SERIES IN OPTICS AND OPTOELECTRONICS

Thin-Film Optical Filters

Fourth Edition

H. Angus Macleod

CRC Press
Taylor & Francis Group
A TAYLOR & FRANCIS BOOK

SERIES IN OPTICS AND OPTOELECTRONICS

Series Editors: **E. Roy Pike**, Kings College, London, UK
Robert G. W. Brown, University of California, Irvine

Recent titles in the series

Optical Tweezers: Methods and Applications
Miles J. Padgett, Justin Molloy, David McGloin (Eds.)

Principles of Nanophotonics
Motoichi Ohtsu, Kiyoshi Kobayashi, Tadashi Kawazoe
Tadashi Yatsui, Makoto Naruse

The Quantum Phase Operator: A Review
Stephen M. Barnett, John A. Vaccaro (Eds.)

An Introduction to Biomedical Optics
R Splinter, B A Hooper

High-Speed Photonic Devices
Nadir Dagli

Lasers in the Preservation of Cultural Heritage: Principles and Applications
C Fotakis, D Anglos, V Zafiropulos, S Georgiou, V Tornari

Modeling Fluctuations in Scattered Waves
E Jakeman, K D Ridley

Fast Light, Slow Light and Left-Handed Light
P W Milonni

Diode Lasers
D Sands

Diffractional Optics of Millimetre Waves
I V Minin, O V Minin

Handbook of Electroluminescent Materials
D R Vij

Handbook of Moire Measurement
C A Walker

Next Generation Photovoltaics
A Martí, A Luque

Stimulated Brillouin Scattering
M J Damzen, V Vlad, A Mocofanescu, V Babin

Laser Induced Damage of Optical Materials
R M Wood

Thin-Film Optical Filters

Fourth Edition

H. Angus Macleod
Thin Film Center Inc.
Tucson, Arizona, USA

CRC Press
Taylor & Francis Group
Boca Raton London New York

CRC Press is an imprint of the
Taylor & Francis Group, an **informa** business
A TAYLOR & FRANCIS BOOK

CRC Press
Taylor & Francis Group
6000 Broken Sound Parkway NW, Suite 300
Boca Raton, FL 33487-2742

© 2010 by Taylor and Francis Group, LLC
CRC Press is an imprint of Taylor & Francis Group, an Informa business

No claim to original U.S. Government works

Printed in the United States of America on acid-free paper
10 9 8 7 6 5 4 3 2 1

International Standard Book Number: 978-1-4200-7302-7 (Hardback)

This book contains information obtained from authentic and highly regarded sources. Reasonable efforts have been made to publish reliable data and information, but the author and publisher cannot assume responsibility for the validity of all materials or the consequences of their use. The authors and publishers have attempted to trace the copyright holders of all material reproduced in this publication and apologize to copyright holders if permission to publish in this form has not been obtained. If any copyright material has not been acknowledged please write and let us know so we may rectify in any future reprint.

Except as permitted under U.S. Copyright Law, no part of this book may be reprinted, reproduced, transmitted, or utilized in any form by any electronic, mechanical, or other means, now known or hereafter invented, including photocopying, microfilming, and recording, or in any information storage or retrieval system, without written permission from the publishers.

For permission to photocopy or use material electronically from this work, please access www.copyright.com (http://www.copyright.com/) or contact the Copyright Clearance Center, Inc. (CCC), 222 Rosewood Drive, Danvers, MA 01923, 978-750-8400. CCC is a not-for-profit organization that provides licenses and registration for a variety of users. For organizations that have been granted a photocopy license by the CCC, a separate system of payment has been arranged.

Trademark Notice: Product or corporate names may be trademarks or registered trademarks, and are used only for identification and explanation without intent to infringe.

Library of Congress Cataloging-in-Publication Data

Macleod, H. A. (Hugh Angus)
Thin-film optical filters / H. Angus Macleod. -- 4th ed.
p. cm. -- (Series in optics and optoelectronics)
Includes bibliographical references and index.
ISBN 978-1-4200-7302-7 (hardcover : alk. paper)
1. Light filters. 2. Thin films--Optical properties. I. Title. II. Series.

QC373.L5.M34 2010
681'.42--dc21 2009052758

Visit the Taylor & Francis Web site at
http://www.taylorandfrancis.com

and the CRC Press Web site at
http://www.crcpress.com

In memory of my Mother and Father

Agnes Donaldson Macleod

John Macleod

Thin-Film Optical Filters

Fourth Edition

Contents

Preface to the Fourth Edition xiii
Symbols and Abbreviations xv

1. Introduction 1
1.1 Early History 1
1.2 Thin-Film Filters 5
References 10

2. Basic Theory 13
2.1 Maxwell's Equations and Plane Electromagnetic Waves 13
2.1.1 The Poynting Vector 18
2.2 The Simple Boundary 21
2.2.1 Normal Incidence 23
2.2.2 Oblique Incidence 27
2.2.2.1 *p*-Polarized Light 28
2.2.2.2 *s*-Polarized Light 30
2.2.3 The Optical Admittance for Oblique Incidence 31
2.2.4 Normal Incidence in Absorbing Media 33
2.2.5 Oblique Incidence in Absorbing Media 38
2.3 The Reflectance of a Thin Film 42
2.4 The Reflectance of an Assembly of Thin Films 45
2.5 Reflectance, Transmittance, and Absorptance 48
2.6 Units 51
2.7 Summary of Important Results 52
2.8 Potential Transmittance 57
2.9 A Theorem on the Transmittance of a Thin-Film Assembly 60
2.10 Coherence 61
2.11 Incoherent Reflection at Two or More Surfaces 66
References 71

3. Theoretical Techniques 73
3.1 Quarter- and Half-Wave Optical Thicknesses 73
3.2 Admittance Loci 74
3.3 Electric Field and Losses in the Admittance Diagram 80
3.4 The Vector Method 87
3.5 The Herpin Index 89
3.6 Alternative Method of Calculation 89
3.7 Smith's Method of Multilayer Design 92
3.8 The Smith Chart 95

3.9 Reflection Circle Diagrams 97
References 103

4. Antireflection Coatings 105
4.1 Antireflection Coatings on High-Index Substrates 106
4.1.1 The Single-Layer Antireflection Coating 106
4.1.2 Double-Layer Antireflection Coatings 112
4.1.3 Multilayer Coatings 121
4.2 Antireflection Coatings on Low-Index Substrates 129
4.2.1 The Single-Layer Antireflection Coating 130
4.2.2 Two-Layer Antireflection Coatings 130
4.2.3 Multilayer Antireflection Coatings 140
4.3 Equivalent Layers 156
4.4 Antireflection Coatings for Two Zeros 168
4.5 Antireflection Coatings for the Visible and the Infrared 172
4.6 Inhomogeneous Layers 179
4.7 Further Information 182
References 183

5. Neutral Mirrors and Beam Splitters 185
5.1 High-Reflectance Mirror Coatings 185
5.1.1 Metallic Layers 185
5.1.2 Protection of Metal Films 187
5.1.3 Overall System Performance, Enhanced Reflectance 193
5.1.4 Reflecting Coatings for the Ultraviolet 196
5.2 Neutral Beam Splitters 198
5.2.1 Beam Splitters Using Metallic Layers 198
5.2.2 Beam Splitters Using Dielectric Layers 201
5.3 Neutral-Density Filters 205
References 207

6. Multilayer High-Reflectance Coatings 209
6.1 The Fabry–Perot Interferometer 209
6.2 Multilayer Dielectric Coatings 215
6.2.1 All-Dielectric Multilayers with Extended High-Reflectance Zones 225
6.2.2 Coating Uniformity Requirements 230
6.3 Losses 234
References 238

7. Edge Filters 241
7.1 Thin-Film Absorption Filters 241
7.2 Interference Edge Filters 242
7.2.1 The Quarter-Wave Stack 243

7.2.2 Symmetrical Multilayers and the Herpin Index 244
7.2.2.1 Application of the Herpin Index to the Quarter-Wave Stack 248
7.2.2.2 Application of the Herpin Index to Multilayers of Other Than Quarter-Waves....... 253
7.2.3 Performance Calculations............ 256
7.2.3.1 Transmission at the Edge of a Stop Band.......... 256
7.2.3.2 Transmission in the Center of a Stop Band 258
7.2.3.3 Transmission in the Pass Band............ 260
7.2.3.4 Reduction of Pass-Band Ripple 262
7.2.3.5 Summary of Design Procedure so Far 265
7.2.3.6 More Advanced Procedures for Eliminating Ripple 266
7.2.3.7 Practical Filters 281
7.2.3.8 Extending the Rejection Zone by Interference Methods............ 283
7.2.3.9 Extending the Transmission Zone............ 287
7.2.3.10 Reducing the Transmission Zone 295
7.2.3.11 Edge Steepness............ 296
References 297

8. Band-Pass Filters............ 299
8.1 Broadband-Pass Filters 299
8.2 Narrowband Filters............ 302
8.2.1 The Metal–Dielectric Single–Cavity Filter 302
8.2.2 The All-Dielectric Single-Cavity Filter 310
8.2.2.1 Case 1: Even Number ($2x$) of Layers 313
8.2.2.2 Case II: Odd Number ($2x + 1$) of Layers 315
8.2.2.3 Phase Shift: Case I............ 316
8.2.2.4 Phase Shift: Case II............ 317
8.2.3 The Solid Etalon Filter............ 325
8.2.4 The Effect of Varying the Angle of Incidence............ 329
8.2.4.1 Simple Tilts in Collimated Light............ 329
8.2.4.2 Case I: High-Index Cavities 332
8.2.4.3 Case II: Low-Index Cavities 333
8.2.4.4 Effect of an Incident Cone of Light............ 335
8.2.5 Sideband Blocking 341
8.3 Multiple Cavity Filters............ 342
8.3.1 Thelen's Method of Analysis............ 349
8.4 Higher Performance in Multiple-Cavity Filters............ 356
8.4.1 Effect of Tilting............ 364
8.4.2 Losses in Multiple Cavity Filters 367
8.4.2.1 Case I: High-Index Cavities 368
8.4.2.2 Case II: Low-Index Cavities 369
8.4.3 Further Information 369

8.5 Phase Dispersion Filter ... 370
8.6 Multiple Cavity Metal–Dielectric Filters ... 377
8.6.1 The Induced-Transmission Filter ... 380
8.6.1.1 Potential Transmittance ... 381
8.6.1.2 Optimum Exit Admittance ... 382
8.6.1.3 Maximum Potential Transmittance ... 384
8.6.1.4 Matching Stack ... 384
8.6.1.5 Front Surface Equivalent Admittance ... 386
8.6.2 Examples of Filter Designs ... 386
8.7 Measured Filter Performance ... 396
References ... 399

9. Tilted Coatings ... 403
9.1 Modified Admittances and the Tilted Admittance Diagram ... 403
9.2 Application of the Admittance Diagram ... 411
9.3 Polarizers ... 425
9.3.1 The Brewster Angle Polarizing Beam Splitter ... 425
9.3.2 Plate Polarizer ... 430
9.3.3 Cube Polarizers ... 431
9.4 Nonpolarizing Coatings ... 431
9.4.1 Edge Filters at Intermediate Angle of Incidence ... 432
9.4.2 Reflecting Coatings at Very High Angles of Incidence ... 437
9.4.3 Edge Filters at Very High Angles of Incidence ... 441
9.5 Antireflection Coatings ... 442
9.5.1 *p*-Polarization Only ... 442
9.5.2 *s*-Polarization Only ... 443
9.5.3 *s*- and *p*-Polarization Together ... 444
9.6 Retarders ... 447
9.6.1 The Ellipsometric Parameters and Relative Retardation ... 447
9.6.2 Series of Coated Surfaces ... 448
9.6.3 Retarders ... 449
9.6.4 Simple Retarders ... 451
9.6.5 Multilayer Retarders at One Wavelength ... 455
9.6.6 Multilayer Retarders for a Range of Wavelengths ... 459
9.7 Optical Tunnel Filters ... 464
References ... 467

10. Color in Optical Coatings ... 471
10.1 Color Definition ... 471
10.2 The 1964 Supplementary Colorimetric Observer ... 478
10.3 Metamerism ... 479
10.4 Other Color Spaces ... 480
10.5 Hue and Chroma ... 481

10.6 Brightness and Optimal Stimuli 482
10.7 Colored Fringes 485
References 487

11. Production Methods and Thin-Film Materials 489
11.1 The Production of Thin Films 490
11.1.1 Thermal Evaporation 491
11.1.2 Energetic Processes 501
11.1.3 Other Processes 513
11.1.4 Baking 517
11.2 Measurement of the Optical Properties 520
11.3 Measurement of the Mechanical Properties 540
11.4 Toxicity 550
11.5 Summary of Some Properties of Common Materials 551
References 561

12. Factors Affecting Layer and Coating Properties 569
12.1 Microstructure and Thin-Film Behavior 569
12.2 Sensitivity to Contamination 584
References 592

13. Layer Uniformity and Thickness Monitoring 595
13.1 Uniformity 595
13.1.1 Flat Plate 597
13.1.2 Spherical Surface 598
13.1.3 Rotating Substrates 598
13.1.4 Use of Masks 603
13.2 Substrate Preparation 604
13.3 Thickness Monitoring and Control 607
13.3.1 Optical Monitoring Techniques 608
13.3.2 The Quartz-Crystal Monitor 618
13.3.3 Monitoring by Deposition Time 620
13.4 Tolerances 621
References 636

14. Specification of Filters and Environmental Effects 641
14.1 Optical Properties 641
14.1.1 Performance Specification 641
14.1.2 Manufacturing Specification 644
14.1.3 Test Specification 644
14.2 Physical Properties 648
14.2.1 Abrasion Resistance 648
14.2.2 Adhesion 651
14.2.3 Environmental Resistance 652
References 653

15. System Considerations: Applications of Filters and Coatings 655
15.1 Potential Energy Grasp of Interference Filters 659
15.2 Narrowband Filters in Astronomy 665
15.3 Atmospheric Temperature Sounding 670
15.4 Order Sorting Filters for Grating Spectrometers 679
15.5 Glare Suppression Filters and Coatings 691
15.6 Some Coatings Involving Metal Layers 695
15.6.1 Electrode Films for Schottky-Barrier Photodiodes 695
15.6.2 Spectrally Selective Coatings for Photothermal Solar Energy Conversion 698
15.6.3 Heat Reflecting Metal–Dielectric Coatings 703
References 705

16. Other Topics 707
16.1 Rugate Filters 707
16.2 Ultrafast Coatings 718
16.3 Automatic Methods 729
16.4 Gain in Optical Coatings 740
16.4.1 Oblique Incidence 744
16.5 Photonic Crystals 748
16.5.1 What Is a Photonic Crystal? 750
16.5.2 Two-Dimensional Photonic Crystals 750
16.5.3 One-Dimensional Photonic Crystals 751
References 756

17. Characteristics of Thin-Film Dielectric Materials 759
References 766

Bibliography 771
Index 773

Preface to the Fourth Edition

In some ways first editions are easier, or perhaps I should say, less difficult, to prepare than subsequent editions. By the time a fourth edition is required, there is a strong expectation among readers of the character and content of the book. Thus, the author must somehow try to maintain the style at the same time as bringing the book up to date. What to omit and what to include are very difficult questions. Modern optical coating design is virtually entirely performed by computer, frequently using automatic techniques. However, computers do not remove the need for understanding, and I think it is understanding that readers look for in the book. Also, I am conscious that a reader, having perhaps rejected an earlier edition in favor of a later and remembering something important in the earlier, might well expect to find it in the later. I made the decision, therefore, to retain most of the descriptions of the earlier design techniques because of their importance in understanding how designs work. Then, although some of the applications that I describe are rather old, nevertheless they do illustrate how optical coatings are incorporated into a system, and so I retained them. I have tried to incorporate a reasonable amount of new material throughout the book. I added a chapter on color because it is increasing in importance in optical coatings, and, although it is of largely academic interest, I could not resist a section on the effects of gain in optical coatings, because I find it a fascinating topic. Then I struggled with coatings for the soft x-ray region and, with some regret, decided not to include them at this time. It is the old design synthesis problem: one has to stop somewhere.

I am fortunate in my friends and colleagues who have helped me immeasurably with suggestions, advice, and, I have to admit it, corrections. The field of optical thin films has been very good to me. I cannot imagine a more friendly, supportive, and open group of people than the international optical thin-film community. It sets an example the rest of the world would do well to follow.

Thank you, all of you, my readers, publishers, friends, colleagues, family, and especially my wife, Ann.

H. Angus Macleod

Symbols and Abbreviations

The following list gives those more important symbols that have been used in at least several places in the text. We have tried as far as possible to create a consistent set of symbols, but there are several well-known and accepted symbols that are universally used in the field for certain quantities and changing them would probably lead to even greater confusion than would retaining them. This has meant that in some cases the same symbol is used in different places for different quantities. We hope the list will make it clear. Less important symbols, defined and used only in very short sections, have been omitted.

A Absorptance; ratio of the power absorbed in the structure to the power incident on it.

$\mathcal{A}$ Potential absorptance; quantity used in the calculation of the absorptance of coatings. It is equivalent to $(1 - \psi)$ where ψ is the potential transmittance.

B Normalized total tangential electric field at an interface, usually the front interface of an assembly of layers. It is also used very briefly at the beginning of Chapter 2 as the magnetic induction.

C Normalized total tangential magnetic field at an interface, usually the front interface of an assembly of layers.

d_q Physical thickness of the qth layer in a thin film coating.

$\boldsymbol{E}$ Electric vector in the electromagnetic field.

$\mathfrak{E}$ Total tangential electric field amplitude, that is, the field parallel to the thin film boundaries.

$\mathcal{E}$ Electric field amplitude.

E Equivalent admittance of a symmetrical arrangement of layers.

F Function used in the theory of the Fabry–Perot interferometer.

$\mathcal{F}$ Finesse. The ratio of the separation of adjacent fringes to the half-width of the fringe in the Fabry–Perot interferometer.

g $g = \lambda_0/\lambda = \nu/\nu_0$ sometimes called the relative wavelength, or the relative wave number, or the wavelength ratio. λ_0 and ν_0 are the reference wavelength and reference wave number, respectively. The optical thicknesses of the layers in a coating are defined with respect to these quantities that are usually chosen to make the more important layers in the coating as close to quarter-waves as possible.

$\boldsymbol{H}$ Magnetic vector in the electromagnetic field.

$\mathcal{H}$ Total tangential magnetic field amplitude, that is, the field parallel to the thin-film boundaries.

$\mathscr{H}$ Magnetic field amplitude.

H Represents a quarter-wave of high index in shorthand notation.

I Irradiance of the wave, that is power per unit area. Unfortunately, the standard SI symbol for irradiance is E but to use E would cause great confusion between irradiance and electric field. It is even more unfortunate that I is the SI symbol for intensity that is the power per unit solid angle from a point source. Doubly unfortunate is that the older definition of intensity is identical to the current definition of irradiance.

k Extinction coefficient. The extinction coefficient denotes the presence of absorption. The complex refractive index, N, is given by $N = n - ik$.

L Represents a quarter-wave of low index in shorthand notation.

M Represents a quarter-wave of intermediate index in shorthand notation. Also used for a matrix element, or to indicate an array of matrix elements.

N Denotes the complex refractive index, $n - ik$.

n Refractive index or, sometimes, the real part of refractive index.

n^* Effective index of a narrowband filter, that is, the index of an equivalent layer that yields a shift of its fringes in wavelength, by the same amount as the peak of the narrowband filter, when tilted with respect to the direction of incidence.

p Packing density, that is the ratio of the solid volume of a film to its total volume.

p p-Polarization, that is the polarization where the electric field direction is in the plane of incidence. It is sometimes known as TM for transverse magnetic.

R Reflectance. The ratio at a boundary of the normal components of reflected and incident irradiance or, alternatively, the ratio of the total reflected beam power to the total incident beam power.

s s-Polarization, that is the polarization where the electric field direction is normal to the plane of incidence. It is sometimes known as TE for transverse electric.

T Transmittance. The ratio of the normal components of transmitted and incident irradiance or, alternatively, the ratio of the total transmitted beam power to the total incident beam power.

TE See s for s-polarization.

TM See p for p-polarization.

x, y, z — Coordinate axes. In the case of a thin film or surface the z-axis is usually taken positive into the surface in the direction of incidence. The x-axis is usually arranged in the plane of incidence and the x-, y-, and z-axes, in that order, make a right-handed set.

$\bar{x}, \bar{y}, \bar{z}$ — Three color-matching functions that define the CIE 1931 Standard Colorimetric Observer.

X, Y, Z — Tristimulus values. They are the three basic responses defining a color.

x, y, z — Chromaticity coordinates, $X/(X + Y + Z)$, $Y/(X + Y + Z)$, $Z/(X + Y + Z)$. Usually z is omitted because they are normalized to add to unity.

$X + iZ$ — Complex surface admittance.

y — Characteristic admittance of a material given in SI units (siemens) by $N\mathcal{Y}$, that is $(n - ik)\mathcal{Y}$ and in units of the admittance of free space, $\mathcal{Y}$, by N or $n - ik$.

Y — Surface admittance, that is the ratio of the total tangential components of magnetic and electric field at any surface parallel to the film boundaries. $Y = C/B$.

$\mathcal{Y}$ — Admittance of free space (2.6544×10^{-3} S).

y_0 — Characteristic admittance of the incident medium.

y_m or y_{sub} — Characteristic admittance of the emergent medium, or substrate.

α — Absorption coefficient, given by $4\pi k/\lambda$ usually in units of cm^{-1}.

α, β, γ — Three direction cosines, that is, the cosines of the angle the direction makes with the three coordinate axes.

β — Symbol for $2\pi kd/\lambda$ usually with reference to a metal.

γ — Equivalent phase thickness of a symmetrical arrangement of layers.

Δ — Relative retardation. It is given by $\varphi_p - \varphi_s \pm 180°$ in reflection and $\varphi_p - \varphi_s$ in transmission, where the normal thin-film sign convention for φ_p is used.

Δ — η_p/η_s where η is the modified tilted admittance. The quantity is used in the design of polarization-free coatings.

δ — Phase thickness of a coating, given by $2\pi(n - ik)d/\lambda$.

ε — Indicates a small error in the discussion of tolerances, etc.

ε — Permittivity of a medium.

η — Tilted optical admittance.

ϑ — Angle of incidence.

κ	Sometimes called the wave number, κ is given by $2\pi(n - ik)/\lambda$ where λ is the free space wavelength. Note the confusing use of the term wave number. It is also applied to ν.
λ	Wavelength of light. In the book, except at the very beginning of Chapter 2, it always indicates the wavelength in free space.
λ_0	Reference wavelength. The optical thicknesses of the layers in a coating are defined with respect to the reference wavelength that is usually chosen to make the more important layers in the coating as close to quarter-waves as possible.
ν	Wave number. $\nu = 1/\lambda$ and is frequently expressed in units of cm^{-1} (also sometimes known as kayser. The SI unit is, strictly, inverse meters or m^{-1}).
ν_0	Reference wave number, $1/\lambda_0$.
μ	Permeability. Used in early part of Chapter 2.
ρ	Amplitude reflection coefficient. Used also as electric charge density in early Chapter 2.
τ	Amplitude transmission coefficient.
φ	Phase difference, often in reflection or transmission.
ψ	Potential transmittance, $T/(1 - R)$ or the ratio of the quantities $\mathrm{Re}(BC^*)$ evaluated at two different interfaces. It represents the power emerging from a system divided by the power entering and is unity if there is no loss.

1

Introduction

This book is intended to form an introduction to thin-film optical filters for both the manufacturer and the user. It does not pretend to present a detailed account of the entire field of thin-film optics, but it is hoped that it will form a supplement to those works already available in the field that only briefly touch on the principles of filters. For the sake of a degree of completeness, it has been thought desirable to repeat some of the information that is found elsewhere in textbooks, referring the reader to more complete sources for greater detail. The topics covered are a mixture of design, manufacture, performance, and application, including enough of the basic mathematics of optical thin films to enable the reader to carry out thin-film calculations. The aim has been to present, as far as possible, a unified treatment, and there are some alternative methods of analysis that are not discussed.

When the book was first written in 1968 to 1969, there were just a few books that covered aspects of the field. Now the situation has changed somewhat and there is an array of relevant books; some are listed in this chapter's reference list. However, the half-life of a work these days is so short that knowledge can actually disappear. It is worthwhile to go back to some of the earlier books. Heavens [1], Holland [2], Anders [3], and Knittl [4] provide some of the texts that will repay study, as well as more recent volumes.

In a work of this size, it is not possible to cover the entire field of thin-film optical devices in the detail that some of them may deserve. The selection of topics is due, at least in part, to the author's preferences and knowledge. Optical filters have been interpreted fairly broadly to include such items as antireflection and high-reflectance coatings.

1.1 Early History

History in general is impossibly complicated, and we can have only an imperfect view of it, told generally through the medium of an historian who will, because culture changes, attempt to interpret it in a way the intended audience can understand. The history of technology is no exception. To simplify the telling, we will usually pick certain events and individuals and connect them as a kind of series, one depending on the other. Technology, however, develops over a very broad front, rather like the advance of the tide. It depends on a network of effort. If one individual does not make a

required advance, another certainly will. Technology adopts the advances it needs at the time and ignores those it does not. Over and over again, we find that discoveries credited to a particular individual were actually anticipated by others but the time was not right so little or no notice was taken of them, and this is true of the abbreviated account of the history of the subject that follows. A true account is beyond us, so we pick a few events and a few individuals and connect them, but there are many other routes through history. This one is based on the preferences and limited knowledge of the author.

Thin metal layers were known from very early times, but if we consider interference as the hallmark of modern thin-film optics then the earliest of what might be called modern thin-film optics was the work of Robert Boyle and Robert Hooke on colors exhibited by materials in thin film form. Sir Isaac Newton [5] related the colors to exact measurements of film thickness and placed the subject on a firm quantitative base with his brilliant technique now known as "Newton's rings." The explanation of colors is now thought to be a very simple matter, being due to interference in a single thin film of varying thickness. However, at that time, the theory of the nature of light was not far advanced. Newton struggled with his concept of the interval of fits that we now understand is a half wavelength, but it was an additional 100 years before the idea of light as a wave would be accepted. On November 12, 1801, in a Bakerian Lecture to the Royal Society, Thomas Young [6] enunciated the principle of the interference of light and produced a satisfactory explanation of the effect. As Henry Crew [7, pg. 7] put it, "This simple but tremendously important fact that two rays of light incident upon a single point can be added together to produce darkness at that point is, as I see it, the one outstanding discovery which the world owes to Thomas Young."

Young's theory was far from achieving universal acceptance. Indeed Young became the victim of a bitter personal attack, against which he had the greatest difficulty defending himself. Recognition came slowly and depended much on the work of Augustin Jean Fresnel and colleagues [8], who, quite independently, also arrived at a wave theory of light. Fresnel's discovery, in 1816, that two beams of light that are polarized at right angles could never interfere established the transverse nature of light waves. Then Fresnel combined Young's interference principle and Huygens's ideas of light propagation into an elegant theory of diffraction. It was Fresnel who put the wave theory of light on such a firm foundation that it has never been shaken. For the thin-film worker, Fresnel's laws, governing the amplitude and phase of light reflected and transmitted at a single boundary, are of major importance. Knittl [9] reminded us that it was Fresnel who first summed an infinite series of rays to determine the transmittance of a thick sheet of glass and that it was Simeon Denis Poisson, in correspondence with Fresnel, who included interference effects in the summation to arrive at the important results that a half-wave–thick film does not change the reflectance of a surface and that a quarter-wave–thick film of index $(n_0n_1)^{½}$ will reduce to zero the reflectance

of a surface between two media of indices n_1 and n_0. Fresnel died in 1827, at the early age of 39.

In 1873, the great work of James Clerk Maxwell, *A Treatise on Electricity and Magnetism* [10], was published, and, in his system of equations, we have the basic theory for the analysis of thin-film optical problems.

Meanwhile, in 1817, Joseph von Fraunhofer had made what are probably the first ever antireflection coatings. It is worth quoting his observations at some length because they show the considerable insight that he had, even at that early date, into the physical causes of the effects that were produced. The following is a translation of part of the paper as it appears in the collected works [11].

> Before I quote the experiments which I have made on this I will give the method which I have made use of to tell in a short time whether the glass will withstand the influence of the atmosphere. If one grinds and then polishes, as finely as possible, one surface of glass which has become etched through long exposure to the atmosphere, then wets one part of the surface, for example half, with concentrated sulfuric or nitric acid and lets it work on the surface for twenty-four hours, one finds after cleaning away the acid that that part of the surface on which the acid was, reflects much less light than the other half, that is it shines less although it is not in the least etched and still transmits as much light as the other half, so that one can detect no difference on looking through. The difference in the amount of reflected light will be most easily detected if one lets the light strike approximately vertically. It is the greater the more the glass is liable to tarnish and become etched. If the polish on the glass is not very good, this difference will be less noticeable. On glass which is not liable to tarnish, the sulfuric and nitric acid does not work.... Through this treatment with sulfuric or nitric acid some types of glasses get on their surfaces beautiful vivid colors which alter like soap bubbles if one lets the light strike at different angles.

Then, in an appendix to the paper added in 1819:

> Colors on reflection always occur with all transparent media if they are very thin. If for example, one spreads polished glass thinly with alcohol and lets it gradually evaporate, towards the end of the evaporation, colors appear as with tarnished glass. If one spreads a solution of gum-lac in a comparatively large quantity of alcohol very thinly over polished warmed metal the alcohol will very quickly evaporate, and the gum-lac remains behind as a transparent hard varnish which shows colors if it is thinly enough laid on. Since the colors, in glasses which have been colored through tarnishing, alter themselves if the inclination of the incident light becomes greater or smaller, there is no doubt that these colors are quite of the same nature as those of soap bubbles, and those which occur through the contact of two polished flat glass surfaces, or generally as thin transparent films of material. Thus, there must be on the

> surface of tarnished glass that shows colors, a thin layer of glass that is different in refractive power from the underlying. Such a situation must occur if a component is partly removed from the surface of the glass or if a component of the glass combines at the surface with a related material into a new transparent product.

It seems that Fraunhofer did not follow this particular line into the development of an antireflection coating for glass, perhaps because optical components were not, at that time, sufficiently complicated for the need for antireflection coatings to be obvious. Possibly the important point that not only was the reflectance less but also the transmittance was greater had escaped him.

In 1886, Lord Rayleigh reported to the Royal Society an experimental verification of Fresnel's reflection law at near-normal incidence [12]. To attain a sufficiently satisfactory agreement between measurement and prediction, he had found it necessary to use freshly polished glass, because the reflectance of older material, even without any visible signs of tarnish, was too low. One possible explanation, which he suggested, was the formation, on the surface, of a thin layer of different refractive index from the underlying material. He was apparently unaware of the earlier work of Fraunhofer.

Then, in 1891, Dennis Taylor published the first edition of his famous book *On the Adjustment and Testing of Telescopic Objectives* and mentioned, "As regards the tarnish which we have above alluded to as being noticeable upon the flint lens of an ordinary objective after a few years of use, we are very glad to be able to reassure the owner of such a flint that this film of tarnish, generally looked upon with suspicion, is really a very good friend to the observer, inasmuch as it increases the transparency of his objective" [13,14, pg. 59].

In fact, Taylor went on to develop a method of artificially producing the tarnish by chemical etching [15]. This work was followed up by Kollmorgen, who developed the chemical process still further for different types of glasses [16].

At the same time, in the nineteenth century, a great deal of progress was being made in the field of interferometry. The most significant development, from the thin-film point of view, was the Fabry-Perot interferometer [17] described in 1899, which has become one of the basic structures for thin-film filters.

Developments became much more rapid in the 1930s, and indeed, it is in this period that we can recognize the beginnings of modern thin-film optical coating. In 1932, Rouard [18] observed that a very thin metallic film reduced the internal reflectance of a glass plate, although the external reflectance was increased. In 1934, Bauer [19], in the course of fundamental investigations of the optical properties of halides, produced reflection-reducing coatings, and Pfund [20] evaporated zinc sulfide layers to make low-loss beam splitters for Michelson interferometers, noting, incidentally, that titanium dioxide could be a better material. In 1936, Strong [21] produced antireflection

coatings through the evaporation of fluorite to give inhomogeneous films, which reduced the reflectance of glass to visible light by as much as 89%, a most impressive figure. Then, in 1939, Geffcken [22] constructed the first thin-film metal-dielectric interference filters. A fascinating account of Geffcken's work is given by Thelen [23], who describes Geffcken's search for improved antireflection coatings and his creation of the famous quarter–half-quarter design.

Several factors were probably responsible for this sudden expansion of the field. Optical systems, particularly photographic objectives, were becoming more complex, bringing a need for antireflection coatings. Telescopes and binoculars, especially for military applications, were also much improved by antireflection coatings. Then the manufacturing process was also becoming more reliable. Although sputtering was discovered about the middle of the nineteenth century, and vacuum evaporation around the beginning of the twentieth century, they had not yet been adopted as useful manufacturing processes. One difficulty was the lack of really suitable pumps, and it was not until the early 1930s that the work of C. R. Burch on diffusion pump oils introduced the oil diffusion pump. This helped enormously, although, particularly in Germany, mercury diffusion pumps were still used very effectively for some time. World War II saw a great expansion in the production of antireflection coatings. This certainly accelerated developments, but the expansion would have taken place without the war, because optics had now reached the stage where coatings were necessary. Since then, tremendous strides have been made. Modern optics without coating is unthinkable. It is almost impossible to imagine an optical instrument that would not rely on optical coatings to ensure its performance. Filters with more than 100 layers are not uncommon, and uses have been found for them in almost every branch of science and technology.

1.2 Thin-Film Filters

First, we assume for the purposes of this section that the materials in thin-film form are free from absorption or other loss. Then, to understand in a qualitative way the performance of thin-film optical devices, it is necessary to accept several simple statements. The first is that the amplitude reflectance of light at any boundary between two media is given by $(1 - \rho)/(1 + \rho)$, where ρ is the ratio of the optical admittances at the boundary, which, in the optical region, is also the ratio of the refractive indices. The reflectance (the ratio of irradiances) is the square of this quantity. The second is that there is a phase shift of 180° when the reflectance takes place in a medium of lower refractive index than the adjoining medium and of zero if the medium has a higher index than the one adjoining it. The third statement is that if light

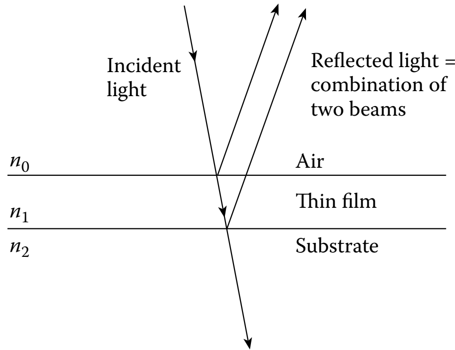

FIGURE 1.1
A single thin film.

is split into two components by reflection at the top and bottom surfaces of a thin film, then the beams will recombine in such a way that the resultant amplitude will be the difference of the amplitudes of the two components if the relative phase shift is 180° or the sum of the amplitudes if the relative phase shift is either zero or a multiple of 360°. In the former case, we say that the beams interfere destructively, and in the latter case, constructively. Other cases where the phase shift is different will be intermediate between these two possibilities.

The antireflection coating depends for its operation on the more or less complete cancellation of the light reflected at the upper and lower of the two surfaces of the thin film (Figure 1.1). Let the index of the substrate be n_{sub}, that of the film be n_1, and that of the incident medium, which will in almost all cases be air, be n_0. For complete cancellation of the two beams of light, the amplitudes of the light reflected at the upper and lower boundaries of the film should be equal, which implies that the ratios of the refractive indices at each boundary should be equal [i.e., $n_0/n_1 = n_1/n_{sub}$, or $n_1 = (n_0 n_{sub})^{1/2}$]. This shows that the index of the thin film should be intermediate between the indices of air, which may be taken as unity, and of the substrate, which may be taken as at least 1.52. At both the upper and lower boundaries of the antireflection film, the reflection takes place in a medium of lower refractive index than the adjoining medium. Thus, to ensure that the relative phase shift is 180° so that the beams cancel, the optical thickness of the film should be made one-quarter wavelength.

A simple antireflection coating should, therefore, consist of a single film of refractive index equal to the square root of that of the substrate and of optical thickness of one quarter of a wavelength. As will be explained in the chapter on antireflection coatings, there are other, improved coatings covering wider wavelength ranges involving greater numbers of layers.

Another basic type of thin-film structure is a stack of alternate high- and low-index films, all one-quarter–wavelength thick (Figure 1.2). Light reflected within the high-index layers will not sustain any phase shift on

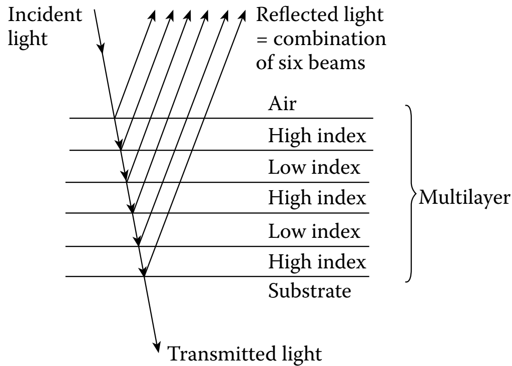

FIGURE 1.2
A multilayer consisting of alternate high and low index quarterwaves.

reflection, while that reflected within the low-index layers will sustain a change of 180°. It is fairly easy to see that the various components of the incident light produced by reflection at successive boundaries throughout the assembly will reappear at the front surface all in phase so that they will recombine constructively. This implies that the effective reflectance of the assembly can be made very high indeed, as high as may be desired, merely by increasing the number of layers. This is the basic form of the high-reflectance coating. When such a coating is constructed, it is found that the reflectance remains high over only a limited range of wavelengths, depending on the ratio of high and low refractive indices. Outside this zone, the reflectance changes abruptly to a low value. Because of this behavior, the *quarter-wave stack,* as it is called, is used as a basic building block for many types of thin-film filters. It can be used as a longwave-pass filter, a shortwave-pass filter, a bandstop filter, a straightforward high-reflectance coating (e.g., in laser mirrors), and a reflector in a thin-film Fabry-Perot interferometer (Figure 1.3), which is another basic filter type described in some detail in Chapters 5 and 7. Here, it is sufficient to say that it consists of a spacer or cavity layer that is usually half a wavelength thick, bounded by two high-reflectance coatings. Multiple-beam interference in the spacer or cavity layer causes the transmission of the filter to be extremely high over a narrow band of wavelengths around that for which the spacer is a multiple of one-half–wavelength thick. It is possible, as with lumped electric circuits, to couple two or more Fabry-Perot filters in series to give a more rectangular shape to the pass band.

Our assumption of vanishingly small absorption and other losses so that the films are completely transparent is true in the great majority of cases. Because no energy is lost, the filter characteristic in reflection is the complement of that in transmission. This fact is used in the construction of such devices as dichroic beam splitters for color separation in, for example, color projection engines.

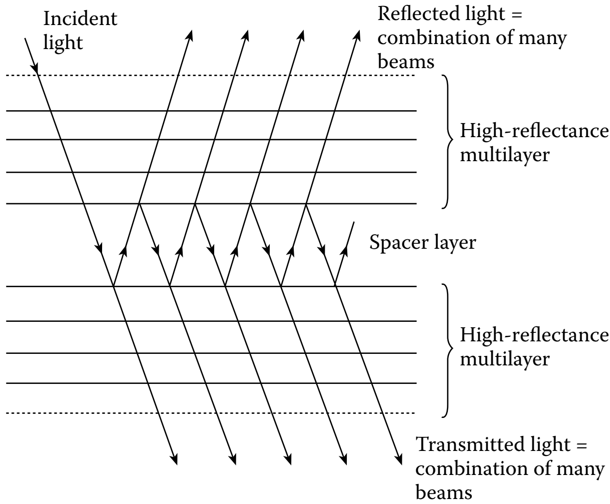

FIGURE 1.3
A Fabry-Perot filter showing multiple reflections in the spacer or cavity layer.

This brief description has neglected the effect of multiple reflections in most of the layers and, for an accurate evaluation of the performance of a filter, these extra reflections must be taken into account. This involves extremely complex calculations, and an alternative, and more effective, approach has been found in the development of entirely new forms of solution of Maxwell's equations in stratified media. This is, in fact, the principal method used in Chapter 2, where basic theory is considered. The solution appears as a very elegant product of 2 × 2 matrices, each matrix representing a single film. Unfortunately, despite the apparent simplicity of the matrices, calculation by hand of the properties of a given multilayer, particularly if there are absorbing layers present and a wide spectral region is involved, is an extremely tedious and time-consuming task. The preferred method of calculation is to use a computer. This makes calculation so rapid and straightforward that it makes little sense to use anything else. Even pocket calculators, especially the programmable kind, can be used to great effect. However, despite the enormous power of the modern computer, it is still true that skill and experience play a major part in successful coating design. The computer brings little in the way of understanding, and understanding is the emphasis in the bulk of this book. There are many techniques that date back to times when computers were expensive, cumbersome, and scarce and alternatives, usually approximate, were required. These would not be used for calculation today, but they bring an insight that straightforward calculation cannot deliver, even if it is very fast. Thus, we include many such techniques and it is convenient to introduce them often in a historical context. The matrix method itself brings many advantages. For example, it has made possible the development of exceedingly powerful design techniques based on the

algebraic manipulation of the matrices; these are also included. Graphical techniques are of considerable usefulness in visualization of the properties of coatings. There are many such techniques, but in this book, we pay particular attention to one such method known as the *admittance diagram.* The author has found this method to be of considerable assistance over the years. It is an accurate technique in the sense that it contains no approximations other than those involved perhaps in sketching it, but it is used normally as an aid to understanding rather than as a calculation tool.

In the design of a thin-film multilayer, we are required to find an arrangement of layers to give a performance specified in advance, and this is much more difficult than straightforward calculation of the properties of a given multilayer. There is no precise analytical solution to the general problem. The normal method of design is to arrive at a possible structure for a filter, using techniques to be described that consist of a mixture of analysis, experience, and the use of well-known building blocks. The evaluation is then completed by calculating the performance on a computer. Depending on the results of the computations, adjustments to the proposed design may be made and then recomputed, until a satisfactory solution is found. This adjustment process can itself be undertaken with a computer and is often known by the term *refinement.* A related term is *synthesis,* which implies an element of construction as well as adjustment. The ultimate in synthesis is the complete construction of a design with no starting information beyond the performance specification, but it is normal to provide some starting information, such as materials to be used and, possibly, the total thickness of coating or a very rough starting design.

The successful application of refinement techniques depends largely on a starting solution that has a performance close to that required. Under these conditions, it has been made to work exceedingly well. The operation of a refinement process involves the adjustment of the parameters of the system to minimize a merit coefficient (in some, less common versions, a measure of merit may be maximized) representing the gap between the performance achieved by the design at any stage and the desired performance. The main difference between the various techniques is in the details of the rules used in adjusting the design. A major problem is the enormous number of parameters that can potentially be involved. Refinement is usually kept within bounds by limiting the search to small changes in an almost acceptable starting design. In synthesis with no starting design, the possibilities are virtually infinite, and so the rules governing the search procedure have to be very carefully organized. The most effective techniques incorporate two elements—an effective refinement technique that operates until it reaches a limit and a procedure for complicating the design that is then applied. These two elements alternate as the design is gradually constructed. Automatic design synthesis is undoubtedly increasing in importance in step with developments in computers, but it is still true that, in the hands of a skilled practitioner, the achievements of both refinement and synthesis are much more impressive than when no skill

is involved. It is still true that someone who knows well what he or she is doing will succeed much better than someone who does not. This branch of the subject is much more a matter of computing techniques than fundamental to the understanding of thin-film filters, and so it is largely outside the scope of this book. The text by Liddell [24] and the more recent text by Furman and Tikhonravov [25] give good accounts of various methods. The real limitation to what is, at the present time, possible in optical thin-film filters and coatings is the capability of the manufacturing process to produce layers of precisely the correct optical constants and thickness, rather than any deficiency in design techniques.

The common techniques for the construction of thin-film optical coatings can be classified as *physical vapor deposition,* or vacuum processes where a solid film condenses from the vapor phase. The most straightforward method, which is also the traditional method, is known as *thermal evaporation,* and this is still much used. Because of defects of solidity possessed by thermally evaporated films, there has been, in recent years, a shift, now accelerating, toward what are described as the *energetic processes*. Here, mechanical momentum is transferred to the growing film, either by deliberate bombardment or by an increase in the momentum of the arriving film material, and this added momentum drives the outermost material deeper into the film, increasing its solidity. These processes are described briefly in the later chapters of the book, but much more information will be found in the books listed in the following reference list.

References

1. Heavens O S 1955 *Optical Properties of Thin Solid Films* (London: Butterworths Scientific Publications)
2. Holland L 1956 *Vacuum Deposition of Thin Films* (London: Chapman and Hall)
3. Anders H 1965 *Dünne Schichten für die Optik* (English translation: *Thin films in optics, Focal Press, 1967*) (Stuttgart: Wissenschaftliche Verlagsgesellschaft mbH)
4. Knittl Z 1976 *Optics of Thin Films* (London: John Wiley and Sons)
5. Newton S I 1704 *Opticks or a Treatise of the Reflections, Refractions, Inflections and Colours of Light* (London: The Royal Society)
6. Young T 1802 On the theory of light and colours (The 1801 Bakerian Lecture) *Philosophical Transactions of the Royal Society of London* **92** 12–48
7. Crew H 1930 Thomas Young's place in the history of the wave theory of light *Journal of the Optical Society of America* **20** 3–10
8. de Senarmont H, Verdet E, and Fresnel L eds 1866–1870 *Oeuvres Completes d'Augustin Fresnel* (Paris: Imprimerie Impériale)
9. Knittl Z 1978 Fresnel historique et actuel *Optica Acta* **25** 167–173
10. Maxwell J C 1873 *A Treatise on Electricity and Magnetism* (Oxford: Clarendon Press)

11. von Fraunhofer J 1888 *Versuche über die Ursachen des Anlaufens und Mattwerdens des Glases und die Mittel, denselben zuvorzukommen,* in *Joseph von Fraunhofer's Gesammelte Schriften* (München: Verlag der Koniglich Bayerischen Akademie der Wissenschaften)
12. Rayleigh L 1886 On the intensity of light reflected from certain surfaces at nearly perpendicular incidence *Proceedings of the Royal Society of London* **41** 275–294
13. Taylor H D 1891 *On the adjustment and testing of Telescopic Objectives* (York/London: T Cooke & Sons)
14. Taylor H D 1983 *The Adjustment and Testing of Telescopic Objectives* ed 5 (Bristol: Adam Hilger)
15. Taylor H D 1904 *Lenses* United Kingdom Patent 29561
16 F Kollmorgen 1916 Light transmission through telescopes. *Transactions of the American Illumination Engineering Society* **11** 220–228
17. Fabry C and Perot A 1899 Theory et applications d'une nouvelle méthode de spectroscopie interférentielle *Annales des Chimie et des Physique, Paris, 7th Series* **16** 115–144
18. Rouard P 1932 Sur le pouvoir réflecteur des métaux en lames très minces *Contes Rendus de l'Academie de Science* **195** 869–872
19. Bauer G 1934 Absolutwerte der optischen Absorptionskonstanten von Alkalihalogenidkristallen im Gebiet ihrer ultravioletten Eigenfrequenzen *Annalen der Physik Lpz 5th Series* **19** 434–464
20. Pfund A H 1934 Highly reflecting films of zinc sulphide *Journal of the Optical Society of America* **24** 99–102
21. Strong J 1936 On a method of decreasing the reflection from non-metallic substances *Journal of the Optical Society of America* **26** 73–74
22. Geffcken W 1939 *Interferenzlichtfilter* Germany Patent 716153
23. Thelen A 1997 *The pioneering contributions of W Geffcken*, in *Thin Films on Glass* Bach H and Krause D Editors (Berlin/Heidelberg: Springer-Verlag) 227–239
24. Liddell H M 1981 *Computer-aided techniques for the design of multilayer filters* (Bristol: Adam Hilger)
25. Furman S A and Tikhonravov A V 1992 *Basics of Optics of Multilayer Systems* (Gif-sur-Yvette: Editions Frontières)

2

Basic Theory

The next part of the book is a long and rather tedious account of some basic theory that is necessary to make calculations of the properties of multilayer thin-film coatings. It is perhaps worth reading just once, or when some deeper insight into thin-film calculations is required. To make it easier for those who have read it to find the basic results or for those who do not wish to read it at all, to proceed with the remainder of the book, the principal results are summarized, beginning on page 52.

2.1 Maxwell's Equations and Plane Electromagnetic Waves

For those readers who are still with us, we begin our attack on thin-film problems by solving Maxwell's equations together with the appropriate material equations. In isotropic media, these are:

$$\mathrm{curl}\boldsymbol{H} = \nabla \times \boldsymbol{H} = \boldsymbol{j} + \partial \boldsymbol{D}/\partial t \tag{2.1}$$

$$\mathrm{curl}\boldsymbol{E} = \nabla \times \boldsymbol{E} = -\partial \boldsymbol{B}/\partial t \tag{2.2}$$

$$\mathrm{div}\boldsymbol{D} = \nabla \bullet \boldsymbol{D} = \rho \tag{2.3}$$

$$\mathrm{div}\boldsymbol{B} = \nabla \bullet \boldsymbol{B} = 0 \tag{2.4}$$

$$\boldsymbol{j} = \sigma \boldsymbol{E} \tag{2.5}$$

$$\boldsymbol{D} = \varepsilon \boldsymbol{E} \tag{2.6}$$

$$\boldsymbol{B} = \mu \boldsymbol{H} \tag{2.7}$$

where the symbols in bold are vector quantities. In anisotropic media, Equations 2.1 through 2.7 become much more complicated with σ, ε, and μ being tensor rather than scalar quantities. Anisotropic media are covered by Yeh [1] and Hodgkinson and Wu [2].

The International System of Units (SI) is used as extensively as possible throughout this book. Table 2.1 shows the definitions of the quantities in the equations together with the appropriate SI units.

TABLE 2.1

SI Units and Symbols

Symbol	Physical Quantity	SI Unit	Symbol for SI Unit
E	Electric field strength	Volt per meter	Vm^{-1}
D	Electric displacement	Coulomb per square meter	Cm^{-2}
H	Magnetic field strength	Ampere per meter	Am^{-1}
j	Electric current density	Ampere per square meter	Am^{-2}
B	Magnetic flux density or magnetic induction	Tesla	T
ρ	Electric charge density	Coulomb per cubic meter	Cm^{-3}
σ	Electric conductivity	Siemens per meter	Sm^{-1}
μ	Permeability	Henry per meter	Hm^{-1}
ε	Permittivity	Farad per meter	Fm^{-1}

To the equations, we can add

$$\varepsilon = \varepsilon_r \varepsilon_0 \tag{2.8}$$

$$\mu = \mu_r \mu_0 \tag{2.9}$$

$$\varepsilon_0 = 1/(\mu_0 c^2) \tag{2.10}$$

where ε_0 and μ_0 are the permittivity and permeability of free space, respectively; ε_r and μ_r are the relative permittivity and permeability, respectively; and c is a constant that can be identified as the velocity of light in free space. ε_0, μ_0, and c are important constants, the values of which are given in Table 2.2.

In the normal way, the parameters in Equations 2.8 through 2.10 do not depend on either $\boldsymbol{E}$ or $\boldsymbol{H}$ and so the phenomena are linear.

The following analysis is brief and incomplete. For a full, rigorous treatment of the electromagnetic field equations, the reader is referred to Born and Wolf [3].

First we assume an absence of space charge so that ρ is zero. This implies

$$div\boldsymbol{D} = \varepsilon(\nabla \bullet \boldsymbol{E}) = 0 \tag{2.11}$$

and solving for $\boldsymbol{E}$

$$\nabla \times (\nabla \times \boldsymbol{E}) = \nabla(\nabla \bullet \boldsymbol{E}) - \nabla^2 E = -\mu \frac{\partial}{\partial t}(\nabla \times \boldsymbol{H}) = -\mu\sigma \frac{\partial \boldsymbol{E}}{\partial t} - \mu\varepsilon \frac{\partial^2 \boldsymbol{E}}{\partial t^2} \tag{2.12}$$

i.e.,

$$\nabla^2 \boldsymbol{E} = \varepsilon\mu \frac{\partial^2 \boldsymbol{E}}{\partial t^2} + \mu\sigma \frac{\partial \boldsymbol{E}}{\partial t} \tag{2.13}$$

TABLE 2.2

Values of c, μ_0, and ε_0

Symbol	Physical Quantity	Value
c	Velocity of light in free space	2.997925×10^8 ms^{-1}
μ_0	Permeability of free space	$4\pi \times 10^{-7}$ Hm^{-1}
ε_0	Permittivity of free space = $1/(\mu_0 c^2)$	$8.8541853 \times 10^{-12}$ Fm^{-1}

A similar expression holds for $\boldsymbol{H}$.

First, we look for a solution of Equation 2.13 in the form of a linearly polarized plane harmonic wave (or *plane polarized,* a term meaning the same as *linearly polarized*), and we choose the complex form of this wave, the physical meaning being associated with either the real or the imaginary part of the expression.

$$\boldsymbol{E} = \boldsymbol{\mathcal{E}} \exp[i\omega(t - z/v)] \tag{2.14}$$

represents such a wave propagating along the z-axis with velocity v. $\boldsymbol{\mathcal{E}}$ is the vector amplitude and ω is the angular frequency of this wave. Note that because we are dealing with linear phenomena, ω is invariant as the wave propagates through media with differing properties. The advantage of the complex form of the wave is that phase changes can be dealt with very readily by including them in a complex amplitude. If we include a relative phase, φ, in Equation 2.14, then it becomes

$$\boldsymbol{E} = \boldsymbol{\mathcal{E}} \exp[i\omega(t - z/v + \varphi)] = \boldsymbol{\mathcal{E}} \exp(i\varphi)\exp[i\omega(t - z/v)] \tag{2.15}$$

where $\boldsymbol{\mathcal{E}}\exp(i\varphi)$ is the complex vector amplitude. The complex scalar amplitude is given by $\mathcal{E}\exp(i\varphi)$ where $\mathcal{E} = |\boldsymbol{\mathcal{E}}|$. Equation 2.15, which has phase φ relative to Equation 2.14, is simply Equation 2.14 with the amplitude replaced by the complex amplitude.

In Equation 2.14, we chose to place the time variable first and the spatial variable second in the argument of the exponential. This is a convention, because we could have chosen the alternative of the spatial variable first. However, to reverse the direction of the wave in this convention, we simply change the minus sign to a plus sign, reversing the spatial direction. In the alternative convention, it is tempting to reverse the wave again by changing the sign from minus to plus, but that would reverse the time axis, not the spatial direction. We shall stick to the convention in Equation 2.14 throughout this book.

For Equation 2.14 to be a solution of Equation 2.13, it is necessary that

$$\omega^2/v^2 = \omega^2\varepsilon\mu - i\omega\mu\sigma \tag{2.16}$$

In a vacuum, we have $\sigma = 0$ and $v = c$, so that from Equation 2.16

$$c^2 = 1/\varepsilon_0\mu_0 \tag{2.17}$$

which is identical to Equation 2.10. Multiplying Equation 2.16 by Equation 2.17 and dividing through by ω^2, we obtain

$$\frac{c^2}{v^2} = \frac{\varepsilon\mu}{\varepsilon_0\mu_0} - i\frac{\mu\sigma}{\omega\varepsilon_0\mu_0}$$

where c/v is clearly a dimensionless parameter of the medium, which we denote by N:

$$N^2 = \varepsilon_r\mu_r - i\frac{\mu_r\sigma}{\omega\varepsilon_0} \tag{2.18}$$

This implies that N is of the form

$$N = c/v = n - ik \tag{2.19}$$

There are two possible values of N from Equation 2.18, but for physical reasons we choose that which gives a positive value of n. N is known as the complex refractive index, n is known as the real part of the refractive index (or often simply as the refractive index, because N is real in an ideal dielectric material), and k is known as the extinction coefficient.

If the various parameters are real (which is not always the case), then from Equation 2.18

$$n^2 - k^2 = \varepsilon_r\mu_r \tag{2.20}$$

$$2nk = \frac{\mu_r\sigma}{\omega\varepsilon_0} \tag{2.21}$$

Equation 2.14 can now be written

$$\boldsymbol{E} = \boldsymbol{\mathcal{E}}\exp[i\omega t - (2\pi N/\lambda)z] \tag{2.22}$$

where we have introduced the wavelength in free space, $\lambda = (2\pi c/\omega)$.

Substituting $n - ik$ for N in Equation 2.22 gives

$$\boldsymbol{E} = \boldsymbol{\mathcal{E}}\exp[-(2\pi k/\lambda)z]\exp[i\omega t - (2\pi n/\lambda)z] \tag{2.23}$$

and the significance of k emerges as being a measure of absorption in the medium. The distance $\lambda/(2\pi k)$ is that in which the amplitude of the wave falls to $1/e$ of its original value. The way in which the power carried by the wave falls off will be considered shortly.

The change in phase produced by a traversal of distance z in the medium is the same as that produced by a distance nz in a vacuum. Because of this, nz

is known as the optical distance, as distinct from the physical or geometrical distance. Generally, in thin-film optics, one is more interested in optical distances and optical thicknesses than in geometrical ones.

Since $\boldsymbol{E}$ is constant, Equation 2.18 represents a linearly polarized plane wave propagating along the z-axis. For a similar wave propagating in a direction given by direction coefficient (α, β, γ), the expression becomes

$$\boldsymbol{E} = \boldsymbol{\mathcal{E}} \exp[i\omega t - (2\pi N/\lambda)(\alpha x + \beta y + \gamma z)] \tag{2.24}$$

This is the simplest type of wave in an absorbing medium. In an assembly of absorbing thin films, we shall see that we are occasionally forced to adopt a slightly more complicated expression for the wave.

There are some important relationships for this type of wave which can be derived from Maxwell's equations. Let the direction of propagation of the wave be given by unit vector $\hat{\boldsymbol{s}}$ where

$$\hat{\boldsymbol{s}} = \alpha \boldsymbol{i} + \beta \boldsymbol{j} + \gamma \boldsymbol{k}$$

and where $\boldsymbol{i}$, $\boldsymbol{j}$ and $\boldsymbol{k}$ are unit vectors along the x, y and z axes, respectively. From Equation 2.24 we have

$$\partial \boldsymbol{E}/\partial t = i\omega \boldsymbol{E}$$

and from Equations 2.1, 2.5, and 2.6

$$\begin{aligned} \text{curl}\boldsymbol{H} &= \sigma \boldsymbol{E} + \varepsilon \partial \boldsymbol{E}/\partial t \\ &= (\sigma + i\omega\varepsilon)\boldsymbol{E} \\ &= i\frac{\omega N^2}{c^2\mu}\boldsymbol{E} \end{aligned}$$

Now

$$\text{curl} = \left(\frac{\partial}{\partial x}\boldsymbol{i} + \frac{\partial}{\partial y}\boldsymbol{j} + \frac{\partial}{\partial z}\boldsymbol{k}\right)\times$$

where × denotes the vector product. But

$$\frac{\partial}{\partial x} = -i\frac{2\pi N}{\lambda}\alpha = -i\frac{\omega N}{c}\alpha$$

$$\frac{\partial}{\partial y} = -i\frac{\omega N}{c}\beta \qquad \frac{\partial}{\partial z} = -i\frac{\omega N}{c}\gamma$$

so that

$$\text{curl}\boldsymbol{H} = -i\frac{\omega N}{c}(\hat{\boldsymbol{s}} \times \boldsymbol{H})$$

Then

$$-i\frac{\omega N}{c}(\hat{s}\times \boldsymbol{H}) = i\frac{\omega N^2}{c^2\mu}\boldsymbol{E}$$

i.e.,

$$(\hat{s}\times \boldsymbol{H}) = -\frac{N}{c\mu}\boldsymbol{E} \tag{2.25}$$

and similarly

$$\frac{N}{c\mu}(\hat{s}\times \boldsymbol{E}) = \boldsymbol{H} \tag{2.26}$$

For this type of wave, therefore, ***E***, ***H***, and $\hat{s}$ are mutually perpendicular and form a right-handed set. The quantity $N/c\mu$ has the dimensions of an admittance and is known as the characteristic optical admittance of the medium, written y. In free space, it can be readily shown that the optical admittance is given by

$$\mathcal{Y} = (\varepsilon_0/\mu_0)^{1/2} = 2.6544\times 10^{-3}\ S \tag{2.27}$$

Now

$$\mu = \mu_r\mu_0 \tag{2.28}$$

Direct magnetic interactions at optical frequencies are vanishingly small so that μ_r is effectively unity. Thus we can write

$$y = N\mathcal{Y} \tag{2.29}$$

and

$$\boldsymbol{H} = y(\hat{s}\times \boldsymbol{E}) = N\mathcal{Y}(\hat{s}\times \boldsymbol{E}) \tag{2.30}$$

2.1.1 The Poynting Vector

An important feature of electromagnetic radiation is that it is a form of energy transport, and it is the energy associated with the wave, which is normally observed. The instantaneous rate of flow of energy across unit area is given by the Poynting vector

$$\boldsymbol{S} = \boldsymbol{E}\times \boldsymbol{H} \tag{2.31}$$

The direction of the vector is the direction of energy flow.

When we add or subtract complex numbers, or multiply them by a real number, the real parts and imaginary parts remain independent. Such operations are known as *linear.* Interference calculations involve adding the waves, so we can happily use the complex wave with all its advantages in such calculations. Multiplication of two complex numbers, however, mixes the real and imaginary parts in the result. Such operations are known as nonlinear, and we are unable to use the complex form of the wave directly in them. The Poynting expression is a nonlinear one (***E*** is *multiplied* by ***H***) and so we have a problem with the complex form of the wave. Either the real or the imaginary part of the wave expression should be used. The real sine or cosine form of the wave implies its square in the result and so the instantaneous value of the Poynting vector must oscillate at twice the frequency of the wave. We turn our attention to the mean value because it is the mean that is significant in our measurements. This is defined as the *irradiance* or, in the older systems of units, *intensity.* [**Beware:** Intensity is defined differently in the SI system as the power per unit solid angle from a point source.] In the SI system of units, irradiance is measured in watts per meter squared. An unfortunate feature of the SI system, for our purposes, is that the symbol for irradiance is E. Use of this symbol would make it very difficult for us to distinguish between irradiance and electric field. Because both are extremely important in almost everything we do, we must be able to differentiate between them, and so we adopt a nonstandard symbol, I, for irradiance (which, unfortunately, is the SI symbol for intensity). The mean of the Poynting vector involves integrating the real expression over a cycle, but the complex form of the wave actually comes to our rescue. For a harmonic wave, we find that we can derive a very attractive and simple expression for the irradiance using the complex form of the wave and thus avoiding the integration. This is

$$\boldsymbol{I} = \frac{1}{2}\text{Re}(\boldsymbol{E} \times \boldsymbol{H}^*) \tag{2.32}$$

where * denotes complex conjugate. It should be emphasized that the complex form *must* be used in Equation 2.32. The irradiance $\boldsymbol{I}$ is written in Equation 2.32 as a vector quantity, when it has the same direction as the flow of energy of the wave. The more usual scalar irradiance I is simply the magnitude of $\boldsymbol{I}$. Because $\boldsymbol{E}$ and $\boldsymbol{H}$ are perpendicular, Equation 2.32 can be written

$$I = \frac{1}{2}\text{Re}(EH^*) \tag{2.33}$$

where E and H are the scalar magnitudes.

It is important to note that for the net irradiance, the electric and magnetic vectors in Equation 2.32 should be the total resultant fields due to all the waves involved. This is implicit in the derivation of the Poynting vector expression. We will return to this point when calculating reflectance and transmittance.

For a single, homogeneous, harmonic wave of the form in Equation 2.24:

$$\boldsymbol{H} = y\,(\hat{\boldsymbol{s}} \times \boldsymbol{E})$$

so that

$$\boldsymbol{I} = \mathrm{Re}\left(\frac{1}{2}y\boldsymbol{E}\boldsymbol{E}^*\hat{\boldsymbol{s}}\right)$$

$$= \frac{1}{2}n\mathscr{Y}\boldsymbol{E}\boldsymbol{E}^*\hat{\boldsymbol{s}} \tag{2.34}$$

Now, from Equation 2.24, the magnitude of E is given by

$$\boldsymbol{E} = \mathcal{E}\exp[i\omega t - (2\pi[n - ik]/\lambda)(\alpha x + \beta y + \gamma z)]$$

$$= \mathcal{E}\exp[-(2\pi k/\lambda)(\alpha x + \beta y + \gamma z)]\exp[i\omega t - (2\pi n/\lambda)(\alpha x + \beta y + \gamma z)]$$

implying

$$\boldsymbol{E}\boldsymbol{E}^* = \mathcal{E}\mathcal{E}^*\exp[-(4\pi k/\lambda)(\alpha x + \beta y + \gamma z)]$$

and

$$I = \frac{1}{2}n\mathscr{Y}|\mathcal{E}|^2\exp[-(4\pi k/\lambda)(\alpha x + \beta y + \gamma z)]$$

The expression $(\alpha x + \beta y + \gamma z)$ is simply the distance along the direction of propagation, and thus the irradiance drops to $1/e$ of its initial value in a distance given by $\lambda/4\pi k$. The inverse of this distance is defined as the absorption coefficient α; that is

$$\alpha = 4\pi k/\lambda \tag{2.35}$$

The absorption coefficient α should not be confused with the direction cosine.

However,

$$|\mathcal{E}|\exp[-(2\pi k/\lambda)(\alpha x + \beta y + \gamma z)]$$

is really the amplitude of the wave at the point (x, y, z) so that a much simpler way of writing the expression for irradiance is

$$I = \frac{1}{2}n\mathscr{Y}(\text{amplitude})^2 \tag{2.36}$$

or

$$I \propto n \times (\text{amplitude})^2 \tag{2.37}$$

This expression is a better form than the more usual

$$I \propto (\text{amplitude})^2 \tag{2.38}$$

The expression will frequently be used for comparing irradiances, in calculating reflectance or transmittance, for example, and if the media in which the two waves are propagating are of different index, then errors will occur unless n is included as above.

2.2 The Simple Boundary

Thin-film filters usually consist of a number of boundaries between various homogeneous media, and it is the effect of these boundaries on an incident wave that we will wish to calculate. A single boundary is the simplest case. First, we consider absorption-free media, i.e., $k = 0$.

The arrangement is sketched in Figure 2.1. A plane harmonic wave is incident on a plane surface separating the incident medium from a second, or emergent, medium. The plane containing the normal to the surface and the direction of propagation of the incident wave is known as the *plane of incidence* and the sketch corresponds to this plane. We take the z-axis as the normal into the surface in the sense of the incident wave and the x-axis as normal to it and also in the plane of incidence. At a boundary, the tangential

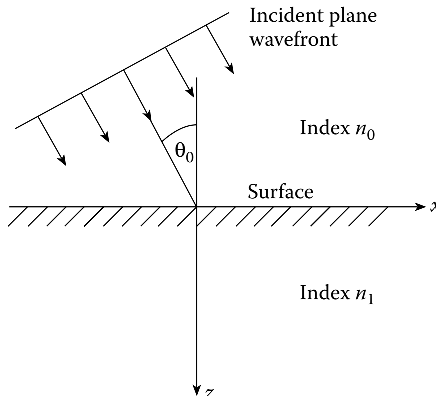

FIGURE 2.1
Plane wave front incident on a single surface.

components of $\boldsymbol{E}$ and $\boldsymbol{H}$—that is, the components along the boundary—are continuous across it because there is no mechanism that will change them. This boundary condition is fundamental in our thin-film theory.

The first problem we have is that the boundary conditions are incompatible with a simple traversal of the boundary by the incident wave. The discontinuity in the characteristic admittance implies a power discontinuity impossible in a simple boundary. This problem is immediately solved by introducing a reflected wave in the incident medium, and this, of course, is directly in line with our experience. Our objective then becomes the calculation of the relative parameters of the three waves: incident, reflected, and transmitted. However, this introduces a further complication. We will use the boundary conditions to set up a set of equations from which we will extract the required relations. The complication is that the reflected wave will certainly be traveling in a different sense from the others so that there will be differences in the phase factors that will considerably complicate the calculations. We can help ourselves enormously by defining the boundary by $z = 0$, eliminating the z term from the phase factors at the boundary. Then the tangential components must be continuous for all values of x, y, and t.

We therefore have three harmonic waves: an incident, a reflected, and a transmitted wave. Let the direction cosines of the $\hat{s}$ vectors of the transmitted and reflected waves be given by $(\alpha_t, \beta_t, \gamma_t)$ and $(\alpha_r, \beta_r, \gamma_r)$, respectively. We already know the direction of the incident wave. We can therefore write the phase factors in the form:

Incident wave	$\exp\{i[\omega t - (2\pi n_0/\lambda_i)(x\sin\vartheta_0 + z\cos\vartheta_0)]\}$
Reflected wave	$\exp\{i[\omega t - (2\pi n_0/\lambda_r)(\alpha_r x + \beta_r y + y_r z)]\}$
Transmitted wave	$\exp\{i[\omega t - (2\pi n_1/\lambda_t)(\alpha_t x + \beta_t y + y_t z)]\}$

The relative phases of these waves are included in the complex amplitudes. For waves with these phase factors to satisfy the boundary conditions for all x, y, t at $z = 0$, implies that the coefficients of these variables must be separately identically equal. Had we not already known that there would be no change in frequency, this would have confirmed it. Because the frequencies are constant, so, too, will be the free space wavelengths. Next

$$0 \equiv n_0\beta_r \equiv n_1\beta_t \tag{2.39}$$

That is, the directions of the reflected and transmitted or refracted beams are confined to the plane of incidence. This, in turn, means that the direction cosines of the reflected and transmitted waves are of the form

$$\alpha = \sin\vartheta \qquad \gamma = \cos\vartheta \tag{2.40}$$

Also

$$n_0 \sin \vartheta_0 \equiv n_0 \alpha_r \equiv n_1 \alpha_t$$

so that if the angles of reflection and refraction are ϑ_r and ϑ_t, respectively, then

$$\vartheta_0 = \vartheta_r \tag{2.41}$$

that is, the angle of reflection equals the angle of incidence, and

$$n_0 \sin \vartheta_0 = n_1 \sin \vartheta_t$$

The result appears more symmetrical if we replace ϑ_t by ϑ_1, giving

$$n_0 \sin \vartheta_0 = n_1 \sin \vartheta_1 \tag{2.42}$$

This is the familiar relationship known as Snell's law. γ_r and γ_t are then given either by Equation 2.40 or by

$$\alpha_r^2 + \gamma_r^2 = 1 \quad \text{and} \quad \alpha_t^2 + \gamma_t^2 = 1 \tag{2.43}$$

Note that for the reflected beam, we must choose the *negative* root of Equation 2.43 so that the beam will propagate in the correct direction.

2.2.1 Normal Incidence

Let us limit our initial discussion to normal incidence and let the incident wave be a linearly polarized plane harmonic wave. The coordinate axes are shown in Figure 2.2. The xy plane is the plane of the boundary. The incident wave we can take as propagating along the z-axis with the positive direction of the $\boldsymbol{E}$ vector along the x-axis. Then, the positive direction of the $\boldsymbol{H}$ vector will be the y-axis. It is clear that the only waves that satisfy the boundary conditions are linearly polarized in the same plane as the incident wave.

A quoted phase difference between two waves traveling in the same direction is immediately meaningful. A phase difference between two waves traveling in opposite directions is absolutely meaningless, unless a reference plane at which the phase difference is measured is first defined. This is simply because the phase difference between oppositely propagating waves of the same frequency has a term $(\pm 4\pi ns/\lambda)$ in it where s is a distance measured along the direction of propagation. Before proceeding further, therefore, we need to define the reference point for measurements of relative phase between the oppositely propagating beams. Because we have already used the device of defining the boundary as $z = 0$, we can continue this idea and define the boundary as that plane where the reflected phase shift should be defined.

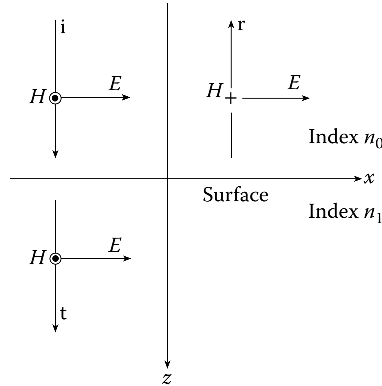

FIGURE 2.2
Convention defining positive directions of the electric and magnetic vectors for reflection and transmission at an interface at normal incidence.

Then there is another problem. The waves have electric and magnetic fields that with the direction of propagation form right-handed sets. Because the direction of propagation is reversed in the reflected beam, the orientation of electric and magnetic fields cannot remain the same as that in the incident beam; otherwise, we would no longer have a right-handed set. We need to decide on how we are going to handle this. Because the electric field is the one that is most important from the point of view of interaction with matter, we will define our directions with respect to it.

The matter of phase references and electric field directions are what we call *conventions* because we do have complete freedom of choice, and any self-consistent arrangement is possible. We must simply ensure that once we have made our choice, we adhere to it. A good rule, however, is never to make things difficult when we can make them easy, and so we will normally choose the rule that is most convenient and least complicated. We define the positive direction of $\boldsymbol{E}$ along the x-axis for all the beams that are involved. Because of this choice, the positive direction of the magnetic vector will be along the y-axis for the incident and transmitted waves but along the negative direction of the y-axis for the reflected wave.

We now consider the boundary conditions. Because we have already made sure that the phase factors are satisfactory, we have only to consider the amplitudes, and we will be including any phase changes in these.

(a) Electric vector continuous across the boundary.

$$\mathcal{E}_i + \mathcal{E}_r = \mathcal{E}_t \tag{2.44}$$

(b) Magnetic vector continuous across the boundary.

$$\mathcal{H}_i - \mathcal{H}_r = \mathcal{H}_t$$

where we must use a minus sign because of our convention for positive directions. The relationship between magnetic and electric field through the characteristic admittance, gives

$$y_0\mathcal{E}_i - y_0\mathcal{E}_r = y_1\mathcal{E}_t \tag{2.45}$$

This can also be derived using the vector relationship, Equation 2.30, and Equation 2.44. We can eliminate $\mathcal{E}_t$ to give

$$y_1(\mathcal{E}_i + \mathcal{E}_r) = y_0(\mathcal{E}_i - \mathcal{E}_r)$$

i.e.,

$$\frac{\mathcal{E}_r}{\mathcal{E}_i} = \frac{y_0 - y_1}{y_0 + y_1} = \frac{n_0 - n_1}{n_0 + n_1} \tag{2.46}$$

With the second part of the relationship being correct only because at optical frequencies we can write

$$y = n\mathcal{Y}$$

Similarly, eliminating $\mathcal{E}_r$,

$$\frac{\mathcal{E}_t}{\mathcal{E}_i} = \frac{2y_0}{y_0 + y_1} = \frac{2n_0}{n_0 + n_1} \tag{2.47}$$

These quantities are called the *amplitude reflection* and *transmission coefficients* and are denoted by ρ and τ, respectively. Thus

$$\rho = \frac{y_0 - y_1}{y_0 + y_1} = \frac{n_0 - n_1}{n_0 + n_1} \tag{2.48}$$

$$\tau = \frac{2y_0}{y_0 + y_1} = \frac{2n_0}{n_0 + n_1} \tag{2.49}$$

In this particular case, all y real, these two quantities are real. τ is always a positive real number, indicating that according to our phase convention there is no phase shift between the incident and transmitted beams at the interface. The behavior of ρ indicates that there will be no phase shift between the incident and reflected beams at the interface provided $n_0 > n_1$, but that if $n_0 < n_1$ there will be a phase change of π because the value of ρ becomes negative.

We now examine the energy balance at the boundary. The total tangential components of electric and magnetic field are continuous across the

boundary but also, because the boundary is of zero thickness, it can neither supply energy to nor extract energy from the various waves. On both counts, the Poynting vector will be continuous across the boundary, so that we can write:

$$\text{net irradiance} = \text{Re}\left[\frac{1}{2}(\mathcal{E}_i + \mathcal{E}_r)(y_0\mathcal{E}_i - y_0\mathcal{E}_r)^*\right]$$

$$= \text{Re}\left[\frac{1}{2}\mathcal{E}_i(y_1\mathcal{E}_t)^*\right]$$

[using $\text{Re}\left(\frac{1}{2}\boldsymbol{E}\times\boldsymbol{H}^*\right)$ and Equations 2.44 and 2.45]. Now

$$\mathcal{E}_r = \rho\mathcal{E}_i \qquad \text{and} \qquad \mathcal{E}_t = \tau\mathcal{E}_i$$

i.e.,

$$\text{net irradiance} = \frac{1}{2}y_0\mathcal{E}_i\mathcal{E}_i^*(1-\rho^2) = \frac{1}{2}y_0\mathcal{E}_i\mathcal{E}_i^*(y_1/y_0)\tau^2 \qquad (2.50)$$

We recognize $(1/2)y_0\mathcal{E}_i\mathcal{E}_i^*$ as the irradiance of the incident beam I_i. We can identify $\rho^2(1/2)y_0\mathcal{E}_i\mathcal{E}_i^* = \rho^2 I_i$ as the irradiance of the reflected beam I_r and $(y_1/y_0)\times\tau^2(1/2)y_0\mathcal{E}_i\mathcal{E}_i^* = (y_1/y_0)\tau^2 I_i$ as the irradiance of the transmitted beam I_t. We define the reflectance R as the ratio of the reflected and incident irradiances and the transmittance T as the ratio of the transmitted and incident irradiances. Then

$$T = \frac{I_t}{I_i} = \frac{y_1}{y_0}\tau^2 = \frac{4y_0y_1}{(y_0+y_1)^2} = \frac{4n_0n_1}{(n_0+n_1)^2}$$

$$R = \frac{I_r}{I_i} = \rho^2 = \left(\frac{y_0-y_1}{y_0+y_1}\right)^2 = \left(\frac{n_0-n_1}{n_0+n_1}\right)^2 \qquad (2.51)$$

From Equation 2.50 we have, using Equations 2.51,

$$(1-R) = T \qquad (2.52)$$

Equations 2.50, 2.51, and 2.52 are therefore consistent with our ideas of splitting the irradiances into incident, reflected, and transmitted irradiances, which can be treated as separate waves, the energy flow into the second medium being simply the difference of the incident and reflected irradiances. Remember that all this, so far, assumes that there is no absorption. We shall shortly see that the situation changes slightly when absorption is present.

2.2.2 Oblique Incidence

Now let us consider oblique incidence, still retaining our absorption-free media. For any general direction of the vector amplitude of the incident wave, we quickly find that the application of the boundary conditions leads us into complicated and difficult expressions for the vector amplitudes of the reflected and transmitted waves. Fortunately, there are two orientations of the incident wave that lead to reasonably straightforward calculations: the vector electrical amplitudes aligned in the plane of incidence (i.e., the xy plane of Figure 2.1) and the vector electrical amplitudes aligned normal to the plane of incidence (i.e., parallel to the y-axis in Figure 2.1). In each of these cases, the orientations of the transmitted and reflected vector amplitudes are the same as for the incident wave. Any incident wave of arbitrary polarization can therefore be split into two components having these simple orientations. The transmitted and reflected components can be calculated for each orientation separately and then combined to yield the resultant. Because, therefore, it is necessary to consider two orientations only, they have been given special names.

A wave with the electric vector in the plane of incidence is known as p-polarized or, sometimes, as TM (for transverse magnetic), and a wave with the electric vector normal to the plane of incidence as s-polarized or, sometimes, TE (for transverse electric). p and s are derived from the German *parallel* and *senkrecht* (perpendicular). Before we can actually proceed to the calculation of the reflected and transmitted amplitudes, we must choose the various reference directions of the vectors from which any phase differences will be calculated. We have, once again, complete freedom of choice, but once we have established the convention we must adhere to it, just as in the normal incidence case. The conventions that we will use in this book are illustrated in Figure 2.3. They have been chosen to be compatible with those for normal incidence already established. In some works, an opposite convention for

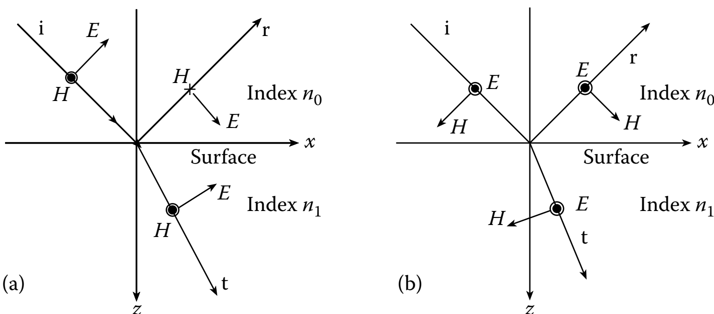

FIGURE 2.3
(a) Convention defining the positive directions of the electric and magnetic vectors for p-polarized light (TM waves). (b) Convention defining the positive directions of the electric and magnetic vectors for s-polarized light (TE waves).

the p-polarized reflected beam has been adopted, but this leads to an incompatibility with results derived for normal incidence, and we prefer to avoid this situation. [Note that for reasons connected with consistency of reference directions for elliptically polarized light, the convention normal in ellipsometric calculations is opposite that of Figure 2.3 for reflected p-polarized light. When ellipsometric parameters are compared with the results of the expressions we shall use, it will usually be necessary to introduce a shift of $180°$ in the p-polarized reflected results.]

We can now apply the boundary conditions. Because we have already ensured that the phase factors will be correct, we need only consider the vector amplitudes.

2.2.2.1 p-Polarized Light

(a) Electric component parallel to the boundary, continuous across it.

$$\mathcal{E}_i \cos\vartheta_0 + \mathcal{E}_r \cos\vartheta_0 = \mathcal{E}_t \cos\vartheta_1 \tag{2.53}$$

(b) Magnetic component parallel to the boundary, continuous across it.

Here we need to calculate the magnetic vector amplitudes, and we can do this either by using Equation 2.30 to operate on Equation 2.53 directly or, because the magnetic vectors are already parallel to the boundary, we can use Figure 2.3 and then convert, because $\mathcal{H} = y\mathcal{E}$.

$$y_0\mathcal{E}_i - y_0\mathcal{E}_r = y_1\mathcal{E}_t \tag{2.54}$$

At first sight, it seems logical just to eliminate first $\mathcal{E}_t$ and then $\mathcal{E}_r$ from these two equations to obtain $\mathcal{E}_r/\mathcal{E}_i$ and $\mathcal{E}_t/\mathcal{E}_i$

$$\begin{aligned}\frac{\mathcal{E}_r}{\mathcal{E}_i} &= \frac{y_0\cos\vartheta_1 - y_1\cos\vartheta_0}{y_0\cos\vartheta_1 + y_1\cos\vartheta_0}\\ \frac{\mathcal{E}_t}{\mathcal{E}_i} &= \frac{2y_0\cos\vartheta_0}{y_0\cos\vartheta_1 + y_1\cos\vartheta_0}\end{aligned} \tag{2.55}$$

and then simply to set

$$R = \left(\frac{\mathcal{E}_r}{\mathcal{E}_i}\right)^2 \quad \text{and} \quad T = \frac{y_1}{y_0}\left(\frac{\mathcal{E}_t}{\mathcal{E}_i}\right)^2$$

but when we calculate the expressions that result, we find that $R + T \neq 1$. In fact, there is no mistake in the calculations. We have computed the irradiances measured along the direction of propagation of the waves and the transmitted wave is inclined at an angle that differs from that of the incident

wave. This leaves us with the problem that to adopt these definitions will involve the rejection of the ($R + T = 1$) rule.

We could correct this situation by modifying the definition of T to include this angular dependence, but an alternative, preferable, and generally adopted approach is to use the components of the energy flows that are normal to the boundary. The ***E*** and ***H*** vectors that are involved in these calculations are then parallel to the boundary. Because these are those that enter directly into the boundary, it seems appropriate to concentrate on them when we are dealing with the amplitudes of the waves. Note that reflectance and transmittance defined for infinite plane waves in terms of normal flows of irradiance are absolutely consistent with reflectance and transmittance defined in terms of the ratios of total beam power when using confined beams such as the output from a laser.

The thin-film approach to all this, then, is to use the components of ***E*** and ***H*** parallel to the boundary, what are called the tangential components, in the expressions ρ and τ that involve amplitudes. Note that the normal approach in other areas of optics is to use the full components of ***E*** and ***H*** in amplitude expressions but to use the components of irradiance in reflectance and transmittance. The amplitude coefficients are then known as the Fresnel coefficients. The thin-film coefficients are *not* the Fresnel coefficients except at normal incidence, although the only coefficient that actually has a different value is the amplitude transmission coefficient for p-polarization.

The tangential components of ***E*** and ***H***, that is, the components parallel to the boundary, have already been calculated for use in Equations 2.53 and 2.54. However, it is convenient to introduce special symbols for them—$\mathcal{E}$ and $\mathcal{H}$.

Then we can write

$$E_i = \mathcal{E}_i \cos\vartheta_0 \qquad H_i = \mathcal{H}_i = y_0\mathcal{E}_i = \frac{y_0}{\cos\vartheta_0} E_i \tag{2.56}$$

$$E_r = \mathcal{E}_r \cos\vartheta_0 \qquad H_r = \frac{y_0}{\cos\vartheta_0} E_r \tag{2.57}$$

$$E_t = \mathcal{E}_t \cos\vartheta_1 \qquad H_t = \frac{y_1}{\cos\vartheta_1} E_t \tag{2.58}$$

The orientations of these vectors are exactly the same as for normally incident light.

Equations 2.53 and 2.54 can then be written as follows.

(a) Electric field parallel to the boundary

$$E_i + E_r = E_t$$

(b) Magnetic field parallel to the boundary

$$\frac{y_0}{\cos\vartheta_0}\mathcal{H}_i - \frac{y_0}{\cos\vartheta_0}\mathcal{H}_r = \frac{y_1}{\cos\vartheta_1}\mathcal{H}_t$$

giving us, by a process exactly similar to that we have already used for normal incidence,

$$\rho_p = \frac{\mathcal{E}_r}{\mathcal{E}_i} = \left(\frac{y_0}{\cos\vartheta_0} - \frac{y_1}{\cos\vartheta_1}\right) \Big/ \left(\frac{y_0}{\cos\vartheta_0} + \frac{y_1}{\cos\vartheta_1}\right) \tag{2.59}$$

$$\tau_p = \frac{\mathcal{E}_t}{\mathcal{E}_i} = \left(\frac{2y_0}{\cos\vartheta_0}\right) \Big/ \left(\frac{y_0}{\cos\vartheta_0} + \frac{y_1}{\cos\vartheta_1}\right) \tag{2.60}$$

$$R_p = \left[\left(\frac{y_0}{\cos\vartheta_0} - \frac{y_1}{\cos\vartheta_1}\right) \Big/ \left(\frac{y_0}{\cos\vartheta_0} + \frac{y_1}{\cos\vartheta_1}\right)\right]^2 \tag{2.61}$$

$$T_p = \left(\frac{4y_0y_1}{\cos\vartheta_0\cos\vartheta_1}\right) \Big/ \left(\frac{y_0}{\cos\vartheta_0} + \frac{y_1}{\cos\vartheta_1}\right)^2 \tag{2.62}$$

where $y_0 = n_0\mathcal{Y}$ and $y_1 = n_1\mathcal{Y}$ and the $(R + T = 1)$ rule is retained. The suffix p has been used in the above expressions to denote p-polarization.

It should be noted that the expression for τ_p is now different from that in Equation 2.55, the form of the Fresnel amplitude transmission coefficient. Fortunately, the reflection coefficients in Equations 2.55 and 2.61 are identical, and because much more use is made of reflection coefficients, confusion is rare.

2.2.2.2 *s*-Polarized Light

In the case of s-polarization, the amplitudes of the components of the waves parallel to the boundary are

$$\mathcal{E}_i = \mathscr{E}_i \quad \mathcal{H}_i = \mathscr{H}_i\cos\vartheta_0 = (y_0\cos\vartheta_0)\mathcal{E}_i$$

$$\mathcal{E}_r = \mathscr{E}_r \quad \mathcal{H}_r = \mathscr{H}_r\cos\vartheta_0 = (y_0\cos\vartheta_0)\mathcal{E}_r$$

$$\mathcal{E}_t = \mathscr{E}_t \quad \mathcal{H}_t = (y_1\cos\vartheta_1)\mathcal{E}_t$$

and here we have again an orientation of the tangential components exactly as for normally incident light, and so a similar analysis leads to

$$\rho_s = \frac{\mathcal{E}_r}{\mathcal{E}_i} = (y_0\cos\vartheta_0 - y_1\cos\vartheta_1)/(y_0\cos\vartheta_0 + y_1\cos\vartheta_1) \tag{2.63}$$

$$\tau_s = \frac{\mathcal{E}_t}{\mathcal{E}_i} = (2y_0 \cos\vartheta_0) / (y_0 \cos\vartheta_0 + y_1 \cos\vartheta_1) \quad (2.64)$$

$$R_s = [(y_0 \cos\vartheta_0 - y_1 \cos\vartheta_1) / (y_0 \cos\vartheta_0 + y_1 \cos\vartheta_1)]^2 \quad (2.65)$$

$$T_p = (4y_0 \cos\vartheta_0 y_1 \cos\vartheta_1) / (y_0 \cos\vartheta_0 + y_1 \cos\vartheta_1)^2 \quad (2.66)$$

where again, $y_0 = n_0\mathcal{Y}$ and $y_1 = n_1\mathcal{Y}$ and the ($R + T = 1$) rule is retained. The suffix s has been used in the above expressions to denote s-polarization.

2.2.3 The Optical Admittance for Oblique Incidence

The expressions that we have derived so far have been in their traditional form (except for the use of the tangential components rather than the full vector amplitudes) and they involve the characteristic admittances of the various media, or their refractive indices together with the admittance of free space, $\mathcal{Y}$. However, the notation is becoming increasingly cumbersome and will appear even more so when we consider the behavior of thin films.

Equation 2.30 gives $\boldsymbol{H} = y(\hat{\boldsymbol{s}} \times \boldsymbol{E})$ where $y = N\mathcal{Y}$ is the optical admittance. We have found it convenient to deal with $\mathcal{E}$ and $\mathcal{H}$, the components of E and H parallel to the boundary, and so we introduce a tilted optical admittance, η, which connects $\mathcal{E}$ and $\mathcal{H}$ as

$$\eta = \frac{\mathcal{H}}{\mathcal{E}} \quad (2.67)$$

At normal incidence, $\eta = y = n\mathcal{Y}$, while at oblique incidence

$$\eta_p = \frac{y}{\cos\vartheta} = \frac{n\mathcal{Y}}{\cos\vartheta} \quad (2.68)$$

$$\eta_s = y\cos\vartheta = n\mathcal{Y}\cos\vartheta \quad (2.69)$$

where the ϑ and the y in Equations 2.68 and 2.69 are those appropriate to the particular medium. In particular, Snell's law, Equation 2.42, must be used to calculate ϑ

Then, in all cases, we can write

$$\rho = \left(\frac{\eta_0 - \eta_1}{\eta_0 + \eta_1}\right) \qquad \tau = \left(\frac{2\eta_0}{\eta_0 + \eta_1}\right) \quad (2.70)$$

$$R = \left(\frac{\eta_0 - \eta_1}{\eta_0 + \eta_1}\right)^2 \qquad T = \frac{4\eta_0\eta_1}{(\eta_0 + \eta_1)^2} \quad (2.71)$$

These expressions can be used to compute the variation of reflectance of simple boundaries between extended media. Examples are shown in Figure 2.4 of the variation of reflectance with angle of incidence. In this case, there is no absorption in the material, and it can be seen that the reflectance for *p*-polarized light (TM) falls to zero at a definite angle. This particular angle is known as the *Brewster angle* and is of some importance. There are many applications where the windows of a cell must have close to zero reflection loss. When it can be arranged that the light will be linearly polarized, a plate tilted at the Brewster angle will be a good solution. The light that is reflected at the Brewster angle is also linearly polarized with electric vector normal to the plane of incidence. This affords a way of identifying the absolute direction of polarizers and analyzers—very difficult in any other way.

The expression for the Brewster angle can be derived as follows. For the *p*-reflectance to be zero, from Equation 2.61

$$\frac{y_0}{\cos\vartheta_0} = \frac{n_0\mathcal{Y}}{\cos\vartheta_0} = \frac{y_1}{\cos\vartheta_1} = \frac{n_1\mathcal{Y}}{\cos\vartheta_1}$$

Snell's law gives another relationship between ϑ_0 and ϑ_1.

$$n_0 \sin\vartheta_0 = n_1 \sin\vartheta_1$$

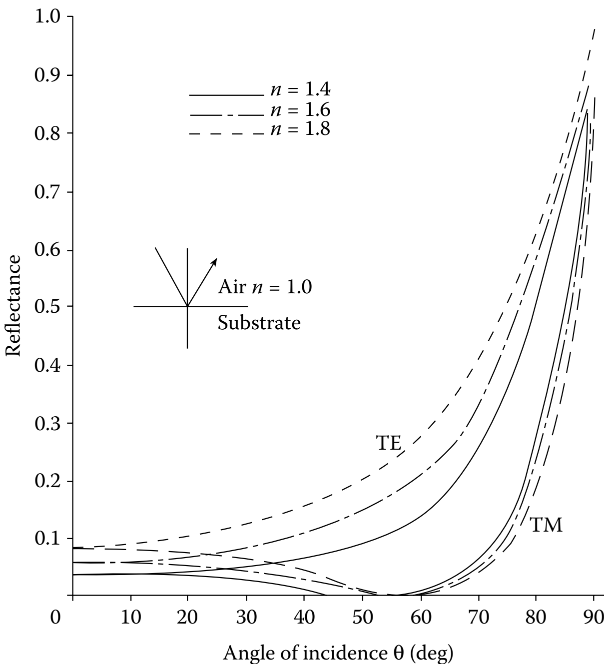

FIGURE 2.4
Variation of reflectance with angle of incidence for various values of refractive index.

Eliminating ϑ_1 from these two equations gives an expression for ϑ_0

$$\tan \vartheta_0 = n_1/n_0 \tag{2.72}$$

Note that this derivation depends on the relationship $y = n\mathscr{Y}$, valid at optical frequencies.

Figure 2.5 shows the variation of tilted admittance of a number of dielectric materials as a function of the angle of incidence in air. Note that the divergence of the two tilted admittances, the polarization splitting, becomes less as the index of refraction increases.

2.2.4 Normal Incidence in Absorbing Media

We must now examine the modifications necessary in our results in the presence of absorption. First, we consider the case of normal incidence and write

$$N_0 = n_0 - ik_0$$

$$N_1 = n_1 - ik_1$$

$$y_0 = N_0\mathscr{Y} = (n_0 - ik_0)\mathscr{Y}$$

$$y_1 = N_1\mathscr{Y} = (n_1 - ik_1)\mathscr{Y}$$

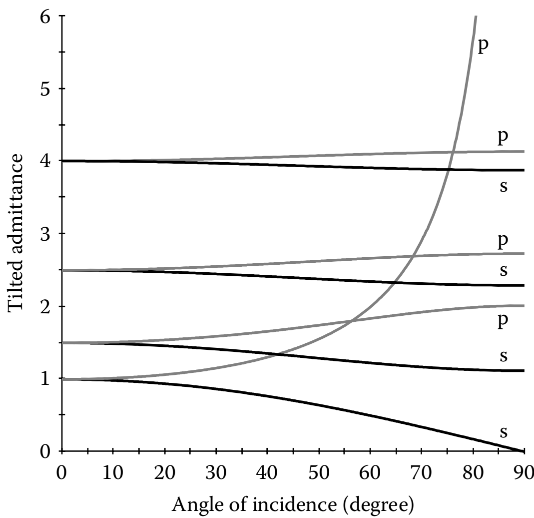

FIGURE 2.5
Tilted admittances of several dielectric (absorption-free) materials as a function of angle of incidence in air.

The analysis follows that for absorption-free media. The boundaries are, as before:

(a) Electric vector continuous across the boundary:

$$\mathcal{E}_i + \mathcal{E}_r = \mathcal{E}_t$$

(b) Magnetic vector continuous across the boundary:

$$y_0\mathcal{E}_i - y_0\mathcal{E}_r = y_1\mathcal{E}_t$$

and eliminating first $\mathcal{E}_t$ and then $\mathcal{E}_r$, we obtain the expressions for the amplitude coefficients

$$\rho = \frac{\mathcal{E}_r}{\mathcal{E}_i} = \frac{y_0 - y_1}{y_0 + y_1} = \frac{(n_0 - ik_0)\mathcal{Y} - (n_1 - ik_1)\mathcal{Y}}{(n_0 - ik_0)\mathcal{Y} + (n_1 - ik_1)\mathcal{Y}} = \frac{(n_0 - n_1) - i(k_0 - k_1)}{(n_0 + n_1) - i(k_0 + k_1)} \tag{2.73}$$

$$\tau = \frac{\mathcal{E}_t}{\mathcal{E}_i} = \frac{2y_0}{y_0 - y_1} = \frac{2(n_0 - ik_0)\mathcal{Y}}{(n_0 - ik_0)\mathcal{Y} + (n_1 - ik_1)\mathcal{Y}} = \frac{2(n_0 - ik_0)}{(n_0 + n_1) - i(k_0 + k_1)} \tag{2.74}$$

Our troubles begin when we try to extend this to reflectance and transmittance. We remain at normal incidence. Following the method for the absorption-free case, we compute the Poynting vector at the boundary in each medium and equate the two values obtained. In the incident medium, the resultant electric and magnetic fields are

$$\mathcal{E}_i + \mathcal{E}_r = \mathcal{E}_i(1 + \rho)$$

and

$$\mathcal{H}_i - \mathcal{H}_r = y_0(1 - \rho)\mathcal{E}_i$$

respectively, where we have used the notation for tangential components, and in the second medium the fields are

$$\tau\mathcal{E}_i \quad \text{and} \quad y_1\tau\mathcal{E}_i$$

respectively. Then the net irradiance on either side of the boundary is

Medium 0: $$I = \mathrm{Re}\left\{\frac{1}{2}[\mathcal{E}_i(1 + \rho)][y_0^*(1 - \rho^*)\mathcal{E}_i^*]\right\}$$

Medium 1: $$I = \mathrm{Re}\left\{\frac{1}{2}[\tau\mathcal{E}_i][y_1^*\tau^*\mathcal{E}_i^*]\right\}$$

We then equate these two values, which gives, at the boundary,

$$\mathrm{Re}\left[\frac{1}{2}y_0^*\mathcal{E}_i\mathcal{E}_i^*(1+\rho-\rho^*-\rho\rho^*)\right]=\frac{1}{2}\mathrm{Re}(y_1)\tau\tau^*\mathcal{E}_i\mathcal{E}_i^*$$

$$\frac{1}{2}\mathrm{Re}(y_0^*)\mathcal{E}_i\mathcal{E}_i^*-\frac{1}{2}\mathrm{Re}(y_0^*)\rho\rho^*\mathcal{E}_i\mathcal{E}_i^*+\frac{1}{2}\mathrm{Re}[y_0^*(\rho-\rho^*)]\mathcal{E}_i\mathcal{E}_i^*=\frac{1}{2}\mathrm{Re}(y_1)\tau\tau^*\mathcal{E}_i\mathcal{E}_i^* \tag{2.75}$$

We can replace the different parts of Equation 2.75 with their normal interpretations to give

$$I_i-RI_i+\frac{1}{2}\mathrm{Re}[y_0^*(\rho-\rho^*)]\mathcal{E}_i\mathcal{E}_i^*=TI_i \tag{2.76}$$

$(\rho-\rho^*)$ is imaginary. This implies that if y_0 is real, the third term in Equation 2.76 is zero. The other terms then make up the incident, the reflected and the transmitted irradiances, and these terms balance. If y_0 is complex, then its imaginary part will combine with the imaginary $(\rho-\rho^*)$ to produce a real result that will imply that $T+R\neq 1$. The irradiances involved in the analysis are those actually at the boundary, which is of zero thickness, and it is impossible that it should either remove or donate energy to the waves. Our assumption that the irradiances can be divided into separate incident, reflected, and transmitted irradiances is therefore incorrect. The source of the difficulty is a coupling between the incident and reflected fields, which occurs only in an absorbing medium and which must be taken into account when computing energy transport. The expressions for the amplitude coefficients are perfectly correct. The phenomenon is well understood and has been described by a number of people; the account by Berning [4] is probably the most accessible.

The extra term is of the order of (k^2/n^2). For any reasonable experiment to be carried out, the incident medium must be sufficiently free of absorption for the necessary comparative measurements to be performed with acceptably small errors. In such cases, the error is vanishingly small. Although we will certainly be dealing with absorbing media in thin-film assemblies, our incident media will never be heavily absorbing and it will not be a serious lack of generality if we assume that our incident media are absorption free. Because our expressions for the amplitude coefficients are valid, then any calculations of amplitudes in absorbing media will be correct. We simply have to ensure that calculations of reflectances are carried out in a transparent medium. With this restriction, then, we have

$$R=\left(\frac{y_0-y_1}{y_0+y_1}\right)\left(\frac{y_0-y_1}{y_0+y_1}\right)^* \tag{2.77}$$

$$T=\frac{4y_0\,\mathrm{Re}(y_1)}{(y_0+y_1)(y_0+y_1)^*} \tag{2.78}$$

where y_0 is real.

We have avoided the problem connected with the definition of reflectance in a medium with complex y_0 simply by not defining it unless the incident medium is sufficiently free of either gain or absorption. Without a definition of reflectance, however, we have trouble with the meaning of antireflection and there are cases such as the rear surface of an absorbing substrate where an antireflection coating would be relevant. We do need to deal with this problem, and although we have not yet discussed antireflection coatings, it is most convenient to include the discussion here where we have already the basis for the theory. The discussion was originally published in 1995 [5].

The usual purpose of an antireflection coating is the reduction of reflectance. But frequently, the objective of the reflectance reduction is the corresponding increase in transmittance. Although an absorbing or amplifying medium will rarely present with a problem in terms of a reflectance measurement, we must occasionally treat a slab of such material on both sides to increase overall transmittance. In this context, therefore, we define an antireflection coating as one that increases transmittance and, in the ideal case, maximizes it. But to accomplish that, we need to define what we mean by *transmittance.*

We have no problem with the measurement of irradiance at the emergent side of our system, even if the emergent medium is absorbing. The incident irradiance is more difficult. This we can define as the *irradiance* if the transmitting structure were removed and replaced by an infinite extent of incident medium material. Then, the transmittance will simply be the ratio of these two values.
i.e.,

$$I_{inc} = \frac{1}{2}\mathrm{Re}(y_0)\mathcal{E}_i\mathcal{E}_i^*$$

and then

$$T = \frac{\frac{1}{2}\mathrm{Re}(y_1)\mathcal{E}_t\mathcal{E}_t^*}{\frac{1}{2}\mathrm{Re}(y_0)\mathcal{E}_i\mathcal{E}_i^*}$$

This is completely consistent with Equation 2.76—that is, with a slight manipulation,

$$T = 1 - \rho\rho^* + \frac{\mathrm{Re}[y_0^*(\rho - \rho^*)]}{\mathrm{Re}(y_0)} \tag{2.79}$$

An alternative form uses

$$\mathcal{E}_t = \frac{2y_0}{(y_0 + y_1)}\mathcal{E}_i$$

so that

$$T = \frac{4y_0 y_0^* \,\mathrm{Re}(y_1)}{\mathrm{Re}(y_0)\cdot\left[(y_0+y_1)(y_0+y_1)^*\right]} \tag{2.80}$$

Now let the surface be coated with a dielectric system so that it presents the admittance Y. Then, since, in the absence of absorption, the net irradiance entering the thin-film system must also be the emergent irradiance,

$$T = \frac{4y_0 y_0^* \,\mathrm{Re}(Y)}{\mathrm{Re}(y_0)\cdot\left[(y_0+Y)(y_0+Y)^*\right]} \tag{2.81}$$

Let $Y = \alpha + i\beta$; then

$$T = \frac{4\alpha(n_0^2 + k_0^2)}{n_0\left[(n_0+\alpha)^2 + (k_0-\beta)^2\right]}$$

and T can readily be shown to be a maximum when

$$Y = \alpha + i\beta = n_0 + ik_0 = (n_0 - ik_0)^* \tag{2.82}$$

The matching admittance should therefore be the *complex conjugate* of the incident admittance. For this perfect matching, the transmittance becomes

$$T = \left(1 + \frac{k_0^2}{n_0^2}\right)$$

and this is greater than unity. This is not a mistake but rather a consequence of the definition of transmittance. Irradiance falls by a factor of roughly $4\pi k_0$ in a distance of one wavelength, rather larger than any normal value of k_0^2/n_0^2, so that the effect is quite small. It originates in a curious pattern in the otherwise exponentially falling irradiance. It is caused by the presence of the interface and is a cyclic fluctuation in the rate of irradiance reduction. Note that the transmittance is unity if the coating is designed to match $n_0 - ik_0$ rather than its complex conjugate.

A dielectric coating that transforms an admittance of y_1 to an admittance of y_0^* will also, when reversed, exactly transform an admittance of y_0 to y_1^*. This is dealt with in more detail later when induced transmission filters are discussed. Thus, the optimum coating to give highest transmittance will be the same in both directions. This implies that an absorbing substrate in identical dielectric incident and emergent media should have exactly similar antireflection coatings on both front and rear surfaces.

Although also a little premature, it is convenient to mention here that the calculation of the properties of a coated slice of material involves multiple beams that are combined either coherently or incoherently. The coherent case is simply the usual interference calculation and we will return to that when we deal with induced transmission filters. We will see then that as the absorbing film becomes thicker, the matching rules for an induced transmission filter tend to Equation 2.82. The incoherent case is at first sight less obvious. An estimate of the reflected beam is necessary for a multiple beam calculation. Such calculations imply that the absorption is not sufficiently high to eliminate completely a beam that sustains two traversals of the system. This implies, in turn, a negligible absorption in the space of one wavelength; in other words, $4\pi k_0$ is very small. The upper limit on the size of the effect under discussion is k_0^2/n_0^2, and this will still be less significant. For an incoherent calculation to be appropriate, there must be a jumbling of phase that washes out its effect. We can suppose for this discussion that the jumbling comes from a variation in the position of the reflecting surface over the aperture. The variation of the extra term in Equation 2.82 is locked for its phase to the reflecting surface, so at any exactly plane surface that may be chosen as a reference, an average of the extra term is appropriate and this will be zero because ρ will have a phase that varies throughout the four quadrants. For multiple beam calculations, therefore, the reflectance can be taken simply as $\rho\rho^*$. Where k_0^2/n_0^2 is significant, the absorption will be very high and certainly enough for the influence of the multiple beams to be automatically negligible.

2.2.5 Oblique Incidence in Absorbing Media

Remembering what we said in the previous section, we limit this to a transparent incident medium and an absorbing second, or emergent, medium. Our first aim must be to ensure that the phase factors are consistent. Taking advantage of some of the earlier results, we can write the phase factors as follows:

Incident $\quad \exp\{i[\omega t - (2\pi n_0/\lambda)(x\sin\vartheta_0 + z\cos\vartheta_0)]\}$

Reflected $\quad \exp\{i[\omega t - (2\pi n_0/\lambda)(x\sin\vartheta_0 - z\cos\vartheta_0)]\}$

Transmitted $\quad \exp\{i[\omega t - (2\pi\{n_1 - ik_1\}/\lambda)(\alpha x + \gamma z)]\}$

where α and γ in the transmitted phase factors are the only unknowns. The phase factors must be identically equal for all x and t with $z = 0$. This implies

$$\alpha = \frac{n_0 \sin\vartheta_0}{(n_1 - ik_1)}$$

and, since $\alpha^2 + \gamma^2 = 1$

$$\gamma = (1 - \alpha^2)^{1/2}$$

There are two solutions to this equation and we must decide which is to be adopted. We note that it is strictly $(n_1 - ik_1)\alpha$ and $(n_1 - ik_1)\gamma$ that are required.

$$\begin{aligned}(n_1 - ik_1)\gamma &= \left[(n_1 - ik_1)^2 - n_0^2 \sin^2 \vartheta_0\right]^{1/2} \\ &= \left[n_1^2 - k_1^2 - n_0^2 \sin^2 \vartheta_0 - i2n_1k_1\right]^{1/2}\end{aligned} \tag{2.83}$$

The quantity within the square root is in either the third or fourth quadrant, and so the square roots are in the second quadrant (of the form $-a + ib$) and in the fourth quadrant (of the form $a - ib$). If we consider what happens when these values are substituted into the phase factors, we see that the fourth quadrant solution must be correct because this leads to an exponential fall-off with z of amplitude together with a change in phase of the correct sense. The second quadrant solution would lead to an increase with z and a change in phase of the incorrect sense, which would imply a wave traveling in the opposite direction. The fourth quadrant solution is also consistent with the solution for the absorption-free case. The transmitted phase factor is therefore of the form

$$\begin{aligned}&\exp\{i[\omega t - (2\pi n_0 \sin \vartheta_0 x/\lambda) - (2\pi/\lambda)(a - ib)z]\} \\ &\qquad = \exp(-2\pi bz/\lambda)\exp\{i[\omega t - (2\pi n_0 \sin \vartheta_0 x/\lambda) - (2\pi az/\lambda)]\}\end{aligned}$$

where

$$(a - ib) = [n_1^2 - k_1^2 - n_0^2 \sin^2 \vartheta_0 - i2n_1k_1]^{1/2}$$

A wave that possesses such a phase factor is known as inhomogeneous. The exponential fall-off in amplitude is along the z-axis, while the propagation direction in terms of phase is determined by the direction cosines, which can be extracted from

$$(2\pi n_0 \sin \vartheta_0 x/\lambda) + (2\pi az/\lambda)$$

The existence of such waves is another good reason for our choosing to consider the components of the fields parallel to the boundary and the flow of energy normal to the boundary.

We should note at this stage that provided we include the possibility of complex angles, the formulation of the absorption-free case applies equally well to absorbing media and we can write

$$(n_1 - ik_1)\sin\vartheta_1 = n_0 \sin\vartheta_0$$

$$\alpha = \sin\vartheta_1$$

$$\gamma = \cos\vartheta_1$$

$$(a - ib) = (n_1 - ik_1)\cos\vartheta_1$$

The calculation of amplitudes follows the same pattern as before. However, we have not previously examined the implications of an inhomogeneous wave. Our main concern is the calculation of the tilted admittance connected with such a wave. Because the x, y, and t variations of the wave are contained in the phase factor, we can write

$$\text{curl} \equiv \left(\frac{\partial}{\partial x}\boldsymbol{i} + \frac{\partial}{\partial x}\boldsymbol{j} + \frac{\partial}{\partial x}\boldsymbol{k}\right) \times$$

$$\equiv \left(-i\frac{2\pi N}{\lambda}\alpha\boldsymbol{i} - i\frac{2\pi N}{\lambda}\gamma\boldsymbol{k}\right) \times$$

and

$$\frac{\partial}{\partial t} \equiv i\omega$$

where the k is a unit vector in the z direction and should not be confused with the extinction coefficient k.

For p-waves, the H vector is parallel to the boundary in the y direction, and so $H = \mathcal{H}_y\boldsymbol{j}$. The component of E parallel to the boundary will then be in the x direction, $\mathcal{E}_x\boldsymbol{i}$. We follow the analysis leading up to Equation 2.25 and, as before,

$$\text{curl}\boldsymbol{H} = \sigma\boldsymbol{E} + \varepsilon\frac{\partial \boldsymbol{E}}{\partial t}$$

$$= (\sigma + i\omega\varepsilon)\boldsymbol{E}$$

$$= \frac{i\omega N^2}{c^2\mu}\boldsymbol{E}$$

Now the tangential component of curl H is in the x direction so that

$$-i\frac{2\pi N}{\lambda}\gamma\,(\boldsymbol{k}\times\boldsymbol{j})\,\mathcal{H}_y = i\frac{\omega N^2}{c^2\mu}\,\mathcal{E}_x\boldsymbol{i}$$

But

$$-(\boldsymbol{k}\times\boldsymbol{j}) = \boldsymbol{i}$$

so that

$$\eta_p = \frac{\mathcal{H}_y}{\mathcal{E}_x} = \frac{\omega N\lambda}{2\pi c^2\mu\gamma} = \frac{N}{c\mu\gamma}$$
$$= \frac{N\mathcal{Y}}{\gamma} = \frac{y}{\gamma}$$

For the *s*-waves, we use

$$\text{curl}\boldsymbol{E} = -\frac{\partial \boldsymbol{B}}{\partial t} = -\mu\frac{\partial \boldsymbol{H}}{\partial t}$$

E is now along the *y*-axis and a similar analysis to that for *p*-waves yields

$$\eta_s = \frac{\mathcal{H}_x}{\mathcal{E}_y} = N\mathcal{Y}\gamma = y\gamma \tag{2.84}$$

Now γ can be identified as cos ϑ, provided that ϑ is permitted to be complex, and so

$$\eta_p = y/\cos\vartheta$$
$$\eta_s = y\cos\vartheta \tag{2.85}$$

Alternatively, we can use the expressions in Equations 2.83 and 2.84 together with the fact that $y = (n - ik)\mathcal{Y}$ to give

$$\eta_s = \mathcal{Y}\left[n_1^2 - k_1^2 - n_0^2\sin^2\vartheta_0 - i2n_1k_1\right]^{1/2} \tag{2.86}$$

The fourth quadrant is the correct solution, and then

$$\eta_p = \frac{y^2}{\eta_s} \tag{2.87}$$

This second form is completely consistent with Equation 2.85 but avoids any problems with the quadrant. Then, the amplitude and irradiance coefficients become, as before,

$$\rho = \frac{\eta_0 - \eta_1}{\eta_0 + \eta_1} \tag{2.88}$$

$$\tau = \frac{2\eta_0}{\eta_0 + \eta_1} \tag{2.89}$$

$$R = \left(\frac{\eta_0 - \eta_1}{\eta_0 + \eta_1}\right)\left(\frac{\eta_0 - \eta_1}{\eta_0 + \eta_1}\right)^* \tag{2.90}$$

$$T = \frac{4\eta_0 \operatorname{Re}(\eta_1)}{(\eta_0 + \eta_1)(\eta_0 + \eta_1)^*} \tag{2.91}$$

And, of course, these expressions are valid for absorption-free media as well.

2.3 The Reflectance of a Thin Film

A simple extension of the above analysis occurs in the case of a thin, plane parallel film of material covering the surface of a substrate. The presence of two (or more) interfaces means that a number of beams will be produced by successive reflections and the properties of the film will be determined by the summation of these beams. We say that the film is *thin* when full interference effects can be detected in the reflected or transmitted light. We describe such a case as *coherent.* When no interference effects can be detected, the film is described as *thick* and the case is described as *incoherent.* The coherent and incoherent cases depend on the presence or absence of a constant phase relationship between the various beams, and this will depend on the nature of the light and the receiver and on the quality of the film. The same film can appear thin or thick under differing illumination conditions. Normally, we will find that the films on the substrates can be treated as thin, while the substrates supporting the films can be considered thick. Thick films and substrates will be considered toward the end of this chapter. Here, we concentrate on the thin case.

The arrangement is illustrated in Figure 2.6. At this stage, it is convenient to introduce a new notation. We denote waves in the direction of incidence by the symbol + (i.e., positive-going) and waves in the opposite direction by – (i.e., negative-going).

The interfaces between the film and the incident medium and the substrate, denoted by the symbols *a* and *b*, can be treated in exactly the same way as the simple boundary already discussed. We consider the tangential components of the fields. There is no negative-going wave in the substrate and the waves in the film can be summed into one resultant positive-going wave and one resultant negative-going wave. At this interface, then, the tangential components of ***E*** and ***H*** are

$$\mathcal{E}_b = \mathcal{E}_{1b}^+ + \mathcal{E}_{1b}^-$$

$$\mathcal{H}_b = \eta_1 \mathcal{E}_{1b}^+ - \eta_1 \mathcal{E}_{1b}^-$$

where we are neglecting the common phase factors and where $\mathcal{E}_b$ and $\mathcal{H}_b$, represent the resultants. Hence

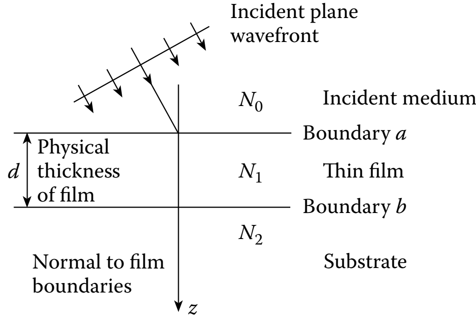

FIGURE 2.6
Plane wave incident on a thin film.

$$\mathcal{E}_{1b}^{+} = \frac{1}{2}(\mathcal{H}_b/\eta_1 + \mathcal{E}_b) \tag{2.92}$$

$$\mathcal{E}_{1b}^{-} = \frac{1}{2}(-\mathcal{H}_b/\eta_1 + \mathcal{E}_b) \tag{2.93}$$

$$\mathcal{H}_{1b}^{+} = \eta_1\mathcal{E}_{1b}^{+} = \frac{1}{2}(\mathcal{H}_b + \eta_1\mathcal{E}_b) \tag{2.94}$$

$$\mathcal{H}_{1b}^{-} = -\eta_1\mathcal{E}_{1b}^{-} = \frac{1}{2}(\mathcal{H}_b - \eta_1\mathcal{E}_b) \tag{2.95}$$

The fields at the other interface *a* at the same instant and at a point with identical *x* and *y* coordinates can be determined by altering the phase factors of the waves to allow for a shift in the *z* coordinate from 0 to –*d*. The phase factor of the positive-going wave will be multiplied by exp($i\delta$) where

$$\delta = 2\pi N_1 d\cos\vartheta_1/\lambda$$

and ϑ_1 may be complex, while the negative-going phase factor will be multiplied by exp($-i\delta$). We imply that this is a valid procedure when we say that the film is thin. The values of E and H at the interface are now, using Equations 2.92 through 2.95:

$$\mathcal{E}_{1a}^{+} = \mathcal{E}_{1b}^{+}e^{i\delta} = \frac{1}{2}(\mathcal{H}_b/\eta_1 + \mathcal{E}_b)e^{i\delta}$$

$$\mathcal{E}_{1a}^{-} = \mathcal{E}_{1b}^{-}e^{i\delta} = \frac{1}{2}(-\mathcal{H}_b/\eta_1 + \mathcal{E}_b)e^{-i\delta}$$

$$\mathcal{H}_{1a}^{+} = \mathcal{H}_{1b}^{+} e^{i\delta} = \frac{1}{2}(\mathcal{H}_b + \eta_1 \mathcal{E}_b) e^{i\delta}$$

$$\mathcal{H}_{1a}^{-} = \mathcal{H}_{1b}^{+} e^{i\delta} = \frac{1}{2}(\mathcal{H}_b - \eta_1 \mathcal{E}_b) e^{-i\delta}$$

so that

$$\begin{aligned}
\mathcal{E}_a &= \mathcal{E}_{1a}^{+} + \mathcal{E}_{1a}^{-} \\
&= \mathcal{E}_b \left(\frac{e^{i\delta} + e^{-i\delta}}{2} \right) + \mathcal{H}_b \left(\frac{e^{i\delta} - e^{-i\delta}}{2\eta_1} \right) \\
&= \mathcal{E}_b \cos\delta + \mathcal{H}_b \frac{i \sin\delta}{\eta_1}
\end{aligned}$$

$$\begin{aligned}
\mathcal{H}_a &= \mathcal{H}_{1a}^{+} + \mathcal{H}_{1a}^{-} \\
&= \mathcal{E}_b \eta_1 \left(\frac{e^{i\delta} - e^{-i\delta}}{2} \right) + \mathcal{H}_b \left(\frac{e^{i\delta} + e^{-i\delta}}{2} \right) \\
&= \mathcal{E}_b i\eta_1 \sin\delta + \mathcal{H}_b \cos\delta
\end{aligned}$$

These two simultaneous equations can be written in matrix notation as

$$\begin{bmatrix} \mathcal{E}_a \\ \mathcal{H}_a \end{bmatrix} = \begin{bmatrix} \cos\delta & (i\sin\delta)/\eta_1 \\ i\eta_1 \sin\delta & \cos\delta \end{bmatrix} \begin{bmatrix} \mathcal{E}_b \\ \mathcal{H}_b \end{bmatrix} \tag{2.96}$$

Because the tangential components of ***E*** and ***H*** are continuous across a boundary and because there is only a positive-going wave in the substrate, this relationship connects the tangential components of ***E*** and ***H*** at the incident interface with the tangential components of ***E*** and ***H*** transmitted through the final interface. The 2 × 2 matrix on the right-hand side of Equation 2.96 is known as the characteristic matrix of the thin film.

We define the input optical admittance of the assembly by analogy with Equation 2.67 as

$$Y = \mathcal{H}_a / \mathcal{E}_a \tag{2.97}$$

when the problem becomes merely that of finding the reflectance of a simple interface between an incident medium of admittance η_0 and a medium of admittance Y, i.e.,

$$\rho = \frac{\eta_0 - Y}{\eta_0 + Y}$$

$$R = \left(\frac{\eta_0 - Y}{\eta_0 + Y}\right)\left(\frac{\eta_0 - Y}{\eta_0 + Y}\right)^* \tag{2.98}$$

We can normalize Equation 2.96 by dividing through by $\mathcal{E}_b$ to give

$$\begin{bmatrix} \mathcal{E}_a/\mathcal{E}_b \\ \mathcal{H}_a/\mathcal{E}_b \end{bmatrix} = \begin{bmatrix} B \\ C \end{bmatrix} = \begin{bmatrix} \cos\delta & (i\sin\delta)/\eta_1 \\ i\eta_1 \sin\delta & \cos\delta \end{bmatrix} \begin{bmatrix} 1 \\ \eta_2 \end{bmatrix} \tag{2.99}$$

and B and C, the normalized electric and magnetic fields at the front interface are the quantities from which we will be extracting the properties of the thin-film system. Clearly, from Equations 2.97 and 2.99, we can write

$$Y = \frac{\mathcal{H}_a}{\mathcal{E}_a} = \frac{C}{B} = \frac{\eta_2 \cos\delta + i\eta_1 \sin\delta}{\cos\delta + i(\eta_2/\eta_1)\sin\delta} \tag{2.100}$$

and from Equations 2.100 and 2.98 we can calculate the reflectance.

$$\begin{bmatrix} B \\ C \end{bmatrix}$$

is known as the characteristic matrix of the assembly.

2.4 The Reflectance of an Assembly of Thin Films

Let another film be added to the single film of the previous section so that the final interface is now denoted by c, as shown in Figure 2.7. The characteristic matrix of the film nearest the substrate is

$$\begin{bmatrix} \cos\delta & (i\sin\delta_2)/\eta_2 \\ i\eta_2 \sin\delta_2 & \cos\delta_2 \end{bmatrix} \tag{2.101}$$

and from Equation 2.96

$$\begin{bmatrix} \mathcal{E}_b \\ \mathcal{H}_b \end{bmatrix} = \begin{bmatrix} \cos\delta_2 & (i\sin\delta_2)/\eta_2 \\ i\eta_2 \sin\delta_2 & \cos\delta_2 \end{bmatrix} \begin{bmatrix} \mathcal{E}_c \\ \mathcal{H}_c \end{bmatrix}$$

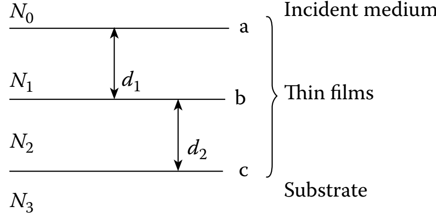

FIGURE 2.7
Notation for two films on a surface.

We can apply Equation 2.96 again to give the parameters at interface a, i.e.,

$$\begin{bmatrix} \mathcal{E}_a \\ \mathcal{H}_a \end{bmatrix} = \begin{bmatrix} \cos\delta_1 & (i\sin\delta_1)/\eta_1 \\ i\eta_1\sin\delta_1 & \cos\delta_1 \end{bmatrix} \begin{bmatrix} \cos\delta_2 & (i\sin\delta_2)/\eta_2 \\ i\eta_2\sin\delta_2 & \cos\delta_2 \end{bmatrix} \begin{bmatrix} \mathcal{E}_c \\ \mathcal{H}_c \end{bmatrix}$$

and the characteristic matrix of the assembly, by analogy with Equation 2.99 is,

$$\begin{bmatrix} B \\ C \end{bmatrix} = \begin{bmatrix} \cos\delta_1 & (i\sin\delta_1)/\eta_1 \\ i\eta_1\sin\delta_1 & \cos\delta_1 \end{bmatrix} \begin{bmatrix} \cos\delta_2 & (i\sin\delta_2)/\eta_2 \\ i\eta_2\sin\delta_2 & \cos\delta_2 \end{bmatrix} \begin{bmatrix} 1 \\ \eta_3 \end{bmatrix}$$

Y is, as before, C/B, and the amplitude reflection coefficient and the reflectance are, from Equation 2.98,

$$\rho = \frac{\eta_0 - Y}{\eta_0 + Y}$$

$$R = \left(\frac{\eta_0 - Y}{\eta_0 + Y}\right)\left(\frac{\eta_0 - Y}{\eta_0 + Y}\right)^* \tag{2.102}$$

This result can be immediately extended to the general case of an assembly of q layers, when the characteristic matrix is simply the product of the individual matrices taken in the correct order, i.e.,

$$\begin{bmatrix} B \\ C \end{bmatrix} = \left\{ \prod_{r=1}^{q} \begin{bmatrix} \cos\delta_r & (i\sin\delta_r)/\eta_r \\ i\eta_r\sin\delta_r & \cos\delta_r \end{bmatrix} \right\} \begin{bmatrix} 1 \\ \eta_m \end{bmatrix} \tag{2.103}$$

where

$$\delta_r = \frac{2\pi N_r d_r \cos\vartheta_r}{\lambda}$$

$$\eta_r = \mathscr{Y} N_r \cos\vartheta_r \qquad \text{for } s\text{-polarization (TE)}$$

$$\eta_r = \mathscr{Y} N_r / \cos\vartheta_r \qquad \text{for } p\text{-polarization (TM)}$$

and where we have now used the suffix *m* to denote the substrate or emergent medium.

$$\eta_m = \mathscr{Y} N_m \cos\vartheta_m \qquad \text{for } s\text{-polarization (TE)}$$

$$\eta_m = \mathscr{Y} N_m / \cos\vartheta_m \qquad \text{for } p\text{-polarization (TM)}$$

If ϑ_0 the angle of incidence, is given, the values of ϑ_r, can be found from Snell's law, i.e.,

$$N_0 \sin\vartheta_0 = N_r \sin\vartheta_r = N_m \sin\vartheta_m \tag{2.104}$$

Equation 2.103 is of prime importance in optical thin-film work and forms the basis of almost all calculations.

A useful property of the characteristic matrix of a thin film is that the determinant is unity. This means that the determinant of the product of any number of these matrices is also unity.

It avoids difficulties over signs and quadrants if, in the case of absorbing media, the arrangement used for computing phase thicknesses and admittances is:

$$\delta_r = (2\pi/\lambda) d_r (n_r^2 - k_r^2 - n_0^2 \sin^2\vartheta_0 - 2in_r k_r)^{1/2} \tag{2.105}$$

With the correct solution being in the fourth quadrant. Then

$$\eta_{rs} = \mathscr{Y}(n_r^2 - k_r^2 - n_0^2 \sin^2\vartheta_0 - 2in_r k_r)^{1/2} \tag{2.106}$$

also in the fourth quadrant, and

$$\eta_{rp} = \frac{y_r^2}{\eta_{rs}} = \frac{\mathscr{Y}^2 (n_r - ik_r)^2}{\eta_{rs}} \tag{2.107}$$

It is useful to examine the phase shift associated with the reflected beam. Let $Y = a + ib$. Then with η_0 real

$$\rho = \frac{\eta_0 - a - ib}{\eta_0 + a + ib}$$

$$= \frac{(\eta_0^2 - a^2 - b^2) - i(2b\eta_0)}{(\eta_0 + a)^2 + b^2}$$

i.e.,

$$\tan\varphi = \frac{(-2b\eta_0)}{(\eta_0^2 - a^2 - b^2)} \tag{2.108}$$

where φ is the phase shift. This must be interpreted, of course, on the basis of the sign convention we have already established in Figure 2.3. It is important to preserve the signs of the numerator and denominator separately as shown; otherwise, the quadrant cannot be uniquely specified. The rule is simple. It is the quadrant in which the vector associated with ρ lies and the following scheme can be derived by treating the denominator as the x coordinate and the numerator as the y coordinate.

Numerator	+	+	−	−
Denominator	+	−	+	−
Quadrant	1st	2nd	4th	3rd

Note particularly that the reference surface for the calculation of phase shift on reflection is the front surface of the multilayer.

2.5 Reflectance, Transmittance, and Absorptance

Sufficient information is included in Equation 2.103 to allow the transmittance and absorptance of a thin-film assembly to be calculated. For this to have a physical meaning, as we have already seen, the incident medium should be transparent, that is, η_0 must be real. The substrate need not be transparent, but the transmittance calculated will be the transmittance into, rather than through, the substrate.

First, we calculate the net irradiance at the exit side of the assembly, which we take as the kth interface. This is given by

$$I_k = \frac{1}{2}\mathrm{Re}(\mathcal{E}_k \mathcal{H}_k^*)$$

where, again, we are dealing with the component of irradiance normal to the interfaces.

$$\begin{aligned} I_k &= \frac{1}{2}\mathrm{Re}(\mathcal{E}_k \eta_m^* \mathcal{E}_k^*) \\ &= \frac{1}{2}\mathrm{Re}(\eta_m^*)\mathcal{E}_k \mathcal{E}_k^* \end{aligned} \tag{2.109}$$

If the characteristic matrix of the assembly is

$$\begin{bmatrix} B \\ C \end{bmatrix}$$

then the net irradiance at the entrance to the assembly is

$$I_a = \frac{1}{2}\text{Re}(BC^*)\mathcal{E}_k\mathcal{E}_k^* \tag{2.110}$$

Let the incident irradiance be denoted by I_i; then Equation 2.110 represents the irradiance actually entering the assembly, which is $(1 - R)I_i$:

$$(1 - R)I_i = \frac{1}{2}\text{Re}(BC^*)\mathcal{E}_k\mathcal{E}_k^*$$

i.e.,

$$I_i = \frac{\text{Re}(BC^*)\mathcal{E}_k\mathcal{E}_k^*}{2(1 - R)}$$

Equation 2.109 represents the irradiance leaving the assembly and entering the substrate, and so the transmittance T is

$$T = \frac{I_k}{I_i} = \frac{\text{Re}(\eta_m)(1 - R)}{\text{Re}(BC^*)} \tag{2.111}$$

The absorptance A in the multilayer is connected with R and T by the relationship

$$1 = R + T + A$$

so that

$$A = 1 - R - T = (1 - R)\left(1 - \frac{\text{Re}(\eta_m)}{\text{Re}(BC^*)}\right) \tag{2.112}$$

In the absence of absorption in any of the layers, it can readily be shown that the above expressions are consistent with $A = 0$ and $T + R = 1$, for the individual film matrices will have determinants of unity and the product of any number of these matrices will also have a determinant of unity. The product of the matrices can be expressed as

$$\begin{bmatrix} \alpha & i\beta \\ i\gamma & \delta \end{bmatrix}$$

where $\alpha\delta + \gamma\beta = 1$ and, because there is no absorption, α, β, γ and δ are all real.

$$\begin{bmatrix} B \\ C \end{bmatrix} \begin{bmatrix} \alpha & i\beta \\ i\gamma & \delta \end{bmatrix} \begin{bmatrix} 1 \\ \eta_m \end{bmatrix} = \begin{bmatrix} \alpha + i\beta\eta_m \\ \delta\eta_m + i\gamma \end{bmatrix}$$

$$\begin{aligned} \mathrm{Re}(BC^*) &= \mathrm{Re}[(\alpha + i\beta\eta_m)(\delta\eta_m - i\gamma)] = (\alpha\delta + \gamma\beta)\,\mathrm{Re}(\eta_m) \\ &= \mathrm{Re}(\eta_m) \end{aligned}$$

and the result follows.

We can manipulate Equations 2.111 and 2.112 into slightly better forms. From Equation 2.98

$$R = \left(\frac{\eta_0 B - C}{\eta_0 B + C}\right)\left(\frac{\eta_0 B - C}{\eta_0 B + C}\right)^* \tag{2.113}$$

so that

$$(1 - R) = \frac{2\eta_0(BC^* + B^*C)}{(\eta_0 B + C)(\eta_0 B + C)^*} \tag{2.114}$$

Inserting this result in Equation 2.111 we obtain

$$T = \frac{4\eta_0\,\mathrm{Re}(\eta_m)}{(\eta_0 B + C)(\eta_0 B + C)^*} \tag{2.115}$$

and in Equation 2.112

$$A = \frac{4\eta_0\,\mathrm{Re}(BC^* - \eta_m)}{(\eta_0 B + C)(\eta_0 B + C)^*} \tag{2.116}$$

Equations 2.113, 2.115, and 2.116 are the most useful forms of the expressions for R, T, and A.

An important quantity that we shall discuss in a later section of this chapter is $T/(1 - R)$, known as the potential transmittance ψ. From Equation 2.111

$$\psi = \frac{T}{(1 - R)} = \frac{\mathrm{Re}(\eta_m)}{\mathrm{Re}(BC^*)} \tag{2.117}$$

The phase change on reflection (Equation 2.108) can also be put in a form compatible with Equations 2.113 through 2.116.

$$\varphi = \arctan\left(\frac{\mathrm{Im}\left[\eta_m\left(BC^* - CB^*\right)\right]}{\left(\eta_m^2 BB^* - CC^*\right)}\right) \tag{2.118}$$

The quadrant of φ is given by the same arrangement of signs of numerator and denominator as Equation 2.108. The phase change on reflection is measured at the front surface of the multilayer.

Phase shift on transmission is sometimes important. This can be obtained in a way similar to the phase shift on reflection. We denote the phase shift by ζ, and we define it as the difference in phase between the resultant transmitted wave as it enters the emergent medium and the incident wave exactly at the front surface—that is, as it enters the multilayer. The electric field amplitude at the emergent surface has been normalized to unity, and so the phase may be taken as zero. Then we simply have to find the expression, which will involve B and C, for the incident amplitude.

These are the normalized total tangential electric and magnetic fields. So we can write:

$$\mathcal{E}_i + \mathcal{E}_r = B$$

$$\eta_0 \mathcal{E}_i - \eta_0 \mathcal{E}_r = C$$

Then we eliminate E_r to give

$$\mathcal{E}_i = \frac{1}{2}\left(B + \frac{C}{\eta_0}\right)$$

and the amplitude transmission coefficient as

$$\tau = \frac{2\eta_0}{(\eta_0 B + C)} = \frac{2\eta_0(\eta_0 B + C)^*}{(\eta_0 B + C)(\eta_0 B + C)^*}$$

so that

$$\zeta = \arctan\left[\frac{-\mathrm{Im}(\eta_0 B + C)}{\mathrm{Re}(\eta_0 B + C)}\right] \tag{2.119}$$

Again, it is important to keep the signs of the numerator and the denominator separately. Then the quadrant is given by the same arrangement of signs as Equation 2.108.

2.6 Units

We have been using the SI units in the work so far. In this system, y, η, and Y are measured in siemens. Much thin-film literature, especially the early literature, has been written in Gaussian units. In Gaussian units, $\mathscr{Y}$, the admittance

of free space, is unity, and so, since $y = N\mathcal{Y}$, y (the optical admittance) and N (the refractive index) are numerically equal at normal incidence, although N is a number without units. The position is different in SI units, where $\mathcal{Y}$ is 2.6544×10^{-3} S. We could, if we choose, measure y and η in units of $\mathcal{Y}$ siemens, which we can call free space units, and in this case y becomes numerically equal to N, just as in the Gaussian system. This is a perfectly valid procedure, and all the expressions for ratioed quantities, notably reflectance, transmittance, absorptance, and potential transmittance, are unchanged. This applies particularly to Equations 2.103 and 2.113 through 2.117. We must simply take due care when calculating absolute rather than relative irradiance and also when deriving the magnetic field. In particular, Equation 2.96 becomes

$$\begin{bmatrix} \mathcal{E}_a \\ \mathcal{H}_a/\mathcal{Y} \end{bmatrix} = \begin{bmatrix} \cos\delta & (i\sin\delta)/\eta_1 \\ i\eta_1\sin\delta & \cos\delta \end{bmatrix} \begin{bmatrix} \mathcal{E}_b \\ \mathcal{H}_b/\mathcal{Y} \end{bmatrix} \tag{2.120}$$

where η is now measured in free space units. In most cases in this book, either arrangement can be used. In some cases, particularly where we are using graphical techniques, we shall use free space units, because otherwise the scales become quite cumbersome.

2.7 Summary of Important Results

We have now covered all the basic theory necessary for the understanding of the remainder of the book. It has been a somewhat long and involved discussion, so we now summarize the principal results. The statement numbers refer to those in the text where the particular quantities were originally introduced.

Refractive index is defined as the ratio of the velocity of light in free space c to the velocity of light in the medium v. When refractive index is real, it is denoted by n, but it is frequently complex and then is denoted by N.

$$N = c/v = n - ik \tag{2.19}$$

N is often called the complex refractive index, n the real refractive index (or often simply refractive index), and k the extinction coefficient. N is always a function of λ.

k is related to the absorption coefficient α by

$$\alpha = 4\pi k/\lambda \tag{2.35}$$

Light waves are electromagnetic and a homogeneous, plane, linearly polarized harmonic (or monochromatic) wave may be represented by expressions of the form.

$$\boldsymbol{E} = \mathcal{E}\exp[i\omega t - (2\pi N/\lambda)z + \varphi] \tag{2.22}$$

where z is the distance along the direction of propagation, $\boldsymbol{E}$ is the electric field, $\mathcal{E}$ is the electric amplitude, and φ is an arbitrary phase. A similar expression holds for $\boldsymbol{H}$, the magnetic field:

$$\boldsymbol{H} = \mathcal{H}\exp[i\omega t - (2\pi N/\lambda)z + \varphi'] \tag{2.121}$$

where φ, φ', and N are not independent. The physical significance is attached to the real parts of the above expressions (or the imaginary parts).

The phase change suffered by the wave on traversing a distance d of the medium is, therefore,

$$-\frac{2\pi Nd}{\lambda} = -\frac{2\pi nd}{\lambda} + i\frac{2\pi kd}{\lambda} \tag{2.122}$$

and the imaginary part can be interpreted as a reduction in amplitude (by substituting in Equation 2.22). Note that in our convention, a wave suffers a phase lag on traversal of the distance d.

The optical admittance is defined as the ratio of the magnetic and electric fields (Equations 2.25 to 2.30)

$$y = H/E$$

and y is usually complex. In free space, y is real and is denoted by $\mathcal{Y}$.

$$\mathcal{Y} = 2.6544 \times 10^{-3}\,\mathrm{S} \tag{2.123}$$

The optical admittance of a medium is connected with the refractive index by

$$y = N\mathcal{Y} \tag{2.124}$$

(In Gaussian units, $\mathcal{Y}$ is unity and y and N are numerically the same. In SI units, we can make y and N numerically equal by expressing y in units of $\mathcal{Y}$, i.e., free space units. All expressions for reflectance, transmittance, etc. involving ratios will remain valid, but care must be taken when computing absolute irradiances, although these are not often needed in thin-film optics, except where damage studies are involved.)

The irradiance of the light, defined as the mean rate of flow of energy per unit area carried by the wave, is given by

$$I = \frac{1}{2}\mathrm{Re}(EH^*) \tag{2.33}$$

This can also be written

$$I = \frac{1}{2} n\mathcal{Y}EE^{*} \tag{2.125}$$

where * denotes complex conjugate.

At a boundary between two media, denoted by suffix 0 for the incident medium and by suffix 1 for the exit medium, the incident beam is split into a reflected beam and a transmitted beam. For *normal incidence,* we have

$$\rho = \frac{\mathcal{E}_r}{\mathcal{E}_i} = \frac{y_0 - y_1}{y_0 + y_1} = \frac{(n_0 - ik_0)\mathcal{Y} - (n_1 - ik_1)\mathcal{Y}}{(n_0 - ik_0)\mathcal{Y} + (n_1 - ik_1)\mathcal{Y}} = \frac{(n_0 - n_1) - i(k_0 - k_1)}{(n_0 + n_1) - i(k_0 + k_1)} \tag{2.73}$$

$$\tau = \frac{\mathcal{E}_t}{\mathcal{E}_i} = \frac{2y_0}{y_0 - y_1} = \frac{2(n_0 - ik_0)\mathcal{Y}}{(n_0 - ik_0)\mathcal{Y} + (n_1 - ik_1)\mathcal{Y}} = \frac{2(n_0 - ik_0)}{(n_0 + n_1) - i(k_0 + k_1)} \tag{2.74}$$

where ρ is the amplitude reflection coefficient and τ is the amplitude transmission coefficient.

There are fundamental difficulties associated with the definitions of reflectance and transmittance unless the incident medium is absorption-free, i.e., N_0 and y_0 are real. For that case:

$$R = \rho\rho^{*} \left(\frac{y_0 - y_1}{y_0 + y_1} \right) \left(\frac{y_0 - y_1}{y_0 + y_1} \right)^{*} \tag{2.77}$$

$$T = \frac{4y_0 \,\mathrm{Re}(y_1)}{(y_0 + y_1)(y_0 + y_1)^{*}} \tag{2.78}$$

Oblique incidence calculations are simpler if the wave is split into two linearly polarized components, one with the electric vector in the plane of incidence, known as *p*-polarized (or TM, for transverse magnetic field) and one with the electric vector normal to the plane of incidence, known as *s*-polarized (or TE, for transverse electric field). The propagation of each of these two waves can be treated quite independently of the other. Calculations are further simplified if only energy flows normal to the boundaries and electric and magnetic fields parallel to the boundaries are considered, because then we have a formulation that is equivalent to a homogeneous wave.

We must introduce the idea of a tilted optical admittance η, which is given by

$$\eta_p = \frac{N\mathcal{Y}}{\cos\vartheta} \quad \text{(for p-waves)}$$

$$\eta_s = N\mathcal{Y}\cos\vartheta \quad \text{(for s-waves)} \tag{2.85}$$

where N and ϑ denote either N_0 and ϑ or N_1 and ϑ_1 as appropriate. ϑ_1 is given by Snell's law, in which complex angles may be included

$$N_0 \sin \vartheta_0 = N_1 \sin \vartheta_1 \tag{2.126}$$

Denoting η_p or η_s by η, we have, for either direction of polarization,

$$\rho = \frac{\eta_0 - \eta_1}{\eta_0 + \eta_1} \tag{2.88}$$

$$\tau = \frac{2\eta_0}{\eta_0 + \eta_1} \tag{2.89}$$

If η_0 is real, we can write

$$R = \left(\frac{\eta_0 - \eta_1}{\eta_0 + \eta_1}\right)\left(\frac{\eta_0 - \eta_1}{\eta_0 + \eta_1}\right)^* \tag{2.90}$$

$$T = \frac{4\eta_0 \,\mathrm{Re}(\eta_1)}{(\eta_0 + \eta_1)(\eta_0 + \eta_1)^*} \tag{2.91}$$

The phase shift experienced by the wave as it traverses a distance d normal to the boundary is then given by $-2\pi Nd\cos\vartheta/\lambda$.

The reflectance of an assembly of thin films is calculated through the concept of optical admittance. We replace the multilayer by a single surface, which presents an admittance Y that is the ratio of the total tangential magnetic and electric fields and is given by

$$Y = C/B \tag{2.127}$$

where

$$\begin{bmatrix} B \\ C \end{bmatrix} = \left\{ \prod_{r=1}^{q} \begin{bmatrix} \cos\delta_r & (i\sin\delta_r)/\eta_r \\ i\eta_r \sin\delta_r & \cos\delta_r \end{bmatrix} \right\} \begin{bmatrix} 1 \\ \eta_m \end{bmatrix} \tag{2.103}$$

$\delta_r = 2\pi Nd\cos\vartheta/\lambda$ and η_m = substrate admittance.

The order of multiplication is important. If q is the layer next to the substrate, then the order is

$$\begin{bmatrix} B \\ C \end{bmatrix} = [M_1][M_2]\cdots[M_q]\begin{bmatrix} 1 \\ \eta_m \end{bmatrix} \tag{2.128}$$

M_1 indicates the matrix associated with layer 1, and so on. Y and η are in the same units. If η is in siemens, then so also is Y, or if η is in free space units (i.e., units of Y), then Y will be in free space units also. As in the case of a single surface, η_0 must be real for reflectance and transmittance to have a valid meaning. With that proviso, then

$$R = \left(\frac{\eta_0 B - C}{\eta_0 B + C}\right)\left(\frac{\eta_0 B - C}{\eta_0 B + C}\right)^* \tag{2.113}$$

$$T = \frac{4\eta_0 \operatorname{Re}(\eta_m)}{(\eta_0 B + C)(\eta_0 B + C)^*} \tag{2.115}$$

$$A = \frac{4\eta_0 \operatorname{Re}(BC^* - \eta_m)}{(\eta_0 B + C)(\eta_0 B + C)^*} \tag{2.116}$$

$$\psi = \text{potential transmittance} = \frac{T}{(1-R)} = \frac{\operatorname{Re}(\eta_m)}{\operatorname{Re}(BC^*)} \tag{2.117}$$

Phase shift on reflection, measured at the front surface of the multilayer, is given by

$$\varphi = \arctan\left(\frac{\operatorname{Im}\left[\eta_m\left(BC^* - CB^*\right)\right]}{\left(\eta_m^2 BB^* - CC^*\right)}\right) \tag{2.118}$$

and that on transmission, measured between the emergent wave as it leaves the multilayer and the incident wave as it enters, by

$$\zeta = \arctan\left[\frac{-\operatorname{Im}(\eta_0 B + C)}{\operatorname{Re}(\eta_0 B + C)}\right] \tag{2.119}$$

The signs of the numerator and denominator in these expressions must be preserved separately. Then the quadrants are given by the arrangement in the table:

Numerator	+	+	−	−
Denominator	+	−	+	−
Quadrant	1st	2nd	4th	3rd

Despite the apparent simplicity of Equation 2.103, numerical calculations without some automatic aid are tedious in the extreme. Even with the help of a calculator, the labor involved in determining the performance of an assembly of more than a very few transparent layers at one or two wavelengths

is completely discouraging. At the very least, a programmable calculator of reasonable capacity is required. Extended calculations are usually carried out on a computer.

However, insight into the properties of thin-film assemblies cannot easily be gained simply by feeding the calculations into a computer, and insight is necessary if filters are to be designed and if their limitations in use are to be fully understood. Studies have been made of the properties of the characteristic matrices and some results that are particularly helpful in this context have been obtained. Approximate methods, especially graphical ones, have also been found useful.

2.8 Potential Transmittance

We find transmittance a rather less accessible parameter from the point of view of the theory than reflectance. Reflectance is immediately a function of the admittance of the front surface of the multilayer. To calculate transmittance, we need further information. A useful concept related to transmittance but rather more accessible is potential transmittance.

The potential transmittance of a layer or an assembly of layers is the ratio of the irradiance leaving by the rear, or exit, interface to that entering by the front interface. The concept was introduced by Berning and Turner [6], and we will make considerable use of it in designing metal-dielectric filters and in calculating losses in all-dielectric multilayers. Potential transmittance is denoted by ψ and is given by

$$\psi = \frac{I_{exit}}{I_{enter}} = \frac{T}{(1-R)} \tag{2.129}$$

that is the ratio between the irradiance leaving the assembly and the net irradiance actually entering. For the entire system, the net irradiance actually entering is the difference between the incident and reflected irradiances. Note that in accordance with the definition of *reflectance* and *transmittance,* the irradiances concerned are the normal components.

The potential transmittance of a series of subassemblies of layers is simply the product of the individual potential transmittances. Figure 2.8 shows a series of film subunits making up a complete system. Clearly

$$\psi = \frac{I_e}{I_i} = \frac{I_d}{I_a} = \frac{I_b}{I_a}\frac{I_c}{I_b}\frac{I_b}{I_c} = \psi_1\psi_2\psi_3 \tag{2.130}$$

The potential transmittance is fixed by the parameters of the layer, or combination of layers, involved, and by the characteristics of the structure at the

exit interface, and it represents the transmittance that this particular combination would give if there were no reflection losses. Thus, it is a measure of the maximum transmittance that could be expected from the arrangement. By definition, the potential transmittance is unaffected by any transparent structure deposited over the front surface—which can affect the transmittance as distinct from the potential transmittance—and to ensure that the transmittance is equal to the potential transmittance, the layers added to the front surface must maximize the irradiance actually entering the assembly. This implies reducing the reflectance of the complete assembly to zero or, in other words, adding an antireflection coating. The potential transmittance is, however, affected by any changes in the structure at the exit interface, and it is possible to maximize the potential transmittance of a subassembly in this way.

There is, however, a problem with Equation 2.129. Reflectance, as we have seen, is defined only in media that are free of absorption. Equation 2.130 is correct as long as we interpret the irradiances as the net irradiance passing through the appropriate interface. In our matrix expression for the properties of any combination of thin films, we use B and C to denote the appropriate normalized electric and magnetic fields at any particular interface. Then, the net normalized irradiance is given by (½)Re(BC^*). Because we are dealing with ratios, we can drop the factor (½) and replace the irradiances in Equations 2.129 and 2.130 with Re(BC^*).

We now show that the parameters of the layer, or subassembly of layers, together with the optical admittance at the rear surface, are sufficient to define the potential transmittance. Let the complete multilayer performance be given by

$$\begin{bmatrix} B \\ C \end{bmatrix} = [M_1][M_2]\cdots[M_a][M_b][M_c]\cdots[M_p][M_q]\begin{bmatrix} 1 \\ \eta_m \end{bmatrix}$$

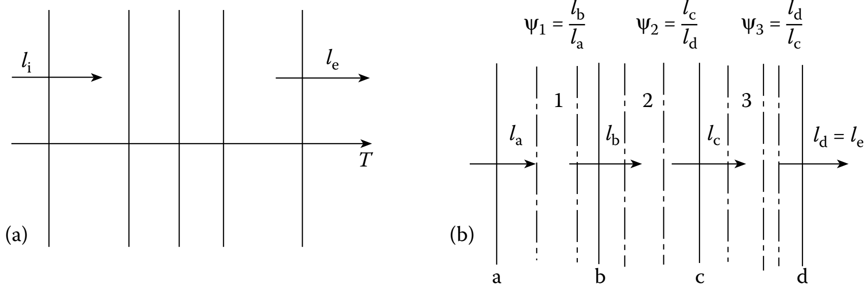

FIGURE 2.8
(a) An assembly of thin films. (b) The potential transmittance of an assembly of thin film consisting of a number of subunits.

where we want to calculate the potential transmittance of the subassembly $[M_a]$ $[M_b]$ $[M_c]$. Let the product of the matrices to the right of the subassembly be given by

$$\begin{bmatrix} B_e \\ C_e \end{bmatrix}$$

Now, if

$$\begin{bmatrix} B_i \\ C_i \end{bmatrix} = [M_a][M_b][M_c]\begin{bmatrix} B_e \\ C_e \end{bmatrix} \tag{2.131}$$

Then

$$\psi = \frac{\mathrm{Re}\left(B_e C_e^*\right)}{\mathrm{Re}\left(B_i C_i^*\right)} \tag{2.132}$$

By dividing Equation 2.131 by B_e we have

$$\begin{bmatrix} B_i' \\ C_i' \end{bmatrix} = [M_a][M_b][M_c]\begin{bmatrix} 1 \\ Y_e \end{bmatrix}$$

where $Y_e = C_e/B_e$, $B_1' = B_1/B_e$, $C_1' = C_1/C_e$, and the potential transmittance is

$$\begin{aligned} \psi &= \frac{\mathrm{Re}(Y_e)}{\mathrm{Re}\left(B_i' C_i'^*\right)} \\ &= \frac{\mathrm{Re}\left(C_e/B_e\right)}{\mathrm{Re}\left[\left(B_i/B_e\right)\left(C_i^*/B_e^*\right)\right]} = \frac{B_e B_e^* \,\mathrm{Re}\left(C_e/B_e\right)}{\mathrm{Re}\left(B_i C_i^*\right)} \\ &= \frac{\mathrm{Re}\left(B_e^* C_e\right)}{\mathrm{Re}\left(B_i C_i^*\right)} = \frac{\mathrm{Re}\left(B_e C_e^*\right)}{\mathrm{Re}\left(B_i C_i^*\right)} \end{aligned}$$

which is identical to Equation 2.132. Thus, the potential transmittance of any subassembly is determined solely by the characteristics of the layer or layers of the subassembly together with the optical admittance of the structure at the exit interface.

Further expressions involving potential transmittance will be derived as they are required.

2.9 A Theorem on the Transmittance of a Thin-Film Assembly

The transmittance of a thin-film assembly is independent of the direction of propagation of the light. This applies regardless of whether the layers are absorbing.

A proof of this result, from Abelès [7,8], who was responsible for the development of the matrix approach to the analysis of thin films, follows quickly from the properties of the matrices.

Let the matrices of the various layers in the assembly be denoted by

$$[M_1],[M_2],\ldots[M_q]$$

and let the two massive media on either side be transparent. The two products of the matrices corresponding to the two possible directions of propagation can be written as

$$[M]=[M_1][M_2][M_3],\ldots[M_q]$$

and

$$[M']=[M_q][M_{q-1}]\ldots[M_2][M_1]$$

Now, because the form of the matrices is such that the diagonal terms are equal, regardless of whether there is absorption, we can show that if we write

$$[M]=[a_{ij}] \quad \text{and} \quad [M']=[a'_{ij}]$$

then

$$a_{ij}=a'_{ij}\,(i\neq j),\, a_{11}=a'_{22} \text{ and } a_{22}=a'_{11}$$

This can be proved simply by induction.

We denote the medium on one side of the assembly by η_0 and on the other by η_m, where η_0 is next to layer 1. In the case of the first direction, the characteristic matrix is given by Equation 2.103

$$\begin{bmatrix} B \\ C \end{bmatrix}=[M]\begin{bmatrix} 1 \\ \eta_m \end{bmatrix}$$

and

$$B = a_{11} + a_{12}\eta_m \qquad C = a_{21} + a_{22}\eta_m$$

In the second case

$$B = a'_{11} + a'_{12}\eta_0 = a_{22} + a_{12}\eta_0$$

$$C = a'_{21} + a'_{22}\eta_0 = a_{21} + a_{11}\eta_0$$

The two expressions for the transmittance of the assembly are, then, from Equation 2.115,

$$T = \frac{4\eta_0\eta_m}{\left|\eta_0\left(a_{11} + a_{12}\eta_m\right) + a_{21} + a_{22}\eta_m\right|^2}$$

$$T' = \frac{4\eta_m\eta_0}{\left|\eta_m\left(a_{22} + a_{12}\eta_0\right) + a_{21} + a_{11}\eta_0\right|^2}$$

which are identical.

This rule does not, of course, apply to the *reflectance* of an assembly, which will necessarily be the same on both sides of the assembly only if there is no absorption in any of the layers.

Among other things, this expression shows that the one-way mirror, which allows light to travel through it in one direction only, cannot be constructed from simple optical thin films. The common so-called one-way mirror has a high reflectance with some transmittance and relies for its operation on an appreciable difference in the illumination conditions existing on either side.

2.10 Coherence

Coherence is a concept that quantifies the ability to produce detectable interference effects. Although often used to describe the properties of a beam of light, it is much better considered as a property of the complete optical system. We usually use the adjectives *coherent* to describe the presence of maximum interference effects and *incoherent* to describe their complete absence. Cases between these limits are described as *partially coherent*. Here, we take a brief look at some of the aspects of coherence that are important in optical coating applications. There are few preconditions. We can imagine that we are carrying out an experiment. We would find it difficult if there were serious fluctuations in the measurements. The same considerations apply to the ideas of coherence. We assume that in all the cases we discuss, we can describe the phenomena as stationary. This implies that although the waves may exhibit variations, their

statistical properties do not vary with time. Thus, in what follows we will simply average them over a sufficiently long time, or will average a sufficiently large number of cases, just as though we were conducting an experiment.

As always, we take advantage of the linear nature of the interactions and represent an arbitrary wave by a corresponding spectrum of harmonic waves. We first consider two beams derived from one single spectral element. Let two beams be linearly polarized plane waves with identical polarization, propagating together along the z-direction, and with complex amplitudes $\mathcal{E}_1$ and $\mathcal{E}_2$. Let the phases of these two waves at $z = 0$ and $t = 0$ be φ_1 and φ_2, with φ_1 and φ_2 contained in the complex amplitudes. Now let us combine the waves. Because the polarizations are exactly equal, the electric and magnetic fields of the resultants will be the simple sums of the components. The resultant irradiance will therefore be:

$$I = \frac{1}{2}\mathrm{Re}\left[(E_1 + E_2)(H_1 + H_2)^*\right] = \frac{1}{2}\mathrm{Re}\left[(E_1 + E_2)y^*(E_1 + E_2)^*\right]$$
$$= \frac{1}{2}\mathrm{Re}(y)E_1E_1^* + \frac{1}{2}\mathrm{Re}(y)E_2E_2^* + \mathrm{Re}(y)\mathrm{Re}(E_1E_2^*) \quad (2.133)$$

$$I = I_1 + I_2 + \mathrm{Re}(y)\mathrm{Re}(\mathcal{E}_1\mathcal{E}_2^*)$$
$$= I_1 + I_2 + 2\sqrt{I_1I_2}\cos(\varphi_1 - \varphi_2) \quad (2.134)$$

Now imagine that many more light waves are involved. These may have different frequencies and/or different phases and/or different amplitudes. They will also contribute to the resultant irradiance that will then be the sum of the individual irradiances together with a sum of interference terms. Everything depends on the spread of parameters across the various light waves. The interference term may remain just as strong or, because the terms may be positive or negative, may cancel out altogether or may take on some intermediate value. We describe the first case as coherent, the second as incoherent, and the intermediate case as partially coherent.

The jumbling of the interference term may result from variations in the source of illumination but equally well from variations in any other feature of the system. For example, if a thin film is involved, there could be variations in thickness across the aperture of the film. Substrates usually are thick enough and sufficiently variable in their thicknesses that no interference effects are observed—that is, substrates normally exhibit incoherent behavior.

The light in any real system is never a single infinite, plane, linearly polarized harmonic wave and the components of the system are never perfect. There are some simple parameters that help in our assessment of coherence. For convenience, we will first think of them as a function of the light yet bear in mind that the system is ultimately what is important. Let us extract two rays from exactly the same point in a beam of light and let them produce

some kind of interference effect involving fringes. Now let us gradually move apart the points where we extract the two rays. As the distance between the two points increases, so the interference fringes become gradually less pronounced. When the fringes just disappear, we can take the distance between the two points as a measure of coherence. If the two points are separated along the direction of propagation of the primary light, then we call that distance the *coherence length.* If the light, instead of being extracted from two points, is instead taken from a complete area of the primary light, then that area where the fringes just disappear is called the *coherence area,* and if from a volume, the *coherence volume.* If, instead of moving the points, we delay one sample by a variable time, then the delay at which the fringes just disappear is the *coherence time.* Clearly, coherence time is just the time it takes for the light to travel the coherence length. Coherence length and coherence time are particularly useful concepts. They are quite simple and yet can explain many otherwise puzzling phenomena.

Let us express our primary light in terms of its spectral components and let the spectrum be a continuous band of wavelengths centered on λ and with a bandwidth of $\Delta\lambda$. We produce interference fringes using this light with a variable path difference. Each elemental wavelength will produce its own set of fringes, and as we increase the path difference, the fringes will be smeared out and the contrast will fall. The path difference at that point where they just disappear will be a measure of the coherence length. We can define the point as that where the fringes will become smeared out over the interval between fringes. In other words, a fringe of order m at the smallest wavelength will just coincide with one of order $m - 1$ at the longest wavelength.

$$\text{Path difference} = m\left(\lambda - \frac{\Delta\lambda}{2}\right) = (m-1)\left(\lambda + \frac{\Delta\lambda}{2}\right) \tag{2.135}$$

$$\text{Coherence length} = \left(m - \frac{1}{2}\right)\cdot\lambda = \frac{\lambda^2}{\Delta\lambda} \tag{2.136}$$

$$\text{Coherence time} = \frac{\lambda^2}{c\Delta\lambda} \tag{2.137}$$

where c is 299.792458 nm/fs.

Cones of illumination also have coherence effects and we can calculate an effective coherence length that can be useful. If ϑ is the cone semiangle and the cone axis is at normal incidence then, using an aproximate two-dimensional model, we can rewrite Equation 2.135 as

$$m\lambda = (m+1)\lambda\cos\vartheta \tag{2.138}$$

and a similar extraction process yields:

$$\text{Coherence length} = m\lambda = \frac{\lambda\cos\vartheta}{1-\cos\vartheta} \simeq \frac{2\lambda}{\vartheta^2} \tag{2.139}$$

or, if ϑ is given in degree

$$\text{Coherence length} = \frac{7 \times 10^3 \lambda}{\vartheta^2} \tag{2.140}$$

This ϑ is the angle within the particular thin film structure. If the incident medium is of a different index then we can make an approximate correction to Equation 2.140 to give:

$$\text{Coherence length} = \frac{7 \times 10^3 \lambda \eta_1^2}{n_0^2 \vartheta^2} \tag{2.141}$$

where n_0 is the incident medium index and n_1 is either the index of the film concerned or the effective index of the coating. This particular coherence length is a function of the properties of the cone and the properties of the film.

When several independent effects are present, such as both cone and bandwidth, then a reasonable rule for combining coherence lengths is:

$$\frac{1}{L} = \sqrt{\frac{1}{L_a^2} + \frac{1}{L_b^2} + \cdots} \tag{2.142}$$

Figure 2.9 shows the appearance of fringes calculated for a 1-mm-thick glass substrate where the uncoated surfaces are perfectly parallel. The fringes are scanned with light of zero bandwidth, that is, infinite coherence length, where the fringes have their maximum theoretical amplitude. This is the completely coherent case. Scanning with 0.2-nm bandwidth corresponds to a

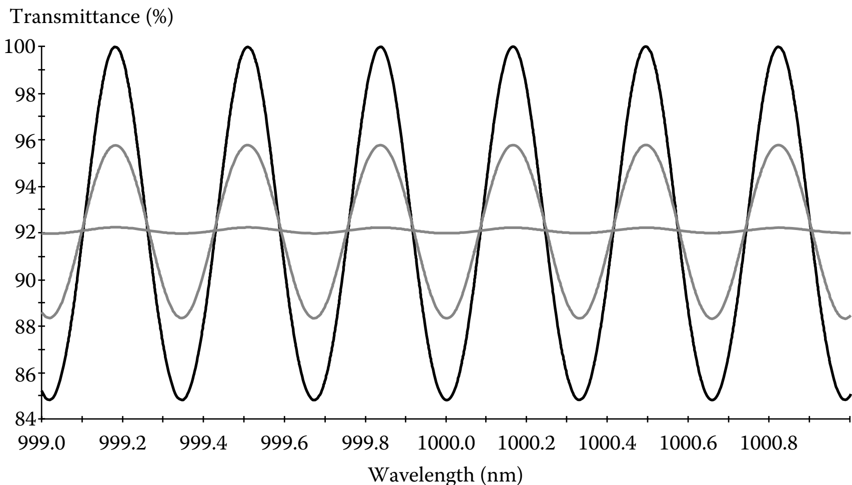

FIGURE 2.9
The appearance of fringes in a perfectly parallel 1-mm-thick glass substrate illuminated with light of zero bandwidth, 0.2-nm bandwidth (coherence length 5 mm), and 2-nm bandwidth (0.5 mm coherence length). The fringes show reducing amplitude with decreasing coherence length.

coherence length of 5 mm, and the fringes are roughly halved in amplitude. This is partial coherence. Finally, with a bandwidth of 2 nm, the coherence length becomes 0.5 mm and the fringes virtually disappear to give the incoherent case.

In the bulk of this book, we shall assume complete coherence when discussing the properties of the thin-film coatings and complete incoherence when dealing with the substrates. However, it is perhaps worthwhile here to look just a little further at the concept of partial coherence. The key lies in the interference term of Equation 2.133, $\mathrm{Re}(y)\mathrm{Re}(E_1E_2^*)$. Although the discussion of this expression assumed that E_1 and E_2 represented harmonic waves, the derivation is quite general. E_1 and E_2 can represent any arbitrary waves, the only condition being that the characteristic admittance of the medium, y, should be constant so that the magnetic field, H, can be replaced by yE.

We began by assuming that the essential difference between E_2 and E_1 was the phase angle φ, and the interference phenomenon was, therefore, a function of φ. If we are now permitting E_1 and E_2 to represent quite general waves, φ has no meaning and makes no sense, because it applies only to a harmonic wave. However, E_1 and E_2 are both functions of time, and so we can introduce a variable time delay τ, to take the place of φ. To keep matters simple, we take just the $E_1E_2^*$ part. Now that we have made the waves much more general, we should take an average over a sufficiently long time or over a sufficiently large number of measurements. We then obtain what is called the *mutual coherence function:*

$$\Gamma_{12}(\tau)=\langle E_1(t+\tau)E_2^*(t)\rangle=\lim_{T\to\infty}\frac{1}{2T}\int_{-T}^{T}E_1(t+\tau)E_2^*(t)\,dt \tag{2.143}$$

$$\gamma_{12}(\tau)=\frac{\Gamma_{12}(\tau)}{\sqrt{\Gamma_{11}(0)}\sqrt{\Gamma_{22}(0)}}=\frac{\langle E_1(t+\tau)E_2^*(t)\rangle}{\sqrt{\langle E_1(t)E_1^*(t)\rangle}\sqrt{\langle E_2(t)E_2^*(t)\rangle}} \tag{2.144}$$

where $\gamma_{12}(\tau)$ is known as the complex degree of coherence.

We can now rewrite Equation 2.133 as:

$$\begin{aligned}I&=\frac{1}{2}\mathrm{Re}(y)\langle E_1(t)E_1^*(t)\rangle+\frac{1}{2}\mathrm{Re}(y)\langle E_2(t)E_2^*(t)\rangle\\&\quad+\mathrm{Re}(y)\mathrm{Re}\left(\langle E_1(t+\tau)E_2^*(t)\rangle\right)\\&=\frac{1}{2}\mathrm{Re}(y)\langle E_1(t)E_1^*(t)\rangle+\frac{1}{2}\mathrm{Re}(y)\langle E_2(t)E_2^*(t)\rangle\\&\quad+\mathrm{Re}(y)\sqrt{\langle E_1(t)E_1^*(t)\rangle\langle E_2(t)E_2^*(t)\rangle}\,\mathrm{Re}\left[\gamma_{12}(\tau)\right]\\&=I_1+I_2+2\sqrt{I_1I_2}\,\mathrm{Re}\left[\gamma_{12}(\tau)\right]\end{aligned} \tag{2.145}$$

when we can see that the real part of the complex degree of coherence is related to the fringe shape. When we have fringes that are not too far from a cosine or a sine profile we can define a fringe visibility that is given by:

$$V = \frac{I_{\text{max}} - I_{\text{min}}}{I_{\text{max}} + I_{\text{min}}} \tag{2.146}$$

The fringe is a cyclic function. How do we find the maximum and minimum extrema? This is where the complex degree of coherence turns out to be particularly useful. Although the real part is a fluctuating function, the full complex form is essentially a rotating vector. The magnitude, therefore, represents the amplitude of the fringe function and the visibility is given by:

$$V = \frac{2\sqrt{I_1 I_2}\,|\gamma_{12}(\tau)|}{I_1 + I_2} \tag{2.147}$$

When I_1 and I_2 are equal, the fringe visibility is at a maximum with value $|\gamma|$.

Direct evaluation of the complex degree of coherence from Equation 2.144 is not easy but Equation 2.147 connects it simply to the visibility of the fringes.

We have concentrated on time as the variable in generating the coherence functions but clearly this could also be in terms of distance. The coherence time and coherence length are simply that time or distance at which the magnitude of the complex degree of coherence falls to a sufficiently low figure. This level tends to be chosen as whatever is most convenient in the particular calculation concerned.

There is much more to coherence, but this abbreviated account has covered the major aspects of importance in thin-film optical coatings.

2.11 Incoherent Reflection at Two or More Surfaces

So far, we have treated substrates as being one-sided slabs of material of infinite depth. In almost all practical cases, the substrate will have finite depth with rear surfaces that reflect some of the energy and affect the performance of the assembly.

The depth of the substrate will usually be much greater than the wavelength of the light, and variations in the flatness and parallelism of the two surfaces will be appreciable fractions of a wavelength. Generally, the incident light will not be particularly well collimated. Under these conditions, it will not be possible with a finite aperture to observe interference effects between light reflected at the front and rear surfaces of the substrate, and because of this, the substrate is known as thick. The coherence length is small compared with the double

traversal of the substrate, which is the basic path difference in any interference effects. We describe the addition of the various waves as incoherent rather than coherent. In Equation 2.134, the interference term vanishes and we are left with the sum of the irradiances instead of the vector sum of the amplitudes.

The symbols used are illustrated in Figure 2.10. Waves are reflected successively at the front and rear surfaces. The sums of the irradiances are given by

$$R = R_a^+ + T_a^+ R_b^+ T_a^- \left[1 + R_a^- R_b^+ + \left(R_a^- R_b^+\right)^2 + \ldots\right]$$
$$= R_a^+ + \left[T_a^+ R_b^+ T_a^- / \left(1 - R_a^- R_b^+\right)\right]$$

i.e., since T^+ and T^- are always identical

$$T_a^+ = T_a^- = T_a$$

and so

$$R = \frac{R_a^+ + R_b^+\left(T_a^2 - R_a^- R_b^+\right)}{1 - R_a^- R_b^+}$$

If there is no absorption in the layers,

$$R_a^+ = R_a^- = R_a \quad \text{and} \quad 1 = \mathrm{R}_a + T_a$$

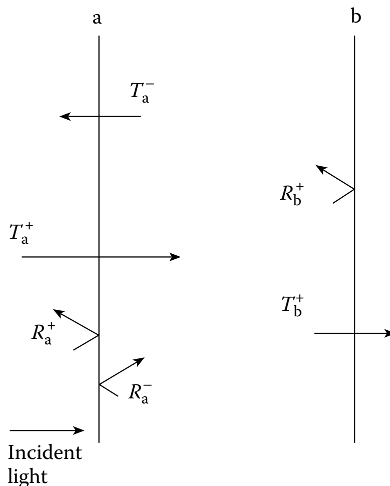

FIGURE 2.10
Symbols used in calculation of incoherent reflection at two or more surfaces.

so that

$$R = \frac{R_a + R_b - 2R_aR_b}{1 - R_aR_b}$$

Similarly

$$T = T_a^+T_b^+\left[1 + R_a^-R_b^+ + \left(R_a^-R_b^+\right)^2 + \ldots\right]$$

$$= \frac{T_aT_b}{1 - R_a^-R_b^+}$$

and again, if there is no absorption,

$$T = \frac{T_aT_b}{1 - R_aR_b} \tag{2.148}$$

or

$$T = \left(\frac{1}{T_a} + \frac{1}{T_b} - 1\right)^{-1} \tag{2.149}$$

because

$$R_a = 1 - T_a \qquad R_b = 1 - T_b$$

A nomogram for solving Equation 2.149 can easily be constructed. Two axes at right angles are laid out on a sheet of graph paper and, taking the point of intersection as the zero, two linear equal scales of transmittance are marked out on the axes. One of these is labeled T_a and the other, T_b. The angle between T_a and T_b is bisected by a third axis that is to have the T scale marked out on it. To do this, a straight edge is placed so that it passes through the 100% transmittance value on, say, the T_a-axis and any chosen transmittance on the T_b-axis. The value of T to be associated with the point where the straight edge crosses the T-axis is then that of the intercept with the T_b-axis. The entire scale can be marked out in this way. A completed nomogram of this type is shown in Figure 2.11.

In the absence of absorption, the analysis can be very simply extended to further surfaces. Consider the case of two substrates, i.e., four surfaces. These we can label T_a, T_b, T_c, and T_d. Then, from Equation 2.149, we have for the first substrate

$$T_1 = \left(\frac{1}{T_a} + \frac{1}{T_b} - 1\right)^{-1}$$

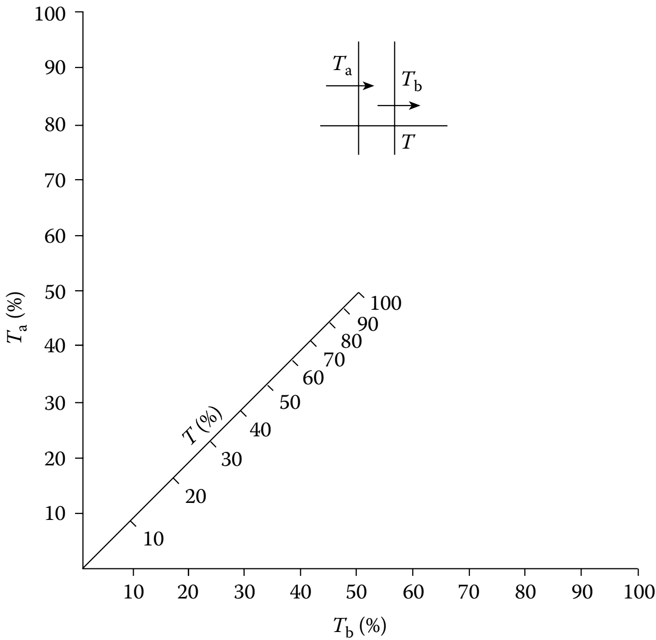

FIGURE 2.11
A nomogram for calculating the overall transmittance of a thick transparent plate given the transmittance of each individual surface.

i.e.,

$$\frac{1}{T_1} = \frac{1}{T_a} + \frac{1}{T_b} - 1$$

and similarly for the second

$$\frac{1}{T_2} = \frac{1}{T_c} + \frac{1}{T_d} - 1$$

The transmittance through all four surfaces is then obtained by applying Equation 2.149 again:

$$\frac{1}{T} = \frac{1}{T_1} + \frac{1}{T_2} - 1$$

i.e.,

$$T = \left(\frac{1}{T_a} + \frac{1}{T_b} + \frac{1}{T_c} + \frac{1}{T_d} - 3 \right)^{-1} \tag{2.150}$$

The iterative nature of these calculations can be clumsy when dealing with a succession of surfaces. A technique based on a study by Baumeister et al.

[9] yields a rather more useful matrix form of the calculation. The emphasis is placed on the flows of irradiance. Absorption in the media between the coated surfaces is supposed sufficiently small so that the coupling problem mentioned earlier is negligible. The symbols are defined in Figure 2.12.

The direction of the light is denoted by the usual plus and minus signs. *a* and *b* are two coatings separated by a medium *m* with internal transmittance $T_{m\text{int}}$. The final medium will be the emergent medium and there, the negative-going irradiance will be zero. The procedure to be outlined will derive the values of I_{ma}^{+} and I_{ma}^{-} from $I_{(m+1)b}^{+}$ and $I_{(m+1)b}^{-}$. The rest is straightforward.

The irradiances on either side of the coating with label *b* are related through the equations

$$I_{(m+1)b}^{+} = T_b I_{mb}^{+} + R_b^{-} I_{(m+1)b}^{-}$$

$$I_{mb}^{-} = R_b^{+} I_{mb}^{+} + T_b I_{(m+1)b}^{-}$$

These can be manipulated into the form

$$I_{mb}^{-} = \frac{1}{T_b}\left\{R_b^{+} I_{(m+1)b}^{+} + \left(T_b^2 - R_b^{-} R_b^{+}\right) I_{(m+1)b}^{-}\right\}$$

$$I_{mb}^{+} = \frac{1}{T_b}\left\{I_{(m+1)b}^{+} - R_b^{-} I_{(m+1)b}^{-}\right\}$$

and in matrix form, this is

$$\begin{bmatrix} I^{-}{}_{mb} \\ I^{+}{}_{mb} \end{bmatrix} = \begin{bmatrix} \dfrac{\left(T_b^2 - R_b^{-} R_b^{+}\right)}{T_b} & \dfrac{R_b^{+}}{T_b} \\ \dfrac{-R_b^{-}}{T_b} & \dfrac{1}{T_b} \end{bmatrix} \begin{bmatrix} I^{-}{}_{(m+1)b} \\ I_{(m+1)b}^{+} \end{bmatrix} \tag{2.151}$$

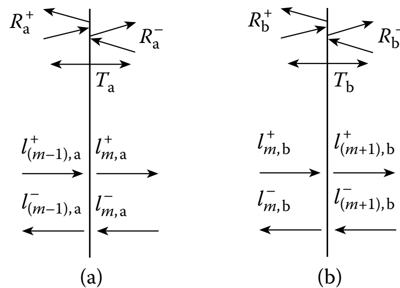

FIGURE 2.12
Symbols defining two successive coatings (a) and (b) with intervening medium in a stack.

The conversion through the medium is given by

$$\begin{bmatrix} I^{-}_{ma} \\ I^{+}_{ma} \end{bmatrix} = \begin{bmatrix} T_{m\,\mathrm{int}} & 0 \\ 0 & \dfrac{1}{T_{m\,\mathrm{int}}} \end{bmatrix} \begin{bmatrix} I^{-}_{mb} \\ I^{+}_{mb} \end{bmatrix} \tag{2.152}$$

Equations 2.151 and 2.152 can be applied to the various coatings and intervening media in succession.

References

1. Yeh P 1988 *Optical Waves in Layered Media* (New York: John Wiley and Sons)
2. Hodgkinson I J and Wu Q h 1997 *Birefringent Thin Films and Polarizing Elements* (Singapore: World Scientific Publishing Co Pte Ltd)
3. Born M and Wolf E 2002 *Principles of Optics: Electromagnetic Theory of Propagation, Interference and Diffraction of Light* ed 7 (New York: Cambridge University Press)
4. Berning P H 1963 *Theory and calculations of optical thin films*, in *Physics of Thin Films* Hass G, Editor (New York/London: Academic Press) 69–121
5. Macleod H A 1995 *Antireflection coatings on absorbing substrates* in 38th Annual Technical Conference, Chicago, Society of Vacuum Coaters, 172–175
6. Berning P H and Turner A F 1957 Induced transmission in absorbing films applied to band pass filter design *Journal of the Optical Society of America* **47** 230–239
7. Abelès F 1950 Recherches sur la propagation des ondes électromagnétiques sinusoïdales dans les milieus stratifiés. Applications aux couches minces. I *Annales de Physique, 12th Series* **5** 596–640
8. Abelès F 1950 Recherches sur la propagation des ondes électromagnétiques sinusoïdales dans les milieus stratifiés. Applications aux couches minces. II *Annales de Physique, 12th Series* **5** 706–784
9. Baumeister P, Hahn R, and Harrison D 1972 The radiant transmittance of tandem arrays of filters *Optica Acta* **19** 853–864

3

Theoretical Techniques

The previous chapter dealt with the fundamental theory culminating in exact expressions for the basic properties of thin-film systems. These are the expressions that we normally use in computing coating performance. There is more to designing, manufacturing, and using coatings than simple calculation. There are many additional techniques that can help us. Some of these are based on older approximate methods of calculation that predate digital computers and nowadays are used more for rapid understanding than for performance calculation. Others are accurate techniques that we will tend to use in an approximate way. Some are based on properties of the characteristic matrices themselves.

3.1 Quarter- and Half-Wave Optical Thicknesses

The characteristic matrix of a dielectric thin film takes on a very simple form if the optical thickness is an integral number of quarter- or half-waves. That is, if

$$\delta = m(\pi/4) \qquad m = 0, 1, 2, 3...$$

For m even, $\cos\delta = \pm 1$ and $\sin\delta = 0$, so that the layer is an integral number of half-wavelengths thick, and the matrix becomes

$$\pm\begin{bmatrix} 1 & 0 \\ 0 & 1 \end{bmatrix}$$

This is the unity matrix and can have no effect on the reflectance or transmittance of an assembly. It is as if the layer were completely absent. This is a particularly useful result and, because of it, half-wave layers are sometimes referred to as *absentee* layers. In the computation of the properties of any assembly, layers that are an integral number of half-wavelengths thick can be omitted completely without altering the result. Of course this is true only at the wavelength for which the layers are half-waves.

For m odd, $\sin\delta = \pm 1$ and $\cos\delta = 0$, so that the layer is an odd number of quarter-wavelengths thick, and the matrix becomes

$$\pm\begin{bmatrix} 0 & i/\eta \\ i\eta & 0 \end{bmatrix}$$

This is not quite as simple as the half-wave case, but such a matrix is still easy to handle in calculations. In particular, if a substrate, or combination of thin films, has an admittance of Y, then the addition of an odd number of quarter-waves of admittance η alters the admittance of the assembly to η^2/Y. This makes the properties of a succession of quarter-wave layers very easy to calculate. The admittance of, say, a stack of five quarter-wave layers is

$$Y = \frac{\eta_1^2\eta_3^2\eta_5^2}{\eta_2^2\eta_4^2\eta_m}$$

where the symbols have their usual meanings.

Because of the simplicity of assemblies involving quarter- and half-wave optical thicknesses, designs are often specified in terms of fractions of quarter-waves at a reference wavelength. Usually only two, or perhaps three, different materials are involved in designs and a convenient shorthand notation for quarter-wave optical thicknesses is *H*, *M*, or *L*, where *H* refers to the highest of the three indices, *M* is the intermediate, and *L* is the lowest. Half-waves are denoted by *HH*, *MM*, *LL* or 2*H*, 2*M* and so on.

3.2 Admittance Loci

The admittance diagram, in common with the Smith Chart and the Reflection Circle Diagram, described later, is a graphic technique based on an exact solution of the appropriate equations. We imagine that the multilayer is gradually built up on the substrate layer by layer, immersed all the time in the final incident medium. As each layer in turn increases from zero thickness to its final value, the admittance of the multilayer at that stage of its construction is calculated and the locus is plotted. Alternatively, we may imagine the multilayer as already constructed and then a reference plane is slid continuously through the layers and the locus of admittance of the structure up to that plane plotted. Either of these views is equally valid and the results are identical. [Note that only the first possibility applies to the reflection circle diagram and only the second to the Smith Chart.] The loci for dielectric layers take the form of a series of circular arcs or even complete circles, each corresponding to a single layer, which are connected at points corresponding to the interfaces between the different layers. Perfect metals are also represented by arcs of circles. Absorbing materials give spiral loci. Although the technique can be used for quantitative calculation it cannot

compete even with a small programmable calculator, and its great value is in the visualization of the characteristics of a particular multilayer.

As the reference plane moves from the surface of the substrate to the front surface of the multilayer, let us calculate and plot the variation of the input optical admittance at the reference plane. The matrix expression is

$$\begin{bmatrix} B \\ C \end{bmatrix} = \left\{ \prod_{r=1}^{q} \begin{bmatrix} \cos\delta_r & (i\sin\delta_r)/\eta_r \\ i\eta_r \sin\delta_r & \cos\delta_r \end{bmatrix} \right\} \begin{bmatrix} 1 \\ \eta_m \end{bmatrix}$$

where $Y = C/B$ is the input optical admittance of the assembly. For the rth layer we can write

$$\begin{bmatrix} B \\ C \end{bmatrix} = \begin{bmatrix} \cos\delta_r & (i\sin\delta_r)/\eta_r \\ i\eta_r \sin\delta_r & \cos\delta_r \end{bmatrix} \begin{bmatrix} B' \\ C' \end{bmatrix}$$

and, since it is optical admittance we are interested in, we can divide throughout by B' to give

$$\begin{bmatrix} B/B' \\ C/B' \end{bmatrix} = \begin{bmatrix} \cos\delta_r & (i\sin\delta_r)/\eta_r \\ i\eta_r \sin\delta_r & \cos\delta_r \end{bmatrix} \begin{bmatrix} 1 \\ Y' \end{bmatrix}$$

where $Y' = C/B'$ represents the admittance of the structure at the exit side of the layer. We now find the locus of the input admittance

$$Y = \frac{C}{B} = \frac{C/B'}{B/B'}$$

Let

$$Y = x + iy$$

and

$$Y' = \alpha + i\beta$$

and let the layer in question be dielectric so that η_r and δ_r are both real. Then

$$\begin{aligned} Y = x + iy &= \frac{(\alpha + i\beta)\cos\delta_r + i\eta_r \sin\delta_r}{\cos\delta_r + (\alpha + i\beta)(i\sin\delta_r)/\eta_r} \\ &= \frac{\alpha\cos\delta_r + i(\beta\cos\delta_r + \eta_r\sin\delta_r)}{[\cos\delta_r - (\beta/\eta_r)\sin\delta_r] + i(\alpha/\eta_r)\sin\delta_r} \end{aligned}$$

Equating real and imaginary parts:

$$x\left[\cos\delta_r - (\beta/\eta_r)\sin\delta_r\right] - (y\alpha/\eta_r)\sin\delta_r = \alpha\cos\delta_r \tag{3.1}$$

$$y\left[\cos\delta_r - (\beta/\eta_r)\sin\delta_r\right] + (x\alpha/\eta_r)\sin\delta_r = \beta\cos\delta_r + \eta_r\sin\delta_r \tag{3.2}$$

Eliminating δ_r yields

$$x^2 + y^2 - x\left[\left(\alpha^2 + \beta^2 + \eta_r^2\right)/\alpha\right] + \eta_r^2 = 0 \tag{3.3}$$

that is the equation of a circle with center $[(\alpha^2 + \beta^2 + \eta_r^2)/2\alpha, 0]$, i.e., on the real axis and with radius such that it passes through the point (α, β), i.e., its starting point. The circle is traced out in a clockwise direction, which can be shown by setting $\beta = 0$ in Equation 3.2.

We can plot the locus in the complex plane in the same way as the locus of the amplitude reflection coefficient.

The scale of δ_r can also be plotted on the diagram. Let $\beta = 0$ and then, from Equations 3.1 and 3.2,

$$x - (y\alpha/\eta_r)\tan\delta_r = \alpha$$

$$y + (x\alpha/\eta_r)\tan\delta_r = \eta_r\tan\delta_r$$

Eliminating α, we have

$$x^2 + y^2 - y(\tan\delta_r - 1/\tan\delta_r) - \eta_r^2 = 0 \tag{3.4}$$

This is a circle with center

$$(0, (\eta_r/2)(\tan\delta_r - 1/\tan\delta_r))$$

i.e., on the imaginary axis and passing through the point $(\eta_r, 0)$. The simplest contours of equal δ_r are $\delta_r = 0, \pi/2, \pi, 3\pi/2, \ldots$, which coincide with the real axis, and $\delta_r = \pi/4, 3\pi/4, 5\pi/4, \ldots$, which is the circle with center the origin passing through the point $(\eta_r, 0)$. For layers starting at a point not on the real axis, the same set of contours of equal δ_r will still apply, with a correction to the value of δ_r that each represents.

Figure 3.1a shows the locus of a film deposited on a transparent substrate of admittance α. The starting point is $(\alpha, 0)$ and, as the thickness is increased to a quarter-wave, a semicircle is traced out clockwise that reintersects the real axis in the point $(\eta_r^2/\alpha, 0)$. A second quarter-wave completes the circle. We could have had any point on the locus as starting point without changing its form. The only difference would have been an offset in the scale of δ_r.

We could add isoreflectance contours to the diagram if we wished. These are circles with centers on the real axis, centers and radii being given by

$$(\eta_0(1+R)/(1-R), 0) \quad \text{and} \quad 2\eta_0(R)^{1/2}/(1-R) \tag{3.5}$$

respectively, where η_0 is the admittance of the incident medium. Since the addition of incident medium material to a surface has no effect on its reflectance, the isoreflectance circles must also be admittance circles of material with admittance η_0.

The phase of the reflectance can also be important and isophase contours are not unlike the contours of constant δ_r. We can carry through a similar procedure to determine the contours and the most important ones are 0, $\pi/2$, π, and $3\pi/2$, that is, the boundaries between the quadrants. The boundary between the first and fourth and between the second and third is simply the real axis, while that between the first and second and the third and fourth is a circle with center the origin which passes through the point $(\eta_0, 0)$. These contours are shown in Figure 3.1b where the various quadrants are labeled.

For the purpose of drawing an admittance diagram, it is most convenient to set η in units of Y, the admittance of free space. Then the optical admittances will have the same numerical value as the refractive indices (at normal incidence only, of course).

The method can be illustrated by the same example as in the amplitude reflection coefficient loci

Air | LH | Glass

where glass has index 1.52, air 1.0, and H and L are quarter-waves of zinc sulfide ($n = 2.35$) and cryolite ($n = 1.35$), respectively.

In free space units, the starting admittance is simply 1.52, the admittance of glass. The termination of the first layer, since it is a quarter-wave, will be at an admittance of $2.35^2/1.52 = 3.633$ on the real axis, and of the second, which is also a quarter-wave, at $1.35^2/3.633 = 0.5016$ on the real axis. The circles are traced out clockwise and each is a semicircle with center on the real axis. Figure 3.2 shows the complete locus.

Metal and other absorbing layers can also be included, although we find the calculations sufficiently involved to require the assistance of a computer. Figure 3.3 shows two loci applying to metal layers, one starting from an admittance of 1.0 and the other from 1.52 (free space units). The higher the ratio k/n for the metal, the nearer the locus is to a circle with center the origin. In the case of Figure 3.3, the locus is somewhat distorted from the ideal case, with a loop bowing out along the direction of the real axis. If we were to add isoreflectance contours to the diagram, corresponding to admittances of 1.52 for the starting admittance of 1.0, and of 1.0 for the starting admittance of 1.52, so that the loci correspond to internal and external reflection from such a metal layer on glass in air, we would see that the observed reduction in internal reflectance when the metal is very thin is predicted by the diagram as well as the constantly increasing external reflectance for the same

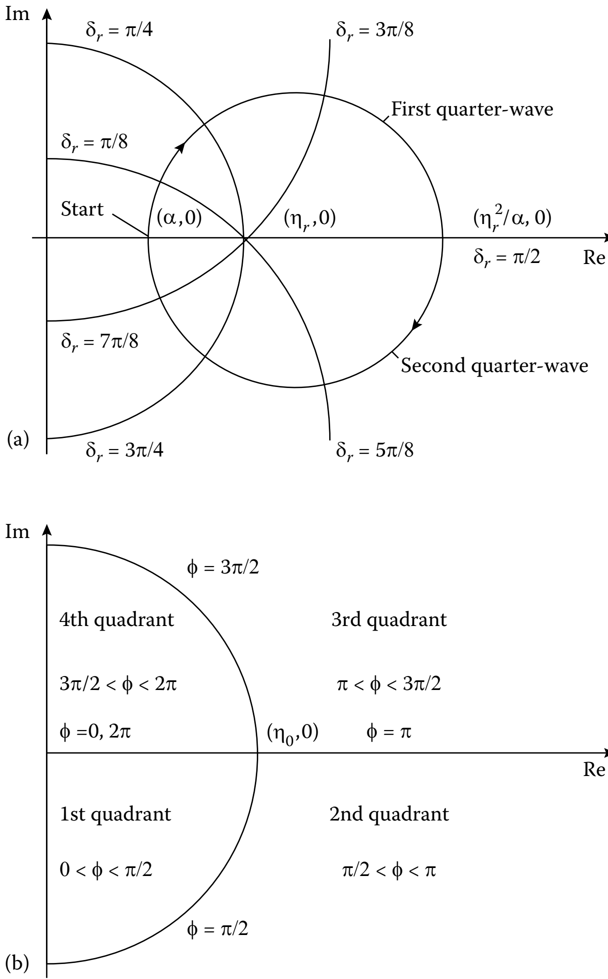

FIGURE 3.1
(a) Admittance locus of a single dielectric film. The locus is a circle centered on the real axis and described clockwise. The film of characteristic admittance Y is assumed to be deposited over a substrate or structure with real admittance α. Note that the product of the admittance of the two points of intersection of the locus with the real axis is always Y^2, the square of the characteristic admittance of the film. Equi-phase-thickness contours have also been added to the diagram. (b) Contours of constant phase shift on reflection φ can be added to the admittance diagram. These contours are all circles with centers on the imaginary axis and passing through the point on the real axis corresponding to the admittance η_0 of the incident medium. The four most important contours correspond to 0, $\pi/2$, π, $3\pi/2$, and these are represented by portions of the real axis and the circle centered on the origin and passing through the point η_0. These are indicated on the diagram and the regions corresponding to the various quadrants of φ are marked.

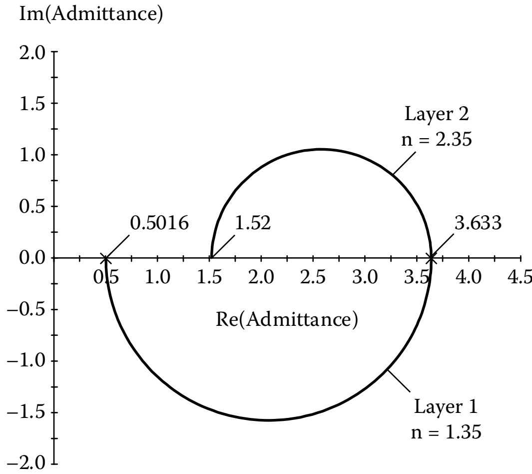

FIGURE 3.2
The admittance of the coating: Air $|LH|$ Glass, with L a quarter-wave of index 1.35, H of 2.35. The indices of air and glass are 1.00 and 1.52, respectively. This is the same coating as in Figure 3.12; note the similarity in shape to that figure.

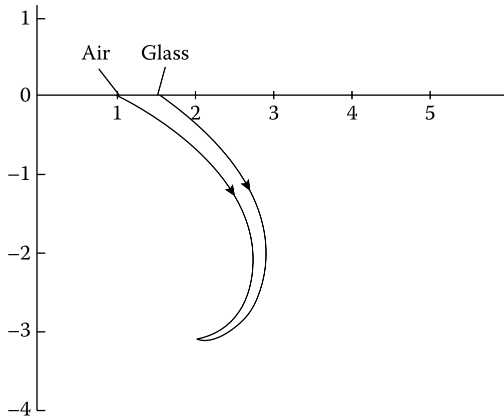

FIGURE 3.3
Admittance loci corresponding to a metal such as chromium with $n - ik = 2 - i3$. Loci are shown for starting points 1.00 and 1.52, corresponding to air and glass, respectively. Note that the initial direction toward the lower right of the diagram implies that in the case of the internal reflectance of the film deposited on glass (i.e., air as substrate and glass as incident medium and the left of the two loci), the reflectance initially falls and then rises, whereas the external reflectance (glass as substrate and air as incident medium and the right of the two admittance loci) always increases, even for very thin layers. When the layers are very thick, they terminate at the point $2 - i3$, so that the film is optically indistinguishable from the bulk material.

range of thicknesses (we can see such an effect in Figure 5.7). Metals with still lower ratios of k/n depart still further from the ideal circle, and in fact those starting at 1.0 can initially loop into the first quadrant so that they actually cut the real axis again, even sometimes at the point 1.52 to give zero internal reflectance.

We have gained much in simplicity by choosing to deal in terms of optical admittance throughout the assembly. It has not affected in any way our ability to calculate either the amplitude reflection coefficient or reflectance. Transmittance is another matter. Strictly, we need to preserve the values of B and C in the matrix calculation. The optical admittance is not sufficient. For dielectric assemblies, we know that the transmittance is given by $(1-R)$, but for assemblies containing absorbing layers, subsidiary calculations are necessary. For many purposes, reflectance is sufficient and, since the graphic technique is used for visualization rather than calculation, a lack of transmission information is not a serious defect. Nevertheless there are concepts that do yield useful information about transmittance and about losses in layers, directly from the admittance diagram. These are dealt with in the following section.

3.3 Electric Field and Losses in the Admittance Diagram

The optical properties of any material are determined largely by the electrons and their interaction with electromagnetic disturbances. Any optical material is made up of atoms or molecules consisting of heavy positively charged masses surrounded by negatively charged electrons. These electrons are light and mobile compared with the heavy positively charged nuclei. An electric field can exert a force on a charged particle even while it is stationary, but a magnetic field can interact only when the charged particle moves, and for any significant interaction, the particle must be moving at an appreciable fraction of the speed of light. At the very high frequencies of optical waves the magnetic interaction is virtually zero. We have already used the fact that the relative permeability is unity in setting up the basic theory. The interaction between light and a material is, therefore, entirely through the electric field. Where the electric field amplitude is high the potential for interaction is high. When thin film optical coatings are illuminated by light, standing wave patterns form that can exhibit considerable variations in electric field amplitude both in terms of wavelength and in terms of position within the coating. The admittance diagram permits a simple technique for assessing these amplitude variations and from them deductions about losses can be made, sometimes with surprising results.

In this discussion we limit ourselves to normal incidence. Oblique incidence represents only a very slight extension.

The basic matrix technique for the calculation of the properties of an optical coating actually contains already the electric field and so only a slight modification is required to extract it. The matrix expression, with the usual meaning for the symbols, is:

$$\begin{bmatrix} B \\ C \end{bmatrix} = \begin{bmatrix} \cos\delta & \dfrac{i\sin\delta}{y} \\ iy\sin\delta & \cos\delta \end{bmatrix} \begin{bmatrix} 1 \\ y_{exit} \end{bmatrix}$$

In this expression, B and C, and the corresponding terms in the other column matrix, are normalized total tangential electric and magnetic fields. The admittances, too, are normalized so that they are in free space units rather than SI units. The first thing we do, therefore, is to restore the expressions to their fundamental form.

$$\begin{bmatrix} E' \\ H' \end{bmatrix} = \begin{bmatrix} \cos\delta & \dfrac{i\sin\delta}{y} \\ iy\sin\delta & \cos\delta \end{bmatrix} \begin{bmatrix} E \\ H \end{bmatrix}$$

Here y is in free space units and so to change it to SI units we must write

$$y = (n - ik)\mathcal{Y}$$

where $\mathcal{Y}$ is the admittance of free space. E and H indicate the complex tangential amplitudes that include the relative phase.

To have absolute values for the total tangential electric field amplitude through the multilayer, it remains simply to give an absolute value to one of the E's. This can be done in a number of ways.

The easiest is to put a value on the final tangential component at the emergent interface, that is, the interface with the substrate. This is related to the incident irradiance through the transmittance. If the incident irradiance is I_{inc}, then

$$\frac{1}{2}\mathrm{Re}\left(E_{exit} \cdot H^{*}_{exit}\right) = T \cdot I_{inc}$$

but

$$H_{exit} = y_{exit}E_{exit}$$

and so

$$\frac{1}{2}\mathrm{Re}\left(E_{exit}\cdot y^{*}_{exit}E^{*}_{exit}\right)=T\cdot I_{inc}$$

Now

$$E\cdot E^{*}=\mathcal{E}^{2}$$

giving, with a little manipulation,

$$E_{exit}=\mathcal{E}_{exit}=\sqrt{\frac{2T\cdot I_{inc}}{y_{exit}}}$$

where y_{exit} must be in SI units, that is, siemens.

If the multilayer system is completely free of absorption, then there is a simple connection between the variation of admittance through the multilayer, which is the quantity we plot in the admittance diagram, and the electric field amplitude.

The admittance at any point in the multilayer is simply the ratio of the total tangential magnetic and electric fields. These total tangential fields also yield the total net irradiance transmitted by the multilayer. Since this multilayer is free of losses, the transmitted irradiance is constant through the multilayer. Putting all this together gives

$$\begin{aligned}I_{out}&=\frac{1}{2}\mathrm{Re}\left(E\cdot H^{*}\right)\\&=\frac{1}{2}\mathrm{Re}\left(E\cdot Y^{*}E^{*}\right)\\&=\frac{1}{2}\mathcal{E}^{2}\cdot\mathrm{Re}\left(Y\right)\end{aligned}$$

i.e.,

$$\mathcal{E}=\sqrt{\frac{2I_{out}}{\mathrm{Re}(Y)}}=\sqrt{\frac{2T\cdot I_{inc}}{\mathrm{Re}(Y)}}\propto\frac{1}{\sqrt{\mathrm{Re}(Y)}}\tag{3.6}$$

Contours of constant electric field are therefore lines, normal to the real axis in the admittance diagram. If we put Y in free space units, then Equation 3.6 becomes:

$$\mathcal{E}=27.46\sqrt{\frac{T\cdot I_{inc}}{\mathrm{Re}(Y)}}\ \text{volt/meter}\tag{3.7}$$

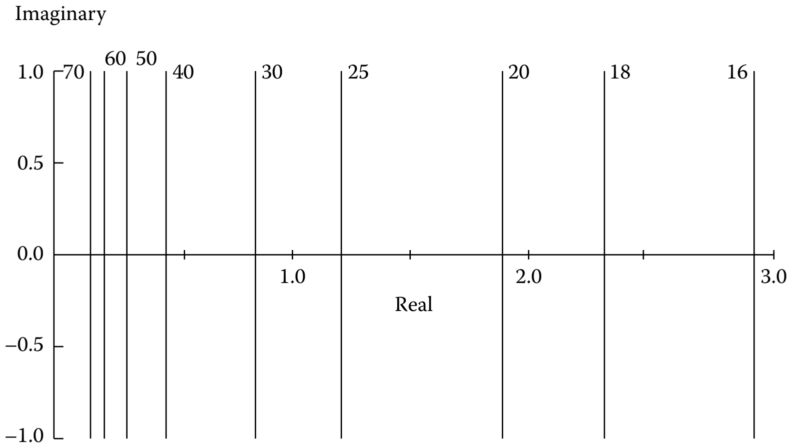

FIGURE 3.4
Lines of constant electric field amplitude for dielectric materials in the admittance diagram. The figures are in volt/meter if the transmitted irradiance is 1 watt/square meter.

Now let us consider a very thin slice of absorbing material embedded in a multilayer. What can we say about the absorption of this slice?

The result is contained in the expression:

$$\begin{bmatrix} E' \\ H' \end{bmatrix} = \begin{bmatrix} \cos\delta & \dfrac{i\sin\delta}{y} \\ iy\sin\delta & \cos\delta \end{bmatrix} \begin{bmatrix} E \\ H \end{bmatrix}$$

where the input and exit irradiances are given by

$$I_{in} = \frac{1}{2}\mathrm{Re}(E' \cdot H'^{*}) \quad \text{and} \quad I_{exit} = \frac{1}{2}\mathrm{Re}(E \cdot H^{*})$$

The irradiance lost by absorption in the layer is the difference between these two quantities. Now let the layer be extremely thin. Since the layer is absorbing δ is given by

$$\delta = \frac{2\pi\left(n - ik\right)d}{\lambda} = \alpha - i\beta \tag{3.8}$$

Equation 3.8 defines the quantities α and β. By extremely thin, we mean that d/λ should be sufficiently small to make both α and β vanishingly small, whatever the size of either n or k.

Then,

$$\begin{bmatrix} E' \\ H' \end{bmatrix} = \begin{bmatrix} \cos(\alpha - i\beta) & \dfrac{i\sin(\alpha - i\beta)}{y} \\ iy\sin(\alpha - i\beta) & \cos\left(\alpha - i\beta\right) \end{bmatrix} \begin{bmatrix} E \\ H \end{bmatrix}$$

$$= \begin{bmatrix} 1 & \dfrac{i(\alpha - i\beta)}{(n - ik)\mathcal{Y}} \\ i(\alpha - i\beta)(n - ik)\mathcal{Y} & 1 \end{bmatrix} \begin{bmatrix} E \\ H \end{bmatrix}$$

$$= \begin{bmatrix} E + \dfrac{i(\alpha - i\beta)H}{(n - ik)\mathcal{Y}} \\ i(\alpha - i\beta)(n - ik)\mathcal{Y}E + H \end{bmatrix}$$

where we are including terms up to the first order only in α and β.

The irradiance at the entrance to this thin layer will then be given by

$$I_{in} = \frac{1}{2}\mathrm{Re}\left[\left\{E + \frac{i(\alpha - i\beta)H}{(n - ik)\mathcal{Y}}\right\}\cdot\left\{i\left(\alpha - i\beta\right)\left(n - ik\right)\mathcal{Y}E + H\right\}^*\right]$$

$$= \frac{1}{2}\mathrm{Re}\left[E\cdot H^* + E\cdot\left\{-i\left(\alpha + i\beta\right)\left(n + ik\right)\mathcal{Y}E^*\right\}\right]$$

$$+ \frac{1}{2}\mathrm{Re}\left[\frac{i\left(\alpha - i\beta\right)H\cdot H^*}{\left(n - ik\right)\mathcal{Y}}\right] \tag{3.9}$$

The second of the two terms in Equation 3.9 simplifies to

$$\frac{1}{2}\mathrm{Re}\left[\frac{i(\alpha - i\beta)H\cdot H^*}{(n - ik)\mathcal{Y}}\right] = \frac{1}{2}\mathrm{Re}\left[\frac{i(\alpha - i\beta)(n + ik)H\cdot H^*}{(n^2 + k^2)\mathcal{Y}}\right]$$

$$= \frac{1}{2}\mathrm{Re}\left[\frac{\left\{\beta n - \alpha k + i(\alpha n + \beta k)\right\}H\cdot H^*}{(n^2 + k^2)\mathcal{Y}}\right]$$

$$= \frac{1}{2}\left[\frac{(\beta n - \alpha k)H\cdot H^*}{(n^2 + k^2)\mathcal{Y}}\right]$$

But

$$\beta n - \alpha k = \frac{2\pi kd}{\lambda}n - \frac{2\pi nd}{\lambda}k = 0$$

The first term gives

$$I_{in} = \frac{1}{2}\mathrm{Re}\left[E \cdot H^* + E \cdot \left\{-i(\alpha + i\beta)(n + ik)\mathcal{Y}E^*\right\}\right]$$
$$= \frac{1}{2}\mathrm{Re}\left[E \cdot H^*\right] + \frac{1}{2}\left[(\alpha k + \beta n)\mathcal{Y}E \cdot E^*\right]$$

where

$$\alpha k + \beta n = \frac{4\pi nkd}{\lambda} \quad \text{and} \quad E \cdot E^* = \mathcal{E}^2$$

The irradiance that has been absorbed is therefore given by the difference between the irradiance incident on the thickness element, I_{in}, and that emerging on the exit side, I_{exit}, and this is

$$I_{absorbed} = \frac{2\pi nkd}{\lambda} \cdot \mathcal{Y} \cdot \mathcal{E}^2 \tag{3.10}$$

The magnitude of the absorbed energy is directly proportional to the produce of n and k. Both must be nonzero for absorption to occur. The absorption will be small for both a metal with vanishingly small n and a dielectric with vanishingly small k. The factor involving n and k may be thought of as a phase thickness multiplied by k or as a quantity β multiplied by n. The quantity nk is therefore a useful indicator of the potential for loss in any given material.

Now we need to consider the contribution to the absorption A of the multilayer. This is a little more difficult and we need to introduce a further concept that will be used in subsequent chapters.

Potential transmittance, ψ, of any element of a coating system is defined as the ratio of the output to the input irradiances, the input being the net irradiance rather than the incident. Potential transmittance has several advantages over transmittance when dealing with absorbing systems because it completely avoids any problems associated with the mixed Poynting vector in absorbing media. The potential transmittance of a complete system is simply the product of the individual potential transmittances.

$$\psi = \frac{I_{exit}}{I_{in}}$$

$$\psi_{system} = \psi_1 \cdot \psi_2 \cdot \psi_3 \cdot \psi_4 \cdot \psi_5 \cdots \psi_q$$

with the eventual overall transmittance given by

$$T = (1 - R) \cdot \psi_{system}$$

The potential transmittance of the thin elemental film is given by

$$\psi = \frac{I_{exit}}{I_{in}} = 1 - \frac{I_{absorbed}}{I_{in}} = 1 - \mathcal{A}$$

where $\mathcal{A}$ is the potential absorptance. But

$$I_{in} = \frac{1}{2}\mathcal{Y} \cdot \mathrm{Re}\left(Y\right) \cdot \mathcal{E}^2$$

where Y is given in free space units. Then

$$\psi = 1 - \mathcal{A} = 1 - \frac{2\pi nkd}{\lambda} \cdot \frac{2}{\mathrm{Re}(Y)} \tag{3.11}$$

This result allows interpretation of an admittance locus in terms of potential absorption.

To move from potential absorption to absorption is straightforward when the absorption is confined to a very thin layer, the rest of the multilayer being essentially transparent. Then the absorption, A, is given by:

$$A = (1 - R)\mathcal{A}$$

If, however, the absorption is distributed through the layer, then the calculation is rather more involved. Normally the absorption would be calculated by the normal matrix expression for the entire film and then would be completely accurate. We, however, are looking for a way of estimating the absorption and its variation through a layer given the locus in the admittance diagram or the electric field distribution. Let us assume that the absorption is rather small. The layer may be considered as a succession of slices of equal optical thickness and extinction coefficient and so the first factor in the expression for $\mathcal{A}$ is a constant. Each slice has a potential absorptance that depends on the real part of the optical admittance, following Equation 3.11. Then the potential transmittance is given by the product of the individual potential transmittances,

$$\begin{aligned}\psi &= \psi_1 \cdot \psi_2 \cdot \psi_3 \cdot \psi_4 \cdots \\ &= (1 - \mathcal{A}_1) \cdot (1 - \mathcal{A}_2) \cdot (1 - \mathcal{A}_3) \ldots \\ &= 1 - (\mathcal{A}_1 + \mathcal{A}_2 + \mathcal{A}_3 + \mathcal{A}_4 + \ldots) + \mathcal{A}_1\mathcal{A}_2 + \ldots\end{aligned}$$

Provided the potential absorptances are small enough, the product terms can be neglected and then the total potential absorptance is given by the sum of the individual absorptances,

$$\mathcal{A} = \mathcal{A}_1 + \mathcal{A}_2 + \mathcal{A}_3 + \mathcal{A}_4 + \ldots \tag{3.12}$$

In terms of an integral, this can be written as

$$\mathcal{A} = \sum_j \mathcal{A}_j = \int_\delta \frac{2k}{\mathrm{Re}(Y)} d\delta = \int_\beta \frac{2n}{\mathrm{Re}(Y)} d\beta \tag{3.13}$$

If an accurate answer is required, we will always turn to the computer and a very simple rapid calculation. To understand the result, usually we would like to know what to do either to increase or decrease the absorptance or to find sensitive regions where contamination or scattering roughness is especially to be avoided. To answer such questions, usually a rough answer that shows trends is all that is needed.

3.4 The Vector Method

The vector method is a valuable technique, especially in design work associated with antireflection coatings. Two assumptions are involved: first, that there is no absorption in the layers, and, second, that the behavior of a multilayer can be determined by considering one reflection of the incident wave at each interface only. The errors involved in using this method can be, in some cases, significant, especially where high overall reflectance from the multilayer exists, but they are small in most types of antireflection coating.

Consider the assembly sketched in Figure 3.5. If there is no absorption in the layers, then $N_r = n_r$ and $k_r = 0$. The amplitude reflection coefficient at each interface is given by

$$\rho = \frac{n_{r-1} - n_r}{n_{r-1} + n_r}$$

which may be positive or negative depending on the relative magnitudes of n_{r-1} and n_r.

The phase thicknesses of the layers are given by δ_1, δ_2, …, where

$$\delta_r = 2\pi n_r d_r / \lambda.$$

A quarter-wave optical thickness is represented by 90°, and a half-wave by 180°.

As the diagram shows, the resultant amplitude reflection coefficient is given by the vector sum of the coefficients for each interface, where each is associated with the appropriate phase lag corresponding to the passage of the wave from the front surface to the interface and back to the front surface again.

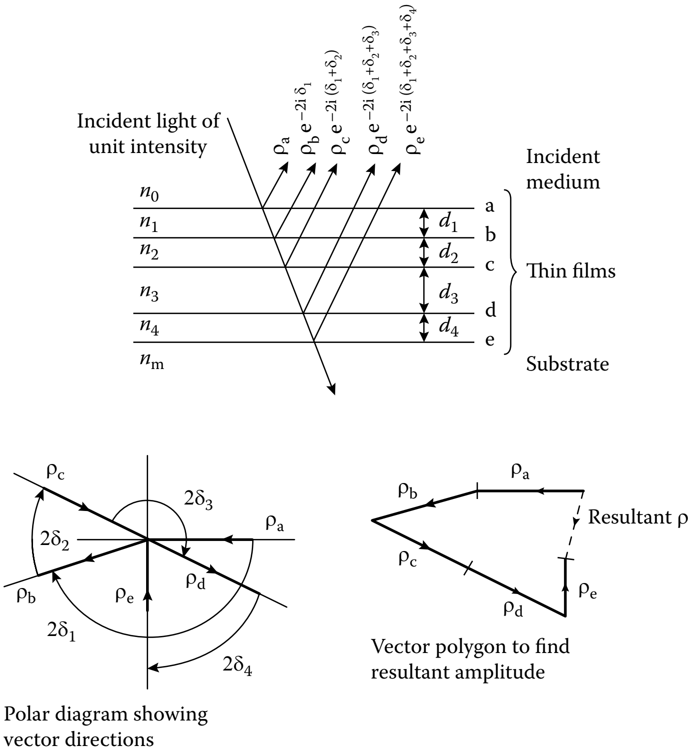

FIGURE 3.5
The vector method. The lengths of the vectors and the phase angles are given by:

$$\rho_a = (n_0 - n_1)/(n_0 + n_1) \ \delta_1 = 2\pi n_1 d_1/\lambda$$

$$\rho_b = (n_1 - n_2)/(n_1 + n_2) \ \delta_2 = 2\pi n_2 d_2/\lambda$$

etc. Note that the sign of the expression for the vector lengths is important and must be included. In the diagram, ρ_a, ρ_c, and ρ_e, are shown as having a negative sign. Note also that the angles between successive vectors are phase lags, so that the sense of all the angles in the polar diagram, 25,, 26,, etc, is also negative.

$$\rho = \rho_a + \rho_b \exp(-2i\delta_1) + \rho_c \exp[-2i(\delta_1 + \delta_2)]$$
$$+\rho_d \exp[-2i(\delta_1 + \delta_2 + \delta_3)] + \ldots$$

The sum can be found analytically or, as is more usual, graphically. The graphic case is easier because the angles between successive vectors are merely $2\delta_1$, $2\delta_2$, $2\delta_3$, and so on.

The calculation of the angles for any wavelength is simplified if, as is usual, the optical thicknesses of the layers are given in terms of quarter-wave optical thicknesses at a reference wavelength λ_0. If the optical thickness of the *r*th

layer is t_r quarter-waves at λ_0, then the value of δ_r at λ is just $\delta_r = (90°t_r\lambda_0/\lambda)$ degrees of arc.

In practice, it will be found extremely easy to confuse angles and directions, particularly where negative reflectances are involved. The task of drawing the vector diagram is greatly eased by plotting first the vectors with directions on a polar diagram and then transferring the vectors to a vector polygon rather than attempting to draw the vector polygon straight away. An important point to remember is that the resultant vector represents the amplitude reflection coefficient and its length must be squared in order to give the reflectance.

A typical arrangement is shown in Figure 3.5. The vector method is used to a considerable extent in Chapter 4 which deals with antireflection coatings.

3.5 The Herpin Index

An extremely important result for filter design is derived in Chapter 7, which deals with edge filters. Briefly, this is the fact that any symmetrical product of three thin-film matrices can be replaced by a single matrix, which has the same form as that of a single film and therefore possesses an equivalent thickness and an equivalent optical admittance. Of course, this is a mathematical device rather than a case of true physical equivalence, but the result is of considerable use in giving an insight into the properties of a great number of filter designs, which can be split into a series of symmetrical combinations. The method also allows the replacement, under certain conditions, of a layer of intermediate index by a symmetrical combination of high and low index material. This is especially useful in the design of antireflection coatings, which frequently require quarter-wave thicknesses of unobtainable intermediate indices. These difficult layers can be replaced by symmetrical combinations of existing materials with the additional advantage of limiting the total number of materials required for the structure.

The equivalent admittance is frequently known as the Herpin Index, after the originator, and the symmetrical combination as an Epstein period, after the author of two of the most important early papers dealing with the application of the result to the design of filters.

The detailed derivation of the relevant formulae is left until Chapter 6, which will make considerable use of the concept.

3.6 Alternative Method of Calculation

The success of the vector method prompts one to ask whether it can be made more accurate by considering second and subsequent reflections at the

various boundaries instead of just one. In fact, an alternative solution of the thin-film problem can be obtained in this way and this was the earlier way of formulating film properties dating back to Poisson (see Chapter 1). It is simpler to consider normal incidence only. The expressions can be adapted for non-normal incidence quite simply when the materials are transparent and with some difficulty when they are absorbing. We consider first the case of a single film. Figure 3.6 defines the various parameters.

The resultant amplitude reflection coefficient is given by

$$\begin{aligned}\rho^+ &= \rho_a^+ + \tau_a^+\rho_b^+\tau_a^- e^{-2i\delta} + \tau_a^+\rho_b^+\rho_a^-\rho_b^+\tau_a^- e^{-4i\delta}\\ &\quad + \tau_a^+\rho_b^+\rho_a^-\rho_b^+\rho_a^-\rho_b^+\tau_a^- e^{-6i\delta}\\ &= \rho_a^+ + \frac{\rho_b^+\tau_a^+\tau_a^- e^{-2i\delta}}{1-\rho_b^+\rho_a^- e^{-2i\delta}}\end{aligned}$$

However

$$\tau_a^+\tau_a^- = \frac{4N_0N_1}{\left(N_0+N_1\right)^2} = 1-\rho$$

and $\rho_a^- = -\rho_a^+$ so that

$$\rho^+ = \frac{\rho_a^+ + \rho_b^+ e^{-2i\delta}}{1+\rho_b^+\rho_a^+ e^{-2i\delta}} \tag{3.14}$$

Similarly

$$\tau^+ = \tau_a^+\tau_b^+\rho_b^+ e^{-i\delta} + \tau_a^+\rho_b^+\rho_a^-\tau_b^+ e^{-3i\delta} + \tau_a^+\rho_b^+\rho_a^-\rho_b^+\rho_a^-\tau_b^+ e^{-5i\delta}$$

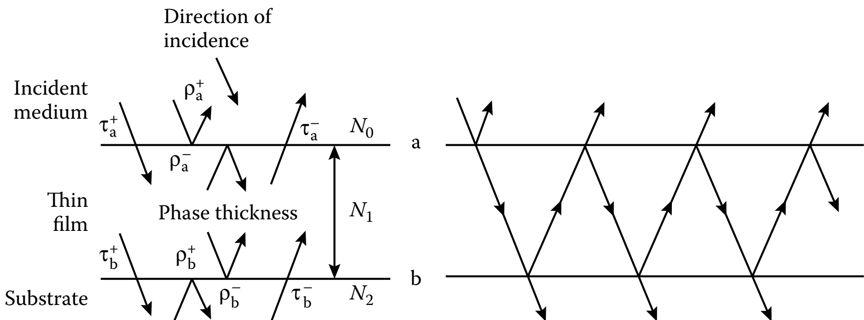

FIGURE 3.6
Parameters in the multiple beam summation.

which reduces to

$$\begin{aligned}\tau^+ &= \frac{\tau_a^+\tau_b^+e^{-i\delta}}{1-\rho_a^-\rho_b^+e^{-2i\delta}} \\ &= \frac{\tau_a^+\tau_b^+e^{-i\delta}}{1+\rho_a^+\rho_b^+e^{-2i\delta}}\end{aligned} \tag{3.15}$$

These expressions can be used in calculations of assemblies of more than one film by applying them successively, first to the final two interfaces, which can then be replaced by a single interface with the resultant coefficients, and then to this equivalent interface and the third last interface, and so on.

The resultant amplitude transmission and reflection coefficients τ^+ and ρ^+ can be converted into transmittance and reflectance using the expressions

$$R = \left(\rho^+\right)\left(\rho^+\right)^*$$

$$T = \frac{n_2}{n_0}\left(\tau^+\right)\left(\tau^+\right)^*$$

n_2 and n_0 are the refractive indices of the substrate, or exit medium, and the incident medium respectively. For these expressions to be meaningful, we must, as before, restrict the incident medium to be transparent so that $N_0 = n_0$. No such restriction applies to the exit medium, which can have complex $N_2 = n_1 - ik_2$, the real part being used in the above expression for T.

It is also possible to develop a matrix approach along these lines. The electric field vectors $\mathcal{E}_0^+$ and $\mathcal{E}_0^-$ in medium 0 at interface a can be expressed in terms of $\mathcal{E}_1^+$ and $\mathcal{E}_1^-$ in film 1 at interface b (see Figure 3.7).

$$\begin{bmatrix}\mathcal{E}_0^+ \\ \mathcal{E}_0^-\end{bmatrix} = \frac{1}{\tau_a^+}\begin{bmatrix} e^{i\delta_1} & \rho_a^+e^{-i\delta_1} \\ \rho_a^+e^{i\delta_1} & e^{-i\delta_1}\end{bmatrix}\begin{bmatrix}\mathcal{E}_1^+ \\ \mathcal{E}_1^-\end{bmatrix} \tag{3.16}$$

If $\mathcal{E}_2^+$ is the tangential component of amplitude in medium 2, then, since there is only a positive-going wave in that medium

$$\begin{bmatrix}\mathcal{E}_1^+ \\ \mathcal{E}_1^-\end{bmatrix} = \frac{1}{\tau_b^+}\begin{bmatrix} 1 \\ \rho_b^+\end{bmatrix}\mathcal{E}_2^+ \tag{3.17}$$

Equations 3.16 and 3.17 can be extended in the normal way to cover the case of many layers. The only point to watch is that ρ_a^+ and τ_a^+ must refer to the coefficients of the boundary in the correct medium. That is, all the

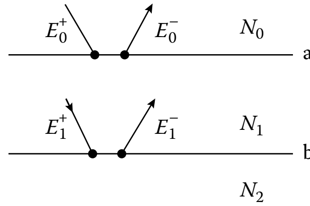

FIGURE 3.7
The positive- and negative-going waves at the two interfaces.

reflection coefficients, ρ, and transmission coefficients, τ, must be calculated for the boundaries as they exist in the multilayer. Thus, if we take an existing multilayer and add an extra layer, not only do we add an extra interface but we alter the amplitude reflection and transmission coefficients of what now becomes the second last interface. Thus, two layers must be recomputed and not just one.

If absorption is included, the formulae remain the same, but the parameters ρ, τ, and δ become complex.

3.7 Smith's Method of Multilayer Design

In 1958, Smith [1], then of the University of Reading, published a useful design method based on Equation 3.15. The technique is also known as *the method of effective interfaces*. It consists of choosing any layer in the multilayer and then considering multiple reflections within it, the reflection and transmission coefficients at its boundaries being the resultant coefficients of the complete structures on either side. The method of summing multiple beams is, of course, quite old and the novel feature of the present technique is the way in which it is applied. Although the technique described by Smith was principally concerned with dielectric multilayers, it can be extended to deal with absorbing layers. As before, we limit ourselves, in the derivation, to normal incidence. When the layers are transparent, the expressions can be extended to oblique incidence without major difficulty. The notation is illustrated in Figure 3.8.

From Equation 3.15

$$\tau^+ = \frac{\tau_a^+ \tau_b^+ e^{-i\delta}}{1 - \rho_a^- \rho_b^+ e^{-2i\delta}}$$

where

$$\delta = 2\pi Nd/\lambda$$

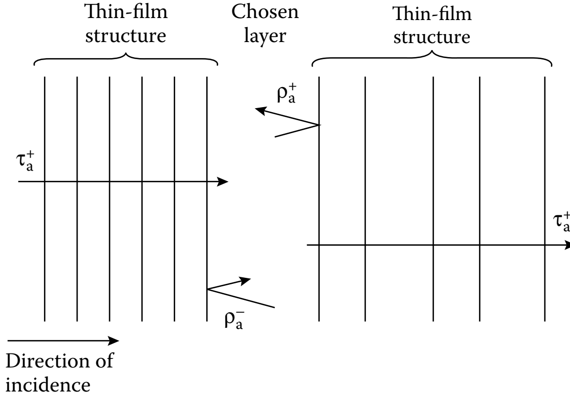

FIGURE 3.8
The quantities associated with the effective interfaces in Smith's technique.

Now $N = n - ik$ and we can write δ as

$$\delta = 2\pi\left(n - ik\right)d/\lambda = \alpha + i\beta$$

and

$$e^{-i\delta} = e^{-\beta}e^{-i\alpha}$$

where $\alpha = 2\pi nd/\lambda$, the phase thickness of the layer, and $\beta = 2\pi kd/\lambda$. Now

$$T = \frac{n_m}{n_0}\left(\tau^+\right)\left(\tau^+\right)^*$$

where n_m is the real part of the exit medium index and n_0 is the refractive index of the incident medium.

$$T = \frac{n_m}{n_0}\frac{\left(\tau_a^+\right)\left(\tau_a^+\right)^*\left(\tau_b^+\right)\left(\tau_b^+\right)^* e^{-2\beta}}{\left(1-\rho_a^-\rho_b^+e^{-2\beta}e^{-2i\alpha}\right)\left(1-\rho_a^-\rho_b^+e^{-2\beta}e^{-2i\alpha}\right)^*}$$

Now, let

$$\tau_a^+ = \left|\tau_a^+\right|e^{i\varphi_a'} \qquad \rho_a^- = \left|\rho_a^-\right|e^{i\varphi_a}$$

$$\tau_b^+ = \left|\tau_b^+\right|e^{i\varphi_b'} \qquad \rho_b^+ = \left|\rho_b^+\right|e^{i\varphi_b}$$

Then,

$$T = \frac{n_m}{n_0}\frac{\left|\tau_a^+\right|^2\left|\tau_b^+\right|^2 e^{-2\beta}}{\left(1-\left|\rho_a^-\right|\left|\rho_b^+\right|e^{i(\varphi_a+\varphi_b)}e^{-2\beta}e^{-2i\alpha}\right)\left(1-\left|\rho_a^-\right|\left|\rho_b^+\right|e^{-i(\varphi_a+\varphi_b)}e^{-2\beta}e^{2i\alpha}\right)}$$

i.e.

$$T = \frac{n_m}{n_0} \frac{\left|\tau_a^+\right|^2 \left|\tau_b^+\right|^2 e^{-2\beta}}{\left[1 - \left|\rho_a^-\right|^2 \left|\rho_b^+\right|^2 e^{-4\beta} - 2\left|\rho_a^-\right|\left|\rho_b^+\right| e^{-2\beta} \cos(\varphi_a + \varphi_b - 2\alpha)\right]} \tag{3.18}$$

A marginally more convenient form of the expression can be obtained by substituting $1 - 2\sin^2\left[\left(\varphi_a + \varphi_b\right)/2 - \alpha\right]$ for $\cos\left(\varphi_a + \varphi_b - 2\alpha\right)$, and with some rearrangement

$$T = \frac{n_m}{n_0} \frac{\left|\tau_a^+\right|^2 \left|\tau_b^+\right|^2 e^{-2\beta}}{\left(1 - \left|\rho_a^-\right|\left|\rho_b^+\right| e^{-2\beta}\right)^2} \cdot \left[1 + \frac{4\left|\rho_a^-\right|\left|\rho_b^+\right| e^{-2\beta}}{\left(1 - \left|\rho_a^-\right|\left|\rho_b^+\right| e^{-2\beta}\right)^2} \times \sin^2\left(\frac{\varphi_a + \varphi_b}{2} - \frac{2\pi nd}{\lambda}\right)\right]^{-1} \tag{3.19}$$

If there is no absorption in the chosen layer, i.e., $\beta = 0$, then the restrictions on reflectances in absorbing media no longer apply and we can write

$$T_a = \frac{n}{n_0}\left|\tau_a^+\right|^2 \qquad R_a^- = \left|\rho_a^-\right|^2$$

$$T_b = \frac{n_m}{n}\left|\tau_b^+\right|^2 \qquad R_a^- = \left|\rho_b^+\right|^2$$

$$T = \frac{T_a T_b}{\left[1 - \left(R_a^- R_b^+\right)^{1/2}\right]^2} \cdot \left[1 + \frac{4R_a^- R_b^+}{\left[1 - \left(R_a^- R_b^+\right)^{1/2}\right]^2} \times \sin^2\left(\frac{\varphi_a + \varphi_b}{2} - \frac{2\pi nd}{\lambda}\right)\right]^{-1} \tag{3.20}$$

which is the more usually quoted version.

The usefulness of this method is mainly in providing an insight into the properties of a particular type of filter, and it is of considerable value in design. It is certainly not the easiest method of determining the performance of a given multilayer—this is best tackled by a straightforward application of the matrix method. What Equations 3.19 or 3.20 do is to make it possible to isolate a layer, or a combination of several layers, and to examine the influence that these layers and any changes in them have on the performance of the filter as a whole. Smith's original paper includes a large number of examples of this approach and repays close study.

3.8 The Smith Chart

The Smith Chart [2,3] is one of a number of different devices of the same broad type that were originally intended to simplify calculation. The Smith Chart is the one that appears most frequently in the literature and so it is included here, although little use is made of it in the remainder of the book. The method depends on three properties of a thin-film structure.

1. Since the tangential components of ***E*** and ***H*** are continuous across a boundary, so also is the equivalent admittance. This has been implied in the section dealing with the matrix method but has not, perhaps, been explicitly stated there.
2. In any thin film, for example, layer q in Figure 3.9, the amplitude reflectance ρ at any plane within the layer is related to that at the edge of the layer remote from the incident wave ρ_m by

$$\rho = \rho_m e^{-2i\delta} \tag{3.21}$$

   where δ is the phase thickness of that part of the layer between the far boundary m and the plane in question.

   This second point is almost self-evident but may be shown by putting $\rho_a^+ = 0$ in Equation 3.15, since the boundary under consideration is an imaginary one between two media of identical admittance.
3. The amplitude reflection coefficient of any thin-film assembly, with optical admittance at the front surface of Y, is given by Equation 3.14, i.e.,

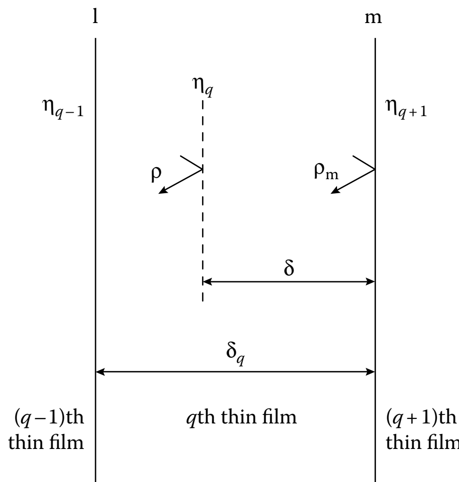

FIGURE 3.9
Parameters used in the Smith Chart description.

$$\rho = \frac{\eta_0 - Y}{\eta_0 + Y} = \frac{1 - Y/\eta_0}{1 + Y/\eta_0} \tag{3.22}$$

where η_0 is the admittance of the incident medium. Y/η_0 is sometimes known as the reduced admittance.

The procedure for calculating the effect of any layer in a thin-film assembly by using these properties is as follows.

1. ρ_m, the amplitude reflection coefficient at the boundary of the layer remote from the side of incidence, is given.
2. The amplitude reflection coefficient within the layer just inside the boundary l is then given by Equation 3.21:

$$\rho = \rho_m e^{-2i\delta_q} \tag{3.23}$$

3. The optical admittance just inside the boundary l is given by Equation 3.22:

$$\rho = \frac{1 - Y/\eta_q}{1 + Y/\eta_q} \tag{3.24}$$

i.e.,

$$\frac{Y}{\eta_q} = \frac{1 - \rho}{1 + \rho} \tag{3.25}$$

4. The optical admittance on the incident side of the boundary l is still Y because of condition 1 above. The reduced admittance is Y/η_{q-1} where

$$\frac{Y}{\eta_{q-1}} = \frac{\eta_q}{\eta_{q-1}} \cdot \frac{Y}{\eta_q} \tag{3.26}$$

5. The amplitude reflection coefficient ρ_l on the incident side of the boundary l is given by

$$\rho_l = \frac{1 - Y/\eta_{q-1}}{1 + Y/\eta_{q-1}} \tag{3.27}$$

Calculation of the amplitude reflection coefficient of any thin-film assembly is merely the successive application of Equations 3.23 to 3.27 to each layer in the system, starting with that at the end of the assembly remote from the incident wave.

The calculation can be carried out in any convenient way and can even be used as the basis for a computer program. The problem is similar to one

found in the study of high-frequency transmission lines and a simple graphic approach has been devised. The most awkward parts of the calculation are in Equations 3.25 and 3.27. A chart connecting values of X and Z, where

$$X = \frac{1 - Z}{1 + Z} \tag{3.28}$$

is shown in Figure 3.10 and is known as a Smith Chart after the originator, P. H. Smith [2] (not to be confused with the S. D. Smith of the previous section). Z is plotted in polar coordinates on the diagram, and the corresponding real and imaginary parts of X are read off from the sets of orthogonal circles. A slide rule is capable of the other part of the calculation, the multiplication by η_q/η_{q-1}.

A scale is provided around the outside of the chart to enable the calculation involved in Equation 3.23 to be very simply carried out by rotating the point corresponding to ρ_m around the center of the chart through the appropriate angle $2\delta_q$. The scale is calibrated in terms of optical thickness measured in fractions of a wavelength, taking into account that the angle is actually $2 \times \delta_q$.

3.9 Reflection Circle Diagrams

This technique, sometimes referred to simply as a circle diagram, was described by Berning [4] and its use in coating design was considerably developed and described in much detail by Apfel [5]. According to Apfel, Frank Rock originated this technique in the mid-1950s. The technique results in diagrams that have an appearance similar to that of the admittance diagram.

The scale and shape of the diagram are similar to that of the Smith Chart and, indeed, the identical set of coordinates and prepared graph paper may be used for both. This leads to a confusion of the two techniques with the name Smith Chart being applied to the circle diagram. They are really quite different. The Smith Chart slides a reference plane through an already existing multilayer and plots the net amplitude reflection coefficient at the plane. There are discontinuities in the locus, therefore, when an interface is crossed. Dielectric loci are circles centered at the origin. The circle diagram assumes that the multilayer is under construction so that the incident medium for the amplitude reflection coefficient is the incident medium for the entire multilayer.

This results also in circles, but there are no discontinuities in the resulting locus and the individual dielectric circles are no longer centered at the origin.

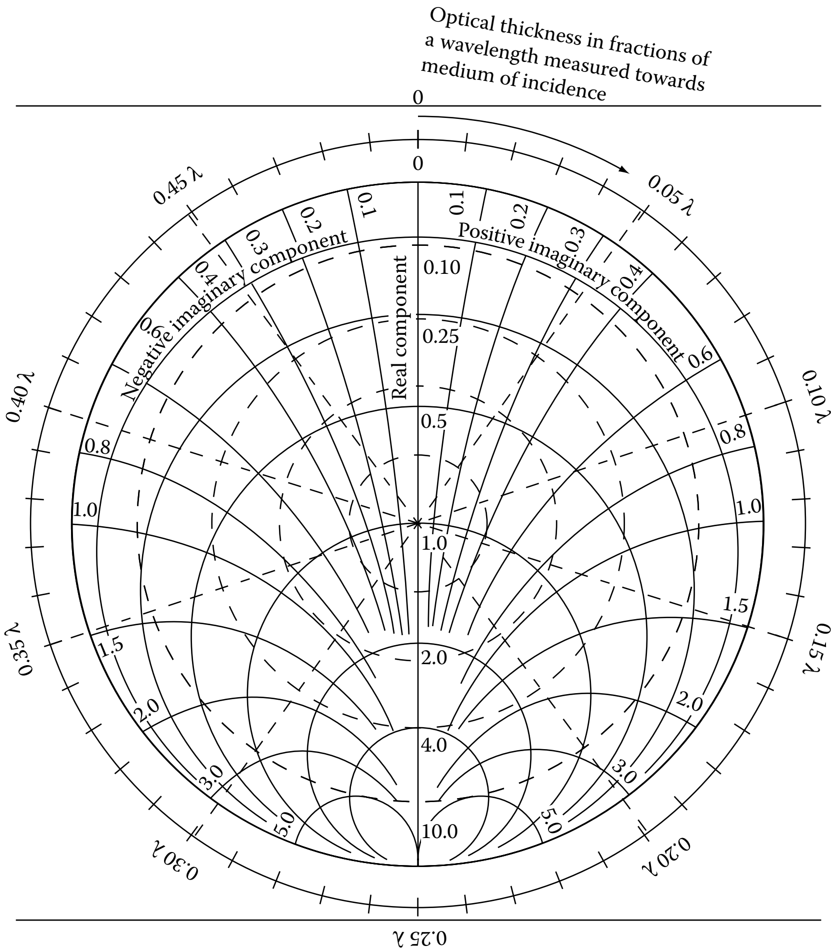

FIGURE 3.10
The Smith Chart. Broken circles are circles of constant amplitude reflection coefficient ρ. From the smallest to the largest they correspond to $\rho = 0.2$, 0.4, 0.6, 0.8 and 1.0, the outer solid circle. Solid circles are circles of constant real part and constant imaginary part of the reduced optical admittance. Note: An optical thickness of 0.25λ corresponds to a phase thickness of 90°. (Based on details given in *High frequency transmission lines*, Willis Jackson, pp. 129 and 146, 3rd edition, London: Methuen 1951.)

Equation 3.14 gives an expression for calculating the change in amplitude reflection coefficient resulting from the addition of a single layer:

$$\rho^+ = \frac{\rho_a^+ + \rho_b^+ e^{-2i\delta}}{1 + \rho_b^+ \rho_a^+ e^{-2i\delta}}$$

We can calculate the properties of a multilayer by successive applications of this formula, as has already been indicated. Let us imagine that we

have arrived at the pth layer in the calculation. The quantities involved are indicated in Figure 3.11. ρ_f^+ is the amplitude reflection coefficient of the $(p-1)$th layer at the outer interface, which we have labeled f.

$$\rho_f^+ = \frac{\eta_{p-1} - \eta_p}{\eta_{p-1} + \eta_p}$$

ρ' in Figure 3.11 is the resultant amplitude reflection coefficient at the inner interface of the pth layer due to the entire structure on that side and is not to be confused with ρ_q, the amplitude reflection coefficient of the qth interface. The resultant amplitude reflection coefficient ρ at the fth interface is given by

$$\rho = \frac{\rho_f^+ + \rho' e^{-2i\delta}}{1 + \rho_f^+ \rho' e^{-2i\delta}} \tag{3.29}$$

Provided we are dealing with dielectric ρ_f^+ materials will be real. ρ' may be complex but we can include any phase angle due to ρ' in the factor $e^{-2i\delta}$. Let us plot the locus of ρ in the complex plane as δ varies. To simplify the analysis, we can replace ρ by $x + iy$ and $\rho' e^{-2i\delta}$ by $\alpha + i\beta$, where

$$\left(\alpha^2 + \beta^2\right)^{1/2} = |\rho'|$$

Then

$$x + iy = \frac{\rho_f^+ + \alpha + i\beta}{1 + \rho_f^+ (\alpha + i\beta)}$$

Multiplying both sides by the denominator of the right-hand side and then equating real and imaginary parts of the resulting expressions yields

$$x\left(1 + \rho_f^+ \alpha\right) - y\rho_f^+ \beta = \rho_f^+ + \alpha$$

$$y\left(1 + \rho_f^+ \alpha\right) + x\rho_f^+ \beta = \beta$$

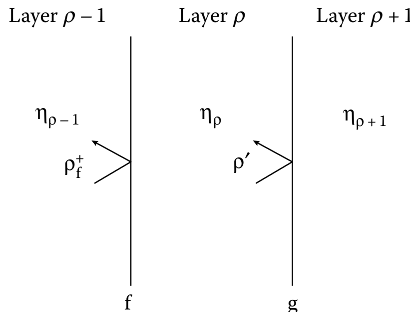

FIGURE 3.11
Quantities in the method of reflection circles.

i.e.,

$$\left(x-\rho_f^+\right)=\alpha x\left(1-x\rho_f^+\right)+\beta y\rho_f^+$$

$$y=-\alpha y\rho_f^+ + \beta(1-x\rho_f^+)$$

To find the locus, we square and add these equations to give

$$\left(x-\rho_f^+\right)^2+y^2=\left(\alpha^2+\beta^2\right)\left[\left(1-x\rho_f^+\right)^2+\left(\rho_f^+y\right)^2\right]$$

$$=\left|\rho'\right|^2\left[\left(1-x\rho_f^+\right)^2+\left(\rho_f^+y\right)^2\right]$$

which can be manipulated to

$$x^2\left(1-\left|\rho'\right|^2\rho_f^{+2}\right)+y^2\left(1-\left|\rho'\right|^2\rho_f^{+2}\right)-2x\rho_f^+\left(1-\left|\rho'\right|^2\right)+\rho_f^{+2}-\left|\rho'\right|^2=0 \qquad (3.30)$$

This is the equation of a circle with center

$$\left(\frac{\rho_f^+\left(1-\left|\rho'\right|^2\right)}{\left(1-\left|\rho'\right|^2\rho_f^{+2}\right)},0\right)$$

i.e., on the real axis, and radius

$$\frac{\left|\rho'\right|\left(1-\rho_f^{+2}\right)}{\left(1-\left|\rho'\right|^2\rho_f^{+2}\right)}$$

The locus of the reflection coefficient as the layer thickness is allowed to increase steadily from zero is therefore a circle. A half-wave layer traces out a complete circle, while a quarter-wave layer, if it starts on the real axis, will trace out a semicircle; otherwise it will be slightly more or less than a semicircle, depending on the exact starting point. In all cases, the circle is traced clockwise.

The locus corresponding to a single layer is straightforward. The plotting of the locus corresponding to two or more layers is slightly more complicated. The form of the locus of each layer is an arc of a circle traced from the terminal point of the previous layer. The complication arises from the subsidiary calculation that must be performed each time to calculate the current value of ρ' from the terminal value of the previous layer. An example will serve to illustrate the point.

Let us consider a glass substrate of index 1.52, on which is deposited first a layer of zinc sulfide of index 2.35 and thickness of one quarter-wave, followed

by a layer of cryolite of index 1.35 and of thickness also one quarter-wave. Air, of index 1.0, is the incident medium.

Calculation of the circles is most easily performed by using Equation 3.29 to calculate the terminal points. The starting point is known and that, together with the fact that the center is on the real axis, completes the specification of the circles.

The values of ρ_f^+ and ρ' for the first layer are

$$\rho_f^+ = \frac{1.0 - 2.35}{1.0 + 2.35} = -0.4030$$

$$\rho' = \frac{2.35 - 1.52}{2.35 + 1.52} = 0.2144$$

The starting point for the layer is

$$\rho = \frac{\rho_f^+ + \rho'}{1 + \rho_f^+ \rho'} = -0.2063$$

which corresponds to the amplitude reflection coefficient of bare glass in air.

For a quarter-wave layer $e^{-2i\delta} = -1$ and so the terminal value of ρ is given by

$$\rho = \frac{\rho_f^+ - \rho'}{1 - \rho_f^+ \rho'} = -0.5683$$

and the locus up to this point is a semicircle. This value of ρ corresponds to the amplitude reflection coefficient of a quarter-wave of zinc sulfide on glass in air. To continue the locus into the next layer, we need new values of ρ_f^+ and ρ'.

$\left(\rho_f^+\right)_{new}$ is straightforward, being the external reflection coefficient at an air-cryolite boundary:

$$\left(\rho_f^+\right)_{new} = \frac{1.0 - 1.52}{1.0 + 1.52} = -0.1489$$

$\left(p'\right)_{new}$ is more difficult. This is the amplitude reflection coefficient that the substrate plus a quarter-wave of zinc sulfide will have, no longer in a medium of air, but in one of cryolite. It can be calculated either using the normal matrix method or simply by inverting the equation

$$\rho = \left(\rho\right)_{old} = \frac{\left(\rho_f^+\right)_{new} + \left(\rho'\right)_{new}}{1 + \left(\rho_f^+\right)_{new}\left(\rho'\right)_{new}}$$

which must be satisfied if the start of the new layer is to coincide with $(\rho)_{old}$, the termination of the old.

$$(\rho')_{new} = \frac{(\rho)_{old} - (\rho_f^+)_{new}}{1 - (\rho)_{old}(\rho_f^+)_{new}}$$

and in this case $(\rho)_{old}$ is –0.5683, so that

$$(\rho')_{new} = \frac{-0.5683 - (-0.1489)}{1 - (-0.5683)(-0.1489)} = -0.4582$$

The new locus, which is another semicircle, then starts at the point –0.5683 on the real axis and terminates at

$$\rho = \frac{(\rho_f^+)_{new} - (\rho')_{new}}{1 - (\rho_f^+)_{new}(\rho')_{new}} = 0.3319$$

The loci are shown in Figure 3.12.

The advantage of the technique over the Smith Chart is especially that the locus is a continuous one, since the termination of each layer is the starting

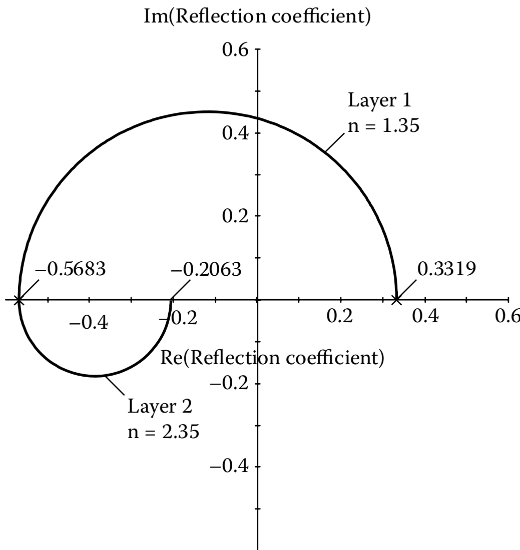

FIGURE 3.12
Reflection circles, or amplitude reflection locus, for the coating: Air |*LH*| Glass, where *L* indicates a quarter-wave of index 1.35, *H* of 2.35, and the indices of air and glass are 1.00 and 1.52, respectively.

point for the next. All possible loci corresponding to a particular refractive index form a set of nested circles centered on the real axis of the diagram. Enough of these circles can be drawn to form a separate template or overlay for each of the materials involved in a design and these can considerably ease the task of drawing the diagram.

Since the method of the Smith Chart is based on the real and imaginary axes of the amplitude reflection coefficient, the loci can actually be drawn on the same diagram as a Smith Chart. Strictly, in that case, the chart should not be referred to as a Smith Chart because it is not being used in that way.

Many examples of the use of this technique in design are given by Apfel [5] who has also extended it to include absorbing layers such as metals.

References

1. Smith S D 1958 Design of multilayer filters by considering two effective interfaces *Journal of the Optical Society of America* **48** 43–50
2. Smith P H 1939 Transmission line calculator *Electronics* **12** 29–31
3. Smith P H 1969 *Electronic applications of the Smith Chart* (New York: McGraw Hill Book Company)
4. Berning P H 1963 *Theory and calculations of optical thin films*, in *Physics of Thin Films* Hass G Editor (New York/London: Academic Press) 69–121
5. Apfel J H 1972 Graphics in optical coating design *Applied Optics* **11** 1303–1312

4

Antireflection Coatings

As previously mentioned in Chapter 1, antireflection coatings were the principal objective of much of the early work in thin-film optics. Of all the possible applications, antireflection coatings have had the greatest impact on technical optics, and even today, in sheer volume of production, they still exceed all other types of coating. In some applications, antireflection coatings are simply required for the reduction of surface reflection. In others, not only must surface reflection be reduced, but the transmittance must also be increased. The crown glass elements in a compound lens have a transmittance of only 96% per untreated surface, while the flint components can have a surface transmittance as low as 90%. The net transmittance of even a modest number of untreated elements in series can therefore be quite low. Additionally, part of the light reflected at the various surfaces eventually reaches the focal plane, where it appears as ghosts or as a veiling glare, thus reducing the contrast of the images. This is especially true of the zoom lenses used in television or photography, where 20 or more elements may be included, and which would be completely unusable without antireflection coatings.

Antireflection coatings can range from a simple single layer having virtually zero reflectance at just one wavelength, to a multilayer system of more than a dozen layers, having virtually zero reflectance over a range of several octaves. The type used in any particular application will depend on a variety of factors, including the substrate material, the wavelength region, the required performance, and the cost.

In the visible region, crown glass, which has a refractive index of around 1.52, is most commonly used. As we shall see, this presents a very different problem from infrared materials, which can have very much higher refractive indices. It is convenient, therefore, to split what follows into antireflection coatings for low-index substrates and antireflection coatings for high-index substrates, corresponding roughly to the visible and infrared. Since, from the point of view of design, antireflection coatings for high-index substrates are more straightforward, they are considered first.

There is no systematic method for the design of antireflection coatings. Trial and error, assisted by approximate techniques (frequently one or other of the graphic methods mentioned in Chapter 2) backed up by accurate computer calculation, is frequently used. Very promising designs can be further improved by computer refinement. Several different approaches are used in this chapter, partly to illustrate their use and partly because they are complementary. All the performance curves have been computed by application of

the matrix method. In most cases, the materials are considered completely transparent.

The vast majority of antireflection coatings are required for matching an optical element into air. Air has an index of around 1.0003 at standard temperature and pressure, which, for practical purposes, can be considered as unity.

The earliest antireflection coatings were on glass for use in the visible region of the spectrum. As shall become apparent later, a single-layer antireflection coating on glass, for the center of the visible region, has a distinct magenta tinge when examined visually in reflection. This gives an appearance not unlike tarnish; indeed, in Chapter 1, we mentioned the beneficial effects of the tarnish layer on aged flint objectives, and so the term "bloom," in the sense of tarnish, has been used in this connection. The action of applying the coating is referred to as "blooming" and the element is said to be "'bloomed."

4.1 Antireflection Coatings on High-Index Substrates

The term *high-index* in this context cannot be defined precisely in the sense of a range with a definite lower bound. It simply means that the substrate has an index sufficiently higher than the available thin-film materials to enable the design of high-performance antireflection coatings consisting entirely, or almost entirely, of layers with indices lower than that of the substrate. These high-index substrates are principally of use in the infrared. Semiconductors, such as germanium, with an index of around 4.0, giving a reflection loss of around 36% per surface, and silicon, with index around 3.5 and reflection loss of 31%, are common, and it would be completely impossible to use them in the vast majority of applications without some form of antireflection coating. For many purposes, the reduction of a 30% reflection loss to one of a few percent would be considered adequate. It is only in a limited number of applications where the reflection loss must be reduced to less than 1%.

4.1.1 The Single-Layer Antireflection Coating

The simplest form of antireflection coating is a single layer. Consider Figure 4.1. Here we have a vector diagram, which, since two interfaces are involved contains two vectors, each representing the amplitude reflection coefficient at an interface.

If the incident medium is air, then, provided the index of the film is lower than the index of the substrate, the reflection coefficient at each interface will be negative, denoting a phase change of 180°. The resultant locus is a circle with a minimum at the wavelength for which the phase thickness of the layer is 90°, that is, a quarter-wave optical thickness, when the two vectors are completely opposed. Complete cancellation at this wavelength, that is,

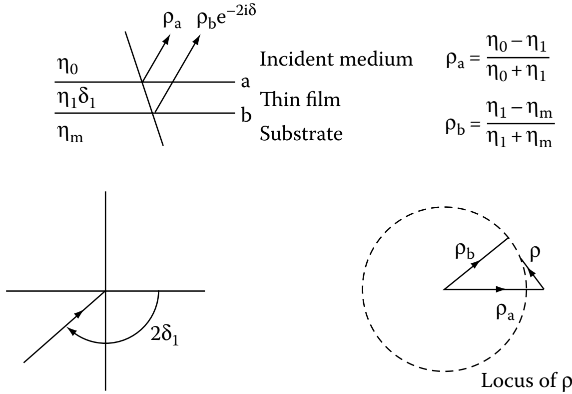

FIGURE 4.1
Vector diagram of a single-layer antireflection coating.

zero reflectance, will occur if the vectors are of equal length. This condition, in the notation of Figure 4.1, is

$$\frac{y_0 - y_1}{y_0 + y_1} = \frac{y_1 - y_m}{y_1 + y_m}$$

which requires

$$\frac{y_1}{y_0} = \frac{y_m}{y_1}$$

or

$$y_1 = \left(y_0 y_m\right)^{1/2} \tag{4.1}$$

This at optical frequencies can also be written

$$n_1 = \left(n_0 n_m\right)^{1/2}$$

At oblique incidence, the admittances, y, in Equation 4.1 should be replaced by the appropriate tilted values, η.

Although this result was derived by an approximate technique, the result is exactly correct. We recall that in Chapter 2 it was shown that the optical admittance of a substrate coated with a quarter-wave optical thickness is

$$Y = y_1^2 / y_m$$

where y_1 is the admittance of the film material and y_m that of the substrate. The reflectance is therefore given by

$$R = \left(\frac{y_0 - Y}{y_0 + Y}\right)^2 = \left(\frac{y_0 - y_1^2/y_m}{y_0 + y_1^2/y_m}\right)^2$$

This is an exact result and clearly, the reflectance is zero if y_1 is given by Equation 4.1.

The condition for a perfect single-layer antireflection coating is, therefore, a quarter-wave optical thickness of material with optical admittance equal to the square root of the product of the admittances of substrate and medium. It is seldom possible to find a material of exactly the optical admittance that is required. If there is a small error, ε, in y_1 such that

$$y_1 = (1+\varepsilon)\cdot(y_o y_m)^{1/2}$$

then

$$R = \left(\frac{-2\varepsilon - \varepsilon^2}{2 + 2\varepsilon + \varepsilon^2}\right)^2 \approx \varepsilon^2$$

provided that ε is small. A 10% error in y_1, therefore, leads to a residual reflectance of 1%.

Zinc sulfide has an index of around 2.2 at 2 µm and 2.15 at 15 µm. It has sufficient transparency for use as a quarter-wave antireflection coating over the range 0.4–25 µm. Germanium, silicon, gallium arsenide, indium arsenide, and indium antimonide can all be treated satisfactorily by a single layer of zinc sulfide. The procedure to be followed for hard, rugged zinc sulfide films is described in a paper by Cox and Hass [1]. The substrate should be maintained at around 150° C during coating and cleaned by a glow discharge immediately before coating. The transmittance of a germanium plate with a single-layer zinc sulfide antireflection coating is shown in Figure 4.2.

Zinc sulfide, even deposited under the best conditions, can deteriorate after prolonged exposure to humid atmospheres. Somewhat harder and more robust coatings are produced with cerium oxide or silicon monoxide. Cerium oxide, when deposited at a substrate temperature of 200° C or more, forms very hard and durable films of refractive index 2.2 at 2 µm. Unfortunately, in common with many other materials it displays a slight absorption band at 3 µm owing to adsorbed water vapor. Silicon monoxide does not show this water vapor band to the same degree, and so Cox and Hass have recommended this material as the most satisfactory for coating germanium and silicon in the near infrared. The index of silicon monoxide evaporated in a good vacuum at a high rate is around 1.9. The transmittance of a silicon plate coated on both sides with silicon monoxide is shown in Figure 4.3.

So far, we have considered only normal incidence in the numerical calculations that we have made. At angles of incidence other than normal, the

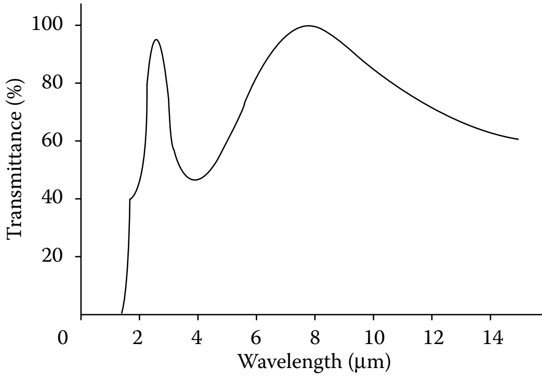

FIGURE 4.2
Transmittance of a germanium plate bloomed on both sides with zinc sulfide for 8 μm. (Courtesy of Sir Howard Grubb, Parsons & Co Ltd.)

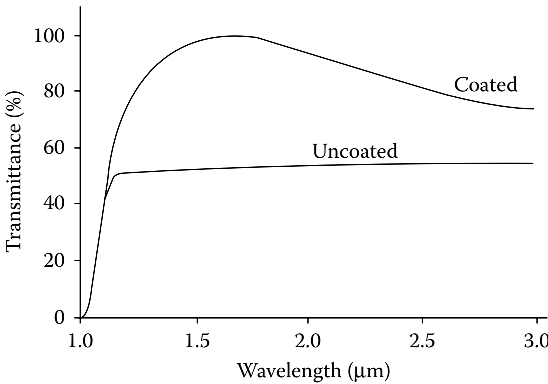

FIGURE 4.3
Transmittance of a 1.5-mm-thick silicon plate with and without antireflection coatings of silicon monoxide, a quarter-wavelength thick at 1.7 μm. (After Cox, J.T. and Hass, G. *Journal of the Optical Society of America*, 48, 677–680, 1958.)

behavior is similar, but the effective phase thickness of the layer is reduced as the incidence increases due to the cosine term in the phase thickness

$$\delta = (2\pi nd \cos\vartheta)/\lambda$$

and so the optimum wavelength is shorter. For the optical admittance we must use the appropriate η_p or η_s, and, as these are different, polarization effects become evident. For high-index substrates and coatings, the effects are much less than for the low-index coatings for the visible region, as we shall see later. Figure 4.4 shows the calculated variation with angle of incidence of the performance of a zinc sulfide coating ($n = 2.2$) on a germanium substrate ($n = 4.0$).

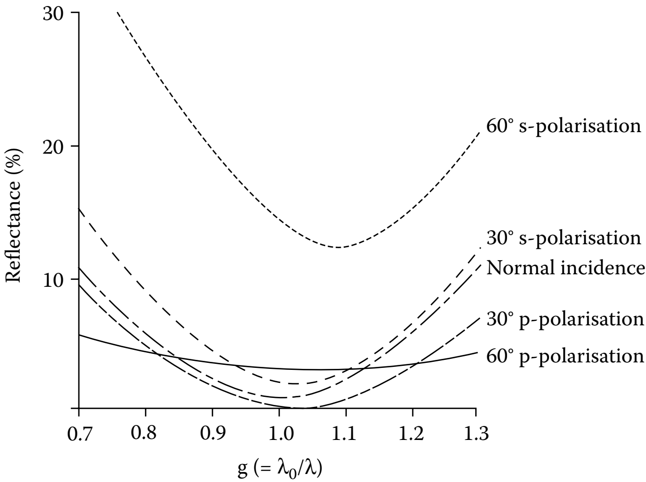

FIGURE 4.4
Calculated performance at various angles of incidence of a zinc sulfide coating (n = 2.2) on a germanium substrate (n = 4.0).

Such calculations are relatively straightforward. We use the matrix method. The characteristic matrix of a single film on a substrate is given by

$$\begin{bmatrix} B \\ C \end{bmatrix} = \begin{bmatrix} \cos\delta_1 & \dfrac{i\sin\delta_1}{\eta_1} \\ i\eta_1 \sin\delta_1 & \cos\delta_1 \end{bmatrix} \begin{bmatrix} 1 \\ \eta_m \end{bmatrix}$$

i.e.,

$$\begin{bmatrix} B \\ C \end{bmatrix} = \begin{bmatrix} \cos\delta_1 + i(\eta_m/\eta_1)\sin\delta_1 \\ \eta_m \cos\delta_1 + i\eta_1 \sin\delta_1 \end{bmatrix}$$

where the symbols have the meanings, defined in Chapter 2,

$$\left.\begin{aligned} \eta_p &= y/\cos\vartheta \\ \eta_s &= y\cos\vartheta \end{aligned}\right\}\text{for each material}$$

$$\delta_1 = (2\pi n_1 d_1 \cos\vartheta_1)/\lambda$$

and where

$$n_0 \sin\vartheta_0 = n_1 \sin\vartheta_1 = n_m \sin\vartheta_m$$

If λ_0 is the wavelength for which the layer is a quarter-wave optical thickness at normal incidence, then $n_1 d_1 = \lambda_0/4$ and

$$\delta_1 = \frac{\pi}{2}\left(\frac{\lambda_0}{\lambda}\right)\cos\vartheta_1$$

so that the new optimum wavelength is $\lambda_0 \cos\vartheta_1$.

The amplitude reflection coefficient is

$$\rho = \frac{\eta_0 - Y}{\eta_0 + Y} = \frac{\eta_0 - C/B}{\eta_0 + C/B}$$

$$= \frac{(\eta_0 - \eta_m)\cos\delta_1 + i\left[(\eta_0\eta_m/\eta_1) - \eta_1\right]\sin\delta_1}{(\eta_0 + \eta_m)\cos\delta_1 + i\left[(\eta_0\eta_m/\eta_1) + \eta_1\right]\sin\delta_1} \tag{4.2}$$

and the reflectance

$$R = \frac{(\eta_0 - \eta_m)^2\cos^2\delta_1 + \left[(\eta_0\eta_m/\eta_1) - \eta_1\right]^2\sin^2\delta_1}{(\eta_0 + \eta_m)^2\cos^2\delta_1 + \left[(\eta_0\eta_m/\eta_1) + \eta_1\right]^2\sin^2\delta_1} \tag{4.3}$$

This expression is deceptively simple. An increase in the number of layers or a move to an absorbing system immediately increases the complexity to a degree that is completely discouraging.

It is instructive to prepare an admittance diagram (Figure 4.5) for the single-layer coating. We recall that admittance loci were discussed in Chapter 2. We consider normal incidence only and use free space units for the admittances so that they are numerically equal to the refractive indices. The locus for a single layer is a circle, and in this case, it begins at the point 4.0 on the real axis, corresponding to the admittance of the germanium substrate. The center of the circle is on the real axis and the circle cuts the real axis again at the point $2.2^2/4.0 = 1.21$, corresponding to a quarter-wave optical thickness. Note especially that since the two points of intersection with the real axis are defined, we do not need to calculate the position of the center. We can mark a scale of δ_1 along the locus. Since $\delta_1 = 2\pi n_1 d_1/\lambda$, we can either assume λ constant and replace the scale with one of optical thickness or, provided that we assume that the refractive index remains constant with wavelength, for a given layer optical thickness we can mark the scale in terms of $g(= \lambda_0/\lambda)$. These various scales have been added. The scale of g assumes that λ_0 is the wavelength for which the layer has an optical thickness of one quarter-wave.

This is a particularly simple admittance locus and it is included principally to illustrate the method. We will make some use of admittance diagrams in this chapter. Normally these will be drawn for one value of wavelength and for one value of optical thickness for each layer.

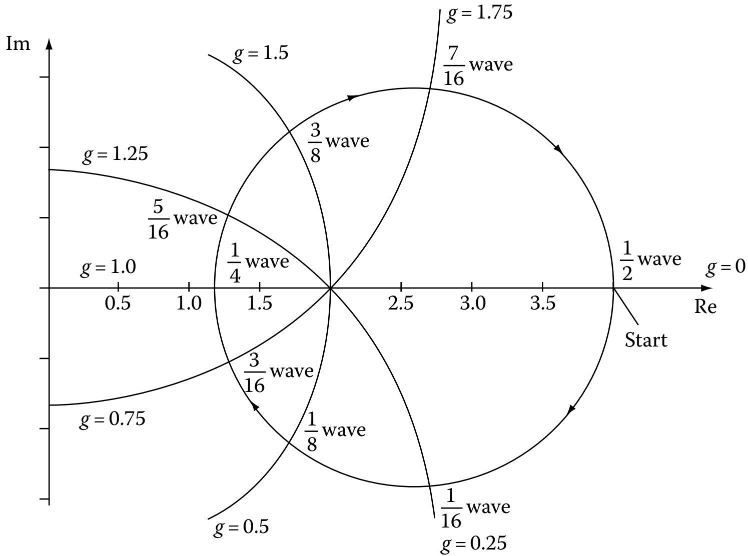

FIGURE 4.5
Admittance diagram for a single-layer zinc sulfide ($n = 2.2$) coating on germanium ($n = 4.0$).

4.1.2 Double-Layer Antireflection Coatings

The disadvantage of the single-layer coating, as far as the design is concerned, is the limited number of adjustable parameters. We can see from the admittance locus of Figure 4.5 that only where the locus passes through the point (1, 0) will zero reflectance be obtained (or more generally when the locus passes through the point (y_0, 0)) and this must correspond to a semicircle or a quarter-wave optical thickness (or, strictly, an odd integral multiple thereof). The refractive index, or optical admittance, of the layer is also uniquely determined as $y_1 = (y_0 y_m)^{½}$. There is thus no room for maneuver in the design of a single-layer coating. In practice, the refractive index is not a parameter that can be varied at will. Materials suitable for use as thin films are limited in number and the designer has to use what is available. A more rewarding approach, therefore, is to use more layers, specifying obtainable refractive indices for all layers at the start, and to achieve zero reflectance by varying the thickness. Then, too, there is the limitation that the single-layer coating can give zero reflectance at one wavelength only and low reflectance over a narrow region. A wider region of high performance demands additional layers.

Much of this design work nowadays is carried out by automatic methods, and this is a perfectly sensible and efficient development. Automatic methods are briefly described elsewhere in this book. They are particularly valuable for antireflection coatings and are strongly recommended. Here, however, we are concerned also with the understanding of the structures of the coatings

and particularly with the parts played by the individual layers. Without such understanding, we are completely vulnerable when things go wrong and the results are not as expected. Also, automatic design techniques function more efficiently when they are furnished with good starting designs. We therefore spend much time in this chapter with some of the traditional design techniques, not so much because all are still used in actual design work but because they require a knowledge of the structure and working of the coatings, and because they are interesting.

We will consider first the problem of ensuring zero reflectance at one single wavelength and we shall attempt to achieve this with a two-layer coating. Since we are dealing with high-index substrates, we look initially at combinations of layers having refractive indices lower than that of the substrate. A vector diagram of one possibility is shown in Figure 4.6. Provided the vectors are not such that any one is greater in length than the sum of the other two, then there are two sets of thicknesses for which zero reflectance can be obtained at one wavelength. The thinner combination, as in Figure 4.6a, will give the broadest characteristic and should normally be chosen. In some ways, it is easier to visualize the design using an admittance plot. As usual, we plot admittance in free space units so that it is numerically the

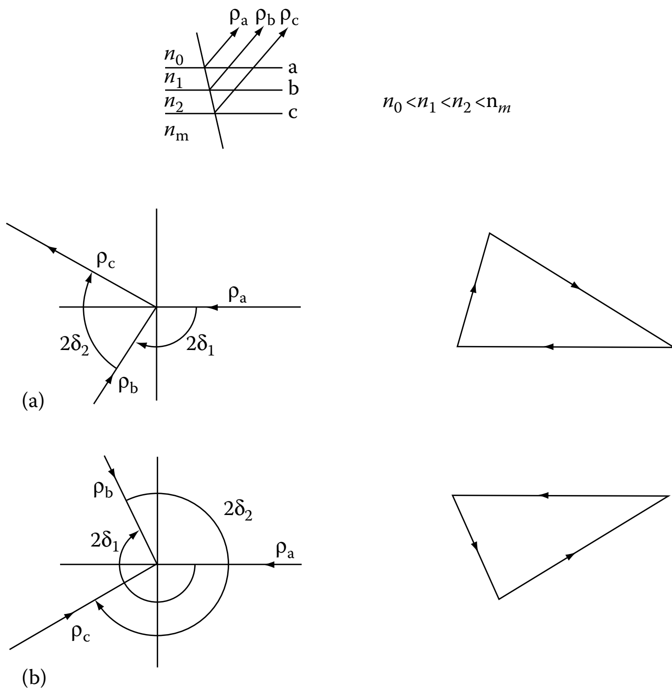

FIGURE 4.6
Vector diagram for double-layer antireflection coating. The thickness of the layers can be chosen to close the vector triangle and give zero reflectance in two ways, (a) and (b).

same as refractive index. Two possible arrangements are shown in Figure 4.7, which can be obtained simply by drawing the circle corresponding to index n_1, passing through the point n_0, and the circle corresponding to index n_2 passing through the point n_m. Provided these circles intersect, then an anti-reflection coating using them is possible. The two sets of thicknesses correspond to the two points of intersection.

This is a very important coating with wider implications than just the blooming of a high-index substrate and so it is worth examining in greater detail. We use the matrix method and follow an analysis by Catalan [2], changing the notation to agree with the system used here.

The characteristic matrix of the assembly is

$$\begin{bmatrix} B \\ C \end{bmatrix} = \begin{bmatrix} \cos\delta_1 & \dfrac{i\sin\delta_1}{y_1} \\ iy_1\sin\delta_1 & \cos\delta_1 \end{bmatrix} \begin{bmatrix} \cos\delta_2 & \dfrac{i\sin\delta_2}{y_2} \\ iy_2\sin\delta_2 & \cos\delta_2 \end{bmatrix} \begin{bmatrix} 1 \\ y_m \end{bmatrix}$$

$$= \begin{bmatrix} \cos\delta_1\left[\cos\delta_2 + i(y_m/y_2)\sin\delta_2\right] + i\sin\delta_1\left(y_m\cos\delta_2 + iy_2\sin\delta_2\right)/y_1 \\ iy_1\sin\delta_1\left[\cos\delta_2 + i(y_m/y_2)\sin\delta_2\right] + \cos\delta_1\left(y_m\cos\delta_2 + iy_2\sin\delta_2\right) \end{bmatrix}$$

The reflectance will be zero if the optical admittance Y is equal to y_0, i.e.,

$$iy_1\sin\delta_1\left[\cos\delta_2 + i(y_m/y_2)\sin\delta_2\right] + \cos\delta_1\left(y_m\cos\delta_2 + iy_2\sin\delta_2\right)$$
$$= y_0\left\{\cos\delta_1\left[\cos\delta_2 + i(y_m/y_2)\sin\delta_2\right] + i\sin\delta_1\left(y_m\cos\delta_2 + iy_2\sin\delta_2\right)/y_1\right\}$$

The real and imaginary parts of these expressions must be equated separately giving

$$-(y_1y_m/y_2)\sin\delta_1\sin\delta_2 + y_m\cos\delta_1\cos\delta_2$$
$$= y_o\cos\delta_1\cos\delta_2 - (y_0y_2/y_1)\sin\delta_1\sin\delta_2$$

and

$$y_1\sin\delta_1\cos\delta_2 + y_2\cos\delta_1\sin\delta_2$$
$$= (y_0y_m/y_2)\cos\delta_1\sin\delta_2 + (y_0y_m/y_1)\sin\delta_1\cos\delta_2$$

i.e.,

$$\tan\delta_1\tan\delta_2 = (y_m - y_0)\left[(y_1y_m/y_2) - (y_0y_2/y_1)\right]$$
$$= y_1y_2(y_m - y_0)/(y_1^2y_m - y_0y_2^2) \quad (4.4)$$

and

$$\tan\delta_2/\tan\delta_1 = y_2\left(y_0y_m - y_1^2\right)/\left[y_1\left(y_2^2 - y_0y_m\right)\right] \tag{4.5}$$

giving

$$\tan^2\delta_1 = \frac{(y_m - y_0)(y_2^2 - y_0y_m)y_1^2}{(y_1^2y_m - y_0y_2^2)(y_0y_m - y_1^2)}$$

$$\tan^2\delta_2 = \frac{(y_m - y_0)(y_0y_m - y_1^2)y_2^2}{(y_1^2y_m - y_0y_2^2)(y_2^2 - y_0y_m)} \tag{4.6}$$

The values of δ_1 and δ_2 found from these equations must be correctly paired, and this is most easily done either by ensuring that they also satisfy the two preceding equations or by sketching a rough admittance diagram.

For solutions to exist, or, putting it in another way, for the circles in the admittance diagram to intersect, the right-hand sides of Equations 4.6 must be positive. δ_1 and δ_2 are then real. This requires that, of the expressions

$$(y_2^2 - y_0y_m) \tag{4.7}$$

$$(y_1^2y_m - y_0y_2^2) \tag{4.8}$$

$$(y_0y_m - y_1^2) \tag{4.9}$$

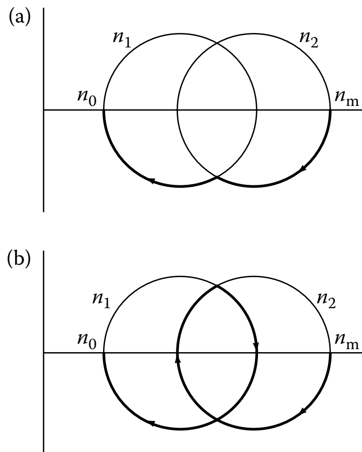

FIGURE 4.7
Admittance diagram for the double-layer antireflection coating. The two possible solutions are shown in (a) and (b).

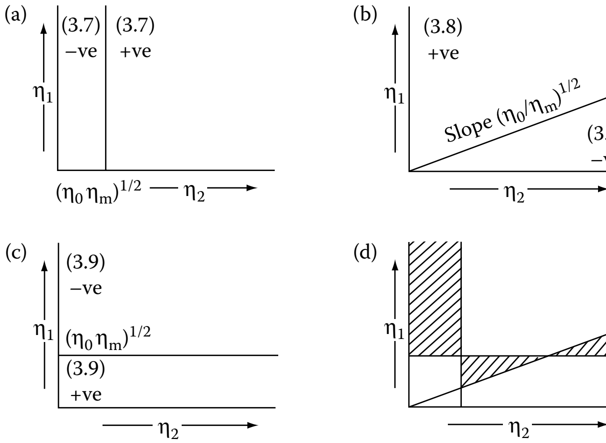

FIGURE 4.8
The construction of a Schuster diagram. (a), (b), and (c) are combined in one diagram in (d), and the shaded areas are those in which real solutions exist.

either all three must be positive, or, any two are negative and the third positive. This can be summarized in a useful diagram (Figure 4.8) known as a Schuster diagram after one of the originators [3]. The bottom right portion of the diagram corresponds to the validity conditions given in Figure 4.7.

One useful coating is given by the area at the top left edge of the diagram where $y_1 \geq (y_0 y_m)^{1/2} \geq y_2$. For germanium at normal incidence in air, $(y_0 y_m)^{1/2} = 2.0$. There is no upper limit to the magnitude of y_1, which can be conveniently chosen to be germanium with index 4.0, while y_2 can be magnesium fluoride with index 1.38, didymium fluoride with index 1.57, cerium fluoride with index 1.59, or any other similar material. The advantage of this arrangement is that the low-index film, which tends to be less robust, is protected by the high-index layer. Germanium layers are particularly good in this respect. Figure 4.9 gives an example of this type of coating. Generally, the total thickness, as in the example, is rather thinner than a quarter-wave, which adds to the durability. Cox [4] has discussed a number of different possibilities along these lines.

Unfortunately, this type of double-layer coating tends to have rather narrower useful ranges than the single-layer coating, which itself may not be broad enough for certain applications. It is possible to broaden the region of reflectance by using two, or even more, layers. A common approach is to choose layer thicknesses that are whole numbers of quarter-waves and then to determine the refractive indices that should be used to give the desired performance.

An effective coating is one consisting of two quarter-wave layers (see Figure 4.10). The appearance of the vector diagram at three different wavelengths is shown in (a), (b) and (c). At $\lambda = (3/4)\lambda_0$ and $\lambda = (3/2)\lambda_0$, the three vectors in the triangle are inclined at 60° to each other. Provided the vectors

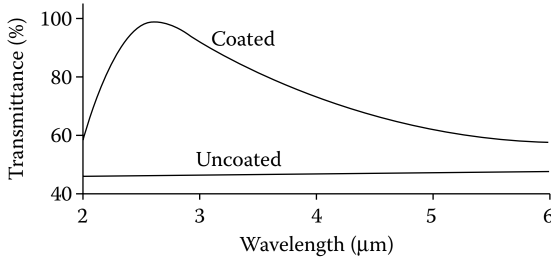

FIGURE 4.9
Transmittance of a germanium plate with two-layer antireflection coatings of MgF_2 ($nd = \lambda/4$ at 1.03 μm) and germanium ($nd = \lambda/4$ at 0.61 μm), the germanium being the outermost layer. (After Cox, J.T., *Journal of the Optical Society of America*, 51, 1406–1408, 1961.)

are all of equal length, the triangles will be closed and the reflectance will be zero at these wavelengths. This condition can be written

$$\frac{y_1}{y_0} = \frac{y_2}{y_1} = \frac{y_m}{y_2}$$

and solved for y_1 and y_2:

$$y_1^3 = y_0^2 y_m$$

$$y_2^3 = y_0 y_m^2 \tag{4.10}$$

The reflectance at the reference wavelength λ_0 where the layers are quarter-waves is given by

$$R = \left(\frac{y_0 - (y_1^2/y_2^2) y_m}{y_0 + (y_1^2/y_2^2) y_m} \right)^2$$

$$= \left(\frac{1 - (y_m/y_0)^{1/3}}{1 + (y_m/y_0)^{1/3}} \right)^2$$

a considerable improvement over the bare substrate.

For germanium of refractive index 4.0 in air, at normal incidence, the values required for the indices are $n_1 = 1.59$ and $n_2 = 2.50$ and the reflectance at λ_0 is 5.6%. The theoretical curve of this coating is shown in Figure 4.11a. Theoretical and measured curves of a similar coating on arsenic trisulfide and triselenide are given in Figure 4.11b and Figure 4.11c.

The coating just described is a special case of a general coating where the layers are of equal thickness. To compute the general conditions, it is easiest to return to the analysis leading up to equations (4.6).

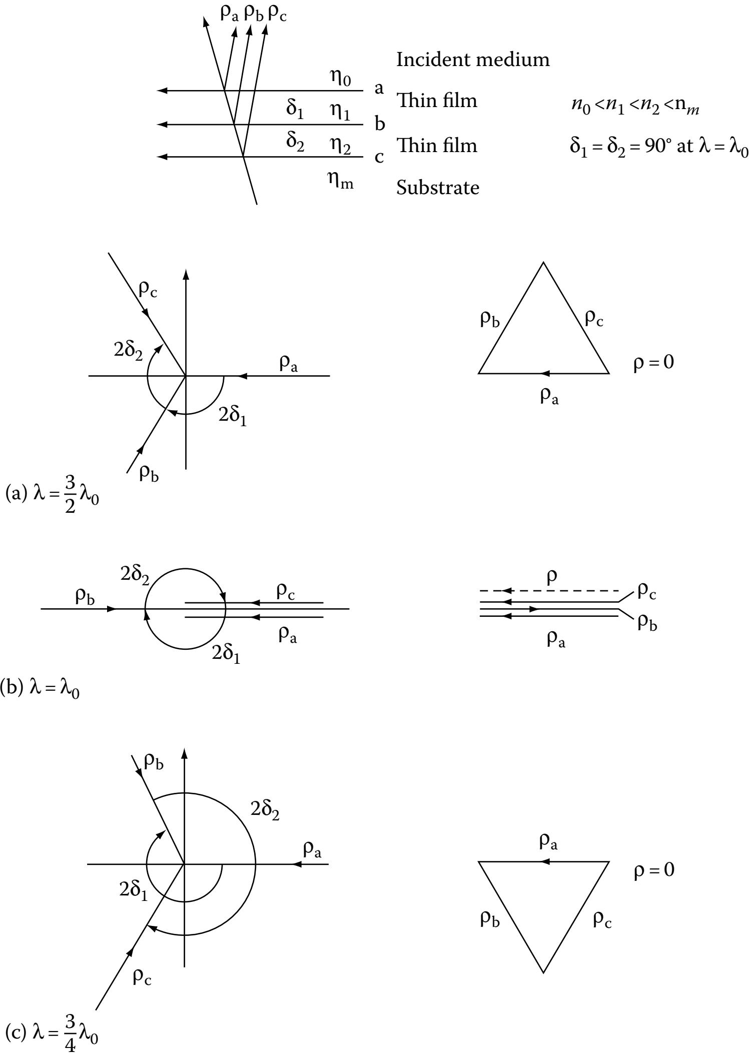

FIGURE 4.10
Vector diagrams for quarter-quarter antireflection coatings on a high-index substrate; (a), (b), and (c) represent wavelengths of $(3/2)\lambda_0$, λ_0, and $(3/4)\lambda_0$, respectively.

Let δ_1 be set equal to δ_2 and denoted by δ, where we recall that if λ_0 is the wavelength for which the layers are quarter-waves, then

$$\delta = \frac{\pi}{2}\left(\frac{\lambda_0}{\lambda}\right)$$

From Equation 4.5

$$y_2\left(y_0 y_m - y_1^2\right) = y_1\left(y_2^2 - y_0 y_m\right)$$

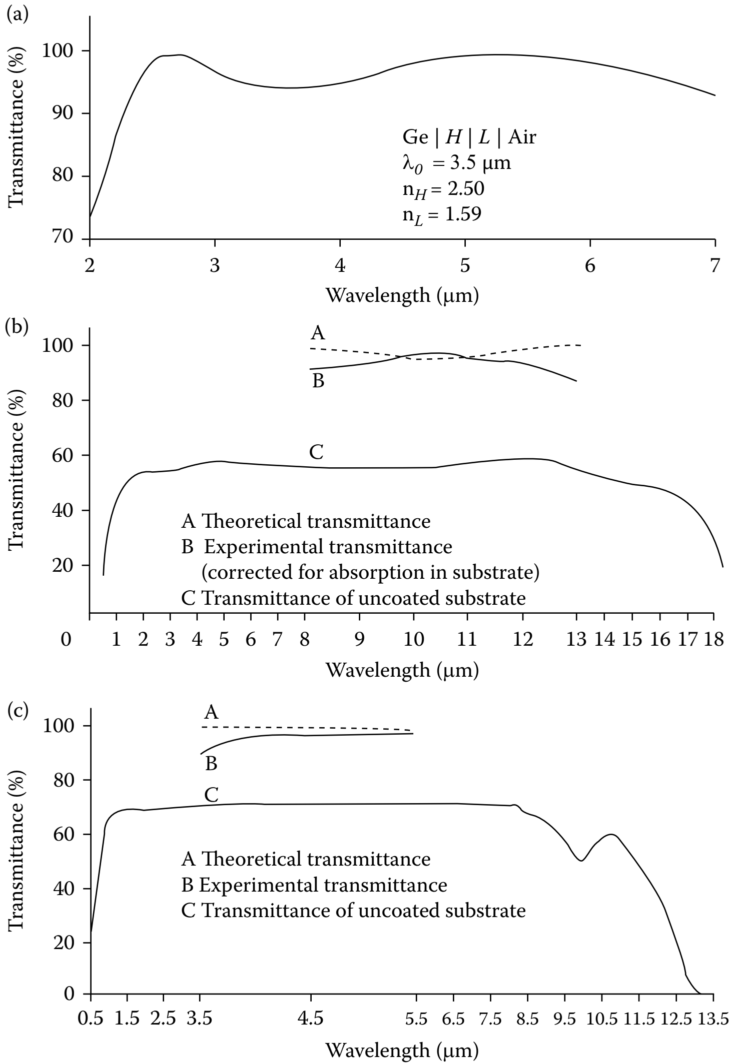

FIGURE 4.11
Double-layer antireflection coatings for high-index substrates. (a) Theoretical transmittance of a quarter-quarter coating on germanium (single surface). (b) Theoretical and measured transmittance of a similar coating on arsenic trisulfide glass (double surface). (c) Theoretical and measured transmittance of a similar coating on arsenic triselenide glass (double surface). [(b) and (c) by courtesy of Barr and Stroud Ltd.]

i.e.,

$$y_0 y_m = y_1 y_2$$

This is a necessary condition for zero reflectance.

From Equation 4.4, we find the wavelengths λ corresponding to zero reflectance:

$$\tan^2\delta = \frac{y_1 y_2 (y_m - y_0)}{y_1^2 y_m - y_0 y_2^2} = \frac{y_0 y_m (y_m - y_0)}{y_1^2 y_m - y_0 y_2^2}$$

If δ is the solution in the first quadrant, then there are two solutions

$$\delta = \delta' \quad \text{or} \quad \delta = \pi - \delta'$$

and the two values of λ are

$$\lambda = \left(\frac{\pi/2}{\delta}\right)\lambda_0$$

In all practical cases, y_{m} will be greater than y_0 and the above equation for $\tan^2\delta$ will have a real solution provided

$$y_1^2 y_m - y_0 y_2^2 \geq 0$$

The left side of this inequality is identical to Expression 4.8.

Figure 4.12 gives the allowed values of y_1 and y_2 for germanium in air plotted on a Schuster diagram assuming normal incidence. The form of

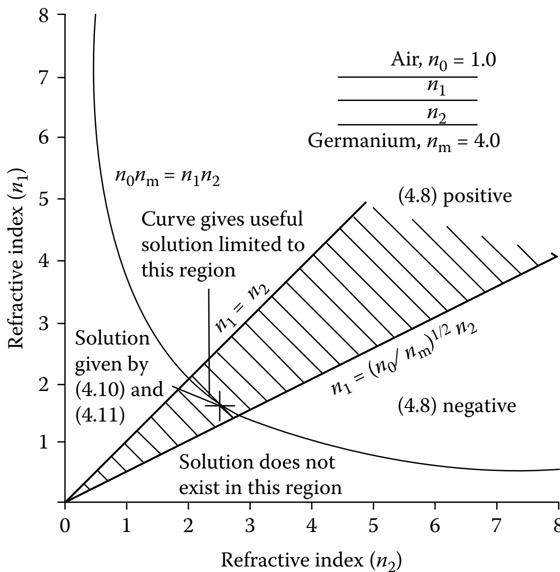

FIGURE 4.12
A Schuster diagram showing possible values of film indices for a quarter-quarter coating on germanium.

the characteristic curve of the coating is similar to that of Figure 4.11. The reflectance rises to a maximum value at the reference wavelength λ_0 situated between the two zeros. The reflectance at λ_0 can be found quite simply. At this wavelength, $\delta = \pi/2$ and the layers are quarter-waves. The optical admittance is given, therefore, by

$$\frac{y_1^2}{y_1^2} y_m$$

and the reflectance by

$$R = \left(\frac{y_0 - \left(y_1^2/y_2^2\right) y_m}{y_0 + \left(y_1^2/y_2^2\right) y_m} \right)^2 \tag{4.11}$$

We are considering cases where y_m is large. For $y_1 = y_2$, the reflectance at λ_0 is that of the bare substrate. If $y_1 > y_2$, the reflectance is even higher. Thus, for the solution to be at all useful, y_1 should be less than y_2 and the region where this condition holds is indicated on the diagram.

4.1.3 Multilayer Coatings

Figure 4.13 shows a vector diagram for a three-layer coating on germanium. Each layer is a quarter-wave thick at λ_0. If $y_m > y_3 > y_2 > y_1 > y_0$, then the vectors will oppose each other, as shown, at $(2/3)\lambda_0$, λ_0 and $2\lambda_0$, and, provided the vectors are all of equal length, will completely cancel at these wavelengths, giving zero reflectance.

The coating is similar to the quarter-quarter coating of Figure 4.10, but where the two zeros of the two-layer coating are situated at $(3/4)\lambda_0$ and $(3/2)\lambda_0$, those of this three-layer coating stretch from $(2/3)\lambda_0$ to $2\lambda_0$, a much broader region.

The condition for the vectors to be of equal length is

$$\frac{y_1}{y_0} = \frac{y_2}{y_1} = \frac{y_3}{y_2} = \frac{y_m}{y_3}$$

which, with some manipulation, becomes

$$y_1^4 = y_0^3 y_m$$

$$y_2^4 = y_0^2 y_m^2$$

$$y_3^4 = y_0 y_m^3 \tag{4.12}$$

For germanium in air at normal incidence

$$n_0 = 1.00 \qquad n_m = 4.00$$

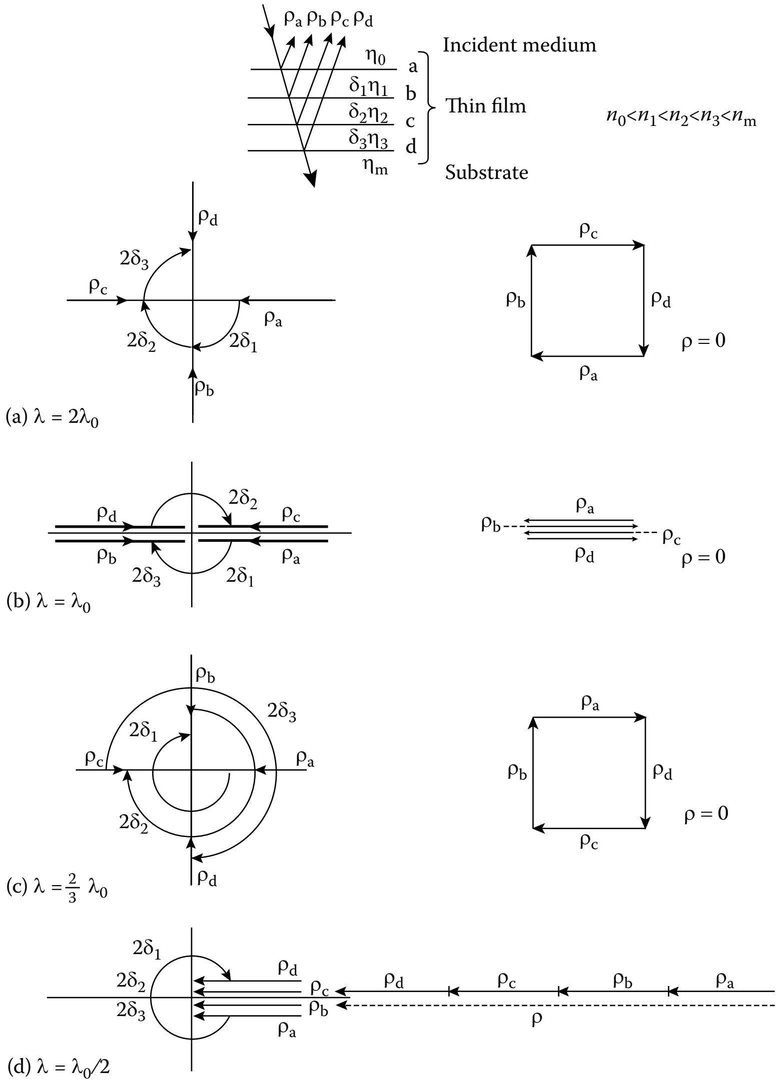

FIGURE 4.13
Vector diagram for a quarter-quarter-quarter coating on a high-index substrate ; (a), (b), (c), and (d) represent wavelengths of $2\lambda_0$, λ_0, (2/3) λ_0, and $\lambda_0/2$ respectively.

and the refractive indices required for the layers are

$$n_1 = 1.41$$
$$n_2 = 2.00$$
$$n_3 = 2.83$$

A coating, which is not far removed from these theoretical figures, is silicon, next to the substrate, of index 3.3, followed by cerium oxide of index 2.2,

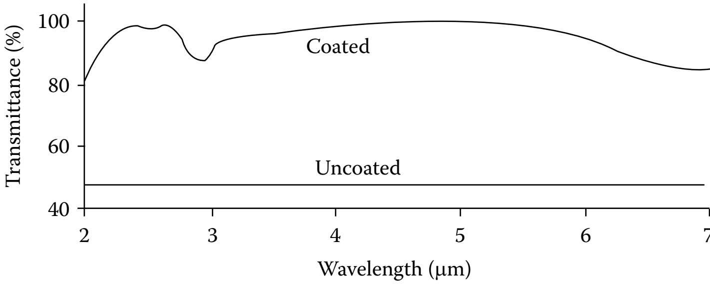

FIGURE 4.14
Measured transmittance of a germanium plate with coatings consisting of $MgF_2 + CeO_2 + Si$ ($n_1d_1 = n_2d_2 = n_3d_3 = \lambda/4$ at 3.5 μm). (After Cox, J.T., Hass, G., and Jacobus, G.F., *Journal of the Optical Society of America*, 51, 714–718, 1961.)

followed by magnesium fluoride, index 1.35. The performance of such a coating with $\lambda_0 = 3.5$ μm is shown in Figure 4.14. This coating, along with other one- and two-layer coatings for the infrared, is described by Cox et al. [5]. The exact theory of this coating may be developed in the same way as that of the two-layer coating, but the calculations are more involved.

It is relatively easy to extend the vector method to deal with four layers, where the zeros of reflectance are found at $(5/8)\lambda_0$, $(5/6)\lambda_0$, $(5/4)\lambda_0$, and $(5/2)\lambda_0$, an even broader region than the three-layer coating. Five layers are equally straightforward. Whether such coatings are of practical value depends very much on the application. For many purposes, the two-layer coating is quite adequate.

The addition of an extra layer makes the exact theory of the three-layer coating very much more involved than that of the two-layer coating. The number of possible groups of designs is enormous. It therefore becomes profitable to use techniques that, rather than calculate performance in detail, simply indicate arrangements that are likely to be capable of acceptable performance and eliminate those that are not. Performance can then be accurately calculated by the procedures of Chapter 2.

A particularly useful technique of this type has been developed by Musset and Thelen [6]. It is based on Smith's method—that is, the method of effective interfaces. We recall from Chapter 2 that this involves the breaking down of the assembly into two subsystems. These we can label *a* and *b*. The overall transmittance of the multilayer is then given by

$$T = \left(\frac{T_a T_b}{\left(1 - R_a^{1/2} R_b^{1/2}\right)^2}\right) \times \left[1 + \frac{4R_a^{1/2} R_b^{1/2}}{\left(1 - R_a^{1/2} R_b^{1/2}\right)^2} \sin^2\left(\frac{\varphi_a + \varphi_b - 2\delta}{2}\right)\right]^{-1} \tag{4.13}$$

We assume that there is no absorption, so that $Ta = 1 - Ra$ and $Tb = 1 - Rb$.

Both of the expressions multiplied together on the right-hand side of Equation 4.13 have maximum possible values of unity, and for maximum transmittance, therefore, both must be separately maximized. The first expression

$$\frac{T_a T_b}{\left(1 - R_a^{1/2} R_b^{1/2}\right)^2}$$

will be unity if, and only if, $R_a = R_b$, while the second,

$$\left[1 + \frac{4R_a^{1/2} R_b^{1/2}}{\left(1 - R_a^{1/2} R_b^{1/2}\right)} \sin^2\left(\frac{\varphi_a + \varphi_b - 2\delta}{2}\right)\right]^{-1}$$

will be unity if, and only if,

$$\sin^2\left(\frac{\varphi_a + \varphi_b - 2\delta}{2}\right) = 0$$

The conditions for a perfect antireflection coating are then

$$R_a = R_b$$

called the *amplitude condition* by Musset and Thelen, and

$$\frac{\varphi_a + \varphi_b - 2\delta}{2} = m\pi$$

called the *phase condition*. The amplitude condition is a function of the two subsystems. The phase condition can be satisfied by adjusting the thickness of the spacer layer. The amplitude condition can, using a method devised by Musset and Thelen, be satisfied for all wavelengths, but it is difficult to satisfy the phase condition except at a limited number of discrete wavelengths. At other wavelengths, the performance departs from ideal to a varying degree.

The transmittance and reflectance of a multilayer remain constant when the optical admittances are all multiplied by a constant factor or when they are all replaced by their reciprocals, in both cases keeping the optical thicknesses constant. These properties can readily be demonstrated from the structure of the characteristic matrices [7]. They enable the design of pairs of substructures having identical reflectance so that only the phase condition need be satisfied for perfect antireflection. We can, following Musset and Thelen, imagine a multilayer consisting of two subsections *a* and *b*, as shown in Figure 4.15, with a medium of admittance y_i in between. At this stage, we put no restrictions on this medium in terms either of refractive index or of thickness but, as we shall see, they will become defined at a later stage. Subsection *a* is bounded by y_m on one side and y_i on the other, while *b* is bounded in the same way by y_i and y_0. We can now apply the appropriate rules for ensuring that the amplitude condition is satisfied. We set up any

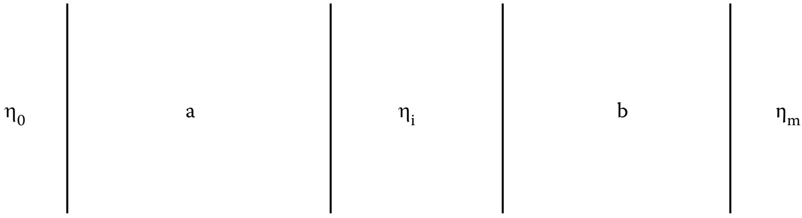

FIGURE 4.15
Multilayer antireflection coating consisting of two subsystems *a* and *b* separated by a central layer.

subsystem *a* and then convert it into subsystem *b* by retaining the optical thicknesses and either multiplying the admittances by a constant multiplier, or taking the reciprocals of the admittances and multiplying them by a constant multiplier. Systems derived by the former procedure are classified by Musset and Thelen as of Type I, and those by the latter as Type II.

For Type I systems we must have

$$y_m f = y_i$$

$$y_i f = y_0$$

so that

$$y_i = (y_0 y_m)^{1/2}$$

and

$$f = (y_0 / y_m)^{1/2}$$

In this way, any y_a gives a corresponding y_b of $y_a(y_0/y_m)^{1/2}$.

Type II systems, on the other hand, convert so that

$$f/y_m = y_0$$

$$f/y_i = y_i$$

$$f/y_a = y_b$$

i.e.

$$y_i = (y_0 y_m)^{1/2} \quad \text{and} \quad f = y_0 y_m$$

so that any y_a gives a corresponding y_b of $y_0 y_m / y_a$.

There are no restrictions on layer thickness or on the number of layers in each subsystem except that they must be equal in number, and it is simpler if quarter-wave layers are used. Once the individual subsystems *a* and *b* are established, the amplitude condition is automatically satisfied at all wavelengths and it remains to satisfy the phase condition. This involves the coupling arrangement. It is impossible to meet the phase condition at all wavelengths and the problem is so complex that it is best to take the easy way out and adopt a layer of admittance y_i with thickness zero, in which case the layer is omitted, or a quarter-wave like the remaining layers of the assembly.

The method can be illustrated by application to the antireflection of germanium at normal incidence. In this case, n_0 = 1.00 and n_m = 4.00. Hence $n_i = (n_0 n_m)^{1/2}$ = 2.0 in both Type I and II systems. First, we take, for subsystem *a*, a straightforward single quarter-wave matching the substrate to the coupling medium:

n_1	n_a $(n_i n_m)^{1/2}$	n_m
2.0	2.826	4.0

Subsystem *b* is, then, for both Type I and II systems

n_0	n_b	n_i
1.0	1.414	2.0

Putting the two subsystems together, we have either a two-layer coating if we permit the thickness of the coupling layer to shrink to zero, or a three-layer coating if the coupling layer is a quarter-wave. In the former case, we have the design:

Air	1.414	2.282	Ge
1.0	$0.25\lambda_0$	$0.25\lambda_0$	4.0

and in the latter

Air	1.414	2.0	Ge
1.0	$0.25\lambda_0$	$0.25\lambda_0$	4.0

The first design gives a single minimum. The second, which is similar to the three-layer design already obtained by the vector method, has a broad three-minimum characteristic (Figure 4.16).

The subsystems need not be perfect matching systems for n_m to n_i and n_i to n_0. We could, for instance, use

$$n_0 = 1.0$$

$$n_b = (1.0 \times 4.0)^{1/3} = 1.587$$

$$n_m = 2.0$$

from the two-layer coating derived by the vector method. This gives complete two- and three-layer coatings, as follows.

Type I

Air	1.587	3.174	Ge
1.0	$0.25\lambda_0$	$0.25\lambda_0$	4.0

Air	1.587	2.0	3.174	Ge
1.0	$0.25\lambda_0$	$0.25\lambda_0$	$0.25\lambda_0$	4.0

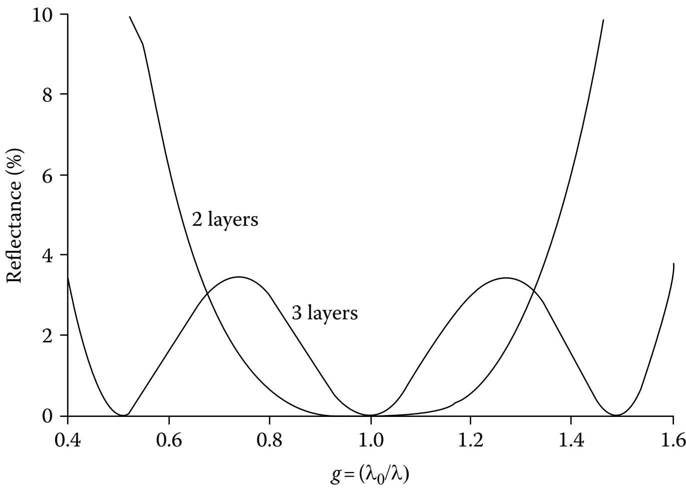

FIGURE 4.16
Theoretical performance of antireflection coatings on germanium designed by the method of Mussett and Thelen (Musset, A. and Thelen, A., Multilayer antireflection coatings, in *Progress in Optics, Wolf*, E., Ed., North Holland, Amsterdam, 201–237, 1966).

Two layers:	Air	1.414	2.858	3.174	Ge
	1.00	$0.25\lambda_0$	$0.25\lambda_0$	$0.25\lambda_0$	4.00

Three layers:	Air	1.414	2.00	2.858	Ge
	1.00	$0.25\lambda_0$	$0.25\lambda_0$	$0.25\lambda_0$	4.00

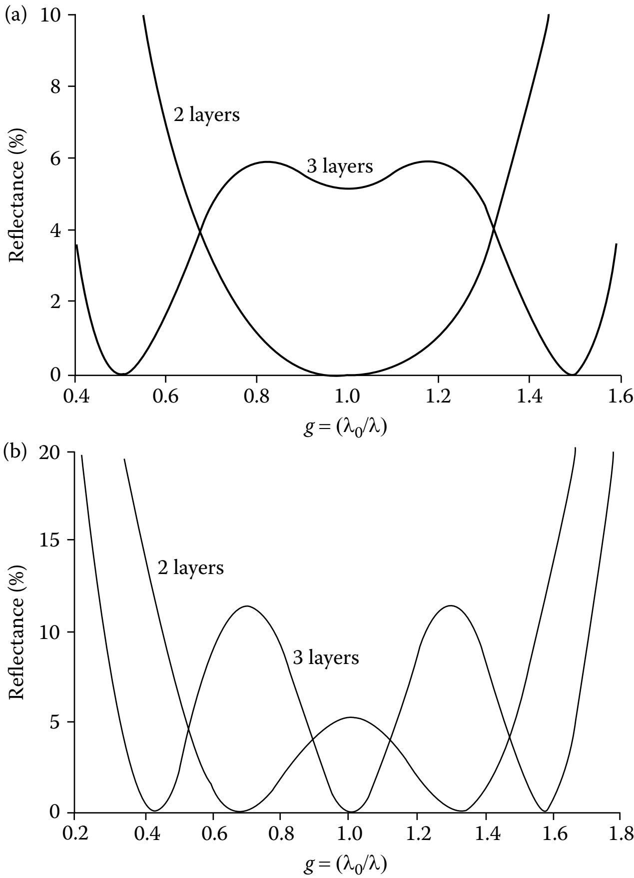

FIGURE 4.17

(a). Theoretical performance of Type I antireflection coatings on germanium designed by the method of Mussett and Thelen (Musset, A. and Thelen, A., Multilayer antireflection coatings, in *Progress in Optics*, Wolf, E., Ed., North Holland, Amsterdam, 201–237, 1966).

Two layers:	Air	1.587	3.174	Ge
	1.00	$0.25\lambda_0$	$0.25\lambda_0$	4.00

Two layers:	Air	1.587	2.00	3.174	Ge
	1.00	$0.25\lambda_0$	$0.25\lambda_0$	$0.25\lambda_0$	4.00

(b). Theoretical performance of Type II antireflection coatings on germanium designed by the method of Mussett and Thelen [6].

Two layers:	Air	1.587	2.520	Ge
	1.00	$0.25\lambda_0$	$0.25\lambda_0$	4.00

Two layers:	Air	1.587	2.00	2.520	Ge
	1.00	$0.25\lambda_0$	$0.25\lambda_0$	$0.25\lambda_0$	4.00

Type II

Air	1.587	2.520	Ge
1.0	$0.25\lambda_0$	$0.25\lambda_0$	4.0

Air	1.587	2.0	2.520	Ge
1.0	$0.25\lambda_0$	$0.25\lambda_0$	$0.25\lambda_0$	4.0

The first of the Type II designs is identical with the vector method coating. Performance curves are given in Figure 4.17.

Analytical expressions for calculating the positions of the zeros and the residual reflectance maxima of two- and three-layer coatings of the above types are given by Musset and Thelen. The method can be readily extended to four and more layers.

Young [8] has developed alternative techniques for coatings consisting of quarter-wave optical thicknesses based on the correspondence between the theory of thin-film multilayers and that of microwave transmission lines. He gives a useful set of tables for the design of multilayer coatings where all thicknesses are quarter-waves. Given the bandwidth and the maximum permissible reflectance, it is possible quickly to derive the coating that meets the specification with the least number of layers. The method, of course, takes no account of the possibility of achieving the given indices in practice, as with many of the other methods we have been discussing, but the optimum solution is a very useful point of departure in the design of coatings using real indices.

4.2 Antireflection Coatings on Low-Index Substrates

Although the theory developed for antireflection coatings on high-index materials applies equally well to low-index materials, the problem is made much more severe by the lack of any rugged thin-film materials of very low index. Magnesium fluoride, with an index of around 1.38, represents the lowest practical index that can be achieved. This immediately makes the manufacture of designs arrived at by the straightforward application of the techniques so far discussed, largely impossible. Design techniques for antireflection coatings on low-index materials are less well organized and involve much more intuition and trial and error than those for high-index materials.

A very common low-index material is crown glass, and coatings are most frequently required for the visible region of the spectrum, which extends from around 400 nm to around 700 nm. Plastic materials of similar or higher refractive index are increasing in use, especially in lenses for spectacles.

For the purposes of most of the coatings that we will discuss here, we will assume glass of index of 1.52, although this varies somewhat with the particular glass and also with wavelength. Although much of what follows is applied directly to the antireflection coating of crown glass, the techniques apply equally well to the coating of other low-index materials. We begin with the simplest coating, a single layer.

4.2.1 The Single-Layer Antireflection Coating

We can make use of the expressions already developed for high-index materials.

The optimum single-layer coating is a quarter-wave optical thickness for the central wavelength λ_0 with optical admittance given by

$$y_1 = \left(y_0 y_m\right)^{1/2} \tag{4.14}$$

For crown glass in air, this represents

$$y_1 = \left(1.0 \times 1.52\right)^{1/2} = 1.23$$

As already mentioned, the lowest useful film index that can be obtained at present is that of magnesium fluoride, around 1.38 at 500 nm. While not ideal, this does give a worthwhile improvement. The reflectance at the minimum is given by

$$R = \left(\frac{y_0 - y_1^2/y_m}{y_0 + y_1^2/y_m}\right)^2 \tag{4.15}$$

i.e., 1.3% per surface.

At angles of incidence other than normal, the phase thickness of the layer is reduced, so that for a given layer thickness the wavelength corresponding to the minimum becomes shorter. The optical admittance appropriate to the angle of incidence and the plane of polarization should also be used in calculating the reflectance. Figure 4.18 indicates the way in which the reflectance of a single layer of magnesium fluoride on a substrate of index 1.52 can be expected to vary with angle of incidence.

4.2.2 Two-Layer Antireflection Coatings

The single-layer coating cannot achieve zero reflectance even at the minimum because of the absence of suitable low-index materials. Instinct suggests that a thin layer of high-index material placed next to the substrate might make it appear to have a higher index so that a subsequent layer of magnesium fluoride would be more effective. This proves to be the case. Two-layer coatings have already been considered with regard to high-index substrates and a complete analysis has been derived.

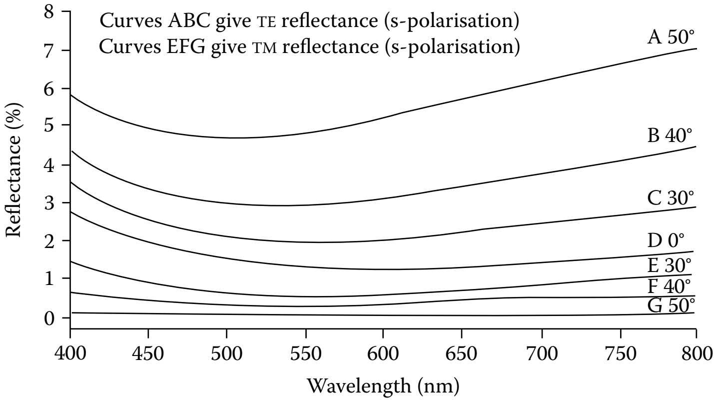

FIGURE 4.18
The computed reflectance at various angles of incidence of a single surface of glass of index 1.52 coated with a single layer of magnesium fluoride of index 1.38 and optical thickness at normal incidence one quarter-wave at 600 nm.

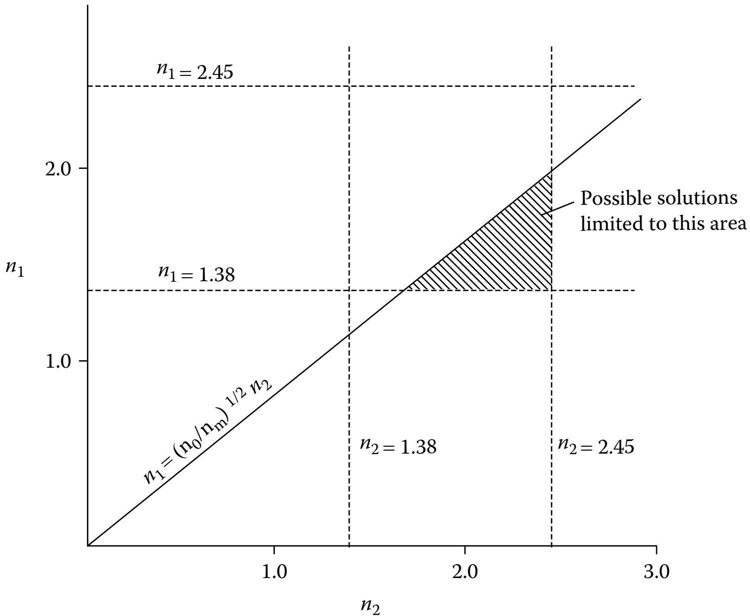

FIGURE 4.19
A Schuster diagram for two-layer coatings on glass ($n = 1.52$) in air ($n = 1.0$). Possible layer indices are assumed to be limited to the range 1.38–2.45.

We can study the Schuster diagram (Figure 4.8) for coatings on glass of index 1.52, and this is reproduced as Figure 4.19. We can assume 1.38 as the lowest possible index, while a realistic upper bound to the range of possible indices is 2.45. Possible solutions are then limited to the shaded area of the diagram. This area is bounded by the lines

$$y_1 = 1.38 \qquad y_2 = 2.45 \qquad y_1 = y_2(y_0/y_m)^{1/2}$$

Solutions on the line

$$y_1 = y_2(y_0/y_m)^{1/2}$$

will consist of two quarter-wave layers. Solutions elsewhere will consist of two layers of unequal thickness, one greater and the other less than a quarter-wave. The thicknesses are given by the expressions

$$\tan^2\delta_1 = \frac{(y_m - y_0)(y_2^2 - y_0 y_m)y_1^2}{(y_1^2 y_m - y_0 y_2^2)(y_0 y_m - y_1^2)}$$

$$\tan^2\delta_2 = \frac{(y_m - y_0)(y_0 y_m - y_2^2)y_1^2}{(y_1^2 y_m - y_0 y_2^2)(y_1^2 - y_0 y_m)} \tag{4.16}$$

As an example, we can take a value of 2.2 for the high-index layer, corresponding to, say, cerium oxide, and of 1.38 for the low-index layer, corresponding to magnesium fluoride. The two possible solutions are then

$$\delta_1/2\pi = 0.3208 \qquad \delta_2/2\pi = 0.05877$$

and

$$\delta_1/2\pi = 0.1792 \qquad \delta_2/2\pi = 0.4412$$

respectively.

These two solutions are plotted in Figure 4.20 and it can be clearly seen that the characteristic of the coating is a single minimum with a narrower bandwidth than the single layer and that the broader of the two possible solutions is associated with the thinner high-index layer. The coating is also an effective one for other values of substrate index. The higher the index of the substrate, the thinner the high-index layer must be and the broader is the characteristic of the coating.

We can follow Catalan [2] and plot curves showing how the values of δ_1 and δ_2 vary with the index of the layer next to the substrate. Such curves are shown in Figure 4.21 and from them several points of interest emerge. First, as already predicted by the Schuster plot, there is a region in which no

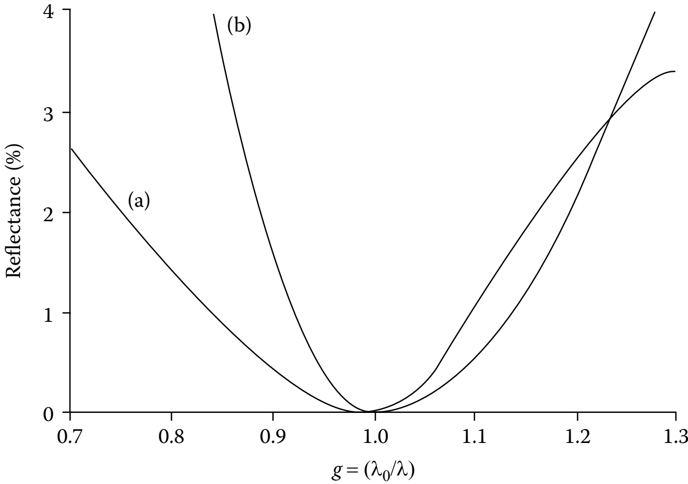

FIGURE 4.20
Two-layer antireflection coatings for glass.

(a)

Air	1.38	2.20	Glass
1.00	$0.321\lambda_0$	$0.0588\lambda_0$	1.52

(b)

Air	1.38	2.20	Glass
1.00	$0.179\lambda_0$	$0.441\lambda_0$	1.52

(a), the broader characteristic, is usually selected. Because of the characteristic single minimum the coating is often known as a V-coat.

solution is possible. Second, and more important, the curves flatten out as the index of the layer increases and changes in refractive index are accompanied by only small changes in optical thickness. One of the problems in manufacturing coatings is the control of the refractive index of the layers, particularly of the high-index layers, and the curves indicate good stability of the performance of the coating in this respect.

The equations are not limited to normal incidence. Catalan has also computed, for various angles of incidence, values of reflectance of a two-layer coating consisting of bismuth oxide, with index 2.45, and magnesium fluoride, with index 1.38, on glass of index 1.5. Curves showing the variation of reflectance with angle of incidence are given in Figure 4.22 and Figure 4.23. The performance is very good up to an angle of incidence of 20° but beyond that, it begins to fall off.

It may also be necessary to design coatings for angles of incidence other than normal. Turbadar [9] has considered this problem and published designs for angle of incidence 45°. The materials were once again bismuth oxide and magnesium fluoride, of indices 2.45 and 1.38, respectively, on glass of index

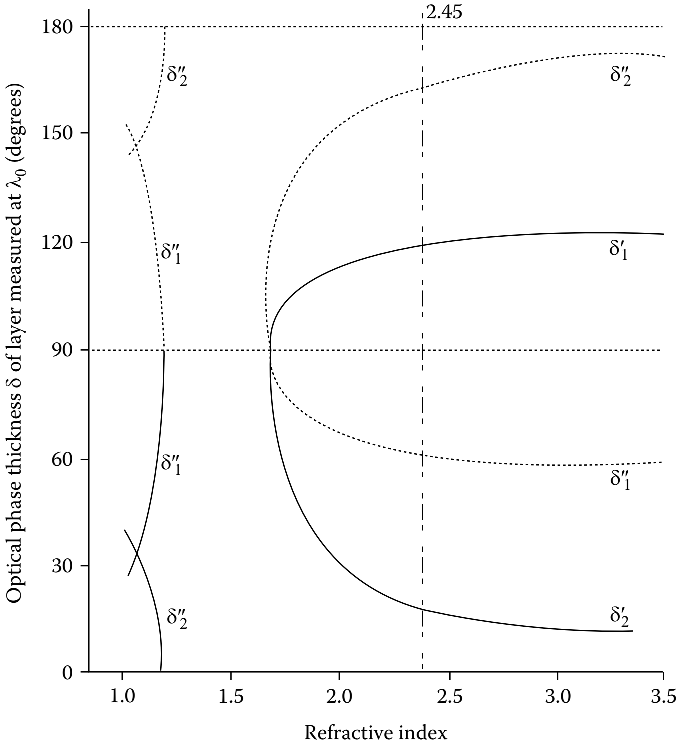

FIGURE 4.21
Optimum thicknesses of the layers in a double-layer antireflection coating at normal incidence. δ_1 and δ_2, the optical phase thicknesses given by Equations 4.7 and 4.8, are plotted against n_2, the refractive index of the high-index layer. The low-index layer is assumed to be magnesium fluoride of index 1.38 and the coating is deposited onto glass of index 1.50. Two pairs of solutions of Equations 4.7 and 4.8 are possible for each set of refractive indices and are denoted by δ_1' and δ_2' and δ_1'' and δ_2''. The value, 2.45, of refractive index, shown by the broken line, corresponds to bismuth oxide and was used by Catalan in his calculations. (After Cox, J.T., *Journal of the Optical Society of America*, 51, 1406–1408, 1961.)

1.5. Four possible solutions were given, which are reproduced as Table 4.1, where the bismuth oxide is next to the glass.

Many performance curves of the various designs under different conditions, including the effect of errors, were produced. Today this is something we can do at great speed on a desktop computer. At the time, this was not possible and the plots that were included of equireflectance contours over a grid of angle of incidence against wavelength were particularly valuable. The fact that they can be more readily created does not reduce their usefulness and so they are given in Figure 4.24.

It is useful to consider an admittance plot for a two-layer coating, which can be a great help in visualizing performance. The plot consist of two circles, the first corresponding to the low-index layer y_1 that passes through the point $(y_0, 0)$ if the reflectance is to be zero and that must, therefore, also pass

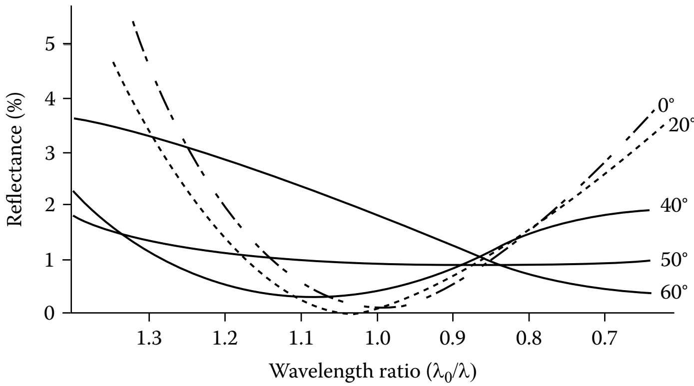

FIGURE 4.22
Theoretical p-reflectance (TM) as a function of wavelength ratio g (= λ_0/λ) of a double-layer antireflection coating. $n_0 = 1.00$, $n_1 = 1.38$, $n_2 = 2.45$, $n_m = 1.50$. (After Cox, J.T., *Journal of the Optical Society of America*, 51, 1406–1408, 1961.)

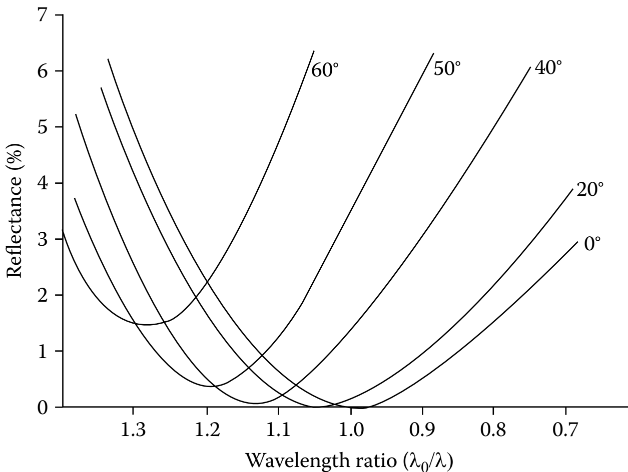

FIGURE 4.23
Theoretical *s*-reflectance (TE) as a function of wavelength ratio g (=λ_0/λ) of a double-layer antireflection coating. $n_0 = 1.00$, $n_1 = 1.38$, $n_2 = 2.45$, $nm = 1.50$. (After Cox, J.T., *Journal of the Optical Society of America*, 51, 1406–1408, 1961.)

TABLE 4.1

Turbadar's two-layer designs for glass (n = 1.5) at 45° incidence.

		Bismuth Oxide	Magnesium Fluoride
s-Polarization (TE wave)	s'	$0.065\lambda_0$	$0.376\lambda_0$
	s''	$0.457\lambda_0$	$0.206\lambda_0$
p-Polarization (TM wave)	p'	$0.021\lambda_0$	$0.382\lambda_0$
	p''	$0.501\lambda_0$	$0.201\lambda_0$

Source: Turbadar, T., *Optica Acta*, 11, 159–170, 1964.

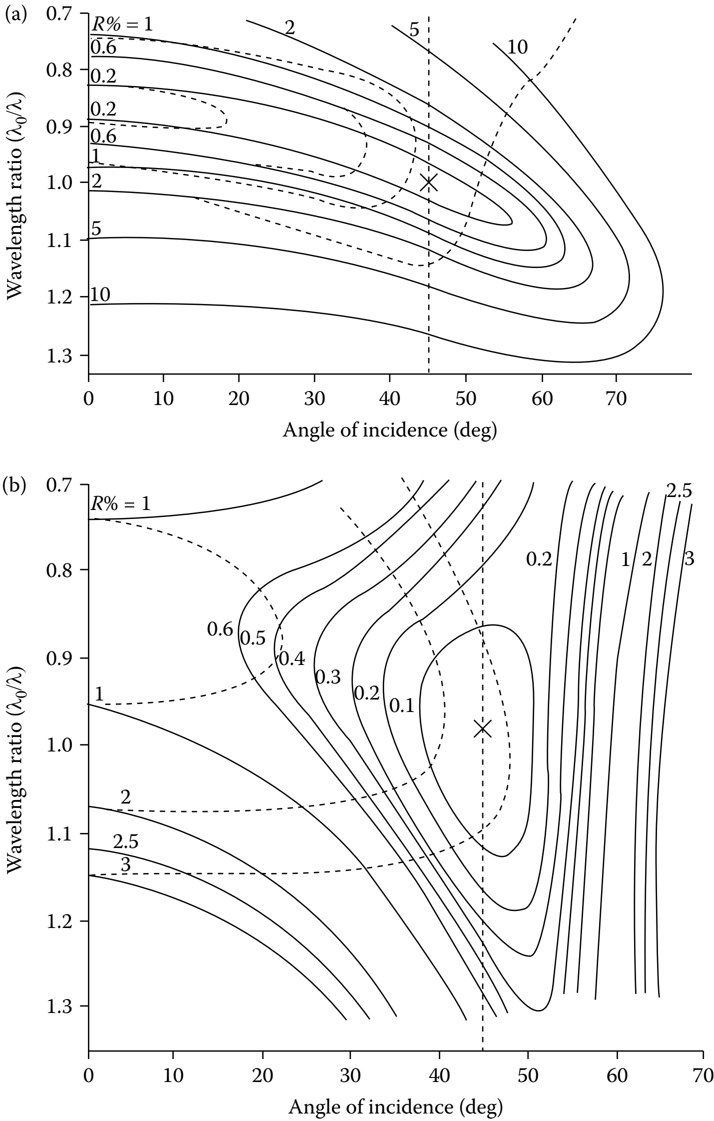

FIGURE 4.24
(a) Equireflectance contours for double-layer antireflection coatings on glass. $n_0 = 1.00$, $n_1 = 1.38$, $n_2 = 2.45$, $n_m = 1.50$, with layer thicknesses optimized for polarization (TE) at 45° angle of incidence, given by S′ in Table 4.1. Solid curves, *s*-reflectance (TE); broken curves, *p*-reflectance (TM). (After Turbadar, T., *Optica Acta*, 11, 159–170, 1964.) (b) Equireflectance contours for double-layer antireflection coatings on glass. $n_0 = 1.00$, $n_1 = 1.38$, $n_2 = 2.45$, $n_m = 1.50$, with layer thicknesses optimized for polarization (TM) at 45° angle of incidence, given by P′ in Table 4.1. Solid curves, *p*-reflectance (TM); broken curves, *s*-reflectance (TE). (After Turbadar, T., *Optica Acta*, 11, 159–170, 1964.)

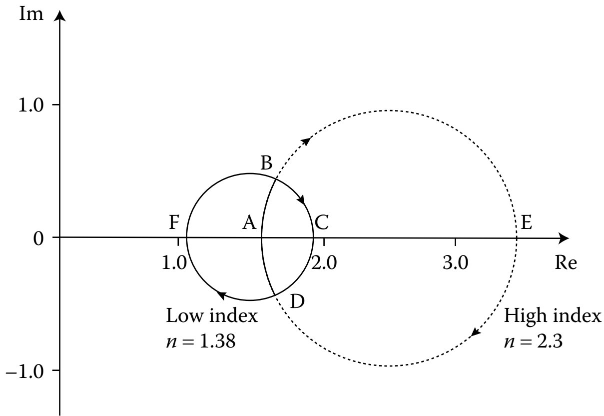

FIGURE 4.25
Admittance diagram showing the two possible double-layer antireflection coating designs.

through the point (y_1^2/y_0, 0). The second circle corresponds to the high-index layer y_2, which must pass through the point (y_m, 0) corresponding to the substrate and, therefore, also through the point (y_2^2/y_m, 0). Provided that these two circles intersect, then a two-layer antireflection coating of this type is possible. Such a plot is shown in Figure 4.25. There are two possible arrangements of the admittance circles, which will give the required zero reflectance. If we recall that a semicircle starting and finishing on the real axis corresponds to a quarter-wave, then we can see that either the high-index layer will be thinner than a quarter-wave with the low-index layer thicker, or the reverse, just as we have already established.

The special case where the layers are both quarter-waves can then be seen to occur when the y_2 circle just touches the y_1 circle internally. In that case

$$y_1^2/y_0 = y_2^2/y_m$$

or

$$y_1 = y_2\left(y_0/y_m\right)^{1/2}$$

which is the equation of the oblique line in the Schuster plot. The admittance plot for $\lambda = \lambda_0$ and the theoretical performance curve for such a coating are shown in Figure 4.26.

All the two-layer coatings considered so far exhibit one single minimum, which can be theoretically zero, at $\lambda = \lambda_0$. On either side of the minimum, the reflectance rises rather more rapidly than for the single-layer coating. An alternative two-layer coating makes use of the broadening effects of a half-wave layer to produce an improvement over the single-layer performance.

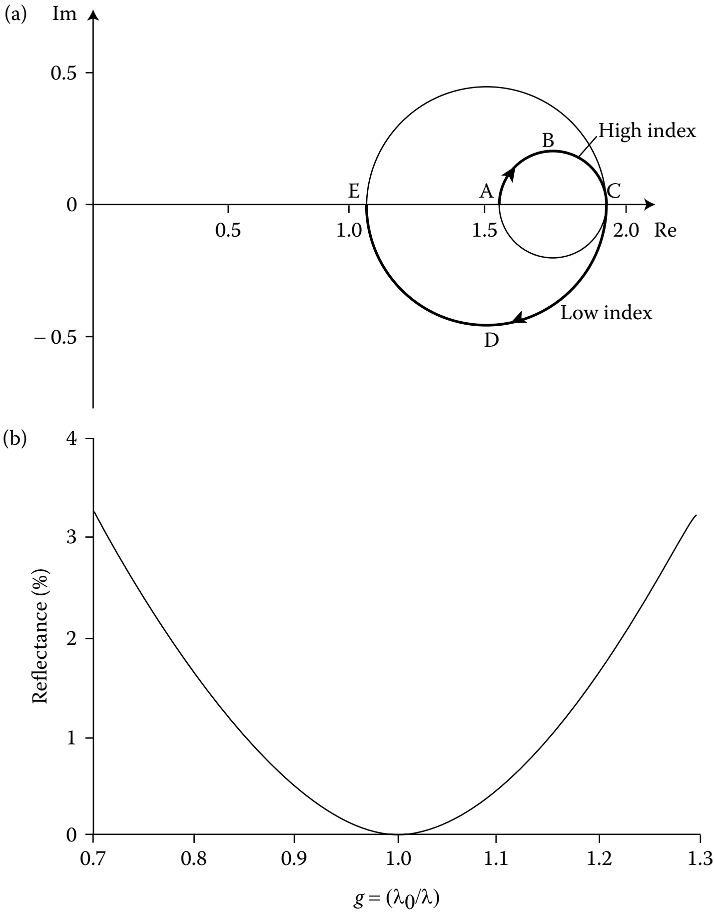

FIGURE 4.26
Special case of the two-layer antireflection coating where the layers become quarter-waves and the two solutions of Figure 4.25 merge into one. The design is

Air	1.38	1.70	Glass
1.00	$0.25\lambda_0$	$0.25\lambda_0$	1.52

(a) The admittance locus. (b) The theoretical performance curve.

A half-wave layer of index higher than the substrate is inserted between the substrate and the quarter-wave low-index film. If magnesium fluoride, of index 1.38, is once again chosen for the low-index film, then, for a substrate of index 1.52, the high-index layer should preferably be in the range 1.7–1.9, while, for a substrate of index 1.7, the range should be increased to 1.9–2.1. The way in which the half-wave layer acts to improve the performance can readily be understood by sketching an admittance plot, as in Figure 4.27. The

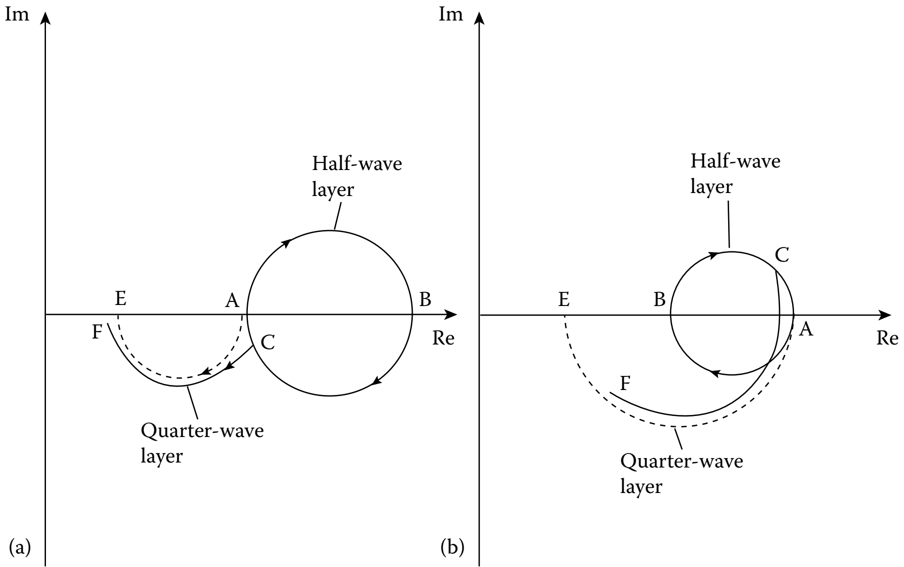

FIGURE 4.27
The operation of a half-wave flattening layer. The contour AE represents a low-index quarter-wave coating and, in ABA, a half-wave layer is inserted between it and the substrate. In (a), the half-wave is of index higher than the substrate, and as g (= λ_0/λ) varies, the action of the half-wave keeps the end of the quarter-wave near the point E and the reflectance remains low. ABCF represents the locus with g somewhat less than unity. g greater than unity would give a similar effect with the point C now above the real axis and the loci slightly longer than full circle and semicircle. (b) shows the corresponding diagram for a low-index half-wave. Here the end point is dragged rapidly away from E as g varies and the reflectance rises rapidly. Flattening is therefore effective in (a) but not in (b). Note that the reflectance curve for another coating with half-wave flattening layer of design:

Air	1.38	1.90	Glass
1.00	$0.25\lambda_0$	$0.5\lambda_0$	1.52

is shown as curve (a) of Figure 4.31. This latter coating is sometimes called a W-coat because of the shape of the characteristic.

opening of the end of the high-index locus as the value of g decreases from 1.0 partially compensates for the shortening of the low-index locus. A similar effect exists as g increases from 1.0, when the lengthening of the low-index locus is compensated by an overlapping with the high-index locus. The half-wave layer must be of an index higher than that of the substrate; otherwise, the opening of the half-wave circle would pull the low-index locus even farther from the point $g = 1.0$, hence increasing the reflectance further and effectively narrowing the characteristic. The important feature of the arrangement is that at the reference wavelength, the second quarter-wave portion of the half-wave layer and the following quarter-wave layer should have loci on the same side of the real axis.

4.2.3 Multilayer Antireflection Coatings

There is little further improvement in performance that can be achieved with two-layer coatings, given the limitations existing in usable film indices. For higher performance, further layers are required.

Thetford [10] has devised a technique for designing three-layer antireflection coatings where the reflectance is zero at two wavelengths and low over a wider range than in the two-layer coating. The arrangement consists of a layer of intermediate index next to the substrate, followed by a high-index layer and finally by a low-index layer on the outside. The indices are chosen at the outset and the method yields the necessary layer thicknesses. There is an advantage in specifying layer indices rather than thicknesses because of the limited range of materials available. Although the actual design of a coating would probably be most efficiently tackled by a process of refinement of a likely starting design, our working through the Thetford method is nevertheless worthwhile because it is an excellent example of reasoning using the vector diagram and it gives great insight.

The technique is based on both the vector method and Smith's method (the method effective interfaces). We recall that the transmittance of an assembly will be unity if, and only if, the reflectances of the structures on either side of the chosen spacer layer are equal and the thickness of the spacer layer is such that the phase change suffered by a ray of the appropriate wavelength, after having completed a round trip in the layer, being reflected once at each of the boundaries, is zero or an integral multiple of 2π. If the phase thickness of the layer is δ, then this is equivalent to saying that

$$\varphi + \varphi' - 2\delta = 2s\pi \qquad s = 0, \pm 1, \pm 2, \ldots \tag{4.17}$$

where φ and φ' are the phases of the amplitude reflection coefficients at the boundaries of the layer. Thetford split the assembly into two parts on either side of the middle layer and then computed the two amplitude reflection coefficients by the vector method, combining the calculations on one diagram. He chose thicknesses for the layers that made the reflectances equal at a reference wavelength. He then found expressions for the change in reflectance with wavelength for each of the two structures and, from them, a second value of wavelength, shorter than the first, at which the reflectances were again equal. The next step was to compute the thickness of the middle layer to satisfy the phase condition at the first wavelength and hence to give zero reflectance for the complete coating at that wavelength, and then to check whether the phase condition was also satisfied at the second wavelength. If it was, then the reflectance of the complete coating was known to be zero at this wavelength and the design was complete. If it was not, then the procedure was repeated with slightly different initial conditions at the reference wavelength. This trial and error procedure turned out to be a very quick method of arriving at the final solution. The only

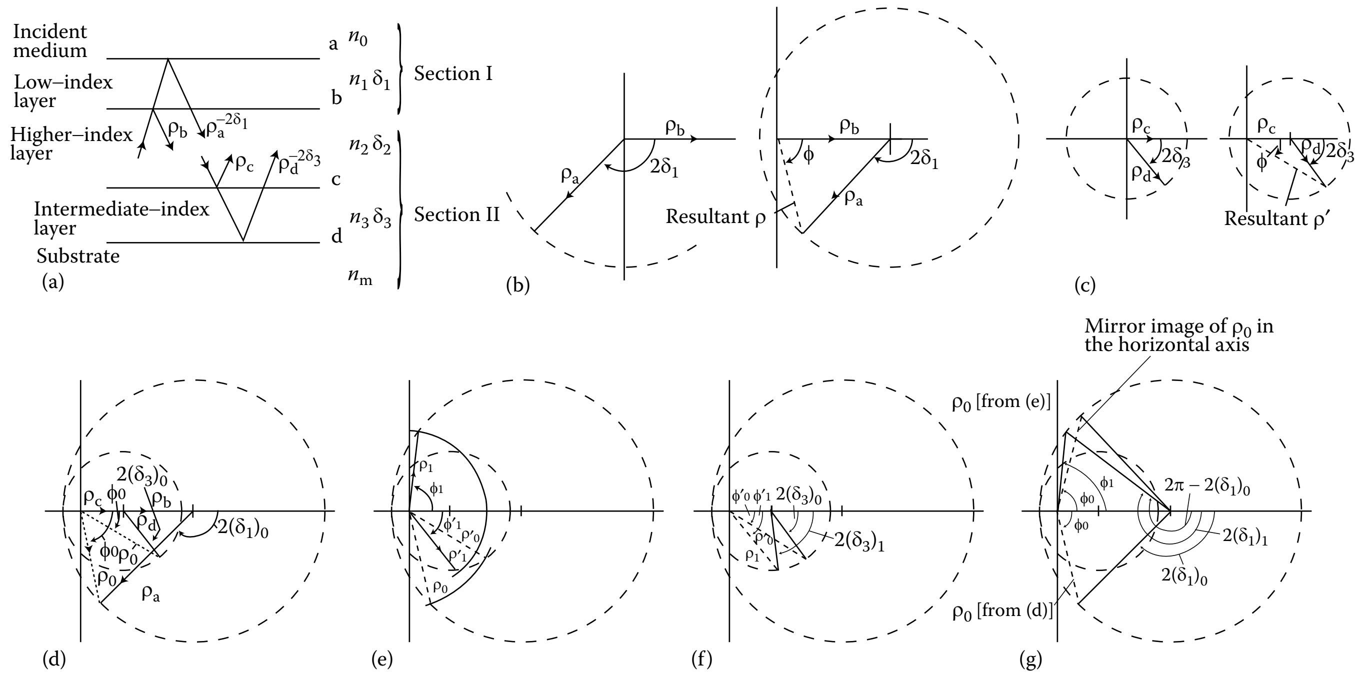

FIGURE 4.28

Thetford's method for antireflection coating design. (a) The three-layer coating split into two sections, I and II, on either side of the central high-index layer. (b) The vector diagram of section I. (c) The vector diagram of section II. (d) The vector diagrams of sections I and II superimposed, showing one possible orientation of ρ and ρ' so that they are of equal length. (e) An alternative orientation of ρ and ρ' where again they are of equal length. The arrangement in (d) is also shown. The vectors ρ_a, ρ_b, ρ_c, and ρ_d have been omitted. (f) The two possible orientations of φ' from (d) and (e). Also shown, (g), is the mirror image of ρ_0 in the horizontal axis. (After Thetford, A., *Optica Acta*, 16, 37–44, 1969.)

step that remained was the accurate calculation of the performance of the design as a check.

The three-layer coating is shown in Figure 4.28. Thetford's notation has been altered to fit in with the practice in this book. The vector diagrams for the two structures are shown at (b) and (c) and then combined at (d), with vectors in such a position that the resultant amplitude reflection coefficients ρ and ρ' are equal in length but not necessarily in phase. In the solution shown, both ρ and ρ' are in the fourth quadrant. It is very easy to arrive at this initial condition. All that is required is a circle with center the origin that cuts both the loci of vectors ρ_a and ρ_d. This initial condition we can take as corresponding to our reference wavelength λ_0. Figure 4.28e shows a second solution for a shorter wavelength λ_1 plotted on top of the first. The values of δ_1 and δ_3 that correspond to this solution are given by λ_0/λ_1 times the values corresponding to λ_0, and ρ is now in the first quadrant while ρ' remains in the fourth. To find this second solution, Thetford has derived approximate expressions for the change in reflectance with change in wavelength, which turn out to give surprisingly accurate results.

The reflectances corresponding to ρ and ρ' are given, from the diagram, by

$$\rho^2 = \rho_a^2 + \rho_b^2 + 2\rho_a\rho_b \cos 2\delta_1 \tag{4.18}$$

and

$$(\rho')^2 = \rho_c^2 + \rho_d^2 + 2\rho_c\rho_d \cos 2\delta_3 \tag{4.19}$$

For a reasonably small change in wavelength, we can find the corresponding change in ρ^2 and $(\rho')^2$ by differentiating Equations 4.18 and 4.19, i.e.,

$$\Delta(\rho)^2 = -4\rho_a\rho_b \sin 2\delta_1 \times \Delta\delta_1$$

$$\Delta\left[(\rho')^2\right] = -4\rho_c\rho_d \sin 2\delta_3 \times \Delta\delta_3$$

Now since the two values of $(\rho')^2$ in which we are interested are in the fourth quadrant, and well clear of any turning values, we can apply this approximate expression directly, giving

$$\Delta\left[(\rho')^2\right] = -4\rho_c\rho_d \sin 2(\delta_3)_0 \times \Delta\delta_3$$

$$\Delta\delta_3 = \left(\frac{\lambda_0}{\lambda_1} - 1\right)(\delta_3)_0$$

for the change in $(\rho')^2$ corresponding to the shift in wavelength from λ_0 to λ_1, where $(\delta_3)_0$ is the value at λ_0.

ρ^2, however, is not so simple. It passes through a turning value between the two solutions. Thetford observed that in Figure 4.28c, the mirror image of ρ, in the horizontal axis would also give the same resultant ρ^2 (although with a different phase angle) and that this would be fairly near the desired solution. This new position of ρa has angle $2\delta_1$, with value $2\pi - 2(\delta_1)_0$, and a change in this angle of

$$\Delta\delta_1 = \left[\left(1+\frac{\lambda_0}{\lambda_1}\right)(\delta_1)_0 - \pi\right] \tag{4.20}$$

would swing it round exactly into the correct position. We can therefore find the change in ρ^2 that we want by using the approximate expression but calculating it as a change of $\Delta\delta_1$ (Equation 4.20) from this fictitious position of ρ_a. $\Delta(\rho^2)$ is then given by

$$\begin{aligned}\Delta\left(\rho^2\right) &= -4\rho_a\rho_b \sin\left[2\pi - 2(\delta_1)_0\right]\left[\left(1+\frac{\lambda_0}{\lambda_1}\right)(\delta_1)_0 - \pi\right]\\ &= 4\rho_a\rho_b \sin 2(\delta_1)_0\left[\left(1+\frac{\lambda_0}{\lambda_1}\right)(\delta_1)_0 - \pi\right]\end{aligned}$$

We must now set $\Delta[(\rho')^2] = \Delta(\rho^2)$, which permits us to solve for λ_1. Next, we investigate the phase condition and the thickness of the middle layer.

From the vector diagram for the first solution, we can find the phase angles φ_0 and φ_0' associated with ρ and ρ' and λ_0. The necessary phase thickness of the middle layer to satisfy the condition for zero reflectance is given from Equation 4.17 by

$$2(\delta_2) = 2\pi + \varphi_0 + \varphi'_0$$

where we must remember to include the signs of φ_0 and φ_0' (both negative in Figure 4.28d) and where we have taken s as + 1 to give the thinnest possible positive value for $(\delta_2)_0$. Next, from the vector diagram we find the values of phase angle φ_1 and φ_1' associated with λ_1. If these satisfy the expression

$$2(\delta_2)_0\frac{\lambda_0}{\lambda_1} = 2\pi + \varphi_1 + \varphi'_1 \tag{4.21}$$

then we know we have a valid solution. The phase angles of the layers at λ_0 are then given by $(\delta_1)_0$, $(\pi_1)_0$, and $(\delta_1)_0$, respectively, and the optical thicknesses of the layers in terms of a quarter-wave at λ_0 can be found by dividing by $\pi/2$. If, however, the phase condition is not met at λ_1, then it is necessary to go back to the beginning and try a new set of solutions. In fact, a satisfactory solution will be found quickly, especially if the error in Equation 4.21 is plotted against, say, $(\delta_1)_0$.

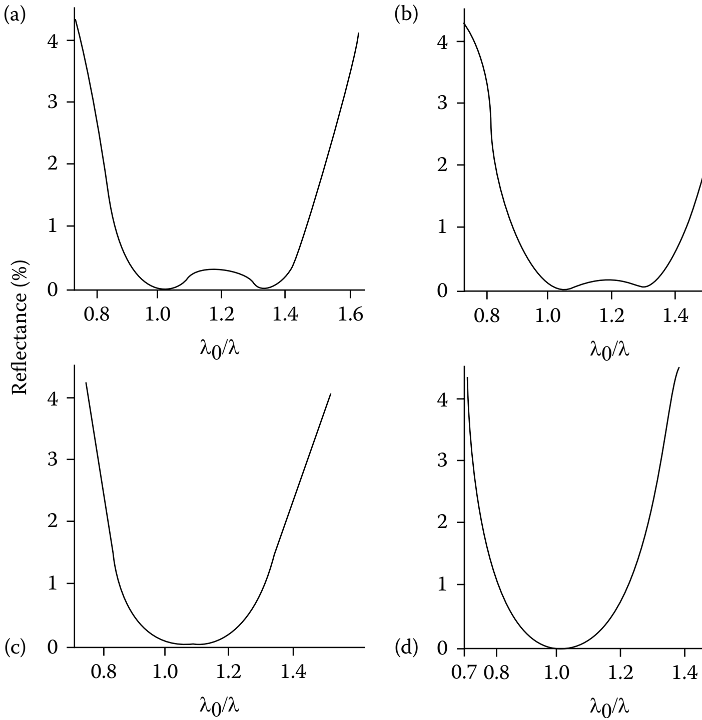

FIGURE 4.29
Calculated reflectance of some three-layer antireflection coatings designed by Thetford. The designs are as follows (after Thetford, A., *Optica Acta*, 16, 37–44, 1969):

(a) $n_0 = 1.00$, $n_1 = 1.38$, $n_2 = 2.00$, $n_3 = 1.80$, $n_4 = n_m = 1.52$, $n_1d_1 = 0.205\lambda_0$, $n_2d_2 = 0.336\lambda_0$, $n_3d_3 = 0.132\lambda_0$.
(b) $n_0 = 1.00$, $n_1 = 1.38$, $n_2 = 2.10$, $n_3 = 1.80$, $n_4 = n_m = 1.52$, $n_1d_1 = 0.225\lambda_0$, $n_2d_2 = 0.359\lambda_0$, $n_3d_3 = 0.152\lambda_0$.
(c) $n_0 = 1.00$, $n_1 = 1.38$, $n_2 = 2.20$, $n_3 = 1.80$, $n_4 = n_m = 1.52$, $n_1d_1 = 0.227\lambda_0$, $n_2d_2 = 0.338\lambda_0$, $n_3d_3 = 0.170\lambda_0$.
(d) $n_0 = 1.00$, $n_1 = 1.38$, $n_2 = 2.40$, $n_3 = 1.80$, $n_4 = n_m = 1.52$, $n_1d_1 = 0.247\lambda_0$, $n_2d_2 = 0.445\lambda_0$, $n_3d_3 = 0.181\lambda_0$.

One advantage that Thetford has pointed out for this type of coating is that once the phase condition has been satisfied at both λ_0 and λ_1 it will be approximately satisfied at all wavelengths between them. This means that the design will possess a broad region of low reflectance without any pronounced peaks of high reflectance. Some of Thetford's designs are shown in Figure 4.29, which also demonstrates how the characteristic varies with the index of the middle layer. This coating is clearly a considerable improvement over the two-layer coating.

It is not easy to establish analytical expressions for the ranges of n_1, n_2, and n_3 that will give an acceptable reflectance characteristic. Generally, if the admittance diagram is not too far removed in appearance from the

form of Figure 4.28 where the two positions of ρ are near the minimum, which corresponds to $2\delta_1 = \pi$, then a good antireflection coating will be obtained.

If it should be a requirement that only two values of refractive index, rather than three, be used in the construction of the coating, then it is possible to achieve a similar performance if four layers of alternate high and low index are used. Thetford [11] has used a similar technique for the design of such a coating. He split the coating (which has a high-index layer next to the glass) at the high-index layer nearest the air, so that the high-low combination next to the glass took the place of the intermediate index layer of the three-layer design. If the thicknesses of these two layers are fairly small, then an Argand diagram is obtained, which is not too different from that for the three-layer design. Because the expressions would be much more complicated in this case, Thetford did not attempt an analytical solution but rather arrived at a design that appeared reasonable, by trial and error. The reflectance characteristic of such a design is shown in Figure 4.30. This solution was then refined by C. Butler, using a computer technique, to give optimum performance. This improved coating is also shown in Figure 4.30.

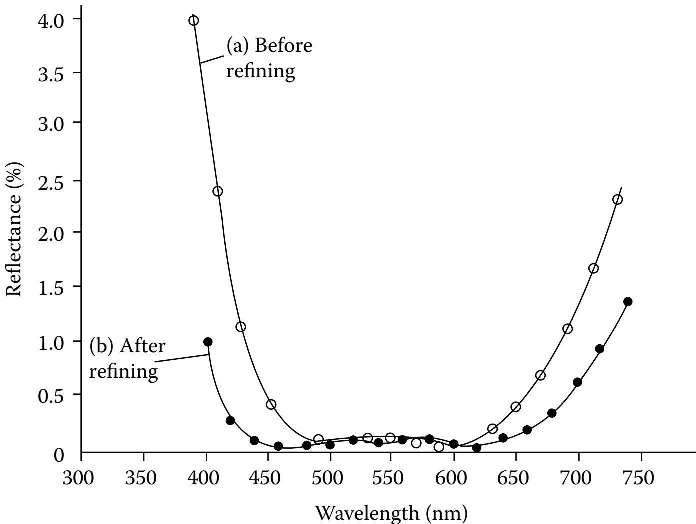

FIGURE 4.30
Calculated reflectance of four-layer antireflection coatings on glass showing the performance before and after the design was refined by computer. The two designs are (communicated by Thetford):

(a) Before refining: $n_0 = 1.00$, $n_1 = n_3 = 1.38$, $n_2 = n_4 = 2.10$, $n_3 = 1.80$, $n_5 = nm = 1.52$, $n_1d_1 = 0.21\lambda_0$, $n_2d_2 = 0.37\lambda_0$, $n_3d_3 = 0.036\lambda_0$, $n_4d_4 = 0.070\lambda_0$.

(b) After refining: $n_0 = 1.00$, $n_1 = n_3 = 1.38$, $n_2 = n_4 = 2.10$, $n_3 = 1.80$, $n_5 = nm = 1.52$, $n_1d_1 = 0.216\lambda_0$, $n_2d_2 = 0.458\lambda_0$, $n_3d_3 = 0.072\lambda_0$, $n_4d_4 = 0.049\lambda_0$.

There are also many coatings that involve layers of either quarter-wave or half-wave optical thicknesses. A number of these can be looked upon as modifications of some of the two-layer designs already considered.

First, we take the two-layer coating consisting of a half-wave layer next to the substrate followed by a quarter-wave layer. This has a peak reflectance in the center of the low-reflectance region. This peak corresponds to the minimum reflectance of a single-layer coating because the inner layer, being a half-wave at that wavelength, is an absentee. We can reduce the peak but retain to some extent the flattening effect of the half-wave layer by splitting it into two quarter-waves, only slightly different in index. The first layer we can retain as 1.9, although it is in no way critical, and then if we make the second quarter-wave of slightly higher index, 2.0, say, the design now becoming

Air	1.38	2.0	1.9	Glass
1.0	$0.25\lambda_0$	$0.25\lambda_0$	$0.25\lambda_0$	1.52

we find a reduction in the reflectance at λ_0 from 1.26% to 0.38%. The characteristic remains fairly broad. Increasing the index of the central layer still further, to 2.13, i.e., a design

Air	1.38	2.13	1.9	Glass
1.0	$0.25\lambda_0$	$0.25\lambda_0$	$0.25\lambda_0$	1.52

reduces the reflectance at λ_0 to virtually zero, but the width of the coating becomes much more significantly reduced. The characteristic curves of these two coatings are shown in Figure 4.31.

Yet a further increase in the width of the coating can be achieved by adding a half-wave layer of low index next to the substrate. The admittance plot is shown in Figure 4.32, and we see the characteristic shape where the final part of the locus of the half-wave layer and the start of the following layer are on the same side of the real axis. A half-wave layer in the same position with index higher than the substrate would be ineffective. A certain amount of trial and error leads to the designs shown in Figure 4.32, that is

Air	1.38	1.905	1.76	1.38	Glass
1.0	$0.25\lambda_0$	$0.25\lambda_0$	$0.25\lambda_0$	$0.5\lambda_0$	1.52

and

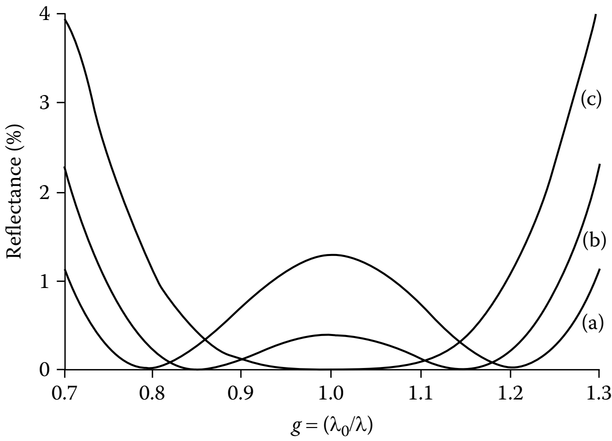

FIGURE 4.31
Progressive changes in an antireflection coating consisting of three quarter-wave layers. (a) The original coating:

Air	1.38	1.90	1.9	Glass
1.00	0.25_0	0.25_0	0.25_0	1.52

The two 1.90 index layers combine to form a single half-wave layer. This is known as a W-coat because of the shape of the characteristic. (b) The index of the central layer is increased to 2.00. (c) The index of the central layer is increased further to 2.13.

Air	1.38	2.13	1.38	2.30	1.38	Glass
1.0	$0.25\lambda_0$	$0.25\lambda_0$	$0.25\lambda_0$	$0.25\lambda_0$	$0.5\lambda_0$	1.52

An alternative approach is to broaden the quarter-quarter design of Figure 4.26 by inserting a half-wave layer between the two quarter-waves. To achieve the broadening effect, it must, of course, be of high index, so that the admittance plot will be of the form shown in Figure 4.33. The coating is frequently referred to as the quarter-half-quarter coating. Coatings that fit into this general type date back to the 1940s and were described by Luther, Lockhart, and King [12]. A systematic design technique explaining the functions of the various layers, however, was not available until the detailed study of Cox, Hass, and Thelen [13]. A certain amount of trial and error leads to the characteristics of Figure 4.34. However, good results are obtained with values of the index of the half-wave layer in the range 2.0–2.4. Cox et al. also investigated the effect of varying the indices of the quarter-wave layers and found that for the best results on crown glass the outermost layer index should be between 1.35 and 1.45, and the innermost layer index between 1.65 and 1.70. The outermost layer is the most critical in the design.

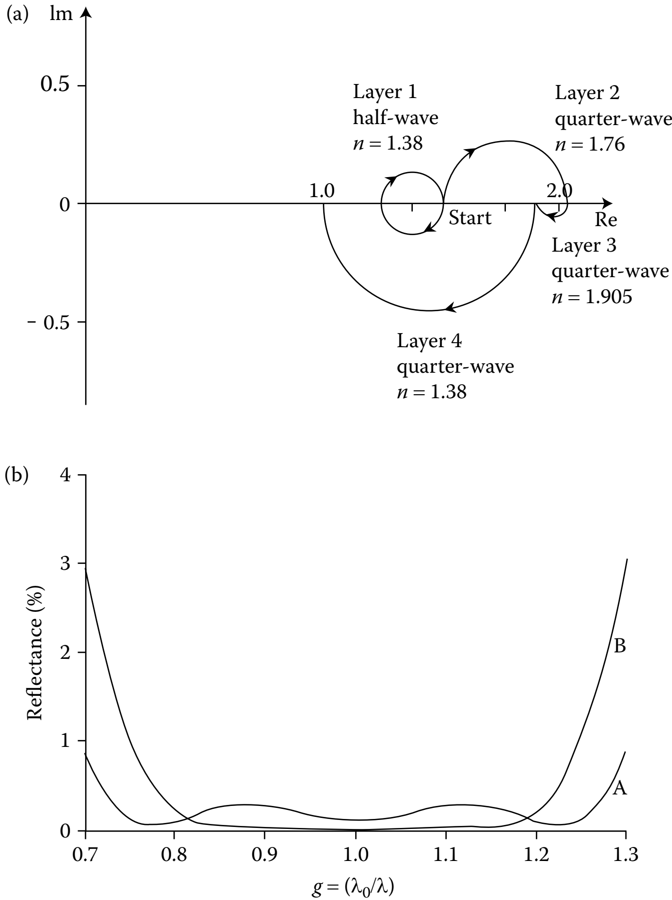

FIGURE 4.32
(a) The admittance locus of the coating:

Air	1.38	1.905	1.76	1.38	Glass
1.00	$0.25\lambda_0$	$0.25\lambda_0$	$0.25\lambda_0$	$0.5\lambda_0$	1.52

(b) The characteristics of (1) the coating of Figure 4.32a and (2) the coating (c) of Figure 4.31 with a half-wave flattening layer of index 1.38 added next to the substrate.

Figure 4.35 also comes from their paper and shows the measured reflectance of an experimental coating consisting of magnesium fluoride, index 1.38, zirconium oxide, index 2.1, and cerium fluoride, which was evaporated rather too slowly and had an index of 1.63, which accounting for the slight rise in the middle of the range. Otherwise, the coating is an excellent practical confirmation of the theory.

The effect of variations in angle of incidence has also been, examined. Cox et al.'s results for tilts up to 50° of a coating designed for normal incidence

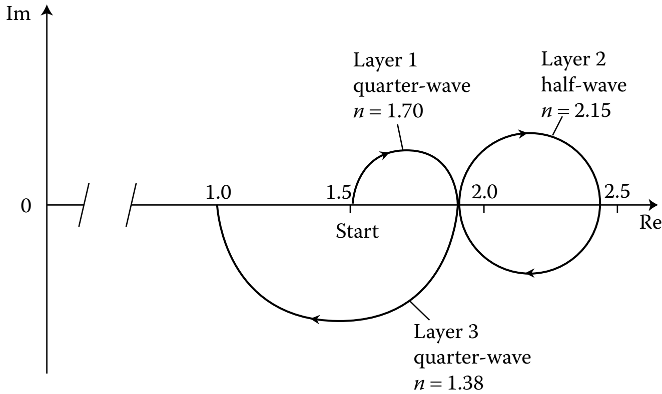

FIGURE 4.33
Admittance locus of the quarter-half-quarter coating:

Air	1.38	2.15	1.70	Glass
1.0	$0.25\lambda_0$	$0.5\lambda_0$	$0.25\lambda_0$	1.52

The half-wave layer acts to flatten the performance of the two quarter-waves.

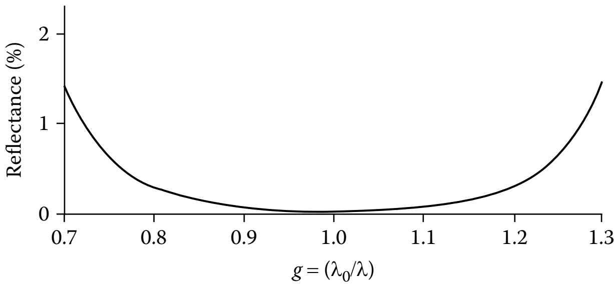

FIGURE 4.34
The calculated reflectance of the quarter-half-quarter coating shown in Figure 4.33.

are shown in Figure 4.36. The performance of the coating is excellent up to 20° but begins to fall off beyond 30°. The coatings can, of course, be designed for use at angles of incidence other than normal, and Turbadar [14] has published a full account of a design for use at 45°. The particular design depends on whether light is *s*- or *p*-polarized, and Figure 4.37 shows sets of equireflectance contours for both designs.

The quarter-half-quarter coating is certainly the most significant of the early multilayer coatings for low-index glass and it has had considerable influence on the development of the field.

The success of the broadening effect of the half-wave layer on the quarter-quarter coating prompts us to consider inserting a similar half-wave in the two-layer coating of Figure 4.25. In this case, there is an advantage in using a

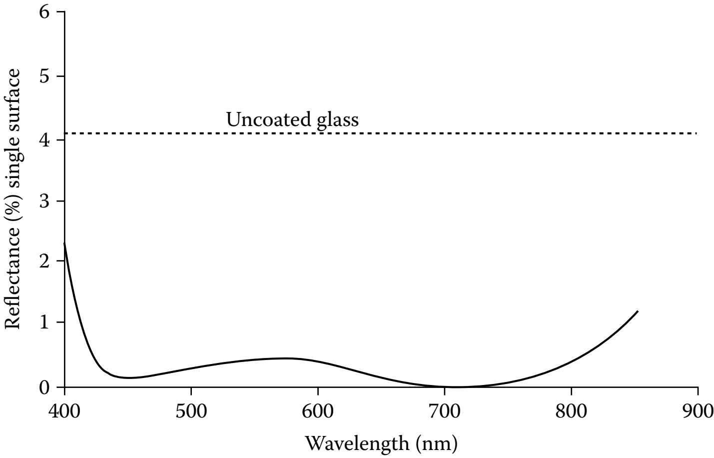

FIGURE 4.35
Measured reflectance of a quarter-half-quarter antireflection coating of $MgF_2 + ZrO_2 + CeF_3$ on crown glass. $\lambda_0 = 550$ nm. (After Cox, J.T., Hass, G., and Thelen, A., *Journal of the Optical Society of America*, 52, 965–969, 1962.)

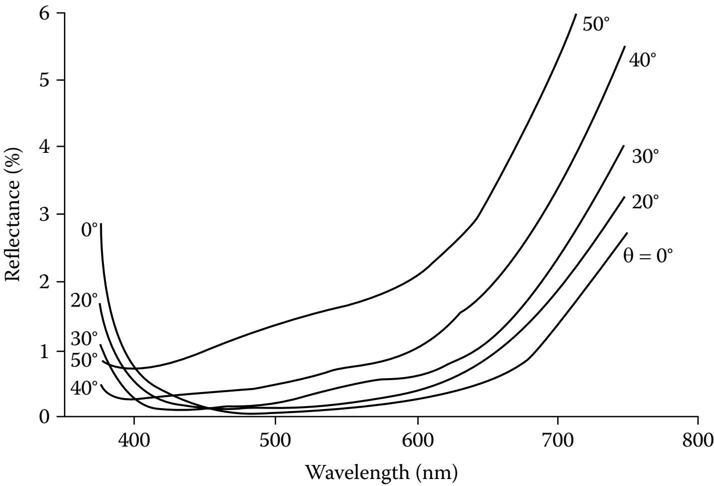

FIGURE 4.36
Calculated reflectance as a function of wavelength for quarter-half-quarter antireflection coatings on glass at various angles of incidence. $n_0 = 1.00$, $n_1 = 1.38$, $n_2 = 2.2$, $n_3 = 1.70$, $nm = 1.51$. (After Cox, J.T., Hass, G., and Thelen, A., *Journal of the Optical Society of America*, 52, 965–969, 1962.)

layer of the same index as that next to the substrate. Here we cannot split the coating at the interface between the high- and the low-index layers, because the admittance plot would not show the correct broadening configuration. Instead, we must split the coating at the point where the low-index locus cuts the real axis so that the plot appears as in Figure 4.38. The design of the coating is then

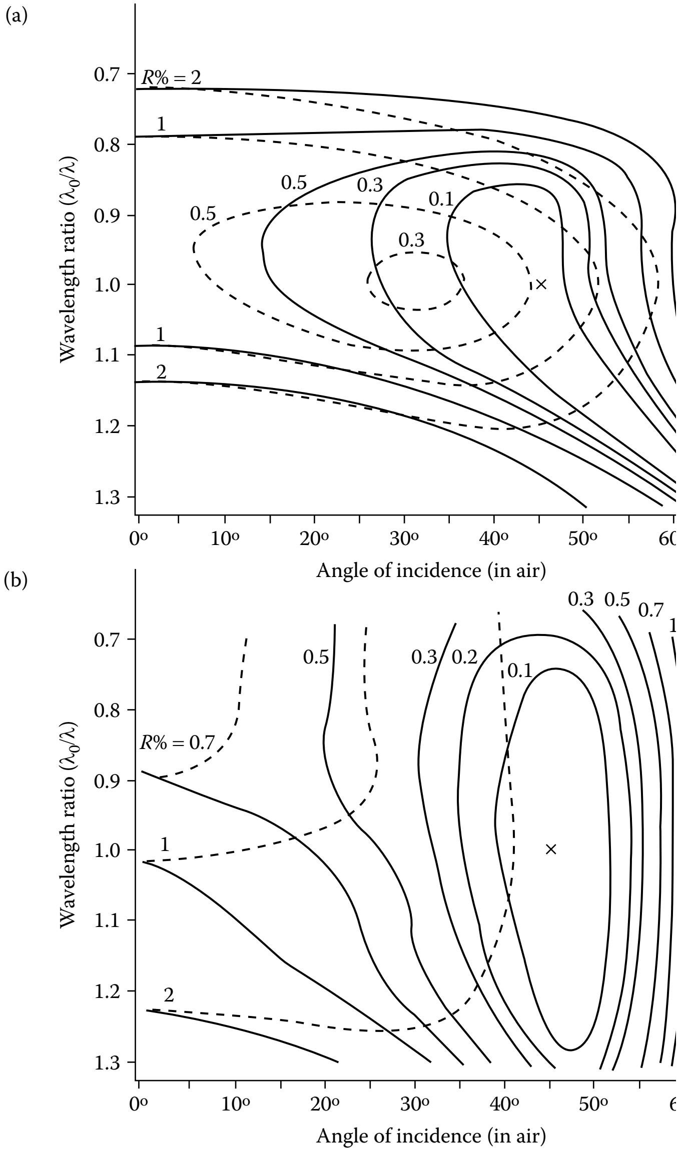

FIGURE 4.37
(a) Equireflectance contours for a quarter-half-quarter antireflection coating designed for use at 45° on crown glass. The indices are chosen for best performance with *s*-polarization (TE). n_0 = 1.00, n_1 = 1.35, n_2 = 2.45, n_3 = 1.70, nm = 1.50. Solid curves, polarization (TE); broken curves, polarization (TM). (After Turbadar, T., *Optica Acta*, 11, 195–205, 1964.) (b) Equireflectance contours for a quarter-half-quarter antireflection coating designed for use at 45° on crown glass. The indices are chosen for best performance with *p*-polarization (TM). n_0 = 1.00, n_1 = 1.40, n_2 = 1.75, n_3 = 1.58, nm = 1.50. Solid curves, polarization (TM); broken curves, polarization (TE). (After Turbadar, T., *Optica Acta*, 11, 195–205, 1964.)

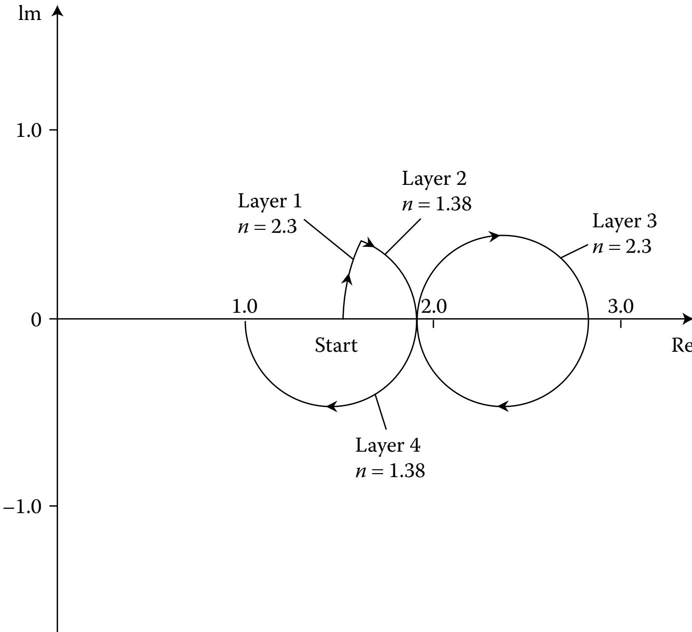

FIGURE 4.38
The two-layer coating of Figure 4.25 with the low-index layer split where it intersects the real axis and a high-index flattening layer inserted.

Air	1.38	2.30	1.38	2.30	Glass
1.0	$0.25\lambda_0$	$0.5\lambda_0$	$0.0734\lambda_0$	$0.0522\lambda_0$	1.52

where this time we have used a value of 2.30 for the high index, and the performance is shown in Figure 4.39. There is a considerable resemblance between this admittance plot and that of the quarter-half-quarter design. This design approach can be attributed originally to Frank Rock, who used the properties of reflection circles in deriving it rather than admittance loci.

Vermeulen [15] arrived independently at an ultimately similar design in a completely different way. There is a difficulty in achieving the correct value for the intermediate index in the quarter-half-quarter design in practice and Vermeulen realized that the deposition of a low-index layer over a high-index layer of less than a quarter-wave would lead to a maximum turning value in reflectance rather lower than would have been achieved with a quarter-wave of high index on its own. He therefore designed a two-layer high-low combination to give an identical turning value to that which should be obtained with the 1.70 index layer of the quarter-half-quarter coating, and he discovered that good performance was maintained. The turning value in reflectance must, of course, correspond to the intersection

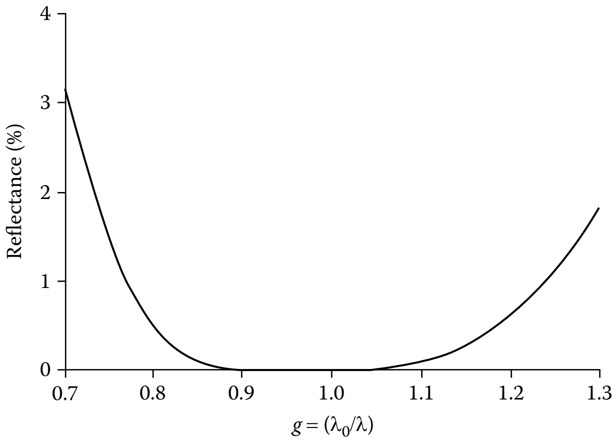

FIGURE 4.39
The performance of the coating of Figure 4.38. Although arrived at by way of the admittance plot of Figure 4.38, the design is virtually identical to one published by Vermeulen, whose design technique was quite different (see text).

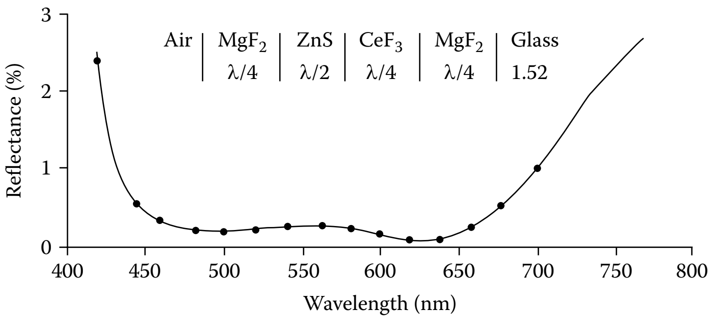

FIGURE 4.40
Measured reflectance of a four-layer antireflection coating on crown glass. The results are for a single surface. (After Shadbolt, M.J., Measured results of four-layer antireflection coating deposition. Sira Institute, Chislehurst, Kent, UK Private Communication, 1967.)

of the locus with the real axis, and the rest follows. We shall return to this coating later.

The quarter-half-quarter coating can be further improved by replacing the layer of intermediate index by two quarter-wave layers. The layer next to the substrate should have an index lower than that of the substrate. A practical coating of this general type is shown in Figure 4.40. Trial and error leads to a design

Air	1.38	2.05	1.60	1.45	Glass
1.0	$0.25\lambda_0$	$0.5\lambda_0$	$0.25\lambda_0$	$0.25\lambda_0$	1.52

the theoretical performance of which is shown in Figure 4.41. Similar designs with slightly different index values are given by Cox and Hass [17] and by Musset and Thelen [6]. Ward [18] has published a particularly useful version of this coating with indices chosen to match those of available materials rather than to achieve optimum performance. Examples of four-layer coatings for substrates of indices other than 1.52 are also given by Ward and by Musset and Thelen [6].

Yet a further four-layer design can be obtained by splitting the half-wave layer of the quarter-half-quarter coating into two quarter-waves and adjusting the indices to improve the performance. A five-layer design derived in a similar way from the design of Figure 4.41 is:

Air	1.38	1.86	1.94	1.65	1.47	Glass
1.0	$0.25\lambda_0$	$0.25\lambda_0$	$0.25\lambda_0$	$0.25\lambda_0$	$0.25\lambda_0$	1.52

The possibilities are clearly enormous and problems are found much more in the construction of the coatings because not all the required indices are readily available. One solution is discussed in the next section.

A rather interesting design based on four layers of alternate high and low index has been published by C. Reichert Optische Werke AG [19]. Full details of the design method are, unfortunately, not given. The thicknesses

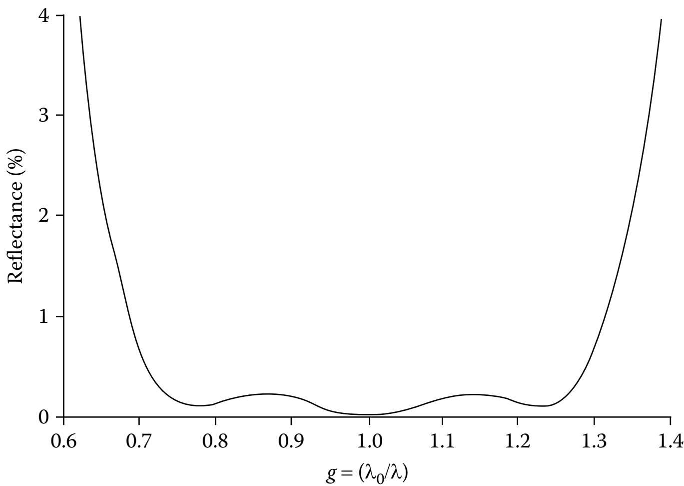

FIGURE 4.41
The performance of the four-layer coating of design:

Air	1.38	2.05	1.60	1.45	Glass
1.00	$0.25\lambda_0$	$0.5\lambda_0$	$0.25\lambda_0$	$0.25\lambda_0$	1.52

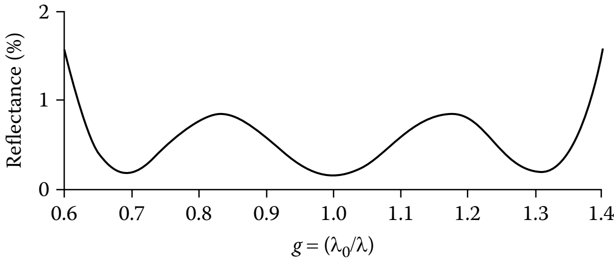

FIGURE 4.42
A five-layer design derived from Figure 3.41 by replacing the half-wave layer by two quarter-wave layers and adjusting the values of the indices. Design:

Air	1.38	1.86	1.94	1.65	1.47	Glass
1.00	$0.25\lambda_0$	$0.25\lambda_0$	$0.25\lambda_0$	$0.25\lambda_0$	$0.25\lambda_0$	1.52

TABLE 4.2
The Reichert design.

Material	Index	Optical Thickness (nm)
Air	1.00	Massive
MgF_2	1.37	161
TiO_2	2.28	78.5
MgF_2	1.37	56.5
TiO_2	2.28	54
Glass	1.52	Massive

Source: Reichert, C., Optische Werke, A.G., *Improvements in or relating to optical components having reflection-reducing coatings*, UK Patent 991,635, 1962.

and materials are given in Table 4.2. Note that the thicknesses are quoted as optical. The reflectance of this coating, Figure 4.43, is slightly better than the unrefined performance of Figure 4.30 but inferior to the refined curve.

Although the Reichert design technique is not described, nevertheless it is a good exercise to attempt to understand how the coating functions. For this, it is easiest if we simply draw an admittance diagram. Since the coating is clearly centered on 550 nm, we draw the diagram for that wavelength.

The admittance diagram, Figure 4.44, shows that the Reichert design can be considered as derived by applying two Vermeulen equivalents to the W-coat and its three-layer variations in Figure 4.31. A particularly interesting feature of the Reichert coating is that it is quite thin compared with the W-coat from which it is derived. This double Vermeulen equivalent is a powerful replacement for a flattening half-wave in a design. We shall return to this structure later when we consider buffer layers.

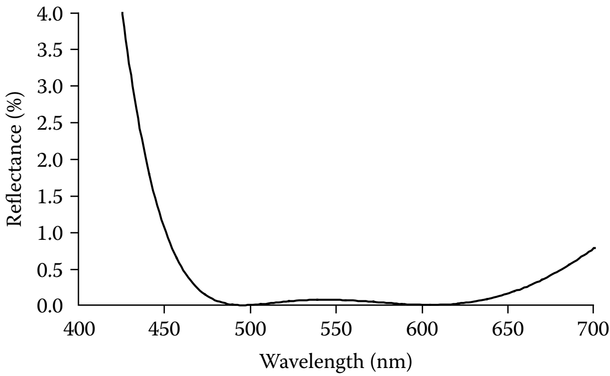

FIGURE 4.43
The Reichert four-layer two-material antireflection coating.

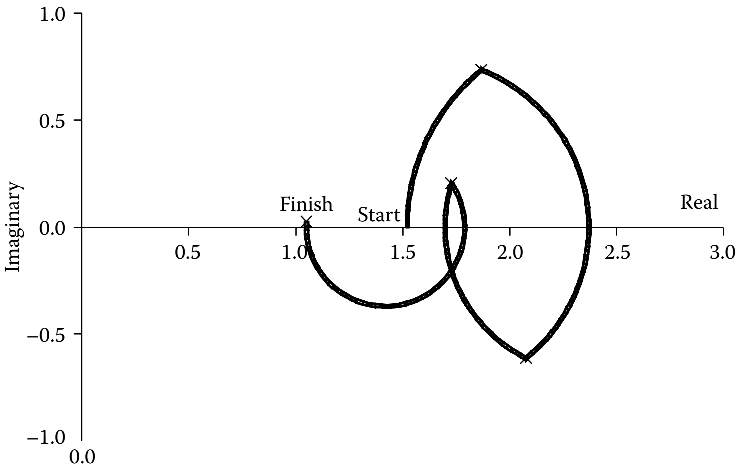

FIGURE 4.44
The admittance locus of the Reichert design at 550 nm.

4.3 Equivalent Layers

There are great advantages in using a series of quarter-waves or multiples of quarter-waves in the first stages of the design of antireflection coatings because the characteristic curves of such coatings are symmetrical about $g = 1.0$. However, problems are presented in construction because the indices, which are specified in this way, do not often correspond exactly with indices that are readily available. Using mixtures of materials of higher and lower indices to produce a layer of intermediate index is a technique that has been used successfully (see Chapter 11), but a more straightforward method is to

replace the layers by equivalent combinations involving only two materials, one of high index and one of low index. These two materials can be well tried, stable materials, the characteristics of which have been established over many production runs in the plant that will be used for, and under the conditions that will apply to, the production of the coatings. To illustrate the method, we assume two materials of index 2.30 and 1.38, corresponding approximately to titanium dioxide and magnesium fluoride, respectively.

The first technique to mention is that of Vermeulen [15], which has already been referenced. It involves the replacing of a quarter-wave by a two-layer equivalent. The analysis is exactly that already given for the two-layer antireflection coating, and it is assumed that the quarter-wave to be replaced has a locus that starts and terminates at predetermined points on the real axis. The replacement is, therefore, valid for the particular starting and terminating points used in its derivation only, and for that single wavelength for which the original layer is a quarter-wave. Under conditions that are increasingly remote from these ideal ones, the two-layer replacement becomes increasingly less satisfactory. It is advisable, when calculating the parameters of the layers, to sketch a rough admittance plot because otherwise there is a real danger of picking incorrect values of layer thickness. In this particular case, we are considering, the starting admittance is 1.52 on the real axis and the terminating admittance is 1.9044, which will ensure that the outermost 1.38 index quarter-wave layer will terminate at the point 1.00 on the real axis. Clearly, the high-index layer should be next to the substrate. The thicknesses are then, using Equations 4.6 and selecting the appropriate pair of solutions, 0.05217 and 0.07339 full waves for the high- and low-index layers, respectively. We complete the design by adding a half-wave of index 2.30 and a quarter-wave of index 1.38. The characteristic curve of this coating is shown in Figure 4.39, which, we recall, was arrived at in a completely different way.

As already mentioned, the four-layer Reichert coating, Table 4.2, can be thought of as a Vermeulen equivalent of the coatings of Figure 4.31.

To obtain a replacement for a quarter-wave that does not depend on the starting point, we turn to a technique originated by Epstein [20] involving the symmetrical periods and the Herpin admittance mentioned briefly in Chapter 2. We recall that any symmetrical combination of layers acts as a single layer with an equivalent phase thickness and equivalent optical admittance. In this particular application, we consider combinations of the form ABA only. We choose for the indices of A and B those of the two materials from which the coating is to be constructed. Then for each quarter-wave layer of the coating, we construct a three-layer symmetrical period that has an equivalent thickness of one quarter-wave and an equivalent admittance equal to that required from the original.

To proceed further, we need expressions for the equivalent thickness and admittance of a symmetrical period. These are derived later in Chapter 7. Since the symmetrical period is of the form ABA, then

$$y_E = y_A \times \left(\frac{\sin 2\delta_A \cos\delta_B + \frac{1}{2}\left[(y_B/y_A)+(y_A/y_B)\right]\cos 2\delta_A \sin\delta_B + \frac{1}{2}\left[(y_B/y_A)-(y_A/y_B)\right]\sin\delta_B}{\sin 2\delta_A \cos\delta_B + \frac{1}{2}\left[(y_B/y_A)+(y_A/y_B)\right]\cos 2\delta_A \sin\delta_B - \frac{1}{2}\left[(y_B/y_A)-(y_A/y_B)\right]\sin\delta_B} \right)^{1/2} \tag{4.22}$$

$$\cos\gamma = \cos 2\delta_A \cos\delta_B - \frac{1}{2}\left[(y_B/y_A)+(y_A/y_B)\right]\sin 2\delta_A \sin\delta_B \tag{4.23}$$

where y_E is the equivalent optical admittance and γ is the equivalent phase thickness. The important feature of the symmetrical combination is that it behaves as a single layer of phase thickness γ and admittance y_E regardless of the starting point for the admittance locus.

In our particular case, the equivalent thickness of the combination should be a quarter-wave. That is

$$\begin{aligned}\cos\gamma &= \cos(\pi/2) = 0 \\ &= \cos 2\delta_A \cos\delta_B - \frac{1}{2}\left[(y_B/y_A)+(y_A/y_B)\right]\sin 2\delta_A \sin\delta_B\end{aligned}$$

which gives

$$\tan 2\delta_A \tan\delta_B = \frac{2y_A y_B}{y_A^2 + y_B^2} \tag{4.24}$$

Substituting in Equation 4.22 and manipulating the expression, we have

$$y_E = y_A \left(\frac{1+\left[(y_B^2 - y_A^2)/(y_B^2 + y_A^2)\right]\cos 2\delta_A}{1-\left[(y_B^2 - y_A^2)/(y_B^2 + y_A^2)\right]\cos 2\delta_A} \right)^{1/2} \tag{4.25}$$

Which yields

$$\cos 2\delta_A = \frac{(y_B^2 + y_A^2)/(y_E^2 - y_A^2)}{(y_B^2 - y_A^2)/(y_E^2 + y_A^2)} \tag{4.26}$$

δ_B is given by Equation 4.24, i.e.,

$$\tan\delta_B = \frac{2y_A y_B}{y_A^2 + y_B^2}\cdot\frac{1}{\tan 2\delta_A} \tag{4.27}$$

and the optical thicknesses are then

$$\frac{n_A d_A}{\lambda_0} = \frac{\delta_A}{2\pi} \text{ full waves at } \lambda_0$$

$$\frac{n_B d_B}{\lambda_0} = \frac{\delta_B}{2\pi} \text{ full waves at } \lambda_0 \tag{4.28}$$

If an equivalent combination for a half-wave layer is required, then it is considered as two quarter-waves in series.

As an example of the application of this technique, we take the four-layer coating of Figure 4.32.

Air	1.38	2.13	1.9	1.38	Glass
1.0	$0.25\lambda_0$	$0.25\lambda_0$	$0.25\lambda_0$	$0.25\lambda_0$	1.52

The layers that must be replaced are the quarter waves with indices 2.13 and 1.90. There are two possible combinations, *HLH* or *LHL*, for each of these layers.

$$\begin{matrix} 2.13 \\ 0.25\lambda_0 \end{matrix} \rightarrow \begin{cases} \begin{array}{c|c|c} 1.38 & 2.30 & 1.38 \\ 0.04128\lambda_0 & 0.15861\lambda_0 & 0.04128\lambda_0 \end{array} \\ \\ \begin{array}{c|c|c} 2.30 & 1.38 & 2.30 \\ 0.11193\lambda_0 & 0.0230\lambda_0 & 0.11198\lambda_0 \end{array} \end{cases}$$

$$\begin{matrix} 1.90 \\ 0.25\lambda_0 \end{matrix} \rightarrow \begin{cases} \begin{array}{c|c|c} 1.38 & 2.30 & 1.38 \\ 0.06793\lambda_0 & 0.10438\lambda_0 & 0.06793\lambda_0 \end{array} \\ \\ \begin{array}{c|c|c} 2.30 & 1.38 & 2.30 \\ 0.09216\lambda_0 & 0.05868\lambda_0 & 0.09216\lambda_0 \end{array} \end{cases}$$

As an indication of the closeness of fit between the symmetrical periods and the layers they replace, the variation, with *g*, of equivalent admittance and equivalent optical thickness is plotted in Figure 4.45.

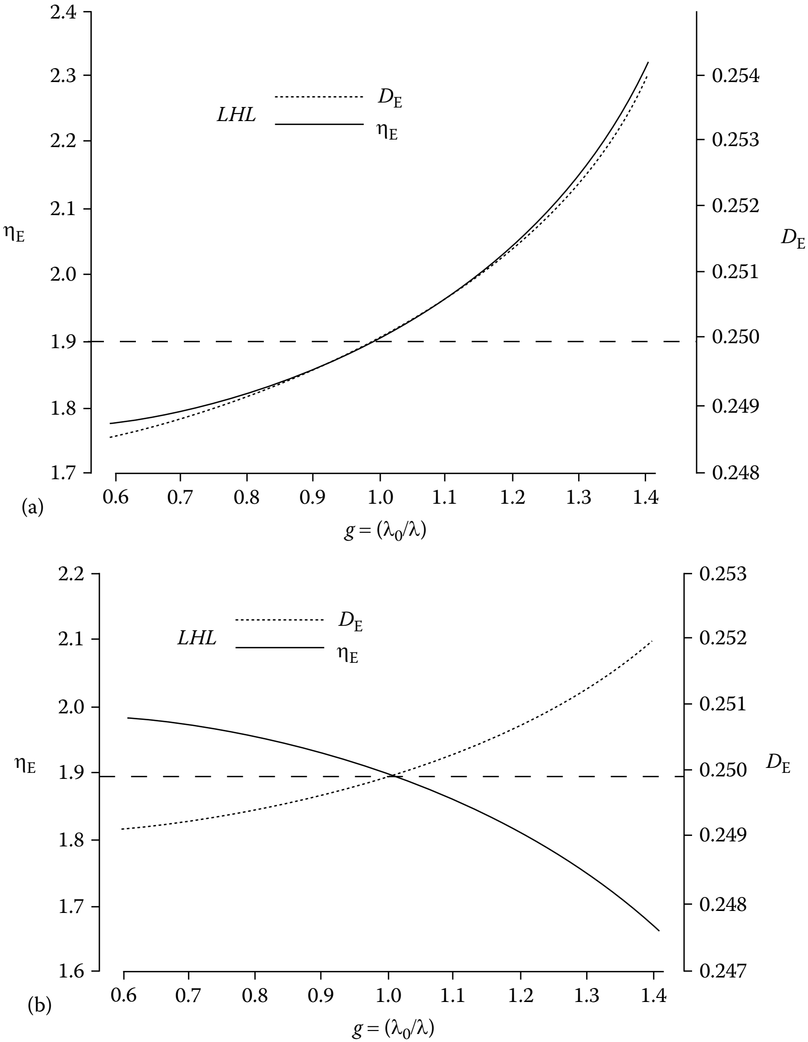

FIGURE 4.45
The equivalent admittances and optical thickness as a function of g (= λ_0/λ) of symmetrical period replacements for a single quarter-wave of index 1.90. The indices used in the symmetrical replacement are 2.30 for the high index and 1.38 for the low index. (a) *LHL* combination. (b) *HLH* combination. For a perfect match, D_E and y_E should both be constant at $0.25\lambda_0$ and 1.9, respectively, whatever the value of g.

We can now replace the layers in the actual design of antireflection coating. There are two possible replacements for each of the relevant layers, but where *HLH* and *LHL* combinations are mixed, there is a tendency toward an excessive number of layers in the final design, and so we consider two possibilities only, one based on *HLH* periods and one on *LHL*. These are shown in Table 4.3.

TABLE 4.3
Designs Shown in Figure 4.46

	Design Based on *LHL* Periods		Design Based on *HLH* Periods	
Layer Number	**Index**	**Thickness**	**Index**	**Thickness**
0	1.0	Incident medium	1.0	Incident medium
1	1.38	$0.29128\lambda_0$	1.38	$0.25\lambda_0$
2	2.30	$0.15861\lambda_0$	2.30	$0.11198\lambda_0$
3	1.38	$0.10921\lambda_0$	1.38	$0.02302\lambda_0$
4	2.30	$0.10438\lambda_0$	2.30	$0.20414\lambda_0$
5	1.38	$0.56793\lambda_0$	1.38	$0.05868\lambda_0$
6	1.52	Substrate	2.30	$0.09216\lambda_0$
7			1.38	$0.5\lambda_0$
8			1.52	Substrate

The spectral characteristics of these coatings along with the original design are shown in Figure 4.46. The replacements have a slightly inferior performance due to the effective dispersion that can be seen in Figure 4.45. The process of design need not stop at this point, however, because the designs are excellent starting points for refinement. Figure 4.47 shows the performance of a refined version of one of the coatings. In practice, the refinement will include an allowance for the dispersion of the indices of the materials and there will be a certain amount of adjustment of the coating during the production trials.

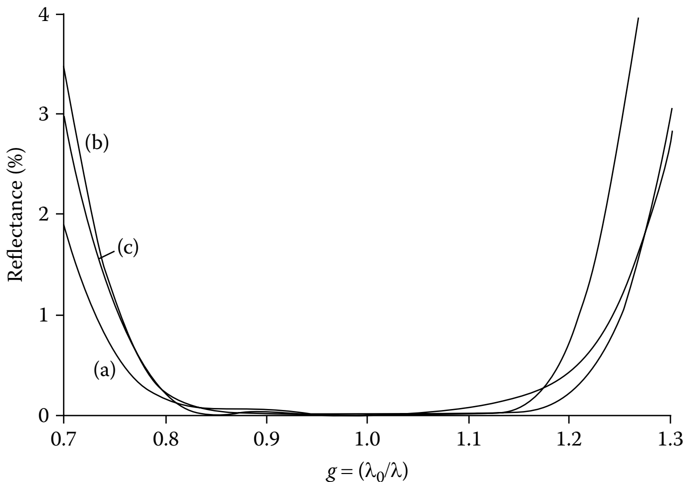

FIGURE 4.46
The performance of the designs of Table 4.3: (a) Five-layer design based on *LHL* periods. (b) Seven-layer design based on *HLH* periods. (c) The original four-layer design from which (a) and (b) were derived

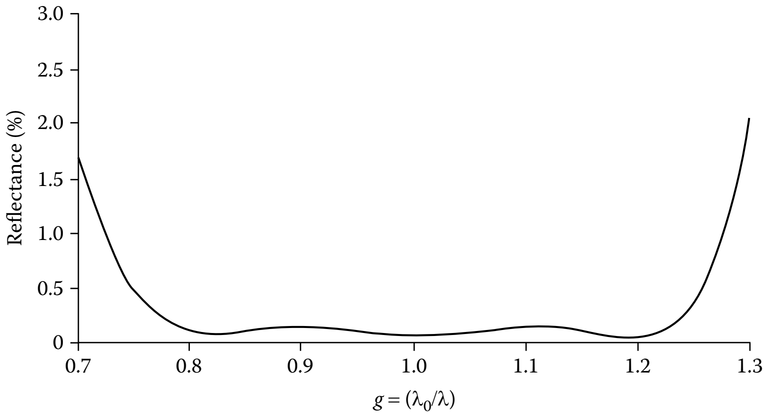

FIGURE 4.47
Refined version of the five-layer design of Figure 4.46 and Table 4.3. Design:

Air	1.38	2.30	1.38	2.30	1.38	Glass
1.0	$0.29735\lambda_0$	$0.1252\lambda_0$	$0.1244\lambda_0$	$0.0874\lambda_0$	$0.5597\lambda_0$	1.52

If performance over a much wider region is required, then the apparent dispersion of the equivalent periods may become a problem. This dispersion can be reduced by using equivalent periods of one-eighth-wave thickness instead of quarter-wave. Each quarter wave in the original design is then replaced by two periods in series. This adds considerably to the number of layers and the solution of the appropriate equations is no longer simple.

An interesting design approach involving equivalent layers has been devised by Schulz et al. [21]. We start with a substrate that has index higher than that of the incident medium. Then, provided we have the materials, we can construct very efficient antireflection coatings consisting of a series of quarter-waves of index gradually descending from that of the substrate to that of the incident medium. The earlier part of this chapter described several coatings of this general type. The most important aspect of the index variation is that it should be reasonably smooth and especially should not show a sudden reversal in its sense. There are, also, many systematic techniques for arriving at optimum values depending on the details of the desired performance. Further information on these can be found in Thelen [22]. Here we shall use a quite simple distribution based on the ideas in Section 4.1.3.

Let the quarter-wave indices be based on an equal amplitude reflection coefficient at all interfaces. Then

$$\frac{y_0}{y_1} = \frac{y_1}{y_2} = \frac{y_2}{y_3} = \cdots = \frac{y_q}{y_{sub}} = f \tag{4.29}$$

and

$$f = \sqrt[q+1]{\frac{y_0}{y_{sub}}} \tag{4.30}$$

allowing the calculation of the various necessary layer indices.

The performance of a six-layer coating designed in this way is shown in Figure 4.49 and Figure 4.50. The performance as a function of g is excellent except at those values of g where the individual layers have optical thicknesses of an integral number of half-waves.

Unfortunately, we cannot construct such a coating because we lack the necessary low-index materials. However, as shown in Figure 4.49, the performance repeats itself at every odd value of g. The region between value of

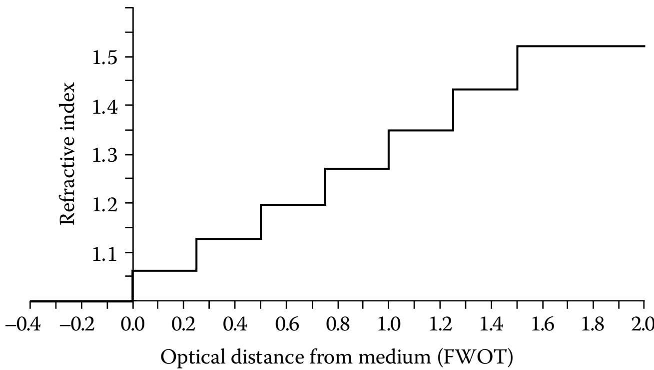

FIGURE 4.48
The index profile of a 6-layer stepped antireflection coating to match index of 1.52 (glass) to 1.00 (air).

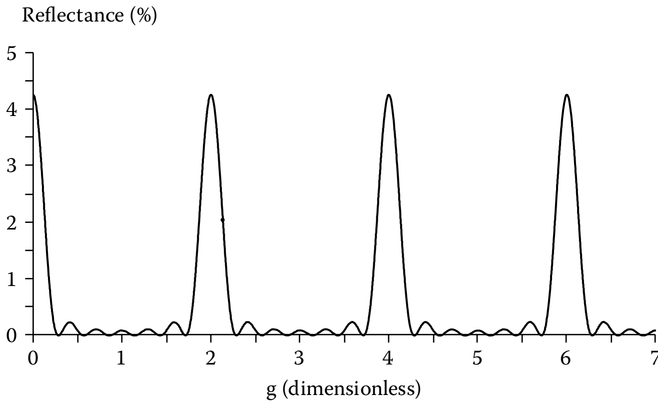

FIGURE 4.49
The performance of the six-layer stepped antireflection coating of Figure 4.48 as a function of g. The peaks of reflectance occur where the layers are an integral number of half-waves thick.

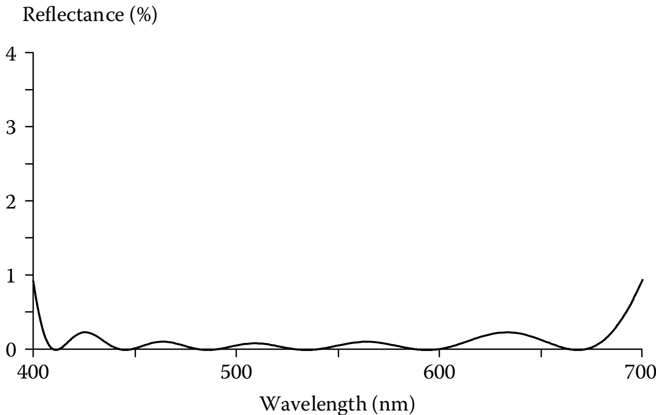

FIGURE 4.50
The antireflection region between *g* of 2 and 4 in Figure 4.49 just covers the visible region.

g of 2 and 4, where the layers are three quarterwaves thick is wide enough just to cover the visible region, Figure 4.50. Although we are unable to replace the low-index quarter-waves, we have no such difficulty where three quarter-wave layers are concerned. There are several possible solutions but a particularly useful one is where the bulk of the combination is of low index and there is a central, quite thin high-index layer.

Replacing the layers by a three-layer symmetrical arrangement and then gently refining the resulting design yields the profile shown in Figure 4.51 with performance in Figure 4.52.

Although this present design was based on symmetrical periods, the principle of thin high-index layers in a matrix of low index can be extended to systems that are not so based and with broader regions of low reflectance. The designs are normally fairly thick, 1.6-μm physical thickness in the case of the design of Figure 4.51, but this is of particular advantage in the case of antireflection coatings for plastic materials, because the coating itself can also play the role of what is called a *hard coat*. The material of normal antireflection coatings is brittle and tends to crack easily when point loads are applied because of the yielding nature of the underlying plastic. It is normal to strengthen the plastic surface by applying a hard coat, which is a layer of hard, less yielding material, often acrylic. The thick silicon dioxide material of the present coating is tough and hard and can support point loads much better than normal antireflection coatings, and so the hard coat can be omitted.

So far, most of our equivalents have been based on symmetrical structures. A different kind of equivalence has been proposed by Schallenberg et al. [23–25]. We can reduce the calculation of the reflectance of any arbitrary multilayer to the following matrix expression, where the individual characteristic matrices have been multiplied to give just one product matrix representing

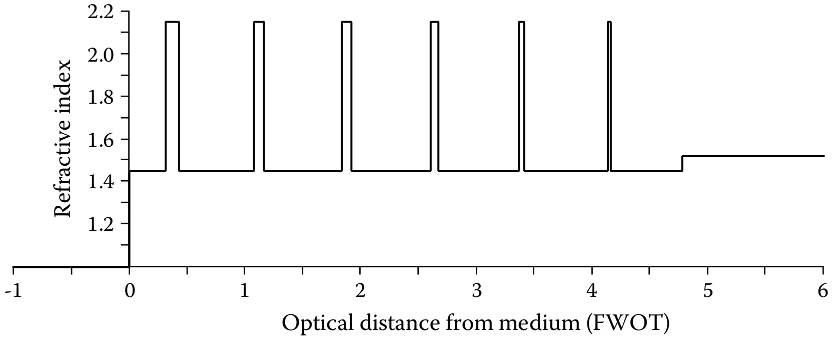

FIGURE 4.51
Replacement of the three quarter-wave layers by their three-layer equivalents followed by slight refinement gives this design with performance shown in Figure 4.52.

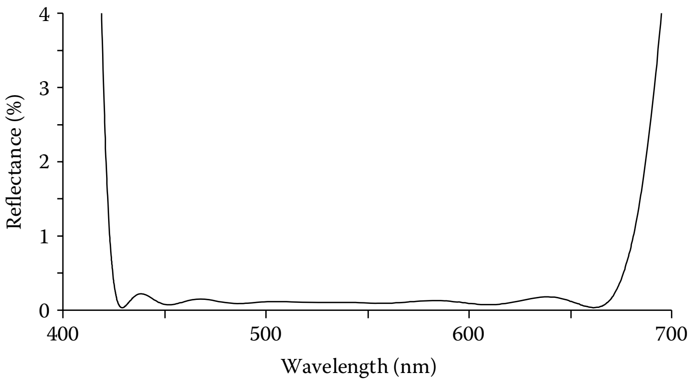

FIGURE 4.52
The performance of the design of Figure 4.51. The width of the coating can be increased at the expense of a slight increase in residual reflectance.

the entire multilayer. As long as the layers are perfect dielectrics then the quantities, *Mxy*, will all be real.

$$\begin{bmatrix} B \\ C \end{bmatrix} = \begin{bmatrix} M_{11} & iM_{12} \\ iM_{21} & M_{22} \end{bmatrix} \begin{bmatrix} 1 \\ y_{sub} \end{bmatrix} = \begin{bmatrix} M_{11} + iy_{sub}M_{12} \\ y_{sub}M_{22} + iM_{21} \end{bmatrix} \tag{4.31}$$

Then the reflectance is given by

$$R = \left| \frac{y_0 B - C}{y_0 B + C} \right|^2 = \frac{M_{11}^2 \left(y_0 - y_{sub} \dfrac{M_{22}}{M_{11}} \right)^2 + M_{12}^2 \left(y_0 y_{sub} - \dfrac{M_{21}}{M_{12}} \right)^2}{M_{11}^2 \left(y_0 + y_{sub} \dfrac{M_{22}}{M_{11}} \right)^2 + M_{12}^2 \left(y_0 y_{sub} + \dfrac{M_{21}}{M_{12}} \right)^2} \tag{4.32}$$

We can define two new quantities

$$E = \sqrt{\frac{M_{21}}{M_{12}}} \quad \text{and} \quad S = y_{sub}\frac{M_{22}}{M_{11}} \tag{4.33}$$

where E is known as the equivalent stack admittance and S as the equivalent substrate admittance. Substituting these values in Expression 1.32 gives:

$$R = \frac{M_{11}^2(y_0 - s)^2 + M_{12}^2(y_0 y_{sub} - E^2)^2}{M_{11}^2(y_0 + s)^2 + M_{12}^2(y_0 y_{sub} + E^2)^2} \tag{4.34}$$

Clearly, the reflectance will be zero if

$$s = y_0 \quad \text{and} \quad E = \sqrt{y_0 y_{sub}} \tag{4.35}$$

However, if the conditions in Expression 1.35 are not met, then, if the coating consists of a series of quarter-waves, M_{11} and M_{12} will oscillate such that each shows a maximum value while the other is zero. Then, the reflectance will vary between two extrema, RE and RS, given by

$$R_s = \frac{(y_0 - S)^2}{(y_0 + S)^2} \quad \text{and} \quad R_E = \frac{(y_0 y_{sub} - E^2)^2}{(y_0 y_{sub} + E^2)^2} \tag{4.36}$$

It is possible without too much difficulty to develop analytical solutions for coatings with a few layers, and some examples are given by Schallenberg et al. [23–25].

We digress for a moment to consider designs that consist of a descending series of quarter-waves, on the lines of the design of Figure 4.48. The series mimics an inhomogeneous layer (see later in this chapter), and a true inhomogeneous layer antireflects all wavelengths shorter than that for which the total thickness is one-half wavelength. Thus, if all the layers are quarter-waves at $g = 1$, then a system of q quarter-waves would exhibit a lower limit at roughly $g = 1/q$. In this case, though, the antireflection breaks down when the individual layers become half-waves, that is as we reach $g = 2$. Since the interference condition around $g = 2$ is identical to that around $g = 0$, the antireflection region will stretch from $g = 1/q$ to $g = 2 - 1/q$, that is a ratio of $2q - 1$. Clearly the greater q, the greater is the region of low reflectance. This rough value applies reasonably well to sequences of quarter-waves like that of Figure 4.48 but gives a rather too optimistic estimate when a class of antireflection coatings known as maximally flat is concerned. Maximally flat antireflection coatings also consist of a descending series of quarter-waves,

TABLE 4.4
Schallenberg's Arrangement for Maximally Flat Antireflection Coatings

1 Layer	2 Layers	3 Layers	4 Layers	5 Layers	6 Layers
					y_0
				y_0	
			y_0		$y_0^{63/64}y_{sub}^{1/64}$
		y_0		$y_0^{31/32}y_{sub}^{1/32}$	
	y_0		$y_0^{15/16}y_{sub}^{1/16}$		$y_0^{57/64}y_{sub}^{7/64}$
y_0		$y_0^{7/8}y_{sub}^{1/8}$		$y_0^{26/32}ysub^{6/32}$	
	$y_0^{3/4}y_{sub}^{1/4}$		$y_0^{11/16}y_{sub}^{5/16}$		$y_0^{42/64}y_{sub}^{22/64}$
$y_0^{1/2}y_{sub}^{1/2}$		$y_0^{4/8}ysub^{4/8}$		$y_0^{16/32}y_{sub}^{16/32}$	
	$y_0^{1/4}ysub^{3/4}$		$y_0^{5/16}y_{sub}^{11/16}$		$y_0^{22/64}y_{sub}^{42/64}$
y_{sub}		$y_0^{1/8}y_{sub}^{7/8}$		$y_0^{6/32}y_{sub}^{26/32}$	
	y_{sub}		$y_0^{1/16}y_{sub}^{15/16}$		$y_0^{7/64}y_{sub}^{57/64}$
		y_{sub}		$y_0^{1/32}y_{sub}^{31/32}$	
			y_{sub}		$y_0^{1/64}y_{sub}^{63/64}$
				y_{sub}	

but the particular sequence is chosen not to exhibit ripple in the antireflected region. Although they have wide bands of low reflectance, the removal of the ripple implies somewhat smaller bandwidths than those given earlier in this paragraph.

Schallenberg [25] noted that the maximally flat designs also obey the expressions in Equation 4.36 and in particular the equivalent stack admittance must be $(y_0 y_{\text{sub}})^{½}$. The expression for R_E in Equation 4.36 is just the quarter-wave rule. Adding a quarter-wave to the substrate transforms the admittance to E^2/y_{sub}. This new admittance can be antireflected in the normal way using another quarter-wave with admittance given by the square root of $y_0 \times E^2/y_{\text{sub}}$. We can apply this in a quite regular way to a series of quarter-waves. A single quarter-wave will bridge from y_{sub} to y_0 and so must have an admittance of $y_1 = (y_0 y_{\text{sub}})^{½}$. A two-quarter-wave design can bridge with the first quarter-wave from *ysub* to y_1 and then with the second quarter-wave from y_1 to y_0. The admittances of the two quarter-waves will be $y_{sub}^{¾}y_0^{¼}$ and $y_{sub}^{¼}y_0^{¾}$. For a three-layer coating, we bridge the gap from y_{sub} to $y_{sub}^{¾}y_0^{¼}$, from $y_{sub}^{¾}y_0^{¼}$ to $y_{sub}^{¼}y_0^{¾}$, and from $y_{sub}^{¼}y_0^{¾}$ to y_0. This gives layers of admittance $y_{\text{sub}}^{7/8}y_0^{1/8}$, $y_{\text{sub}}^{4/8}y_0^{4/8}$, and $y_{\text{sub}}^{1/8}y_0^{7/8}$. Schallenberg's arrangement is shown in Table 4.4 and can be very easily extended to greater numbers of layers. It avoids the complicated calculations that are usually required for these coatings.

The required indices for a six-layer coating of this type on germanium assuming an index of 4.00 and air as the incident medium, are given in Table 4.5. Because of the unobtainable indices, the design, as it stands, could not be constructed but it will serve to illustrate the method and it could be used as the basis for a replacement technique, such as has just been described. The calculated performance with a reference wavelength of 3 µm is shown in Figure 4.53 and the corresponding admittance locus in Figure 4.54.

4.4 Antireflection Coatings for Two Zeros

There are occasional applications where antireflection coatings are required which have zeros at certain well-defined wavelengths rather than over a wide spectral region. One of the most frequent of these applications is frequency doubling, where antireflection is required at two wavelengths, one of which is twice the other.

The simplest coating that will satisfy this requirement is the quarter-quarter that has already been considered. We recall that the coating has two zeros at $\lambda = 3\lambda_0/4$ and $\lambda = 3\lambda_0/2$, just what is required. The conditions are

$$\begin{aligned} n_1 &= (n_0^2 n_m)^{1/2} \\ n_2 &= (n_0 n_m^2)^{1/2} \end{aligned} \tag{4.37}$$

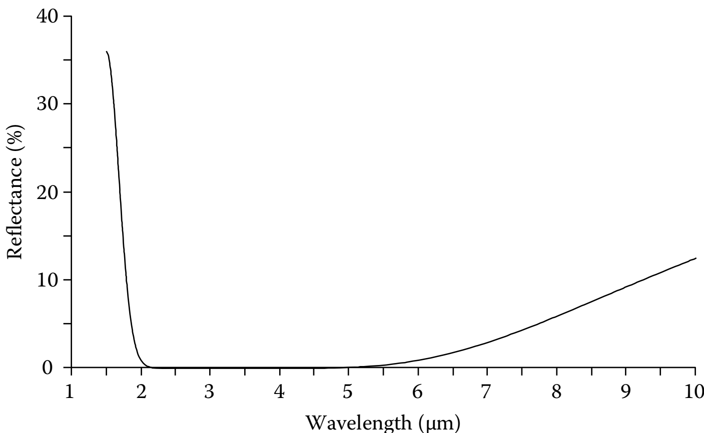

FIGURE 4.53
The performance of the coating of Table 4.5 assuming a reference wavelength of 3 µm. Unfortunately, the coating as it stands requires unrealistic material indices, and so could not be constructed directly.

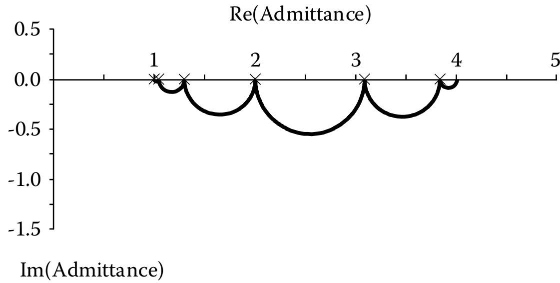

FIGURE 4.54
The admittance diagram of the maximally flat coating of Figure 4.53 at the reference wavelength.

The principal problem with this coating is once again the low-index substrate. With an index of 1.38 as the lowest value for n, the lowest value of substrate index that can be accommodated, from Equation 4.1, is $1.38^3 = 2.63$. Thus, the coating is suitable only for high-index substrates.

A common material that requires antireflection coatings at λ and 2λ is lithium niobate, which has an index of around 2.25. The quarter-quarter coating should have indices of 1.310 and 1.717. Indices of 1.38 and 1.717 give a reflection loss of 0.2%, which will probably be adequate for many applications, and indeed similar performance is obtained with any index between 1.7 and 1.8 for the high-index layer.

Should this performance be inadequate, then an additional layer can be added. Provided we keep to quarter-waves and multiples of quarter-waves, we retain the symmetry about $g = 1$ and therefore have to consider the performance at $g = 2/3$ only since that at $g = 3/4$ will be automatically equivalent. From the point of view of the vector diagram, the problem with the quarter-quarter coating is ρ_a, the amplitude reflection coefficient from the first interface, which is too large. The vectors are inclined at 120° to each other, and for zero reflectance, they should be of equal length so that they form an equilateral triangle. If an extra quarter-wave n_3 is added, there will

TABLE 4.5
The Design of Figures 4.53 and 4.54

Layer Number	Refractive Index
Incident	1.00
1	1.0219
2	1.1637
3	1.6105
4	2.4837
5	3.4372
6	3.9143
Substrate	4.00

be four vectors and the fourth, ρ_d, will be along the same direction as ρ_a. If ρ_d is made to be of opposite sense to ρ_a, that is, if $n_3 > n_m$, then it is possible to reduce the resultant of the two vectors to the same length as the other two. This can be achieved by the design

Air	1.38	1.808	2.368	Lithium niobate
1.0	$0.25\lambda_0$	$0.25\lambda_0$	$0.25\lambda_0$	2.25

We can take 2.35, the index of zinc sulfide, for n_3, and then any index in the range 1.75–1.85 for n_2, to keep the minimum reflectance at $g = 2/3$ to below 0.1%.

There are many other possible arrangements. A coating with the first layer a half-wave, instead of a quarter-wave, can give a similar improvement, this time through a combination with ρ_c, which means that $n_2 > n_3$. Here the ideal design is

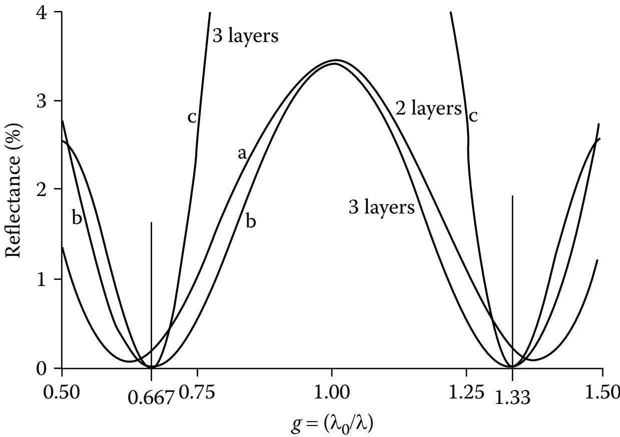

FIGURE 4.55
The performance of various two-zero 2:1 antireflection coatings on a high-index substrate such as lithium niobate with $n = 2.25$. The ideal positions for the two zeros are $g = 0.667$ and $g = 1.333$.

Air	1.38	1.72	Lithium niobate
1.0	$0.25\lambda_0$	$0.25\lambda_0$	2.25

Air	1.38	1.808	2.368	Lithium niobate
1.0	$0.25\lambda_0$	$0.25\lambda_0$	$0.25\lambda_0$	2.25

Air	1.38	1.81	1.72	Lithium niobate
1.0	$0.5\lambda_0$	$0.25\lambda_0$	$0.25\lambda_0$	2.25

Air	1.38	1.81	1.72	Lithium niobate
1.0	$0.5\lambda_0$	$0.25\lambda_0$	$0.25\lambda_0$	2.25

and again, there is reasonable flexibility in the values of n_2 and n_3 if the aim is simply a reflectance of less than 0.1%. It is interesting to note the similarity between this coating and the quarter-quarter. The quarter-quarter has another zero at $g = 8/3$. If the inner quarter-waves in the above design were merged into a single half-wave of index around 1.75, then the coating would be identical with the quarter-quarter used at $g = 4/3$ and $g = 8/3$. Figure 4.55 shows the performance of these coatings.

This idea of using the fourth vector to trim the length of one of the other three so that a low reflectance is obtained can be extended to low-index substrates. The coating now, of course, departs considerably from the original quarter-quarter coating. A quarter-quarter-quarter design based on this approach is

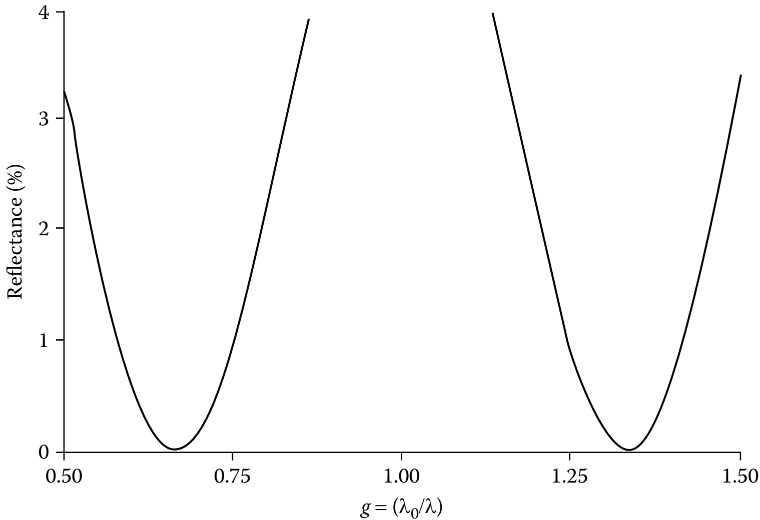

FIGURE 4.56
A three-layer two-zero 2:1 antireflection coating for a low-index substrate. Design ($\lambda_0 = 707$ nm):

Air	1.38	1.585	1.82	Glass
1.0	$0.25\lambda_0$	$0.25\lambda_0$	$0.25\lambda_0$	1.52

The method can be extended to four and even more quarter-waves, although the derivation of the final designs is very much more of a trial-and-error process because of the rather cumbersome expressions that cannot be reduced to explicit formulae for the various indices. Indeed, there are now too many parameters for there to be just one solution and the surplus can be used in an optimizing process for broadening the reflectance minima. A number of interesting designs is given by Baumeister et al. [26].

Air	1.38	1.808	2.368	Glass
1.0	$0.25\lambda_0$	$0.25\lambda_0$	$0.25\lambda_0$	2.25

and its performance is shown in Figure 4.56 where the monitoring wavelength has been assumed to be 707 nm and the two zeros are situated at 530 nm and 1.06 μm.

Mouchart [27], too, has considered the derivation of antireflection coatings intended to eliminate reflection at two wavelengths. In coatings where all layers have thicknesses that are specified in advance to be multiples of a quarter-wave at $g = 1$, it is possible arbitrarily to choose the indices of all the layers except the final two, which can then be calculated from the values given to the others. The calculation involves the solution of an eighth-order equation that can be set up using expressions derived by Mouchart. The values of $\partial^2 R/\partial\lambda^2$ at the antireflection wavelength, which is inversely related to the bandwidth of the coating, can be used to assist in choosing the more promising designs from the enormous number that can be produced. Mouchart considers three-layer coatings of this type in some detail.

4.5 Antireflection Coatings for the Visible and the Infrared

There are frequent requirements for coatings that span the visible region and also reduce the reflectance at an infrared wavelength corresponding to a laser line. Such coatings are required in instruments where visual information and laser light share common elements, such as surgical instruments, surveying devices, and the like. There are very many designs for such coatings and manufacturers seldom publish them. Design is largely a process of trial and error, and frequently the final operation is to replace the unobtainable or difficult indices by symmetrical combinations of better behaved materials and to refine the design so obtained to take account of the dispersion of the optical constants of real materials and to compensate for the apparent dispersion that occurs in connection with the symmetrical periods. In this section, we consider the fundamental design process only, neglecting dispersion and in most cases retaining the ideal values of index. We assume that the substrate is always glass of index 1.52 and that, as usual, the incident medium is air of index 1.0.

The simplest type of coating that has low reflectance in the visible region and at a wavelength in the near infrared is a single layer of low-index material of thickness three quarter-waves. This has low reflectance at both λ_0 and $3\lambda_0$. Unfortunately, the lowest index, of 1.38, corresponding to magnesium fluoride, gives a residual reflectance of 1.25% at the minima and the performance in the visible region is rather narrower than that for the single

quarter-wave coating since the layer is three times thicker. The magnesium fluoride layer could be considered as an outer quarter-wave over an inner half-wave and a high-index half-wave flattening layer, of index 1.8, could be introduced between them giving the design

$$\text{Air} \mid LHHLL \mid \text{Glass}$$

Unfortunately, the half-wave layer, while it flattens the performance in the visible region, destroys the performance in the infrared at $3\lambda_0$, where it is two thirds of a quarter-wave thick. The solution is to make the layer three half-waves thick in the visible, so that it is still a half-wave, and therefore an absentee, at $3\lambda_0$. The design then becomes

$$\text{Air} \mid L6H2L \mid \text{Glass}$$

and the performance is shown in Figure 4.57, where the reference wavelength is 510 nm. The performance in the visible region is indeed flattened in the normal way, although, because the flattening layer is three times thicker than normal, the characteristic rises sharply in the blue and red regions. The minimum in the infrared around 1.53 μm is still present, although slightly skewed because of the half-wave layer. However, perhaps the most surprising feature is the appearance of a third and very deep minimum at 840 nm. We use the admittance diagram to help in understanding the origin of this dip.

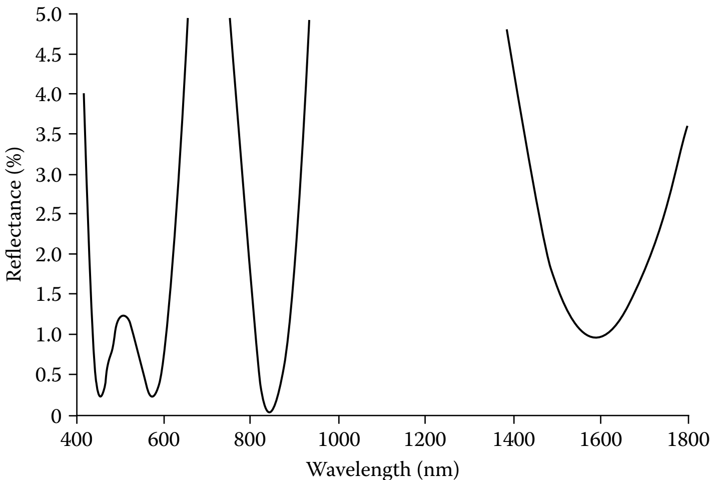

FIGURE 4.57
The performance of the coating: Air (1.0) | $L\,6H\,2L$ | Glass (1.52) with L a quarter-wave of index 1.38 and H of 1.8. λ_0 is 510 nm.

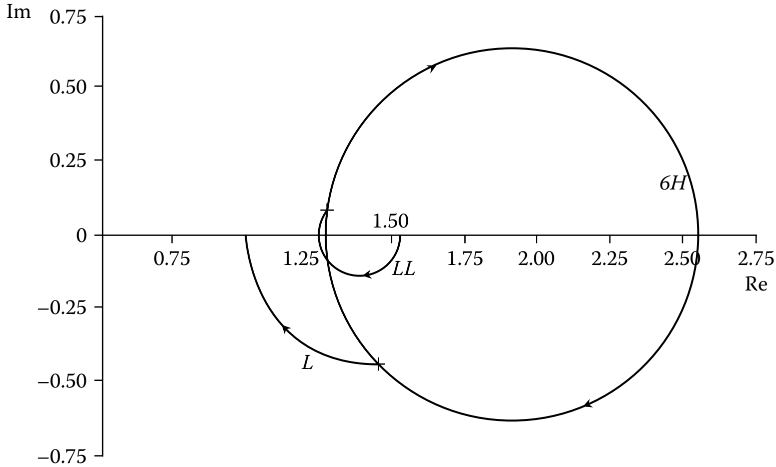

FIGURE 4.58
The admittance diagram for the coating of Figure 4.57 at 840 nm, corresponding to the unexpected sharp zero, explains the occurrence of the dip.

Figure 4.58 shows the admittance diagram for the coating at the wavelength 840 nm. Layer 2, the 1.8 index layer, is almost two half-waves thick at this wavelength and so describes almost two complete revolutions, linking the ends of the loci of the two 1.38 index layers in such a way that almost zero reflectance is obtained. The loci of the two low-index layers are not very sensitive to changes in wavelength, and therefore the position of the dip is fixed almost entirely by the high-index layer. Changes in its thickness will change the position of the dip. Making it thinner, 1.0 full waves instead of 1.5, for example, will move the dip to a longer wavelength. The performance characteristic of a coating of design

$$\text{Air} \mid L4H2L \mid \text{Glass}$$

is shown in Figure 4.59. The dip is now fairly near the desired wavelength of 1.06 μm.

A coating that gives good performance over the visible region but has high reflectance at 1.06 μm is the quarter-half-quarter coating. The admittance diagram at λ_0 for such a coating is shown in Figure 4.33. The locus intersects or crosses the real axis at the points 1.9 and 2.45. It is possible to insert layers of index 1.9 or 2.45, respectively, at these points in the design without any effect on the performance at λ_0. The loci of these layers, whatever their thicknesses, would simply be points. Such layers are known as "buffer layers" and were devised by Mouchart [28]. At the reference wavelength, they exert no influence whatsoever, but at other wavelengths, where the starting points of their loci move away from their reference wavelength positions, the loci appear in the normal way and can have important effects on performance.

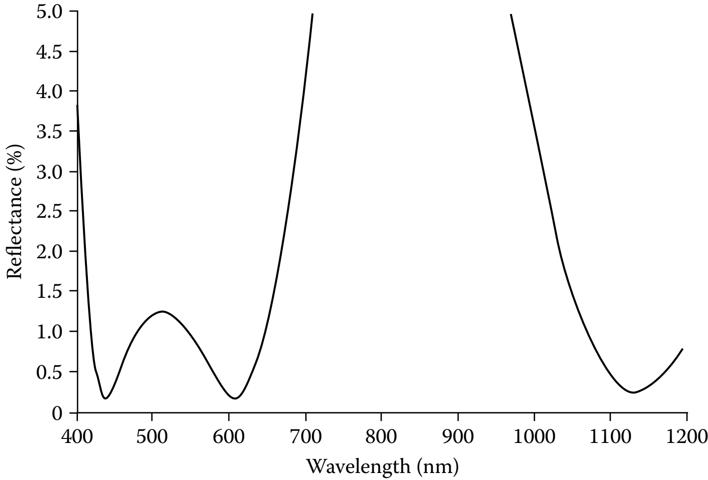

FIGURE 4.59
The performance of the coating: Air (1.0) | *L* 4*H* 2*L* | Glass (1.52) with *L* a quarter-wave of index 1.38, *H* of 1.8, and reference wavelength, λ_0, 510 nm. Note that the dip has moved to a longer wavelength than in Figure 4.57.

They are similar in some respects to half-wave layers, that by virtue of their precise thickness are absentees at λ_0 but that have considerable influence on other wavelengths. The index can be chosen to sharpen or flatten a characteristic. The buffer layer has a precise value of index but can have any thickness, which can be chosen to adjust performance at wavelengths other than λ_0. Here we attempt to use buffer layers to alter the performance at 1.06 μm. One buffer layer is not sufficient and we need to insert the two possible 1.9 index layers so that the design becomes:

$$\text{Air} \mid LB'HHB''N \mid \text{Glass}$$

where $y_L = 1.38$, $y_H = 2.15$, and $y_N = 1.70$. B' and B'' are buffer layers of admittance 1.9. Trial and error establishes thicknesses for B' of $0.342\lambda_0$, and for B'' of $0.084\lambda_0$. However, although the reflectance at 1.06 μm is reduced considerably, the buffer layers do distort the performance characteristic somewhat in the visible region (Figure 4.60), and only by refining the design is a completely satisfactory performance obtained. The final design, also illustrated in Figure 4.60, is:

Air	1.38	1.90	2.15	1.90	1.70	Glass
1.00	$0.2667\lambda_0$	$0.3085\lambda_0$	$0.5395\lambda_0$	$0.1316\lambda_0$	$0.1796\lambda_0$	

Many of the designs currently used for the visible and 1.06 μm involve just two materials of high and low index. Designs of this type can be arrived at

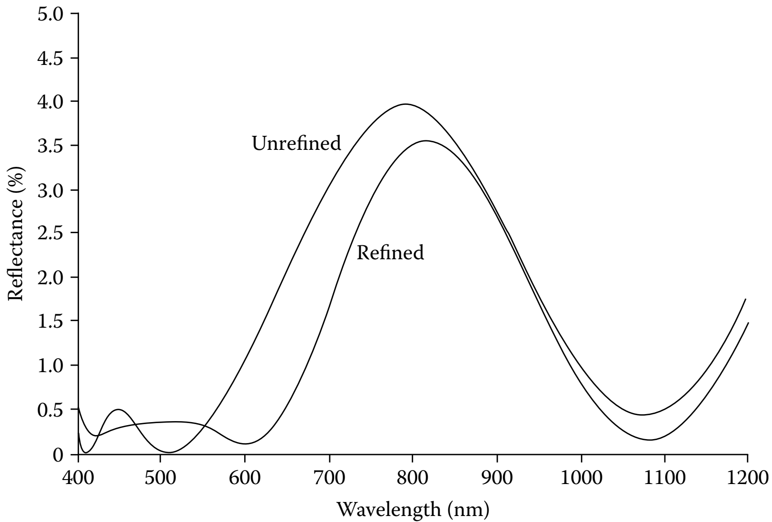

FIGURE 4.60
The performance of the design: Air (1.0) | *LB′HHB″M* | Glass (1.52) with *L*, *H*, and *M* quarter-waves of indices 1.38, 2.15, and 1.70, respectively. *B′* and *B″* are buffer layers of index 1.9 (see text) and thicknesses $0.342\lambda_0$ and $0.084\lambda_0$, respectively. λ_0 is 510 nm. The design has also been refined to yield the second performance curve. The refined design is given in the text.

in a number of ways. The arrangements above that use ideal layers can be replaced by symmetrical periods in the way already discussed. This type of design is seldom immediately acceptable because the very wide wavelength range makes it difficult exactly to match the layers with symmetrical periods and they are therefore usually refined by computer.

Figure 4.61 shows the performance of a six-layer design arrived at by computer synthesis:

Air	1.38	2.25	1.38	2.25	1.38	2.25	Glass
1.00	$0.3003\lambda_0$	$0.1281\lambda_0$	$0.0657\lambda_0$	$0.6789\lambda_0$	$0.0718\lambda_0$	$0.0840\lambda_0$	

Buffer layers are very useful in such coatings. Half-wave absentee layers correct performance rapidly as the wavelength moves from that for which they are half-waves. Buffer layers react more slowly and therefore are very helpful when reflectance must remain low over a wide spectral region. The difficulty with buffer layers is that their refractive index is fixed by the axis crossings of the admittance locus of the coating in which they are to be inserted. We normally have a limited set of indices corresponding to the particular materials we are using and to use such layers as buffers, we must engineer an axis crossing at the appropriate value of admittance. The double Vermeulen structure makes this possible. In Figure 4.44, the axis crossing on the extreme

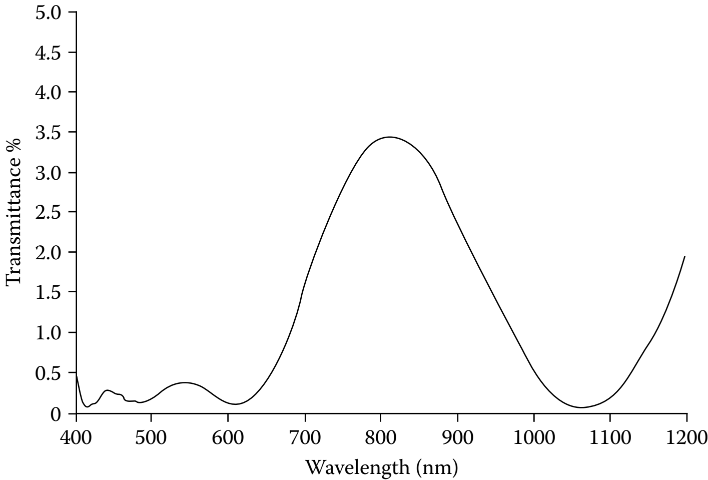

FIGURE 4.61
The performance of a six-layer design of antireflection coating for the visible region and 1.06 μm, arrived at purely by computer synthesis. The reference wavelength is 510 nm and the design is given in the text.

right can be moved simply by adjusting the thicknesses of the layers making up the structure. It is straightforward to arrange that the axis crossing should actually coincide with the index of the high-index layer already used in the design. This has been achieved with the first of the designs in Table 4.6. Note that the thicknesses are optical so that they can be directly compared with those in Table 4.2.

Figure 4.62 shows the admittance locus of the adjusted coating. The axis crossing has been arranged and the final three layers of the design have been adjusted to give good performance over the visible region. The performance

TABLE 4.6

Introduction of Buffer Layers

		Starting Design	With Buffer	With Buffer and Absentee
Material	**Index**	**Optical Thickness (nm)**	**Optical Thickness (nm)**	**Optical Thickness (nm)**
Air	1.00	Massive	Massive	Massive
MgF_2	1.37	154.47	154.47	140.80
TiO_2	2.28	57.96	57.96	50.70
MgF_2	1.37	22.66	22.66	17.46
TiO_2	2.28	…	247.50	240.84
MgF_2	1.37	35.06	35.06	44.31
TiO_2	2.28	49.23	49.23	39.99
MgF_2	1.37	…	…	294.54
Glass	1.52	Massive	Massive	Massive

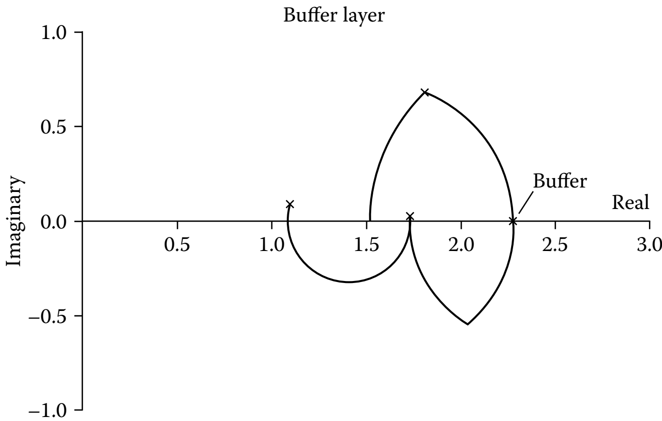

FIGURE 4.62
The admittance locus of the adjusted coating showing the axis crossing at 2.28. A buffer layer has been inserted there.

of the coating is shown in Figure 4.63. The design is given in the first design column of Table 4.6. Then, the buffer layer of TiO_2 is added, and the appearance of the admittance locus does not change with buffer layer thickness. Adjustment of the buffer layer by trial and error gives the improvement shown in Figure 4.63.

Addition of a half-wave layer of low index between the coating and the glass substrate followed by refinement of all layers yields the performance shown in Figure 4.64. This is as good a performance as we are likely to get with seven layers of the given indices. Significant improvement in performance demands more layers.

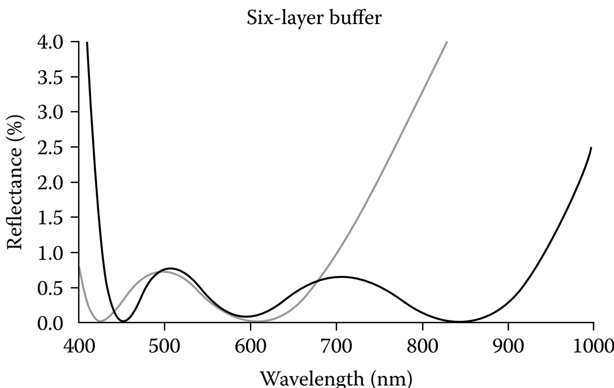

FIGURE 4.63
The starting four-layer coating performance is shown in gray. The addition of the buffer layer makes the coating into a six-layer system. Adjustment of the buffer layer thickness until just less than a half wave gives the performance shown by the black line. The designs are given in Table 4.6.

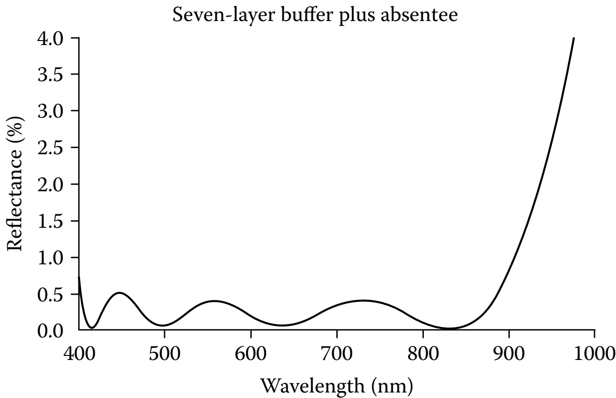

FIGURE 4.64
Performance of the seven-layer coating containing in Table 4.6.

The major determinant of antireflection-coating performance for low-index substrates is the lowest index of refraction of the design materials. Magnesium fluoride is the usual choice but, unfortunately, it is not ideal. It suffers from high tensile stress and for reasonable durability must be deposited on a heated substrate. Silicon dioxide is much tougher and more stable and would be preferred over magnesium fluoride were it not for the fact that the refractive index is rather higher at around 1.45 compared with magnesium fluoride's 1.38. In multilayer coatings, therefore, it is quite common practice to use silicon dioxide as the low-index material through the coating but to continue to use magnesium fluoride as the outermost layer. The layer next to the air is critical. The layers distributed within the coating are less so.

4.6 Inhomogeneous Layers

Inhomogeneous layers are ones in which the refractive index varies through the thickness of the layer. As we shall see in Chapter 11, many of the thin-film materials that are commonly used give films that are inhomogeneous. This inhomogeneity is often quite small and the layers can safely be treated as if they were homogeneous in all but the most precise and exacting coatings. There are, however, a number of films that show sufficient inhomogeneity to affect the performance of an antireflection coating perceptibly. If such a layer is used instead of a homogeneous one in a well-corrected antireflection coating then a reduction in performance is the normal result. Provided the inhomogeneity is not large, an adjustment of the indices of the other layers is usually sufficient correction and, as Ogura [29] has pointed out, an index that decreases slightly with thickness associated with the high-index layer

in the quarter-half-quarter coating can actually broaden the characteristic. Zirconium oxide is a much-used material that exhibits an index increasing with film thickness when deposited at room temperature, but decreasing with thickness when deposited at substrate temperatures above 200° C. Vermeulen [30] has considered the effect of the inhomogeneity of zirconium oxide on the quarter-half-quarter coating and has shown how it is possible to correct for the inhomogeneity by varying the index of the intermediate-index layer, which for virtually complete compensation should be of the two-layer composite type [15] already referred to in this chapter. This type of inhomogeneity is one that is intrinsic and relatively small. By arranging for the evaporation of mixtures of composition varying with film thickness, it is possible to produce layers that show an enormous degree of inhomogeneity and that permit the construction of entirely new types of antireflection coating.

Accurate calculation techniques for such layers are reviewed by Jacobsson [31] and Knittl [32]. The simplest method involves the splitting of the inhomogeneous layer into a very large number of thin sublayers. Each sublayer is then replaced by a homogeneous layer of the same thickness and mean refractive index so that the smoothly varying index of the inhomogeneous layer is represented by a series of small steps. Computation can then be carried out as for a multilayer of homogeneous layers. There is no difficulty with modern computers in accommodating very large numbers of sublayers so that, although an approximation, the method can be made to yield results identical for all practical purposes with those that would have been obtained by exact calculation (in cases where exact calculation techniques exist).

For our purposes, we can approach the theory of such coatings from the starting point of the multilayer antireflection coating for high-index substrates. As more and more layers are added to the coating, the performance, both the bandwidth and the maximum reflectance in the low-reflectance region, steadily improves. In the limit, there will be an infinite number of layers with infinitesimal steps in optical admittance from one layer to the next. If, as layers are added, the total optical thickness of the multilayer is kept constant, the thickness of the individual layers will tend to zero and the multilayers will become indistinguishable from a single layer of identical optical thickness, but with optical admittance varying smoothly from that of the substrate to that of the incident medium.

If there are n layers in the multilayer, then the total optical thickness of the coating will be $n\lambda_0/4$, which may be denoted by T. There will be n zeros of reflectance extending from a shortwave limit

$$\lambda_S = \frac{(n+1)}{n}\cdot\frac{\lambda_0}{2}$$

to a longwave limit

$$\lambda_L = (n+1)\cdot\frac{\lambda_0}{2}$$

In terms of T, the total optical thickness, these limits are

$$\lambda_S = \frac{2(n+1)}{n^2} \cdot T$$

$$\lambda_L = \frac{2(n+1)}{n} \cdot T$$

At wavelengths of $2\lambda_L$ or longer, the arrows in the vector diagram are confined to the third and fourth quadrants so that the antireflection coating is no longer effective.

If now n tends to infinity but T remains finite, the multilayer tends to a single inhomogeneous layer, λ_S tends to zero, and λ_L tends to $2T$. For all wavelengths between these limits, the reflectance of the assembly is zero. Thus, the inhomogeneous film with smoothly varying refractive index is a perfect antireflection coating for all wavelengths shorter than twice the optical thickness of the film. At wavelengths longer than this limit the performance falls off, and at the wavelength given by four times the optical thickness of the film, the coating is no longer effective.

Of course, in practice there is no useful thin-film material with refractive index as low as unity and any inhomogeneous thin film must terminate with an index of around 1.35, say, which, in the infrared, is the index of magnesium fluoride. The reflectance of such a coated component will be equal to that of a plate of magnesium fluoride, 2.2% per surface.

Jacobsson and Martensson [33] have produced an inhomogeneous antireflection coating of this type on a germanium plate. The films were manufactured by the simultaneous evaporation of germanium and magnesium fluoride, the relative proportions of which were varied throughout the deposition to give a smooth transition between the indices of the two materials. An example of the performance attained is shown in Figure 4.65. For this particular coating, the physical thickness is quoted as 1.2 μm. To find the optical thickness, we assume that the variation of refractive index with physical thickness is linear (mainly because any other assumed law of variation would lead to very difficult calculations, although possibly more accurate results). The optical thickness is then given by the physical thickness times the mean of the two terminal indices. For this present film, starting with an index of 4.0 and finishing with 1.35, the mean is 2.68 and the optical thickness, therefore, 2.68 × 1.2 μm, i.e., 3.2 μm. This implies that the coating should give excellent antireflection for wavelengths out to 6.4 μm, after which it should show a gradually reducing transmission until a wavelength of 4 × 3.2 μm, i.e., 12.8 μm. The curve of the coated component in Figure 4.65 shows that this is indeed the case.

Berning [34] has suggested the use of the Herpin index concept for the design of antireflection coatings that are composed of homogeneous layers

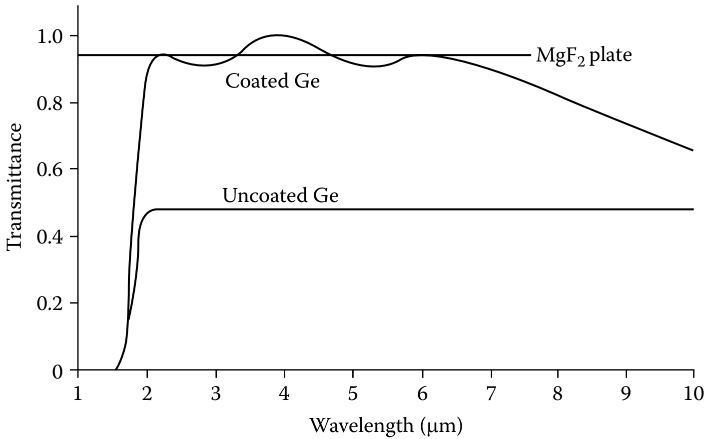

FIGURE 4.65
Measured transmittance of a germanium plate, coated on both sides with an inhomogeneous Ge-MgF_2 film with geometrical thickness 1.2 μm. (After Jacobsson, R. and Martensson, J.O., *Applied Optics*, 5, 29–34, 1966.)

of two materials, one of high index and the other of low index, which are step approximations to the inhomogeneous layer and which, because they involve homogeneous layers of well-understood and stable materials, might be easier to manufacture than the ideal inhomogeneous layers. He has suggested designs for the antireflection coating of germanium consisting of up to 39 alternate layers of germanium and magnesium fluoride equivalent to 20 quarter-waves of gradually decreasing index.

As with coatings consisting of homogeneous layers, the most serious limitation is the lack of low-index materials. A single inhomogeneous layer to match a substrate to air must terminate at an index of around 1.38, which means that the best that can be done with such a layer is a residual reflectance of 2.5%. This limits their direct use to high-index substrates. For low-index substrates, it is likely that their role will remain the improving of the performance of designs incorporating homogeneous materials.

4.7 Further Information

It has not been possible in a single chapter in this book to cover completely the field of antireflection coatings. Further information will be found in Cox and Hass [17] and Musset and Thelen [6]. There is also a very useful account of antireflection coatings in Knittl [32], which contains some alternative techniques.

References

1. Cox J T and Hass G 1958 Antireflection coatings for germanium and silicon in the infrared *Journal of the Optical Society of America* **48** 677–680
2. Catalan L A 1962 Some computed optical properties of antireflection coatings *Journal of the Optical Society of America* **52** 437–440
3. Schuster K 1949 Anwendung der Vierpoltheorie auf die Probleme der optischen Reflexionsminderung, Reflexionsverstarkung, und der interferenzfilter *Annalen der Physik, 6th Series* **4** 352–356
4. Cox J T 1961 Special type of double-layer antireflection coefficient for infrared optical materials with high refractive index *Journal of the Optical Society of America* **51** 1406–1408
5. Cox J T, Hass G, and Jacobus G F 1961 Infrared filters of antireflected Si, Ge, InAs and InSb *Journal of the Optical Society of America* **51** 714–718
6. Musset A and Thelen A 1966 *Multilayer antireflection coatings*, in *Progress in Optics* Wolf E Editor (Amsterdam: North Holland) 201–237
7. Thelen A 1969 *Design of multilayer interference filters*, in *Physics of Thin Films* Hass G and Thun R E Editors (New York/London: Academic Press) 47–86
8. Young L 1961 Synthesis of multiple antireflection films over a prescribed frequency band *Journal of the Optical Society of America* **51** 967–974
9. Turbadar T 1964 Equireflectance contours of double layer antireflection coatings *Optica Acta* **11** 159–170
10. Thetford A 1969 A method of designing three-layer anti-reflection coatings *Optica Acta* **16** 37–44
11. Thetford A 1968 *Four-layer coating design* University of Reading, UK Private Communication
12. Luther B, Lockhart J, and King P 1947 Three-layered reflection-reducing coatings *Journal of the Optical Society of America* **37** 689–694
13. Cox J T, Hass G, and Thelen A 1962 Triple-layer antireflection coating on glass for the visible and near infrared *Journal of the Optical Society of America* **52** 965–969
14. Turbadar T 1964 Equireflectance contours of triple-layer antireflection coatings *Optica Acta* **11** 195–205
15. Vermeulen A J 1971 Some phenomena connected with the optical monitoring of thin-film deposition and their application to optical coatings *Optica Acta* **18** 531–538
16. Shadbolt M J 1967 *Measured results of four-layer antireflection coating deposition* Sira Institute, Chislehurst, Kent, UK Private Communication
17. Cox J T and Hass G 1964 *Antireflection coatings*, in *Physics of Thin Films* Hass G and Thun R E Editors (New York and London: Academic Press) 239–304
18. Ward J 1972 Towards invisible glass *Vacuum* **22** 369–375
19. C Reichert Optische Werke AG 1962 *Improvements in or relating to optical components having reflection-reducing coatings* UK Patent 991,635
20. Epstein L I 1952 The design of optical filters *Journal of the Optical Society of America* **42** 806–810
21. Schulz U, Schallenberg U B, and Kaiser N 2003 Symmetrical periods in antireflective coatings for plastic optics *Applied Optics* **42** 1346–1351

22. Thelen A 1988 *Design of Optical Interference Coatings* (New York: McGraw-Hill Book Company)
23. Schallenberg U B, Schulz U, and Kaiser N 2004 Multicycle AR coatings: a theoretical approach *Proceedings of the Society of Photo-Optical Instrumentation Engineers* **5250** 357–366
24. Schallenberg U B 2006 Antireflection design concepts with equivalent layers *Appl Opt* **45** 1507–1514
25. Schallenberg U 2008 Design principles for broadband AR coatings *Proceedings of the Society of Photo-Optical Instrumentation Engineers* **7101** 710103-1–710103-8
26. Baumeister P W, Moore R, and Walsh K 1977 Application of linear programming to antireflection coating design *Journal of the Optical Society of America* **67** 1039–1045
27. Mouchart J 1978 Thin film optical coatings. 6: Design method for two given wavelength antireflection coatings *Applied Optics* **17** 1458–1465
28. Mouchart J 1978 Thin film optical coatings. 5: Buffer layer theory *Applied Optics* **17** 72–75
29. Ogura S 1975 *Some features of the behaviour of optical thin films* PhD Thesis Newcastle upon Tyne Polytechnic
30. Vermeulen A J 1976 Influence of inhomogeneous refractive indices in multilayer anti-reflection coatings *Optica Acta* **23** 71–79
31. Jacobsson R 1975 Inhomogeneous and coevaporated homogeneous films for optical applications *Physics of Thin Films* **8** 51–98
32. Knittl Z 1976 *Optics of Thin Films* (London: John Wiley and Sons)
33. Jacobsson R and Martensson J O 1966 Evaporated inhomogeneous thin films *Applied Optics* **5** 29–34
34. Berning P H 1962 Use of equivalent films in the design of infrared multilayer antireflection coatings *Journal of the Optical Society of America* **52** 431–436

5

Neutral Mirrors and Beam Splitters

5.1 High-Reflectance Mirror Coatings

Almost as important as the transmitting optical components of the previous chapter are those whose function is to reflect a major portion of the incident light. In the vast majority of cases, the sole requirement is that the specular reflectance should be as high as conveniently possible, although, as we shall see, there are specialized applications where not only should the reflectance be high, but also the absorption should be extremely low. For mirrors in optical instruments, simple metallic layers usually give adequate performance and these will be examined first. For some applications where the reflectance must be higher than can be achieved with simple metallic layers, their reflectance can be boosted by the addition of extra dielectric layers. Multilayer all-dielectric reflectors, which combine maximum reflectance with minimum absorption, and which transmit the energy that they do not reflect, are reserved for the next chapter.

5.1.1 Metallic Layers

The performance of the commonest metals used as reflecting coatings is shown [1] in Figure 5.1.

Silver was once the most popular material. Until the middle 1930s, it was the principal reflecting material for precision optics, usually deposited chemically in a liquid process. Liquid chemical deposition is still used for the production of second surface architectural mirrors. In that application, the bonding of the silver to the glass surface is assured by a very thin layer of tin and the silver is protected by an outer layer of copper followed by an additional layer of paint. In front surface applications, silver reacts with atmospheric oxygen and tarnishes by the formation of silver sulfide, but the initial high reflectance and the extreme ease of evaporation still make it a common choice for components used only for a short period. Silver is also useful where it is necessary to coat temporarily a component, such as an interferometer plate, for a test of flatness. We shall deal more fully with protected silver in the next section.

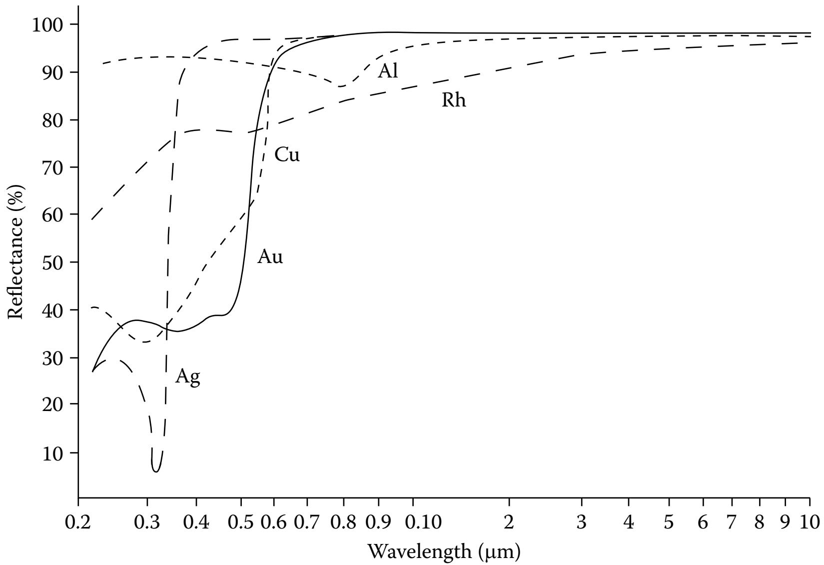

FIGURE 5.1
Reflectance of freshly deposited films of aluminum, copper, gold, rhodium and silver as a function of wavelength from 0.2 to 10 μm. (After Hass, G., *Journal of the Optical Society of America*, 45, 945–952, 1955.)

John Strong [2] working with astronomical mirrors, pioneered, in the 1930s, the replacement of chemically deposited silver by evaporated aluminum. Aluminum is easy to evaporate and has good ultraviolet, visible and infrared reflectance, together with the additional advantage of adhering strongly to most substances, including plastics. As a result, it is the most frequently used film material for the production of reflecting coatings. The reflectance of an aluminum coating does drop gradually in use, although the thin oxide layer, which always forms on the surface very quickly after coating, helps to protect it from further corrosion. In use, especially if the mirror is at all exposed, dust and dirt invariably collect on the surface and cause a fall in reflectance. The performance of most instruments is not seriously affected by a slight drop in reflectance, but in some cases where it is important to collect the maximum amount of light, as it is difficult to clean the coatings without damaging them, the components are recoated periodically. This applies particularly to the mirrors of large astronomical reflecting telescopes. The primary mirrors of these are recoated with aluminum usually around once a year in coating plants that are installed in the observatories for this purpose. Because the primaries are very large and heavy, it is not usually to rotate them during coating and the uniformity of coating is achieved using multiple sources. Aluminum is still used for the vast majority of telescope mirrors, but some of the very latest telescopes are being coated with a more advanced coating consisting of protected silver.

Gold is probably the best material for infrared reflecting coatings. Its reflectance drops off rapidly in the visible region and it is really useful only beyond 700 nm. On glass, gold tends to form rather soft, easily damaged films, but it adheres strongly to a film of chromium or Nichrome (trade name of a resistance wire usually of composition 80% nickel/20% chromium), and this is often used as an underlayer between the gold and the glass substrate.

The reflectance of rhodium and platinum is rather less than that of the other metals mentioned, and these metals are used only where stable films very resistant to corrosion are required. Both materials adhere very strongly to glass. Dental mirrors that are subjected to a quite difficult environment and have to be sterilized by heating are usually rhodium coated. Rhodium is also used for some automobile rear-view mirrors. These are frequently front-surface mirrors and on the outside of a vehicle are subjected to the weather, washing and cleaning, and a general level of serious abuse. An early paper pointing out the advantages of rhodium with its great stability over films of aluminum is that of Auwärter [3].

Chromium is somewhat cheaper than rhodium and is also much used for automobile rear-view mirrors.

5.1.2 Protection of Metal Films

Most metal films are rather softer than hard dielectric films and can be scratched easily. Unprotected evaporated aluminum layers, for example, can be badly damaged if wiped with a cloth, while gold and silver films are even softer. This is a serious disadvantage, especially when periodic cleaning of the mirrors is necessary. One solution, as we have seen, is periodic recoating. An alternative, which improves the ruggedness of the coatings and also protects them from atmospheric corrosion, is overcoating with an additional dielectric layer. The behavior of a single dielectric layer on a metal is a useful illustration of the calculation techniques of Chapter 2. We shall also require some related results later and so it is useful to spend a little time on the problem.

First, the admittance diagram, Figure 5.2, gives us a qualitative picture of the behavior of the system as the dielectric layer is added. The metal layer will normally be thick enough for the optical admittance at its front surface to be simply that of the metal, the substrate optical constants having no effect. The optical admittance of the metal will always be in the fourth quadrant and so, as a dielectric layer is added, the reflectance must fall until the locus of the admittance of the assembly crosses the real axis. (We recall that the reflectance associated with the locus of a dielectric layer in an incident medium of lower admittance, always falls as the locus is traced out in the fourth quadrant [that is below the real axis] and always rises in the first [that is above the real axis]. This minimum of reflectance will occur at a dielectric layer thickness of less than a quarter-wave. For layer thicknesses of up to twice this figure, therefore, the reflectance of the protected metal film will be

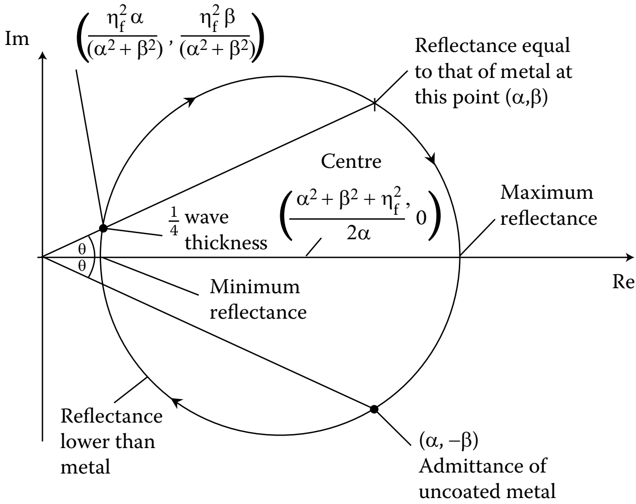

FIGURE 5.2
Admittance diagram of a dielectric layer deposited over a metal. The metal admittance would usually be much closer to the imaginary axis but have been moved for greater clarity in the diagram. The dielectric locus starts at the admittance of the uncoated metal. The construction to find the quarter-wave point is explained in the text, as are the other parameters.

reduced. The reduction in reflectance depends very much on the particular metal and the index of the dielectric film.

We can mark the position of the quarter-wave dielectric layer thickness by a simple construction. We draw the line from the origin to the starting point of the dielectric locus, that is the metal admittance $\alpha - i\beta$, which lies in the fourth quadrant. This line makes an angle ϑ with the real axis. Then, also through the origin, we draw a line in the first quadrant making the same angle ϑ with the real axis. This cuts the dielectric locus in two points. One is the point $\alpha + i\beta$, the image of the starting point in the real axis, and at this point the reflectance of the assembly is identical to that of the uncoated metal. The second point of intersection is

$$\left(\frac{\eta_f^2\alpha}{\left(\alpha^2+\beta^2\right)}, \frac{\eta_f^2\beta}{\left(\alpha^2+\beta^2\right)}\right) \text{i.e. } \frac{\eta_f^2}{(\alpha - i\beta)}$$

and here the layer is clearly one quarter-wave thick. In fact, this is a useful construction to find the terminal point of a quarter-wave layer.

We can derive straightforward analytical expressions for the various parameters and, in particular, the points of intersection of the locus with the real axis, which we know correspond to the points of maximum and minimum reflectance.

The characteristic matrix is given by

$$\begin{bmatrix} B \\ C \end{bmatrix} = \begin{bmatrix} \cos\delta_f & i(\sin\delta_f/\eta_f) \\ i\eta_f\sin\delta_f & \cos\delta_f \end{bmatrix} \begin{bmatrix} 1 \\ \alpha - i\beta \end{bmatrix} \tag{5.1}$$

where $\alpha - i\beta$ is the characteristic admittance of the metal, i.e., $Y(n_m - ik_m)$ at normal incidence, $\delta_f = 2\pi n_f d_f \cos\vartheta_f/\lambda$ and η_f is the characteristic admittance of the film material. Then

$$\begin{bmatrix} B \\ C \end{bmatrix} = \begin{bmatrix} \cos\delta_f + (\beta\sin\delta_f/\eta_f) + i(\alpha\sin\delta_f/\eta_f) \\ \alpha\cos\delta_f + i(\eta_f\sin\delta_f - \beta\cos\delta_f) \end{bmatrix}$$

Now, at the points of intersection of the locus with the real axis, we must have that the admittance, which we can denote by μ, is real. But

$$\mu = C/B$$

And, equating real and imaginary parts,

$$\alpha\cos\delta_f = \mu\left[\cos\delta_f + (\beta\sin\delta_f/\eta_f)\right] \tag{5.2}$$

$$\eta_f\sin\delta_f - \beta\cos\delta_f = \mu(\alpha\sin\delta_f/\eta_f) \tag{5.3}$$

Hence, first eliminating μ,

$$(\alpha\cos\delta_f)(\alpha\sin\delta_f)/\eta_f = (\eta_f\sin\delta_f - \beta\cos\delta_f)\left[\cos\delta_f + (\beta\sin\delta_f/\eta_f)\right]$$

i.e.,

$$\left[(\alpha^2 + \beta^2 - \eta_f^2)/(2\eta_f)\right]\sin(2\delta_f) = -\beta\cos(2\delta_f)$$

Thus

$$\tan(2\delta_f) = 2\beta\eta_f/(\eta_f^2 - \alpha^2 - \beta^2)$$

So that

$$\delta_f = \frac{1}{2}\arctan\left[2\beta\eta_f/(\eta_f^2 - \alpha^2 - \beta^2)\right] + \frac{m\pi}{2} \qquad m = 0, 1, 2, 3, \cdots \tag{5.4}$$

Or, in full waves

$$D_f/\lambda_0 = [1/(4\pi)]\arctan\left[2\beta\eta_f/\left(\eta_f^2-\alpha^2-\beta^2\right)\right] + m/4 \quad (5.5)$$

where the arctangent is to be taken in either the first or second quadrant so that δ_f for $m = 0$ is positive and represents the first intersection with the real axis where the film is less than, or at the very most, equal to, a quarter-wave. A similar result has been derived by Park [4] using a slightly different technique.

The value of μ can be found by rearranging Equations 5.2 and 5.3 slightly

$$(\mu-\alpha)\cos\delta_f + (\beta\mu/\eta_f)\sin\delta_f = 0$$

$$\beta\cos\delta_f + \left[(\mu\alpha/\eta_f) - \eta_f\right]\sin\delta_f = 0$$

and, eliminating δ_f,

$$(\mu-\alpha)\left[(\mu\alpha/\eta_f) - \eta_f\right] - \beta(\mu\beta/\eta_f) = 0$$

The two solutions are

$$\mu = \left[\left(\alpha^2+\beta^2+\eta_f^2\right)/(2\alpha)\right] \pm \left\{\left[\left(\alpha^2+\beta^2+\eta_f^2\right)/(2\alpha)\right]^2 - \eta_f^2\right\}^{1/2}$$

but this is not the best form for calculation. We know that the two solutions μ_1 and μ_2 are related by $\mu_1\mu_2 = \eta_f^2$ and so we write

$$\mu_1 = 2\alpha\eta_f^2 \Big/ \left\{\left(\alpha^2+\beta^2+\eta_f^2\right) + \left[\left(\alpha^2+\beta^2+\eta_f^2\right)^2 - 4\alpha^2\eta_f^2\right]^{1/2}\right\} \quad (5.6)$$

$$\mu_2 = \left[\left(\alpha^2+\beta^2+\eta_f^2\right)/(2\alpha)\right] + \left\{\left[\left(\alpha^2+\beta^2+\eta_f^2\right)/(2\alpha)\right]^2 - \eta_f^2\right\}^{1/2} \quad (5.7)$$

and the value that corresponds to the first intersection ($m = 0$ in Equation 5.4) is

$$\mu_1 = 2\alpha\eta_f^2 \Big/ \left\{\left(\alpha^2+\beta^2+\eta_f^2\right) + \left[\left(\alpha^2+\beta^2+\eta_f^2\right)^2 - 4\alpha^2\eta_f^2\right]^{1/2}\right\} \quad (5.6)$$

Often

$$\left(\alpha^2+\beta^2+\eta_f^2\right)^2 \gg 4\alpha^2\eta_f^2$$

and in that case

$$\mu_1 = \alpha\eta_f^2 / \left(\alpha^2 + \beta^2 + \eta_f^2\right) \tag{5.8}$$

$$\mu_2 = \left(\alpha^2 + \beta^2 + \eta_f^2\right) / \alpha \tag{5.9}$$

The limits of reflectance are given by

$$R_{\text{minimum}} = \left[(\eta_0 - \mu_1)/(\eta_0 + \mu_1)\right]^2 \tag{5.10}$$

$$R_{\text{minimum}} = \left[(\eta_0 - \mu_2)/(\eta_0 + \mu_2)\right]^2 \tag{5.11}$$

The higher the index of the dielectric film, the greater is the fall in reflectance at the minimum. The reflectance rises above that of the bare metal at the maximum, but, for the metals commonly used as reflectors, the increase is not great, and so the lower-index films are to be preferred as protecting layers. As an example, we can consider aluminum, which has a refractive index of 0.82 – i5.99 at 546 nm [5] with protecting layers of silica of index 1.45 or a high-index layer, 2.3, such as cerium oxide. The results in Table 5.1 were calculated from Equations 5.5 through 5.7, 5.10, and 5.11. Clearly, if high-index films are used for protecting metal layers, then the monitoring of layer thickness must be accurate, otherwise there is a risk of a sharp drop in reflectance. Also, the high reflectance region associated with the high-index protecting layer is rather narrow.

Aluminum is probably the commonest mirror coating material for the visible region, and, in addition to the silicon dioxide and cerium oxide mentioned above, there is a large number of materials that can be used for protecting it. The best overall material is definitely silicon dioxide, often referred to as silica or quartz (although strictly quartz refers to the natural mineral). If highest luminous reflectance is required then a half-wave of silicon dioxide is best. Silicon monoxide (SiO), for example, is also a very effective protecting material, but it has strong absorption at the blue end of the spectrum, where it causes the reflectance of the composite coating to be rather low, and, since it has a higher index, it presents a greater reduction of reflectance at the

TABLE 5.1

Reflectance Extrema for Overcoated Aluminum

Aluminum (0.82–i5.99)	**$R_{uncoated}$ (%)**	**R_{min} (%)**	**D_{min} (full waves)**	**R_{max} (%)**	**D_{max} (full waves)**
SiO2 (1.45)	91.63	83.64	0.2128	91.86	0.4628
CeO2 (2.30)	91.63	65.90	0.1925	92.44	0.4425

minimum than does silicon dioxide. Another useful coating is aluminum oxide (Al_2O_3), also often known as sapphire (although sapphire is strictly a crystalline form). This can be vacuum deposited, or the aluminum at the surface of the coating can be anodized by an electrolytic technique [1], forming a very hard layer of aluminum oxide. Gold and silver are more difficult to protect because of the difficulty of getting films to stick to them. Gold is sometimes protected with silicon monoxide, but the sticking is not always entirely satisfactory. Since gold resists tarnishing much better than silver, if it is not going to be handled it is often preferable not to overcoat it. It has been found that aluminum oxide sticks very well to silver [6,7]. Aluminum oxide does not appear to be a very effective barrier against moisture and so it has been used principally as a bonding layer between the silver and a layer of silicon oxide, which affords good moisture resistance and which, although it adheres only weakly to silver, adheres strongly to the aluminum oxide. Further details of the coating are given by Hass and his colleagues [7]. The starting material can be silicon monoxide, but to reduce the absorption at the blue end of the spectrum, the silicon oxide should be reactively deposited (see Chapter 11) when the actual oxide produced will lie between SiO and SiO_2. With such a coating, it is possible to achieve a reflectance greater than 95% over the visible and infrared from 0.45 to 20 μm.

Aluminum oxide and silicon oxide are absorbing at wavelengths longer than 8 μm and it has been discovered by Pellicori [8] and confirmed theoretically by Cox and Hass [9] that reflectors protected by these materials exhibit a sharp dip in reflectance at high angles of incidence, that is, 45° and above. The dip can be avoided by the use of a protecting material that does not absorb in this region. Magnesium fluoride is such a material, but it must be deposited on a hot substrate (temperatures in excess of 200° C) if it is to be robust. The metals have their best performance if deposited at room temperature, and thus the substrates should be heated only after they have been coated with the metal.

In the 1930s, John Strong [2] introduced the evaporated aluminum coating for the mirrors in reflecting telescopes, replacing chemically deposited silver. This aluminum coating has remained essentially unchanged for 70 years. Astronomical telescopes are normally expected to operate over as wide a spectral region as possible and aluminum covers the ultraviolet, visible, and infrared to a wider extent than any other material. However, there is a problem, particularly in the infrared. The faintness of an infrared source that can be observed is largely determined by the thermal radiation from the mirrors themselves and this, of course, depends on the thermal emittance of the mirror coatings. The material with the highest reflectance and lowest emissivity in the infrared is silver. Silver has some disadvantages. It has low reflectance in the ultraviolet, and it is environmentally weak. Attempts have been made to develop a silver-based coating that would be more rugged and would reflect more strongly in the ultraviolet [10]. So far, no universal coating based on silver has been adopted. However, some of the new generation of telescopes are optimized for the infrared, and the coating being used for these instruments

is based on protected silver [11,12]. The two Gemini telescopes sited in Chile and Hawaii with their 8-meter-diameter primaries have already been coated with this silver-based coating. The technique used is magnetron sputtering. The mirror is rotated underneath the magnetron targets that cover the entire mirror in three passes. A thin layer of $NiCrN_x$ over the glass acts to bond the silver layer. The silver is then protected by a very thin layer of $NiCrN_x$ followed by a thicker layer of silicon nitride. The standard coating [11] consists of 6.5 nm of $NiCrN_x$, 110 nm of silver, 0.6 nm of $NiCrN_x$ and 8.5 nm of SiN_x. Uniformity of the coating is better than 1 nm. The success of the Gemini coatings will certainly encourage its use for other telescopes.

5.1.3 Overall System Performance, Enhanced Reflectance

In optical instruments of any degree of complexity, there will be a number of reflecting components in series, and the overall transmission of the system will be given by the product of the reflectances of the various elements. Figure 5.3 gives the overall transmission of any system with a number of components in series, with identical values of reflectance. It is obvious from the diagram that even with the best metal coatings, the performance with 10 elements, say, is low. If the instrument is to be used over a wide range, little can be done to alleviate the situation. Most spectrometers, for instance, have 10 or more reflections with a consequent severe drop in transmission, but are required to work over a wide region—possibly as much as a 25:1 variation in wavelength. The spectrometer designer normally just accepts this loss and designs the rest of the instrument accordingly.

In cases where the wavelength range is rather more limited, say, to the visible region or to a single wavelength, it is possible to increase the reflectance of a simple metal layer by overcoating it with extra dielectric layers.

The characteristic admittance of a metal can be written $n-ik$ and the reflectance in air at normal incidence is

$$R=\left|\frac{1-(n-ik)}{1+(n-ik)}\right|^2=\frac{(1-n)^2+k^2}{(1+n)^2+k^2}=\frac{1-\left[2n/\left(1+n^2+k^2\right)\right]}{1+\left[2n/\left(1+n^2+k^2\right)\right]} \tag{5.12}$$

In Chapter 3 it was shown that the optical admittance of an assembly Y becomes n^2/Y when a quarter-wave optical thickness of index n, that is admittance in free space units, is added.

If the metal is overcoated with two quarter-waves of material of indices n_1 and n_2, n_2 being next to the metal, then the optical admittance at normal incidence is

$$\left(\frac{n_1}{n_2}\right)^2(n-ik)$$

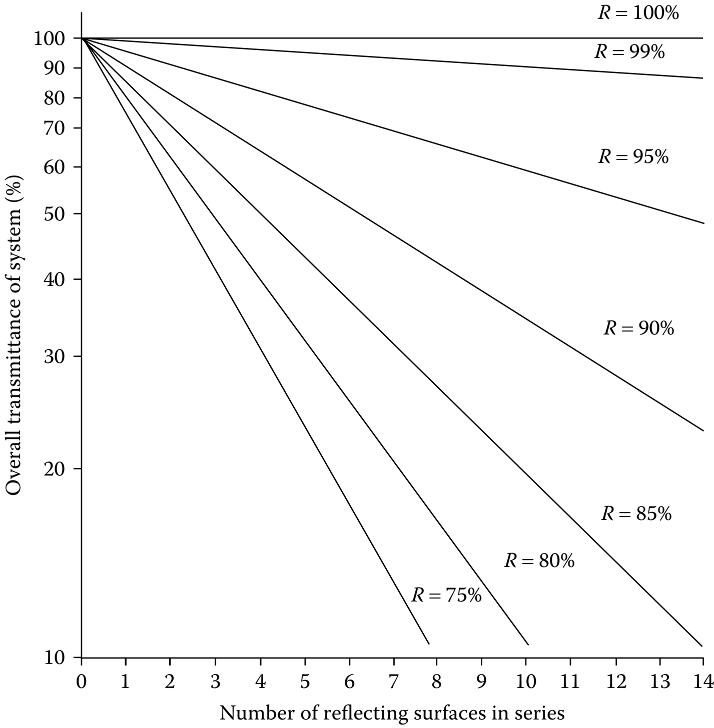

FIGURE 5.3
Overall transmittance of an optical system with a number of reflecting elements in series.

and the reflectance in air, also at normal incidence,

$$R = \left|\frac{1-(n_1/n_2)^2(n-ik)}{1+(n_1/n_2)^2(n-ik)}\right|^2 = \frac{\left[1-(n_1/n_2)^2 n\right]^2 + (n_1/n_2)^4 k^2}{\left[1+(n_1/n_2)^2 n\right]^2 + (n_1/n_2)^4 k^2}$$

i.e.,

$$R = \frac{1 - \left[2(n_1/n_2)^2 n\right] \Big/ \left[1+(n_1/n_2)^4(n^2+k^2)\right]}{1 + \left[2(n_1/n_2)^2 n\right] \Big/ \left[1+(n_1/n_2)^4(n^2+k^2)\right]} \quad (5.13)$$

This will be greater than the reflectance of the bare metal, given by Expression 5.12, if

$$\frac{2(n_1/n_2)^2 n}{1+(n_1/n_2)^4(n^2+k^2)} < \frac{2n}{1+n^2+k^2} \quad (5.14)$$

which is satisfied by either

$$\left(\frac{n_1}{n_2}\right)^2 > 1 \text{ or } \left(\frac{n_1}{n_2}\right)^2 < \frac{1}{n^2+k^2} \tag{5.15}$$

assuming that $n^2 + k^2 \geq 1$.

The first solution is of greater practical value than the second, which can be ignored. This shows that the reflectance of any metal can be enhanced by a pair of quarter-wave layers for which $(n_1/n_2) > 1$, n_1 being on the outside and n_2 next to the metal. The higher this ratio, the greater is the increase in reflectance.

As an example, consider aluminum at 550 nm with $n - ik = 0.92 - i5.99$. From Equation 5.12, the untreated reflectance of this is approximately 91.6%. If the aluminum is covered by two quarter-waves consisting of silicon oxide of index 1.45, next to the aluminum, followed by titanium oxide of index 2.40, then $(n_1/n_2) = 1.655$ and, from Equation 5.13, the reflectance jumps to 96.4%.

An approximate result can be obtained very quickly using $A = (1 - R)$. When the two layers are added, A is reduced roughly to $A/(n_1/n_2)^2$. Inserting the above figures, for aluminum, A is 9.4% initially, and on addition of the layers drops to 3.45%, corresponding to an enhanced reflectance of 96.5% (instead of the more accurate figure of 96.4%).

A second similar pair of dielectric layers will raise the reflectance even higher, to approximately 99%, and greater numbers of quarter-wave pairs may be used to give a still higher reflectance.

Unfortunately, the region over which the reflectance is enhanced, is limited. In the visible region, the gain is essentially in luminous reflectance. Outside the enhanced zone the reflectance is less than it would be for the bare metal. Jenkins [13] has measured the reflectance of an aluminum layer overcoated with six quarter-wave layers of cryolite, of index 1.35, and zinc sulfide of index 2.35. With layers monitored at 550 nm, the reflectance of the boosted aluminum was greater than 95% over a region 280 nm wide, and greater than 99% over the major part. Coatings that are more robust can be obtained using magnesium fluoride, silicon dioxide or aluminum oxide as the low-index layers, and cerium oxide or titanium oxide as the high-index layers. To attain maximum toughness, the dielectric layers should be deposited on a hot substrate. Aluminum, however, if deposited hot, tends to scatter badly and so the substrates should be heated only after deposition of the aluminum is complete. Figure 5.4 shows the reflectance of aluminum enhanced by four quarter-wave layers increasing the reflectance over the visible region.

We have already considered more exactly the behavior of a single dielectric layer on a metal, and have shown, as did Park [4], that the thickness of the dielectric layer for minimum reflectance should be (5.5),

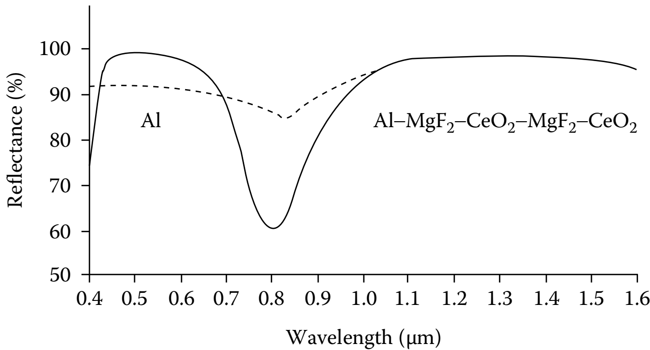

FIGURE 5.4
Reflectance of evaporated aluminum with (*solid curve*) and without (*broken*) two reflectance-increasing film pairs of MgF_2 and CeO_2 as a function of wavelength from 0.4 to 1.6 μm. (After Hass, G., *Journal of the Optical Society of America*, 45, 945–952, 1955.)

$$D_f = \left\{\arctan\left[2\beta\eta_f \Big/ \left(\eta_f^2 - \alpha^2 - \beta^2\right)\right]\right\}\left[\lambda_o \Big/ (4\pi)\right]$$

where $(\alpha - i\beta)$ is the admittance of the metal and the angle is in the first or second quadrant. This is the thickness that the low-index layer next to the metal should have if the maximum possible increase in reflectance is to be achieved. A moment's consideration of the admittance diagram will show that this is indeed the case. Layers other than that next to the metal will, of course, retain their quarter-wave thicknesses. Usually, however, the layer is simply made a quarter-wave because the resulting difference in performance over the visible region is not great.

5.1.4 Reflecting Coatings for the Ultraviolet

The production of high-reflectance coatings for the ultraviolet is a much more exacting task than for the visible and infrared. A very full review of the topic is given by Madden [14], supplemented in great detail by a later account by Hass and Hunter [15]. The following is a very brief summary.

The most suitable material known for the production of reflecting coatings for the ultraviolet out to around 100 nm is aluminum. To achieve the best results, the aluminum should be evaporated at a very high rate, 40 nm s^{-1} or more if possible, on to a cold substrate, the temperature of which should not be permitted to exceed 50° C, and at pressures of 10^{-6} torr (1.33×10^{-4} Pa) or lower. The aluminum should be of the purest grade. Hass and Tousey [16] have quoted results showing a significant improvement (as high as 10% at 150 nm) in the ultraviolet reflectance of aluminum films if 99.99% pure aluminum is used in preference to 99.5% pure. Aluminum should, in theory, have a much higher reflectance than is usually achieved in practice, particularly at the shortwave end of the range. This has been found to be due

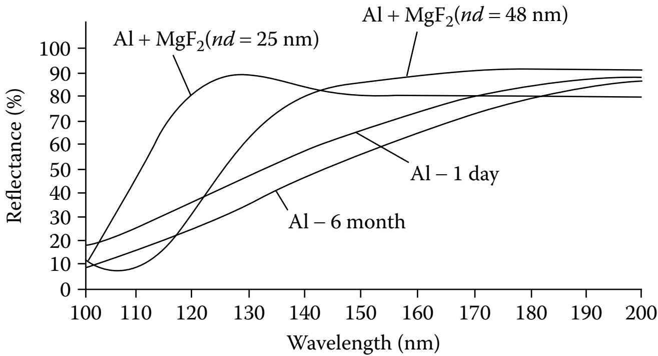

FIGURE 5.5
Reflectance of evaporated aluminum from 100 to 200 nm with and without protective layers of MgF_2 of two different thicknesses. (After Canfield, L.R., Hass, G., and Waylonis, J.E., *Applied Optics*, 5, 5–50, 1966.)

to the formation of a thin oxide layer on the surface, and as we have already shown, such a layer must, unless it is very thick, lead to a reduction in reflectance. This oxidation takes place even at partial pressures of oxygen below 10^{-6} torr (1.33×10^{-4} Pa). Unprotected aluminum films, therefore, inevitably show a rapid fall in reflectance with time when exposed to the atmosphere. The reflectance stabilizes when the layer is of sufficient thickness to inhibit further oxidation, but this occurs only when the reflectance at short wavelengths has fallen catastrophically.

Attempts have been made to find suitable protecting material for aluminum to prevent oxidation, and very promising results have been obtained with magnesium fluoride (very robust coatings) and lithium fluoride (less robust), which in crystal form are very useful window materials for the ultraviolet. Figure 5.5 and Figure 5.6 show the effect of an extra protecting

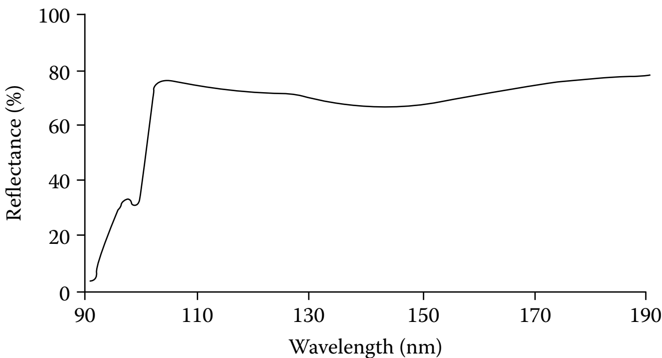

FIGURE 5.6
Reflectance of an evaporated aluminum film with a 14-nm-thick LiF overcoating in the region of 90–190 nm. Measurements were begun about 10 minutes after the evaporation was completed. (After Cox, J.T., Hass, G., and Waylonis, J.E. *Applied Optics*, 7, 1535–1539, 1968.)

layer of magnesium fluoride [17] or lithium fluoride [18] on the reflectance of aluminum. The increase in reflectance is partly due to the lack of oxide layer, but also to interference effects.

It is necessary to evaporate the protecting layer immediately after the aluminum in order that the minimum amount of oxidation should be allowed to take place. This is usually achieved by running the two sources simultaneously and arranging for the shutter that covers the aluminum source at the end of the deposition of the aluminum layer to uncover at the same time the magnesium or lithium fluoride source. The use of magnesium fluoride–overcoated aluminum as a reflecting coating for the ultraviolet is now becoming standard practice.

The aluminum and magnesium fluoride coating is examined in some detail by Canfield et al. [17]. Among other results, they show that provided the magnesium fluoride is thicker than 10 nm, the coatings will withstand, without deterioration, exposure to ultraviolet radiation and to electrons (up to 10^{16} 1-MeV electrons/cm^2) and protons (up to 10^{12} 5-MeV protons/cm^2).

5.2 Neutral Beam Splitters

A device that divides a beam of light into two parts is known as a *beam splitter*. The functional part of a beam splitter generally consists of a plane surface coated to have a specified reflectance and transmittance over a certain wavelength range. The incident light is split into a transmitted and a reflected portion at the surface, which is usually tilted so that the incident and reflected beams are separated. The ideal values of reflectance and transmittance may vary from one application to another. The beam splitters considered in this section are known as neutral beam splitters, because reflectance and transmittance should ideally be constant over the wavelength range concerned.

Neutral beam splitters are usually specified by the ideal values of transmittance and reflectance expressed as a percentage and written T/R. The 50/50 beam splitters are probably the most common.

5.2.1 Beam Splitters Using Metallic Layers

Apart from a single uncoated surface, which is sometimes used, the simplest type of beam splitter consists of a metal layer deposited on a glass plate. Silver, which has least absorption of all the common metals used in the visible region, is traditionally the most popular material for this. The 50/50 beam splitters are frequently referred to as being “half-silvered,” although commercial beam splitters nowadays are usually constructed from metals, such as chromium, which are less prone to damage by abrasion and corrosion.

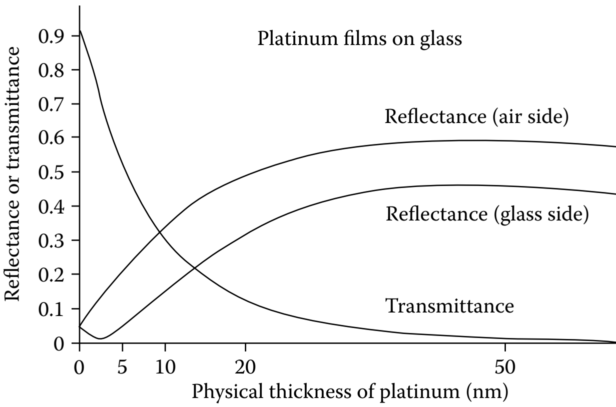

FIGURE 5.7
Reflectance and transmittance curves for a platinum film on glass, calculated from the optical constants on the bulk metal. (After Heavens, O.S. *Optical Properties of Thin Solid Films*, Butterworths Scientific Publications, London, 1955.)

All metallic beam splitters suffer from absorption. The transmittance of a metal film is the same, regardless of the direction in which it is measured. This is not so for reflectance, and that measured at the air side is slightly higher than that measured at the glass side. This effect does not appear with a transparent film. Since $T + A + R = 1$, the reduction in reflectance at the substrate side means that the absorption from that side must always be higher. Figure 5.7 shows curves for platinum demonstrating this behavior [19]. Because of this difference in reflectance, metallic beam splitters should always be used in the manner shown in Figure 5.8 if the highest efficiency is to be achieved.

It is possible to decrease the absorption in metallic beam splitters by adding an extra dielectric layer. The method has been applied to chromium films by Pohlack [20], and Figure 5.9 gives some of the measurements made.

The first pair of results is for a simple chromium film on glass of index 1.52 measured both from the air side and from the glass side. The second pair of

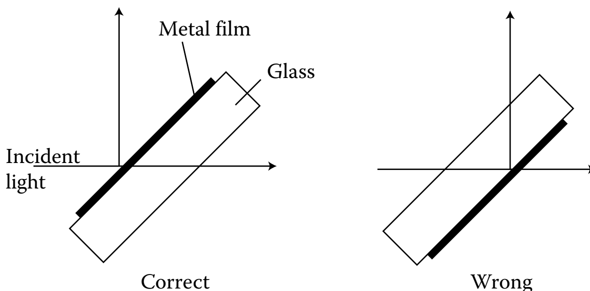

FIGURE 5.8
Correct use of a metallic beam splitter.

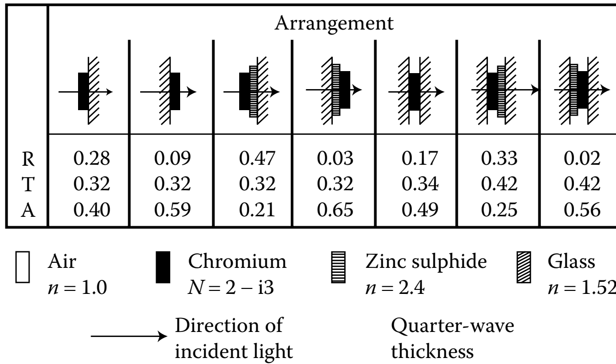

	Arrangement						
	1	2	3	4	5	6	7
R	0.28	0.09	0.47	0.03	0.17	0.33	0.02
T	0.32	0.32	0.32	0.32	0.34	0.42	0.42
A	0.40	0.59	0.21	0.65	0.49	0.25	0.56

FIGURE 5.9
Values of reflectance, transmittance, and absorptance at 550 nm and normal incidence for semireflecting films of chromium on glass showing the effect of adding a quarter-wave layer of zinc sulfide. (After Pohlack, H., Beitrag zur Optik dünnster Metallschichten, in *Jenaer Jahrbuch*, VEB Carl Zeiss, Jena, 241–245, 1953.)

results shows how the absorption in the chromium can be reduced by the presence of a quarter-wave layer of high refractive index material (zinc sulfide of index approximately 2.4 in this case) between the metal and the glass. This layer forms an antireflection coating on the rear surface of the metal, and the effect can be seen particularly strongly in the results for reflectance and transmission from the glass side. There, the transmission remains exactly as before, but the reflectance is considerably reduced. Results are also given for a chromium layer protected by a glass cover cemented on the front surface with and without the antireflecting layer. The metallic absorption again is very much less when the antireflection layer is on the side of the metal remote from the incident light.

Shkliarevskii and Avdeenko [21] increased the transparency and decreased the absorption in metallic coatings using an antireflection coating in a similar manner. The antireflection coating in this case, instead of being dielectric, was a thin metallic layer. They found that a layer of silver deposited on a substrate heated to around 300° C increased the transparency of an aluminum coating, deposited on top of the silver at room temperature, by a factor as high as 3.5 at 1 μm and 2.5 at 700 nm without any decrease in reflectance at the aluminum-air interface. Since a simple layer of silver would not normally do this, there is presumably some microstructural effect involved or the silver at this high temperature is perhaps being converted toward a dielectric.

If the beam splitter is used correctly, the reduction in reflectance at the glass–film interface can be useful in reducing the stray light derived from reflection, first from the back surface of the glass blank and then from the glass–film interface.

One complication found with beam splitters is a difference in the values of reflectance for the two planes of polarization when the beam splitter is tilted. The *s*-reflectance (or TE) is higher than the *p*-reflectance (or TM). Anders [22] describes a method for calculating efficiency and stray light performance.

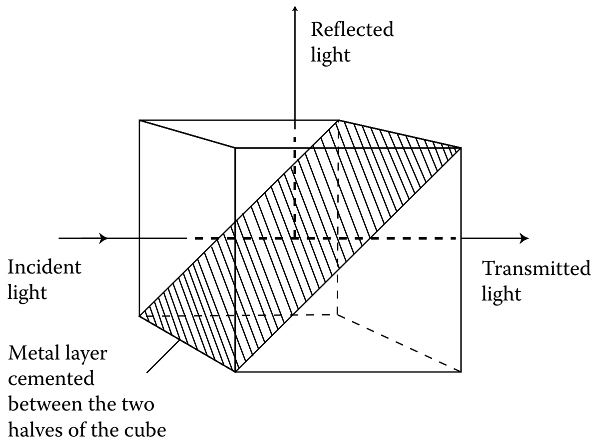

FIGURE 5.10
A cube beam splitter.

It is not always possible to use the flat plate beam splitter in some optical systems. Reflections from the rear surface can be a problem despite the antireflection layer behind the metal film, and in applications where the light passing through the plate is not collimated, aberrations are introduced. To overcome these difficulties a beam-splitting cube, as shown in Figure 5.10, can be used, although the absorption in the metal is greater in this configuration because both surfaces, instead of just one, are now in contact with a medium whose index is greater than unity. Since the cemented assembly protects the metal layers, the choice of materials is wide. Silver is probably most frequently used, although chromium, aluminum and gold are also popular.

Chromium gives almost neutral beam splitting over the visible region, with an absorptance of approximately 55% for both planes of polarization, the *s*-reflectance being approximately 30% and the *p*-reflectance 15%. Silver varies more with wavelength, the reflectance falling toward the blue end of the spectrum, but the absorptance is rather less than for chromium, around 15% at 550 nm, with *s*-reflectance of 50% and *p*-reflectance of 30%. Curves of the performance of several different metallic beam splitters are given by Anders [22].

5.2.2 Beam Splitters Using Dielectric Layers

There are many optical instruments where the light undergoes a transmission followed by a reflection, or vice versa, both at the same, or at the same type of, beam splitter. In two-beam interferometers, for example, the beams are first of all separated by one pass through a beam splitter and then combined again by a further pass either through the same beam splitter, as in the Michelson interferometer, or through a second beam splitter, as in the Mach-Zehnder interferometer. The effective transmittance of the instrument is given by the product of the transmittance and the reflectance of the beam

splitter, taking into account the particular polarization involved. For a perfect beam splitter, the product, *TR*, would be 0.25; for most metallic beam splitters, it is around 0.08 or 0.10. The absorption in the film is the primary source of loss.

A beam splitter of improved performance, as far as the *TR* product is concerned, can be obtained by replacing the metallic layer with a transparent high-index quarter-wave. At normal incidence the reflectance of a quarter-wave is given by

$$R = \left[\frac{y_0 - y_1^2/y_{sub}}{y_0 + y_1^2/y_{sub}}\right]^2 = \left[\frac{\eta_0 - \eta_1^2/\eta_{sub}}{\eta_0 + \eta_1^2/\eta_{sub}}\right]^2$$

At 45° angle of incidence, the position of the peak is shifted to a shorter wavelength, and the appropriate optical admittances must be used in calculating peak reflectance.

$$R = \left[\frac{\eta_0 - \eta_1^2/\eta_{sub}}{\eta_0 + \eta_1^2/\eta_{sub}}\right]^2$$

and since η varies with the plane of polarization, R will have two values: R_s and R_p.

Figure 5.11 shows the peak reflectance of a quarter-wave of index between 1.0 and 3.0 on glass of index 1.52 for both 45° incidence and normal incidence. At 45°, the peak reflectance for unpolarized light, $1/2\,(R_s + R_p)$, is within 1.5% of the peak value for normal incidence.

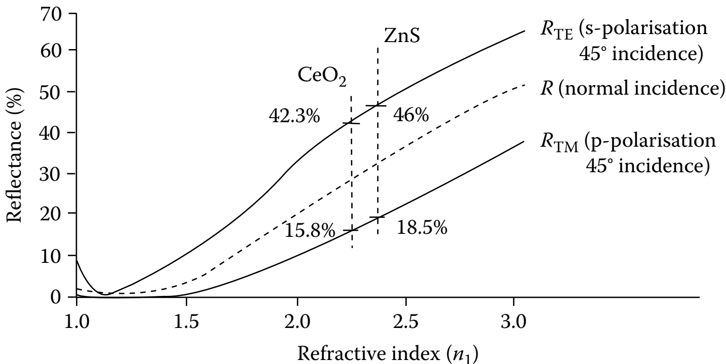

FIGURE 5.11
Peak reflectance in air of a quarter-wave of index on glass of index n_1 on glass of index 1.52 at normal and 45° incidence.

Zinc sulfide, with index 2.35, is a popular material for beam splitters. At 45° we have

$$(TR)_s = (0.46 \times 0.54) = 0.248$$

$$(TR)_p = (0.185 \times 0.815) = 0.151$$

and

$$(TR)_{unpolarized} = \frac{1}{2}(0.248 + 0.151) = 0.200$$

$(TR)_{unpolarized}$ cannot be calculated using $T_{mean}R_{mean}$ because the light, after having undergone one reflection or transmission, is then partly polarized.

If a more robust film is required, titanium dioxide or cerium dioxide is a good choice. Cerium dioxide, with an index approximately 2.25, gives

$$(TR)_s = (0.423 \times 0.577) = 0.244$$

$$(TR)_p = (0.158 \times 0.842) = 0.133$$

$$(TR)_{unpolarized} = 0.189$$

Clearly the dielectric beam splitter, even if it does tend to have characteristics that more nearly correspond to 70/30 rather than 50/50, has a considerably better performance than the metallic beam splitter. The transmittance curve of a typical 70/30 beam splitter in Figure 5.12 shows how the transmittance varies on either side of the peak.

Beam splitters with 55/45 characteristics can be made by evaporating pure titanium in a good vacuum and subsequently oxidizing it to TiO_2 by heating

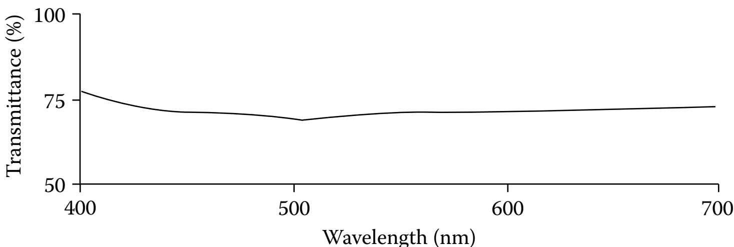

FIGURE 5.12
Measured transmittance curve of a dielectric 70/30 beam splitter at 45° angle of incidence. (Courtesy of Sir Howard Grubb, Parsons & Co Ltd.)

at 420° C in air at atmospheric pressure. The titanium oxide thus formed has rutile structure and a refractive index of 2.8. Titanium films produced in a poor vacuum oxidize subsequently to the anatase form, having rather lower refractive index. The production of very large beam splitters, of this type, 17 × 13 inches, is described in a paper by Holland et al. [23].

The single-layer beam splitter suffers from a fall in reflectance on either side of the central wavelength. In the same way that single-layer antireflection coatings can be broadened by adding a half-wave layer, so the single quarter-wave beam splitter can be broadened. The same basic pattern of admittance circles can be achieved either by a low-index half-wave layer between the high-index quarter-wave and the glass substrate or an even higher index half-wave deposited over the quarter-wave. Since no suitable materials for the latter solution exist in practice, the low-index half-wave is the only feasible approach. The admittance diagram is shown in Figure 5.13 and the performance in Figure 5.14.

The technique is effective also for multilayer systems to give a higher reflectance. Approximately 50% reflectance can be achieved by a four-layer coating—Air | *LHLH* | Glass, and this can be flattened by an additional low-index half-wave at the glass end of the multilayer, that is, Air | *LHLHLL* | Glass. Figure 5.14 shows the performance calculated for this design of beam splitter. A detailed discussion of the role of half-wave layers is given by Knittl [24].

As mentioned, beam-splitting cubes must be used in some applications where plate beam splitters are unsuitable. Unfortunately, the main problem connected with dielectric beam splitters, the low reflectance for *p*-polarization, waves, becomes even worse with cube beam splitters. The reason for this is simply that 45° incidence in glass is effectively a much greater angle of

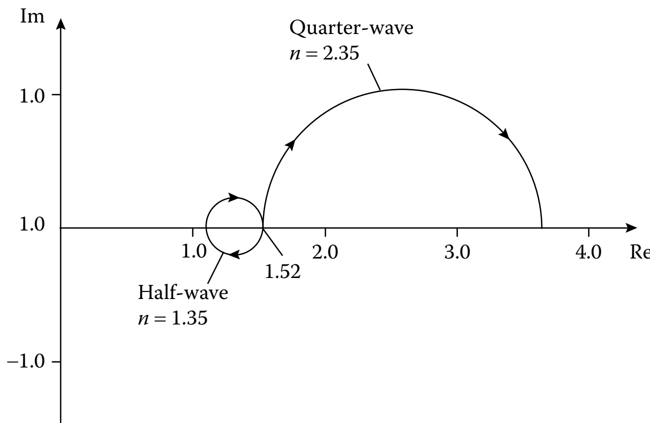

FIGURE 5.13
Admittance diagram at λ_0 of a two-layer beam splitter. The high-index quarter-wave layer gives the required high reflectance. The low-index half-wave layer flattens the performance over the visible region.

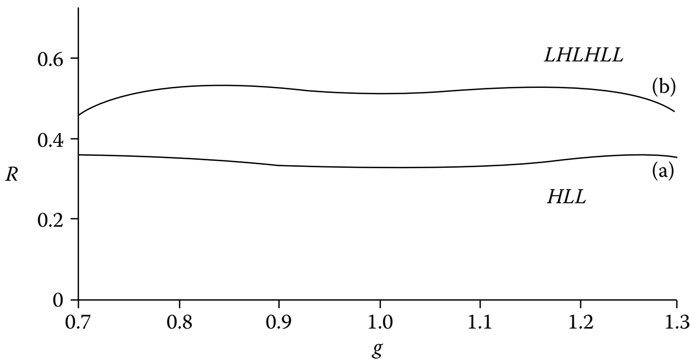

FIGURE 5.14
(a) The performance of the beam splitter shown in Figure 5.13. Design: Air (1.00) | *HLL* | Glass (1.52) with *L* a quarter-wave of index 1.35 and *H* of 2.35. (b) The performance of a beam splitter of design: Air (1.00) | *LHLHLL* | Glass (1.52) with indices as for (a).

incidence than 45° in air. Consequently, for simple designs, the polarization splitting is even greater and the performance becomes so poor that the beam splitter is unusable in most applications. Metal layers are, therefore, required for straightforward cube beam splitters and combiners. This disadvantage of the dielectric layer can, however, be turned to advantage in the construction of polarizers as we shall see in Chapter 9.

If we forget about practical issues and think of theory, then we can see that with only two dielectric materials there is little flexibility in the design of those coatings at oblique incidence where a given performance is required for both polarizations. The *p* and *s* phase thicknesses are equal, and, except for the outer surfaces of the coating where it contacts the two surrounding media, there is essentially one kind of interface only. The problem can be very slightly eased by adopting three, rather than two, materials because now we have three different kinds of interface. This does not convert an impossible problem into an easy one. It simply converts a virtually impossible problem into a very difficult one. Published designs achieved by powerful computer synthesis do exist but are exceedingly complex. A useful paper dealing principally with a two-material plate beam splitter that is nonpolarizing over a very limited spectral region, but which also includes a useful commentary on the whole question of dielectric nonpolarizing beam splitters, is that by Ciosek et al. [25].

5.3 Neutral-Density Filters

A filter that is intended to reduce the power of an incident beam of light evenly over a wide spectral region is known as a neutral-density filter.

The performance of neutral-density filters is usually defined in terms of the optical density, D:

$$D = \log_{10}(I_0/I_T) = -\log_{10} T$$

where I_0 is the incident irradiance, I_T is the transmitted irradiance, and T is given in a scale of 0 to 1.

Absorption and *absorptance* are terms not correctly used of neutral-density filters because they represent the fraction of energy actually absorbed in the film, and in neutral-density filters, a proportion of the incident energy is removed by reflection.

The advantage of using the logarithmic term if that the effect of placing two or more neutral-density filters in series is easily calculated. The overall density is simply the sum of the individual densities (provided that multiple reflections are not permitted to occur between the individual filters. Such reflections would affect the result in the way shown in Chapter 2, Equation 2.148).

Thin-film neutral-density filters consist of single metallic layers with thicknesses chosen to give the correct transmission values. Rhodium, palladium, tungsten, and chromium, as well as other metals, are all used to some extent, but very good performance is obtained by the evaporation of a nickel chromium alloy, approximately 80% nickel and 20% chromium. Chromel A and Nichrome are trade names of standard resistance wires having suitable composition that can be readily obtained. The method is described by Banning [26]. The Chromel or Nichrome should be evaporated at 10^{-4} torr (1.33×10^{-2} Pa), or better, from a thick tungsten spiral. Neutral films, having densities up to around 1.5, corresponding to a transmittance of 3% can be manufactured in this way. If the films are made

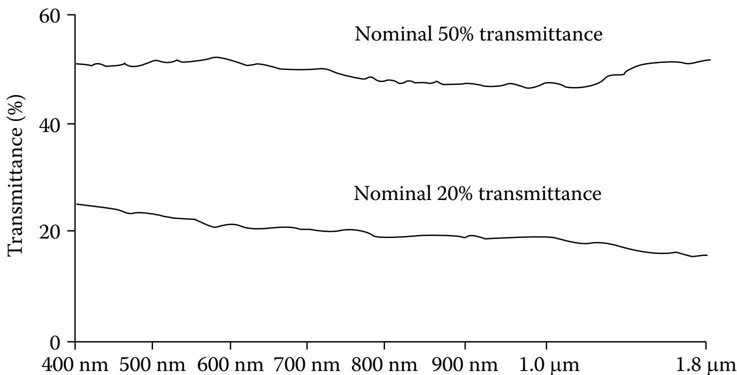

FIGURE 5.15
Measured transmittance curves of neutral density filters consisting of Nichrome films on glass substrates. (Courtesy of Sir Howard Grubb, Parsons & Co Ltd.)

thicker, they are not as neutral and tend to have higher transmittance in the red, owing to excess chromium. The films are very robust and do not need any protection, especially if they are heated to around 200° C after evaporation.

Figure 5.15 shows some response curves of neutral-density filters made from Nichrome on glass. The filters are reasonably neutral over the visible and near infrared out to 2 μm. In fact, if quartz substrates are used the filters will be good over the range 0.24–2 μm.

References

1. Hass G 1955 Filmed surfaces for reflecting optics *Journal of the Optical Society of America* **45** 945–952
2. Strong J 1936 The evaporation process and its application to the aluminizing of large telescope mirrors *Astrophysical Journal* **83** 401–423
3. Auwärter M 1939 Rhodium mirrors for scientific purposes *Journal of Applied Physics* **10** 705–710
4. Park K C 1964 The extreme values of reflectivity and the condition for zero reflection from thin dielectric films on metal *Applied Optics* **3** 877–881
5. Hass G and Hadley L 1972 *Optical constants of metals*, in *American Institute of Physics Handbook* Gray D E Editor (New York/London: McGraw-Hill Book Company) 6.124–6.156
6. Cox J T, Hass G, and Hunter W R 1975 Infrared reflectance of silicon oxide and magnesium fluoride protected aluminum mirrors at various angles of incidence from 8μm to 12μm *Applied Optics* **14** 1247–1250
7. Hass G, Heaney J B, Herzig H, Osantowski J F, and Triolo J J 1975 Reflectance and durability of Ag mirrors coated with thin layers of Al_2O_3 plus reactively deposited silicon oxide *Applied Optics* **14** 2639–2644
8. Pellicori S F 1974 Private communication (Santa Barbara Research Center, Goleta, CA)
9. Cox J T and Hass G 1978 Protected Al mirrors with high reflectance in the 8-12 μm region from normal to high angles of incidence *Applied Optics* **17** 2125–2126
10. Song D Y, Sprague R W, Macleod H A, and Jacobson M R 1985 Progress in the development of a durable silver-based high-reflectance coating for astronomical telescopes *Applied Optics* **24** 1164–1170
11. Boccas M 2004 Coating Gemini's mirrors with protected silver *Gemini Newsletter* **29** 9–13
12. Jacobson M R, Kneale R C, Gillett F C, Raybould K, Filhaber J F, Carniglia C K, Laird R, Kitchens D, Shimshock R P, and Booth D C 1998 Development of silver coating options for the Gemini 8-m telescopes project. *Proceedings of the Society of Photo-Optical Instrumentation Engineers* **3352** 477–502
13. Jenkins F A 1958 Extension du domaine spectral de pouvoir réflecteur élevé des couches multiples diélectriques *Journal de Physique et le Radium* **19** 301–306
14. Madden R P 1963 *Preparation and Measurement of Reflecting Coatings for the Vacuum Ultraviolet*, in *Physics of Thin Films, Vol 1* Hass G Editor (New York/London: Academic Press) 123–186

15. Hass G and Hunter W R 1978 *The Use of Evaporated Films For Space Applications: Extreme Ultraviolet Astronomy and Temperature Control of Satellites*, in *Physics of Thin Films* Hass G and Francombe M H Editors (New York/San Francisco/London: Academic Press) 71–166
16. Hass G and Tousey R 1959 Reflecting coatings for the extreme ultraviolet *Journal of the Optical Society of America* **49** 593–602
17. Canfield L R, Hass G, and Waylonis J E 1966 Further studies on MgF_2-overcoated aluminium mirrors with highest reflectance in the vacuum ultraviolet *Applied Optics* **5** 45–50
18. Cox J T, Hass G, and Waylonis J E 1968 Further studies on LiF-overcoated aluminium mirrors with highest reflectance in the vacuum ultraviolet *Applied Optics* **7** 1535–1539
19. Heavens O S 1955 *Optical Properties of Thin Solid Films* (London: Butterworths Scientific Publications)
20. Pohlack H 1953 *Beitrag zur Optik dünnster Metallschichten*, in *Jenaer Jahrbuch* (Jena: VEB Carl Zeiss) 241–245
21. Shkliarevskii I N and Avdeenko A A 1959 Increasing the transparency of metallic coatings *Optics and Spectroscopy* **6** 439–443
22. Anders H 1965 *Dünne Schichten für die Optik* (English translation: *Thin Films in Optics, Focal Press, 1967*) (Stuttgart: Wissenschaftliche Verlagsgesellschaft mbH)
23. Holland L, Hacking K, and Putner T 1953 The preparation of titanium dioxide beam-splitters of large surface area *Vacuum* **3** 159–161
24. Knittl Z 1976 *Optics of Thin Films* (London: John Wiley and Sons)
25. Ciosek J, Dobrowolski J A, Clarke G A, and Laframboise G 1999 Design and manufacture of all-dielectric nonpolarizing beam splitters *Applied Optics* **38** 1244–1250
26. Banning M 1947 Neutral density filters of Chromel A *Journal of the Optical Society of America* **37** 686–687

6

Multilayer High-Reflectance Coatings

The metal reflecting layers of the previous chapter suffer from a considerable absorption loss that, although unfortunate, still permits a high level of performance in most simple systems. There are applications where the absorption in metal layers is too high and their reflectance too low. These include multiple-beam interferometers and resonators, where the large number of successive reflections magnifies the effects of absorption, and high-power systems, where the energy absorbed can be sufficient to damage or destroy the coating. One way of increasing the reflectance of an opaque metal coating, as we have seen, is to enhance the reflectance by adding dielectric layers. This also reduces the absorptance, but the transmittance remains effectively zero. For high-reflecting coatings that must transmit what they do not reflect, all-dielectric multilayers are required. The description that follows begins with the most successful of the multiple-beam interferometers, the Fabry–Perot interferometer. As we shall see later, this interferometer is also of considerable importance in the development of thin-film band-pass filters, and this is a further reason for dealing with it in some detail here.

6.1 The Fabry–Perot Interferometer

First described in 1899 by Fabry and Perot [1], the interferometer known by their names has profoundly influenced the development of thin-film optics. It belongs to the class of interferometers known as multiple-beam interferometers because a large number of beams is involved in the interference. The theory of each of the various types of multiple-beam interferometer is similar. They differ mainly in physical form. Their common feature is that their fringes are much sharper than those in two-beam interferometers, thus improving both measuring accuracy and resolution. Multiple-beam interferometers are described in almost all textbooks on optics, such as that by Born and Wolf [2].

The heart of the Fabry–Perot interferometer is the etalon consisting of two flat plates separated by a distance d_s and aligned so that they are parallel to a very high degree of accuracy. The separation is usually maintained by a spacer ring made of Invar or quartz. The inner surfaces of the two plates are usually coated to enhance their reflectance.

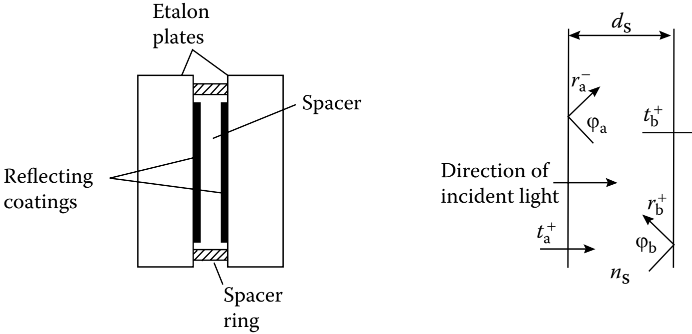

FIGURE 6.1
A Fabry–Perot etalon. The amplitude coefficients in the diagram are converted to the coefficients of irradiance in Equation 6.1 as shown in Equation 3.20.

Figure 6.1 shows an etalon in diagrammatic form. The amplitude reflection and transmission coefficients are defined as shown. The basic theory has already been given in Chapter 3, Equation 3.20, where it was shown that the transmission for a plane wave is given by

$$T = \frac{T_a T_b}{\left[(1-R_a^- R_b^+)^{1/2}\right]^2}\left[1+\frac{4(R_a^- R_b^+)^{1/2}}{\left[(1-R_a^- R_b^+)^{1/2}\right]^2}\sin^2\left(\frac{\varphi_a+\varphi_b}{2}-\delta\right)\right]^{-1} \quad (6.1)$$

where $\delta = (2\pi n_s d_s \cos\vartheta_s)/\lambda$, with d_s and n_s being the physical thickness and refractive index of the spacer layer. This is similar to Expression 3.20 except that δ has been modified to include oblique incidence ϑ_s. In order to simplify the discussion, let the reflectances and transmittances of the two surfaces be equal and let there be no phase change on reflection, i.e., let $\varphi_a = \varphi_b = 0$.

Then

$$T = \frac{T_s^2}{(1-R_s)^2}\frac{1}{1+\left[4R_s/(1-R_s)^2\right]\sin^2\delta} \quad (6.2)$$

and, writing

$$F = \frac{4R_s}{(1-R_s)^2} \quad (6.3)$$

Then

$$T = \frac{T_s^2}{(1-R_s)^2}\frac{1}{1+F\sin^2\delta} \quad (6.4)$$

If there is no absorption in the reflecting layers, then

$$1 - R_s = T_s$$

and

$$T = \frac{1}{1 + F\sin^2\delta} \tag{6.5}$$

The form of this function is shown in Figure 6.2 where T is plotted against δ. T is a maximum for $\delta = m\pi$, where $m = 0, \pm1, \pm2, \ldots$, and a minimum halfway between these values. The successive peaks of T are multiple-beam fringes and m is the order of the appropriate fringe.

As F increases, the widths of the fringes become very much narrower. The ratio of the separation of adjacent fringes to the half-width (the fringe width measured at half the peak transmittance) is called the "finesse" of the interferometer and is written $\mathcal{F}$. From Equation 6.5, the value of δ corresponding to a transmittance of half the peak value is given by

$$0.5 = \frac{1}{1 + F\sin^2\delta}$$

and if δ is sufficiently small so that we can replace $\sin^2\delta$ with δ^2, then

$$\delta = \frac{1}{F^{1/2}}$$

which is *half* the width of the fringe. The separation between values of δ representing successive fringes is π, so that

$$\mathcal{F} = \frac{\pi F^{1/2}}{2} = \frac{\pi R_s^{1/2}}{(1 - R_s)} \tag{6.6}$$

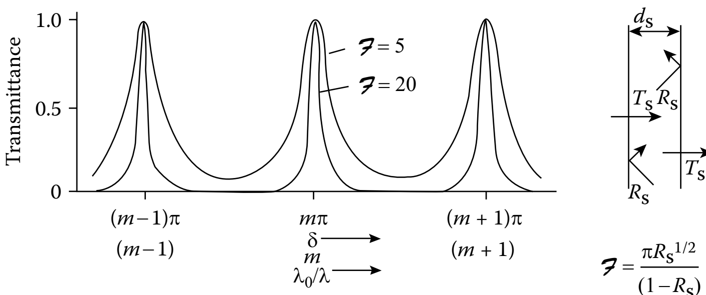

FIGURE 6.2
Fabry–Perot fringes.

The Fabry–Perot interferometer is used principally for the examination of the fine structure of spectral lines. The fringes are produced by passing light from the source in question through the interferometer. Measurement of the fringe pattern as a function of the physical parameters of the etalon can yield very precise values of the wavelengths of the various components of the line. The two most common arrangements are either to have the incident light highly collimated and incident normally, or at some constant angle, when the fringes can be scanned by varying the spacer thickness, or it is possible to keep the spacer thickness constant and scan the fringes by varying ϑ_s, the angle of incidence. Possible arrangements corresponding to these two methods are shown in Figure 6.3.

Practical considerations limit the achievable finesse to a maximum normally of around 25, or perhaps 50 in exceptional cases. This is due mainly to imperfections in the plates themselves. It is extremely difficult to manufacture a plate with flatness better than $\lambda/100$ at, say, 546 nm. Variations in flatness of the plates gives rise to local variations of d_s and hence δ, causing the fringes to shift. These variations should not be greater than the fringe width, otherwise the luminosity of the instrument will suffer. Chabbal [3] has considered this problem in great detail, but for our present purpose it

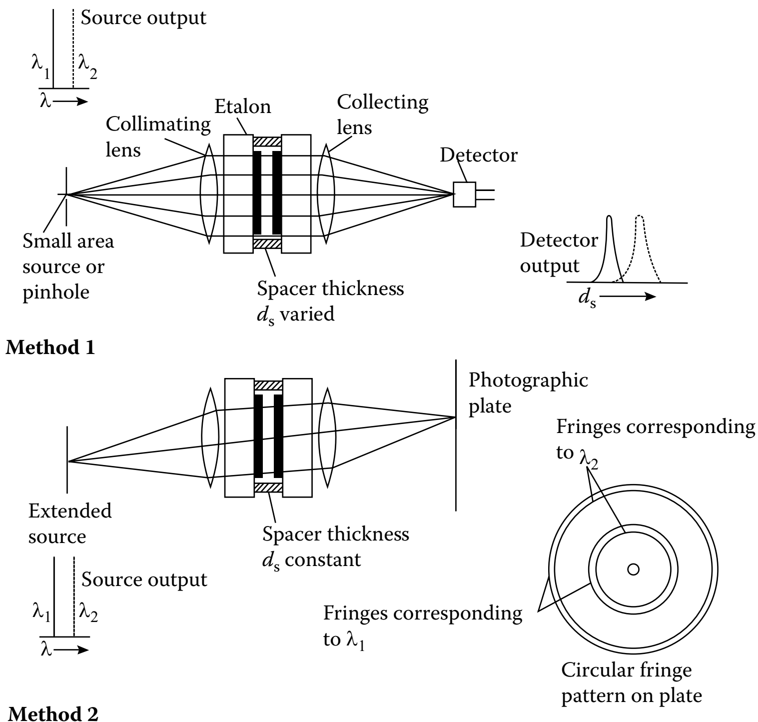

FIGURE 6.3
Two possible arrangements of a Fabry–Perot interferometer.

is sufficient to assume that, for a pair of $\lambda/100$ plates (i.e., having errors not greater than $\pm\lambda/200$ about the mean), the variation in thickness of the spacer layer will be of the order of $\pm\lambda/100$ about the mean. This will occur when the defects in the plates are in the form of either spherical depressions in both plates or else protrusions. This in turn means a change in δ of $\pm 2\pi/100$ corresponding to a total excursion of $2\pi/50$. Any decrease in fringe width below this will not increase the resolution of the system but merely reduce the overall luminosity, so that $2\pi/50$ represents a lower limit on the fringe width. Since the interval between fringes is π, this condition is equivalent to an upper limit on finesse of $\pi/(2\pi/50)$, i.e., 25. In more general terms, if the plates are good enough to limit the total thickness variation in the space to λ/p (not quite the same as saying that each plate is good to λ/p), then the finesse should be not greater than $p/2$.

The resolving power of an optical instrument is normally determined by the Rayleigh criterion that is particularly concerned with power distributions of the form

$$I(\delta) = \left[\frac{\sin(\delta/2)}{\delta/2}\right]^2 I_{\text{max}} \tag{6.7}$$

which are of a type produced by diffraction rather than interference effects. Two wavelengths are considered just resolved by the instrument if the power maximum of one component falls exactly over the first intensity zero of the other component. This implies that if the two components are of equal power, then, in the combined fringe pattern, the minimum that will exist between the two maxima will be of a power $8/\pi^2$ times that at either of them. In the Fabry–Perot interferometer the fringes are of rather different form, and the pattern of zeros and successively weaker maxima associated with the Equation 6.7 function is missing. The Rayleigh criterion cannot, therefore, be applied directly. Born and Wolf [2] suggest that a suitable alternative form of the criterion that could be applied in this case might be that two equally intense lines are just resolved when the resultant response between the peaks in the combined fringe pattern is $8/\pi^2$ that at either peak. On this basis, they have shown that the resolving power of the Fabry–Perot interferometer is

$$\frac{\lambda}{\Delta\lambda} = 0.97m\mathcal{F}$$

which is virtually indistinguishable from

$$\frac{\lambda}{\Delta\lambda} = m\mathcal{F} \tag{6.8}$$

and which is the ratio of the peak wavelength of the appropriate order to the half-width of the fringe. Thus, the half-width of the fringe is a most useful parameter because it is directly related to the resolution of the instrument in a most simple manner. We shall make much use of the concept of half-width in Chapter 8.

Since resolving power is the product of finesse and order number, a low finesse does not necessarily mean low resolution, but it does mean that to achieve high resolution the interferometer must be used in high order. This in its turn means that the separation of neighboring orders in terms of wavelength is small—in high order, this is given approximately by λ/m. If steps are not taken to limit the range of wavelengths accepted by the interferometer, then the interpretation of the fringe patterns becomes impossible. This limiting of the range can be achieved by using a suitable filter in series with the etalon. This filter could be a thin-film filter of a type discussed in Chapter 8. Another method is to use, in series with the etalon, other etalons of lower order, and hence resolving power, arranged so that the fringes coincide only at the wavelength of interest and at wavelengths very far removed. The wide fringe interval or, as it is also called, *free spectral range,* of the low-order, low-resolution instrument is thus combined with the high resolution and narrow free spectral range of the high-order instrument. A simpler and more convenient method, probably that most often used, involves a spectrograph and is generally used in conjunction with the second method of scanning the interferometer: variation of ϑ_s keeping d_s constant. The resolving power of the spectrograph need not be high and the entrance slit can be quite broad. It is usually placed where the photographic plate is in Figure 6.3, so that it accepts a broad strip down the center of the circular fringe pattern. The plate from the spectrograph then shows a low-resolution spectrum with a fringe pattern along each line corresponding to the fine-structure components within the line.

So far in our examination of the Fabry–Perot interferometer we have neglected to consider absorption in the reflecting coatings. Equation 6.4 contains the information we need.

$$T = \frac{T_s^2}{(1-R_s)^2}\frac{1}{1+F\sin^2\delta} \tag{6.4}$$

Let A_s be the absorptance of each coating. Then

$$1 = R_s + T_s + A_s$$

So that Equation 6.4 becomes

$$T = \frac{T_s^2}{(T_s+A_s)^2}\frac{1}{1+F\sin^2\delta}$$

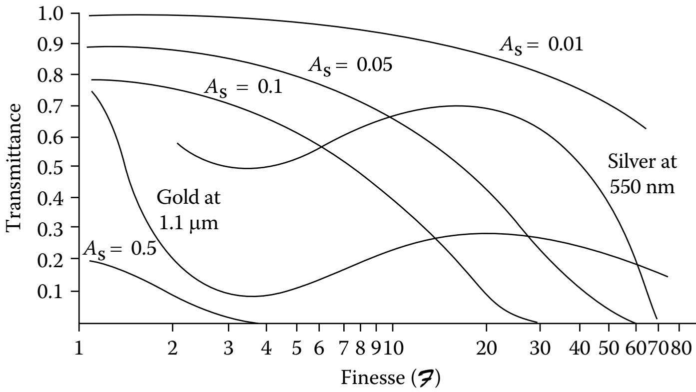

FIGURE 6.4
Etalon transmittance against finesse for various values of absorptance of the coatings.

i.e.

$$T = \frac{1}{(1 + A_s/T_s)^2} \frac{1}{1 + \sin^2 \delta} \tag{6.9}$$

Clearly the all-important parameter is A_s/T_s.

Curves are shown in Figure 6.4 connecting the transmittance of the etalon with finesse, given the absorptance of the coatings. It is possible on this diagram to plot the performance of any type of coating if the way in which R_s, T_s, and A_s vary is known. This has been done for silver layers at 550 nm and gold at 1.1 μm. The figures from which these curves were plotted were taken from Mayer [4]. Other sources of information, particularly on silver films, are available [5–7], and results may differ from those plotted in some respects. However, the curves are adequate for their primary purpose, which is to show that the performance of silver, the best metal of all for the visible and near infrared, begins to fall off rapidly beyond a finesse of 20 and is inadequate for the very best interferometer plates. An enormous improvement is possible with all-dielectric multilayer coatings.

6.2 Multilayer Dielectric Coatings

In Chapter 1, it was mentioned that a high reflectance can be obtained from a stack of quarter-wave dielectric layers of alternate high and low index. This is because the beams reflected from all the interfaces in the assembly are of equal phase when they reach the front surface, where they combine constructively. An expression is given in Section 3.1 for the optical admittance

of a series of quarter-waves. If n_H and n_L are the indices of the high- and low-index layers and if the stack is arranged so that the high-index layers are outermost at both sides, then

$$Y = \frac{n_H^{2p+2}}{n_L^{2p} n_{sub}} \tag{6.10}$$

where n_{sub} is the index of the substrate and $(2p + 1)$ is the number of layers in the stack.

The reflectance in air or free space is then

$$R = \left[\frac{1 - n_H^{2p+2}/\left(n_L^{2p} n_{sub}\right)}{1 + n_H^{2p+2}/\left(n_L^{2p} n_{sub}\right)} \right]^2 \tag{6.11}$$

The greater the number of layers, the greater is the reflectance. Maximum reflectance for a given odd number of layers is always obtained with the high-index layers outermost.

If

$$\frac{n_H^{2p+2}}{n_L^{2p} n_{sub}} > 1$$

then

$$R \simeq 1 - 4\frac{n_L^{2p} n_{sub}}{n_H^{2p+2}}$$

And

$$T \simeq 4\frac{n_L^{2p} n_{sub}}{n_H^{2p+2}} \tag{6.12}$$

which shows that when reflectance is high, then the addition of two extra layers reduces the transmittance by a factor of $(n_L/n_H)^2$.

Provided the materials are transparent, the absorption in a multilayer stack can be made very small indeed. We shall return later to this topic, but we can note here that in the visible region of the spectrum, the absorptance can be less than 0.01%.

Dielectric multilayers, however, suffer from two defects. The first, more of a complication than a fault, is that there is a variable change in phase associated with the reflection. The second, more serious, is that the high reflectance is obtained over a limited range of wavelengths only.

We can see, qualitatively, how the phase shift varies, using the admittance diagram. If, as is usual, the multilayer consists of an odd number of layers

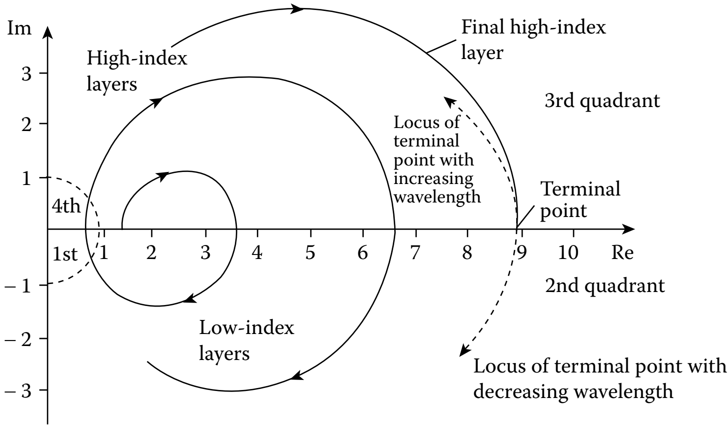

FIGURE 6.5
Admittance diagram for a quarter-wave stack ending with a high-index layer. The quadrants for the phase shift on reflection, φ, are marked on the diagram and correspond to those in Figure 3.1b. For decreasing wavelength, the terminal point moves into the region associated with values of φ in the second quadrant, while for increasing wavelength, φ moves into the third quadrant.

with high-index layers on the outside, then at the outer surface of the final layer the admittance will be on the real axis with a high positive value. This is shown diagrammatically in Figure 6.5. The quadrants are marked on the figure in the same way as Figure 3.1b. Clearly, the phase shift associated with the coating is π at the reference wavelength for which all the layers are quarter-waves. For slightly longer wavelengths, the circles shrink slightly from the semicircles associated with the quarter-waves and so the terminal point of the locus moves upwards into the region associated with the third quadrant. If the wavelength decreases, the terminal point moves into the second quadrant. The phase shift, therefore, increases with wavelength. If, on the other hand, the coating ends with a quarter-wave of low-index material so that at the reference wavelength the admittance is real, but less than unity, then the phase shift on reflection will be zero, moving into the first quadrant as the wavelength increases or into the fourth as it decreases.

To investigate the effect of the phase change, and also of the dispersion of phase change, on the operation of the interferometer, we return to the original formula, Equation 6.1. In our analysis we made the assumption that the phase change on reflection was zero and concluded that transmission peaks would be obtained at wavelengths given by

$$\delta = m\pi$$

where $m = 0, \pm 1, \pm 2, \ldots$ If we now permit φ_a and φ_b to be non-zero, then the positions of the transmission peaks will be given by

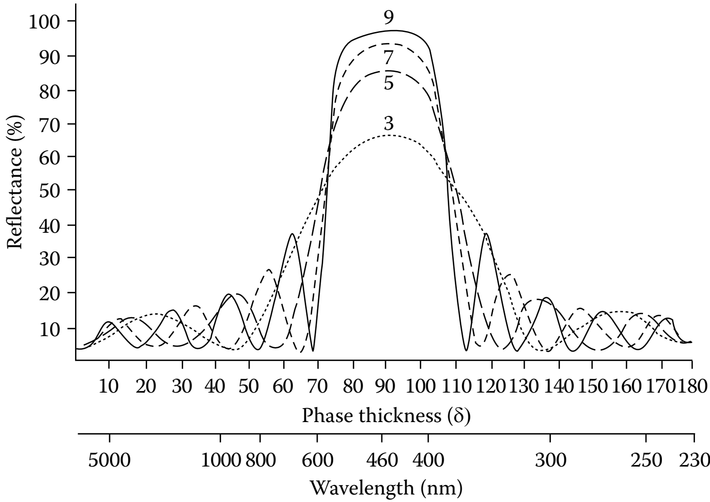

FIGURE 6.6
Reflectance R for normal incidence of alternating $\lambda/4$ layers of high-index (n_H = 2.3) and low-index (n_L = 1.38) dielectric materials on a transparent substrate (n_{sub} = 1.52) as a function of the phase thickness $\delta = 2\pi nd/\lambda$ (*upper scale*) or the wavelength λ for λ_0 = 460 nm (*lower scale*). The number of layers is shown as a parameter on the curves. (After Penselin, S. and Steudel, A., *Zeitschrift für Physik*, 142, 21–41, 1955.).

$$\delta = q\pi - \frac{\varphi_a + \varphi_b}{2}$$

where $q = 0, \pm 1, \pm 2, \ldots$ The effect of the phase changes φ_a and φ_b is simply to shift the positions of the peak wavelengths. If the order is fairly high (and as we have seen most interferometers are used in high order), the shift is quite small. The effect of the phase change, and of any phase dispersion, can be completely eliminated from the determination of wavelength with the interferometer, by a method described by Stanley and Andrew [8] involving the use of two spacers of different thickness.

The behavior of a typical quarter-wave stack is shown in Figure 6.6. The high-reflection zone can be seen to be limited in extent. On either side of a plateau, the reflectance falls abruptly to a low, oscillatory value. The addition of extra layers does not affect the width of the zone of high reflectance but increases the reflectance within it and the number of oscillations outside.

The width of the high-reflectance zone can be computed using the following method. If a multilayer consists of q repetitions of a fundamental period consisting of two, three, or indeed any number of layers, then the characteristic matrix of the multilayer is given by

$$[\mathcal{M}] = [M]^q$$

where $[M]$ is the matrix of the fundamental period. Let $[M]$ be written

$$\begin{bmatrix} M_{11} & M_{12} \\ M_{21} & M_{22} \end{bmatrix}$$

Then it can be shown that for wavelengths that satisfy

$$\left| \frac{M_{11} + M_{22}}{2} \right| \geq 1 \tag{6.13}$$

the reflectance increases steadily with increasing number of periods. This is therefore the condition that a high-reflectance zone should exist, and the boundaries are given by

$$\left| \frac{M_{11} + M_{22}}{2} \right| = 1 \tag{6.14}$$

A rigorous proof of this result is somewhat involved. One version is given by Born and Wolf [2], and another by Welford [10]. A justification of the result, rather than a proof, was given by Epstein [11] and it is his method that is followed here.

If the characteristic matrix of a thin-film assembly on a substrate of admittance η_{sub} is given by

$$\begin{bmatrix} B \\ C \end{bmatrix}$$

then if η_{sub} is real, Equation 2.115 shows that

$$T = \frac{4\eta_0\eta_{sub}}{(\eta_0 B + C)(\eta_0 B + C)^*} = \frac{4\eta_0\eta_{sub}}{|\eta_0 B + C|^2}$$

where η_0 is the admittance of the incident medium. Let the characteristic matrix of the assembly of thin films be, as above,

$$[\mathcal{M}] = \begin{bmatrix} \mathcal{M}_{11} & \mathcal{M}_{12} \\ \mathcal{M}_{21} & \mathcal{M}_{22} \end{bmatrix}$$

Then

$$\begin{bmatrix} B \\ C \end{bmatrix} = \begin{bmatrix} \mathcal{M}_{11} & \mathcal{M}_{12} \\ \mathcal{M}_{21} & \mathcal{M}_{22} \end{bmatrix} \begin{bmatrix} 1 \\ \eta_{sub} \end{bmatrix} = \begin{bmatrix} \mathcal{M}_{11} + \eta_{sub}\mathcal{M}_{12} \\ \eta_{sub}\mathcal{M}_{22} + \mathcal{M}_{21} \end{bmatrix}$$

giving

$$T = \frac{4\eta_0\eta_{sub}}{\left|\eta_0(\mathcal{M}_{11} + \eta_{sub}\mathcal{M}_{12}) + \eta_{sub}\mathcal{M}_{22} + \mathcal{M}_{21}\right|^2}$$

If there is no absorption, $\mathcal{M}_{11}$ and $\mathcal{M}_{22}$ are real and $\mathcal{M}_{12}$ and $\mathcal{M}_{21}$ are imaginary. Then

$$T = \frac{4\eta_0\eta_{sub}}{\left|\eta_0\mathcal{M}_{11} + \eta_{sub}\mathcal{M}_{22}\right|^2 + \left|\eta_0\eta_{sub}\mathcal{M}_{12} + \mathcal{M}_{21}\right|^2} \tag{6.15}$$

In the absence of the multilayer, the transmittance of the substrate will be

$$T_{sub} = \frac{4\eta_0\eta_{sub}}{(\eta_0 + \eta_{sub})^2} \tag{6.16}$$

To simplify the discussion, let $\eta_0 = \eta_{\mathrm{sub}}$. Then, from equations (6.15) and (6.16), T will be less than T_{sub} if

$$\left|\frac{\mathcal{M}_{11} + \mathcal{M}_{22}}{2}\right| > 1$$

Regardless of the value of M_{12} and M_{21}. Now if

$$\left|\frac{M_{11} + M_{22}}{2}\right| > 1$$

where $[M]$ is the matrix of the fundamental period in the multilayer; then, generally, as the number of periods increases, that is, as q tends to infinity,

$$\left|\frac{\mathcal{M}_{11} + \mathcal{M}_{22}}{2}\right| \to \infty$$

That this is plausible may be seen by first of all squaring $[M]$, whence, writing N_{ab} for the terms in $[M]^2$,

$$N_{11} + N_{22} = M_{11}^2 + 2M_{12}M_{21} + M_{22}^2$$

Since the determinant of $[M] = 1$,

$$2M_{12}M_{21} = 2M_{11}M_{22} - 2$$

so that

$$N_{11}+N_{22}=M_{11}^2+2M_{11}M_{22}+M_{22}^2-2=(M_{11}+M_{22})^2-2$$

Let

$$\left|\frac{M_{11}+M_{22}}{2}\right|=1+\varepsilon$$

Then

$$N_{11}+N_{22}=(2+2\varepsilon)^2-2=2+8\varepsilon+4\varepsilon^2$$

so that by squaring [*M*] and resquaring the result and so on, it can be seen that

$$\left|\frac{\mathcal{M}_{11}+\mathcal{M}_{22}}{2}\right|\to\infty \quad \text{as } q\to\infty$$

The quarter-wave stack, which we have so far been considering, consists of a number of two-layer periods, together with one extra high-index layer. Each period has a characteristic matrix:

$$[M]=\begin{bmatrix}\cos\delta & (i\sin\delta)/n_L\\ in_L\sin\delta & \cos\delta\end{bmatrix}\begin{bmatrix}\cos\delta & (i\sin\delta)/n_H\\ in_H\sin\delta & \cos\delta\end{bmatrix}$$

Since the two layers are of equal optical thickness, δ, without any suffix, has been used for phase thickness.

$$\frac{M_{11}+M_{22}}{2}=\cos^2\delta-\frac{1}{2}\left(\frac{n_H}{n_L}+\frac{n_L}{n_H}\right)\sin^2\delta$$

The right side of this expression cannot be greater than +1, and so to find the boundaries of the high-reflectance zone we must set

$$-1=\cos^2\delta-\frac{1}{2}\left(\frac{n_H}{n_L}+\frac{n_L}{n_H}\right)\sin^2\delta_e$$

which, with some rearrangement, gives

$$\cos^2\delta_e=\left(\frac{n_H-n_L}{n_H+n_L}\right)^2$$

Now,

$$\delta = \frac{\pi}{2}\frac{\lambda_0}{\lambda} = \frac{\pi}{2}g$$

where λ_0 is, as usual, the wavelength for which the layers have quarter-wave optical thickness and g is λ_0/λ. Let the edges of the high-reflectance zone be given by

$$\delta_e = \frac{\pi}{2}g_e = \frac{\pi}{2}(1 \pm \Delta g)$$

so that

$$\cos^2 \delta_e = \sin^2\left(\pm\frac{\pi\Delta g}{2}\right)$$

and the width of the zone is $2\Delta g$. Then

$$\Delta g = \frac{2}{\pi}\arcsin\left(\frac{n_H - n_L}{n_H + n_L}\right)$$

This shows that the width of the zone is a function only of the indices of the two materials used in the construction of the multilayer. The higher the ratio, the greater is the width of the zone. Figure 6.7 shows Δg plotted against the ratio of refractive indices.

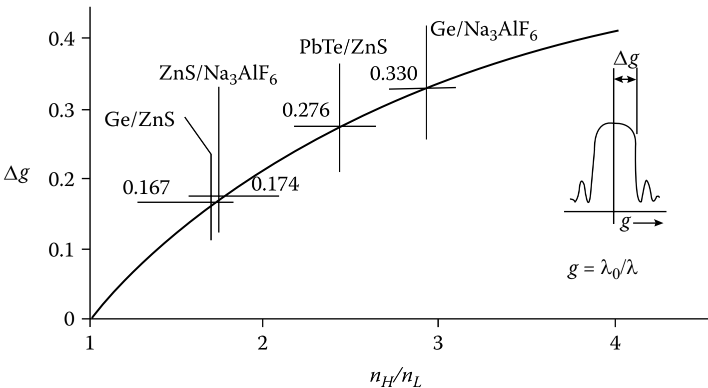

FIGURE 6.7
The width of the high-reflectance zone of a quarter-wave stack plotted against the ratio of the refractive indices, n_H/n_L.

So far we have considered only the fundamental reflectance zone for which all the layers are one-quarter of a wavelength thick. It is obvious that high-reflectance zones will exist at all wavelengths for which the layers are an odd number of quarter-wavelengths thick. That is, if the center wavelength of the fundamental zone is λ_0, then there will also be high-reflectance zones with center wavelengths $\lambda_0/3$, $\lambda_0/5$, $\lambda_0/7$, $\lambda_0/9$, and so on.

At wavelengths where the layers have optical thickness equivalent to an even number of quarter-waves, which is the same as an integral number of half-waves, the layers will all be absentee layers and the reflectance will be that of the uncoated substrate.

The analysis determining Δg for the fundamental zone is valid also for all higher-order zones so that the boundaries are given by

$$g_0 \pm \Delta g,\ 3g_0 \pm \Delta g,\ 5g_0 \pm \Delta g$$

and so on. Higher-order reflectance curves are shown in Figure 6.8.

The materials used in the visible region depend very much on the application. Zinc sulfide plus cryolite is an old combination that is still often used. Although these materials present rather poorer environmental resistance than coatings based on oxides, they do possess some advantages. Both materials are easy to evaporate from simple thermal sources and give high optical performance even when evaporated onto a cold substrate. This means that the risk of distortion of very accurate interferometer plates through heating is eliminated. The layers are rather susceptible to attack by moisture and care should be taken to avoid any condensation, such as might happen when cold plates are exposed to a warmer atmosphere; otherwise, the coatings will be ruined. Touching by fingers is also to be avoided at all costs.

The softness of the coatings can, however, be turned to advantage. Etalon plates are extremely expensive and if the coatings are easily removable, the plates can be recoated for use at other wavelengths. Prolonged soaking in warm water is often sufficient to remove zinc sulfide and cryolite coatings. In cases where the coatings are not completely removed in this way, the addition of two or three drops of hydrochloric acid to the water will

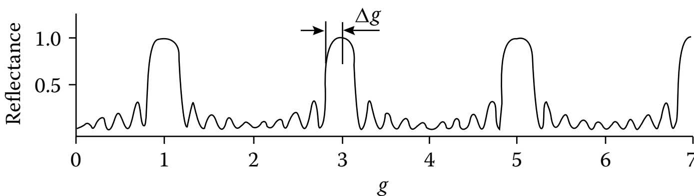

FIGURE 6.8
Reflectance of a nine-layer stack of zinc sulfide (n_H = 2.35) and cryolite (n_L = 1.35) on glass (n_{sub} = 1.52) showing the high-reflectance bands.

quickly complete the operation. This should obviously be done with great care and the plates immediately rinsed in running water to avoid any risk of surface damage.

For more demanding applications, particularly where the coating may have to be exposed to a more aggressive environment, hard oxide layers would normally be chosen, silicon dioxide as low index and titanium dioxide, tantalum pentoxide, or niobium pentoxide as high-index materials. Hafnium oxide is frequently used as high-index material when high laser damage threshold is a requirement. Levels of absorption of less than 0.5% can be achieved with ease, 0.1% with some extra care, and 0.001% with minute attention to detail. Levels still lower are required for the reflecting structures in more advanced narrowband filters, dealt with in a later chapter. In thermal evaporation, the oxide materials demand higher source temperatures and the simple directly heated boat sources applicable to zinc sulfide and cryolite must be replaced by electron beam sources, described in more detail in a later chapter. Magnesium fluoride, the tough material much used in antireflection coatings for the visible region, has an attractive low index of refraction but does suffer from rather high intrinsic tensile stress, and so can be a somewhat unreliable material in high-reflectance multilayers.

Zinc sulfide absorbs in the ultraviolet region. In the 300- to 400-nm region, it can be replaced by antimony trioxide that, with cryolite, can be evaporated on to a cold substrate from simple thermal sources. This combination should be handled at least as carefully as zinc sulfide and cryolite. Tougher materials are hafnium dioxide and silicon dioxide.

For the infrared, germanium for the region beyond 1.8 μm with an index around 4.0, or lead telluride for the region beyond 3.5 μm, with an index around 5.7, is a good high-index material for filter applications. Both are useful beyond 12 μm. Zinc sulfide, with an index of 2.35, is a useful low-index material out to 20 μm. In the near infrared, silicon monoxide is frequently used as the low-index material accompanying germanium. Thorium fluoride has many desirable properties as a low-index material except that it is radioactive and so its use is limited to those few applications where it is still necessary, notably high-power high-reflectance coatings for CO_2 laser applications where it is frequently coupled with zinc selenide as high-index material. Germanium, unfortunately, along with most high-index semiconductors, suffers from an extinction coefficient that increases significantly with temperature and so it exhibits thermal runaway in high-power applications. Many fluorides, cerium fluoride and yttrium fluoride, for example, and mixtures of fluorides are also used as low-index materials out to around 12 μm. Materials are dealt with in much more detail later.

The losses experienced in the coatings are as much a function of the technique used as of the materials themselves. Great care in preparing the machine and substrates is needed. Everything should be scrupulously clean. Two papers that are useful if the maximum performance is required are by

Perry [12] and Heitmann [13]. Both these authors are concerned with laser mirrors, where losses must be of an even lower order than in the case of the Fabry–Perot interferometer.

6.2.1 All-Dielectric Multilayers with Extended High-Reflectance Zones

The limited range over which high reflectance can be achieved with a quarter-wave stack is a difficulty in some applications, and a number of attempts have been made to extend the range by altering the design. Most of these have involved the staggering of the thicknesses of successive layers throughout the stack to form a regular progression, the aim being to ensure that at any wavelength in a fairly wide range, enough of the layers in the stack have optical thickness sufficiently near a quarter-wave to give high reflectance.

Penselin and Steudel [9] were probably the first workers to try this method. They produced a number of multilayers where the layer thicknesses were in a harmonic progression. Their best 13-layer results are shown as curve B in Figure 6.9. Baumeister and Stone [14] developed a simple computer-based technique to optimize their reflectors. Curve C in Figure 6.9 represents their best 15-layer design.

Heavens and Liddell [15] used a similar approach. By this time computers had developed further, but the user still had to book time in advance and travel to the machine. They were able to compute a large number of reflection curves for assemblies of layers for which the thicknesses were in either arithmetic or geometric progression. With the same number of layers, the geometric progression gave very slightly broader reflection zones. In the computations the high index was assumed to be 2.36 (zinc sulfide), the low index 1.39 (magnesium fluoride), and the substrate index 1.53 (glass). Values of common difference for the arithmetic progression ranged from −0.05 to

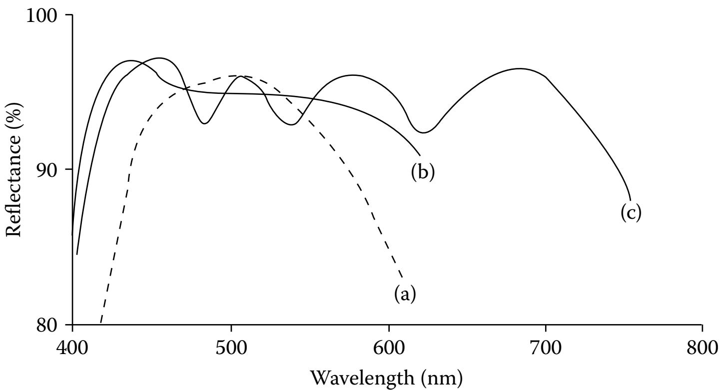

FIGURE 6.9
Broadband multilayer reflectors. (a) Computed curve for a seven-layer quarter-wave stack. (b) Measured reflectance of a 13-layer broadband design (Penselin, S. and Steudel, A., *Zeitschrift für Physik*, 142, 21–41, 1955). (c) Measured reflectance of a 15-layer alternative design (Baumeister, P.W. and Stone, J.M., *Journal of the Optical Society of America*, 46, 228–229, 1956).

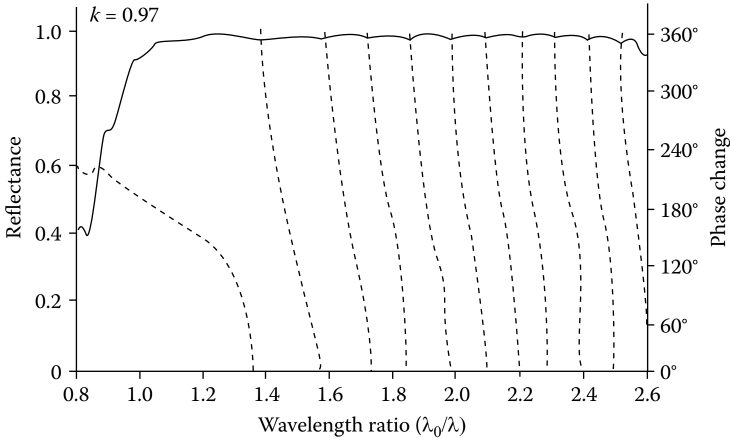

FIGURE 6.10
Reflectance of a 35-layer geometric stack on glass. Reflectance (*full curve*) and phase change on reflection (*broken curve*); $n_0 = 1.00$, $n_H = 2.36$, $n_L = 1.39$, $n_{sub} = 1.53$, common difference $k = 0.97$. (After Heavens, O.S. and Liddell, H.M., *Applied Optics*, 5, 373–376, 1966.)

+0.05, and for the common ratio of the geometric progression, from 0.95 to 1.05. A 35-layer geometric curve is shown in Figure 6.10.

As in the case of antireflection coatings, computer refinement can be used to improve an initial, less-satisfactory performance. Baumeister and Stone [14,16] pioneered the use of this technique in optical thin films. By trial and error, they arrived at a preliminary 15-layer design with high reflectance over an extended range but with unacceptably large dips. The aim was to produce a reflectance of around 95% using zinc sulfide (n = 2.3) and cryolite (n = 1.35) on glass (n not given), and the final result is shown as curve C of Figure 6.9 with design details listed in Table 6.1. Computer limitations forced the use of a very coarse net for the relaxation—only five points were involved—and, in addition, arbitrary relationships between the various layers were used to reduce the number of independent variables to five. This was in 1956. The computer was described as an IBM card-programmed calculator. Since then, advances in the technique have kept pace with the increasing power of computers. By 1971, Pelletier et al. [17] described the computer design and refinement of reflectors like that shown in Figure 6.11 where dispersion of the optical properties of the materials was included in the calculations.

A particularly simple method is to place a quarter-wave stack for one wavelength on top of another for a different wavelength. This process has been considered in detail by Turner and Baumeister [18]. Unfortunately, if each stack consists of an odd number of layers with outermost layers of the same index, then a peak of transmission is found in the center of the high-reflectance zone. This peak arises because the two stacks act in much the same way as Fabry–Perot reflectors. In a Fabry–Perot interferometer, as we have seen, provided the reflectances and transmittances of the structures on

TABLE 6.1

The 15-Layer Baumeister and Stone Design [14]

Layer Number	Material	Index	Wavelength for which Layer is a Quarter-Wave (nm)
	Air incident medium	1.00	Massive
1	ZnS	2.30	414.0
2	Na_3AlF_6	1.35	414.0
3	ZnS	2.30	414.0
4	Na_3AlF_6	1.35	434.8
5	ZnS	2.30	463.7
6	Na_3AlF_6	1.35	463.7
7	ZnS	2.30	520.5
8	Na_3AlF_6	1.35	517.0
9	ZnS	2.30	626.2
10	Na_3AlF_6	1.35	701.3
11	ZnS	2.30	575.7
12	Na_3AlF_6	1.35	666.7
13	ZnS	2.30	690.8
14	Na_3AlF_6	1.35	690.8
15	ZnS	2.30	690.8
	Glass		Massive

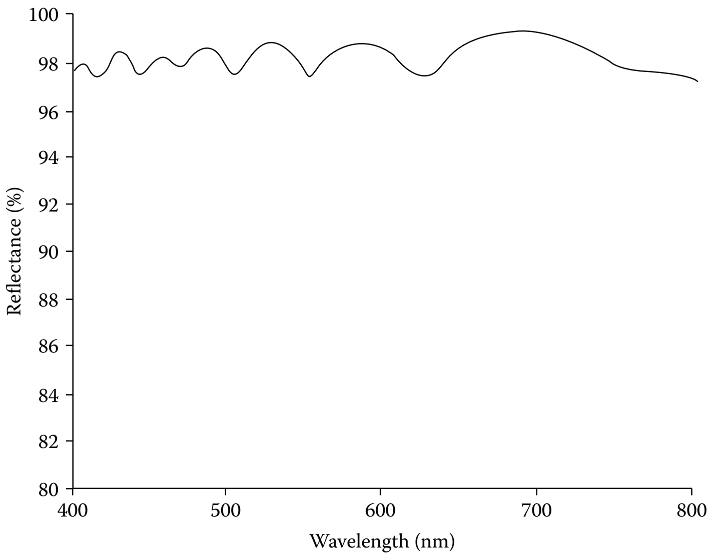

FIGURE 6.11
The calculated performance and the design of a 21-layer high-reflectance coating for the visible and near infrared. Dispersion of the indices of the materials has been taken into account in both design by refinement and in performance calculation. (After Pelletier, E., Klapisch, M., and Giacomo, P., *Nouvelle Revue d'Optique Appliquée*, 2, 247–254, 1971.)

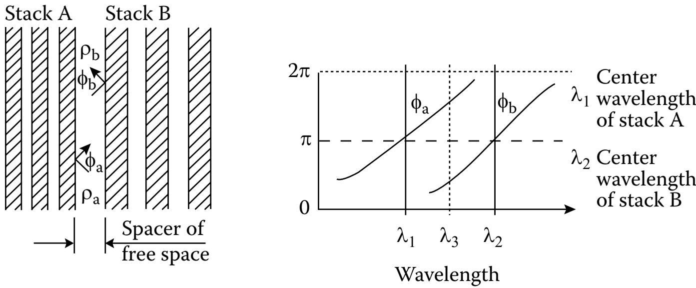

FIGURE 6.12
At λ_3, $(\varphi_a + \varphi_b) = \pi$. Also, by symmetry, at λ_3, $(\lambda_2/\lambda_3) - 1 = 1 - (\lambda_1/\lambda_3)$, i.e., $\lambda_3 = (\lambda_1 + \lambda_2)/2$.

either side of the spacer layer are equal in magnitude, then the transmittance of the assembly will be unity for

$$\frac{\varphi_a + \varphi_b - 2\delta}{2} = q\pi$$

where $q = 0, \pm 1, \pm 2, \ldots$

The situation is sketched in Figure 6.12. The assembly of the two stacks is divided at the boundary between them and spaced apart leaving a layer of free space that forms a spacer layer. The phase angle φ associated with each reflection coefficient is also shown. At one wavelength, given by the mean of the center wavelengths of the stacks, it can be seen that

$$\varphi_a + \varphi_b = 2\pi$$

Also by symmetry, at this wavelength the reflectances of both stacks are equal and, therefore, the condition for unity transmittance will be completely satisfied if $2\delta = 0$—that is, if the intervening layer is allowed to shrink until it vanishes completely. A peak of transmission will always exist, therefore, if two stacks are deposited so that they are overlapping at the mean of the two reference wavelengths. This is shown in Figure 6.13, which is reproduced from Turner and Baumeister [18]. Curves A and B are measured reflectance of two high-reflectance quarter-wave stacks, each with the same odd number of layers, starting and finishing with a high-index layer. Curve C shows the measured reflectance of a coating made by combining the two stacks. The peak of transmission can be clearly seen as a dip in the reflectance curve. Experimental errors, either in monitoring or measurement, prevent its reaching the theoretical minimum.

The dip can be removed by destroying the relationship

$$\frac{\varphi_a + \varphi_b - 2\delta}{2} = q\pi$$

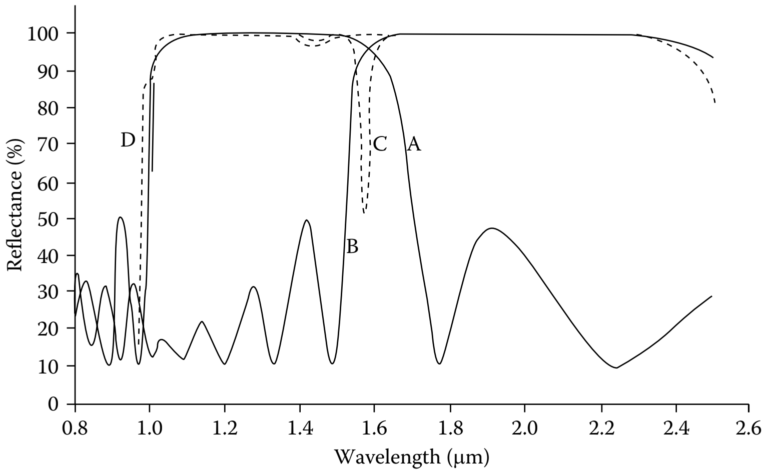

FIGURE 6.13
Measured reflectances of two quarter-wave stacks with slightly overlapping high-reflectance bands. Individual stacks, *full curves*: curve A: A|0.8(*HLHLHLHLHLH*)|G, curve B: A|1.2(HLHLHLHLHLH)|G. When these are combined in a single coating, there is a minimum in the overlap region resulting from the condition in Figure 6.12: curve C (*broken*): A|0.8(HLH LHLHLH) 1.2(HLHLHLHLHLH)|G. An inserted *L* layer eliminates the minimum by destroying the π phase shift. Curve D (*dotted*): A|0.8(HLHLHLHLHLH) *L* 1.2(HLHLHLHLHLH)|G. *G* denotes the glass substrate (n = 1.52), *A* the air incident medium (n = 1.00), *H* the stibnite high-index films, and *L* the chiolite low-index films. *H* and *L* are quarter-wave thicknesses at the reference wavelength, λ_0, of 1.6 μm. (After Turner, A.F. and Baumeister. P.W., *Applied Optics*, 5, 69–76, 1966.)

in the region where both stacks have high reflectance. Turner and Baumeister [18] achieved the result quite simply by adding a low-index layer, one quarter-wave thick at the mean wavelength, in between the stacks. This gave value for δ of $\pi/2$ and for $(\varphi_a + \varphi_b - 2\delta)/2$ of $\pi/2$, which corresponds to minimum possible transmission and maximum reflectance. This is illustrated by curve D. The dip has disappeared completely, leaving a broad flat-topped reflectance curve.

Turner and Baumeister [18] have also considered the design of broadband reflectors from a slightly different point of view and achieved similar results to the above, although the reasoning is completely different. If a stack is made up of a number of symmetrical periods such as

$$\frac{H}{2}L\frac{H}{2} \quad \text{or} \quad \frac{L}{2}H\frac{L}{2}$$

it can be represented mathematically by a single layer of thickness similar to the actual thickness of the multilayer and with a real optical admittance. This relationship holds good for all regions except the zones of high reflectance where the thickness and optical admittance are both imaginary. This result has already been referred to in Chapter 4 and will be examined

in much greater detail in the following two chapters. For our present purpose, it is sufficient to note that the relationship does exist. If a single layer of real refractive index is deposited on top of a 100% reflector, no interference maxima and minima can possibly exist. For reflectors falling short of the 100% condition, maxima and minima can exist but are very weak. Thus, in the region where the overlapping stack has a real refractive index, the high reflectance of the lower stack remains virtually unchanged, provided enough layers are used. The high-reflectance zones can either just touch without overlapping, in which case no reflectance minima will exist, or overlap, in which case the minima will be suppressed because the central layer, composed of an eighth-wave from each stack, is a quarter-wavelength thick at the mean of the two monitoring wavelengths, and, as has been shown above, this effectively removes any reflectance minima. Figure 6.14a shows the measured reflectance of two stacks

$$\left(\frac{L}{2}H\frac{L}{2}\right)^4$$

on a barium fluoride substrate together with the measured reflectance of two similar stacks superimposed on the same substrate in such a way that the high-reflectance zones just touch.

6.2.2 Coating Uniformity Requirements

One feature of the broadband reflectors that we have been considering is that the change in phase on reflection varies very rapidly with wavelength, much more rapidly than in the case of the simple quarter-wave stack. The difficulty that this could cause if such coatings were used in the determination of wavelength in a Fabry–Perot interferometer has frequently been mentioned. The method proposed by Stanley and Andrew [8] that uses two spacers does completely eliminate the effect of even the most rapid phase change with wavelength, but there is another effect, the subject of a dramatic report by Ramsay and Ciddor [19]. They used a 13-layer coating of a design similar to that of Baumeister and Stone and listed in Table 6.2.

The coating was deposited with layer uniformity in the region of 1–2 nm from center to edge of the 75 mm diameter plates. When tested, however, after coating, the plates appeared to be $\lambda/60$ concave at 546 nm, very uniform at 588 nm, and $\lambda/10$ convex at 644 nm. This curvature is, of course, only apparent. Tests on the plates using silver layers showed that they were probably $\lambda/60$ concave. The apparent curvature results from changes both in the thickness of the coatings and in the phase change on reflection.

In fact, a theory sufficient to explain the effect was published, together with some estimates of required uniformity, by Giacomo [20] in 1958. He obtained the result that the apparent variation of spacer thickness (measured

TABLE 6.2
Design of the Ramsay and Ciddor Reflector

Layer Number	Material	Wavelength for which Layer is a Quarter-Wave (nm)
	Air incident medium	Massive
1	ZnS	454
2	Na_3AlF_6	355
3	ZnS	385
4	Na_3AlF_6	392
5	ZnS	571
6	Na_3AlF_6	535
7	ZnS	539
8	Na_3AlF_6	573
9	ZnS	562
10	Na_3AlF_6	594
11	ZnS	720
12	Na_3AlF_6	671
13	ZnS	589
	Fused silica substrate	

in units of phase) was equal to the error in uniformity of the coating (measured as the variation in physical thickness) times a factor

$$\left(\frac{\nu}{e}\frac{\partial\varphi}{\partial\nu}+4\pi\nu\right)$$

where e is the total thickness of the coating (physical thickness), $\nu = 1/\lambda$ is the wave number, and φ is the phase change on reflection at the surface of the coating. Another way of stating the result is to take $\Delta\rho_m$ as the maximum allowable error in spacer thickness (measured in units of phase) due to this cause, and then the uniformity in coating must be better than

$$\frac{\Delta e}{e}=\frac{\Delta\rho_m}{\left[(\partial\varphi/\partial\nu)+4\pi e\right]\nu}$$

Giacomo showed that the two terms in the expression, $\partial\varphi/\partial\nu$ (which is generally negative) and $4\pi e$, could cancel, or partially cancel, so that some designs of coating would be more sensitive to uniformity errors than others. Ramsay and Ciddor [19] carried this further by pointing out that the two terms in the expression vary in magnitude throughout the high-reflectance zone of the coating, and, although the cancellation or partial cancellation does occur, in addition, the varying magnitudes mean that it is possible in some cases

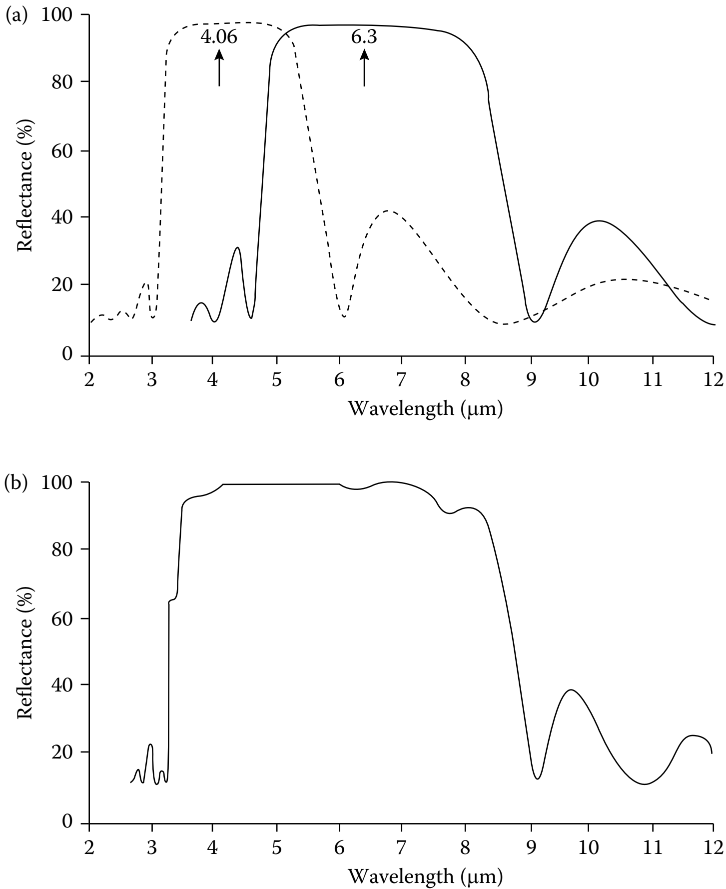

FIGURE 6.14
(a) Measured reflectances of two stacks A|(0.5*L* *H* 0.5*L*)^4|G on BaF_2 substrates. *G* denotes the BaF_2\$ and A air; *H* and *L* are films of stibnite and chiolite a quarter-wave thick at reference wavelengths λ_0 = 4.06 μm (*broken curve*) or 6.3 μm (*full curve*). (After Turner and Baumeister [18].) (b) Measured reflectance of the two stacks of (a) superimposed in a single coating for an extended high-reflectance region. (After Turner, A.F. and Baumeister. P.W., *Applied Optics*, 5, 69–76, 1966.)

for the apparent curvature due to uniformity errors to vary from concave to convex or vice versa throughout the range. This is so for the particular coating they considered, and it is this change in apparent curvature that is particularly awkward, implying that the interferometer must be tested for flatness over the entire working range, not, as is normal, at one convenient wavelength.

For the conventional quarter-wave coating, the magnitude of $\partial\varphi/\partial\nu$ falls far short of $4\pi e$; for example, in the case of a seven-layer coating of zinc sulfide and cryolite, for the visible region $\partial\varphi/\partial\nu$ is only –1.5 μm compared with $4\pi e$ of around +21.5 μm, and the uniformity that is required can readily be

calculated from the finesse requirement and the physical thickness of the coating, neglecting the effect of the variations in phase angle altogether. In the case of the broadband multilayer, however, the magnitude of $\partial\varphi/\partial\nu$ is very much greater, and at some wavelengths will exceed the value of $4\pi e$. For example, Giacomo quotes a case where $\partial\varphi/\partial\nu$ reached –125 μm, completely swamping the thickness effect, $4\pi e$. Heavens and Liddell [15] quote values of $\partial\varphi/\partial\nu$ varying from 10 to 26 μm for the staggered multilayers. The change in apparent curvature can therefore occur with these staggered systems, and it is dangerous to attempt to calculate the required uniformity simply from the coating thickness and the finesse requirement. An analysis that is very similar in certain respects, especially in the end result, has been carried out for random errors in the layers of certain types of band-pass filters and is considered in Chapter 8.

One point that does arise is the possibility of designing a coating where the two terms cancel almost completely throughout the entire working range. This is mentioned by Ramsay and Ciddor [19]. Since then, Ciddor [21] has carried this one stage further and produced several possible designs. Particularly successful is a design for a reflector to give approximately 75% reflectance over the major part of the visible, which is approximately three times less sensitive to thickness variations than would be the case with a reflector exhibiting no phase change with change in thickness. The design is intended for film indices of 2.30 and 1.35 on a substrate of index 1.46, corresponding to zinc sulfide and cryolite on fused silica. The thicknesses are given in Table 6.3. The reflectance is constant within around ±2% over the region 650 nm to 400 nm, and an interferometer plate with such a coating would behave as if it were much flatter than the purely geometrical lack of uniformity of the coating would suggest.

TABLE 6.3

Ciddor's Design of Reflector

Layer Number	Index	Wavelength for which Layer is a Quarter-Wave (nm)
	1.00	Massive
1	1.35	309
2	2.30	866
3	1.35	969
4	2.30	436
5	1.35	521
6	2.30	369
7	1.35	484
8	2.30	441
9	1.35	795
10	2.30	768
	1.46	Massive—substrate

6.3 Losses

If lossless materials are used, then the reflectance attainable by a quarter-wave stack depends solely on the number of layers. If the reflectance is high, then the addition of a further pair of layers reduces the transmittance by a factor $(n_L/n_H)^2$. In practice, the reflectance that can be ultimately achieved is limited by losses in the layers. These losses can be scattering or absorption.

Scattering losses are principally due to defects such as dust in the layers or to surface roughness, and techniques for reducing them are essentially attention to detail and good housekeeping. Absorption losses are a property of the material, and may be intrinsic or due to impurities or to composition or to structure. Absorption losses are related to the extinction coefficient of the material, and it is useful to consider the absorption losses of a quarter-wave stack composed of weakly absorbing layers having small but non-zero extinction coefficients. Expressions for this have been derived by several workers. The technique we use here is adapted from an approach devised by Hemingway and Lissberger [22].

We use the concept of potential transmittance introduced in Chapter 2. We split the multilayer into subassemblies of single layers, each with its own value of potential transmittance. The potential transmittance of the assembly is then the product of the individual transmittances.

For the entire multilayer, we can write

$$\psi = \frac{T}{1-R}$$

Then, if A is the absorptance

$$1-\psi = \frac{1-R-T}{1-R} = \frac{A}{1-R}$$

and

$$A = (1-R)(1-\psi)$$

Now $0 \le \psi \le 1$, so we can introduce a quantity $\mathcal{A}_f$, and write

$$\psi_f = 1-\mathcal{A}_f$$

for each individual layer, and since we are considering only weak absorption, the potential transmittance will be very near unity and so $\mathcal{A}_f$ will be very small. Then the potential transmittance of the entire assembly will be given by:

$$\psi = \prod_{f=1}^{p} \psi_f = \prod_{f=1}^{p} (1 - \mathcal{A}_f)$$
$$= 1 - \sum_{f=1}^{p} \mathcal{A}_f + \cdots$$

Now let us consider one single layer. The relevant parameters are contained in

$$\begin{bmatrix} B \\ C \end{bmatrix} = \begin{bmatrix} \cos\delta_f & i(\sin\delta_f)/y_f \\ iy_f \sin\delta_f & \cos\delta_f \end{bmatrix} \begin{bmatrix} 1 \\ y_e \end{bmatrix}$$

and

$$\psi = \frac{\text{Re}\,(y_e)}{\text{Re}\,(BC^*)}$$

from Equation 2.132. Also

$$\begin{aligned} y_f &= n_f - ik_f \text{ (free space units)} \\ \delta_f &= 2\pi(n_f - ik_f)d_f/\lambda \\ &= 2\pi n_f d_f/\lambda - i2\pi k_f d_f/\lambda \\ &= \alpha - i\beta \end{aligned}$$

where k_f, and hence β, is small.

If we consider layers that are approximately quarter-waves, we can set

$$\alpha = [(\pi/2) + \varepsilon]$$

where ε is small. Then

$$\cos\delta_f \approx (-\varepsilon + i\beta)$$
$$\sin\delta_f \approx 1$$

and the matrix expression becomes

$$\begin{bmatrix} B \\ C \end{bmatrix} = \begin{bmatrix} (-\varepsilon + i\beta) & i/(n - ik) \\ i(n - ik) & (-\varepsilon + i\beta) \end{bmatrix} \begin{bmatrix} 1 \\ y_e \end{bmatrix}$$

whence

$$\begin{bmatrix} B \\ C \end{bmatrix} = \begin{bmatrix} (-\varepsilon + i\beta) + iy_e/(n - ik) \\ i(n - ik) + y_e(-\varepsilon + i\beta) \end{bmatrix}$$

so that

$$BC^* = \left[(-\varepsilon + i\beta) + iy_e/(n - ik)\right]\left[i(n - ik) + y_e(-\varepsilon + i\beta)\right]^*$$

and, assuming that y_e is real, since we are dealing with a quarter-wave stack, and neglecting terms of second order and above in k, β, and ε

$$\text{Re}(BC^*) = (\beta n + y_e + y_e^2\beta/n)$$

and

$$\psi_f = \frac{y_e}{(\beta n + y_e + y_e^2\beta/n)} = \frac{1}{1 + \beta\left[(y_e/n) + (y_e/n)\right]}$$

Then, since β is small,

$$\psi_f = 1 - \beta\left[(n/y_e) + (y_e/n)\right]$$

and

$$\mathcal{A}_f = 1 - \psi_f = \beta\left[(n/y_e) + (y_e/n)\right]$$

Next we must find

$$(1 - R)\sum \mathcal{A}_f$$

For this we need the value of y_e at each interface. Let the stack of quarter-wave layers end with a high-index layer. Then the admittance of the whole assembly will be Y, where Y is large and real. If we denote the admittance of the incident medium by y_0 (n_0 in free space units and also real), then

$$R = \left[\frac{y_0 - Y}{y_0 + Y}\right]^2$$

If Y is sufficiently large,

$$1 - R = 1 - [1 - 4y_0/Y] = 4y_o/Y$$

Further, since Y is the terminating admittance and the layers are all quarter-waves, the admittances at each of the interfaces follow the pattern:

Y	$\dfrac{y_H^2}{Y}$	$\dfrac{y_L^2 Y}{y_H^2}$	$\dfrac{y_H^4}{y_L^2 Y}$	$\dfrac{y_L^4 Y}{y_H^4}$	$\dfrac{y_H^6}{y_L^4 Y}$	$\dfrac{y_L^6 Y}{y_H^6}$
y_0	n_H	n_L	n_H	n_L	n_H	n_L

Then

$$A = (1 - R)\sum_{f=1}^{p} \mathcal{A}_f$$

$$= \frac{4y_0}{Y}\left[\left(\frac{y_H}{y_H^2/Y} + \frac{y_H^2/Y}{y_H}\right)\beta_H + \left(\frac{y_L}{y_L^2 Y/y_H^2} + \frac{y_L^2 Y/y_H^2}{y_L}\right)\beta_L\right.$$

$$\left. + \left(\frac{y_H}{y_H^4/y_L^2 Y} + \frac{y_H^4/y_L^2 Y}{y_H}\right)\beta_H + \cdots\right]$$

i.e.,

$$A = 4y_0\left[\left(\frac{1}{y_H} + \frac{y_H}{Y^2}\right)\beta_H + \left(\frac{y_L}{y_H^2} + \frac{y_H^2}{y_L Y^2}\right)\beta_L + \left(\frac{y_L^2}{y_H^3} + \frac{y_H^3}{y_L^2 Y^2}\right)\beta_H + \cdots\right]$$

Since β_H and β_L are small and Y is large, we can neglect terms in β/Y^2 and the absorptance is then given by

$$A = 4y_0\left[\left(\frac{1}{y_H} + \frac{y_L^2}{y_H^3} + \frac{y_L^4}{y_H^5} + \cdots\right)\beta_H + \left(\frac{y_L}{y_H^2} + \frac{y_L^3}{y_H^4} + \frac{y_L^5}{y_H^6} + \cdots\right)\beta_L\right]$$

$(y_L/y_H)^2$ is less than unity and, although the series are not infinite, we can assume that they have a sufficiently large number of terms so that any error involved in assuming that they are in fact infinite is very small.

Thus

$$A = 4y_0\left(\frac{\beta_H/y_H}{1-(y_L/y_H)^2} + \frac{y_L\beta_L/y_H^2}{1-(y_L/y_H)^2}\right) = \frac{4y_0(y_H\beta_H + y_L\beta_L)}{(y_H^2 - y_L^2)}$$

Now

$$y\beta = y\left(\frac{2\pi kd}{\lambda}\right) = \left(\frac{2\pi nd}{\lambda}\right)k$$

where, since we are working in free space units, we are replacing y with n. Since the layers are quarter-waves,

$$\frac{2\pi nd}{\lambda} = \frac{\pi}{2}$$

so that

$$A = \frac{2\pi n_0 \left(k_H + k_L\right)}{\left(n_H^2 - n_L^2\right)} \quad \text{(final layer of high index)}$$

The case of a multilayer terminating with a low-index layer can be dealt with in the same way. The final low-index layer acts to reduce the reflectance and so increase the absorptance that is given by

$$A = \frac{2\pi}{n_0}\left[\frac{\left(n_H^2 k_L + n_L^2 k_H\right)}{\left(n_H^2 - n_L^2\right)}\right] \quad \text{(final layer of low index)}$$

As an example, we can consider a multilayer with $k_H = k_L = 0.0001$, $n_H = 2.35$ and $n_L = 1.35$, in air $n_0 = 1.00$.

A = 0.03% (high index layer outermost)

A = 0.12% (low index layer outermost)

In fact, in the red part of the spectrum, the losses in a zinc sulfide and cryolite stack can be less than 0.001%, indicating that the value of k must be less than 6×10^{-6} assuming that the loss is entirely in one material. For tantalum pentoxide and silicon dioxide multilayer quarter-wave stacks, losses as low as 1 ppm at 1 µm (i.e., 0.0001%) have been reported. This is consistent with values of k an order of magnitude lower. At this level, small amounts of contamination on the reflector surfaces become important additional sources of loss.

In absolute terms, the absorption loss affects the reflectance more than the transmittance in any given quarter-wave stack. Giacomo [23,24] has shown that $\Delta T/T$ and $\Delta R/R$ are of the same order, and therefore, since $R \gg T$, then $\Delta R \gg \Delta T$. We shall return to this question of loss later.

References

1. Fabry C and Perot A 1899 Theory et applications d'une nouvelle méthode de spectroscopie interférentielle *Annales des Chimie et des Physique, Paris, 7th Series* **16** 115–144
2. Born M and Wolf E 2002 *Principles of Optics: Electromagnetic Theory of Propagation, Interference and Diffraction of Light* ed 7 (New York: Cambridge University Press)

3. Chabbal R 1958 Finesse limité d'un Fabry–Perot formé de lames imparfaites *Journal de Physique et le Radium* **19** 295–300
4. Mayer H 1950 *Physik dünner Schichten* (Stuttgart: Wissenschaftliche Verlagsgesellschaft mbH)
5. Kuhn H and Wilson B A 1950 Reflectivity of thin silver films and their use in interferometry *Proceedings of the Physical Society B* **63** 745–755
6. Oppenheim U 1956 Semireflecting silver films for infrared interferometry *Journal of the Optical Society of America* **46** 628–633
7. Palik E D ed 1985 *Handbook of Optical Constants of Solids* (New York: Academic Press Inc)
8. Stanley R W and Andrew K L 1964 Use of dielectric coatings in absolute wavelength measurements with a Fabry–Perot interferometer *Journal of the Optical Society of America* **54** 625–627
9. Penselin S and Steudel A 1955 Fabry–Perot-Interferometerverspiegelungen aus dielektrischen Vielfachschichten *Zeitschrift für Physik* **142** 21–41
10. Welford W T (writing as W Weinstein) 1954 Computations in thin film optics *Vacuum* **4** 3–19
11. Epstein L I 1955 Improvements in heat reflecting filters *Journal of the Optical Society of America* **45** 360–362
12. Perry D L 1965 Low loss multilayer dielectric mirrors *Applied Optics* **4** 987–991
13. Heitmann W 1966 Extrem hochreflektierende dielektrische Spiegelschichten mit Zincselenid *Zeitschrift für Angewandte Physik* **21** 503–508
14. Baumeister P W and Stone J M 1956 Broad-band multilayer film for Fabry–Perot interferometers *Journal of the Optical Society of America* **46** 228–229
15. Heavens O S and Liddell H M 1966 Staggered broad-band reflecting multilayers *Applied Optics* **5** 373–376
16. Baumeister P W 1958 Design of multilayer filters by successive approximations *Journal of the Optical Society of America* **48** 955–958
17. Pelletier E, Klapisch M, and Giacomo P 1971 Synthèse d'empilements de couches minces *Nouvelle Revue d'Optique Appliquée* **2** 247–254
18. Turner A F and Baumeister P W 1966 Multilayer mirrors with high reflectance over an extended spectral region *Applied Optics* **5** 69–76
19. Ramsay J V and Ciddor P E 1967 Apparent shape of broad band multilayer reflecting surfaces *Applied Optics* **6** 2003–2004
20. Giacomo P 1958 Proprietes chromatiques des couches reflechissantes multidielectriques *Journal de Physique et le Radium* **19** 307–311
21. Ciddor P E 1968 Minimization of the apparent curvature of multilayer reflecting surfaces *Applied Optics* **7** 2328–2329
22. Hemingway D J and Lissberger P H 1973 Properties of weakly absorbing multilayer systems in terms of the concept of potential transmittance *Optica Acta* **20** 85–96
23. Giacomo P 1956 Les couches réfléchissantes multidiélectriques appliquées a l'interférometre de Fabry–Perot. Etude théorique et expérimentale des couches réelles. I *Revue d'Optique* **35** 317–354
24. Giacomo P 1956 Les couches réfléchissantes multidiélectriques appliquées a l'interférometre de Fabry–Perot. Etude théorique et expérimentale des couches réelles. II *Revue d'Optique* **35** 442–467

7

Edge Filters

Filters in which the primary characteristic is an abrupt change between a region of rejection and a region of transmission are known as *edge filters*. Edge filters are divided into two main groups: longwave-pass and shortwave-pass. The operation may depend on many different mechanisms and the construction may take a number of different forms. The following account is limited to thin-film edge filters. These rely for their operation on absorption or interference or both.

7.1 Thin-Film Absorption Filters

A thin-film absorption filter consists of a thin film of material with an absorption edge at the required wavelength and is usually longwave-pass in character. Semiconductors that exhibit a very rapid transition from opacity to transparency at the intrinsic edge are particularly useful in this respect, making excellent longwave-pass filters. The edges are not generally as steep as can be achieved with the interference filters to be described, but they are simple and easy to make. The primary complication is connected with the reflection loss in the pass region due to the high refractive index of the film. Germanium, for example, with an edge at 1.65 µm, has an index of 4.0, and, as the thickness of germanium necessary to achieve useful rejection will be at least several quarter-waves, there will be prominent interference fringes in the pass zone showing variations from substrate level, at the half-wave positions, to a reflectance of 68% (in the case of a glass substrate) at the quarter-wave position. The problem can be readily solved by placing antireflection coatings between the substrate and the germanium layer, and between the germanium layer and the air. Single quarter-wave antireflection coatings are usually quite adequate. For optimum matching the values required for the indices of the antireflecting layers are 2.46 between glass and germanium, and 2.0 between germanium and air. The index of zinc sulfide, 2.35, is sufficiently near to both values and, with it, the reflectance near the peak of the quarter-wave coatings will oscillate between

$$\left[\frac{1-(2.35^4)/(4^2\times 1.52)}{1+(2.35^4)/(4^2\times 1.52)}\right]^2 = 1.3\%$$

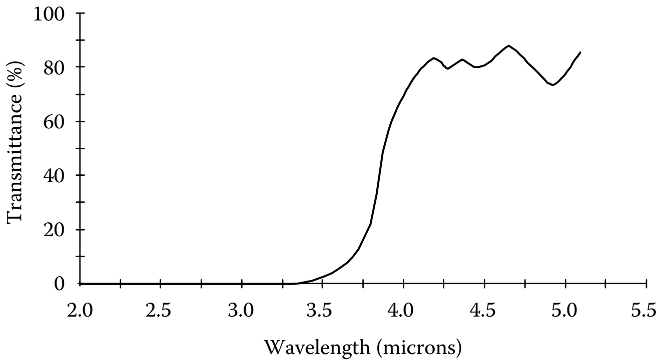

FIGURE 7.1
The measured characteristic of a lead telluride filter. Design:

$\lambda/4$	$30 \times \lambda/4$	$\lambda/4$	CaF_2
ZnS	PbTe	ZnS	substrate

$\lambda_0 = 3.0$ μm.
The small dip at 4.25 μm is probably due to a slight unbalance of the measuring spectrometer caused by atmospheric CO_2. (Courtesy of Sir Howard Grubb, Parsons & Co Ltd.)

for wavelengths where the germanium layer is equal to an integral odd number of quarter-waves, and 4%, that is the reflectance of the bare substrate, where the germanium layer is an integral number of half-waves thick (for at such a wavelength the germanium layer acts as an absentee layer and the two zinc sulfide layers combine also to form a half-wave and, therefore, an absentee layer).

Other materials used to form single-layer absorption filters in this way include cerium dioxide, giving an ultraviolet rejection-visible transmitting filter, silicon, giving a longwave-pass filter with an edge at 1 μm, and lead telluride, giving a longwave-pass filter at 3.4 μm.

A practical lead telluride filter characteristic is shown in Figure 7.1, along with its design. The two zinc sulfide layers were arranged to be quarter-waves at 3.0 μm. Better results would probably have been obtained if the thicknesses had been increased to quarter-waves at 4.5 μm.

7.2 Interference Edge Filters

The basic dielectric reflecting structure is the quarter-wave stack. It is characterized by a limited zone of high reflectance surrounded by regions of relatively high transmittance that exhibit rather pronounced ripple. The transition from reflecting to transmitting is a quite sharp one, the sharpness

increasing with the number of layers in the structure. The performance is, therefore, already of the form of a shortwave or longwave-pass filter. To convert this coating into a useful edge filter implies reduction of the ripple in the pass region. This used to be a quite difficult task but nowadays is greatly simplified by the use of powerful computers in a process of refinement or even complete synthesis. We shall come to this process later in this chapter. Although older analytical techniques are being replaced by newer machine-aided design, their study is still useful in that it leads to an understanding that is difficult to obtain from computer-aided processes only. We begin, therefore, by looking at some of the fundamental theory.

7.2.1 The Quarter-Wave Stack

The basic type of interference edge filter is the quarter-wave stack of the previous chapter. As was explained, the principal characteristic of the optical transmission curve plotted as a function of wavelength is a series of high-reflection zones, i.e., low transmission, separated by regions of high transmission. The shape of the transmission curve of a quarter-wave stack is shown in Figure 7.2. The particular combination of materials shown is useful in the infrared beyond 2 μm, but the curve is typical of any pair of materials having a reasonably high ratio of refractive indices.

The system of Figure 7.2 can be used either as a longwave-pass filter with an edge at 5.0 μm or a shortwave-pass filter with an edge at 3.3 μm. These wavelengths can be altered at will by changing the monitoring wavelength.

It sometimes happens that the width of the rejection zone is adequate for the particular application, as, for example, where light of a particularly

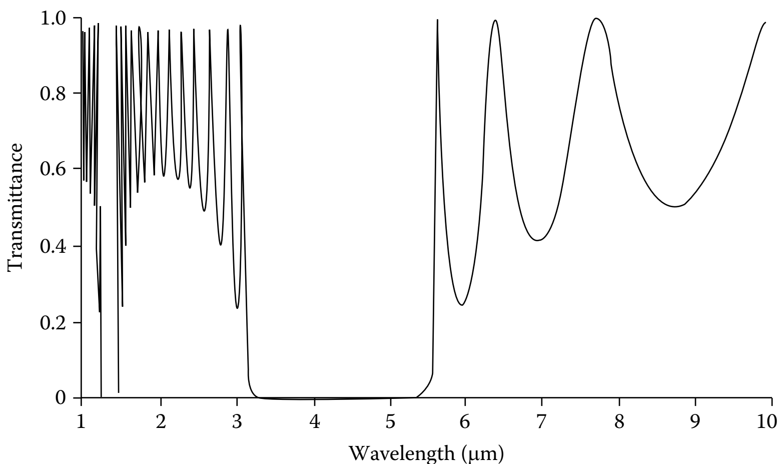

FIGURE 7.2
Computed characteristic of a 13-layer quarter-wave stack of germanium (index 4.0) and silicon monoxide (index 1.70) on a substrate of index 1.42. The reference wavelength, λ_0, is 4.0 μm.

narrow spectral region only is to be eliminated, or where the detector itself is insensitive to wavelength beyond the opposite edge of the rejection zone. In most cases, however, it is desirable to eliminate all wavelengths shorter than, or longer than, a particular value. The rejection zone, shown in Figure 7.2, must somehow be extended. This is usually done by adding additional filters.

Absorption filters usually have very high rejection in the stop region, but, as they depend on the fundamental optical properties of the basic materials, they are inflexible in character and the edge positions are fixed. Using interference and absorption filters together combines the best properties of both—the deep rejection of the absorption filter with the flexibility of the interference filter. The interference layers can be deposited on an absorption filter, which acts as the substrate, or the interference section can sometimes be made from material, which itself has an absorption edge within the interference rejection zone. Within the absorption region, the filter behaves in much the same way as the single layers of the previous section.

Other methods of improving the width of the rejection zone will be dealt with shortly, but now we must turn our attention to the more difficult problem created by the magnitude of the ripple in transmission in the pass region. As the curve of Figure 7.2 shows, the ripple is severe and the performance of the filter would be very much improved if somehow the ripple could be reduced.

Before we can reduce the ripple, we must first investigate the reason for its appearance, and this is not an easy task, because of the complexity of the mathematics. A paper published by Epstein [1] in 1952 is of immense importance, in that it lays the foundation of a method that gives the necessary insight into the problem to enable the performance to be not only predicted but also improved.

7.2.2 Symmetrical Multilayers and the Herpin Index

The 1952 Epstein paper [1] dealt with the mathematical equivalence of a symmetrical combination of films and a single layer and was the beginning of what has become one of the most powerful design method to date for thin-film filters.

Any thin-film combination is known as symmetrical if each half is a mirror image of the other half. The simplest example of this is a three-layer combination in which a central layer is sandwiched between identical outer layers. When such a symmetrical arrangement is used as a component of a thin-film design, it is usually called a *symmetrical period*. It can be shown that a symmetrical period can be treated as a single equivalent layer with a calculable phase thickness and equivalent characteristic admittance. If a multilayer consists of a number of repeats of an identical symmetrical period, then it becomes equivalent in performance to a single layer. Of course, analytical expressions for the equivalent optical properties are

rather involved, but the basic form of the result can be established relatively easily and used as a qualitative guide while the accurate calculation can be left to the computer.

Consider first a symmetrical three-layer period *pqp*, made up of dielectric materials free from absorption. The characteristic matrix of the combination is given by

$$\begin{bmatrix} M_{11} & M_{12} \\ M_{21} & M_{22} \end{bmatrix} = \begin{bmatrix} \cos\delta_p & (i\sin\delta_p)/\eta_p \\ i\eta_p\sin\delta_p & \cos\delta_p \end{bmatrix} \begin{bmatrix} \cos\delta_q & (i\sin\delta_q)/\eta_p \\ i\eta_q\sin\delta_q & \cos\delta_q \end{bmatrix} \times \begin{bmatrix} \cos\delta_p & (i\sin\delta_p)/\eta_p \\ i\eta_p\sin\delta_p & \cos\delta_p \end{bmatrix} \tag{7.1}$$

(where we have used the more general tilted optical admittance η. Note that the p suffix is an indication of layer p and not of polarization type). By performing the multiplication we find:

$$M_{11} = \cos 2\delta_p \cos\delta_q - \frac{1}{2}\left(\frac{\eta_q}{\eta_p} + \frac{\eta_p}{\eta_q}\right)\sin 2\delta_p \sin\delta_q \tag{7.2}$$

$$M_{12} = \frac{i}{\eta_p}\left[\sin 2\delta_p \cos\delta_q + \frac{1}{2}\left(\frac{\eta_q}{\eta_p} + \frac{\eta_p}{\eta_q}\right)\cos 2\delta_p \sin\delta_q + \frac{1}{2}\left(\frac{\eta_p}{\eta_q} - \frac{\eta_q}{\eta_p}\right)\sin\delta_q\right] \tag{7.3}$$

$$M_{12} = i\eta_p\left[\sin 2\delta_p \cos\delta_q + \frac{1}{2}\left(\frac{\eta_q}{\eta_p} + \frac{\eta_p}{\eta_q}\right)\cos 2\delta_p \sin\delta_q - \frac{1}{2}\left(\frac{\eta_p}{\eta_q} - \frac{\eta_q}{\eta_p}\right)\sin\delta_q\right] \tag{7.4}$$

and

$$M_{22} = M_{11} \tag{7.5}$$

There are four elements in this product matrix. However, Expression 7.5 implies that only three of the elements are independent. Then it can be shown that, since the determinant of each of the individual matrices is unity, the determinant of the product matrix is also unity. This adds one further relationship and so the matrix can be represented by two independent variables. These two independent variables can be chosen in any way we wish. All that is necessary is that we should be able to use them to reconstruct the product matrix unambiguously.

Let the two independent variables be denoted by γ and E such that

$$M_{11} = \cos\gamma = M_{22} \tag{7.6}$$

$$M_{12} = \frac{i\sin\gamma}{E} \tag{7.7}$$

and

$$M_{21} = iE\sin\gamma \tag{7.8}$$

The determinant of the matrix remains at unity and the elements are single-valued functions of the two independent variables. These quantities have, intentionally, exactly the same form as a single layer of phase thickness γ and admittance E. We call these two quantities the equivalent phase thickness and the equivalent admittance, respectively. E is also known sometimes as the Herpin admittance after the name of an early worker in this area.

Equations 7.6 to 7.8 can be solved for γ and admittance E. Of course, the solutions are multivalued, but since we are going to use them to reconstruct the matrix, we can choose the values that are of greatest significance to us. We therefore choose γ to have a value that is nearest to the total phase thickness of the period. The solution for E is derived from a square root, and usually we will take the positive root.

$$\gamma = \arccos\ M_{11} \tag{7.9}$$

$$E = \sqrt{\frac{M_{21}}{M_{12}}} \tag{7.10}$$

M_{11} does not equal M_{22} in an unsymmetrical arrangement and such a combination cannot, therefore, be replaced by a single layer.

It can easily be shown that this result can be extended to cover any symmetrical period consisting of any number of layers. First, the central three layers that, by definition, will form a symmetrical assembly on their own can be replaced by a single layer. This equivalent layer can then be taken along with the next layers on either side as a second symmetrical three-layer combination that can, in its turn, be replaced by a further single layer. The process can be repeated until all the layers have been so replaced.

The importance of this result lies both in the ease of interpretation (the properties of a single layer can be visualized much more readily than those of a multilayer) and in the ease with which the result for a single period may be extended to that for a multilayer consisting of many periods.

If a multilayer is made up of, say, s identical symmetrical periods, each of which has an equivalent phase thickness γ and equivalent admittance E,

then physical considerations show that the multilayer will be equivalent to a single layer of thickness $s\gamma$ and admittance E.

This result also follows because of an easily derived analytical result:

$$\begin{bmatrix} \cos\gamma & i\sin\gamma/E \\ iE\sin\gamma & \cos\gamma \end{bmatrix}^s = \begin{bmatrix} \cos(s\gamma) & i\sin(s\gamma)/E \\ iE\sin(s\gamma) & \cos(s\gamma) \end{bmatrix} \tag{7.11}$$

It must be emphasized that the equivalent single layer is not an exact replacement for the symmetrical combination in every respect physically. It is merely a mathematical expression for the product of a number of matrices and is valid only for those cases where such a product is involved. The effect of changes in angle of incidence, for instance, cannot be estimated by converting the multilayer to a single layer in this way.

So far everything we have done applies to layers that are absorbing as well as those free from loss. Let us now limit the discussion to lossless layers, that is, ones where k, the extinction coefficient, is zero. Now M_{11} and M_{22} (equal to M_{11}) will be real and M_{12} and M_{21}, imaginary. In any practical case, when the matrix elements are computed, it will be found that there are regions where $M_{11} < -1$, i.e., $\cos\gamma < -1$. This expression cannot be solved for real γ, and in this region, γ must be imaginary. Since the determinant of the matrix must be unity, M_{12} and M_{21} must have opposite sign and E, therefore, must also be imaginary. We can think of this result in two different ways. The imaginary γ and E simply form a matrix that is not unlike the matrix of a perfect metallic layer. Increasing the thickness of metal results in higher reflectance. Alternatively, since $|M_{11} + M_{12}|/2 > 1$, as the number of basic periods is increased, the reflectance must tend to unity. This condition of imaginary γ and E implies a high-reflectance zone or, in other words, a stop band. Outside the stop band, γ and E are real, and the multilayer appears as a dielectric slab of material exhibiting fringes becoming more and more closely packed with an increase in the number of periods. This dielectric region corresponds to a pass band. The edges of the pass bands and stop bands are given by $M_{11} = -1$.

We can write expressions for γ and E. The expression for the equivalent admittance in the pass band is quite a complicated one. From Equations 7.3 through 7.8

$$E = +\left(\frac{M_{21}}{M_{12}}\right)^{1/2}$$

$$= +\left[\frac{\eta_p^2\left\{\sin 2\delta_p\cos\delta_q + \frac{1}{2}\left(\frac{\eta_q}{\eta_p} + \frac{\eta_p}{\eta_q}\right)\cos 2\delta_p\sin\delta_q - \frac{1}{2}\left(\frac{\eta_p}{\eta_q} - \frac{\eta_q}{\eta_p}\right)\sin\delta_q\right\}}{\sin 2\delta_p\cos\delta_q + \frac{1}{2}\left(\frac{\eta_q}{\eta_p} + \frac{\eta_p}{\eta_q}\right)\cos 2\delta_p\sin\delta_q + \frac{1}{2}\left(\frac{\eta_p}{\eta_q} - \frac{\eta_q}{\eta_p}\right)\sin\delta_p}\right] \tag{7.12}$$

For γ we have, from Expression 7.2

$$\gamma = \arccos\left[\cos 2\delta_p \cos\delta_q - \frac{1}{2}\left(\frac{\eta_q}{\eta_p} + \frac{\eta_p}{\eta_q}\right)\sin 2\delta_p \sin\delta_q\right] \tag{7.13}$$

Let us begin our discussion of these expressions with the particular and simpler case of the quarter-wave stack.

7.2.2.1 Application of the Herpin Index to the Quarter-Wave Stack

Returning for the moment to our quarter-wave stack, we see that it is possible to apply the above results directly if a simple alteration to the design is made. This is simply to add a pair of eighth-wave layers to the stack, one at each end. Low-index layers are required if the basic stack begins and ends with quarter-wave high-index layers and vice versa. The two possibilities are

$$\frac{H}{2}LHLHLH\ldots HL\frac{H}{2}$$

and

$$\frac{L}{2}HLHLHL\ldots LH\frac{L}{2}$$

These arrangements we can replace immediately by

$$\frac{H}{2}L\frac{H}{2}\frac{H}{2}L\frac{H}{2}\frac{H}{2}L\frac{H}{2}\frac{H}{2}\cdots\frac{H}{2}\frac{H}{2}L\frac{H}{2}$$

and

$$\frac{L}{2}H\frac{L}{2}\frac{L}{2}H\frac{L}{2}\frac{L}{2}H\frac{L}{2}\frac{L}{2}\cdots\frac{L}{2}\frac{L}{2}H\frac{L}{2}$$

respectively, which can then be written as

$$\left[\frac{H}{2}L\frac{H}{2}\right]^s \quad\text{and}\quad \left[\frac{L}{2}H\frac{L}{2}\right]^s$$

$(H/2)L(H/2)$ and $(L/2)H(L/2)$ being the basic periods in each case. The results in Equations 7.1 through 7.11 can then be used to replace both the above stacks by single layers, making the performance in the pass bands and also the

extent of the stop bands easily calculable. We shall examine first the width of the stop bands, given by $M_{11} = -1$. Equation 7.2 shows this is equivalent to

$$\cos 2\delta_p \cos \delta_q - \frac{1}{2}\left(\frac{\eta_q}{\eta_p} + \frac{\eta_p}{\eta_q}\right)\sin 2\delta_p \sin \delta_q = -1 \tag{7.14}$$

and this is exactly the same expressions as was obtained in the previous chapter for the width of the unaltered quarter-wave stack. There, δ was replaced by $(\pi/2)g$, where $g = \lambda_0/\lambda$ (or ν/ν_0, where ν is the wave number), and the edges of the stop band were defined by

$$\delta_e = \frac{\pi}{2}(1 \pm \Delta g)$$

The total width is therefore

$$2\Delta g = 2\Delta\left(\frac{\lambda_0}{\lambda}\right)$$

where

$$\Delta g = \frac{2}{\pi}\arcsin\left|\frac{\eta_q - \eta_p}{\eta_q + \eta_p}\right| \tag{7.15}$$

This expression is already plotted in Figure 6.7. The width of the stop band is exactly the same regardless of whether the basic period is $(H/2)L(H/2)$ or $(L/2)H(L/2)$. Of course, it is possible to have other three-layer combinations where the width of the central layer is not equal to twice the thickness of the two outer layers, and some of the other possible arrangements will be examined, both in this chapter and the next, as they have some interesting properties, but, as far as the width of the stop band is concerned, it has been shown by Vera [2] that the maximum width for a three-layer symmetrical period is obtained when the central layer is a quarter-wave and the outer layers an eighth-wave each.

Let us now turn our attention to the pass band—first the equivalent admittance and then the equivalent optical thickness. The expression for the equivalent admittance in the pass band is given in Equation 7.12 and for γ in Equation 7.13. Figure 7.3 shows the equivalent admittance and optical thickness calculated for combinations of zinc sulfide and cryolite. The form of this curve is quite typical of such periods. Once the equivalent admittance and thickness have been evaluated, the calculation of the performance of the filter in the pass region, and its subsequent improvement, becomes much more straightforward. They are dealt with in greater detail later in this chapter.

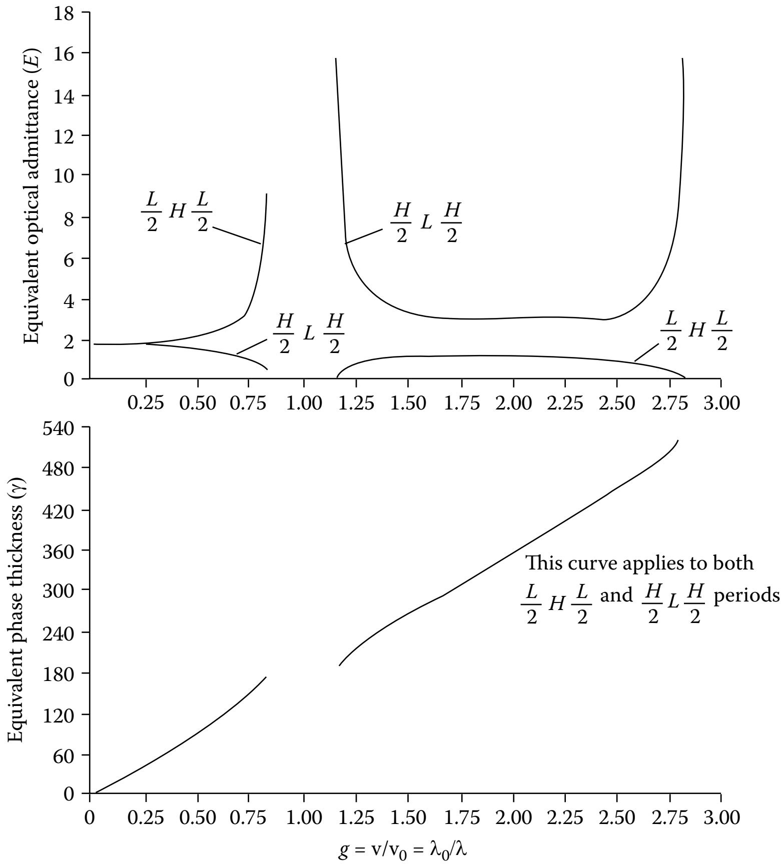

FIGURE 7.3
Equivalent optical admittance, E, and phase thickness, γ, of a symmetrical period of zinc sulfide ($n = 2.35$) and cryolite ($n = 1.35$) at normal incidence.

The expressions are not particularly easy to handle analytically, but there is some simplification in the $(H/2)L(H/2)$ and $(L/2)H(L/2)$ periods. First, we shall examine some of the properties of the expression for the equivalent optical admittance, Equation 7.12.

We can normalize Expression 7.12 by dividing both sides by η_p. E is then solely a function of δ_p, δ_q, and the ratio η_p/η_q. Next, we can make the further simplification, which we have not done so far, that $2\delta_p = \delta_q$. The expression for E/η_p then becomes

$$\frac{E}{\eta_p} = \left[\frac{\left\{1+\frac{1}{2}\left[\rho+\left(1/\rho\right)\right]\right\}\cos\delta_q\sin\delta_q - \frac{1}{2}\left[\rho-\left(1/\rho\right)\right]\sin\delta_q}{\left\{1+\frac{1}{2}\left[\rho+\left(1/\rho\right)\right]\right\}\cos\delta_q\sin\delta_q + \frac{1}{2}\left[\rho-\left(1/\rho\right)\right]\sin\delta_q}\right]^{1/2} \tag{7.16}$$

where $\rho = \eta_p/\eta_q$.

It is now easy to see that the following relationships are true. We write $(E/\eta_p)(\rho, \delta_q)$ to indicate that it is a function of the variables ρ and δ_q.

$$\frac{E}{\eta_p}(\rho, \pi - \delta_q) = \frac{1}{(E/\eta_p)(\rho, \delta_q)} \tag{7.17}$$

$$\frac{E}{\eta_p}\left(\frac{1}{\rho}, \delta_q\right) = \frac{1}{(E/\eta_p)(\rho, \delta_q)} \tag{7.18}$$

These relationships are, in fact, true for all symmetrical periods, even ones that involve inhomogeneous layers, and general statements and proofs of these and other theorems are given by Thelen [3].

Thelen showed how these relationships can be used to reduce the labor in calculating the equivalent admittance for various values of the ratio of admittances. This is less important today when the personal computer can make all the necessary calculations for us. However, a good sense of the variation of the parameters and their dependence on the optical constants of the layers can readily be obtained from the curves Thelen published, and they are reproduced in Figure 7.4 and Figure 7.5. The vertical scale has been made logarithmic, which has the advantage of making the various sections of the curve repetitions of the first section. This follows directly from the

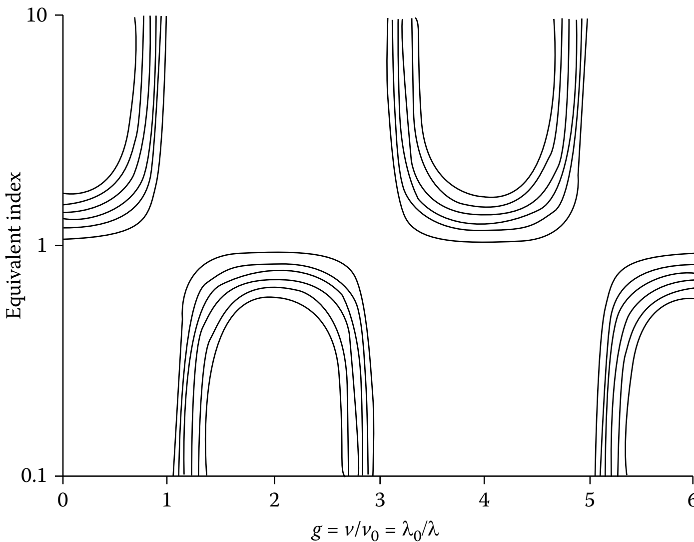

FIGURE 7.4
Equivalent admittance for the system $(L/2)H(L/2)$. $n_L = 1.00$ and n_H/n_L is a parameter with values 1.23, 1.50, 1.75, 2.0, 2.5, 3.0. The curves with the wider stop bands have the higher n_H/n_L values. (After Thelen, A., *Journal of the Optical Society of America*, 56, 1533–1538, 1966.)

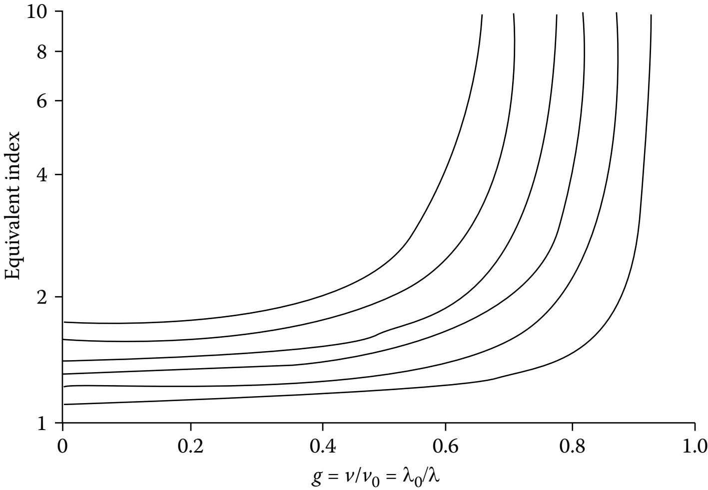

FIGURE 7.5
Enlarged first part of Figure 7.4. (After Thelen, A., *Journal of the Optical Society of America*, 56, 1533–1538, 1966.)

relations 7.17 and 7.18. The values of the ratios of optical admittances used are all greater than unity. Values less than unity can be derived from the plotted curves using relation 7.18. Again the logarithmic scale means that it is necessary only to reorient the curve for $\eta_p/\eta_q = k$ to give that for $\eta_p/\eta_q = 1/k$. All the information necessary to plot the curves is therefore given in the enlarged version of the first section of Figure 7.4 reproduced in Figure 7.5.

It is also useful to note the limiting values of E:

$$E \to (\eta_p \eta_q)^{1/2} \text{ as } \delta_q \to 0 \tag{7.19}$$

and

$$E \to \eta_p (\eta_p/\eta_q)^{1/2} \text{ as } \delta_q \to \pi \tag{7.20}$$

The equivalent phase thickness of the period is given by Equation 7.2 as

$$\gamma = \arccos\left[\cos^2 \delta_q - \frac{1}{2}\left(\rho + \frac{1}{\rho}\right)\sin^2 \delta_q\right] \tag{7.21}$$

This expression for γ is multivalued, and the value chosen is that nearest to $2\delta_p + \delta_q$, the actual sum of the individual phase thicknesses, which is the most easily interpreted value. It is clear from the expression for γ that it does not matter whether the ratio of the admittances is greater or less than unity. The phase thickness for ρ is the same as that for $1/\rho$. Figure 7.6, also from

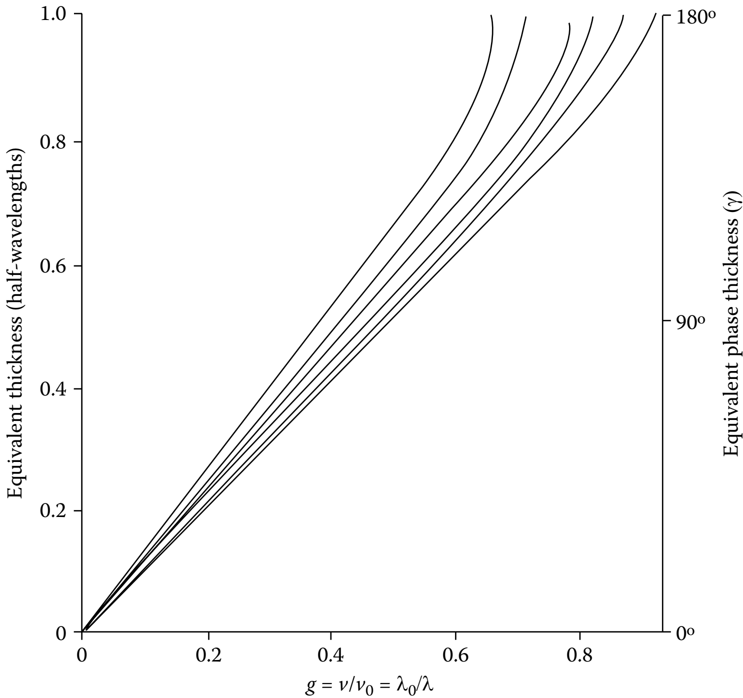

FIGURE 7.6
Equivalent thickness of the system described in Figure 7.4. (After Thelen, A., *Journal of the Optical Society of America*, 56, 1533–1538, 1966.)

Thelen's paper, shows the phase thickness of the combinations in Figure 7.4 and Figure 7.5. Because of the obvious symmetries, all the information necessary for the complete curve of the equivalent phase thickness is given in this diagram. The equivalent thickness departs significantly from the true thickness only near the edge of the high-reflectance zone. At any other point in the pass bands, the equivalent phase thickness is almost exactly equal to the actual phase thickness of the combination.

7.2.2.2 Application of the Herpin Index to Multilayers of Other Than Quarter-Waves

All the curves shown so far are for |eighth-wave|quarter-wave|eighth-wave| periods. If the relative thicknesses of the layers are varied from this arrangement, then the equivalent admittance is altered. It has already been mentioned that the reflectance zones for a combination other than the above must be narrower. Some idea of the way in which the equivalent admittance alters can be obtained from the value as $g \to 0$. Let $2\delta_p/\delta_q = \psi$. Then, from Equation 7.12

$$E = \eta_p \left[\frac{\dfrac{\sin 2\delta_p}{\sin \delta_q}\cos\delta_q + \dfrac{1}{2}\left(\dfrac{\eta_q}{\eta_p} + \dfrac{\eta_p}{\eta_q}\right)\cos 2\delta_p - \dfrac{1}{2}\left(\dfrac{\eta_p}{\eta_q} - \dfrac{\eta_q}{\eta_p}\right)}{\dfrac{\sin 2\delta_p}{\sin \delta_q}\cos\delta_q + \dfrac{1}{2}\left(\dfrac{\eta_q}{\eta_p} + \dfrac{\eta_p}{\eta_q}\right)\cos 2\delta_p + \dfrac{1}{2}\left(\dfrac{\eta_p}{\eta_q} - \dfrac{\eta_q}{\eta_p}\right)} \right]^{1/2} \tag{7.22}$$

Now $\sin 2\delta_p/\sin\delta_q \to \psi$ as $g \to 0$, i.e.,

$$E \to \eta_p \left[\frac{\psi + \dfrac{1}{2}\left(\dfrac{\eta_q}{\eta_p} + \dfrac{\eta_p}{\eta_q}\right) - \dfrac{1}{2}\left(\dfrac{\eta_p}{\eta_q} - \dfrac{\eta_q}{\eta_p}\right)}{\psi + \dfrac{1}{2}\left(\dfrac{\eta_q}{\eta_p} + \dfrac{\eta_p}{\eta_q}\right) + \dfrac{1}{2}\left(\dfrac{\eta_p}{\eta_q} - \dfrac{\eta_q}{\eta_p}\right)} \right]^{1/2}$$

Rearranging this, we obtain

$$E = \eta_p \left[\frac{\psi + (\eta_q/\eta_p)}{\psi + (\eta_p/\eta_q)} \right]^{1/2} \tag{7.23}$$

This result shows that, for small g, it is possible, by varying the relative thicknesses of the two materials, to vary the equivalent admittance throughout the range of values between η_p and η_q but not outside that range. This result has already been referred to in the chapter on antireflection coatings, where it was shown how to use the concept of equivalent admittance to create replacements for layers having indices difficult to reproduce.

Epstein [1] has considered in more detail the variation of equivalent admittance by altering the thickness ratio and gives tables of results of zinc sulfide/cryolite multilayers. Ufford and Baumeister [4] give sets of curves that assist in the use of equivalent admittance in a wide range of design problems.

Some results that are, at first sight, rather surprising are obtained when the value of the equivalent admittance around $g = 2$ is investigated. As $g \to 2,\ 2\delta_p \to \pi$ and $\delta_q \to \pi$ so that, from Equation 7.22

$$E \to \eta_p \left[\frac{-1 - \dfrac{1}{2}\left(\dfrac{\eta_q}{\eta_p} + \dfrac{\eta_p}{\eta_q}\right)\cos 2\delta_p - \dfrac{1}{2}\left(\dfrac{\eta_p}{\eta_q} - \dfrac{\eta_q}{\eta_p}\right)}{-1 - \dfrac{1}{2}\left(\dfrac{\eta_q}{\eta_p} + \dfrac{\eta_p}{\eta_q}\right) + \dfrac{1}{2}\left(\dfrac{\eta_p}{\eta_q} - \dfrac{\eta_q}{\eta_p}\right)} \right]^{1/2} = \left(\frac{\eta_p}{\eta_q}\right)^{1/2} \tag{7.24}$$

This is quite a straightforward result. Now let $2\delta p/\delta q = \psi$, as in the case just considered where $g \to 0$. Let $g \to 2,$ so that $2\delta_p + \delta_q \to 2\pi\cdot$ (In this case, we define $g = \lambda_0/\lambda$ by defining λ_0 as that wavelength making $2\delta_p + \delta_q = \pi\cdot$)

We have, as $g \to 2$

$$\cos 2\delta_p \to \cos(2\pi - \delta_q) = \cos\delta_q$$

$$\sin 2\delta_p \to \sin(2\pi - \delta_q) = -\sin\delta_q$$

and $\delta_q \to 2\pi/(1+\psi)$ so that

$$E = \eta_p \left[\frac{-\sin\delta_q \cos\delta_q + \frac{1}{2}\left(\frac{\eta_q}{\eta_p} + \frac{\eta_p}{\eta_q}\right)\cos\delta_q \sin\delta_q - \frac{1}{2}\left(\frac{\eta_p}{\eta_q} - \frac{\eta_q}{\eta_p}\right)\sin\delta_q}{-\sin\delta_q \cos\delta_q + \frac{1}{2}\left(\frac{\eta_q}{\eta_p} + \frac{\eta_p}{\eta_q}\right)\cos\delta_q \sin\delta_q - \frac{1}{2}\left(\frac{\eta_p}{\eta_q} - \frac{\eta_q}{\eta_p}\right)\sin\delta_q} \right]^{1/2}$$

$$= \eta_p \left[\frac{-\cos\delta_q \left\{1 - \frac{1}{2}\left(\frac{\eta_q}{\eta_p} + \frac{\eta_p}{\eta_q}\right)\right\} - \frac{1}{2}\left(\frac{\eta_p}{\eta_q} - \frac{\eta_q}{\eta_p}\right)}{-\cos\delta_q \left\{1 - \frac{1}{2}\left(\frac{\eta_q}{\eta_p} + \frac{\eta_p}{\eta_q}\right)\right\} + \frac{1}{2}\left(\frac{\eta_p}{\eta_q} - \frac{\eta_q}{\eta_p}\right)} \right]^{1/2} \quad (7.25)$$

where $\cos\delta_q = \cos[2\pi/(1+\psi)]$.

Whatever the value of ψ, the quantities within the square root brackets have opposite signs, which means that the equivalent admittance is imaginary. Even as $\psi \to 1$, where one would expect the limit to coincide with the result in Equation 7.24, the admittance is still imaginary. The explanation of this apparent paradox is as follows. An imaginary equivalent admittance, as we have seen, indicates a zone of high reflectance. Consider first the ideal eighth-wave|quarter-wave|eighth-wave stack of Equation 7.24. At the wavelength corresponding to $g = 2$, the straightforward theory predicts that the reflectance of the substrate shall not be altered by the presence of the multilayer, because each period of the multilayer is acting as a full wave of real admittance and is therefore an absentee layer. Looking more closely at the structure of the multilayer we can see that this can also be explained by the fact the all the individual layers are a half-wavelength thick. If the ratio of the thicknesses is altered, the layers are no longer a half-wavelength thick and cannot act as absentees. In fact, the theory of the above result shows that a zone of high reflectance occurs.

The transmittance of a shortwave-pass filter at the wavelength corresponding to $g = 2$ is therefore very sensitive to errors in the relative thicknesses of the layers. Even a small error leads to a peak of reflection. The width of this spurious high-reflectance zone is quite narrow if the error is small. Thus, the appearance of a pronounced narrow dip in the transmission curve of a shortwave-pass filter is quite a common feature and is difficult to eliminate. The dip is referred to sometimes as a "half-wave hole."

7.2.3 Performance Calculations

We are now in a position to make some performance calculations.

7.2.3.1 Transmission at the Edge of a Stop Band

The level of transmission in the high-reflectance region, or stop band, is an important parameter of the filter. Thelen [3] gives a useful method for calculating this at the edges of the band. His analysis is as follows.

Let the multilayer be made up of s fundamental periods so that the characteristic matrix of the multilayer is

$$[M]^s = \begin{bmatrix} \cos\gamma & i\sin\gamma/E \\ iE\sin\gamma & \cos\gamma \end{bmatrix}^s = \begin{bmatrix} \cos(s\gamma) & i\sin(s\gamma)/E \\ iE\sin(s\gamma) & \cos(s\gamma) \end{bmatrix}$$

At the edges of the stop band we know that $\cos(s\gamma) \to 1, \sin(s\gamma) \to 0,$ and $E \to 0$ or ∞ depending on the particular combination of layers. Now,

$$\frac{\sin(s\gamma)}{\sin\gamma} \to s \text{ as } \sin\gamma \to 0$$

so that the matrix tends to

$$\begin{bmatrix} 1 & is\sin\gamma/E \\ iEs\sin\gamma & 1 \end{bmatrix} = \begin{bmatrix} 1 & sM_{12} \\ sM_{21} & 1 \end{bmatrix}$$

at the stop band limits. Either M_{12} or M_{21} will also tend to zero because

$$M_{11}M_{22} - M_{12}M_{21} = 1$$

and, depending on which tends to zero, we have either

$$\begin{bmatrix} 1 & sM_{12} \\ 0 & 1 \end{bmatrix} \text{ or } \begin{bmatrix} 1 & 0 \\ sM_{21} & 1 \end{bmatrix}$$

for the matrix.

If η_0 is the admittance of the incident medium and η_{sub} of the substrate, then the transmittance of the multilayer at the edge of the stop band is given by Equation 2.115:

$$T = \frac{4\eta_0\eta_m}{(\eta_0 B + C)(\eta_0 B + C)^*}$$

where

$$\begin{bmatrix} B \\ C \end{bmatrix} = \begin{bmatrix} 1 & sM_{12} \\ 0 & 1 \end{bmatrix} \begin{bmatrix} 1 \\ \eta_{sub} \end{bmatrix} = \begin{bmatrix} 1 + n_{sub} sM_{12} \\ \eta_{sub} \end{bmatrix} \quad \text{for} \quad M_{21} = 0$$

or

$$\begin{bmatrix} B \\ C \end{bmatrix} = \begin{bmatrix} 1 & 0 \\ sM_{21} & 1 \end{bmatrix} \begin{bmatrix} 1 \\ \eta_{sub} \end{bmatrix} = \begin{bmatrix} 1 \\ n_{sub} + sM_{21} \end{bmatrix} \quad \text{for} \quad M_{12} = 0$$

If there is no absorption, M_{12} and M_{21} are imaginary. Then

$$T = \frac{4\eta_0\eta_{sub}}{(\eta_0 + \eta_{sub})^2 + (s\eta_0\eta_{sub} + |M_{12}|)^2} \quad \text{when } M_{21} = 0 \tag{7.26}$$

and

$$T = \frac{4\eta_0\eta_{sub}}{(\eta_0 + \eta_{sub})^2 + (s|M_{21}|)^2} \quad \text{when } M_{12} = 0 \tag{7.27}$$

We can take this a stage further. For M_{12} or M_{21} to be zero requires that

$$\sin 2\delta_p \cos\delta_q + \frac{1}{2}\left(\frac{\eta_q}{\eta_p} + \frac{\eta_p}{\eta_q}\right)\cos 2\delta_p \sin\delta_q = \mp\frac{1}{2}\left(\frac{\eta_p}{\eta_q} - \frac{\eta_q}{\eta_p}\right)\sin\delta_q$$

If M_{12} is zero, we can deduce that

$$|M_{21}| = \left|\eta_p\left(\frac{\eta_p}{\eta_q} - \frac{\eta_q}{\eta_p}\right)\sin\delta_q\right| \tag{7.28}$$

or, if M_{21} is zero, that

$$|M_{12}| = \left|\frac{1}{\eta_p}\left(\frac{\eta_p}{\eta_q} - \frac{\eta_q}{\eta_p}\right)\sin\delta_q\right| \tag{7.29}$$

This is as far as it is easy to go in a completely general way. Now let us restrict the remainder of the discussion to the eighth-wave |quarter-wave| eighth-wave

configuration. At the limits of the high-reflectance zone, Expression 7.14 becomes

$$\cos^2\delta_q - \frac{1}{2}\left(\frac{\eta_q}{\eta_p} + \frac{\eta_p}{\eta_q}\right)\sin^2\delta_q = -1$$

which, with a little simplification, yields

$$\sin^2\delta_q = \frac{4\eta_p\eta_q}{(\eta_p + \eta_q)^2} \tag{7.30}$$

Then

$$|M_{21}|^2 = \left|\frac{4\eta_p(\eta_p - \eta_q)^2}{\eta_q}\right| \quad \text{for} \quad M_{12} = 0 \tag{7.31}$$

$$|M_{12}|^2 = \left|\frac{4(\eta_p - \eta_q)^2}{\eta_p^3\eta_q}\right| \quad \text{for} \quad M_{21} = 0 \tag{7.32}$$

To give the transmittance at the edges of the high-reflectance zone, these expressions should be used in Equations 7.26 and 7.27 according to the rules

> If E, the equivalent admittance, is zero, then M_{21} is zero.
>
> If E, the equivalent admittance, is ∞, then M_{12} is zero.

7.2.3.2 Transmission in the Center of a Stop Band

For the simple quarter-wave stack, an expression for transmittance at the center of the high-reflectance zone has already been given in Chapter 6. For the present multilayer, the transmittance is of a similar order of magnitude but the eighth-wave layers at the outer edges of the stack complicate matters. The stack may be represented by

$$\frac{p}{2}q\frac{p}{2}\frac{p}{2}q\frac{p}{2}\cdots\frac{p}{2}q\frac{p}{2}$$

which is

$$\frac{p}{2}qpqpqp\cdots q\frac{p}{2}$$

If there are s periods, then the layer q appears s times in this expression. At the center of the high-reflectance zone, the matrix product becomes:

$$\begin{bmatrix} \frac{1}{\sqrt{2}} & \frac{i}{\eta_p\sqrt{2}} \\ \frac{i\eta_p}{\sqrt{2}} & \frac{1}{\sqrt{2}} \end{bmatrix} \begin{bmatrix} 0 & \frac{i}{\eta_q} \\ i\eta_q & 0 \end{bmatrix} \begin{bmatrix} 0 & \frac{i}{\eta_p} \\ i\eta_p & 0 \end{bmatrix} \cdots \begin{bmatrix} 0 & \frac{i}{\eta_q} \\ i\eta_q & 0 \end{bmatrix} \begin{bmatrix} \frac{1}{\sqrt{2}} & \frac{i}{\eta_p\sqrt{2}} \\ \frac{i\eta_p}{\sqrt{2}} & \frac{1}{\sqrt{2}} \end{bmatrix}$$

$$= \begin{bmatrix} \frac{1}{\sqrt{2}} & \frac{i}{\eta_p\sqrt{2}} \\ \frac{i\eta_p}{\sqrt{2}} & \frac{1}{\sqrt{2}} \end{bmatrix} \begin{bmatrix} 0 & \frac{i}{\eta_q} \\ i\eta_q & 0 \end{bmatrix} \begin{bmatrix} -\frac{\eta_q}{\eta_p} & 0 \\ 0 & -\frac{\eta_p}{\eta_q} \end{bmatrix}^{s-1} \begin{bmatrix} \frac{1}{\sqrt{2}} & \frac{i}{\eta_p\sqrt{2}} \\ \frac{i\eta_p}{\sqrt{2}} & \frac{1}{\sqrt{2}} \end{bmatrix}$$

$$= \frac{1}{2} \begin{bmatrix} \left(-\frac{\eta_q}{\eta_p}\right)^s + \left(-\frac{\eta_p}{\eta_q}\right)^s & \frac{i}{\eta_p}\left\{\left(-\frac{\eta_q}{\eta_p}\right)^s - \left(-\frac{\eta_p}{\eta_q}\right)^s\right\} \\ i\eta_p\left\{\left(-\frac{\eta_p}{\eta_q}\right)^s - \left(-\frac{\eta_q}{\eta_p}\right)^s\right\} & \left(-\frac{\eta_q}{\eta_p}\right)^s + \left(-\frac{\eta_p}{\eta_q}\right)^s \end{bmatrix} \tag{7.33}$$

Let η_{sub} be the admittance of the substrate. Then

$$\begin{bmatrix} B \\ C \end{bmatrix} = \frac{1}{2} \begin{bmatrix} \left(-\frac{\eta_q}{\eta_p}\right)^s + \left(-\frac{\eta_p}{\eta_q}\right)^s + \frac{i\eta_{sub}}{\eta_p}\left\{\left(-\frac{\eta_q}{\eta_p}\right)^s - \left(-\frac{\eta_p}{\eta_q}\right)^s\right\} \\ \eta_{sub}\left\{\left(-\frac{\eta_q}{\eta_p}\right)^s + \left(-\frac{\eta_p}{\eta_q}\right)^s\right\} + i\eta_p\left\{\left(-\frac{\eta_p}{\eta_q}\right)^s - \left(-\frac{\eta_q}{\eta_p}\right)^s\right\} \end{bmatrix} \tag{7.34}$$

Equation 2.115 gives

$$T = \frac{4\eta_0\eta_{sub}}{(\eta_0 B + C)(\eta_0 B + C)^*}$$

$$= \frac{16\eta_0\eta_{sub}}{\left[(\eta_0 + \eta_{sub})\left\{\left(-\frac{\eta_q}{\eta_p}\right)^s + \left(-\frac{\eta_p}{\eta_q}\right)^s\right\}\right]^2 + \left[\left(\frac{\eta_0\eta_{sub}}{\eta_p} - \eta_p\right)\left\{\left(-\frac{\eta_q}{\eta_p}\right)^s - \left(-\frac{\eta_p}{\eta_q}\right)^s\right\}\right]^2} \tag{7.35}$$

If s is sufficiently large so that

$$\left(\frac{\eta_H}{\eta_L}\right)^s \gg \left(\frac{\eta_L}{\eta_H}\right)^s$$

which will usually be the case, this expression reduces to

$$T = \frac{16\eta_0\eta_{sub}}{(\eta_H/\eta_L)^{2s}\left[(\eta_0+\eta_{sub})^2+\left\{(\eta_0\eta_{sub}/\eta_p)-\eta_p\right\}^2\right]} \tag{7.36}$$

where η_p will be either η_H or η_L depending on which is outermost in the symmetrical period.

7.2.3.3 Transmission in the Pass Band

In the pass band, the multilayer behaves as if it were a single layer of slightly variable optical thickness and admittance. Let us consider the case of $[(L/2)H(L/2)]^s$. Figure 7.7 shows part of the curve of equivalent admittance E for $[(L/2)H(L/2)]$. γ, the equivalent phase thickness, is also shown. In the case of a real single transparent layer on a transparent substrate the reflectance oscillates between two limiting values that correspond to layer thicknesses of an integral number of quarter-waves. When the layer is equivalent to an even number of quarter-waves, that is a whole number of half-waves, it is an absentee layer and behaves as if it did not exist, so that the reflectance is that of the bare substrate. When the layer is equivalent to an odd number of quarter-waves, then, according to whether the index is higher or lower than that of the substrate, the reflectance will either be a maximum or a minimum.

Thus if η_f is the admittance of the film, η_{sub} of the substrate, and η_0 of the incident medium, the reflectance will be $[(\eta_0-\eta_{sub})/(\eta_0+\eta_{sub})]^2$, corresponding to an even number of quarter-waves, and

$$\left(\frac{\eta_0-\eta_f^2/\eta_{sub}}{\eta_0+\eta_f^2/\eta_{sub}}\right)^2$$

corresponding to an odd number of quarter-waves. Regardless of the actual thickness of the film, we can draw two lines

$$R = \left(\frac{\eta_0-\eta_{sub}}{\eta_0+\eta_{sub}}\right)^2 \tag{7.37}$$

and

$$R = \left(\frac{\eta_0-\eta_f^2/\eta_{sub}}{\eta_0+\eta_f^2/\eta_{sub}}\right)^2 \tag{7.38}$$

which are the loci of maximum and minimum reflectance values, that is, the envelope of the reflectance curve of the film. If the optical thickness of the film is D, then the actual positions of the turning values will be given by

$$D = 2m\lambda/4 \quad m = 0, 1, 2, 3, 4, \ldots$$

for those in Equation 7.37, and by

$$D = (2m + 1)\lambda/4$$

for those in Equation 7.38, that is at wavelengths given by

$$\lambda = 4D/2m = 2D/m$$

and

$$\lambda = 4D/(2m + 1)$$

respectively.

We can now return to our multilayer. Since the multilayer can be replaced by a single film, the reflectance will oscillate between two values: the reflectance of the bare substrate

$$R = \left(\frac{\eta_0 - \eta_{sub}}{\eta_0 + \eta_{sub}}\right)^2 \tag{7.39}$$

and that given by

$$R = \left(\frac{\eta_0 - E^2/\eta_{sub}}{\eta_0 + E^2/\eta_{sub}}\right)^2 \tag{7.40}$$

where we have replaced η_f in Equation 7.38 by E, the equivalent admittance of the period. Equation 7.40 now represents a curve rather than a line, since E is variable. To find the positions of the maxima and minima, we look for values of $g = \lambda_0/\lambda$ for which the total thickness of the multilayer is a whole number of quarter-waves, which is the same as saying that the total equivalent phase thickness of the multilayer must be a whole number times $\pi/2$; an odd number corresponds to Equation 7.40 and an even number to Equation 7.39. If there are s periods in the multilayer, then the equivalent phase thickness will be $s\gamma$, which will be a multiple of $\pi/2$ when the equivalent phase thickness of a single period, γ, is a multiple of $\pi/2s$, i.e.

$$\gamma = m\pi/2s \quad m = 1, 3, 5, 7, \ldots \text{ corresponding to Equation 7.40}$$

and

$$\gamma = m\pi/s \quad m = 1, 2, 3, 4, \ldots \text{ corresponding to Equation 7.39}$$

At the very edge of the pass band, the equivalent phase thickness is π and so we might expect that the multilayer should act as an absentee layer. However,

the equivalent admittance at that point is either zero or infinite and so the multilayer cannot be treated in this way, and, in fact, we apply Expressions 7.26 through 7.36 already derived.

Figure 7.7 illustrates the situation where a four-period multilayer has been taken as an example. The important point, however, is that the envelopes of the reflectance curve do not vary with the number of periods. The reason for the excessive ripple in the pass band of a filter is now clear. It is due to mismatching of the equivalent admittances of the substrate, multilayer stack, and medium. To reduce the ripple, better matching is required.

7.2.3.4 Reduction of Pass-Band Ripple

There are a number of different approaches for reducing ripple. The simplest approach is to choose a combination having an equivalent admittance

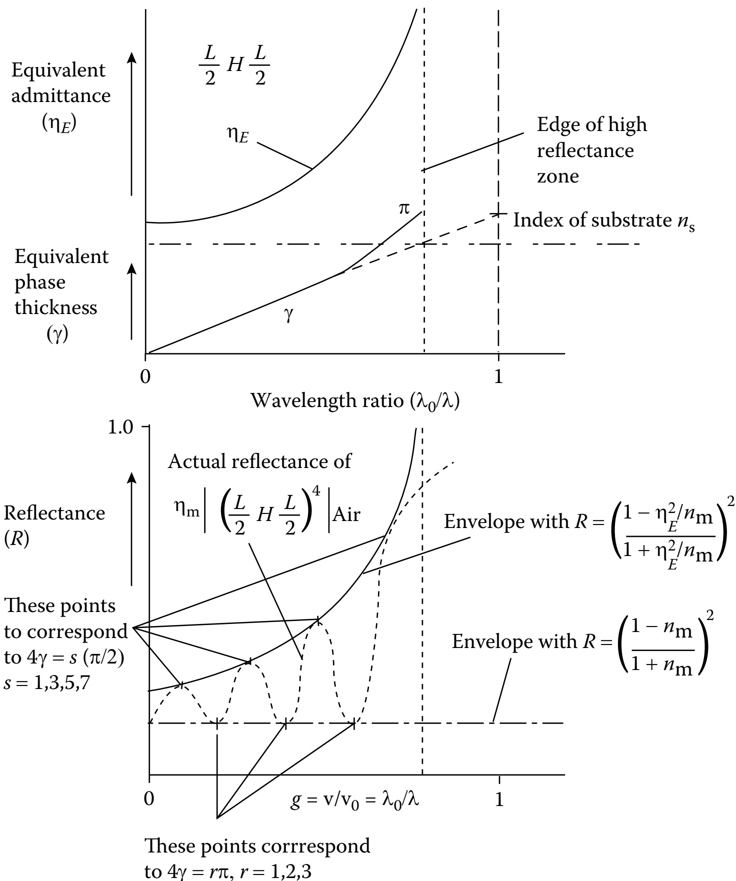

FIGURE 7.7
Diagram explaining the origin of the ripple in the pass band of an edge filter.

similar to that of the substrate. Provided the reflection loss due to the bare substrate is not too great, this method should yield an adequate result. Figure 7.3 shows that the combination $[(H/2)L(H/2)]$ where $\eta_H = 2.35$, $\eta_L = 1.35$, should give a reasonable performance as a longwave-pass filter on glass, and this is indeed the case. The performance of such a filter is shown in Figure 7.8. For a shortwave-pass filter, the combination $[(L/2)H(L/2)]$ is better and this is also shown in Figure 7.8. Often, however, the materials that are available do not yield a suitable equivalent admittance and other measures to reduce ripple must be adopted.

One method that is very straightforward has been suggested by Welford [5] but does not seem to have been much used. This is simply to vary the thicknesses of the films in the basic period so that the equivalent admittance is altered to bring it nearer to the desired value. For this method to be successful, the reflectance from the bare substrate must be kept low and the substrate should have a low index. Glass in the visible region is quite satisfactory, but the method could not be used with, for example, silicon and germanium in the infrared without modification.

The more usual approach is to add matching layers at either side of the multilayer to match it to the substrate and to the medium. If a quarter-wave layer of admittance η_3 is inserted between the multilayer and substrate, and a quarter-wave layer of admittance η_1 between the multilayer and incident medium, then good matching will be obtained if

$$\eta_3 = (\eta_{sub}E)^{1/2} \text{ and } \eta_1 = (\eta_0 E)^{1/2} \tag{7.41}$$

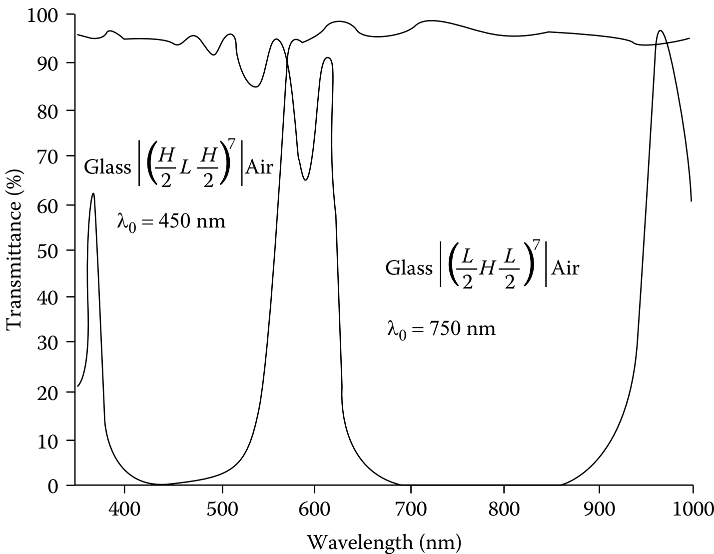

FIGURE 7.8
Computed transmittance of a 15-layer longwave-pass filter and a 15-layer shortwave-pass filter.

The layers are simply acting as antireflection layers between the multilayer and its surroundings. As a quick check that this does give the required performance we can compute the behavior of the multilayer, considering just those wavelengths where the multilayer is equivalent either to an odd or to an even number of quarter-waves and to plot as before the envelope of the reflectance curve. At wavelengths where the multilayer acts like a quarter-wave, the equivalent admittance of the assembly is just

$$Y = \frac{\eta_1^2\eta_3^2}{E^2\eta_{sub}}$$

so that the reflectance is

$$R = \left[\frac{\eta_0 - \left(\eta_1^2\eta_3^2\right)/\left(E^2\eta_{sub}\right)}{\eta_0 + \left(\eta_1^2\eta_3^2\right)/\left(E^2\eta_{sub}\right)}\right]^2 \tag{7.42}$$

which will be zero for

$$\eta_1^2\eta_3^2 = E^2\eta_0\eta_{sub} \tag{7.43}$$

When the multilayer acts like a half-wave it is an absentee, and the reflectance is

$$R = \left[\frac{\eta_0 - \eta_1^2\eta_{sub}/\eta_3^2}{\eta_0 + \eta_1^2\eta_{sub}/\eta_3^2}\right]^2 \tag{7.44}$$

which is zero if

$$\frac{\eta_1^2}{\eta_3^2} = \frac{\eta_0}{\eta_{sub}} \tag{7.45}$$

Solving Equations 7.43 and 7.45 for η_1 and η_3 gives Equation 7.41, as we would expect. If ideal matching layers do not exist, the suitability of any available materials can quickly be checked by substituting the appropriate values in Equations 7.42 and 7.44.

Figure 7.9 shows a shortwave-pass filter before and after the matching layers have been added. The final reflectance envelopes are given by Equations 7.42 and 7.44. The computed performance of the filter is shown in Figure 7.10. As the value of g increases from 1.25, the ripple becomes a little greater than that predicted by the envelopes. This is because the envelopes were

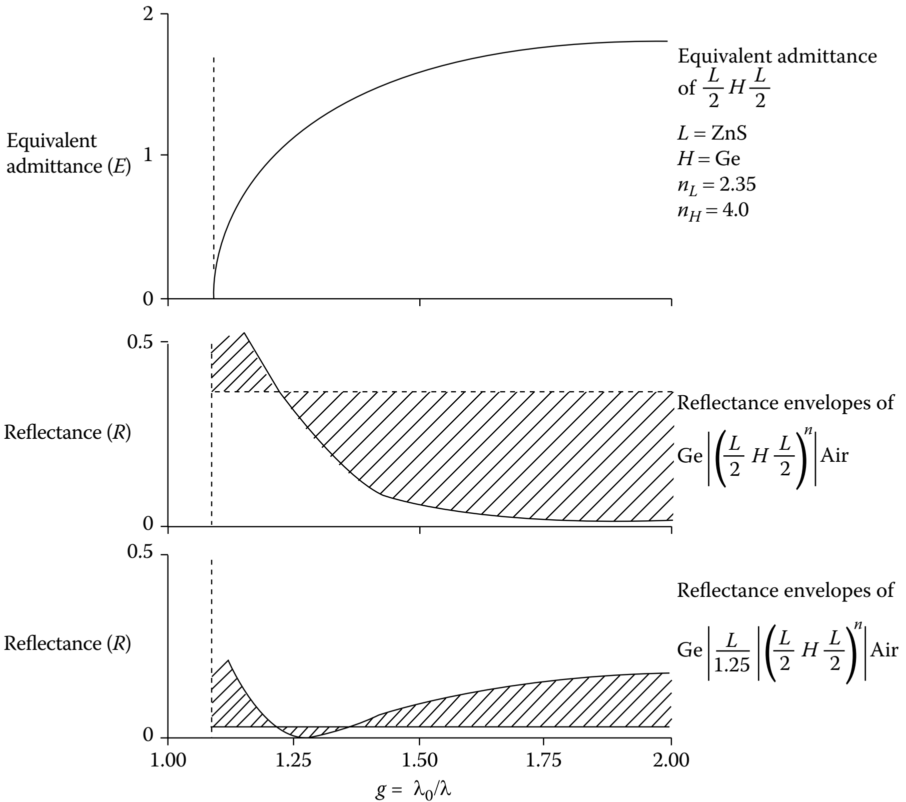

FIGURE 7.9
Steps in the design of a shortwave-pass filter using zinc sulfide and germanium on a germanium substrate.

calculated based on quarter-wave matching layers, and this is strictly true for $g = 1.25$ only.

7.2.3.5 Summary of Design Procedure so Far

We have now established a simple design procedure for edge filters. First, two materials, of different refractive index and transparent in the region where transmission is required, are chosen and used to form a multilayer of the form $[(L/2)H(L/2)]^s$ or $[(H/2)L(H/2)]^s$. Generally, it is better to choose as high a ratio of refractive indices as possible to give the widest rejection zone and also the maximum rejection for a given number of periods. The width of the rejection zone is given by Equation 7.15 and is plotted in Figure 6.7. The level of rejection at the edges of the zone is given by Equations 7.26, 7.27, 7.31, and 7.32 and at the center of the zone by Equation 7.36. Next, the equivalent admittance of the stack should be calculated. The

design curves given in Figure 7.5 can help in this. The formulae given in Equations 7.19 and 7.20 for limiting values of E will be found useful as a guide to interpolating curves. The reflectance envelopes can now be estimated using the formulae in Equations 7.39 and 7.40. This will immediately give some idea of the likely ripple. The positions of the peaks and troughs of the ripple can, if necessary, be found using the curves of γ in Figure 7.6 and the method given in Section 7.2.3.4. If this ripple is adequate, the next step can be omitted and the design can proceed to the final step. If the ripple is not adequate, then matching layers between multilayer and substrate, and multilayer and medium, are required. These should be quarter-wavelength films at the most important wavelength and should have admittances as nearly as possible given by

$$\eta_3 = (\eta_{sub}E)^{1/2} \text{ and } \eta_1 = (\eta_0 E)^{1/2} \tag{7.41}$$

where η_1 is between the multilayer and medium and η_3 is between the multilayer and substrate. Generally, materials with the exact values will not be available and a compromise must be made. To test the effectiveness of the compromise, the new reflectance envelope curves can be calculated using Equations 7.42 and 7.44.

We illustrate the method in the design of a shortwave-pass filter made from germanium and zinc sulfide on a germanium substrate as shown in Figure 7.9 and Figure 7.10.

The description so far is largely of a systematic analytical approach because such an approach brings with it a degree of understanding. Although there is a degree of manual labor involved in its application, in practice we make much more use of the computer. Calculation of the equivalent parameters and the ripple performance is fast and easy.

7.2.3.6 More Advanced Procedures for Eliminating Ripple

At the present time, probably the most common technique for eliminating ripple is computer refinement, which is dealt with in more detail later in this book. Computers are unable to make use of terms like "improve," "better," or "worse." They deal with numbers and their logic is based on whether one number is greater or less than another number. For a computer to be able to improve a design, the assessment of any improvement has to be based on a number, changes in which correspond to what we would understand as an improvement or a deterioration in performance. Usually, but not always, a decreasing number is used to indicate an improving performance. This number, called the *figure of merit*, therefore represents the performance to the computer. It is calculated by a set of rules, called the *function of merit*, that reside in the computer. The figure of merit is generally the expression in one single number of the difference between the current

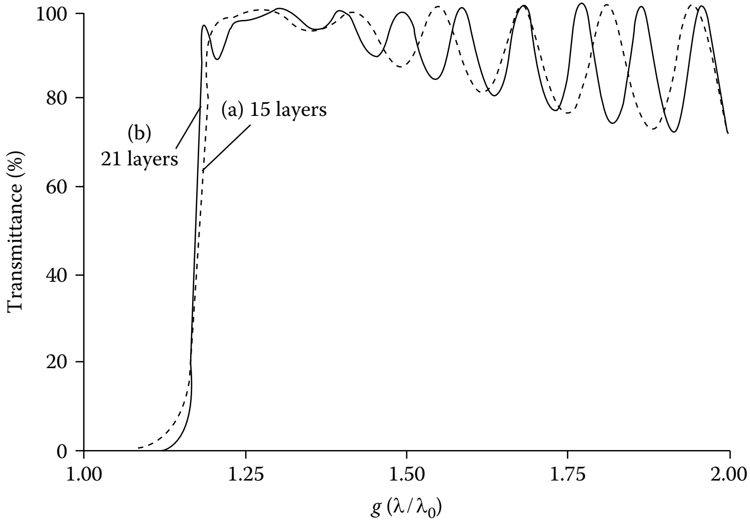

FIGURE 7.10
The calculated performance of filters designed according to Figure 6.9 with design: Air |(0.5*L* *H* 0.5*L*)^s *L*/1.25| Ge with $n_L = 2.35$, $n_H = 4.0$, $n_{Ge} = 4.0$, and $n_{Air} = 1.00$. (a) $q = 7$ (b) $q = 10$.

design performance and a desired or target performance. In the refinement process, the computer makes changes to a design in a process that gradually reduces the gap, as defined by the figure of merit, between the current design performance and target performance. The various refinement processes differ in the instructions followed by the computer in altering the design, but all have the intension of ensuring convergence to as favorable a figure of merit as possible.

Computer refinement was introduced into optical coating design by Baumeister [6], who programmed a computer to estimate the effects of slight changes in the thicknesses of the individual layers on a merit function representing the deviation of the performance of the coating from the ideal. An initial design, not too far from ideal, was adopted and the thicknesses of the layers were modified, successively, gradually to improve the performance. The optimum thickness of any one layer is not independent of the thicknesses of the other layers so that the changes in thickness at each iteration could not be large without running the risk of instability. Computer speed and capacity have increased considerably since the early work of Baumeister, but the essentials of the method are still the same. Rather than change the layers successively, it is now more usual to estimate changes to be made in all the adjustable layers. These changes are then made simultaneously and the new function of merit computed. Further changes are then estimated and the process repeated. The way in which changes to be made are assessed is the principal difference between the techniques in frequent use. If the function of merit is considered as

a surface in $(p + 1)$-dimensional space with p independent variables being layer thicknesses, then a common method involves determining the direction of slope of the merit surface and then altering the layer thicknesses so as to move along it. An enormous number of different techniques exist. Comparisons of various methods have tended to show that there is no universal best technique [7].

Computer refinement is a very powerful design aid, but it can function only with an initial design. It then modifies the design to improve the performance. Less usual is complete design synthesis with no starting solution. This adds to refinement a process for complicating the design when the refinement reaches an impasse, that is, a minimum merit figure that is still unsatisfactory. Synthesis was introduced in the 1960s by Dobrowolski [8]. The use of both refinement and synthesis in design has grown in pace with improvements in and availability of computers.

Refinement processes, and synthesis, search parameter space for acceptable designs. They cannot find what is not present in parameter space. Computer techniques, no matter how powerful, are unable to find designs that do not, or cannot, exist. They have no appreciation of feasibility. The existence of efficient computer refinement techniques, therefore, does not in any way imply that the analytical design methods are obsolete and can be discarded. The analytical techniques inform us about feasibility and existence of designs. They save us from wasting time in unrealistic searches. They help us to set up designs for computer refinement. Thus, we will spend a little time looking at some historical analytical techniques before considering the use of computer refinement.

It should always be remembered, however, that the manufacture of edge filters or, indeed, of any optical coating is not altogether an easy task, and unless the expected performance of a simple design is being achieved in manufacture, there is little point in attempting anything more complicated until the sources of error have been eliminated.

The first and obvious method for improving our edge filter designs is to improve the efficiency of the matching layers. In the chapter on antireflection coatings, there were many multilayer coatings discussed that gave a rather better performance than the single layer. The ultimate performance was obtained with an inhomogeneous layer. Unfortunately, as we have seen, the major problem with inhomogeneous layers is the attainment of an index of refraction less than around 1.35 and we require this if we are to match to air. Jacobsson [9] has, however, considered briefly the matching of a multilayer longwave-pass filter $[(H/2)L(H/2)]^6$, consisting of germanium with an index of 4.0 and silicon monoxide with an index of 1.80, to a germanium substrate by means of an inhomogeneous layer. His paper shows the three curves reproduced in Figure 7.11. The first curve 1 is the multilayer on a glass substrate of index 1.52. Since, in the pass band, the equivalent admittance of the multilayer falls gradually from $(1.8 \times 4.0)^{½} = 2.7$ to zero as the wavelength approaches the edge, it will be a value not too different from the index of

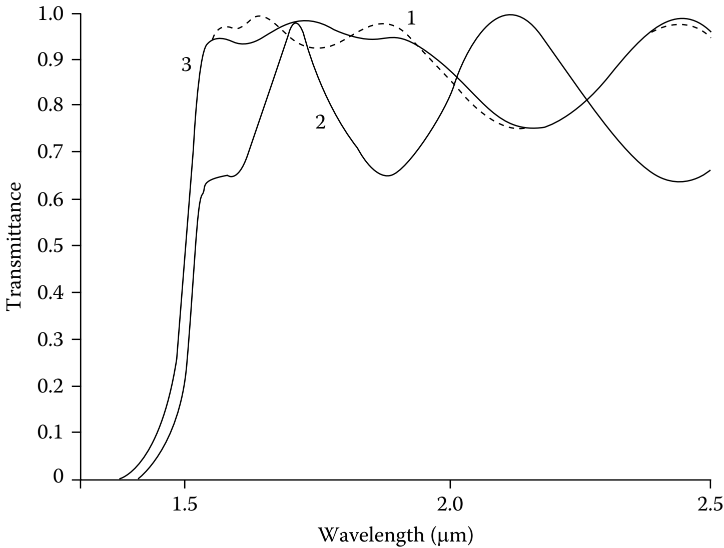

FIGURE 7.11
Reflectance versus wavelength of a multilayer on a substrate with index nsub = 1.52 (curve 1), n_{sub} = 4.00 (curve 2), and on a substrate with n_{sub} = 4.00 with an inhomogeneous layer between substrate and multilayer (curve 3). (After Jacobsson, R., *Journal of the Optical Society of America*, 54, 422–423, 1964.)

the substrate in the vicinity of the edge. The transmittance near the edge is, therefore, high, as we might expect. When, as in curve 2, the same multilayer is deposited on a germanium substrate of index 4.0, the severe mismatching causes a very large ripple to appear. With an inhomogeneous layer between the germanium substrate and the multilayer and with the index varying from that of germanium next to the substrate to 1.52 next to the multilayer, the performance achieved, curve 3, is almost exactly that of the original multilayer on the glass substrate.

One of the examples examined by Baumeister [6] was a shortwave-pass filter, and the design that he eventually obtained suggested a new approach to Young and Cristal [10]. It was mentioned in Chapter 3 that Young had devised a method for designing antireflection coatings based on the quarter-wave transformer used in microwave filters. The antireflection coating takes the form of a series of quarter-waves with refractive indices in steady progression from the index of one medium to the index of the other. Young has given a series of tables enabling antireflection coatings of given bandwidth and ripple to be designed.

In their paper, Young and Cristal explain that they examined Baumeister's filter and realized that the design might be written as a series of symmetrical periods with thicknesses increasing steadily from the middle of the stack to the outside, and they were struck by the resemblance that this bore to an antireflection coating in which each layer had

been replaced by a symmetrical period. They then designed a coating by microwave techniques, to match the admittance at the center of the filter, which they arbitrarily took as 0.6, to air, with admittance 1.0, at the outside, each layer being replaced by an equivalent period. The arrangement is shown as filter B in Table 7.1, where the thicknesses given by Young and Cristal for one of their filters have been broken down into their symmetrical periods. The performance of the filter is shown in Figure 7.12 along with one other filter of their design and Baumeister's original design. The thicknesses are all shown in Table 7.2. To simplify the discussion, Young and Cristal designed the filter to match with air on both sides of the multilayer, instead of, as would be more usual, glass on one side and air on the other.

Young and Cristal do not discuss their design procedure in detail, but, from the final design of the filter, it is possible to deduce it. Following Baumeister, the indices assumed for their films were 1.38 for the low index and 2.30 for the high index. First, the equivalent admittance of a single period was calculated, as in Figure 7.13. The wavelength corresponding to 240° was chosen for optimizing. From the value of equivalent admittance at 240°, the value of 0.6 was probably selected intuitively as the value to use for the center of the stack. An antireflection coating consisting of four layers, each three-quarter wavelengths thick, was designed to match this value to air, and the admittances of the layers computed. The admittances were then matched by that of three-layer symmetrical periods by altering thicknesses of each period, following the scheme shown in Figure 7.13. This meant that the admittances were ideal but the thicknesses were not. However, the antireflection coating is not very susceptible to errors in layer thickness, and as can be seen from the curve in Figure 7.12, the performance achieved is excellent.

A similar approach is to use one of the multilayer antireflection coatings mentioned in Chapter 4. Since the equivalent admittance of a symmetrical period varies with wavelength, any optimizing at one wavelength is strictly correct over only a narrow range, and a simple approach, such as this, is probably as good as a more complicated one. Taking 240° as corresponding to the design wavelength, we find the value for equivalent admittance of the single period to be 0.8. We want the periods in the final design to be symmetrically placed around this period, so we find the starting admittance at the center of the stack by assuming that this period should be able to act as a $3\lambda/4$ antireflection coating between the center and the outside air. The admittance at the center of the filter should therefore be $0.8^2 = 0.64$. Next, we design a four-layer antireflection coating to replace this basic period, using the formulae

$$\eta_1 = \eta_0(\eta_c/\eta_0)^{1/5} \quad \eta_3 = \eta_0(\eta_c/\eta_0)^{3/5}$$

$$\eta_2 = \eta_0(\eta_c/\eta_0)^{2/5} \quad \eta_4 = \eta_0(\eta_c/\eta_0)^{4/5}$$

TABLE 7.1

Designs of Filters B from Figure 7.13 and D from Figure 7.14

Layer Number	Index	Filter B Layer Thickness		Period	Filter D Layer Thickness		Period
1	1.38	47.50°	47.50°		48.56°	48.56°	
2	2.35	95.00°	95.00°	1	97.12°	97.12°	1
3	1.38	93.25°	47.50° 45.75°		94.69°	48.56° 46.13°	
4	2.35	91.50°	91.50°	2	92.25°	92.25°	2
5	1.38	90.00°	45.75° 44.25°		90.38°	46.13° 44.25°	
6	2.35	88.50°	88.50°	3	88.50°	88.50°	3
7	1.38	87.50°	44.25° 43.25°		87.38°	44.25° 43.13°	
8	2.35	86.50°	86.50°	4	86.25°	86.25°	4
9	1.38	86.50°	43.25° 43.25°		86.26°	43.13° 43.13°	
10	2.35	86.50°	86.50°	5	86.25°	86.25°	5
11	1.38	87.50°	43.25° 44.25°		87.38°	43.13° 44.25°	
12	2.35	88.50°	88.50°	6	88.50°	88.50°	6
13	1.38	90.00°	44.25° 45.75°		90.38°	44.25° 46.13°	
14	2.35	91.50°	91.50°	7	92.25°	92.25°	7
15	1.38	93.25°	45.75° 47.50°		94.69°	46.13° 48.56°	
16	2.35	95.00°	95.00°	8	97.12°	97.12°	8
17	1.38	47.50°	47.50°		48.50°	48.56°	

The second column in each case gives the filter split into its component periods.

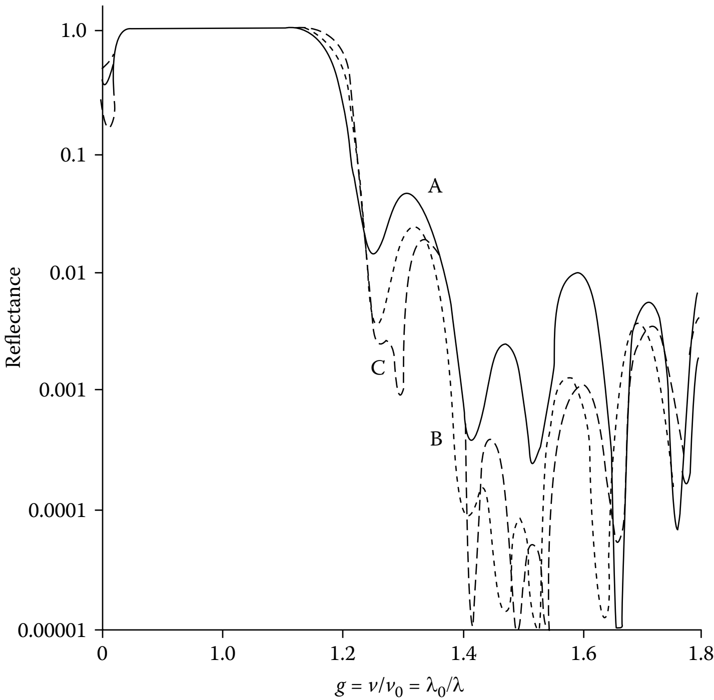

FIGURE 7.12
Reflectance of the three shortwave-pass filter designs, A, B, and C, having unequal layer thickness. (After Young, L. and Crystal, E.G., *Applied Optics*, 5, 77–80, 1966.)

where η_0 is air and η_c is the admittance at the center. Taking $\eta_0 = 1.0$ and $\eta_c = 0.64$, these admittances are then

$$\eta_1 = 0.91 \quad \eta_2 = 0.84 \quad \eta_3 = 0.76 \quad \eta_4 = 0.70$$

The values of total phase thickness πg at which the single period has equivalent admittance corresponding to these values are

$$\pi g_1 = 259^\circ \quad \pi g_2 = 246^\circ \quad \pi g_3 = 236^\circ \quad \pi g_4 = 230^\circ$$

For each period to have the appropriate admittance at the design wavelength, the phase thicknesses of the layers measured at the monitoring wavelength are given by

TABLE 7.2

Designs of the Three Filters in Figure 7.12

Layer Number	Thickness (Degrees)		
	Filter A	**Filter B**	**Filter C**
1	46.00	47.50	46.60
2	96.00	95.00	93.20
3	93.20	93.25	91.70
4	91.70	91.50	90.20
5	91.10	90.00	89.15
6	89.75	88.50	88.10
7	87.50	87.50	87.30
8	86.05	86.50	86.50
9	86.70	86.50	86.50
10	86.05	86.50	86.50
11	87.50	87.50	87.30
12	89.75	88.50	88.10
13	91.10	90.00	89.15
14	91.70	91.50	90.20
15	93.20	93.25	91.70
16	96.00	95.00	93.20
17	46.00	47.50	46.60

Filter A: The half of Baumeister's filter on the air side repeated symmetrically. (The design is referred to as design IX in Baumeister's paper [6].)

Filter B: New design based on a prototype transformer with a fractional bandwidth of 1.5.

Filter C: New design based on a prototype transformer with a fractional bandwidth of 1.6.

$$\text{Period 1}\begin{cases}\dfrac{L}{2}45^\circ \times \dfrac{\pi g_1}{240^\circ}\\ H90^\circ \times \dfrac{\pi g_1}{240^\circ}\\ \dfrac{L}{2}45^\circ \times \dfrac{\pi g_1}{240^\circ}\end{cases} \qquad \text{Period 2}\begin{cases}\dfrac{L}{2}45^\circ \times \dfrac{\pi g_2}{240^\circ}\\ H90^\circ \times \dfrac{\pi g_2}{240^\circ}\\ \dfrac{L}{2}45^\circ \times \dfrac{\pi g_2}{240^\circ}\end{cases}$$

and so on. The results are shown in Table 7.1, filter D. The transmittance of filter D is shown in Figure 7.14 compared with that of filter A.

Thelen [3] has pointed out that the rapid variation of equivalent admittance near the edge of the filter is the major source of difficulty in edge filter design. It is a simple matter to match the multilayer to the substrate where the equivalent admittance curve is flat, some distance from the edge, but

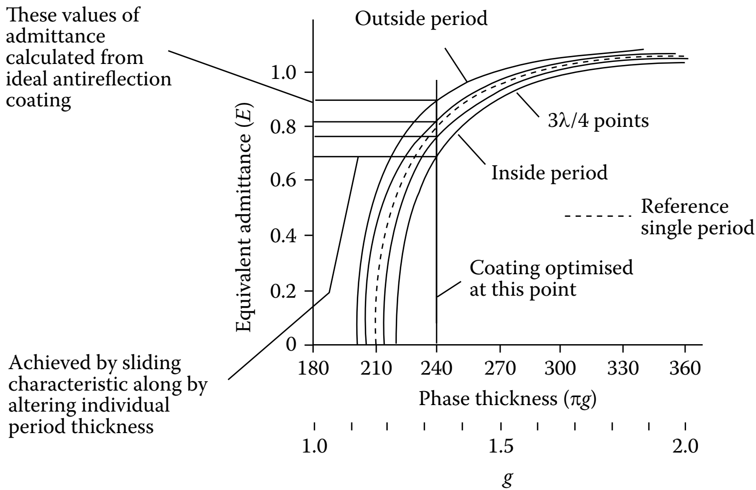

FIGURE 7.13
The admittance of the ideal four-layer antireflection coating to match air to the admittance of 0.6 is marked along the equivalent admittance axis. The reference single period is shown *dotted*, and the values marked on the *g*-axis refer to this period. By altering the total thickness of each period relative to this reference, the four displaced solid line curves are obtained in such a way that the four symmetrical periods have the desired admittances at the wavelengths that correspond to a reference phase thickness of 240°.

the variations near the edge usually give rise, with simple designs, to a pronounced dip in the transmission curve. Thelen has devised an ingenious method of dealing with this dip, involving the equivalent of a single-layer antireflection coating. Between the substrate and/or the incident medium and the main or primary multilayer, which consists of a number of equal basic periods, Thelen places a secondary multilayer, similar to the first but shifted in thickness so that, in the center of the steep portion of the admittance curve, the equivalent admittance of the secondary is made equal to the square root of the equivalent admittance of the primary times the admittance of the substrate. The number of secondary periods is chosen to make the thickness at this point an odd number of quarter-waves and to satisfy completely the antireflection condition. Figure 7.15 shows the performance he achieved.

Seeley and Smith [11] developed a different method of adapting results obtained in the synthesis of lumped electrical circuits for use in thin-film optical filters. One of the features of Young's method is that the refractive indices cannot be specified in advance, and as the range of available indices is limited this can lead to difficulties. In certain cases this can be avoided, as we have seen, by constructing three-layer periods with the appropriate equivalent indices, but even this has its limitations. Seeley, therefore, searched for another method that would permit the designer to specify the indices right from the start and to achieve the final performance by

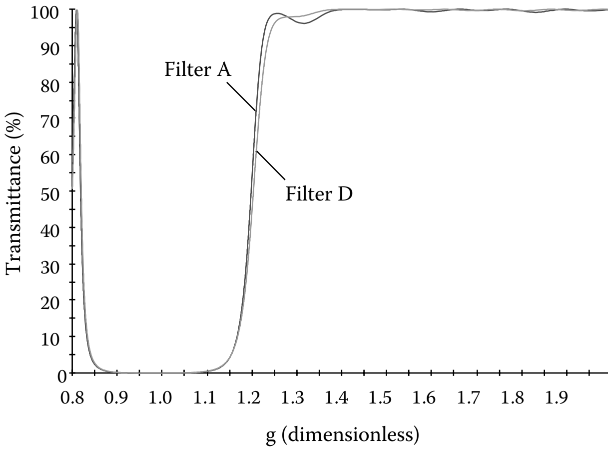

FIGURE 7.14
The computer transmittance of the shortwave-pass filter of design D of Table 7.1 compared with filter A.

varying the thicknesses of the various layers. In a lumped electrical filter, consisting of inductances and capacitances, one parameter only is specified—the admittance. In the thin-film filter, there are two parameters for each layer—the refractive index and the thickness. Thus, it is possible for the optical designer to fix the values of the refractive indices of the

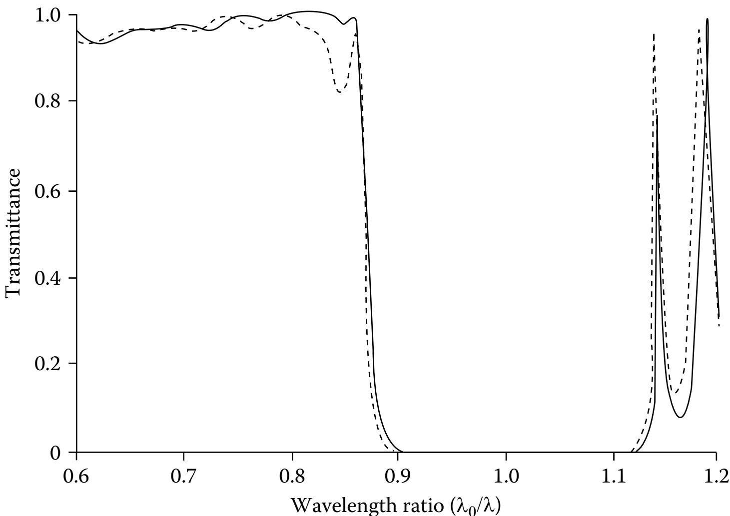

FIGURE 7.15
Comparison of the computed performance of the filters: $1.00|(0.5H\ L\ 0.5H)^{15}|1.52$ (*dashed line*) and $1.00|(0.5H\ L\ 0.5H)^{12}[(1/1.05)(0.5H\ L\ 0.5H)^{3}]|1.52$ (*solid line*) with $n_H = 2.3$, $n_L = 1.56$. (After Thelen, A., *Journal of the Optical Society of America*, 56, 1533–1538, 1966.)

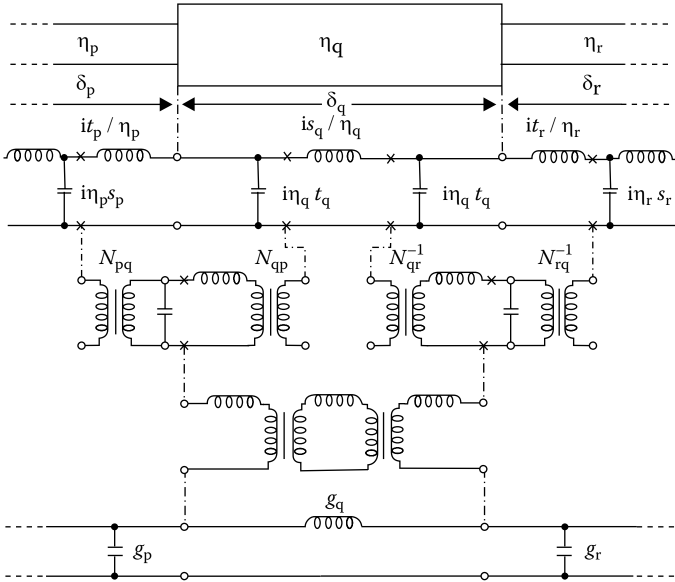

FIGURE 7.16
The conversion used by Seeley in diagrammatic form. High-index layers are first replaced by a T circuit and low-index ones by a π circuit. This figure shows the step-by-step process by which Seeley converts a multilayer thin-film filter into a lumped electric filter in such a way that the elements of the electric filter can be identified with the optical thickness of the films, the indices of the films being specified completely independently. (Courtesy of Dr. J. S. Seeley.)

multilayer filter in advance and then to compute the layer thickness by analogy with the lumped filter. As Welford [5] has pointed out, the analogy between thin-film assemblies and lumped electric filters is not exact. Thin films behave, in fact, in the same manner as lengths of transmission line. Seeley, however, devised a way of making the analogy exact, although only at one frequency. At all other frequencies, the analogy is only approximate. If the frequency chosen for exact correspondence is made the cut-off point of the filter, then the performance of the optical filter is found to be sufficiently close to that of the electrical filter over the usual working range. The techniques for optimizing the performance of electrical filters are well established.

Seeley's method starts with an electrical filter of the desired type—longwave-pass, shortwave-pass, or band-pass—whose performance is known to be optimum. The elements of the electrical filter are then converted by a step-by-step process into an equivalent circuit that is an exact analogue of the thin-film multilayer at one frequency. The process is shown in Figure 7.16 and Figure 7.17. In his design work, Seeley usually chooses electrical filters that have been designed using the Tchebyshev equal ripple polynomial. This polynomial allows the best fit to a square pass band when both

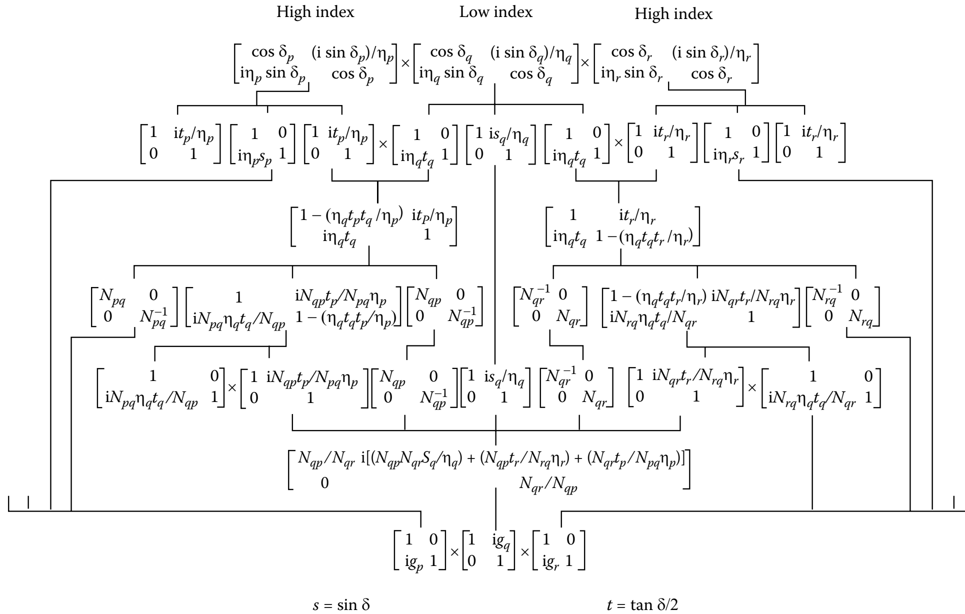

FIGURE 7.17
The Seeley conversion: the manipulation takes place at the cut-off frequency of the lumped circuit and all variable quantities are normalized to that frequency. The arrangement leads to a fairly complicated set of equations for ... δ_p, δ_q, δ_r ... in terms of ... g_p, g_q, g_r … , which cannot be solved analytically but require iteration. Approximate solutions have been derived and are as follows:

$$\text{High-Index layers: } \sin\delta_p = \frac{g_p}{(\eta_H/\eta_{sub}) + (\eta_L/\eta_{sub})} \qquad \text{Low-Index layers: } \sin\delta_q = \frac{g_q}{(\eta_{sub}/\eta_L) + (\eta_{sub}/\eta_H)}$$

δ being between 0 and $\pi/2$ for longwave-pass filters and $\pi/2$ and π for shortwave-pass filters. The admittance levels in the derivation of these two expressions have been normalized to the terminating admittance (of the substrate), so that for η_p we have written η_H/η_{sub} and for η_q, η_L/η_{sub}, η_H and η_L being the admittances of the high- and low-index layers, respectively.

TABLE 7.3

Designs of Filters from Figure 7.18

	Relative Thickness	
Layer Number	**Longwave-Pass**	**Shortwave-Pass**
1 and 14	0.55	1.25
2 and 13	0.82	1.11
3 and 12	0.92	1.05
4 and 11	0.96	1.025
5 ands 10	0.98	1.015
6 and 9	0.99	1.01
7 and 8	1.00	1.00
15 (antireflection)	2.00	0.50

edge steepness and ripple in the pass band are taken into account. From this, Seeley and Smith [12] have given simple rules for longwave-pass filters.

1. The optical admittance of the substrate η_{sub} should lie between η_H and η_L, the admittances of the high- and low-index layers of the multilayer. If this is not satisfied, then a matching layer or combination of layers will be necessary between the substrate and the multilayer.
2. The first layer at the substrate should be high if $\eta_H/\eta_{sub} > \eta_{sub}/\eta_L$, and low if $\eta_{sub}/\eta_L > \eta_H/\eta_{sub}$.
3. The fractional ripple in the pass band will be

$$\left(\frac{\eta_H}{\eta_{sub}} - \frac{\eta_{sub}}{\eta_L}\right)^2 \left(\frac{\eta_H}{\eta_{sub}} + \frac{\eta_{sub}}{\eta_L}\right)^{-2}$$

4. For filters on germanium substrates using as layer materials lead telluride and zinc sulfide, the phase thicknesses should be in the proportions shown in Table 7.3. The first layer at the substrate and all other odd layers, including the antireflection layer, are ZnS (n = 2.2). The remaining (even) layers are PbTe (n = 5.1). The substrate, germanium, has an index of 4.0.
5. Since the low-index material is usually good for matching the substrate to air, the front layer of the multilayer section of the filter should have a high index. The computed transmittances of the designs given in Table 7.3 are given in Figure 7.18. The method is described in greater detail by Seeley et al. [11].

The computed transmittances of the designs given in Table 7.3 are shown in Figure 7.18. The method is described in greater detail elsewhere [11,12].

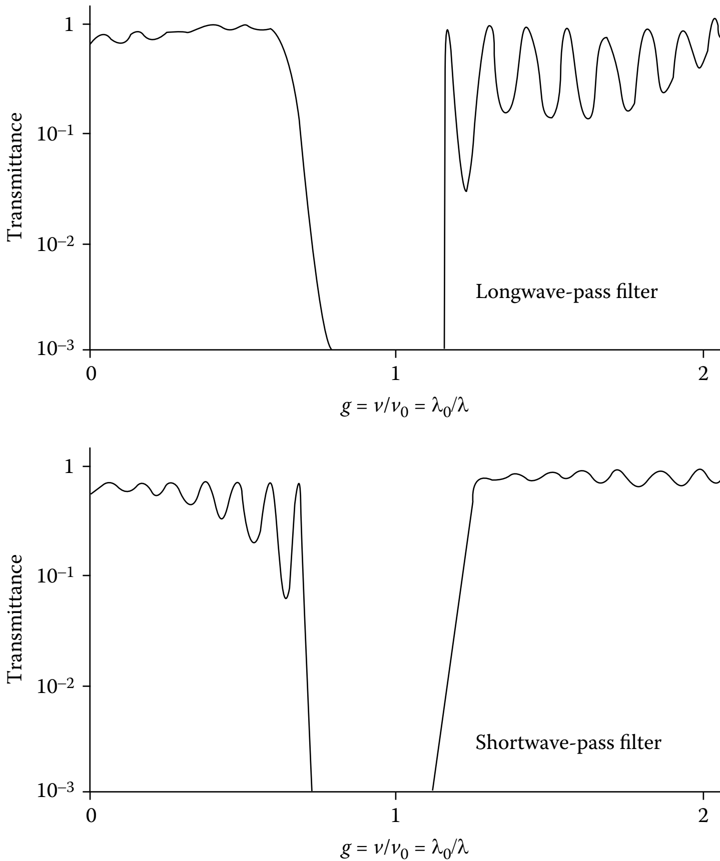

FIGURE 7.18
Computed transmittance of the 14-layer filters given in Table 7.3. ν_0 and λ_0 are the frequency and wavelength, respectively, at which the central layers are a quarter-wave in thickness. (After Seeley, J.S. and Smith, S.D., *Applied Optics*, 5, 81–85, 1966.)

All of these techniques that have been discussed so far trace their origins to the time when only the mainframe computer was available. It was important to carry out as much preliminary design work as possible before submitting the design to the machine. We repeat these techniques here because they contribute much to our understanding of design and the problems that can and cannot be solved. The more modern approach makes much greater use of computers in what is usually called *computer-aided design*.

We know from the previous pages that the edge filter consists essentially of a structure based on the quarter-wave stack. The properties are derived from a mismatch between this structure and the surrounding media. In the rejection, or high-reflectance, zones, the mismatch is so serious that high reflectance is achieved. The mismatch is in the nature of a

real admittance and an imaginary admittance. Inserting dielectric layers in between these two media has virtually no effect on the high reflectance. In the pass, or potential pass, zones, the mismatch is essentially between two real admittances and this leads to interference fringes that are usually known as *ripple*. Here dielectric layers in the form of matching assemblies can be used to reduce the mismatch and, hence, the ripple. Thus, a useful procedure is to establish a structure, usually based on the quarter-wave stack that has the correct rejection and potential pass zones, and to design suitable matching structures to reduce the ripple to acceptable levels. This is rather like the design of an antireflection coating except that the thin-film structure exhibits dispersion very much more complex than a simple dielectric material. However, the computer is just as successful at handling the complicated dispersion as it is at simple dispersion. The user simply has to set the problem up in the form of the correct instructions. We illustrate the method in the design of a straightforward edge filter of a longwave-pass type. To simplify the demonstration, we will use dispersionless materials of indices 1.45 and 2.15 for the thin films and 1.52 for the substrate. We will arrange for the longwave edge of the rejection region to be at 700 nm.

Edge is a vague term. It means what the supplier of the filter intends it to mean. In some cases, the 5% transmittance point is taken as the edge wavelength. In other cases it can be the 50% wavelength. We use it here in the rather imprecise sense of the start of the pass region and, therefore, of rather high transmittance. If this is not satisfactory, then the reference wavelength can readily be adjusted to achieve whatever is the desired definition. We start with a quarter-wave stack with reference wavelength 608 nm. How many layers to use is always a difficult question. Fortunately, with a relatively fast computer, a little trial and error is a completely feasible and simple method. The design process is going to construct matching assemblies on either side of the core of the filter that we will retain as a set of quarter-waves. These matching assemblies will reduce a little, the steepness of edge. We start with a quarter-wave stack that has roughly the desired shape. This will be the core of the filter. Next we add sufficient quarter-wave layers on either side to form the matching structures. We lock the quarter-wave stack core so that it does not take part in the refinement. We specify the transmittance in the pass region as the targets for refinement, and the result of this procedure with a 28-layer core and 10-layer matching structures on either side is shown in Figure 7.19.

This is normally a very fast procedure, and it has the advantage of avoiding the need for specifying the rejection region. It also avoids the appearance of spikes between target points in the rejection region, which can be a problem when all layers take part in the refinement.

Some refinement processes, particularly very fast ones, can be rather eager in their travel over the merit surface, shutting down some layer thicknesses

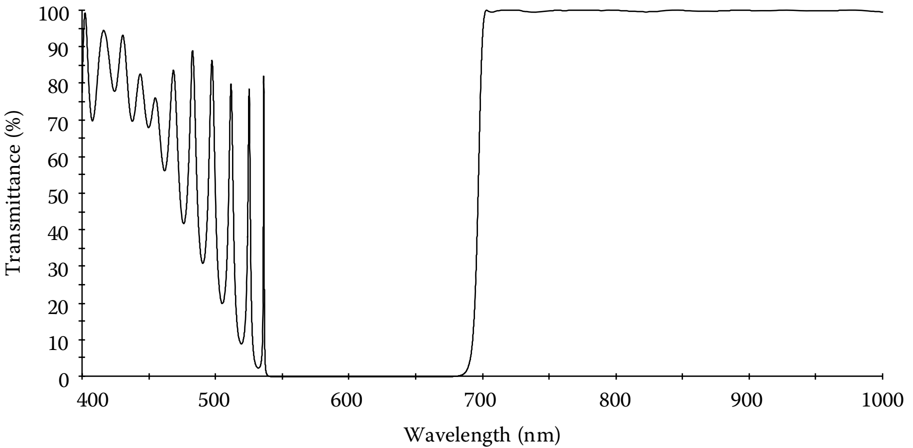

FIGURE 7.19
The transmittance of a 48-layer longwave-pass filter. The outermost 10 layers on each side were refined to reduce the ripple in the pass region. The remaining layers form a quarter-wave core.

to zero. It can be difficult to recover from this. A good technique, especially in such cases, is to open up the matching systems for refinement gradually.

Once a design has been established, it is easy to check the rejection performance and make appropriate changes to the starting design by adding or subtracting layers.

Shortwave-pass filters can be designed using essentially the same technique. It should be remembered, however, that the possible width of the pass region is limited by the appearance of the higher reflecting orders. They cannot be eliminated simply by the outer matching layers but need a rather different approach, dealt with a little later in this chapter.

7.2.3.7 Practical Filters

Because the stop band of the multilayer edge filter is limited in extent, it is usually necessary for practical filters to consist of a multilayer filter together with additional filters to give the broad rejection region that is almost always required. These additional filters may be multilayer, and some methods of broadening the stop band in this way are mentioned in the following section. Usually they are absorption filters having wide rejection regions but inflexible characteristics. These absorption filters may be combined with multilayer filters in a number of different ways. They may simply be placed in series with the substrates carrying the multilayers, the substrates may themselves be the absorption filters, or the multilayer materials may also act as thin-film absorption filters.

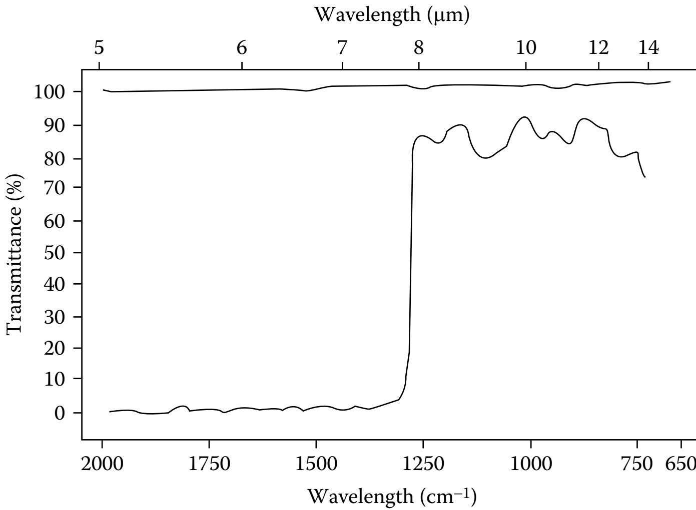

FIGURE 7.20
Measured transmittance of a practical longwave-pass filter with edge at 1250 cm^{-1} (8 μm). (Courtesy of OCLI Optical Coatings Ltd.)

In the visible and near ultraviolet regions, there is available a wide range of glass filters that solve most of the problems, particularly those connected with longwave-pass filters. In the infrared, the position is rather more difficult, and often the complete filter consists of several multilayers, which are necessary to connect the edge of the stop band to the nearest suitable absorption filter. Figure 7.20 shows a longwave-pass filter for the infrared. Figure 7.21 gives some of the infrared absorption filters that have shortwave-pass characteristics.

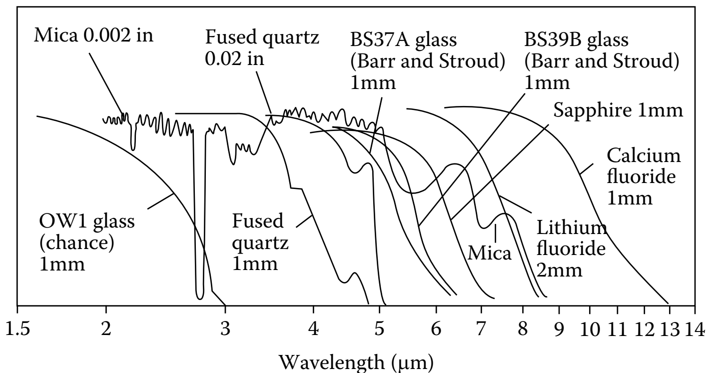

FIGURE 7.21
A selection of infrared materials that can be used as shortwave-pass absorption filters. (Courtesy of Sir Howard Grubb, Parsons & Co. Ltd.)

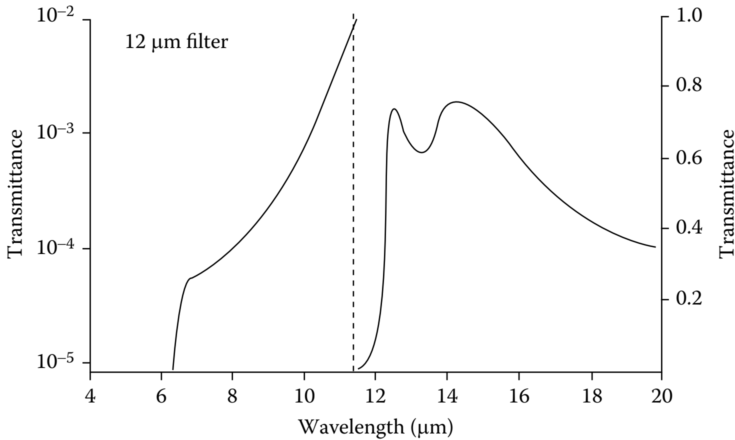

FIGURE 7.22
Measured transmittance of a multilayer blocking filter with edge at 12 μm. A subsidiary indium antimonide filter is included to ensure good blocking at wavelengths shorter than 7 μm. (After Seeley, J.S. and Smith, S.D., *Applied Optics*, 5, 81–85, 1966.)

Unfortunately, not all of these materials are currently easily available. For longwave-pass characteristics, semiconductors such as silicon, with an edge at 1 μm, and germanium, with an edge at 1.65 μm, are the most suitable. Indium arsenide, with an edge at 3.4 μm, and indium antimonide, with edge at 7.2 μm, are also useful, but because of the rather higher absorption they can only be used in very thin slices, around 0.013 cm for indium antimonide and only a little thicker for indium arsenide. This means that they tend to be extremely fragile and can only be produced in a circular shape of rather limited diameter, not usually greater than 2.0 cm.

The measured transmittance for a longwave-pass filter consisting of an edge filter together with an absorption filter is given in Figure 7.22. This filter was originally designed to be used as a shortwave blocking filter with narrowband filters at 15 μm. It consists of two components—a multilayer filter made from a lead telluride and zinc sulfide multilayer on a germanium substrate and placed in series with an indium antimonide filter. The very high rejection achieved can be seen from the logarithmic plot.

7.2.3.8 Extending the Rejection Zone by Interference Methods

The most convenient and straightforward way of extending the reflectance zone is to place a second quarter-wave stack in series with the first, and to ensure that their rejection zones overlap. The second stack is best placed either on a second substrate or on the opposite side of the substrate from the first stack. This avoids some unfortunate interference consequences.

However, there are also some multiple beam effects that can lead to disappointing performance.

We would like the transmittance of the combined components to be given by

$$T = T_a T_b \tag{7.46}$$

where T_a and T_b are the individual transmittances. This will be the case if the transmission loss is purely by absorption but if there are multiple beams reflected back and forth between the surfaces and these beams reach the receiver then the transmittance will be higher.

The worst case occurs when all the multiple beams are collected and contribute to the signal. The full theory is given in Chapter 2. In the complete absence of absorption and collection of all beams, that is the worst case, then the transmittance is given by

$$T = \frac{1}{(1/T_a) + (1/T_b) - 1} \tag{7.47}$$

If T_a and T_b are both small and equal, then, instead of their product, the resultant transmittance is just one half of their individual transmittance. Whatever the arrangement, the net transmittance can never be larger than the smaller of T_a and T_b.

To avoid this, the substrate should be made reasonably thick and, if possible, slightly wedged. Anything that can be done to reduce the power of the reflected beams is also worthwhile. Absorbing material, even if only slightly absorbing, placed between the two surfaces can also help.

A more difficult situation occurs when it is impossible to place the stacks on separate surfaces, and one stack must be deposited directly on top of the other. In this case, it is necessary to take precautions to avoid the creation of transmission maxima. The problem has already been dealt with in Chapter 6 where the extension of the high-reflectance zone of a quarter-wave stack was discussed.

If we consider the assembly split into two separate multilayers, then a transmission maximum will occur at any wavelength for which $(\varphi_a + \varphi_b)/2 = m\pi$, where $m = 0, \pm 1, \pm 2, \ldots$. The height of this maximum is given by

$$T = \frac{|\tau_a^+|^2 |\tau_b^+|^2}{\left(1 - |\rho_a^-||\rho_b^+|\right)^2} = \frac{T_a T_b}{\left[1 - (R_a R_b)^{1/2}\right]^2} \tag{7.48}$$

If there is no absorption, this expression implies that, for low transmittance at the maxima, R_a and R_b should be as dissimilar as possible. This can be

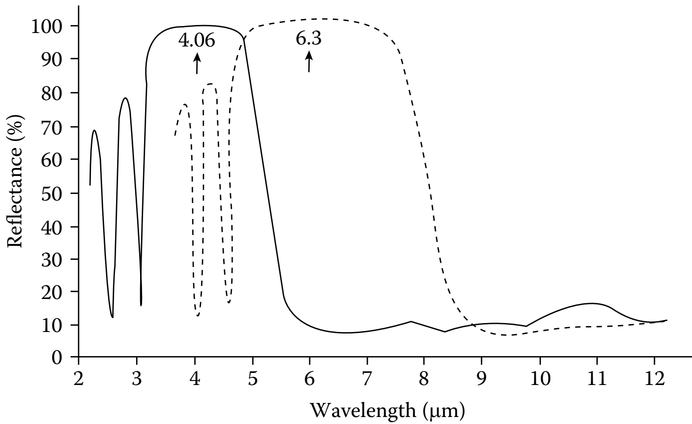

FIGURE 7.23
Measured reflectance of two longwave-pass stacks: A|(0.5*H L* 0.5*H*)^4|BaF_2 H and L are films of stibnite and chiolite a quarter-wave thick at $\lambda_0 = 4.06$ μm or 6.3 μm. A is air and the substrate is barium fluoride. (After Turner, A.F. and Baumeister, P.W., *Applied Optics*, 5, 69–76, 1966.)

achieved by using many layers to keep the reflectance of one multilayer as high as possible in the pass region of the other.

In slightly more quantitative terms, from the reflectance envelope, which does not vary with the number of periods, we can find the highest reflectance in the pass region of either multilayer making up the composite filter. If we denote this reflectance by R_p, then we can be certain that the design will be acceptable if we choose a sufficiently high number of periods to make R_s, the lowest reflectance in the stop band of the other multilayer, sufficiently high to ensure that

$$\frac{(1-R_p)(1-R_s)}{\left[1-(R_pR_s)^{1/2}\right]^2} \leq T_c \tag{7.49}$$

where T_c is some acceptable level for the transmission in the rejection zone of the complete filter. This formula will give a pessimistic result; the actual transmission achieved in practice will depend on the phase change as well as the reflectance.

The other danger area is the region where the two high-reflectance bands are overlapping. There, it must be arranged that on no account is $(\varphi_a + \varphi_b)/2 = m\pi$. The method for dealing with this was described in the previous chapter where a layer of intermediate thickness was placed between the two quarter-wave stacks. The result is equivalent to placing two similar multilayers, both of the form $[(L/2)H(L/2)]^m$ or $[(H/2)L(H/2)]^m$, together.

Equation 7.49 also implies that some of the sections of the composite filter should have more periods than others. In the reduction of the ripple in the

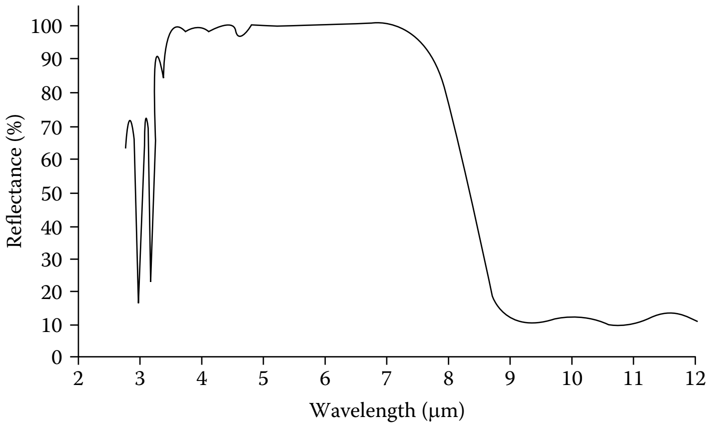

FIGURE 7.24
Measured reflectance of the two longwave-pass stacks of Figure 7.23 superimposed in a single coating for an extended high-reflectance region. (After Turner, A.F. and Baumeister, P.W., *Applied Optics*, 5, 69–76, 1966.)

pass band of the basic multilayer, the ripple on the other side of the stop band is almost invariably increased. Thus, in the combination of, say, two multilayers, the rejection zone of one stack will overlap a region of high ripple, while the rejection zone of the other stack will overlap a region of relatively low ripple. Since high ripple means that R_p is high, the former stack should have more periods than the latter if the same level of rejection is required throughout the combined rejection region. Figure 7.23 shows two component edge filters which are combined in a single filter in Figure 7.24. The severe ripple that occurs in one of the multilayers can be seen reflected in the rejection zone of the composite filter. This ripple is limited to part of the rejection zone only, and in order to reduce the effect, more periods are necessary in the appropriate multilayer.

The same procedure is valid for shortwave-pass filters but there is the additional problem of the higher reflecting orders, which is dealt with in the next section.

A common current requirement is for a shortwave-pass filter to block the near infrared and transmit the visible region. These filters are used in different applications, but a common one is the reduction of the infrared sensitivity of a silicon receiver that might be used in a digital camera. The width of the rejection region is beyond the capabilities of a single quarter-wave stack, so we need to broaden the rejection zone. We can do this using one or other of the methods already discussed. Fortunately, the usual requirement can be satisfied without the need for suppression of a third-order peak, so a straightforward two-material structure is sufficient.

The filter in Figure 7.25 was created by refinement of all layers, starting with a tapered design as shown and involving all layers in the refinement.

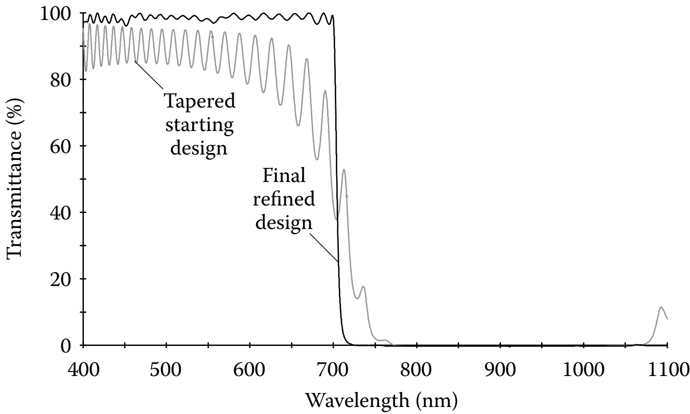

FIGURE 7.25
The performance of a shortwave pass filter with extended rejection zone. This is a 40-layer design with $n_L = 1.45$ and $n_H = 2.35$, corresponding roughly to SiO_2 and TiO_2. The substrate is glass with index 1.52 and the incident medium air with $n = 1.00$. A linearly tapered 40-layer stack with low index outermost was created as starting design and then the entire system was refined to yield the final performance.

A virtually indistinguishable final design can also be obtained by starting with air$\left|(LH)^{20}\right|$Glass at $\lambda_0 = 800$ nm. The refinement process achieved the sharp edge by assembling the first half of the filter into what is essentially a quarter-wave stack with the required sharpness of shortwave edge. It adjusted the remaining layers to fill in the longwave part of the rejection region. By a slight tuning of all the layer thicknesses, it achieved the matching in the pass region. Different refinement techniques all appear to converge on much the same final design.

This approach, using refinement, where a starting design, sufficiently close to the requirements, can be created and where there is reasonable certainty of the existence of a satisfactory end point, is typical of the more modern way of designing optical coatings. It does require knowledge of the structures likely to be successful, but it removes the tedious manual labor that used to be the primary feature of thin-film coating design.

7.2.3.9 Extending the Transmission Zone

The shortwave-pass filter, as it has been described so far, possesses a limited pass band because of the higher-order stop bands. These are not always particularly embarrassing, but occasionally, as for example with some types of heat reflecting filters, a much wider pass band is required. The problem was first considered by Epstein [14] and was studied more extensively by Thelen [15].

Epstein's analysis was as follows. Let the multilayer be represented by s periods each of the form

$$M = \begin{bmatrix} M_{11} & M_{12} \\ M_{21} & M_{22} \end{bmatrix}.$$

If a single period is considered as if it were immersed in a medium of admittance η, then the transmission coefficient of the period is given by

$$\tau = \frac{2\eta_0}{\eta_0 B + C} = \frac{2\eta}{\eta\left[\left(M_{11} + M_{22}\right) + \left\{\eta M_{12} + \left(M_{21}/\eta\right)\right\}\right]}$$

where η_0, B, and C have the usual meaning as explained in Chapter 2.
Let $\tau = |\tau| e^{i\varphi}$; then

$$\frac{1}{2}\left[\left(M_{11} + M_{22}\right) + \left\{\eta M_{12} + \left(M_{21}/\eta\right)\right\}\right] = \frac{\cos\varphi - i\sin\varphi}{|\tau|}$$

If the period is transparent, equating real parts gives

$$\frac{1}{2}\left(M_{11} + M_{22}\right) = \frac{\cos\varphi}{|\tau|}$$

Now, if light that has suffered two or more reflections at interfaces within the period is ignored, then

$$\varphi \simeq \sum \delta$$

the total phase thickness of the period.
When $\sum\delta = m\pi$, $\cos\varphi = \pm 1$, and, if $|\tau| < 1$, then

$$\frac{1}{2}\left|\left(M_{11} + M_{22}\right)\right| > 1$$

and a high-reflectance zone results. If, however, $|\tau| = 1$, then

$$\frac{1}{2}\left|\left(M_{11} + M_{22}\right)\right| = 1$$

and the high-reflectance zone is suppressed. In the simple form of stack, $[(L/2)H(L/2)]^s$ or $[(H/2)L(H/2)]^s$, $|\tau| = 1$ for $\varphi = 2m\pi$ $m = 1, 2, 3, 4, \ldots$ and the

even-order high-reflectance zones are therefore suppressed. As noted earlier, only a slight change in the relative thicknesses of the layers is enough to reduce τ and turn the band into a high-reflectance zone.

Putting this result in another way, a zone of high reflectance potentially exists whenever the total optical thickness of an individual period of the multilayer is an integral number of half-waves, and the high-reflectance zone is prevented from appearing if, and only if, $|\tau| = 1$. This result was then used by Epstein in his paper to design a multilayer in which the fourth- and fifth-order reflectance bands were suppressed. Thelen has extended Epstein's analysis to deal with cases where any two and any three successive orders are suppressed, and it is this method we shall follow.

Following Epstein, Thelen [15] assumed a five-layer form, *ABCBA*, involving three materials, as the basic period of the multilayer, and noted that if the period is thought of as immersed in a medium *M*, the combination *AB* becomes an antireflection coating for *C* in *M* at the wavelengths where suppression is required. In the construction of the final multilayer, the medium *M* can be considered first to exist between successive periods and then to suffer a progressive decrease in thickness until it just vanishes. The shrinking procedure leaves unchanged the suppression of the various orders that has been arranged. *M* can, therefore, be chosen quite arbitrarily during the design procedure to be discarded later. The antireflection coating *AB* is of a type studied originally by Muchmore [16], and Thelen adapted his results as follows.

The various parameters of the layers are denoted by the usual symbols with the appropriate suffixes *A, B, C*, and *M*.

Let layers *A* and *B* be of equal optical thickness, i.e.,

$$\delta_A = \delta_B \tag{7.50}$$

and let

$$\eta_A \eta_B = \eta_C \eta_M \tag{7.51}$$

Then the wavelengths for which unity transmittance will be achieved will be given by

$$\tan^2 \delta_A' = \frac{\eta_A \eta_B - \eta_C^2}{\eta_B^2 - \left(\eta_A \eta_C^2 / \eta_B\right)} \tag{7.52}$$

(This result can be derived from Equations 4.4 and 4.5. If we replace, in these equations, suffixes 1, 2, *sub*, and 0 by *A, B, C*, and *M*, respectively, then the condition for $\delta_A = \delta_B$ is, from Equation 4.5: $\eta_A \eta_B = \eta_C \eta_M$ and Equation 7.52 then follows immediately from Equation 4.4.)

Two solutions given by Equation 7.52, δ'_A and $(\pi - \delta'_A)$, are possible. We can specify that δ'_A correspond to λ_1 and $(\pi - \delta'_A)$ to λ_2 where λ_1 and λ_2 are the two wavelengths where suppression is to be obtained. Solving these two equations for δ'_A gives

$$\delta'_A = \frac{\pi}{1+(\lambda_1/\lambda_2)} \tag{7.53}$$

This can be entered in Equation 7.52, whence

$$\tan^2 \frac{\pi}{1+(\lambda_1/\lambda_2)} = \frac{\eta_A\eta_B - \eta_C^2}{\eta_B^2 - (\eta_A\eta_C^2/\eta_B)} \tag{7.54}$$

This determines the complete design of the coating. The optical thickness of the layer *A* can be found from Equation 7.53 to be

$$\frac{\lambda_1\lambda_2}{2(\lambda_1 + \lambda_2)} \tag{7.55}$$

The only other quantity to be found is the optical thickness of layer *C*, and we note first that the total optical thickness of the period is $\lambda_0/2$, where λ_0 is the wavelength of the first high-reflectance zone. The optical thicknesses of layers *A* and *B* have already been defined as equal, so that the optical thickness of layer *C* is

$$\frac{\lambda_0}{2} - \frac{2\lambda_1\lambda_2}{2(\lambda_1 + \lambda_2)} \tag{7.56}$$

This medium *M* introduced as an artificial aid to calculation, disappears, and does not figure at all in the results. Any two of the optical admittances η_A, η_B, and η_C can be chosen at will. The third one is then found from Equation 7.54.

Thelen gives a large number of examples of multilayers with various zones suppressed. Particularly useful is a multilayer with the second- and third-order zones suppressed. For this,

$$\lambda_1 = \lambda_0/2 \qquad \lambda_2 = \lambda_0/3$$

and all the layers are found to be of equal optical thickness $\lambda_0/10$. Two of the refractive indices of the layers are then chosen and Equation 7.54 is solved for the remaining one. For rapid calculation, Thelen gives a nomogram

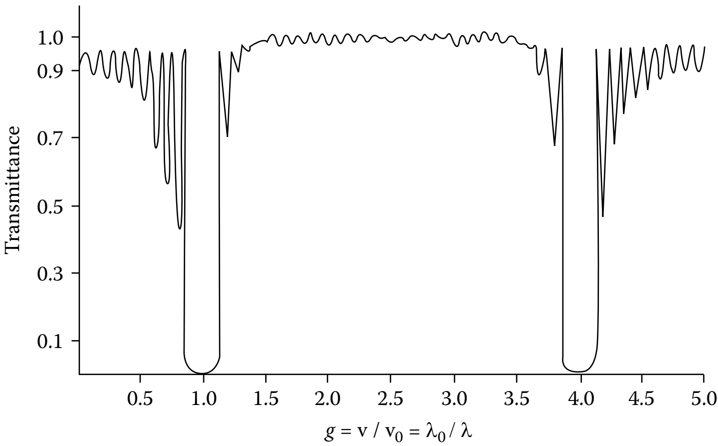

FIGURE 7.26
Calculated transmittance as a function of g of the design: Incident|$(ABCBA)^{10}A$|sub with n_{sub} = 1.50, $n_0 = 1.00$, $n_A = 1.38$, $n_B = 1.90$ and $n_C = 2.30$. (After Thelen, A., *Journal of the Optical Society of America*, 53, 1266–1270, 1963.)

connecting the three quantities. The transmittance of a multilayer with the second and third orders suppressed is given in Figure 7.26.

Thelen also considered a multilayer in which the second, third, and fourth orders were all suppressed and found the conditions to be as follows. Layer thicknesses:

$$A\colon\ \lambda_0/12$$

$$B\colon\ \lambda_0/12$$

$$C\colon\ \lambda_0/6$$

The indices are given by

$$\eta_B = (\eta_A \eta_C)^{1/2}$$

Figure 7.27 shows the transmittance of a multilayer where the second, third, and fourth orders have been suppressed in this way.

A heat-reflecting filter using a combination of stacks in which the second and third, and second, third, and fourth orders, have been suppressed, together with the normal quarter-wave stacks, has been designed. The calculated transmittance spectrum is shown in Figure 7.28. The production of such a coating would indeed be a formidable task.

The so-called half-wave hole is a common problem with shortwave-pass filters. The visible symptom is a narrow dip in transmittance at around one-half of the fundamental reference wavelength where the layers are

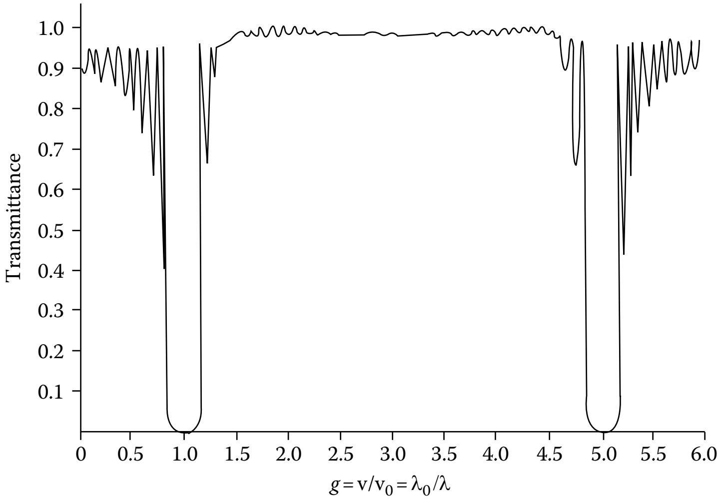

FIGURE 7.27
Calculated transmittance as a function of g of the design: Incident $|(AB2CBA)^{10}A|$ sub with $n_{sub} = 1.50$, $n_0 = 1.00$, $n_A = 1.38$, $n_B = 1.781$ and $n_C = 2.30$. (After Thelen, A., *Journal of the Optical Society of America*, 53, 1266–1270, 1963.)

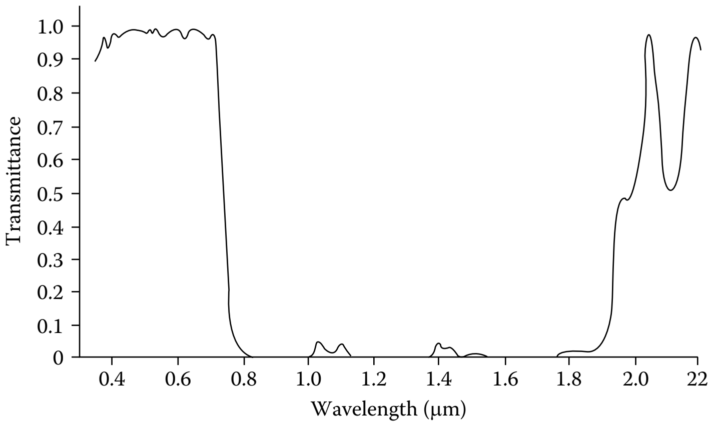

FIGURE 7.28
Calculated transmittance of a triple-stack heat reflector. Design:

$$Incident \left\| \left[1.1\left(\frac{1}{2}AC\frac{1}{2}A \right) \right] \left(\frac{1}{2}AC\frac{1}{2}A \right)^5 \left[1.25\left(\frac{1}{2}AC\frac{1}{2}A \right) \right] \right.$$

$$\left. \left[0.57(ADCDA) \right]^8 \left[0.642(ADCDA) \right]^8 \frac{1}{2}A \right| sub$$

with $\lambda 0 = 860$ nm, $n_{sub} = 1.50$, $n_M = 1.00$, $n_A = 1.38$, $n_B = 1.781$, $n_C = 2.30$, and $n_D = 1.90$. (After Thelen, A., *Journal of the Optical Society of America*, 53, 1266–1270, 1963.)

quarter-waves. The reason for the absence of a second order peak in structures based on the quarter-wave stack is that the quarter-waves become half-waves simultaneously and are, together, absentees. Anything that disturbs this relationship causes the missing order to appear as the half-wave hole. We have already commented on that in the discussion on Equation 7.25. We will briefly examine the half-wave hole using a structure of dispersionless materials of indices 1.45 and 2.15 corresponding roughly to silicon dioxide and tantalum pentoxide.

The performance of a classic shortwave-pass filter based on a structure $(0.5L\ H\ 0.5L)^{25}$ with a reference wavelength of 1000 nm and in which the outermost six layers on either side have been refined, is shown in Figure 7.29 along with a modified design to be discussed shortly. When this filter is tilted to an angle of incidence of 40° in the incident medium of air, the result is as shown in Figure 7.30. A severe dip in transmittance has appeared at the left-hand side of the characteristic corresponding roughly to a wavelength of $\lambda_0/2$. This is the half-wave hole.

We apply a method similar to that of Thelen to the problem of suppressing this hole. In this case, we want to eliminate only one reflecting order, the second. This requires an antireflection coating at every interface between the high- and low-index materials that is effective only at the second-order wavelength. To simplify the manufacturing problems, we shall use the same two materials as are already used in the basic design.

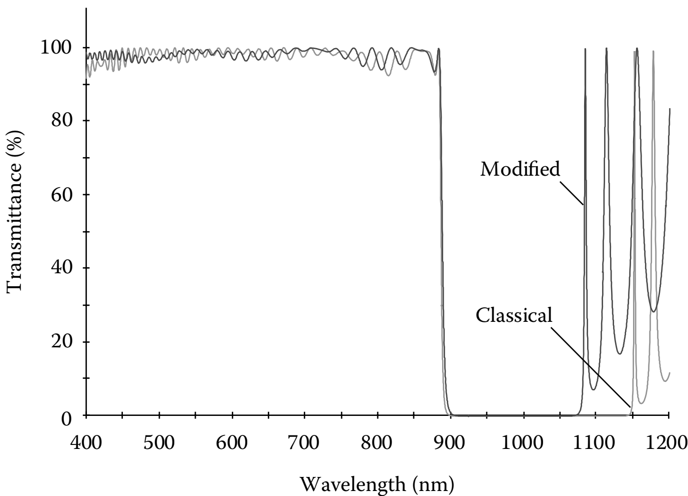

FIGURE 7.29
Two shortwave-pass filters at normal incidence. The classic one is based on a 51-layer quarter-wave stack with adjusted outermost layers to reduce ripple. The modified one is the 51-layer stack with inserted antireflection coatings as discussed in the text. The materials used in the designs are dispersionless with indices of refraction 1.45 and 2.15 corresponding roughly to silicon dioxide and tantalum pentoxide.

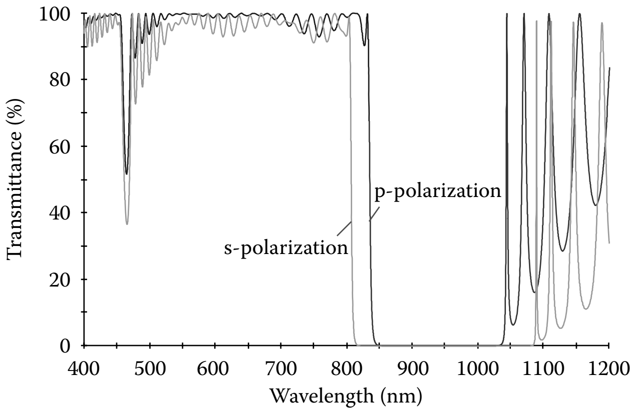

FIGURE 7.30
The classic filter of Figure 7.29 at an angle of incidence of 40° in the air incident medium. The half-wave hole can clearly be seen in the 450- to 500-nm region.

It is always possible to match two layers with a two-layer coating consisting of the same two materials. The admittance diagram, Figure 7.31, makes that clear. The point on the real axis corresponding to the admittance of the material of an admittance circle is always inside the circle. Thus, each of the two admittance points will be on the periphery of one circle and inside the other so that the two circles must always intersect. Therefore, there will be a continuous path from one admittance to the other and a valid antireflection coating. It can be shown that in this special case the optical thicknesses of the two layers are equal. Clearly, there are two solutions and we take the thinner.

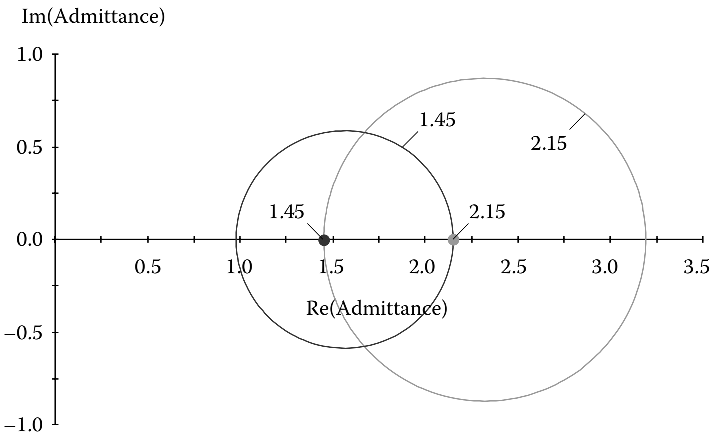

FIGURE 7.31
The geometry of the admittance diagram shows that two admittance circles passing through the admittances of the alternate material will always intersect so that there is a continuous path from one admittance to the other.

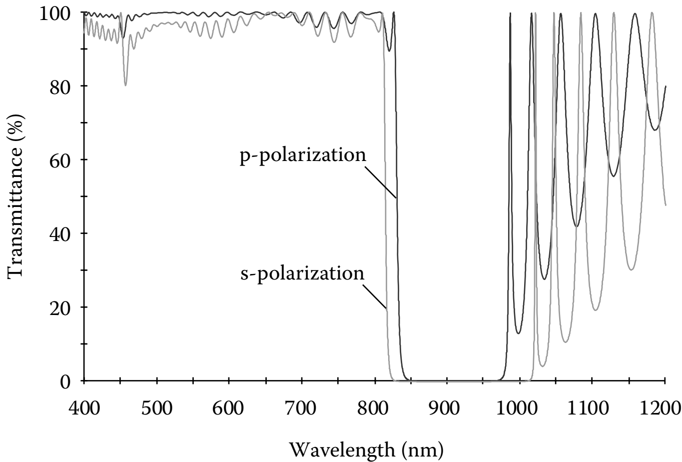

FIGURE 7.32
The performance of the modified design of Figure 7.29 showing the 40° incidence performance. The half-wave hole has almost disappeared.

For these two materials, the optical thicknesses required at the wavelength for the antireflecting action are both 0.08159. At the reference wavelength, the thickness will be just one half of that. Insertion of the antireflection coating implies the removal of an equal optical thickness from each of the layers of the original quarter-wave structure. The starting design is, therefore

$$(0.3368L\ 0.1632H\ 0.1632L\ 0.6737H\ 0.1632L\ 0.1632H\ 0.3368L)^{25}$$

Next the outermost five of the original layers (not the antireflection sections) were refined to give the performance shown as modified in Figure 7.29. The width of the high reflectance zone has suffered from the changes in the original quarter-waves and so, before refining, the edge was adjusted in position to coincide with the edge of the classic design. This implied changing the reference wavelength to 965 nm.

Tilting this filter to 40° in air yields the performance curves shown in Figure 7.32. The half-wave hole has almost disappeared. The residual dip is a consequence of the fact that the antireflection coating was designed for normal incidence. It can be further reduced by adjusting slightly the antireflection coating thicknesses, although too much adjustment will begin to cause a half-wave hole to appear at normal incidence.

7.2.3.10 Reducing the Transmission Zone

The simple quarter-wave multilayer has the even-order high-reflectance bands missing. Sometimes it is useful to have these high-reflectance bands

present. The method of the previous section can also be applied to this problem, and the enhancement of the reflectance at the even orders is a relatively simple business. Because it makes the analysis simpler, we assume that the basic period is of the form *AB* rather than (*A*/2)*B*(*A*/2). Once the basic result is established, it can easily be converted to the form (*A*/2)*B*(*A*/2) if required. The reason that the even-order peaks are suppressed in the ordinary quarter-wave stack is that each of the layers is an integral number of half-waves thick and so are absentee layers. All that is required for a reflectance peak to appear is the destruction of this condition. To achieve this, the thickness of one of the layers must be increased and the other decreased, keeping the overall optical thickness constant. The greater the departure from the half-wave condition, the more pronounced is the reflectance peak.

Consider the case where reflectance bands are required at $\lambda_0, \lambda_0/2$, and $\lambda_0/3$, but not necessarily at $\lambda_0/4$. This will be satisfied by making $n_A d_A = n_B d_B/3$ and $n_A d_A = \lambda_0/8$ so that the basic stack becomes either

$$\frac{H}{2}\frac{3L}{2}\frac{H}{2}\frac{3L}{2}\frac{H}{2}\frac{3L}{2}\cdots\frac{3L}{2}$$

or

$$\frac{L}{2}\frac{3H}{2}\frac{L}{2}\frac{3H}{2}\frac{L}{2}\frac{3H}{2}\cdots\frac{3H}{2}$$

The reflectance peak at $\lambda_0/4$ will be suppressed because the layers at that wavelength have integral half-wave thicknesses.

The method can be used to produce any number of high-reflectance zones. However, it should be noted that the further the thicknesses depart from ideal quarter-waves at λ_0, the narrower will be the first-order reflectance band.

7.2.3.11 Edge Steepness

In longwave- and shortwave-pass filters, the steepness of edge is not usually a parameter of critical importance. The number of layers necessary to produce the required rejection in the stop band of the filter will generally produce an edge steepness, which is quite acceptable. If, however, an exceptional degree of edge steepness is required, then the easiest way of improving it is to use still more layers. Increasing the number of layers will cause an apparent increase in the ripple in the pass band, because the first minimum in the pass band will be brought nearer to the edge, and usually will be on a part of the reflectance envelope, which is increasing in width towards the edge. If the increase in number of layers is considerable, then it will probably be advisable to use one of the more advanced techniques for reducing ripple.

An alternative method for increasing the steepness of edge without major alterations to the basic design concept is the use of higher-order stacks. The steepness of edge for a given number of layers will increase in proportion with the order. There are two snags here. The first is that the rejection zone width varies inversely with the order number. This can be dealt with by adding a further first-order stack to extend the rejection zone. The second snag is more serious. The permissible errors in layer thickness are also reduced in inverse proportion with the order number. This is because the performance does not depend directly on the phase thickness of the layers but rather on the sines and cosines of the layer thicknesses, and in the case of the fifth order, for example, these are layer thicknesses greater than 2π. Thus, if for a first-order edge filter, the acceptable random errors in layer thickness are of the order of, say, 5%, those tolerable in the fifth order will be of the order of 1%. Optical monitoring can be arranged to take account of this and so for that reason would be preferred over crystal monitoring. A possible further practical difficulty with higher-order filters is that considerably more material is required for each layer.

References

1. Epstein L I 1952 The design of optical filters *Journal of the Optical Society of America* **42** 806–810
2. Vera J J 1964 Some properties of multilayer films with periodic structure *Optica Acta* **11** 315–331
3. Thelen A 1966 Equivalent layers in multilayer filters *Journal of the Optical Society of America* **56** 1533–1538
4. Ufford C and Baumeister P 1974 Graphical aids in the use of equivalent index in multilayer-filter design *Journal of the Optical Society of America* **64** 329–334
5. Welford W T (writing as W Weinstein) 1954 Computations in thin film optics *Vacuum* **4** 3–19
6. Baumeister P W 1958 Design of multilayer filters by successive approximations *Journal of the Optical Society of America* **48** 955–958
7. Dobrowolski J A and Kemp R A 1990 Refinement of optical multilayer systems with different optimization procedures *Applied Optics* **29** 2876–2893
8. Dobrowolski J A 1965 Completely automatic synthesis of optical thin film systems *Applied Optics* **4** 937–946
9. Jacobsson R 1964 Matching a multilayer stack to a high-refractive-index substrate by means of an inhomogeneous layer *Journal of the Optical Society of America* **54** 422–423
10. Young L and Crystal E G 1966 On a dielectric fiber (sic) by Baumeister *Applied Optics* **5** 77–80
11. Seeley J S, Liddell H M, and Chen T C 1973 Extraction of Tschebysheff design data for the klowpass dielectric multilayer *Optica Acta* **20** 641–661

12. Seeley J S and Smith S D 1966 High performance blocking filters for the region 1 μ to 20 μ *Applied Optics* **5** 81–85
13. Turner A F and Baumeister P W 1966 Multilayer mirrors with high reflectance over an extended spectral region *Applied Optics* **5** 69–76
14. Epstein L I 1955 Improvements in heat reflecting filters *Journal of the Optical Society of America* **45** 360–362
15. Thelen A 1963 Multilayer filters with wide transmission bands *Journal of the Optical Society of America* **53** 1266–1270
16. Muchmore R B 1948 Optimum band width for two layer anti-reflection films *Journal of the Optical Society of America* **38** 20–26

8

Band-Pass Filters

A filter possessing a region of transmission bounded on either side by regions of rejection is known as a *band-pass filter*. For the broadest band-pass filters, the most suitable construction is a combination of longwave-pass and shortwave-pass filters, already mentioned in Chapter 7. For narrower filters, however, this method is not very successful because of difficulties associated with obtaining both the required precision in positioning and the steepness of edges. Other methods are therefore used, involving a single assembly of thin films to produce simultaneously the pass and rejection bands. The simplest of these is the thin-film Fabry–Perot filter, a development of the interferometer already described in Chapter 6. The spacer layer in the Fabry–Perot etalon acts rather like a resonant cavity and so is usually called a cavity layer. The Fabry–Perot filter then becomes known as a *single-cavity filter*. The single-cavity filter has a triangular pass band shape and it has been found possible to improve this, by coupling simple filters in series, in much the same way as tuned circuits. These coupled arrangements are known as *multiple-cavity filters*. The terminology has not always been as simple. The cavities are usually a half-wave, or integral multiples of half-waves, thick. Thus, an older term that is still sometimes used is *multiple half-wave filter*. The two-cavity filter was earlier called a double half-wave filter, abbreviated to DHW filter, while the three-cavity was called a triple half-wave, or THW, filter.

8.1 Broadband-Pass Filters

Band-pass filters can be very roughly divided into broadband-pass filters and narrowband-pass filters. There is no definite boundary between the two types and the description of one particular filter usually depends on the application and the filters with which it is being compared. For the purpose of the present work, by *broadband filters* we mean filters with bandwidths of perhaps 20% or more, which are made by combining longwave-pass and shortwave-pass filters. The best arrangement is probably to deposit the two components on opposite sides of a single substrate. To give maximum possible transmission, each edge filter should be designed to match the substrate into the surrounding medium, a procedure already examined in Chapter 7. Such a filter is shown in Figure 8.1.

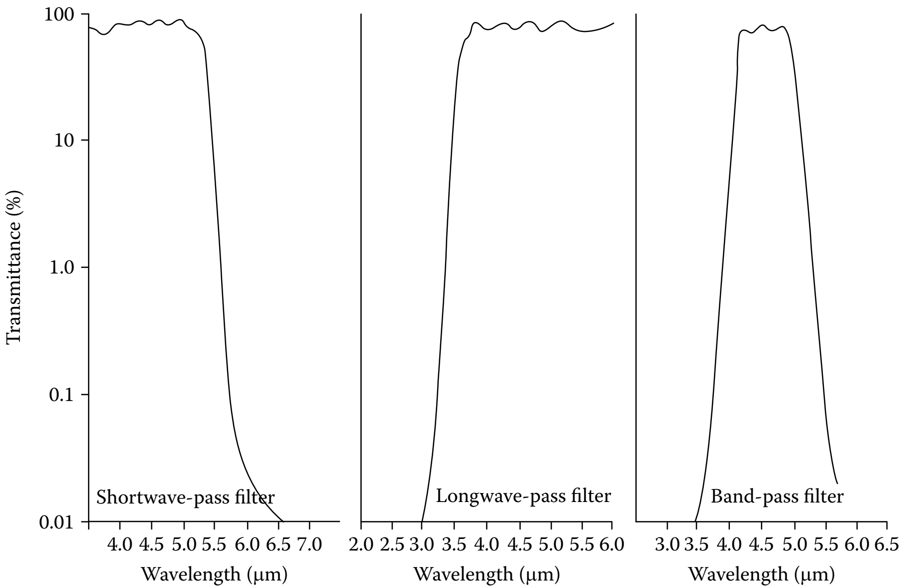

FIGURE 8.1
The construction of a band-pass filter by placing two separate edge filters in series. (Courtesy of Standard Telephones and Cables Ltd.)

It is also possible, however, to deposit both components on the same side of the substrate. This was a problem which Epstein [1] examined in his early paper on symmetrical periods. The main difficulty is the combining of the two stacks so that the transmission in the pass band is a maximum and so that one stack does not produce transmission peaks in the rejection zone of the other. The transmission in the pass band will depend on the matching of the first stack to the substrate, the matching of the second stack to the first, and the matching of the second stack to the surrounding medium. Depending on the equivalent admittances of the various stacks, it may be necessary to insert quarter-wave matching layers or to adopt any of the more involved matching techniques.

In the visible region, with materials such as zinc sulfide and cryolite, or titanium dioxide and silicon dioxide, the combination $[(H/2)L(H/2)]^S$ acts as a good longwave-pass filter with an equivalent admittance at normal incidence and at wavelengths in the pass region not too far removed from the edge of near unity. This can therefore be used next to the air without mismatch. The combination $[(L/2)H(L/2)]^S$ acts as a shortwave pass filter, with equivalent admittance only a little lower than the first section, and can be placed next to it, between it and the substrate, without any matching layers. The mismatch between this second section and the substrate, which in the visible region will be glass of index 1.52, is sufficiently large to require a matching layer. Happily, the $[(H/2)L(H/2)]$ combination with a total phase thickness of 270° (i.e., effectively three quarter-waves) has admittance

exactly correct for this. The transmittance of the final design is shown in Figure 8.2b with the appropriate admittances of the two sections in Figure 8.2a. Curve A refers to a $[(L/2)H(L/2)]^4$ shortwave-pass section and B to a $[(H/2)L(H/2)]^4$ longwave-pass. The complete design is shown in Table 8.1. The edges of the two sections have been chosen quite arbitrarily and could be moved as required.

To avoid the appearance of transmission peaks in the rejection zones of either component, it is safest to deposit them so that high-reflectance zones do not overlap. The complete rejection band of the shortwave-pass section will always lie over a pass region of the longwave-pass filter, but the higher-order bands should be positioned, if at all possible, clear of the rejection zone of the longwave-pass section. The combination of edge filters of the same type has already been investigated in Chapter 7 and the principles discussed there apply to this present situation. It should also be remembered that, although in the normal shortwave-pass filter the second-order reflection peak is missing, a small peak can appear if any thickness errors are present. This can, if superimposed on a rejection zone of the other section, cause the appearance of a transmission peak if the errors are sufficiently pronounced. The expression for maximum transmission is

$$T_{\max} = \frac{T_a T_b}{[1-(R_a R_b)^{1/2}]^2}$$

but this only holds if the phase conditions are met.

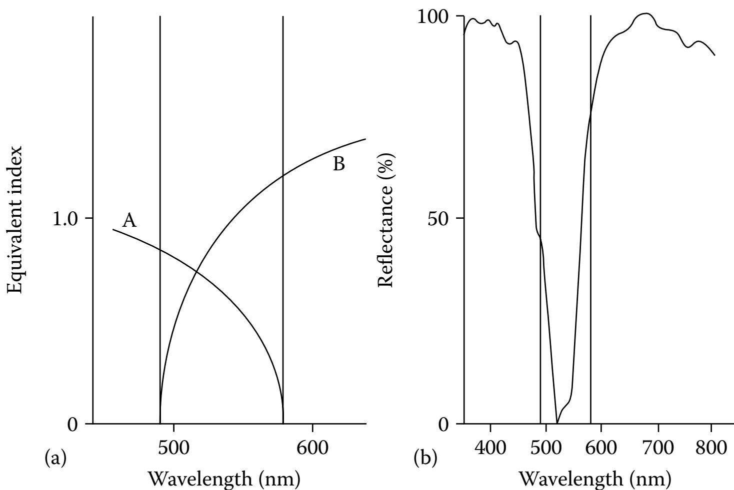

FIGURE 8.2
(a) Equivalent admittances of two stacks made up of symmetrical periods used to form a band-pass filter. A: (0.5*LH*0.5*L*); B: (0.5*HL*0.5*H*), where $n_L = 1.38$, $n_H = 2.30$. (b) Calculated reflectance curve for a band-pass filter. For the complete design of this filter, made up of two superimposed stacks, one of type A and one of type B, refer to Table 8.1. (After Epstein, L.I., *Journal of the Optical Society of America*, 42, 806–810, 1952.)

TABLE 8.1
Epstein's Band-Pass Filter Design

Layer Index	Phase Thickness of each Layer Measured at 546 nm (degrees)	Layer Index	Phase Thickness of each Layer Measured at 546 nm (degrees)
1.52	Massive	2.30	55.4
1.38	67.3	1.38	33.9
2.30	134.5	2.30	67.9
1.38	122.7	1.38	67.9
2.30	110.8	2.30	67.9
1.38	110.8	1.38	67.9
2.30	110.8	2.30	67.9
1.38	110.8	1.38	67.9
2.30	110.8	2.30	67.9
1.38	110.8	1.38	67.9
2.30	110.8	2.30	33.9
1.38	110.8	1.00	Massive

Source: Epstein, L.I., *Journal of the Optical Society of America*, 42, 806–810, 1952.

8.2 Narrowband Filters

8.2.1 The Metal–Dielectric Single–Cavity Filter

The simplest type of narrowband thin-film filter is based on the Fabry–Perot interferometer discussed in Chapter 6. In its original form, the Fabry–Perot interferometer consists of two identical parallel reflecting surfaces spaced apart at distance d. In collimated light, the transmission is low for all wavelengths except for a series of very narrow transmission bands spaced at intervals that are constant in terms of wave number. This device can be replaced by a complete thin-film assembly consisting of a dielectric layer bounded by two metallic reflecting layers (Figure 8.3). The dielectric layer takes the place of the spacer. The old term for such a layer is the *spacer layer* but the tendency nowadays is to call it the *cavity layer*. Except that the cavity or spacer layer now has an index greater than unity, the analysis of the performance of this thin-film filter is exactly the same as for the conventional etalon, but in other respects there are some significant differences.

While the surfaces of the substrates should have a high degree of polish, their figures need not be worked to the exacting tolerances necessary for etalon plates. Provided the vapor stream in the chamber is uniform, the films will follow the contours of the substrate without exhibiting thickness variations. This implies that it is possible for the thin-film Fabry–Perot filter to be used in a much lower order than the conventional etalon. Indeed, it turns out

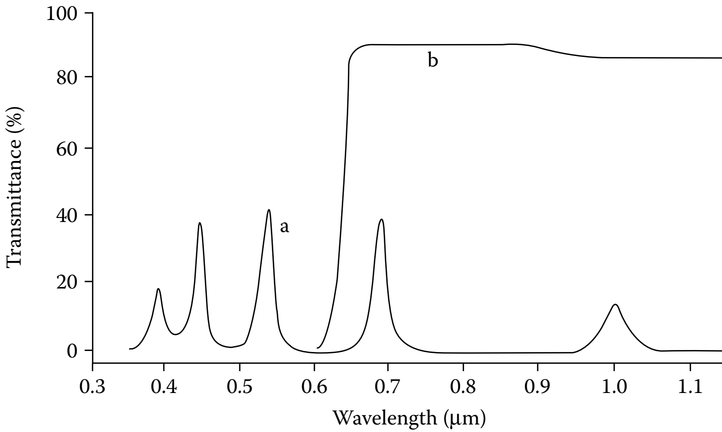

FIGURE 8.3
Characteristics of a metal–dielectric filter for the visible region (curve a). Curve b is the transmittance of an absorption glass filter that can be used for the suppression of the short wavelength sidebands. (Courtesy of Barr & Stroud Ltd.)

in practice that lower orders must be used, because the thin-film cavity layers tend to exhibit an increasing roughness with increasing thickness so that their use beyond the fourth of fifth order becomes problematic. The roughness broadens the pass band and reduces the peak transmittance reducing any advantage of a very high order. This simple type of filter is known as a metal–dielectric Fabry–Perot, or single-cavity, to distinguish it from the all-dielectric equivalent to be described later.

It is worthwhile briefly to analyze the performance of the single cavity filter again, this time including the effects of phase shift at the reflectors. The starting point for this analysis is Equation 3.20

$$T_F = \frac{T_a T_b}{[1-(R_a R_b)^{1/2}]^2} \frac{1}{1+F\sin^2\left[\frac{1}{2}(\varphi_a+\varphi_b)-\delta\right]} \tag{8.1}$$

where

$$F = \frac{4(R_a R_b)^{1/2}}{[1-(R_a R_b)^{1/2}]^2}$$

and

$$\delta = \frac{2\pi nd\cos\vartheta}{\lambda}.$$

We have adapted Equation 3.20 slightly by removing the + and − signs on the reflectances. The following analysis is similar to that already performed in Chapter 5 except that here we are including the effects of φ_a and φ_b. The transmittance maxima are given by

$$\frac{2\pi nd\cos\vartheta}{\lambda}-\frac{\varphi_a+\varphi_b}{2}=m\pi \quad \text{where } m=0,\pm1,\pm2,\pm3,\ldots \tag{8.2}$$

and where we have chosen $-m$ rather than $+m$ because $(\varphi_a+\varphi_b)/2<\pi$ by definition. The analysis is marginally simpler if we work in terms of wave number, ν, instead of wavelength. The positions of the peaks are then given by

$$\frac{1}{\lambda}=\nu=\frac{m\pi+(\varphi_a+\varphi_b)/2}{2\pi nd\cos\vartheta}=\frac{1}{2nd\cos\vartheta}\left(m+\frac{\varphi_a+\varphi_b}{2\pi}\right) \tag{8.3}$$

Depending on the particular metal, the thickness, the index of the substrate, and the index of the cavity layer, the phase shift on reflection φ will be in either the first or second quadrant. Therefore, $(\varphi_a+\varphi_b)/(2\pi)$ will be positive between 0 and 1 and, for silver in the middle of the visible region, roughly 0.7. If we take m as the order number, then there will actually be a zeroth order peak. At normal incidence this peak will be given roughly by $nd/0.35$ so that for this peak to be at λ_0, the cavity layer should have an optical thickness around $0.35\lambda_0$. In the first order, the cavity layer should be around $0.85\lambda_0$ in optical thickness.

The resolving power of the thin-film single-cavity, or Fabry–Perot, filter may be defined in the same way as for the interferometer. As we saw in Chapter 6, a convenient definition is

$$\frac{\text{Peak wavelength}}{\text{Halfwidth of pass band}}$$

where the half-width is the width of the band measured at half the peak transmittance. Because the half-width can be rapidly converted into resolving power, and because it is so easily visualized, it tends to be the parameter of choice to express the performance of all types of narrowband filter, not just the single-cavity filter. Other measures of bandwidth sometimes quoted along with the half-width are widths measured at different fractions of peak transmittance, 0.9 or 0.1, for example. Sometimes, particularly in telecommunication applications, these levels are expressed in dB below the peak level.

We digress for a moment to explain this different scale. dB is the symbol for decibel, which is a unit of comparison of power levels and, in our case, a comparison of irradiances. The scale is a logarithmic one. The decibel is

not included in the SI system but it is internationally accepted and used. It is based on the bel, a unit that originated at Bell Telephone Laboratories and is named after Alexander Graham Bell. The bel is defined as the base 10 logarithm of the ratio of the two power levels. A drop in power leads to a negative value. The numbers become a little more convenient when multiplied by 10 and this leads to the decibel scale. The level in decibel of irradiance I_1 compared with irradiance I_0 is, therefore:

$$L(d\text{B}) = 10\log_{10}\left(\frac{I_1}{I_0}\right) \tag{8.4}$$

a negative value representing a loss, and a positive value, a gain. The ratio I_1/I_0 can represent a transmittance or reflectance in absolute units. To convert transmittance into decibels, we use:

$$T(\text{dB}) = 10\log_{10}[T(\text{abs})] \tag{8.5}$$

For example, a transmittance of 50% becomes 0.5 in absolute terms and the value in decibel is –3.01 dB. This is sometimes referred to as an insertion loss of 3.01 dB because it represents a reduction in power. The advantage of the decibel scale is that it is additive. Two components in series, one with an insertion loss of 2 dB and the other of 4 dB, would give a total insertion loss of (2 + 4) dB = 6 dB.

It is worthwhile spending just a little longer on this question of resolving power and resolution. Let the pass band be sufficiently narrow, which is the same as F being sufficiently large, so that near a peak we can replace

$$\frac{\varphi_a + \varphi_b}{2} - \delta \quad \text{with} \quad -m\pi - \Delta\delta$$

and

$$\sin^2\left(\frac{\varphi_a + \varphi_b}{2} - \delta\right) \quad \text{with} \quad (\Delta\delta)^2$$

where we are assuming that φ_a and φ_b are constant, or vary very much more slowly than δ over the pass band.

The half-peak bandwidth, or half-width, can be found by noting that at the half-peak transmission points

$$F\sin^2\left(\frac{\varphi_a + \varphi_b}{2} - \delta\right) = 1$$

Then, by using the approximation given above, this becomes

$$(\Delta\delta_h)^2 = \frac{1}{F}$$

i.e., the half-width of the pass band

$$2\Delta\delta_h = 2/F^{1/2}$$

The *finesse* is defined as the ratio of the interval between fringes to the fringe half-width and is written $\mathcal{F}$. The change in δ in moving from one fringe to the next is just π, and the finesse, therefore, is

$$\mathcal{F} = \frac{\pi F^{1/2}}{2} \tag{8.6}$$

Since $\nu \propto \delta$, $\nu_0/\Delta\nu_h = \delta_0/2\Delta\delta_h$, where ν_0 and δ_0 are, respectively, the values of the wave number and cavity layer phase thickness associated with the transmission peak, and $\Delta\nu_h$ and $2\Delta\delta_h$ are the corresponding values of half-width. The ratio of the peak wave number to the half-width is then given by

$$\frac{\nu_0}{\Delta\nu_h} = F\left(m + \frac{\varphi_a + \varphi_b}{2\pi}\right)$$

for a peak of order m, since

$$\delta_0 = m\pi + \frac{\varphi_a + \varphi_b}{2}$$

The ratio of peak position to half-width expressed in terms of wave number is exactly the same in terms of wavelength,

$$\frac{\nu_0}{\Delta\nu_h} = \frac{\lambda_0}{\Delta\lambda_h} \tag{8.7}$$

where λ_0 is given by

$$\lambda_0 = \frac{2nd\cos\vartheta}{m + (\varphi_a + \varphi_b)/2\pi}$$

and this was discussed in Chapter 6.

The manufacture of the metal–dielectric filter is straightforward. The main point to watch is that the metallic layers should be evaporated as quickly as possible on to a cold substrate. In the visible and near infrared regions, the best results are probably achieved with silver and cryolite, while in the

ultraviolet region, the best combination is aluminum and either magnesium fluoride or cryolite. Wherever possible, the layers should be protected by cementing a cover slip over them as soon as possible after deposition. This also serves to balance the assembly by equalizing the refractive indices of the media outside the metal layers.

Turner [2] quoted some results for metal–dielectric filters constructed for the visible region that may be taken as typical of the performance to be expected. The filters were constructed from silver reflectors and magnesium fluoride cavities. For a first-order cavity, a bandwidth of 13 nm with a peak transmittance of 30% was obtained at a peak wavelength of 531 nm. A similar filter with a second-order cavity gave a bandwidth of 7 nm with peak transmittance of 26% at 535 nm. With metal–dielectric filters, the third order is usually the highest used. Because of scattering in the space layer, which becomes increasingly apparent in the fourth and higher orders, any benefit that would otherwise arise from using these orders is largely lost. A typical curve for a metal–dielectric filter for the visible region is shown in Figure 7.3. The particular peak to be used is that at 0.69 μm, which is of the third order. The shortwave sidebands due to the higher-order peaks can be suppressed quite easily by the addition of an absorption glass filter, which can be cemented over the metal–dielectric element to act as a cover glass. Such a filter is also shown in the figure and is one of a wide range of absorption glasses that are available for the visible and near infrared and that have longwave-pass characteristics. There are, unfortunately, few absorption filters suitable for the suppression of the longwave sidebands. If the detector that is to be used is not sensitive to these longer wavelengths, then no problem exists and commercial metal–dielectric filters for the visible and near infrared usually possess long-wavelength sidebands beyond the limit of the photocathodes or photographic emulsions, which are the usual detectors for this region. If the longwave-sideband suppression must be included as part of the filter assembly, then there is an advantage in using metal– dielectric filters in the first order, even though the peak transmission for a given bandwidth is much lower, since they do not usually possess long-wavelength sidebands. Theoretically, there will always be a peak corresponding to the zero order at very long wavelengths, but this will not usually appear, partly because the substrate will cut off long before the zero order is reached, and also because the properties of the thin-film materials themselves will change radically. We shall discuss later a special type of metal–dielectric filter, the induced transmission filter, that can be made to have a much higher peak transmission, although with a rather broader half-width, without introducing long-wavelength sidebands, and that is often used as a long-wavelength suppression filter.

Silver does not have an acceptable performance for ultraviolet filters and aluminum has been found to be the most suitable metal, with magnesium fluoride as the preferred dielectric. In the ultraviolet beyond 300 nm, there are few suitable cements (none at all beyond 200 nm) and it is not possible to

use cover slips cemented over the layers in the way in which filters for the visible region are protected. The normal technique, therefore, is to attempt to protect the filter by the addition of an extra dielectric layer between the final metal layer and the atmosphere. These layers are effective in that they slow down the oxidation of the aluminum, which otherwise takes place rapidly and causes a reduction in performance even at quite low pressures. This oxidation has been referred to in Chapter 5. They cannot completely stabilize the filters, however, and slight longwave drifts can occur, as reported by Bates and Bradley [3]. A second function of the final dielectric layer is to act as a reflection-reducing layer at the outermost metal surface and hence to increase the transmittance of the filter. This is not a major effect—the problem of improving metal–dielectric filter performance is dealt with later in this chapter—but any technique that helps to improve performance, even marginally, in the ultraviolet, is very welcome. Some performance curves of first-order metal–dielectric single-cavity filters are shown in Figure 8.4.

The formula for transmittance of the single-cavity filter can also be used to determine both the peak transmittance in the presence of absorption in the reflectors and the tolerance that can be allowed in matching the two reflectors. First, let the reflectances be equal and let the absorptance be denoted by A, so that

$$R + T + A = 1 \tag{8.8}$$

The peak transmittance will then be given by

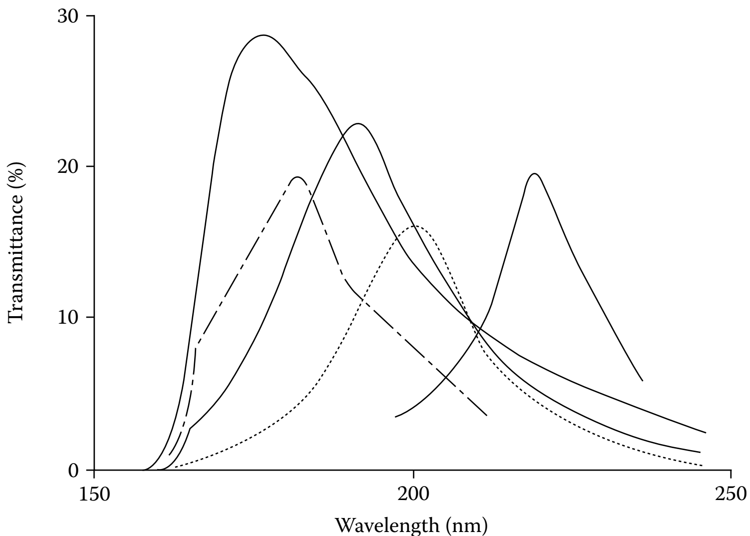

FIGURE 8.4
Experimental transmittance curves of first-order metal–dielectric filters for the far ultraviolet deposited on Spectrosil B substrates. (After Bates, B. and Bradley, D.J., *Applied Optics*, 5, 971–975, 1966.)

$$(T_F)_{\text{peak}} = \frac{T^2}{(1-R)^2}$$

and, using Equation 8.8,

$$(T_F)_{\text{peak}} = \frac{1}{(1+A/T)^2} \tag{8.9}$$

exactly as for the Fabry–Perot interferometer, which shows that when absorption is present, the value of peak transmission is determined by the ratio A/T.

To estimate the accuracy of matching that is required for the two reflectors, we assume that the absorption is zero. The peak transmission is given by the expression

$$(T_F)_{\text{peak}} = \frac{T_a T_b}{[1-(R_a R_b)^{1/2}]^2} \tag{8.10}$$

where the subscripts *a* and *b* refer to the two reflectors. Let

$$R_b = R_a - \Delta_a \tag{8.11}$$

where Δ_a is the error in matching, so that $T_b = T_a + \Delta_a$. Then we can write

$$\begin{aligned}(T_F)_{\text{peak}} &= \frac{T_a(T_a+\Delta_a)}{\{1-[R_a(R_a-\Delta_a)]^{1/2}\}^2} \\ &= \frac{T_a(T_a+\Delta_a)}{\left\{1-R_a\left[1-\frac{1}{2}(\Delta_a/R_a)+\ldots\right]\right\}^2}\end{aligned} \tag{8.12}$$

Now assume that Δ_a is sufficiently small compared with R_a so that we can take only the first two terms of the expansion in Equation 8.12. With some rearrangement, the equation becomes

$$(T_F)_{\text{peak}} = \frac{T_a^2}{(1-R_a)^2}\frac{1+(\Delta_a/T_a)}{\left[1+\frac{1}{2}(\Delta_a/T_a)\right]^2} \tag{8.13}$$

The first part of the equation is the expression for peak transmission in the absence of any error in the reflectors, while the second part shows how the peak transmission is affected by errors. The second part of the expression is plotted in Figure 8.5 where the abscissa is $T_b/T_a = 1 + \Delta_a/T_a$. Clearly, the single-cavity filter is surprisingly insensitive to errors. Even with reflector transmittance unbalanced by a factor of three, it is still possible to achieve 75% peak transmittance.

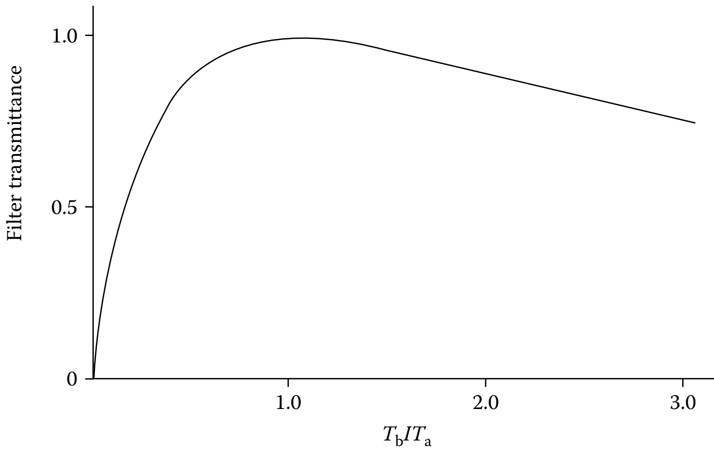

FIGURE 8.5
Theoretical peak transmittance of a single-cavity, or Fabry–Perot, filter with unbalanced reflectors.

8.2.2 The All-Dielectric Single-Cavity Filter

In the same way as we found for the conventional Fabry–Perot etalon, if improved performance is to be obtained, then all-dielectric multilayers should replace the metallic reflecting layers.

An all-dielectric filter is shown in diagrammatic form in Figure 8.6. Basically, this is the same as a conventional etalon with dielectric coatings and with a solid thin-film cavity, or spacer, and the observations made for the metal–dielectric filter are also valid. Again, the substrate need not be worked to a high degree of flatness, although the polish must be good, because, provided the geometry of the coating machine is adequate, the films will follow any reasonable substrate contours without showing changes in thickness.

The bandwidth of the all-dielectric filter can be calculated as follows. If the reflectance of each of the multilayers is sufficiently high, then

FIGURE 8.6
The structure of an all-dielectric single-cavity filter.

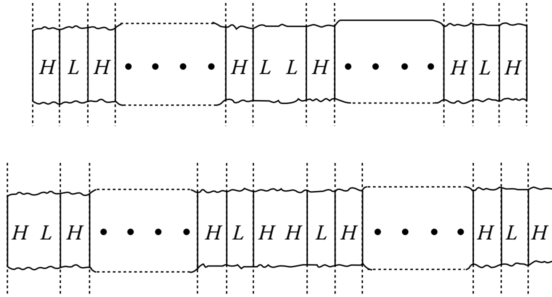

FIGURE 8.7
The structure of the two basic types of all-dielectric single-cavity, or Fabry–Perot, filter.

$$F = \frac{4R}{(1-R)^2} \simeq \frac{4}{T^2}$$

and

$$\frac{\lambda_0}{\Delta\lambda_h} = m\mathcal{F} = \frac{m\pi F^{1/2}}{2} \simeq \frac{m\pi}{T} \tag{8.14}$$

Since the maximum reflectance for a given number of layers will be obtained with a high-index layer outermost, there are really only two cases that need be considered and these are shown in Figure 8.7. If x is the number of high-index layers in each stack, not counting the cavity layer, then in the case of the high-index cavity, the transmittance of the stack will be given by

$$T = \frac{4n_L^{2x} n_s}{n_H^{2x+1}}$$

and in the case of the low-index cavity by

$$T = \frac{4n_L^{2x-1} n_s}{n_H^{2x}}$$

Substituting these results into the expression for bandwidth, we find, for the high-index cavity,

$$\frac{\Delta\lambda_h}{\lambda_0} = \frac{4n_L^{2x} n_s}{m\pi n_H^{2x+1}} \tag{8.15}$$

and, for the low-index cavity,

$$\frac{\Delta\lambda_h}{\lambda_0} = \frac{4n_L^{2x-1} n_s}{m\pi n_H^{2x}} \tag{8.16}$$

where we are adopting the fractional half-width $\Delta\lambda_h/\lambda_0$ rather than the resolving power $\lambda_0/\Delta\lambda_h$ as the important parameter. This is customary practice.

In these formulae, we have completely neglected any effect due to the dispersion of phase change on reflection from a multilayer. As we have already noted in Chapter 6, the phase change is not constant. The sense of the variation is such that it increases the rate of variation of $[(\varphi_a + \varphi_b)/2] - \delta$ with wavelength in the formula for transmittance of the single-cavity filter and, hence, reduces the bandwidth and increases the resolving power in Equations 8.15 and 8.16.

Seeley [4] has studied the all-dielectric filter in detail and, by making some approximations in the basic expressions for the filter transmittance, has arrived at formulae for the first-order half-widths, which, with a little adjustment, become equal to Expressions 8.15 and 8.16 multiplied by a factor $(n_H - n_L)/n_H$. We can readily extend Seeley's analysis to all-dielectric filters of order m.

We recall that the half-peak points are given by

$$F\sin^2[(2\pi D/\lambda) - \varphi] = 1 \tag{8.17}$$

where, since the filter is quite symmetrical, we have replaced $(\varphi_a + \varphi_b)/2$ by φ. It is simpler to carry out the analysis in terms of $g = \lambda_0/\lambda = \nu/\nu_0$. At the peak of the filter, we have $g = 1.0$. We can assume for small changes Δg in g that

$$2\pi D/\lambda = m\pi(1 + \Delta g)$$

and

$$\varphi = \varphi_0 + \frac{d\varphi}{dg}\Delta g$$

so that Equation 8.17 becomes

$$F\sin^2\left(m\pi(1 + \Delta g) - \varphi_0 - \frac{d\varphi}{dg}\Delta g\right) = 1$$

φ_0, we know, is 0 or π, and so, using the same approximation as before,

$$F\left(m\pi\Delta g - \frac{d\varphi}{dg}\Delta g\right)^2 = 1$$

or

$$\Delta g = F^{-1/2}\left(m\pi - \frac{d\varphi}{dg}\right)^{-1}$$

The half-width is $2\Delta g$ so that

$$2\Delta g = \frac{\Delta\nu_h}{\nu_0} = \frac{\Delta\lambda_h}{\lambda_0} = 2F^{-1/2}\left(m\pi - \frac{d\varphi}{dg}\right)^{-1}$$
$$= \frac{2}{m\pi F^{1/2}}\left(1 - \frac{1}{m\pi}\frac{d\varphi}{dg}\right)^{-1} \quad (8.18)$$

We now need the quantity $d\varphi/dg$. We use Seeley's technique, but, rather than follow him exactly, we choose a slightly more general approach because we shall require the results later. The matrix for a dielectric quarter-wave layer is

$$\begin{bmatrix} \cos\delta & i\sin\delta/\eta \\ i\eta\sin\delta & \cos\delta \end{bmatrix}$$

where, as usual, we are writing η for the optical admittance, which is in free space units. Now, for layers that are almost a quarter-wave we can write

$$\delta = \pi/2 + \varepsilon$$

where ε is small. Then

$$\cos\delta \simeq -\varepsilon \qquad \sin\delta \simeq 1$$

so that the matrix can be written

$$\begin{bmatrix} -\varepsilon & i/\eta \\ i\eta & -\varepsilon \end{bmatrix}$$

We limit our analysis to quarter-wave multilayer stacks having high index next to the substrate. There are two cases, even and odd numbers of layers.

8.2.2.1 Case 1: Even Number (2x) of Layers

The resultant multilayer matrix is given by

$$\begin{bmatrix} B \\ C \end{bmatrix} = [L][H][L]\ldots[L][H]\begin{bmatrix} 1 \\ \eta_{sub} \end{bmatrix}$$

where

$$[L] = \begin{bmatrix} -\varepsilon_L & i/\eta_L \\ i\eta_L & -\varepsilon_L \end{bmatrix}$$

$$[L]=\begin{bmatrix} -\varepsilon_H & i/\eta_H \\ i\eta_H & -\varepsilon_H \end{bmatrix}$$

Then

$$\begin{aligned}
\begin{bmatrix} B \\ C \end{bmatrix} &= \{[L][H]\}^x \begin{bmatrix} 1 \\ \eta_{sub} \end{bmatrix} \\
&= \begin{bmatrix} -\left(\dfrac{\eta_H}{\eta_L}\right) & -i\left(\dfrac{\varepsilon_L}{\eta_H}+\dfrac{\varepsilon_H}{\eta_L}\right) \\ -i(\eta_L\varepsilon_H+\eta_H\varepsilon_L) & -\left(\dfrac{\eta_L}{\eta_H}\right) \end{bmatrix}^x \begin{bmatrix} 1 \\ \eta_{sub} \end{bmatrix} \\
&= \begin{bmatrix} M_{11} & iM_{12} \\ iM_{21} & M_{22} \end{bmatrix} \begin{bmatrix} 1 \\ \eta_{sub} \end{bmatrix}
\end{aligned}$$

Our problem is to find expressions for M_{11}, M_{12}, M_{21}, and M_{22}. In the evaluation, we neglect all terms of second and higher order in ε. Terms in ε appearing in M_{11} and M_{22} are of second and higher order and therefore

$$M_{11}=(-1)^x\left(\frac{\eta_H}{\eta_L}\right)^x$$

$$M_{22}=(-1)^x\left(\frac{\eta_L}{\eta_H}\right)^x$$

M_{12} and M_{21} contain terms of first, third, and higher orders in ε. The first-order terms are

$$\begin{aligned}
M_{12} &= -\left(\frac{\varepsilon_L}{\eta_H}+\frac{\varepsilon_H}{\eta_L}\right)\left(-\frac{\eta_L}{\eta_H}\right)^{x-1} + \left(-\frac{\eta_H}{\eta_L}\right)\left[-\left(\frac{\varepsilon_L}{\eta_H}+\frac{\varepsilon_H}{\eta_L}\right)\right]\left(-\frac{\eta_L}{\eta_H}\right)^{x-2} + \cdots \\
&\quad + \left(-\frac{\eta_H}{\eta_L}\right)^p\left[-\left(\frac{\varepsilon_L}{\eta_H}+\frac{\varepsilon_H}{\eta_L}\right)\right]\left(-\frac{\eta_L}{\eta_H}\right)^{x-p-1} + \cdots \\
&\quad + \left(-\frac{\eta_H}{\eta_L}\right)^{x-1}\left[-\left(\frac{\varepsilon_L}{\eta_H}+\frac{\varepsilon_H}{\eta_L}\right)\right] \\
&= (-1)^x\left(\frac{\varepsilon_L}{\eta_H}+\frac{\varepsilon_H}{\eta_L}\right)\left[\left(\frac{\eta_L}{\eta_H}\right)^{x-1}+\left(\frac{\eta_L}{\eta_H}\right)^{x-3}+\cdots+\left(\frac{\eta_H}{\eta_L}\right)^{x-1}\right]
\end{aligned}$$

$$M_{12} = (-1)^x \left(\frac{\varepsilon_L}{\eta_H} + \frac{\varepsilon_H}{\eta_L}\right)\left(\frac{\eta_L}{\eta_H}\right)^{x-1}$$

$$\times\left[\left(\frac{\eta_L}{\eta_H}\right)^{2x-2} + \left(\frac{\eta_L}{\eta_H}\right)^{2x-4} + \cdots + \left(\frac{\eta_L}{\eta_H}\right)^{2} + 1\right]$$

i.e.,

$$= (-1)^x \left(\frac{\varepsilon_L}{\eta_H} + \frac{\varepsilon_H}{\eta_L}\right)\left(\frac{\eta_L}{\eta_H}\right)^{x-1}\left[1 - \left(\frac{\eta_L}{\eta_H}\right)^{2x}\right]\left[1 - \left(\frac{\eta_L}{\eta_H}\right)^{2}\right]^{-1}$$

Since $(\eta_L/\eta_H) < 1$.

Now, provided x is large enough and (η_L/η_H) small enough, we can neglect $(\eta_L/\eta_H)^{2x}$ in comparison with 1, and after some adjustment, the expression becomes

$$M_{12} = \frac{(-1)^x \eta_H \eta_L \left(\frac{\eta_H}{\eta_L}\right)^x \left(\frac{\varepsilon_L}{\eta_H} + \frac{\varepsilon_H}{\eta_H}\right)}{(\eta_H^2 - \eta_L^2)}$$

A similar procedure yields

$$M_{21} = \frac{(-1)^x \eta_H \eta_L \left(\frac{\eta_H}{\eta_L}\right)^x (\eta_L \varepsilon_L + \eta_H \varepsilon_H)}{\left(\eta_H^2 - \eta_L^2\right)}$$

8.2.2.2 Case II: Odd Number (2x + 1) of Layers

The resultant matrix is given by

$$\begin{bmatrix} B \\ C \end{bmatrix} = [H][L][H][L]\ldots[L][H]\begin{bmatrix} 1 \\ \eta_{sub} \end{bmatrix}$$

$$= [H]\{[L][H]\}^x \begin{bmatrix} 1 \\ \eta_{sub} \end{bmatrix}$$

which we can denote by

$$\begin{bmatrix} N_{11} & iN_{12} \\ iN_{21} & N_{22} \end{bmatrix}\begin{bmatrix} 1 \\ \eta_{sub} \end{bmatrix}$$

and which is simply the previous result multiplied by

$$\begin{bmatrix} -\varepsilon_H & i/\eta_H \\ i\eta_H & -\varepsilon_H \end{bmatrix}$$

Then

$$N_{11} = -\varepsilon_H M_{11} - M_{21}/\eta_H = (-1)^{x+1}\left(\frac{\eta_H}{\eta_L}\right)^x \frac{(\varepsilon_L\eta_H\eta_L + \varepsilon_H\eta_H^2)}{(\eta_H^2 - \eta_L^2)}$$

$$N_{12} = -\varepsilon_H M_{12} + M_{22}/\eta_H = (-1)^x\left(\frac{\eta_L}{\eta_H}\right)^x \frac{1}{\eta_H}$$

$$N_{21} = \eta_H M_{11} - \varepsilon_H M_{21} = (-1)^x\left(\frac{\eta_H}{\eta_L}\right)^x \eta_H$$

$$N_{22} = -\varepsilon_H M_{22} - \eta_H M_{12} = (-1)^{x+1}\left(\frac{\eta_H}{\eta_L}\right)^x \frac{\eta_H^2\eta_L(\varepsilon_L/\eta_H + \varepsilon_H/\eta_L)}{(\eta_H^2 - \eta_L^2)}$$

where terms in $(\eta_L/\eta_H)^x$ are neglected in comparison with $(\eta_H/\eta_L)^x$.

8.2.2.3 Phase Shift: Case I

We are now able to compute the phase shift on reflection. We take, initially, the admittance of the incident medium to be η_0. Then

$$\begin{bmatrix} B \\ C \end{bmatrix} = \begin{bmatrix} M_{11} & iM_{12} \\ iM_{21} & M_{22} \end{bmatrix}\begin{bmatrix} 1 \\ \eta_{sub} \end{bmatrix} = \begin{bmatrix} M_{11} + i\eta_{sub}M_{12} \\ \eta_{sub}M_{22} + iM_{21} \end{bmatrix}$$

$$\begin{aligned}\rho &= \frac{\eta_0 B - C}{\eta_0 B + C} = \frac{\eta_0(M_{11} + i\eta_{sub}M_{12}) - \eta_{sub}M_{22} - iM_{21}}{\eta_0(M_{11} + i\eta_{sub}M_{12}) + \eta_{sub}M_{22} + iM_{21}} \\ &= \frac{(\eta_0 M_{11} - \eta_{sub}M_{22}) + i(\eta_0\eta_{sub}M_{12} - M_{21})}{(\eta_0 M_{11} + \eta_{sub}M_{22}) + i(\eta_0\eta_{sub}M_{12} + M_{21})}\end{aligned} \tag{8.19}$$

$$\tan\varphi = \frac{2\eta_0\eta_{sub}^2 M_{12}M_{22} - 2\eta_0 M_{11}M_{21}}{\eta_0^2 M_{11}^2 - \eta_{sub}^2 M_{22}^2 + \eta_0^2\eta_{sub}^2 M_{12}^2 - M_{21}^2} \tag{8.20}$$

Inserting the appropriate expressions and once again neglecting terms of second and higher order in ε and terms in $(\eta_L/\eta_H)^x$, we obtain for φ

$$\tan\varphi = \frac{-2\eta_H\eta_L(\eta_L\varepsilon_H + \eta_H\varepsilon_L)}{\eta_0(\eta_H^2 - \eta_L^2)} \tag{8.21}$$

(for $LH\ldots LHLH|\eta_{sub}$).

8.2.2.4 Phase Shift: Case II

ρ is given by an expression similar to Equation 7.19, in which M is replaced by N. Then, following the same procedure as for case I, we arrive at

$$\tan\varphi = \frac{-2\eta_0(\eta_L\varepsilon_L + \eta_H\varepsilon_H)}{(\eta_H^2 - \eta_L^2)} \tag{8.22}$$

(for $HLH\ldots LHLH|\eta_{sub}$).

Equations 8.21 and 8.22 are in a general form that we will need later. For our present purposes, we can introduce some slight simplification.

$$\delta = \frac{2\pi nd}{\lambda} = 2\pi nd\nu = 2\pi nd\nu_0(\nu/\nu_0) = (\pi/2)g$$

so that

$$\varepsilon_H = \varepsilon_L = (\pi/2)g - \pi/2 = (\pi/2)(g-1)$$

Also, when we consider the construction of the Fabry–Perot filters, we see that the incident medium in case I will be a high-index spacer layer, and in case II, a low-index spacer. Thus, for Fabry–Perot filters,

$$\tan\varphi = \frac{-\pi n_L}{(n_H - n_L)}(g-1)$$

for both case I and case II.

Now, φ is nearly π or 0. Then

$$\frac{d\varphi}{dg} = \frac{-\pi\eta_L}{(\eta_H - \eta_L)}$$

which is the result obtained by Seeley. This can then be inserted in Equation 8.18 to give

$$\frac{\Delta\nu_h}{\nu_0} = \frac{\Delta\lambda_h}{\lambda_0} = \frac{2}{m\pi F^{1/2}}\left(\frac{\eta_H - \eta_L}{\eta_H - \eta_L + \eta_L/m}\right).$$

Then the expressions for the half-width of all-dielectric Fabry–Perot filters of mth order become

High-index cavity:

$$\left(\frac{\Delta\lambda_h}{\lambda}\right)_H = \frac{4\eta_{sub}\eta_L^{2x}}{m\pi\eta_H^{2x+1}} \frac{(\eta_H - \eta_L)}{(\eta_H - \eta_L + \eta_L/m)} \tag{8.23}$$

Low-index cavity:

$$\left(\frac{\Delta\lambda_h}{\lambda}\right)_L = \frac{4\eta_{sub}\eta_L^{2x-1}}{m\pi\eta_H^{2x}} \frac{(\eta_H - \eta_L)}{(\eta_H - \eta_L + \eta_L/m)} \tag{8.24}$$

which are simply the earlier results multiplied by the factor $(\eta_H - \eta_L)/(\eta_H - \eta_L + \eta_L/m)$. It should be noted that these results are for first-order reflecting stacks and mth-order cavity. Clearly, the effect of the phase is much greater the closer the two indices are in value and the lower the cavity order m. For the common visible and near infrared materials, zinc sulfide and cryolite, the factor for first-order cavities is equal to 0.43, while for infrared materials such as zinc sulfide and lead telluride it is greater, around 0.57. Figure 8.8 and Figure 8.9 show the characteristics of typical all-dielectric narrowband single-cavity, or Fabry–Perot, filters.

Since the all-dielectric multilayer reflector is effective over a limited range only, transmission sidebands appear on either side of the peak and, in most applications, must be suppressed. The shortwave sidebands can be removed very easily by adding to the filter a longwave-pass absorption filter, readily available in the form of polished glass disks from a large number of manufacturers. Unfortunately, it is not nearly as easy to obtain shortwave-pass absorption filters and the rather shallow edges of those that are available tend considerably to reduce the peak transmittance of the filter if the sidebands are effectively suppressed. The best solution to this problem is not to use an absorption type of filter at all, but to employ as a blocking filter a metal–dielectric filter of the type already discussed, or, preferably, of the multiple cavity type to be considered shortly. Because metal–dielectric filters used in the first order do not have longwave sidebands, they are very successful in this application. The metal–dielectric blocking filter can, in fact, be deposited over the all-dielectric filter in the same deposition cycle, provided that the

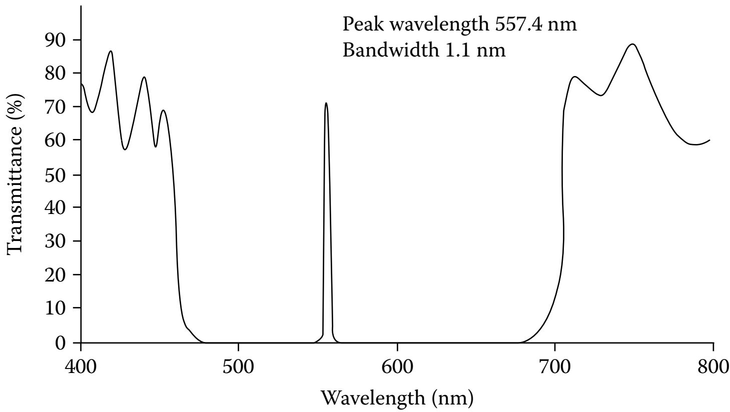

FIGURE 8.8
Measured transmittance of a narrowband all-dielectric filter with unsuppressed sidebands. Zinc sulfide and cryolite were the thin-film materials used. (Courtesy of Sir Howard Grubb, Parsons & Co. Ltd.)

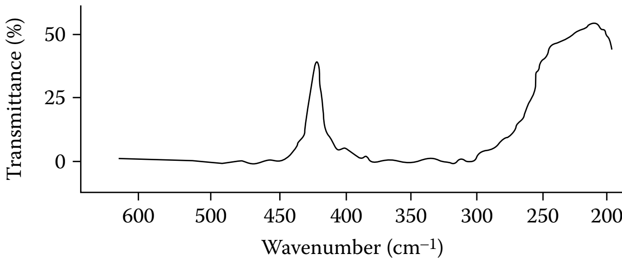

FIGURE 8.9
Measured transmittance of a Fabry–Perot filter for the far infrared. Design: Air|*LHLHHLH*|Ge with *H* indicating a quarter-wave of germanium and *L* of cesium iodide. The rear surface of the substrate is unbloomed so that the effective transmittance of the filter is 50%. (Courtesy of Sir Howard Grubb, Parsons & Co. Ltd.)

layers are monitored using the narrowband filter itself as the test glass—this is known as direct monitoring—but, more frequently, a completely separate metal–dielectric filter is used. The various components that go to make up the final filter are cemented together in one assembly.

Before we leave the single-cavity filter, we can examine the effects of absorption losses in the layers in a manner similar to that already employed in Chapter 6, where we were concerned with quarter-wave stacks. Many workers have investigated the problem. The following account relies heavily on the work of Hemingway and Lissberger [5], but with slight differences.

We apply the method of Chapter 6 directly. There, we recall, we showed that the loss in a weakly absorbing multilayer was given by

$$A = (1 - R)\sum \mathcal{A}$$

where, for quarter-waves,

$$\mathcal{A} = \beta\left(\frac{n}{y_e} + \frac{y_e}{n}\right)$$

$$\beta = \frac{2\pi kd}{\lambda} = \frac{2\pi nd}{\lambda}\frac{k}{n} = \frac{\pi}{2}\frac{k}{n}$$

y_e is the admittance of the structure on the emergent side of the layer, in free space units, $n - ik$ is the refractive index of the layer and d is the geometrical thickness. For quarter-waves, $nd = \lambda/4$.

The arrangement is shown in Table 8.2 where the admittance y_e is given at each interface and where expressions for either high- or low-index cavities are included. The reflecting stacks are assumed to begin with high-index layers of which there are x per reflector, not counting the cavity layer.

We consider the case of low-index cavities first.

$$\begin{aligned}\sum\mathcal{A} &= \beta_H\left(\frac{n_{sub}}{n_H} + \frac{n_H}{n_{sub}}\right) + \beta_L\left(\frac{n_H^2}{n_L n_{sub}} + \frac{n_L n_{sub}}{n_H^2}\right) \\ &+ \beta_H\left(\frac{n_L^2 n_{sub}}{n_H^3} + \frac{n_H^3}{n_L^2 n_{sub}}\right) + \beta_L\left(\frac{n_H^4}{n_L^2 n_{sub}} + \frac{n_L^2 n_{sub}}{n_H^4}\right) + \cdots \\ &+ \beta_L\left(\frac{n_H^{2x-2}}{n_L^{2x-3} n_{sub}} + \frac{n_L^{2x-3} n_{sub}}{n_H^{2x-2}}\right) + \beta_H\left(\frac{n_H^{2x-1}}{n_L^{2x-2} n_{sub}} + \frac{n_L^{2x-2} n_{sub}}{n_H^{2x-1}}\right) \\ &+ m\left[\beta_L\left(\frac{n_H^{2x}}{n_L^{2x-1} n_{sub}} + \frac{n_L^{2x-1} n_{sub}}{n_H^{2x}}\right) + \beta_H\left(\frac{n_H^{2x}}{n_L^{2x-1} n_{sub}} + \frac{n_L^{2x-1} n_{sub}}{n_H^{2x}}\right)\right] \\ &+ \beta_H\left(\frac{n_H^{2x-1}}{n_L^{2x-2} n_{sub}} + \frac{n_L^{2x-2} n_{sub}}{n_H^{2x-1}}\right) + \cdots + \beta_H\left(\frac{n_{sub}}{n_H} + \frac{n_H}{n_{sub}}\right)\end{aligned}$$

where the final set of terms is a repeat of the first and where the cavity consists of $2m$ quarter-waves. Rearranging, we find

$$\begin{aligned}\sum\mathcal{A} &= 2\beta_H\left(\frac{n_{sub}}{n_H} + \frac{n_L^2 n_{sub}}{n_H^3} + \frac{n_L^4 n_{sub}}{n_H^5} + \cdots + \frac{n_L^{2x-2} n_{sub}}{n_H^{2x-1}}\right) \\ &+ 2\beta_H\left(\frac{n_H}{n_{sub}} + \frac{n_H^3}{n_L^2 n_{sub}} + \frac{n_H^5}{n_L^4 n_{sub}} + \cdots + \frac{n_H^{2x-1}}{n_L^{2x-2} n_{sub}}\right)\end{aligned}$$

TABLE 8.2

Parameters for the Calculation of Losses in Narrowband Filters

Left Layer	Left Value	Center Layer	Center Value	Right Layer	Right Value
		Direction of Incidence ↓	$n_{sub} = n_0$		
		n_H	n_H^2 / n_{sub}		
		n_L	$n_L^2 n_{sub} / n_H^2$		
		n_H	$n_H^4 / (n_L^2 n_{sub})$		
		n_L	$n_L^4 n_{sub} / n_H^4$		
		⋮	$n_H^{2x-2} / (n_L^{2x-4} n_{sub})$		
		n_L	$n_L^{2x-2} n_{sub} / n_H^{2x-2}$		
		n_H	$n_H^{2x} / (n_L^{2x-2} n_{sub})$		
		↙			$n_H^{2x} / (n_L^{2x-2} n_{sub})$
	$n_H^{2x} / (n_L^{2x-2} n_{sub})$		↘	n_L	$n_L^{2x} n_{sub} / n_H^{2x}$
n_L	$n_L^{2x} n_{sub} / n_H^{2x}$			n_H	$n_H^{2x+2} / (n_L^{2x} n_{sub})$
Cavity ⋮	$n_L^{2x} n_{sub} / n_H^{2x}$			Cavity ⋮	$n_H^{2x+2} / (n_L^{2x} n_{sub})$
n_L	$n_H^{2x} / (n_L^{2x-2} n_{sub})$			n_L	$n_L^{2x} n_{sub} / n_H^{2x}$
		↘	↙	n_H	$n_H^{2x} / (n_L^{2x-2} n_{sub})$
			$n_H^{2x} / (n_L^{2x-2} n_{sub})$		
		n_H	$n_L^{2x-2} n_{sub} / n_H^{2x-2}$		
		⋮	$n_H^4 / (n_L^2 n_{sub})$		
		n_H	$n_L^2 n_{sub} / n_H^2$		
		n_L	n_H^2 / n_{sub}		
		n_H	n_{sub}		

$$+2\beta_L\left(\frac{n_L n_{sub}}{n_H^2}+\frac{n_L^3 n_{sub}}{n_H^4}+\cdots+\frac{n_L^{2x-3} n_{sub}}{n_H^{2x-2}}\right)$$
$$+2\beta_L\left(\frac{n_H^2}{n_L n_{sub}}+\frac{n_H^4}{n_L^3 n_{sub}}+\cdots+\frac{n_H^{2x-2}}{n_L^{2x-3} n_{sub}}\right)$$
$$+2m\beta_L\left(\frac{n_H^{2x}}{n_L^{2x-1} n_{sub}}+\frac{n_L^{2x-1} n_{sub}}{n_H^{2x}}\right)$$

where we have combined similar terms due to the two mirrors and where the final term is due to the cavity layer. The first four terms are geometric series and therefore, since $(n_L/n_H) < 1$,

$$\sum \mathcal{A} = 2\beta_H \frac{n_{sub}}{n_H}\frac{[1-(n_L/n_H)^{2x}]}{[1-(n_L/n_H)^2]}$$
$$+2\beta_H \frac{n_H^{2x-1}}{n_L^{2x-2} n_{sub}}\frac{[1-(n_L/n_H)^{2x-2}]}{[1-(n_L/n_H)^2]}$$
$$+2\beta_L \frac{n_L n_{sub}}{n_H^2}\frac{[1-(n_L/n_H)^{2x-2}]}{[1-(n_L/n_H)^2]}$$
$$+2\beta_L \frac{n_H^{2x-2}}{n_H^{2x-3} n_{sub}}\frac{[1-(n_L/n_H)^{2x-2}]}{[1-(n_L/n_H)^2]}$$
$$+2m\beta_L + \frac{n_H^{2x}}{n_L^{2x-1} n_{sub}}+\frac{n_L^{2x-1} n_{sub}}{n_H^{2x}}$$

(n_L/n_H) will usually be rather less than unity and x will normally be large and so we can make the usual approximations and neglect terms such as $(n_L/n_H)^{2x}$ in the numerators and also those terms that have (n_{sub}/n_H) as a factor compared with $(n_L/n_{sub})(n_H/n_L)^{2x-1}$, etc. Then, the expression simplifies to

$$\sum \mathcal{A} = 2\beta_H \frac{n_H^{2x-1}}{n_L^{2x-2} n_{sub}}\frac{1}{[1-(n_L/n_H)^2]}$$
$$+2\beta_L \frac{n_H^{2x-2}}{n_L^{2x-3} n_{sub}}\frac{1}{[1-(n_L/n_H)^2]}$$
$$+2m\beta_L \frac{n_H^{2x}}{n_L^{2x-1} n_{sub}}$$

but

$$\beta_H = \frac{2\pi n_H d}{\lambda}\frac{k_H}{n_H} = \frac{\pi}{2}\frac{k_H}{n_H}$$
$$\beta_L = \frac{\pi}{2}\frac{k_L}{n_L}$$

Thus

$$\sum \mathcal{A} = \frac{\dfrac{\pi k_H n_H^{2x}}{n_{sub} n_L^{2x-2}} + \dfrac{\pi k_L n_H^{2x}}{n_{sub} n_L^{2x-2}}}{(n_H^2 - n_L^2)} + \frac{\pi m k_L n_H^{2x}}{n_L^{2x} n_{sub}}$$

$$= \frac{\pi n_H^{2x}}{n_{sub} n_L^{2x}} \left[\frac{n_L^2 (k_H + k_L)}{(n_H^2 - n_L^2)} + m k_L \right]$$

The absorptance is then given by $A = (1 - R)\Sigma\mathcal{A}$. If the incident medium has index n_0, then, since the terminating admittance in Table 8.2 is n_{sub},

$$R = \left[\frac{n_0 - n_{sub}}{n_0 + n_{sub}} \right]^2$$

and therefore

$$(1 - R) = \frac{4 n_0 n_{sub}}{(n_0 + n_{sub})^2}$$

The above expression for $\Sigma\mathcal{A}$ should, therefore, be multiplied by the factor $4n_0 n_{sub}/(n_0 + n_{sub})^2$ to yield the absorptance. However, the filters should be designed so that they are reasonably well matched into the incident medium and therefore this factor will be unity, or sufficiently near unity. The absorptance is then given by $\Sigma\mathcal{A}$. That is:

$$A = \frac{\pi n_H^{2x}}{n_{sub} n_L^{2x}} \left[\frac{n_L^2 (k_H + k_L)}{(n_H^2 - n_L^2)} + m k_L \right] \tag{8.25}$$

for low-index cavities.

For high-index cavities we work through a similar analysis and, with the same approximations, we arrive at

$$A = \frac{\pi n_H^{2x}}{n_{sub} n_L^{2x}} \left[\frac{n_L^2 k_H + n_H^2 k_L}{(n_H^2 - n_L^2)} + m k_H \right] \tag{8.26}$$

for high-index cavities.

It should be noted that, since x is the number of high-index layers, the filter represented by Equation 8.26 will be narrower than that represented by Equation 8.25 for equal x.

A useful set of alternative expressions can be obtained if we substitute Equations 8.23 and 8.24 into Equations 8.25 and 8.26 to give:
High-index cavity

$$A = 4\frac{\lambda_0}{\Delta\lambda_h}\frac{\{k_H[m+(1-m)(n_L/n_H)^2]+k_L\}}{(n_H+n_L)[m+(1-m)(n_L/n_H)]} \tag{8.27}$$

Low-index cavity

$$A = 4\frac{\lambda_0}{\Delta\lambda_h}\frac{\{k_L(n_H/n_L)[m+(1-m)(n_L/n_H)^2]+(n_L/n_H)k_H\}}{(n_H+n_L)[m+(1-m)(n_L/n_H)]} \tag{8.28}$$

Figure 8.10 shows the value of A plotted for Fabry–Perot filters with $n_H = 2.35$ and $n_L = 1.35$, typical of zinc sulfide and cryolite. $(\lambda_0/\Delta\lambda_h)$ is taken as 100 and k_H and k_L as either zero or 0.0001. The effect of other values of $(\lambda_0/\Delta\lambda_h)$ or k can be estimated by multiplying by an appropriate factor. The approximations are reasonable for $k(\lambda_0/\Delta\lambda_h)$ less than around 0.1.

It is difficult to draw any general conclusions from Figure 8.10 because the results depend on the relative magnitudes of k_H and k_L. However, except in the case of very low k_L, the high-index cavity is to be preferred. There are very good reasons connected with performance when tilted, with energy grasp and with the manufacture of filters, for choosing high- rather than low-index cavities.

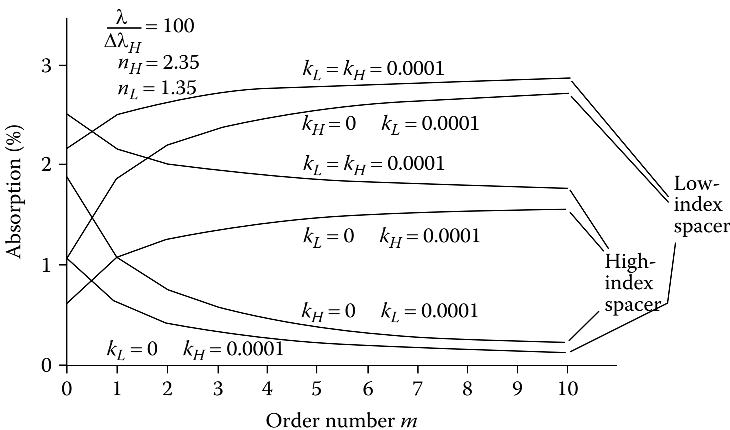

FIGURE 8.10
The value (expressed as a percentage) of the absorptance, as a function of the order number m, of single-cavity filters with $\lambda_0/\Delta\lambda_h$ of 100 and values of extinction coefficients k_H and k_L of 0.0001 or zero. Other values can be accommodated by multiplying by an appropriate factor. n_H is taken as 2.35 and n_L as 1.35. The results are derived from Equations 8.27 and 8.28.

In the visible and near infrared regions of the spectrum, materials such as zinc sulfide and cryolite are capable of half-widths of less than 0.1 nm with useful peak transmittance. Uniformity is, however, a major difficulty for filters of such narrow bandwidths. At the 90%-of-peak points, the single-cavity filter has a width that is one-third of the half-width. It is a good guide that the uniformity of the filter should be such that the peak wavelength does not vary by more than one-third of the half-width over the entire surface of the filter. This means that the effective increase in half-width due to the lack of uniformity is kept within some 4.5% of the half-width and the reduction in peak transmittance to less than 3% (these figures can be calculated using the expressions derived later for assessing the performance of filters in uncollimated incident light). For filters of less than 0.1 nm half-width, this rule implies a variation of not more than 0.03 nm or 0.006% in terms of layer thickness, a very severe requirement even for quite small filters. Half-widths of 0.3–0.5 nm are less demanding and can be produced more readily provided considerable care is taken. For narrower filters, use is often made of the solid etalon filters now to be described.

8.2.3 The Solid Etalon Filter

A solid etalon filter, or, as it is sometimes called, a solid spacer filter is a very high-order single-cavity or Fabry–Perot filter in which the cavity consists of an optically worked plate or a cleaved crystal. Thin-film reflectors are deposited on either side of the cavity, or spacer, in the normal way, so that the cavity also acts as the substrate. The problems of uniformity that exist with all-thin-film narrowband filters are avoided and the thick cavity does not suffer from the increased scattering losses that always seem to accompany the higher-order thin-film cavities. The solid etalon filter is very much more robust and stable than the conventional air-spaced Fabry–Perot etalon, while the manufacturing difficulties are comparable. The high order implies a small interval between orders and a conventional thin-film narrowband filter must be used in series with it to eliminate the unwanted orders.

An early account of the use of mica for the construction of filters of this type is that of Dobrowolski [6], who credits Billings with being the first to use mica in this way, achieving half-widths of 0.3 nm. Dobrowolski obtained rather narrower pass bands and his is the first complete account of the technique. Mica can be cleaved readily to form thin sheets with flat parallel surfaces, but there is a complication due to the natural birefringence of mica, which means that the position of the pass band depends on the plane of polarization. This splitting of the pass band can be avoided by arranging the thickness of the mica such that it is a half-wave plate, or multiple half-wave, at the required wavelength. If the two refractive indices are n_o and n_e, this implies

$$\frac{2\pi(n_o - n_e)d}{\lambda} = p\pi \quad p = 0, \pm 1, \pm 2, \ldots$$

The order of the cavity will then be given by

$$m = \frac{n_o p}{(n_o - n_e)} \quad \text{or} \quad m = \frac{n_e p}{(n_o - n_e)}$$

depending on the plane of polarization. The difference between these two values is p, but, since p is small, the bandwidths will be virtually identical. The separation of orders for large m is given approximately by λ/m. Dobrowolski found that the maximum order separation, corresponding to $p = 1$, was given by 1.64 nm at 546.1 nm. With such cavities, around 60 μm thick, filters with half-widths around 0.1 nm, the narrowest 0.085 nm, were constructed. Peak transmittance ranged up to 50% for the narrower filters and up to 80% for slightly broader ones with around 0.3 nm half-width.

More recent work on solid etalon filters has concentrated on the use of optically worked materials as cavities. These must be ground and polished so that the faces have the necessary flatness and parallelism. The most complete account so far of the production of such filters is by Austin [7]. Fused silica discs as thin as 50 μm have been produced with the necessary parallelism for half-widths as narrow as 0.1 nm in the visible region, while thicker discs can give bandwidths as narrow as 0.005 nm. A 50-μm fused silica cavity gives an interval between orders of around 1.4 nm in the visible region, which allows the suppression of unwanted orders to be fairly readily achieved by conventional thin-film narrowband filters.

The process of optical working tends to produce an error in parallelism over the surface of the cavity, which is ultimately independent of its thickness. Let us denote the total range of thickness due to this lack of parallelism and to any deviation from flatness by Δd. This variation in cavity thickness causes the peak wavelength of the filter to vary. We can take an absolute limit for these variations as half the bandwidth of the filter. Then, the resultant half-width will be increased by just over 10% and the peak transmittance reduced by just over 7% (once again using the expressions that we will shortly establish for filter performance in uncollimated light). We can write

$$\Delta\lambda_0/\lambda_0 = \Delta D/D = \Delta d/d \leq 0.5\Delta\lambda_h/\lambda_0$$

where D is the optical thickness nd of the cavity, $\Delta\lambda_0$ is the error in peak wavelength, and $\Delta\lambda_h$ is the half-width. But

$$\text{Resolving power} = \lambda_0/\Delta\lambda_h = m\mathcal{F}$$

and hence, since

$$D = m\lambda_0/2$$

$$\mathcal{F} = \frac{0.25\lambda_0}{\Delta D}$$

Now the attainable ΔD in the visible region is of the order of $\lambda/100$ and this means that the limiting finesse is around 25, independent of the cavity thickness. High resolving power then has to be achieved by the order number m that determines both the cavity thickness, $D = m\lambda_0/2$, and the interval between orders, λ_0/m. For a half-width of 0.01 nm at, say, 500 nm, the resolving power is 50,000. The finesse of 25 implies an order number of 2000, a cavity optical thickness of 500 μm and an interval between orders of 0.25 nm. This very restricted range between orders means that it is very difficult to carry out sideband blocking by a thin-film filter directly. Instead, a broader solid etalon filter can be used with its corresponding greater interval between orders. It, in its turn, can be suppressed by a thin-film filter. For a half-width of 0.1 nm, a cavity optical thickness of 50 μm is required, which gives an interval between orders of 2.5 nm.

The temperature coefficient of peak wavelength change of solid etalon filters with fused silica cavities is 0.005 nm $°C^{-1}$ and the filters may be finely tuned by altering this temperature.

Candille and Saurel [8] have used Mylar foil as the cavity. Their filters were strictly of the multiple cavity type described later in this chapter. The Mylar acted as a substrate and a high-order cavity. One of the reflectors included a low-order single-cavity filter that served both as blocking filter to eliminate the additional unwanted orders of the Mylar section and as an additional cavity to steepen the sides of the pass band. The position of the pass band could be altered by varying the tension in the Mylar. The filters were not as narrow as the other solid etalon filters mentioned, half-widths of 0.8–1.0 nm being obtained.

Solid etalon filters have also been constructed for the infrared. Smith and Pidgeon [9] used a polished slab of germanium some 780 μm thick working at around 700 cm^{-1} in the 400th order. Both faces were coated with a quarter-wave of zinc sulfide followed by a quarter-wave of lead telluride to give a reflectance of 62%, a fringe half-width of 0.1 cm^{-1} and an interval between orders of 1.6 cm^{-1}. This particular arrangement was designed so that the lines in the R-branch of the CO_2 spectrum, which are spaced at 1.6 cm^{-1} apart at around 14.5 μm, should be exactly matched by a number of adjacent orders. Order sorting was not, therefore, a problem.

Roche and Title [10] have reported a range of solid etalon filters for the infrared. These filters are some 13 mm in diameter, have resolving powers in the region of 3×10^4 and the techniques used for their construction are as reported by Austin [7]. For wavelengths equal to or shorter than 3.5 μm, fused silica cavities are quite satisfactory. For longer wavelengths, Yttralox, a combination of yttrium and thorium oxides, was found to be most satisfactory. With this material, solid etalon filters were produced that at 3.334 μm had half-widths as low as 0.2 nm and at 4.62 μm, 0.8 nm. At these wavelengths, the attainable finesse was 30–40 and the current limit to the half-width that can be achieved is the permissible interval between orders, which determines the arrangement of subsidiary blocking filters.

Recently, Floriot et al. [11] made some significant advances in the use of solid etalon filters for telecommunication applications. These are actually multiple-cavity filters, rather than single-cavity, but it is convenient to refer to the work here. We shall see shortly that the sloping edges of the single-cavity filter can be considerably steepened, so that the response of the filter becomes more rectangular, when multiple cavities are coherently coupled together to present a single, combined, interferometric response. The coupling between successive cavity structures is usually accomplished by means of a single quarter-wave layer called the *coupling layer.* Multiple-cavity filters present challenges in production that are well beyond those of single-cavity filters. The very narrowband filters required for telecommunication applications may require designs of well above 100 discrete layers, sometimes more than 200. If such filters are constructed from solid etalons, then the same reduction in design complexity and greater ease of deposition enjoyed by the single-cavity solid etalon filters are realized. Of course, there is the difficulty of coupling together the cavities, and this has been accomplished by using air as the coupling material and finely adjusting the thickness using piezoelectric translators. The air coupling layers can actually have thicknesses considerably in excess of quarter-waves and, in the filters described, were arranged at usually slightly more than 20 quarter-waves, and to achieve optimum performance, the coupling layers together with the two layers on either side of each coupling layers were refined in thickness. In practical filters, this refinement process is repeated at the appropriate point in the production of the filters to compensate for any committed errors in deposition. When first produced, the cavities are not necessarily of exactly the required thicknesses. They consist of 10 mm × 10 mm silica plates and are measured by examining the interference fringes produced by a tunable laser. They are then adjusted in thickness by depositing a silica film over their surface. The final filter is required to accommodate only the 250 μm beam waist of a Gaussian beam, and so the initial parallelism of 3 arc sec meets the requirements. The problem of the limited free spectral range is partially met by arranging different thicknesses for the cavities so that those peaks close to the fundamental wavelength in the various etalons do not exactly coincide.

A typical example using four cavity structures has a design as follows:

$$1.09H(LH)^2\ 246C\ (HL)^2\ 1.05H\ 20.66A\ 1.13H(LH)^2\ 500C$$
$$(HL)^2\ 1.09\text{H}\ 24.79\text{A}\ 1.06\text{H}\ (LH)^2\ 412C\ (HL)^2\ 1.02H\ 31.11A$$
$$0.73\text{H}\ (LH)2\ 298\text{C}\ (HL)2\ 1.27H$$

where the symbols indicate quarter-wave thicknesses at the reference wavelength of 1550 nm. *C* is the silica cavity material of index 1.44, *H* a high-index quarter-wave of index 2.09 (Ta_2O_5), and *L* a low-index quarter-wave of index 1.46 (SiO_2), and *A* represents a quarter-wave of air. The incident and emergent media are both air. The calculated performance of this design is shown in Figure 8.11. The ripple performance is exceptionally good. Filters with this

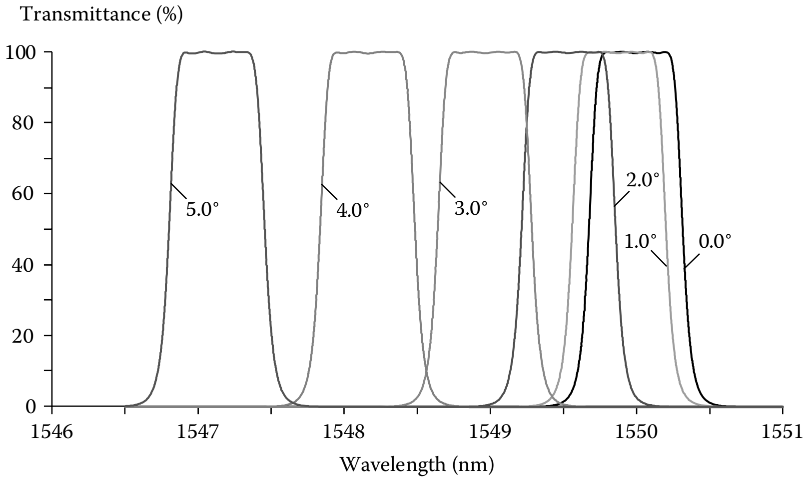

FIGURE 8.11
The calculated performance of the solid etalon filter, with design as in the text, at normal incidence and at increasing angle of incidence. The ripple performance is exceptional and remains so even at elevated angles of incidence. (After Floriot. J., Lemarchand, F., and Lequime, M., *Applied Optics*, 45, 1349–1355, 2006.)

level of performance will often exhibit rather poorer performance at oblique incidence where the profile becomes distorted. This solid etalon filter exhibits virtually no perceptible distortion as evidenced by the figure.

8.2.4 The Effect of Varying the Angle of Incidence

As we have seen with other types of thin-film assembly, the performance of the all-dielectric single-cavity filter varies with angle of incidence, and this effect is particularly important when considering, for instance, the allowable focal ratio of the pencil being passed by the filter or the maximum tilt angle in any application. The variation with angle of incidence is not altogether a bad thing because the effect can be used to tune filters that would otherwise be off the desired wavelength—this is very important from the manufacturer's point of view because it enables an easing of the otherwise almost impossibly tight production tolerances.

The effect of tilting has been studied by a number of workers, particularly by Dufour and Herpin [12], Lissberger [13], Lissberger and Wilcock [14], and Pidgeon and Smith [15]. For our present purposes, we follow Pidgeon and Smith since their results are in a slightly more suitable form.

8.2.4.1 Simple Tilts in Collimated Light

The phase thickness of a thin film at oblique incidence is $\delta = 2\pi nd \cos\vartheta/\lambda$. This can be interpreted as an apparent optical thickness of $nd \cos\vartheta$ that varies with angle of incidence so that layers seem thinner when tilted. Although

the optical admittance changes as the tilt angle varies, in narrowband filters the predominant effect is the apparent change in thickness that moves the filter pass band to shorter wavelengths.

For an ideal single-cavity filter with cavity layer index n^*, where the reflectors have constant phase shift of zero or π regardless of the angle of incidence or wavelength, we can write for the position of peak wavelength in the mth order

$$\frac{2\pi n^* d\cos\vartheta}{\lambda} = \frac{2\pi n^* d}{\lambda_0}\frac{\lambda_0}{\lambda}\cos\vartheta = m\pi$$

where λ is the new, tilted, peak wavelength and λ_0 the peak at normal incidence. We can replace λ_0/λ by g, which can then be written as $1 + \Delta g$. Then, since $2\pi n^* d/\lambda_0 = m\pi$,

$$1+\Delta g = \frac{1}{\cos\vartheta}$$

so that

$$\Delta g = \frac{1}{\cos\vartheta} - 1$$

If the angle of incidence is ϑ_0 in air then

$$\vartheta = \arcsin(\sin\vartheta_0/n^*)$$

and Δg is given in terms of ϑ_0 and n^*. The effect of tilting, then, in this ideal filter can be estimated simply from a knowledge of the index of the cavity and the angle of incidence.

For small angles of incidence, the shift is given by

$$\Delta g = \frac{\Delta\nu}{\nu_0} = \frac{\Delta\lambda}{\lambda_0} = \frac{\vartheta_0^2}{2n^{*2}} \tag{8.29}$$

The index of the cavity, n^*, determines its sensitivity to tilt: the higher the index, the less the filter is affected.

In the case of a real filter, the reflectors are also affected by the tilting and so the calculation of the shift in peak wavelength is more involved. It has, however, been shown by Pidgeon and Smith [15] that the shift is similar to what would have been obtained from an ideal filter with cavity index n^*, intermediate between the high and low indices of the layers of the filter. n^* is known as the effective index. This concept of the effective index holds good

for quite high angles of incidence, up to 20° or 30°, or even higher, depending on the indices of the layers making up the filter.

We can estimate the effective index for the filter by a technique similar to that already used for finding the peak position of metal–dielectrics (Equation 8.3). We retain our assumption of small angle of incidence and small changes in g around the value corresponding to the peak at normal incidence.

The peak position is given, as before, by

$$\sin^2\left[\frac{2\pi nd\cos\vartheta}{\lambda}-\varphi\right]=0 \tag{8.30}$$

with, at normal incidence

$$\sin^2\left[\frac{2\pi nd}{\lambda_0}-\varphi_0\right]=0 \tag{8.31}$$

Now φ_0 is 0 or π and so Equation 8.31 is satisfied by

$$2\pi nd/\lambda_0 = m\pi \quad m=0,1,2,\ldots$$

The analysis is once again easier in terms of g (= $\lambda_0/\lambda = \nu/\nu_0$). Equation 8.30 becomes

$$\sin^2[(2\pi nd/\lambda_0)g\cos\vartheta-\varphi_0-\Delta\varphi]=0 \tag{8.32}$$

We write

$$g=1+\Delta g \text{ and } \cos\vartheta \simeq 1-\vartheta^2/2$$

However, we should work in terms of ϑ_0, the external angle of incidence, which we will assume is referred to free space (if not, then we make the appropriate correction). Then

$$n\sin\vartheta = n_0\sin\vartheta_0 = \sin\vartheta_0$$

and, using Equation 8.32,

$$\sin^2[(2\pi nd/\lambda_0)-\varphi_0+m\pi\Delta g-(m\pi\vartheta_0^2/2n^2)-\Delta\varphi]=0$$

is the condition for the new peak position. This requires

$$m\pi\Delta g-(m\pi\vartheta_0^2/2n^2)-\Delta\varphi=0 \tag{8.33}$$

Now $\Delta\varphi$ is a function of ϑ and Δg and to evaluate it we return to Equations 8.20 and 8.21, but, because we are dealing with a perturbation from a reference condition of normal incidence, we replace η by n. The layers in the reflectors are all quarter-waves and so ε is given by

$$\frac{\pi}{2}+\varepsilon=\left[\frac{2\pi nd}{\lambda_0}\right]g\cos\vartheta=\left(\frac{\pi}{2}\right)(1+\Delta g)\left(1-\frac{\vartheta^2}{2}\right)$$

but

$$\vartheta=\frac{\vartheta_0}{n}$$

so that

$$\varepsilon=\frac{\pi}{2}\Delta g-\frac{\pi\vartheta_0^2}{4n^2}$$

with n being either n_L or n_H for ε_L or ε_H, respectively.

At this stage, we are forced to consider high-index and low-index cavities separately.

8.2.4.2 Case I: High-Index Cavities

From Equation 8.20, we have, inserting n_H for η_0,

$$\begin{aligned}\Delta\varphi&=\frac{2n_L^2}{(n_H^2-n_L^2)}\varepsilon_H-\frac{2n_Hn_L}{(n_H^2-n_L^2)}\varepsilon_L\\&=-\frac{2n_L^2}{(n_H^2-n_L^2)}\left(\frac{\pi}{2}\Delta g-\frac{\pi\vartheta_0^2}{4n_H^2}\right)-\frac{2n_Hn_L}{(n_H^2-n_L^2)}\left(\frac{\pi}{2}\Delta g-\frac{\pi\vartheta_0^2}{4n_L^2}\right)\\&=-\frac{\pi n_L}{(n_H-n_L)}\Delta g+\frac{\pi}{2}\frac{(n_L^2+n_H^2-n_Ln_H)}{n_H^2n_L(n_H-n_L)}\vartheta_0^2\end{aligned}$$

and Equation 8.33 becomes

$$m\pi\Delta g-\frac{m\pi\vartheta_0^2}{2n_H^2}+\frac{\pi n_L}{(n_H-n_L)}\Delta g-\frac{\pi}{2}\frac{(n_L^2+n_H^2-n_Ln_H)}{n_H^2n_L(n_H-n_L)}\vartheta_0^2=0$$

giving, after some manipulation and simplification

$$\Delta g=\frac{1}{n_H^2}\left[\frac{m-1-(m-1)\dfrac{n_L}{n_H}+\dfrac{n_H}{n_L}}{m-(m-1)\dfrac{n_L}{n_H}}\right]\frac{\vartheta_0^2}{2}$$

But, comparing the expression with Equation 8.29, we find

$$n^{*2} = \frac{n_H^2\left[m - (m-1)\dfrac{n_L}{n_H}\right]}{\left[m - 1 - (m-1)\dfrac{n_L}{n_H} + \dfrac{n_H}{n_L}\right]}$$

or

$$n^* = n_H\left[\frac{m - (m-1)\dfrac{n_L}{n_H}}{m - 1 - (m-1)\dfrac{n_L}{n_H} + \dfrac{n_H}{n_L}}\right]^{1/2} \tag{8.34}$$

For first-order filters

$$n^* = (n_H n_L)^{1/2} \tag{8.35}$$

which is the result obtained by Pidgeon and Smith. As $m \to \infty$ then $n^* \to n_H$, as we would expect.

8.2.4.3 Case II: Low-Index Cavities

The analysis is exactly as for case I except that Equation 8.22 is used and the n in Equation 8.33 becomes n_L:

$$n^* = n_L\left[\frac{m - (m-1)\dfrac{n_L}{n_H}}{m - m\dfrac{n_L}{n_H} + \left(\dfrac{n_L}{n_H}\right)^2}\right]^{1/2} \tag{8.36}$$

For first-order filters

$$n^* = \frac{n_L}{\left[1 - \dfrac{n_L}{n_H} + \left(\dfrac{n_L}{n_H}\right)^2\right]^{1/2}} \tag{8.37}$$

which is, again, the expression given by Pidgeon and Smith and we note again that as $m \to \infty$ then $n^* \to n_L$.

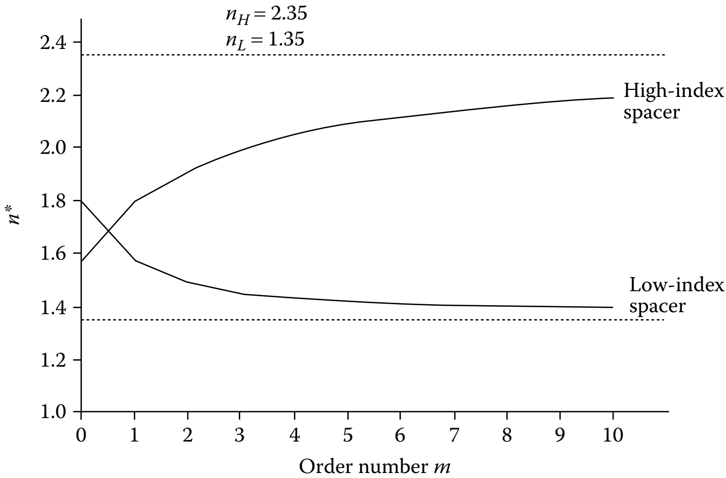

FIGURE 8.12
The effective index n^* plotted against order number m for single-cavity filters constructed of materials such as zinc sulfide, $n = 2.35$, and cryolite, $n = 1.35$. The results were calculated from Expressions 8.34 and 8.36.

Typical curves showing how the effective index n^* varies with order number for both low- and high-index cavities are given in Figure 8.12.

Pidgeon and Smith made experimental measurements on narrowband filters for the infrared. The designs in question were

$$\text{(a) } L|\text{Ge}|LHLH\ LL\ HLH|\text{Air}$$

$$\text{(b) } L|\text{Ge}|LHLHL\ HH\ LHLH|\text{Air}$$

where H represents a quarter-wave thickness of lead telluride and L of zinc sulfide, and where the peak wavelength was approximately 15 μm. Calculations of shift were carried out by the approximate method using n^* and by the full matrix method without approximations. The results using n^* matched the accurate calculations up to angles of incidence of 40° to an accuracy representing ±2% change in n^*. The experimental points showed good agreement with the theoretical estimates. Some of the results are shown in Figure 8.13 and Figure 8.14.

The angle of incidence may be in a medium other than free space, in which case Equation 8.29 becomes

$$\Delta g = \frac{\Delta \nu}{\nu_0} = \frac{\Delta \lambda}{\lambda_0} = \frac{n_0 \vartheta_0^2}{2n^{*2}} \tag{8.38}$$

where ϑ_0 is measured in radians.

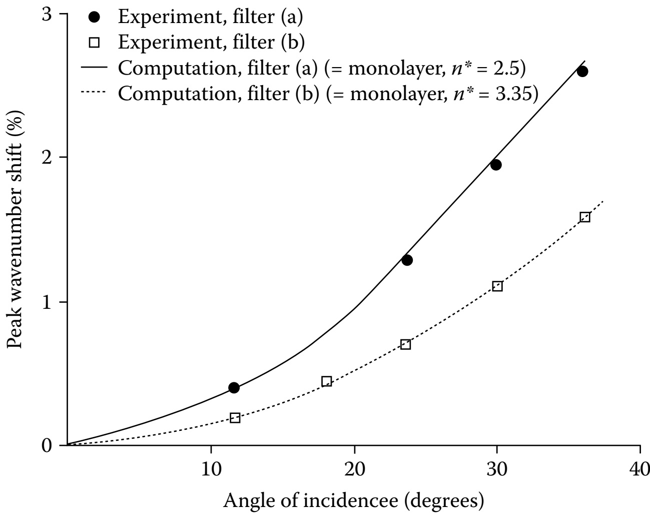

FIGURE 8.13
The shift of peak wave number with scanning angle for two single-cavity filters in collimated light. In both cases the monolayer curves fit the computed curves to ±2% in n. (After Pidgeon, C.R. and Smith, S.D., *Journal of the Optical Society of America*, 54, 1459–1466, 1964.)

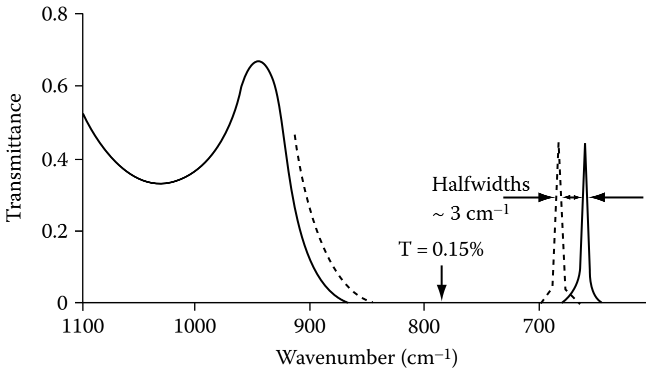

FIGURE 8.14
Measured transmittance of two filters of type (b). Design: Air|*HLHL HH LHLHL*|Ge substrate |*L*|Air (*H* = PbTe, *L* = ZnS). (After Pidgeon, C.R. and Smith, S.D., *Journal of the Optical Society of America*, 54, 1459–1466, 1964.)

If ϑ_0 is measured in degrees, then

$$\Delta g = \frac{\Delta \nu}{\nu_0} = \frac{\Delta \lambda}{\lambda_0} = 1.5 \times 10^{-4} \frac{n_0 \vartheta_0^2}{n^{*2}} \tag{8.39}$$

8.2.4.4 Effect of an Incident Cone of Light

The analysis can be taken a stage further to arrive at expressions for the degradations of peak transmission and bandwidth, which become apparent

when the incident illumination is not perfectly collimated. Essentially the same results have been obtained by Lissberger and Wilcock [14] and by Pidgeon and Smith [15].

It is assumed first that, in collimated light, the sole effect of tilting a filter is a shift of the characteristic towards shorter wavelengths, or greater wave numbers, leaving the peak transmittance and bandwidth virtually unchanged. The performance in convergent or divergent light is then given by integrating the transmission curve over a range of angles of incidence. The analysis is simpler in terms of wave number or of g, rather than wavelength. If ν_0 is the wave number corresponding to the peak at normal incidence and ν_Θ to the peak at angle of incidence Θ, then it is plausible that the resultant peak, when all angles of incidence in the cone from 0 to Θ are included, should appear at a wave number given by the mean of the above extremes. We shall show, shortly, that this is indeed the case. The new peak is given by

$$\nu_{peak} = \nu_0 + \frac{1}{2}\Delta\nu' \tag{8.40}$$

where

$$\Delta\nu' = \nu_\Theta - \nu_0 = \nu_0 \frac{\Theta^2}{2n^{*2}}$$

The effective bandwidth of the filter will, of course, appear broader, and, since the process is, in effect, a convolution of a function with bandwidth W_0, which is the width of the filter at normal incidence, and another function with bandwidth $\Delta\nu'$, the change in peak position produced by altering the angle of incidence from 0 to Θ, it seems likely that the resultant bandwidth might be given by the square root of the sum of their squares. This, too, is indeed the case, as we shall also show.

$$W_\Theta^2 = W_0^2 + (\Delta\nu')^2 \tag{8.41}$$

The peak transmission falls and is given by

$$\hat{T}_\Theta = \left(\frac{W_0}{\Delta\nu'}\right)\arctan\left(\frac{\Delta\nu'}{W_0}\right) \tag{8.42}$$

The analysis is as follows.

We consider incident light in the form of a cone with semiangle Θ, that is a cone of focal ratio 1/(2tanΘ). We assume that in collimated light the effect of tilting the filter is simply to move the characteristic toward shorter wavelengths, leaving the bandwidth and peak transmittance unchanged. We can think of the illumination as in the form of a uniform spherical wavefront

with the filter located exactly at the center. Then, the flux at any angle will be proportional to the area subtended on the spherical surface.

For small values of ϑ, the flux incident on the filter is proportional to $\vartheta d\vartheta$. The resultant transmittance of the filter is then given by the total flux transmitted divided by the total flux incident. We can forget about the constants of proportionality because they cancel in this operation.

With that simplification, the total flux incident is proportional to

$$\int_0^\Theta \vartheta d\vartheta = \frac{1}{2}\Theta^2$$

The total flux transmitted is proportional to

$$\int_0^\Theta \vartheta T(\vartheta) d\vartheta$$

We can, for small values of ϑ and Δg, set

$$T = \frac{1}{1 + \left\{\frac{2}{\Delta g_h}\left(\Delta g - \frac{\vartheta_0^2}{2n^{*2}}\right)\right\}^2}$$

where Δg_h is the half-width at normal incidence of the filter in units of g. This expression follows directly from the concept of n^*. The transmittance of the filter is then given by

$$\begin{aligned} T &= \frac{2}{\Theta^2}\int_0^\Theta \frac{\vartheta_0 d\vartheta_0}{1 + \left\{\frac{2}{\Delta g_h}\left(\Delta g - \frac{\vartheta_0^2}{2n^{*2}}\right)\right\}^2} \\ &= -\frac{2}{\Theta^2}\frac{n^{*2}\Delta g_h}{2}\left[\arctan\left\{\frac{2}{\Delta g_h}\left(\Delta g - \frac{\vartheta_0^2}{2n^{*2}}\right)\right\}\right]_0^\Theta \\ &= \frac{1}{2}\frac{\Delta g_h}{(\Theta^2/2n^{*2})}\left[\arctan\left(2\frac{\Delta g}{\Delta g_h}\right) - \arctan\left\{2\left(\frac{\Delta g}{\Delta g_h} - \frac{\Theta^2}{2n^{*2}}\frac{1}{\Delta g_h}\right)\right\}\right] \end{aligned} \tag{8.43}$$

The expression inside the square brackets is the difference of two angles. We can take the tangent of that difference and then the arctangent of the resulting expression to yield an improved form:

$$T = \frac{1}{2}\frac{\Delta g_h}{\left(\Theta^2/2n^{*2}\right)}\left[\arctan\left(\frac{\left(\frac{2}{\Delta g_h}\right)\left(\frac{\Theta^2}{2n^{*2}}\right)}{1 + \left(\frac{2}{\Delta g_h}\right)^2\left\{\Delta g\left(\Delta g - \frac{\Theta^2}{2n^{*2}}\right)\right\}}\right)\right] \tag{8.44}$$

Differentiating this with respect to Δg, we find zero derivative and, therefore, maximum transmittance at

$$\Delta g = \frac{1}{2}\frac{\Theta^2}{2n^{*2}}$$

However, $\Theta^2/(2n^{*2})$ is the shift in the position of the peak at angle of incidence Θ. Thus, in a cone of light of semiangle Θ, the peak wavelength of the filter is given by the mean of the value at normal incidence and that at the angle Θ corresponding to Equation 8.40. The value of the peak transmittance is then, from Equation 8.43,

$$T = \frac{1}{2}\frac{\Delta g_h}{(\Theta^2/2n^{*2})}\left[\arctan\left(\frac{(\Theta^2/2n^{*2})}{\Delta g_h}\right) - \arctan\left(-\frac{(\Theta^2/2n^{*2})}{\Delta g_h}\right)\right]$$

$$= \frac{\Delta g_h}{(\Theta^2/2n^{*2})}\arctan\left(\frac{(\Theta^2/2n^{*2})}{\Delta g_h}\right)$$

which corresponds to Equation 8.42.

The half-peak points are given by those values of Δg that yield half the peak transmittance in Expression 8.44. That is

$$\frac{1}{2}\frac{\Delta g_h}{(\Theta^2/2n^{*2})}\left[\arctan\left(\frac{\left(\frac{2}{\Delta g_h}\right)\left(\frac{\Theta^2}{2n^{*2}}\right)}{1+\left(\frac{2}{\Delta g_h}\right)^2\left\{\Delta g\left(\Delta g - \frac{\Theta^2}{2n^{*2}}\right)\right\}}\right)\right]$$

$$= \frac{1}{2}\frac{\Delta g_h}{(\Theta^2/2n^{*2})}\arctan\left(\frac{(\Theta^2/2n^{*2})}{\Delta g_h}\right)$$

and this is satisfied by

$$1+\left(\frac{2}{\Delta g_h}\right)^2\left\{\Delta g\left(\Delta g - \frac{\Theta^2}{2n^{*2}}\right)\right\} = 2$$

i.e.,

$$\Delta g\left(\Delta g - \frac{\Theta^2}{2n^{*2}}\right) - \left(\frac{\Delta g_h}{2}\right)^2 = 0$$

We are interested in the difference between the roots of the equation, which gives the width of the characteristic

$$(\Delta g_1 - \Delta g_2) = \left[\left(\frac{\Theta^2}{2n^{*2}} \right) + (\Delta g_h)^2 \right]^{1/2}$$

exactly corresponding to Equation 8.41.
Since

$$\arctan x = x - \frac{x^3}{3} + \frac{x^5}{5} - \frac{x^7}{7} + \cdots \quad \text{for } |x| \leq 1$$

for small values of ($\Delta\nu'/W_0$), we can write

$$\hat{T}_\Theta = 1 - \frac{1}{3}\left(\frac{\Delta\nu'}{W_0} \right)^2 \tag{8.45}$$

If *FR* denotes the focal ratio of the incident light, then, for values of around 2 to infinity, it is a reasonably good approximation that

$$\Theta = 1/[2FR]$$

Using this, we find another expression for $\Delta\nu'$ that can be useful:

$$\Delta\nu' = \frac{\nu_0}{8n^{*2}(FR)^2}$$

We can extend this analysis still further to the case of a cone of semiangle Θ incident at an angle other than normal, provided we make some simplifying assumptions. If the angle of incidence of the cone is χ, then the range of angles of incidence will be $\chi \pm \Theta$.

If $\chi < \Theta$, then we can assume that the result is simply that for a normally incident cone of semiangle $\chi + \Theta$.

If $\chi > \Theta$ then we have three frequencies, ν_0 corresponding to normal incidence, ν_1 to angle of incidence $\chi - \Theta$, and ν_2 to angle of incidence $\chi + \Theta$. The new filter peak can be assumed to be

$$\nu_{peak} = \frac{1}{2}(\nu_1 + \nu_2) = \frac{\chi^2 + \Theta^2}{2n^{*2}}\nu_0 \qquad (\chi \text{ and } \Theta \text{ in radians}) \tag{8.46}$$

or alternatively

$$\nu_{peak} = \frac{1.52 \times 10^{-4}(\chi^2 + \Theta^2)}{n^{*2}}\nu_0 \qquad (\chi \text{ and } \Theta \text{ in degrees}) \tag{8.47}$$

The half-width is

$$[W_0^2 + (\nu_2 - \nu_1)^2]^{1/2} \tag{8.48}$$

where

$$(\nu_2 - \nu_1) = \frac{2\chi\Theta}{n^{*2}}\nu_0 \qquad (\chi \text{ and } \Theta \text{ in radians}) \tag{8.49}$$

or

$$(\nu_2 - \nu_1) = \frac{6.09 \times 10^{-4}\chi\Theta}{n^{*2}}\nu_0 \qquad (\chi \text{ and } \Theta \text{ in degrees}) \tag{8.50}$$

The peak transmittance is

$$\frac{W_0}{(\nu_2 - \nu_1)}\arctan\left[\frac{(\nu_2 - \nu_1)}{W_0}\right] \simeq 1 - \frac{1}{3}\left[\frac{(\nu_2 - \nu_1)}{W_0}\right]^2 \tag{8.51}$$

$(\nu_2 - \nu_1)$ is proportional to $\chi\Theta$, and Hernandez [16] has found excellent agreement between measurements made on real filters and calculations from these expressions for values of $\chi\Theta$ up to $(10^\circ)^2$.

We can illustrate the use of these expressions in calculating the performance of a zinc sulfide and cryolite filter for the visible region. We assume that this is a low-index first-order filter with a bandwidth of 1%.

For this filter, we calculate that $n^* = 1.55$. We take 10% reduction in peak transmittance as the limit of what is acceptable. Then, from Equation 8.51

$$(\nu_2 - \nu_1)/W_0 = 0.55$$

and the increased half-width corresponding to this reduction in peak transmittance is

$$(1 + 0.55^2)^{1/2}W_0 = 1.14W_0$$

or an increase of 14% over the basic width.

At normal incidence, the tolerable cone semiangle is given by

$$1.5 \times 10^{-4}\left(\frac{\Theta^2}{n^{*2}}\right) = \Delta\nu = 0.55W_0 = 0.55 \times 0.01 \qquad (\Theta \text{ in degrees})$$

i.e.,

$$\Theta = \left[\frac{1.55^2 \times 0.55 \times 0.01}{1.5 \times 10^{-4}}\right]^{1/2} = 9.4°$$

Such a cone at normal incidence will cause a shift in the position of the peak toward shorter wavelengths or higher frequencies of

$$\frac{1}{2}\frac{\Delta\nu'}{\nu_0} = \frac{0.55 \times 0.01}{2} = 0.275\%$$

Used at oblique incidence in a cone of illumination, we have

$$\frac{6.09 \times 10^{-4}\chi\Theta}{n^{*2}}\nu_0 = \nu_2 - \nu_1 = 0.55 \times 0.01$$

i.e.,

$$\chi\Theta = \frac{1.55^2 \times 0.55 \times 0.01}{6.09 \times 10^{-4}} = 21.7 \text{ degree squared}$$

This implies that the filter can be used in a cone of semiangle 2° up to an angle of incidence of 21.7°/2° = 10.9° or of semiangle 3° up to an angle of incidence of 7° and so on.

One very important result is the shift in peak wavelength in a cone at normal incidence, which indicates that if a filter is to be used at maximum efficiency in such an arrangement, its peak wavelength at normal incidence in collimated light should be slightly longer to compensate for this shift.

8.2.5 Sideband Blocking

There is a disadvantage in the all-dielectric filter: the high-reflectance zone of the reflecting coating is limited in extent and hence the rejection zone of the filter is also limited. In the near ultraviolet, visible, and near infrared regions, the transmission sidebands on the shortwave side of the peak can usually be suppressed, or blocked, by an absorption filter with a longwave-pass characteristic in the same way as for metal–dielectric filters. The longwave sidebands are more of a problem. These may be outside the range of sensitivity of the detector and therefore may not require elimination, but if they are troublesome then the usual technique for removing them is the addition of a metal–dielectric first-order filter with no longwave sidebands. It is usually very much broader than the narrowband component in order

that the peak transmittance may be high. The metal–dielectric component is usually added as a separate component, but it can be deposited over the basic Fabry–Perot. Rather than a simple Fabry–Perot filter, a double cavity metal–dielectric is commonly used. Multiple cavity filters are the next topic of discussion.

8.3 Multiple Cavity Filters

The transmission curve of the basic all-dielectric single-cavity, or Fabry–Perot, filter is not of ideal shape. It can be shown that one-half of the energy transmitted in any order lies outside the half-width (assuming an even distribution of energy with frequency in the incident beam). A more nearly rectangular curve would be a great improvement. Further, the maximum rejection of the single-cavity filter is completely determined by the half-width and the order. The broader filters, therefore, tend to have poor rejection as well as a somewhat unsatisfactory shape.

When tuned electric circuits are coupled, the resultant response curve is rather more rectangular and the rejection outside the pass band rather greater than a single tuned circuit, and a similar result is found for the single-cavity filter. If two or more of these filters are placed in series, much the same sort of curve is obtained with a much more promising shape. The filters may be either metal–dielectric or all-dielectric and the basic form is

|reflector | half-wave cavity | reflector | half-wave cavity | reflector|

The outer reflectors being rather weaker than the central one. This type of structure has been known by many different names. Old terms are *double half-wave*, or DHW, filter but the more usual modern terms are either a *double cavity filter* or a *two-cavity filter*. Some typical examples of all-dielectric two-cavity filters are shown in Figure 8.15.

Such filters were certainly constructed by A. F. Turner and his co-workers at Bausch and Lomb in the early 1950s, but the results were published only as quarterly reports in the Fort Belvoir Contract Series over the period 1950–1968 [17]. The earliest filters were of the three-cavity (triple half-wave) type, known at Bausch and Lomb as WADIs (wide-band all-dielectric interference filters) [18]. Two-cavity (double half-wave) filters came later but were in routine use at Bausch and Lomb certainly by 1957. They were initially known as TADIs. The Fort Belvoir Contract Reports make fascinating reading and show just how advanced the work at Bausch and Lomb was at that time. Use was being made of the concept of equivalent admittance for the design both of WADI filters and of the edge filters for blocking the sidebands. Multilayer antireflection coatings were also well understood.

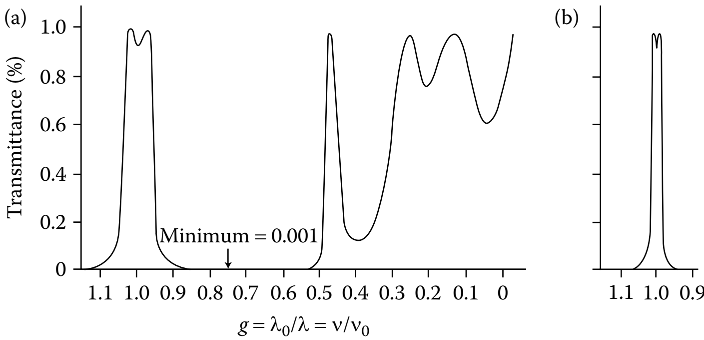

FIGURE 8.15
(a) Computed transmittance of *HLLHLHLLH*. (b) Computed transmittance of *HLHHLHLHHLH*. In both cases, $n_H = 4.0$ and $n_L = 1.35$. (After Smith, S.D., *Journal of the Optical Society of America*, 48, 43–50, 1958.)

The first complete account in the archival literature of a theory applicable to multiple half-wave filters is due to Smith [19], and it is his method that we follow first.

The reflecting stacks in the classic single-cavity or Fabry–Perot filter have more or less constant reflectance over the pass band of the filter. A dispersion of phase change on reflection does, as we have seen, help to reduce the bandwidth, but this does so without altering the basic shapes of the pass-band shape. Smith suggested the idea of using reflectors with much more rapidly varying reflectance to achieve a better shape. The essential expression for the transmittance of the complete filter has already been derived in Section 3.7 where we have assumed $\beta = 0$, that is, no absorption in the cavity layer. From Smith's formula, Equation 3.19,

$$T = \frac{|\tau_a^+|^2 |\tau_b^+|^2}{\left(1 - |\rho_a^-||\rho_b^+|\right)^2} \left[1 + \frac{4|\rho_a^-||\rho_b^+|}{\left(1 - |\rho_a^-||\rho_b^+|\right)^2} \sin^2 \frac{\varphi_a + \varphi_b - 2\delta}{2}\right]^{-1} \tag{8.52}$$

it can be seen that high transmission can be achieved at any wavelength if, and only if, the reflectances on either side of a chosen spacer layer are equal. Of course, there is a phase condition that must be met, too, but this can be arranged by choosing the correct cavity thickness to make

$$\left|\frac{\varphi_a + \varphi_b}{2} - \delta\right| = m\pi$$

In these expressions, the symbols have the same meanings as given in Figure 3.8.

Smith pointed out the advantage of having reasonably low reflectance in the region around the peak wavelength, which implies that absorption is

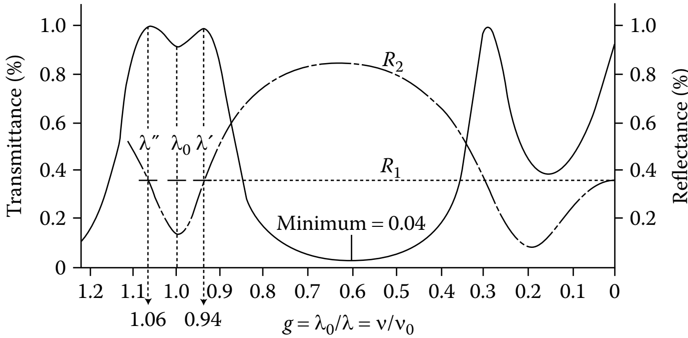

FIGURE 8.16
Computed transmittance of *HHLHH* and explanatory reflectance curves R_1 and R_2 (n_H = 4.0, n_L = 1.35). (After Smith, S.D., *Journal of the Optical Society of America*, 48, 43–50, 1958.)

less effective in limiting the peak transmittance. In the single-cavity filter, low reflectance means wide bandwidth, but Smith limited the bandwidth by arranging for the reflectances to begin to differ appreciably at wavelengths only a little removed from the peak. This is illustrated in Figure 8.16. The figure shows what is probably the simplest type of two-cavity filter with construction *HHLHH*. The *HH* layers are the two cavities and the *L* layer is a coupling layer. For simplicity, in the following discussion we shall ignore any substrate. The behavior of the filter is described in terms of the reflectances on either side of one of the two cavities. R_1 is the reflectance of the interface between the high index and the surrounding medium, which we take as air with index unity, and is a constant. R_2 is the reflectance of the assembly on the other side of the cavity and is low at the wavelength at which the cavity is a half-wave (i.e., absentee) and rises on either side. The residual reflectance is due to the quarterwave *L* layer. At wavelengths λ' and λ'', the reflectances R_1 and R_2 are equal and we would expect to see high transmission if the phase condition is met, which in fact it is. The transmittance of the assembly is also shown in the figure and the shape can be seen to consist of a steep-sided pass band with two peaks close together and only a slight dip in transmission between the peaks, much more like the ideal rectangle than the shape of a single-cavity filter.

Smith's formula for the transmittance of a filter can be written:

$$T(\lambda) = T_0(\lambda)\frac{1}{1 + F(\lambda)\sin^2[(\varphi_1 + \varphi_2)/2 - \delta]} \tag{8.53}$$

where

$$T_0(\lambda) = \frac{(1 - R_1)(1 - R_2)}{[1 - (R_1R_2)^{1/2}]^2} \tag{8.54}$$

$$F(\lambda) = \frac{4(R_1R_2)^{1/2}}{[1-(R_1R_2)^{1/2}]^2} \tag{8.55}$$

Both these quantities are now variable since they involve R_2, which varies as in Figure 8.16. The form of the functions is also shown in Figure 8.17. At wavelengths removed from the peak, $T_0(\lambda)$ is low and $F(\lambda)$ is high, the combined effect being to increase the rejection. In the region of the peak, $T_0(\lambda)$ is high, and, just as important, $F(\lambda)$ is low, producing high transmittance that is insensitive to the effects of absorption. As we have shown before, the peak transmittance is dependent on the quantity A/T, where A is the absorptance and T the transmittance of the reflecting stacks. Clearly, the greater is T, the higher A can be for the same overall filter transmittance.

The typical double-peaked shape of the two-cavity filter results from the intersection of the R_1 and R_2 curves at two separate points. Two other cases can arise. The curves can intersect at one point only, in which case the system has a single peak with transmittance theoretical unity, provided the phase condition is met, or the curves may never intersect at all, in which case the system will usually show a single peak of transmittance rather less than unity, the exact magnitude depending on the relative magnitudes of R_1 and R_2 at their closest approach. This third case is to be avoided in design. For the twin-peaked filter, a requirement is that the trough in the center between the two peaks should be shallow, which means that R_1 and R_2 should not be very different at λ_0.

Having examined the simplest type of two-cavity filter, we are in a position to study more complicated ones. What we have to look for is a system of two reflectors, where one of the reflectors remains reasonably constant over the range of interest and where the other should be equal, or nearly equal, to the first over the pass-band region, but should increase sharply outside the pass band. The straightforward single-cavity filter has effectively zero reflectance at the peak wavelength, but the reflectance rapidly rises on either side

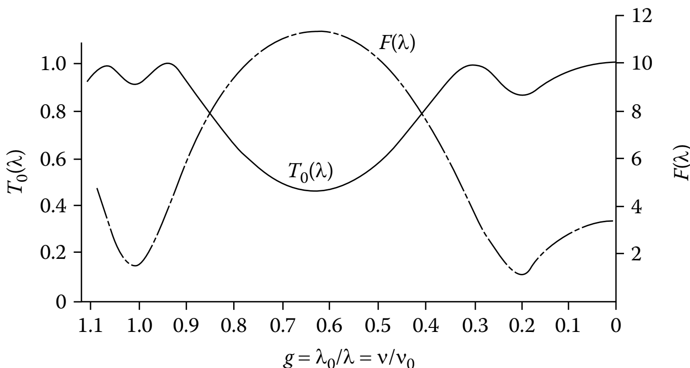

FIGURE 8.17
$T_0(\lambda)$ and $F(\lambda)$ for *HHLHH*. (After Smith, S.D., *Journal of the Optical Society of America*, 48, 43–50, 1958.)

of the peak. If, then, a simple quarter-wave stack is added to a single-cavity structure, the resultant combination should have the desired property, that is, the reflectance equal or close to that of the simple stack at the center wavelength and increasing sharply on either side. We can therefore use a simple stack as one reflector, with more or less constant reflectance, on one side of the cavity, and, on the other side, an exactly similar stack combined with the additional single-cavity filter. This will result in a single-peaked filter if the reflectances will be exactly matched at λ_0. The double-peaked transmission curve will be obtained if the reflectance of the stack plus the single-cavity filter is arranged to be just a little different from the reflectance of the stack by itself. This is the arrangement that is more often used, and it generally occurs naturally because of an extra quarter-wave layer that is inserted in between the stack and the additional single-cavity structure. This avoids the existence of a half-wave layer that would otherwise tend to perturb the form of the reflectance variation remote from the peak. This layer appears as a sort of coupling layer in the filter. Figure 8.18 should make the situation clear.

So far, we have not considered the substrate of the filter, but, of course, it is part of the structure and must be included. The substrate will be on one side of the filter and will alter the reflectance of the system on that side. This change in reflectance can easily be calculated, particularly if the substrate is considered to be on the same side of the cavity, or spacer, as the simple stack. The constant reflectance R_1 of the simple stack will generally be large, and if the substrate index is given by n_{sub}, then the transmittance of the stack on its own $(1 - R_1)$ will become either $(1 - R_1)/n_{sub}$ if the index of the layer next to the substrate is low or $n_{sub}(1 - R_1)$ if it is high.

This change in reflectance could be considerable, especially if n_{sub} is large, and so the substrate must be taken into account in the design and it is usually convenient to do this from the beginning of the design process. The substrate

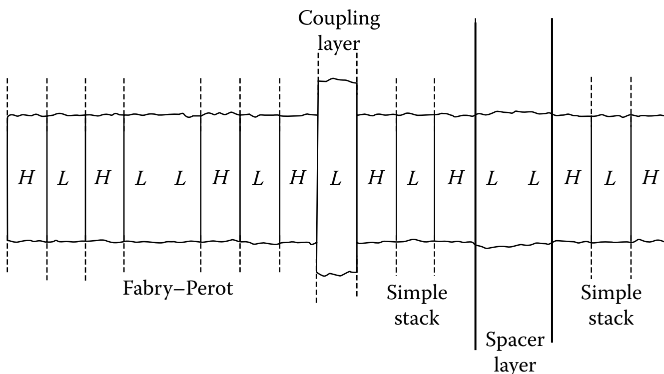

FIGURE 8.18
The construction of a two-cavity filter. The Fabry–Perot or single-cavity filter combined with the adjacent simple stack forms one reflector. The other reflector is the simple stack on the right of the cavity, or spacer, layer.

can be considered part of the simple stack and R_1 can be adjusted to include it. Provided the reflectances of the two assemblies on either side of the spacer layer are arranged always to be equal at the appropriate wavelengths, the transmittance of the complete filter will be unity.

As an example, let us consider the case of a filter deposited on a germanium substrate using zinc sulfide for the low-index layers and germanium for the high ones. Let the cavity be of low index and let the reflecting stack on the germanium substrate be represented by Ge|*LHLL*, where the *LL* layer is the cavity. The transmittance of the stack into the cavity layer will be approximately $T_1 = 4n_L^3/n_H^2 n_{Ge}$, which, since the substrate is the same material as the high-index layer, becomes $4n_L^3/n_H^3$. On the other side of the cavity layer, we make a start with the combination *LLHLH*|Air, representing the basic reflecting stack, where *LL* once again is the cavity layer. This has transmission $T_2 = 4n_L^3/n_H^4$, which is $1/n_H$ times T_1. Clearly, this is too unbalanced and an adjustment to this second stack must be made. If a low-index layer is added next to the air, then the transmittance becomes $T_2 = 4n_L^5/n_H^4$. Since n_L^2 is approximately equal to the index of germanium, the transmittances T_1 and T_2 are now equal and the single-cavity filter can now be added to the second stack to give the desired shape to the reflectance curve. This additional single-cavity filter can take any form, but it is convenient here to use a combination almost exactly the same as the already existing arrangement. The complete design of the filter is then

$$\text{Ge}|LH\ LL\ HLH\ L\ HLH\ LL\ HLH|\text{Air}$$

and the performance of the filter is shown in Figure 8.19.

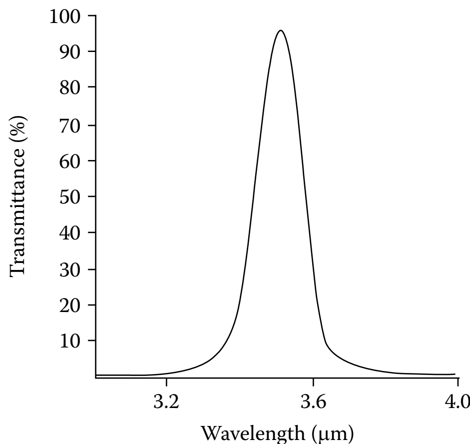

FIGURE 8.19
Computed transmittance of the two-cavity filter. Design: Air|*LHLLHLHLHLHLLHLH*|Ge. The substrate is germanium (n = 4.0); H = germanium (n = 4.0) and L = zinc sulfide (n = 2.35); and the incident medium is air (n = 1.0).

An alternative way of checking whether the filter is going to have high transmittance uses the concept of absentee half-wave layers. The layers in two-cavity filters are usually either of quarter- or half-wave thickness at the center of the pass band, as in the above filter, and we can take it as an example to illustrate the method. First we note that the two cavities are both half-wave layers and that they can be eliminated without affecting the transmission. The filter, at the center wavelength, will have the same transmittance as

$$\text{Ge}|LH\ HLH\ L\ HLH\ HLH|\text{Air}$$

In this, there are two sets of *HH* layers that can be eliminated in the same way, leaving two sets of *LL* layers that can be removed in their turn. Almost all the layers in the filter can be eliminated in this way leaving ultimately

$$\text{Ge}|L|\text{Air}.$$

As we already know, a single quarter-wave of zinc sulfide is a good antireflection coating for germanium, and so the transmittance of the filter will be high in the center of the pass band.

Knittl [20,21] has used an alternative multiple-beam approach to study the design of two-cavity filters. Essentially, he has applied a multiple beam summation to the first cavity, the results of which are then used in a multiple beam summation for the second cavity. This yields an expression not unlike Smith's, although slightly more complicated, but with the advantage that it is only the phase that varies across the pass band. The magnitude of the reflection and transmission coefficients can be safely assumed constant and this means that the parameters involving these quantities are also constant. The form of the expression for overall transmittance is then very much easier to manipulate so that the positions and values of maxima and minima in the pass band can be readily determined. We shall not deal further with the method here, because it is already well covered by Knittl [21].

Of course, the possible range of designs does not end with the two-cavity, or DHW, filter. Other types of filter exist, involving even more half-wave cavities. An early type of filter, already mentioned, was the WADI devised by Turner, which consisted of a straightforward single-cavity filter, to either side of which was added a half-wave layer together with several quarter-wave layers. The function of these extra layers was to alter the phase characteristics of the reflectors on either side of the primary cavity layer, so that the pass band was broadened and at the same time, the sides became steeper. Similarly, it is possible to repeat the basic single-cavity element used in the two-cavity filter once more to give a three-cavity filter also known as a triple half-wave or THW filter, which has a similar bandwidth but steeper sides. WADI and three-cavity, or THW, filters are much the same thing, although the original design philosophy was a little different, and nowadays, the term *three-cavity filter* is more usual. Even more cavity layers may be used yielding

multiple-cavity filters. The method we have been using for the analysis of the filters becomes rather cumbersome when many cavities are involved—even the simple method for checking that the transmittance is high in the pass band breaks down, for reasons that will be made clear in the next section, where we shall consider a very powerful design method that has been devised by Thelen.

8.3.1 Thelen's Method of Analysis

We have not yet arrived at any ready way of calculating the bandwidth of two- and three-cavity filters. The design method has merely ensured that the transmittance of the filter is high in the pass band and that the shape of the transmission curve is steep-sided. The bandwidth can be calculated, but trial and error is necessary to arrive at a prescribed bandwidth in the design. It can indeed be calculated using the formula for transmittance

$$T = T_0 \frac{1}{1 + F_0 \sin^2 \delta}$$

but this can be very laborious as the phases of the reflectances have to be included in δ. This expression has been very useful in achieving an insight into the basic properties of the multiple-cavity filter, but, for systematic design, a method based on the concept of equivalent admittance will be found much more useful.

As was shown in Chapter 7, any symmetrical assembly of thin films can be replaced by a single layer of equivalent admittance and optical thickness, both of which vary with wavelength but can be calculated. This concept has been used by Thelen [22] in the development of a very powerful systematic design method that predicts all the performance features of the filters including the bandwidth. The basis of the method is the splitting of the multiple cavity filter into a series of symmetrical periods, the properties of which can be predicted by finding their equivalent admittances. Take, for example, the design we have already examined.

$$\text{Ge}|LHLLHLHLHLHLLHLH|\text{Air}$$

This can be split up into the arrangement

$$\text{Ge}|LHL\ LHLHLHLHL\ LHLH|\text{Air}$$

The part that determines the properties of the filter is the central section, *LHLHLHLHL*, which is a symmetrical assembly. It can therefore be replaced by a single layer having the usual series of high-reflectance zones, where the admittance is imaginary, and pass zones, where the admittance is real.

We are interested in the latter because they represent the pass bands of the final filter. The symmetrical section must then be matched to the substrate and the surrounding air, and matching layers are added for that purpose on either side. This is the function of the remaining layers of the filter. The condition for perfect matching is easily established because the layers are all of quarter-wave optical thicknesses.

A most useful feature of this design approach is that the central section of the filter can be repeated many times, steepening the edges of the pass band and improving the rejection without affecting the bandwidth to any great extent.

To make predictions of performance straightforward, Thelen has computed formulae for the bandwidth of the basic sections. We use Thelen's technique here, with some slight modifications, to fit in with the pattern of analysis already carried out for the single-cavity filter. To include filters of order higher than the first, we write the basic period as

$$H^mLHLHLH\ldots LH^m \text{ or } L^mHLHLHL\ldots HL^m$$

where there are $2x+1$ layers, $x+1$ of the outermost index and x of the other, and m is the order number. We have already mentioned how Seeley [4], in the course of developing expressions for the single-cavity filter, arrived at an approximate formula for the product of the characteristic matrices of quarter-wave layers of alternating high and low indices. Using an approach similar to Seeley's, we can put the characteristic matrix of a quarter-wave layer in the form

$$\begin{bmatrix} -\varepsilon & i/n \\ in & -\varepsilon \end{bmatrix} \tag{8.56}$$

where $\varepsilon = (\pi/2)(g-1)$, $g = \lambda_0/\lambda$, and we are using n to indicate both refractive index and characteristic admittance. This expression is valid for wavelengths close to that for which the layer is a quarter-wave. First let us consider m odd, and write m as $2q+1$. Then, to the same degree of approximation, the matrix for H^m or L^m is

$$(-1)^q\begin{bmatrix} -m\varepsilon & i/n \\ in & -m\varepsilon \end{bmatrix}$$

Neglecting terms of second and higher order in ε, then the product of the $2x-1$ layers making up the symmetrical period is

$$\begin{bmatrix} M_{11} & iM_{12} \\ iM_{21} & M_{22} \end{bmatrix} \tag{8.57}$$

where

$$M_{11} = M_{22} = (-1)^{x+2q}(-\varepsilon)\left[m\left(\frac{n_1}{n_2}\right)^{x} + \left(\frac{n_1}{n_2}\right)^{x-1} + \left(\frac{n_1}{n_2}\right)^{x-2} + \cdots + \left(\frac{n_2}{n_1}\right)^{x-1} + m\left(\frac{n_2}{n_1}\right)^{x}\right]$$

$$iM_{12} = i(-1)^{x}/[(n_1/n_2)^{x} n_1]$$

and

$$iM_{12} = i(-1)^{x}[(n_1/n_2)^{x} n_1]$$

Now it is not easy from this expression to derive the half-width of the final filter analytically. Instead of deriving the half-width, therefore, Thelen chose to define the edges of the pass band as those wavelengths for which

$$\frac{1}{2}\left|M_{11} + M_{22}\right| = 1$$

or, since $M_{11} = M_{22}$

$$\left|M_{11}\right| = 1$$

These points will not be too far removed from the half peak transmission points, especially if the sides of the pass band are steep. Applying this to Expression 8.57, we obtain

$$\left|M_{11}\right| = \varepsilon\left[m\left(\frac{n_1}{n_2}\right)^{x} + \left(\frac{n_1}{n_2}\right)^{x-1} + \left(\frac{n_1}{n_2}\right)^{x-2} + \cdots + \left(\frac{n_2}{n_1}\right)^{x-1} + m\left(\frac{n_2}{n_1}\right)^{x}\right] = 1 \quad (8.58)$$

This expression is quite symmetrical in terms of n_1 and n_2. Then if we replace n_1 and n_2 by n_H and n_L, regardless of which is which, we will obtain the same expression

$$\varepsilon\left[m\left(\frac{n_H}{n_L}\right)^{x} + \left(\frac{n_H}{n_L}\right)^{x-1} + \left(\frac{n_H}{n_L}\right)^{x-2} + \cdots + \left(\frac{n_L}{n_H}\right)^{x-1} + m\left(\frac{n_L}{n_H}\right)^{x}\right] = 1$$

i.e.,

$$\varepsilon\left[(m-1)\left(\frac{n_H}{n_L}\right)^x+(m-1)\left(\frac{n_L}{n_H}\right)^x+\left(\frac{n_H}{n_L}\right)^x\left(\frac{1-(n_L/n_H)^{x+1}}{1-(n_L/n_H)}\right)\right]=1$$

where we have used the formula for the sum of a geometric series just as in the case of the single-cavity filter. We now neglect terms of power x or higher in (n_L/n_H) to give

$$\varepsilon\left(\frac{n_H}{n_L}\right)^x\left\{(m-1)+\frac{1}{1-(n_L/n_H)}\right\}=1$$

i.e.,

$$\varepsilon=\left(\frac{n_L}{n_H}\right)^x\frac{[1-(n_L/n_H)]}{[m-(m-1)(n_L/n_H)]} \tag{8.59}$$

The bandwidth will be given by

$$\left|\frac{\Delta\lambda_B}{\lambda_0}\right|=\left|\frac{\Delta\nu_B}{\nu_0}\right|=2(g-1)=\frac{4\varepsilon}{\pi}$$

so that, manipulating Equation 8.59 slightly

$$\left|\frac{\Delta\lambda_B}{\lambda_0}\right|=\frac{4}{m\pi}\left(\frac{n_L}{n_H}\right)^x\frac{(n_H-n_L)}{(n_H-n_L+n_L/m)} \tag{8.60}$$

The equivalent admittance is given by

$$E=\left(\frac{M_{21}}{M_{12}}\right)^{1/2}=\left(\frac{n_1}{n_2}\right)^x n_1 \tag{8.61}$$

The case of m even, i.e., $m = 2q$, is arrived at similarly. Here, the matrix of H^m or L^m is

$$(-1)^q\begin{bmatrix}1 & im\varepsilon/n\\ im\varepsilon n & 1\end{bmatrix}$$

and a similar multiplication, neglecting terms higher than first in ε gives

$$\left|\frac{\Delta\lambda_B}{\lambda_0}\right| = \frac{4}{m\pi}\left(\frac{n_L}{n_H}\right)^x \frac{(n_H - n_L)}{(n_H - n_L + n_L/m)}$$

that is, exactly as Equation 8.60, but

$$E = \left(\frac{M_{21}}{M_{12}}\right)^{1/2} = \left(\frac{n_2}{n_1}\right)^{x-1} n_2$$

for equivalent admittance. This is to be expected since the layers L^m or H^m act as absentees because of the even value of m.

Expression 8.60 should be compared with the single-cavity Expressions 8.23 and 8.24. If we split the multiple cavity filter into a series of single cavities, then the number of layers in each reflector is half that in the basic symmetrical period. Equations 8.23, 8.24, and 8.60 are, therefore, consistent.

To complete the design, we need to match the basic period to the substrate and the surrounding medium. We first consider the case of first-order filters, and the modifications that have to be made in the case of higher order will become obvious. For a first-order filter, then, matching will best be achieved by adding a number of quarter-wave layers to the period. The first layer should have index n_1, the next, n_2, and so on, alternating the indices in the usual manner. The equivalent admittance of the combination of symmetrical period and matching layers will then be

$$\frac{n_1^{2y}}{n_2^{2(y-1)}}\left(\frac{n_2}{n_1}\right)^x \frac{1}{n_2} \quad \text{or} \quad \left(\frac{n_2}{n_1}\right)^{2y} n_2 \left(\frac{n_1}{n_2}\right)^x$$

where there are y layers of index n_1 and either $(y - 1)$ or y layers of index n_2, respectively. We have also used the fact that the addition of a quarter-wave of index n to an assembly of equivalent admittance E alters the admittance presented by the structure to n^2/E, the quarter-wave rule.

This equivalent admittance should be made equal to that of the substrate on the appropriate side, and of the surrounding medium on the other. The following discussion should make the method clear.

When we try to apply this formula to the design of multiple half-wave filters, we find to our surprise that quite a number of designs we have looked at previously, and which seemed satisfactory, do not satisfy the conditions. For example, let us consider the design arrived at in the earlier part of this section:

Ge | *LH LL HLH L HLH LL HLH* | Air

where L indicates zinc sulfide of index 2.35 and H germanium of index 4.0. The central period is *LHLHLHLHL*, which has equivalent admittance n_L^5/n_H^4. The *LHL* combination alters this equivalent admittance to

$$\frac{n_L^4}{n_H^2}\frac{n_H^4}{n_L^5} = \frac{n_H^2}{n_L}$$

which is a gross mismatch to the germanium substrate. The *LHLH* combination on the other side alters the admittance to

$$\frac{n_H^4}{n_L^4}\frac{n_L^5}{n_H^4} = n_L$$

which in turn is not a particularly good match to air.

The explanation of this apparent paradox is that in this particular case the total filter, taking the phase thickness of the central symmetrical period into account, has unity transmittance because it satisfies Smith's conditions given in the previous section but, over a wide range of wavelengths, pronounced transmission fringes would be seen if the bandwidth of the filter were not much narrower than a single fringe. Adding extra periods to the central symmetrical one has the effect of decreasing this fringe width, bringing them closer together. Eventually, given enough symmetrical periods, the width of the fringes becomes less than the filter bandwidth and they appear as a pronounced ripple superimposed on the pass band. This is illustrated clearly in Figure 8.20.

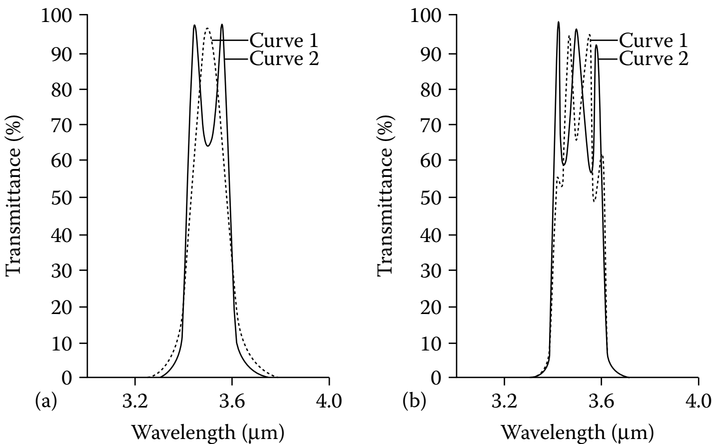

FIGURE 8.20
(a) Curve 1: Computed transmittance of the three-cavity filter: Air|*LHLHL*(*LHLHLHLHL*)^2 *LHL*|Ge. Curve 2: shows the effect of omitting the L layer next to the air in the design of curve 1: Air|*HLHL*(*LHLHLHLHL*)^2 *LHL*|Ge. (b) Computed transmittance of five-cavity filters. Curve 3: Air|*HLHL*(*LHLHLHLHL*)^4 *LHL*|Ge. Curve 4: As curve 3 but with an extra L layer: Air|*LHLHL*(*LHLHLHLHL*)^4 *LHL*|Ge. The presence or absence of the L layer has little effect on the ripple in the pass band. For all curves, H = germanium (n_H = 4.0) and L = zinc sulfide (n_L = 2.35).

The three-cavity version is still acceptable when an extra *L* layer is added, but the five-cavity version is quite unusable. The presence or absence of an outermost *L* layer has no effect on the performance, other than inverting the fringes. The simple method of cancelling out half-waves for predicting the pass-band transmission therefore breaks down, because it merely ensures that λ_0 will coincide with a fringe peak.

It is profitable to look at the possible combinations of the two materials that can be made into a filter on germanium and where the center section can be repeated as many times as required. The combinations for up to 11 layers in the center section are given in Table 8.3.

The validity of any of these combinations can easily be tested. Take, for example, the fourth one, with the nine-layer period in the center. Here the equivalent admittance of the symmetrical period is $E = n_H^5/n_L^4$. The *LHLH* section between the germanium substrate and the center section transforms the admittance into

$$\frac{n_L^4}{n_H^4}\frac{n_H^5}{n_L^4} = n_H$$

which is a perfect match for germanium. The matching section at the other end is *HLH* and this transforms the admittance into

$$\frac{n_H^4}{n_L^2}\frac{n_L^4}{n_H^5} = \frac{n_L^2}{n_H}$$

which, because zinc sulfide is a good antireflection material for germanium, gives a good match for air.

For higher-order filters, the method of designing the matching layers is similar. However, we can choose, if we wish, to add half-wave layers to that part of the matching assembly next to the symmetrical period in order to make the resulting cavity of the same order as the others. For example, the period *HHHLHLHLHLHHH*, based on the fourth example of Table 8.3, can be

TABLE 8.3

Suitable Components for Multiple Cavity Filters

Matching Combination for Germanium	Symmetrical Period	Matching Combination for Air
Ge | *L*	*LHL*	| Air (already matched)
Ge | *LH*	*HLHLH*	*H* | Air
Ge | LHL	*LHLHLHL*	*LH* | Air
Ge | *LHLH*	*HLHLHLHLH*	*HLH* | Air
Ge | *LHLHL*	*LHLHLHLHLHL*	*LHLH* | Air

L: ZnS, $n_L = 2.35$ *H*: Ge, $n_H = 4.0$.

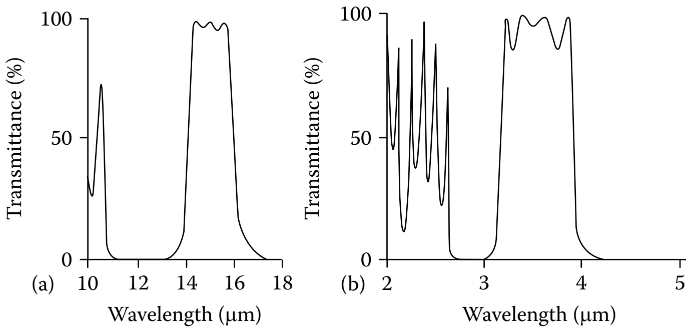

FIGURE 8.21
(a) Transmittance of a multiple half-wave filter. Design: Air|*HHL H LHHL LHHLH*|Ge with H = PbTe (n = 5.0); L = ZnS (n = 2.35), λ_0 = 15 μm. (b) Transmittance of a multiple half-wave filter. Design: Air|*HHLH LHHLH LHHL H LHHLH LHH*|silica H = Ge (n = 4.0); L = ZnS (n = 2.35); silica substrate (n = 1.45) λ_0 = 3.5 μm. (Courtesy of Sir Howard Grubb, Parsons & Co. Ltd.)

matched either by Ge|*LHLH* and *HLH*|Air, as shown, or by Ge|*LHLHHH* and *HHHLH*|Air, making all cavities of identical order regardless of the number of periods.

This method, then, gives the information necessary for the design of multiple half-wave filters. The edge steepness and rejection in the stop bands will determine the number of basic symmetrical periods in any particular case. Usually, because of the approximations in the various formulae, and because the definition used for bandwidth is not necessarily the half-width, although not far removed from it, it is advisable to check the design by accurate computation before actually manufacturing the filter. It may also be advisable to make an estimate of the permissible errors that can be tolerated in the manufacture because it is pointless attempting to achieve a performance beyond the capabilities of the process. The result will just be worse than if a less-demanding specification had been attempted. The estimation of manufacturing errors is discussed in Chapter 13. Typical multiple-cavity filters are shown in Figure 8.21.

8.4 Higher Performance in Multiple-Cavity Filters

The curve of Figure 8.21b shows the square shape of the pass band of a multiple cavity filter but also illustrates one of the problems inherent in this type of design, the "rabbit's ears," or the rather prominent peaks at either side of the pass band. This can become even worse with increasing numbers of periods. Figure 8.22 shows this clearly.

The reason for this problem feature is the dispersion of the equivalent admittance of the symmetrical period. In the design approach, this is assumed constant across the pass band but in reality, it varies considerably, tending to

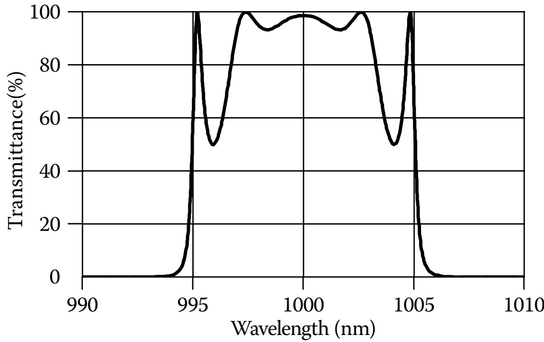

FIGURE 8.22
A multiple cavity filter with a central core of five symmetrical periods. Design: Glass|*HLHLHLH* (*HLHLHLHLHLHLHLH*)^5 *HLHLHLH*|Glass, with $n_H = 2.35$, $n_L = 1.35$, $n_{\text{glass}} = 1.52$, $\lambda_0 = 1000$ nm. Note the very prominent peaks at the edges of the pass band sometimes called "rabbit's ears."

either zero or infinity at the pass-band edges (see Figure 8.23). It is, in fact, exactly the same problem as in edge filters where better ripple suppression near the edge demands a matching system that exhibits similar dispersion. Shifted periods are, however, difficult to arrange in the case of band-pass filters because of the need for ripple suppression at both edges of the pass band. However, inspired by the shifted periods technique, we seek a solution, where part of the matching is due to a symmetrical system that has a dispersion of the appropriate form so that its matching remains reasonably good even when the equivalent admittance to be matched to the surrounding media varies. Any of the symmetrical periods we are dealing with will have an odd number of quarter-waves so that the equivalent phase thickness at $g = 1$ will be an odd number of $\pi/2$. This implies that the period could, itself,

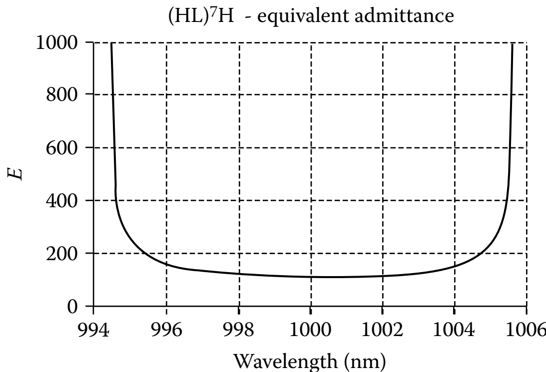

FIGURE 8.23
The equivalent admittance of $(HL)^7H$ over the potential pass band. Note the rapid change near the edges of the pass band. This dispersion of equivalent admittance is very difficult to match to an essentially dispersionless medium.

be used as a simple matching assembly. Since the pass band in this type of filter is usually narrow, the matching condition will not vary too much over the pass-band width. To make use of this possibility, we have to find at least pairs of symmetrical periods that will permit one to be used as a matching assembly for the other. Attempting to find two, or more, periods that have the correct relationship at $g = 1$ for one to match the other to the substrate or incident medium is difficult. If, however, we could find two periods of different width but with the same central admittance, then we could continue to use the straightforward matching illustrated in Table 8.3, which uses a series of quarter-wave layers and is perfectly satisfactory at the center of the pass band. A solution lies with higher-order periods.

The addition of further half-wave layers to the outside of a symmetrical period does not change its equivalent admittance at the pass-band center, nor does it change the sense of curvature of the variation of equivalent admittance. Figure 8.24 shows the admittances of *HLHLHLHLHLH*, *HHHLHLHLHLHLHHH*, *HLLLHLHLHLHLLLH*, and *HHHLLLHLHLHLHLLLHHH*. All have the value n_H^6/n_L^5 at $g = 1$, and all exhibit a gradually increasing admittance as the value of g moves away from unity. The wider curves have values of admittance intermediate between the narrower curves and the value that all possess at $g = 1$. All represent an odd number of quarter-waves at $g = 1$, but the broader curves remain closer to an odd number of quarter-waves than the narrower curves as g varies. These broader curves could therefore be used to match the narrower ones to a notional medium of constant admittance, n_H^6/n_L^5. The best one, that is, the period closest to the ideal values of the required admittance, is chosen. The use of more than one of the wider matching systems does not usually give very good results because of their differing dispersion curves. Matching of the dispersionless notional medium to the incident and emergent media is then a straightforward matter of a series of quarter-waves, as before.

A simple example uses two of the periods from Figure 8.24, *HLHLHLHLHLH* and *HHHLHLHLHLHLHHH*

Glass|*HLHLH HLHLHLHLHLH* (*HHHLHLHLHLHLHHH*)^q *HLHLHLHLHLH HLHLH*|Glass

The characteristic curves of two such filters are shown in Figure 8.25 and Figure 8.26.

We need an expression for the width of such filters. This is determined principally by the highest-order periods. If we write the expression for the highest order period as:

$$mABABA\ldots BmA$$

where there are $2x + 1$ layers including the layers mA, then we can show that the bandwidth, defined in the same way as before, is given by

$$\frac{\Delta\lambda}{\lambda_0} = \frac{4}{m\pi}\left(\frac{n_L}{n_H}\right)^x \frac{(n_H - n_L)}{(n_H - n_L + n_L/m)} \tag{8.62}$$

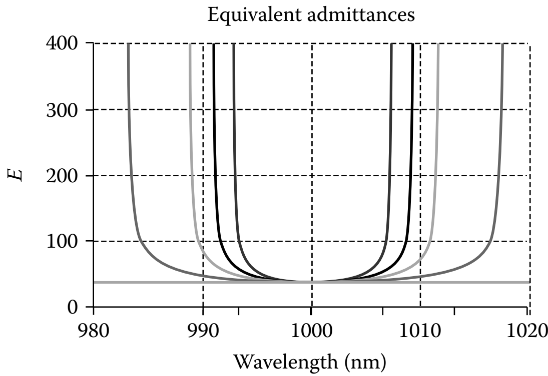

FIGURE 8.24
The equivalent admittances of symmetrical periods from narrower to broader in order *HHHLLLHLHLHLHLLLHHH*, *HHHLHLHLHLHLHHH*, *HLLLHLHLHLHLLLH*, and *HLHLH-LHLHLH* with *H* representing characteristic admittance 2.35 and *L* 1.35. The straight line represents the admittance that all have at $g = 1$.

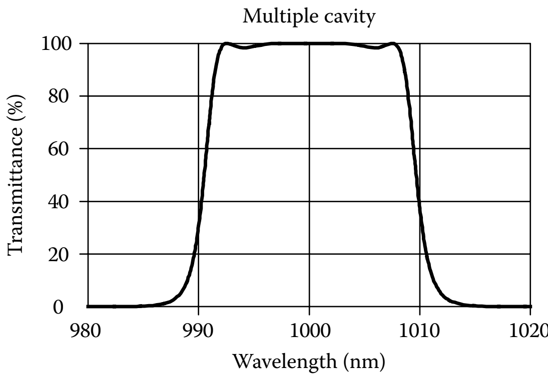

FIGURE 8.25
A multiple cavity filter similar to that of Figure 8.22 but using periods of increasing order to improve the pass-band ripple. Design: Glass|*HLHLH HLHLHLHLHLH*(*HHHLHLHLHLH LHHH*)^2 *HLHLHL HLHLH HLHLH*|Glass with $n_H = 2.35$, $n_L = 1.35$, $n_{glass} = 1.52$, $\lambda_0 = 1000$ nm. Note the much flatter pass-band top compared with Figure 8.22.

This expression reduces to that already derived if $m = 1$. Using the expression to calculate the bandwidth of the filters of Figure 8.25 and Figure 8.26, we find 0.018, implying pass-band edges at 991.1 nm and 1009.1 nm.

Of course, it will be clear that Figure 8.24 shows a special case where all the symmetrical periods have identical equivalent admittance at the reference wavelength. This feature is not absolutely necessary. It is possible to have matching systems with differing central equivalent admittances as long as the final combination matches the surrounding media and the dispersion of the admittances gives good ripple performance. Thus, for any given bandwidth, there is usually a very large number of possible alternative designs.

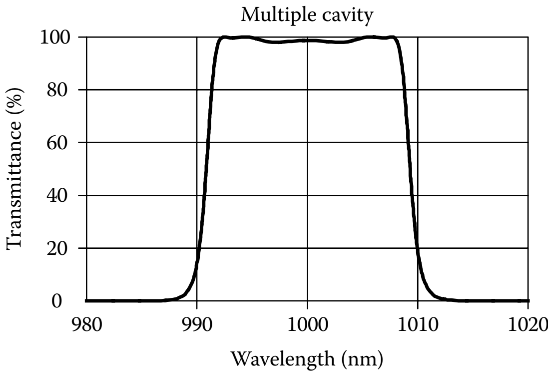

FIGURE 8.26
A multiple cavity filter similar to that of Figure 8.25 but with three central high-order periods rather than two. Design: Glass|*HLHLH HLHLHLHLHLH* (*HHHLHLHLHLHLHHH*)^3 *HLHLHLHLHLH HLHLH*|Glass with $n_H = 2.35$, $n_L = 1.35$, $n_{glass} = 1.52$, $\lambda_0 = 1000$ nm.

The search for the best performance is generally a computer operation where the definition of best involves a function of merit that includes ripple, bandwidth, edge steepness, and so on, appropriately weighted.

The design procedures so far have all made use of quarter-wave layers. We shall see later that this is necessary for their manufacture. Powerful natural deposition error compensation processes exist in systems of quarter-waves but are largely absent for non–quarter-wave designs.

The designs of Figure 8.25 and Figure 8.26 assume that the incident and emergent media are virtually identical. This would fit the case where the filter is embedded in a system or, perhaps, a cemented cover is attached to its outer surface. Because of the symmetry of their structure, the admittance presented at the reference wavelength to the exterior media is the characteristic admittance of the coupling layers. In the designs just considered, these are of low index, quite close to the index of glass. Thus, the match with the surrounding media at the reference wavelength is necessarily good. There are instances, however, where the incident and emergent media are quite different or when the index of the coupling layers does not match that of the media quite so well. Recently, driven by telecommunication applications in the main, there has been a shift to very stable materials like silica and tantala and processes like ion-assisted deposition or ion-beam sputtering that yield very stable and tough layers. These permit use of the filter without any protection over the front surface. This can be a great advantage in well-corrected systems. However, it brings the complication of the lack of symmetry. Of course, the earlier, infrared, narrow-band filters that we considered were not symmetrical, but there, the requirements for peak transmittance and lack of ripple were much less demanding.

In such cases it is often sufficient to construct a two-layer antireflection coating of the V-coat type to match the otherwise unmatched medium, normally

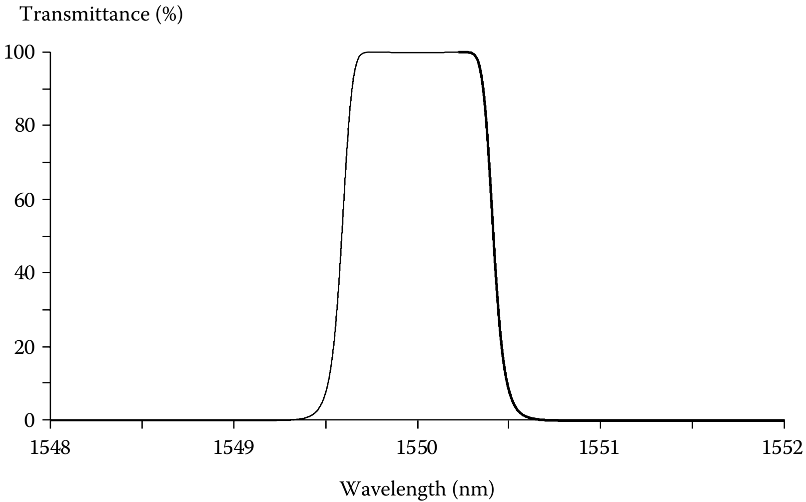

FIGURE 8.27
Performance of a filter of design: Air|[1.2462 L 0.3458H] $(HL)^7$ H $(HL)^{15}$ H $(HHHH$ $(HL)^{15}$ H $HHHH)^2$ $(HL)^{15}$ H $(HL)^7$ H|Glass with $\lambda_0 = 1550$ nm, $n_H = 2.15$, $n_L = 1.45$ (corresponding roughly to Ta_2O_5 and SiO_2 respectively) $n_{glass} = 1.52$ and $n_{air} = 1.00$. The structure within the square brackets is the antireflection coating of the V-coat type.

the air on the side of incidence. This matching coating does not suffer from the same sensitivity to errors of the remainder of the structure and the normal tolerances for such an antireflection coating apply. An example of such a filter is shown in Figure 8.27. Note, however, that there is an enhanced sensitivity of the shape of this filter to changes in angle of incidence. We deal with this in the next section.

Usually the V-coat approach will be sufficient but if still greater levels of performance are required, then three-, four-, and even five-layer antireflection coatings can be used, between either the filter and incident medium or substrate, or even both. The antireflection coatings are seldom subject to the same tight tolerances as the remainder of the filter.

The design of very high-performance narrowband filters is considerably constrained by the need for structures that can be successfully produced. This has meant adherence to quarter-waves and exact multiples of quarter-waves of a limited range of materials. These limitations may be ultimately relaxed as manufacturing techniques advance. Techniques borrowed from the microwave region that ignore such constraints can be harnessed in the optical region to produce outstanding theoretical designs that assume the availability of a continuous range of refractive indices and/or completely unconstrained thicknesses. Baumeister [23–25] explains the technique.

Baumeister's design technique is based on the parameter standing wave ratio. In an incident medium, the net electric field amplitude varies with

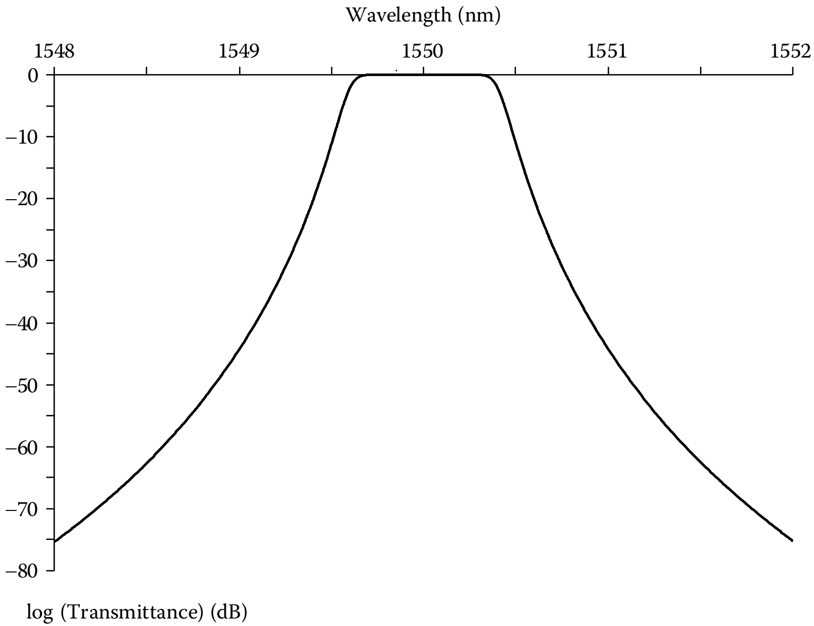

FIGURE 8.28
The performance of the filter of Figure 8.27 plotted on a logarithmic scale. This filter has performance typical of a DWDM beam splitter intended for 200 GHz channel spacing.

position, varying from $\mathcal{E}_1 + \mathcal{E}_2$ to $\mathcal{E}_1 - \mathcal{E}_2$, where $\mathcal{E}_1$ and $\mathcal{E}_2$ are the amplitudes of the two beams. The standing wave ratio is defined as

$$V = \frac{\mathcal{E}_1 + \mathcal{E}_2}{\mathcal{E}_1 - \mathcal{E}_2} = \frac{1 + \sqrt{R}}{1 - \sqrt{R}} \tag{8.63}$$

where R is the reflectance. An advantage of the standing wave ratio parameter is that it takes a very simple form when the admittance of the system concerned is real. Let the admittance of the surface be Y and the characteristic admittance of the incident medium be y_0, both real, then the standing wave ratio is given by

$$V = \frac{y_0}{Y} \quad \text{or} \quad V = \frac{Y}{y_0} \tag{8.64}$$

whichever is greater than unity.

The design of the microwave structure that is the starting design for the operation is based on a series of iris diaphragm reflectors in a waveguide, each of which is adjusted to a given standing wave ratio, assuming that the particular reflector is isolated from the others, and which are spaced apart by

what are equivalent to cavity layers. In Baumeister's method, these reflectors are replaced by thin-film structures that are bounded by the materials of the successive cavities. For example, if the indices of two successive cavities are n_L and the cavities are separated by five alternate quarter-waves of n_H and n_L, then standing wave ratio will be n_H^6/n_L^6. To achieve the exact standing wave ratios that are required, the method necessarily makes use of fractional thicknesses or special characteristic admittances. These characteristic admittances can be achieved by introducing symmetrical periods, although these will contain fractional thicknesses. Once the correct standing wave ratios are achieved, dispersion of the properties of the structures must be taken into account and a certain amount of manual adjustment, involving such operations as replacing single quarter-waves by three quarter-waves, and altering the order of the cavity layers, is normal.

An example of a two-material 13-cavity design arrived at by this technique is shown in Figure 8.29. This design uses quarter-wave structures for each reflector, but the final layer in each structure is a quarter-wave of admittance adjusted to yield the exact required standing wave ratio. The adjusted admittance is then achieved through the use of a three-layer symmetrical period. The final design that uses 346 layers is

$$\text{Air} \mid 0.241L\ 2.499H\ 1.241L\ H\ (L\ H)^3\ 2L\ (H\ L)^5\ 1.3257H\ 0.3329L\ 1.3257H\ (LH)^5$$
$$2L\ (H\ L)^5\ \mathrm{H}\ 1.2077L\ 0.5671H\ 1.2077L\ H\ (L\ H)^5\ 2L\ (H\ L)^6\ 1.4654H\ 0.0654L$$
$$1.4654H\ (L\ H)^6\ 2L\ (H\ L)^6\ 1.4251H\ 0.1419L\ 1.4251H\ (L\ H)^6\ 2L\ (H\ L)^6\ 1.4072H$$
$$0.1759L\ 1.4072H\ (L\ H)^6\ 2L\ (H\ L)^6\ 1.4001H\ 0.1894L\ 1.4001H\ (\mathrm{L\ H})^6\ 2L\ (H\ L)^6$$

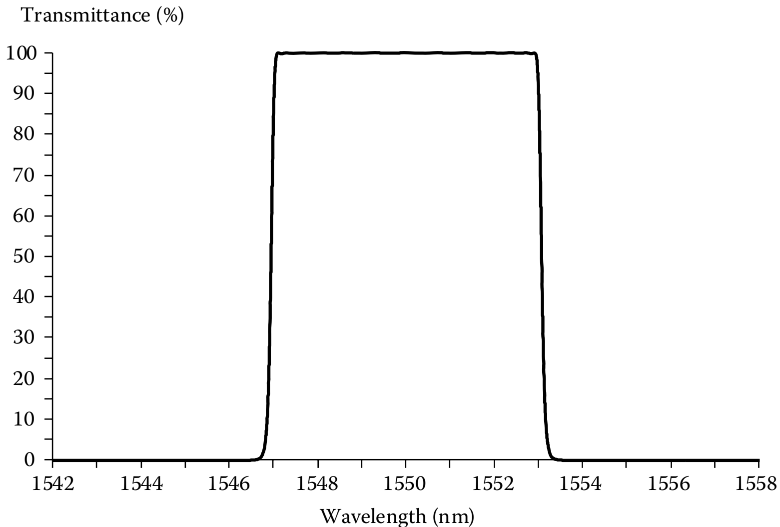

FIGURE 8.29
The performance of the 346-layer filter designed by Baumeister with design as in the text. (After Baumeister, P., *Applied Optics*, 42, 2407–2414, 2003.)

$$1.4001H\ 0.1894L\ 1.4001H\ (L\ H)^6\ 2L\ (H\ L)^6\ 1.4072H\ 0.1759L\ 1.4072H\ (L\ H)^6$$
$$2L\ (H\ L)^6\ 1.4251H\ 0.1419L\ 1.4251H\ (L\ H)^6\ 2L\ (H\ L)^6\ 1.4654H\ 0.0654L\ 1.4654H$$
$$(L\ H)^6\ 2L\ (H\ L)^5\ H\ 1.2077L\ 0.5671H\ 1.2077L\ H\ (L\ H)^5\ 2L\ (H\ L)^5\ 1.3257H\ 0.3329L$$
$$1.3257H\ (L\ H)^5\ 2L\ (H\ L)^4\ H\ 2.628L\ 1.818H|\text{Glass}$$

where $n_{air} = 1.00$, $n_H = 2.065$, $n_L = 1.47$, and $n_{glass} = 1.50$.

If the designs are constrained to use only quarter-waves, or multiple quarter-waves, of only two materials, then it is generally no longer possible to match the required standing wave ratios exactly, and so the design operation simply attempts as close a match as possible with the inevitable increase in pass-band ripple.

8.4.1 Effect of Tilting

A feature of the multiple-cavity designs not mentioned so far is the sensitivity to changes in angle of incidence. Thelen [22] has examined this aspect and for those types that involve symmetrical periods consisting of quarter-waves of alternating high and low index and where the spacers are of the first order, he arrived at exactly the same expressions as those of Pidgeon and Smith for the single cavity. As far as angular dependence is concerned, the filter behaves as if it were a single layer with an effective index of

$$n^* = (n_1 n_2)^{1/2}$$

where $n_1 > n_2$ or

$$n^* = \frac{n_1}{[1-(n_1/n_2)+(n_1/n_2)^2]^{1/2}}$$

where $n_2 > n_1$.

For higher-order filters, therefore, we should be safe in making use of Expressions 8.34 and 8.36.

Figure 8.30 shows the tilted performance of a simple three-cavity narrow-band filter of design:

$$\text{Air}\ |\ 1.21L\ 0.38H\ (HL)^7\ HHHHHH\ (LH)^7\ L\ (HL)^7\ HHHHHH\ (LH)^7$$
$$\text{L (HL)7}\ HHHHHH\ (LH)^7\ |\ \text{Glass}$$

with $n_{air} = 1.00$, $n_H = 2.065$, $n_L = 1.47$, and $n_{glass} = 1.50$.

Unfortunately, there can be complications. The filter of Figure 8.27 uses cavities of different orders to achieve the excellent ripple performance. These cavities move at slightly different rates with changing angle because their effective indices differ slightly. Detuned cavities have a seriously degrading effect on multiple-cavity filters. This can clearly be seen in Figure 8.31. The filter pass-band shape degrades considerably as angle of incidence increases.

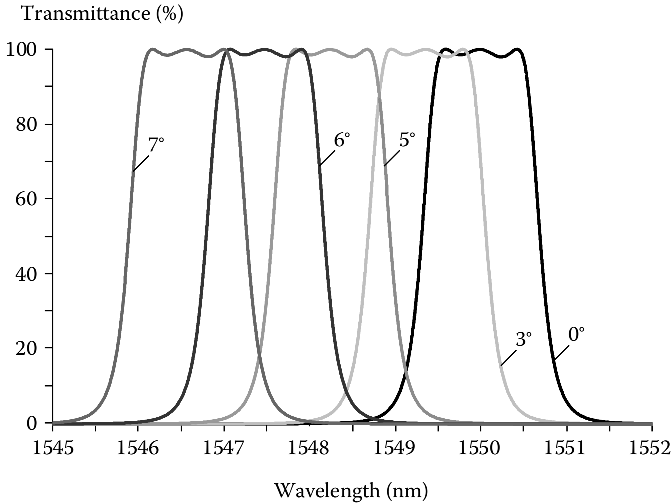

FIGURE 8.30
Performance as a function of angle of incidence in air of a simple 3-cavity narrowband filter where all cavities are exactly the same. There is no perceptible distortion of the characteristic as the angle is increased. By 15° incidence (not shown) polarization splitting is becoming perceptible but otherwise the characteristic is still undistorted.

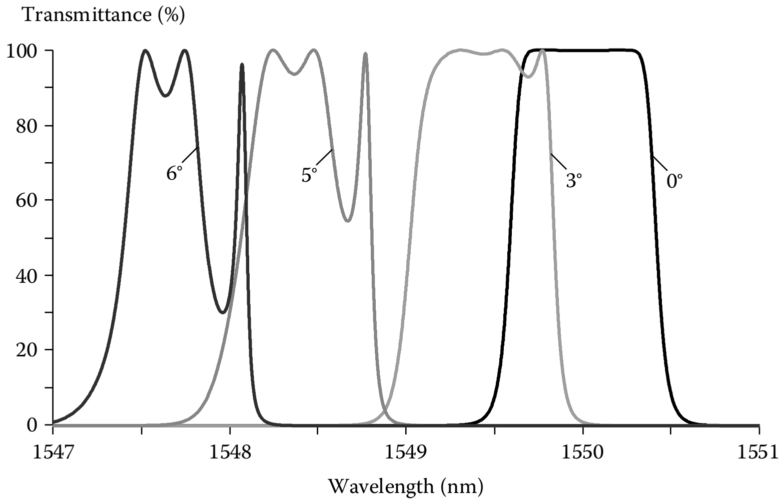

FIGURE 8.31
The performance of the filter of Figure 8.27 at normal incidence (extreme right) and angles of incidence of 3°, 5°, and 6°. Serious distortion is already visible at 3° and increases with angle. Polarization splitting is negligible.

To improve the tilted performance, we need to bring the effective indices of the cavities closer together. The design of this filter involves high-index cavities and so the higher-order ones will have higher effective index. Incorporating more low-index material in these cavity structures is the most direct route. Here, some trial and error is usually the most straightforward way to proceed. Various tricks are possible, such as changing some single quarter-wave low-index layers to three-quarters, but in the case of this particular filter, changing one or more of the high-index half-waves in the cavity layers to low-index half-waves works reasonably well. The best arrangement appears to be

$$\text{Air}|1.2676L\ 0.3379H\ (HL)^7\ H\ (HL)^{15}\ H\ (HLLH\ (HL)^{15}\ H\ HLLH)^2$$
$$(\text{HL})^{15}\ \text{H}\ (\text{HL})^7\ \text{H}|\text{Glass}$$

With the values of indices exactly as in Figure 8.27; this gives the tilted performance shown in Figure 8.32.

The design of Figure 8.29 uses cavities that are of the same order and so presents a similar tilted performance to that shown in Figure 8.32.

Another advantage to filters that exhibit this insensitivity of shape to tilt angle is their general inherent insensitivity to a particular type of uniformity error. Deposition thickness monitoring of narrowband filters is usually what is termed *direct*—that is, it takes place on an actual filter that is being produced. This permits the error compensation necessary for successful narrowband filter production. Away from the monitoring area, however, the deposited thicknesses may vary and, in fact, such variation is frequently

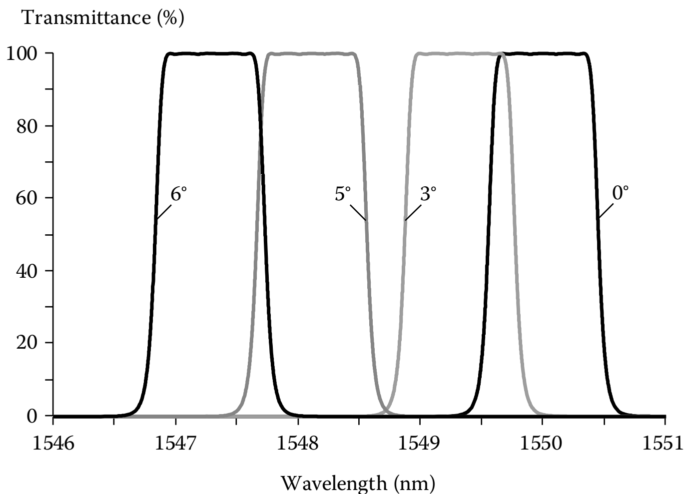

FIGURE 8.32
Tilted performance of the modified design where the cavities now move at similar rates with angle. Note that the effective index of this filter is now very slightly less than that of Figure 8.31. Even at 15° incidence (not shown) the filter characteristic remains undistorted but there is perceptible polarization splitting.

encouraged in the production of telecom filters. Here, after deposition, a large filter disk is eventually diced into smaller filters, and a spread of peak wavelength yields filters for different channels. It is very difficult to ensure that such varying thicknesses of high- and low-index films remain always exactly in step. Relative thickness errors have an effect on filter shape similar to that of changing angle of incidence. Insensitivity of shape to angle of incidence changes, therefore, implies similar insensitivity also to relative errors in uniformity and improves the yield of usable components.

8.4.2 Losses in Multiple Cavity Filters

Losses in multiple cavity filters can be estimated in the same way as for the Fabry–Perot filter. There are so many possible designs that a completely general approach would be very involved. However, we can begin by assuming that the basic symmetrical unit is perfectly matched at either end. The scheme of admittances through the basic unit will then be as shown in Table 8.4.

Then, in the same way as for the single-cavity filter, we can write

$$\sum \mathcal{A} = \beta_1\left[\left(\frac{n_1}{n_2}\right)^{x-1} + \left(\frac{n_2}{n_1}\right)^{x-1}\right] + \beta_2\left[\left(\frac{n_1}{n_2}\right)^{x-2} + \left(\frac{n_2}{n_1}\right)^{x-2}\right]$$
$$+ \beta_1\left[\left(\frac{n_1}{n_2}\right)^{x-3} + \left(\frac{n_2}{n_1}\right)^{x-3}\right] + \cdots + \beta_2\left[\left(\frac{n_2}{n_1}\right)^{x-2} + \left(\frac{n_1}{n_2}\right)^{x-2}\right]$$
$$\beta_1\left[\left(\frac{n_2}{n_1}\right)^{x-1} + \left(\frac{n_1}{n_2}\right)^{x-1}\right]$$

i.e.,

TABLE 8.4

Admittances through Basic Symmetrical Unit

Layer	Admittance
	n_1^x/n_2^{x-1}
n_1	
	n_2^{x-1}/n_1^{x-2}
n_2	
	n_1^{x-2}/n_2^{x-3}
n_1	
	n_2^{x-3}/n_1^{x-4}
⋮	
	n_1^{x-2}/n_2^{x-3}
n_2	
	n_2^{x-1}/n_1^{x-2}
n_1	
	n_1^x/n_2^{x-1}

$$\sum \mathcal{A} = \beta_1 \left\{ \left[\left(\frac{n_1}{n_2}\right)^{x-1} + \left(\frac{n_1}{n_2}\right)^{x-3} + \cdots + \left(\frac{n_2}{n_1}\right)^{x-1} \right] \right.$$
$$\left. + \left[\left(\frac{n_2}{n_1}\right)^{x-1} + \left(\frac{n_2}{n_1}\right)^{x-3} + \cdots + \left(\frac{n_1}{n_2}\right)^{x-1} \right] \right\}_1$$
$$+ \beta_2 \left\{ \left[\left(\frac{n_2}{n_1}\right)^{x-1} + \left(\frac{n_2}{n_1}\right)^{x-3} + \cdots + \left(\frac{n_1}{n_2}\right)^{x-1} \right] \right.$$
$$\left. + \left[\left(\frac{n_1}{n_2}\right)^{x-1} + \left(\frac{n_1}{n_2}\right)^{x-3} + \cdots + \left(\frac{n_2}{n_1}\right)^{x-1} \right] \right\}$$

We note that the second expression of each pair is the same as the first with inverse order.

The layers are quarter-waves and so we can write, as before,

$$\beta_1 = \frac{\pi}{2}\frac{k_1}{n_1} \quad \text{and} \quad \beta_2 = \frac{\pi}{2}\frac{k_2}{n_2}$$

Once again we divide the cases into high- and low-index cavities.

8.4.2.1 Case I: High-Index Cavities

We replace n_1 by n_H, k_1 by k_H, n_2 by n_L, and k_2 by k_L. Then, neglecting, as before, terms in $(n_L/n_H)^x$ compared with unity,

$$\sum \mathcal{A} = \frac{\pi(k_H/n_H)(n_H/n_L)^{x-1}}{1-(n_L/n_H)^2} + \frac{\pi(k_L/n_L)(n_H/n_L)^{x-2}}{1-(n_L/n_H)^2}$$
$$= \pi\left(\frac{n_H}{n_L}\right)^x \frac{n_L(k_H+k_L)}{(n_H^2-n_L^2)}$$

Now Expression 8.60 with $m = 1$ is

$$\left|\frac{\Delta\lambda_B}{\lambda_0}\right| = \frac{4}{\pi}\left(\frac{n_L}{n_H}\right)^x \frac{(n_H-n_L)}{n_H}$$

so that

$$\sum \mathcal{A} = 4\left(\frac{\lambda_0}{\Delta\lambda_B}\right)\frac{n_L(k_H+k_L)}{n_H(n_H+n_L)}$$

Now, this is the loss of one basic symmetrical unit. If further basic units are added, each will have the same loss. In addition, there are the matching stacks at either end of the filter. We will not be far in error if we assume that they add a further loss equal to one of the basic symmetrical units. The total number of units is then equal to the number of cavities. If we denote this by q, then $q = 2$ for a two-cavity filter and so on. We can also assume that $R = 0$ so that the absorption loss becomes

$$A = q\pi\left(\frac{n_H}{n_L}\right)^x \frac{n_L(k_H + k_L)}{(n_H^2 - n_L^2)} \tag{8.65}$$

or

$$A = 4q\left(\frac{\lambda_0}{\Delta\lambda_B}\right)\frac{n_L(k_H + k_L)}{n_H(n_H + n_L)} \tag{8.66}$$

8.4.2.2 Case II: Low-Index Cavities

In the same way

$$A = q\pi\left(\frac{n_H}{n_L}\right)^x \frac{(n_H^2 k_L + n_L^2 k_H)}{n_H(n_H^2 - n_L^2)} \tag{8.67}$$

or

$$A = 4q\left(\frac{\lambda_0}{\Delta\lambda_B}\right)\left(\frac{n_L}{n_H}\right)\frac{[k_L(n_H/n_L) + k_H(n_L/n_H)]}{(n_H + n_L)} \tag{8.68}$$

Expressions 8.66 and 8.68 are approximately q times the absorption of single-cavity, filters with the same half-width, a not surprising result.

8.4.3 Further Information

The examples of multiple cavity filters so far described have been for the visible and infrared, but of course they can be designed for any region of the spectrum where suitable thin-film materials exist. An account of filters for the visible and ultraviolet that is still relevant is given by Barr [26]. All-dielectric filters, both of the single-cavity and multiple-cavity types for the near ultraviolet, are described by Nielson and Ring [27], who used combinations of cryolite and lead fluoride, and of cryolite and antimony trioxide,

the former for the region 250–320 nm and the latter for 320–400 nm. Apart from the techniques required for the deposition of these materials, the main difference between such filters and those for the visible or infrared is that the values of the high and low refractive indices are much closer together, requiring more layers for the same rejection. Nielson and Ring's filters contained basic units of 17 or 19 layers, in most cases, so that complete DHW filters consisted of 31 or 39 layers, respectively. Malherbe [28] has described a lanthanum fluoride and magnesium fluoride filter for 205.5 nm in which the basic unit had 51 layers (high-index first-order cavity), the full design being $(HL)^{12}H\ H(LH)^{25}H(LH)^{12}$ with a total number of 99 layers, giving a measured bandwidth of 2.5 nm.

8.5 Phase Dispersion Filter

The phase dispersion filter predates the successes of the narrowband filters for telecom applications and was an attempt to find an approach to the design of narrowband filters that would avoid some of the manufacturing difficulties inherent in conventional narrowband filters. At the time, the conventional filter was found to be increasingly difficult to manufacture as half-widths were reduced below around 0.3% of peak wavelength. Attempts to improve the position by using higher-order cavities appeared ineffective when the cavity became thicker than perhaps the fourth order because of what was considered to be increased roughness of the cavity. Much more is now known about narrowband filters and the causes of manufacturing difficulties, and those will be dealt with in some detail in a subsequent chapter. A principal problem at the time was moisture-induced drifts, although that was not recognized until somewhat later. Although the phase dispersion filter was not, as it turned out, the solution to the narrowband filter problem; nevertheless, it does have very interesting properties and the philosophy behind the design is worth discussing.

The reflecting stack with extended bandwidth, which was originally intended for classic Fabry–Perot etalons, and described in Chapter 6, shows a large dispersion of the phase change on reflection, and this suggested to Baumeister and Jenkins [29] that it might form the basis for a new type of filter in which the narrow bandwidth would depend almost entirely on this phase dispersion rather than on the very high reflectances of the reflecting stacks. They called this type of filter a "phase dispersion filter." It consists quite simply of a single-cavity all-dielectric filter that has, instead of the conventional dielectric quarter-wave stacks on either side of the cavity layer, reflectors consisting of staggered multilayers. The rapid change in phase causes the bandwidth of the filter and the position of its peak to be much less sensitive to the errors in thickness of the cavity layer than would otherwise be the case.

The results, which they themselves [29] and with Jeppesen [30] eventually achieved, were good, although they never quite succeeded in attaining the performance possible in theory. This prompted a study [31] of the influence of errors in any of the layers of a filter on the position of the peak. The idea behind this study was that random errors in both thickness and uniformity in layers other than the cavity might be responsible for the discrepancy between theory and practice. If, in a practical filter, the errors were causing the peak to vary in position over the surface of the filter, then the integrated response would exhibit a rather wider bandwidth and lower transmittance than those of any very small portion of the filter, which might well be attaining the theoretical performance. It seemed possible that there might be a design of filter that could yield the minimum sensitivity to errors and therefore give the minimum possible bandwidth with a given layer "roughness."

Giacomo et al.'s findings [31] can be summarized as follows (the notation in the paper has been slightly altered to agree with that used throughout this book): the peak of an all-dielectric multilayer filter is given by

$$\frac{\varphi_a + \varphi_b}{2} - \delta = m\pi \tag{8.69}$$

where

$$\delta = \frac{2\pi n_c d_c}{\lambda} = 2\pi n_c d_c \nu$$

d_c being the physical thickness of the cavity layer and the other symbols having their usual meanings.

For a change Δd_i in the ith layer, Δd_j in the jth layer, and Δd_c in the cavity, the corresponding change in the wave number of the peak $\Delta\nu$ is given by

$$\sum_i \frac{\partial \varphi_a}{\partial d_i}\Delta d_i + \sum_j \frac{\partial \varphi_b}{\partial d_j}\Delta d_j - 2\frac{\partial \delta}{\partial d_c}\Delta d_c + \left(\frac{\partial \varphi_a}{\partial \nu} + \frac{\partial \varphi_b}{\partial \nu} - 2\frac{\partial \delta}{\partial \nu}\right)\Delta \nu = 0 \tag{8.70}$$

Now

$$\frac{\partial \delta}{\partial d_c} = 2\pi n_c \nu = \frac{\delta}{d_c} \tag{8.71}$$

and

$$\frac{\partial \delta}{\partial \nu} = 2\pi n_c d_c = \frac{\delta}{\nu} \tag{8.72}$$

and also, since d_i and ν appear in the individual thin-film matrices only in the value of $\delta_i = 2\pi n_i d_i \nu$, then

$$\sum_i \frac{\partial \varphi_a}{\partial d_i}\Delta_0 d_i = \frac{\partial \varphi_a}{\partial \nu}\Delta_0 \nu$$

and similarly for φ_b, where Δ_0 indicates that the changes in d_i are related by

$$\frac{\Delta_0 d_i}{d_i} = \frac{\Delta_0 \nu}{\nu}$$

This gives

$$\frac{\partial \varphi_a}{\partial \nu} = \sum_i \left(\frac{\partial \varphi_a}{\partial d_i}\frac{d_i}{\nu} \right) \tag{8.73}$$

which is independent of the particular choice of Δ_0 used to arrive at it. A similar expression holds for φ_b. Using Equations 8.71, 8.72, and 8.73 in Expression 8.70:

$$\sum_i \left(\frac{\partial \varphi_a}{\partial d_i}\Delta d_i \right) + \sum_j \left(\frac{\partial \varphi_b}{\partial d_j}\Delta d_j \right) - 2\delta \frac{\Delta d_c}{d_c} + \left[\sum_i \left(\frac{\partial \varphi_a}{\partial d_i} d_i \right) + \sum_j \left(\frac{\partial \varphi_b}{\partial d_j} d_j \right) - 2\delta \right] \frac{\Delta \nu}{\nu} = 0$$

i.e.,

$$\frac{\Delta \nu}{\nu} = -\frac{\left[\sum_i \left(\frac{\partial \varphi_a}{\partial d_i} d_i \alpha_i \right) + \sum_j \left(\frac{\partial \varphi_b}{\partial d_j} d_j \alpha_j \right) - 2\delta \alpha_c \right]}{\left[\sum_i \left(\frac{\partial \varphi_a}{\partial d_i} d_i \right) + \sum_j \left(\frac{\partial \varphi_b}{\partial d_j} d_j \right) - 2\delta \right]} \tag{8.74}$$

where

$$\alpha_i = \frac{\Delta d_i}{d_i} \text{ etc.}$$

Now, in a real filter, the fluctuations in thickness, or "roughness," will be completely random in character, and to deal with the performance of any appreciable area of the filter, we must work in terms of the mean square deviations. Each layer in the assembly can be thought of as being a combination of a large number of thin elementary layers of similar mean thicknesses

but that fluctuate in a completely random manner quite independently of each other. The RMS variation in thickness of any layer in the filter can then be considered to be proportional to the square root of its thickness. This can be written:

$$\varepsilon_i = kd_i^{1/2}$$

where k can be assumed to be the same for all layers regardless of thickness. If a_i is the RMS fractional variation of the ith layer, then

$$a_i = \frac{\varepsilon_i}{d_i} = \frac{k}{d_i^{1/2}}$$

where

$$a_i = \overline{\alpha_i^2}.$$

We now define β as being

$$\beta^2 = \overline{\left(\frac{\Delta\nu}{\nu}\right)^2}.$$

Then

$$\beta^2 = \frac{\left[\sum_i \left[\left(\frac{\partial\varphi_a}{\partial d_i} d_i\right)^2 a_i^2\right] + \sum_j \left[\left(\frac{\partial\varphi_b}{\partial d_j} d_j\right)^2 a_j^2\right] + 4\delta^2\alpha_c^2\right]}{\left[\sum_i \left(\frac{\partial\varphi_a}{\partial d_i} d_i\right) + \sum_j \left(\frac{\partial\varphi_b}{\partial d_j} d_j\right) - 2\delta\right]^2}$$

which gives

$$\beta^2 = \frac{k^2 \sum_{k=1}^{q} \left(\frac{1}{d_k} A_k^2\right)}{\left(\sum_{k=1}^{q} A_k\right)^2} \tag{8.75}$$

where

$$A_k = \frac{\partial\varphi_a}{\partial d_k} d_k \quad \text{or} \quad \frac{\partial\varphi_b}{\partial d_k} d_k \quad \text{or} \quad -2\delta$$

whichever is appropriate. q is the number of layers in the filter. The expression will be a minimum when

$$\frac{A_k}{d_k} = \frac{A_l}{d_l} = \cdots. \tag{8.76}$$

Then

$$\beta^2 = k^2/T \tag{8.77}$$

where T is the total thickness of the filter.

In the general case,

$$\beta \geq k/T^{1/2}$$

and one might hope to attain a limiting resolution of

$$R = T^{1/2}/k \tag{8.78}$$

The condition written in Equation 8.76 can be developed with the aid of Equation 8.73 into

$$\frac{\partial \varphi_a}{\partial d_k} = \frac{\partial \varphi_b}{\partial d_j} = -4\pi n_c \nu$$

so that

$$\nu\left(\frac{\partial \varphi_a}{\partial \nu}\right) = \sum_i \left(\frac{\partial \varphi_a}{\partial d_i} d_i\right) = -4\pi n_c d_m \nu$$

and likewise for reflector b, where d_m = total thickness of the appropriate reflector. This gives

$$\frac{\partial \varphi_a}{\partial \nu} = -4\pi n_c d_m \tag{8.79}$$

This condition is necessary but not sufficient for the resolution to be a maximum and it can be used as a preliminary test of the suitability of any particular multilayer reflector that may be employed.

The classic quarter-wave stack is very far from satisfying it but the staggered multilayer is much more promising. In their paper, Giacomo et al. [31] compare a staggered multilayer reflector with a conventional quarter-wave

stack. Both reflectors have 15 layers, and the results are quoted for the broadband reflector at 17 000 cm^{-1} and for the conventional reflector at 20 000 cm^{-1}.

Equation 8.79 can be written

$$\sum_i \left(\frac{\partial \varphi_a}{\partial d_i} d_i \right) = \sum_i \frac{\partial \varphi_a}{\partial \alpha_i} = -4\pi n_c d_m \nu$$

Now, from Table 8.5,

$$-\sum_i \frac{\partial \varphi_a}{\partial \alpha_i} = 30.662$$

and

$$4\pi n_c d_m \nu = 34.5$$

so that on the preliminary basis of Equation 8.79, the prospects look extremely good.

However, this is not a sufficient condition. We must calculate the actual relationship between β and k and compare it with the theoretical condition given by Equation 8.77. Now

$$A_i = d_i \frac{\partial \varphi}{\partial d_i} = \frac{\partial \varphi}{\partial \alpha_i}$$

which is the last column given for each reflector. This can be used in Equation 8.75 giving for a filter using the broadband reflector

$$\beta = 1.023k$$

which can be compared with the value obtained in the same way for the conventional quarter-wave stack of Table 8.5:

$$\beta = 1.289k.$$

For a total filter thickness of 2.35 μm, the theoretical minimum value of β is given by Expression 8.77 as

$$\beta = 0.652k$$

(k having units of μm$^{1/2}$).

TABLE 8.5

Parameters of Broadband and Conventional Reflectors

	Broadband Film				Classical Film		
Layer Number	Thickness d_i (μm)	Index (n)	$\partial\varphi/\partial d_i$ (μm^{-1})	$\partial\varphi/\partial\alpha_i$	Thickness d_i (μm)	$\partial\varphi/\partial d_i$ (μm^{-1})	$\partial\varphi/\partial\alpha_i$
Substrate		1.52					
1	0.0751	2.30	0.32	0.024	0.0543	0.01	0.001
2	0.1279	1.35	0.60	0.076	0.0926	0.02	0.002
3	0.0751	2.30	1.97	0.148	0.0543	0.05	0.003
4	0.1235	1.35	1.85	0.229	0.0926	0.06	0.005
5	0.0626	2.30	4.75	0.298	0.0543	0.16	0.009
6	0.1299	1.35	4.60	0.597	0.0926	0.16	0.015
7	0.0681	2.30	11.68	0.795	0.0543	0.48	0.026
8	0.0957	1.35	10.63	1.018	0.0926	0.48	0.044
9	0.0566	2.30	30.85	1.746	0.0543	1.39	0.075
10	0.0859	1.35	30.37	2.608	0.0926	1.39	0.128
11	0.0504	2.30	78.33	3.948	0.0543	4.03	0.219
12	0.0805	1.35	62.33	5.019	0.0926	4.03	0.373
13	0.0450	2.30	121.58	5.471	0.0543	11.69	0.635
14	0.0767	1.35	65.41	5.015	0.0926	11.69	1.082
15	0.0450	2.30	81.59	3.672	0.0543	33.92	1.843
Incident medium		1.35					
Σ	1.1978		506.8	30.662	1.0829	69.53	4.460

Source: After Giacomo. P., Baumeister, P.W., and Jenkins, F.A., *Proceedings of the Physical Society*, 73, 480–489, 1959.

Thus, although the phase dispersion filter using the reflectors shown in Table 8.5 appears to be promising based on the criterion (Expression 8.79), in the event, its performance is somewhat disappointing. It is, however, certainly better than the straightforward classic filter. So far no design that better meets the condition of Equation 8.76 has been proposed.

Some otherwise unpublished results obtained by Ritchie [32] are shown in Figure 8.33. This filter used zinc sulfide and cryolite as the materials on glass as substrate. Its design is given in Table 8.6. An experimental filter monitored at 1.348 μm gave peaks with corresponding bandwidths of

1.047 μm, bandwidth 3.0 nm
1.159 μm, bandwidth 2.5 nm
1.282 μm, bandwidth 4.0 nm

Theoretically, the bandwidths should have been 0.8 nm, 1.7 nm, and 4.6 nm, respectively.

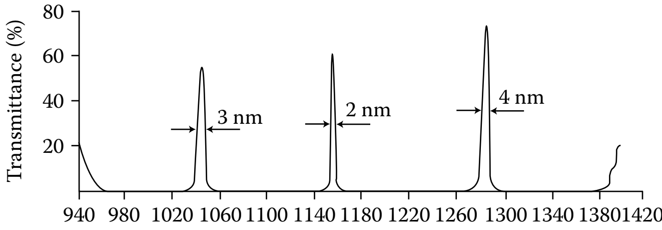

FIGURE 8.33
The measured transmittance of a 35-layer phase-dispersion filter. The design is given in Table 8.6. (After Ritchie, F.S., Unpublished work on Ministry of Technology Contract KX/LSO/C.B.70(a).)

TABLE 8.6
Reflector Design for Figure 8.33 Filter

Layer Number	Material	Optical Thickness Units of λ_0
1	ZnS	0.2375
2	Na_3AlF_6	0.2257
3	ZnS	0.2143
4	Na_3AlF_6	0.2036
5	ZnS	0.1934
6	Na_3AlF_6	0.1838
7	ZnS	0.1746
8	Na_3AlF_6	0.1649
9	ZnS	0.1576
10	Na_3AlF_6	0.1498
11	ZnS	0.1423
12	Na_3AlF_6	0.1352
13	ZnS	0.1285
14	Na_3AlF_6	0.1220
15	ZnS	0.1159
16	Na_3AlF_6	0.1101
17	ZnS	0.1046
Cavity	Na_3AlF_6	0.5000

These 17 layers are followed by another 17 that are a mirror image of the first 17.

8.6 Multiple Cavity Metal–Dielectric Filters

Metal–dielectric filters are indispensable in suppressing the longwave side-bands of narrowband all-dielectric filters, and as filters in their own right, especially in the extreme shortwave region of the spectrum. Unlike all-dielectric filters, however, they possess the disadvantage of high intrinsic

absorption. In single-cavity filters, this means that the pass bands must be wide to achieve reasonable peak transmission and the shape is far from ideal. It is possible to combine metal–dielectric elements into multiple cavity filters that, because of their more rectangular shape, are more satisfactory but, again, losses can be high.

The accurate design procedure for such metal–dielectric filters can be lengthy and tedious and frequently they are simply designed by trial and error as they are manufactured. We have already mentioned the metal–dielectric single-cavity filter. These filters may be coupled together simply by depositing them one on top of the other with no coupling layer in between.

We can illustrate this by choosing silver as our metal, which we can give an index of $0.055 - i3.32$ at 550 nm [33]. The thickness of the cavity layer in the single-cavity filter, as we have already noted, should be rather thinner than a half-wave at the peak wavelength to allow for the phase changes in reflection at the silver–dielectric interfaces. This phase change varies only slowly with silver thickness when it is thick enough to be useful as a reflector and we can assume, as a reasonable approximation, that it is equal to the limiting value for infinitely thick material. We can then use Equation 5.5 to calculate the thickness of the cavity. Equation 5.5 calculates for us exactly one-half of the filter because it gives the thickness of the dielectric material to yield real admittance with zero phase change at the outer surface of the metal–dielectric combination. Adding a second exactly similar structure with the two dielectric layers facing each other, so that they join to form a single cavity, yields a filter in which the phase condition, Equation 8.2, is satisfied.

Let us choose a cavity of index 1.35, similar to that of cryolite. Then half the cavity thickness is given by

$$D_c = \frac{1}{4\pi}\arctan\left(\frac{2\beta n_c}{n_c^2 - \alpha^2 - \beta^2}\right) \tag{8.80}$$

where $\alpha - i\beta$ is the index of the metal and n_c that of the cryolite cavity and the angle is taken in the first or second quadrant.

With $\alpha - i\beta = 0.055 - i3.32$ and $n_c = 1.35$ we find

$$D_c = 0.18855$$

so that the cavity thickness should be 0.3771 full waves.

We can choose a metal layer thickness of 35 nm, quite arbitrarily, simply for the sake of illustration. Our single-cavity filter is then

Glass	Ag 35 nm	Cryolite 0.3771 waves	Ag 35 nm	Glass

(the geometrical thickness being quoted for the silver and the optical thickness for the cryolite) and the two-cavity filter is exactly double this structure:

Glass	Ag 35 nm	Cryolite 0.3771 waves	Ag 70 nm	Cryolite 0.3771 waves	Ag 35 nm	Glass

Transmittance curves of these filters are shown in Figure 8.34. The peaks are slightly displaced from 550 nm because of the approximations inherent in the design procedure.

The single cavity has reasonably good peak transmittance but its typical triangular shape means that its rejection is quite poor even at wavelengths far from the peak. The two-cavity filter has better shape but rather poorer peak transmittance. The rejection can be improved by increasing the metal thickness, but at the expense of peak transmittance.

The design approach we have described is quite crude and simply concentrates on ensuring that the peak of the filter is centered near the desired wavelength. Peak transmittance and bandwidth are either accepted as they are or a new metal thickness is tried. Performance is in no way optimized.

The unsatisfactory nature of this design procedure led Berning and Turner [34] to develop a new technique for the design of metal–dielectric filters in which the emphasis is on ensuring that maximum transmittance is achieved

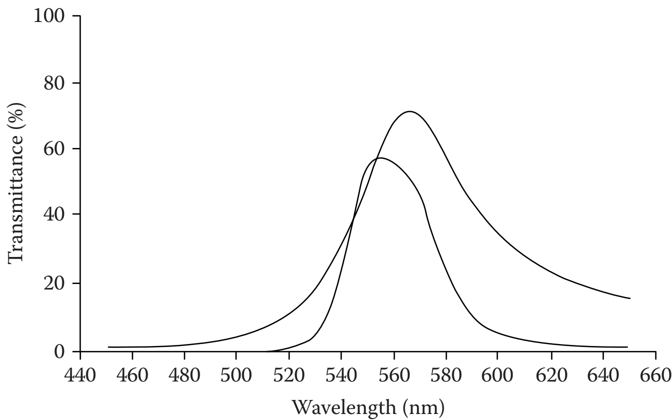

FIGURE 8.34
The transmittance as a function of wavelength of filters of design:

Glass	Ag 35 nm	Cryolite $0.3771\lambda_0$	Ag 35 nm	Glass

and

Glass	Ag 35 nm	Cryolite $0.3771\lambda_0$	Ag 70 nm	Cryolite $0.3771\lambda_0$	Ag 35 nm	Glass

where $\lambda_0 = 550$ nm, $n - ik = 0.055 - i3.32$, $n_{glass} = 1.52$, and $n_{cryolite} = 1.35$. Dispersion in the materials has been neglected.

in the filter pass band. For this purpose they devised the concept of potential transmittance and created a new type of metal–dielectric filter known as the induced-transmission filter.

8.6.1 The Induced-Transmission Filter

Given a certain thickness of metal in a filter, what is the maximum possible peak transmittance, and how can the filter be designed to realize this transmittance? This is the basic problem tackled and solved by Berning and Turner [34]. The development of the technique as given here is based on their approach, but it has been adjusted and adapted to conform more nearly to the general pattern of this book.

The concept of potential transmittance has already been touched on in Chapter 2 and used in the analysis of losses in dielectric multilayers. We recall that the potential transmittance ψ of a layer or assembly of layers is defined as the ratio of the irradiance leaving the rear surface to that actually entering at the front surface, and it represents the transmittance that the layer or assembly of layers would have if the reflectance of the front surface were reduced to zero. Once the parameters of the metal layer are fixed, its potential transmittance is determined entirely by the admittance of the structure at the exit face of the layer. Furthermore, it is possible to determine that particular admittance that gives maximum potential transmittance. To achieve this transmittance once the correct exit admittance is established, it is sufficient to add a coating to the front surface to reduce the reflectance to zero. The maximum potential transmittance is a function of the thickness of the metal layer.

The design procedure is then as follows. The optical constants of the metal layer at the peak wavelength are given. Then the metal layer thickness is chosen and the maximum potential transmittance together with the matching admittance at the exit face of the layer, which is required to produce that level of potential transmittance, is found. Often a minimum acceptable figure for the maximum potential transmittance will exist and that will put an upper limit on the metal layer thickness. A dielectric assembly to give the correct matching admittance at the rear of the layer, which will usually be deposited directly on the substrate, must then be designed. The filter is then completed by the addition of a dielectric system to match the front surface of the resulting metal–dielectric assembly to the incident medium. Techniques for each of these steps will be developed. The matching admittances for the metal layer are such that the dielectric stacks are efficient in matching over a limited region only, outside which their performance falls off rapidly. It is this rapid fall in performance that defines the limits of the pass band of the filter.

Before we can proceed further, we require some analytical expressions for the potential transmittance and for the matching admittance. This leads to some lengthy and involved analysis that is not difficult but rather involved and time consuming.

8.6.1.1 Potential Transmittance

We limit the analysis to an assembly in which there is only one absorbing layer, the metal. The potential transmittance is then related to the matrix for the assembly, as shown in Chapter 2. For the film in question, we have

$$\begin{bmatrix} B_i \\ C_i \end{bmatrix} = [M]\begin{bmatrix} 1 \\ Y_e \end{bmatrix}$$

where $[M]$ is the characteristic matrix of the metal layer and Y_e is the admittance of the terminating structure. Then the potential transmittance ψ is given by

$$\psi = \frac{\text{Re}(Y_e)}{\text{Re}(B_i C_i^*)} \tag{8.81}$$

Let the exit admittance be given by $X + iZ$. Then

$$\begin{bmatrix} B_i \\ C_i \end{bmatrix} = \begin{bmatrix} \cos\delta & (i\sin\delta)/y \\ iy\sin\delta & \cos\delta \end{bmatrix}\begin{bmatrix} 1 \\ X+iZ \end{bmatrix}$$

where

$$\begin{aligned} \delta &= 2\pi(n-ik)d/\lambda = (2\pi nd)/\lambda - i(2\pi kd)/\lambda \\ &= \alpha - i\beta \\ \alpha &= (2\pi nd)/\lambda \\ \beta &= (2\pi kd)/\lambda \end{aligned}$$

If free space units are used, then

$$y = n - ik.$$

Now,

$$\begin{aligned} (B_i C_i^*) &= [\cos\delta + i(\sin\delta/y)(X+iZ)][iy\sin\delta + \cos\delta(X+iZ)]^* \\ &= [\cos\delta + i(\sin\delta/y)(X+iZ)][-iy^*\sin\delta^* + \cos\delta^*(X-iZ)] \\ &= -iy^*\cos\delta\sin\delta^* + \frac{\sin\delta\sin\delta^* y^{*2}(X+iZ)}{yy^*} \\ &\quad + \cos\delta\cos\delta^*(X-iZ) + \frac{i\sin\delta\cos\delta^* y^*(X+iZ)(X-iZ)}{yy^*} \end{aligned}$$

We require the real part of this and we take each term in turn.

$$-iy^* \cos\delta \sin\delta^* = -i(n+ik)(\cos\alpha\cosh\beta - i\sin\alpha\sinh\beta) \\ \times(\sin\alpha\cosh\beta + i\cos\alpha\sinh\beta)$$

and the real part of this, after a little manipulation, is

$$\mathrm{Re}(-iy^* \cos\delta \sin\delta^*) = n\sinh\beta\cosh\beta + k\cos\alpha\sin\alpha$$

Similarly

$$\mathrm{Re}\left(\frac{\sin\delta\sin\delta^* y^{*2}(X+iZ)}{yy^*}\right) = \frac{X(n^2-k^2)-2nkZ}{(n^2+k^2)} \\ \times(\sin^2\alpha\cosh^2\beta + \cos^2\alpha\sinh^2\beta)$$

$$\mathrm{Re}[\cos\delta\cos\delta^*(X-iZ)] = X(\cos^2\alpha\cosh^2\beta + \sin^2\alpha\sinh^2\beta)$$

$$\mathrm{Re}\left(\frac{i\sin\delta\cos\delta^* y^*(X+iZ)(X-iZ)}{yy^*}\right) = \frac{X^2+Z^2}{(n^2+k^2)}(n\sinh\beta\cosh\beta - k\sin\alpha\cos\alpha)$$

The potential transmittance is then

$$\begin{aligned}\psi = \Bigg[&\frac{(n^2-k^2-2nkZ/X)}{(n^2+k^2)}(\sin^2\alpha\cosh^2\beta + \cos^2\alpha\sinh^2\beta) \\ &+(\cos^2\alpha\cosh^2\beta + \sin^2\alpha\sinh^2\beta) \\ &+(1/X)(n\sinh\beta\cosh\beta + k\cos\alpha\sin\alpha) \\ &+\frac{X^2+Z^2}{X(n^2+k^2)}(n\sinh\beta\cosh\beta - k\cos\alpha\sin\alpha)\Bigg]^{-1}\end{aligned} \tag{8.82}$$

8.6.1.2 Optimum Exit Admittance

Next we find the optimum values of X and Z. From Equation 8.82

$$\frac{1}{\psi} = \left[\frac{p(n^2-k^2-2nkZ/X)}{(n^2+k^2)} + q + \frac{r}{X} + \frac{s(X^2+Z^2)}{X(n^2+k^2)}\right] \tag{8.83}$$

where p, q, r, and s are shorthand for the corresponding expressions in

Equation 8.82. ψ is always positive and is a well-behaved function, so for an extremum in ψ we have also an extremum in $1/\psi$, of the opposite sense. We can safely write that the optimum exit admittance is given by:

$$\frac{\partial}{\partial X}\left(\frac{1}{\psi}\right)=0 \quad \text{and} \quad \frac{\partial}{\partial Z}\left(\frac{1}{\psi}\right)=0$$

i.e.,

$$\frac{p\cdot 2nkZ}{X^2(n^2+k^2)}-\frac{r}{X^2}+\frac{s}{(n^2+k^2)}-\frac{sZ^2}{X^2(n^2+k^2)}=0 \tag{8.84}$$

and

$$\frac{p(-2nk)}{X(n^2+k^2)}+\frac{2sZ}{X(n^2+k^2)}=0 \tag{8.85}$$

From Equation 8.85:

$$Z=\frac{nkp}{s}$$

and, substituting in Equation 8.84,

$$X^2=\frac{r(n^2+k^2)}{s}-\frac{n^2k^2p^2}{s^2}$$

Then, inserting the appropriate expressions for p, r, and s, from Equations 8.82 and 8.83

$$X=\left[\frac{(n^2+k^2)(n\sinh\beta\cosh\beta+k\sin\alpha\cos\alpha)}{(n\sinh\beta\cosh\beta-k\sin\alpha\cos\alpha)} -\frac{n^2k^2(\sin^2\alpha\cosh^2\beta+\cos^2\alpha\sinh^2\beta)^2}{(n\sinh\beta\cosh\beta-k\sin\alpha\cos\alpha)^2}\right]^{\frac{1}{2}} \tag{8.86}$$

$$Z=\frac{nk(\sin^2\alpha\cosh^2\beta+\cos^2\alpha\sinh^2\beta)}{(n\sinh\beta\cosh\beta-\sin\alpha\cos\alpha)} \tag{8.87}$$

We note that for β large $X \to n$ and $Z \to k$, that is:

$$Y_e \to (n + ik) = (n - ik)^*$$

8.6.1.3 Maximum Potential Transmittance

The maximum potential transmittance can then be found by substituting the values of X and Z, calculated by Equations 8.86 and 8.87, into Equation 8.82. All these calculations are best performed by computer or calculator, so there is little advantage in developing a separate analytical solution for maximum potential transmittance.

8.6.1.4 Matching Stack

We have to devise an assembly of dielectric layers that, when deposited on the substrate, will have an equivalent admittance of

$$Y = X + iZ$$

This is illustrated diagrammatically in Figure 8.35 where a substrate of admittance $(n_s - ik_s)$ has an assembly of dielectric layers terminating such that the final equivalent admittance is $(X + iZ)$. Now, the dielectric layer circles are executed in a clockwise direction always. If we therefore reflect the diagram in the x axis and then reverse the direction of the arrows, we get exactly the same set of circles—that is, the layer thicknesses are exactly the same—but the order is reversed (it was ABC and is now CBA) and they match a starting admittance of $X - iZ$, i.e., the complex conjugate of (X + iZ), into a terminal admittance of $(n_s + ik_s)$, i.e., the complex conjugate of the substrate index. In our filters, the substrate will have real admittance, i.e., $k_s = 0$, and it is a more straightforward problem to match $(X - iZ)$ into n_s than n_s into $(X + iZ)$.

There is an infinite number of possible solutions, but the simplest involves adding a phase-matching dielectric layer to change the admittance $(X - iZ)$ into a real value and then to add a series of quarter-waves to match the resultant real admittance into the substrate. We will illustrate the technique shortly with several examples. At the moment, we recall that the necessary analysis was carried out in Chapter 5. There we showed that a film of optical thickness D given by

$$D = \frac{1}{4\pi}\arctan\left[\frac{2Zn_f}{(n_f^2 - X^2 - Z^2)}\right] \tag{8.88}$$

(where the tangent is taken in the first or second quadrant) will convert an admittance $(X - iZ)$ into a real admittance of value

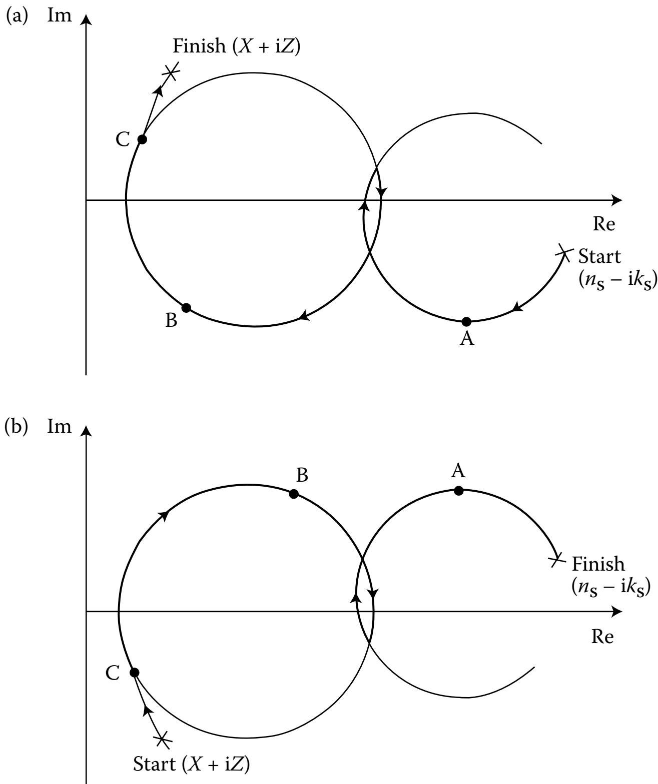

FIGURE 8.35
(a) A sketch of the admittance diagram of an arbitrary dielectric assembly of layers matching a starting admittance of $(n_s - ik_s)$ to the final admittance of $(X + iZ)$. (b) The curves of figure (a) reflected in the real axis and with the directions of the arrows reversed. This is now a multilayer identical to (a) but in the opposite order and connecting an admittance of $(X - iZ)$ [i.e., $(X + iZ)^*$] to one of $(n_s + ik_s)$ [i.e., $(n_s - ik_s)^*$].

$$\mu = \frac{2Xn_f^2}{(X^2 + Z^2 + n_f^2) + [(X^2 + Z^2 + n_f^2)^2 - 4X^2 n_f^2]^{1/2}} \tag{8.89}$$

n_f, the characteristic admittance of the film, can be high or low, but μ will always be lower than the substrate admittance (except in very unlikely cases) because it is the first intersection of the locus of n_f with the real axis, which is given by Equations 8.88 and 8.89.

Since the admittance of the substrate will always be greater than unity, the quarter-wave stack to match μ to n_s should start with a quarter-wave of low index. Alternate high- and low-index layers follow, the precise number being found by trial and error.

To complete the design, we need to know the equivalent admittance at the front surface of the metal layer and then we construct a matching stack to match it to the incident medium.

8.6.1.5 Front Surface Equivalent Admittance

If the admittance of the structure at the exit surface of the metal layer is the optimum value $(X + iZ)$ given by Equations 8.86 and 8.87, then it can be shown that the equivalent admittance that is presented by the front surface of the metal layer is simply the complex conjugate $(X - iZ)$. The analytical proof of this requires a great deal of patience, although it is not particularly difficult. Instead, let us use a logical justification.

Consider a filter consisting of a single metal layer matched on either side to the surrounding media by dielectric stacks. Let the transmittance of the assembly be equal to the maximum potential transmittance and let the admittance of the structure at the rear of the metal layer be the optimum admittance $(X + iZ)$. Let the admittance at the front surface be $(\xi + i\eta)$ and let this be matched perfectly to the incident medium. Now we know that the transmittance is the same regardless of the direction of incidence. Let us turn the filter around, therefore, so that the transmitted light proceeds in the opposite direction. The transmittance of the assembly must be the maximum potential transmittance once again. The admittance of the structure at what was earlier the input, but is now the new exit face of the metal layer, must therefore be $(X + iZ)$. But, since the layers are dielectric and the medium is of real admittance, this must also be the complex conjugate of $(\xi + i\eta)$, that is, $(\xi - i\eta)$. $(\xi + i\eta)$ must therefore be $(X - iZ)$, which is what we set out to prove.

The procedure for matching the front surface to the incident medium is therefore exactly the same as that for the rear surface and, indeed, if the incident medium is identical to the rear exit medium, as in a cemented filter assembly, then the front dielectric section can be an exact repetition of the rear.

8.6.2 Examples of Filter Designs

We can now attempt some filter designs. We choose the same material, silver, as we did for the metal–dielectric filters earlier. Once again, arbitrarily, we select a thickness of 70 nm. The wavelength we retain as 550 nm, at which the optical constants of silver can be taken as $0.055 - i3.32$ [33].

The filter is to use dielectric materials of indices 1.35 and 2.35, corresponding to cryolite and zinc sulfide, respectively. The substrate is glass, $n = 1.52$, and the filter will be protected by a cemented cover slip, so that we can also use $n = 1.52$ for the incident medium.

$$\alpha = 2\pi nd/\lambda = 0.04398$$

$$\beta = 2\pi kd/\lambda = 2.6549$$

and from Equations 8.86 and 8.87, we find the optical admittance

$$X + iZ = 0.4572 + i3.4693$$

Substituting this in Equation 8.82 gives

$$\psi = 80.50\%$$

We can choose to have either a high- or low-index phase-matching layer. Let us choose first a low index and from Equation 8.88 we obtain an optical thickness for the 1.35 index layer of 0.19174 full waves. Equation 8.89 yields a value of 0.05934 for μ that must be matched to the substrate index of 1.52. We start with a low-index quarter-wave and simply work through the sequence of possible admittances:

$$\frac{n_L^2}{\mu}, \quad \frac{n_H^2\mu}{n_L^2}, \quad \frac{n_L^4}{n_H^2\mu}, \quad \frac{n_H^4\mu}{n_L^4} \quad \text{etc.}$$

until we find one sufficiently close to 1.52. The best arrangement in this case involves three layers of each type.

$$\frac{n_H^6\mu}{n_L^6} = 1.6511$$

equivalent to a loss of 0.2% at the interface with the substrate.

The structure so far is then

$$|Ag|\, L''\ LHLHLH|\, \text{Glass} \tag{8.90}$$

with $L'' = 0.19174$ full waves. This can be combined with the following L layer into a single layer $L' = 0.25 + 0.19174 = 0.44174$ full waves, i.e.,

$$|Ag|\, L'\ HLHLH|\, \text{Glass}$$

Since the medium is identical to the substrate, then the matching assembly at the front will be exactly the same as that at the rear, so that the complete design is

$$Glass|\, HLHLH\ L'\ Ag\ L'\ HLHLH|\, \text{Glass}$$

with

Ag 70 nm (physical thickness)
L'' 0.44174 full waves (optical thickness)
H, *L* 0.25 full waves
λ_0 550 nm

The performance of this design is shown in Figure 8.36. Dispersion of the silver has not been taken into account to give a clearer idea of the intrinsic characteristics. The peak is indeed centered at 550 nm with transmittance virtually that predicted.

A high-index matching layer can be handled in exactly the same way. For an index of 2.35, Equation 8.88 yields an optical thickness of 0.1561 and Equation 8.89 gives a value of 0.1426 for μ. Again, the matching quarter-wave stack should start with a low-index layer. There are two possible arrangements, each with H' representing 0.1561 full waves:

$$Ag|H'LHLH|\text{Glass}$$

with $n_H^4\mu/n_L^4 = 1.310$, i.e., a loss of 0.6% at the glass interface, or

$$Ag|H'LHLHL|\text{Glass}$$

with $n_L^6/n_H^4\mu = 1.392$, representing a loss of 0.2% at the glass interface. We choose the second alternative and the full design can then be written

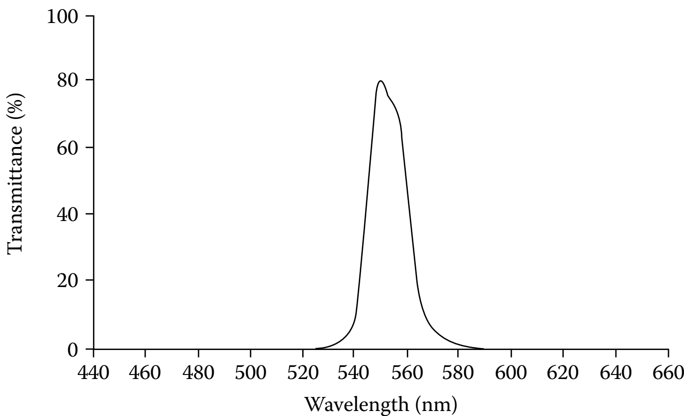

FIGURE 8.36
Calculated performance of the design: Glass|*HLHLH L'* Ag *L' HLHLH*|Glass where $n_{Glass} = 1.52$, Ag = 70 nm (physical thickness) of index 0.055 − *i*3.32, $H = 0.25\lambda_0$ (optical thickness) of index 2.35, $L = 0.25\lambda_0$ (optical thickness) of index 1.35, $L' = 0.4417\lambda_0$ (optical thickness) of index 1.35, and $\lambda_0 = 550$ nm. Dispersion has been neglected.

Glass|$LHLHL\,H'\,Ag\,H'\,LHLHL$| Glass

with

Ag 70 nm (physical thickness)
H' 0.1561 full waves (optical thickness)
H, L 0.25 full waves

The performance of this design is shown in Figure 8.37, where, again, the dispersion of silver has not been taken into account. Peak transmission is virtually as predicted.

When, however, we plot, over an extended wavelength region, the performance of any of these designs, including the metal–dielectric filters from the early part of this chapter, we find that the performance at longer wavelengths appears disappointing. One example, the low-index matched induced-transmission filter is shown in Figure 8.38. In the case of the filters from the early part of this chapter, the rise is smoother but is of a similar order of magnitude. The reason for the rise is, in fact, our assumption of zero dispersion. This means that β is reduced as λ increases. α is always quite small and the performance of the metal layers is determined principally by β. Silver, however, over the visible and near infrared, shows an increase in k that corresponds roughly to the increase in λ so that k/λ is roughly constant (to within around ±20%) over the region 400 nm–2.0 μm. In fact, this behavior is common to most high-performance metals. The dispersion completely alters the picture and is the reason why the first-order metal–dielectric filters do not show longwave sidebands.

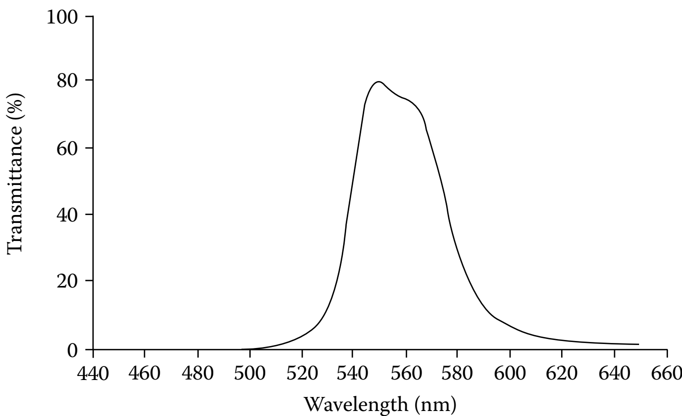

FIGURE 8.37
Calculated performance neglecting dispersion of the design: Glass|$LHLHL\ H'$ Ag H' $LHLHL$|Glass where $n_{Glass} = 1.52$, Ag = 70 nm (physical thickness) of index $0.055 - i3.32$, $H = 0.25\lambda_0$ (optical thickness) of index 2.35, $L = 0.25\lambda_0$ (optical thickness) of index 1.35, $H' = 0.1561\lambda_0$ (optical thickness) of index 2.35, and $\lambda_0 = 550$ nm.

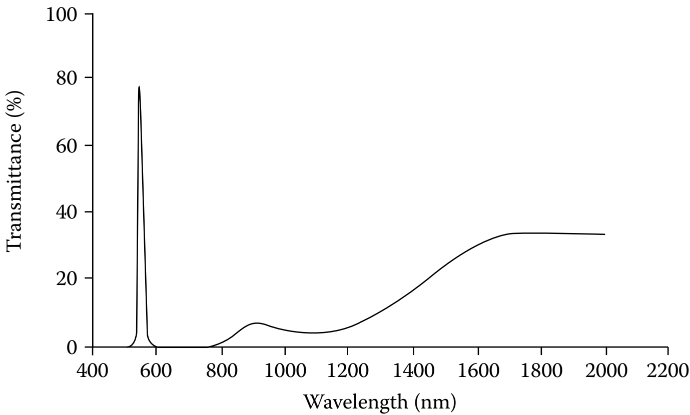

FIGURE 8.38
The design of Figure 8.36 computed over a wider spectral region neglecting dispersion.

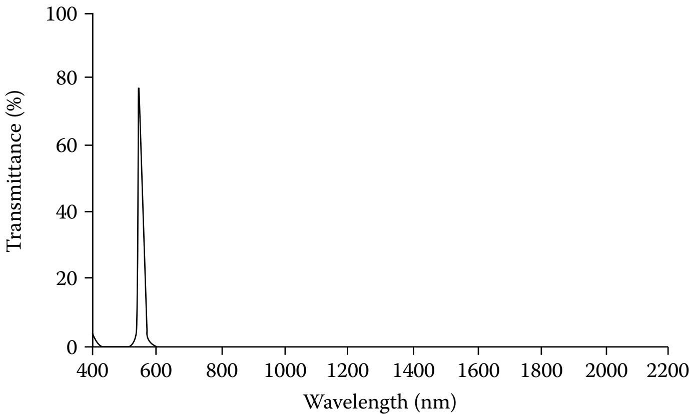

FIGURE 8.39
The design of Figure 8.36 and Figure 8.38 computed this time including dispersion. The rise in transmittance at longer wavelengths has vanished but there is now obvious transmittance at 400 nm.

Taking dispersion into account, the performance of the induced transmission filter improves considerably and is shown in Figure 8.39. Close examination of the rejection, however, Figure 8.40, shows that it is not particularly high, being between 0.01% and 0.1% transmittance over most of the range with an increase to 0.15% in the vicinity of 850 nm. This level of rejection can be acceptable in some applications and the induced-transmission filter represents a very useful, inexpensive general-purpose filter. The dispersion that improves the performance on the longwave side of the peak degrades it on the

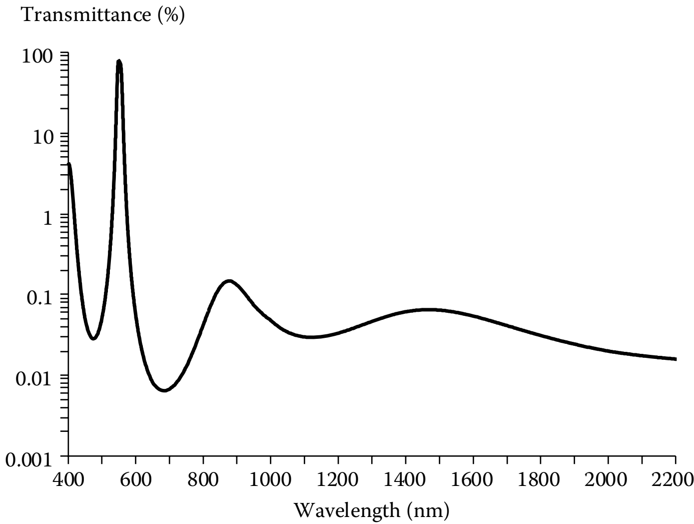

FIGURE 8.40
The filter of Figure 8.39 with performance displayed on a logarithmic scale.

shortwave side, and to complete the filter it is normal to add a longwave-pass absorption glass filter cemented to the induced transmission component.

To improve the rejection of the basic filter, it is necessary to add further metal layers. The simplest arrangement is to have these extra metal layers of exactly the same thickness as the first. The potential transmittance of the complete filter will then be the product of the potential transmittances of the individual layers. The terminal admittances for all the metal layers can be arranged to be optimum quite simply, giving optimum performance for the filter. All that is required is a dielectric layer in between the metal layers, which is twice the thickness given by Equation 8.88 for the first matching layer. We can see why this is so, by imagining a matching stack on the substrate overcoated with the first metal layer. Since its terminal admittance will be optimum, the input admittance will be the complex conjugate, as we have discussed already. Addition of the thickness given by Equation 8.88 renders the admittance real; that is, the admittance locus has reached the real axis. Addition of a further identical thickness must give an equivalent input admittance that is the complex conjugate of the metal input admittance and hence is equal to the optimum admittance. This can be repeated as often as desired.

Returning to our example, a two-metal layer induced-transmission filter will have peak transmittance, if perfectly matched, of $\psi^2 = (0.80501)^2$, that is, 64.8%; a three-metal layer filter should have $\psi^3 = (0.80501)^3$, that is, 52.17%; and so on.

The designs, based on the low-index matching layer version, are then, from Expression 8.90

$$\begin{aligned} &\text{Glass}|HLHLHL\,L''\,Ag\,L''\,L''\,Ag\,L''\,LHLHLH\ \text{Glass} \\ &= \text{Glass}|HLHLH\,L'\,Ag\,L'''\,Ag\,L'\,HLHLH\,|\text{Glass} \end{aligned} \tag{8.91}$$

where

$L' = 0.25 + 0.19174 = 0.44174$ full waves
$L'' = 0.19174$ full waves
$L''' = 2 \times 0.191\,74 = 0.38348$ full waves
Ag = 70 nm

and

$$\text{Glass}|HLHLH\,L'\,Ag\,L'''\,Ag\,L'''\,Ag\,L'\,HLHLH\,|\text{Glass} \tag{8.92}$$

The performance of these two filters on a logarithmic scale is plotted in Figure 8.41 and a considerable improvement is evident.

Unfortunately, these designs, although they do have the peak transmittance predicted, possess a poor pass-band shape, in that it has a hump on the longwave side. The hump can be eliminated by adding an extra half-wave layer to those layers with label L''', i.e.,

$$\text{Glass}\,|HLHLH\,L'\,Ag\,L^{IV}\ Ag\,L'\,HLHLH\,|\text{Glass} \tag{8.93}$$

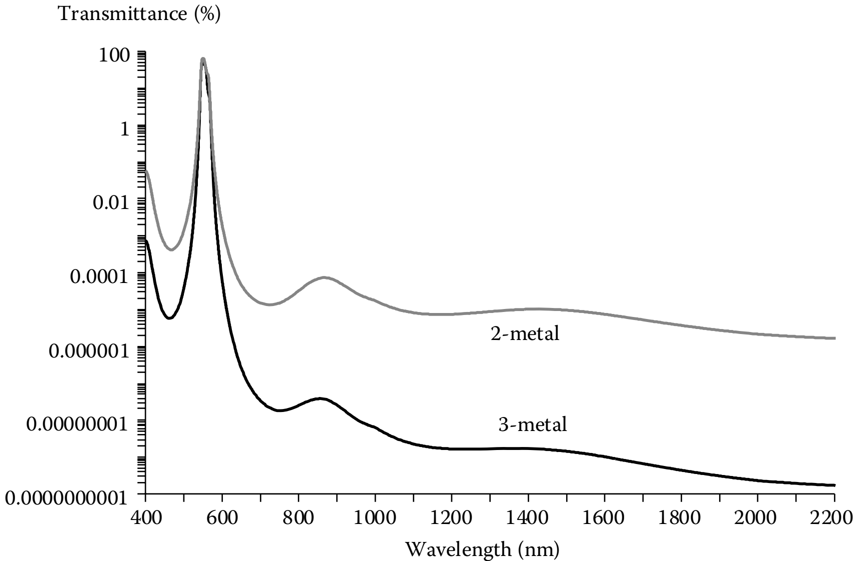

FIGURE 8.41
The performance on a logarithmic scale of the filters of the two-metal design (8.91) and the three-metal (8.92). The rejection is several orders of magnitude better than that of the single-metal design of Figure 8.40.

and

$$\text{Glass}|HLHLHL'\ AgL^{IV}\ AgL^{IV}\ AgL'\ HLHLH|\text{Glass} \tag{8.94}$$

where

$$L^{IV} = 0.5 + 0.38348 = 0.88348 \text{ full waves.}$$

Figure 8.42 shows the form of Designs 8.91 and 8.92 and the hump can clearly be seen together with the improved shape of Designs 8.93 and 8.94.

Dispersion was not included in the computation of Figure 8.42. The rejection over an extended region, including the effects of dispersion, is plotted in Figure 8.43. Unfortunately, the modified Designs 8.93 and 8.94 act as metal–dielectric–metal (M–D–M is a frequently used shorthand notation for such a filter) and metal–dielectric–metal–dielectric–metal (M–D–M–D–M) filters at approximately 1100 nm, which gives a very narrow leak, rising to around 0.15% in the former and 0.05% in the latter. Elsewhere, the rejection is excellent, of the order of 0.0001% at 900 nm and 0.000015% at 1. 5 μm for the former and 0.0000001% at 900 nm and 3×10^{-9}% at 1.5 μm for the latter.

If the leak is unimportant, then the filters can be used as they are, with the addition of a longwave-pass filter of the absorption type as before. For

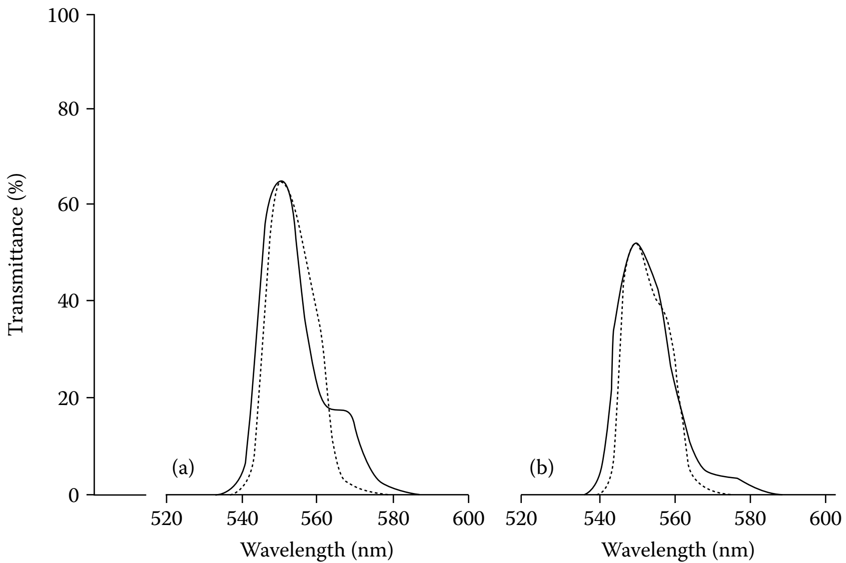

FIGURE 8.42
Performance, neglecting dispersion, of (a) two-metal-layer designs and (b) three-metal-layer designs of induced-transmission filter. The full curves denote Expressions 8.91 and 8.92 and there is a spurious shoulder on the longwave side of the peak in each case. This can be eliminated by the addition of half-wave decoupling layers as the *dashed lines* show. They are derived from Expressions 7.89 and 7.90, respectively.

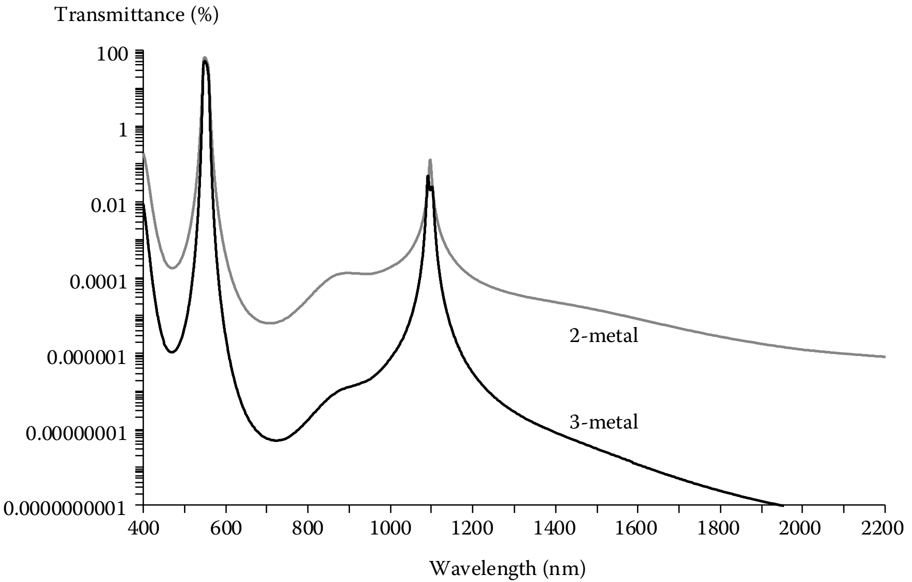

FIGURE 8.43
The extended performance of the filters of Designs 8.93 and 8.94. The spikes at 1050 nm occur because the thick dielectric structures between the metal layers act as rather poor cavities.

the suppression of all-dielectric filter sidebands, it is better to use filters of type 8.91 and 8.92 since the shape of the sides of the pass band is relatively unimportant. The rejection of these filters is excellent and, of course, the leak is missing.

The bandwidth of the filters is not an easy quantity to predict analytically and the most straightforward approach is simply to compute the filter profile. Berning and Turner [34] suggest a figure of merit indicating the potential usefulness of a metal in induced transmission filters as the ratio k/n. The higher this ratio, the better should be the performance of the completed filter. We saw in Chapter 3 that a useful indicator of potential loss in a material is the product nk. The smaller is this quantity, the lower the level of loss.

Induced-transmission filters for the visible region having only one single metal layer are relatively straightforward to manufacture. The thickness of the metal layer can be arrived at by trial and error. If the metal layer is less than optimum in thickness, the effect will be a broadening of the pass band and a rise in peak transmission at the expense of an increase in background transmission remote from the peak. A splitting of the pass band will also become noticeable with the appearance eventually, if the thickness is further reduced, of two separate peaks. If, on the other hand, the silver layer is made too thick, the effect will be a narrowing of the peak with a reduction of peak transmission. The best results are usually obtained with a compromise thickness where the peak is still single in shape but where any further reduction in silver thickness would cause the splitting to appear. A good approximation in practice,

which can be used as a first attempt at a filter, is to deposit the first dielectric stack and to measure the transmittance. The silver layer can then be deposited using a fresh monitor glass so that the optical density is twice that of the dielectric stack. The second cavity and stack can then be added on yet another fresh monitor. A measurement of the transmittance of the complete filter will quickly indicate which way the thickness of the silver layer should be altered in order to optimize the design. Usually, one or two tests are sufficient to establish the best parameters. If, after this optimizing, the background rejection remote from the peak is found to be unsatisfactory, then not enough silver is being used. As the thickness was chosen to be optimum for the two dielectric sections, a pair of quarter-wave layers should be added to each in the design and the trial-and-error optimization repeated. This will also narrow the bandwidth, but this is usually preferable to high background transmission.

In the ultraviolet the available metals do not have as high a performance as, for instance, silver in the visible, and it is very important, therefore, to ensure that the design of a filter is optimized as far as possible; otherwise a very inferior performance will result. An important paper in this field is that by Baumeister et al. [35]. Aluminum is the metal commonly used for this region, and measured and computed results obtained by these workers for filters with aluminum layers are shown in Figure 8.44. The performance achieved is most satisfactory, and the agreement between practical and theoretical curves is good.

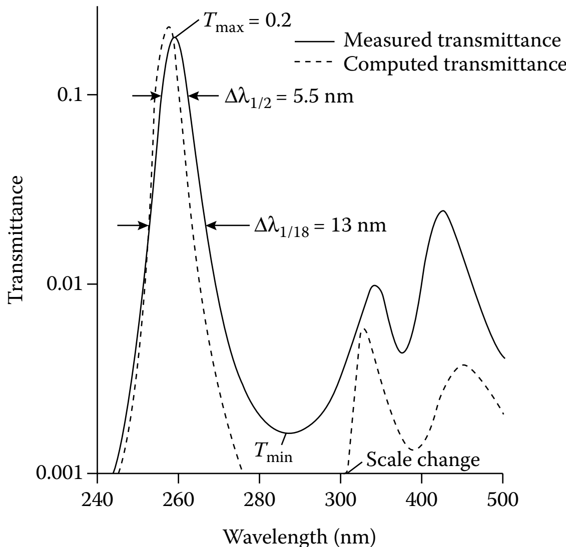

FIGURE 8.44
Computed and measured transmittance of an induced transmission filter for the ultraviolet. Design: Air|*HLHLHLH* 1.76*L* Al 1.76*L* *HLHLHLH*|Quartz where *H* = PbF2 (n_H = 2.0) and *L* = Na_3AlF_6 (n_L = 1.36). The physical thickness of the aluminum layer is 40 nm and λ_0 = 253.6 nm. (After Baumeister, P.W., Costich, V.R., and Pieper, S.C., *Applied Optics* 4, 911–913, 1965.)

Induced-transmission filters have been the subject of considerable study by many workers. Metal–dielectric multilayers are reviewed by MacDonald [36]. A useful, account of induced-transmission filters is given by Lissberger [37]. Multiple cavity induced-transmission filters have been described by Maier [38]. An alternative design technique for metal–dielectric filters involving symmetrical periods has been published by Macleod [39]. Symmetrical periods for metal–dielectric filter design have also been used by McKenney [40] and by Landau and Lissberger [41].

8.7 Measured Filter Performance

Not a great deal has been published on the measured performance of actual filters, and the main source of information for a prospective user is always the literature issued by manufacturers. Performance of current production filters tends to improve all the time so that inevitably such information does not remain up to date for long. Two papers [42,43] quote the results of a number of tests on commercial filters, and, although they were written some time ago, they will still be found useful sources of information.

Blifford examined the performance of the products of four different manufacturers, covering the region 300–1000 nm. The variation of peak wavelength with angle of incidence was found to be similar to the relationship already established (see Section 8.2.4). Unfortunately, information on the design and materials is lacking, so that the expression for the effective index cannot be checked. The sensitivities to tilt varied from $P = 0.22$ to $P = 0.51$, where P corresponds to the quantity $1/n^{*2}$ in Equations 8.29, 8.38, and 8.39. Blifford suggests that an average value of 0.35 for P would probably be the best value to assume in any case where no other data were available. Changes in peak transmittance with angle of incidence were found, but were not constant from one filter to another and apparently must always be measured for each individual filter. Possibly, the effect is due to the absorption filters that are used for sideband suppression and that, because they do not show any shift in edge wavelength with angle of incidence, may cut into the pass band of the interference section at large angles of incidence. In most cases examined, the change in peak transmission was less than 10% for angles of 5°–10°.

The variation in peak transmittance over the surface of the filter was also measured in a few cases. For a typical filter with a peak wavelength of 500 nm and a bandwidth not explicitly mentioned, but probably 2.1 nm (from information given elsewhere in the paper), the extremes of peak transmission were 54% and 60%. This is, in fact, one aspect of a variation of peak wavelength, bandwidth, and peak transmittance that frequently occurs, although the magnitude can range from very small to very large. The cause

is principally the adsorption of water vapor from the atmosphere before a cover slip can be cemented over the layers, and it is dealt with in greater detail in Chapter 12. Infrared filters appear to suffer less from this defect than visible and near infrared filters.

Another parameter measured by Blifford was the variation of peak wavelength with temperature. Variation of the temperature from –60° C to +60° C resulted in changes of peak wavelength from +0.01 nm $°C^{-1}$ to +0.03 nm $°C^{-1}$. The relationship was found to be linear over the whole of this temperature range with little, if any, change in the pass-band shape and peak transmittance. In most cases, the temperature coefficients of bandwidth and peak transmittance were found to be less than 0.01 $°C^{-1}$. Filters for the visible region have also been the subject of a detailed study by Pelletier and his colleagues [44]. The shift with temperature for any filter is a function of the coefficients of optical thickness change with temperature, depending on the design of the filter and especially on the material used for the cavities. Measurements made on different filter designs yielded the following coefficients of optical thickness for the individual layer materials:

$$\text{zinc sulfide } (4.8 \pm 1.0) \times 10^{-5}\ °C^{-1}$$
$$\text{cryolite } (3.1 \pm 0.7) \times 10^{-5}\ °C^{-1}$$

Hysteresis is frequently found with temperature cycling narrowband filters over an extended temperature range. The hysteresis is particularly pronounced when the filters are uncemented and when they are heated toward 100 °C. It is usually confined to the first cycle of temperature, takes the form of a shift of peak wavelength toward shorter wavelengths and is caused by the desorption of water, discussed again in Chapter 12.

Our ideas of the effects of temperature on optical coatings were completely revolutionized by an important paper by Takahashi [45]. Films that have been deposited by the energetic processes (see Chapter 11) usually exhibit lower temperature coefficients than thermally evaporated, even when the effects of moisture desorption and adsorption are discounted. This is at first sight a quite surprising result. But the explanation appears to lie in the microstructure. The lateral thermal expansion of the loosely packed columns in the thermally evaporated films enhances the drifts due to temperature changes. In the energetically deposited films, the material is virtually bulk-like in that there are no voids in between any residual columns and so the material exhibits bulk like properties. The change in characteristics with a change in temperature now corresponds to what would be expected from bulk materials. Indeed, Takahashi [45] has shown that for multiple-cavity narrowband filters, and surely for other filter types, once the design and materials are chosen, the expansion coefficient of the substrate dominates the behavior and can even change the sense of the induced spectral shift. The stress induced in the coating by the differential lateral expansion and contraction of substrate and coating is translated by Poisson's ratio into

a swelling or contraction normal to the film surfaces. Since the expansion coefficients of film materials are usually higher than that of the substrate, the birefringence together with the film swelling increases the optical thickness and, with increasing temperature, moves the characteristic to a longer wavelength. Increasing the expansion coefficient of the substrate reduces the long-wave shift. As a result of this modeling and improved understanding, temperature coefficients of peak wavelength shift at 1550 nm of 3 pm °C^{-1} (pm is picometer, i.e., 0.001 nm, so this figure represents 0.0002% °C^{-1}) have routinely been achieved in energetically deposited tantala/silica filters for communication purposes and shifts as low as 1 pm °C^{-1} are possible. We shall return to this model in more detail in Chapter 12.

An effect of a different kind, although related, is the subject of a contribution by Title and his colleagues [46,47]. A permanent shift of a filter characteristic toward shorter wavelengths amounting to a few tenths of nanometers accompanied by a distortion of pass-band shape was produced by a high level of illumination. The filters were for the Hα wavelength, 656.3 nm, and the changes were interpreted as due to a shift in the properties of the zinc sulfide material, the fundamental nature of the shift being unknown. Zinc sulfide can be transformed into zinc oxide by the action of ultraviolet light, especially in the presence of moisture, and the shifts that were observed could probably have been caused by such a mechanism.

The possibility of variations in filter properties both over the surface of the filter and as a function of time, temperature and illumination level should clearly be borne in mind in the designing of apparatus incorporating filters.

A useful survey that compares the performance achievable from different types of narrowband filters was the subject of a report by Baumeister [48].

Baker and Yen [42] studied the variations in properties of infrared filters with angle of incidence and temperature, and reported both theoretical and experimental results. Accurate calculation of the effects of changes in the angle of incidence yielded a variation of peak wavelength of the expected form, but no significant variation of bandwidth for angles of incidence up to 50°. They also calculated that the peak transmittance and the shape of the pass band should remain unchanged for angles up to 45°. For angles above 50°, both the shape and the peak transmittance gradually deteriorated. The calculations were confirmed by measurements on real filters.

The effects of varying temperatures were also investigated both theoretically and practically. As in the case of the shorter wavelength filters examined by Blifford, they measured a shift towards longer wavelengths with increasing temperature. For temperatures down to liquid helium the filters show little loss of peak transmittance or variation of characteristic pass-band shape. However, serious losses in transmittance occurred above 50 °C. Although not mentioned in the paper, this is probably due to the use of germanium, either as substrate or as one of the layer materials. Germanium always exhibits a marked fall in transmittance at elevated temperatures above 50 °C. Baker and Yen make the point that filters designed to be least sensitive to variations

in the angle of incidence are usually most sensitive to temperature and vice versa. The temperature coefficients of peak wavelength that they quote vary from +0.0035% °C^{-1} to +0.0125% °C^{-1}. Unfortunately, neither the materials used in the filters nor the designs are quoted in the paper, but it is likely that the figures will apply to most interference filters for the infrared.

Similar measurements of the temperature shift of infrared filters were made at Grubb Parsons. The materials used were zinc sulfide and lead telluride, and the filters that had first-order high-index cavities gave temperature coefficients of peak wavelength of −0.0135% °C^{-1}. These filters were of the type used in the selective chopper radiometer described in Chapter 15. The negative temperature coefficient is usual with filters having lead telluride as one of the layer materials. This negative coefficient in lead telluride is especially useful as it tends to compensate for the positive coefficient in zinc sulfide, and Evans et al. [49] have succeeded in designing and constructing filters using lead telluride that have zero temperature coefficient.

References

1. Epstein L I 1952 The design of optical filters *Journal of the Optical Society of America* **42** 806–810
2. Turner A F 1950 Some current developments in multilayer optical films *Journal de Physique et le Radium* **11** 443–460
3. Bates B and Bradley D J 1966 Interference filters for the far ultraviolet (1700A to 2400A) *Applied Optics* **5** 971–975
4. Seeley J S 1964 Resolving power of multilayer filters *Journal of the Optical Society of America* **54** 342–346
5. Hemingway D J and Lissberger P H 1973 Properties of weakly absorbing multilayer systems in terms of the concept of potential transmittance *Optica Acta* **20** 85–96
6. Dobrowolski J A 1959 Mica interference filters with transmission bands of very narrow half-widths *Journal of the Optical Society of America* **49** 794–806
7. Austin R R 1972 The use of solid etalon devices as narrow band interference filters *Optical Engineering* **11** 65–69
8. Candille M and Saurel J M 1974 Réalisation de filtres “double onde” a bandes passantes très étroites sur supports en matière plastique (mylar) *Optica Acta* **21** 947–962
9. Smith S D and Pidgeon C R 1963 Application of multiple beam interferometric methods to the study of CO2 emission at 15μm *Mémoires de la Société Royale des Sciences Liège 5th Series* **9** 336–349
10. Roche A E and Title A M 1974 Tilt tunable ultra narrow-band filters for high resolution photometry *Applied Optics* **14** 765–770
11. Floriot J, Lemarchand F, and Lequime M 2006 Solid-spaced filters: an alternative for narrow-bandpass applications *Applied Optics* **45** 1349–1355

12. Dufour C and Herpin A 1954 Applications des methodes matricielles au calcul d'ensembles complexes de couches minces alternees *Optica Acta* **1** 1–8
13. Lissberger P H 1959 Properties of all-dielectric filters. I. A new method of calculation *Journal of the Optical Society of America* **49** 121–125
14. Lissberger P H and Wilcock W L 1959 Properties of all-dielectric interference filters. II. Filters in parallel beams of light incident obliquely and in convergent beams *Journal of the Optical Society of America* **49** 126–130
15. Pidgeon C R and Smith S D 1964 Resolving power of multilayer filters in non-parallel light *Journal of the Optical Society of America* **54** 1459–1466
16. Hernandez G 1974 Analytical description of a Fabry Perot spectrometer. 3: Off-axis behaviour and interference filters *Applied Optics* **13** 2654–2661
17. For example, Reports 4, 5 and 6 of Contract DA-44-009-eng-1113 covering the period January–October 1953. The contract reports were once obtainable from the Engineer Research and Development Laboratories, Fort Belvoir, Virginia 22060, USA, but are now, unfortunately, out of print.
18. Turner A F 1952 Wide pass band multilayer filters *Journal of the Optical Society of America* **42** 878(a)
19. Smith S D 1958 Design of multilayer filters by considering two effective interfaces *Journal of the Optical Society of America* **48** 43–50
20. Knittl Z 1965 *Dielektrische Interferenzfilter mit rechteckigem Maximum*, in *Proc Coll on Thin Films* (Budapest: 153–161
21. Knittl Z 1976 *Optics of Thin Films* (London: John Wiley and Sons)
22. Thelen A 1966 Equivalent layers in multilayer filters *Journal of the Optical Society of America* **56** 1533–1538
23. Baumeister P 2001 Design of a coarse WDM bandpass filter using the Thelen bandpass design method *Opt. Express* **9** 652–657
24. Baumeister P 2003 Application of microwave technology to design an optical multilayer bandpass filter *Applied Optics* **42** 2407–2414
25. Baumeister P W 1982 Use of microwave prototype filters to design multilayer dielectric bandpass filters *Applied Optics* **21** 2965–2967
26. Barr E E 1974 Visible and ultraviolet bandpass filters *Proceedings of the Society of Photo-Optical Instrumentation Engineers* **50** 87–118
27. Neilson R G T and Ring J 1967 Interference filters for the near ultra-violet *Journal de Physique* **28** C2,270–C2,275
28. Malherbe A 1974 Interference filters for the far ultraviolet *Applied Optics* **13** 1275–1276
29. Baumeister P W and Jenkins F A 1957 Dispersion of the phase change for dielectric multilayers. Application to the interference filter *Journal of the Optical Society of America* **47** 57–61
30. Baumeister P W, Jenkins F A, and Jeppesen M A 1959 Characteristics of the phase-dispersion interference filter *Journal of the Optical Society of America* **49** 1188–1190
31. Giacomo P, Baumeister P W, and Jenkins F A 1959 On the limiting bandwidth of interference filters *Proceedings of the Physical Society* **73** 480–489
32. Ritchie F S. Unpublished work on Ministry of Technology Contract KX/LSO/C.B.70(a).
33. Hass G and Hadley L 1972 *Optical constants of metals*, in *American Institute of Physics Handbook* Gray D E Editor (New York/London: McGraw-Hill Book Company) 6.124–6.156

34. Berning P H and Turner A F 1957 Induced transmission in absorbing films applied to band pass filter design *Journal of the Optical Society of America* **47** 230–239
35. Baumeister P W, Costich V R, and Pieper S C 1965 Bandpass filters for the ultraviolet *Applied Optics* **4** 911–913
36. MacDonald J 1971 *Metal-Dielectric Multilayers* (London: Adam Hilger)
37. Lissberger P H 1981 Coatings with induced transmission *Applied Optics* **20** 95–104
38. Maier R L 1967 2M interference filters for the ultraviolet *Thin Solid Films* **1** 31–37
39. Macleod H A 1978 A new approach to the design of metal-dielectric thin-film optical coatings *Optica Acta* **25** 93–106
40. McKenney D B 1969 *Ultraviolet interference filters with metal-dielectric stacks* PhD Dissertation University of Arizona
41. Landau B V and Lissberger P H 1972 Theory of induced-transmission filters in terms of the concept of equivalent layers *Journal of the Optical Society of America* **62** 1258–1264
42. Baker M L and Yen V L 1967 Effects of the variation of angle of incidence and temperature on infrared filter characteristics *Applied Optics* **6** 1343–1351
43. Blifford I H 1966 Factors affecting the performance of commercial interference filters *Applied Optics* **5** 105–111
44. Pelletier E, Roche P, and Bertrand L 1974 On the limiting bandwidth of interference filters: influence of temperature during production *Optica Acta* **21** 927–946
45. Takahashi H 1995 Temperature stability of thin-film narrow-bandpass filters produced by ion-assisted deposition *Applied Optics* **34** 667–675
46. Title A M 1974 Drift in interference filters. 2: Radiation effects *Applied Optics* **13** 2680–2684
47. Title A M, Pope T P, and Andelin J P 1974 Drift in interference filters. Part 1 *Applied Optics* **13** 2675–2679
48. Baumeister P W 1973 Thin films and interferometry. 13 March 1973 *Applied Optics* **12** 1993–1994
49. Evans C S, Hunneman R, Seeley J S, and Whatley A 1976 Filters for *v*2 band of CO2: monitoring and control of layer deposition *Applied Optics* **15** 2736–2745

9

Tilted Coatings

We have already seen in Chapter 2 that the characteristics of coatings change when they are tilted with respect to the incident illumination and that the particular way in which they change depends on the angle of incidence. We have studied the shifts that are induced in narrowband filters. Narrowband filters are a simple case because the tilt angle is usually small and we can assume that the major effect is in the phase thickness of the layers, which is affected equally for each plane of polarization. For larger tilts, however, the admittances are also affected and then the performance for each plane of polarization differs. Some important applications involve the difference in performance between one plane and the other, which can be controlled to some extent, making possible the construction of phase retarders and polarizers. On the other hand, the differences in performance can create problems, and although it is impossible to cancel the effects completely, there are ways of modifying it so that a more acceptable performance may be achieved. Then there are some, at first sight, strange effects that occur with dielectric-coated reflectors. Under certain conditions and at reasonably high angles of incidence, sharp absorption bands can exist for one plane of polarization. This can create difficulties with dielectric-overcoated reflectors such as protected silver. The chapter begins with the addition of tilting effects to the admittance diagram, which allows us to explain qualitatively the behavior of many different types of tilted coatings including overcoated reflectors and which involves a slight modification to the traditional form of the tilted admittances. Next, there is a description of polarizers followed by an account of phase retarders. Some coatings where the polarization splitting is undesirable, such as dichroic filters, are described with ways of reducing this splitting. Finally, some antireflection coatings at high angles of incidence are included.

Some of the material in this chapter has already been mentioned and discussed in earlier chapters but here we attempt to introduce a consistent and connected account and so there are some advantages in repeating what has been said before in the present context.

9.1 Modified Admittances and the Tilted Admittance Diagram

The form of the admittances and the phase thickness of a film illuminated at oblique incidence are given in Chapter 2 and have already been used in

considering the performance of some coatings including narrowband filters. For dielectric materials they are:

$$\delta = \frac{2\pi n d \cos\vartheta}{\lambda} \tag{9.1}$$

$$\eta_s = y \cos\vartheta \tag{9.2}$$

$$\eta_p = \frac{y^2}{\eta_s} = \frac{y}{\cos\vartheta} \tag{9.3}$$

where

$$n_0 \sin\vartheta_0 = n_1 \sin\vartheta_1 = n_2 \sin\vartheta_2 = \cdots \tag{9.4}$$

and n, y, d, and ϑ are the values appropriate to the particular material, the suffix zero indicating, as usual, the incident medium.

The problem presented when the values of n and y are permitted to be complex, is solved by adopting a slightly different form of Expressions 9.1 through 9.3. The incident medium retains its real characteristics so that it is free from absorption. Then, ϑ, the angle of incidence, has to be permitted to become complex to support a complex $\sin\vartheta$. However, we can avoid the complex angle by noting that it is $\cos\vartheta$ that we need and $\cos^2\vartheta$ is just $1 - \sin^2\vartheta$. Then the arrangement when absorbing materials are concerned becomes

$$\delta = \frac{2\pi d(n^2 - k^2 - n_0^2 \sin^2\vartheta_0 - 2ink)^{1/2}}{\lambda} \tag{9.5}$$

where the square root must be taken in the fourth quadrant, and

$$\eta_s = (n^2 - k^2 - n_0^2 \sin^2\vartheta_0 - 2ink)^{1/2} \tag{9.6}$$

and

$$\eta_p = \frac{(n - ik)^2}{\eta_s} \tag{9.7}$$

where we are working in free space units.

The two sets of relationships are completely compatible. Equations 9.1 through 9.3 become Equations 9.5 to 9.7 when $\cos\vartheta$ is permitted to become complex.

The calculation of multilayer properties at angles of incidence other than normal simply involves the use of the above expressions instead of those for normal incidence. It should be emphasized that the appropriate tilted values are to be adopted for incident medium and substrate as well as for the films. Unfortunately, the use of the admittance diagram is rendered much more

complicated because of the change in the incident admittance. The isoreflectance and isophase contours depend on the admittance of the incident medium and we therefore need one set for *s*-polarization and one quite different set for *p*-polarization, as well as completely new sets each time the angle of incidence is changed. Fortunately, there is a way round this problem, which carries some other advantages as well.

It has been shown by Thelen [1] that the properties of a multilayer are unaffected if all the admittances are multiplied or divided by a constant factor, and indeed it is usual to divide the admittances by $\mathscr{Y}$, the admittance of free space, so that the normal incidence admittance is numerically equal to the refractive index. We now propose an additional correction to the admittances, the dividing of the *s*-polarized admittances, and the multiplying of the *p*-polarized admittances, by $\cos\vartheta_0$. This has the effect of preserving, for both *s*- and *p*-polarization, the admittance of the incident medium at its normal incidence value, regardless of the angle of incidence, and means that the isoreflectance and isophase contours of the admittance diagram retain their normal incidence values whatever the angle of incidence or plane of polarization. We can call these admittances simply the *modified admittances,* and the expressions for them become for dielectric materials

$$\eta_s = \frac{y\cos\vartheta}{\cos\vartheta_0} \tag{9.8}$$

and

$$\eta_p = \frac{y\cos\vartheta_0}{\cos\vartheta} \tag{9.9}$$

and for absorbing materials

$$\eta_s = \frac{(n^2 - k^2 - n_0^2\sin^2\vartheta_0 - 2ink)^{1/2}}{\cos\vartheta_0} \tag{9.10}$$

and

$$\eta_p = \frac{(n - ik)^2}{\eta_s} \tag{9.11}$$

the fourth quadrant solution being the correct one for the square root.

The values of reflectance, transmittance, absorptance, and phase changes on either transmission or reflection are completely unchanged by the adoption of these values for the admittances. Since the expressions involve $\cos\vartheta_0$ and $\cos\vartheta$, which are connected by the admittance of the incident medium, then the dependence of the modified admittances on the index of the incident medium will be somewhat different from the unmodified, traditional ones. Nevertheless, we shall see that this does carry some advantages.

We consider first purely dielectric materials. In this case, provided that $n_0 \sin \vartheta_0$ is less than n, the film index, then the two values for the modified admittances are real and positive. If, however, n_0 is greater than n, then there is a real value of ϑ_0 at which $n_0 \sin \vartheta_0$ is equal to n. This angle is known as the *critical angle,* and, for angles of incidence greater than this value, the admittances are imaginary. We will consider what happens for angles of incidence beyond critical later. First, we will limit ourselves to angles less than critical where the admittances are real.

First, let us consider air of index unity as the incident medium. We recall that all transparent thin-film materials have refractive index greater than unity. In Figure 9.1 the modified admittance is shown for a number of thin-film materials as a function of angle of incidence. The p-admittances of all materials cross the line $n = 1$ at the value known as the Brewster angle for which the single-surface p-reflectance is zero. The s-admittances all increase away from the line $n = 1$, so that the single-surface s-reflectance simply increases with angle of incidence. Since all these materials are dielectric, their modified optical thickness is real and, therefore, although a correction has to be made for the effect of angle of incidence, quarter- and half-wave layers

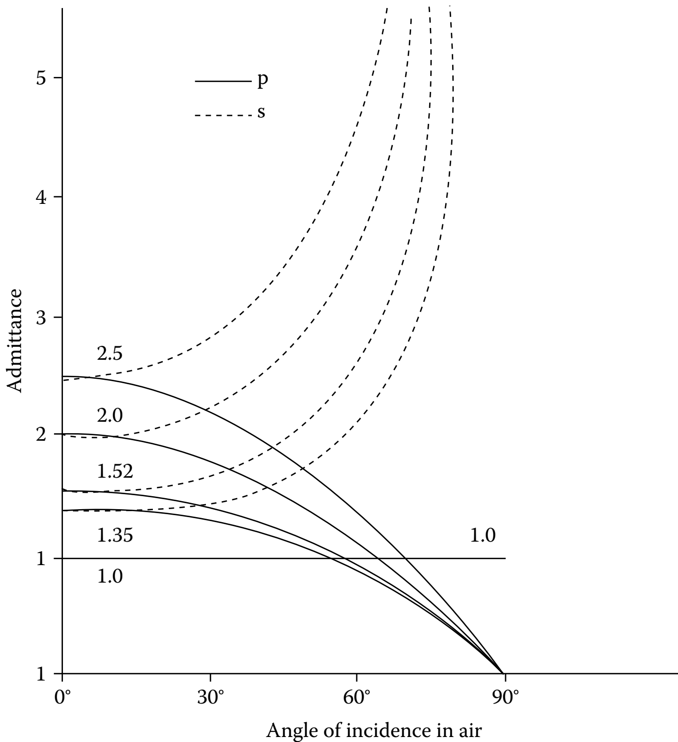

FIGURE 9.1
Modified p- and s-admittances (i.e., including the extra factor of $\cos \vartheta_0$) of materials of indices 1.0, 1.35, 1.52, 2.0, and 2.5 for an incident medium of index 1.0.

can be produced at non-normal incidence just as readily as at normal. It cannot be too greatly emphasized that although the optical thickness changes with angle of incidence, it does not vary with the plane of polarization.

It is possible to make several deductions directly from Figure 9.1. The first is that, for any given pair of indices, the ratio of the *s*-admittances increases with angle of incidence, while that for *p*-admittances reduces. Since the width of the high-reflectance zone of a quarter-wave stack decreases with decreasing ratio of these admittances, the width will be less for *p*-polarized light than for *s*-polarized. As we shall shortly see, this effect is used in a useful type of polarizer. The splitting of the admittance of dielectric layers means also that there is a relative phase shift between *p*- and *s*-polarized light reflected from a high-reflectance coating when the layers depart from quarter-waves. This effect can be used in the design of phase retarders and we will give a brief account of this. The diagram also helps us to consider the implications of antireflection coatings for high angles of incidence. A frequent requirement is an antireflection coating for a crown glass of index around 1.52. For a perfect single-layer coating, we should have a quarter wave of material of optical admittance equal to the square root of the product of the admittances of the glass and the incident medium. At normal incidence in air there is, of course, no sufficiently robust material with index as low as 1.23. For greater angles of incidence, the *s*-polarized reflectance increases still further from its normal incidence value and the admittance required for a perfect single-layer antireflection coating remains outside the range of practical materials, corresponding to still lower indices of refraction. The *p*-polarized behavior is, however, completely different, and in the range from approximately 50° to 70° the admittance required for the antireflection coating is within the range of what is possible. No coating is required, of course, at the Brewster angle. For angles greater than the Brewster angle, the index required is *greater* than that of the glass. Note, however, that the Brewster condition implies two solutions to the antireflection coating for *p*-polarization. The other solution usually corresponds to a very low unobtainable index. Antireflection coatings for high angles of incidence will also be discussed shortly.

The behavior of dielectric materials when the incident medium is of a higher index (one that is within the range of available thin-film materials) is somewhat more complicated. Figure 9.2 illustrates the variation of the admittances when the incident medium is glass of index 1.52. There is the familiar splitting of the *s*- and *p*-polarized admittances, increasing, as before, with angle of incidence. For indices lower than that of the glass, it is possible to reach the critical angle, and, at that point, the admittances reach either zero or infinity and disappear from the diagram. Their behavior beyond the critical angle will be discussed shortly. A further, very important feature is that, while for indices higher than that of the incident medium the *p*-polarized admittance falls with angle of incidence, for indices lower than the incident medium the *p*-polarized admittance rises. All cut the incident medium

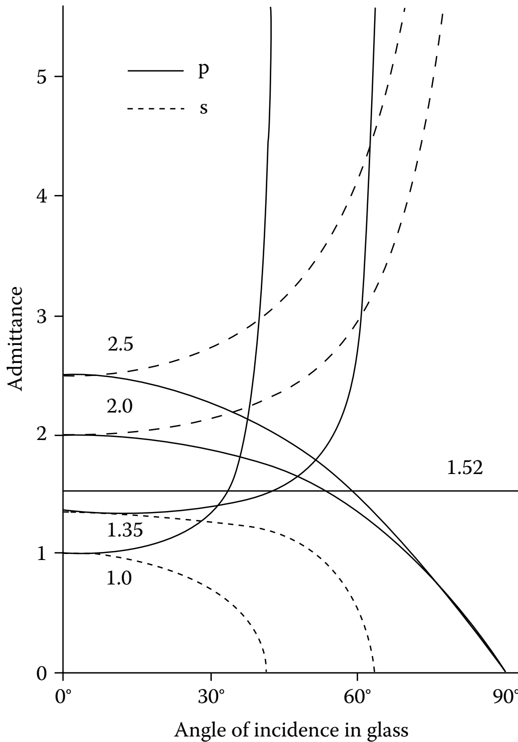

FIGURE 9.2
Modified p- and s-admittances (i.e., including the extra factor of cos ϑ_0) of materials of indices 1.0, 1.35, 1.52, 2.0, and 2.5 for an incident medium of index 1.52.

admittance at the Brewster angle, but now a new phenomenon is apparent. The p-admittance curves for materials of index lower than that of the incident medium intersect the curves corresponding to higher indices. An immediate deduction is that a quarter-wave stack, composed of such pairs of materials, will simply behave, at the angle of incidence corresponding to the point of intersection, as a thick slab of material. Provided the admittances of substrate, thin films and incident medium are not too greatly different, the p-reflectance will be low. The ratio of the s-admittances is large, because their splitting increases with angle of incidence, and so the corresponding s-reflectance is high and the width of the high-reflectance zone, large. This is the basic principle of the MacNeille polarizing beam splitter [2] that we will return to in a later section. The range of useful angles of incidence will depend partly on the rate at which the curves of p-polarized admittance diverge on either side of the intersection, and this can be estimated from the diagram.

Apart from the polarization-splitting of the admittance, the behavior of dielectric layers at angles of incidence less than critical is reasonably straightforward and does not involve difficulties of a more severe order than exist at

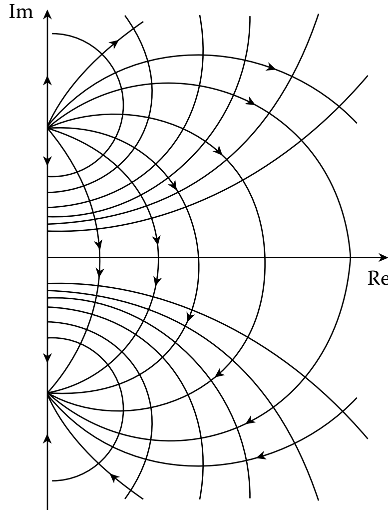

FIGURE 9.3
Admittance loci for an ideal metal with admittance $-ik$. The loci begin at the point ik and terminate on $-ik$. Equi-thickness contours are also shown at no fixed intervals. Similar loci are obtained for *s*-polarized frustrated total reflectance (*FTR*) layers. For *p*-polarized *FTR* layers, the shape of the loci is similar but they are traced in the opposite direction.

normal incidence. The behavior becomes rather more complicated, and interesting, with angles beyond critical, and then, when metal films are introduced, however, the behavior becomes still stranger especially when metal and dielectric films are combined.

We know already that the admittance locus of a dielectric layer at normal incidence is a circle centered on the real axis. Tilted dielectric layers at angles of incidence less than critical still have circular loci that can be calculated from the tilted admittances in exactly the same way. Provided the modified admittances are used in constructing the loci then the isoreflectance and isophase circles on the admittance diagram will remain exactly the same as at normal incidence for both *p*- and *s*-polarization.

The admittance of a metal layer is a little more complicated than a dielectric. For a lossless metal in which the refractive index, and hence the optical admittance, is purely imaginary and given by $-ik$, the loci are a set of circles with centers on the real axis and passing through the points ik and $-ik$ on the imaginary axis. Figure 9.3 shows the typical form. The circles, like the dielectric ones, are traced out clockwise starting on ik and ending on $-ik$. Real metallic layers do depart from this ideal model but if the metal is of high performance, i.e., if the ratio k/n is high, then the loci are similar to the perfect case. It is as if the diagram were rotated slightly about the origin so that the points where all circles intersect are $(n, -k)$ and $(-n, k)$, respectively, although the circles can never reach the point $(-n, k)$ since admittance loci are constrained to the first and second quadrants of the admittance diagram.

Figure 9.4 shows a set of optical admittance loci calculated for silver, $n - ik$ = 0.075 – i3.41 [3] demonstrating this typical behavior, although the departure from ideal can be seen as very small. The direction of the loci is perhaps now better described as terminating on (n, –k), because although most are still described in a clockwise direction, it is possible for some very truncated loci now to come from the left of the end point, and some of these are strictly counter clockwise in direction. We will omit from the discussion in this chapter metals not of high optical quality for which the loci resemble a set of spirals terminating at (n, –k). What happens at oblique incidence?

The phase thickness at normal incidence is

$$\delta = \frac{2\pi(n - ik)d}{\lambda} \tag{9.12}$$

dominated by the imaginary part. At oblique incidence, it becomes

$$\delta = \frac{2\pi(n^2 - k^2 - n_0^2 \sin^2 \vartheta_0 - 2ink)^{1/2} d}{\lambda} \tag{9.13}$$

still in the fourth quadrant. Since $n_0 \sin \vartheta_0$ is normally small compared with k, it has little effect on the phase thickness. It reduces the real part slightly and increases the imaginary part, but the effect is small, and the behavior is essentially similar to that at normal incidence. At an angle of incidence of 80° in air, for example, the phase thickness of silver changes from $2\pi(0.075 - i3.41)d/\lambda$ to $2\pi(0.00721 - i3.549)d/\lambda$. The change in the modified admittance, therefore, is mainly due to the $\cos \vartheta_0$ term. The ratio of real to

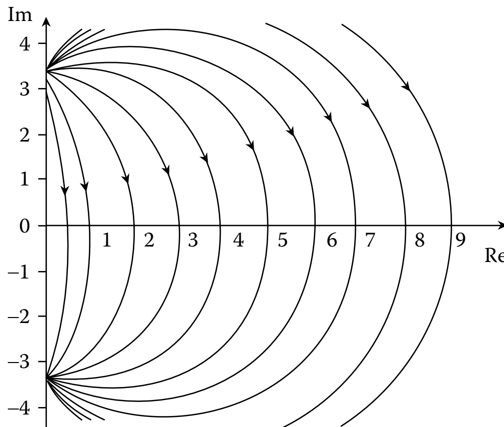

FIGURE 9.4
Admittance loci for silver at normal incidence in the visible region. The value assumed for the optical constants is 0.075 – i3.51 (Berning, P.H. and Turner, A.F., *Journal of the Optical Society of America*, 47, 230–239, 1957.).

imaginary parts remains virtually the same, and the *p*-admittance simply moves toward the origin (both real and imaginary parts reduced) and the *s*-admittance away from the origin. Thus, the principal effect for high-performance metal layers with tilt is an expansion of the circular loci for *s*-polarization and a contraction for *p*-polarization. The basic form remains the same.

9.2 Application of the Admittance Diagram

The shift in the modified optical admittance does mean that the phase shift on reflection from a massive metal will vary with angle of incidence. For silver, or most other high-performance metals, at normal incidence, the phase shift will be in the second quadrant. As the angle of incidence increases, the movement of the *p*-polarized admittance toward the origin implies that the *p*-polarized phase shift moves toward the first quadrant. We know that isoreflectance circles interest the real axis in two points with product y_0. We know, therefore, that the isoreflectance circle in Figure 9.5, *ACB*, which is tangent to the metal admittance line at point *C*, must have $OA \cdot OB = y_0^2$. Geometry tells us that OC^2 is equal to $OA \cdot OB$ and must be given by y_0^2. The circle centered on the origin and passing through the point y_0 on the

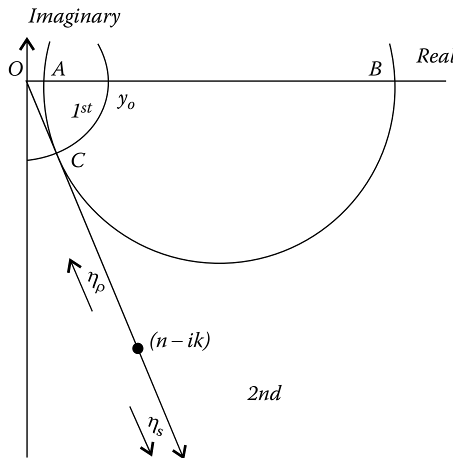

FIGURE 9.5
The variation of the modified admittance of a typical high-performance metal as the angle of incidence is increased. At normal incidence, both *s* and *p*-polarizations have admittance $(n - ik)$. As ϑ_0 increases, $\cos \vartheta_0$ gradually drops from unity at normal incidence to zero at grazing incidence. The modified η_p, therefore, drops toward the origin while η_s moves away. Geometry tells us that a minimum *p*-reflectance occurs at point *C* where the phase shift on reflection crosses the boundary between second and first quadrants.

real axis divides the lower quadrant of the admittance diagram into reflectance phase shifts in the first and second quadrants, as shown in Figure 9.5 and must also pass through *C*. The point C, therefore, marks a minimum *p*-reflectance and a phase shift on reflection of 90°. Because the behavior resembles somewhat the Brewster phenomenon with dielectric surfaces, the angle is known as the pseudo-Brewster angle. At the pseudo-Brewster angle, the phase shift for *s*-reflectance is not quite 180° and so the angle of incidence has to increase slightly for the difference in phase shift between the two polarizations to become 90°. This slightly greater angle is called the *principal angle*. We can see that a reasonable approximation for the pseudo-Brewster angle is given by $\cos\vartheta_0 = y_0/(n^2 + k^2)^{1/2}$. For silver with optical constants ($0.075 - i3.41$) in air, this gives about 73°. Accurate calculation makes it slightly nearer 72°. The reflectance for *s*-polarized light increases, while for *p*-polarized light it shows a very slight drop initially to a shallow minimum, that occurs, it is readily shown, just as the modified admittance crosses the boundary in the admittance diagram between the first and second quadrants. After the minimum, the *p*-reflectance rises to 100% at grazing incidence.

Now we examine what happens when a metal layer is overcoated with a dielectric layer. The arrangement is sketched schematically in Figure 9.6. Provided the admittance η_f of the dielectric layer is less than $(\eta_m\eta_m^*)^{1/2}$, where η_m is the admittance of the metal layer, the admittance locus will loop outside the line joining the origin to the starting point, as in the diagram. For dielectric layers having admittance greater than that of the incident medium, the reflectance falls with increasing thickness while the locus is in the fourth quadrant of the admittance diagram. At the intersection with the real axis, the reflectance is a minimum. It then begins to rise, but, at the quarter-wave

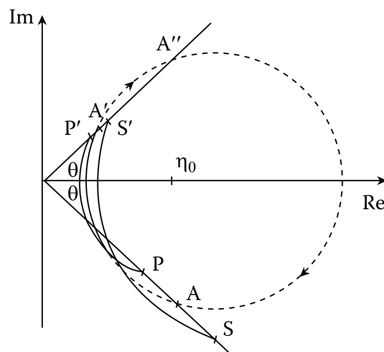

FIGURE 9.6
Schematic diagram of a dielectric overcoat on a metal surface. At normal incidence, the metal admittance is at point A. A′ represents a quarter-wave thickness of material, while A″ represents the point at which the reflectance returns to the starting value. The lowest reflectance is given by the intersection with the real axis between the points A and A′. When tilted, the *p*-locus is given by PP′ and the *s*-locus by SS′.

point A′ given by η_f^2/η_m, it is still below the reflectance of the bare metal. Only at point A″ does the reflectance return to its initial level. The drop in reflectance for silver is usually slight, but for aluminum, it can be catastrophic. Silver is therefore usually overcoated with a quarter-wave protective layer, but aluminum, especially if luminous reflectance is what is required, with a half-wave. The higher the index of the overcoat, the lower is the reflectance at the minimum and so low-index protecting layers like silica are much to be preferred.

As the metal–dielectric combination is tilted, the *p*-admittance of the metal slides toward the origin, with a drop in reflectance, while the *s*-admittance moves away from the origin with a rise in reflectance. The dielectric layer shows a drop in admittance for *p*-polarized light and an increase for *s*-polarized. For dielectric coatings that are near a quarter-wave, these changes tend to compensate, and, indeed, in silver, slightly overcompensate, the changes in reflectance of the bare metal. The *p*-reflectance of the overcoated metal tends to be slightly higher than the *s*-reflectance.

Eventually, for very high angles of incidence, the *p*-polarized admittance of the dielectric layer falls below the admittance of the incident medium, and now the fourth quadrant portion of the locus represents increasing reflectance. This means that the dielectric overcoating, when thin, instead of reducing the reflectance of the metal, actually slightly enhances it. Thus, although it depends on the final thickness of the dielectric layer, the *p*-reflectance will tend to be high. For *s*-polarized light, the admittance of the dielectric layer tends to infinity as the angle of incidence tends to 90°. The locus of the dielectric overcoat, therefore, tends more and more toward a vertical line. As the admittance of the metal moves away from the origin, its projection in the real axis moves farther to the right, eventually crossing the incident medium admittance and continuing toward infinity. There must, therefore, be an angle of incidence, very high, where the locus of the dielectric overcoat will intersect the real axis at the admittance of the incident medium. If the thickness is chosen so that the locus terminates at this point, then the reflectance of the metal–dielectric combination will be zero. This will occur for one particular value of angle of incidence and for a precise value of the dielectric layer thickness, and the dip in reflectance will show a rapid variation with angle of incidence. Such behavior, for *s*-polarized light, of a metal overcoated with a thin dielectric layer was predicted by Nevière and Vincent [4] from a quite different analysis based on a Brewster absorption phenomenon in a lossy waveguide used just under its cutoff thickness. Since the modified admittance for *s*-polarized light increases with angle of incidence only in the case where its refractive index is greater than that of the incident medium, this is a necessary condition for the observation of the effect. The increased flexibility given by two dielectric layers deposited on a metal has been used to advantage in the design of reflection polarizers [5].

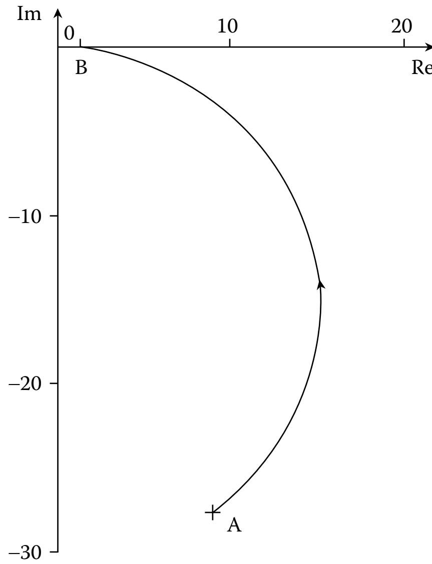

FIGURE 9.7
p-Polarized admittance locus for 150 nm thickness of SiO_2 (0.39 − *i*0.29), on aluminum (18.35−*i*55.75), at an angle of incidence of 60°. A is the point corresponding to the modified admittance of aluminum and the anticlockwise curvature of the spiral locus carries it into the region of low reflectance.

A different phenomenon was reported by Cox et al. [6] in connection with an infrared mirror of aluminum with a protective overcoat of silicon dioxide. The silicon dioxide is heavily absorbing in the region beyond 8 μm. At a wavelength of just over 8 μm, n and k have values around 0.4 and 0.3, respectively. At normal incidence, the admittance loci of the silicon dioxide are spirals that end on the admittance of the silicon dioxide and are described in a clockwise manner in much the same way as the silver loci already discussed. At non-normal incidence, the *s*-polarized admittance and the phase factor for the layer remain in the fourth quadrant, and so the behavior of the silicon oxide is similar to that at normal incidence. The *p*-polarized admittance, however, moves toward the first quadrant, and enters it at an angle of incidence around 40°. The behavior of such a material, where the phase thickness is in the fourth quadrant but the optical admittance is in the first, is different from normal materials in that the spirals are now traced out anticlockwise, rather than clockwise. The admittance of aluminum at 8.1 μm is around 18.35 − *i*55.75 and, for *p*-polarized light at an angle of incidence of 60°, the modified admittance becomes 9.176 − *i*27.87. The dielectric locus sweeps down toward the real axis, as in Figure 9.7, and, in a thickness of 150 nm, terminates near the point (1, 0), so that the reflectance is near zero.

This behavior is quite unlike the normal behavior to be expected with lossless dielectric overcoats that have refractive index greater than that of the

incident medium. However, we shall see that it does have a certain similarity with one of the techniques for generating surface electromagnetic waves, which we shall be dealing with shortly, where the coupling medium is a dielectric layer of index lower than that of the incident medium, and where the angle of incidence is beyond the critical angle.

We now turn back to dielectric materials and investigate what happens when angles of incidence exceed the critical angle. Equations 9.10, 9.11, and 9.13 are the relevant equations and we have $k = 0$ and $n_0\sin\vartheta_0 > n$. The phase thickness at normal incidence, $2\pi nd/\lambda$, becomes, from Equation 9.13,

$$\delta = \frac{2\pi(n^2 - n_0^2\sin^2\vartheta_0)^{1/2}d}{\lambda}$$

i.e.,

$$\delta = -i\frac{2\pi(n_0^2\sin^2\vartheta_0 - n^2)^{1/2}d}{\lambda} \tag{9.14}$$

at oblique incidence, where, again, the fourth rather than second quadrant solution is correct. The modified admittances are then

$$\begin{aligned}\eta_s &= -i\frac{(n_0^2\sin^2\vartheta_0 - n^2)^{1/2}}{\cos\vartheta_0}\\ \eta_p &= \frac{n^2}{\eta_s}\end{aligned} \tag{9.15}$$

Since η_s is negative imaginary, η_p must be positive imaginary. The behavior of the modified admittance is shown diagrammatically in Figure 9.8. For a thin film of material used beyond the critical angle, then, the *s*-polarized behavior is indistinguishable from that of an ideal metal. We have a set of circles centered on the real axis, described clockwise and ending on the point η_s on the negative imaginary axis. For *p*-polarized light, the behavior is, in one important respect, different. Here, the combination of negative imaginary phase thickness and positive imaginary admittance inverts the way in which the circles are described, so that although they are still centered on the origin, they are anticlockwise and terminate at η_p on the positive imaginary axis. This behavior plays a significant part in what follows. We assume a beam of light incident on the hypotenuse of a prism beyond the critical angle. Simply for plotting some of the following figures, we assume a value for the index of the incident medium of 1.52.

For an uncoated hypotenuse, the second medium is air of refractive index unity. The modified admittance for *p*-polarized light is positive imaginary

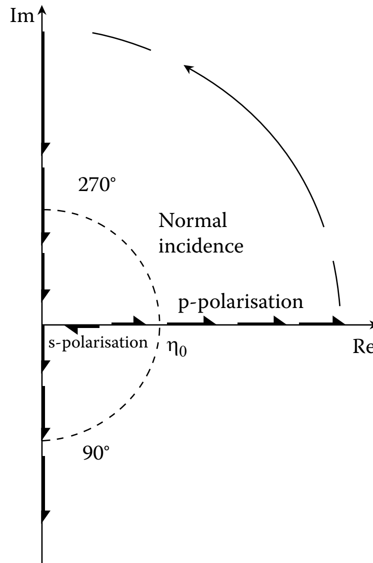

FIGURE 9.8
The variation of the *s*-polarized and *p*-polarized modified admittances of free space with respect to an incident medium of higher index. η_0 is the incident admittance. The *s*-admittance falls along the real axis until zero at the critical angle and then it turns along the negative direction of the imaginary axis tending to negative imaginary infinity as the angle of incidence tends to 90°. The *p*-admittance rises along the real axis, passing the point η_0 at the Brewster angle, becoming infinite at the critical angle, switching over to positive imaginary infinity, and then sliding down the imaginary axis tending to zero as the angle of incidence tends to 90°.

and, as ϑ_0 increases, falls down the imaginary axis toward the origin. The reflectance is unity and Figure 9.8 shows that the phase shift varies from 180° through the third and fourth quadrants toward 0°. The *s*-polarized reflectance is likewise unity, but the admittance is negative imaginary, and falls from zero to infinity along the imaginary axis so that the *s*-polarized phase shift increases with ϑ_0 from zero, through the first and second quadrants toward 180°. Since the incident medium has admittance 1.52, the circle separating the first and second quadrants and the third and fourth quadrants, which has center the origin, has radius 1.52.

Now let a thin film be added to the hypotenuse. Since we are treating our glass prism as the incident medium, we should treat the surrounding air as the substrate. Thus, the starting admittance for the film is on the imaginary axis. Provided the thin film has no losses, then the admittance of the film–substrate combination must remain on the imaginary axis. If the film admittance is imaginary, the combination admittance will simply move toward the film admittance. If, however, the film admittance is real, the admittance of the combination will move along the imaginary axis in a positive direction, returning to the starting point every half-wave. The lower the

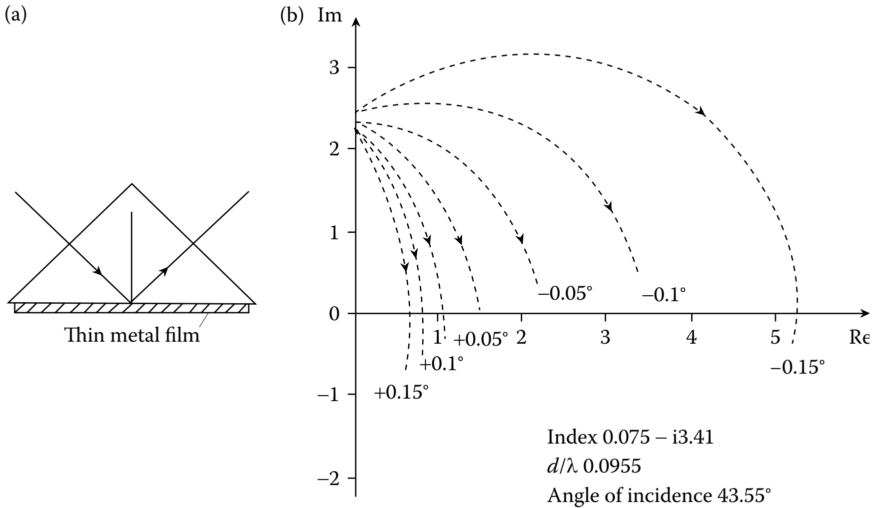

FIGURE 9.9
(a) Coupling to a surface plasma wave. (After Kretschmann and Raether [7].) (b) *p*-polarized admittance locus corresponding to the arrangement in (a). The *solid curve* corresponds to the optimum angle of incidence and thickness of metal (silver) film. The *dashed curves* correspond to changes in the angle of incidence as marked on each curve.

modified admittance, the slower the locus moves near the origin and the faster at points far removed from the origin. The variation of phase change between the fourth quadrant and the start of the first quadrant is, therefore, slower, while that between the third and second quadrants is faster than for a higher admittance. Thus there is a wide range of possibilities for varying the relative phase shifts for *p*- and *s*-polarizations by choosing an overcoat of higher or lower index and varying the thickness, or even by adding additional layers [8–10].

Given that the starting point is on the axis, then the only way in which the admittance can be made to leave it is by an absorbing layer. We turn to the set of metal loci (Figure 9.4) and we can see that for a range of values of starting admittance on the imaginary axis, the metal loci loop around, away from the axis, to cut the real axis. Although Figure 9.4 shows the behavior of metal layers for an incident medium of unity at normal incidence, the tilted behavior for an incident admittance of 1.52 is quite similar. Figure 9.9 shows the illuminating arrangement and the loci. For a very narrow range of starting values, the metal locus cuts the real axis near the incident admittance, and, if the metal thickness is such that the locus terminates there, then the reflectance of the combination will be low. For one particular angle of incidence and metal thickness, the reflectance will be zero. It should not be too much of a surprise to find that the condition is very sensitive to angle of incidence. Since the admittance of the metal varies much more slowly than the air substrate, the zero reflectance condition will no longer

hold, even for quite small tilts. One can think of it in terms of a rather long lever with a fulcrum and a forced movement very close to it so that the end of the lever magnifies considerably the movement. This very narrow drop in reflectance to a very low value, which has all the hallmarks of a sharp resonance, can be interpreted as the generation of a surface plasma wave, or plasmon, on the metal film. This coupling arrangement, devised by Kretschmann and Raether [7], cannot operate for *s*-polarized light without modification. The admittance of the substrate for *s*-polarization is now on the negative part of the real axis and, therefore, any metal that is deposited will simply move the admittance of the combination toward the admittance of the bulk metal.

An alternative coupling arrangement, devised by Otto [11], involves the excitation of surface waves through an evanescent wave in an FTR layer (frustrated total reflectance). We recall that the admittance locus for *p*-polarization of a layer used beyond the critical angle is a circle described in an anticlockwise direction. This means that such a layer can be used to couple into a massive metal. Here the metal acts as the substrate, with a starting admittance in the fourth quadrant of the admittance diagram. For *p*-polarized light, the dielectric FTR layer has a circular locus that cuts the real axis. Clearly, then, for the correct angle of incidence and dielectric layer thickness, the reflectance can be made zero. Surface plasma oscillations and their applications are extensively reviewed by Raether [12]. Abelès [13] includes an account of the optical features of such effects in his review of the optical properties of very thin films.

Now let us return to the first case of coupling and let us examine what happens when a thin layer is deposited over the metal next to the surrounding air. The starting admittance is, as before, on the imaginary axis, but now the dielectric layer modifies that position, so that the starting point for the metal locus is changed. Because the metal loci at the imaginary axis are clustered closely together, almost intersecting, a small change in starting point produces an enormous change in the locus, and hence in the point at which it cuts the real axis, leading to a substantial change in reflectance (Figure 9.10). This very large change that a thin external dielectric film makes to the internal reflectance of the metal film, has been used in the study of contaminant films adsorbed on metal surfaces. Film thicknesses of a few ångströms have been detected in this way. Provided that the film is very thin, then an additional tilt of the system will be sufficient to pull the intersection of the metal locus with the real axis back to the incident admittance, and so the effect can be interpreted as a shift in the resonance rather than a damping.

This result helps us to devise a method for exciting a similar resonance with *s*-polarized light. The essential problem is the starting point on the negative imaginary axis, which means that the subsequent metal locus remains within the fourth quadrant, never crossing the real axis to make it possible to have zero reflectance. The addition of a dielectric

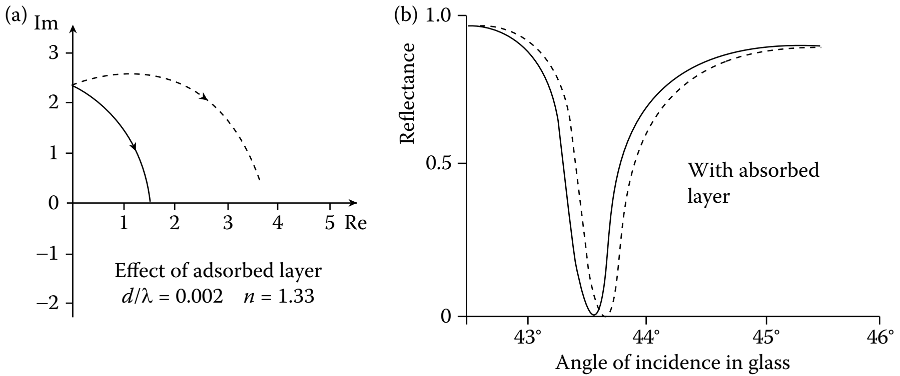

FIGURE 9.10
(a) The effect of a thin adsorbed layer on the surface of the silver in Figure 9.9. The *solid line* is the optimum while the *dashed line* is the change in the metal locus due to the adsorbed layer. (b) Calculated reflectance as a function of angle of incidence with and without the adsorbed layer.

layer between the metal surface and the surrounding air can move the starting point for the metal on to the positive part of the imaginary axis so that the coated metal locus can cut the real axis for *s*-polarized light in just the same way as the uncoated metal in *p*-polarized light. Moreover, for both *p*- and *s*-polarized light, the low reflectance will be repeated for each additional half-wave dielectric layer that is added. This behavior was used by Greenland and Billington [14] for the monitoring of optical layers intended as spacer layers for metal–dielectric interference filters. The operation of the cavities for inducing absorption devised by Harrick and Turner [15], although designed on the basis of a different approach, can also be explained this way.

Under certain conditions it is also possible to arrange the dielectric overcoat such that an *s*-polarized resonance and a *p*-polarized resonance should be sufficiently close together in angle to make it possible to measure both together [16,17]. The electric field is still high at the outermost surface, so the sensitivity to a thin added layer of material is undiminished. The added *s*-polarization resonance yields additional information on the structure of the detected material. Figure 9.11 shows typical resonances. The outer medium is water, common in biochemical investigations. The rugged nature of the outer SiO_2 layer implies that the detector can be cleaned and reused, an additional advantage over bare metal.

The long-range surface plasmon is a phenomenon of some interest [18,19]. Again, the light must be *p*-polarized for the effect to be possible. A thinner metal layer than in the classic case is used, and it is surrounded by dielectric media that are beyond the critical angle so that they support evanescent waves. A resonance that is exceedingly narrow is induced in the reflectance of the assembly. This implies lower losses, and hence

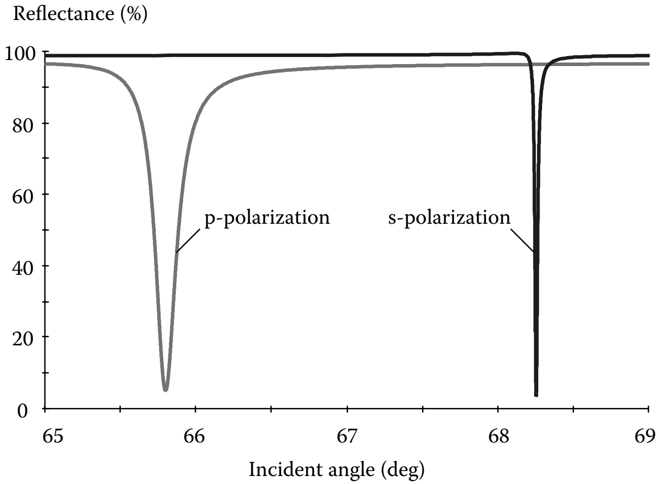

FIGURE 9.11
Resonances at 632.8 nm for both *p*- and *s*-polarizations achieved by overcoating the silver layer with a thick low-index layer (SiO_2). The outer medium is water rather than air and the thickness of silver is 51.1 nm and of SiO_2, 502.3 nm. The incident medium is borosilicate glass. Note that both resonances are considerably narrower than that in Figure 9.10.

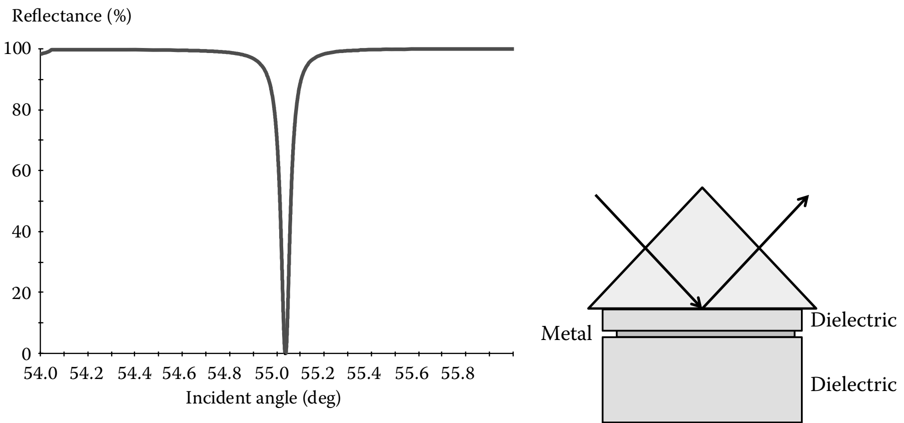

FIGURE 9.12
The long-range surface plasmon resonance. As before, the resonance exists for *p*-polarized light. It is shown here for an incident medium of index 1.8 with a thin silver film, 20.64 nm thick surrounded by SiO_2 1037 nm thick in front and massive behind. The wavelength is 632.8 nm.

greater range, than the classic surface plasmon. We use, again, an infinite plane wave to excite the resonance. We can understand it by using an admittance diagram.

Figure 9.13 shows the admittance diagram at resonance. The massive material, SiO_2, behind the silver is effectively the substrate for the system. Since it

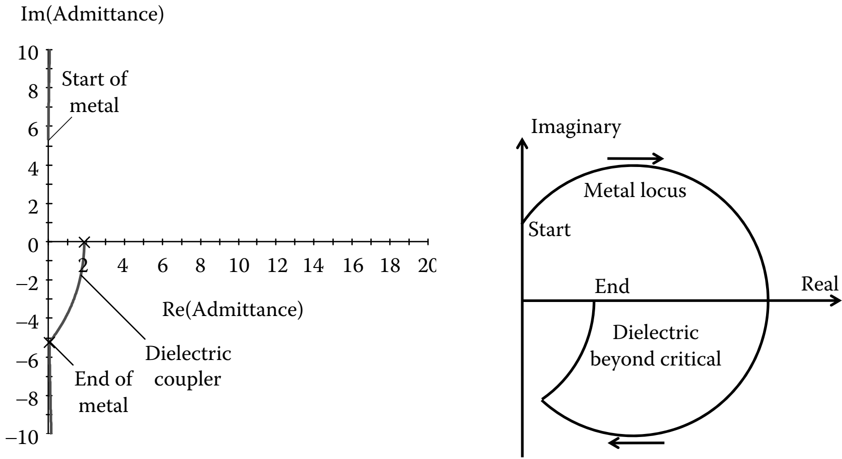

FIGURE 9.13
The *p*-polarized admittance locus associated with the long-range surface plasmon. The angle of incidence in the 1.8 index incident material is 55.035°. The massive material, SiO_2, behind the silver is beyond critical and therefore the starting point for the locus is on the positive limb of the imaginary axis. The silver locus loops round and ends close to the imaginary axis and below the real axis so that the subsequent SiO_2 locus that is beyond critical loops round to terminate at the admittance of the incident medium, in this case 1.8. Note that the modified admittances are used. Note further that the loci of dielectric materials beyond critical for *p*-polarized light are circles described *counterclockwise*.

is beyond critical, its *p*-admittance is positive imaginary and so the starting point for the locus is on the positive limb of the imaginary axis. The silver locus loops round in a huge circle and ends such that the starting point for the subsequent SiO_2 locus is below the real axis and close to the imaginary axis. The final (front) layer is also SiO_2 and also beyond critical. Its *p*-admittance is, therefore, also positive imaginary.

This implies a counterclockwise direction for its admittance locus that loops round to terminate at the admittance of the incident medium—in this case, 1.8. The enormous length of the admittance locus implies a rapid change in the conditions as the angle of incidence changes and hence a very narrow dip in the *p*-reflectance of the system and a lower loss for the plasmon. The total electric field amplitude is shown in Figure 9.14. The field in the metal layer is extremely small explaining the low loss. The field is largely, but not completely, perpendicular to the metal surfaces.

An unexpected transparency of metal layers surrounded by dielectric layers beyond the critical angle, Figure 9.15, was described by Dragila et al. [20], who explained it by coupled plasma waves on either side of the metal layer. This is virtually the same as the long-range plasmon except that now we are dealing with enhanced transmission rather than enhanced plasmon range. The problem [21,22] can readily be treated as an induced transmission filter and the transmittance maximized, all in a simple three-layer,

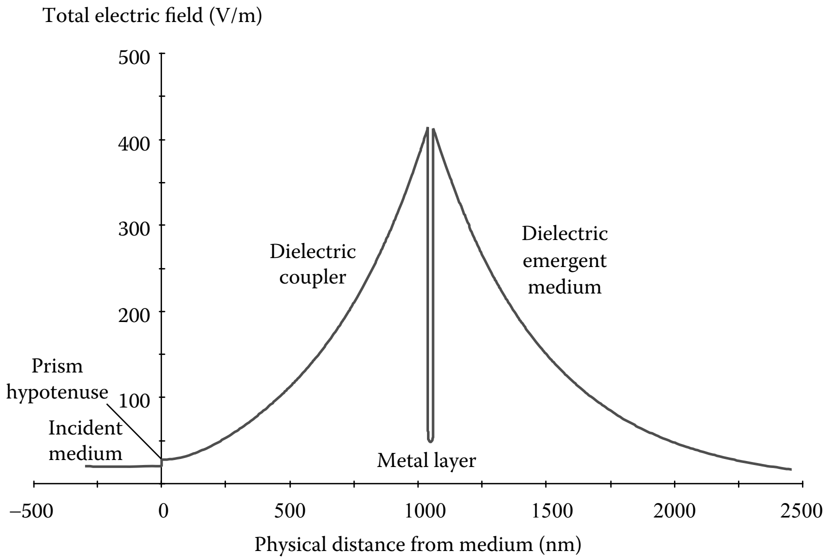

FIGURE 9.14
The total electric field amplitude through the system at resonance. Note that the electric field in the metal, that is silver, layer is exceedingly low and so the loss is smaller than for the conventional one-sided surface plasmon. The field is plotted in V/m assuming 1 Wm^{-2} input power.

dielectric–metal–dielectric design. Maximum potential transmittance from any given absorbing layer is achieved when the admittance at the rear surface is an optimum value that depends solely on the geometric thickness (that is d/λ) of the layer and its optical constants. The theory is dealt with in Chapter 8. This optimum admittance is in the first quadrant and can be calculated from the analytical expressions already given. Here we have

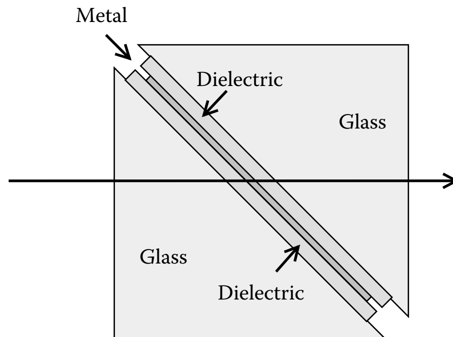

FIGURE 9.15
The arrangement of the metal layer (silver) surrounded by two dielectric layers operating beyond the critical angle described by Dragila, R., Lutherda, B., and Vukovic, S., *Physical Review Letters*, 55, 1117–1120, 1985.

identical incident and exit media. The p-polarized locus for the low-index material next to the substrate sweeps round in a counterclockwise manner in the first quadrant from the admittance of the exit medium toward the imaginary axis, where it will eventually intersect it in the point that corresponds to the modified tilted admittance. Over the range of angles beyond critical, the p-admittance varies from infinity to zero along the positive limb of the imaginary axis. The metal optimum admittance varies more slowly, and it is straightforward to identify the appropriate angle for which the optimum admittance for a given metal thickness lies on the dielectric locus. This fixes the dielectric layer thickness, and the remainder of the design is then the addition of a layer in front of the metal exactly the same as that behind.

Figure 9.16 shows the admittance diagrams for a filter of this type, and Figure 9.17, the performance. The incident and exit media are high index glass (n = 1.8); the wavelength is taken as 632.8 nm, and the thickness of the metal layer, silver, as 80 nm with optical constants (0.0666 – i4.0452). The low index material is silica (n = 1.45) and both first and third layers are of physical thickness 314 nm. Once the wavelength and thickness of the silver, and the index of the matching dielectric layers, are chosen, the thickness of the dielectric layers and angle of incidence are then fixed.

Note the similarity between the loci of the metal layer followed by the dielectric layer in Figure 9.16, that is layers 2 and 3, and the corresponding

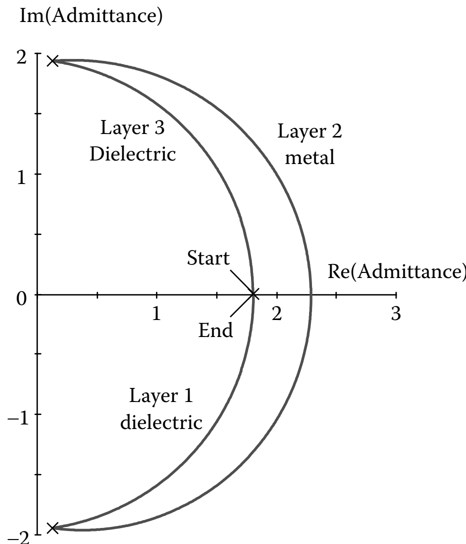

FIGURE 9.16
Admittance diagrams for the induced transmission filter described in the text. The counterclockwise p-loci of the dielectric layers are in opposition to the clockwise rotation of the silver loci. Design : 1.8 | 1.45, 344 nm (0.0666 – i4.0452), 80 nm, 1.45, 344 nm | 1.8, λ = 632.8 nm, ϑ_0 = 59.44°.

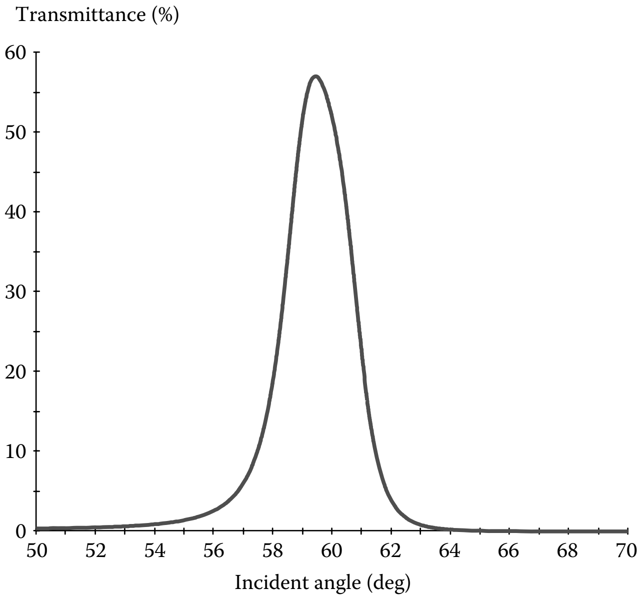

FIGURE 9.17
The performance of the filter of Figure 9.16 as a function of angle of incidence at $\lambda = 632.8$ nm. The peak transmittance is the maximum possible from a silver layer of this thickness at this angle of incidence.

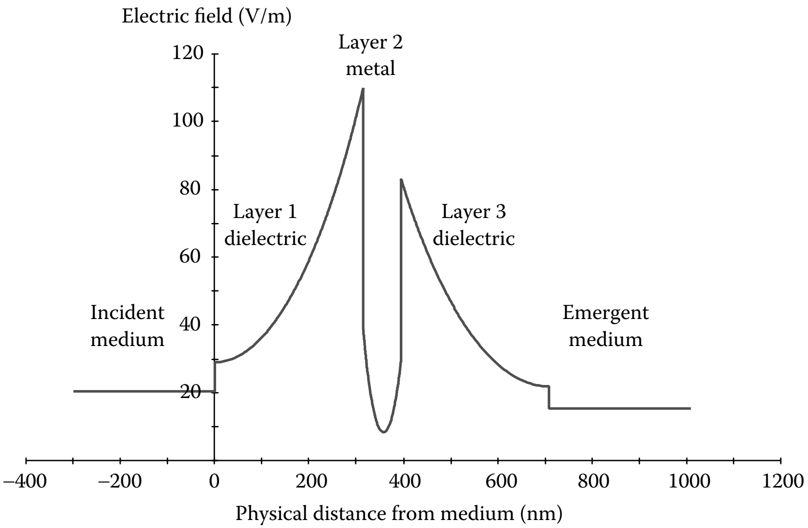

FIGURE 9.18
The distribution of total electric field amplitude through the filter of Figure 9.16 and Figure 9.17. Note the similarity with the long-range plasmon distribution in Figure 9.14

layers in Figure 9.13. In fact, the mechanism that assures the high transparency of the metal layer in this filter is virtually the same as ensures the low loss in the long-range surface plasmon. An almost identical mechanism is responsible for the curious induced transparency of metal films pierced with regular arrays of small holes [23,24]. Bonod et al. [25] explain the phenomenon as a scattering of the light by the array of holes into a surface plasmon on the side of incidence. This induces a similar plasmon on the other side of the metal that is then scattered by the holes back into the direction of incidence. Indeed, a diffraction grating on either side is calculated to perform in the same way. The electric field in the metal is reduced and, hence, also the losses. The great advantage of this arrangement is that it can operate at normal incidence. The maximum possible transmittance is that predicted by the theory of induced transmission in Chapter 8.

9.3 Polarizers

9.3.1 The Brewster Angle Polarizing Beam Splitter

This type of beam splitter was first constructed by Mary Banning [26] at the request of S. M. MacNeille, the inventor of the device [2], which is frequently known as a MacNeille polarizer.

The principle of the device is that it is always possible to find an angle of incidence so that the Brewster condition for an interface between two materials of differing refractive index is satisfied. When this is so, the reflectance for the p-plane of polarization vanishes. The s-polarized light is partially reflected and transmitted. To increase the s-reflectance, retaining the p-transmittance at or very near unity, the two materials may then be made into a multilayer reflecting stack. The layer thickness should be quarter-wave optical thicknesses at the appropriate angle of incidence.

When the Brewster angle for normal thin-film materials is calculated, it is found to be greater than 90° referred to air as the incident medium. In other words, it is beyond grazing incidence for the materials. This presents a problem that is solved by building the multilayer filter into a glass prism so that the light can be incident on the multilayer at an angle greater than is possible with air as incident medium. The arrangement is shown in Figure 9.19.

The calculation of the design is quite straightforward. Consider two materials with refractive indices n_H and n_L (where H and L refer to high and low relative indices, respectively). The Brewster condition is satisfied when the angle of incidence is such that

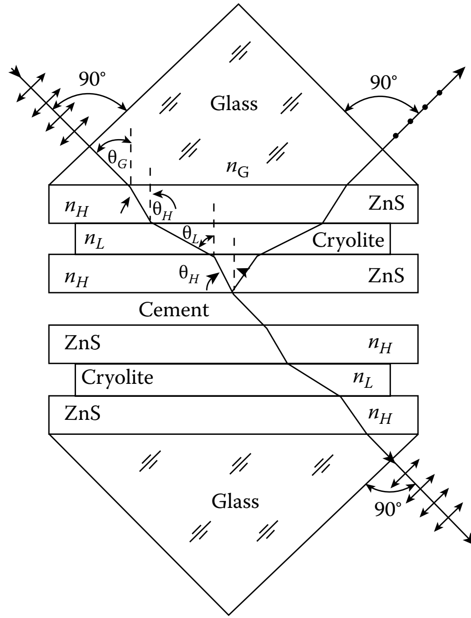

FIGURE 9.19
Schematic diagram of a polarizing beam splitter. (After Banning, M., *Journal of the Optical Society of America*, 37, 792–792, 1947.)

$$\frac{n_H}{\cos\vartheta_H} = \frac{n_L}{\cos\vartheta_L} \tag{9.16}$$

where

$$n_H \sin\vartheta_H = n_L \sin\vartheta_L = n_G \sin\vartheta_G \tag{9.17}$$

G refers to the glass of the prism. These equations can be solved easily for ϑ_H

$$\sin^2\vartheta_H = \frac{n_L^2}{n_H^2 + n_L^2} \tag{9.18}$$

the form in which we shall use the result. (A more familiar form is $\tan^2\vartheta_H = n_L^2/n_H^2$.)

Given the layer indices, there are two possible approaches to the design. Either we can decide on the refractive index of the glass and then calculate the angle at which the prism must be set, or we can decide on the prism angle, 45° being a convenient figure, and calculate the necessary refractive index of the glass. The approach used by Banning was the latter.

First suppose that the condition $\vartheta_G = 45°$ must be met. Using Equations 9.17 and 9.18, we obtain

$$\sin^2\vartheta_H = \frac{n_G^2 \sin^2\vartheta_G}{n_H^2} = \frac{n_G^2}{2n_H^2} \text{ for } \vartheta_G = 45°$$

i.e.,

$$n_G^2 = \frac{2n_H^2 n_L^2}{n_H^2 + n_L^2} \tag{9.19}$$

the condition obtained by Banning.

If, however, n_G is fixed, then Equations 9.17 and 9.18 give

$$\frac{n_G^2 \sin^2\vartheta_G}{n_H^2} = \sin^2\vartheta_H = \frac{n_L^2}{n_H^2 + n_L^2}$$

i.e.,

$$\sin^2\vartheta_G = \frac{n_H^2 n_L^2}{n_G^2(n_H^2 + n_L^2)} \tag{9.20}$$

Banning used zinc sulfide with an index of 2.30 and cryolite evaporated at a pressure of 10^{-3} Torr (0.133 Pa) to give a porous layer of index around 1.25. With these indices, it is necessary to have an index of 1.55 for the glass if the prism angle is to be 45°. For an index of 1.35, a more usual figure for cryolite, together with zinc sulfide with an index of 2.35, the glass index should be 1.66. Alternatively, for glass of index 1.52, the angle of incidence using the second pair of materials should be 50.5°.

The degree of polarization at the center wavelength can also be calculated.

$$R = \left[\frac{\eta_G - (\eta_H^2/\eta_G)(\eta_H/\eta_L)^{q-1}}{\eta_G + (\eta_H^2/\eta_G)(\eta_H/\eta_L)^{q-1}}\right] \tag{9.21}$$

where q is the number of layers and we are assuming q to be odd.

For s-waves	For p-waves:
$\eta_G = n_G \cos\vartheta_G$	$\eta_G = n_G/\cos\vartheta_G$
$\eta_H = n_H \cos\vartheta_H$	$\eta_H = n_H/\cos\vartheta_H$
$\eta_L = n_L \cos\vartheta_L$	$\eta_L = n_L/\cos\vartheta_L$

Now, for p-waves, by the condition we have imposed, $\eta_H = \eta_L$ and

$$R_p = \left[\frac{\eta_G - (\eta_H^2/\eta_G)}{\eta_G + (\eta_H^2/\eta_G)}\right]^2$$
$$= \left[\left(\frac{n_G^2 \cos^2\vartheta_H}{n_H^2 \cos\vartheta_G} - 1\right)\bigg/\left(\frac{n_G^2 \cos^2\vartheta_H}{n_H^2 \cos^2\vartheta_G} + 1\right)\right] \tag{9.22}$$

Similarly,

$$R_s = \left[\frac{n_G^2 \cos^2\vartheta_G - n_H^2 \cos^2\vartheta_H \left(\dfrac{n_H \cos\vartheta_H}{n_L \cos\vartheta_L}\right)^{q-1}}{n_G^2 \cos^2\vartheta_G + n_H^2 \cos^2\vartheta_H \left(\dfrac{n_H \cos\vartheta_H}{n_L \cos\vartheta_L}\right)^{q-1}}\right]^2 \tag{9.23}$$

Now

$$\frac{n_H \cos\vartheta_L}{n_L \cos\vartheta_H} = 1$$

so that

$$\frac{n_H \cos\vartheta_H}{n_L \cos\vartheta_L} = \frac{n_H^2}{n_L^2}$$

and

$$R_s = \left[\frac{n_G^2 \cos^2\vartheta_G - n_H^2 \cos^2\vartheta_H \left(\dfrac{n_H}{n_L}\right)^{2(q-1)}}{n_G^2 \cos^2\vartheta_G + n_H^2 \cos^2\vartheta_H \left(\dfrac{n_H}{n_L}\right)^{2(q-1)}}\right]^2 \tag{9.24}$$

The degree of polarization in transmission is given by

$$P_T = \frac{T_p - T_s}{T_p + T_s} = \frac{1 - R_p - 1 + R_s}{1 - R_p + 1 - R_s} = \frac{R_s - R_p}{2 - R_p - R_s} \tag{9.25}$$

and in reflection by

$$P_R = \frac{R_s - R_p}{R_s + R_p} \tag{9.26}$$

It can be seen that in general, for a small number of layers, the polarization in reflection is better than the polarization in transmission, but for a large number of layers, it is inferior to that in transmission.

The construction of the beam splitter is similar to the cube beam splitter that was considered in Chapter 5. Any number of layers can be used in the coating. Banning's original coating consisted of three layers, probably because of practical difficulties at that time. Two coatings were therefore prepared, one on the hypotenuse of each prism making up the cube, as shown in Figure 9.19. The two prisms were then cemented together. Nowadays there is little difficulty in depositing 21 layers, or more if need be, and these can be conveniently placed on just one prism and the other untreated prism simply cemented to it.

The very great advantage that this type of polarizing beam splitter has over the other polarizers such as the pile-of-plates is its wide spectral range coupled with a large physical aperture. Unfortunately, it does suffer from a limited angular field, particularly at the center of its range, partly because the Brewster condition is met exactly only at the design angle. As the angle of incidence moves away from this condition, a residual reflectance peak for p-polarization gradually appears in the center of the range. The performance well away from the center remains high even for quite large tilts away from optimum. As an example, we can consider a seven-layer ZnS and cryolite beam splitter in glass of index 1.52 designed so that a wavelength of 510 nm corresponds to the center of the range. At the design angle of 50.4° and at 510 nm the residual p-reflectance is 1.6%, due to the mismatch between the materials of the stack and the glass prism. (The Brewster angle condition cannot be met for both film materials and the substrate simultaneously—see Figure 9.2.) A tilt in the plane of incidence to 55° in glass (that is a tilt to 7° in air) raises the reflectance to 25% at 510 nm and over 30% at 440 nm, since the band center moves to shorter wavelengths. The reflectance at 650 nm, on the other hand, shows little change. Skew rays present a further difficulty. Polarization performance is measured with reference to the s- and p-directions associated with the principal plane of incidence containing the axial ray. A skew ray possesses a plane of incidence that is rotated with respect to the principal plane. Thus, the s- and p-planes for skew rays are not quite those of the axial ray and, although the s-polarized transmittance can be very low, there can be a component of the p-polarized light, parallel to the axial s-direction and representing leakage that can be significant. In fact, given the apex angle of a cone of incident illumination, there is a limit to the degree of polarization that cannot be exceeded even by adding further layers to the design.

The leakage can be reduced by moving to higher angles of incidence. Li and Dobrowolski [27] describe such a polarizer where one of the materials is operating beyond the critical angle. This also improves considerably the possible p-polarized performance that can be obtained. The disadvantage is that more glass is required than for smaller incidence angles.

A detailed study of the polarizing prism has been carried out by Clapham [28].

9.3.2 Plate Polarizer

The width of the high-reflectance zone of a quarter-wave stack is a function of the ratio of the admittances of the two materials involved. This ratio varies with the angle of incidence and is different for *s*- and *p*-polarizations. We recall that

$$\eta_s = n\cos\vartheta \text{ while } \eta_p = n/\cos\vartheta$$

so that

$$\eta_{Hs}/\eta_{Ls} = \cos\vartheta_H/\cos\vartheta_L$$

and

$$\eta_{Hp}/\eta_{Lp} = \cos\vartheta_L/\cos\vartheta_H$$

whence

$$\frac{(\eta_H/\eta_L)_s}{(\eta_H/\eta_L)_p} = \frac{\cos^2\vartheta_H}{\cos^2\vartheta_L} \tag{9.27}$$

The factor $\cos^2\vartheta_H/\cos^2\vartheta_L$ is always less than unity so that the width of the high-reflectance zone for *p*-polarized light is always less than that for *s*-polarized light. Within the region outside the *p*-polarized but inside the *s*-polarized high-reflectance zone, the transmittance is low for *s*-polarized light but high for *p*-polarized so that the component acts as a polarizer. The region is quite narrow, so that such a polarizer will not operate over a wide wavelength range; but for single wavelengths, such as a laser line, it can be very effective. To complete the design of the component it is necessary to reduce the ripple in transmission for *p*-polarized light and this can be performed using any of the techniques of Chapter 7, probably the most useful analytical technique being Thelen's shifted-period method because it is the performance right at the edge of the pass region that is important. Nowadays, computer refinement of the few outermost layers is more common. It is normal to use the component as a longwave-pass filter because this involves thinner layers and less material than would a shortwave-pass filter. The rear surface of the component requires an antireflection coating for *p*-polarized light. We can omit this altogether if the component is used at the Brewster angle. The design of such a polarizer is described by Songer [29] who gives the design shown in Figure 9.20. Plate polarizers are used in preference to the prism, or MacNeille, type when high powers are concerned.

Virtually any coating possessing a sharp edge between transmission and reflection can potentially be used as a polarizer. It has been suggested that narrowband filters have advantages over simple quarter-wave stacks as the basis of plate polarizer coatings, because the monitoring of the component during deposition is a more straightforward procedure [30].

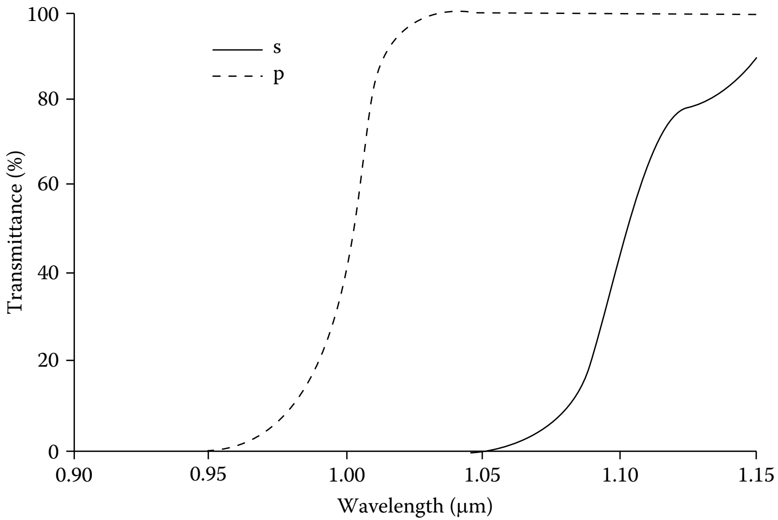

FIGURE 9.20
Characteristic curve of a plate polarizer for 1.06 µm. Design:

$$\text{Air} \mid (0.5H'\ L'\ 0.5H')^3\ (0.5H''\ L''\ 0.5H'')^8\ (0.5H'\ L'\ 0.5H')^3 \mid \text{Glass}$$

where $H' = 1.010H$, $L' = 1.146L$, $H'' = 1.076H$, and $L'' = 1.220L$ and with $n_H = 2.25$, $n_L = 1.45$, $\lambda_0 = 0.9$ µm, and $\vartheta_0 = 56.5°$. The solid line indicates *s*-polarization and the dashed line, *p*-polarization. (After Songer, L., *Optical Spectra*, 12, 45–50, 1978.)

9.3.3 Cube Polarizers

An advantage of the polarizer immersed in a prism is that the effective angle of incidence can be very high—much higher than if the incident medium were air. This enhances the polarization splitting and gives broader regions of high degree of polarization than could be the case with air as the incident medium. Even if the Brewster angle condition cannot be reached, there is an advantage in using an immersed design, provided the incident power is not too high. Netterfield [31] has considered the design of such polarizers in some detail and his paper should be considered for further information.

9.4 Nonpolarizing Coatings

The design of coatings that avoid polarization problems is a much more difficult task than that of polarizer design and there is no completely effective method. The changes in the phase thickness of the layers and in the optical

admittances are fundamental and cannot be avoided. The best we can hope to do, therefore, is to arrange a sequence of layers to give as far as possible similar performance for *p*- and *s*-polarization. Clearly, the wider the range of either angle of incidence or of wavelength, the more difficult is the task. The techniques currently available operate only over very restricted ranges of wavelength and angle of incidence (effectively over a very narrow range of angles). There is a small body of published work but the principal analytical techniques we shall use here rely heavily on techniques devised by Thelen [32,33].

9.4.1 Edge Filters at Intermediate Angle of Incidence

This section is based entirely on an important paper by Thelen [33]. However, the expressions found in the original paper have been altered to make the notation consistent with the remainder of this book. Care should be taken, therefore, in reading the original paper. In particular, the x found in the original is defined in a slightly different way.

At angles of incidence not so severe that the *p*-reflectance suffers, the principal effect of operating edge filters at oblique incidence is the splitting between the two planes of polarization. This limits the edge steepness that can be achieved for unpolarized light. Edge filters with quite limited pass regions can be constructed from band-pass filters but, because band-pass filters also suffer from polarization splitting, the bandwidth for *s*-polarized light shrinking, and for *p*-polarized light expanding, they still present the same problem. However, there is a technique that can displace the pass bands of a band-pass filter to make one pair of edges coincide. This results in an edge filter of rather limited extent, which for a given angle of incidence has no polarization splitting. The position of the peak of a band-pass filter can be considered to be a function of both the cavity thickness and the phase shift of the reflecting stacks on either side. At oblique incidence, the relative phase shift between *s*- and *p*-polarized light reflected by the stacks can be adjusted by adding or removing material. This alters the relative positions of the peaks of the pass bands for the two planes of polarization and, if the adjustment is correctly made, it can make a pair of edges coincide. This, of course, is for one angle of incidence only. As the angle of incidence moves away from the design value, the splitting will gradually reappear.

Rather than apply this technique exactly as we have just described it, we instead adapt the techniques for the design of multiple cavity filters based on symmetrical periods. Let us take a typical multiple cavity filter design:

Incident medium | matching (symmetrical stack)^q matching | substrate

The symmetrical stack that forms the basis of this filter can be represented as a single matrix with the same form as that of a single film, as we have already seen in Chapter 8. The limits of the pass band are given by those

wavelengths for which the diagonal terms of the matrix are unity and the off-diagonal terms are zero. That is, if the matrix is given by

$$\begin{bmatrix} N_{11} & iN_{12} \\ iN_{21} & N_{22} \end{bmatrix}$$

then the edges of the pass band are given by

$$N_{11} = N_{22} = \pm 1$$

The design procedure simply ensures that this condition is satisfied for the appropriate angle of incidence.

We can consider the symmetrical period as a quarter-wave stack of $2x + 1$ layers with two identical additional layers, one on either side:

$$fB\,ABAB\ \ldots A\ fB$$

where A and B indicate quarter-wave layers and f is a correction factor to be applied to the quarter-wave thickness to yield the thicknesses of the detuned outer layers. We can write the overall matrix as $fB\ M\,fB$ where $M = ABAB\ldots A$, giving the product:

$$\begin{bmatrix} \cos\alpha & i\sin\alpha/\eta_B \\ i\eta_B\sin\alpha & \cos\alpha \end{bmatrix} \begin{bmatrix} M_{11} & iM_{12} \\ iM_{21} & M_1 \end{bmatrix} \begin{bmatrix} \cos\alpha & i\sin\alpha/\eta_B \\ i\eta_B\sin\alpha & \cos\alpha \end{bmatrix}$$

Then N_{11} is given by

$$N_{11} = N_{22} = M_{11}\cos 2\alpha - 0.5(M_{12}\eta_B - M_{21}/\eta_B)\sin 2\alpha = \pm 1 \qquad (9.28)$$

for the edge of the zone for each plane of polarization. This must be satisfied for both planes of polarization simultaneously for the edges of the pass bands to coincide. In fact, symmetrical periods made up of thicknesses other than quarter-waves can also be used, when some trial and error will be required to satisfy Equation 9.28. A computer can be of considerable help. For quarter-wave stacks, we seek assistance in the expressions derived in Chapter 8 for narrowband filter design. We use the analysis starting with Expression 8.57, with $m = 1$ and $q = 0$, giving

$$\begin{aligned} M_{11} &= (M_{22} =)(-1)^x(-\varepsilon)[(\eta_A/\eta_B)^x + \cdots + (\eta_B/\eta_A)^x] \\ iM_{12} &= i(-1)^x/[(\eta_A/\eta_B)^x\eta_A] \\ iM_{21} &= i(-1)^x[(\eta_A/\eta_B)^x\eta_A] \end{aligned} \qquad (9.29)$$

ε indicating, as before, a small departure from a quarter-wave, that is $\varepsilon = (\pi/2)(g - 1)$. Note that $2x + 1$ is now the number of layers in the inner stack.

The total number of layers, including the detuned ones, is $2x + 3$. Now, using exactly the same procedure as in Chapter 8, we can write expressions for the coefficients in Equation 9.29 as

$$M_{11} = \frac{(-1)^x(-\varepsilon)(\eta_H/\eta_L)^x}{(1-\eta_L/\eta_H)} = (-1)^x(-\varepsilon)P$$

and

$$0.5(M_{12}\eta_B - M_{21}/\eta_B) = 0.5(-1)^x[(\eta_B/\eta_A)^{x+1} + \cdots + (\eta_A/\eta_B)^{x+1}] = (-1)^x Q$$

where

$$P = \frac{(\eta_H/\eta_L)^x}{(1-\eta_L/\eta_H)} \text{ and } Q = 0.5(\eta_H/\eta_L)^{x+1}$$

Then the two equations become

$$\begin{aligned} \pm 1 &= \varepsilon P_p \cos 2\alpha + Q_p \sin 2\alpha \\ \pm 1 &= \varepsilon P_s \cos 2\alpha + Q_s \sin 2\alpha \end{aligned} \quad (9.30)$$

and give for α and ε

$$\sin 2\alpha = \pm \frac{P_s - P_p}{(P_sQ_p - P_pQ_s)} \quad (9.31)$$

$$\varepsilon = \frac{\pm 1 - Q_p \sin 2\alpha}{P_p \cos 2\alpha} \quad (9.32)$$

Now,

$$\varepsilon = (\pi/2)(1-g) \text{ where } g = \lambda_0/\lambda$$

$$\alpha = (\pi/2)(\lambda_R/\lambda) = (\pi/2)(\lambda_R/\lambda_0)g = (\pi/2)fg$$

so that

$$f = \alpha/(\pi g/2) = \alpha/[(\pi/2) - \varepsilon] \quad (9.33)$$

Two values for f will be obtained. Usually, the larger corresponds to a shortwave-pass and the smaller to a longwave-pass filter.

There are some important points about the particular values of α and ε, which are best discussed within the framework of a numerical example. Let us attempt the design of a longwave-pass filter at 45° in air having a symmetrical period of

$$fL\ HLHLHLH\ fL$$

where H represents an index of 2.35 and L of 1.35. The inner stack has seven layers, which corresponds to $2x + 1$, so that x in this example is 3. We will use the modified admittances that for this combination are [the subscripts S and A referring to the substrate ($n = 1.52$) and to air ($n = 1.00$), respectively]:

$$\eta_{Hs} = 3.1694 \qquad \eta_{Ls} = 1.6264$$
$$\eta_{Ss} = 1.9028 \qquad \eta_{As} = 1.0000$$
$$\eta_{Hp} = 1.7425 \qquad \eta_{Lp} = 1.1206$$
$$\eta_{Sp} = 1.2142 \qquad \eta_{Ap} = 1.0000$$

Then

$$P_s = 15.201 \qquad P_p = 10.535$$
$$Q_s = 7.211 \qquad Q_p = 1.0000$$

giving $\sin\alpha = \pm 0.1480$.

Now, the outer tuning layers in their unperturbed state will be quarter-waves and so the two solutions we look for will be near $2\alpha = \pi$, that is, in the second and third quadrants. We continue to keep the results in the correct order and find

$$2\alpha = \pi \pm 0.1485 = 3.2901 \text{ or } 2.9931.$$

Then, in both cases, $\cos 2\alpha = 0.9890$ and so

$$\varepsilon = \pm(1 + 2.923 \times 0.148)/(-10.535 \times 0.9890) = \pm(-0.1375)$$

whence

$$f = (3.2901/2)/[(\pi/2) - 0.1375] = 1.148$$

with

$$g = 1 - (2 \times 0.1375)/\pi = 0.9125$$

and

$$f = (2.9931/2)/[(\pi/2) + 0.1375] = 0.876$$

with

$$g = 1 + (2 \times 0.1375)/\pi = 1.088$$

We take the second of these, which will correspond to a longwave-pass filter. We now need to consider the matching requirements. Since we are attempting to obtain coincident edges for both planes of polarization in an edge filter of limited pass band extent, we will interest ourselves in having good performance right at the edge of the pass band with little regard for performance

farther away. We use the method based on symmetrical periods. The basic period is

$$0.876L\ HLHLHLH\ 0.876L$$

with H and L quarter-waves of indices 2.35 and 1.35, respectively, and tuned for 45°. Calculation of the equivalent admittances for the symmetrical period gives the values for s- and p-polarization shown in Table 9.1. (Again, they are modified admittances.) We will arrange matching at $g = 1.08$. Adding an $HLHL$ combination to the period with the L layer next to it yields admittances of 0.9625 for p-polarization and 1.416 for s-polarization. The media we have to match have modified admittances of 1.0 for air and 1.214 for glass for p-polarization and 1.0 and 1.903, respectively, for s-polarization. As an initial attempt, therefore, this matching is probably adequate. Since the matching is to be at $g = 1.08$, the thicknesses of the four layers in the matching assemblies must be corrected by the factor 1.0/1.08. To complete the design, we need to make sure all layers are tuned for 45°, which means multiplying their effective thicknesses for 45° by the factor $1/\cos\vartheta$.

The final design with all thicknesses quoted as their normal incidence values is then

$$\text{Air} \mid (0.971\,H\ 1.087\,L)^2(1.028\,L(1.049\,H\ 1.174\,L)^3\ 1.049\,H\ 1.028\,L)^q$$
$$(1.087\,L\ 0.971\,H)^2 \mid \text{Glass}$$

The performance with $q = 4$ is shown in Figure 9.21. Since the p-admittances are less effective than the s-admittances in achieving high reflectance, the steepness of the edge for s-polarization is somewhat greater and so the two edges coincide at their upper ends. Adjustment of the factor f can move this point of coincidence up and down the edges. Thelen gives many examples

TABLE 9.1

Equivalent Admittances and Phase Thicknesses of the Symmetrical Period (0.876*L* *HLHLHLH* 0.876*L*) Where *L* and *H* Indicate Quarter-Waves at 45° Angle of Incidence of Index 1.35 and 2.35, Respectively

	***s*-Polarization**		***p*-Polarization**	
g	***E* (modified)**	**γ/π**	***E* (modified)**	**γ/π**
1.04	Imaginary values		0.1946	4.4372
1.05	0.0949	4.2955	0.2018	4.4372
1.06	0.1190	4.4454	0.1993	4.5884
1.07	0.1202	4.5786	0.1861	4.6652
1.08	0.0982	4.7211	0.1588	4.7486
1.09	Imaginary values		0.1049	4.8530
1.10	Imaginary values		Imaginary values	

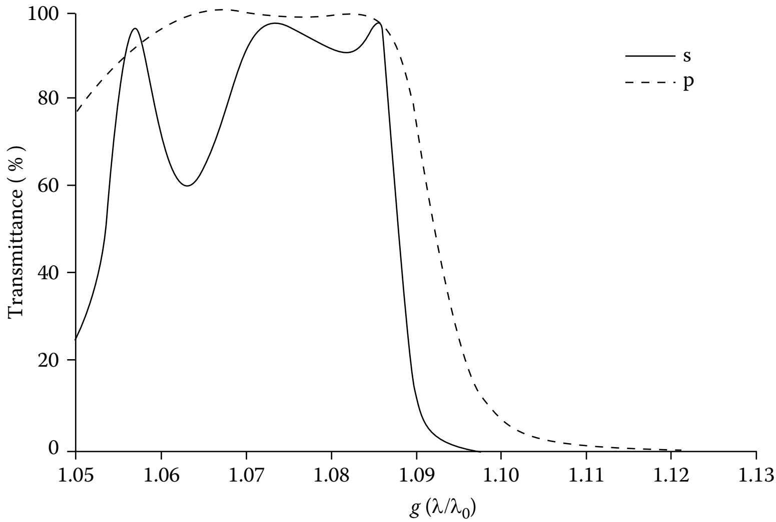

FIGURE 9.21
Calculated performance of a polarization-free edge filter designed for use at 45° in air using the method of Thelen [33]. The multilayer structure is given in the text. The *solid curve* indicates s-polarization and the *dashed curve* p-polarization.

of designs including some that are based on symmetrical periods containing thicknesses other than quarter-waves.

9.4.2 Reflecting Coatings at Very High Angles of Incidence

Reflecting coatings at very high angles of incidence suffer catastrophic reductions in reflectance for p-polarization. This is especially true for coatings that are embedded in glass, such as cube beam splitters, and we have already seen how they are well suited to making good polarizers. The admittances for p-polarized light are not favorable for high reflectance, and so to increase the p-reflectance we must use a large number of layers—many more than is usual at normal incidence. The s-reflectance must also at the same time be considerably reduced; otherwise, it will vastly exceed what is possible for p-polarization. The technique we use here is based on yet another method originated by Thelen [32]. A number of authors have studied the problem. For a detailed account of the use of symmetrical periods in the design of reflecting coatings for oblique incidence, the paper by Knittl and Houserkova [34] should be consulted.

We consider a quarter-wave stack. The surface admittance of such a stack on a substrate is given at normal incidence by

$$Y = \frac{y_1^2 y_3^2 y_5^2 \cdots y_{sub}}{y_2^2 y_4^2 y_6^2 \cdots} \tag{9.34}$$

with y_{sub} in the numerator, as shown, if the number of layers is even or in the denominator if odd.

The reflectance is

$$R = \left[\frac{y_0 - Y}{y_0 + Y}\right]^2$$

in the normal way. Now, if the stack of quarter-waves is considered to be tilted, with the thicknesses tuned to the particular angle of incidence, the expression for reflectance will be similar except that the appropriate tilted admittances must be used. Here we will use the modified admittances so that y_0 will remain the same. Then Y becomes

$$Y = \frac{\eta_1^2 \eta_3^2 \eta_5^2 \ldots \ \eta_{sub}}{\eta_2^2 \eta_4^2 \eta_6^2 \ldots} \tag{9.35}$$

and in order for the reflectances for p- and s-polarizations to be equal, the modified admittances for p- and s-polarization must be equal, or, alternatively,

$$\frac{y_0 - Y_p}{y_0 + Y_p} = \frac{Y_s - y_0}{Y_s - y_0}$$

However, this second condition reduces to $Y_s Y_p = y_0{}^2$ and since $\eta_p \eta_s = y^2$, then this is equivalent to a set of quarter-waves that would yield zero reflectance if they were quarter-waves at normal incidence, not an encouraging result if we are looking for high reflectance.

If we write Δ_1 for (η_{1p}/η_{1s}), and similarly for the other layers, then the first condition is

$$\frac{\Delta_1^2 \Delta_3^2 \Delta_5^2 \ldots \ \Delta_{sub}}{\Delta_2^2 \Delta_4^2 \Delta_6^2} = 1 \tag{9.36}$$

(Note that Thelen's paper does not use modified admittances and so includes the incident medium in the formula.) The procedure then is to attempt to find a combination of materials such that condition 9.36 is satisfied and the value of admittance is such that the required reflectance is achieved. This is a matter of trial and error.

An example may help to make the method clear. Table 9.2 gives some figures for modified admittances in glass (n = 1.52) and at an angle of incidence of 45°. In this particular case, the substrate and incident medium are of the same material. There is a number of possible arrangements but the most straightforward is to find three materials H, L, and M, with M being of intermediate index, such that

$$\Delta_H \Delta_L = \Delta_M^2 \tag{9.37}$$

TABLE 9.2

Modified Admittances of Different Materials at 45° in Incident Medium of Index 1.52

n_f	**1/cos ϑ**	η_p	η_s	$\Delta(=\eta_p/\eta_s)$
1.35	1.6526	1.5776	1.1553	1.3656
1.38	1.5943	1.5558	1.2241	1.2710
1.45	1.4898	1.5275	1.3765	1.1097
1.52	1.4142	1.5200	1.5200	1.0000
1.57	1.3719	1.5230	1.6185	0.9410
1.65	1.3180	1.5377	1.7705	0.8685
1.70	1.2907	1.5515	1.8627	0.8330
1.75	1.2672	1.5680	1.9531	0.8028
1.80	1.2466	1.5867	2.0419	0.7771
1.85	1.2286	1.6072	2.1295	0.7548
1.90	1.2127	1.6292	2.2158	0.7353
1.95	1.1985	1.6525	2.3010	0.7182
2.00	1.1858	1.6770	2.3853	0.7030
2.05	1.1744	1.7023	2.4687	0.6895
2.10	1.1640	1.7285	2.5514	0.6775
2.15	1.1546	1.7554	2.6334	0.6666
2.20	1.1461	1.7829	2.7147	0.6568
2.25	1.1383	1.8110	2.7955	0.6478
2.30	1.1311	1.8396	2.8757	0.6397
2.35	1.1245	1.8686	2.9554	0.6323
2.40	1.1184	1.8980	3.0347	0.6254

Modified admittances
Incident medium index = 1.52
Angle of incidence = 45°

Then the multilayer structure can be . . . *HMLMHMLMHMLM* . . . so that the form of admittance is

$$Y = \frac{\eta_H^2 \eta_L^2 \eta_H^2 \cdots}{\eta_M^2 \eta_M^2 \eta_M^2 \cdots} \tag{9.38}$$

The number of layers can then be chosen so that the required reflectance is achieved. The substrate does not appear in Expression 9.38 because, as already mentioned, if is of the same material as the incident medium and therefore $\Delta_{sub} = 1$. When the substrate is of a different material there may be a slight residual mismatch, but practical difficulties will usually make achievement of an exact match difficult. Theoretically, it is always possible to remove the residual mismatch by adding an extra section that matches the substrate to the incident medium.

From Table 9.2 we see that a set of layers giving an approximate match at 45° has indices 1.35, 2.25, and 1.57. For this combination

$$\frac{\Delta_H \Delta_L}{\Delta_M^2} = \frac{1.3656 \times 0.6478}{0.941^2} = 0.999.$$

The p-admittance increase due to one four-layer period of that type is

$$\frac{\eta_{Hp}^2 \eta_{Lp}^2}{\eta_{Mp}^4} = \frac{1.811^2 \times 1.578^2}{1.523^2} = 1.518$$

Eight periods give a value of 28.2—that is a reflectance of 87% for 32 layers. The particular arrangement of H, L, and M layers is flexible as long as H or L are odd and M is even. The performance of a coating to this design is shown in Figure 9.22. The basic period is four quarter-waves thick. High-reflectance zones exist wherever the basic period is an integral number of half-waves thick. Since in this case we have four quarter-waves we expect extra-high-reflectance zones at g = 0.5 and g = 1.5. The peak at g = 0.5 (i.e., $\lambda = 2 \times 510 = 1020$ nm) is visible at the long wavelength end of the diagram.

Examination of the modified admittances for the materials shows how the coating does yield the desired performance. Each second pair of layers

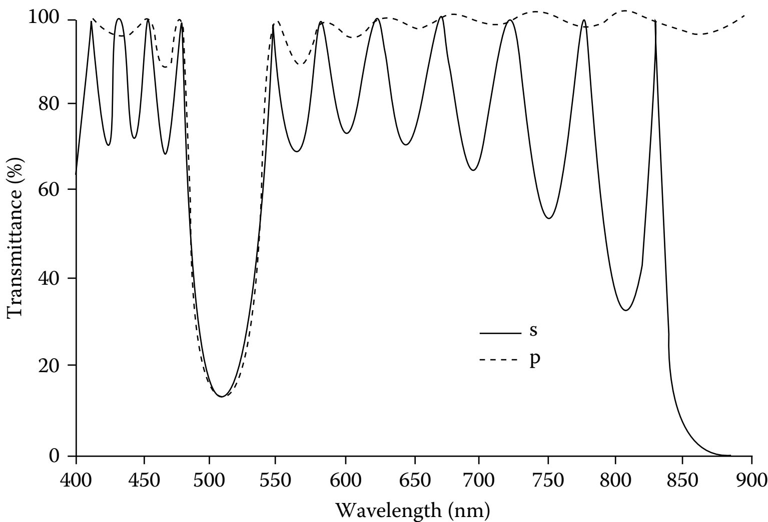

FIGURE 9.22
Calculated performance of a polarization-free reflector at an angle of incidence of 45° in glass. The coating was designed using the method of Thelen [32]. Design: Glass | (1.38H 1.372M 1.653L 1.372M)^8 | Glass with $n_H = 2.25$, $n_M = 1.57$, $n_L = 1.35$, $n_{Glass} = 1.52$, and $\lambda_0 = 510$ nm. The *solid line* indicates s-polarization and the *dashed line* p-polarization.

tends to reduce the *s*-reflectance of the preceding pair but slightly to increase the *p*-reflectance. To achieve high reflectance, large numbers of layers are needed. Angular sensitivity is quite high and there is little that can be done to improve it.

9.4.3 Edge Filters at Very High Angles of Incidence

It is possible to adapt the treatment of the previous section to design edge filters for use at high angles of incidence. We cannot expect to be able to do this with a modest number of layers. Let us illustrate the method by using the example we have just calculated. Figure 9.22 shows the performance. We wish to use this component as a longwave-pass filter and hence to eliminate the ripple on the longwave side of the peak. However, the rejection is not good enough. We need to use more layers. An arrangement with 20 repeats gives lower than 0.1% over most of the rejection region but then there is the ripple. We therefore choose 24 repeats and use the outermost eight layers on either side as the basis for our matching. Computer refinement is the simplest way to achieve this. For this number of layers we need a somewhat more accurate estimate of the layer thicknesses. The final design, before refinement, is then:

$$\text{Glass} \mid (1.13827H\ 1.37187M\ 1.65262L\ 1.37187M)^{24} \mid \text{Glass}$$

The performance after refinement is shown in Figure 9.23.

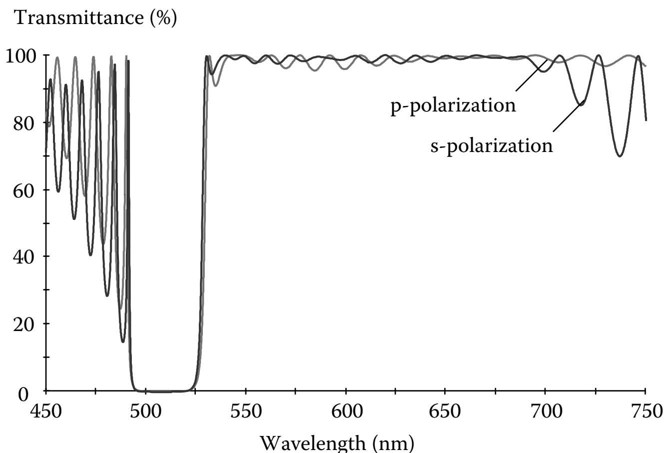

FIGURE 9.23
Calculated performance of a polarization-free edge filter at an angle of incidence of 45° in glass. Design: Glass | $(1.13827H\ 1.37187M\ 1.65262L\ 1.37187M)^{24}$ | Glass with $n_H = 2.35$, $n_M = 1.57$, $n_L = 1.35$, $n_{Glass} = 1.52$, and $\lambda_0 = 510$ nm.

Shortwave-pass filters or filters with different materials can be designed in the same way. Such designs are fairly sensitive to materials and to angle of incidence.

The width of the rejection region is very limited, and less than the width of the split region in a conventional two-material edge filter. Provided the requirements are not too severe, adding a glass absorption filter is probably the most practical way of dealing with the problem. Otherwise, a second interference component at a slightly shorter wavelength will be additionally required.

9.5 Antireflection Coatings

Antireflection coatings at high angles of incidence are rather more difficult than the design of coatings for normal incidence. Some simplification occurs when only one plane of polarization has to be considered. Then it is a case of converting the admittances into tilted or modified optical admittances at the appropriate angle of incidence and then using these values to design coatings in much the same way as for normal incidence. The major complication is that the range of admittances available is different from the range at normal incidence and, especially in the case of *s*-polarization less favorable. We will consider briefly the problem of antireflection coatings for one polarization first and then treat both polarizations where there is the additional problem of a completely different set of admittances for each polarization.

To simplify the discussion of design, we will assume an angle of incidence of 60° in air with a substrate of index 1.5 and possible film indices of 1.3, 1.4, 1.5, … , 2.5. Real designs will be based on available indices, will therefore be more constrained, and may require more layers. The modified admittances with values of $\Delta(=\eta_p/\eta_s)$ are given in Table 9.3.

9.5.1 *p*-Polarization Only

At 60° the modified *p*-admittance of the substrate is only 0.9186, giving a single-surface reflectance for *p*-polarized light of less than 0.2%, acceptable for most purposes. The angle of incidence of 60° is only just greater than the Brewster angle. If still lower reflectance is required, then a single quarter-wave of admittance given by $(0.9186 \times 1.0000)^{1/2}$, that is 0.9584, is required. This corresponds from Table 9.3 to an index of just over 1.6, that is *greater* than the index of the substrate. As the angle of incidence increases, still farther from 60° the required index will become still greater. Eventually, at very high angles of incidence indeed, the required single layer index will be greater than the highest index available, and at that stage, designs based on combinations such as Air | *HL* | Glass will be required with quarter-wave thicknesses at the appropriate angle

TABLE 9.3

Modified Admittances of Different Materials at 60° in Incident Medium of Index 1.00

n_f	$1/\cos\vartheta$	η_p	η_s	$\Delta(=\eta_p/\eta_s)$
1.00	2.0000	1.0000	1.0000	1.0000
1.30	1.3409	0.8716	1.9391	0.4495
1.40	1.2727	0.8909	2.2000	0.4050
1.50	1.2247	0.9186	2.4495	0.3750
1.60	1.1893	0.9514	2.6907	0.3536
1.70	1.1621	0.9878	2.9258	0.3376
1.80	1.1407	1.0266	3.1560	0.3253
1.90	1.1235	1.0673	3.3823	0.3156
2.00	1.1094	1.1094	3.6056	0.3077
2.10	1.0977	1.1526	3.8262	0.3012
2.20	1.0878	1.1966	4.0448	0.2958
2.30	1.0794	1.2414	4.2615	0.2913
2.40	1.0722	1.2867	4.4766	0.2874
2.50	1.0660	1.3325	4.6904	0.2841

Modified admittances
Incident medium index = 1.00
Angle of incidence = 60°

of incidence. Such coatings operate over a very small range of angles of incidence only and are very difficult to produce because of the required accuracy. If at all possible, it is better to avoid such designs altogether by redesigning the optical system.

9.5.2 *s*-Polarization Only

The modified *s*-admittance for the substrate is 2.449, and the required single-layer admittance for perfect antireflection is $(2.4495 \times 1.0000)^{1/2}$ or 1.5650, well below the available range. The problem is akin to that at normal incidence where we do not have materials of sufficiently low index. Here the solution is similar. We begin by raising the admittance of the substrate to an acceptable level by adding a quarter-wave of higher admittance. In this case a layer of index 1.9 or admittance 3.3823 is convenient and gives a resultant admittance of 3.38232/2.449 or 4.6713 that requires a quarter-wave of admittance $(4.6713 \times 1.0000)^{1/2}$ or 2.1613 to complete the design. This corresponds most nearly to an index of 1.4, admittance of 2.2000, and the residual reflectance with such a combination is 0.03%, a considerable improvement over the 17.7% reflectance of the uncoated substrate. We cannot expect that such a coating will have a broad characteristic, and Figure 9.24 confirms it. A small improvement can be made by adding a high-admittance half-wave layer between the two quarter-waves or a low-admittance half-wave next to the substrate. The

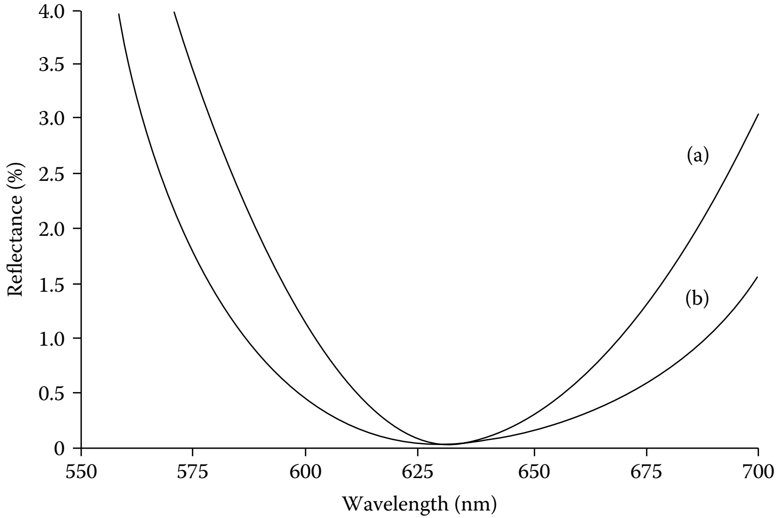

FIGURE 9.24
Antireflection coatings for *s*-polarized light at an angle of incidence of 60° in air. (a) Air | 1.273*L* 1.123*H* | Glass, (b) Air | 1.273*L* 1.123*H* 2.682*A* | Glass with $n_L = 1.4$, $n_H = 1.9$, $n_A = 1.3$, $n_{Glass} = 1.5$, and $\lambda_0 = 632.8$ nm.

latter is also shown in the figure. In terms of normal incidence thicknesses, the two designs are:

$$\text{Air} \mid 1.273L\ 1.123H \mid \text{Glass}$$

and

$$\text{Air} \mid 1.273L\ 1.123H\ 2.682A \mid \text{Glass}$$

where *L, H,* and *A* indicate quarter-waves at normal incidence of films of index 1.4, 1.9, and 1.3 respectively. The *p*-reflectance of these designs is very high, and they are definitely suitable for *s*-polarization only.

Again, it is better wherever possible to avoid the necessity for such antireflection coatings by rearranging the optical design of the instrument so that *s*-polarized light is reflected and *p*-polarized light is transmitted.

9.5.3 *s*- and *p*-Polarization Together

The task of ensuring low reflectance for both *s*- and *p*-polarized light is almost impossible and should only be attempted as a last and very expensive resort. It is possible to arrive at designs that are effective over a narrow wavelength region and one such technique is included here. Again, we use the range of indices given in Table 9.3 and design a coating to give low *s*- and *p*-reflectance on a substrate of index 1.5 in air.

We use quarter-wave layer thicknesses only and a design technique similar to the procedure we have already used for high-reflectance coatings but with an additional condition that the admittance of both substrate and coating for both *p*- and *s*-polarizations should be unity to match the incident medium. This implies

$$\frac{\Delta_1^2\Delta_3^2\Delta_5^2 \dots \Delta_{sub}}{\Delta_2^2\Delta_4^2\Delta_6^2} = 1 \tag{9.39}$$

and

$$Y = \frac{\eta_{1s}^2\eta_{3s}^2\eta_{5s}^2 \dots \eta_{sub,s}}{\eta_{2s}^2\eta_{4s}^2\eta_{6s}^2 \dots} = 1 \tag{9.40}$$

Equation 9.39 ensures that the *p*-reflectance equals the *s*-reflectance and Equation 9.40 that the *s*-reflectance, and, therefore, also the *p*-reflectance, is zero. From Table 9.3 the starting values are $\Delta_{sub} = 0.3750$ and $\eta_{sub} = 2.4495$. Trial and error shows that with the addition of one single quarter-wave layer, the best result corresponds to an index of 1.3 for which $\Delta_1^2/\Delta_{sub} = 0.4495^2/0.3750 = 0.5387$ and $\eta_{1s}^2/\eta_{sub} = 1.9391^2/2.4495 = 1.5350$. Other combinations give values that are farther from unity in each case. Adopting a quarter-wave of index 1.3 as the first layer of the coating, we need a further combination of layers that will provide a correction factor of 1.3624 in Δ and of 0.8071 in η_s. An additional single layer will not do, but two-layer combinations of a high-index followed by a low-index layer can be found that will correct Δ but that are inadequate in terms of η_s. The two-layer combination that comes nearest to satisfying the requirements is a layer of index 1.8 followed by one of index 1.3, making the design so far:

$$\text{Air} \mid n = 1.3 \mid n = 1.8 \mid n = 1.3 \mid \text{Glass}$$

This has an overall Δ of (0.44952 × 0.44952)/(0.32532 × 0.375) = 1.0288 and a η_s of (1.93912 × 0.93912)/(3.15602 × 2.4495) = 0.5795. However, the combination of index 2.5 followed by 1.4 gives approximately the same correction for Δ but a different correction for η_s. This gives the opportunity of using both combinations in a four-layer arrangement to adjust the value of η_s without altering Δ. The correction factor for Δ is given by (0.44952 × 0.28412)/(0.40502 × 0.32532) = 0.9396 and for η_s by (1.93912 × 4.69042)/(2.20002 × 3.15602) = 1.7159. This then yields an overall value for Δ of 0.9396 × 1.0288 = 0.9667 and for η_s of 1.7159 × 0.5795 = 0.9944. The seven layers can be put in various orders without altering the reflectance at the reference wavelength. All that is required is that the 1.3 and 2.5 indices should be odd, and the 1.4 and 1.8 indices, even. Here we put them in descending value of index from the substrate so that the final design is:

$$\text{Air} \mid 1.3409L\ 1.2727A\ 1.3409L\ 1.1407B\ 1.3409L\ 1.1407B\ 1.066H \mid \text{Glass}$$

with $n_L = 1.30$, $n_A = 1.40$, $n_B = 1.80$, and $n_H = 2.50$.

The calculated performance of this coating for a reference wavelength of 632.8 nm is shown in Figure 9.25. As we might have suspected, the width of the zone of low reflectance is narrow. An alternative design arrived at in the same way but for a substrate of index 1.52 and a range of film indices from 1.35 to 2.40 uses 10 layers:

$$\text{Air} \mid 1.3036L\ 1.1748A\ 1.3036L\ 1.1748A\ 1.3036L\ 1.1407B\ 1.0722H\ 1.1235C\ 1.0722H\ 1.1235C \mid \text{Glass}$$

with $n_L = 1.35$, $n_A = 1.65$, $n_B = 1.80$, $n_C = 1.90$, $n_H = 2.40$, $n_{Glass} = 1.52$, and $n_{air} = 1.00$. The performance is similar to that of Figure 9.25.

The most successful designs for equal *p*- and *s*-performance in the last two sections have illustrated the usefulness of using more than two materials. It is fairly easy to see why. The phase thickness at oblique incidence is exactly the same for both polarizations and, with only two materials, there is no flexibility in the properties of the interfaces. An interface of material *A* to material *B* has virtually the same properties as material *B* to material *A*, except for a 180° difference in the phase shifts. Altering the polarization-sensitive properties independently is, therefore, virtually impossible. A slight increase in flexibility can be obtained by the use of three materials, with three different interface properties. There is a price to pay in that the properties of coatings at oblique incidence exhibit considerable sensitivity to the precise values of refractive index.

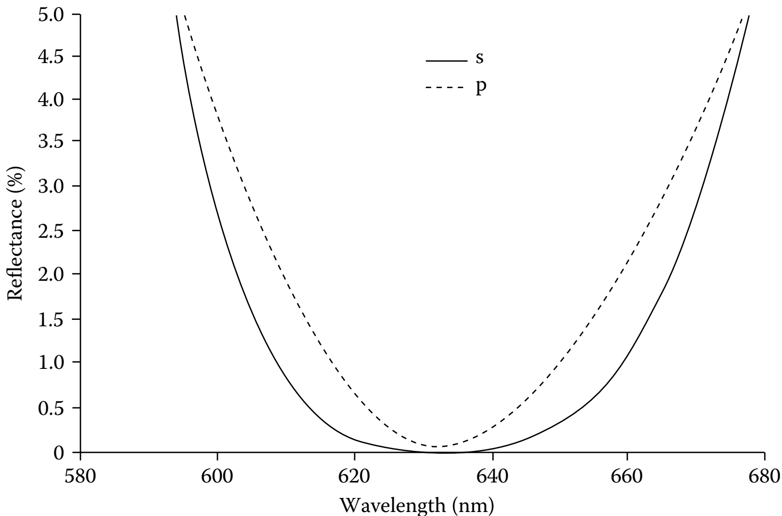

FIGURE 9.25
Calculated performance of an antireflection coating for glass to have low reflectance for both *p*- and *s*-polarization at an angle of incidence of 60° in air. The *solid line* indicates *s*-polarization and the *dashed line* *p*-polarization. $\lambda_0 = 632.8$ nm and the design is given in the text.

The ideal antireflection coating is, of course, the inhomogeneous layer, already discussed in Chapter 4. The properties of the coating are not very sensitive to the profile of index as long as it is smooth and gradual. It acts as an efficient antireflection coating as long as its total phase thickness is greater than one-half wavelength. Thus, when tilted, although the profile changes slightly, as long as the angle of incidence is below that at which the phase thickness would become less than one-half wavelength, the antireflecting properties will be maintained.

Unfortunately, the difficulty of finding a sufficiently low refractive indices for the outermost parts of the inhomogeneous layer exists also at oblique incidence.

9.6 Retarders

In many applications, the polarization state of a ray is of great importance. Optical surfaces, with or without coatings, modify these properties. Knowledge of nature of the modification is necessary for an investigation of the initial polarization. Measurement of the modification is an important surface and coating characterization tool. Deliberate manipulation of the polarization is possible with specially designed coatings. Before we can examine and quantify these properties, we need to define some terms and conventions.

9.6.1 The Ellipsometric Parameters and Relative Retardation

We assume a completely polarized beam defined by two orthogonal components of electric field that exhibit complete coherence. Then, the ellipsometric parameters ψ and Δ (psi and Delta) are defined as:

$$\tan\psi = \left|\frac{\mathcal{E}_x}{\mathcal{E}_y}\right| \text{ and } \Delta = \varphi_x - \varphi_y \tag{9.41}$$

Δ is also known as the relative retardation or retardance. Note that ψ and Δ depend on the choice of the reference axes. Note also that this Δ should not be confused with that in Equations 9.36 and the following ones. When reflection at a surface is concerned, it is convenient to make the reference axes coincide with the *p*- and *s*-directions. Then we can introduce the idea of a ψ and Δ that are properties of the surface, or of the coating. We can define them as:

$$\tan\psi = \left|\frac{\rho_p}{\rho_s}\right| \text{ or } \left|\frac{\tau_p}{\tau_s}\right| \text{ and } \Delta = \varphi_p - \varphi_s \tag{9.42}$$

However, there is a mild problem. The convention needs a consistent handedness of the reference axes together with the propagation direction, that is p, s, and direction, *in that order*. The thin film convention, detailed in Chapter 2, is right-handed in incidence and transmission but *left-handed* in reflection. To keep the complications to a minimum, the ellipsometric convention then flips the p-direction in the reflected ray. This creates problems at normal incidence where there is no plane of incidence and where there can be no orientational dependence in the behavior of linearly polarized light. The thin-film community, therefore, retains the Chapter 2 convention for positive directions and simply amends the definition of Δ to be:

$$\begin{aligned} \Delta &= \varphi_p - \varphi_s \quad \text{in transmission} \\ \Delta &= \varphi - \varphi_s \pm \pi \quad \text{in reflection} \end{aligned} \tag{9.43}$$

This also helps to remove a complication at normal incidence. Circularly polarized light that is reflected from the surface of a coating at normal incidence remains circularly polarized, but it changes its handedness. This implies a relative retardance, or Δ, of π, or 180°, which, fortunately, is in accordance with Expression 9.43. The value of ψ is, therefore, 45° and Δ, 180°, or π. Any pair of orthogonal axes making up a right-handed set with the direction of propagation can therefore be used without requiring any change in the values of ψ and Δ.

A reflection at normal incidence is sometimes referred to as a half-wave plate or a half-wave retarder. This is an unsatisfactory way of referring to it because it does not behave as a normal half-wave retarder. We cannot use it to rotate a plane of polarization, for example. We shall deal with retarders in more detail shortly.

9.6.2 Series of Coated Surfaces

A knowledge of the absolute phase of a light ray demands an exact knowledge of the path length traversed by the ray. In an optical system, this is not usually known or even constant to the necessary precision. For the understanding of the effects on the polarization of the light, the absolute phase is not required but only the difference in phase between the reference components. Thus, unless there is some optical activity that would introduce a differential phase shift between the components, we normally ignore the phase change that results from the passage between components and include simply the changes that take place at the surfaces. Since it is the difference in phase that is important, we can simply use Δ. Should we need separate phases for each polarization, we can adopt the net Δ for the final p-polarized component and zero for s.

At oblique incidence, ψ and Δ are initially defined with respect to the plane of incidence. Provided the plane of incidence for any subsequent reflection or transmission does not change, then combining the effect of multiple surfaces

is straightforward. Since the p-direction and s-direction are completely independent, then, ignoring the phase shift between elements, we can write

$$\begin{aligned} \rho_p &= \rho_{p1} \cdot \rho_{p2} \cdot \rho_{p3} \cdots \\ \rho_s &= \rho_{p1} \cdot \rho_{p2} \cdot \rho_{p3} \cdots \end{aligned} \tag{9.44}$$

where each ρ may be replaced by a τ for a transmission, and where we must use the ellipsometric convention for ρ_p. Then

$$\begin{aligned} \tan\psi &= \tan\psi_1 \cdot \tan\psi_2 \cdot \tan\psi_2 \cdots \\ \Delta &= \Delta_1 + \Delta_2 + \Delta_3 + \ldots \end{aligned} \tag{9.45}$$

The combination becomes much more complicated if the planes of incidence are not coincident. Then it is not particularly helpful to think in terms of ψ and Δ. Since the plane of incidence always contains the ray, we will be dealing with a rotation of each fresh plane of incidence about the ray direction. This can be handled as an application of the Jones matrices [35–37] for rotation.

First, we need to choose reference directions for the input electric field of the wave and these can conveniently be the p- and s-directions of the beam as it emerges from the previous element. Then, let ϑ is the angle of rotation of the new set of p- and s-directions around the direction of propagation. The calculation can be written as:

$$\begin{bmatrix} \mathcal{E}_{p'} \\ \mathcal{E}_{s'} \end{bmatrix} = \begin{bmatrix} \rho_{p'} & 0 \\ 0 & \rho_{s'} \end{bmatrix} \begin{bmatrix} \cos\vartheta & \sin\vartheta \\ -\sin\vartheta & \cos\vartheta \end{bmatrix} \begin{bmatrix} \mathcal{E}_p \\ \mathcal{E}_s \end{bmatrix} \tag{9.46}$$

The components $\mathcal{E}_{p'}$ and $\mathcal{E}_{s'}$ are referred to the p- and s-directions of the final emergent beam. Once again, the ellipsometric convention is used for ρ_p.

The Jones matrix approach involves keeping track of the reference directions and their rotations. This can be quite difficult and include awkward subsidiary calculations, especially when transmission rather than reflection is involved. An alternative approach involves setting up a set of three-dimensional reference axes and referring everything to them. Vector analysis is the most straightforward way of handling the calculations. Once the framework is set up, it is then necessary only to specify the directions of the various surface normals, the materials and coatings, and whether reflection or transmission is involved.

The most important prerequisite for such calculations is a clear head.

9.6.3 Retarders

Phase retarders introduce a relative phase shift between two orthogonal planes of polarization and are characterized by their relative retardance, Δ.

Most commonly, these are plates of birefringent materials with different indices of refraction for each polarization. If these indices are given by n_a and n_b, then, ignoring any effect of the surfaces of the plate, the relative phase shift that is introduced is $2\pi(n_a - n_b)d/\lambda$ where d is the physical thickness of the plate. Usually, the direction in the plate that corresponds to the electric field direction for the lower refractive index is called the fast axis. This helps to determine the sense of the relative phase shift, but the terminology is not well organized. The birefringent retarder is a very straightforward component that is easy to use and possesses the great advantage of preserving the direction of the light beam. There are limitations, however. Retarders of large size may be impossible or prohibitively expensive. The surfaces have the usual reflection loss and may need antireflection coatings to minimize them. Then there is the dependence on $1/\lambda$. Achromatic retarders, therefore, are more complicated generally using two or more different materials. Thin-film retarders can avoid some of these problems.

Isotropic materials show no polarization-sensitive effects at normal incidence. Once they are tilted, there is a difference in the properties for *s*- and *p*-polarized light and this is the basis for their application in retarders.

The phase thickness of a layer is the same for both *s*- and *p*-polarizations. For a device to operate in transmission, the reflectance should be low, and the light then tends to be transmitted with almost identical phase shift for both polarizations. Only in narrowband filters where the light is stored in cavities do we find any very significant differences between the polarizations and such components are rather more useful as polarizers than as retarders. Useful thin-film retarders are almost invariably reflecting devices. Since the polarization state of the light can be perturbed by a simple difference in reflectance even when there is no difference in the relative phase, these devices should have *p*- and *s*-reflectances that are as closely equal as possible. This normally implies making the reflectances as high as possible.

Before we consider the design of thin-film retarders, we need to consider our conventions. We are dealing exclusively with tilted reflectances and with changes in the polarization state of the light. It is therefore convenient to use the ellipsometric parameters ψ and Δ of the coating or device, Equations 9.42 and 9.43, to describe the performance. Since we will attempt to have no influence on polarization from reflectance differences, ψ will normally be 45°.

We should consider briefly the implications of a value of ψ that differs from 45°. We imagine linearly polarized light incident with polarization direction at 45° to the plane of incidence. This gives equal amplitude of both *s*- and *p*-polarizations. Then, on suffering a reflection characterized by ψ, the new plane of polarization will be rotated to angle ψ with respect to the direction of *s*-polarization. In fact, errors in ψ always result in a rotation of the plane of polarization of linearly polarized light. The largest effect is produced when the incident light has polarization direction at 45° to the plane of incidence. The ellipsometric convention measures angles with respect to the *s*-direction (this is in accordance with the convention for ψ) and so the rotation in that

case will be $\varepsilon = (45° - \psi)$. Circularly polarized light will become slightly elliptical, as if the original linearly polarized light used to generate it were rotated through ε away from the ideal 45° with the axis of a quarter-wave plate. We will use ψ as one characteristic of our thin-film retarders.

9.6.4 Simple Retarders

The simplest form of this type of retarder is not strictly a thin-film system at all. Below the critical angle, the ψ and Δ associated with reflection at a simple dielectric surface are of little interest. ψ varies from 45° to zero and back to 45°, while Δ starts at 180° and flips to zero as the angle of incidence, ϑ, rises either to grazing incidence or the critical angle, whichever comes first. Beyond the critical angle, which requires an incident medium of greater refractive index than the emergent, the situation changes. Then ψ remains fixed at 45° and Δ rises from zero to a maximum in the first quadrant and then falls back to zero. The behavior is illustrated in Figure 9.26. There are two angles of incidence at which the retardance is exactly 45°. With two such reflections, a total Δ of 90°, that is, a quarter-wave retardance, can be obtained. A device that employs this effect is known as a *Fresnel rhomb* (Figure 9.27).

A high-performance metal layer can be used as a very simple retarder. As the angle of incidence changes, the admittance (modified) of a high-performance metal layer is given to a good degree of accuracy by $\eta_s = (n - ik)/\cos\vartheta_0$ and $\eta_p = (n - ik)\cos\vartheta_0$. As the angle of incidence increases, therefore, the *s*- and *p*-admittances move along a straight line from $(n - ik)$ at normal incidence toward the origin for *p*-polarization and away from the origin for *s*-polarization. The behavior is illustrated in Figure 9.5. The phase shifts at normal incidence are equal and then move gradually apart, the *p*-phase shift reducing to zero at grazing incidence and the *s*-phase shift increasing to 180°

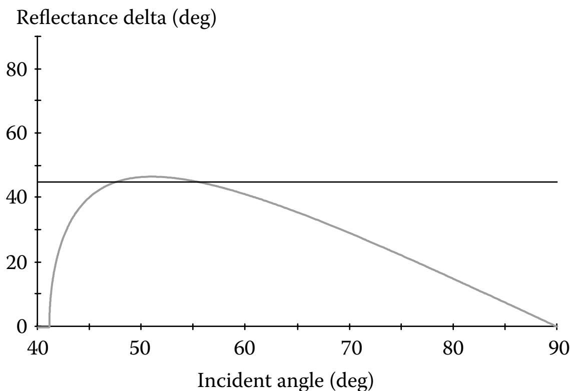

FIGURE 9.26
The variation of Δ with angle of incidence (degrees) for total internal reflection at a glass surface (index 1.52). Δ is 45° for angles of 47.6° and 55.4°.

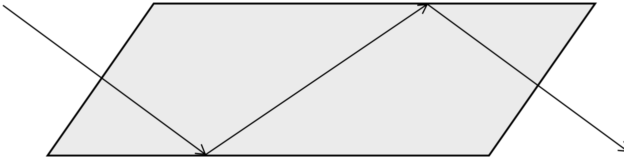

FIGURE 9.27
Sketch of a Fresnel rhomb. The double reflection inside the device gives a total retardance, Δ, of 90°.

at grazing incidence. The retardance, Δ, then, is 180° at normal incidence and falls to zero at grazing incidence. (Remember the extra 180° that must be included in Δ.) The calculated behavior of silver at 600 nm is shown in Figure 9.28. ψ is close to 45° falling to around 44.5° near the pseudo-Brewster angle where R_p is a minimum.

The effect of a thin dielectric overcoat, like a layer of tarnish, for example, is to reduce the retardation slightly. Figure 9.29 shows the effect of 3 nm of a material of index 1.70. The *p*-polarization locus falls faster than the *s*-polarization and so the *p*-phase shift moves more rapidly into the first quadrant. This implies a reduction in the value of Δ and, at its maximum, there is a reduction of around 4°.

Of course, the retardation varies with wavelength as well as angle of incidence, but this simple retarder can be quite useful, especially soon after deposition in a reasonably benign laboratory atmosphere.

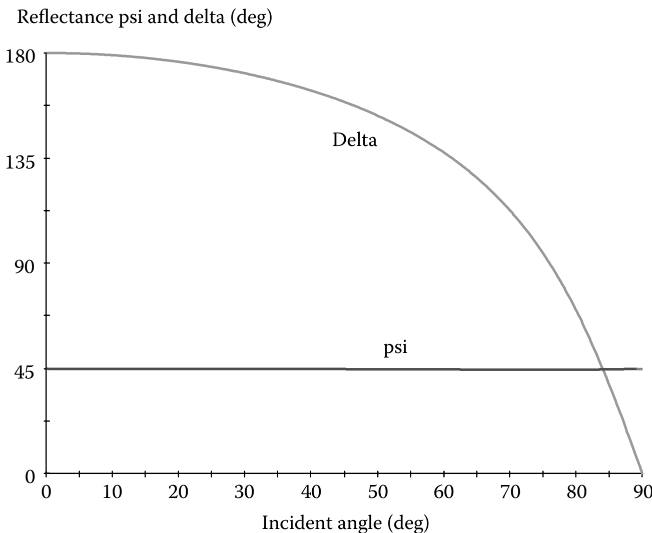

FIGURE 9.28
The calculated retardance, Δ, and ψ for an opaque silver layer at 600 nm where the optical constants are (0.06 – *i*3.75).

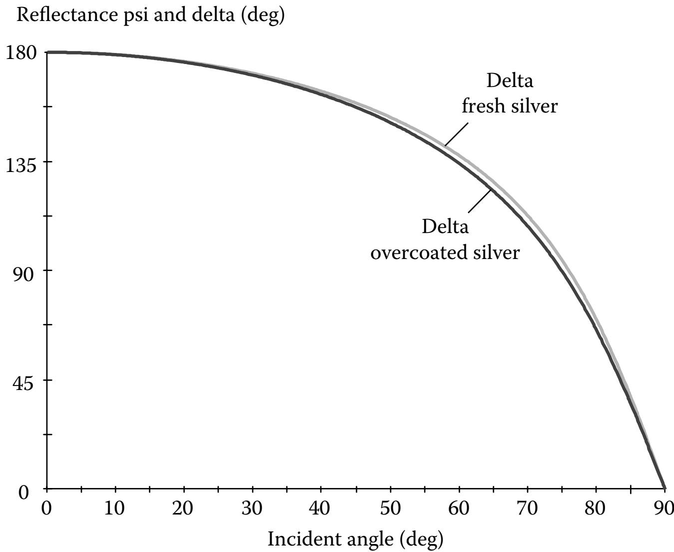

FIGURE 9.29
The effect of a thin dielectric layer over the silver of Figure 9.28. A 3-nm-thick layer of index 1.70 reduces slightly the retardation. The original silver upper curve is compared with an overcoat of 3 nm of material of index 1.70. The two curves are almost identical on this scale but there is a reduction of around 4° in the center.

The retardance of a simple surface beyond critical can be altered by a thin-film overcoat. For example, the Fresnel rhomb is almost achromatic in performance, but the dispersion of the glass causes the retardation to increase gradually with decrease in wavelength. A further disadvantage of the Fresnel rhomb is its sensitivity to angle of incidence changes. The performance of the Fresnel rhomb can be considerably improved in both these directions by the addition of a thin-film coating to both surfaces of the rhomb. King [38] has manufactured Fresnel rhombs exhibiting a phase retardation varying by less than 0.4° over the wavelength range 330–600 nm. These were made from hard crown glass with one surface coated with magnesium fluoride 20 nm thick. Then Lostis [9] gives an early example of the considerable modification possible in the retardance of a prism hypotenuse by the addition of a single thin film.

We begin with 45° as the angle of incidence, glass (n = 1.52) as the prism material and air as the outermost medium. This incidence is beyond the critical angle. To achieve a qualitative understanding, we start by imagining that a dielectric film is added, at oblique incidence, to the hypotenuse of the prism where the light is totally reflected. Provided there are no losses, the light will still be totally reflected but the value of Δ will have changed. We can understand the change by considering a simple hypothetical case where the base of the prism has $\varphi_s = \varphi_p = 0$. This means that the admittance is at the origin. We imagine that the film is of sufficiently high index that its

p- and s-admittances are real, but, of course, of different value. If the index is high, compared with glass, then the s-admittance will be high and the p-admittance low (note that these are the *modified* admittances). A low-index film will have the p-admittance higher than the s. Figure 9.2 should make this clear. Eighth-wave thicknesses arrive at η_p and η_s on the imaginary axis, while the boundary between the fourth and third quadrants is the point y_0 in between these two values.

The addition of an eighth-wave then, takes the loci for p- and s-polarizations to points that correspond to different phase shifts on reflection and, for a high-index film, the p-admittance will be lagging behind the s-admittance. Subsequently as the thickness becomes a quarter-wave, the s- and p-admittance are in step and the retardance is again 180°. For the second quarter-wave, the situation is reversed and the retardance rises above 180°. For a low index film, the p- and s-admittances are reversed, and so the variation of retardance will tend to be opposite to that of the high-index film, although the low index film will exhibit tighter cycles because of the larger $\cos\vartheta$ term. The extent of the polarization splitting in Figure 9.2 is also an indication of the maximum value of Δ attainable.

Figure 9.30 shows the accurately calculated variation of retardance of a high-index film (n = 2.40) and low-index film (n = 1.38). A thin (around 0.08 full wave for 2.40) layer of high admittance can clearly transform the retardance so that it is 90° in just one reflection at 45° incidence.

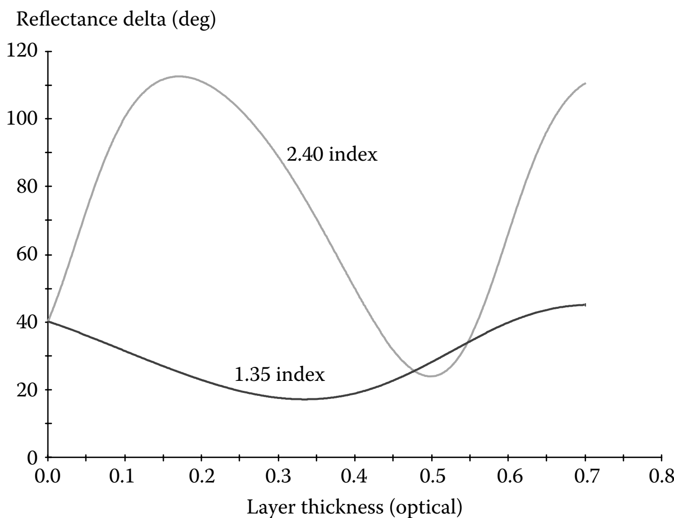

FIGURE 9.30
The retardance, or Δ, produced by total internal reflection at 45° in a prism of index 1.52 when a layer of index 2.40 or 1.38 is added to the outer surface of the hypotenuse. Air is the outer medium. A thickness of around 0.08 full waves (measured at normal incidence) of index 2.40 gives a retardance of 90° in one reflection.

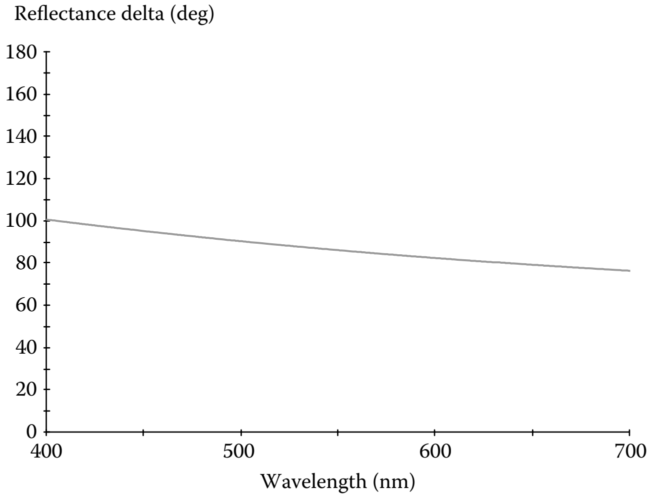

FIGURE 9.31
The variation with wavelength of the retardance at 45° incidence of the design: Glass (n = 1.52) | $0.062\lambda_0$ n = 2.40 | Air with λ_0 = 510 nm.

9.6.5 Multilayer Retarders at One Wavelength

There has been a number of applications where reflecting coatings have been required that introduced specified phase retardances between *s*- and *p*-polarization. In particular, certain types of high-power laser resonators have required coatings that introduce a 90° phase shift between *s*- and *p*-polarization at an angle of incidence of 45°. Coatings designed and manufactured for this purpose have generally been designed for wavelengths in the infrared and have taken the form of silver films with a multilayer dielectric overcoat.

The first published designs were due to Southwell [39,40] who used a computer synthesis technique. Then Apfel [41,42] devised an analytical approach that we follow here. The principle of operation of the coatings is that an added dielectric layer will not affect the reflectance of a system that already has a reflectance of unity. It will simply alter the phase change on reflection. When the component is used at oblique incidence, the alteration in phase will be different for each plane of polarization. By adding layers in the correct sequence, eventually any desired phase difference between *p*- and *s*-polarization for a single specified angle of incidence and wavelength can be achieved. In practice, a silver layer is used as the basic reflecting coating and, although this has reflectance slightly less than unity, in the infrared it is high enough for it to be possible to neglect any error that might otherwise be introduced. It is, of course, not necessary to use a metal layer as starting reflector. A dielectric stack would be equally effective but would simply have more layers.

The basis of Apfel's method is a plot of phase retardance, denoted by Apfel as D, against the average phase shift A as a function of thickness of added layer of a given index. For simplicity, we retain this notation but in the rest of what follows we alter both notation and derivation to agree with the remainder of the book. [Note especially that Apfel defines D as the difference between p and s-phase shifts. We will rather use the normal sign convention for Δ so that $D = \Delta$.]

We will use the modified admittances so that $\eta_0 = y_0$. The starting point of the treatment is a reflector with a reflectance of unity, that is, a surface with imaginary admittance. Let this imaginary admittance be $i\beta$ for p-polarization and $-i\beta$ for s. Then for this surface

$$\left|\rho_p\right| e^{i\varphi_p} = e^{i\varphi_p} = \frac{(\eta_0 - i\beta)}{(\eta_0 + i\beta)} = \frac{(y_0 - i\beta)}{(y_0 + i\beta)} \tag{9.47}$$

i.e.,

$$\tan\left(\frac{\varphi_p}{2}\right) = \frac{-\beta}{y_0} \tag{9.48}$$

and

$$\tan\left(\frac{\varphi_s}{2}\right) = \frac{\beta}{y_0} \tag{9.49}$$

These two values of φ are identical numerically but inverted in sign. They can be represented by $\pm\xi$ when

$$\beta = -y_0 \tan\left(\frac{\xi}{2}\right) \tag{9.50}$$

From the form of the admittance diagram, we can see that for β positive, φ_p should be in the third or fourth quadrant and hence $\tan(\varphi_p/2)$ is negative, confirming the sign in Expressions 9.48 and 9.50.

Now let us add a film of admittance η_1 and phase thickness δ_1 to the substrate, η_1 corresponding to the appropriate polarization,

$$\begin{aligned}\begin{bmatrix} B \\ C \end{bmatrix} &= \begin{bmatrix} \cos\delta_1 & i(\sin\delta)/\eta_1 \\ i\eta_1 \sin\delta_1 & \cos\delta_1 \end{bmatrix} \begin{bmatrix} 1 \\ i\beta \end{bmatrix} \\ &= \begin{bmatrix} \cos\delta_1 - (\beta/\eta_1)\sin\delta_1 \\ i(\eta_1 \sin\delta_1 + \beta\cos\delta_1) \end{bmatrix}\end{aligned} \tag{9.51}$$

The phase shift, φ_p, is now given, from Equation 9.51, as

$$\tan(\varphi_p/2) = \frac{-(\eta_1 \sin\delta_1 + \beta\cos\delta_1)}{y_0[\cos\delta_1 - (\beta/\eta_1)\sin\delta_1]}. \tag{9.52}$$

While that for φ_s becomes:

$$\tan(\varphi_s/2) = \frac{-(\eta_1 \sin\delta_1 - \beta\cos\delta_1)}{y_0[\cos\delta_1 + (\beta/\eta_1)\sin\delta_1]} \tag{9.53}$$

with appropriate adjustments to Expressions 9.52 and 9.53 should $\beta \to \infty$.

To draw a *D*–*A* curve, we choose a starting point given by $D = \Delta = 2\xi \pm 180°$ and $A = 0$, and plot the difference in phase against the average phase, all calculated from Expressions 9.52 and 9.53. Different values of ξ yield a family of curves. There is, however, a slight problem connected with principal range. If this is limited to 360°, then there are two values of *D* for every possible value of *A*. Apfel's plots show only one of the solutions. It is better to permit *D* to range from –360° to +360° so as to separate the two solutions. Then a certain amount of manipulation of the results into the correct range is sometimes necessary for the results to plot cleanly. This family of curves can

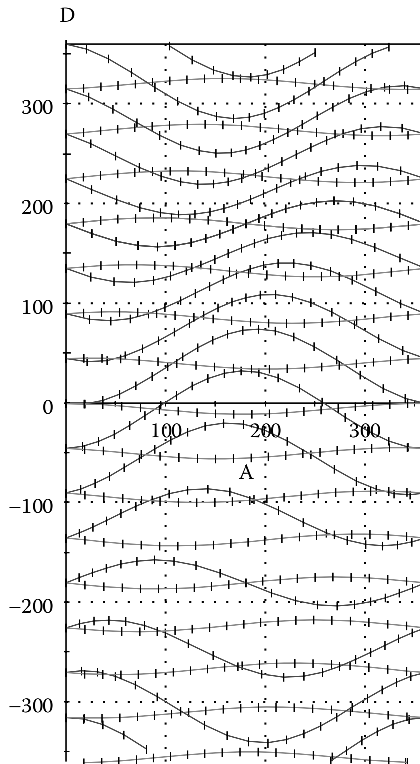

FIGURE 9.32
D–*A* plot for films of index 1.45 (*flatter orange curves*) and 2.15 (*steeper blue curves*) over the hypotenuse of a glass prism of index 1.52 illuminated internally at angle of incidence 45°. The tick marks are spaced at intervals of one tenth of a quarter-wave at the appropriate angle of propagation. (See color insert following page 398.)

have a scale of thickness marked along them, in the manner of Figure 9.32. Thickness increases with movement toward the left. Note that as curves disappear off the left side of the diagram they reappear at the right side and the same with the top and the bottom of the diagram.

The curves now make it possible to determine the phase retardation produced by any combination of thicknesses of layers of the given dielectric materials that are added to any substrate of unity reflectance. Since the curves for different materials do not coincide, it is possible to reach any point of the diagram simply by moving from one set of curves to the other in succession.

The method is illustrated by Figure 9.32, where we design a phase retarder to have a retardance of 180°. The start point is a glass–air interface beyond critical. The layers follow the appropriate curves and, as can be seen, terminate at the extrema. This ensures the most efficient design. The final retardance in this case is 172° and the design is optimum for four layers. To do

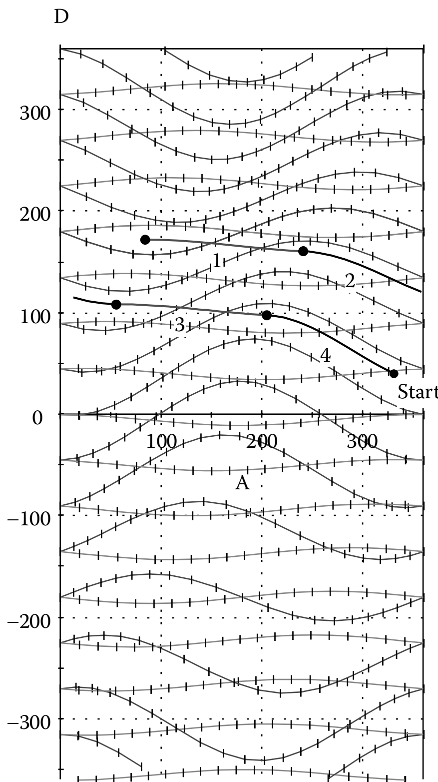

FIGURE 9.33
The design of a retarder to give 180° retardance at one wavelength and consisting of four layers with final design: 1.52 | 1.2533*L* 0.8950*H* 1.1935*L* 0.6902*H* | Air. With $\lambda_0 = 600$ nm, $n_H = 2.15$ and $n_L = 1.45$. The angle of incidence in the incident medium of index 1.52 is 45°. The final retardance is 172°. To do better will require another layer. (See color insert following page 398.)

better will require yet another layer. The performance as a function of wavelength is shown in Figure 9.34.

Computer refinement and synthesis are powerful techniques that work very well with retarders. A useful aspect of this graphical technique is that it does indicate very clearly the least number of layers that will be required and their approximate thicknesses. Once this information is available, the automatic design processes can then be used to great effect.

9.6.6 Multilayer Retarders for a Range of Wavelengths

There is no body of published knowledge on analytical design techniques for thin-film retarders over a wide range of wavelengths. Fortunately, as mentioned earlier, the existence of powerful computer programs for refinement and synthesis with the capability of targeting retardance makes the design of such systems relatively straightforward. As emphasized in the previous section, the use of reflection rather than transmission is strongly advised and, if possible, operating on a surface with incidence beyond critical, with its natural total reflection, reduces considerably the difficulties in, and the complexity of the design.

A typical design for a 90° retarder is given in Table 9.4 with performance plotted in Figure 9.35. For simplicity, no dispersion in the materials was assumed. The complexity of the design depends very much on the tolerances required. Over the range 400–700 nm, the variation in Δ is largely within ±0.5°, rising slightly at the very ends of the range. To reduce this variation it is sufficient to amply more layers.

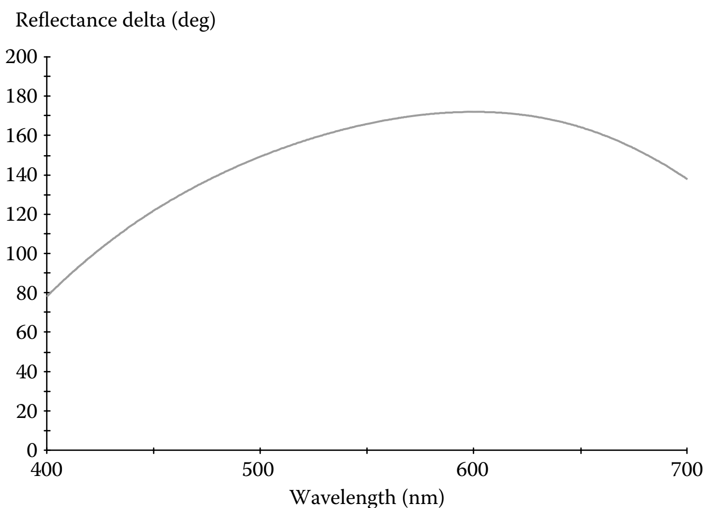

FIGURE 9.34
The retardance as a function of wavelength, at 45° in glass, of the design of Figure 9.33. At 600 nm, the design wavelength, it is 172°.

TABLE 9.4

Design of the Retarder of Figure 9.35

Layer	Material	Refractive Index	Thickness (optical)
Medium	1.52	1.5200	
1	2.40	2.4000	0.06390
2	1.38	1.3800	0.13084
3	2.40	2.4000	0.08567
Substrate	Air	1.0000	

Reference wavelength 510 nm
Angle of incidence 45°

The advantage of the use of prisms beyond the critical angle is that whatever thicknesses are used for the dielectric layers, provided they have very low losses, then the reflectance will always be total. In addition, at the very high angles of propagation in the film materials, the large splitting between the *p*- and *s*-admittances also helps greatly in simplifying the design. At angles that are less than critical, these advantages are lacking. Otherwise, the design operation is similar. We need high reflectance and we can achieve that by a dielectric or metal–dielectric assembly. This must have sufficient layers so that the additional retardance-trimming layers do not cause too great a fall in reflectance.

Since it usually makes little difference whether the relative retardance is positive or negative, the best choice is to have the targets represent as small as possible a *reduction* from the starting values. This makes use of the natural tendency of the dielectric overcoating layers. It cannot be expected that such retarders could have performance equivalent to the totally internally

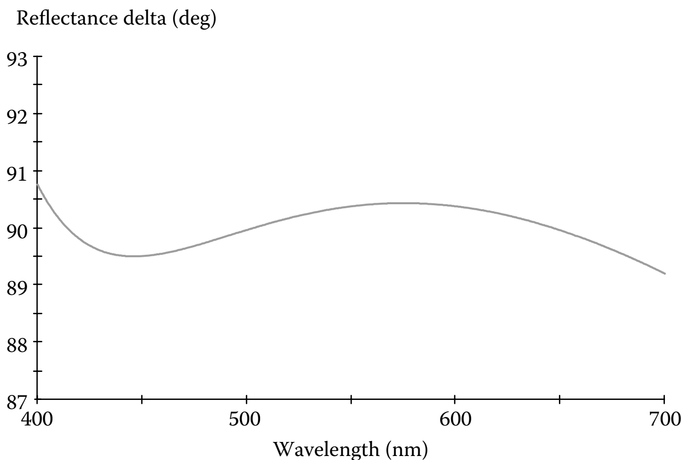

FIGURE 9.35
The retardance, Δ, of a three-layer system on the base of a prism of index 1.52 with internal incident angle 45°. The design of the coating is given in Table 9.4.

TABLE 9.5

Design of the Retarder of Figures 9.36 and 9.37

Layer	Refractive Index	Thickness (optical)
Medium	1.0000	
1	1.4500	0.185990
2	2.4000	0.360087
3	1.4500	0.408571
4	2.4000	0.364333
5	1.4500	0.374153
6	2.4000	0.344197
7	1.4500	0.380938
8	2.4000	0.329630
9	1.4500	0.344621
10	2.4000	0.291818
11	1.4500	0.368586
12	2.4000	0.079470
13	2.4000	0.261612
14	1.4500	0.286358
15	2.4000	0.261612
Layers 16 to 31 are repeats of 14 and 15		
32	1.4500	0.286358
33	2.4000	0.261612
Substrate	1.5200	

Reference wavelength 600 nm
Angle of incidence in air 45°

reflecting retarders. The performance is generally inferior and, unless starting with a high performance metal, the number of layers large.

An example of the design of a 90° retarder that operates at 45° in air and uses a completely dielectric approach is given in Table 9.5 with performance in terms both of retardance and ψ in Figure 9.36 and Figure 9.37. The basic reflector is a 21-layer quarter-wave stack at a reference wavelength of 600 nm and tuned to 45°. It is constructed from material with indices 1.45 and 2.40. The target specification of 90° is defined over 550–650 nm. The eventual variation in retardance is clearly rather larger than in the internally reflected cases, and the range of wavelengths over which the performance is achieved, rather less. The overcoat that ensures the retardance has 12 layers. The value of ψ for this coating is shown in Figure 9.37, and any errors from this source are clearly well below those from the achieved values of Δ.

Prism systems are frequently used in visual optical instruments to manipulate the image in some way. This might be a translator in a periscope or an erector in a telescope. Internal reflection plays an important part in such systems. The single totally reflecting surface reverses the parity of the image —that is, it changes the handedness of the image. The reversal of parity is

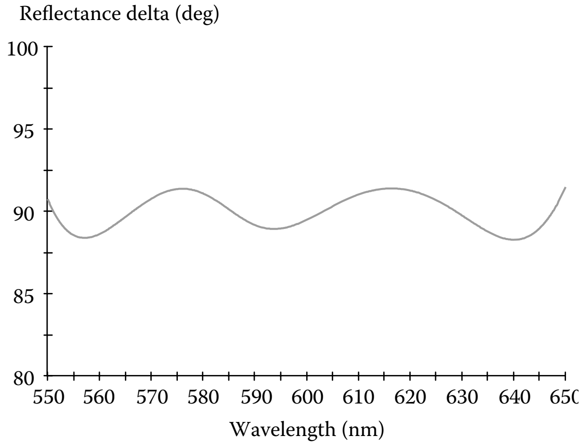

FIGURE 9.36
The retardance Δ at 45° in air from a dielectric reflector of materials 2.40 and 1.45 arranged as a basic reflector for 45° with outer correcting layers. See Table 9.5 for the design.

usually in itself undesirable in a visual image, but, further, it is normally accompanied by a sensitivity of the system to rotation. A reflector that retains parity and, solves most of these problems, is the roof.

This consists of two internally reflecting surfaces arranged accurately at 90° to each other so that the appearance is exactly that of the roof of a house. Many erecting prism systems have an odd number of reflecting surfaces arranged with coplanar normals. Their reversal of parity and their sensitivity to rotation make them useless in instruments like binoculars. The

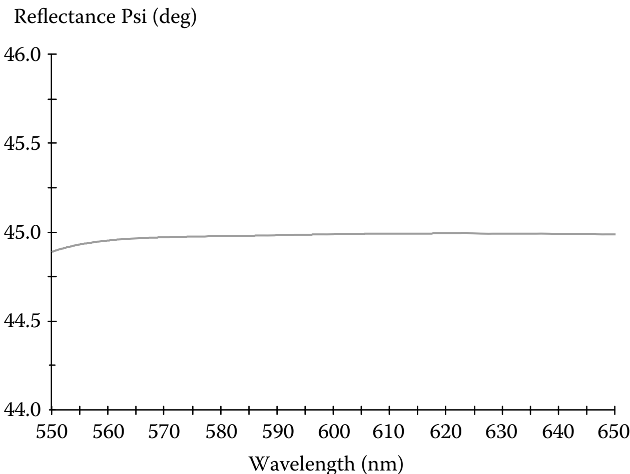

FIGURE 9.37
The value of ψ for the retarder of Figure 9.36 and Table 9.5.

replacement of one of the surfaces by a roof restores the parity and removes the rotational sensitivity. The Pechan prism, often used instead of a double Porro prism in compact binoculars, is a good example.

However, the roof, in solving the parity and rotation sensitivity problems, introduces another different problem. Half the light contributing to the image meets the two surfaces in the reverse order to the other half. At each reflection, there is an effect on the polarization state of the light, even if perfectly collimated. The composite effect of the two surfaces depends on the order in which they are encountered. If the resulting polarization states are sufficiently different for the two halves, then the resulting image will consist of a point-spread function for each half rather than a single, narrower function for the complete aperture. When the perturbation of polarization consists essentially of two equal parts with identical orientation of polarization but with a half-wave difference in phase, the central maximum of the point spread function disappears and there is a serious doubling of the image. This is an old problem that was explained in detail by Mahan [43,44]. See Rabinovitch and Toker [10] for some more recent information on this and other similar problems.

To avoid this problem, the relative retardation, Δ, at each of the reflecting surfaces of the roof should be 180°. If the incident ray direction is at 45° to the roof with the plane of incidence bisecting the angle between the two surfaces, then the angle of incidence of the ray on each surface is 60°. The angle between the two planes of incidence for the ray as it crosses the roof is 70.5°. Let us assume that the light is linearly polarized. Δ of 180° implies that the p-component (note this is the ellipsometric convention, not the normal thin-film convention) of the polarization is flipped. This is equivalent to a rotation of the direction of polarization, around the ray, through twice the angle between it and the s-direction. The two s-directions lie in the planes of the roof, and the double rotation turns the plane of polarization through 180°. This is the same for either order in which the surfaces are encountered and so the two alternative passages through the roof yield identical emerging polarizations. This is not the case for a Δ of zero or of some intermediate value. Then the orientation depends not only on the properties of the surfaces but also on the angle of incidence. The question of allowable tolerances in visual systems has been studied by Ito and Noguchi [45], who, using a slightly different theoretical approach, arrived at an identical conclusion. Experimental evidence led Ito and Noguchi to suggest that for best images the error in Δ should under no circumstances be greater than 90° and preferably should be less than 20°.

At 60° internal incidence, uncoated glass surfaces, of index 1.52 used in a roof, rotate the polarization in opposite directions and can also introduce large ellipticity into a linearly polarized input beam. The relative rotation angle is around 66°. This is clearly unsatisfactory. Simple silver coatings, sometimes used to reduce the polarization perturbations of simple plane surfaces at incidence beyond critical, give retardations a little greater than

90° (Figure 9.38), better than uncoated glass but not very satisfactory compared with 180° ± 20°.

A very simple coating consisting of a thin layer of a material like tantalum pentoxide (around 80 nm in physical thickness) overcoated with opaque silver can achieve a value of Δ of around 180°, at the expense of a small reduction in reflectance, particularly at the blue end of the visible. Figure 9.39 shows such a performance. This is inside the ±20° tolerance suggested by Ito and Noguchi [45]. For improved performance, a dielectric multilayer is required and with five or so layers, accuracies within 5° can readily be achieved.

9.7 Optical Tunnel Filters

At an earlier stage in the development of narrowband filters, a main barrier to their construction was the fabrication of reflecting stacks of sufficiently low loss, and it appeared that the phenomenon of frustrated total internal reflection might offer some hope as a possible solution. This phenomenon has been known for some time. If light is incident on a boundary beyond the critical angle, it will normally be completely reflected. However, the incident light does in fact penetrate a short distance into the second medium, where it decays exponentially. Provided the second medium is somewhat thicker than a wavelength or so, the decay will be more or less complete

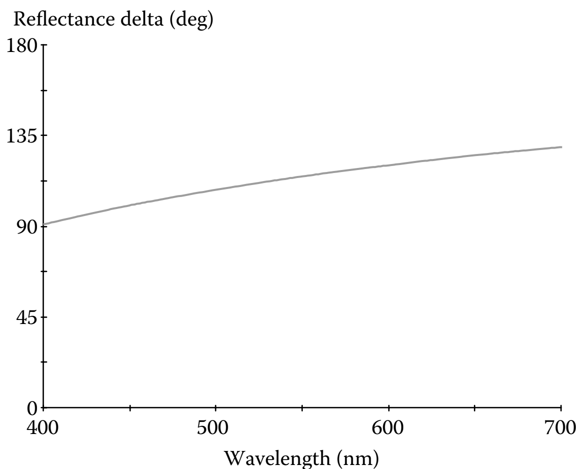

FIGURE 9.38
The relative retardation of a silver coating at 60°, the angle of incidence in a roof used at 45°. Although the difference between the retardation and ideal 180° is less that 90°, it is well outside the ideal 20°.

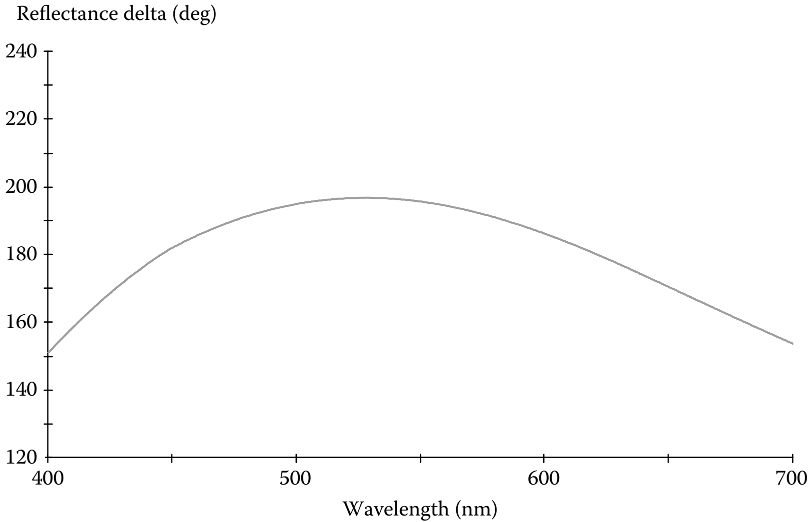

FIGURE 9.39
The relative retardation at 60° internal incidence of a simple two-layer coating of 80 nm of Ta_2O_5 next to the glass covered by a thick layer of silver.

and the reflectance unity. If, on the other hand, the second medium is made extremely thin, then the decay may not be complete when the wave meets the boundary with the third medium. Then, if the angle of propagation is then no longer greater than critical, a proportion of the incident light will appear in the third medium and the reflectance at the first boundary will be something short of total. This, as Baumeister [46] has pointed out, is very similar to the behavior of fundamental particles in tunneling through a potential barrier, and he has used the term *optical tunneling* to describe the phenomenon. The most important feature of the effect, as far as the thin-film filter is concerned, is that the frustrated total reflection can be adjusted to any desired value, simply by varying the thickness of the frustrating layer between the first and third media.

The method of constructing a filter using this effect is very similar to the polarizing beam splitter (see Section 9.3.1). The hypotenuse of a prism is first coated with a frustrating layer of lower index so that the light will be incident at an angle greater than critical. This is a function of the prism angle, refractive index, and the refractive index of the frustrating layer. Next follows the cavity layer that must necessarily be of higher index, so that a real angle of propagation will exist. This in turn is followed by yet another frustrating layer. The whole is then cemented into a prism block by adding a second prism. The angle at which light is incident on the diagonal face must be greater than the angle ψ given by

$$\sin\psi = n_F / n_G$$

where n_F is the index of the frustrating layer and n_G is the index of the glass of the prism. For $n_F = 1.35$ and $n_G = 1.52$, we find $\psi = 63°$, a quite appreciable angle. Usually glass of rather higher index, nearer 1.7, is used to reduce the angle as far as possible.

Although at first sight the optical tunnel or frustrated total reflectance (FTR) filter appears most attractive and simple, there are some tremendous theoretical disadvantages. First, there is an enormous shift in peak wavelength between the two planes of polarization. Typical figures quoted are of the order of 100 nm in the visible region, the peak corresponding to the *p*-plane of polarization being at a shorter wavelength. This large polarization splitting is due to the large angle of incidence at which the device must be used. Although the phase thickness of the cavity does not vary with polarization, the phase changes at the interface do vary. Another effect of this large angle is that the angle sensitivity of the filter is extremely large. Shifts of 5 nm/degree of arc have been calculated [46].

Added to these disadvantages is the fact that the attempts made to produce FTR filters have been very disappointing in their results, the performance appearing to fall far short of what was expected theoretically. It seems that the difficulties inherent in the construction of the FTR filter are at least as great as those involved in the conventional Fabry–Perot filter. Because of this, interest in the FTR filter has been mainly theoretical and the filter does not appear ever to have been in commercial production.

The theory is given in great detail by Baumeister [46], who also surveys the quite extensive literature at the time. Not only did he cover the FTR filter but he also pointed out that, as far as the theory is concerned, the frustrating layer or, as he renamed it, the tunnel layer, behaves exactly as a loss-free metal layer. This implies that all sorts of filters including induced-transmission filters are possible using tunnel layers. Designs for a number of these are included in the paper. One conclusion that Baumeister reaches is that there appears to be no practical application for the tunnel-layer filter of the induced-transmission and FTR single-cavity types. However, he does mention the possibility of a longwave-pass filter constructed from an assembly of many tunnel layers separated by dielectric layers with the advantage of a limitless rejection zone on the shortwave side of the edge. Even with this type of filter, there are some disadvantages that could be serious. The characteristics of the filter near the edge suffer from strong polarization splitting. This could be overcome by adding a conventional edge filter to the assembly at the front face of the prism. However, the second disadvantage is rather more serious: the appearance of pass bands in the stop region when the filter is tilted in the direction so as to make the angle of incidence more nearly normal. Curves given by Baumeister show a small transmission spike appearing even with a tilt of only 1° internal or 2.7° external with respect to the design value.

Despite the slightly pessimistic conclusion in the Baumeister paper, the concept has been revitalized by Li and Dobrowolski [27] in the construction

of highly efficient thin-film polarizers. The difficulties of very low admittance contrast between high- and low-index materials for *p*-polarization at angles around 45° in glass disappear at high angles of incidence when one of the materials is operating beyond critical as a tunnel layer. The design concepts are rather more complex, but the use of computers is not at all inhibited by such complexity and so automatic refinement and synthesis are particularly useful methods.

References

1. Thelen A 1966 Equivalent layers in multilayer filters *Journal of the Optical Society of America* **56** 1533–1538
2. MacNeille S M Eastman Kodak Company 1946 *Beam splitter* US Patent 2,403,731
3. Berning P H and Turner A F 1957 Induced transmission in absorbing films applied to band pass filter design *Journal of the Optical Society of America* **47** 230–239
4. Nevière M and Vincent P 1980 Brewster phenomena in a lossy waveguide used just under the cut-off thickness *Journal d'Optique* **11** 153–159
5. Ruiz-Urbieta M, Sparrow E M, and Parikh P D 1975 Two-film reflection polarizers: theory and application *Applied Optics* **14** 486–492
6. Cox J T, Hass G, and Hunter W R 1975 Infrared reflectance of silicon oxide and magnesium fluoride protected aluminum mirrors at various angles of incidence from 8µm to 12µm *Applied Optics* **14** 1247–1250
7. Kretschmann E and Raether H 1968 Radiative decay of non-radiative surface plasmons excited by light *Zeitschrift für Naturforschung* **23A** 2135–2136
8. Clapham P B, Downs M J, and King R J 1969 Some applications of thin films to polarization devices *Applied Optics* **8** 1965–1974
9. Lostis M P 1957 Etude et realisation d'une lame demi-onde en utilisant les proprietes des couches minces *Journal de Physique et le Radium* **18** 51S–52S
10. Rabinovitch K and Toker G 1994 Polarization effects in optical thin films *Proceedings of the Society of Photo-Optical Instrumentation Engineers* **2253** 89–102
11. Otto A 1968 Excitation of non-radiative surface plasma waves in silver by the method of frustrated total reflection *Zeitschrift für Physik* **216** 398–410
12. Raether H 1977 *Surface plasma oscillations and their applications*, in *Physics of Thin Films* Hass G and Francombe M H Editors (New York/San Francisco/London: Academic Press) 145–261
13. Abelès F 1976 Optical properties of very thin films *Thin Solid Films* **34** 291–302
14. Greenland K M and Billington C 1950 The construction of interference filters for the transmission of specified wavelengths *Journal de Physique et le Radium* **11** 418–421
15. Harrick J and Turner A F 1970 A thin film optical cavity to induce absorption of thermal emission *Applied Optics* **9** 2111–2114
16. Salamon Z, Macleod H A, and Tollin G 1997 Coupled plasmon-waveguide resonators: A new spectroscopic tool for probing proteolipid film structure and properties *Biophysical Journal* **73** 2791–2797

17. Salamon Z, Tollin G, Macleod H A, and Stevenson I C 1998 *Thin layer surface resonators: a new spectroscopic tool for probing dielectric film structure and properties* in *41st Annual Technical Conference Proceedings* Boston Society of Vacuum Coaters 238–242
18. Craig A E, Olson G A, and Sarid D 1983 Experimental observation of the long-range surface-plasmon polariton *Optics Letters* **8** 380–382
19. Quail J C, Rako J G, and Simon H J 1983 Long-range surface-plasmon modes in silver and aluminum films *Optics Letters* **8** 377–379
20. Dragila R, Lutherda B, and Vukovic S 1985 High transparency of classically opaque metallic films *Physical Review Letters* **55** 1117–1120
21. Macleod H A 1992 *Unconventional coatings*, in *Tutorials in Optics* Moore D T Editor (Washington, DC: Optical Society of America) 121–135
22. Macleod A and Clark C 2001 *Evanescent waves and some of their applications* in *44rd Annual Technical Conference Proceedings* Philadelphia Society of Vacuum Coaters 75–80
23. Ebbesen T W, Ghaemi H F, Thio T, and Wolff P A NEC Research Institute, Inc 1999 *Sub-wavelength aperture arrays with enhanced light transmission* US Patent 5,973,316
24. Ebbesen T W, Lezec H J, Ghaemi H F, Thio T, and Wolff P A 1998 Extraordinary optical transmission through subwavelength hole arrays *Nature* **391** 667–669
25. Bonod N, Enoch S, Li L, Popov E, and Nevière M 2003 Resonant optical transmission through thin metallic films with and without holes *Optics Express* **11** 482–490
26. Banning M 1947 Practical methods of making and using multilayer filters *Journal of the Optical Society of America* **37** 792–792
27. Li L and Dobrowolski J A 2000 High-performance thin-film polarizing beam splitter operating at angles greater than the critical angle *Applied Optics* **39** 2754–2771
28. Clapham P B 1969 *The preparation of thin film polarizers* Report OP. MET. 7 (Teddington, UK, National Physical Laboratory)
29. Songer L 1978 The design and fabrication of a thin film polarizer *Optical Spectra* **12** (10) 45–50
30. Blanc D, Lissberger P H, and Roy A 1979 The design, preparation and optical measurement of thin film polarizers *Thin Solid Films* **57** 191–198
31. Netterfield R P 1977 Practical thin-film polarizing beam splitters *Optica Acta* **24** 69–79
32. Thelen A 1976 Nonpolarizing interference films inside a glass cube *Applied Optics* **15** 2983–2985
33. Thelen A 1981 Nonpolarizing edge filters *Journal of the Optical Society of America* **71** 309–314
34. Knittl Z and Houserkova H 1982 Equivalent layers in oblique incidence: the problem of unsplit admittances and depolarization of partial reflectors *Applied Optics* **11** 2055–2068
35. Jones R C 1941 A new calculus for the treatment of optical systems. I Description and discussion of the calculus *Journal of the Optical Society of America* **31** 488–493
36. Henry Hurwitz J and Jones R C 1941 A new calculus for the treatment of optical systems. II Proof of three general equivalence theorems *Journal of the Optical Society of America* **31** 493–499
37. Jones R C 1941 A new calculus for the treatment of optical systems. III The Sohnke theory of optical activity *Journal of the Optical Society of America* **31** 500–503

38. King R J 1966 Quarter wave retardation systems based on the Fresnel rhomb *Journal of Scientific Instruments* **43** 617–622
39. Southwell W H 1979 Multilayer coatings producing 90° phase change *Applied Optics* **18** 1875
40. Southwell W H 1980 Multilayer coating design achieving a broadband 90° phase shift *Applied Optics* **19** 2688–2692
41. Apfel J H 1981 Graphical method to design multilayer phase retarders *Applied Optics* **20** 1024–1029
42. Apfel J H 1984 Graphical method to design internal reflection phase retarders *Appl. Opt.* **23** 1178–1183
43. Mahan A I 1945 Focal plane anomalies in roof prisms *Journal of the Optical Society of America* **35** 623–645
44. Mahan A I 1947 Focal plane anomalies in telescopic systems *Journal of the Optical Society of America* **37** 852–867
45. Ito T and Noguchi M 2001 *Viewing optical instrument having roof prism and a roof prism* US Patent 6,304,395
46. Baumeister P W 1967 Optical tunneling and its application to optical filters *Applied Optics* **6** 897–905

10

Color in Optical Coatings

Anyone who works with optical coatings knows that they can present exceedingly attractive colors. These colors originate in interference effects that enhance reflectance or transmittance in certain parts of the visible spectrum and inhibit it in others. Although colors occur with both transmitted and reflected light, it has long been observed that the most vivid effects are usually found in reflection. In the same way that coatings can be designed to have desired spectral properties, they can also be designed to present desired colors. This is a little more complicated than the usual design processes, because of the subjective nature of color itself. Color is strictly a human response to a luminous stimulus. The response varies with the individual observer. Since the coating is not luminous in itself, a source of light is also required before the colors can be observed. We avoid the obvious difficulties inherent in the variations between individual observers and light sources by using theoretical standards that represent more or less well the average properties, and permit us to remove the subjective nature of the problem. The design goals can then be presented in unambiguous terms but there remain some complications. To observe the color there must be an acceptable level of reflected or transmitted light. This, in turn, has a major influence on what can be achieved. A frequent further requirement is that the coatings should be sufficiently simple for large-scale production at reasonable cost. This chapter is a quite abbreviated account of certain aspects of color that are particularly relevant to optical coatings.

10.1 Color Definition

Color [1] is a subjective, human, response to the spectral quality of light. The human eye has two different types of receptors, known as cones and rods. Cones predominate in the center of the retina, while rods are more plentiful toward the periphery. The cones look very much like the rods but are very slightly conical and it is they that are sensitive to color. The rods respond to weaker levels of illumination. In the normal eye, there are three different types of cones distinguished by their spectral responses. We describe the sensations they produce as being red, or green, or blue. There is overlap of the different responses, especially in the case of green and red. It appears

that around 95% of the world's population can agree on the quality of the response to any particular color and it is this agreement that allows us to devise objective definitions of color.

We are unable to measure directly the color response and so, as with other subjective phenomena, we must content ourselves with comparative measurements involving certain agreed standards. These standards may take, and have taken, different forms, such as sets of colored objects like tiles, but the now generally accepted system is based on the use of three standard sources of illumination, one emitting light to produce a red sensation, one green, and one blue.

Since the eye operates by converting the light into a combination of red, green, and blue responses, we can represent any color as a combination of red, green, and blue stimuli derived from standard sources, or *primary stimuli* as they are more properly called, in a process known as *color matching*. The measure of the color, then, is the three amounts of light that must be delivered from the primary stimuli and combined, to produce exactly the same response as the color to be measured. Fortunately, the nature of the human color response is such that we can treat the three amounts of standard light as three independent color coordinates. Since there is a high degree of agreement on the results of such color matching experiments, we can convert the results of large numbers of subjective tests into a representative objective measure.

The concept of color purity is one that we can readily understand and we can accept that the purest color response would be derived from a single spectral element, or line. We are quite used to the representation of illumination in terms of its spectrum. If we know the color coordinates of every spectral line, that is the amounts of the standard light in each, then, because the process is linear, we can simply add the appropriate amounts to derive the coordinates of the particular color concerned. This is the basis of the objective measure of color. The sets of coordinates for each spectral line are known as the *color matching functions*.

Although there are different systems of color representation and specification in existence in different countries and professions, the most significant, and now almost universal, is the system defined by the Commission Internationale de l'Eclairage (CIE). This organization was established in 1913 and is the body internationally agreed as setting standards for colorimetry and photometry. In 1931, the CIE defined a Standard Observer consisting of three color matching functions based on three fixed primary color stimuli, the color matching functions being normalized sets of values of relative amounts of the primary stimuli required to reproduce the stimuli of all the lines of the visible spectrum, with the lines having equal radiant power.

As might be expected, it turns out that it is impossible to match all the lines of the spectrum with mixtures of any three practical primary stimuli. Negative amounts are necessary. Negative amounts can be accommodated in actual experiments by adding the appropriate amount of the primary stimulus to the color to be matched, but this complicates the color specification

to an undesirable extent. The solution adopted by the CIE is exceptionally clever. Since the color matching functions depend on the nature of the primary stimuli, these were defined so as to require only positive values in color matching. As a result, although the stimuli correspond roughly to red, green and blue, they have a color purity well beyond that of any single spectral line. They are completely unattainable practically, but it is not necessary that they be constructed. Their purpose is simply to define the color matching functions. So that we can refer to the primary stimuli, they have been given quite simple names, **X**, **Y,** and **Z**, corresponding to red, green, and blue, respectively. The corresponding color matching functions are named $\bar{x}(\lambda)$, $\bar{y}(\lambda)$, and $\bar{z}(\lambda)$, respectively. However, the CIE went still further. The flexibility in the definition of the primary stimuli permitted the arrangement that the areas of the color matching functions, plotted against a linear scale of wavelength, should be identical. Still further, the $\bar{y}(\lambda)$ color matching function was made identical to the standard photopic response curve of the human eye. This last is of great importance to thin-film practitioners. The color matching functions are illustrated in Figure 10.1.

The cone receptors in the human eye are responsible for the response to normal levels of illumination and, of course, for the color response. The photopic response curve of the human eye is the relative response of the cones to monochromatic light of identical power but varying wavelength. It is a measure of the spectral variation of the apparent luminosity, or brightness, of the light. The correspondence of the $\bar{y}(\lambda)$ color matching function and the standard photopic response function means that we can derive luminous properties readily from our color calculations.

Optical coatings are not self-luminous. A source of illumination is necessary for us to be able to perceive their color. Obviously, the spectral variation of the illumination will affect that of the light reflected or transmitted by

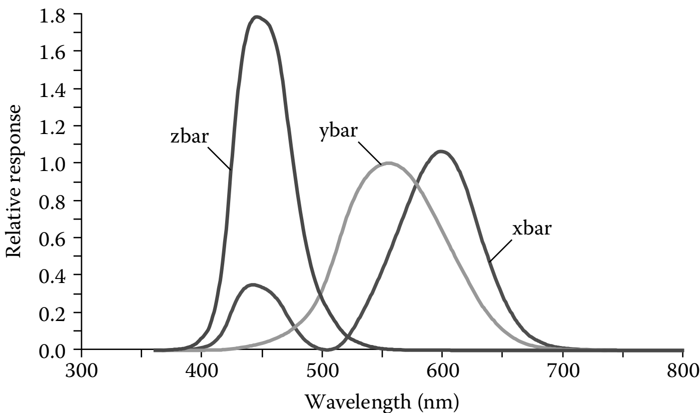

FIGURE 10.1
The 1931 color matching functions defined by the CIE. The y-bar curve corresponds to the standard photopic response curve of the human eye.

the coating, that is, the color of the coating. The specification of the source of illumination, then, is a necessary component of the definition of coating color. Standard definitions of sources of illumination are therefore included in the CIE system. The CIE definitions give special meanings to the terms *sources* and *illuminants.* A source is a practical device that can be constructed and used in an actual measurement of color. An illuminant is a theoretical distribution of relative output to be used purely in calculation. Some sources correspond sufficiently well to illuminants to be defined as equivalent but there are illuminants that have no exact corresponding source. In this chapter, we will be concerned more with illuminants than sources.

There are many different defined illuminants in the CIE system but of particular interest in optical coatings are Standard Illuminants A, E, and D_{65}. Illuminant A represents black body radiation at a temperature of 2856K and the corresponding source is a gas-filled coiled-tungsten filament lamp operating at a correlated color temperature of 2856K. *Correlated Color Temperature* implies a close relationship between the source color and that of a black body at that temperature. E is the Equal Energy illuminant emitting equal power per wavelength unit over the visible spectrum. This illuminant can be considered as that assumed in all normal calculations of spectral coating characteristics. The corresponding source does not exist in practice. D_{65} is a representation of daylight (but not direct sunlight) with a correlated color temperature of 6504K. Unfortunately, there is no artificial source that exactly matches this and so the CIE has developed a technique for quantifying the usefulness of artificial sources in representing D_{65} and other artificial daylight sources. The spectral distributions of Illuminants A, E, and D_{65} are illustrated in Figure 10.2. The spectral distributions are normalized so that the relative outputs are 100 at 560 nm.

All color calculations start with three basic color coordinates, known as the *tristimulus values,* denoted by *X, Y,* and *Z*. Let the spectral output of the source of illumination be $S(\lambda)$ and the response of the coating be $R(\lambda)$. Then

$$X = 100\frac{\int_{\lambda} S(\lambda)R(\lambda)\bar{x}(\lambda)d\lambda}{\int_{\lambda} S(\lambda)\bar{y}(\lambda)d\lambda} \tag{10.1}$$

$$X = 100\frac{\int_{\lambda} S(\lambda)R(\lambda)\bar{y}(\lambda)d\lambda}{\int_{\lambda} S(\lambda)\bar{y}(\lambda)d\lambda} \tag{10.2}$$

$$Z = 100\frac{\int_{\lambda} S(\lambda)R(\lambda)\bar{z}(\lambda)d\lambda}{\int_{\lambda} S(\lambda)\bar{y}(\lambda)d\lambda} \tag{10.3}$$

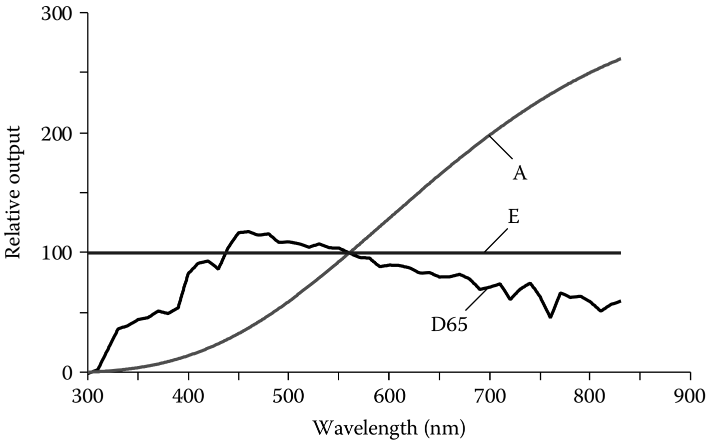

FIGURE 10.2
The relative outputs of illuminants A, E, and D_{65}.

where the factor 100 is omitted should $R(\lambda)$ be given in percent rather than absolute terms.

Because of the way in which $\bar{y}(\lambda)$ is defined, Y is also the luminous reflectance or luminous transmittance, in percent, depending on the nature of the response R. It is therefore also known as the *luminance factor*.

X, Y, and Z are components of a vector in three-dimensional space, making it difficult to visualize the color. Two dimensions are easier. We can retain the relationship between the tristimulus values but reduce the number of necessary dimensions by normalizing the components so that their sum is always unity. This leads to what are known as the *chromaticity coordinates*, x and y, defined as:

$$x = \frac{X}{X + Y + Z} \tag{10.4}$$

$$y = \frac{Y}{X + Y + Z} \tag{10.5}$$

The chromaticity coordinates define points in a rectangular plot known as a *chromaticity diagram*.

We can take as an example a quite simple decorative coating consisting of a titanium oxide layer some 300 nm thick deposited over an opaque titanium metal foil or layer. The variation of reflectance as a function of wavelength is shown in Figure 10.3. We can deduce from the form of the curve that the color of the coating will be green.

The results of calculating the chromaticity coordinates of the coating using the three illuminants from Figure 10.2 are shown in Figure 10.4. We would describe a color as white if it were to introduce no further spectral variation in the color of the reflected light so that the reflected light has

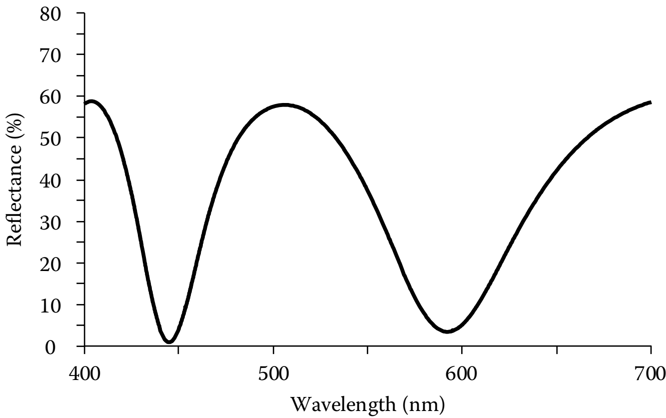

FIGURE 10.3
The spectral variation of reflectance of a titanium oxide layer, 300 nm thick, over titanium metal.

exactly the color of the source. In fact, the human eye adapts to the color of the source of illumination. A white paper looks white, even when the general illumination has a blue or yellow cast to it. The point corresponding to the particular illuminant in the chromaticity diagram, therefore, is referred to as the white point and the appropriate white points are plotted along with the coating in Figure 10.4. Note that because of the way in which the parameters are defined, the white point corresponding to illuminant E has coordinates (1/3, 1/3). A spectrum line stimulates the purest possible color response and the locus of the chromaticity coordinates of the lines of the spectrum is also shown on the diagram with the appropriate wavelengths marked off on it. Purple is not a spectral color. The line joining the two ends of the spectrum line is the locus of the purest purple colors, known as the purple line.

It is difficult to make any deductions about the color of the coating from the chromaticity coordinates on their own until we see how they compare with the coordinates of the illuminants, or white points. Then we can see that the chromaticity coordinates represent, in each case, a move toward the green part of the spectrum locus.

We can quantify this procedure by drawing a straight line from the white point, through the color coordinates of the sample, to meet the spectrum locus. The wavelength that corresponds to the point of intersection is then known as the *dominant wavelength*. The color associated with this dominant wavelength is then of the same quality as that of the sample. In fact, we can think of the sample color as being a mixture of the spectrum line color and white. The purity of the resulting color is less, the greater the proportion of white light that must be added. This then leads to a definition of color purity. There are two definitions of purity in common use. Colorimetric purity is an expression of purity based on the idea just expressed, the fraction of the total

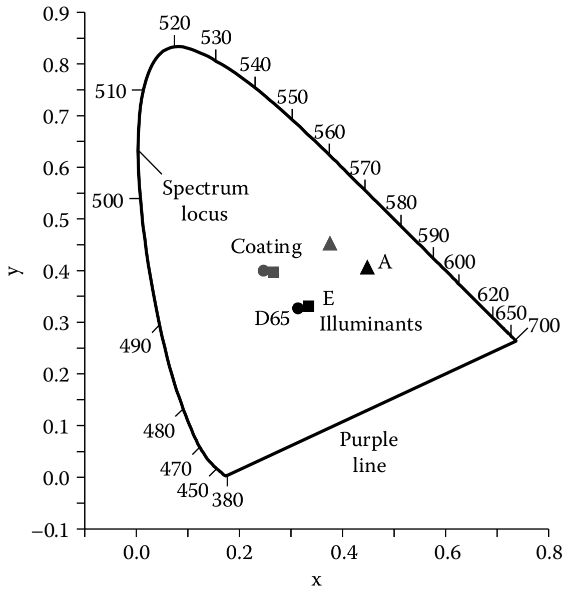

FIGURE 10.4
The chromaticity coordinates of the coating of Figure 10.3 calculated with illuminants D_{65}, E, and A. The locus of the lines of the spectrum is shown and marks the purest colors. The scale around it is wavelength in nm. Purple is not a spectral color and the purest purples lie on the line labeled purple. The color white corresponds to the particular illuminant and so the corresponding point is also known as the white point.

luminance of the color that is due to the monochromatic stimulus. Excitation purity is a simpler definition that is the fraction of the total distance from the white point to the spectrum line that corresponds to the color stimulus in question. Excitation purity corresponds roughly to what is often termed the saturation of the color.

Both expressions of purity can be reduced to measurements taken from the chromaticity diagram. If we indicate the chromaticity of the white point by (x_w, y_w), of the spectral line by (x_λ, y_λ) and of the point in question by (x, y) then the two measures of purity are given by:

$$p_e = \frac{x - x_w}{x_\lambda - x_w} = \frac{y - y_w}{y_\lambda - y_w}$$
$$p_c = \frac{y_\lambda}{y} \cdot \frac{x - x_w}{x_\lambda - x_w} = \frac{y_\lambda}{y} \cdot \frac{y - y_w}{y_\lambda - y_w} \tag{10.6}$$

where the particular formula to be used is the one that gives least rounding error.

If the coating chromaticity is beneath the white point it will be of a purple hue and the line from the white point through the color stimulus will

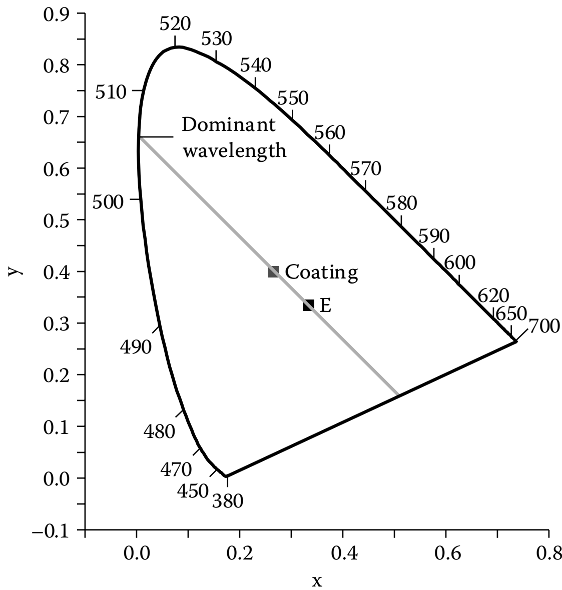

FIGURE 10.5
Dominant wavelength is found by drawing a line from the white point, through the color stimulus in question to meet the spectrum locus. The wavelength corresponding to the point of intersection is the dominant wavelength.

intersect the purple line rather than the spectrum locus. In that case, there is no dominant wavelength. The line, produced backward, will, however, intersect the spectrum locus and that point of intersection is known as the complementary wavelength. All chromaticities will have one or other of dominant wavelength or complementary wavelength. Some blue and some red chromaticities will have both.

The expressions for purity in Equation 10.6 need to be extended to accommodate color stimuli without a dominant wavelength. In the case of excitation purity, the coordinates used for (x_w, y_w) are those of the point of intersection with the purple line. In the case of colorimetric purity, (x_w, y_w) are replaced by the coordinates of the complementary wavelength.

Purity and dominant or complementary wavelength are rarely used as a specification for color but rather as an aid to the appreciation of the color.

10.2 The 1964 Supplementary Colorimetric Observer

Human color vision is a complicated process in which the brain and eye are both involved and the perception of color is found to depend not just on the spectral content of the stimulus but also on the size of the retinal area that is

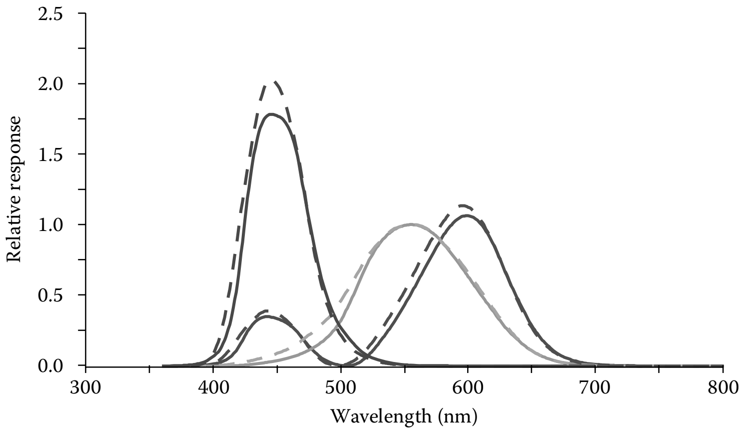

FIGURE 10.6
The 1964 supplementary color matching functions (*broken lines*) compared with the 1931 functions (*solid lines*).

stimulated, or, more usefully for interpretation, on the angular subtense of the area. The experiments that were carried out to establish the parameters of the 1931 Standard Observer used fields that subtended 2°. Experiments demonstrated the validity of the functions for fields subtending from 1° to 4° but larger fields exhibit an increasing difference. For this reason, the CIE in 1964 defined a set of color matching functions for fields subtending 10° at the eye. The associated color matching functions are usually written as $\bar{y}_{10}(\lambda)$, $\bar{y}_{10}(\lambda)$, and $\bar{z}_{10}(\lambda)$. This supplementary observer was arranged so that the equal energy stimulus still has the value 1/3 for its chromaticity coordinates, but the function $\bar{y}_{10}(\lambda)$ in this observer does not correspond to the photopic response function. Figure 10.6 compares the two sets of color matching functions.

10.3 Metamerism

It is clear from the nature of the definition of the tristimulus values that it is possible for color stimuli with quite different radiant power distributions to have identical tristimulus values. Such stimuli are said to be metamers, the adjective being metameric and the concept metamerism.

In the case of optical coatings (and indeed of any non–self-luminous stimulus), the spectral distribution of the source of illumination must be included. Since this will vary from one type of source to another, a pair of optical coatings that are metamers for one type of illumination will not be so for another. Only if the spectral response of two coatings is identical will they

exhibit the same color response under all possible qualities of illumination. Such color matches are said to be nonmetameric.

Metamerism is important in the design of coatings that are required to have a particular color response. The illuminant under which the response is to be achieved must be specified. In the case of pairs of coatings that are to be always matched in their color qualities, then their spectral responses must be equal.

10.4 Other Color Spaces

The X, Y, and Z tristimulus values define a color unambiguously, and the derived chromaticity coordinates allow us to plot color information in two dimensions. How closely do we have to match a particular set of tristimulus values so that the perceived colors should be the same, or within some acceptable error? Here the chromaticity diagram is of less use. It makes appreciation of color straightforward, but the distances between points are not simply related to the perceived color differences. This leads to the idea of a uniform color space, where the linear distance between two points is directly proportional to the perceived color difference. There is still progress to be made in this area, but two color spaces that go a long way toward this concept of a uniform color space are recommended by the CIE. These were both defined in 1976. The first is the CIE ($L^*u^*v^*$)-Space and the second is the CIE ($L^*a^*b^*$)-Space, frequently referred to as CIELUV and CIELAB, respectively. Both are derived from the tristimulus values, but the expressions are quite complicated. In both, the coordinates are plotted with rectangular axes in three dimensions and the perceived color difference is proportional to the linear distance between points.

The quantities L^*, u^*, and v^* are defined by the expressions:

$$\begin{aligned} L^* &= 116\left(\frac{Y}{Y_w}\right)^{\frac{1}{3}} - 16 \text{ for } \frac{Y}{Y_{\mathrm{w}}} > 0.008856 \\ L^* &= 903.3\frac{Y}{Y_w} \text{ for } \frac{Y}{Y_{\mathrm{w}}} \le 0.008856 \end{aligned} \tag{10.7}$$

$$\begin{aligned} u^* &= 13L^*(u' - u'_w) \\ v^* &= 13L^*(v' - v'_w) \end{aligned} \tag{10.8}$$

where

$$u' = \frac{4X}{X + 15Y + 3Z} \text{ and } u'_w = \frac{4X_w}{X_w + 15Y_w + 3Z_w}$$
$$v' = \frac{9Y}{X + 15Y + 3Z} \text{ and } v'_w = \frac{9Y_w}{X_w + 15Y_w + 3Z_w} \tag{10.9}$$

and the suffix w indicates the attributes of the white point.

The quantity L^*, in the ($L^*a^*b^*$)-Space is, defined exactly as in the ($L^*u^*v^*$)-Space. Then a^* and b^* are given by:

$$a^* = 500\left[f\left(\frac{X}{X_w}\right) - f\left(\frac{Y}{Y_w}\right)\right]$$
$$b^* = 200\left[f\left(\frac{Y}{Y_w}\right) - f\left(\frac{Z}{Z_w}\right)\right] \tag{10.10}$$

where

$$f(\varphi) = \varphi^{\frac{1}{3}} \quad \text{if} \quad \varphi > 0.008856$$
$$f(\varphi) = 7.787\varphi + \frac{16}{116} \quad \text{if} \quad \varphi \le 0.008856 \tag{10.11}$$

The advantage of these spaces is the closer agreement between perceived color difference and linear distance, but because the coordinates u^* and v^* and a^* and b^* involve the value of L^*, a plot of u^* against v^* or of a^* against b^* does not yield unique chromaticity coordinates. This makes it difficult to appreciate the color and so these color spaces do not diminish the importance of the chromaticity diagram.

These spaces are very frequently used for the specification of a required color.

10.5 Hue and Chroma

The terms *hue* and *chroma* are used in descriptions of color. Hue is essentially what we mean when we commonly say "color." Red, green, yellow, blue, and purple are all hues. Chroma is much the same as "purity." In other words, chroma indicates how closely the color response matches that of a monochromatic stimulus. The most common use of the terms is in the Munsell system of color, which uses a color space with essentially cylindrical

coordinates. There are three attributes of any color, chroma, hue, and value, that we can associate with the cylindrical coordinates ρ, ϑ, and z. We can visualize the Munsell system roughly as a vertical cylinder. The value of the color, what we refer to as *lightness,* is the vertical position on the cylinder axis. The chroma is the distance toward the periphery of the cylinder and the hue is the intercept on the circumference of the cylinder that is marked off as a ring of the colors red, yellow, green, blue, and purple. In the actual Munsell system, the periphery of the figure departs somewhat from a perfect cylinder but otherwise the coordinates are as described.

The CIE recognizes the usefulness of such coordinates in that they are closely related to color perception and so the 1976 ($L^*u^*v^*$)-Space and ($L^*a^*b^*$)-Space include the possibility of calculating what are called correlates of lightness, chroma, and hue. L^* is the correlate of lightness. Correlates of chroma are:

$$\begin{aligned} C^*_{uv} &= [(u^*)^2 + (v^*)^2]^{\frac{1}{2}} \\ C^*_{ab} &= [(a^*)^2 + (b^*)^2]^{\frac{1}{2}} \end{aligned} \tag{10.12}$$

The hue correlate is defined as an angle in degrees by:

$$\begin{aligned} h_{uv} &= \arctan\left(\frac{v^*}{u^*}\right) \\ h_{ab} &= \arctan\left(\frac{b^*}{a^*}\right) \end{aligned} \tag{10.13}$$

where the signs of u^*, v^* or a^*, b^* are kept separate so that the quadrant of the angle can be unambiguously assigned. Note that these are not in any way a conversion to the Munsell system. They are simply cylindrical coordinates in the appropriate CIE space.

10.6 Brightness and Optimal Stimuli

Decorative coatings modify the spectral quality of illumination to produce a particular color sensation. While it is not a universal rule, most decorative coatings operate in reflection, and for the sake of simplicity, we shall assume reflection in what follows, although the results will be equally applicable to transmitting coatings.

Color purity is a straightforward concept that we can readily appreciate, but there is another important attribute, usually referred to as *brightness.* Brightness is easily understood, but perhaps slightly more difficult to

define. It is an attribute that describes the tendency of a stimulus to appear more or less intense than another. A brighter stimulus emits more light. It appears that our perception of brightness follows a 1/3 power law, hence the 1/3 power in the $L^*a^*b^*$ and $L^*u^*v^*$ color space definitions, but for the purposes of this section we shall concentrate on the *luminance factor*, that is the Y tristimulus value. The larger Y, the greater is the brightness.

Let us imagine that we have a decorative coating that is completely white in appearance and has a luminance factor of 100. Now let us gradually modify the spectral profile of the coating so that the reflected light is gradually reduced in spectral bandwidth. As the bandwidth is reduced, the reflected color gains in purity until it reaches a single spectral element. This gain in purity must be accompanied by a reduction in the amount of light that is reflected, that is, the brightness of the coating. Thus, there is a relationship between color and brightness, or luminance factor. Indeed, we can use the luminance factor to compare the quality of two coatings with similar chromaticity coordinates. This leads us directly to the idea of an optimal color stimulus that exhibits the greatest possible luminance factor for that set of chromaticity coordinates.

As might be guessed, optimal color stimuli have a perfectly rectangular spectral response. The response is uniformly 100% between two edge wavelengths outside of which the response is uniformly zero. Alternatively, it can be zero within a band and uniformly 100% outside. It is perhaps easier instinctively to sense the validity of this than to prove it. Given the form of this optimal stimulus, it becomes possible to calculate the maximum luminance factor for any given chromaticity and to plot the locus in the chromaticity diagram of the optimal stimuli for a given value of luminance factor, which forms a closed curve in the chromaticity diagram. This locus will depend, of course, on the particular illuminant but such loci have been calculated and are tabulated. See, for example Wyszecki and Styles [1]. Figure 10.7 shows loci calculated for the D_{65} illuminant.

Now that we know unambiguously the maximum possible luminance factor for any given chromaticity, we can use it in an objective assessment of the quality of any given decorative coating. Probably the most useful approach is to plot, in the chromaticity diagram, the chromaticity concerned together with the locus of a constant maximum luminance factor corresponding to the luminance factor of the coating.

Let us use the diagram to assess the quality of a simple coating. Figure 10.8 shows the performance of a simple nine-layer optical coating with design as listed in the figure caption. Its chromaticity coordinates for the D_{65} illuminant and 1931 Standard Observer are plotted in Figure 10.9. The luminance factor, Y, is calculated as 54.85 and the locus of the optimal stimuli corresponding to this luminance factor is also plotted in the diagram. The coating is clearly not quite optimum, principally because the reflectance is only 90% rather than 100% but the gap between current performance and optimum is small.

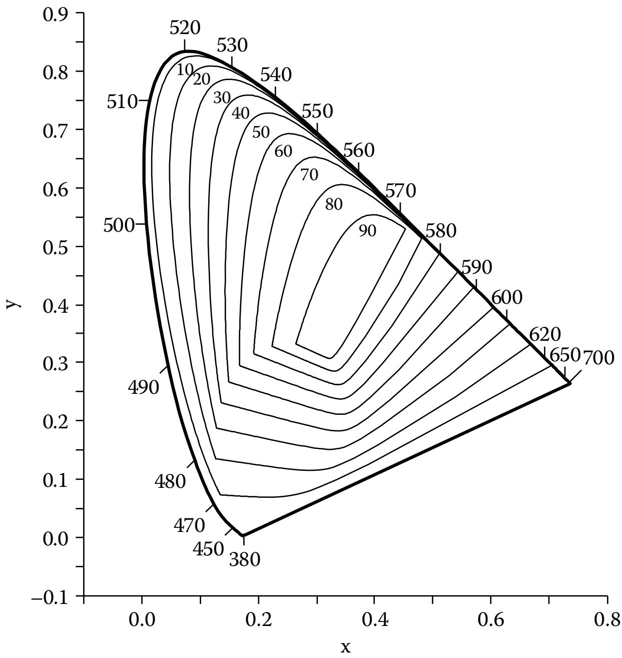

FIGURE 10.7
Chromaticity loci of optimal object-color stimuli for D_{65} Illuminant and values of Y from 10 to 90.

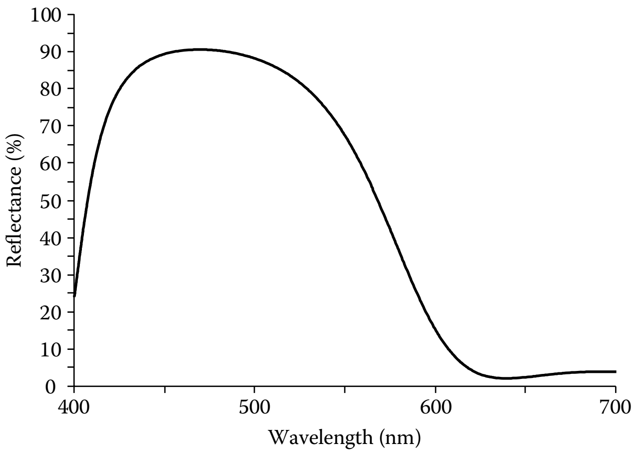

FIGURE 10.8
Reflectance over the visible region of a simple coating consisting of the design: Air | $(0.5H\ L\ 0.5H)^4$ | Glass with $\lambda_0 = 500$ nm. H represents a quarter-wave of Ta_2O_5 and L of SiO_2.

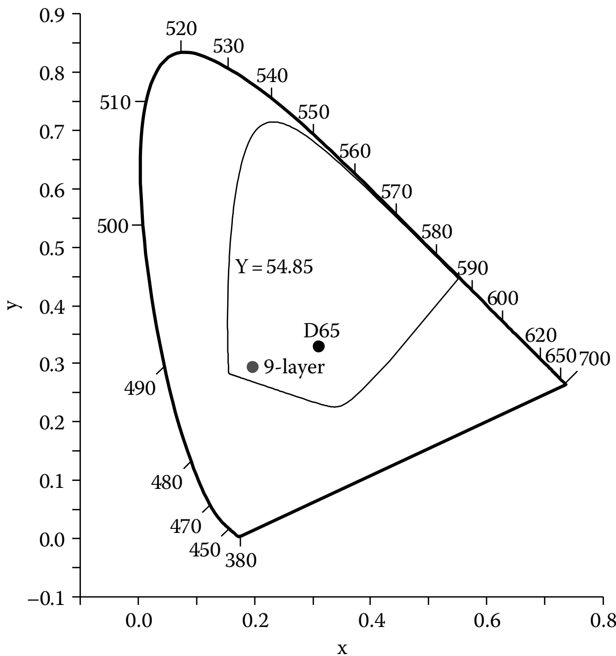

FIGURE 10.9
The dot labeled nine-layer represents the calculated chromaticity of the coating of Figure 10.8 with illuminant D_{65}. The dot to the right is the white point. The luminance factor of the coating is calculated to be 54.85 and the locus of the optimal stimuli for that value is also plotted in the diagram. The coating is only a little short of the possible optimum.

Knowledge of the optimum luminance factor helps us to avoid unrealistic targets for color performance in the design of optical coatings.

10.7 Colored Fringes

Colored fringes of constant thickness can often be seen in simple film systems like oil on water or protective lacquer over metal and the like. Since they are localized in the film, they are very easy to see. They are sometimes known as Newton's rings because the first very detailed study of such fringes was carried out by Isaac Newton and described in his *Optiks* [2]. The appearance of such fringes depends very much on both viewing conditions and the source of illumination.

The idea of coherence was introduced in Chapter 2 along with coherence length, a simple quantitative parameter that can be used to predict the appearance or nonappearance of interference effects. Coherence and coherence length should be thought of as properties of the entire system. Coherence

length is the path difference where interference just disappears. Of course, one could argue about the exact point where interference effects disappear, but a very useful and much used expression for coherence length, is $\lambda^2/\Delta\lambda$, where $\Delta\lambda$ is the limiting bandwidth of the system and can be a property of the light source, the receiver, or the intervening components. Fringes in a film tend to disappear when a double traversal of the film becomes greater than the applicable coherence length.

When we use broadband sources of illumination, like daylight, the spectral bandwidth of the source is very large and it is the spectral response of the cones in the retina that possess the limiting bandwidth. The bandwidth of a cone we can take roughly as 100 nm that would, at, say, 550 nm, yield a coherence length of $550^2/100$ nm, that is, just over 3 μm. This implies that roughly slightly greater than 1.5 μm would be the limiting film optical thickness. However, there are other sources of illumination. Fluorescent lights are mainly based on a mercury discharge, and despite the broadening of the lines in the discharge and the effect of the phosphor that coats the inside of the discharge vessel, there are still strong lines in the output spectrum. We can illustrate this with the CIE F10 illuminant that represents a daylight fluorescent source (Figure 10.10). A significant component of the fluorescent light is in the form of narrow spikes that are some 10 nm wide. This gives a coherence length at 550 nm of around 30 μm and, since this is very much greater than that of the human eye, will be the dominant determinant of the coherence. Thus, we can expect, in such fluorescent light to perceive fringes in films up to around 15 μm in optical thickness.

Let us use a very simple example as an illustration. We assume oil of refractive index 1.5 over water that has refractive index approximately 1.33.

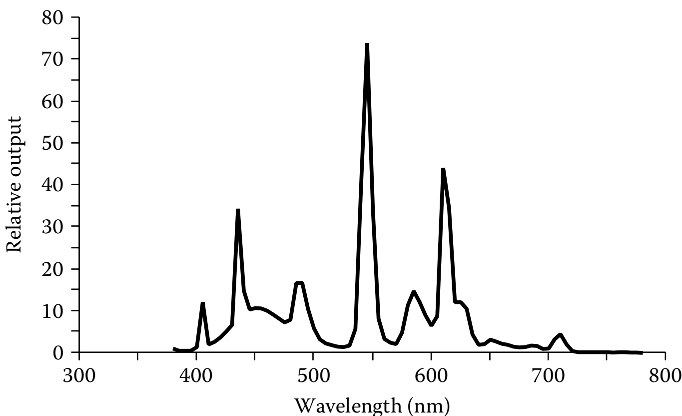

FIGURE 10.10
The relative output of the CIE F10 illuminant representing a daylight fluorescent source. Apart from the pronounced spikes in the output, the blue content is slightly less than in the D_{65} illuminant.

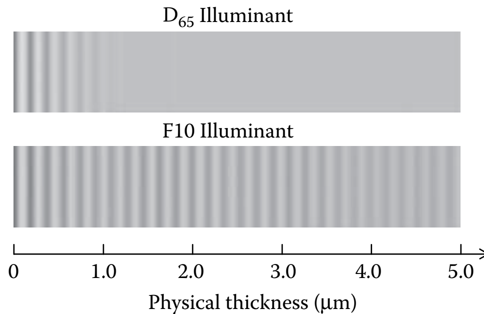

FIGURE 10.11
The appearance of fringes in an oil film (n = 1.5) over water (n ≈ 1.33). (See color insert following page 398.)

We will assume that the physical thickness of the oil varies from zero to 5 μm and, using the 1931 Standard Observer, we will calculate the appearance of the fringes in the oil in both D_{65} andF10 illuminants. The appearance of the fringes will be affected to some extent by the reproduction process but the comparison will be valid. This is shown in Figure 10.11. The oil with its refractive index of 1.5 shows fringes vanishing at a physical thickness of 1 μm, that is an optical thickness of 1.5 μm, just as predicted, while in F10 illumination the fringes are still clearly visible at a physical thickness of 5 μm, that is, an optical thickness of 7.5 μm.

This effect is often seen in decorative metal objects that are protected by transparent lacquer, such as door handles, faucets, and so on.

References

1. Wyszecki G and Styles W S 1982 *Color science* ed 2 (New York: John Wiley & Sons)
2. Newton S I 1704 *Opticks or a Treatise of the Reflections, Refractions, Inflections and Colours of Light* (London: The Royal Society)

11

Production Methods and Thin-Film Materials

In this chapter, we shall deal briefly with the fundamental process, the machines that are used for the thin-film deposition, and we shall discuss some aspects of the properties of thin-film materials. Subsequent chapters will include a more detailed examination of some of the problems met in production.

Much of this chapter is concerned with the properties of materials, ways of measuring them, and some examples of the results of the measurements of the important parameters. Probably the most important properties from the thin-film point of view are given in the following list, although the order is not that of relative importance, which will vary from one application to another.

1. Optical properties such as refractive index and region of transparency
2. The method that must be used for the production of the material in thin-film form
3. Mechanical properties of thin films such as hardness or resistance to abrasion, and the magnitude of any built-in stresses
4. Chemical properties such as solubility and resistance to attack by the atmosphere, and compatibility with other materials
5. Toxicity
6. Price and availability
7. Other properties that may be important in particular applications, for example, electrical conductivity or dielectric constant

Item 7 is not one on which we comment further here. On the question of price and availability, item 6, also little can be said. The situation is changing all the time. Note, however, that price is of secondary importance to suitability. The cost of a failed batch of coatings is very great compared with the price of the source materials. Many companies are able to offer a wide range of materials completely ready for thin-film production, together with all the necessary information on the techniques that should be used.

11.1 The Production of Thin Films

There is a considerable number of processes that can be and are used for the deposition of optical coatings. The commonest take place under vacuum and can be classified as *physical vapor deposition* (sometimes abbreviated to PVD). In these processes, the thin film condenses directly in the solid phase from the vapor. The word "physical" as distinct from "chemical" does not imply the complete absence of chemical parameters in the formation of the film. Chemical reactions are, in fact, involved, but the term *chemical vapor deposition* (sometimes abbreviated to CVD) is reserved for a family of techniques where the growing film is formed by a chemical reaction between precursors so that the growing film differs substantially in composition and properties from the starting materials.

The physical vapor deposition processes can be classified in various ways but the most useful classifications for our purposes are based on the methods used for producing the vapor and on the energy that is involved in the deposition and growth of the films. Vacuum, or thermal, evaporation has for years been the principal physical vapor deposition process and because of its simplicity, its flexibility, and its relatively low cost and because of the enormous number of existing deposition systems, it is likely to continue so for some considerable time. It is, however, clear that it possesses major shortcomings, especially in respect of the microstructure of the films, and, particularly for high-performance specialized coatings, alternative processes, such as sputtering, are being adopted. In thermal evaporation, the material to be deposited, the evaporant, is simply heated to a temperature at which it vaporizes. The vapor then condenses as a solid film on the substrates, which are maintained at temperatures below the freezing point of the evaporant. Molecules travel virtually in straight lines between source and substrate and the laws governing the thickness of deposit are similar to the laws that govern illumination. In sputtering, the vapor is produced by bombarding a target with energetic particles, mostly ions, so that the atoms and molecules of the target are ejected from it. Such vapor particles have much more energy than the products of thermal evaporation and this energy has considerable influence on the condensation and film-growth processes. In particular, the films are usually much more compact and solid. In other variants of physical vapor deposition, the condensation of thermally evaporated material is supplied with additional energy by direct bombardment by energetic particles. Such processes, together with sputtering, are known collectively as the *energetic processes.*

Although physical vapor deposition is the predominant class of deposition processes in optical coatings, the application of chemical vapor deposition is gradually increasing. The chemical reactions between the starting materials, the precursors, to form the material of the coating may be triggered in various ways but the most common is probably by means of an electrically induced plasma in the active vapor. Such processes are known collectively

as *plasma enhanced*. Chemical vapor deposition is complementary to, rather than a direct competitor of, physical vapor deposition. Physical vapor deposition is an exceedingly flexible process in terms of materials, substrate shape, and coating type. Chemical vapor deposition is somewhat less so because the reactor where the reaction and deposition take place, usually has to be designed, or at least modified, to fit the particular product. It has been used with great success in the production of large numbers of similar components. It is also capable of the deposition of films that present a challenge for physical vapor deposition. The boundary between the two classes of process is rather blurred.

In Chapter 1, we saw how the subject could be said to begin with Fraunhofer's preparing of thin films by the chemical etching of glass and also by deposition from solution. These and similar methods have been used to some extent in optical thin-film work. Other techniques that, at different stages in the development of the subject, have been, and are still sometimes, employed include anodic oxidation of aluminum to form a protective coating and the spraying of material onto a surface either in solution or in the form of a substance that can be chemically converted into the desired material later. Even the substance itself is sometimes sprayed on, possibly after vaporization in a hot flame. Polymerization of monomers deposited on surfaces by condensation or from solution is also used occasionally. Extrusion of self-supporting thin-film multilayers is yet another technique.

It is impossible to cover everything, or even anything, to the depth it deserves. There is a number of books that deal specifically with processes. Useful works include those by Vossen and Kern [1,2] and Glocker and Shah [3]. We shall deal primarily with physical vapor deposition and especially with thermal evaporation since that is still the staple process.

11.1.1 Thermal Evaporation

In thermal evaporation, the vapor is produced simply by heating the material, known as the evaporant. Because of the reduced pressure in the chamber, the vapor is given off in an even stream, the molecules appearing to travel in straight lines so that any variation in the thickness of the film that is formed is smooth, and depends principally on the position and orientation of the substrate with respect to the vapor source. The properties of the film are broadly similar to those of the bulk material, although, as we shall see, there are important differences in the detailed microstructure. Precautions that have to be taken to ensure good film quality include scrupulous cleanliness of the substrate surface, near normal incidence of the vapor stream and, sometimes, heating the substrate to temperatures of 200–300 °C (or even higher, depending on the material) before commencing deposition. The evaporation is carried out in a sealed chamber that is evacuated to a pressure usually of the order of 10^{-5} mbar (10^{-3} Pa). The materials to be deposited are melted

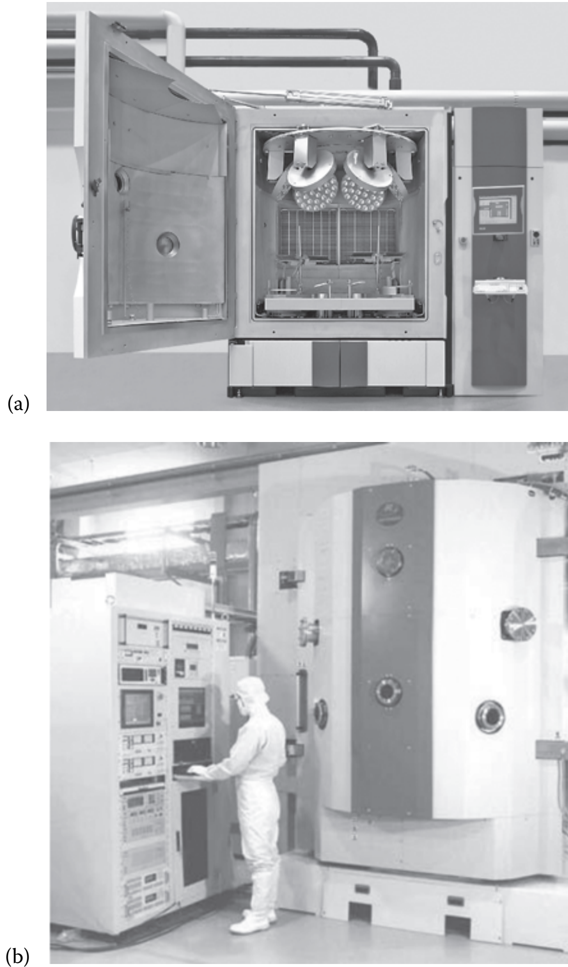

FIGURE 11.1
Thin-film coating machines. These are known as box coaters because the chamber is fabricated in the form of a box with a front door, rather than as a bell jar on a base-plate. They are normally designed to be mounted in the wall of a clean room so that loading and unloading of substrates can take place inside the clean room, while servicing of the equipment is accomplished in the grey area behind the clean-room wall. (a) The SYRUSpro 1510 machine manufactured by Leybold Optics showing a planetary substrate carrier. The front surface heaters, usual with planetary systems, can be seen at the foot of the port to the pumping system at the rear. (Courtesy of Leybold Optics GmbH, Alzenau, Germany.) (b) The OTFC 1800 machine manufactured by Optorun. (Courtesy of Optorun Co. Ltd., Kawagoe, Japan.) (See color insert following page 398.)

within the chamber, using one of a number of possible techniques that will be described. The complete machine consists of the chamber together with the necessary pumps, pressure gauges, power supplies for supplying the energy necessary to melt the evaporant, monitoring equipment for the measurement of the thin-film thickness during the process, substrate holding

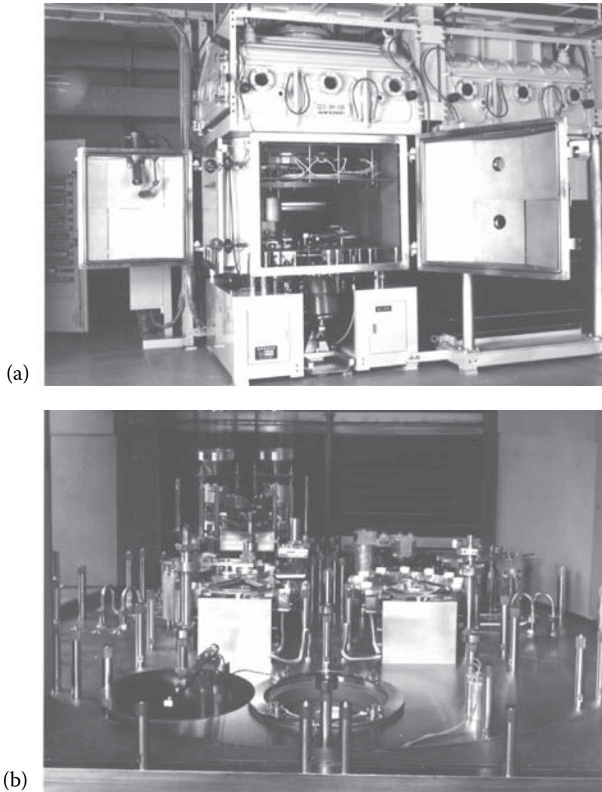

FIGURE 11.2
CES Series Continuous Vacuum Thin Film Coater. The operation is completely automatic. A continuous supply of jigs carrying preloaded substrates are heated under vacuum before passing into the coating chamber. Once coated they pass back out of the system and fresh jigs take their place. (a) The coating chamber. Some of the transport and heating chambers can be seen at the top of the photograph. (b) The interior of the coating chamber showing two electron-beam evaporation sources with automatic feed mechanisms for tablets on the right and granules on the left. (Courtesy of Shincron Co. Ltd., Yokohama, Japan.)

jigs, substrate heaters, and the controls. Modern thin-film coating machines are shown in Figure 11.1 and Figure 11.2. We shall see in the next section that a powerful technique for improving coating quality in thermal evaporation is what is known as ion-assisted deposition.

This consists of thermal evaporation accompanied by bombardment of the growing film by energetic ions to compact it by the impulsive effect of transferred momentum. The machines of Figure 11.1 and Figure 11.2 incorporate suitable sources for the generation of these energetic ions.

To evaporate the material, it must be contained in some kind of crucible and it must be heated until molten with a sufficiently high vapor pressure, unless it sublimes. There is a number of ways of achieving this. The simplest method is to make use of a crucible of refractory metal that acts also

FIGURE 11.3
The base-plate of a thin-film coating machine showing the electrodes and the shutter used for terminating the layers. (Courtesy Balzers AG.)

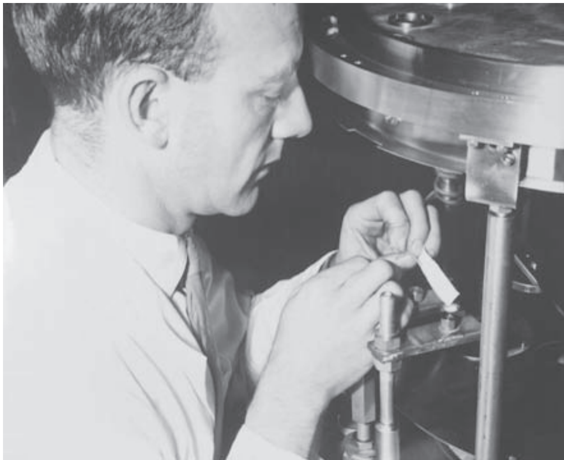

FIGURE 11.4
A molybdenum boat, mounted between electrodes in an Edwards E19E machine, being charged with material (Courtesy Edwards High Vacuum.).

as a heater when an electric current is passed through it. The crucibles are elongated in shape with flat contact areas at either end and are commonly referred to as boats. Electrodes within the machine, which are insulated from the structure, act as both terminals and supports. The resistance of the boats is low, and high currents, several hundred amps at low voltages, are required to heat them. Considerable power is used that heats everything including the electrodes, and, especially to protect their sealing rings, the electrodes are normally water-cooled. Figure 11.3 shows a baseplate of an older bell-jar type of machine complete with a set of electrodes, and Figure 11.4 a molybdenum

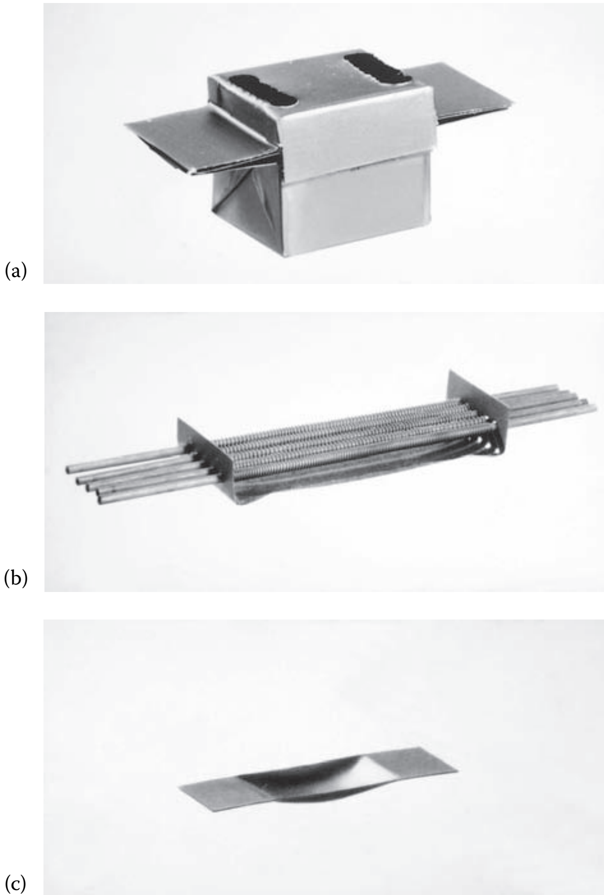

FIGURE 11.5
Various evaporation sources. (a) Tantalum box source (660 A, 1695 W for 1600 °C). (b) Tungsten source for large quantities of metals such as aluminum, silver, and gold (475 A, 1400 W for 1800 °C). (c) Tungsten boat (325 A, 565 W for 1800 °C). (d) Aluminum oxide crucible with molybdenum heater. (e) Aluminum oxide crucible with tungsten filament. Two tungsten boats can also be seen. (Courtesy of Balzers AG.)

boat, mounted between electrodes in a similar machine, being charged with material. Tantalum, molybdenum, and tungsten are all suitable for the manufacture of boats, tantalum and molybdenum being easily bent and formed, and tungsten much less so. Rather less often, in special applications, platinum may be used. A wide range of materials can be evaporated from tantalum, and, of these materials, it is probably that most frequently used. However, some materials react with it (ceric oxide, for example) or with molybdenum and require the less reactive but rather more difficult tungsten.

Considerable skill is required in the manufacture of tungsten boats and they will usually be obtained in final form from specialized manufacturers.

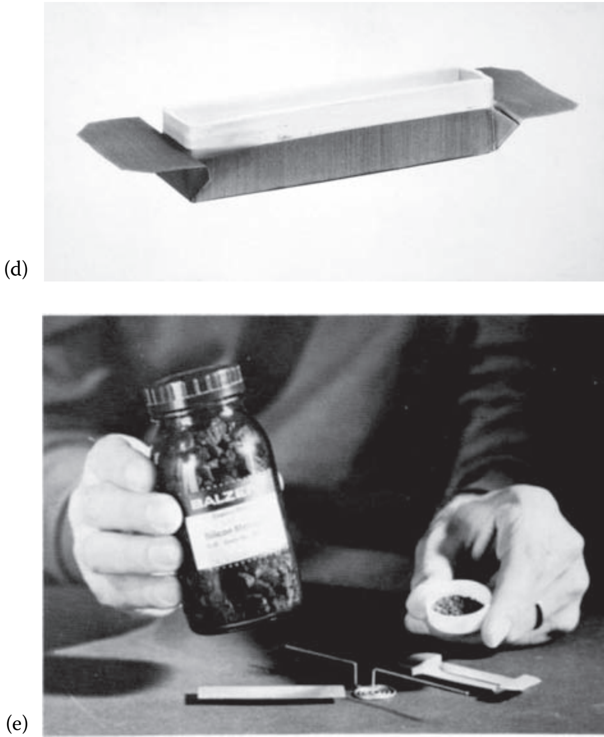

(d)

(e)

FIGURE 11.5 (continued)

If it is necessary, perhaps in an emergency, to construct such a boat from tungsten strip, it should be heated to red heat before bending; otherwise, it will crack. Only the simplest of shapes can be attempted. Certain evaporants react even with tungsten. In some cases, a protective liner of alumina can be added, or an alumina crucible surrounded by a tungsten heater can even be used. In other cases, such as aluminum, the reaction is not very fast, and a tungsten wire helix is a satisfactory source. The aluminum, which wets the tungsten, forms droplets along the helix that has its axis horizontal. The area of tungsten in contact with the aluminum for a given evaporation rate is somewhat less, and the thickness of the wire somewhat greater, than for a boat, so that the tungsten is dissolved away more slowly and a greater proportion can be removed before failure. Even though the tungsten is dissolved in the aluminum, it appears not to contaminate the deposited film. Different types of boat are shown in Figure 11.5.

Materials like zinc sulfide or silicon monoxide, which sublime at not too high a temperature, can be heated in a crucible of alumina, or even fused silica, by radiation from above. A tungsten spiral just above the surface of the material can produce enough heat to vaporize it. This means that the hottest part of the material is the evaporating surface and so the material is

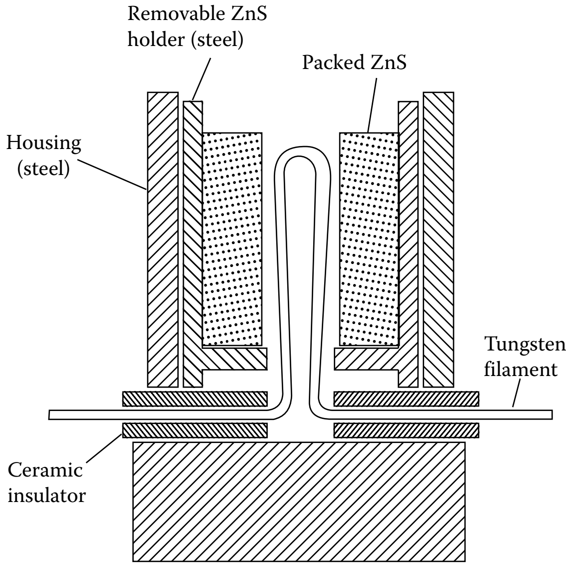

FIGURE 11.6
The howitzer, a source for evaporating large quantities of ZnS at high deposition rates. The removable ZnS holder shown as steel can also be made of fused silica or alumina and the hairpin filament can be replaced by a tungsten helix. (After Cox and Hass [4].)

much less prone to spitting. One example of such a source is shown in Figure 11.5—the crucible is being held in the hand and the spiral is on the table. A development of this type of source is the "howitzer" source that is shown in Figure 11.6, which is particularly useful for zinc sulfide in the infrared as the capacity can be very great [4].

Germanium is an example of a material that reacts even with alumina. The reaction is not particularly fast, but the germanium films become contaminated and show higher longwave infrared absorption than is usual. Graphite has been found to be a useful boat material in this case. Supplied in rod form for use as furnace heating elements, it can be easily machined into almost any desired shape. Copper, graphite, or one of the refractory metals should be used to make the contacts to the graphite boats. At the high temperatures involved, steel and graphite interact so that the former tends to melt and pit badly and is, therefore, quite unsuitable.

A form of heating that avoids many of the difficulties associated with directly and indirectly heated boats is electron-beam heating, and this is now the preferred technique for most materials, especially the refractory oxides. In this method, the evaporant is contained in a suitable crucible, or hearth, of electrically conducting material, and is bombarded with a beam of electrons to heat and vaporize it. The portion of the evaporant that is heated is in the center of the exposed surface, and there is a reasonably long thermal conduction path through the material to the hearth that can therefore be held

at a rather lower temperature than the melting temperature of the evaporant, without prohibitive heat loss. This means that the reaction between the evaporant and the hearth can be inhibited, and the hearth is normally water-cooled to maintain its low temperature.

Copper, because of its high thermal conductivity, is the preferred hearth material. The electrons are emitted by a hot filament, normally tungsten, and are attracted to the evaporant by a potential usually between 6 and 10 kV. Various types of electrodes and forms of focusing have been used at different times, but the arrangement that has now been almost universally adopted is what is known as the bent-beam type of gun. The hearth is at the ground potential and the filament is negative with respect to it. The filament and electrodes are placed under the hearth, well out of reach of the emitted evaporant. There is usually a plate at filament potential situated close to the filament with a beam-defining slit through which the electrons pass, and this is followed closely by the anode at the same potential as the hearth and incorporating a slightly larger slit so that the beam passes through it. The beam is bent around through rather greater than a semicircle by a magnetic field and focused on the material in the hearth. This avoids the problems of early electron beam systems that had filaments in line of sight of the hearth and hence considerably shortened life due to reactions with the evaporant. Supplementary magnetic fields derived from coils allow the position of the spot to be varied so that the mean can be placed in the center of the hearth and a raster can be described that increases the area of heated material. This reduces the temperature necessary to maintain the same rate of deposition, improves the efficiency of use of the material in the crucible, and makes the electron beam source more stable. Typical electron beam sources of this type are shown in Figure 11.7.

The electron beam source is particularly useful for materials that react with boats or require very high evaporation temperatures, or both. Even in quite small sources, beam currents of up to 1 A at voltages of around 10 kV can be achieved and refractory oxides such as aluminum oxide, zirconium oxide, and hafnium oxide, and reactive semiconductors such as germanium and silicon, can be evaporated readily. Furthermore, materials that can be evaporated quite satisfactorily by a directly heated boat can be evaporated still more easily by electron beam, and so the tendency is to use electron beam sources, once they are installed, for virtually all materials. To improve their flexibility, they can be constructed with multiple pockets in the hearth so that the same source can handle up to four different materials in a single coating cycle. Of course the capacity of each individual pocket in a multiple-pocket version is usually rather less than that of the single-pocket version of the same source. In addition, it is not currently possible to maintain the alternative crucibles at near evaporation temperatures implying a delay between layers as the source is brought up to temperature. For large-scale production, therefore, or for coatings for the infrared, it is normal to use two or more single-pocket sources.

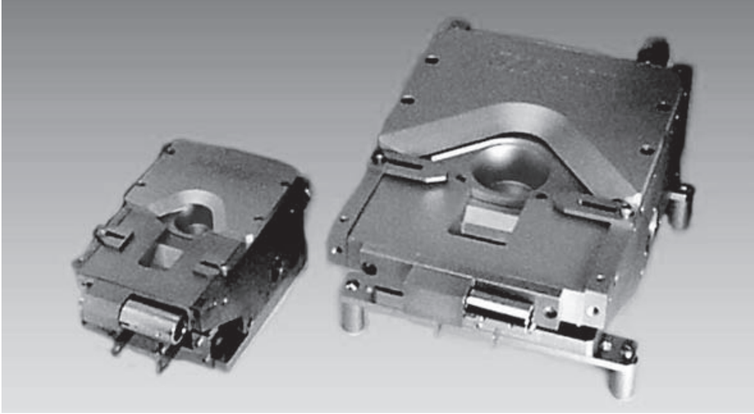

FIGURE 11.7
Electron-beam sources of the bent-beam type. The water-cooled crucibles have several pockets that can be rotated into position at the focus of the electron beam that issues from the slot below the opening in the top of the gun. The sides of the gun are the pole pieces of the focusing and deflecting magnet. Fine-tuning of the field is accomplished by the adjustable tabs on the upper parts of the sources. (Courtesy of Telemark, Hayward, California, USA.) (See color insert following page 398.)

In the operation of an electron-beam source, not all electrons necessarily disappear into the evaporant material in the crucible. Reflected electrons and secondary electrons can exist and may sometimes influence the growing film. Sometimes a grounded plate is fixed behind the source to attempt to trap such electrons. Bangert and Pfefferkorn [5] suggest that in the case particularly of zinc sulfide, the effect of the electrons is actually beneficial. Not much is known about this aspect of the use of electron-beam sources.

The temperature of the substrate also plays a part in determining the properties of the condensed films. Higher substrate temperatures lead to denser and more stable films (see Chapter 12). For refractory oxides temperatures are frequently around 300 °C or slightly higher. Usually it is the consistency of temperature from one coating run to the next that is of greater importance than the absolute level, although Ritchie [6], working in the far infrared beyond 12 μm, found substrate temperature to be of critical importance and devised ways of controlling it to within 2 °C of the experimentally determined optimum. Substrates are often of low thermal conductivity and are mounted on rotating jigs to ensure uniformity of film thickness so that the measurement of the absolute temperature of the substrates is difficult. The heating is usually by means of radiant elements placed a short distance behind the substrates or by tungsten halogen lamps placed so that they illuminate the front surfaces of the substrates, the latter method gaining in popularity.

For planetary arrangements of substrate carriers (see Figure 11.1), it is difficult to arrange rear-surface heating and so front surface heaters are normal. Measurement is most often carried out by placing a thermocouple just in

front of the substrate carrier. This will not measure substrate temperature accurately but will give an indication of the constancy of process conditions; frequently this is the most important characteristic. An improvement can be obtained by embedding the thermocouple in a block of material of the same type as the substrates.

Thermocouples have been placed on the rotating jig and the signal led out through silver slip rings, but even in this case the temperature of the front surface of the substrates is still not necessarily known to any high degree of accuracy, especially if they are of material of low thermal conductivity such as glass or silica. Results that are rather more accurate are achievable with substrates of germanium or silicon, frequently used in the infrared. A more consistent technique that is becoming more common is the use of an infrared remote sensing thermometer that detects infrared radiation from the hot substrates. Usually mounted outside the chamber, this views the substrates through an infrared-transmitting window. The absolute calibration of the device depends on the emittance of the substrate. This varies less for substrates such as glass and dielectric coatings for the visible region than for infrared components. Again, consistency from one run to the next is of prime importance. One tends to find more accurate and complex arrangements in the research laboratory, where very small numbers of samples are the norm and large batches of coatings are rare.

Usually metals should be deposited at low substrate temperatures to avoid scatter—particularly important in metal–dielectric filters and in ultraviolet-reflecting coatings, although there is an exception to this rule of thumb in the cases of rhodium and platinum, both of which give substantially better results when deposited hot [7,8]. There are difficulties in refrigerating substrates, and substrate temperatures below ambient encourage thicker adsorbed gas layers that inhibit the condensation of the films and cause contamination. Thus, it is not normal to operate with substrate temperatures below ambient, at which adequate results are obtained. The softer dielectric materials, such as zinc sulfide and cryolite, can also be deposited at room temperature (except, as we shall see, if zinc sulfide is to be used in the infrared). The harder dielectric materials, however, usually require elevated substrate temperatures, often 200–300 °C. These materials include ceric oxide, magnesium fluoride, and titanium dioxide. Some of the semiconductors for the infrared must be similarly treated. Frequently, optimum mechanical properties demand deposition at a temperature that is different from that for optimum optical properties and a compromise that depends on the particular application is necessary. Further details will be given when individual materials are discussed.

Figure 11.2 is significant for a number of reasons. The exposure of the deposition chamber to the atmosphere every time fresh substrates for coating are to be introduced disturbs enormously the coating environment. The walls of the chamber adsorb considerable quantities of atmospheric gases, particularly water vapor, and the subsequent outgassing during evacuation

is a major contributor to the time to reach final coating conditions, and even then, there are difficulties in determining whether or not the conditions are finally stable. The machine in Figure 11.2 uses what is known as *a load lock system*, the term *load lock* likely being derived from a lock on a river or canal. In such a system, the chamber is maintained under deposition conditions.

Substrates are introduced into a separate load chamber, isolated from the deposition chamber by a gate valve. The gate valve is opened only when the load chamber has reached the correct vacuum conditions when the substrates are transferred to the deposition chamber. The machine of Figure 11.2 takes the concept still further in that the substrates are thermally soaked until the precise deposition conditions are reached and only then are they transferred. Immediately after coating, they are transferred out. The deposition chamber then is used only for deposition. In the normal way, the opening of the deposition chamber to atmosphere affords the opportunity of recharging sources and so ways of doing that remotely under vacuum had also to be devised.

One of the biggest problems in optical coating manufacture is the cleaning of the deposition chamber. Particularly in thermal evaporation, the material in vapor form goes everywhere there is a line of sight from the source, and coats everything. There can also be some deposition of material in the shadows of the chamber fittings even, sometimes, on the rear surfaces of the substrates. It is normal, therefore, to fit shields in the chamber to minimize deposition on any parts that would be difficult to clean later, such as the actual walls of the chamber. These shields can be removed from time to time and cleaned outside the deposition room. To ease still further the problems of cleaning, it is common practice to add disposable sheets of aluminum foil to screen even the shields. The cleaning operation can be mechanical, bead blasting is common, or chemical. It is good practice to bake the shields after cleaning. This removes any races of trapped fluid but also tends to dislodge any loosely bound particles that remain and could cause problems later in the deposition process. The cleaning operation is not only a technical problem. There are all kinds of legal requirements that vary from one area to another.

11.1.2 Energetic Processes

The energetic processes, as the name suggests, are ones that involve energies rather greater than thermal. Thin films deposited by thermal evaporation have a pronounced columnar structure that is a major cause of coating instability and drift. This is discussed later in this chapter. The idea behind the energetic processes is to disrupt the columnar structure with its accompanying voids by supplying extra energy, and this does work well. Some of the energetic processes are old ones that have always involved extra energy and are now recognized as having certain advantages because of it. Although we describe the processes as energetic, it has been shown that momentum is the important quantity.

Sputtering is an old process that predates thermal evaporation. Momentum transfer from incident energetic ions is used to eject atoms and molecules

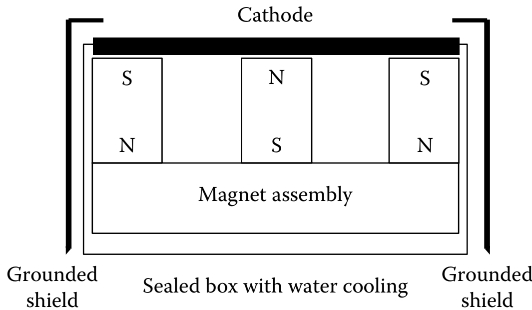

FIGURE 11.8
Schematic representation of a planar magnetron source. The target or cathode is connected to the negative supply. The structure of the coating machine including the grounded shield is the positive side of the supply. Electrons leaving the cathode surface move outward but are turned into a cycloidal path by the field of the magnets. The polarity of the magnets is unimportant as long as they are arranged with the outer poles opposite to the inner as shown.

from a target into the vapor phase. The kinetic energy and momentum of the ejected particles are high and so the growing film is subjected to a much greater impulse each time a fresh particle arrives, which disrupts the void and columnar structure. In the conventional form of sputtering, the target is metallic so that it conducts and the bombarding ions are derived from a DC discharge near the target. This discharge may be confined by crossed electric and magnetic fields when it is known as magnetron sputtering and this is a frequent way of applying the process in optical coating. DC planar magnetron targets are most common; Figure 11.8 shows a schematic form of such a target. The great advantage of magnetron sputtering is the much longer path length of the electrons so that the discharge can be maintained at a considerably lower pressure (0.3 Pa or 0.3×10^{-2} mbar, for example) than is required compared with conventional sputtering in the absence of the magnetic field.

There are, however, some disadvantages. The arrangement of magnets concentrates the discharge in the region between the pole pieces and the erosion of the target is greatest there, while other areas of the target show negligible erosion. With long rectangular targets, the appearance of the eroded region is not unlike the shape of a *racetrack*, a term often used to describe it. Target utilization is therefore not good and so used targets are usually recovered rather than scrapped.

Since the targets in DC magnetron sputtering are metallic, a process of reactive sputtering must be used to produce oxides or nitrides and the sputtering gas, therefore, is usually a mixture of a noble gas such as argon and oxygen or nitrogen. This reactive gas reacts also with the target to produce a skin of oxide or nitride and the skin tends to build up in the less eroded regions. These patches of insulating film have a high capacitance (capacitance is proportional to the inverse of the thickness) and as they are bombarded, they charge gradually and, because their capacitance is high, they

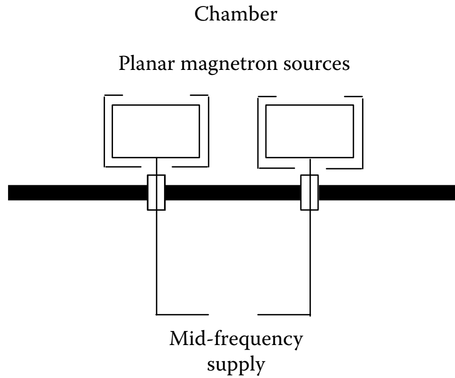

FIGURE 11.9
The twin magnetron arrangement in which two magnetron targets are connected to a mid-frequency power supply so that each is alternately anode and cathode. The arrangement avoids the charging problems of reactive DC sputtering without the complications of radio-frequency sputtering.

store a considerable charge. They are not particularly reliable as capacitors and tend to break down in a sudden and violent discharge that is essentially an arc. This arcing tends to produce molten droplets of material that are often embedded in the film. In the worst case, the discharge can actually seriously damage the target. The insulating skin also modifies the electrical properties of the sputtering system inducing a hysteresis that complicates the control. Such effects are particularly severe with silicon targets, and silicon oxide is the sole low-index material really suitable for sputtering. The problem is often called *target poisoning.*

There are several current solutions to the target-poisoning problem. The target surface may be moved with respect to the magnets so that the region of high erosion moves over the surface and scrubs off the insulating material. In the usual embodiment, the target is made in cylindrical form and rotated about a longitudinal axis around the magnets and inside the grounded shield. Then there are special power supplies that regularly reverse the polarity of the supply so as to discharge the capacitors. Because the capacitance is high, the time constant is quite long, and the discharging can be performed at a relatively low frequency. A more recent solution, and perhaps the most popular in precision optics, involves twin magnetron targets connected to opposite poles of a mid-frequency power supply. The targets are now alternately the anode and cathode of the system. This discharges the effective capacitors before they can cause damage and, because of the long time constant, the frequency can be as low as 10 KHz although the more usual frequency is around 40 KHz. This is sometimes termed *mid-frequency sputtering*, or *twin*, or *dual magnetron sputtering*. This arrangement of alternating anode and cathode solves another problem. In normal single-target sputtering, the chamber structure is usually the anode of the supply, although sometimes there may be an additional rod that functions

also as an anode. The insulating film also gradually covers this structure making the anode less and less effective with serious implications especially for the control of the process. The effect is known as the disappearing anode. Since the mid-frequency arrangement provides the anode that is constantly scrubbed with every alternate half cycle, the technique solves the disappearing anode problem along with the poisoning. Usually the double magnetrons are planar, but the process has also been used with rotating magnetrons.

An alternative process places the magnetron source inside a shroud where it can be operated in argon and thus avoid poisoning. The material escapes through a large aperture above the source in the center of the shroud. Outside the shroud in the main chamber, the material coats the substrates but the growing film is also bombarded with a beam of oxygen or nitrogen ions in the manner of ion-assisted deposition, described shortly. Enormous quantities of gas enter the deposition chamber and to remove the gas very fast, high-capacity pumps are used. The films that grow are amorphous of very high packing density. This process is known as *microplasma*, and most of what is known publicly about the process comes from an issued patent [9]. An advantage of the process appears to be that the geometry of the coating chamber can be similar to that for thermal evaporation. Presumably, the increased positional stability of the magnetron sources is a further advantage over a similar evaporation geometry.

A rather different approach [10,11] uses intermittent deposition on a cylindrical work holder but extends the plasma completely around the cylinder so that the efficiency of conversion of the metal to the oxide or nitride is exceedingly high This is achieved by arranging a number, usually four, of magnetron sources around the periphery of the cylinder, only the one with the appropriate material operating at any particular time. The magnets within the targets are arranged so that always a target with a north magnetic pole outermost is next to one with a south pole outermost. Thus, as we move around the cylinder we have NSN for the first magnetron, then SNS for the next, and so on. This forms a kind of magnetic bottle and the plasma spreads out all around the work holder. Very high-quality coatings are reported. The process is termed *closed field magnetron sputtering.* A machine is shown in Figure 11.10.

There are other solutions. The oxidation or nitriding may take place remote from the deposition. This requires that only a small amount of material be deposited then treated, then more deposited and then treated, and so on. The process is implemented by placing the substrates on a cylindrical drum that is then rotated rapidly and continuously past a linear magnetron-sputtering source, often mid-frequency, then past an ion source and round to the magnetron targets again. The idea originated in the community that coats tools [12] and thermal evaporation was the method uppermost in the minds of the authors for the deposition of the material. Nevertheless, the idea of intermittent deposition can readily be applied to other types of

FIGURE 11.10
CFM450 closed field magnetron coating system. (Courtesy Applied Multilayers, Coalville, Leicestershire, England.) (See color insert following page 398.)

deposition and particularly to the sputtering of optical coatings. An early version of such a process was known as *metamode,* short for "metal mode," and is the subject of an issued patent [13].

A fairly recent innovation in optical coatings is the load lock system for the introduction of substrates into the coating chamber, already mentioned in connection with the machine of Figure 11.2. Since sputtering sources do not need to be renewed after every deposition cycle, they especially lend themselves to load lock design. Figure 11.11 shows a small machine that uses intermittent deposition by sputtering but, in this case, the deposition chamber is isolated from the outside world by a load lock system. This particular machine was originally designed for small batch ophthalmic applications but it has been demonstrated to be very successful also in other types of coating [14].

A machine that goes still further in that the loading system is not only through a load lock but is handled robotically is shown in Figure 11.12. Here, the input and output side of the machine is designed to be situated in a clean room while the chamber is in a gray area where planned maintenance can be performed without exposing any of the other parts of the machine.

The insulating skin that forms over the metallic cathode has a relatively high capacitance and this permits the mid-frequency sputtering approach. The surface of a purely dielectric target has very low capacitance because the thickness of dielectric material is now very large. The small capacitance has a very short time constant and any discharging operation must take place at elevated frequency, that is, at radiofrequency. Radiofrequency (RF) sputtering does avoid the problems of an insulating target. Although it has been much used in other areas of thin-film deposition it has not been as

FIGURE 11.11
The Plasmacoat is a small machine, originally intended principally for the coating of spectacle lenses but also suitable for small batches of other types of coating. The process is one of reactive sputtering and the operation is entirely automatic. The coating chamber is permanently under vacuum. For loading, the substrate carrier drops down into the loading chamber leaving the coating chamber sealed off. The carrier can then be loaded through the access door. Once substrates are loaded, the access door closes and the substrate carrier moves upwards back into the deposition chamber. (Courtesy of Applied Multilayers, Coalville, Leicestershire, England.)

popular in optical coatings, possibly partly because of additional requirements of screening and matching and possibly also because although an excellent process capable of very high-quality films, it seems not to present a sufficiently compelling advantage over other deposition techniques. Nevertheless, in applications where speed is less important than quality, it has been found remarkably reliable and stable, to the extent where even quite complex coatings can be controlled entirely by power, gas pressure, and time with no ongoing layer thickness measurement whatsoever [15]. Even here, however, we find similar stability with the lower frequency forms of sputtering [16].

A completely different approach to sputtering involves the use of a separate chamber to generate the ions that are then extracted and directed toward the target (Figure 11.13 and Figure 11.14). This is known as ion-beam

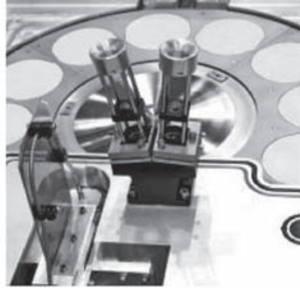

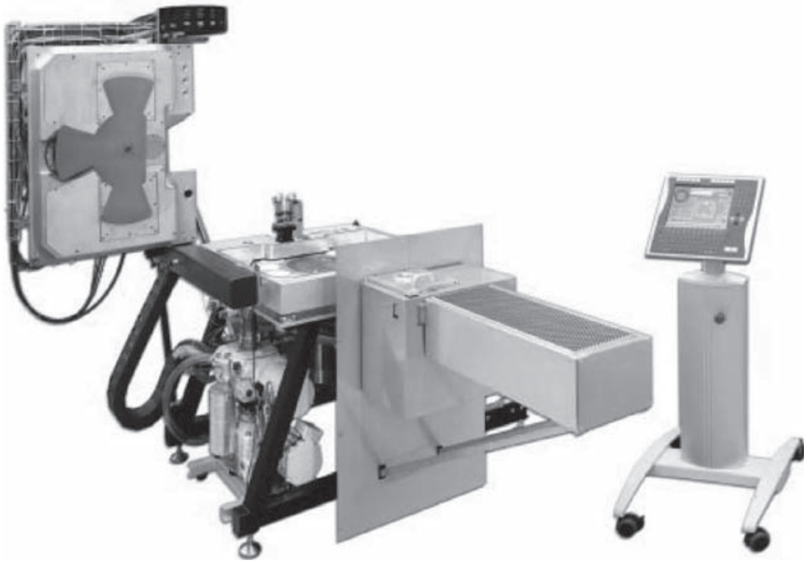

FIGURE 11.12
The Helios magnetron sputtering system of Leybold Optics incorporates the intermittent deposition technique in a chamber that is never opened to atmosphere except for servicing. The substrates are fed into the coating chamber robotically through a load lock system. The loading side is situated in a clean room and the coating chamber in a grey room. The substrate carrier is shown on the left with an optional optical monitoring system. (Courtesy Leybold Optics GmbH, Alzenau, Germany.) (See color insert following page 398.)

sputtering [17]. It is capable of a very high degree of film purity and the lowest published losses in multilayer reflecting coatings, 1 ppm or less, have been achieved with this process [18,19]. Since the ion beam is usually neutralized by adding electrons, charging problems with insulating targets can be avoided and the process is as useful for insulating materials as for conductors. Ion-beam sputtering is slow compared with most other processes and it is not yet able to cope with deposition over large areas. It has, however, made

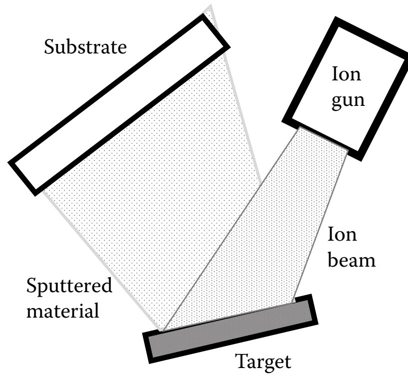

FIGURE 11.13
Ion-beam sputtering schematic. The ion-generating discharge is within the ion gun and therefore removed from the deposition chamber. This gives much higher-quality films.

FIGURE 11.14
A Spector ion-beam sputtering system for the production of high-quality optical coatings especially narrowband filters for dense wavelength division multiplexing. (Courtesy of Ion Tech, Inc., Fort Collins, Colorado, USA.)

big inroads into the area of precision optics. The reason for this is partly the evident success of the process, partly the resolution of a protracted patent dispute involving ion-beam sputtering, but there was also an element of chance. During the 1990s, it had become a significant technique for the production of dense wavelength division multiplexing filters and when that

market contracted, other uses had to be found for the equipment that now happily demonstrated considerable success in the construction of other types of high-quality coatings.

Not all materials are suitable for sputtering. In particular, the fluorides present considerable difficulties because of preferential sputtering of fluorine atoms. The film is then fluorine deficient and optically absorbing. The fluorine vacancies can be filled with oxygen—there is usually plenty of oxygen around—that removes the absorption, at least at longer wavelengths, but the film becomes an oxyfluoride with altered (usually raised) index of refraction and frequently poorer environmental resistance. Various techniques have been proposed for the successful sputtering of fluorides but that they have not so far been generally adopted suggests that difficulties still remain.

In reactive low-voltage ion plating [20,21], a high-current beam of low voltage electrons is directed into the region above the hearth in an electron beam source. This results in a very high degree of ionization of evaporant material, usually a metal or suboxide ensuring that the melt should be conducting. Reactive gases, oxygen or nitrogen, fed separately into the chamber, are also highly ionized. There is a complete circuit from electron source to electron beam source to low-voltage high-current power supply and back to electron beam source and it is completely isolated from the remainder of the structure. The substrate carrier is also electrically isolated.

There are many electrons and they are very mobile and so the isolated substrates acquire a charge that is negative with respect to the electron beam source. This attracts the positive ions from the source so that they arrive at the film surface with additional momentum that is transferred to the film and compact it. Films are tough, hard, and dense and usually amorphous. Because of the very efficient reaction with the additional gas, they are of high optical quality. Recent versions of the process include the possibility of a deliberate bias on the substrate carrier rather than simply leaving it to the accumulation of electrons.

Ion-assisted deposition is an energetic process that has the great advantage that it is easy to implement in traditional thermal equipment. It consists of thermal evaporation to which has been added bombardment of the growing film with a neutral beam of energetic ions (that is, a beam of positive ions injected with sufficient electrons). All that is required to put it into operation in a conventional machine, therefore, is the addition of an ion source. The most common types of ion sources for this purpose are broad-beam, often with extraction grids. Much of the earlier published research and reported successes used the Kaufman, or gridded type of, ion gun.

In that, the source of electrons is a hot filament and the extraction system consists of two closely aligned grids, the inner floating and acquiring the potential of the discharge so that it confines it within the gun, and the second applying a field to draw the positive ions out of the discharge chamber through the apertures in the inner grid. The beam of ions is neutralized

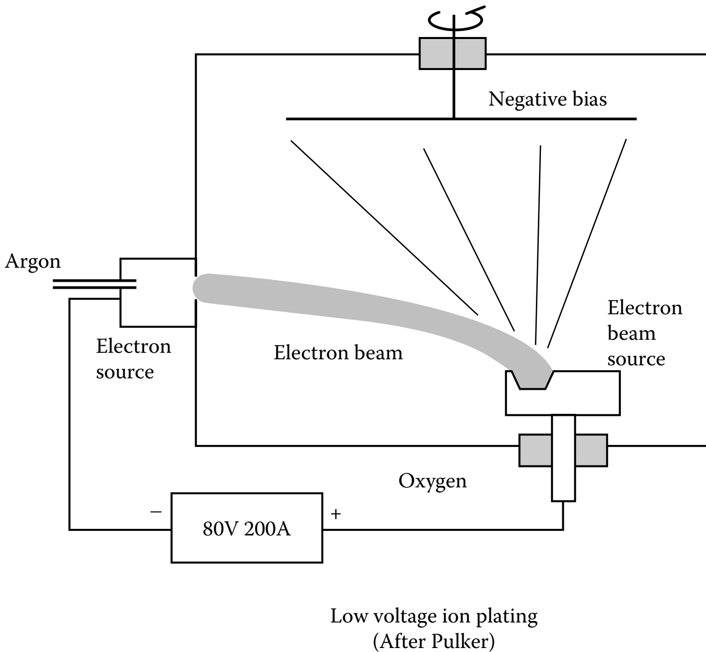

FIGURE 11.15
The low-voltage ion plating process. The negative bias on the electrically isolated substrates is acquired from the free electrons in the chamber. (After Pulker, H.K. and Guenther, K.H., Reactive physical vapor deposition processes, in *Thin Films for Optical Systems*, Flory, F.R., Ed., Marcel Dekker, Inc, New York, 91–115, 1995.)

outside the discharge chamber by adding electrons, often from a hot filament, immersed in the beam to avoid space charge limitation, or, more commonly today, from a separate hollow-cathode electron emitter. The Kaufman source has an advantage in that the ion energy is well controlled, an advantage in research, but the grids are fragile and easily misaligned or damaged and so some effort has been put into the development of sources that do not require extraction grids and they are being used in increasing numbers in production. For further information, see Bovard [22] and Fulton [23].

The ionized plasma-assisted deposition process includes features of both ion-assisted deposition and low-voltage ion plating. It makes use of what is known as an advanced plasma source [24–26]. The source, which is insulated from the chamber and floats in potential, is of simple construction. A central indirectly heated cathode is made of lanthanum hexaboride. This lies along the axis of a vertical cylinder that is the anode. A noble gas, usually argon, is introduced into the source. The cylinder contains a solenoid that produces an axial magnetic field. The crossed electric and magnetic fields make the electrons move in cycloids with the usual increase in path length and degree of ionization, so that an intense plasma is produced in the source. The fields do not confine the plasma axially and so it escapes from the source into the chamber.

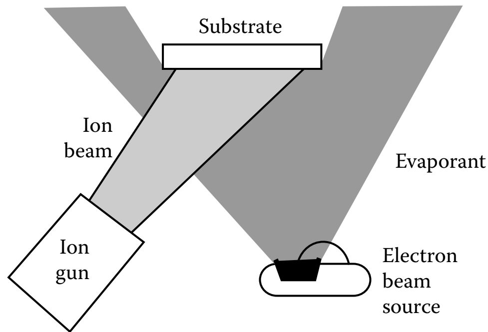

FIGURE 11.16
The addition of ion bombardment of the growing film transforms conventional thermal evaporation into ion-assisted deposition.

There, the electrons, which are very mobile, escape preferentially to the chamber structure leaving the plasma charged positively without the need for isolated substrate holders. The deposition sources are thermal, usually electron beam, and they emit evaporant into the plasma where it gains energy and is partially ionized. The evaporant then condenses on the growing film with additional energy, as in ion plating, and is bombarded simultaneously by ions from the plasma as in ion-assisted deposition. For reactive processes, the reacting gas is not fed into the source, but into the plasma as it leaves the source. The process has been very successful in the production of narrowband filters for dense wavelength division multiplexing and, since the contraction of the telecom market, in precision optics in general.

A quite recent development of some importance is known as *radical assisted sputtering* or RAS [27]. Here the configuration is also of a vertical drum rotating past, this time, dual magnetron sources but the interaction is arranged to be with atomic oxygen or, in some cases nitrogen. There is essentially no bombardment. The reactivity of the atomic oxygen is so high that bombardment to ensure implantation is not necessary and, in fact, is intentionally suppressed. The films are consequently of very high quality. Although this is not strictly an energetic process, nevertheless the films have consistent high packing density and all the attributes of an energetic process. The machines are configured with load locks so that the chamber is exposed to the atmosphere only for maintenance. Again, the stability of the process has been demonstrated in the monitoring of film thickness purely by timing. This is a particularly fast process, and so batch costs are reported as attractively low and the machine is capable of large batches. A machine is shown in Figure 11.18.

It seems clear that a major benefit of the energetic processes is an increase in film packing density. The improvements are achieved at comparatively low substrate temperatures, which helps with the difficult coating of plastic substrates.

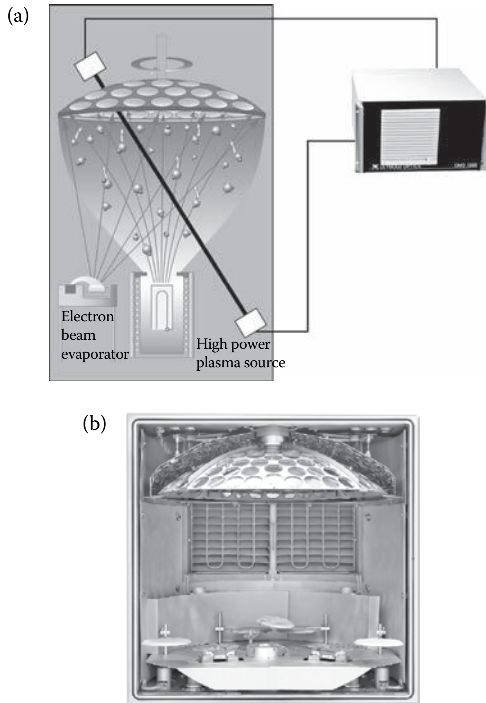

FIGURE 11.17
The advanced plasma source. (a) Diagram of the advanced plasma source (APS) and the arrangement of the machine for plasma ion-assisted deposition (PIAD). The sketch shows also the application of a system of optical monitoring (OMS 5000) that takes its signals directly from one of the batch substrates. The optical properties of the substrate are sampled every time it passes through the beam. (b) Photograph of the interior of a SYRUSpro 1110 system showing two boat sources toward the front and two electron-beam sources toward the rear together with a central advanced plasma source. The single-rotation calotte permits rear surface heating and the shroud that can be seen above the rear half of the calotte carries the heater elements on its lower surface. Electron-beam sources and just slightly to the right of the center the cylindrical advanced plasma source. (Courtesy of Leybold Optics GmbH, Alzenau, Germany.) (See color insert following page 398.)

It has been theoretically demonstrated by advanced computer modeling [28,29] that the major effects are due to the additional momentum of the molecules, either supplied by collisions with the incoming energetic ions, or derived from the additional kinetic energy of the evaporant. Experimental evidence exists [30,31] that shows correlation of the effects with momentum rather than energy of the bombarding ions. Major benefits of these processes are the increased packing density of the films, making them more bulk-like and hence increasing their ruggedness, the improved adhesion resulting from a mixing of materials at the interfaces between layers, and a reduction of the sometimes quite high tensile stress in the layers. The increase in packing density reduces also the moisture sensitivity and can actually eliminate

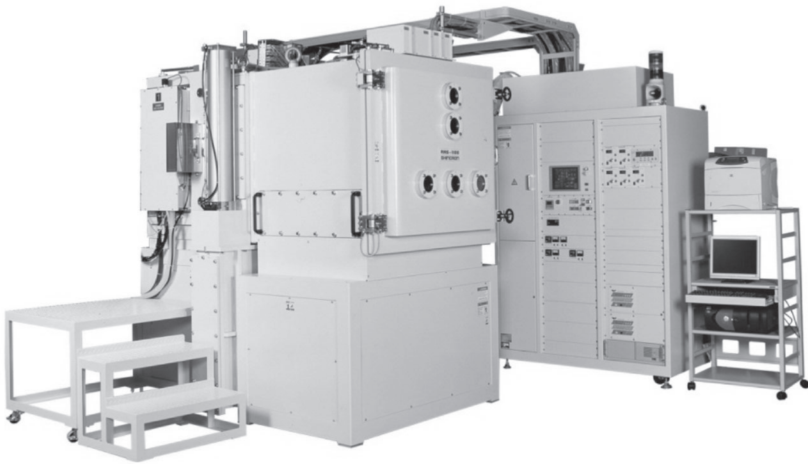

FIGURE 11.18
Machine for implementing the RAS process. The front door opens into the load chamber. The actuator for the gate valve into the deposition chamber is visible on the left-hand wall and behind it a cover giving access to the rear of one of the magnetron sources. (Courtesy Shincron Company Ltd, Yokohama, Japan.)

it altogether [32]. The increased packing density also improves the stability of the films in other ways. Magnesium fluoride films resist high temperature oxidation better, for example, [33]. The hardness and corrosion resistance of metal films, especially with dielectric overcoats [34], are improved by ion-assisted deposition but the optical properties tend to be slightly adversely affected, possibly by the implantation of a small fraction of the bombarding ions [35]. The increased reactivity of the bombarding ions permits the deposition of compounds, such as nitrides [36], that are difficult or impossible by normal vacuum evaporation.

11.1.3 Other Processes

Physical vapor deposition processes are those most often used for the production of optical coatings. However, in the electronic device field, chemical vapor deposition is the principal method for thin-film deposition and there is increasing interest in it for optical purposes, usually with regard to very special requirements.

Chemical vapor deposition differs from physical vapor deposition in that the film material is produced by a reaction amongst components of the vapor that surrounds the substrates. The reaction may be induced by the temperature of the substrates themselves, when the process is the classic thermal chemical vapor deposition, or, and this is more usual in the optical field, it may be a plasma-induced process.

Usually the components, the reactants or precursors, will be introduced into a carrier gas that is permitted to flow through the system. This ensures a constant supply of the reactants to the growing interface and allows sufficient dilution so that the reaction is not so fast as to overwhelm the film growth. In this classic form of chemical vapor deposition, great problems are created by reactions that are too efficient. A reaction that proceeds rapidly tends to produce a film that is poorly packed and poorly adherent. The term *snow* is often used to describe it. The reactions must, therefore, be quite weak and this means that impurities that have strong reactions can play havoc with the process and severely limit the possible range of processes.

Because of all the difficulties, the classic thermal chemical vapor deposition process is not often used for optical coatings. Instead, pulsed processes have been largely adopted. Material added to a thin film is assimilated provided it is not immobilized by material deposited over it before it has had time to relax into favorable positions. The problem is not really the strength of the reaction but rather the large amount of material that arrives in a given time. Earlier material is buried under the later material and cannot relax to a state of equilibrium, and snow is the result. If an efficient reaction can be made to deliver material at a correct rate then the film will be dense. It is the overall rate of deposition that determines the microstructure. Pulsing the reaction gives the control of rate that is required. The pulsing can most conveniently be achieved when a plasma-assisted process is involved [37].

A related process that is sometimes called *plasma polymerization*, and sometimes *plasma-enhanced* (or *-induced*) *chemical vapor deposition* or PECVD [38–40], is used to deposit dense organic layers with stable optical properties over curved and irregular surfaces with good uniformity. Plasma polymerization is quite unlike normal polymerization where monomers are linked into chains of repeat units. The plasma is characterized by energetic electrons that break the reactants into active fragments and these fragments link with each other to form the deposited film. Some of this combination may take place in the gaseous phase, forming clusters that may deposit on the growing film or may be broken into fragments again by the plasma. Strong binding occurs so that the deposited film is tough and hard and dense. It is not strictly polymeric and contains free radicals that may combine with any oxygen that is also present. The mechanical properties can range from plastic to elastic and glass-like. Because the films are insulating, in fact they are used as capacitor dielectrics in some applications, RF discharges are usual for this process. Speed of deposition can be very high, up to 1 μm min^{-1} although rates of one-tenth to one-hundredth of this are more common.

The process has been used for some time in the semiconductor industry to deposit silicon dioxide. The normal precursor is tetraethoxysilane (TEOS) together with oxygen but the substrate temperature is usually quite high, at least 250 °C, much higher than can be possible for plastic substrates. When the temperature is reduced to permit coating of plastic substrates, the film composition becomes much more complicated. Apart from the silicon oxide

content, they include, for example, silanol that results from reactions involving residual water vapor. There are, in fact, many silicone compounds that can be and have been used as precursors in the PECVD deposition of such silica-rich films. The feature that they tend to share is a backbone of alternate silicon and oxygen atoms. Apart from the tetraethoxysilane already mentioned other suitable compounds include hexamethyldisiloxane (HMDSO), tetramethoxysilane (TMOS), methyltrimethoxysilane (MTMOS), and trimethylmethoxysilane (TMMOS). As might be expected, they are toxic, although their toxicity varies. The make-up of the precursors determines to a large extent the character of the film. With organic silicone compounds or silanes present in the gas along with oxygen, the coatings are particularly tough and resistant to abrasion and form the basis for a number of different hard coats. The name hard coat is normally given to an initial layer over a plastic substrate that acts as a transition between the organic plastic and an overlying essentially inorganic optical coating. Fluorine compounds give films that have very low friction and are hydrophobic and are frequently used as the outermost anti-smudge layer in an antireflection coating. The precise details of the precursors are difficult to obtain. They are considered part of the expertise of the process.

A technique that has some features in common with chemical vapor deposition is *atomic layer deposition* or ALD. In atomic layer deposition, the film molecules are assembled from their components on the actual surface to be coated. The substrates are placed in a reactor and a precursor in the gaseous phase is entered. This precursor is chosen so that one of the components is chemisorbed on the surface of the substrate. Ideally this process saturates when complete cover of the surface by a monolayer is achieved, although, in practice, there may not be a complete monolayer, or there may be some multilayer coverage. At saturation, the reactor is purged. A second cycle then involves a precursor for the second component of the molecules. This second component is now chemisorbed over the first, and the same process of saturation ideally ensures the completion of a single monolayer of the compound over the surface, although in practice, there may be some small departure from perfection. The reactor is purged again and the first component is reintroduced to produce the first part of a second molecular layer and the process repeats itself many times to build up the required thickness of film. As might be expected, the process is slower than either conventional chemical vapor deposition or the physical vapor deposition processes we have considered. The various steps of the process must be activated and that can be accomplished in a number of ways including simply heating the substrates, or supplying the energy in the form of ultraviolet radiation, or through a plasma that will be excited at radiofrequency to avoid charging effects over the dielectric materials involved. The basic principle is that the surface controls the growth, not the reaction. Thus, in spite of the low rate of deposition, the process has the great intrinsic advantage of depositing uniformly thick films over even quite complex substrates together with films of very high quality with easily controllable thicknesses because of the stability of the

incremental thickness in each cycle. Titanium dioxide and aluminum oxide have been used very successfully in optical coatings. For aluminum oxide the precursors can be trimethylaluminum [TMA or $Al(CH_3)_3$] and water, alternately pulsed into the reactor. For titanium dioxide, tetrakis (ethylmethylamido) titanium (TEMAT or $Ti[N(CH_3)C_2H_5]_4$) as one of the precursors and water as another, are possible.

The process has proved successful in many different applications outside optics, especially in the semiconductor industry, and has succeeded in the manufacture of telecom quality narrowband filters. At the time of writing, the preferred lower refractive index material for optical purposes is aluminum oxide. If this could be supplemented, or replaced, by silicon dioxide, then broad acceptance of the process in optical coatings in general would be much more likely. The features of uniformity over complex substrates, high-quality essentially pinhole-free films, and accurate control over film thickness, make the process very attractive. Figure 11.19 shows a typical machine.

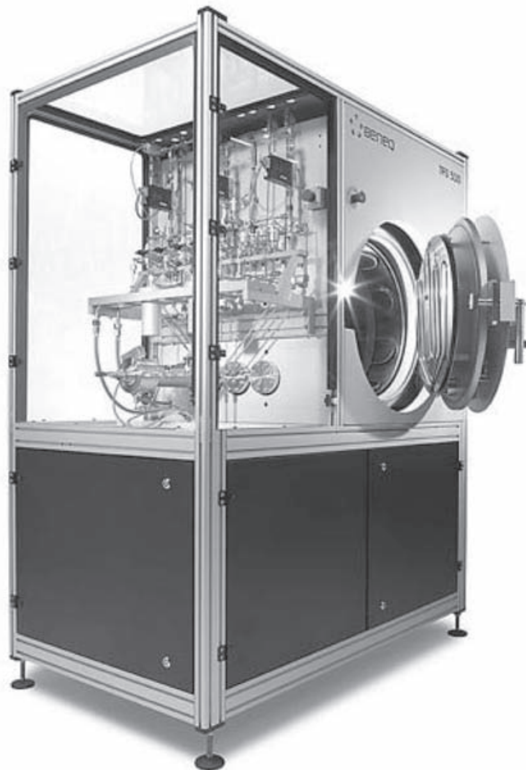

FIGURE 11.19
A TFS 500 system for atomic layer deposition capable of optical coatings. (Courtesy Beneq Oy, Vantaa, Finland. www.beneq.com.)

There are many other techniques for the deposition of optical coatings. Probably the most important of these is the sol-gel process. The name sol-gel refers to those processes that involve a solution that undergoes a transition of the sol-gel type, that is, a solution is transformed into a gel. The common form of the sol-gel process starts with a metal alkoxide. This organometallic compound is hydrolyzed when it is mixed with water in an appropriate mutual solvent. The solution is usually made slightly acidic to control the rates of reaction and to help the formation of a polymeric material with linear molecules. The result is a gradual transition to an oxide polymer with liquid-filled pores. This gel can be deposited over the surface of an optical component by dipping. The coating is then heat treated to remove the liquid in the pores and to densify it; the higher the temperature to which it is raised, the denser is the film. By treating the gel film at temperatures as high as 1000 °C complete densification is achieved. Lower temperatures give partial densification but already by 600 °C, the film is largely impermeable. Typical materials are TEOS (tetraethylorthosilicate, $Si(OC_2H_5)_4$) for eventual films consisting of silica, and titanium tetraethoxide [$Ti(OC_2H_5)_4$] for films of titanium oxide. These materials are dissolved in ethanol and then hydrolyzed by adding a little distilled water. In the case of the titanium compound, the rate of hydrolyzation is much faster. Thus, nitric acid is added to control the transformation and so the solution is made rather weaker.

There are quite considerable difficulties in producing multilayer coatings by the sol-gel process, and so, the principal applications have been in high durability antireflection coatings of a few layers. The process has not competed with vacuum deposition in the production of more complex multilayers.

Interest in the sol-gel process increased enormously when it was discovered that sol-gel deposited antireflection coatings had exceptionally high laser damage threshold [41]. The technique is much used therefore in producing antireflection coatings for components in the very large lasers for fusion experiments. These coatings are unbaked and quite porous; otherwise, the refractive index would not be suitable for single-layer antireflection coatings for low-index materials. In uncontrolled environments, such porous coatings take up moisture and other contaminants and their index tends to vary over a period of time and their performance fall. Regular coatings must be baked at high temperature. However, the environment of the large lasers is tightly controlled and the fragility of the unbaked coatings can be viewed as an advantage if they have to be removed to permit recoating of the component.

11.1.4 Baking

A final stage of the manufacturing process for optical coatings that is seldom discussed is that of baking. This is probably the one aspect of coating production that might still be referred to as an art rather than a science. Baking consists of heating the coated component normally in air at temperatures of usually between 100 °C and 300 °C for a period of perhaps several hours.

A common reaction in most coating departments to a batch of coatings that exhibit less than acceptable properties is to bake the coatings in air for a time simply to see if their properties improve. They frequently do. There is no doubt that such treatment can improve the properties of the coatings in several respects.

Coated substrates that are to be used as laser mirrors cemented to laser tubes are almost invariably baked before mounting because it is believed that this increases their stability. There is no doubt that such treatment does reduce the drift that may occur at the early stages of laser operation but the reason for this is obscure.

Frequently the absorption in the layers falls. This may be simply a case of improved oxidation. We know that baking of titanium suboxides in air improves their transmittance and reduces their absorptance [42]. High-quality films are frequently amorphous and prolonged baking may induce a slow amorphous-to-crystalline transition in such films. This process may compete with the oxidation process so that an optimum period of baking may result. This may be one reason why details of baking are frequently considered proprietary.

Most of the work that has been reported on baking is with regard to narrowband filters, still frequently constructed from zinc sulfide and cryolite. Meaburn [43] was a particularly early worker in this area. He found that a process of baking at 90 °C for 10 hours improved the stability of narrowband filters of zinc sulfide and cryolite enormously. This was especially so if they were protected afterward by a cemented cover slip.

Title et al. [44] reported a baking process called a *hard bake* with filters similar to those described by Meaburn. In the hard bake, filters were subjected to temperatures around 100 °C for a certain time. During the baking process, the peak wavelength moved toward shorter wavelengths. After a critical time the rate of movement suddenly slowed and the filter became much more stable. Details of the shift and the time were considered proprietary and not included in the published account. This is consistent with a desorption process coupled with a diffusion process to be described shortly.

Richmond [45] and Lee [46] both conducted baking experiments on narrowband filters. They were interested in absorption and desorption processes in thin films. They found that the baking process did not appear to alter the amount of moisture absorbed and desorbed by the filters. The stability of the characteristic, in the sense of the total change for a given change in relative humidity, was essentially unaltered. The rate of change, however, was greatly increased so that the characteristic reached equilibrium very much faster. The filters, therefore, appeared to be much more stable in the laboratory environment.

Müller [47] constructed computer models of the annealing process in thin films. The essential features of the models were thermally activated movements of atoms from a filled site to an available neighboring and vacant site. He found that packing density did not change during this process but that

there was a quite definite amalgamation of smaller voids into larger ones. This process appears to be a wandering of the voids through the material of the thin film but is really a process of surface diffusion around the interior of the voids. Once two voids meet there is an energetic advantage in combining, but, once combined, no advantage in splitting. Thus the voids simply increase gradually in size as they reduce in number. The reason for the findings of Richmond and Lee, and probably also Title and Meaburn, now become clear. After deposition, the pore-shaped voids in the material are quite irregular in shape, especially at the interfaces between the layers. The annealing or baking process tends to remove the restrictions in the pores so that although their volume is unchanged their regular shape implies a much faster filling by capillary condensation when exposed to humidity. This means that equilibrium is reached much more rapidly and the filter appears much more stable when the environmental conditions are stable. In the case of already cemented filters, the effective environment is quite stable although the filter stability may be disturbed by changes in temperature. However, when the temperature stabilizes, equilibrium is rapidly established once again.

The improved stability of the integral laser mirror is probably also derived at least partly from this decrease in the time constant for it to reach equilibrium. Any drift of the mirrors after alignment in the laser would immediately cause fluctuations, almost invariably reductions, in laser output. If the mirror can reach equilibrium before the final alignment, then, since the environment within the laser is reasonably stable from the point of view of moisture and consequent adsorption, the laser will be stable.

Müller [47] has also explained why it is that baking never seems to improve poor adhesion but invariably makes it worse. Here if the bonds that bind atoms together across an interface are weaker than those that bind similar atoms together in either material, then there is an energetic advantage for a void that reaches an interface to remain there. Voids therefore collect at such an interface and gradually weaken the adhesion further.

There are a few more recent studies of baking in connection with telecom quality filters, primarily using energetically deposited materials. Prins and colleagues [48] found a curious effect that they termed *creep*, although, as they pointed out, it is not creep in the normal sense of the word, in the baking of narrow-band filters that had been energetically deposited The particular materials were not identified, but it is likely that they were SiO_2 and Ta_2O_5 or, possibly, the chemically similar Nb_2O_5, because at the time, they were the preferred materials in that application. These materials become amorphous when energetically deposited. Exposure to a high temperature (1 minute at 340 °C, for example) of filters on high expansion coefficient substrates caused an expected immediate shift to shorter wavelengths. However, on cooling back down to room temperature, the original wavelength was not immediately restored. Instead, in a gradual recovery that occupied around 5 minutes the wavelength gradually returned toward the original value, although very slight shifts could continue for a period of days. A small permanent shift due

to the baking could also be observed. It seems that relaxation of the films is much slower at lower temperatures. The authors referred to the property of the films as a viscosity that reduced as the temperature increased, and the behavior can certainly be interpreted in that way.

Baking reduces the strain in the films. A particularly useful and informative study of the changes in filters due to baking is due to Brown [49]. Here the filters were definitely constructed from SiO_2 and Ta_2O_5 and the process was ion-beam sputtering, frequently used for telecom quality filters. Annealing at temperatures of around 500 °C induced a shift in the filters toward longer wavelengths. Energetic processes such as ion-beam sputtering induce high levels of compressive strain in the films. Annealing permits redistribution of the material in the film so that it becomes thicker as the strain reduces. The reduction in strain also induces a drop in refractive index since strain birefringence is reduced. The net effect is an increase in optical thickness since the thickness increase dominates. Brown suggested also a packing density effect in which void volume plays a part. It is difficult to say whether these are true voids in the sense of actual empty spaces in the film, or just an expression of the spacing of the elements of the films but the paper repays close study because of the accurate quantitative nature of the results.

Much more work is required on the whole matter of baking and consequent filter stability before all becomes completely clear, but the oven is already an indispensable apparatus in virtually all coating shops.

We return to the matter of moisture adsorption in Chapter 12.

11.2 Measurement of the Optical Properties

Once a suitable method of producing the particular thin film has been determined, the next step is the measurement of the optical properties. Many methods for this exist and a useful earlier account is given by Heavens [50]. Measurement of the optical constants of thin films is also included in the book by Liddell [51]. A more recent survey is that of Borgogno [52]. Recently, the measurement of the optical properties of thin films has increased in importance to the extent that special purpose instruments are now available. These normally include the extraction software and are essentially push-button in operation. As always, however, even when automatic tools are available some understanding of the nature of the process and its limitations is still necessary. Here we shall be concerned with just a few methods that are frequently used.

In all of this, it is important to understand that we never actually measure the optical constants n and k directly. Although thickness, d, is more susceptible to direct measurement, its value too is frequently the product of an indirect process. The extraction of these properties, and others, involves measurements of thin-film behavior followed by a fitting process in which

the parameters of a film model are adjusted so that the calculated behavior of the model matches the measured data. The adjustable parameters of the model are then taken to be the corresponding parameters of the real film. The operation is dependent on a model that corresponds closely to the real film. The appropriateness of the model would be of less importance were we simply trying to recast the measurements in a more convenient form. Even an inadequate model with parameters appropriately adjusted can be expected to reconstitute the original measurements. However, the parameters extracted are rarely used in that role. Rather they are used for predictions of film performance in different situations where film thickness may be quite different and where the film is part of a much more complex structure. This leads to the idea of *stability* of optical constants, a rather different concept from accuracy. Accurate fitting of measured data using an inappropriate model may reproduce the measurements with immense precision yet yield predictions for other film thicknesses that are seriously in error. Such parameters are lacking in stability. Stable optical constants might reproduce the measured results with only satisfactory precision but would have equal success in a predictive role. A good example might be a case where a film that is really inhomogeneous and free from absorption is modeled by a homogeneous and absorbing film. The extracted film parameters in this case can be completely misleading. It must always be remembered that the film model is of fundamental importance.

Almost as important as the model is the accuracy of the actual measurements. Calibration verification is an indispensable step in the measurement of the performance that will be used for the optical constant extraction. Remember that only two parameters are required to define a straight line but to verify linearity requires more. Small errors in measurement can have especially serious consequences in the extinction coefficient and/or assessment of inhomogeneity of the film. The samples themselves should be suitable for the quality of measurement. For example, a badly chosen substrate may deflect the beam partially out of the system so that the measurement is deficient or it may introduce scattering losses that are not characteristic of the film.

The calculation of performance given the design of an optical coating is a straightforward matter. Optical constant extraction is quite different. Each film is a separate puzzle. It may be necessary to try different techniques and different models. Repeat films of different thicknesses or on different substrates may be required. Some films may appear to defy rational explanation. A common film defect is a cyclic inhomogeneity that produces measurements that the usual simpler film models are incapable of fitting with sensible results. It is always worthwhile attempting to recalculate the measurements using the model and extracted parameters to see where deficiencies might lie. Because of all the caveats in this and the previous paragraphs, exact correspondence, however, does not necessarily indicate perfect extraction.

As we saw in Chapter 2, given the optical constants and thicknesses of any series of thin films on a substrate, the calculation of the optical properties

is straightforward. The inverse problem, that of calculating the optical constants and thicknesses of even a single thin film, given the measured optical properties, is much more difficult and there is no general analytical solution to the problem of inverting the equations. For an ideal thin film, there are three parameters involved, n, k, and d, the real and imaginary parts of refractive index and the geometrical thickness, respectively. Both n and k vary with wavelength, which increases the complexity. The traditional methods of measuring optical constants, therefore, rely on special limiting cases that have straightforward solutions.

Perhaps the simplest case of all is represented by a quarter-wave of material on a substrate, both of which are lossless and dispersionless, that is, k is zero and n is constant with wavelength. The reflectance is given by

$$R = \left(\frac{1 - n_f^2 / n_{sub}}{1 + n_f^2 / n_{sub}} \right)^2 \tag{11.1}$$

where n_f is the index of the film and n_{sub} that of the substrate, and the incident medium is assumed to have an index of unity. Then n_f is given by

$$n_f = n_{sub}^{1/2} \left(\frac{1 - R^{1/2}}{1 + R^{1/2}} \right)^{1/2} \tag{11.2}$$

where the refractive index of the substrate, n_{sub} must, of course, be known. The measurement of reflectance must be reasonably accurate. If, for instance, the refractive index is around 2.3, with a substrate of glass, then the reflectance should be measured to around one-third of a percent (absolute ΔR of 0.003) for a refractive index measurement accurate in the second decimal place.

It is sometimes claimed that this method gives a more accurate value for refractive index than the original measure of reflectance since the square root of R is used in the calculation. This may be so, but the value obtained for refractive index will be used in the subsequent calculation of the reflectance of a coating, and therefore the computed figure can be only as good as the original measurement of reflectance.

In the absence of dispersion, the curve of reflectance versus wavelength of the film will be similar to that in Figure 11.20. The extrema correspond to integral numbers of quarter-waves, even numbers being half-wave absentees and giving reflectance equal to that of the uncoated substrate, and odd corresponding to the quarter-wave of Equations 11.1 and 11.2. Thus, it is easy to pick out those values of reflectance that correspond to the quarter-waves.

The technique can be adapted to give results in the presence of slight dispersion. The maxima in Figure 11.20 will now no longer be at the same heights, but, provided the index of the substrate is known throughout the range, the heights of the maxima can be used to calculate values for film

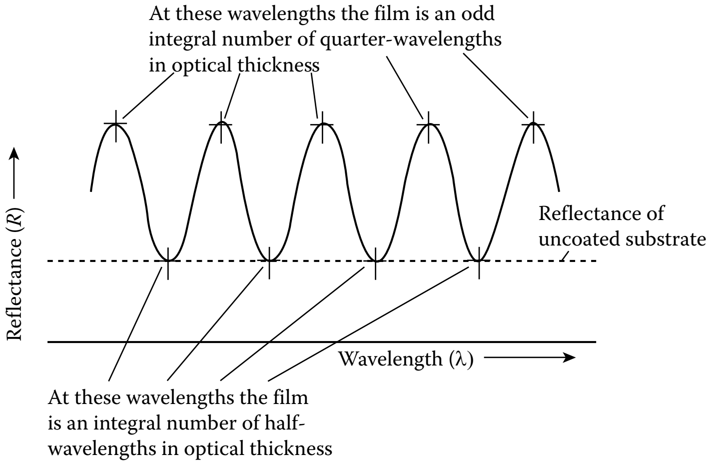

FIGURE 11.20
The reflectance of a simple thin film.

index at the corresponding wavelengths. Interpolation can then be used to construct a graph of refractive index against wavelength. Results obtained by Hall and Ferguson [53] for MgF_2 are shown in Figure 11.21.

This simple method yields results that are usually sufficiently accurate for design purposes. If, however, the dispersion is somewhat greater, or if rather more accurate results are required, then the slightly more involved formulae given by Hass et al. [54] must be applied. It is still assumed that the absorption is negligible. If the curve of reflectance or transmittance of a film possessing dispersion is examined, it will easily be seen that the maxima corresponding to the odd quarter-wave thicknesses are displaced in wavelength from the true quarter-wave points, while the half-wave maxima are unchanged. This shift is due to the dispersion, and measurement of it can yield a more accurate value for the refractive index. In the absence of absorption the turning values of R, T, $1/R$, and $1/T$ must all coincide. Assuming that the refractive index of the incident medium is unity, that of the substrate n_{sub} and of the film *n*f then their expression for T becomes

$$T = \frac{4}{n_{sub} + 2 + n_{sub}^{-1} + 0.5n_{sub}^{-1}(n_f^2 - 1 - n_{sub}^2 + n_{sub}^2 n_f^{-2})[1 - \cos(4\pi n_f d_f/\lambda)]}$$

Since the turning values of T and $1/T$ coincide, the positions of the turning values can be found in terms of d/λ by differentiating the expression for $1/T$ and equating it to zero as follows:

$$\frac{1}{T} = \frac{n_{sub} + 2 + n_{sub}^{-1}}{4} + \frac{1}{8n_{sub}}\left(n_f^2 - 1 - n_{sub}^2 + n_{sub}^2 n_f^{-2}\right)\left[1 - \cos\left(\frac{4\pi n_f d_f}{\lambda}\right)\right]$$

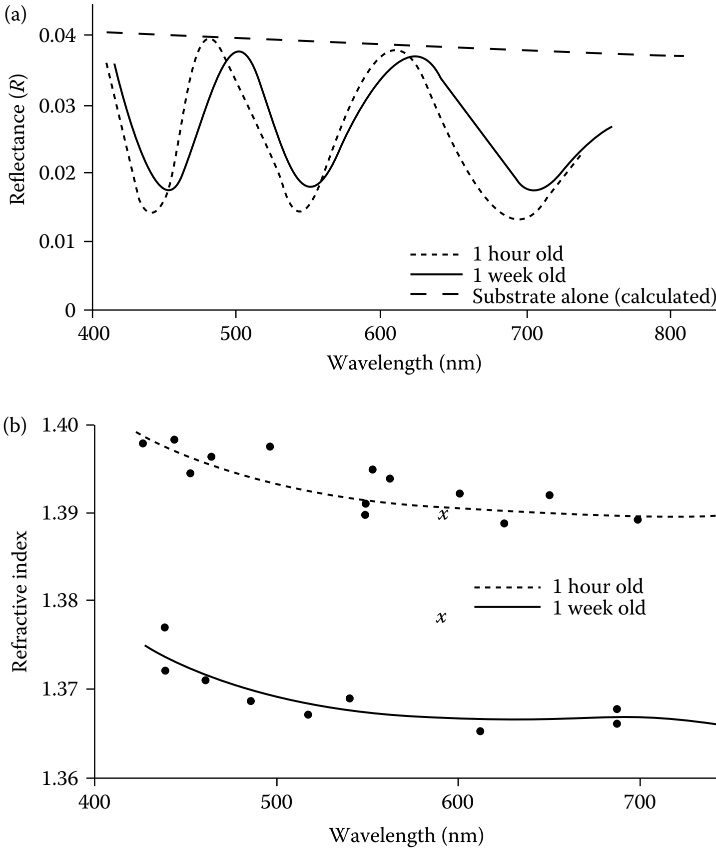

FIGURE 11.21
The refractive index of magnesium fluoride films. (a) The reflectance of a single film. (b) The reflectance result transforms into refractive index. The curves are formed by the results from many films. x denotes bulk indices of the crystalline solid. (After Hall, J.F., Jr. and Ferguson, W.F.C., *Journal of the Optical Society of America*, 45, 74–75, 1955.)

i.e.,

$$0 = \frac{d(1/T)}{d(d/\lambda)} = 0.25n_f'\left(n_{sub}^{-1}n_f - n_{sub}n_f^{-3}\right)\left[1-\cos\left(\frac{4\pi n_f d_f}{\lambda}\right)\right]$$
$$+0.5\pi\left(n_{sub}^{-1}n_f^2 - n_{sub}^{-1} - n_{sub} + n_{sub}n_f^{-2}\right)\left(n_f + n_f'\frac{d_f}{\lambda}\right)\sin\left(\frac{4\pi n_f d_f}{\lambda}\right)$$

where $n_f' = dn_f/d(d/\lambda)$. That the equation is satisfied exactly at all half-wave positions can easily be seen since both $\sin(4\pi n_f d_f/\lambda)$ and $(1 - \cos 4\pi n_f d_f/\lambda)$ are zero. At wavelengths corresponding to odd quarter-waves, a shift does occur and this can be determined by manipulating the above equation into

$$\tan\left(\frac{2\pi n_f d_f}{\lambda}\right) = -2\pi \frac{n_f^5 - \left(1+n_{sub}^2\right)n_f^3 + n_{sub}^2 n_f}{n_f^4 - n_{sub}^2}\left(\frac{n_f}{n_f'} + \frac{d_f}{\lambda}\right) \tag{11.3}$$

Of course, it is impossible to solve this equation immediately for n_f because there are too many unknowns. Generally, the most useful approach is by successive approximations using the simpler quarter-wave formula (11.2) to obtain a first approximation for the index and the dispersion. It should be remembered that the reflection of the rear surface of the test glass should be taken into account in the derivation of the reflectance curve. It is also important that the test glass should be free from dispersion to a greater degree than the film; otherwise, it must also be taken into account with consequent complication of the analysis.

If absorption is present, then Formula 11.3 cannot be used. In the case of heavy absorption, it can safely be assumed that there is no interference and the value of the extinction coefficient can be calculated from the expression

$$\frac{1-R}{T} = \exp\left(\frac{4\pi k_f d_f}{\lambda}\right)$$

($4\pi k_f d_f/\lambda$ because we are dealing with energies not amplitudes) which gives [54] for k_f

$$k_f = \frac{\lambda}{4\pi d_f \log e}\log\left(\frac{1-R}{T}\right) \tag{11.4}$$

where the two logarithms are to the same base, usually 10.

The thin-film designer is not too concerned with very accurate values of heavy absorption. Often it is sufficient merely to know that the absorption is high in a given region and the result given by Expression 11.4 will be more than satisfactory. In regions where the absorption is significant but not great enough to weaken the single-film interference effects, a more accurate method can be used.

Equations 2.122 and 2.125 are valid for any assembly of thin films on a transparent substrate, n_{sub}, and give

$$\frac{T}{1-R} = \frac{\mathrm{Re}(n_{sub})}{\mathrm{Re}(BC^*)} \tag{11.5}$$

For a single film on a transparent substrate, the values of B and C are given by

$$\begin{bmatrix} B \\ C \end{bmatrix} = \begin{bmatrix} \cos\delta_f & (i\sin\delta_f)/N_f \\ iN_f\sin\delta_f & \cos\delta_f \end{bmatrix}\begin{bmatrix} 1 \\ n_{sub} \end{bmatrix} = \begin{bmatrix} \cos\delta_f + i(n_{sub}/N_f)\sin\delta_f \\ n_{sub}\cos\delta_f + iN_f\sin\delta_f \end{bmatrix}$$

Now

$$\delta_f = \frac{2\pi N_f d_f}{\lambda} = \varphi - i\psi = \frac{2\pi n_f d_f}{\lambda} - i\frac{2\pi k_f d_f}{\lambda} \tag{11.6}$$

We shall assume that k is small compared with n and this implies that ψ will be small compared with φ. Now for ψ sufficiently small

$$\cos\delta = \cos\varphi\cosh\psi + i\sin\varphi\sin\psi \approx \cos\varphi + i\psi\sin\varphi$$

and

$$\sin\delta = \sin\varphi\cosh\psi - i\cos\varphi\sinh\psi = \sin\varphi - i\psi\cos\varphi$$

yielding the following expressions for B and C

$$\begin{bmatrix} B \\ C \end{bmatrix} = \begin{bmatrix} [1-(n_{sub}/n_f)\psi]\cos\varphi - \left(n_{sub}k_f/n_f^2\right)\sin\varphi + i[\psi + (n_{sub}/n_f)]\sin\varphi \\ (n_{sub} + n_f\psi)\cos\varphi + k_f\sin\varphi + i(n_f + n_{sub}\psi)\sin\varphi \end{bmatrix} \tag{11.7}$$

At wavelengths where the optical thickness is an integral number of quarter wavelengths, $\sin\varphi$ or $\cos\varphi$ is zero, and we can neglect terms in $\cos\varphi\sin\varphi$. The value of the real part of (BC^*) is then given by

$$\begin{aligned} \mathrm{Re}(BC^*) &= \cos^2\varphi\left(1 + \frac{n_{sub}}{n_f}\psi\right)(n_{sub} + n_f\psi) + \sin^2\varphi\left(\psi + \frac{n_{sub}}{n_f}\right)(n_f + n_{sub}\psi) \\ &= \left[n_{sub} + \left(\frac{n_{sub}^2}{n_f} + n_f\right)\psi\right] \end{aligned} \tag{11.8}$$

and when substituted in Equation 11.5 yields

$$\frac{1-R}{T} = 1 + \left(\frac{n_{sub}}{n_f} + \frac{n_f}{n_{sub}}\right)\psi \tag{11.9}$$

giving for k_f (using Expression 11.6 in Expression 11.9)

$$k_f = \left(\frac{\lambda}{2\pi d_f[(n_{sub}/n_f) + (n_f/n_{sub})]}\right)\left(\frac{1-R-T}{T}\right) \tag{11.10}$$

This expression is accurate only close to the turning values of the reflectance or transmittance curves.

In the case of low absorption, the index should also be corrected. Hall and Ferguson [55] give the following expressions.

$$n_f \left[\frac{n_{sub}\left(1+\sqrt{R}\right)}{1-\sqrt{R}} \right]^{1/2} + \frac{\pi k_f d_f}{\lambda} \left[\frac{1+\sqrt{R}}{1-\sqrt{R}} - n_{sub} \right] \quad (11.11)$$

where R is the value of reflectance of the film at the reflectance maximum.

In the methods discussed so far, we have been assuming that the thickness of the film is unknown, except inasmuch as it can be deduced from the measurements of reflectance and transmittance, and the extrema have been the principal indicator of film thickness. However, it is possible to measure film thickness in other ways, such as multiple beam interferometry, or electron microscopy, or by using a stylus step-measuring instrument. If there could be an independent accurate measure of physical thickness, then the problem of calculating the optical constants would become much simpler. This was the basis of a technique devised by Hadley (see Heavens [50] for a description). Since two optical constants, n_f and k_f, are involved at each wavelength, two parameters must be measured, and these can most conveniently be R and T. In the ideal form of the technique, if now a value of n_f is assumed, then by trial and error one value of k_f can be found, which, together with the known geometrical thickness and the assumed n_f, yields the correct measured value of R, and then a second value of k_f that similarly yields the correct value of T. A different value of n_f will give two further values of k_f, and so on.

Proceeding thus, we can plot two curves of k_f against n_f, one corresponding to the T values and the other to the R values, and, where they intersect, we have the correct values of n_f and k_f for the film. The angle of intersection of the curves gives an indication of the precision of the result.

Hadley, at a time when such calculations were exceedingly cumbersome, produced a book of curves giving the reflectance and transmittance of films as a function of the ratio of geometrical thickness to wavelength, with n_f and k_f as parameters, which greatly speeded up the process. Nowadays, the method can be readily programmed and precision estimates incorporated. This method can be applied to any thickness of film, not just at the extrema, although maximum precision is achieved, as we might expect, near optical thicknesses of odd quarter-waves, while, at half-wave optical thicknesses, it is unable to yield any results. As with many other techniques, it suffers from multiple solutions, particularly when the films are thick, and in practice a range of wavelengths is employed, which adds an element of redundancy and helps to eliminate some of the less probable solutions.

Hadley's method involves simple iteration and does not require any very powerful computing facilities. Even in the absence of Hadley's precalculated curves, it can be accommodated on a programmable calculator of modest capacity. It does, however, involve the additional measurement of film thickness, which is of a different character from the measurements of R and T. This

is the primary disadvantage. There is a problem with virtually all techniques that make independent measurements of thickness. Unless the thickness is very accurately determined and the model used for the thin film is well chosen, the values of optical constants that are derived may have quite serious errors. The source of the difficulty is that the extrema of the reflectance or transmittance curves are essentially fixed in position by the value of n_f and d_f. There is only a very small influence on the part of k_f. Should the value for d_f be incorrect, then there is no way in which a correct choice of n_f can satisfy both the value and the position of the extremum. What happens, then, is that the extremum position is ensured by an apparent dispersion, usually enormous and quite false, and the values of n_f are then seriously in error, sometimes showing abrupt gaps in the curve. The situation is often worse at the half-wave points than at the quarter-wave ones but, even in between the extrema, there are clear errors in level that tend to be alternately too high and then too low in between successive extremum pairs. A technique that has been used to avoid this difficulty is to permit some small variation of d_f around the measured value and to search for a value that removes to the greatest extent the incorrect features of the variation of n_f.

A different approach that has been developed by Pelletier and his colleagues in Marseille [56], and requires the use of powerful computing facilities, retains the measurement of R and T, but, instead of an independent measure of film thickness, adds the measurement of R', the reflectance of the film from the substrate side. Now we have three parameters to calculate at each wavelength and three measurements, and it might appear possible that all three could be calculated by a process of iteration, rather like the Hadley method, but the Marseille group found the possible precision rather poor and it broke down completely when there was no absorption.

To overcome this difficulty, the Marseille method uses the fact that the geometrical thickness of the film does not vary with wavelength, and therefore, if information over a spectral region is used, there will be sufficient redundancy to permit an accurate estimate of geometrical thickness. Then once the thickness has been determined, a computer method akin to refinement finds accurate values of the optical constants n_f and k_f over the whole wavelength region. For dielectric layers of use in optical coatings, k_f will usually be small, and often negligible, over at least part of the region and a preliminary calculation involving an approximate value of n_f is able to yield a value for geometrical thickness, which in most cases is sufficiently accurate for the subsequent determination of the optical constants. Given the thickness, R and T, as we have seen, should in fact be sufficient to determine n_f and k_f. However, this would mean discarding the extra information in R', and so the determination of the optical constants uses successive approximations to minimize a figure of merit consisting of a weighted sum of the squares of the differences between measured T, R, and R' and the calculated values of the same quantities using the assumed values of n_f and k_f. Although seldom necessary, the new values of the optical constants can then be used in

an improved estimate of the geometrical thickness, and the optical constants recalculated. For an estimate of precision, the changes in n_f and k_f to change the values of T, R, and R' by a prescribed amount, usually 0.3%, are calculated. Invariably, there are regions around the wavelengths for which the film is an integral number of half-waves thick, where the errors are greater than can be accepted and results in these regions are rejected. In practice the films are deposited over half of a substrate, slightly wedged to eliminate the effects of multiple reflections, and measurements are made of R and R' and T and T', the transmittance measured in the opposite direction (theoretically identical), on both coated and uncoated portions of the substrate. This permits the optical constants of the substrate to be estimated; the redundancy in the measurements of T and T' gives a check on the stability of the apparatus. A very large number of different dielectric thin film materials have been measured in this way and a typical result is shown in Figure 11.22.

A particularly useful and straightforward family of techniques are known as *envelope methods.* The results that they yield are particularly stable. The envelope method was first described in detail by Manifacier et al. [57] and later elaborated by Swanepoel [58].

Let us imagine that we have a homogeneous dielectric film that is completely free from absorption. Let us deposit this film on a transparent substrate and gradually increase the thickness of this film, all the time measuring the reflectance. Let the maximum reflectance be given by R_{max} and the minimum by R_{min}. We can plot the locus of the film at one wavelength as the thickness increases and this will appear as Figure 11.23.

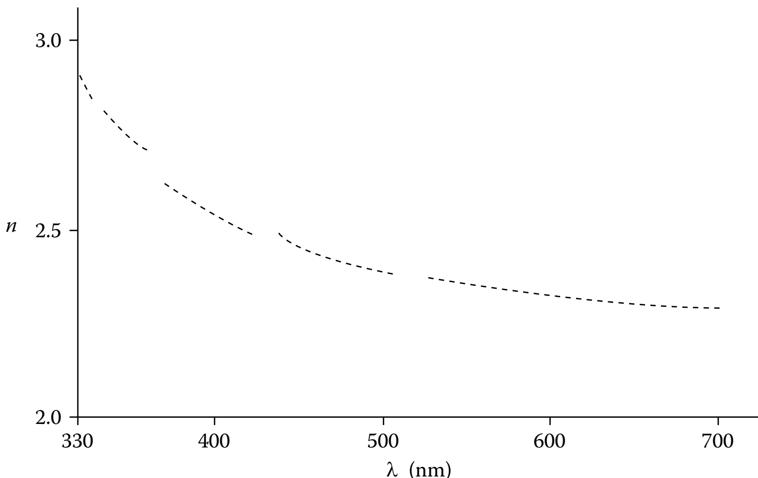

FIGURE 11.22
The refractive index of a film of zinc sulfide. The slight departure from a smooth curve is due to structural imperfections suggesting that even in this case of a very well behaved optical material there is some very slight residual inhomogeneity. (After Pelletier, E., Roche, P., and Vidal, B. *Nouvelle Revue d'Optique*, 7, 353–362, 1976.)

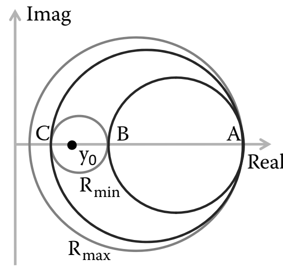

FIGURE 11.23
The circles labeled R_{max} and R_{min} are isoreflectance circles. The two circles tangent to both of them are possible loci for the thin film. Two other possible circular loci, tangent to both circles, are possible geometrically, but would represent admittances less than y_0 and so have been discarded. (See color insert following page 398.)

The maximum and minimum reflectances will each be represented by an isoreflectance circle in the admittance plane. Any possible locus for the thin film must then be a circle tangent to both of them. There could be four such loci but, since the incident medium will usually be air, two of the loci must represent characteristic admittances less than unity, and can therefore be discarded. There are then two possible remaining loci, both shown in the diagram. Should the addition of the film increase the reflectance above that of the uncoated substrate, then the substrate must be represented by the point *B* in the diagram. There is then only one locus that can represent the film, that is, the locus with extreme points *A* and *B*. The reflectances at *A* and *B* can then be converted into admittances, and the square root of their product will be the characteristic admittance of the film. Should the film reduce the reflectance below that of the substrate then the substrate must be represented by the point *A*, and we now have two possible solutions for the admittance of the film. Provided the minimum reflectance is not too low, we should be able to distinguish the correct solution provided we have a sufficiently reasonable idea of the correct value. It is easy to see the danger, however, of a film that is acting as a good antireflection coating for the substrate. Then the two possible values will be close together and it will be very difficult to separate them. In addition, it can be shown that the effect of errors in the measurement of reflectance have a much greater effect on the extracted value of characteristic admittance when the extremum represents a very low value.

So far, to extract the value of the film characteristic admittance, we do not need to calculate the admittance of the substrate separately. Let the film now be slightly inhomogeneous in a simple way where the refractive index changes uniformly and slowly through the film. The locus will no longer be that of a circle but a slowly contracting or expanding spiral and there will be a gap between the notional half-wave points and the actual substrate admittance. Now, separate knowledge of the substrate admittance will allow an estimate also of the inhomogeneity of the film.

Now let the film be also slightly absorbing. A slightly absorbing film shows very little difference in reflectance when compared with an exactly similar but transparent film. However, this is not the case in transmittance. Transmittance is sensitive to both inhomogeneity and absorptance. The expressions are a little more complicated in transmittance, nevertheless, if we add transmittance measurements, T_{max} and T_{min}, to our corresponding reflectance measurements, we will be able to distinguish and separately estimate both absorptance and inhomogeneity.

Finally, provided we know the starting and finishing points for the film locus and the number of circles, or the number of exhibited extrema, then we can calculate the optical thickness, and hence physical thickness of the film.

Unfortunately, we seldom have the necessary information in this form. What we generally have are plots of reflectance and/or transmittance of an already deposited film in terms of wavelength, and similar plots of an uncoated substrate. Figure 11.24 shows typical fringes as a function of wavelength. To these fringes have been added two envelope curves that pass through the fringe extrema. The basis of the envelope technique is the assumption that these envelope curves in both reflectance and in transmittance can be used at any wavelength as substitutes for the R_{max}, R_{min}, T_{max}, and T_{min} that would have been available had the growing film been measured continuously at every wavelength point.

Although, at first sight, this might seem a somewhat inaccurate technique because it depends on envelopes that might be arbitrary, it turns out that films that can be modeled as a straightforward, slightly absorbing, slightly

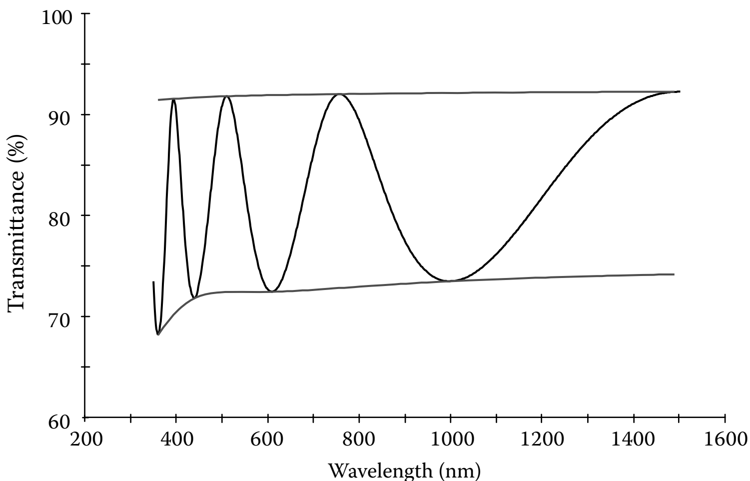

FIGURE 11.24
The fringes measured in transmission of a film of tantalum pentoxide over a substrate of glass. The envelopes of the fringes are shown. With well-behaved films like this one, the adding of the envelopes is a straightforward process.

inhomogeneous dielectric film exhibit well-formed fringes that lend themselves to simple envelope curves, such as in Figure 11.24. Films that show fringes that are more variable in their extrema are invariably more complicated in their structure and unable to be represented by a simple model. A great advantage of this technique is that the extracted values of film parameters are exceptionally stable. Predictions of performance that use them do not give results outside what one would expect from the envelope values.

Manifacier et al. [57] considered transmittance curves only and assumed homogeneous and absorbing films and their analysis was focused on films of index higher than that of the substrate. Let T_{max} and T_{min} be the envelope values. Then we can write

$$\alpha = \frac{C_1[1-(T_{\max}/T_{\min})^{1/2}]}{C_2[1+(T_{\max}/T_{\min})^{1/2}]} \tag{11.12}$$

where

$$\alpha = \exp(-4\pi k_f d_f/\lambda) \tag{11.13}$$

$$4\pi n_f d_f/\lambda = m\pi \quad \text{(quarter- or half-wave thickness)}$$

$$\begin{aligned} C_1 &= (n_f + n_0)/(n_{sub} + n_f) \\ C_2 &= (n_f - n_0)/(n_{sub} - n_f) \\ T_{\max} &= 16 n_0 n_{sub} n_f^2 \alpha/(C_1 + C_2\alpha)^2 \\ T_{\min} &= 16 n_0 n_{sub} n_f^2 \alpha/(C_1 - C_2\alpha)^2 \end{aligned} \tag{11.14}$$

Then, from Expressions 11.12 and 11.13, if we define N as

$$N = \frac{n_0^2 + n_{sub}^2}{2} + 2n_0 n_{sub}\frac{T_{\max} - T_{\min}}{T_{\max}T_{\min}}$$

n_f is given by

$$n_f = \left[N + (N^2 - n_0^2 n_{sub}^2)^{1/2}\right]^{1/2} \tag{11.15}$$

Once n_f has been determined, Equation 11.12 can be used to find a value for α. The thickness d_f can then be found from the wavelengths corresponding to the various extrema and the extinction coefficient k_f from the values of d_f and α. The method has the advantage of explicit expressions for the various quantities, which makes it easily implemented on machines as small as programmable calculators.

Computers bring the advantage that we no longer need to devise methods of optical constant measurement with the principal objective of ease of calculation. Instead, methods can be chosen simply based on precision of results, regardless of the complexity of the analytical techniques that are required. This is the approach advocated by Hansen [59], who has developed a reflectance attachment making it possible to measure the reflectance of a thin film for virtually any angle of incidence and polarization, the particular measurements carried out being chosen to suit each individual film.

For rapid, straightforward measurement of refractive index, a method of Abelès [60] is especially useful. It relies on the fact that the reflectance for *p*-polarization is the same for substrate and film at an angle of incidence that depends only on the indices of film and incident medium, and not at all on either substrate index or film thickness, except, of course, that layers that are a half-wave thick at the appropriate angle of incidence and wavelength will give a reflectance equal to the uncoated substrate regardless of index. It is fairly easy to use Snell's law and the expressions for equal *p*-admittances to give

$$n_f \sin \vartheta_f = n_0 \sin \vartheta_0$$

and

$$n_f / \cos \vartheta_f = n_0 / \cos \vartheta_0$$

so that

$$n_f = n_0 \tan \vartheta_0 \tag{11.16}$$

The measurement of index reduces to the measurement of the angle ϑ_0 at which the reflectances are equal. Heavens [50] shows that the greatest accuracy of measurement is, once again, obtained when the layer is an odd number of quarter-waves thick at the appropriate angle of incidence. This is because there is then the greatest difference in the reflectances of the coated and uncoated substrate for a given angular misalignment from the ideal. It is possible to achieve an accuracy of around 0.002 in refractive index provided the film and substrate indices are within 0.3 of each other, but not equal. Hacskaylo [61] has developed an improved method based on the Abelès technique. It involves incident light that is linearly polarized with the direction of polarization almost, but not quite, parallel to the plane of incidence. The reflected light is passed through an analyzer and the analyzer angle, for which the reflected light from the uncoated substrate and from the film-coated substrate are equal, is plotted against the angle of incidence. A very sharp zero at the angle satisfying the Abelès condition is obtained, which permits accuracies of 0.0002–0.0006 in the measurement of indices in the range of 1.2–2.3. It is not necessary for the film index to be close to the substrate index.

Values of R and φ for an opaque surface define, completely and unambiguously, the optical constants of the surface. Absolute reflectance is a difficult measurement and it is more usual to measure the way in which the unknown surface compares with a known reference—which introduces further difficulties. Phase is even more involved, requiring an interferometric operation as well as a known standard. Phase measurements are, therefore, quite rare and routine measurements of reflectance are almost always comparative. A major problem is the calibration and maintenance of suitable standards. There is a way, however, of avoiding such difficulties. At normal incidence, there is only one value of reflectance and one of phase, but at oblique incidence, there are two, one pair for *s*-polarization and the other for *p*-polarization. In principle, therefore, it should be possible to use one as a reference for the other and this leads to the method known as ellipsometry [62,63]. A full description of ellipsometry and its techniques is beyond the scope of this book but a short discussion is appropriate.

The ellipsometric parameters have already been introduced in the section on retarders in Chapter 9. We recall that they are known as ψ and Δ (psi and Delta), where

$$\tan\psi = \left|\frac{\rho_p}{\rho_s}\right| \quad \text{or} \quad \left|\frac{\tau_p}{\tau_s}\right|$$
$$\Delta = \varphi_p - \varphi_s \quad \text{in transmission} \tag{11.17}$$
$$\Delta = \varphi_p - \varphi_s \pm \pi \quad \text{in reflection}$$

Δ is also known as the relative retardation or retardance.

Ellipsometry has many advantages, especially the ability to use a single illuminated spot for both measurements. Then there is the absence of any reference samples that must be maintained and, although high accuracy is required, the measurement is simple, involving straightforward manipulations of polarized light. Disadvantages are that the measurement is at oblique incident, quite far from more normal measurements of performance, making it difficult to exercise instinct in judging the results. A limitation is that there are two parameters only, rather less than the number that must often be established for a complete description of the system. This limitation is frequently addressed by introducing a physical model and by additionally varying the angle of incidence, or the wavelength, or both. The combination is known as *variable angle spectroscopic ellipsometry*, frequently abbreviated to VASE.

Only two parameters, refractive index and extinction coefficient, are sufficient to define a simple surface. Since there are two ellipsometric parameters, ψ and Δ, then it should be possible to make a determination of the surface parameters from a single ellipsometric measurement. This is indeed the case, and there is a direct analytical connection between the two sets of parameters. Unfortunately, this is not normally the case with a thin film on a substrate. Even with a simple absorbing film on an already characterized

substrate, three parameters, n, k, and d, are necessary to define the film. The properties of films that are absorbing may depart only slightly from a surface of bulk material. In such cases, it is often assumed that the extraction techniques used for a simple surface are applicable. The parameters, n and k, that are extracted in this way are usually referred to as the pseudo-optical constants. They exhibit, usually, the gross features of the real optical constants, although they may not be suitable for thin film calculations and predictions.

In spectroscopic ellipsometry, the wavelength is varied. Since the film physical thickness is not sensitive to wavelength, this introduces an element of redundancy. It is then sufficient to introduce a small amount of additional information. This frequently takes the form of a prescribed spectral variation of optical constants according to some recognized model. Other film parameters may then also be included, and the redundancy in the measurement can be so great that even simple multilayers may be evaluated.

We illustrate the extraction process by considering the simple case of a single wavelength, single angle measurement in reflection of a surface characterized by refractive index n and extinction coefficient k, where $y = (n - ik)$.

Let the incident medium be of index unity and let $\varepsilon = \tan\psi \exp i(\Delta \pm \pi)$. Then

$$\varepsilon = \frac{\rho_p}{\rho_s} = \frac{(\eta_{0p} - \eta_p)}{(\eta_{0p} + \eta_p)} \cdot \frac{(\eta_0 + \eta_s)}{(\eta_{0s} - \eta_s)} \tag{11.18}$$

where the symbols may be taken as the modified admittances and the definition of ε is consistent with the usual thin film sign convention and also with the normal sign convention for Δ. Then, replacing the incident medium admittance by unity and recalling that $\eta_p\eta_s = y^2$,

$$\varepsilon = \frac{(1 - y^2) - (\eta_p - \eta_s)}{(1 - y^2) + (\eta_p - \eta_s)} \tag{11.19}$$

Now

$$\eta_s = \frac{\sqrt{y^2 - \sin^2\vartheta_0}}{\cos\vartheta_0} \tag{11.20}$$

and

$$\eta_p = \frac{y^2 \cos\vartheta_0}{\sqrt{y^2 - \sin^2\vartheta_0}} \tag{11.21}$$

so that after some manipulation we can write

$$\gamma = \frac{1-\varepsilon}{1+\varepsilon} = \frac{(\eta_p - \eta_s)}{(1-y^2)}$$
$$= \frac{\dfrac{y^2 \cos\vartheta_0}{\sqrt{y^2 - \sin^2\vartheta_0}} - \dfrac{\sqrt{y^2 - \sin^2\vartheta_0}}{\cos\vartheta_0}}{(1-y^2)} \tag{11.22}$$
$$= \frac{\sin^2\vartheta_0}{\cos\vartheta_0\sqrt{y^2 - \sin^2\vartheta_0}}$$

This gives

$$y^2 = \frac{\sin^4\vartheta_0}{\gamma^2\cos^2\vartheta_0} + \sin^2\vartheta_0 \tag{11.23}$$

There will be two solutions and the fourth quadrant solution will be the correct one.

Hilfiker et al. [64] give a useful account of the use of spectroscopic ellipsometry in the characterization of absorbing coatings.

Ellipsometry is especially useful for the derivation of the optical constants of opaque metal films. Provided they have a suitable thickness, high-performance metal films can also be characterized by a measurement of a surface plasma resonance, discussed already in Chapter 9. This tool involves a rather simpler optical arrangement than the ellipsometer but it is more limited in its application. The film in question is deposited over the base of a prism and the resonance is measured in the normal way. Usually a quite undemanding optical arrangement involving a simple goniometer with laser and collimator and receiver will suffice. The p-polarized resonance has three attributes: the angular position, the resonance width, and the resonance depth. There are three attributes of the metal coating, n, k, and d. n is primarily associated with the resonance width, k with its position, and d with its depth, so that the extraction process is a simple process of model fitting.

There is one small problem associated with two possible solutions. The two solutions involve quite distinct values of d, except that when the minimum reflectance is zero then the two solutions coincide. A simple technique for distinguishing the correct set of values is to ensure that the two thickness values are sufficiently far apart for the correct one to be recognized. This, of course, means that the sample should be prepared so that the minimum reflectance is sufficiently far from zero, yet the resonance is sufficiently well developed for accurate measurement. This is a limitation on the range of usable thicknesses. Alternatively, measurements at more than one wavelength may be performed. The correct solutions will be those with similar

values of d. The technique has been used, for example, in studies of the influence of small changes in process parameters on the optical constants of metals [35].

Provided there is some measurable finite transmittance then metal layers can be characterized by reflectance and transmittance measurements as a function of wavelength. Dobrowolski et al. [65] used a process termed *reverse synthesis* to extract successfully the optical constants of a range of thin-film materials, including metals, from measurements of reflectance and transmittance. Reverse synthesis is essentially a refinement process where parameters of a model are varied to reduce the error between model predictions and actual measurements. The use of a model reduces the parameters to a reasonable number. The model was a combination of Lorenz and Drude expressions so that both dielectric and metallic layers could be handled.

Unfortunately, the behavior of real thin films is often more complicated than we have been assuming. They are frequently inhomogeneous, that is, their refractive index varies throughout their thickness. They tend also to be anisotropic, although rather less work has been done on this aspect of their behavior.

Provided that the variation of index throughout the film is either a smooth increase or a smooth decrease, so that there are no extrema within the thickness of the film, the highest and lowest values being at the film boundaries, then we can use a very simple technique to determine the difference in behavior at the quarter-wave and half-wave points, which would be obtained with an inhomogeneous film. We assume that the film is absorption free and that its properties can be calculated by a multiple-beam approach, which considers the amplitude reflection and transmission coefficients at the boundary only. We assume that the index of that part of the film next to the substrate is n_b and that next to the surrounding medium is n_a. The corresponding admittances are y_b and y_a. The only reflections that take place are assumed to be at either of the two interfaces. There is one further complication, also indicated in Figure 11.25, before we can sum the multiple beams to arrive at transmittance and reflectance. A beam propagating from the outer surface of the film to the inner is assumed to suffer no loss by reflection and, therefore, the irradiance is unaltered. Since irradiance is proportional to the square of the electric amplitude times admittance, a beam that is of amplitude $\mathcal{E}_a^+$, just inside interface a, will have amplitude $(y_a/y_b)\mathcal{E}_a^+ = \mathcal{E}_b^+$ at interface b. The correction will be reversed in travelling from b back to a. This is in addition to any phase changes. The inverse correction applies to magnetic amplitudes. Since the correction cancels out for each double pass it does not affect the result for resultant reflectance but it must be taken into account when the multiple beams are being summed for the calculation of transmittance. The derivation of the necessary expressions proceeds as in Chapter 2. Here, for simplicity, we restrict ourselves to normal incidence. Oblique incidence is a very simple extension. We start with the total tangential electric and magnetic field amplitudes at interface b.

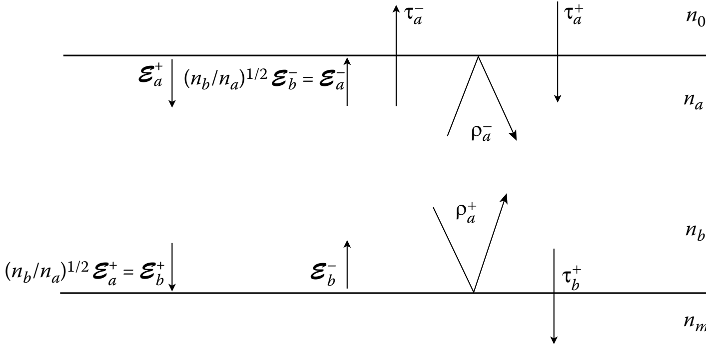

FIGURE 11.25
Inhomogeneous film quantities used in the development in the text of the matrix expression for an inhomogeneous layer.

$$\mathcal{E}_b = \mathcal{E}_b^+ + \mathcal{E}_b^-$$
$$\mathcal{H}_b = y_b\mathcal{E}_b^+ - y_b\mathcal{E}_b^-$$

Giving

$$\mathcal{E}_b^+ = 0.5\,[(\mathcal{H}_b/y_b) + \mathcal{E}_b]$$
$$\mathcal{E}_b^- = 0.5\,[-(\mathcal{H}_b/y_b) + \mathcal{E}_b]$$

Then the various rays are transferred to interface *a*

$$\mathcal{E}_a^+ = 0.5(y_b/y_a)^{1/2}[(\mathcal{H}_b/y_b) + \mathcal{E}_b]e^{i\delta}$$
$$\mathcal{E}_a^- = 0.5(y_b/y_a)^{1/2}[-(\mathcal{H}_b/y_b) + \mathcal{E}_b]e^{-i\delta}$$

giving

$$\mathcal{E}_a = \mathcal{E}_a^+ + \mathcal{E}_a^- = \left(\frac{y_b}{y_a}\right)^{1/2}(\cos\delta)\mathcal{E}_b + \frac{i\sin\delta}{(y_a y_b)^{1/2}}\mathcal{H}_b$$
$$\mathcal{H}_a = y_a\mathcal{E}_a^+ - y_a\mathcal{E}_a^- = i(y_a y_b)^{1/2}(\sin\delta)\mathcal{E}_b + \left(\frac{y_a}{y_b}\right)^{1/2}(\cos\delta)\mathcal{H}_b$$

The characteristic matrix for the layer is then given by

$$\begin{bmatrix} \left(\frac{y_b}{y_a}\right)^{1/2}\cos\delta & \frac{i\sin\delta}{(y_a y_b)^{1/2}} \\ i(y_a y_b)^{1/2}\sin\delta & \left(\frac{y_a}{y_b}\right)^{1/2}\cos\delta \end{bmatrix} \tag{11.24}$$

an expression originally due to Abelès [66,67]. The calculation of inhomogeneous layer properties has been considered in detail by Jacobsson [68].

Now we consider cases where the layer is either an odd number of quarter-waves or an integral number of half-waves. We apply Expression 11.24 in the normal way and find the well-known relations

$$R = \left[\frac{y_0 - y_a y_b / y_{sub}}{y_0 + y_a y_b / y_{sub}}\right] \text{ for a quarter-wave} \tag{11.25}$$

and

$$R = \left[\frac{y_0 - y_a y_{sub} / y_b}{y_0 + y_a y_{sub} / y_b}\right] \text{ for a half-wave} \tag{11.26}$$

The expression for a quarter-wave layer is indistinguishable from that of a homogeneous layer of admittance $(y_a y_b)^{1/2}$, and so it is impossible to detect the presence of inhomogeneity from the quarter-wave result. The half-wave expression is quite different. Here the layer is no longer an absentee layer and cannot therefore be represented by an equivalent homogeneous layer. The shifting of the reflectance of the half-wave points from the level of the uncoated substrate in absorption-free layers is a sure sign of inhomogeneity and can be used to measure it.

The Hadley method of deriving the optical constants takes no account of inhomogeneity. Any inhomogeneity, therefore, introduces errors. The Marseille method, however, includes half-wave points and therefore has sufficient information to accommodate inhomogeneity. The matrix expression is a good approximation when the inhomogeneity is not too large and when the admittances y_a and y_b are significantly different from those of substrate and incident medium. To avoid any difficulties due to the model, the Marseille group actually uses a model for the layer consisting of at least 10 homogeneous sublayers with linearly varying values of n but identical values of k and thickness d. The half-wave points still give the principal information on the degree of inhomogeneity. They are also affected by the extinction coefficient k and this has also to be taken into account. One half-wave point within the region of measurement can be used to give a measure of inhomogeneity that is assumed constant over the rest of the region. Several half-wave points can yield values of inhomogeneity that can be fitted to a Cauchy expression, that is, an expression of the form

$$\frac{\Delta n}{n} = A + \frac{B}{\lambda^2} + \frac{C}{\lambda^4}. \tag{11.27}$$

Details of the technique are given by Borgogno et al. [69]. Some of their results are shown in Figure 11.26.

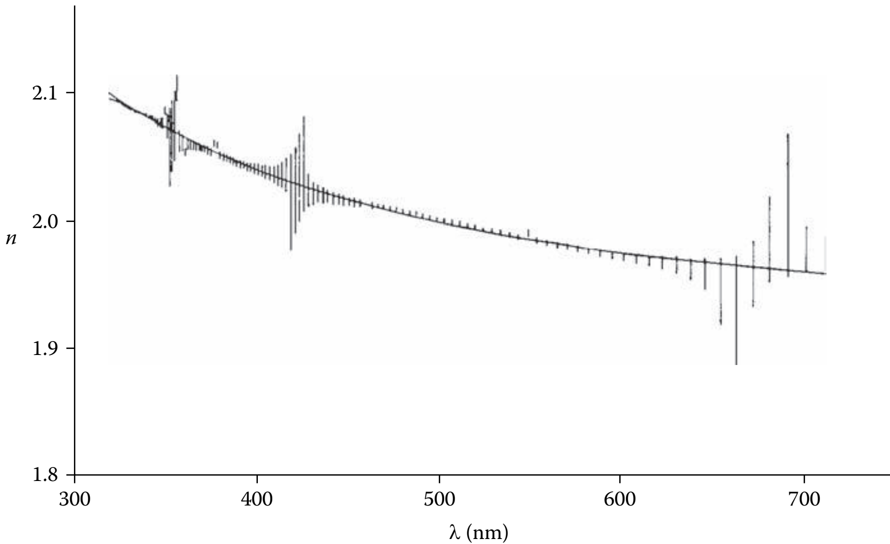

FIGURE 11.26
Values of mean index and the uncertainty n calculated for hafnium oxide using an inhomogeneous film model. The Cauchy coefficients for n are $A = 1.9165$, $B = 2.198 \times 10^4$ nm^2, $C = -3.276 \times 10^8$ nm^4 and for $\Delta n/n$ are: $A' = -5.39 \times 10^{-2}$, $B' = -1.77 \times 10^3$ nm^2. (After Borgogno, J.P., Lazarides, B., and Pelletier, E., *Applied Optics*, 21, 4020–4029, 1982.)

The envelope method has also been extended to deal with inhomogeneous films using the inhomogeneous matrix expression for the calculations [70]. The extinction coefficient k, as in the Marseille method, is assumed constant through the film.

Netterfield [71] measured the variation in reflectance of a film at a single wavelength as it was deposited. If the assumption is made that the part of the film that is already deposited is unaffected by subsequent material, then the values of reflectance associated with extrema can be used to calculate a profile of the refractive index throughout the thickness of the layer. Some results obtained in this way for cryolite, are shown in Figure 11.27.

11.3 Measurement of the Mechanical Properties

From the point of view of optical coatings, the importance of the mechanical properties of thin films is primarily in their relation to coating stability, that is, the extent to which coatings will continue to behave as they did when removed from the coating chamber, even when subjected to disturbances of an environmental and/or mechanical nature. There are many factors involved in stability, many of which are neither easy to define nor to measure, and there are still great difficulties to be overcome. The approach used in quality assurance in

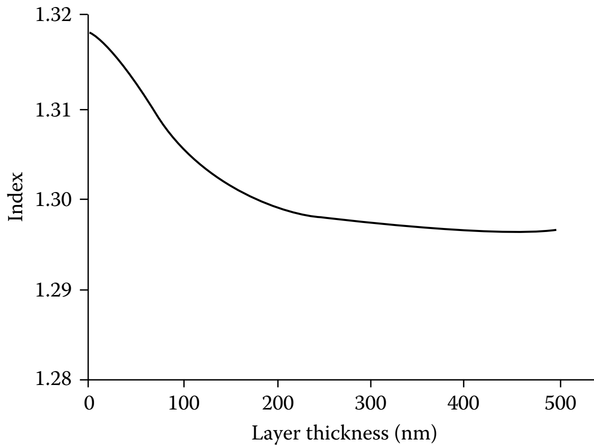

FIGURE 11.27
Graph of the index profile of cryolite layers at $\lambda = 633$ nm, derived from fitting a formula, $n2 = A + [B/(t\ 2 + C)]$, where t is the thickness coordinate, to curves of the variation of reflectance *in vacuo* of a cryolite film deposited over a zinc sulfide film of varying thickness. $A = 1.6773$, $B = 5.0431 \times 10^2$ nm^2, $C = 8.2986 \times 10^3$ nm^2. (After Netterfield, R.P., *Applied Optics*, 15, 1969–1973, 1976.)

manufacture, discussed further in Chapter 12, is entirely empirical. Tests are devised that reproduce, in as controlled a fashion as possible, the disturbances to which the coating will be subjected in practice, and samples are then subjected to these tests and inspected for signs of damage. Sometimes the tests are deliberately made more severe than those expected in use. Coating performance specifications are normally written in terms of such test levels.

Stress is normally measured by depositing the material on a thin flexible substrate that deforms under the stress applied to it by a deposited film. The deformation is measured and the value of stress necessary to cause it calculated. The substrate may be of any suitable material; glass, mica, silica, metal, for example, have all been used. The form of the substrate is often a thin strip, supported so that part of it can deflect. Then, either the deflection is measured in some way, or a restoring force is applied to restore the strip to its original position. Usually the deflection, or the restoring force, is measured continuously during deposition. Optical microscopes, capacitance gauges, piezoelectric devices and interferometric techniques are some of the successful methods.

A useful survey of the field of stress measurement in thin films in general is given by Hoffman [72]. A particularly useful paper that deals solely with dielectric films for optical coatings is that by Ennos [73]. Ennos used a thin strip of fused silica as substrate, simply supported at each end on ball bearings so that the center of the strip was free to move. An interferometric technique with a helium-neon laser as the light source was used to measure the movement of the strip. The strip was made of one mirror of a Michelson

interferometer of novel design, shown in Figure 11.28. Since the laser light was linearly polarized, the upper surface of the prism was set at the Brewster angle to eliminate losses by reflection of the emergent beam. Apart from the more obvious advantages of large coherence length and high collimation, the laser beam made it possible to line up the interferometer with the bell jar of the machine in the raised position (see Figure 11.28b). No high-quality window in the machine was necessary, the glass jar of quite poor optical quality proving adequate. To complete the arrangement, the laser light was also directed on a test flat for the optical monitoring of film thickness. A typical

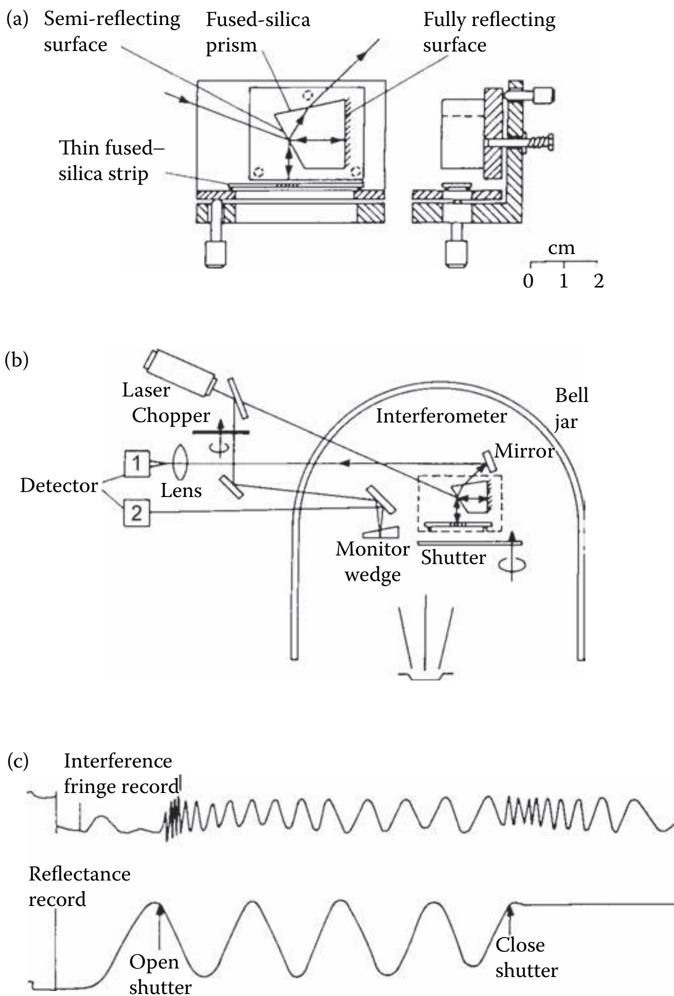

FIGURE 11.28
(a) Film-stress interferometer. (b) Experimental arrangement for continuous measurement of film stress during evaporation. (c) Recorder trace of fringe displacement and film reflectance. (After Ennos, A.E., *Applied Optics*, 5, 51–61, 1966.)

record obtained with the apparatus is also shown in Figure 11.28c. The calibration of the fused-silica strip was determined both by calculation and by measurement of deflection under a known applied load.

Curves plotted for a wide range of materials showing the variation of stress in the films during the actual growth as a function both of film thickness and evaporation conditions are included in the paper, some examples being shown in Figure 11.29. It is of particular interest to note the frequent drop in stress when the films are exposed to the atmosphere. This is principally due to adsorption of water vapor, an effect to be considered further toward the end of this chapter.

The interferometric technique has been further improved by Roll and Hoffman [74,75]. Then Ledger and Bastien [76] have taken the Michelson interferometer of Ennos and replaced it by a cat's-eye interferometer, using circular disks as sensitive elements that are very much less temperature sensitive, and this has enabled the measurement of stress levels in optical films over a wide range of substrate temperatures. Examination of the differences in thermally induced stress for identical films on different substrate materials, when substrate temperature is varied after deposition, has permitted the measurement of the elastic moduli and thermal expansion coefficients of the thin-film materials. Although the measured value of expansion coefficient for bulk thorium fluoride crystals is small and negative, the values for thorium fluoride thin films were consistently large and positive, varying from 11.1×10^{-6} to $18.1 \times 10^{-6}\,°C^{-1}$. Young's modulus for the same samples varies from 3.9×10^5 to 6.8×10^5 kg cm^{-2} (that is 3.9×10^{10} to 6.8×10^{10} Pa).

Ledger and Bastien arranged the interferometer so that fringes were counted as they were generated at the center of the interferometer during the deposition of the film and changes in the stress. An asymmetric shape to the fringes permitted the distinction between a fringe appearing and a fringe disappearing. This meant that the stress level would be lost if the fringe count failed at any stage. A group at the Optical Sciences Center [77] modified the interferometer to view a sufficiently large field that included a number of fringes. The fringe pattern was then interpreted in the manner of an interferogram to give the form of the surface of the deformable substrate. This effectively decoupled each measurement from all the others and permitted the stress to be determined unambiguously at any stage even if some intervening measurements were missed or skipped. The interferometer was used in a detailed study of titanium dioxide films deposited by thermal evaporation with or without ion assist.

Thermally evaporated films usually exhibit a tensile stress that is a consequence of the disorder frozen into the film, as freshly arriving material covers what already exists. An increase in the rate of deposition gives less time for the material on the surface to reorganize itself and therefore should lead to an increase in tensile stress. This is clearly seen in Figure 11.30.

Under bombardment, the tighter packing of the films leads to an increase in compressive stress because of the transfer of momentum to the growing

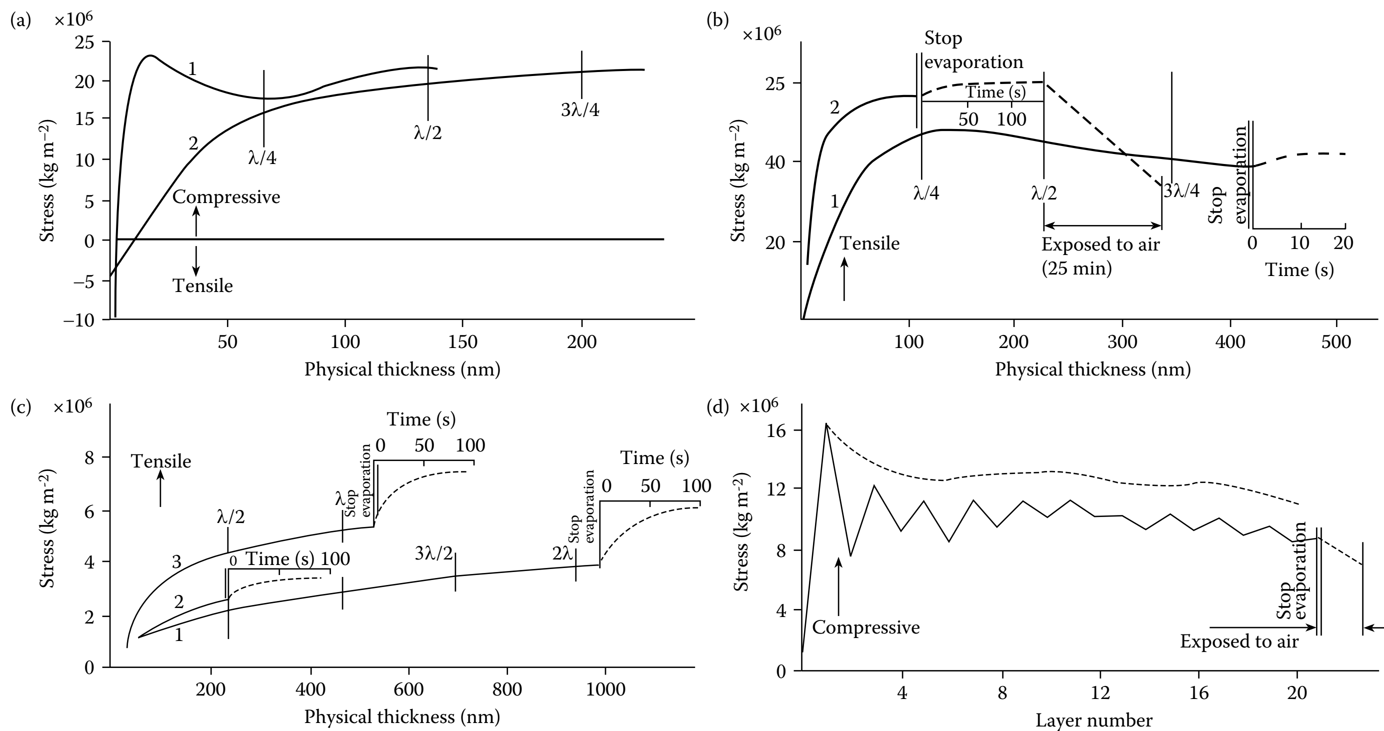

FIGURE 11.29
(a) Film stress in evaporated zinc sulfide on fused silica at ambient temperature. Evaporation rate 1:0.25 nm s^{-1}, 2:2.2 nm s^{-1}. (b) Film stress in magnesium fluoride. 1: Direct evaporation from molybdenum, evaporation rate 4.2 nm s^{-1}. 2: Indirect radiative heating, evaporation rate 1.2 nm s^{-1}. (c) Cryolite and chiolite evaporated by indirect radiative heating. 1: Cryolite, evaporation rate 3.5 nm s^{-1}. 2: Chiolite, evaporation rate 4 nm s^{-1}. (d) Zinc sulfide–cryolite multilayer. Twenty-one layers *(HL)*10*H*. Resultant average stress after each evaporation plotted. *Dashed curve* shows upper limit of film stress reached during the warm-up period before the evaporation of a layer commenced. (After Ennos, A.E., *Applied Optics*, 5, 51–61, 1966.)

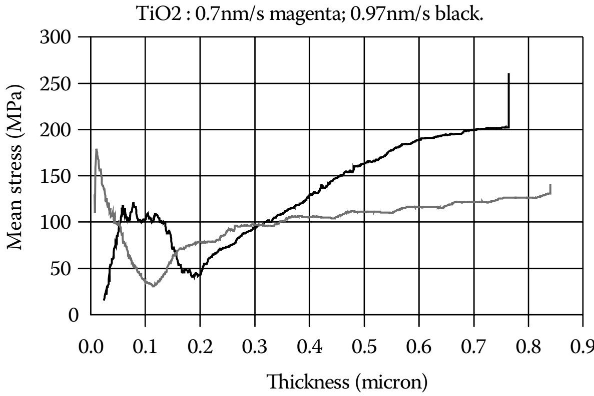

FIGURE 11.30
The mean (tensile) stress as a function of film thickness in titania films deposited at 0.7 nm s^{-1} (gray) and 0.97 nm s^{-1} (black). The higher rate of deposition leads to greater tensile stress. The vertical line at the end of each curve is a relaxation thought to be due to the disappearance of the thermal gradient present during deposition (Bovard, B.G., Lega, X.C.d., Hahn, S.-H., and Macleod, H.A. "Intrinsic stress in titanium dioxide thin films produced by ion-assisted deposition," Optical Sciences Center, University of Arizona, Tucson, Arizona Private Communication).

film (Figure 11.31). In fact, it is possible by careful control of the bombardment to achieve extremely low values. Unfortunately, not all materials exhibit such a simple relationship.

Pulker [78] has studied the relationship between stress levels and the microstructure of optical thin films, developing further some ideas of Hoffman. The work is surveyed eslewhere [79]. Good agreement between measured levels of

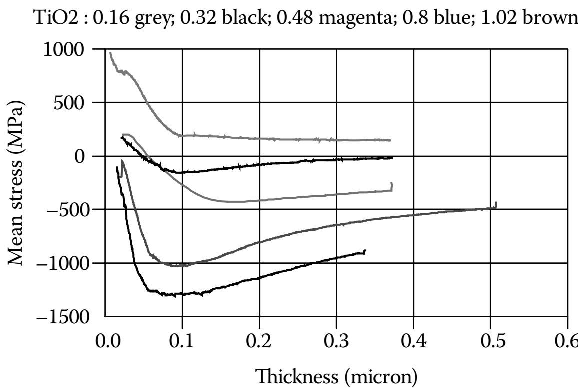

FIGURE 11.31
The mean stress as a function of thickness of a series of titania films deposited by ion-assisted deposition. The background gas was oxygen and the films were bombarded with 500 eV argon ions at levels from top to bottom of 0.16, 0.32, 0.48, 0.80, and 1.02 mA cm^{-2} (Bovard, B.G., Lega, X.C.d., Hahn, S.-H., and Macleod, H.A. "Intrinsic stress in titanium dioxide thin films produced by ion-assisted deposition," Optical Sciences Center, University of Arizona, Tucson, Arizona Private Communication).

stress and those calculated from the model has been achieved, but perhaps the most spectacular feature has been the demonstration, in accord with the theory, that small amounts of impurity can have a major effect on stress. The impurities congregate at the boundaries of the columnar grains of the films and reduce the forces of attraction between neighboring grains, thus reducing stress. Small amounts of calcium fluoride in magnesium fluoride, around 4 mol%, reduce tensile stress by some 50%. Pellicori [80] has shown the beneficial effect of mixtures of fluorides in reducing cracking in low-index films for the infrared.

Windischmann [81] has discussed and modeled the stresses in ion-beam sputtered thin films. He identifies momentum transfer as the important parameter. This is in line with conclusions regarding ion-assisted deposition. The results of Figure 11.31 agree with the Windischmann model.

Strauss has recently reviewed mechanical stress in optical coatings [82].

Abrasion resistance is another mechanical property that is of considerable importance and yet extremely difficult to define in any terms other than empirical. The problem is that abrasion resistance is not a single fundamental property, but rather a combination of factors such as adhesion, hardness, friction, packing density, and so on. Various ways of specifying abrasion resistance exist but all depend on arbitrary empirical standards. The standard sometimes involves a pad, made from rubber, which may be loaded with a particular grade of emery. The pad is drawn over the surface of the film under a controlled load for a given number of strokes. Signs of visible damage show that the coating has failed the test. Because the pad in early versions of the test was a simple eraser, the test is sometimes known as the eraser test. Similar standard tests may be based on the use of cheesecloth or even of steel wool. Wiper blades and sand slurries have also been used to attempt to reproduce the kind of abrasion that results from wiping in the presence of mud. Most of the tests suffer from the fact that they do not give a measure of the degree of abrasion resistance but are merely of a go/no-go nature. There is a modification of the test, described in Chapter 12, which does permit a measure of abrasion resistance to be derived from the extent of the damage caused by a controlled amount of abrasion. This is still probably the best arrangement yet devised, but even here the results vary considerably with film thickness and coating design so that it is far from an absolute measure of a fundamental thin-film property. The scratch test, described shortly, is sometimes used to derive an alternative measure of abrasion resistance. Abrasion resistance is, therefore, primarily a quality-control tool. It will be considered further in Chapter 12.

Adhesion is another important mechanical property that presents difficulties in measurement. What we usually think of as adhesion is the magnitude of the force necessary to detach unit area of the film from the substrate or from a neighboring film in a multilayer. However, accurate measures of this type are impossible. Quality-control testing is, as for many of the other mechanical properties, of a go/no-go nature. A strip of adhesive tape is stuck to the film and removed. The film fails if it delaminates along with the tape.

Jacobsson and Kruse [83] have studied the application of a direct-pull technique to optical thin films. In principle, the adhesive forces between film and substrate can be measured simply by applying a pull to a portion of the film until it breaks away, and, indeed, this is a technique used for other types of coatings, such as paint films. The test technique is straightforward and consists of cementing the flat end of a small cylinder to the film, and then pulling the cylinder, together with the portion of film under it, off the substrate, in as near normal a direction as possible. The force required to accomplish this is the measure of the force of adhesion. Great attention to detail is required. The end of the cylinder must be true, must be cemented to the film so that the thickness of cement is constant and so that the axis of the cylinder is vertical. The pull applied to the cylinder must have its line of action along the cylinder axis, normal to the film surface.

The precautions to be taken, and the tolerances that must be held, are considered by Jacobsson and Kruse. Their cylindrical blocks were optically polished at the ends, and, in order more nearly to ensure a pull normal to the surface, the film and substrate were cemented between two cylinders, the axes of which were collinear. The mean value of the force of adhesion between 250-nm-thick ZnS films and a glass substrate was found to be 2.3×10^7 Pa, which rose to 4.3×10^7 Pa when the glass substrate was subjected to 20 minutes of ion bombardment before coating. Zinc sulfide films evaporated on to a layer of SiO, some 150 nm thick, gave still higher adhesion figures of 5.4×10^7 Pa. The increases in adhesion due to the ion bombardment and the SiO were consistent, and the scatter in successive measures of adhesion was small, some 30% in the worst case.

An alternative method of measuring the force of adhesion is the scratch test, devised by Heavens [84], and improved and studied in detail by Benjamin and Weaver [85,86], who applied it to a range of metal films. Again, in principle, it is a straightforward test that nevertheless is very complex in interpretation. A round-ended stylus is drawn across the film-coated substrate under a series of increasing loads, and the point at which the film under the stylus is removed from the surface is a measure of the adhesion of the film. Benjamin and Weaver were able to show that plastic deformation of the substrate under the stylus subjected the interface between film and substrate to a shear force, directly related to the load on the stylus by the expression [85]

$$F = \left[a / (r^2 - a^2)^{1/2} \right] - P \qquad (11.28)$$

where

$a = [W/(\pi P)]^{1/2}$

P is the indentation hardness of the substrate

r is the radius of the stylus point

a is the radius of the circle of contact

W is the load on the stylus

F is the shear force

The shear force is roughly proportional to the root of the load on the stylus. For the film just to be removed by drawing the stylus across it, the shear force had just to be great enough to break the adhesive bonds. Using this apparatus, Benjamin and Weaver were able to confirm, quantitatively, what had been qualitatively observed before, that the adhesion of aluminum deposited at pressures around 10^{-5} Torr (1.3×10^{-5} mbar or 1.3×10^{-3} Pa) on glass was initially poor, of values similar to van der Waals forces, but that after some 200 hours it improved to reach values consistent with chemical bonding. Aluminum deposited at higher pressures, around 10^{-3} Torr (1.3×10^{-3} mbar or 0.13 Pa), gave consistently high bonding immediately after deposition. This is attributed to the formation of an oxide-bonding layer between aluminum and glass, and a series of experiments demonstrated the importance of such oxide layers in other metal films on glass. On alkali halide crystals, the initial bonding at van der Waals levels showed no subsequent improvement with time. More recently, the scratch test has been studied by Laugier [87,88], who has included the effects of friction during the scratching action in the analysis. Zinc sulfide has been shown to exhibit an unusual ageing behavior in that it occurs in two well-defined stages. After a period of some 18–24 hours after deposition, the adhesion increases by as much as a factor of four from an initially low figure. After a period of 3 days, the adhesion then begins to increase further, and after a further 7 days reaches a final maximum that can be some 20 times the initial figure. This is attributed to the formation of zinc oxide at the interface between layer and substrate, first free zinc at the interface combining with oxygen that has diffused through the layer from the outer surface and then later zinc that has diffused to the boundary from within the layer.

Commercial instruments that apply these tests are now available and help to standardize the tests as far as is possible. Unfortunately, none of these adhesion tests is entirely satisfactory. Some of the difficulties are related to consistency of measurement, but the greatest problem is the nature of the adhesion itself. The forces which attach a film to a substrate, or one film to another, are all very large (usually greater than 100 ton in^{-2} or some 10^9 Pa) but also of very short range. In fact, they are principally between one atom and the next. The short range of the forces has two major consequences. First, the forces can be blocked by a single atom or molecule of contaminant, and so adhesion is susceptible to even the slightest contamination. A single monomolecular layer of contaminant is sufficient to destroy completely the adhesion between film and substrate. A small fraction of a monomolecular layer is enough to affect it adversely. Second, although the force of adhesion is large, the work required to detach the coating, the product of the force and its range, can be quite small. Coatings usually fail in adhesion in a progressive manner rather than suddenly and simultaneously over a significant area, and in such peel failures, it is the work, rather than the force, required to detach the coating—the work of adhesion, as it is usually called—that is the important parameter. This work can be considered as the supply of the necessary surface energy

associated with the fresh surfaces exposed in the adhesion failure together with any work lost in the plastic deformation of film and/or substrate.

With some metal films, particularly deposited on plastic, there is evidence that an electrostatic double layer gradually forms, which contributes positively to the adhesion. In the tape test, the adhesive forces are comparatively very weak, but their long range allows them to be applied simultaneously over a relatively large area. Thus, the film is unlikely to be detached from the substrate unless it is very weakly bonded, and even then, it may not be removed unless there is a stress concentrator that can start the delamination process. Sometimes this is provided by scribing a series of small squares into the coating and the tape will tend to lift out complete squares.

In the case of the direct-pull technique, it is exceedingly difficult to avoid a progressive failure rather than a simultaneous rupturing of the bonds over the entire area of the pin. Unevenness in the thickness of the adhesive, or a pull that is not completely central, can cause a progressive failure with consequent reduction in the force measured. Even when the greatest care is taken, it is unlikely that the true force of adhesion will be obtained and the test is useful principally as a quality control vehicle. Poor adhesion will tend to give a very much-reduced force.

The scratch test suffers from additional problems. Many of the films used in optical coatings shatter when a sufficiently high load is applied before any delamination from the substrate takes place. Such shattering dissipates additional energy and thus film hardness and brittleness enter into the test results. Rarely with dielectric materials does a clean scratch occur. Again, the test becomes useful as a comparison between nominally similar coatings rather than an absolute one. Goldstein and DeLong [89] had some success in the assessment of dielectric films using microhardness testers to scratch the films. Most commercial scratch testers include a microscope, and visual examination of the nature of the failures is an important component of the test. Some also include sensitive acoustical detectors to detect the onset of damage. A stylus skidding over a surface is much quieter than one that is ploughing its way through and shattering the material as it goes.

The chemical resistance of the film is also of some significance, particularly in connection with the effects of atmospheric moisture, to be considered later. In this latter respect, the solubility of the bulk material is a useful guide, although it should always be remembered that, in thin-film form, the ratio of surface area to volume can be extremely large and any tendency toward solubility present in the bulk material greatly magnified. As in so many other thin-film phenomena, the magnitude of the effect depends very much on the particular thickness of material, on the other materials present in the multilayer, on the particular deposition conditions, as well as the type of test used. However, a broad classification into moisture resistant (materials such as titanium oxide, silicon oxide, and zirconium oxide), slightly affected (materials such as zinc sulfide), and badly affected (materials such as sodium fluoride) can be made.

11.4 Toxicity

In thin-film work, as indeed in any other field where much use is made of a variety of chemicals, the possibility that a material may be toxic should always be borne in mind. Fortunately, most of the materials in common use in thin-film work are reasonably innocuous, but there are occasions where distinctly hazardous materials must be used. The thin-film worker would be wise to check this point before using a new material. The technical literature on thin films, being primarily concerned with physical and chemical properties, seldom mentions the toxic nature of the materials. For example, thorium fluoride, oxyfluoride and oxide, are materials that are extensively covered in the literature, but for a long time, there was little or no mention of the radioactivity of thorium (nowadays well recognized). Recently, there has been a growing realization of the dangers associated with them and they are gradually being phased out although there are still some high-power infrared applications where they continue to be necessary. Some of the thallium salts are useful materials for the far infrared, but these are particularly toxic.

Fortunately, manufacturers' literature is becoming a useful source of information on toxicity, and in any cases of doubt, the manufacturer should always be consulted. As long as toxic material is confined to a bottle, there is little danger, but as soon as the bottle is opened, material can escape. A major objective, in the use of toxic materials, is to confine them in a well-defined space, in which suitable precautions may be taken. If material is allowed to escape from this space, so that dangerous concentrations can exist outside, then it may be impossible to prevent an accident. It may be necessary to include the whole laboratory in the danger zone and to take special precautions in cleaning up on leaving. Special clothing, extending to respirators, may even be required while in the laboratory. On the other hand, machines may be isolated from the remainder of the production area by special dust-containing cabinets complete with air circulation and filtration units.

Most of the material evaporated in a process ends up as a coating on the inside of the machine and on the jigs and fixtures, where it usually forms a powdery deposit. The greatest danger is in the subsequent cleaning. Some of the solvents and cleaning fluids that can be used in the process give off harmful vapors. A good rule when dealing with potentially hazardous chemicals is to limit the total quantity on the premises to a minimum and especially the amount that is out of safe storage at any time. This puts an upper bound on the magnitude of any major disaster but also, even if no other precautions are taken, minimizes any leakage. It is also good from the psychological point of view. It should also be remembered that many poisons are cumulative in action, and while a slight dose received in the course of a short experiment may not be particularly harmful, the same dose, repeated many times in the course of several years, may do irreparable damage. Thus,

the research worker may get away with a particular process that is operated only enough times to prove it, but the production worker will be expected to operate this process day in and day out, possibly for years. The safety standards in the production shop must therefore be of the highest standard and workers should be aware of them without being dismayed by them. It should be remembered, too, that in an emergency the laboratory may be vacated rapidly. It is then important, particularly for any emergency workers, that the hazardous materials should be well contained and their situation known. Good housekeeping is indispensable. The thin-film worker in industry should make certain that the medical officer of the works is fully aware of the materials currently in use, so that any necessary precautions can be taken before any trouble occurs.

There are, of course, legal requirements. However, legal requirements may not represent sufficiently prudent precautions. In general, unless positively dangerous materials are involved, the same precautions should be taken as in any chemical laboratory.

11.5 Summary of Some Properties of Common Materials

So far, little has been said about the actual properties of the more useful materials employed in thin-film work. The list that follows is far from being exhaustive, but gives the more important properties of some commonly used materials. Thin film properties are very dependent on process conditions and so the same material may exhibit a range of properties even varying from one machine to another. What is particularly important is that, whatever the achieved properties, they should be sufficiently stable from one production run to another. Random fluctuations can be solved only by tighter control. Published figures, therefore, tend to be a guide to, rather than a precise indication of, film properties.

The material probably used more than any other in thin-film work is magnesium fluoride. This has an index of approximately 1.38 or 1.39 in the visible region (see Figure 11.21) and is used extensively in lens blooming. In the simplest case, this is generally a single layer. Early workers used fluorite but this was found to be rather soft and vulnerable and was subsequently replaced by magnesium fluoride. Magnesium fluoride can be evaporated from a tantalum or molybdenum boat, and the best results are obtained when the substrate is hot at a temperature of some 200–300 °C. When magnesium fluoride is evaporated, trouble can sometimes be experienced through spitting and flying out of material from the boat. This is thought to be caused by thin coatings of magnesium oxide round the grains of magnesium fluoride in the evaporant. Magnesium oxide has a rather higher melting point than magnesium fluoride and the grains tend to explode once they have reached

a certain temperature. It is important, therefore, to use a reasonably pure grade of material, preferably one specifically intended for thin-film deposition and to protect it from atmospheric moisture.

Magnesium fluoride tends to suffer, as do many of the fluorides, from rather high tensile stress. A thin film of infinite area, even if highly stressed, does not exert any shear stress across the interface with the substrate or neighboring material. However, in a film of limited area, the shear stress rises to a maximum at the edge, where delamination often begins. In single films of magnesium fluoride the shear stress is not usually dangerously high but in multilayers containing many magnesium fluoride layers, such as high reflectors, the total strain energy and consequent shear loading can become high enough for spontaneous destruction of the coating to occur. Thus, magnesium fluoride is not recommended for use in structures containing many layers.

Probably the easiest materials of all to handle are zinc sulfide and cryolite. They have a good refractive index contrast in the visible, the index of zinc sulfide being around 2.35 and that of cryolite around 1.35. Both materials sublime rather than melt, and can be deposited from a tantalum or molybdenum boat or else from a howitzer (shown in Figure 11.6). Although these materials are not particularly robust, they are so easy to handle that they are very much used, especially in the construction of multilayer filters for the visible and near infrared that can subsequently be protected by a cemented cover slip. The substrates need not be heated for the deposition of the materials when intended for the visible region. Zinc sulfide is also a particularly useful material in the infrared out to about 25 μm. In the infrared, however, the substrates must be heated for best performance. The conditions are given by Cox and Hass [4], who state the best conditions to be on substrates that have been heated to around 150 °C and cleaned with an effective glow discharge just prior to the evaporation and certainly not more than 5 minutes beforehand. Films produced under these conditions will withstand several hours' boiling in 5% salt water, exposure to humid atmospheres, and cleaning with detergent and cotton wool.

A trick that has sometimes been used with zinc sulfide to improve its durability is bombardment of the growing film with electrons. This can be achieved by positioning a negatively biased hot filament, somewhere near the substrate carrier, in such a way that the filament is shielded from the arriving evaporant but is in line of sight of the substrates. This process is still not entirely understood, but it has been suggested [5] that an important factor is the modification of the crystal structure of the zinc sulfide layers by electron bombardment. Resistively heated boats produce a mixture of the cubic zinc blende and the hexagonal wurtzite structure, while electron-beam sources produce purely the zinc blende modification. The hexagonal form is a high temperature modification, which, it is suspected, will tend to transform into the lower temperature cubic modification, particularly when water vapor is present, a transformation accompanied by a weakening of adhesion, and even delamination. Deliberate electron bombardment of growing zinc

sulfide films from boat sources results in films with entirely cubic structure and with the improved stability expected from that structure.

For more durable films in the visible region, use can be made of a range of refractory oxide layers. More of these are available for the role of high-index layer than low-index.

Cerium dioxide is a high-index material that is not now as commonly used as it once was. It can be evaporated from a tungsten boat (it reacts strongly with molybdenum, producing dense white powdery coatings that completely cover the inside of the system). The procedure to be followed is given by Hass et al. [90]. Unless the material is one of the types prepared especially for vacuum evaporation, it should first be fired in air at a temperature of around 700–800 °C. If this procedure is not followed, the films will have a lower refractive index. Even with these precautions, cerium dioxide is an awkward material to handle. It tends to form inhomogeneous layers and the index varies throughout the evaporation cycle as the material in the tungsten boat is used up. It is therefore difficult to achieve a very high performance from cerium dioxide layers, in terms of maximum transmission from a filter or from an antireflection coating, and its chief use tended to be in the production of high-reflectance coatings, for high-power lasers, for example, where high reflectance coupled with low loss was the primary requirement and transmission in the pass region not as important.

Titanium dioxide is nowadays preferred over cerium oxide and is probably one of the most common high-index materials for the visible and near infrared. It has the advantage of the highest index of any of the transparent high-index materials. It is extremely robust but has a rather high melting point of 1925 °C, which makes it very difficult to evaporate directly from a boat source. Tungsten boats are most useful. One of the most successful early methods [42] was the initial evaporation of pure titanium metal which is then subsequently oxidized in air by heating it to temperatures of 400–500 °C. To obtain the highest possible index it is important to evaporate the titanium metal as quickly as possible at as low a pressure as possible so that little oxygen is dissolved in the film. On oxidation in air, indices of around 2.65 can be attained. If the deposit is partially oxidized beforehand, the index is usually rather lower, of the order of 2.25. Other early methods involved the reaction between atmospheric moisture and titanium tetrachloride. Titanium dioxide forms on a hot surface introduced into the vapor of hot titanium tetrachloride in the presence of atmospheric moisture. Best results on glass are obtained when the temperature of the glass is maintained at around 200 °C.

Both of these methods are useful for single layers but are almost impossibly complicated where multilayers are required. More modern alternative methods involve what is known as reactive deposition using either evaporation from electron-beam sources or sputtering.

Reactive evaporation was developed as a useful process in the early 1950s, Auwärter and colleagues in Europe and Brinsmaid in the United States being major contributors [91–93]. The problem with the direct evaporation of titanium

dioxide is that the very high temperatures that are required cause the titanium dioxide to be reduced so that absorption appears in the film. It was found that the reduced titanium oxide can be reoxidized to titanium dioxide during the deposition by ensuring that there is sufficient oxygen present in the atmosphere within the chamber. It appears that the oxidation takes place actually on the surface of the substrate rather than in the vapor stream, and the pressure of the residual atmosphere of oxygen must be arranged to be high enough for the necessary number of oxygen molecules to collide with the substrate surface. If the pressure is too high, then the film becomes porous and soft. There is therefore a range of pressures over which the process works best, usually 5×10^{-5} to 3×10^{-4} mbar (5×10^{-3} to 3×10^{-2} Pa). However, it is not possible to give hard and fast figures because they vary from machine to machine and depend on the particular evaporation conditions such as substrate temperature and speed of evaporation. The conditions must therefore be established by trial and error in each process. A suboxide is normally used as starting material. There are two reasons for this. The suboxide usually melts at a lower temperature than the dioxide or the metal and so is useful when a tungsten boat must be used. However, the reduction of the oxide in melting and vaporizing has been mentioned. This causes the composition of the vapor to vary unless the evaporation is what is known as congruent, that is the composition of the vapor is the same as the composition of the material in the source. Experimental evidence shows that reasonably congruent evaporation is obtained when the composition is near either Ti_2O_3 or Ti_3O_5 [94]. It is usual to use a starting material that has one or other of these compositions. The evaporation should proceed slowly enough to ensure that complete oxidization takes place. This means that several minutes should be allowed for a thickness corresponding to a quarter-wave in the visible region. Provided the rate of evaporation is kept substantially constant then the refractive index of the film can be as high as 2.45 in the visible region. The titanium dioxide remains transparent throughout the visible, the absorption in the ultraviolet becoming intense at around 350 nm.

Titanium oxide is also used with success in sputtering processes. Sputtering is the process of bombardment of the material to be deposited with high-energy positive ions so that molecules are ejected and deposited on the substrate. Reactive sputtering is the same process except that the gas in the chamber is one that can and does react with the material as it is sputtered. Usually this gas is oxygen and in this case, it reacts with the titanium to produce titanium dioxide without requiring any subsequent oxidation. The problems of poisoning of the sputtering cathodes and the various solutions have already been mentioned in connection with reactive sputtering. The rotating cylindrical magnetron and the mid-frequency double magnetron are two current solutions.

The most complete account of the properties of titanium dioxide, and the way in which they depend on deposition conditions, is that of Pulker et al. [95]. The behavior is exceedingly complicated and the results depend on starting material, oxygen pressure, rate of deposition and substrate temperature.

The evaporation of Ti_3O_5 as the starting material gave more consistent results than were obtained with other possible starting materials. With other forms of titanium oxide, the composition varied as the material was depleted, tending in each case toward Ti_3O_5.

Apfel [96] has pointed out the conflict between high optical properties and durability. Optical absorption falls as the substrate temperature is reduced and the residual gas pressure is raised. At the same time, the durability of the layers is adversely affected, and a compromise, which depends on the actual application, is usually necessary. Substrate temperatures between 200–300 °C are usually satisfactory, with gas pressures around 10^{-4} Torr (1.3×10^{-4} mbar or 1.3×10^{-2} Pa).

The low-index material that is normally used in conjunction with titanium dioxide is silicon dioxide (silica). Indeed, there is virtually no choice amongst the oxides. The usual current method for the evaporation of silicon dioxide uses an electron-beam source. Chunks of silica or machined plates are used as source material and a slight background pressure of oxygen may sometimes be used. The silicon oxide forms amorphous layers that are dense and resistant. As with most materials, a high substrate temperature during deposition is an advantage.

The high melting temperature of silica makes it difficult to evaporate it directly from heated boats. However, it is possible to use a reactive method [91,93] that avoids this problem. Silicon monoxide is a convenient starting material, which, in its own right, is a useful material for the infrared. The silicon monoxide can be evaporated readily from a tantalum boat or, as the material sublimes rather than melts, a howitzer source. Provided there is sufficient oxygen present, the silicon monoxide will oxidize to a form mostly Si_2O_3 that has a refractive index of 1.52–1.55 and exhibits excellent transmission from just on the longwave side of 300 nm out to 8 μm [97].

An interesting effect involving the ultraviolet irradiation of films of Si_2O_3 has been reported [98]. With ultraviolet power density corresponding to a 435 W quartz-envelope Hanovia lamp at a distance of 20 cm, the refractive index of the film, after around five hours' exposure, drops to 1.48 (at 540 nm). This change in refractive index appears to be due to an alteration in the structure of the film, rather than in the composition, that remains Si_2O_3. At the same time as the reduction in refractive index, an improvement in the ultraviolet transmission is observed, the films becoming transparent to beyond 200 nm. Longer exposure to ultraviolet, around 150 hours, does eventually alter the composition of the films to SiO_2. These changes appear to be permanent. Si_2O_3 is a particularly useful material for protecting aluminum mirrors, and this method of improvement by ultraviolet irradiation opens the way to greatly improved mirrors for the quartz ultraviolet. The effect has been studied in some detail by Mickelsen [99] who proposes an explanation involving electron traps.

Heitmann [100] made considerable improvements to the reactive process by ionizing the oxygen in a small discharge tube through which the gas is

admitted to the coating chamber. The degree of ionization is not high, but the reactivity of the oxygen is improved enormously, and the titanium oxide and silicon oxide films produced in this way have appreciably less absorption than those deposited by the conventional reactive process. The silicon oxide films show infrared absorption bands characteristic of the SiO form rather than the more usual Si_2O_3. The technique has been further improved by Ebert [101] and his colleagues who have developed a more efficient hollow-cathode ion source, and extended the method to materials such as beryllium oxide, with useful transmittance in the ultraviolet.

Other materials found useful in thin films are the oxides and fluorides of a number of the lanthanides or rare earths. Ceric oxide [90], although possibly strictly not a rare earth, has already been mentioned. Cerium fluoride forms very stable films of index 1.63 at 550 nm when evaporated from a tungsten boat.

Similarly, the oxides of lanthanum, praseodymium, and yttrium, and their fluorides, form excellent layers when evaporated from tungsten boats. A good account of their properties is given by Hass et al. [54]. The properties of the rare earth oxides have been shown [102] to have improved transparency, especially in the ultraviolet, when electron-beam evaporation is used.

A detailed study of the fluorides of the lanthanides and their usefulness in the extreme ultraviolet, in fact there is little else that can be used in that region, has been performed by Lingg [103,104].

Then there is a number of other hard oxide materials that were extremely difficult to evaporate until the advent of the high-power electron-beam gun, and so were used only relatively infrequently, if at all. Zirconium dioxide [102,105] is a very tough, hard material which has good transparency from around 350 nm to some 10 μm. It tends to give inhomogeneous layers, the degree of inhomogeneity depending principally on the substrate temperature. Hafnium oxide [102,106] has good transparency to around 235 nm, and an index around 2.0 at 300 nm, so that it is a good high-index material for that region. It is a preferred high-index material for high power laser mirrors. Both yttrium and hafnium oxide have been found to be good protecting layers for aluminum in the 8–12 μm region [107,108], which avoid the drop in reflectance at high angles of incidence associated with SiO_2 and with $A1_2O_3$.

In the infrared, many more possibilities are available. Semiconductors all exhibit a sudden transition from opacity to transparency at a certain wavelength known as the intrinsic edge. This wavelength corresponds to the energy gap between the filled valence band of electrons and the empty conduction band. At wavelengths shorter than this gap, photons are absorbed in the material because they are able to transfer their energy to the electrons in the filled valence band by lifting them into the empty conduction band. At wavelengths longer than this value, the photon energy is not sufficient, and apart from a little free carrier absorption, there is no mechanism for absorbing the energy and the material appears transparent until the lattice vibration bands at rather long wavelengths are encountered. For the more

common semiconductors, silicon and germanium, the intrinsic edge wavelengths are 1.1 μm and 1.65 μm, respectively. Thus, both of these materials are potentially useful in the infrared. A great advantage that they possess is their high refractive index, 3.5 for silicon and 4.0 for germanium.

Silicon, however, is not at all easy to evaporate because it reacts strongly with any crucible material, and almost the only way of dealing with it in thermal evaporation is to use an electron gun with a water-cooled crucible so that the cold silicon in contact with the crucible walls acts as its own container. The high thermal conductivity of silicon makes it necessary to use high power. Sputtering is a viable process and, in fact, most large-area silicon dioxide coatings are produced by the reactive sputtering of silicon from magnetron targets. The poisoning problem in reactive sputtering and its solutions have already been mentioned. Germanium, on the other hand, is a most useful material and straightforward techniques have been devised to handle it. Tungsten boats can be used provided that the total thickness of material to be deposited is not too great, 2 or 3 μm say, because germanium does react with tungsten. Molybdenum boats have been used with greater success [106]. A quite satisfactory method is to use a crucible made from graphite and heated directly or indirectly when the germanium films obtained are extremely pure and free from absorption. Again, the method of choice nowadays is the electron-beam source when the hearth material can be graphite or water-cooled copper.

There are other semiconductors of use as follows. Tellurium [109,110] has an index of 5.1 at 5 μm, good transmission from 3.5 μm to at least 12 μm, and can be evaporated easily from a tantalum boat. Lead telluride [6,111–118] has an even higher index of around 5.5 with good transmission from 3.4 μm out to beyond 20 μm. A tantalum boat is the most suitable source. Care must be taken not to overheat the material; the temperature should be just enough to cause the evaporation to proceed, otherwise some alteration in the composition of the film will take place, causing an increase in free-carrier absorption and consequent fall-off in longwave transparency. The substrates should be heated, best results being obtained with temperatures around 250 °C, but as this will be too great for the low-index film, which is usually zinc sulfide, a compromise temperature that is rather lower, usually around 150 °C, is often used for both materials. One difficulty with lead telluride is the ease with which it can be upset by impurities that cause free-carrier absorption. It is extremely important to use pure grades of material and this applies to the accompanying zinc sulfide as well as the lead telluride, especially if the material is to be used at the longwave end of its transparent region. Lead telluride also appears to be incompatible with a number of other materials, particularly some of the halides, presumably because material diffuses into the lead telluride generating free carriers. An annealing process that can in certain circumstances improve the transmission of otherwise absorbing films of lead telluride in the region beyond 12 μm is described by Evans and Seeley [114].

Lead telluride can in some circumstances behave in a curious way immediately after deposition [111,112]. The optical thickness of the material is observed to grow during a period of around 15 minutes while the layer is still under vacuum. Typical gains in optical thickness of a half-wave layer are of the order of 0.007 full wave, although in any particular case it varies considerably and can often be zero. The reasons for this behavior are not clear but the layers do not exhibit any further instability, once they have ceased growing. It is simply a matter of allowing for this behavior in the monitoring process.

A wide range of low-index materials is used in the infrared. Zinc sulfide [4,55] in comparison with the high-index semiconductors has a relatively low index. If an electron-beam source is not available, then zinc sulfide should be deposited from a tantalum boat, or, better still, a howitzer, on substrates freshly cleaned by a glow discharge and held at temperatures of around 150 °C, if the maximum durability is to be obtained. Zinc sulfide films so treated will withstand boiling for several hours in 5% salt solution, cleaning with cotton wool, and exposure to moist air, without damage [4]. Silicon monoxide is another possibility [4,119]. It can also be deposited from a tantalum boat or a howitzer. The deposition rate should be fast and the pressure low, of the order of 10^{-5} Torr (1.3×10^{-5} mbar or 1.3×10^{-3} Pa) or less if possible. The refractive index is around 1.85 at 1 μm and falls to 1.6 at 7 μm. A strong absorption band prevents use of the material beyond 8 μm. Thorium fluoride, unfortunately radioactive, has been much used in the past, although it is less in favor nowadays because of its radioactivity. It is still much used in high power coatings for the CO_2 laser because a completely suitable replacement in that application has not yet been found. Then there are many other materials, such as fluorides of lead, lanthanum, barium, cerium, and oxides such as titanium, yttrium, hafnium and cerium.

The nitrides of silicon and aluminum are tough, hard materials with excellent transparency from the ultraviolet through to around 10 μm in the infrared. They have not been much used in optical coatings because of the difficulty of thermal evaporation. The process of reactive evaporation of the metal in nitrogen does not work because the nitrogen, unless it is in atomic form, does not readily combine with the metal. Evaporation of aluminum, for example, in a residual atmosphere of nitrogen results in bright aluminum films whereas evaporation in oxygen gives aluminum oxide. The situation has changed completely with the introduction of the energetic processes, and especially ion-assisted deposition. The nitrogen beam from the ion source used in these processes reacts strongly with the metal to form dense, hard, and tough nitride films of good transparency. There is another enormous advantage in these materials. The oxynitrides represent a continuous range of compositions between the pure oxide and the pure nitride. The oxide is of rather lower refractive index and the refractive index of the oxynitride ranges smoothly with composition from that of the oxide to that of the nitride. The composition of the film is a function of the reacting gas composition and this can readily be varied to alter the film index in a well-controlled

manner. Hwangbo and colleagues [36] investigated the ion-assisted deposition of aluminum oxynitride. They used aluminum metal as source material. A particularly straightforward way of controlling the index of aluminum oxynitride films from 1.65 to 1.83 at 550 nm was to bombard the growing film with a constant flux of nitrogen from the ion gun and to supply a variable quantity of oxygen to the process simply as a background gas. The reactivity of the oxygen is so great that any small quantity is taken up preferentially by the film. In fact, in the oxynitride process, it is virtually impossible to eliminate oxygen entirely and so the achievable high index does not quite reach the value that would be associated with the pure nitride. Hwangbo et al. [36] were able to construct simple rugate filters with the sole variable during the process being the background pressure of oxygen, all other quantities, bombardment, evaporation rate, and so on, being held constant. Placido [120] has constructed rugate structures of very many accurately controlled cycles from aluminum oxynitride using reactive RF sputtering of aluminum metal in a mixture of oxygen and nitrogen.

Bovard et al. [121] produced silicon nitride films using low-voltage ion plating. Here there was no oxygen in the chamber and the films were pure nitride giving a refractive index of 2.05 at 550 nm. The range of variation in index from silicon oxynitride films is potentially very great.

Mixtures of materials are receiving attention both in deliberately inhomogeneous films and in homogeneous films where an intermediate index between the two components of the mixture is required. Often such a mixture can replace a rather more difficult single component material.

Jacobsson and Martensson [122] used mixtures of cerium oxide and magnesium fluoride, of zinc sulfide and cryolite, and of germanium and magnesium fluoride, with the relative concentration of the two components varying smoothly throughout the films, to produce inhomogeneous films with a refractive index variation of a prescribed law. Some of the results they obtained for antireflection coatings were mentioned in Chapter 4. To produce the mixture, two separate sources, one for each material, were used; they were evaporated simultaneously but with independent rate controls. Apparently no difficulty in obtaining reasonable films was experienced, the mixing taking place without causing absorption to appear.

Fujiwara [123,124] was interested in the production of homogeneous films for antireflection coatings [125]. The three-layer quarter–half–quarter coating for glass requires a film of intermediate index that is rather difficult to obtain with a simple material, and the solution adopted by Fujiwara was to use a mixture of two materials, one having a refractive index lower than the required value and the other higher. The two combinations that were tried successfully were cerium oxide and cerium fluoride, and zinc sulfide and cerium fluoride. These were simply mixed together in powder form in a certain known proportion by weight and then evaporated from a single source. The mixture evaporated giving an index that was sufficiently reproducible for antireflection coating purposes. The range of indices obtainable with the

cerium oxide–cerium fluoride mixture was 1.60–2.13, and with the cerium fluoride–zinc sulfide mixture 1.58–2.40. One interesting feature of the second mixture was that, although zinc sulfide on its own is not particularly robust, in the form of a mixture with more than 20% by weight of cerium fluoride the robustness was greatly increased, the films withstanding boiling in distilled water for 15 minutes without any deterioration. Curves are given for refractive index against mixing ratio in the papers.

Mixtures of zinc sulfide and magnesium fluoride have also been studied by Yadava et al. [126]. The refractive index of the mixture varies between the indices of magnesium fluoride and zinc sulfide, depending on the mixing ratio, and the absorption edge varies from that of zinc sulfide to that of magnesium fluoride in a nonlinear fashion. The same authors [126,127] have studied the use of assemblies of large numbers of alternate very thin discrete layers of the components instead of mixtures. For a wide range of material combinations, ZnS–MgF_2, ZnS–MgF_2–SiO, Ge–ZnS, ZnS–Na_3AIFs, for example, the results were similar to those expected from the evaporation of mixtures of the same materials.

Silica is a particularly difficult material to evaporate because of its high melting point and also because of its transparency to infrared, which makes it difficult to heat. It was found by Morgan at the Libbey-Owens-Ford Glass Company [128] that silica could be thermally evaporated readily if some pretreatment were carried out. This consisted of combining the silica with a metallic oxide, a vast number of different oxides being suitable. The oxide can be mixed intimately with the silica, coated on the outer surface of silica chunks or, in some cases where the oxide has a rather lower melting temperature than the silica, mixed very crudely. Only a small quantity of the oxide is required and the evaporation is carried out in the conventional manner from a tungsten source. The oxides mentioned include aluminum, titanium, iron, manganese, cobalt, copper, cerium, and zinc. Along similar lines, it has been discovered by workers at Balzers AG [129,130] that cerium oxide mixed with other oxides improves the oxidation and increases the transparency and ease of evaporation. Materials such as titanium dioxide are difficult to evaporate without absorption, and the most successful method is reactive evaporation in oxygen, which produces absorption-free films, although the process is rather time consuming because the evaporation must proceed slowly. With the addition of a small amount of cerium oxide—the mixture can vary from 1:1 to 8:1 titanium oxide (the monoxide, the dioxide, or even the pure metal) to cerium oxide—hard films free from absorption, even when evaporated quickly at pressures of 10^{-5} Torr (1.3×10^{-5} mbar or 1.3×10^{-3} Pa), are readily obtained. Apparently, this effect is not limited to titanium oxide, and a vast range of different materials that have been successfully tried is given. Other rare earth oxides and mixtures of rare earth oxides can also take the place of the cerium dioxide.

Stetter et al. [105] have pointed out the advantage of oxygen-depleted materials as source material for electron-beam evaporation, in that composition

changes little if at all during evaporation, which leads to more consistent film properties. The extra oxygen is supplied, in the usual way, from the residual atmosphere in the machine. The depleted materials also have higher thermal and electrical conductivity. A mixture of ZrO_2 and $ZrTiO_4$, sintered at high temperature under high vacuum and oxygen-depleted, was developed. This material, designated 'Substance no 1', when evaporated from an electron-beam system in a residual oxygen pressure of $1–2 \times 10^{-4}$ Torr ($1.3–2.5 \times 10^{-4}$ mbar or $1.3–2.5 \times 10^{-2}$ Pa) with substrate temperature 270 °C, and condensation rate of the order of 10 nm min^{-1}, gives homogeneous layers of refractive index 2.15 (at 500 nm). Such a value of index is ideal for the quarter–half–quarter antireflection coating for the visible region. This has prompted further work on mixtures [131] and there are now several similar materials available. H1 is from the zirconia/titania system with index 2.1 at 500 nm and good transparency from 360 nm to 7 μm but with some difficulties in evaporation because of incomplete melting. H2 from the praseodymium/titanium oxide system has a similar index and the advantage of ease of evaporation but suffers from a more restricted range of good transmittance, 400 nm to 7 μm, and localized slight absorption in the transparent region. H4 is a lanthanum/titanium oxide combination with again refractive index 2.1 at 500 nm and transmission region from 360 nm to 7 μm that melts completely and so is normally preferred over the other two materials. M1 is a mixture of praseodymium/aluminum oxide with index on heated substrates of 1.71 at 500 nm and good transparency from 300 nm to longer wavelengths.

Butterfield [132] has produced films of a mixture of germanium and selenium. For composition varying from 30 to 50 atomic % of germanium, glassy films with refractive index in the range 2.4–3.1, with good transparency from 1.5–15 μm, could be produced. The starting material was an alloy of germanium and selenium in the correct proportions, produced by melting the pure substances in an evacuated quartz tube. The evaporation source was a graphite boat. It is likely that much more work will be carried out on mixtures, because of the apparent ease with which the deposition can be performed to give a wide range of refractive indices, many of which are not available by other means. The theory of the optical properties of mixtures is covered in a useful review by Jacobsson [68], who also gives further information on mixtures and on inhomogeneous layers.

References

1. Vossen J L and Kern W 1978 *Thin Film Processes* (New York/San Francisco/London: Academic Press)
2. Vossen J L and Kern W 1991 *Thin Film Processes II* (San Diego: Academic Press)
3. Glocker D A and Shah S I 1995 *Handbook of Thin Film Process Technology* (Bristol: Institute of Physics)

4. Cox J T and Hass G 1958 Antireflection coatings for germanium and silicon in the infrared *Journal of the Optical Society of America* **48** 677–680
5. Bangert H and Pfefferkorn H 1980 Condensation and stability of ZnS thin films on glass substrates *Applied Optics* **19** 3878–3879
6. Ritchie F S 1970 *Multilayer Filters for the Infrared Region 10–100 microns* PhD Thesis University of Reading
7. Coulter J K, Hass G, and Ramsay J B 1973 Optical constants and reflectance and transmittance of evaporated rhodium films in the visible *Journal of the Optical Society of America* **63** 1149–1153
8. Hass G and Ritter E 1967 Optical film materials and their applications *Journal of Vacuum Science and Technology* **4** 71–79
9. Scobey M A Optical Corporation of America 1996 *Low pressure reactive magnetron sputtering apparatus and method* US Patent 5,525,199
10. Gibson D R, Brinkley I, Waddell E M, and Walls J M 2008 Closed field magnetron sputtering: new generation sputtering process for optical coatings *Proceedings of SPIE* **7101** 710108 1–12
11. Gibson D R, Brinkley I T, Waddell E M, and Walls J M 2008 *Closed field magnetron sputter deposition of carbides and nitrides for optical applications* in *51st Annual Technical Conference Proceedings Chicago* Society of Vacuum Coaters 487–491
12. Schiller S, Heisig U, and Goedicke G 1975 Alternating ion plating: A method of high-rate ion vapor deposition *Journal of Vacuum Science and Technology* **12** 858–864
13. Scobey M A, Seddon R I, Seeser J W, Austin R R, LeFebvre P M, and Manley B W Optical Coating Laboratory, Inc 1989 *Magnetron sputtering apparatus and process* US Patent 4,851,095
14. Spencer A G 1997 *Precision optical coatings from express ophthalmic coaters* in *40th Annual Technical Conference Proceedings New Orleans* Society of Vacuum Coaters 259–265
15. Placido F 1998 *Radio frequency sputtering of optical coatings including rugate filters* Department of Physics Private Communication
16. Pervak V, Tikhonravov A V, Trubetskov M K, Pistner J, Krausz F, and Apolonski A 2007 Band filters: two-material technology versus rugate *Applied Optics* **46** 1190–1193
17. Wei D T, Kaufman H R, and Lee C-C 1995 *Ion beam sputtering*, in *Thin Films for Optical Systems* Flory F R Editor (New York/Basel/Hong Kong: Marcel Dekker, Inc) 133–201
18. Lalezari R, Rempe G, Thompson R J, and Kimble H J 1992 *Measurement of ultralow losses in dielectric mirrors* in *Topical Meeting on Optical Interference Coatings Tucson* Optical Society of America 331–333
19. Mackowski J M, Pinard L, Dognin L, Ganau P, Lagrange B, Michel C, and Morgue M 1998 *Different approaches to improve the wavefront of low-loss mirrors used in the VIRGO gravitational wave antenna*, in *Optical Interference Coatings* (Washington: Optical Society of America) 18–20
20. Pulker H K, Bühler M, and Hora R 1986 Optical films deposited by a reactive ion plating process *Proceedings of the Society of Photo-Optical Instrumentation Engineers* **678** 110–114
21. Pulker H K and Guenther K H 1995 *Reactive physical vapor deposition processes*, in *Thin Films for Optical Systems* Flory F R Editor (New York/Basel/Hong Kong: Marcel Dekker, Inc) 91–115
22. Bovard B G 1995 *Ion-assisted deposition*, in *Thin Films for Optical Systems* Flory F R Editor (New York/Basel/Hong Kong: Marcel Dekker, Inc) 117–132

23. Fulton M L 1994 Applications of ion-assisted-deposition using a gridless end-Hall ion source for volume manufacturing of thin-film optical filters. *Proceedings of the Society of Photo-Optical Instrumentation Engineers* **2253** 374–393
24. Matl K, Klug W, and Zöller A 1991 Ion-assisted deposition with a new plasma source *Materials Science and Engineering* **A140** 523–527
25. Pongratz S and Zöller A 1992 Plasma ion-assisted evaporative deposition of surface layers *Annual Review of Materials Science* **22** 279–295
26. Zöller A, Boos M, Hagedorn H, and Romanov B 1994 Computer simulation of coating processes with monochromatic monitoring *Proceedings of the Society of Photo-Optical Instrumentation Engineers* **7101** 71010G-1–71010G-7
27. Matsumoto S, Kikuchi K, Yamasaki M, Tang Q, and Ogura S Shincron Co., Ltd 2001 *Method of forming a thin film of a composite metal compound and the apparatus for carrying out the method* US Patent 6,207,536 B1
28. Müller K-H 1986 Monte Carlo calculation for structural modifications in ion-assisted thin film deposition due to thermal spikes *Journal of Vacuum Science and Technology, A* **4** 184–188
29. Müller K-H 1988 Models for microstructure evolution during optical thin film growth *Proceedings of the Society of Photo-Optical Instrumentation Engineers* **821** 36–44
30. Targove J D, Lingg L J, and Macleod H A 1988 *Verification of momentum transfer as the dominant densifying mechanism in ion-assisted deposition* in *Optical Interference Coatings Tucson, AZ, USA* Optical Society of America 268–271
31. Targove J D and Macleod H A 1988 Verification of momentum transfer as the dominant densifying mechanism in ion-assisted deposition *Applied Optics* **27** 3779–3781
32. Martin P J, Macleod H A, Netterfield R P, Pacey C G, and Sainty W G 1983 Ion-beam-assisted deposition of thin films *Applied Optics* **22** 178–184
33. Messerly M J 1987 *Ion-beam analysis of optical coatings* PhD Dissertation University of Arizona
34. Sainty W G, Netterfield R P, and Martin P J 1984 Protective dielectric coatings produced by ion-assisted deposition *Applied Optics* **23** 1116–1119
35. Hwangbo C K, Lingg L J, Lehan J P, Macleod H A, Makous J L, and Kim S Y 1989 Ion-assisted deposition of thermally evaporated Ag and Al films *Applied Optics* **28** 2769–2778
36. Hwangbo C K, Lingg L J, Lehan J P, Macleod H A, and Suits F 1989 Reactive ion-assisted deposition of aluminum oxynitride thin films *Applied Optics* **28** 2779–2784
37. Segner J 1995 *Plasma impulse chemical vapor deposition*, in *Thin Films for Optical Systems* Flory F R Editor (New York/Basel/Hong Kong: Marcel Dekker, Inc) 203–229
38. Hora R and Wohlrab C 1993 *Plasma polymerization: A new technology for functional coatings on plastics* in *36th Annual Technical Conference* Society of Vacuum Coaters 51–55
39. Möhl W, Lange U, and Pacquet V 1994 Optical coatings on plastic lenses by PICVD-technique *Proceedings of the Society of Photo-Optical Instrumentation Engineers* **2253** 486–491
40. Wohlrab C and Hofer M 1995 *Plasma polymerization of optical coatings on organic substrates: Equipment and processes* in *38th Annual Technical Conference* Society of Vacuum Coaters 222–230

41. Thomas I M 1993 Sol-gel coatings for high power laser optics: past present and future *Proceedings of the Society of Photo-Optical Instrumentation Engineers* **2114** 232–243
42. Hass G 1952 Preparation, properties and optical applications of thin films of titanium dioxide *Vacuum* **2** 331–345
43. Meaburn J 1967 A search for nebulosity in the high galactic latitude radion spurs *Zeitschrift für Astrophysik* **65** 93–104
44. Title A M, Pope T P, and Andelin J P 1974 Drift in interference filters. Part 1 *Applied Optics* **13** 2675–2679
45. Richmond D 1976 *Thin film narrow band optical filters* PhD Thesis Newcastle upon Tyne Polytechnic
46. Lee C C 1983 *Moisture adsorption and optical instability in thin film coatings* PhD Dissertation University of Arizona
47. Müller K-H 1985 A computer model for postdeposition annealing of porous thin films *Journal of Vacuum Science and Technology, A* **3** 2089–2092
48. Prins S L, Barron A C, Herrmann W C, and McNeil J R 2004 Effect of stress on performance of dense wavelength division multiplexing filters: thermal properties *Applied Optics* **43** 633–637
49. Brown J T 2004 Center wavelength shift dependence on substrate coefficient of thermal expansion for optical thin-film interference filters deposited by ion-beam sputtering *Applied Optics* **43** 4506–4511
50. Heavens O S 1964 *Measurement of optical constants of thin films*, in *Physics of Thin Films* Hass G and Thun R E Editors (New York/London: Academic Press) 193–238
51. Liddell H M 1981 *Computer-aided techniques for the design of multilayer filters* (Bristol: Adam Hilger Ltd)
52. Borgogno J-P 1995 *Spectrophotometric methods for refractive index determination*, in *Thin Films for Optical Systems* Flory F R Editor (New York/Basel/Hong Kong: Marcel Dekker, Inc) 269–328
53. Hall J F, Jr and Ferguson W F C 1955 Dispersion of zinc sulfide and magnesium fluoride films in the visible spectrum *Journal of the Optical Society of America* **45** 74–75
54. Hass G, Ramsay J B, and Thun R 1959 Optical properties of various evaporated rare earth oxides and fluorides *Journal of the Optical Society of America* **49** 116–120
55. Hall J F and Ferguson W F C 1955 Optical properties of cadmium sulphide and zinc sulphide from 0.6 micron to 14 micron *Journal of the Optical Society of America* **45** 714–718
56. Pelletier E, Roche P, and Vidal B 1976 Détermination automatique des constantes optiques et de l'épaisseur de couches minces: application aux couches diélectriques *Nouvelle Revue d'Optique* **7** 353–362
57. Manifacier J C, Gasiot J, and Fillard J P 1976 A simple method for the determination of the optical constants n, k and the thickness of a weakly absorbing thin film *Journal of Physics E* **9** 1002–1004
58. Swanepoel R 1983 Determination of the thickness and optical constants of amorphous silicon *Journal of Physics E* **16** 1214–1222
59. Hansen W 1973 Optical characterization of thin films: theory *Journal of the Optical Society of America* **63** 793–802
60. Abelès F 1950 La détermination de l'indice et de l'épaisseur des couches minces transparentes *Journal de Physique et le Radium* **11** 310–314

61. Hacskaylo M 1964 Determination of the refractive index of thin dielectric films *Journal of the Optical Society of America* **54** 198–203
62. Azzam R M A 1995 *Ellipsometry*, in *Handbook of Optics* Bass M Editor (New York: McGraw Hill) 27.1–27.27
63. Rivory J 1995 *Ellipsometric measurements*, in *Thin Films for Optical Systems* Flory F R Editor (New York/Basel/Hong Kong: Marcel Dekker, Inc) 299–328
64. Hilfiker J N, Synowicki R A, and Tompkins H G 2008 *Spectroscopic Ellipsometry Methods for Thin Absorbing Coatings* in *51st Annual Technical Conference Proceedings Chicago* Society of Vacuum Coaters 511–516
65. Dobrowolski J A, Ho F C, and Waldorf A 1983 Determination of optical constants of thin film coating materials based on inverse synthesis *Applied Optics* **22** 3191–3200
66. Abelès F 1950 Recherches sur la propagation des ondes électromagnétiques sinusoïdales dans les milieus stratifiés. Applications aux couches minces. I *Annales de Physique, 12ième Serie* **5** 596–640
67. Abelès F 1950 Recherches sur la propagation des ondes électromagnétiques sinusoïdales dans les milieus stratifiés. Applications aux couches minces. II *Annales de Physique, 12ième Serie* **5** 706–784
68. Jacobsson R 1975 Inhomogeneous and coevaporated homogeneous films for optical applications *Physics of Thin Films* **8** 51–98
69. Borgogno J P, Lazarides B, and Pelletier E 1982 Automatic determination of the optical constants of inhomogeneous thin films *Applied Optics* **21** 4020–4029
70. Arndt D P, Azzam R M A, Bennett J M, Borgogno J P, Carniglia C K, Case W E, Dobrowolski J A, Arndt D P, Gibson U J, Hart T T, et al. 1984 Multiple determination of the optical constants of thin-film coating materials *Applied Optics* **23** 3571–3596
71. Netterfield R P 1976 Refractive indices of zinc sulphide and cryolite in multilayer stacks *Applied Optics* **15** 1969–1973
72. Hoffman R W 1976 Stresses in thin films: the relevance of grain boundaries and impurities *Thin Solid Films* **34** 185–190
73. Ennos A E 1966 Stresses developed in optical film coatings *Applied Optics* **5** 51–61
74. Roll K 1976 Analysis of stress and strain distribution in thin films and substrates *Journal of Applied Physics* **47** 3224–3229
75. Roll K and Hoffman H 1976 Michelson interferometer for deformation measurements in an UHV system at elevated temperatures *Review of Scientific Instruments* **47** 1183–1185
76. Ledger A M and Bastien R C 1977 *Intrinsic and thermal stress modeling for thin-film multilayers* (The Perkin Elmer Corporation, Norwalk, Connecticut 06856.)
77. Bovard B G, Lega X C d, Hahn S-H, and Macleod H A 1991 *Intrinsic stress in titanium dioxide thin films produced by ion-assisted deposition* Optical Sciences Center, University of Arizona, Tucson, Arizona Private Communication
78. Pulker H K 1982 Stress, adherence, hardness and density of optical thin films *Proceedings of the Society of Photo-Optical Instrumentation Engineers* **325** 84–92
79. Pulker H K 1999 *Coatings on Glass* ed 2nd (Amsterdam: Elsevier)
80. Pellicori S F 1984 Stress modification in cerous fluoride films through admixture with other fluoride compounds *Thin Solid Films* **113** 287–295
81. Windischmann H 1987 An intrinsic stress scaling law for polycrystalline thin films prepared by ion beam sputtering *Journal of Applied Physics* **62** 1800–1807

82. Strauss G N 2003 *Mechanical stress in optical coatings*, in *Optical Interference Coatings* Kaiser N and Pulker H K Editors (Berlin: Springer-Verlag) 207–229
83. Jacobsson R and Kruse B 1973 Measurement of adhesion of thin evaporated films on glass substrates by means of the direct pull method *Thin Solid Films* **15** 71–77
84. Heavens O S 1950 Some features influencing the adhesion of films produced by vacuum evaporation *Journal de Physique et le Radium* **11** 355–360
85. Benjamin P and Weaver C 1960 Measurement of adhesion of thin films *Proceedings of the Royal Society of London, A* **254** 163–176
86. Benjamin P and Weaver C 1960 Adhesion of metal films to glass *Proceedings of the Royal Society of London, A* **254** 177–183
87. Laugier M 1981 Unusual adhesion-aging behaviour in ZnS thin films *Thin Solid Films* **75** L19–L20
88. Laugier M 1981 The development of the scratch test technique for the determination of the adhesion of coatings *Thin Solid Films* **76** 289–294
89. Goldstein I S and DeLong R 1982 Evaluation of microhardness and scratch testing for optical coatings *Journal of Vacuum Science and Technology* **20** 327–330
90. Hass G, Ramsay J B, and Thun R 1958 Optical properties and structure of cerium dioxide films *Journal of the Optical Society of America* **48** 324–327
91. Auwärter M 1960 *Process for the manufacture of thin films* US Patent 2,920,002
92. Brinsmaid D S, Keenan W J, Koch G J, and Parsons W F Eastman Kodak Co 1957 *Method of producing titanium dioxide coatings* US Patent 2,784,115
93. Vogt A 1957 *Improvements in or relating to the manufacture of thin light-transmitting layers* UK Patent 775,002
94. Chiao S-C, Bovard B G, and Macleod H A 1998 Repeatability of the composition of titanium oxide films produced by evaporation of Ti2O3 *Applied Optics* **37** 5284–5290
95. Pulker H K, Paesold G, and Ritter E 1976 Refractive indices of TiO2 films produced by reactive evaporation of various titanium-oxide phases *Applied Optics* **15** 2986–2991
96. Apfel J H 1980 *The preparation of optical coatings for fusion lasers* in *International Conference on Metallurgical Coatings San Diego*
97. Ritter E 1962 Zür Kentnis des SiO und Si2O3-Phase in dünnen Schichten *Optica Acta* **9** 197–202
98. Bradford A P, Hass G, McFarland M, and Ritter E 1965 Effect of ultraviolet irradiation on the optical properties of silicon oxide films *Applied Optics* **4** 971–976
99. Mickelsen R A 1968 Effects of ultraviolet irradiation on the properties of evaporated silicon oxide films *Journal of Applied Physics* **39** 4594–4600
100. Heitmann W 1971 Reactive evaporation in ionized gases *Applied Optics* **10** 2414–2418
101. Ebert J 1982 Activated reactive evaporation *Proceedings of the Society of Photo-Optical Instrumentation Engineers* **325** 29–38
102. Smith D and Baumeister P W 1979 Refractive index of some oxide and fluoride coating materials *Applied Optics* **18** 111–115
103. Lingg L J 1990 *Lanthanide trifluoride thin films: structure, composition and optical properties* PhD Dissertation University of Arizona
104. Lingg L J, Targove J D, Lehan J P, and Macleod H A 1987 Ion-assisted deposition of lanthanide trifluorides for VUV applications *Proceedings of the Society of Photo-Optical Instrumentation Engineers* **818** 86–92

105. Stetter F, Esselborn R, Harder N, Friz M, and Tolles P 1976 New materials for optical thin films *Applied Optics* **15** 2315–2317
106. Baumeister P W and Arnon O 1977 Use of hafnium dioxide in mutilayer dielectric reflectors for the near uv *Applied Optics* **16** 439–444
107. Cox J T and Hass G 1978 Protected Al mirrors with high reflectance in the 8–12-μm region from normal to high angles of incidence *Applied Optics* **17** 2125–2126
108. Lubezky I, Ceren E, and Klein Z 1980 Silver mirrors protected with Yttria for the 0.5 to 14 µm region *Applied Optics* **19** 1895
109. Greenler R G 1955 Interferometry in the infrared *Journal of the Optical Society of America* **45** 788–791
110. Moss T S 1952 Optical properties of tellurium in the infra-red *Proceedings of the Physical Society* **65** 62–66
111. Evans C S, Hunneman R, and Seeley J S 1976 Increments at the interface between layers during infra-red filter manufacture *Optica Acta* **23** 297–303
112. Evans C S, Hunneman R, and Seeley J S 1976 Optical thickness changes in freshly deposited layers of lead telluride *Journal of Physics D* **9** 321–328
113. Evans C S, Hunneman R, Seeley J S, and Whatley A 1976 Filters for $\nu 2$ band of CO2: monitoring and control of layer deposition *Applied Optics* **15** 2736–2745
114. Evans C S and Seeley J S 1968 *Properties of thick evaporated layers of PbTe* in *Paper presented at the Colloquium on IV-VI compounds Paris*
115. Seeley J S, Hunneman R, and Whatley A 1981 Far infrared filters for the Galileo-Jupiter and other missions *Applied Optics* **20** 31–39
116. Smith S D and Seeley J S 1968 *Multilayer filters for the region 0.8 to 100 microns* Air Force Cambridge Research Laboratories)
117. Yen Y-H, Zhu L-X, Zhang W-D, Zhang F-S, and Wang S-Y 1984 Study of PbTe optical coatings *Applied Optics* **23** 3597–3601
118. Zhang K G, Seeley J S, Huneman R, and Hawkins G J 1989 Optical and semiconductor properties of lead telluride coatings *Proceedings of the Society of Photo-Optical Instrumentation Engineers* **1112** 393–402
119. Hass G and Salzberg C D 1954 Optical properties of silicon monoxide in the wavelength region from 0.24 to 14.0 microns *Journal of the Optical Society of America* **44** 181–187
120. Placido F 1997 *RF sputtering of aluminium oxynitride rugates. Micrographs of rugate structures.* Department of Physics Private Communication
121. Bovard B B, Ramm J, Hora R, and Hanselmann F 1989 Silicon nitride thin films by low voltage reactive ion plating: optical properties and composition *Applied Optics* **28** 4436–4441
122. Jacobsson R and Martensson J O 1966 Evaporated inhomogeneous thin films *Applied Optics* **5** 29–34
123. Fujiwara S 1963 Refractive indices of evaporated cerium dioxide-cerium fluoride films *Journal of the Optical Society of America* **53** 880
124. Fujiwara S 1963 Refractive indices of evaporated cerium fluoride-zinc sulphide films *Journal of the Optical Society of America* **53** 1317–1318
125. Kogaku N Nippon Kogaku K K 1965 *Surface-coated optical elements* UK Patent 1,010,038
126. Yadava V N, Sharma S K, and Chopra K L 1974 Optical dispersion of homogeneously mixed ZnS-MgF2 films *Thin Solid Films* **22** 57–66
127. Yadava V N, Sharma S K, and Chopra K L 1973 Variable refractive index optical coatings *Thin Solid Films* **17** 243–252

128. Morgan W L Libbey-Owens-Ford Glass Company 1949 *Method of coating with quartz by thermal evaporation* USA Patent 2,463,791
129. Balzers Patent und Lizenz Anstalt 1962 *Improvements in and relating to the oxidation and/or transparency of thin partly oxidic layers* UK Patent 895,879
130. Kraus T and Rheinberger P Balzers Patent- und Lizenz-Anstalt 1962 *Use of a rare earth metal in vaporizing metals and metal oxides* US Patent 3,034,924
131. Friz M, Koenig F, and Feiman S 1992 *New materials for production of optical coatings* in *35th Annual Technical Conference Proceedings* Society of Vacuum Coaters 143–148
132. Butterfield A W 1974 The optical properties of GexSe1-x thin films *Thin Solid Films* **23** 191–194

12

Factors Affecting Layer and Coating Properties

12.1 Microstructure and Thin-Film Behavior

One of the most significant features of optical thin films is the way in which their properties and behavior differ from those of identical materials in bulk form. This is, of course, also true for thin films in areas other than optics. Almost always, the performance of the film is poorer than that of the corresponding bulk material. Refractive index is usually lower, although, very occasionally, for some semiconductor materials it can be slightly higher with greater losses, less durability, and inferior stability. There is also sensitivity to deposition conditions, especially substrate temperature.

Heitmann [1] has studied the influence of parameters, such as the residual gas pressure within the chamber and the rate of deposition, on the refractive indices of cryolite and thorium fluoride. Raising the residual gas (nitrogen) pressure from 4×10^{-6} Torr (5.3×10^{-6} mbar or 5.3×10^{-4} Pa) in one case, and 2×10^{-6} Torr (2.6×10^{-6} mbar or 2.6×10^{-4} Pa) in another, to 2×10^{-5} Torr (2.6×10^{-5} mbar or 2.6×10^{-3} Pa) had no measurable effect, within the accuracy of the experiment (± 0.1% for thorium fluoride and ±0.3% for cryolite) while a further increase in residual pressure to 2×10^{-4} Torr (2.6×10^{-4} mbar or 2.6×10^{-2} Pa) gave a drop in index of 1.5% for cryolite and 1.4% for thorium fluoride. At this higher pressure, the mean free path of the nitrogen molecules was less than the distance between boat and substrate, and the decrease in refractive index was probably caused by increased porosity of the layers. This tends to confirm that the mean free path of the residual gas molecules should be kept longer than the source–substrate distance but that any further increases in mean free path beyond this have little effect. Heitmann concluded that the mean free path of the molecules is the important parameter, not the ratio of the numbers of evaporant molecules to residual gas molecules impinging on the substrate in unit time, which appeared to have no effect on refractive index. He also found that changes in the rate of deposition, from a quarter-wave in 0.5 min (measured at 632.8 nm) to a quarter-wave in 1.5 min, caused a decrease in refractive index of 0.6% in both cases, but that a further decrease to a quarter-wave in 5 min produced only slight variations.

Heitmann's results are probably best interpreted in terms of slight changes in film microstructure, induced by the variations in deposition conditions. Layer microstructure is, in fact, the most significant factor in determining the properties of optical thin films and the way in which they differ from the same material in bulk form. During the past two decades, there has been an increasing interest in the microstructure of, and microstructural effects in, optical thin films.

A useful technique for the study of thin-film structure, which immediately yielded important results, is electron microscopy. Its use in the examination of thin-film coatings has involved the development of techniques for fracturing multilayers and for replicating the exposed sections. Pearson, Lissberger, Pulker, and Guenther [2–5] have all made substantial contributions in this area and their results show that the layers in optical coatings have, almost invariably, a pronounced columnar structure, with the columns running across the films normal to the interfaces. To their investigations, we can add those of Movchan and Demchishin [6] and then Thornton [7,8], who investigated the effects of substrate temperature and, in Thornton's case, also residual gas pressure, on the microstructure of evaporated and sputtered films. This showed that a critical parameter in vacuum deposition of thin films is the ratio of the temperature of the substrate T_{sub} to the melting temperature T_{melt} of the evaporant. For values of this ratio lower than around 0.5, the structure of the layers is intensely columnar, the columns running along the direction of growth. Increased gas pressure forces the growth into a more pronounced columnar mode even for slightly higher values of substrate temperature.

Because the most useful materials in optical thin films are all of high melting point, substrate temperatures can never be higher than a small fraction of the evaporant melting temperature, and so the structure of thin films is almost invariably a columnar one, with the columns running along the direction of growth, normal to the film interfaces. The columns are several tens of nanometres across and roughly cylindrical in shape. They are packed in an approximately hexagonal fashion with gaps in between the columns, which take the form of pores running completely across the film, and there are large areas of column surface that define the pores and are in this way exposed to the surrounding atmosphere. The columnar structure of a film of zinc sulfide is shown in Figure 12.1 [9].

Packing density p defined as:

$$p = \frac{\text{Volume of solid part of film (i.e., columns)}}{\text{Total volume of film (i.e., pores plus columns)}}$$

It is a very important parameter. It is usually in the range 0.75–1.0 for optical thin films. For thermally evaporated thin films it is most often 0.8–0.95, and seldom as great as unity. A packing density that is less than unity reduces

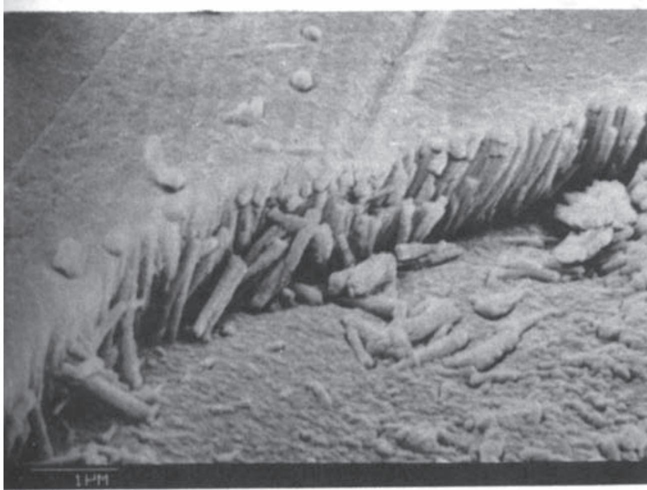

FIGURE 12.1
The columnar structure of a zinc sulfide film. Part of the film has been mechanically removed leaving the columnar structure visible in the cross section. (After Reid, I.M., Macleod, H.A., Henderson, E., and Carter, M.J., The ion plating of optical thin films for the infrared, in *Proc International Conference on Ion Plating and Allied Techniques (IPAT 79), London, July 1979,* CEP Consultants Ltd, Edinburgh, 55–62, 1979.)

the refractive index below that of the solid material of the columns. A useful expression that is reasonably accurate for films of low index [10,11] connects the index of the film n_f, that of the solid part of the film n_s, and of the voids n_v, with the packing density p:

$$n_f = pn_s + (1-p)n_v \tag{12.1}$$

The behavior of films of higher index, 2.0 and above, can be rather more complicated, but in many cases a linear law as in Equation 12.1 is sufficiently accurate and is, therefore, often used. If the value of packing density has been derived from optical measurements by using Equation 12.1, as is frequently the case, then, of course, the expression can, and should, be used. In any event, it gives an indication of the correct trend. For an alternative expression that is more complicated and can give a better fit in many of the more complicated cases, although still not always ideal, the paper by Harris and colleagues [11] can be consulted.

Packing density is a function of substrate temperature, usually, but not always, increasing with substrate temperature, and of residual gas pressure, decreasing with rising pressure. Film refractive index, therefore, is also affected by substrate temperature and residual gas pressure. The columns can vary in cross-sectional area as they grow outward from the substrate surface, which is one cause of film inhomogeneity. Substrate temperature is a difficult parameter to measure and to control so that consistency in technique, heating

for the same period each batch, identical rates of deposition, pumping for the same period before commencing deposition, and so on, is of major importance in ensuring a stable and reproducible process. Changing the substrate dimensions, especially substrate thickness, from one run to the next can cause appreciable changes in film properties. Such changes are even more marked in the case of reactive processes where the residual gas pressure is raised, and where a reaction between evaporant and residual atmosphere takes place at the growing surface of the film. Thus, it should not be surprising that a high proportion of test runs are required in any manufacturing sequence.

Various modeling studies [12–15] have confirmed that the columnar growth results from the limited mobility of the material on the surface of the growing film. It diffuses over the surface under thermal excitation until it is buried by arriving material. Diffusion through the bulk of the material is not significant. Thus lower substrate temperature and higher rates of deposition lead to more pronounced columns and reduced packing density. The energetic processes involve an element of bombardment of the growing films. The transfer of momentum drives the material deeper into the film and, although the columnar structure may persist to some extent, squeezes out the voids. The packing density is normally close to or equal to unity. The results of the higher packing density are almost all favorable. The consequences, described in this chapter, of the columnar microstructure are all less serious in the energetically deposited films. (See Figure 12.2 [16].)

A second level of microstructure in thin films is their crystalline state. Although this is less well understood, considerable progress has been made. Optical thin films are deposited from vapor that has been derived from sources at comparatively very high temperature. The substrates on which the films grow are at relatively very low temperature. There is therefore a great lack of equilibrium between growing film and arriving vapor. The film material is rapidly cooled or quenched, and this not only influences the formation of the columnar microstructure but it also affects the crystalline order. The material that is condensing will attempt to reach the equilibrium form appropriate to the temperature of the substrate, but the correct rearrangement of the molecules will take a certain time, and the film will tend to pass through the higher temperature forms during this rearrangement. If the rate of cooling is greater than the rate of crystallization, then a higher temperature form will be frozen into the layer. The very rapid cooling rate normally existing in thin films implies the presence of quite high temperature forms and there are often mixtures of phases. This explains an, at first sight, curious behavior of thin films. Frequently there is an inversion in the crystalline structure in that at low substrate temperatures a predominance of high temperature crystalline forms are found, whereas at high substrate temperatures, more low-temperature material appears to form. The low substrate temperature leads to a higher quench rate and the rest follows [17]. Amorphous forms, corresponding to a quite high temperature, can often be frozen by very rapid cooling, and are enhanced by a higher temperature

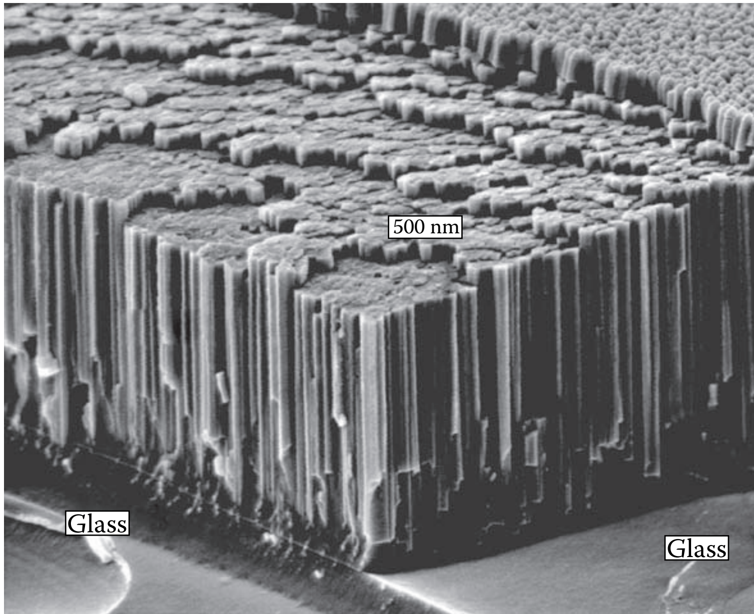

FIGURE 12.2
Compact microstructure of an aluminum oxynitride rugate structure deposited by radio frequency reactive sputtering of aluminum. The packing density is very high but some columnar features remain. The fractures at the outer surface tend to be in the nitrogen-rich parts of the rugate cycle leading to the stepped appearance. (Courtesy of Professor Frank Placido, University of the West of Scotland, Paisley, Scotland.)

of the arriving species. For example, sputtering, where additional kinetic energy is possessed by the arriving molecules, often gives amorphous films. The low voltage ion-plating technique, again with high incident energy, appears virtually invariably to give amorphous films. The high temperature forms are often only metastable and may change their structure at quite low temperatures leading to problems of various kinds. Some films deposited in amorphous form by sputtering may sometimes be induced to recrystallize, in a manner described as explosive, by a slight mechanical disturbance, such as a scratch, or by laser irradiation [18].

Samarium fluoride has two principal crystalline forms, a hexagonal high temperature form and an orthorhombic low-temperature form. Table 12.1 shows the results of thermal evaporation and ion-assisted deposition, which both lead to this apparently inverted structure [17]. Zirconia has three principal structures—monoclinic, tetragonal, and cubic—in ascending temperature. Klinger and Carniglia [19] found that very thin zirconia shows a cubic structure, but becomes monoclinic when thicker than a quarter-wave at 600 nm. This behavior can be explained by a lower rate of quenching when the film is thicker and less thermally conducting. Alumina, normally amorphous in thin-film form, can recrystallize in the electron microscope

TABLE 12.1

Samarium Fluoride (SmF_3) [17]

Normal high temperature form		Hexagonal
Normal low temperature form		Orthorhombic
Thermal evaporation	Substrate temperature of 100 °C	Hexagonal (111)
	Substrate temperature ≥200 °C	Orthorhombic (111) with some hexagonal
Ion-assisted deposition	Substrate temperature of 100 °C	Hexagonal (110) with some (111)
	Higher bombardment at substrate temperature 100 °C	Hexagonal (110) with appearance of new peak consistent with SmF_2 (111)

when subjected to the electron bombardment necessary for viewing [20]. Amorphous zirconia, which can occur when films are very thin, has been shown to exhibit similar behavior [21].

Thin films, therefore, are complicated mixtures of different crystalline phases, some being high-temperature metastable states. Such behavior is clearly very material and process dependent and each specific system requires individual study. What is a good structure for one application may not be so for another. The low scattering of the amorphous phases make them attractive for certain applications, but their high-temperature or high-flux behavior may not be as satisfactory. Much more needs to be done in attempting to improve our understanding.

The columnar structure and the crystalline structure can be considered as essentially regular intrinsic features of film microstructure. Then, in addition, there are defects that can be thought of as local disturbances of the intrinsic features. A principal and very important class of defect is the nodule. Nodules are inverted conical growths that propagate through the film or multilayer. They can occur in all processes. They start at a seed that is usually a very small defect or irregularity and it appears that virtually any irregularity, even minute ones, may act as a seed. Scratches on the substrate, pits, dust, contamination, material particles ejected from the source, loose accumulations of material in the vapor phase, perhaps even local electric charges, can all cause nodules to start growing. Once the nodule starts, it continues to grow until it forms a domed protrusion at the outer surface of the multilayer. The nodule itself is very much larger than the defect that causes it. It is not, in itself, a contaminant. It is made up of exactly the material of the remainder of the coating. It is simply growing in a different way. The outer surface of the nodule is a quite sharp boundary between it and the remainder of the coating. This sharp boundary is a region of weakness and there is frequently a fissure around the nodule, either partially or completely, and the nodule may sometimes be detached from the coating completely, leaving a hole behind. Nodules are present in almost all coatings. The only way of suppressing them appears to be a move toward perfection in the substrate, its surface and

its preparation, and in the coating deposition. The incidence of nodules over superpolished substrates, for example, is much reduced compared with conventional substrates. A typical nodule is shown in Figure 12.3 and the hole left by a detached nodule in Figure 12.4.

Variation in refractive index is not the only feature of film behavior associated with the columnar structure. The pores between the columns permit the penetration of atmospheric moisture into the film, where, at low relative humidity, it forms an adsorbed layer over the surfaces of the columns and, at medium relative humidity, actually fills the pores with liquid water due to capillary condensation. Moisture adsorption has been the subject of considerable study by Ogura [22,23], who used the variation in adsorption with relative humidity to derive information on the pore structure of the films. The moisture, since it has a different refractive index (around 1.33) from the 1.0 of the air that it displaces from the voids, causes an increase in the refractive index of the films. Since the geometrical thickness of the film does not change, the increase of film index during adsorption is accompanied by a corresponding increase in optical thickness. Exposure of a film to

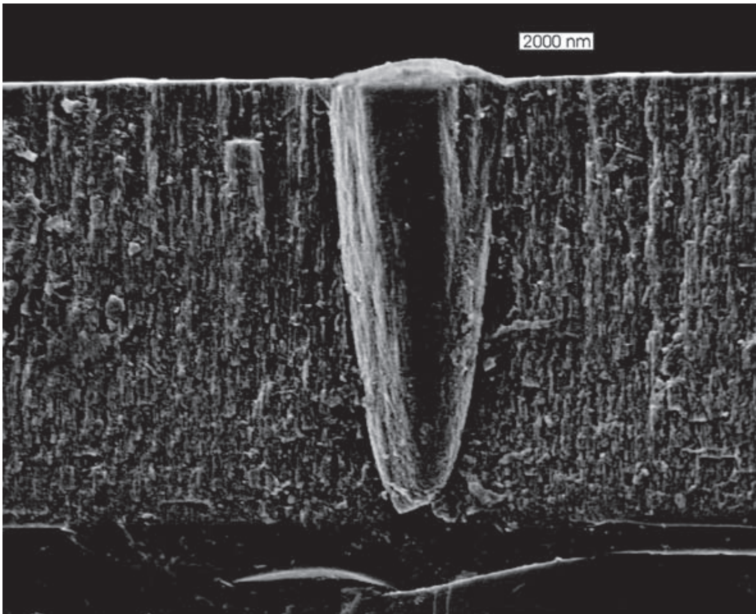

FIGURE 12.3
A nodule. The film is a rugate structure of aluminum oxynitride deposited by radiofrequency (RF) reactive sputtering of aluminum. The film has been broken across its width to show a cross-section that includes a complete nodule. The sharpness of the boundary is clear and the weakness is shown by the fact that the crack in the film circles around the nodule rather than passing through it. The shape and the domed protrusion at the outer surface (upper) of the film system are typical. (Courtesy of Professor Frank Placido, University of the West of Scotland, Paisley, Scotland.)

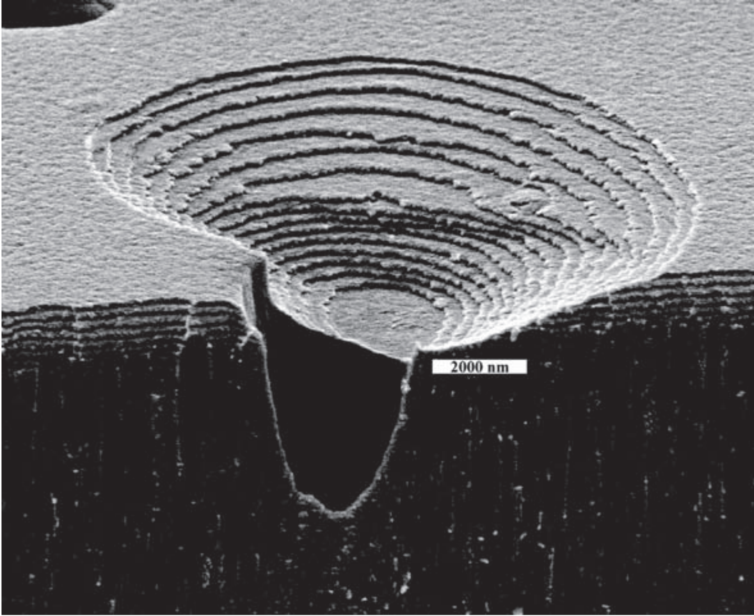

FIGURE 12.4
The hole left by the detachment of a nodule. Part of the outer part of the structure has been removed along with the nodule. The stepped appearance is once again caused by preferential cracking in the nitrogen-rich part of the aluminum oxynitride rugate structure. (Courtesy of Professor Frank Placido, University of the West of Scotland, Paisley, Scotland.)

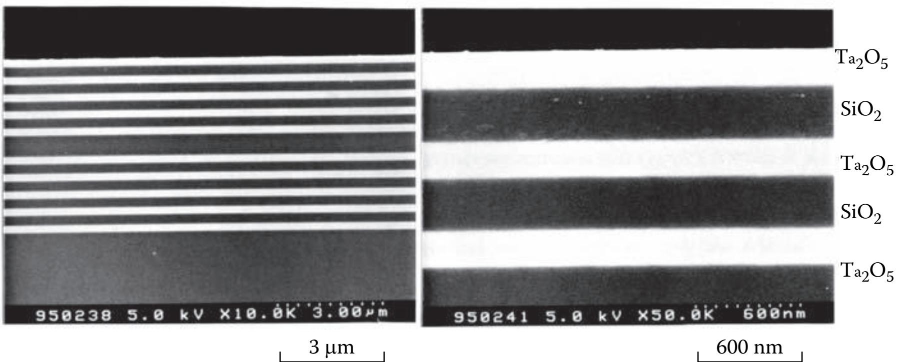

FIGURE 12.5
A micrograph showing the compact amorphous structure of a narrowband filter of silica and tantala produced by ion-assisted deposition using an RF ion-gun. (Courtesy of Shincron Co. Ltd., Tokyo, Japan.)

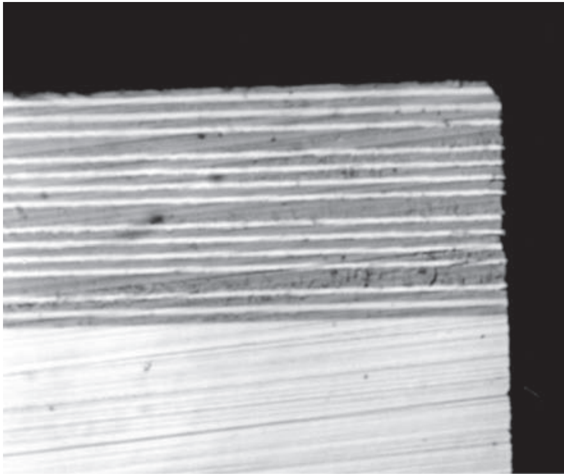

FIGURE 12.6
The structure of a multiple-cavity filter for the far infrared constructed from lead telluride and zinc sulfide. This particular filter was one of a set for the region 6–18 μm required to have a size of 1.2 mm × 0.45 mm for use in the High Resolution Dynamic Limb Sounder (HIRLDS) and the high quality of the diamond sawn edge of the component is clear from the micrograph. The scale of the micrograph can be assessed from the 4 μm physical thickness of the cavity layers. (Courtesy of Roger Hunneman, University of Reading, England.)

the atmosphere, therefore, usually results in a shift of the film characteristic to a longer wavelength. Such shifts in narrowband filters have been the subject of considerable study. Schildt et al. [24] found that for freshly prepared filters of zinc sulfide and magnesium fluoride, constructed for the region 400–500 nm, the variation in peak wavelength could be expressed as

$$\Delta\lambda = q \log_{10} p$$

where q is a constant varying from around 1.4 for filters that had aged, to around 8.3 for freshly prepared filters, and P is the partial pressure of water vapor measured in Torr (P should be replaced by $0.75 \times P$ if P is measured in mbar or $0.0075 \times P$ if P is measured in Pa) and $\Delta\lambda$ is measured in nm. $\Delta\lambda$ was arbitrarily chosen as zero when the pressure was 1 Torr (1.3 mbar or 133 Pa). This relationship was found to hold good for the pressure range 1 to approximately 20 Torr (1.3–26 mbar or 133–2660 Pa). The filters settled down to the new values of peak wavelength some 10–20 minutes after exposure to a new level of humidity began. They found that the shifted values of peak wavelength could be stabilized by cementing cover slips over the layers using an epoxy resin. Koch [25,26] showed that the characteristics of narrowband filters became quite unstable during adsorption until the filters reached an equilibrium state. Macleod and Richmond [27], Richmond [28], and Lee [29] have made detailed studies of the effects of adsorption on the characteristics of narrowband filters. The results are applicable to all types of multilayer coating.

The shifts in the characteristics are due, as we have seen, to the filling of the pores of the film with liquid water. In multilayers, the pores of one film are not always directly connected with the pores of the next, and the penetration of atmospheric moisture is frequently a slow and complex process in which a limited number of penetration pores take part, from which the moisture spreads across the coating in increasing circular patches. The primary entry points for the moisture are thought to be nodules where capillary condensation can take place in the fissures that often surround them. The coating may take several weeks to reach equilibrium and, afterwards, will exhibit some instability should the environmental conditions change. The patches, which can sometimes be seen with the naked eye as a flecked or mottled appearance, can be made more visible if the coating is viewed in monochromatic light, at or near a wavelength for which there is a rapid variation of transmittance (Figure 12.7). The edge of an edge filter, or the pass band of a narrowband filter, is especially suitable. Wet patches show a shift in wavelength that changes them from high to low transmittance, or vice versa, and they can be readily photographed as was done in Figure 12.8 and Figure 12.9.

The drift of the filters toward longer wavelengths, which occurs on exposure to the atmosphere, varies considerably in magnitude with both the materials and the spectral region and there is frequently considerable hysteresis on desorption. In the infrared, the layers are thick, and many of the semiconductor materials that are used as high-index layers have high packing density. This means that moisture-induced drift is less of a general problem than it is in the visible and ultraviolet regions of the spectrum, although it is important in some applications. In the visible region, drifts can be as high as 10 nm, and sometimes greater, toward longer wavelengths. The gradual stabilization of the coating as it reaches equilibrium is frequently referred to as ageing or settling. The energetic processes can usually suppress completely the moisture-induced drifts and have been almost universally adopted for suitable coatings. It should be noted, however, that not all materials respond well to the brutal bombardment that is characteristic of the energetic processes. Metals suffer from the inevitable implantation of the bombarding species. Their optical properties are degraded by the scattering

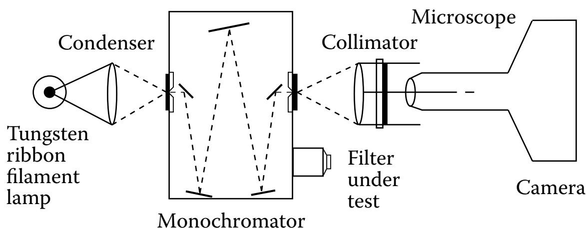

FIGURE 12.7
Sketch of the apparatus for observing moisture-penetration patterns in a multilayer of zinc sulfide and cryolite. Short slits that are virtually pin holes are used in the monochromator. (After Macleod, H.A. and Richmond, D., *Thin Solid Films*, 37, 163–169, 1976.)

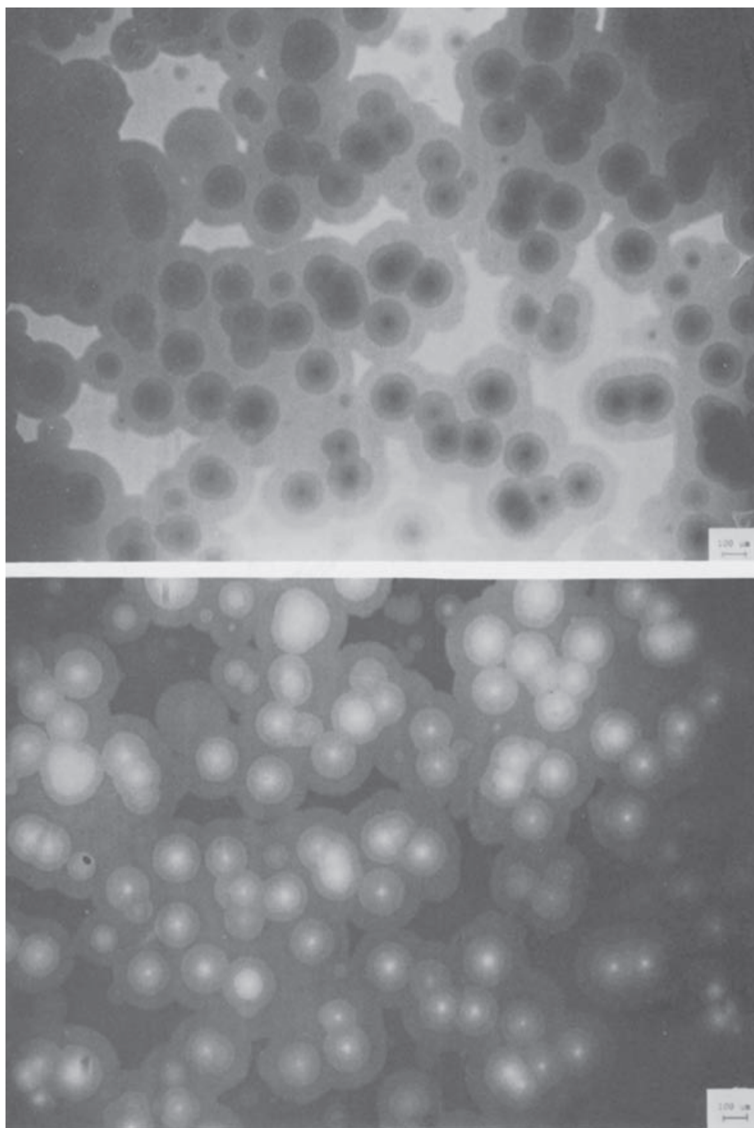

FIGURE 12.8
Photograph of moisture-penetration patterns in a zinc sulfide and cryolite filter some two weeks after coating. The relative humidity was approximately 50% during this time. The upper photograph was taken at a wavelength of 488.5 nm and the lower at 512.8 nm. The dark patches of the upper photograph correspond to the light patches of the lower showing that a wavelength shift rather than absorption is responsible for the patterns. (After Lee, C.C. Moisture adsorption and optical instability in thin film coatings, PhD Dissertation, University of Arizona, 1983.)

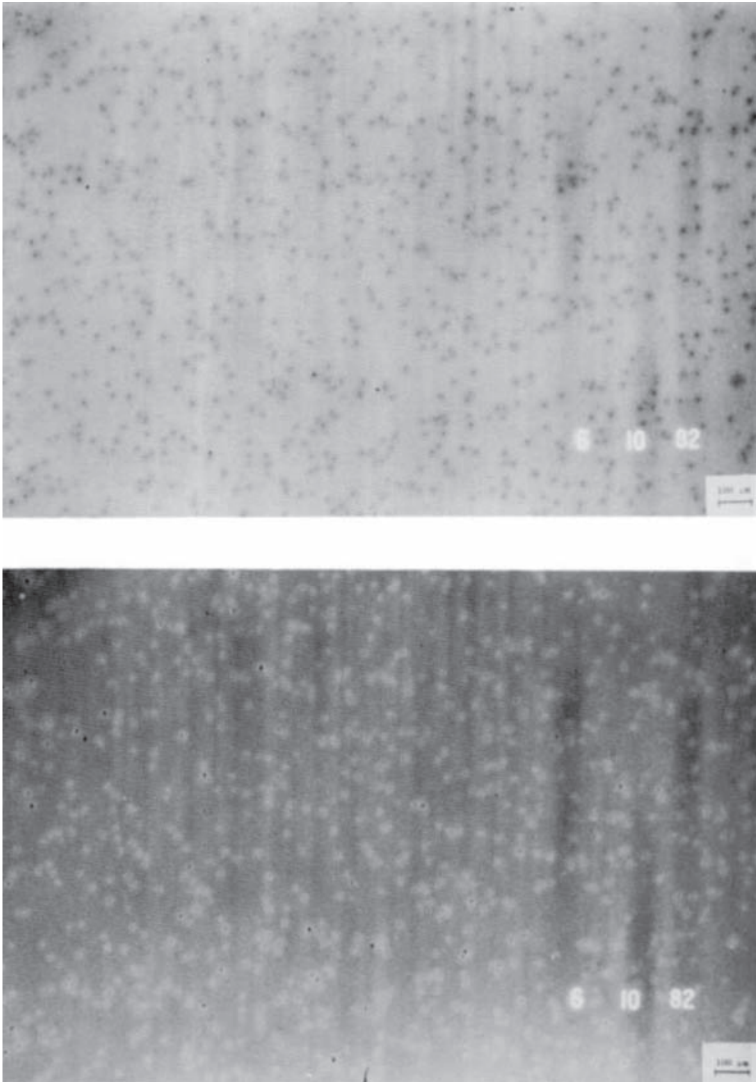

FIGURE 12.9
Moisture-penetration patterns in a multilayer of zirconium dioxide and silicon dioxide. The photographs were taken immediately after removal from the coating chamber. The wavelength for the upper photograph was 543 nm, and that for the lower 553 nm. (After Lee, C.C. Moisture adsorption and optical instability in thin film coatings, PhD Dissertation, University of Arizona, 1983.)

of conduction electrons that results. Fluorides lose fluorine and so the bombardment must be strictly limited otherwise the concentration of vacancy defects becomes too great. Oxygen tends to fill the vacancies and form oxyfluorides that are neither as rugged as the original fluorides nor as useful in the ultraviolet.

It is not simply in generating optical shifts that moisture is a problem for coatings. It has major mechanical and sometimes chemical effects as well. The stress in the coating is transmitted across the gaps between the columns, again by short-range forces. These forces can be very easily blocked by water molecules. An alternative explanation of the phenomenon is that the moisture, which coats the surfaces of the columns, reduces the surface energy to something approaching that of liquid water. Since the surface energy is an important factor in the stress/strain balance in the film, the result of the moisture adsorption is a change in the stress level. The stress is usually tensile and the moisture reduces it, usually significantly. We have already mentioned Pulker's work [30] on impurities in thin films and their reduction of stress levels in a similar way. Adhesion, too, is affected by moisture. The materials used for thin films have usually very high surface energies and then the work of adhesion is correspondingly high. The presence of liquid water in a film can cause a reduction in the surface energy of the exposed surfaces of at least an order of magnitude. If water is present at the site of an adhesion failure and can take part in a process of bond transfer, rather than bond rupture followed by adsorption, then it will reduce the work of adhesion, and it is more likely that the failure will propagate. There is frequently enough strain energy in a film to supply the required work. The penetration sites for the moisture patches are probably associated with defects that may act as stress concentrators where adhesion failures driven by the internal strain energy in the films may originate. All the ingredients for a moisture-assisted adhesion failure are present and it is frequently at such sites that delamination is first observed. Blistering is a similar form of adhesion failure frequently associated with moisture penetration sites and a compressively strained film. Uniform strain in a film is translated into a shear stress across its interface that is zero in the center and a maximum at the edge. Thus, the edges of a coating are particularly vulnerable. Defects at the edge act as stress concentrators and if the forces are sufficiently high, delamination can begin and gradually propagate from the edge across the film. The presence of moisture encourages such failures. It is important, therefore, that defects at the edge of a coating should be kept to an absolute minimum. Great care should be taken with the fixtures that hold the substrates in place during the coating operation. It is very important that they should be designed to avoid any small scratches or other damage to the edges of the substrates.

We have already mentioned in Chapter 7 that changes in temperature cause changes in the spectral characteristics of coatings, narrowband filters having characteristics that are probably most sensitive to such alterations. We must divide the coatings into those that have been simply thermally evaporated and those that have been produced by an energetic process.

Most of the work that has been reported so far in this chapter has been in respect of conventionally thermally evaporated coatings. For small temperature changes, the principal effect is a simple shift toward longer wavelengths with increasing temperature. For the materials commonly used in the visible

region of the spectrum, the shift is of the order of 0.003% °C^{-1}, while for infrared filters it can be greater, and a useful figure is 0.005% °C^{-1}, although it can be as high as 0.0125% °C^{-1}. It must be emphasized that these figures depend strongly on the particular materials used. Filters of lead telluride and zinc sulfide can actually have negative coefficients greater than 0.01% °C^{-1} and, using these materials, it is even possible to design a filter that has zero temperature coefficient [31]. With greater positive changes of, say, 60 °C or more, it is usual for any moisture in the filter to desorb partially, causing an abrupt shift toward shorter wavelengths (see Figure 12.10). This shift is not recovered immediately on cooling to room temperature, and so considerable hysteresis is apparent in the behavior [32]. Subsequent temperature cycling, before readsorption of any moisture, will then exhibit no hysteresis. Eventually, if maintained at room temperature, the filter will readsorb moisture and drift gradually back to its initial wavelength. Exposure to higher temperatures still, over 100 °C, can cause permanent changes that appear to be related to minute alterations in the structure of the layers, altering the adsorption behavior so that some materials become less ready to adsorb moisture while others show more rapid adsorption [27–29]. A frequently applied empirical treatment, already mentioned in Chapter 11, involves baking of filters at elevated temperatures, usually several

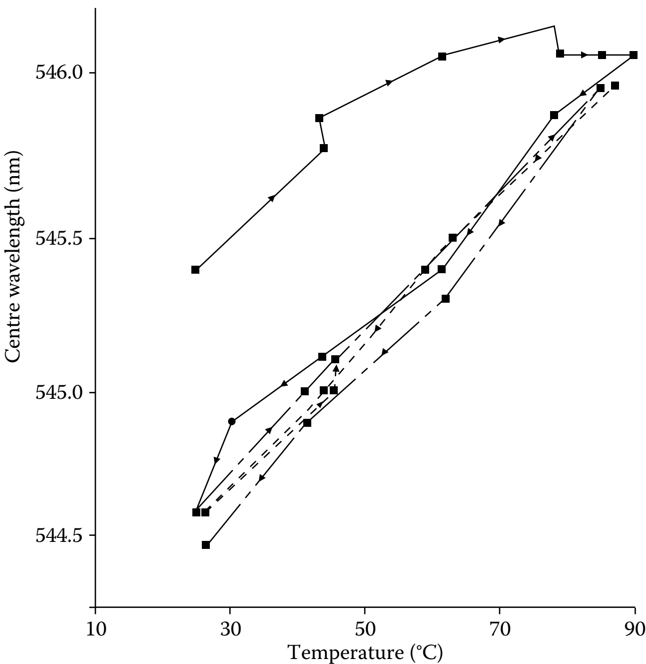

FIGURE 12.10
Record of the variation of peak wavelength with temperature for a filter of design: Air|$(HL)^4$ $6H$ $(LH)^4$|Glass with L = cryolite and H = zinc sulfide. (After Roche, P., Bertrand, L., and Pelletier, E., *Optica Acta*, 21, 927–946, 1974.)

hundred degrees Celsius, for some hours. The baking process reduces residual absorption, particularly in reactively deposited oxide films, and improves the subsequent stability of the coatings. Part of the baking process appears to involve the opening up of the pores in the films, by smoothing out restrictions, so that moisture adsorption processes are more rapid and the films reach equilibrium in normal atmospheres much more quickly.

Films that have been deposited by the energetic processes usually exhibit lower temperature coefficients than thermally evaporated, even when the effects of moisture desorption and adsorption in the conventional films are eliminated. This is, at first sight, a quite surprising result. However, the explanation appears to lie in the microstructure. The lateral thermal expansion of the loosely packed columns in the thermally evaporated films enhances the drifts due to temperature changes. In the energetically deposited films, the material is virtually bulk-like in that there are no voids in between any residual columns and so the material exhibits bulk-like properties. The change in characteristics with a change in temperature now corresponds to what would be expected from bulk materials. Indeed, Takahashi [33] has shown that for multiple-cavity narrowband filters, once the design and materials are chosen, the expansion coefficient of the substrate dominates the behavior and can even change the sense of the induced spectral shift. The stress induced in the coating by the differential lateral expansion and contraction of substrate and coating is translated by Poisson's ratio into a swelling or reduction normal to the film surfaces. As a result of this modeling and improved understanding, temperature coefficients of peak wavelength shift at 1550 nm of 3 pm $°C^{-1}$ (pm is picometre, i.e., 0.001 nm, so that 3 pm $°C^{-1}$ at 1550 nm represents 0.0002% $°C^{-1}$) have routinely been achieved in energetically deposited tantala/silica filters for communication purposes and shifts even lower than 1 pm $°C^{-1}$ are possible. The Takahashi model has been further elaborated by Kim and Hwangbo [34].

Coatings that are subjected to very low temperatures usually shift toward shorter wavelengths, consistent with their behavior at elevated temperatures. The actual coatings are not usually affected mechanically. The substrates tend to be more vulnerable. Laminated components, particularly, run the risk of breaking because of differential contraction and/or expansion.

There are losses associated with all layers, which can be divided into scattering and absorption. In absorption, the energy, which is lost from the primary beam, is dissipated within the coating and usually appears as heat. In scattering, the flux lost is deflected and either re-emerges from the coating in a different direction or is trapped beyond the critical angle within the coating or substrate. Absorption is a material property that may be intrinsic or due to impurities. A deficiency of oxygen, for example, can cause absorption in most of the refractory oxide materials. Scattering is usually due to defects in the coating that can be classified into volume or surface defects. Surface defects are simply a departure from the smooth flat surfaces of the ideal film. Such departures can be due to roughness of the substrate surface that tends to be reproduced at each interface in a multilayer, or to the

columnar structure of the layers that results in a nodular appearance of the film boundaries. Volume defects are local variations of optical constants and are usually dust particles, pinholes or fissures in the coating. Losses in thin films are of particular importance in the laser field where they determine the limiting performance of multilayers. A major problem in the production of high-quality laser coatings is dust that emanates from the sources and from the powdery deposit that forms on the cold walls of the chamber. If this dust can be eliminated, only possible if the strictest attention is paid to detail and the most involved precautions are taken, then the remaining source of scattering loss is the roughness of the interfaces between the layers and between multilayer and substrate. If great care is exercised, then, in the visible and near infrared regions, the total losses, that is, absorption and scattering, can be reduced below 0.001% (for some very special applications losses toward one-tenth of this figure have been achieved) and the power handling capability of the coatings can be of the order of 5 J cm^{-2} for pulses of 1 ns or less at 1.06 μm. Useful surveys of scattering in thin-film systems have been written by Duparré [35–37] and by Amra [38,39].

Laser damage is still a very active research topic. The best bulk crystals can exhibit intrinsic damage thresholds that are ultimately connected with multiphoton events causing the raising of electrons into the conduction band. Damage in thin-film systems, on the other hand, is dominated by the defects in the films so that the intrinsic level is not reached. In continuous wave applications, particularly in the infrared, thermal effects associated with absorption, either local or general, appear to be the principal source of damage, small defects appearing less important. In most other cases local defects are the problem. The particular nature of the defects may vary considerably, from inclusions to cracks or fissures, but considerable attention in recent years has been paid to the nodules that tend to grow through the films from any substrate imperfections. These nodules are poorly connected thermally to the film and this is suspected to be an important factor in the initiation of damage. In those spectral regions where water absorbs strongly, considerable importance is attached to the presence of liquid water within the films. In other parts of the spectrum, its role is less clear, but it may well play a part. Laser damage has been surveyed recently by Koslowski [40] and by Stolz and Génin [41].

12.2 Sensitivity to Contamination

Optical coatings are rarely used in an ideal environment. They are subjected to all kinds of environmental disturbances ranging from abrasion to high temperature and humidity. These cause performance degradation that mostly originates in an actual irreversible and usually visible destruction of

the layers. However, performance may be degraded in a rather less spectacular way by the simple acquisition of a contaminant that may have no aggressive effect on the layers other than a reduction of the level of performance of the coating as a whole. The action of water vapor that is adsorbed by a process of capillary condensation and causes a spectral shift of the coating is well known. Here we are concerned with much smaller amounts of absorbing material, such as carbon, in the form of submolecular thicknesses either at some point during the construction of the coating or, more usually, over the surface after deposition.

Although there are many tests for the assessment of the resistance of a coating to most environmental disturbances, there is no standard test for the measurement of susceptibility to contamination. Yet it can be shown that the response of coatings can vary enormously, depending on many factors including design, wavelength, and even on errors committed during deposition. The reason may be that, often, careful cleaning will restore the performance but this does not avoid the degradation in between cleanings, and cleanings that are more frequent are required for coatings that are more susceptible.

Fortunately, it is possible to make some predictions of coating response to low levels of contamination and, especially, to make assessments of comparative sensitivity [42,43]. Electric field distribution and potential absorption are the keys to understanding the phenomenon.

If the contamination layer is on the front surface, then it receives the full irradiance that enters the multilayer, and the admittance at the contamination layer determines the reflectance as well as the potential absorptance. The key expressions involving absorptance, A, and potential absorptance, $\mathcal{A}$, have already been derived in Chapter 2.

$$\mathcal{A} = \left(\frac{2\pi nkd}{\lambda}\right)\left(\frac{2}{\mathrm{Re}(Y)}\right) \tag{12.2}$$

and

$$A = (1-R)\mathcal{A} \tag{12.3}$$

Then we can write

$$\begin{aligned} A &= (1-R)\mathcal{A} \\ &= \left(\frac{4\pi nkd}{\lambda}\right)\left(\frac{1}{\mathrm{Re}(Y)}\right)\left\{1-\frac{\left[y_0-\mathrm{Re}(Y)\right]^2+\left[\mathrm{Im}(Y)\right]^2}{\left[y_0+\mathrm{Re}(Y)\right]^2+\left[\mathrm{Im}(Y)\right]^2}\right\} \\ &= \left(\frac{4\pi nkd}{\lambda}\right)\left\{\frac{4y_0}{\left[y_0+\mathrm{Re}(Y)\right]^2+\left[\mathrm{Im}(Y)\right]^2}\right\} \end{aligned} \tag{12.4}$$

and Equation 12.4 permits us to put on the admittance diagram contours of absorption due to contamination on the outer surface. Before we draw actual lines, we need to define some of the quantities. It is simplest to use numbers that allow us to scale the diagram easily. We therefore simplify the expression by defining H (not magnetic field) by:

$$H = \frac{4\pi nkd}{\lambda} \tag{12.5}$$

and replacing Y by $x - iz$, then we find

$$\frac{A}{H} = \frac{4y_0}{(y_0 + x)^2 + z^2} \tag{12.6}$$

H is a measure of the absorption capacity of the film, while A is the actual absorptance. We can think of A/H as a measure of the sensitivity to absorptance of an optical coating [44]. This sensitivity is purely a function of the optical admittance of the complete coating. Further, from Expression 12.6, contours of constant sensitivity are circles in the admittance plane that are centered on the point $-y_0$ and exhibit decreasing sensitivity with increasing radius.

To simplify matters still further we take the value of y_0 as 1.00. The contour lines for this case are then as shown in Figure 12.11.

As an example of the magnitude of H we can take the values of amorphous carbon given by Palik [45–47], that is optical constants of $2.26 - i1.025$ at 1000 nm, and assume a thickness of 0.1 nm. A plot of H is shown in Figure 12.12 and over most of the wavelength region shown, it is between 0.003 and 0.006.

Antireflection coatings all attempt to terminate their loci at the point $(y_0, 0)$. This implies a value of A/H of $1/(y_0)$, that is 1.00 for y_0 of unity, and, from Figure 12.12, this gives, for a perfect antireflection coating, a range of absorptance across the visible region from around 0.3%–0.6% with a film of carbon 0.1 nm thick. A slightly less than perfect coating will exhibit figures a little greater or less than these. It all depends on the admittance at termination. Typical results for a four-layer antireflection coating over the visible region are shown in Figure 12.13. The design of the coating has little influence on this result and all coatings that have precisely zero reflectance will have exactly the same level of sensitivity.

Reflectors exhibit much greater variation. A dielectric reflector that is made up of quarter-wave layers and terminates with a final high-admittance layer will end its locus to the far right of the diagram and the sensitivity to contamination will be much reduced. This, however, is not so for extended-zone high-reflectance coatings. In such coatings, at least part of the high-reflectance zone involves the inner part of the coating, and the outer part exhibits an admittance that circles around from far to the right to very near the imaginary axis. The value of A/H can then be almost as large as

FIGURE 12.11
Circles of constant contamination sensitivity in the admittance plane calculated for an incident admittance of 1.0. Greatest sensitivity corresponds to the origin where the value is 4.0. (From Macleod, A., *SVC News Bulletin* 24, 25, 28, 2006. With permission.)

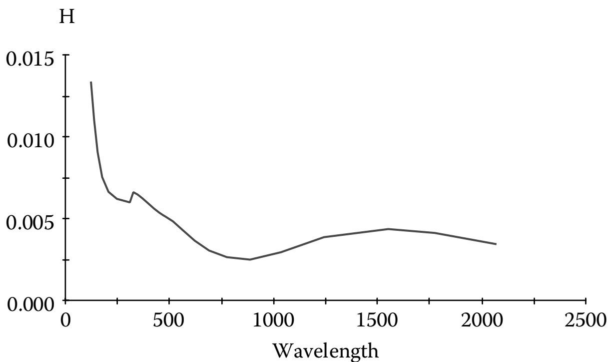

FIGURE 12.12
Plot of H against wavelength for 0.1-nm thickness of carbon film.

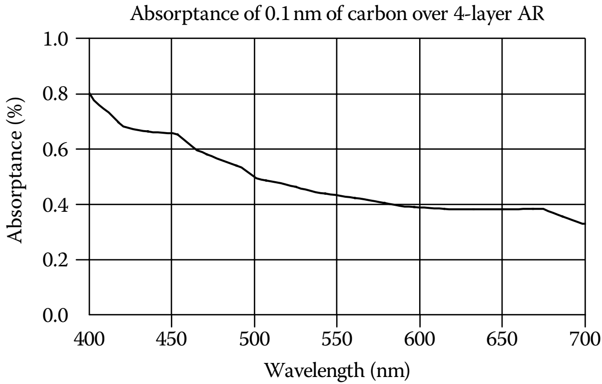

FIGURE 12.13
The absorptance produced by a layer of carbon of thickness 0.1 nm in front of a four-layer antireflection (AR) coating for the visible region.

4.0 so that over parts of the visible region the absorptance due to the 0.1 nm thickness of carbon can rise to between 1.0% and 2.0%. This is illustrated by a 39-layer extended zone reflector with performance as in Figure 12.14 and absorptance behavior as in Figure 12.15.

Aluminum reflectors are normally protected by a thin layer of low index, most often a half-wave in thickness, although a quarter-wave may also be used. The quarter-wave thickness gives a greater fall in reflectance at the reference wavelength and also a higher electric field. The sensitivity to contamination of the two coatings is quite different and shown in Figure 12.16.

The simple quarter-wave stack is of enormous importance as the most common high-performance reflector. We have seen how poor the extended-zone high reflector is. What can we deduce about the quarter-wave stack? We can take the contamination figures as at 1000 nm. At the center wavelength,

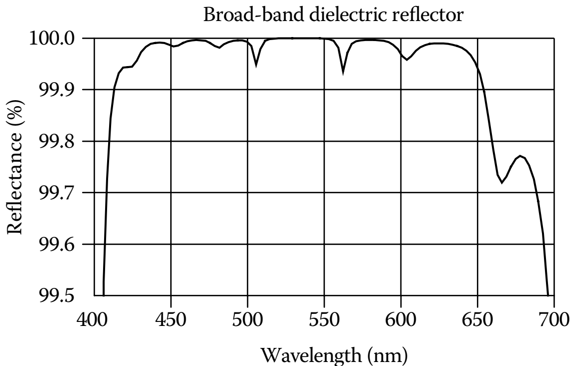

FIGURE 12.14
The reflectance of an extended-zone high-reflectance coating for the visible region. The coating consists of two mutually displaced quarter-wave stacks making up a total of 39 layers.

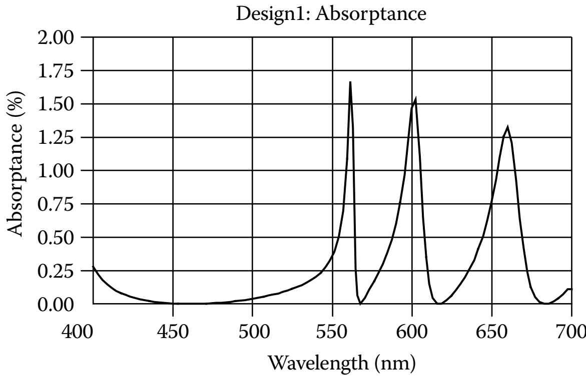

FIGURE 12.15
The absorptance produced by 0.1 nm of carbon deposited over the outer surface of the reflector of Figure 12.14.

where all layers are quarter-waves, the admittance presented by a quarter-wave stack, Y, is real. The absorptance of the layer, using the 1000-nm figures and assuming air as incident medium, is therefore given from Equations 12.5 and 12.6, by

$$A = \frac{0.0116}{(1+Y)^2} \tag{12.7}$$

We take a quarter-wave stack of silica and titania and calculate the absorptance as a function of the (odd) number of layers assuming titania outermost. The result is shown as the dashed line in Figure 12.17. The results were also calculated using the full matrix theory. Agreement is excellent up to

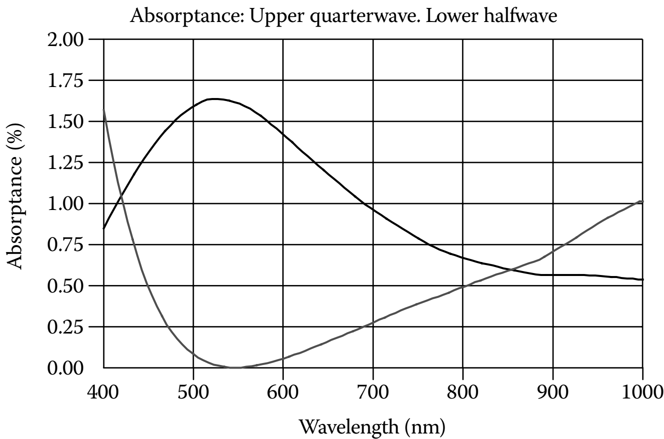

FIGURE 12.16
Effect of contamination by 0.1 nm thick film of carbon on aluminum reflector with quarter-wave of silica protecting layer (*upper curve*) and half-wave of silica (*lower curve*).

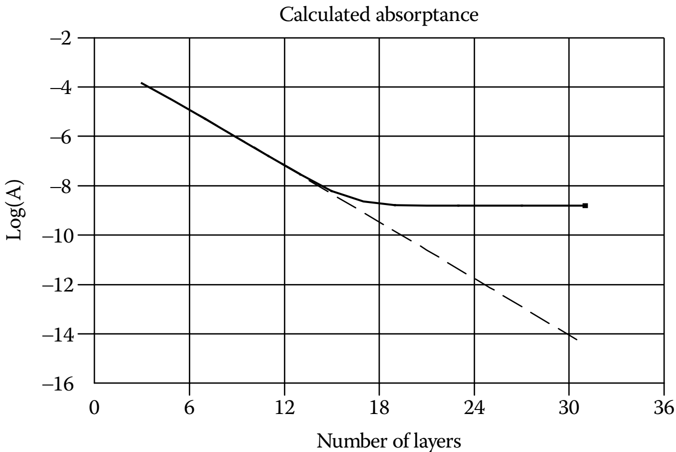

FIGURE 12.17
The predicted absorptance, plotted as log(A), of a quarter-wave stack as a function of the odd number of layers. The dashed line is the simple theory. The full line is calculated using the full matrix theory.

around 15 layers and then the full calculation shows a leveling off. The effect is due to the failure of the thin-layer approximation. The admittance locus of the very thin contamination layer is shifted to the extreme right and now, even though it is exceedingly thin, it swings round toward the imaginary axis. The potential absorptance rises and, when multiplied by the decreasing $(1 - R)$ factor, a constant is obtained. This constant level is very small, less than 10 parts per billion. Equation (12.7) shows that for a quarter-wave stack terminated by a low-admittance layer, where Y would be very small, that the limiting absorptance would be 0.0116, or 1.16%. Accurate calculation confirms this.

As the wavelength changes, however, the admittance locus for the quarter-wave stack begins to unwind. The major effect is that the value of Re(Y) decreases. This is accompanied by a slight decrease also in reflectance. The result is a considerable increase in the level of absorption associated with the contamination layer. Figure 12.18 shows the rapid increase in absorptance up to 500 parts per million from the less than 10 parts per billion at the center wavelength.

Thermally evaporated coatings are known to be affected by moisture. The moisture enters in localized spots and spreads out in the form of circular patches of increasing diameter. This changes the field distribution in a coating and therefore alters the absorptance associated with a contamination layer (Figure 12.18). Monitoring errors that have no perceptible effect on the reflectance of a quarter-wave stack can have major effects on the sensitivity to contamination.

Some additional information on contamination sensitivity at interfaces within the coating are included in the article by Macleod and Clark [42].

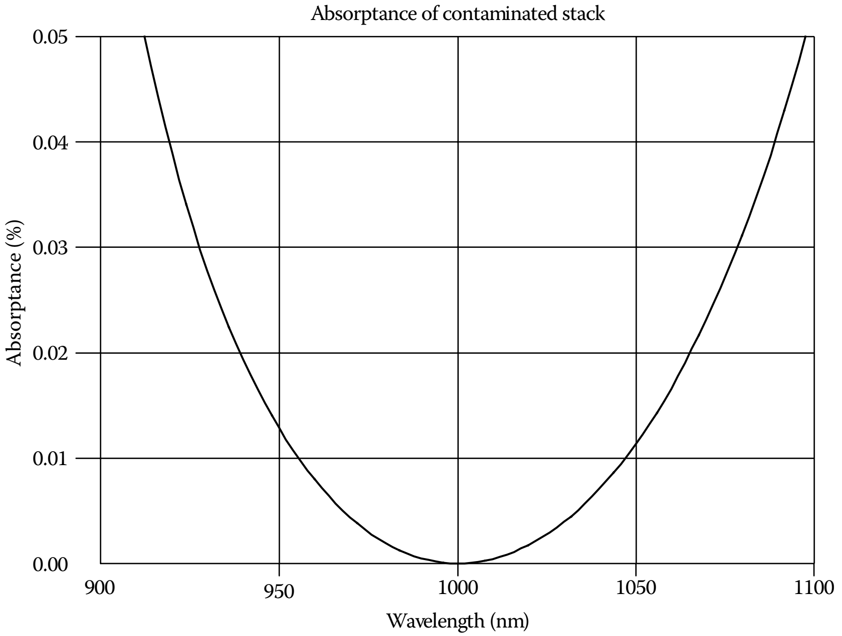

FIGURE 12.18
Absorptance of the quarter-wave stack with contamination layer as a function of wavelength.

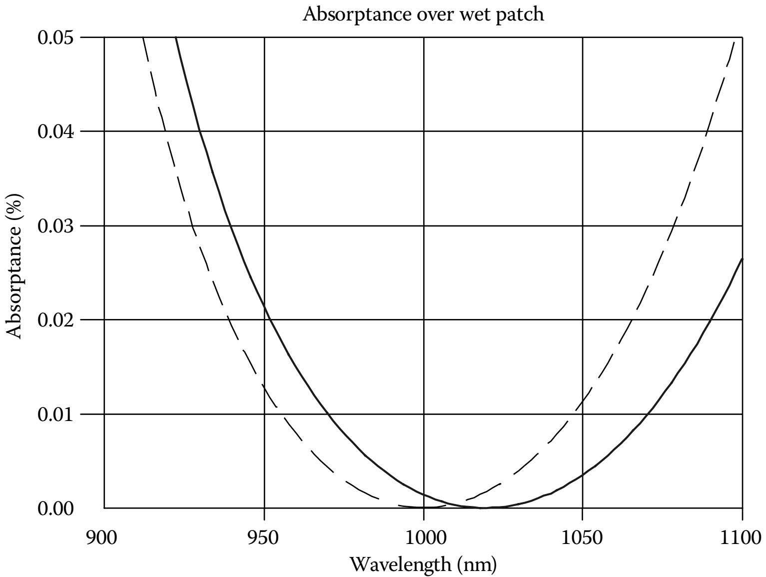

FIGURE 12.19
The *bold line* shows absorptance of a contamination layer over a wet patch in a quarter-wave stack. The *dashed line* shows the absorptance when deposited over a dry area.

References

1. Heitmann W 1968 The influence of various parameters on the refractive index of evaporated dielectric thin films *Applied Optics* **7** 1541–1543
2. Pearson J M 1970 Electron microscopy of multilayer thin films *Thin Solid Films* **6** 349–358
3. Lissberger P H and Pearson J M 1976 The performance and structural properties of multilayer optical filters *Thin Solid Films* **34** 349–355
4. Pulker H K and Jung E 1971 Correlation between film structure and sorption behaviour of vapour deposited ZnS, cryolite and MgF2 films *Thin Solid Films* **9** 57–66
5. Pulker H K and Guenther K H 1972 Electron optical investigation of cross-sectional structure of vacuum-deposited multilayer systems *Vakuum-Technik* **21** 201–207
6. Movchan B A and Demchishin A V 1969 Study of the structure and properties of thick vacuum condensates of nickel, titanium, tungsten, aluminium oxide and zirconium dioxide *Fiz Metal Metalloved* **28** 653–660
7. Thornton J A 1974 Influence of apparatus geometry and deposition conditions on the structure and topography of thick sputtered coatings *Journal of Vacuum Science and Technology* **11** 666–670
8. Thornton J A 1986 The microstructure of sputter-deposited coatings *Journal of Vacuum Science and Technology, A* **4** 3059–3065
9. Reid I M, Macleod H A, Henderson E, and Carter M J 1979 *The ion plating of optical thin films for the infrared*, in *Proc International Conference on Ion Plating and Allied Techniques (IPAT 79), London, July 1979* (Edinburgh: CEP Consultants Ltd) 55–62
10. Kinosita K and Nishibori M 1969 Porosity of MgF2 films—evaluation based on changes in refractive index due to adsorption of vapors *Journal of Vacuum Science and Technology* **6** 730–733
11. Harris M, Macleod H A, Ogura S, Pelletier E, and Vidal B 1979 The relationship between optical inhomogeneity and film structure *Thin Solid Films* **57** 173–178
12. Müller K-H 1986 Model for ion-assisted thin-film densification *Journal of Applied Physics* **59** 2803–2807
13. Müller K-H 1988 Models for microstructure evolution during optical thin film growth *Proceedings of the Society of Photo-Optical Instrumentation Engineers* **821** 36–44
14. Sargent R B 1990 Effects of surface diffusion on thin-film morphology: a computer study *Proceedings of the Society of Photo-Optical Instrumentation Engineers* **1324** 13–31
15. Sargent R B 1989 *Surface diffusion: A computer study of its effects on thin film morphology* PhD Dissertation University of Arizona
16. Placido F 1997 *RF sputtering of aluminium oxynitride rugates. Micrographs of rugate structures.* University of the West of Scotland, *Scotland,* Private Communication
17. Lingg L J 1990 *Lanthanide trifluoride thin films: structure, composition and optical properties* PhD Dissertation University of Arizona
18. Messier R, Takamori T, and Roy R 1975 Observations on the "explosive" crystallization of non-crystalline Ge *Solid State Communications* **16** 311–314
19. Klinger R E and Carniglia C K 1985 Optical and crystalline inhomogeneity in evaporated zirconia films *Applied Optics* **24** 3184–3187

20. Targove J D 1987 *The ion-assisted deposition of optical thin films* PhD Dissertation University of Arizona
21. Boulesteix C and Lottiaux M 1987 *Behavior of zirconia film in electron microscope* University of Aix-Marseille III, Marseille, France Private Communication
22. Ogura S 1975 *Some features of the behaviour of optical thin films* PhD Thesis Newcastle upon Tyne Polytechnic
23. Ogura S and Macleod H A 1976 Water sorption phenomena in optical thin films *Thin Solid Films* **34** 371–375
24. Schildt J, Steudel A, and Walther H 1967 The variation of the transmission wavelength of interference filters by the influence of water vapour *Journal de Physique* **28** C2/276–C2/279
25. Koch H 1965 Optische Untersuchungen zur Wasserdampfsorption in Aufdampfschichten (inbesondere in MgF2 Schichten) *Physica Status Solidi* **12** 533–543
26. Koch H 1967 *Über Sorptionsvorgänge beim Belüften von MgF2 Schichten*, in *Proc Coll on Thin Films, Budapest, 1965* (Budapest: Verlag: Kultura) 199–203
27. Macleod H A and Richmond D 1976 Moisture penetration patterns in thin films *Thin Solid Films* **37** 163–169
28. Richmond D 1976 *Thin film narrow band optical filters* PhD Thesis Newcastle upon Tyne Polytechnic
29. Lee C C 1983 *Moisture adsorption and optical instability in thin film coatings* PhD Dissertation University of Arizona
30. Pulker H K 1982 Stress, adherence, hardness and density of optical thin films *Proceedings of the Society of Photo-Optical Instrumentation Engineers* **325** 84–92
31. Seeley J S, Hunneman R, and Whatley A 1981 Far infrared filters for the Galileo-Jupiter and other missions *Applied Optics* **20** 31–39
32. Roche P, Bertrand L, and Pelletier E 1974 Influence of temperature on the optical properties of narrowband optical filters *Optica Acta* **21** 927–946
33. Takashashi H 1995 Temperature stability of thin-film narrow-bandpass filters produced by ion-assisted deposition *Applied Optics* **34** 667–675
34. Kim S-H and Hwangbo C K 2004 Temperature dependence of transmission center wavelength of narrow bandpass filters prepared by plasma ion-assisted deposition *Journal of the Korean Physical Society* **45** 93–98
35. Duparré A and Kassam S 1993 Relation between light scattering and microstructure of optical thin films *Applied Optics* **32** 5475–5480
36. Duparré A 1995 *Light scattering of thin dielectric films*, in *Handbook of Optical Properties. Volume 1. Thin Films for Optical Coatings* Hummel R E and Guenther K H Editors (Boca Raton: CRC Press Inc) 273–303
37. Duparré A and Kaiser N 1998 AFM helps engineer low-scatter films *Laser Focus World* **34** (4) 147–152
38. Amra C 1993 From light scattering to the microstructure of thin-film multilayers *Applied Optics* **32** 5481–5491
39. Amra C 1995 *Introduction to light scattering in multilayer optics*, in *Thin Films for Optical Systems* Flory F R Editor (New York, Basel, Hong Kong: Marcel Dekker, Inc) 367–391
40. Koslowski M 1995 *Damage-resistant laser coatings*, in *Thin Films for Optical Systems* Flory F R Editor (New York, Basel, Hong Kong: Marcel Dekker, Inc) 521–549
41. Stolz C J and Génin F Y 2003 *Laser resistant coatings*, in *Optical Interference Coatings* Kaiser N and Pulker H K Editors (Berlin: Springer-Verlag) 310–333

42. Macleod A and Clark C 1997 *How sensitive are coatings to contamination?* in *Eleventh International Conference on Vacuum Web Coatings Miami, Florida* Bakish Materials Corporation, New Jersey 176–186
43. Macleod H A and Clark C 1997 *Electric field distribution as a tool in optical coating design* in *40th Annual Technical Conference Proceedings New Orleans* Society of Vacuum Coaters 221–226
44. Macleod A 2006 Potential transmittance *SVC News Bulletin* 24, 25, 28
45. Palik E D ed 1985 *Handbook of Optical Constants of Solids* (New York: Academic Press Inc)
46. Palik E D 1991 *Handbook of Optical Constants of Solids II* (San Diego/London: Academic Press)
47. Palik E D 1998 *Handbook of Optical Constants of Solids III* (San Diego/London: Academic Press)

13

Layer Uniformity and Thickness Monitoring

In the previous chapter we considered what is probably the most difficult aspect of thin-film coating and filter production, that of materials. As we saw, these are not always satisfactory, and there are still problems associated with their stability. Once the materials have been chosen, and their properties are known, the thin-film designer, using the methods discussed in Chapters 4–9, can usually produce a design to meet a given specification. Given suitable materials and an acceptable design, however, there are still further difficulties to be overcome in the construction of a practical filter. The two most important remaining factors are, first, controlling the uniformity of layer thickness over the area of the substrate and, second, controlling the overall thickness of each layer. Lack of uniformity causes a shift of characteristic wavelength over the surface of the filter, without necessarily affecting the performance in other ways, while thickness errors usually cause a reduction in performance. The magnitude of the errors that can be tolerated will vary from one design to another, and the estimation of this is dealt with briefly. The bulk of this chapter is concerned with the general problem of minimizing these two sources of error. One other important topic is substrate preparation, and that is considered in Section 13.2.

13.1 Uniformity

In the evaporation process, it is usual to maintain the pressure within the chamber sufficiently low to ensure that the molecules in the stream of evaporant will travel in straight lines until they collide with a surface. To calculate the thickness distribution in a machine, the assumption is usually made that every molecule of evaporant sticks where it lands. This assumption is not always strictly correct, but it does allow uniformity calculations that are sufficiently accurate for most purposes. The distribution of thickness is then calculated in exactly the same way as intensity of illumination in an optical calculation. All that is required to enable the thickness to be estimated is knowledge of the distribution of evaporant from the source.

Holland and Steckelmacher [1] published an early and detailed account of techniques for the prediction of layer thickness and uniformity and established the theory that is essentially that still used in uniformity predictions.

Their expressions were later extended by Behrndt [2]. Holland and Steckelmacher divided sources into two broad types: those that have even distribution in all directions and can be likened to a point source, and those that have a distribution similar to that from a flat surface, the intensity falling off as the cosine of the angle between the direction concerned and the normal to the surface. The expressions for the distribution of material emitted from the two types of source are as follows.

For the point source:

$$dM = [m/(4\pi)]\,d\omega$$

and for the directed surface source:

$$dM = [m/\pi](\cos\varphi)\,d\omega.$$

where m is the total mass of material emitted from the source in all directions and dM is the amount passing through solid angle $d\omega$ (at angle φ to the normal to the surface in the case of the second type of source).

If the material is being deposited on surface element dS of the substrate that has its normal at angle ϑ to the direction of the source from the element, then the amount that will condense on the surface will be given by:

For the point source:

$$dM = \left(\frac{m}{4\pi}\right)\left(\frac{\cos\vartheta}{r^2}\right)dS$$

and for the directed surface source:

$$dM = \left(\frac{m}{\pi}\right)\left(\frac{\cos\varphi\cos\vartheta}{r^2}\right)dS$$

To estimate the thickness, t, of the deposit we need to know the density of the film. If this is denoted by μ then the thickness will be:

For the point source:

$$t = \left(\frac{m}{4\pi\mu}\right)\left(\frac{\cos\vartheta}{r^2}\right)$$

and for the directed surface source:

$$t = \left(\frac{m}{\pi\mu}\right)\left(\frac{\cos\varphi\cos\vartheta}{r^2}\right)$$

These are the basic equations used by Holland and Steckelmacher for estimating the thickness in uniformity calculations.

13.1.1 Flat Plate

The simplest case is that of a flat plate held directly above and parallel to the source. Here the angle φ is equal to the angle ϑ and the thickness is as follows.

For the point source:

$$t = \left(\frac{m}{4\pi\mu}\right)\left(\frac{\cos\vartheta}{r^2}\right) = \frac{mh}{4\pi\mu(h^2+\rho^2)^{3/2}}$$

and for the directed surface source:

$$t = \left(\frac{m}{\pi\mu}\right)\left(\frac{\cos^2\vartheta}{r^2}\right) = \frac{mh^2}{\pi\mu(h^2+\rho^2)^2}$$

with notation as in Figure 13.1. These expressions simplify, for the point source, to:

$$\frac{t}{t_0} = \frac{1}{[1+(\rho/h)^2]^{3/2}}$$

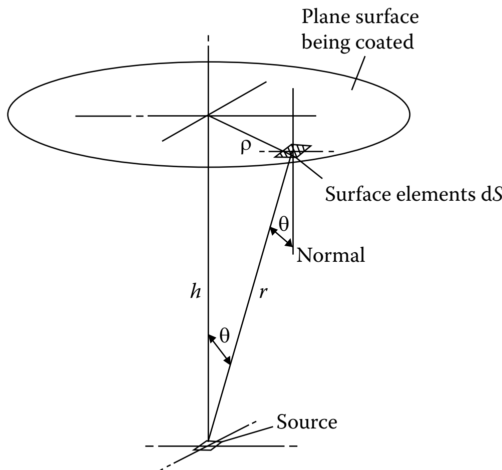

FIGURE 13.1
Diagram showing the geometry of the evaporation from a central source onto a parallel plane surface.

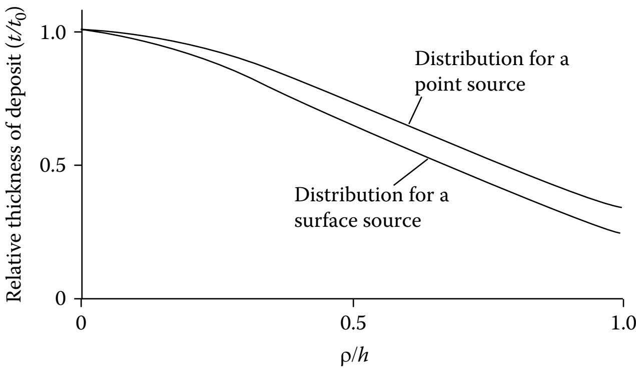

FIGURE 13.2
Film thickness distribution on a stationary substrate from a central source.

and for the directed surface source, to:

$$\frac{t}{t_0} = \frac{1}{[1+(\rho/h)^2]^2}$$

They are plotted in Figure 13.2. t_0 is the thickness immediately above the source where $\rho = 0$. In neither case is the uniformity at all good. Clearly, the geometry is not suitable for any very accurate work unless the substrate is extremely small and in the center of the machine.

13.1.2 Spherical Surface

A slightly better arrangement that can sometimes be used is a spherical geometry where the substrates lie on the surface of a sphere. A point source will give uniform thickness of deposit on the inside surface of a sphere when the source is situated at the center. It can be shown that the directed surface source will give uniform distribution similarly when it is itself made part of the surface. In fact, it was the evenness of the coating within a sphere that led Knudsen [3] first to propose the cosine law for thin-film deposition. The method is often used in machines for simple blooming of components such as lenses where the uniformity need not be better than, say, 10% of the layer thickness at the center of the component. However, for precise work, this uniformity is still not adequate.

A higher degree of uniformity involves rotation of the substrate carrier, which we shall now consider.

13.1.3 Rotating Substrates

The situation here is as if, in Figure 13.1, the surface for coating were rotated about a normal at distance R from the source. As the surface rotates, the

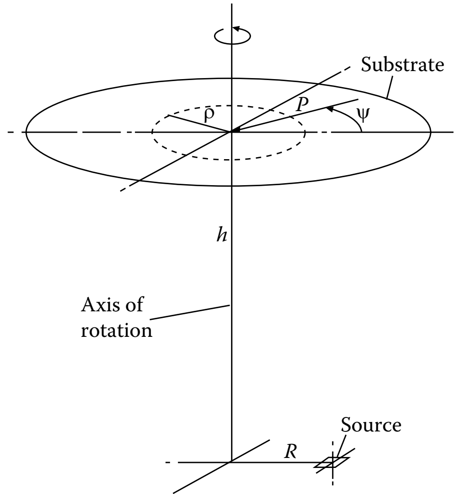

FIGURE 13.3
Diagram showing the geometry of the evaporation from a stationary offset source onto a rotating substrate.

thickness deposited at any point will be equal to the average of the thickness that would be deposited on a stationary substrate around a ring centered on the axis of rotation, provided always that the number of revolutions during the deposition is sufficiently great to make the amount deposited in an incomplete revolution a very small proportion of the total thickness. By choosing the correct distance between source and axis of rotation, the uniformity can be made vastly superior to that for stationary substrates.

We shall consider first the directed surface source. Figure 13.3 shows the situation. The calculation is similar to that for the flat plate with a central source. Here we stop the plate and calculate the mean thickness around the circle containing the point in question and centered on the axis of rotation. The radius of the circle is ρ, and if we define any point P on the circle by the angle ψ, then the thickness at the point is given by

$$t = \frac{m}{\pi\mu} \cdot \frac{h^2}{(h^2 + \rho^2 + R^2 - 2\rho R\cos\psi)^2}$$

where r, the distance from the source to the point, is given by

$$r^2 = h^2 + \rho^2 + R^2 - 2\rho R\cos\psi$$

Then, taking the mean of the thickness around the circle, we have for the thickness of the deposit in the rotating case,

$$t = \frac{m}{\pi\mu} \cdot \frac{1}{2\pi} \int_0^{2\pi} \frac{h^2 d\psi}{(h^2 + \rho^2 + R^2 - 2\rho R \cos\psi)^2}.$$

Now the integral $\int_0^{2\pi} d\psi/(1 - a\cos\psi)^2$ can be evaluated by contour integration to give

$$\int_0^{2\pi} \frac{d\psi}{(1 - a\cos\psi)^2} = \frac{2\pi}{(1 - a^2)^{3/2}}$$

so that the expression for thickness becomes

$$t = \frac{m}{\pi\mu} \cdot \frac{h^2}{(h^2 + \rho^2 + R^2)^2} \cdot \frac{1}{[1 - \{2\rho R/(h^2 + \rho^2 + R^2)\}^2]^{3/2}}$$

$$\frac{t}{t_0} = \frac{(1 + R^2/h^2)(1 + \rho^2/h^2 + R^2/h^2)}{[1 + \rho^2/h^2 + R^2/h^2 - 2(\rho/h)(R/h)]^{3/2}[1 + \rho^2/h^2 + R^2/h^2 + 2(\rho/h)(R/h)]^{3/2}}$$

where t/t_0 is, as before, the ratio of the thickness at the radius in question to that at the center of the substrate holder.

Figure 13.4 shows this function plotted for several different dimensions typical of medium-sized coating machines. The distribution is vastly superior to that when the substrates are stationary. For one particular combination of dimensions, that corresponding to $R = 7$, the distribution is extremely even over the central part (radius 3.75) of the machine. This is the arrangement used in the production of narrowband filters where the uniformity must necessarily be very good. If the uniformity is not quite so important, where rather broader filters or perhaps antireflection coatings are concerned, then the sources can be moved outwards, allowing a larger area to be coated at the expense of a slight reduction in uniformity.

A similar expression is found for a point source but this time involving elliptic integrals. The thickness at the point *P*, assuming that the substrate does not rotate, is given by

$$t = \frac{m}{4\pi\mu} \cdot \frac{h^2}{(h^2 + \rho^2 + R^2 - 2\rho R \cos\psi)^{3/2}}$$

and in the presence of rotation, the thickness at any point around the ring of radius ρ will be the mean of the expression, i.e.

$$t = \frac{m}{4\pi\mu} \cdot \frac{1}{2\pi} \cdot \int_0^{2\pi} \frac{h d\psi}{(h^2 + \rho^2 + R^2 - 2\rho R \cos\psi)^{3/2}}$$

$$= \frac{m}{4\pi^2\mu} \cdot \int_0^{\pi} \frac{h d\psi}{(h^2 + \rho^2 + R^2 - 2\rho R \cos\psi)^{3/2}}$$

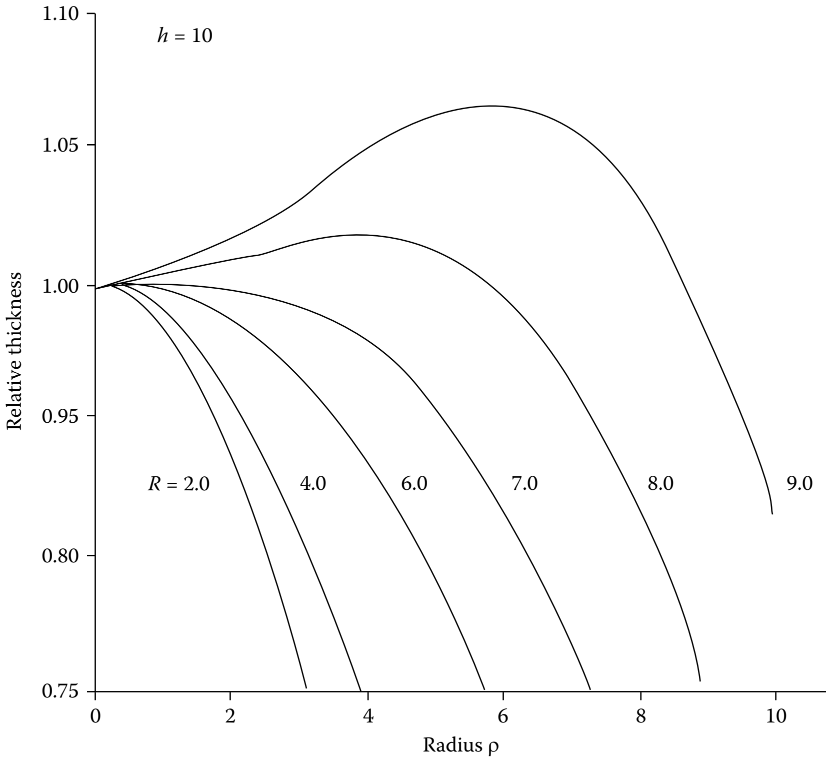

FIGURE 13.4
Theoretical film thickness distribution on substrates rotated about the center of the machine for various source radii and substrate heights. The sources are assumed to be small directed surfaces parallel to the substrates.

Now let $(\pi - \psi)/2 = \gamma$, then $d\psi = -2d\gamma$, and the expression for thickness becomes

$$t = \frac{m}{4\pi^2\mu} \cdot \int_{\pi/2}^{0} \frac{-hd\gamma}{[h^2 + (R+\rho)^2 - 4\rho R \sin^2\gamma]^{3/2}}$$

which can be written

$$t = \frac{m}{4\pi^2\mu} \cdot \frac{h}{[h^2 + (R+\rho)^2]^{3/2}} \cdot \int_{\pi/2}^{0} \frac{d\gamma}{\{1 - [4\rho R/\{h^2 + (R+\rho)^2\}]\sin^2\gamma\}^{3/2}}$$

Now the integral in this expression is a standard form

$$\frac{1}{(1-k^2)} E(k,\alpha) = \int_0^{\alpha} \frac{d\gamma}{(1-k^2\sin^2\gamma)^{3/2}}$$

where $E(k,\alpha)$ is an elliptic integral of the second kind, and is a tabulated function [4]. The expression for thickness then becomes:

$$t = \frac{hm}{4\pi^2\mu} \cdot \frac{E(k,\pi/2)}{[h^2+(R+\rho)^2]^{1/2}[h^2+(R-\rho)^2]}$$

where

$$k^2 = 4\rho R/[h^2+(R+\rho)^2]$$

Curves of this expression are given by Holland and Steckelmacher [1], and the shape is very similar to that for the directed surface source.

Almost all the sources used in the production of thin-film filters, especially the boat type, give distributions similar to the directed surface source. Holland and Steckelmacher also describe some experiments that they carried out to determine this point. Keay and Lissberger [5] have studied the distribution from a howitzer source loaded with zinc sulfide, and it appears that this is somewhere in between the point source and the directed surface source, probably due to scattering in the evaporant stream immediately above the heater where the pressure is high. The cloud of vapor that forms seems to act to some extent as a secondary point source. This behavior of the howitzer probably depends to a considerable extent on the material being evaporated. Graper [6] has studied the distribution of evaporant from an electron beam source and has found that this is somewhat more directional than the directed surface source. Its distribution can be described by a $\cos^x \vartheta$ law where x is somewhere between 1 and 3, and depends on the power input and on the amount of material in the hearth. Using zinc sulfide and cryolite, Richmond [7] found that the distribution from an electron beam source was best represented by a law of the form $\cos \vartheta$.

Normally, in calculating the distribution to be expected from a particular geometry, we assume that we are using directed surface sources, and then, when setting up a machine for the first time, the sources are placed at the theoretically best positions. The first few runs soon show whether any further adjustments are necessary, and if they are, they are usually very slight and can be made by trial and error. Once the best positions are found, it is important to ensure that the sources are always accurately set to reproduce them. Care should be taken to make sure that the angular alignment is correct. A source at the correct geometrical position but tilted away from the correct direction will give uniformity errors just as much as if it were laterally displaced. The frontispiece shows a machine being fitted with a flat plate work holder for the manufacture of narrowband filters.

Where uniformity must be good over as large an area as possible containing many rather smaller substrates, it is possible to use a combination of a spherical surface and rotating plate. A domed work holder, or calotte, is rotated about its center with the sources offset beneath it so that they are approximately on the surface of the sphere, with slight adjustments made

FIGURE 13.5
Interior of a machine with a domed calotte. (Courtesy Balzers AG.)

during setting up. This gives very good results over a much larger area than would be possible with the simple rotating flat plate. Figure 13.5 shows the interior of a machine that uses this arrangement.

When still improved uniformity is required, it is possible to achieve it by what is known as a planetary geometry. In this arrangement, the substrates are held in a number of small carriers that not only rotate about the center of the machine, but also about their own individual centers at much greater speed, so that they execute many revolutions for each single revolution of the carrier as a whole. This carries a stage further the averaging process that occurs with the simple rotating carrier. A planetary system can be seen in the open machine in Figure 11.1a.

13.1.4 Use of Masks

It is possible to make corrections to distribution by careful use of masks. In their simplest form, they are stationary and are placed just in front of

the substrates that rotate on a single carrier about a single axis. The masks are cut so that they modify the radial distribution of thickness. Theoretical calculations give dimensions for masks of approximately the correct shape, which can then be trimmed according to experimental results to arrive at the final form. For a number of reasons, it is normal to leave the central monitor glass uncorrected. It is difficult to correct the central part of the chamber where the mask width tends to zero, and, in any case, the monitor is usually stationary. Furthermore, in some monitoring arrangements, there is an advantage in having more material on the monitor than on the batch.

A further degree of freedom was introduced by Ramsay et al. [8] in the form of a rotating mask. For a large flat substrate approaching the dimensions of the machine, there is little other than simple rotation that can be done, in terms of the carrier, to improve uniformity. Planetary arrangements require much more room. Stationary masks are of some help but they are somewhat sensitive to the characteristic of the sources and are not therefore sufficiently stable for a very high degree of uniformity. A much more stable arrangement, that has been shown capable of uniformities of the order of 0.1% over areas of around 200 mm diameter, involves rotating the mask about a vertical axis at a rotational speed considerably in excess of that of the substrate carrier. This effectively corrects the angular distribution of the source that can then be positioned at the center of the machine. The mask rotation axis is usually placed very near the source and positioned so that the line drawn from the source through the mask center intersects the perimeter of the substrate carrier. In practice, the axis of rotation and the rotating shutter are close to the source position and slight adjustment of the axis can be made for trimming purposes. It has been found to be an exceptionally stable arrangement.

13.2 Substrate Preparation

Before a substrate can be coated, it must be cleaned. The forces that hold films together and to the substrate are all short-range interatomic and intermolecular forces. These forces are extremely powerful, but their short range means that we can think of each atomic layer as being bound to the neighboring layers only, and being little affected by material further removed from it. Thus, the adhesion of a thin film to the substrate depends critically on conditions at the substrate surface. Even a monomolecular layer of a contaminant on the surface can change the force of adhesion by orders of magnitude. Condensation of evaporant, too, is just as sensitive to surface conditions that can alter completely the characteristics of the subsequent layers. Substrate cleaning so that the condensing material attaches itself to the substrate and not an intervening layer of contaminant, is therefore of paramount importance.

The typical symptoms of an inadequately cleaned substrate are a mottled, oily appearance of the coating, coupled usually with poor adhesion and optical performance. This can be caused also by such defects in the machine as backstreaming of oil from the pumps. When these symptoms appear, it is usually advisable to extend any subsequent improvements in cleaning techniques to the machine as well.

A good account of various cleaning methods is given by Holland [9]. A more recent account is that of Mattox [10]. The best cleaning process will depend very much on the nature of the contamination that must be removed, and, although it may seem self-evident, in all cleaning operations it is essential to avoid contaminating the surface rather than cleaning it. For laboratory work, when the substrates are reasonably clean to start with (microscope slide glass is usually in this condition), then for most purposes it will be found sufficient to wash the substrates thoroughly in detergent and warm water (not household detergent, which sometimes has additives that cause smears to appear on the finished films), to rinse them thoroughly in running warm water (in areas where tap water is fairly pure, hot tap water will often be found adequate), and then to dry them thoroughly and immediately with a clean towel or soft paper tissue, or, better still, to blow them dry with a jet of clean dry nitrogen.

The substrates should never be allowed to dry themselves or stains will certainly occur, which are usually impossible to remove. Substrates should be handled as little as possible after cleaning and, since they never remain clean for long, placed immediately in the coating machine and the coating operation started. Wax or grease will probably require treatment with an alcohol such as isopropyl, perhaps rubbing the surface with a clean fresh cotton swab soaked in the alcohol and then flooding the surface with the liquid. Care must be taken to ensure that the alcohol is clean. A bottle of alcohol available to all in a laboratory seldom remains clean for long and a better arrangement is to keep it under lock and key and to allow the alcohol into the laboratory in wash bottles that emit the alcohol when squeezed.

This basic cleaning procedure can be modified and supplemented in various ways, especially if large numbers of substrates are to be handled automatically. Ultrasonic scrubbing in detergent solution or in alcohol is a very useful technique, although prolonged ultrasonic exposure is to be avoided since it can eventually cause surface damage. It is important that the substrates should be kept wet right through the cleaning procedure until they are dried as the final stage. Vapor cleaning is frequently used for final drying. The substrates are exposed to the vapor of alcohol or other degreasing agents so that initially it condenses and runs off, taking any residual contamination or the remains of the agent from the previous cleaning stage with it. The substrates gradually reach the temperature of the vapor. Then no further condensation takes place, and the substrates can be withdrawn perfectly dry. Since the agent is condensing from the vapor phase, it is in an extremely pure form. An alternative end to the cleaning process is a rinse in deionized water followed by drying in a blast of dry, filtered nitrogen.

It is very difficult to see marks on the surface of the substrate with the naked eye. Dust can be picked up by oblique illumination, but wax and grease cannot. An old test for assessing the quality of a cleaning process is to breathe on one of the substrates so that moisture condenses on it in a thin layer. This tends to magnify the effects of any residue. The moisture acts in almost exactly the same way as a condensing film since the condensation pattern depends on the surface conditions. A surface examined in this way is said to exhibit a good or bad "breath figure." A contaminated surface gives a smeared pattern, while a clean surface is completely even. Since even this step can introduce slight residual contamination, it is better used only on a sample as an indication of the condition of the batch.

Once the substrates are in the chamber, and they should always be loaded as soon as possible after cleaning, they can be given a final clean by a glow discharge. The equipment for this, which consists of a high-voltage supply, preferably DC, together with the necessary lead-in electrodes, is fitted as standard in most machines. At a suitable pressure, which will vary with the particular geometry of the electrodes but which will usually be around 0.06 mbar (6 Pa), a glow discharge is struck, and, provided the geometry is correct, the surface of the substrates is bombarded with positive ions. This effectively removes any light residual contamination, although gross contamination will persist. It is not certain whether the cleaning action actually arises from a form of sputtering or whether the glow discharge is merely a convenient way of raising the temperature of the surfaces so that contaminants are baked off. Generally, the glow discharge is limited in duration to 5 or perhaps 10 min. It has been suggested that, although glow discharge cleaning does remove grease, it does encourage dust particles; for coatings where minimum dust is required, such as high-performance laser mirrors, glow discharge cleaning is frequently omitted. Lee [11] found that the omission of glow discharge cleaning led to a very great increase in the incidence of moisture penetration patches in his films and consequently to a fall in the performance of his filters.

The evaporation of the first layer should begin as soon as possible after the glow discharge has stopped. Cox and Hass [12] used a discharge current of 80 mA and a voltage of 5000 V for 5 min to clean substrates before coating them with zinc sulfide, and found that the time between finishing the discharge and starting the evaporation should be not greater than three minutes. If the time was allowed to exceed 5 min, then the quality of the films, especially their adhesion, deteriorated.

If, as sometimes happens, a filter is left for a period, say overnight, in an uncompleted state, it will often be found advisable to carry out a short period of glow discharge cleaning before starting to evaporate the remaining layers.

In the energetic processes such as ion-assisted deposition, the substrate can be readily bombarded by the ion beam before coating. This is a very effective cleaning method. Care should be taken, however, not to prolong this bombardment. The substrate surface is usually sputtered along with the

contaminants. Since this vigorous cleaning process can be carried out at deposition temperature and pressure, the deposition can start immediately the surface is considered clean, even without any pause in the bombardment.

13.3 Thickness Monitoring and Control

Given suitable materials, clean substrates, and a machine with substrate-holder geometry to give the required distribution accuracy, the main remaining problem is that of controlling the deposition of the layers so that they have the characteristics required by the coating or filter design. Of course, many properties are required, but refractive index and optical thickness are the most important. There is no satisfactory way, at present, of measuring the refractive index of that portion of a film actually being deposited. Such measurements can be made later but for closed loop control, dynamic measurements are required. Normal practice, therefore, is simply to control, as far as possible, those deposition parameters that would affect refractive index so that the index produced for any given material, or mixture of materials, is consistent. This procedure, while it usually gives satisfactory results, is not ideal and is used simply because, at the present time, there is no better way. Fortunately, the energetic processes, especially sputtering, do exhibit very good stability in terms of refractive index and other properties.

Film thickness can more readily be measured and, therefore, controlled. The simplest systems display a signal to a machine operator who is responsible for interpreting it and assessing the correct instant to terminate deposition. At the other end of the scale, there are completely automatic systems in which operator judgment plays no part and in which even operator intervention is rarely required. The term *monitoring* strictly means keeping track of a parameter but in the thin-film community, it is understood as including both measurement and control.

There are many ways in which the thickness can be measured. All that is necessary is to find a parameter that varies in a suitable fashion with thickness and to devise a way of monitoring this parameter during deposition. Thus, parameters such as mass, electrical resistance, optical density, reflectance, and transmittance have all been used. Of all the methods, those most frequently used involve optical measurements of reflectance or transmittance, or the measurement of total deposited mass by the quartz-crystal microbalance, or, in some very stable processes, time of deposition.

The question of the best method for the monitoring of thin films is, of course, inseparable from that of how accurately the layers must be controlled. This second question is a surprisingly difficult one to answer. Indeed, it is impossible to separate the two questions: the tolerances that can be allowed and the method used for monitoring are closely related, and one cannot be

considered in depth independently of the other. For convenience, however, we will consider some of the more common arrangements for monitoring, including only the most rudimentary ideas of accuracy, and then, at a later stage, consider the question of tolerances along with some of the more advanced ideas of monitoring and its various classifications.

13.3.1 Optical Monitoring Techniques

Optical monitoring systems consist of a light source of some description illuminating a test substrate that may or may not be one of the filters in the batch, and a detector analyzing the reflected or transmitted light. From the results of that analysis, the evaporation of the layer is stopped as far as possible at the correct point. Usually, so that the layer may be stopped as sharply as possible, the machine is fitted with a shutter that can be inserted in front of the evaporation sources. This is a much more satisfactory method than merely turning off the supply to the boats that always take a finite time to stop emitting. Such a shutter can be seen in Figure 11.3.

Almost all the early workers in the field used the eye as the detector, and the thicknesses of the films were determined by assessing their color appearance in white light. In many cases, they were concerned with simple single-layer coatings such as single-layer blooming, which are not at all susceptible to errors. When the blooming layer is of the correct thickness for visible light, the color reflected from the surface in white light has a magenta tint, owing to the reduction of the reflectance in the green. The visual method is quite adequate for this purpose and is still being widely used. A very clear account of the method is given by Mary Banning [13], who compiled Table 13.1.

In the production of other types of filter where the errors of the visual method would be too large, other methods must be used. The simplest appears to be the use of a receiver in the measurement of the variation of transmittance or reflectance at a single wavelength, known often as *single-point monitoring*. It seems that many workers adopted such a method virtually simultaneously. An early paper by Polster [14] describes a photoelectric method that is basically the same as that used most often today. Holland [9] credits Dufour with an early (1948) version of such a system including a chip changer. Billings [15] mentions, in 1950, a multilayer technique that had already been operated for some years by Fogelsanger at Evaporated Metal Films. We saw in Chapter 2 that if the film is without absorption, then its reflectance and transmittance measured at any one wavelength will vary with thickness in a cyclic manner, similar to a sine wave, although, for the higher indices, the waves will be more flattened at their tops. The turning values correspond to those wavelengths for which the optical thickness of the film is an integral number of quarter wavelengths, the reflectance being equal to that of the substrate when the number is even and a maximum amount removed from the reflectance of the substrate when the number is odd. Figure 13.6 illustrates the behavior of films of different values of refractive index. This affords the means for measurement. If the detector in the system is made highly selective,

TABLE 13.1

Color Changes for Visual Optical Monitoring

Color Change for		Optical Thickness for Green Light
ZnS	**Na_3AlF_6**	
Bluish white	Yellow	
↓	↓	
White	Magenta	$\lambda/4$
↓	↓	
Yellow	Blue	
↓	↓	
Magenta	White	$\lambda/2$
↓	↓	
Blue	Yellow	
↓	↓	
Greenish white	Magenta	$3\lambda/4$
↓	↓	
Yellow	Blue	
↓	↓	
Magenta	Greenish white	λ
↓	↓	
Blue	Yellow	
↓	↓	
Green	Magenta	$5\lambda/4$

Source: After Banning, M., *Journal of the Optical Society of America*, 37, 792–792, 1947.

for example by putting a narrow filter in front of it, then the measured reflectance or transmittance will vary in this cyclic way, and the film may be monitored to an integral number of quarter-waves by counting the number of turning points passed through in the course of the deposition. A typical arrangement to perform this operation is shown in Figure 13.7. The filter may be an interference filter or, more flexible, an adjustable prism or grating monochromator.

Consider the deposition of a high-reflectance multilayer stack where all the layers are quarter-waves. Let the monitoring wavelength be the wavelength for which all the layers are one quarter-wavelength thick. The reflectance of the test piece will vary as shown in Figure 13.8 [16]. The example shown is typical of a reflecting stack for the visible region. The reflectance can be seen to increase during the deposition of the first layer, of high index, to a maximum where the deposition is terminated. During the second layer, the reflectance falls to a minimum where the second layer is terminated. The third layer increases the reflectance once again and the fourth layer reduces it. This behavior is superimposed on a trend towards a reflectance of unity so that the variable part of the signal becomes a gradually smaller part of the total. This puts a limit on the number of layers that can be monitored in

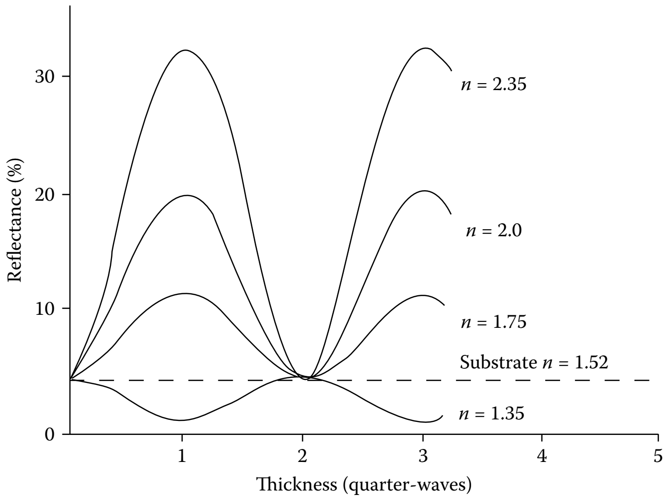

FIGURE 13.6
Curves showing the variation with thickness of the reflectance of several films with different refractive indices.

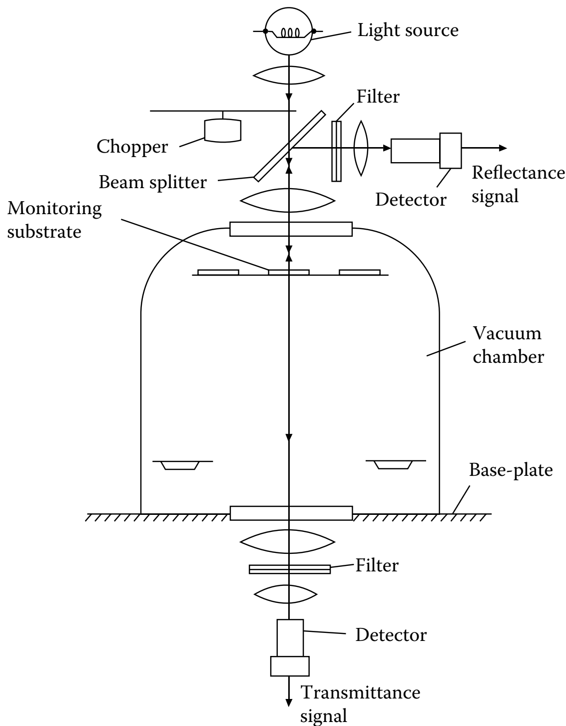

FIGURE 13.7
A possible arrangement of a monitoring system for reflectance and transmittance measurements.

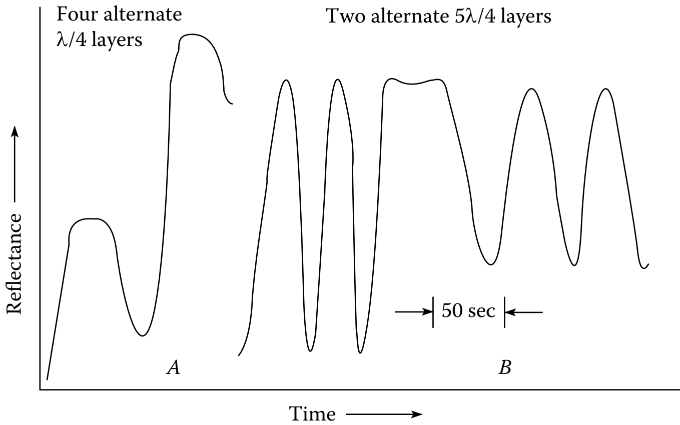

FIGURE 13.8
Record taken from a pen recorder of the reflectance of a monitor glass during film deposition. (After Perry, D.L. *Applied Optics*, 4, 987–991, 1965.)

reflectance in this way to around four, when a fresh monitoring substrate must be inserted. In transmission monitoring, this effect does not exist and the variable part of the signal remains a sufficiently large part of the whole. The only problem is that the overall trend of the signal is towards zero, so that eventually it will become too small in comparison with the noise in the system. With reasonable optics and a photomultiplier detector, the number of layers that may be dealt with in this way is around 21. At this stage, the noise usually becomes too great.

Frequently, automatic methods of detection of the layer end point are used. Automatic methods, however, are not universally used and operator control of the machine is still an important technique. For the greatest accuracy, the output of the detector should be displayed on a chart recorder making it easier to determine the turning values. With such an arrangement, a trained operator can readily terminate the layers to an accuracy on the monitoring substrate of around 5% or better, depending on the index of the film. With care and attention, 2% is a good estimate. Of course, as we shall see, this does not necessarily mean that the actual thickness of the filters in the batch will be as accurate. Other sources of error operate to introduce differences between the monitor and the batch.

To improve the signal-to-noise ratio, it is usual to chop the light before it enters the machine, partly because the evaporation process produces a great deal of light during the heating of the boats, but mainly because, at the signal levels encountered, the electronic noise without some filtering would be impossibly great. The chopper is best placed immediately after the source of light but before the machine, and the filter after the machine. This arrangement reduces the stray light to a greater extent than would placing either the filter before the machine or the chopper after it. It is, of course, always

advisable to limit as far as possible the total light incident on the detector, partly because unchopped radiation can push the detector into a nonlinear region and partly because it can damage the device especially if it is a photomultiplier. If a filter rather than a monochromator is used, then great care should be taken to ensure that the sidebands are particularly well suppressed. Photomultipliers and other detectors have characteristics that can vary considerably with wavelength, and if the monitoring wavelength lies in a rather insensitive region compared with the peak sensitivity, then small leaks in the more sensitive region, which might not be very noticeable in the characteristic curve of the filter, can cause considerable difficulties from stray light, even giving spurious signals of similar or greater magnitude than the true signal. Prism or grating monochromators are often safer for this work, besides being considerably more flexible.

The technique in which the layer termination is at an extremum of the signal is sometimes called turning-value monitoring or turning-point monitoring. We can investigate the errors likely to arise in this type of monitoring as follows. Suppose that in the monitoring of a single quarter-wave layer there is an error γ in the value of reflectance at the termination point.

$$\gamma = \Delta R/R$$

This will give rise to a corresponding error φ in the phase thickness of the layer δ where

$$\delta = (\pi/2) - \varphi$$

The result is symmetrical around the turning value and so we can assume an undershoot rather than overshoot to give a marginally simpler analysis. Because of the nature of the characteristic reflectance curve of the single layer, the error in phase thickness will be rather greater in proportion than the original error in reflectance. The surface admittance of the layer will be given by the characteristic matrix:

$$\begin{bmatrix} \cos\delta & (i\sin\delta)/y \\ iy\sin\delta & \cos\delta \end{bmatrix} \begin{bmatrix} 1 \\ y_{sub} \end{bmatrix}$$

where

$$\cos\delta = \sin\varphi \quad \text{and} \quad \sin\delta = \cos\varphi$$

This gives

$$Y = \frac{y_{sub}\sin\varphi + iy\cos\varphi}{\sin\varphi + i(y_{sub}\cos\varphi)/y}$$

where the symbols have their usual meaning. Introducing approximations for $\sin\varphi$ and $\cos\varphi$ up to and including powers of the second order, we have

$$Y = \frac{y_{sub}\varphi + iy(1-\varphi^2/2)}{\varphi + i(y_{sub}/y)(1-\varphi^2/2)}$$

and the reflectance of the monitor *in vacuo* will be given by

$$R = \left|\frac{(y_{sub}-1)\varphi + i(y - y_{sub}/y)(1-\varphi^2/2)}{(y_{sub}+1)\varphi + i(y + y_{sub}/y)(1-\varphi^2/2)}\right|^2$$

which simplifies to

$$R = \frac{(y - y_{sub}/y)^2}{(y + y_{sub}/y)^2}\left\{1 + \frac{4y_{sub}(1 - y^2 + y_{sub}^2 - y_{sub}^2/y^2)}{(y^2 - y_{sub}^2/y^2)^2}\varphi^2\right\} \tag{13.1}$$

The values of γ and φ are related as follows:

$$\gamma = \frac{4y_{sub}(1 - y^2 + y_{sub}^2 - y_{sub}^2/y^2)}{(y^2 - y_{sub}^2/y^2)^2}\varphi^2 = \sigma\varphi^2 \tag{13.2}$$

since the first factor in Equation 13.1 is just the reflectance when γ and φ are both zero.

Now, in most cases, it will be very difficult to determine the reflectance at the turning value to better than 1% of the true value. In many cases, especially where there is noise, it will not be possible even to do as well as this. However, assuming this value for γ, the expression for the error in the layer thickness becomes

$$\pm 0.01 = \sigma\varphi^2$$

where the sign $\pm$ is taken to agree with $\sigma\varphi^2$ and depends on whether the turning value is a maximum or a minimum. If the error is expressed in terms of a quarter-wave thickness, equivalent to $\pi/2$ radians, the expression becomes

$$Error = \frac{\varphi}{\pi/2} = \frac{0.1}{(\pi/2)\sigma^{1/2}} \tag{13.3}$$

A typical case is the monitoring of a quarter-wave of zinc sulfide on a glass substrate where $y = 2.35$ and $y_{sub} = 1.52$. Substituting these values in Expression 13.2 and using it in Expression 13.3, the fractional error in the quarter-wave becomes 0.08. This is a colossal error compared with the

original error in reflectance and illustrates the basic lack of accuracy inherent in this method.

In the infrared, it is often possible to use wavelengths for monitoring that are shorter than the wavelengths of the desired filter peaks by a factor of perhaps 2 or even 4. This improves the basic accuracy by the same factor. For layers similar to that considered above, the errors would then be 0.04 or 0.02. These errors are on the limit of permissible errors, and it is clear that this simple system of monitoring is not really adequate for any but the simplest of designs.

What makes the method particularly difficult to apply is that it is only the portion of the signal before the turning point that is available to the operator, who has therefore to anticipate the turning value, and the fact that trained machine operators can achieve the theoretical figures for accuracy says much for their skill.

An alternative method, inherently more accurate, involves the termination of the layer at a point remote from a turning value where the signal changes much more rapidly. This consists of the prediction of the reflectance of the monitoring substrate when the layer is of the correct thickness and then the termination of the deposition at that point. One disadvantage is that the reflectance of the monitor, or its transmittance, is not an easy quantity to measure absolutely, because of calibration drifts during the process, due partly to such causes as the gradual coating of the machine windows—which is almost impossible to avoid. Another is that whereas with turning value monitoring it is often possible to use just one single monitor, on which all the layers can be deposited, so that it becomes an exact replica of the other filters in the batch, in this alternative method the prediction of the reflectances used as termination values is very difficult if only one monitor is used, because small errors in early layers affect the shape of the curve for later layers. However, we shall see later in this section that this single-point method is still used effectively—although with some innovations.

Some of these difficulties may be avoided by using a separate monitor for each and every layer. To avoid the errors due to any shift in calibration that may occur in changing from one monitor to the next or in the coating of the machine windows, it is wise if at all possible to choose the parameters of the system so that the layer is thicker than a quarter-wave at the monitoring wavelength. This ensures that the termination point of the layer is beyond at least the first turning value, which can therefore be used as a calibration check. It will also be found necessary to set up the reflectance scale for each fresh monitoring substrate and the initial uncoated reflectance that will be known accurately can be used for this. Because a large number of monitor glasses is required, special monitor changers have been designed and are commercially available, which will accommodate stacks of 40 or more glasses. The low-index material may have rather poor contrast on the monitor substrates and a frequent variant of this method is the deposition of two layers, high index followed by low index, on each monitor substrate. The word *chip* has become the almost universal term for a monitor glass and *chip changer* for the monitor glass changer.

The principal objection that most workers almost instinctively feel toward this system is that the monitor is no longer an exact replica of the batch of filters. This is to some extent a valid objection. The layer being deposited on an otherwise uncoated substrate is condensing on top of what may be quite a different structure from the partially finished filters of the batch. Behrndt and Doughty [17] noticed a definite measurable difference between layers deposited on top of an already existing structure and those deposited on fresh substrates. They compared the deposition of zinc sulfide shown by a crystal monitor (this special type of monitor will be discussed shortly), which already had a number of layers on it, with the layer going down on a fresh glass substrate, and found that the layer began to grow on the crystal immediately the source was uncovered, but that the optical monitor took some time to register any deposition. The difference could amount to several tens of nanometers before the rates became equal. This, they decided, was due to the finite time for nuclei to form on the fresh glass surface and the rather small probability of sticking of the zinc sulfide until the nuclei were well and truly formed. Once the film started to grow, all the molecules reaching the surface would stick. On the crystal where a film already existed, not necessarily of zinc sulfide, nucleation sites were already there and the film started to grow immediately. The sticking coefficient of a material on a fresh monitor surface falls with rising vapor pressure, and zinc sulfide has a particularly large vapor pressure. Similar trouble was not experienced with thorium fluoride that has a much lower vapor pressure. Behrndt and Doughty found that the problem could be solved by providing nucleation sites on the clean monitor slides by precoating them with thorium fluoride that has a refractive index very close to that of glass. Some 20 nm or so of thorium fluoride was found to be sufficient and did not affect the monitoring of zinc sulfide deposited on top. (Since thorium fluoride is radioactive and somewhat out of favor, a different low-index fluoride would be advisable.) This effect becomes greater the greater the surface temperature of the monitor. By changing the type of evaporation source to an electron-beam unit, which produced less radiant heat for the same evaporation rate, it was found possible to operate at monitor temperatures low enough to cause the effect to disappear.

The same authors also remarked on an effect well known in thin-film optics. Thick substrates tend to have layers condensing on them that are thicker than those on thin substrates in the same or similar positions in the machine. In the case cited by the authors, the thin substrates were around 0.040 in thick, while the thick ones were around half an inch thick. The difference in coating thickness was sufficient to shift the reflectance turning values by some 40–50 nm at 632.8 nm. This was shown, qualitatively, to be due to the difference in temperature between the two substrates. The thicker substrates took longer to heat up than the thin ones. The heating in this particular case was almost entirely due to radiation from the sources and, again when electron-beam sources were introduced, the effect was considerably reduced.

The accuracy of the monitoring process can be improved greatly if a system devised by Giacomo and Jacquinot [18], and known usually as the *maximètre,* is employed. This involves the measurement of the derivative of the reflectance versus wavelength curve of the monitor. At points where the reflectance is a turning value, the derivative of the reflectance with respect to wavelength is zero and is rapidly changing from a positive to a negative value in the case of a maximum and vice versa in the case of a minimum. The original apparatus consisted of a monochromator with a small vibrating mirror before the slits on the exit side so that a small spectral interval was scanned sinusoidally. The output signal from the detector consisted of a steady DC component, representing the mean reflectance, or transmittance, over the interval, a component of the same frequency as the scanning mirror representing the first derivative of the reflectance against wavelength, a component of twice the scanning frequency, representing the second derivative of the reflectance, and so on. A slight complication is the variation in sensitivity of the system with wavelength that appears as a change in the reflectance signal and hence the derivative, unless it is compensated. In their arrangement, Giacomo and Jacquinot produced an intermediate image of the spectrum within the monochromator, and a razor blade positioned along it made a linear correction to the intensity over a sufficiently wide region and was found to be accurate enough. A more usual technique today would be to make a correction electronically. The accuracy claimed for this system is a few tenths of a nanometre, typically 0.2–0.3 nm, and this is certainly achieved. A problem, as we have seen in Chapter 9, is that the layers may be insufficiently stable themselves to retain optical thicknesses to this accuracy, especially when exposed to the atmosphere.

A method, similar in some respects, but with some definite advantages in interpretation, was devised by Ring [19] and Lissberger [20]. It consists of measuring the reflectance or transmittance at two wavelengths and finding the difference. In the original system, a monochromator was used, containing a chopping system that switched the output of the monochromator from one wavelength to another and back again. The AC signal from the detector was a measure of the difference. Since the two wavelengths could be placed virtually anywhere within the region of sensitivity of the detector, the method had greater flexibility than the Giacomo and Jacquinot system. Greatest contrast in the two reflectance signals as a layer was being deposited could be obtained by placing the two wavelengths at the points of greatest opposite slope in the characteristic of the thin-film structure at the appropriate stage. When the signals at the two wavelengths were equal, the output of the system passed through a null, and, if displayed on a chart recorder, made detection of the terminal point of a particular layer, usually indicated by the null, particularly easy to detect.

More recently, the ideas inherent in these systems have been extended to broad spectral regions. Although the principles of these more modern methods are not new, it is the advances in detectors and in electronics and data

analysis that have made them practical. Many of the systems have been developed in industry and frequently have not been published. In the cases of those that have been written up, detailed descriptions of the precise way in which they are used have often been lacking. Usually the technique involves a comparison between the spectral characteristic that is actually obtained at any instant, and that required at the instant of termination of the particular layer. In the earlier systems, this was carried out visually by displaying both curves on a monitor. This works well when there is a close match between predicted and measured performance but frequently errors in earlier layers, and changes in the characteristics of layers from what is expected, cause the actual curves to differ to a greater or lesser extent from the predictions. In these circumstances, there can be great difficulty in assessing visually the correct moment to terminate a layer. The most recent systems, therefore, are usually linked to a computer that calculates a figure of merit that can either be displayed to a machine operator or, better still, used in the completely automatic termination of layers.

Details of scanning monochromator systems have been published by a number of authors. An early description of such a system is that of Hiraga et al. [21], where the scanning was carried out by a rotating helical slit assembly. Pelletier and his colleagues in Marseilles [22,23] have developed two such systems. The first uses a stepping motor to rotate a grating and scan the system over a wide wavelength region, the second uses a holographic grating with a flat spectrum plane in which is situated a silicon photodiode array detector that can be scanned electronically. Sullivan and his colleagues [24–26] have had great success in implementing a completely automatic system of monitoring including error compensation. A recent study of broad band optical monitoring from the deep ultraviolet to the near infrared is that of Ristau et al. [27].

From time to time, ellipsometric monitoring has been examined. This has the advantage that an assessment of how stable is the refractive index of the deposited layer can readily be made. The principal disadvantage is the increased difficulty of implementing such a monitoring system that requires a high angle of incidence on the measuring chip. Ellipsometric monitoring has been used to advantage by Dligatch and Netterfield [28].

It should not be thought that such advances in monitoring have superseded the direct single-point system where all the layer are monitored on one single substrate that forms one of the batch under construction. Figure 11.17a shows a sketch of a SYRUSpro machine (Leybold Optics GmbH) where all the layers are monitored using one single wavelength, which is changed from layer to layer, with termination points that are, in general, on the side of the oscillatory monitoring curve, rather than at the turning values. The single, chosen, monitoring substrate is in the midst of the batch and passes through the monitoring beam once per substrate carrier rotation. This sampling of the monitoring signal is, however, sufficiently accurate to allow a high degree of control. There is a large advantage in that the chosen

substrate is much more representative of the coating batch than a centrally placed separate monitoring substrate [29].

13.3.2 The Quartz-Crystal Monitor

The normal modes of mechanical vibration of a quartz crystal have very high Q and can be transformed into electric signals by the piezoelectric properties of the quartz and vice versa. The crystal acts, therefore, as a very efficient tuned circuit that can be coupled into an electrical oscillator by adding appropriate electrodes. Any disturbance of its mechanical properties will cause a change in its resonant frequency. Such a disturbance might be an alteration of the temperature of the crystal or its mass. The principle of monitoring by the quartz-crystal microbalance (as it is called) is to expose the crystal to the evaporant stream and to measure the change in frequency as the film deposits on its face and changes the total mass. In some arrangements, the resonant frequency of the crystal is compared with that of a standard outside the machine and the difference in frequency is measured; in others, the number of vibrations in a given time interval is measured digitally. Usually the frequency shift will be converted internally into a measure of film thickness using film constants fed in by the operator. Since the signal from the quartz-crystal monitor changes constantly in the same direction it can be used more easily in automatic systems than optical signals.

The mechanical vibrational modes of a slice of quartz crystal are very complicated. It has been found possible to limit the possible modes and the coupling between them by cutting the slice with respect to the axes of the crystal in a particular way, by proportioning the dimensions of the slice correctly and by supporting the crystal in its holder in the correct way. Quartz-crystal vibrational modes also vary with temperature, some having positive temperature coefficient and some negative, and it has been found possible to cut the slice in such a way that modes which have opposite temperature dependence are intentionally coupled so that the combined effect is a resonant frequency independent of temperature over a limited temperature range. The usual cut of crystal used in thin-film monitors is the *AT* cut. This is cut from a slice oriented so that it contains the x axis of the crystal and is at an angle of 35° 15′ to the z-axis. The mode of vibration is a high-frequency shear mode (Figure 13.9) and the temperature coefficient is small over the range −40 °C

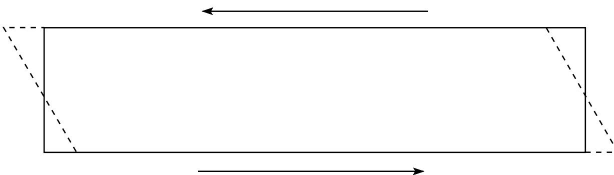

FIGURE 13.9
Quartz crystal operating in shear.

to +90 °C, of the order of $\pm 10^{-6}$ °C^{-1} or slightly greater. The coefficient changes sign several times throughout the range so that the total fractional change in frequency over the complete range is only around 5×10^{-5}. Usually the frequency chosen is around 5 MHz or sometimes 6 MHz, although the range could be anything from 0.5 MHz to 50 or 100 MHz. Generally, the temperature of the crystal must be limited to below 120°C (otherwise, the temperature coefficient becomes excessively large), so it may not always be possible to keep it at the same temperature as the other substrates in the machine and this may be of importance in some applications.

As the thickness of the evaporant builds up, the frequency of the crystal falls and the reduction in frequency is proportional both to the square of the resonant frequency and to the mass of the film deposited. Accuracy depends on a wide range of factors, many related more to the stability of the installation than to the crystal itself, but a good starting rule of thumb for a typical arrangement is that the measurement of mass thickness can be carried out to an accuracy of perhaps 2%, adequate for most optical filters. Unfortunately, the sensitivity of the crystal decreases with increasing build up of mass and the total amount of material that can be deposited before the crystal must be cleaned is limited. With existing crystals, this makes them less useful for multilayer work, especially in the infrared, where a single crystal would have difficulty in accommodating a complete filter. One way round this problem is to place a screen over the crystal that cuts down the material reaching it to a fraction of that reaching the substrates in the batch. This, of course, reduces the accuracy of the system. A more satisfactory solution is to use a multiple crystal head that can change crystals automatically when one is exhausted.

Because the crystal measures mass and not optical thickness, it must be calibrated separately for each material used. The calibration depends on the acoustical properties not only of the crystal but also of the deposited material. Any mismatch in the acoustic impedances for the particular shear mode at a boundary acts in much the same way as a mismatch in optical admittance, and perturbs the natural frequency of the combined crystal and film. This must be taken into account in the calculations, and most commercial crystal monitors include an input for the acoustic impedance values. These values are not always well known for thin film materials, which creates one problem. There are further problems in crystals that are controlling the deposition of a multilayer coating. The discontinuity in acoustic impedance now occurs at every interface and complicates the calculations to a completely impracticable extent. Thus, the control of the deposition of a multilayer coating on one single crystal carries an additional inaccuracy because of the difficulty of allowing for these discontinuities. This has led to the practice of a separate crystal for each material, since that involves only one discontinuity and so only one calibration for each crystal.

Because of these difficulties, some recent crystal monitors employ multiple modes of vibration. The redundancy in the mass of added material, which

is necessarily identical for each mode, permits an estimate of the acoustical impedance mismatch and, therefore, avoids the need for a user-supplied value. This technique can even be extended to the corrections necessary in the deposition of a multilayer on one crystal [30].

There can be considerable advantages in the use of quartz-crystal monitors. Since the output moves in a constant direction and does not reverse, it is more readily accommodated by automatic control systems. Further, the crystal does not need optical windows with their attendant difficulties of maintenance and screening from the evaporant. Alignment is simpler than for optical monitors although the requirements for dimensional stability are just as severe. In recent years, there have been developments in the use of multiple-crystal sensors distributed around the chamber able to sense changes in the plume of material from the sources and make appropriate corrections to the monitoring calculations. The automatic corrections for acoustic impedance remove the associated uncertainty. With such improvements, the results that can be achieved by pure-crystal monitoring are excellent.

In the case of narrowband filters, the optical monitoring is successful because of a built-in error compensation process. This makes it difficult for the crystal monitor to achieve the same yield. For processes where error compensation is necessary to achieve the optical performance, optical monitoring is preferred. In those cases, the crystal monitoring is usually still employed, but for source and rate control sensing rather than primary monitoring.

A useful set of instructions and tips on the quartz-crystal monitor will be found in a paper by Riegert [31], which deals much more fully with the topics mentioned above and, despite its age, is still valid. Manufacturers' manuals include good information also.

13.3.3 Monitoring by Deposition Time

The stability of the sputtering deposition process renders very consistent the thickness of material added in each increment of the incremental processes described in Chapter 11. This makes it possible to control layer thicknesses by time, or, alternatively, by the number of rotations of the substrate drum.

Spencer [32] describes successful experiments in the time control of thickness in a small ophthalmic coater with sputtering sources of ZrO_2 and SiO_2 in the construction of optical coatings including a single-cavity narrowband filter. Pervac et al. [33] with pure time control successfully produced narrowband notch filters using the Helios machine of Figure 11.12. Gibson et al. [34] report run to run reproducibility of ±0.3% in the characteristics of edge filters of TiO_2 and SiO_2 for the visible region produced by the close-field magnetron sputtering system of Figure 11.10.

Figure 13.10 illustrates the stability of time monitoring in the production using the RAS process, Figure 11.18, of successive batches of antireflection coatings with 10-layer design, using SiO_2 and Si_3N_4.

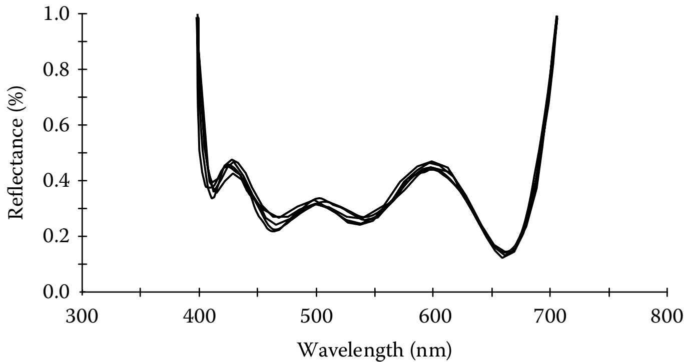

FIGURE 13.10
Performance of a 10-layer antireflection coating monitored by time. There are results from five successive production runs superimposed. The materials are SiO_2 and Si_3N_4 and deposition was by the RAS process (see Chapter 11). (Courtesy Shincron Company Ltd, Yokohama, Japan).

A variant of time control has long been used in in-line sputtering systems where substrates move through the system at a fixed rate. Short-term stability of the process has to be good but there can be slow drifts over long periods of time. Often the thickness of the deposited layers will be measured and the results used in the gradual adjustment of sputtering power so that the long-term stability of the process is assured.

13.4 Tolerances

The question of how accurately we must control the thickness of layers in the deposition of a given multilayer is surprisingly difficult to answer and has attracted a great deal of attention over the years. Nowadays we immediately think of the computer when we wish to carry out numerical studies but this is a relatively recent innovation. The earlier studies lacked this luxury, and so were greatly influenced by the need to limit the volume of calculation. Nevertheless, the results were, and still are, of great value.

One of the earliest approaches to the assessment of errors permissible in multilayers was devised by Heavens [35], who used an approximate method based on the alternative matrix formulation in Equation 3.16. His method, useful mainly when calculations must be performed manually, consisted of a technique for recalculating fairly simply the performance of a multilayer with a small error in thickness in one of the layers. He showed that the final reflectance of a quarter-wave stack is scarcely affected by a 5% error in any one of the layers.

Lissberger [36,37] developed a method for calculating the performance of a multilayer involving the reflectances at the interfaces. In multilayers made up of quarter-waves, the expressions took on a fairly simple form that permitted the effects of small errors, in any or all of the layers, on the phase change caused in the light reflected by the multilayer to be estimated. Lissberger's results, applied to the all-dielectric single-cavity (Fabry–Perot) filter, show that the most critical layer is the cavity layer spacer. The layers on either side of the cavity layer are next most sensitive and the remainder of the layers progressively less sensitive the further they are from the cavity.

We have already mentioned in Chapter 8 the paper by Giacomo et al. [38], who examined the effects on the performance of narrowband filters of local variations in thickness, or "roughness," of the films. This involved the study of the influence of thickness variations in any layer on the peak frequency of the complete filter. The treatment was similar in some respects to that of Lissberger. For the conventional single-cavity filter, layers at the center had the greatest effect. If all layers were assumed equally rough, the design least affected by roughness would have all the layers of equal sensitivity and attempts were made to find such a design. A phase-dispersion filter gave rather better results than the simple conventional single-cavity, but still fell short of ideal.

Baumeister [39] introduced the concept of sensitivity of filter performance to changes in the thickness of any particular layer. The method involved the plotting of sensitivity curves over the whole range of useful performance of a filter, curves that indicated the magnitude of performance changes due to errors in any one layer. His conclusions concerning a quarter-wave stack were that the central layer is the most sensitive and the outermost layers least sensitive. An interesting feature of these sensitivity curves for the quarter-wave stack is that the sensitivity is greatest nearest the edge wavelength. This is confirmed in practice with edge filters, where errors usually produce more pronounced dips near the edge of the transmission zone than appear in the theoretical design.

Smiley and Stuart [40] adopted a different approach using an analog computer. There were some difficulties involved in devising an analogue computer, but, once constructed, it possessed the advantage at the time that any of the parameters of the thin-film assembly could be easily varied. A particular filter, which they examined, was:

$$\text{Air}\,|4H\;L\;4H|\,\text{Air}$$

with $n_H = 5.00$ and $n_L = 1.54$. This is a multiple-cavity filter of simple design. Errors in one of the $4H$ layers and in the L layer were investigated separately. They found that errors greater than 1% in one $4H$ layer had a serious effect; errors of 5%, for example, caused a drop in peak transmittance to 70% and errors of 10% a drop to 50%, together with considerable degradation in the shape of the pass band. Errors of up to 10% in the L layer had virtually no

effect on either the shape of the pass band or on the peak transmittance. This is absolutely in line with what we would nowadays expect from a multiple-cavity filter.

An investigation was performed by Heather Liddell as part of a study reported by Smith and Seeley [41] into some effects of errors in the monitoring of infrared single-cavity filters of designs:

$$\text{Air}\,|\,HLHL\ HH\ LHLHL\,|\,\text{Substrate}$$

and

$$\text{Air}\,|\,HL\ HH\ LHL\,|\,\text{Substrate}.$$

A computer program to calculate the reflectance of a multilayer at any stage during deposition was used. Monitoring was assumed to be at or near a frequency of four times the peak frequency (i.e., a quarter of the desired peak wavelength) of the completed filter. It was shown that, if all layers were monitored on one single substrate, then, provided the form of the reflectance curve during deposition was predicted, and it was possible to terminate layers at reflectances other than turning values, there could be an advantage in choosing a monitoring frequency slightly removed from four times peak frequency. If no corrections were made for previous errors, then a distinct tendency for errors to accumulate in even-order monitoring (that is monitoring frequency an even integer times peak frequency) was noted.

The major problem in tolerancing is that real errors cannot be treated as small; that is to say that first-order approximations are unrealistic. The error in one layer interacts nonlinearly with the errors in other layers and it is not realistic to treat them as though their effects can be calculated in isolation and then linearly combined.

In recent years, the most satisfactory approach for dealing with the effects of errors and the magnitude of permissible tolerances has been found to be the use of Monte Carlo techniques. In this method, the performance of the filter is calculated, first with no errors and then a number of times with errors introduced in all the layers. In the original form of the technique, introduced by Ritchie [42], the errors are thickness errors and completely random and uncorrelated. They belong to the same infinite population, taken as normal with prescribed mean and standard deviation. The performance curves of the filter without errors and of the various runs with errors are calculated. Although statistical analyses of the results can be made, it is almost always sufficient simply to plot the various performance curves together, when visual assessment of the effects of errors of the appropriate magnitude can be made. The method really provides a set of traces that reproduce, as far as possible, what would actually be achieved in a succession of real production batches. The characteristics of the infinite normal population can be varied and the procedure repeated. It is sufficient to calculate some 8 or perhaps 10 curves for a set of error parameters. The level of error at which a

satisfactory process yield would be achieved can then readily be determined. In the earliest version of the technique, the various errors were drawn manually from random number tables and converted into members of a normal population using a table of area under the error curve. (The procedure is described in textbooks of statistics—see Yule and Kendall [43], for example.) Later versions of the technique simply generate the random errors by computer. Although the errors are usually drawn from a normal population, the type of population has little effect on the order of the results. Normal distributions are convenient to program, and since there is no strong reason for not using them and because errors made up of a number of uncorrelated effects are well represented by normal distributions, most error analyses do make use of them.

The level of permissible errors depends to some extent on the index contrast in the filter. Figure 13.11 shows some examples of plots where the errors are simple independent thickness errors of zero mean. From these and similar results we find that the thickness errors that can be tolerated in simple edge filters and antireflection coatings are normally around 2% standard deviation. This correlates quite well with the accuracy usually achievable by normal optical or quartz crystal monitoring. Narrow-band filters require rather better accuracy when random errors in thickness are involved. The two-cavity filter of Figure 13.11 is showing unacceptable pass band distortion with random thickness errors as small as 0.5% standard deviation. This filter has a roughly 2% half-width. For narrower filters or filters with greater number of cavities, the tolerances must be still tighter. In a single-cavity filter, the main effect of random errors is a peak wavelength shift, the shape of the pass band being scarcely affected even by errors as large as 10%. The standard deviation of the scatter in peak wavelength is slightly less than the standard deviation of the layer thickness errors so that some averaging process is operating, although the orders of magnitude are the same.

A system of monitoring in which the thickness errors in different layers are uncorrelated requires that each layer should be controlled independently of the others. In this type of monitoring, therefore, we cannot expect high precision in the centering of narrowband single-cavity filters and we foresee great difficulties in being able to produce narrowband multiple-cavity filters at all.

This monitoring arrangement is what we have called indirect. Systems where each layer is controlled on a separate monitoring chip are of this type. There are difficulties with monitoring of low-index layers on a fresh glass substrate because of the small changes in transmittance or reflectance, and so the monitoring chips are usually changed after a low-index layer and before a high index, two or four layers per chip being normal. Sometimes these layers will be monitored to turning values. More frequently, what is sometimes called *level monitoring* will be used. Here the layer reflectance or transmittance signal is terminated at a point removed from the turning value where the signal is still changing, leading to an inherently greater accuracy. This

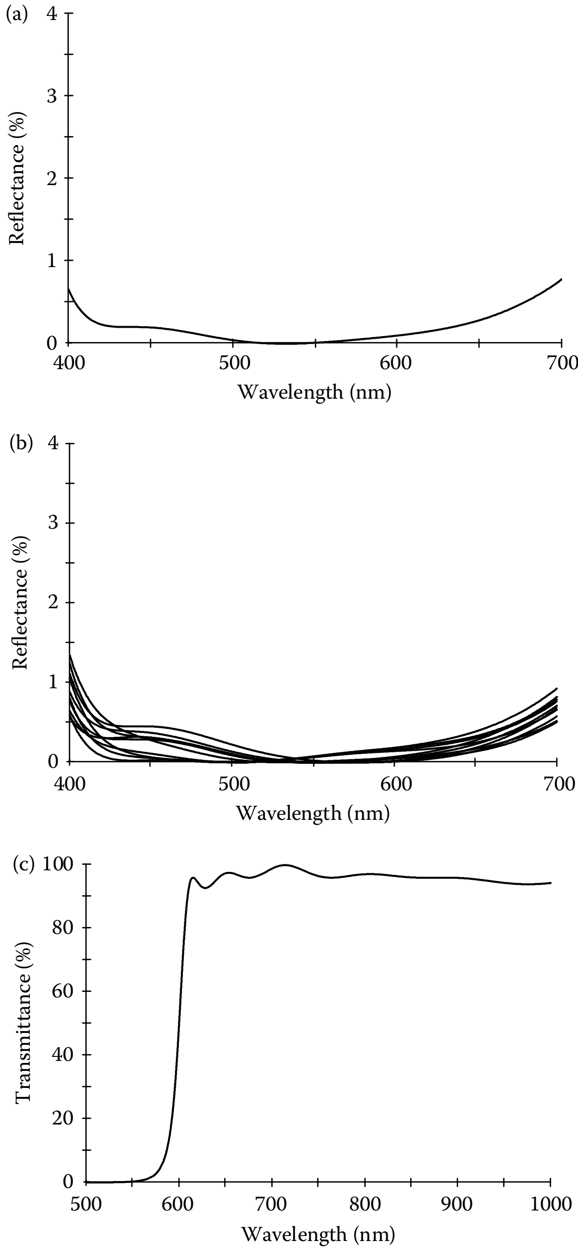

FIGURE 13.11
The effect of random in layer thickness on the performance of thin-film filters. (a) Four-layer antireflection coating with no errors. (b) Four-layer antireflection coating with thickness errors of 2% standard deviation. (c) Long-wave pass filter with no errors. (d) Long-wave pass filter with thickness errors of 2% standard deviation. (e) Two-cavity filter with no errors. (f) Two-cavity filter with thickness errors of 0.5% standard deviation.

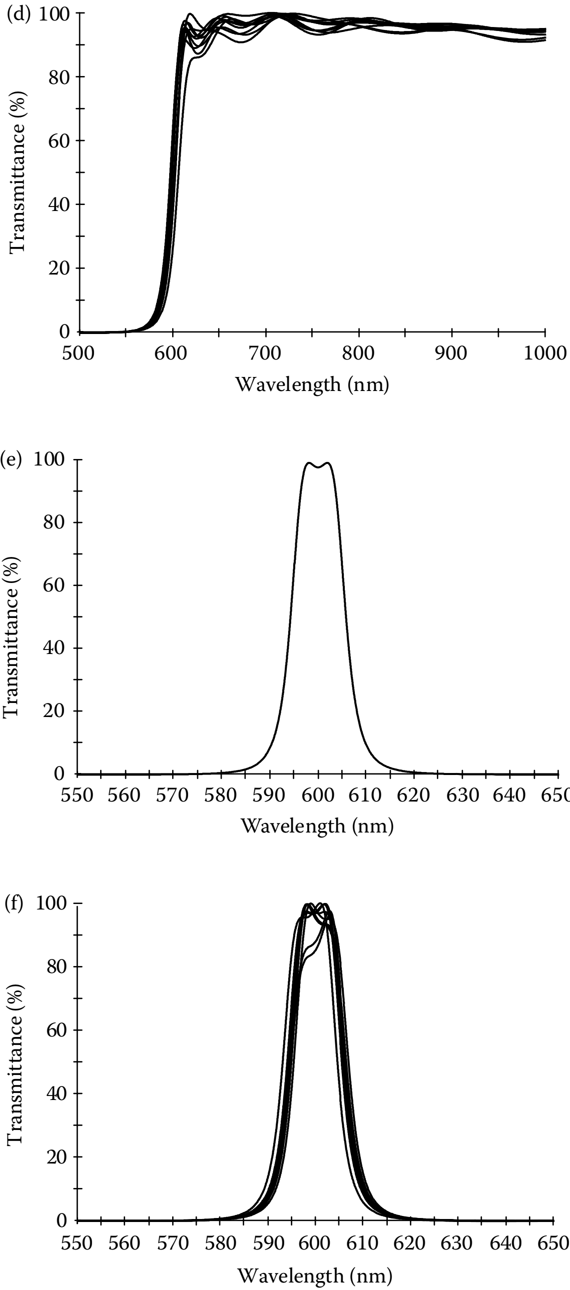

FIGURE 13.11 (continued)

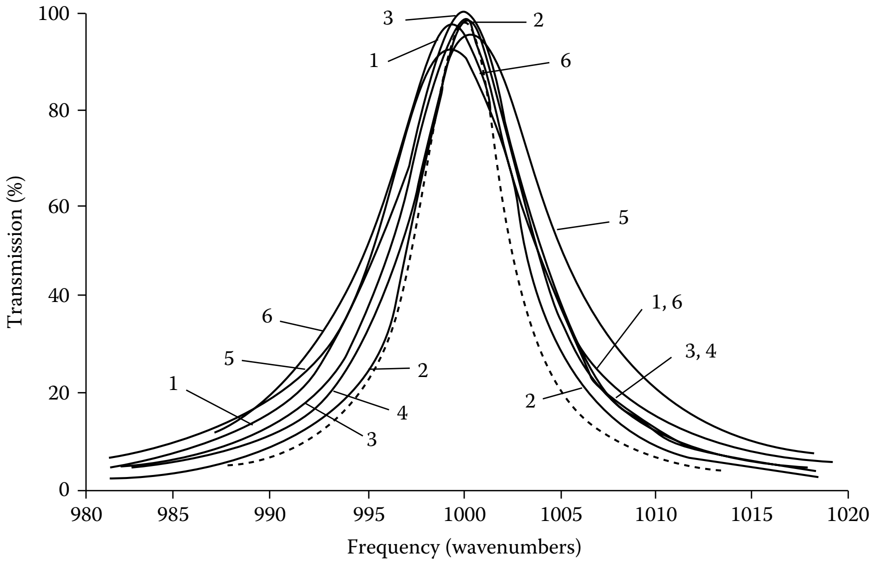

FIGURE 13.12
The effect of 1% standard deviation reflectance error on the performance of the Fabry–Perot filter: Air |*HLHL HH LHLH*| Ge. The substrate is germanium (n = 4.0), L represents a quarter-wave of ZnS (n = 2.3) and H a quarter-wave of PbTe (n = 5.4). The monitoring is in first order. The *dashed curve* is the performance with no errors. (After Macleod, H.A., *Optica Acta*, 19, 1–28, 1972.)

approach involves what is really an absolute measurement of reflectance or transmittance, and so the termination point is frequently chosen to be after a turning value rather than before, so that the extremum can be used as a calibration. This usually implies a shorter wavelength for monitoring or the introduction of a geometrical difference between batch and monitor, placing the monitor nearer the source or placing masks in front of the batch.

Narrowband filters are not normally monitored in this way. Instead, all the layers are monitored on the same substrate, usually the actual filter being produced, a system known as *direct monitoring.* At the peak wavelength of the filter, the layers should all be quarter-waves or half-waves, and so we can expect a signal that reaches an extremum at each termination point. The accuracy cannot therefore be particularly high for any individual layer and, at first sight, it would appear that the achievable accuracy should be far short of what must be required. Since each layer is being deposited over all previous layers on the monitor substrate, then there is an interaction between the errors in any layer and those in the previous layers not included in the tolerancing calculation described above. We really require a technique that models the actual process as far as possible and this is a quite straightforward computing operation. Each layer is simply considered to be deposited on a surface of optical admittance corresponding to that of the multilayer that precedes it, rather than on a completely fresh substrate. The results of

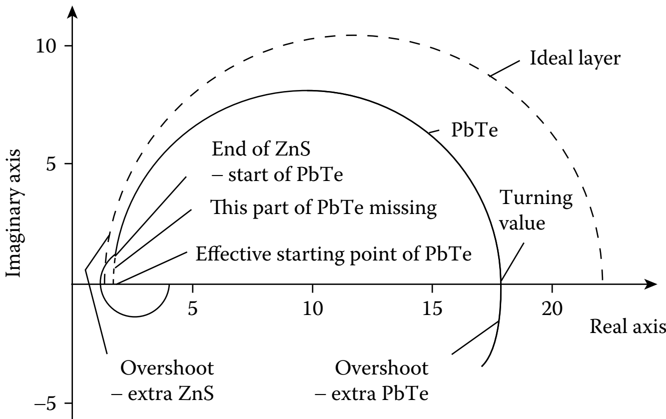

FIGURE 13.13
The admittance locus of the first two layers of the filter in Figure 13.12 when there is an overshoot in the first layer of around one-eighth wave optical thickness. (After Macleod, H.A., *Optica Acta*, 19, 1–28, 1972.)

such a simulation are shown in Figure 13.12 taken from Macleod [44], which demonstrates the powerful error compensation mechanism that has been found to exist. The compensation has also been independently and simultaneously confirmed by Pelletier and his colleagues [45]. Its nature is perhaps best explained by the use of an admittance diagram.

Figure 13.13 shows such a diagram drawn for two quarter-waves. Since both the isoreflectance contours (see Chapter 2) and the individual layer loci are circles centered on the real axis, the turning values must always occur at the intersections of the loci with the real axis, regardless of what has been deposited earlier. At the termination point of each layer, there is the possibility of restoring the phase to zero or to π. As far as any individual layer is concerned, it is principally the overshoot or undershoot of the previous layer that affects it. If the previous layer is too thick, the current one will tend to be thinner to compensate, and vice versa. Of course, it is impossible to cancel completely all effects of an error in a layer. The process is actually transforming the thickness errors into errors in reflectance at each stage since the loci will be slightly displaced from their theoretical position. This is not a serious error. As can be guessed from the shape of the diagram, the reflectance error is a second-order effect. Since the phase is self-corrected each time a layer is deposited, the peak wavelength of the filter will remain at the desired value, that of the monitoring wavelength. The remaining error, the residual one in reflectance, is then translated into changes in peak transmittance and halfwidth. Since the reflectance change is always a reduction, the bandwidth of an actual filter is invariably wider than theoretical. The peak transmittance falls to the extent that the reflectances on either side of the spacer layer are unbalanced. This is usually quite small and the reduction in peak transmittance is generally much less important that the increase in bandwidth.

In this monitoring arrangement, thickness errors in any individual layer are a combination of a compensation of the error in the previous layer together with the error committed in the layer itself. The magnitude of the thickness errors can be quite misleading in interpreting whether or not the filter can be made successfully. In Figure 13.12, for example, thickness errors of the order of 50% occur in some layers and yet the filter characteristics are all useful ones.

The important characteristic is actually the error in reflectance or transmittance in determining the turning values, and it is possible to develop theoretical expressions relating the reflectance or transmittance errors to the reduction in performance of the final filter [44]. This analysis includes an assessment of the sensitivity of each layer to errors that indicate those layers where the greatest care in monitoring should be exercised. These can be different from the thickness sensitivity of Lissberger [36,37] already mentioned. With high-index cavity layers, greatest sensitivity is found in the low-index layers following the cavity, while with low-index cavities, the cavity itself has the highest sensitivity. A feature of this analysis is that it demonstrates that for any particular error magnitude, there is a point where improved half-width does not result from an increase in the number of layers because the effect of errors is increasing more rapidly than the theoretical decrease in bandwidth. Then it is necessary to move to second- and higher-order spacers if decreased bandwidth is to result. This corresponds to what is found in practice. The error analysis also demonstrates that from the point of view of monitoring, high-index cavities are to be preferred over low-index. We have already seen in Chapter 8 that high-index spacers give decreased angular sensitivity and greater tuning range. However, for filters in the visible region where the absorption loss in the high-index layers is greater than that in the low-index layers, low-index cavity layers are more common.

Formulae that permit the calculation of the errors in reflectance, in half-width, and in peak transmittance as a function of the magnitude of the random errors in determining the turning values exist [44], but for most purposes a computer simulation will suffice. It should be noted that the compensation is effective only for the first order. Second-order monitoring, that is monitoring at the wavelength for which the layers are all half-waves, is not effective in preserving the peak wavelength. We can understand this because the admittance diagram is quite different and so the compensation is of a different nature. Likewise, third-order monitoring is not as effective as first-order, and, although the scatter in peak wavelength is less than that obtained with second-order monitoring, it is, nevertheless, quite large.

Multiple-cavity filters are similar in behavior but there are some complications. The coupling layers in between the various Fabry–Perot sections of the filter turn out to be particularly sensitive to errors in a rather peculiar way. Preliminary examination of the admittance diagram for the various layers of a multiple-cavity filter and even the standard error analysis do not immediately reveal any marked difference in terms of error sensitivity

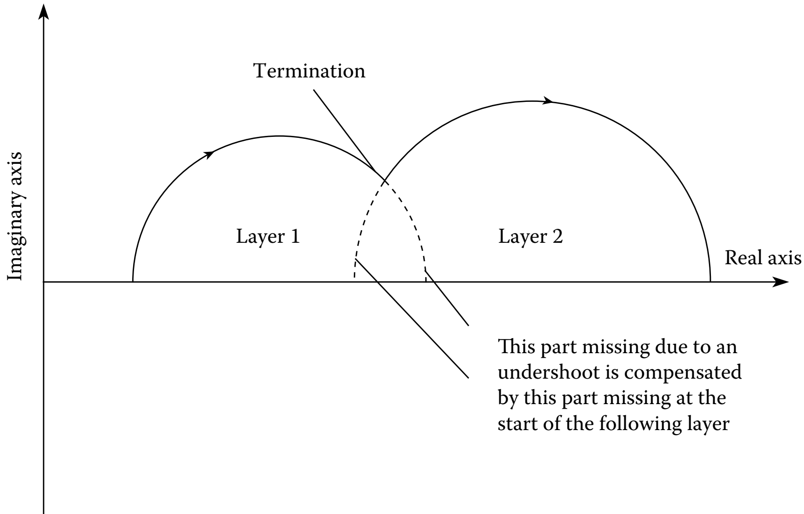

FIGURE 13.14
Error compensation when the admittance circles are on the same side of the real axis. (After Macleod, H.A. and Richmond, D., *Optica Acta*, 21, 429–443, 1974.)

between these layers and those of single-cavity filters. Closer investigation shows that there is always one transition from one layer to the next occurring at or near to the central coupling layer where a thickness error is compensated by an error of the same rather than the opposite sense [46]. The condition is sketched in Figure 13.14. An increase in thickness in the first layer results in an increase in thickness of the subsequent layer and vice versa. This condition must occur once between each pair of cavities. The net result is an increase or decrease in the relative spacing of the cavities causing the appearance of a multiple-peaked characteristic curve. The peaks become more pronounced, the greater the relative error in spacing. One of the peaks always corresponds to the normal control wavelength and is close to the theoretical transmittance. The other peaks (one for a two-cavity, two for a three-cavity, and so on) can appear on either side of the main peak depending on the nature of the particular errors. This false compensation can be destroyed if the second of the two layers concerned can be controlled independently of the others, either on a separate monitor plate or by a quartz-crystal monitor, or even by simple timing. It is essential that it should also be deposited on the regular monitor as well, so that the compensation of the full filter should not be destroyed [46].

Another problem surfaced in the production of narrowband filters for applications in telecommunications. Figure 13.15 shows the specification for a dense wavelength division multiplexing filter together with the effect on a suitable design of ten sets of independent random thickness errors drawn from an infinite normal population with standard deviation of 0.003%. This perturbs the performance of the filter to the limit of what is acceptable by

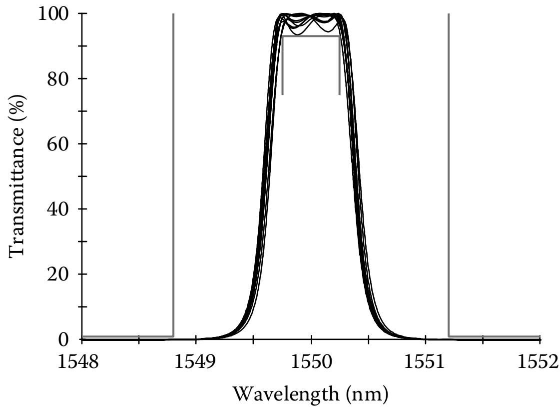

FIGURE 13.15
The effect of random errors in layer thickness of standard deviation 0.003%. The perturbed performance is just within the specification indicated by the straight lines.

the specification. We have already seen in this chapter that turning value monitoring carries with it the automatic compensation of thickness errors but in the case especially of these high performance filters, random thickness errors also have an implication. Uniformity of the filter will be assured by rotating the substrate about its axis above an offset source. These multiplexing and demultiplexing filters are normally quite small, often 1.4 mm^2 in size, and so normal practice is to make a rather larger filter on a disk and to dice it into smaller units after coating. Those parts of the disk that are displaced from the center of rotation will suffer a variable deposition rate as the disk rotates, but each complete rotation will have an incremental thickness added that is equivalent to that at the center or deliberately adjusted so that the filters cut from the disk will span a number of communication channels. However, it is impossible to ensure that each layer will correspond to an exact whole number of rotations. There will therefore be a random error in termination of each layer corresponding to the final fractional turn that will be larger the farther the element is from the center of rotation. This random error must not exceed the already established 0.003%. We can assume for the sake of argument that the largest radius is such that the typical error from this effect is 25% of the thickness that would be deposited in a full turn. Then the total number of turns necessary in order that this error should not exceed our 0.003% figure is 0.25/0.00003, that is 8333 complete rotations. Assuming the deposition of a single quarter-wave takes some 5 min, then the required rotational speed of the disk is 1700 revolutions per minute. Such rotational rates are quite typical of machines for the production of telecommunication-quality filters.

Pelletier and his colleagues [47] have studied theoretically the behavior of the *maximètre* types of monitoring systems in the production of narrowband filters. They conclude that, as we would expect, the accuracy of the

system in the production of single layers is very much better than a single-wavelength system. In the monitoring of narrowband filters all on one substrate, there is a compensation process operating like the turning value method but it is more complex in operation. For very small errors in most layers, the system works adequately, but for large errors in most layers or small errors in certain critical layers, the errors accumulate in such a way as to cause a drastic broadening of the bandwidth of a single-cavity filter or complete collapse of a multiple-cavity filter. Pelletier has introduced two concepts to describe this behavior. Accuracy represents the error that will be committed in any particular layer without reference to the multilayer system as a whole. Stability represents the way in which the errors accumulate as the multilayer deposition proceeds. The accuracy of the *maximètre* is excellent and greater than in the turning value method, but the stability in the control of narrowband filters is very poor and it can easily become completely unstable. Subsidiary measurements are therefore required to ensure stability if advantage is to be taken of the very great accuracy that is possible. Narrowband filters and their monitoring systems have been surveyed by Macleod [48].

The concepts of accuracy and stability and the discovery that the one does not ensure the other imply that different measurements may be necessary to ensure that both are simultaneously assured. This leads to the idea of broadband monitoring in which simultaneous measurements are made at a large number of wavelengths over a wide spectral region and a merit function representing the difference between actual and desired signals is computed. The merit function can then be used as a monitoring signal and layer deposition terminated when the merit function reaches a minimum. Although perfect deposition should ensure a minimum of zero in the figure of merit, inevitable errors in layer index and homogeneity will perturb the result. The accuracy and stability of such a broadband system in the monitoring of certain components such as beam splitters has been investigated by computer simulation [49] and evidence found for useful error compensation. Apart from the very qualitative justification discussed above, no theory for such compensation yet exists and it may operate only in quite specific cases.

Extensions of broadband monitoring to a system that would reoptimize, on the basis of errors measured in earlier layers, those layers of a design yet to be deposited, are possible but there are also considerable dangers. The most important aspect of such processes is that the errors should be correctly characterized. They may be errors in thickness, optical constants, or both and if incorrectly characterized the results can be rather worse than in the absence of compensation [25,26]. Such techniques should not be thought of as removing the need for stable reproducible materials.

As computing power has increased, so has the ability to model the production process. Such modeling, almost invariably of the Monte Carlo type, allows the study of errors and tolerances in an almost completely realistic way. Some results are described by Macleod [50] and Clark [51]. The technique

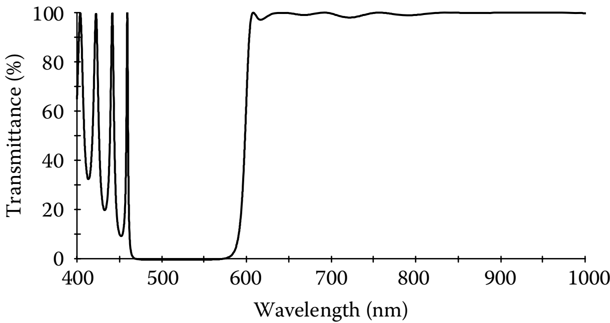

FIGURE 13.16
Theoretical performance of the longwave pass filter used in the simulation exercise.

has recently been termed "computational manufacturing" by Tikhonravov et al. [52–54].

We can illustrate the method with a simple example of a longwave-pass filter for the visible and near infrared. The filter consists of a total of 31 layers of silica and tantala, arranged as a core of quarter-waves bounded on each side by four layers that have been refined to act as ripple-reducing matching systems. The theoretical performance is shown in Figure 13.16.

For this exercise we will limit our model to include signal noise only. We assume transmittance monitoring, and Figure 13.17 shows the signal for the first two layers of the simulation illustrating the level of noise that we will assume, 0.4% standard deviation in terms of transmittance.

Our first task is to decide on the interpretation of the monitoring signal. Because of the difficulty of maintaining accurate calibration of reflectance or transmittance, common practice in optical monitoring is to arrange that the termination point should, wherever possible, follow a signal extremum. The termination level is then specified as a prescribed signal increase or reduction following the extremum. Thus, the monitoring system must be capable of recognizing and extremum and then detecting the necessary

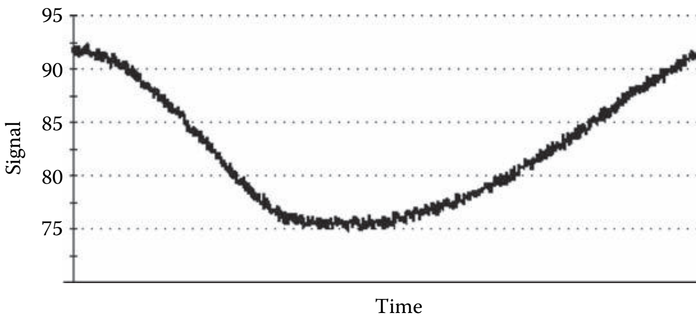

FIGURE 13.17
The simulated monitoring signal for the first two layers of the longwave pass filter shown as if on a strip chart. (Courtesy Thin Film Center Inc, Tucson, Arizona, USA.)

overshoot. We shall use in our simulation a straightforward technique that is mirrored in many commercial systems. The noisy signal will present many extrema, and we will select the correct one by introducing the equivalent of mechanical backlash. The system will accept an extremum once the signal has reversed in sense by a prescribed amount that must be greater than the total noise perturbations of the signal. The result will be a delay in recognition that will increase with the level of noise. Once the extremum has been registered in this way, the prescribed overshoot will be applied to the accepted extremum to derive the termination level. The layer will then be terminated as soon as this level is reached, or, immediately, if it is actually less than the backlash. Figure 13.18 illustrates the method. Noise implies that detection of an extremum will be late but termination at a prescribed level will tend to be early.

Next we need to decide on a monitoring procedure. We will, as is common practice, use multiple chips and initially we choose four layers per chip. Ideally, the first layer on a chip should be of high index to maximize the signals and happily, in this case, the final layer in the design, that is the first layer to be deposited, is of high index. The reference wavelength for the design is 523 nm but for better signals we move the monitoring wavelength to 450 nm, choose a spectral bandwidth of 10 nm, and also increase the tooling factor for both materials in the machine to 1.1, that is 10% more material must be deposited on the chip for the correct thickness on the part. This should ensure as far as possible monitoring signals that exhibit extrema before termination. Beyond 450 nm we are climbing the dispersion curve for tantala and we are also running out of energy without a special source.

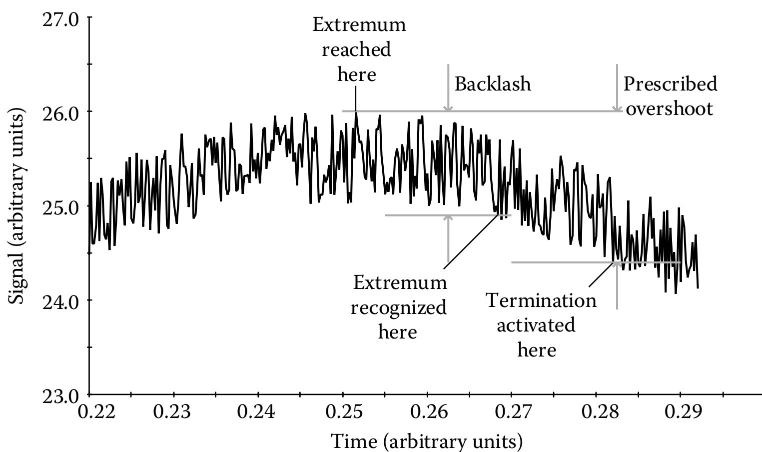

FIGURE 13.18
The noise on the signal implies an enormous numbers of local extrema. The occurrence of the correct extremum will be recognized when the signal has reversed a prescribed amount that must be greater than the total excursion due to the noise. Once the extremum is recognized, the prescribed overshoot will be applied to arrive at the correct termination level for the signal.

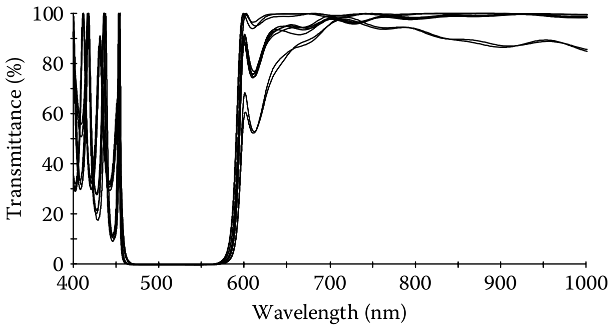

FIGURE 13.19
The first attempt at simulating the construction of the filter results in a poor performance in the pass region. (Courtesy Thin Film Center Inc, Tucson, Arizona, USA.)

For such exercises, 10 separate runs of the Monte Carlo model are usually sufficient. The results of the first 10 runs of this particular model are shown in Figure 13.19. The pass region is poor and the yield quite unacceptable. The advantage of simulation is that the designs that were achieved are all available for inspection. We can quite quickly determine that it is the first chip with the first four layers to be deposited that is the problem. The second pair of layers is suffering from errors accumulated from the first pair. Replacing the first chip by two chips, each with only two layers, results in a successful monitoring arrangement as shown in Figure 13.20. It is difficult to detect it in Figure 13.20, but the inherent shortening of the layers due to noise in level monitoring has moved the edge slightly to the short wave. This can readily be corrected in practice by increasing the monitoring wavelength.

This is, admittedly, a quite simple example. Effects like varying tooling factors, changing temperature, noise varying with time and so on can all be readily simulated. This makes it easy for the design process to include an element of simulation.

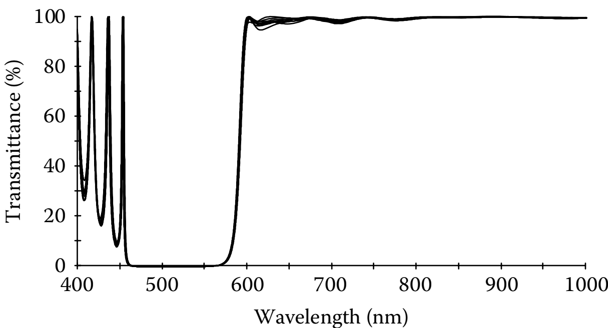

FIGURE 13.20
Changing the first four-layer chip into two two-layer chips solves the problem. The 10 runs now show satisfactory performance. (Courtesy Thin Film Center Inc, Tucson, Arizona, USA.)

Quartz-crystal monitoring, in which the mass rather than optical thickness is measured, seems unlikely to possess powerful compensation. Yet simulation of a simple broadband system for antireflection coatings comparing optical monitoring with quartz crystal gave results that indicate that the quartz crystal is in no way inferior [50]. The relative merits of quartz crystal and optical monitoring form a subject of almost constant debate and published results for quartz crystal are impressive [55,56]. It is clear that narrowband filters, if they are to be controlled in peak wavelength, do require direct optical monitoring, but quartz crystal monitoring is suitable for most other filter types. The general opinion, based to some extent on instinct, is that quartz-crystal monitoring is most suitable for production of successive batches of identical components. For single runs of varying coating types, optical monitoring appears normally to be preferred. Optical monitoring is also preferred in applications such as filters for the far infrared, where very large thicknesses of materials are deposited in each coating run.

References

1. Holland L and Steckelmacher W 1952 The distribution of thin films condensed on surfaces by the vacuum evaporation method *Vacuum* **2** 346–364
2. Behrndt K H 1963 *Thickness uniformity on rotating substrates*, in *Transactions of the 10th AVS National Vacuum Symposium* (London: McMillan) 379–384
3. Knudsen M 1915 Das Cosinusgesetz in der kinetischen Gastheorie *Annalen der Physik, 4th Series* **48** 1113–1121
4. Jancke E and Emde F 1952 *Tables of Higher Functions* ed 5th (Leipzig: Teubner)
5. Keay D and Lissberger P H 1967 Application of the concept of effective refractive index to the measurement of thickness distributions of dielectric films *Applied Optics* **6** 727–730
6. Graper E B 1973 Distribution and apparent source geometry of electron-beam heated evaporation sources *Journal of Vacuum Science and Technology* **10** 100–103
7. Richmond D 1976 *Thin film narrow band optical filters* PhD Thesis Newcastle upon Tyne Polytechnic
8. Ramsay J V, Netterfield R P, and Mugridge E G V 1974 Large-area uniform evaporated thin films *Vacuum* **24** 337–340
9. Holland L 1956 *Vacuum Deposition of Thin Films* (London: Chapman and Hall)
10. Mattox D M 1978 Surface cleaning in thin film technology *Thin Solid Films* **53** 81–96
11. Lee C C 1983 *Moisture adsorption and optical instability in thin film coatings* PhD Dissertation University of Arizona
12. Cox J T and Hass G 1958 Antireflection coatings for germanium and silicon in the infrared *Journal of the Optical Society of America* **48** 677–680
13. Banning M 1947 Practical methods of making and using multilayer filters *Journal of the Optical Society of America* **37** 792–792

14. Polster H D 1952 A symmetrical all-dielectric interference filter *Journal of the Optical Society of America* **42** 21–25
15. Billings B H 1950 A birefringent frustrated total reflection filter *Journal of the Optical Society of America* **40** 471–476
16. Perry D L 1965 Low loss multilayer dielectric mirrors *Applied Optics* **4** 987–991
17. Behrndt K H and Doughty D W 1966 Fabrication of multilayer dielectric films *Journal of Vacuum Science and Technology* **3** 264–272
18. Giacomo P and Jacquinot P 1952 Localisation précise d'un maximum ou d'un minimum de transmission en fonction de la longeur d'onde. Application à la préparation des couches minces *Journal de Physique et le Radium* **13** 59A–64A
19. Ring J 1957 PhD Thesis University of Manchester
20. Lissberger P H and Ring J 1955 Improved methods for producing interference filters *Optica Acta* **2** 42–46
21. Hiraga R, Sugawara N, Ogura S, and Amano S 1974 Measurement of spectral characteristics of optical thin film by rapid scanning spectrophotometer *Japanese Journal of Applied Physics* 689–692
22. Borgogno J P, Bousquet P, Flory F, Lazarides B, Pelletier E, and Roche P 1981 Inhomogeneity in films: limitation of the accuracy of optical monitoring of thin films *Applied Optics* **20** 90–94
23. Flory F, Schmitt B, Pelletier E, and Macleod H A 1983 Interpretation of wide band scans of growing optical thin films in terms of layer microstructure *Proceedings of the Society of Photo-Optical Instrumentation Engineers* **401** 109–116
24. Sullivan B T and Dobrowolski J A 1992 *Optical multilayer coatings produced with automatic deposition error compensation* in *Optical Interference Coatings Tucson, Arizona* Optical Society of America 278–279
25. Sullivan B T and Dobrowolski J A 1992 Deposition error compensation for optical multilayer coatings. 1. Theoretical description *Applied Optics* **31** 3821–3835
26. Sullivan B T and Dobrowolski J A 1993 Deposition error compensation for optical multilayer coatings. II. Experimental results: sputtering system *Applied Optics* **32** 2351–2360
27. Ristau D, Ehlers H, Gross T, and Lappschies M 2006 Optical broadband monitoring of conventional and ion processes *Applied Optics* **45** 1495–1501
28. Dligatch S and Netterfield R P 2007 *In-situ Monitoring and Deposition Control of a Broadband Multilayer Dichroic Filter* in *Optical Interference Coatings* Optical Society of America WC4, 1–3
29. Zoeller A, Boos M, Goetzelmann R, Hagedorn H, and Klug W 2005 Substantial progress in optical monitoring by intermittent measurement technique *Proceedings of the Society of Photo-Optical Instrumentation Engineers* **5963** 59630D 1–9
30. Wajid A 1992 *Measuring and controlling deposition on a piezoelectric monitor crystal* US Patent 5,112,642
31. Riegert R P 1968 *Optimum usage of quartz crystal monitor based devices* in *IVth International Vacuum Congress Manchester* Institute of Physics and the Physical Society 527–530
32. Spencer A G 1997 *Precision optical coatings from express ophthalmic coaters* in *40th Annual Technical Conference Proceedings New Orleans* Society of Vacuum Coaters 259–265

33. Pervak V, Tikhonravov A V, Trubetskov M K, Pistner J, Krausz F, and Apolonski A 2007 Band filters: two-material technology versus rugate *Applied Optics* **46** 1190–1193
34. Gibson D R, Brinkley I, Waddell E M, and Walls J M 2008 Closed field magnetron sputtering: new generation sputtering process for optical coatings *Proceedings of the Society of Photo-Optical Instrumentation Engineers* **7101** 710108-1–710108-12
35. Heavens O S 1954 All-dielectric high-reflecting layers *Journal of the Optical Society of America* **44** 371–373
36. Lissberger P H 1959 Properties of all-dielectric filters. I. A new method of calculation *Journal of the Optical Society of America* **49** 121–125
37. Lissberger P H and Wilcock W L 1959 Properties of all-dielectric interference filters. II. Filters in parallel beams of light incident obliquely and in convergent beams *Journal of the Optical Society of America* **49** 126–130
38. Giacomo P, Baumeister P W, and Jenkins F A 1959 On the limiting bandwidth of interference filters *Proceedings of the Physical Society* **73** 480–489
39. Baumeister P W 1962 Methods of altering the characteristics of a multilayer stack *Journal of the Optical Society of America* **52** 1149–1152
40. Smiley V N and Stuart F E 1963 Analysis of infrared interference filters by means of an analog computer *Journal of the Optical Society of America* **53** 1078–1083
41. Smith S D and Seeley J S 1968 *Multilayer filters for the region 0.8 to 100* microns Final Report on Contract AF61(052)-833 (Air Force Cambridge Research Laboratories)
42. Ritchie F S 1970 *Multilayer filters for the infrared region 10-100 microns* PhD Thesis University of Reading
43. Yule G U and Kendall M G 1958 *An Introduction to the Theory of Statistics* ed Fourteenth (London: Charles Griffin & Co, Ltd)
44. Macleod H A 1972 Turning value monitoring of narrow-band all-dielectric thin-film optical filters *Optica Acta* **19** 1–28
45. Bousquet P, Fornier A, Kowalczyk R, Pelletier E, and Roche P 1972 Optical filters: monitoring process allowing the auto-correction of thickness errors *Thin Solid Films* **13** 285–290
46. Macleod H A and Richmond D 1974 The effect of errors in the optical monitoring of narrow-band all-dielectric thin film optical filters *Optica Acta* **21** 429–443
47. Pelletier E, Kowalczyk R, and Fornier A 1973 Influence du procédé de contrôle sur les tolérances de réalisation des filtres interférentiels à bande étroite *Optica Acta* **20** 509–526
48. Macleod H A 1976 Thin film narrow band optical filters *Thin Solid Films* **34** 335–342
49. Vidal B, Fornier A, and Pelletier E 1978 Optical monitoring of nonquarterwave multilayer optical filters *Applied Optics* **17** 1038–1047
50. Macleod H A 1981 Monitoring of optical coatings *Applied Optics* **20** 82–89
51. Clark C and Macleod H A 1997 *Errors and tolerances in optical coatings* in *40th Annual Technical Conference Proceedings New Orleans* Society of Vacuum Coaters 274–279
52. Tikhonravov A V and Trubetskov M K 2005 Computational manufacturing as a bridge between design and production *Applied Optics* **44** 6877–6884
53. Tikhonravov A V, Trubetskov M K, and Amotchkina T V 2006 Investigation of the effect of accumulation of thickness errors in optical coating production by broadband optical monitoring *Applied Optics* **45** 7026–7034

54. Tikhonravov A V, Trubetskov M K, and Amotchkina T V 2006 Statistical approach to choosing a strategy of monochromatic monitoring of optical coating production *Applied Optics* **45** 7863–7870
55. Pulker H K 1978 Coating production: new ideas at a time of demand *Optical Spectra* **12** 43–46
56. Laan C J v d and Frankena H J 1977 Monitoring of optical thin films using a quartz crystal monitor *Vacuum* **27** 391–397

14

Specification of Filters and Environmental Effects

Ideally, if a filter is to be manufactured for a customer for a given application, then the performance required by the customer, and the design, manufacturing, and test methods, should all be defined, even if only implicitly. These details form different aspects of the specification of the filter.

There is no standard method for setting up the specification of an optical filter or coating, the problem being much the same as for any other device. There are three main aspects to be considered: the performance specification, which lists the details of the performance required from the filter, and is usually the customer's specification; the manufacturing specification, which defines the design and details the steps involved in the manufacture of the filter; and the test specification laying down the tests that must be carried out on the filter to ensure that it meets the performance requirements, these latter aspects being mainly the concern of the manufacturer. In the following notes, a few of the more important points are mentioned, but they do not form a complete guide to the writing of specifications, which is a subject in its own right.

Optical filter specifications can conveniently be divided into two sections, one concerned with optical properties and the other with physical or environmental properties. We shall first consider the optical properties.

14.1 Optical Properties

14.1.1 Performance Specification

The performance specification of a filter is essentially a statement of the capabilities of the filter in a language that can readily be interpreted by system designer, customer, and filter manufacturer alike. It can sometimes be prepared by a filter manufacturer from knowledge of the known achievable performance. This can be either for a customer, or, possibly without having a particular application in mind, as in the case of a standard product in a catalogue. We shall say little about the latter here. Probably more often, the performance specification will be written by the system designer and will state a level of performance required from a filter in order to achieve a

desired level of performance from a system. In writing such a specification, an answer must first of all be given to the question: What is the filter for? The purpose of the filter must be set down as clearly and concisely as possible, and this will form the basis for the work on the performance specification. There is really no systematic method for specifying the details of performance. Sometimes it happens that the performance of the system in which the filter is to be used must be of a certain definite level; otherwise, there will be no point in proceeding further. The filter performance requirements can then be quite readily set down. Often, however, it will not be quite so simple. No absolute requirement for performance may exist, only that the performance should be as high as possible within allowable limits of complexity or perhaps price. In such a case, the performance of the system with different levels of filter performance must be balanced against cost and system complexity, and a decision made as to what is reasonable. The final specification will be a compromise between what is desirable and what is achievable. This will often need the input of much design and manufacturing information and close contact between customer and manufacturer. It should always be remembered in this that specifications that cannot be met in practice can be of only academic interest.

By way of an example, let us briefly consider the case where a spectral line must be picked out against a continuum. Clearly, a narrowband filter will be required, but what will be the required bandwidth and type of filter? The energy from the line to be transmitted by the filter will depend on the peak transmittance (assuming that the peak of the filter can always be tuned to the line in question), while the energy from the continuum will depend on the total area under the transmission curve, including the rejection region at wavelengths far removed from the peak. The narrower the pass band, the higher the contrast between the line and the continuum, especially as narrowing the pass band generally also improves the rejection. However, the narrower the pass band, because of the increased difficulty of manufacture, the higher the price, and, further, because of the increased sensitivity to lack of collimation, the larger is the tolerable focal ratio. This latter point implies that for the same field of view, a filter with a narrower bandwidth must be made larger to permit the use of the larger focal ratio, which in turn will increase still further the difficulties of manufacture and, possibly, the complexity of the entire system. Another way of improving the performance of the filter is by increasing the steepness of edge of the pass band while still retaining the same bandwidth. A rectangular pass-band shape gives higher contrast than a simple Fabry–Perot filter of identical half-width and usually possesses the additional advantage that the rejection remote from the peak of the filter is also rather greater. This edge steepness can be specified by quoting the necessary tenth peak bandwidth or even the hundredth peak bandwidth. Again, inevitably, the steeper the edges, the more difficult is the manufacture and the higher the price.

Because filters, as with any manufactured product, cannot be made exactly to a specification in absolute terms, some tolerances must always be stated.

For a narrowband filter, the principal parameters that should be given tolerances are peak wavelength, peak transmittance, and bandwidth. Since in almost all applications the higher the peak transmittance the better, it is usually sufficient to state a lower limit for it. There are two aspects of peak wavelength tolerance. The first is uniformity of peak wavelength over the surface of the filter. There will always be some grading of the films, although perhaps small, and a limit must be put on this. The effect is similar to that of an incident cone of illumination (which has been discussed in Section 8.2.4.4) and it is usually best to limit the uniformity errors in the specification to not more than one-third of the half-width. The second aspect is error in the mean peak wavelength measured over the whole area of the filter. The tolerance for this is usually made positive so that the filter can always be tuned to the correct wavelength by tilting. For a given bandwidth, the amount of tilt that can be tolerated in any application will be determined to a great extent by the aperture and field of the system, since the total range of angles of incidence that can be accepted by a filter falls as the tilt angle is increased.

The bandwidth of the filter should also be specified and a tolerance put on it, but, because of the difficulty of controlling bandwidth very accurately, it is not usually desirable to tie it up too tightly and the tolerance should be kept as wide as possible, not normally less than 0.2 times the nominal figure unless there is a very good reason for it.

Another important parameter involved in the optical performance specification, is rejection in the stopping zones, which may be defined in a number of different ways. Either the average transmittance over a range, or absolute transmittance at any wavelength in the range, can be given an upper limit. The first would usually apply where the interfering source is a continuum and the second where it is a line source, in which case the wavelengths involved should be stated, if known.

Yet another entirely different method of specifying filter performance is by drawing maximum and minimum envelopes of transmittance against wavelength. The performance of the filter must not fall outside the region laid down by the envelopes. It is important that the acceptance angle of the filter also be stated. This type of specification is rather more definite than the first type mentioned above. A disadvantage, however, is that it may be rather too severe since everything is stated in absolute terms when average values may be just as good. A further point is that it is impossible to devise a test to determine whether or not a filter meets an absolute specification of this type. Finite bandwidth of the measuring apparatus will ultimately be involved. It is advisable, therefore, if specifying a filter in this way, to include a note to the effect that the performance specified at each wavelength is the average over a certain definite interval.

There is little else that can be said in general terms about the optical performance specification. In any one application, these factors will assume different relative importance and each case must to a very great extent be considered on its own merits. Clearly, this is an area where it is of prime importance that the system designer work very closely with the filter designer.

14.1.2 Manufacturing Specification

We shall now consider briefly the manufacturing specification containing the filter design together with details of the manufacturing method. In most cases, this will be intended for the use of the machine operator.

First, the filter design, including the materials, will be given. Most filters contain no more than three different thin-film materials having a relatively low, medium, and high refractive index. Designs are usually written in terms of quarter-wave optical thicknesses at a reference wavelength λ_0 using the symbols *L*, *M*, and *H*. Typical designs may be written:

$$L\,|\,\mathrm{Ge}\,|\,LHLHHLH \quad L = \mathrm{ZnS} \quad H = \mathrm{Ge}$$
$$M\,|\,\mathrm{Si}\,|\,MHLHHLH \quad L = \mathrm{CaF2} \quad M = \mathrm{ZnS} \quad H = \mathrm{Ge}$$

the substrates being indicated by the symbols $|\,\mathrm{Ge}\,|$ and $|\,\mathrm{Si}\,|$. Next, the constructional details should be written down. These consist of the monitoring method to be used, including the wavelengths, and the form of the signals together with other important details such as substrate temperature, special types of evaporation sources, and so on. It will be found useful to arrange the whole manufacturing specification in the form of a table that can be issued to the machine operators for use as a checklist. Operators should always be encouraged to observe critically the operation of the machine so that faults or anomalies can be spotted at an early stage, and it is a help in this if they are expected to list comments in appropriate places on the form. It will also be found convenient to give each filter production batch a different reference number. Once the filters are produced, the completed specification form can then be filed by the machine operator to form the machine logbook. Additional information such as pumping performance can also be recorded on the sheets, useful from the maintenance point of view.

For calculation purposes, there is no consensus on whether the incident medium should be at the top or the foot of a table of design. For manufacture, however, the first layer to be deposited is necessarily next to the substrate and it is usual to list the layers in tables of manufacturing instructions from innermost, next to the substrate, to outermost.

Software products can assist in setting up the manufacturing specification, especially the sequence of monitoring signals. In some cases, these can be automatically fed into the deposition controller so that the printed copy can be simply for reference and record keeping.

14.1.3 Test Specification

Probably the most important specification of all is the test specification. This lays down the complete set of tests that will be carried out on the filters to measure the performance. It should always be remembered that, although the

filter will have been designed to meet a particular performance specification, it is only the performance laid down in the test specification that can actually be guaranteed, and, although it may seem obvious, the test specification must be written with the requirements of the performance specification always in mind. In fact, it is possible simply to specify the performance of a filter as that which will pass the appropriate test specification. It will sometimes be found that the test specification, if it exists at all, is a rather loose document or that sometimes the customer's performance specification will serve both roles. If so, then someone somewhere along the line will be interpreting the performance specification to decide on the tests to be applied, and it is always better to have the tests and the method of interpretation in writing.

The first essential in any test specification is a definite statement of the performance or the make and type of the test equipment to be used. This ensures that results can be repeated if necessary, even if remote from the original testing site. Next, the various tests together with the appropriate acceptance levels can be set down.

It is in the measurement of such factors as uniformity where the tests and the method of interpretation are particularly important. Absolute uniformity is impossible to measure in the ordinary way. The performance would have to be measured at every point on the coating with an infinitesimally small measuring beam. A simpler and usually satisfactory method is to check the performance, for example the peak wavelength, at the center of the filter and at four approximately equally spaced areas around the circumference, using a specified area of measuring beam. The spread over the filter is taken to be the spread in the values of peak wavelength, or other performance attributes, over the five separate measurements. The spectrometer used for the measurement will also have a finite bandwidth and features of the filter that are rather less than this, will, in general, not be picked up. This applies particularly to the measurement of rejection. Rejection must usually be measured over a very wide region, and for the test to be completed in a reasonable time, a fast scanning speed must be used, which in turn requires a broad bandwidth. This averages the measurement over a finite region and is, therefore, unsatisfactory if the energy that is to be rejected has a line rather than a continuous spectrum. In such a case, the lines should be defined and the tests include more careful measurements at the defined lines. A technique for measuring the rejection of films using a Fourier transform spectrometer has been suggested by Bousquet and Richier [1]. While this is difficult to apply in the visible region, the availability of commercial Fourier transform spectrometers for the infrared makes it a feasible technique for infrared filters.

Of course, inevitably, the more extensive the testing that must be carried out on each individual filter, the more expensive that filter is going to be. Performance testing of low-price standard filters is, in the main, carried out on a batch basis, with, at the most, only a few details being checked on each individual filter. This is a point that should be borne in mind by a prospective

customer buying a standard filter from a catalog, that a superlative level of performance cannot be absolutely guaranteed from a single given filter, which, by its price, cannot have had more than the basic testing carried out on it.

So far we have dealt with the directly measurable optical performance of the filter, but there are additional properties of a subjective nature and rather more difficult to measure. These are connected with the quality and finish of the films and substrates. Substrates are specified as for any optically worked component, details such as flatness or curvature of surface, degree of polish and allowable blemishes, sleeks and the like can all be stated. We shall not consider substrates further here. There is a specification, used particularly in the United States, MIL-E13830A, which gives a useful set of standards for optical components including substrates.

The quality of the coating can be measured by the presence or absence of defects such as pinholes, stains, spatter marks, and uncoated areas. Pinholes are important for two reasons. First, they are actually small uncoated, or partially uncoated, areas and as such will allow extra light to be transmitted in the rejection regions, reducing the overall performance of the filter. Second, and this is especially so for filters for the visible region, they are unsightly and detract from the appearance. In fact, they usually look worse to the eye than the effect they actually have on performance. Apart from the purely subjective appearance, the permissible level of pinholes can be defined based on a given maximum number of a certain size per unit area, calculated to reduce the rejection in the stop bands by not more than a given amount. To calculate this figure, a minimum area of filter that will be used at any one time must be assumed. This will depend on the application, but, in the absence of any definite information on this, a suitable figure is 5 mm × 5 mm. Obviously, the smaller this area, the smaller is the size of the largest pinhole. Of course, the actual counting of pinholes in any filter would involve a prohibitive amount of labor and in practice, with visible filters, the measurement is often carried out visually, comparing the filter with limit samples. A simple fixture consisting of a light box with sets of filters laid out on it, some just inside, some on, and some just outside the limit, can be readily constructed. For infrared filters on transparent substrates, this method can also be applied, but for filters on opaque substrates, it is easier to measure actual rejection performance.

Spatter marks are caused by fragments of material ejected from the sources. In themselves, unless gigantic, they have little effect on the optical performance. A major danger is that the fragments may be removed later, leaving pinholes. Sometimes, however, spatter causes nodular growth with their associated problems (see Chapter 12) or, if many spatter fragments are present, the scattering losses may rise. The incidence can be tied down just as with pinholes, but, as the specular optical performance is little affected, unless the number of marks is enormous, the basis for deciding what is permissible is usually subjective. If the spatter is causing pinholes, they will be dealt with separately. Often specifications will state that there must be no spatter

marks visible to the naked eye, but this is vague, particularly when dealing with inspectors with no optical experience. Disagreements can arise between manufacturer and customer especially when, as can happen, the customer's inspectors use an eyeglass to assist the naked eye. The best course is probably to relate the test to agreed limit samples when it can be carried out in exactly the same way as for pinholes.

Stains can be caused in a number of ways. The most common reason is a faulty substrate. One type of mark that is often seen, especially when anti-reflection coatings are involved, is due to a defect in the optical working. The polishing process consists partly of a smoothing out of irregularities in the surface by a movement of material. If the grinding, which always precedes the polishing, has been too coarse, then the deeper pits during the polishing are filled in with material that is only loosely bonded to the surface, although the polish will usually appear completely satisfactory to the eye. In the heating and then coating of the surface, this poorly bonded material breaks away, leaving a patch of surface that is etched in appearance and often possesses well-defined boundaries. The only remedy for this type of blemish is improved polishing techniques. Other stains that may appear can be caused by faulty substrate cleaning. If water or even alcohol is allowed to dry on a surface without wiping, water marks appear. Droplets should always be removed from the surface by a final vapor cleaning stage, or by blowing with clean air (great care must be taken to make sure the air is clean and does not carry oil with it), or by wiping with a clean tissue or cloth during the cleaning process. Water should never be allowed to dry on the surface by itself. Stains, unless particularly bad, do not usually affect the optical performance to anything like the extent their appearance would suggest (except in the case of very high performance components such as Fabry–Perot interferometer plates or laser mirrors), and the basis for judging them is again subjective.

Finally, the filter must be held in a jig during coating so that at least some uncoated areas must exist. These usually take the form of a ring around the periphery of the filter, perhaps around 0.5 mm wide. There will be a slight taper in the coating at the very edge, which must also be allowed for, the combined taper and uncoated area forming a strip perhaps 1.0 mm in width. The uncoated area actually serves a useful purpose because mechanical mounts can grip the component at this point without damaging the coating. Damage near the edge is dangerous because it is there that delamination is frequently initiated. Jigs that allow the substrates to chatter as they rotate can cause such defects. Uncoated areas should not occur within the boundary of the filter proper; when they do, it is usually a sign of adhesion failures that may recur. They may be due to substrate contamination or to moisture penetration with weakening of adhesion, as described in Chapters 11 and 12, but they are always cause for rejection of the component. Blisters, too, which are a slightly different version of the same fault, are also cause for immediate rejection.

14.2 Physical Properties

As far as the physical properties of the filter are concerned, there are two primary aspects. First, the dimensions of the filter must meet the requirements laid down. This is purely a matter of mechanical tolerances that we need not go into any further here. Second, the filter must be capable of withstanding, as far as possible, the handling it will receive in service and also of resisting any attack from the environment. The assessment of the ruggedness, or robustness, of the coating will now be considered in greater detail.

The approach almost invariably used in defining and testing the ruggedness of a coating is to combine the performance and test specifications. A series of controlled tests reproducing typical conditions likely to be met in practice is set up, and then performance is defined as being a measure of the ability to pass the particular tests. This avoids the difficulty in setting up a more general performance specification.

There is one basic difference between the tests of optical performance and those we are about to discuss. Optical tests, except, perhaps, for laser damage threshold, are usually nondestructive in nature while tests of ruggedness are, in the main, destructive. The filters are tested deliberately to cause damage, and the extent of the damage, or the point at which damage can be detected, if it can be measured, used as a measure of the ruggedness of the filter. It is thus not possible to carry out the whole series of tests on the actual filter that is to be supplied to the customer and it is normal to use a system of batch testing. A number of filters is made in a batch and either one or perhaps two chosen at random for testing. Provided these test filters are found acceptable then the complete batch is assumed satisfactory. This arrangement is, of course, not peculiar to thin-film devices. Another aspect of this batch testing is involved in what is known as a type test. Often if a large number of filters, all of the same type and characteristic, are involved, a series of very extensive and severe tests will be carried out on a sample of filters from a number of production batches. The test results will then be assumed to apply to the entire production of this type of filter. Once the filters have passed this type test, normal production testing is carried out on a reduced scale. It is imperative that once the type test has been successful there are no subsequent changes, even of a minor nature, to the production process; otherwise, the type test becomes invalidated.

14.2.1 Abrasion Resistance

Coatings on exposed surfaces, such as the antireflection coating on a lens, will probably require cleaning from time to time. Cleaning usually consists of some sort of rubbing action with a cloth or perhaps lens tissue. Often there

may be dust or grit on the surface of the lens, which may not be removed before rubbing. The result of such treatment is abrasion and it is important to have the abrasion resistance of exposed coatings as high as possible. An absolute measure of abrasion resistance is not at all easy to establish because of the difficulty of defining it in absolute terms, and the approach is to reproduce, under controlled conditions, abrasion similar to that likely to be met in practice only rather more severe. The degree to which the coating withstands the treatment is then a guide to its performance in actual use. In the United Kingdom, a great deal of work was carried out on standardizing this test by the Sira Institute (formerly the British Scientific Instrument Research Association). Their method involved a standard pad made from rubber loaded with emery powder, which, with a precise load, is drawn across the surface under test a given number of times—typically 20 times with a loading of 5 lb in^{-2}. Their work was directed mainly towards the assessment of the performance of magnesium fluoride single-layer antireflection coatings for the visible. It has been established that sufficiently rugged coatings of this type do not show signs of damage under the normal test conditions given above. Abrasion resistance, however, has been found to be not just a function of the film material but also of the thickness. Multilayer coatings are generally much more prone to damage than either of the component materials in single-layer form. It is therefore necessary to establish fresh standards for each and every type of coating.

The U.S. military specification MIL-E-12397B, which dates from 1954 and is still active, specifies the composition of an eraser containing ground pumice abrasive material for testing coated optical components. This eraser is used in many of the U.S. military specifications that include abrasion testing. An important related specification is MIL-C-675C. This specification strictly applies to single-layer magnesium fluoride antireflection coatings but nevertheless is quoted as the standard for a wide range of optical coatings including multilayers and, although it is strictly a military specification, it is applied frequently to optical coatings in general.

There are difficulties in achieving exactly the same abrading performance from different batches of abrading pad. Similar tests using pads that may or may not include abrading particles are widely used. It is not uncommon to find similar tests using rough cloth and even steel wool.

Unfortunately, such tests do not normally produce an actual measure of the abrasion resistance, but merely determine whether a given coating is acceptable. Because of this, some investigations into a better arrangement were carried out by Holland and van Dam [2]. Their test is based on the principle that a measurement of abrasion resistance must involve actual damage to the films. The measure of the damage can then be taken as a measure of the abrasion resistance. Their method was to subject the films to abrasive action that varied in intensity over the surface and that was, at its most intense point, sufficiently severe completely to remove the coating. The point at which the coating just stopped being completely removed was then

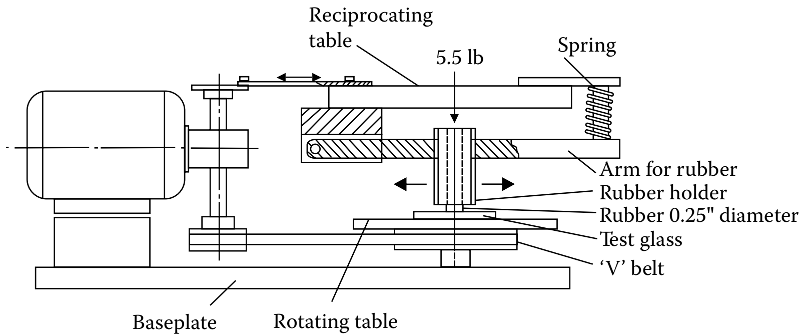

FIGURE 14.1
Schematic arrangement of an abrasion machine. The reciprocating table is supported by two horizontal bars not shown in the diagram. (After Holland, L. and van Dam, E.W. *Journal of the Optical Society of America*, 46, 773–777, 1956.)

found. Of course, the method is still relative in that a different standard must be set up for every thin-film combination, but it does permit comparison of the abrasion resistance of similar coatings, impossible with the previous method. The apparatus is shown in Figure 14.1. It consists of a reciprocating arm carrying the abrasive pad of the Sira type, 0.25 in diameter, and loaded with 5.5 lb. The table carrying the sample under test rotates approximately once for every three strokes of the pad. The pad traces out a series of spirals on the surface of the sample and the geometry is arranged so that the diameter of the abraded area is approximately 1.25 in. The abrasion takes the form of a gradual fall off in intensity towards the outside of the circle, and the test is arranged to carry on for such a time that the central area of the coating is completely removed, while the outside, not at all. Holland and van Dam found that some 200 strokes were sufficient to do this with single layers of magnesium fluoride. They then defined the abrasion resistance measure of the coating by the formula

$$w = (d^2/D^2) \times 100\% \tag{14.1}$$

where d is the diameter of the circle where the coating has been completely removed and D is the diameter of the area that has been subjected to abrasion. Holland and van Dam studied particularly the case, as had Sira, of the single-layer magnesium fluoride antireflection coating for the visible region and they quote a wide range of most interesting results.

They investigated many different conditions of evaporation including angle of incidence and substrate temperature. A common value for the abrasion resistance of a typical magnesium fluoride layer of thickness to give antireflection in the green is between two and five, depending on the exact conditions of deposition. Best results were obtained when the substrate temperature during evaporation was 300 °C and the glow-discharge cleaning

before coating lasted for 10 min. There was a significant reduction in abrasion resistance if either the temperature were allowed to drop to 260 °C or if there were only 5 min of glow discharge cleaning. They also found that the abrasion resistance of the film is increased considerably by burnishing with a Selvyt cloth (a popular cloth for cleaning optics) or by baking further at 400 °C in air after deposition. Another significant result obtained concerns the occurrence of a critical angle of vapor incidence during film deposition, beyond which the abrasion resistance falls off extremely rapidly. This critical angle varies slightly with film thickness but is approximately 40° for thicknesses in excess of 300 nm and rises as the thickness decreases.

The test appears never to have received general recognition in specifications. It should be extremely useful as a quality-control test in manufacture, especially as a reduction in quality can be detected long before it drops below the level of the normal abrasion test, and remedial action can be taken before any coatings are even rejected.

14.2.2 Adhesion

Adhesion has already been discussed in Chapter 11. In the simplest type of adhesion test, a piece of adhesive tape is stuck down on the surface of the coating and pulled off. Whether this removes the film is taken as an indication of whether the adhesion of the film to the substrate is less than or greater than that of the tape to the film. The test is again of the go–no-go, or binary, type.

It is important if consistent results are to be obtained that some precautions are taken in carrying out the test. The first is that the tape should have a consistent peel adhesion rating, which should be stated in the specification. Peel adhesion is measured by sticking a freshly cut piece of tape on a clean surface, usually metal, and then steadily pulling it off, normal to the surface. The tension per unit tape width, usually expressed in grams per inch, is the measure of the peel adhesion rating of the tape. The rating obtained in this way is usually virtually the same as the rating obtained when the tape is removed from a thin-film coating. Some precautions in applying the test are necessary. Fresh tape should always be used. The tape should be stuck firmly to the coating, exerting a little pressure and smoothing it down. It should be removed steadily, pulling it at right angles to the surface, and never snatched off, which would put an uncontrolled impulsive load on the film and would certainly lead to inconsistent results. The same thickness of tape should be used for all testing. With thicker tape of the same peel adhesion rating, the test would be slightly less severe. The width of the tape, however, does not matter. A rating, which is often used, is 1200 g in^{-1} width. If necessary, the adhesion rating of any tape can easily be checked using a spring balance. For obvious reasons the test is often called the "Scotch Tape test."

The major problem with this test is the great difference in the nature of the adhesion between tape and film and film and substrate. The tape adhesive force is relatively low but the range of the force, because the adhesive

stretches, is large. The forces holding the film to the substrate are large but the range is small. The test, therefore, detects those areas where the adhesion is virtually nonexistent rather than areas where it is lower than normal.

Attempts have been made to devise quantitative techniques for adhesion measurement and a number of these have also been discussed in greater detail in Chapter 11. The simplest and most straightforward is the direct-pull test, involving the attachment of the flat end of a cylindrical pin to the coating, followed by measurement of the force necessary to pull it off. Provided the coating is detached with the pin, the force required divided by the area of the pin is then the measure of adhesion. Because the thin-film adhesive forces have such a short range, it is almost impossible to carry out the test in such a way as to avoid completely any progressive fracturing of the film bonds, and so the results will usually show an adhesive force that is lower than is actually the case. Of course, in a test of film quality, this lowering of the test result is a much better feature than one that artificially inflates it.

An alternative test that has some advantages as well as disadvantages is the scratch test, in which a loaded stylus is drawn across the coating with gradually increasing load. At each stroke, the coating is examined under a microscope for signs of damage. The load at which the coating is completely removed is taken as the measure of adhesion. The Goldstein and DeLong [3] technique involving the use of a microhardness tester as a scratch tester has also been mentioned in Chapter 11.

14.2.3 Environmental Resistance

One further aspect of thin-film performance is also of very great importance. This is the resistance that the film assembly offers to environmental attack. Probably the universally important aspect of the environmental performance of a coating is its resistance to the effects of humidity, but, depending on the application, its resistance to other agents, such as temperature, vibration, shock, and corrosive fluids such as saltwater, may also be important.

There are two possible approaches. Either the filter may be expected to operate satisfactorily while actually undergoing the test or it may only be expected to withstand the test conditions without suffering any permanent damage, although the performance need not be adequate during the actual application of the test. The latter is usual as far as interference filters are concerned, and in such a case, the specification is known as a "derangement specification" because it is sufficient that the performance is not permanently deranged by the application of the test conditions. Derangement specifications are easier to apply than the other type because the normal performance measuring equipment can be used remote from the environmental test chamber. However, the user of the coating needs to be aware of the nature of the specification: whether it is of the operational or derangement class.

Of all the agents likely to cause damage, atmospheric moisture is probably the most dangerous. For most applications, particularly where severe environments are excluded, it will be found sufficient for the filter to be tested by exposing it for 24 h to an atmosphere of relative humidity 98% ± 2% at a temperature of 50 °C ± 2 °C. It is often found that although the coatings are not removed by this test they are softened, and it is normal to carry out this test before the adhesion or abrasion-resistance tests, which can follow on immediately after.

A great deal of work has been carried out by government bodies on the environmental testing of equipment and components. This has resulted in specifications that are equivalent to the most severe conditions ever likely to be met in both tropical and polar climates. These specifications include, in the United Kingdom, DEF133 and DTD1085 for aircraft equipment. Relevant specifications in the United States include MIL-C-675, MIL-C-14806, MIL-C-48497, and MIL-M-13508. The tests vary from one specification to another but can include exposure to the effects of high humidity and temperature cycling over periods of 28 days, exposure conditions equivalent to dust storms, exposure to fungus attack, vibration and shock, exposure to salt, fog, and rain, and immersion in saltwater. It is not always possible for coatings to meet all tests in these specifications and concessions are often given if the coatings are to be enclosed within an instrument. Humidity and exposure to salt, fog, and water are particularly severe tests. Fungus does not normally represent as severe a problem to the coatings as it does to the substrates. Certain types of glass can be damaged by fungus, and in such cases, coatings, even if they themselves are not attacked, will suffer along with the substrates. Most instruments likely to be exposed to sand or dust are adequately sealed since their performance is likely to suffer if dust or sand is permitted to enter. Thus, dust storms are usually a danger only to those elements with surfaces on the outside of an instrument.

References

1. Bousquet P and Richier R 1972 Etude du flux parasite transmis par un filtre optique à partir de la détermination de sa fonction de transfert *Optics Communications* **5** 27–30
2. Holland L and van Dam E W 1956 Wear resistance of magnesium fluoride films on glass *Journal of the Optical Society of America* **46** 773–777
3. Goldstein I S and DeLong R 1982 Evaluation of microhardness and scratch testing for optical coatings *Journal of Vacuum Science and Technology* **20** 327–330

15

System Considerations: Applications of Filters and Coatings

It is only rarely that thin-film filters or coatings are used by themselves. They usually form part of an optical system, and it is in integrating coatings into such systems where many problems appear. There is an unfortunate tendency to leave coatings until late in the design process and some of the most severe problems occur during the attempted integration of coatings once the remainder of the design has been frozen. Such problems could frequently have been avoided had the incorporation of coatings been studied at a time when there was still some design flexibility.

Coatings cannot automatically be deposited with equal ease on any surface. Furthermore, some tolerances on coating performance must be permitted. Then there is the shift in coating characteristics with angle of incidence, with temperature and, unless energetically deposited, with atmospheric humidity. Coatings often possess considerable intrinsic strain and the resulting stress can cause distortion that is significant in substrates of interferometric quality if they are not sufficiently thick. Lack of uniformity in coatings can also cause problems. Some of these difficulties arise from coating characteristics that show rapid change of phase with wavelength, characteristics frequently possessed by broadband reflectors. A lack of uniformity in the coating, if it is dielectric, is roughly equivalent to a wavelength variation over the surface, and if the phase dispersion is high, then the resulting phase errors can be out of all proportion to the errors in thickness. The net result is an apparent loss of figure of the coated component that may show surprisingly large variations with wavelength. Extended-zone reflectors frequently exhibit rapid phase dispersion and so should be used with caution in applications where interferometric quality is required. All of these points have been discussed elsewhere in this book, and the intention of repeating them here is simply to reinforce the point that coatings are like any other component and must be designed into the system as an integral part, and not simply added at a later stage.

Coatings rarely stretch right to the edge of a substrate. Substrates must be held in jigs during coating, and it is normal to do this with a lip that obscures the rim of the substrate leaving an uncoated ring. This is not entirely a disadvantage. Delamination is always most likely to start at the edge of a coating, and the uncoated rim around the coating gives it a much more regular edge and reduces the risk of delamination. Further, the mount for the component need not make contact with the coating where it could damage it and increase

the chance of spontaneous delamination. The uncoated ring can, however, be a disadvantage if the component is a filter that rejects certain wavelength regions, because stray light can leak through the uncoated part unless precautions to baffle it are taken. The uncoated area can be considerably reduced by the use of wire clips to hold the substrates by the edges during deposition, a technique frequently used with components such as sunglasses, but problems with stray light leakage can sometimes lead to the requirement that there should be no uncoated area whatsoever. The normal method for achieving this is to cut the component after coating. This should be carried out only if absolutely necessary. It increases the cost considerably because of the risk of failure involved in the cutting operation, and it inevitably leaves a coating edge that is uneven on a microscopic scale and more likely to include stress concentrators that can initiate delamination.

It is always more difficult to coat a curved surface than a plane one, and the difficulties increase with the curvature. Difficult coatings with tight tolerances should, wherever possible, be deposited on plane surfaces. Narrowband filters can be tuned to shorter wavelengths by tilting. If small tilts can be permitted (by the use of wedged holders, for example), then the tolerances on peak wavelength can be relaxed.

Standard size components are always to be preferred. The manufacturer already has the necessary jigs and fixtures, and the substrates are available in quantity. Fewer test runs are required and there are fewer unexpected difficulties. When something goes wrong with the process, an entire batch of components is usually lost. Such failures are more likely with components of unusual shape or size, and so a greater number of uncoated components must be produced to ensure the correct number of final coated components. All of this means that the cost of nonstandard components is considerably greater than standard.

Most filters will consist of a series of components, some of which are designed to reject radiation in regions outside the pass bands. Surprisingly disappointing performance can be achieved in cases where the rejected light is reflected rather than absorbed. We can illustrate this by considering two surfaces having reflectances and transmittances of R_1, T_1, R_2, and T_2. Light can be considered as being reflected backward and forward between the surfaces and being combined incoherently. The net transmittance is then given by Expression 2.11:

$$T = \frac{T_1 T_2}{1 - R_1 R_2}$$

If R_1 and/or R_2 is/are zero, that is, what is not transmitted is absorbed, then we have the expected result

$$T = T_1 T_2.$$

However, if $R_1 = 1 - T_1$ and $R_2 = 1 - T_2$ then the result becomes similar to Expression 2.149:

$$T = \frac{1}{(1/T_1) + (1/T_2) - 1}$$

Consider the case where $T_1 = T_2 = 0.01$. The first expression gives $T = (0.01)^2 = 0.0001$, a very satisfactory figure, while the second expression gives

$$T = \frac{1}{100 + 100 - 1} = \frac{1}{199} = 0.005$$

that is one half of the individual transmittance, and very disappointing from the point of view of rejection. The solution is somehow to reduce the effect of R_1 and R_2, either by ensuring that the reflected beams rapidly walk out of the system aperture, for example, by tilting the components relative to each other or by placing absorbing components in between the two surfaces so that the beams are rapidly attenuated.

Sometimes reflecting and absorbing components will be combined in a system. Examples of this might be a heat-reflecting filter coating consisting of an interference shortwave-pass filter deposited on a heat-absorbing glass or a narrowband filter consisting of an all-dielectric interference section, a metal–dielectric coating, and an absorption glass. It is usually best in such cases to assemble the components such that the low-loss interference section faces the source. This ensures that the maximum amount of energy is rejected by reflection and minimizes the temperature rise and possible resulting long-term damage. In the case of the narrowband filter assembly, the overall rejection performance of the filter is assisted by placing the absorbing glass component in between the two interference sections for the reasons discussed above.

Light that is rejected by reflection does not automatically vanish. It is simply redirected. System design should take this into account. If the rejected light is not trapped, it may return to the rejecting component. If it arrives back at the component at a different angle of incidence, it may be transmitted, frustrating the rejection performance.

Polarization effects can sometimes be the cause of unexpected performance variation. We can illustrate this with the somewhat extreme case of a simple single-layer dielectric beam splitter shown in Figure 15.1. The performance of such a coating, assuming a quarter-wave (monitored at normal incidence) of zinc sulfide ($n = 2.35$) immersed in glass ($n = 1.52$) at an angle of incidence of 45°, is given by

$R_s = 33.15\%$	$R_p = 4.03\%$	$R_{mean} = 33.15\%$
$T_s = 66.85\%$	$T_p = 95.97\%$	$T_{mean} = 81.41\%$

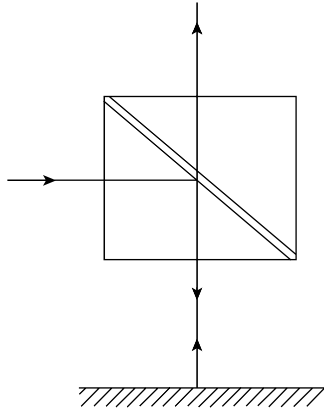

FIGURE 15.1
Arrangement of a single-layer dielectric beam splitter used for calculation of efficiency discussed in the text.

Let us assume that the reflecting surface has a reflectance of 100% and calculate the irradiance of the output beam as a fraction of the input irradiance. A simple calculation involves the unpolarized figures for T and R and yields TR = (18.59% × 81.41%) = 15.13%. However, this calculation has taken no account of the polarizing effect of the beam splitter itself. The true figure for unpolarized incident light should be $0.5(R_sT_s + R_pT_p)$ = 13.01% (a difference greater than 10% of the previous figure). Polarization of the input beam alters the results still further. With *s*-polarized input light the figure would be R_sT_s = 22.16%, while, with *p*-polarized light, it would be as low as R_pT_p = 3.87%. Thus, with varying degrees of polarization of the input light the efficiency of the system can vary from 3.87% to 22.16%. To avoid performance fluctuations resulting from such effects, a quarter-wave plate with axis at 45° to the plane of incidence is often inserted in the input side of a system to convert both *s*- and *p*-polarized light to circularly polarized, which makes the overall performance of the system equivalent to unpolarized light. (It is unlikely that the input light should be already circularly polarized, but of course, in that case the quarter-wave plate could make the situation worse.) Metal layers suffer less from polarization effects, but they, too, do still have significant polarization sensitive behavior.

That was an example of an immersed coating. Note that immersed coatings always have very high effective angles of incidence since the important quantity for Snell's law is $n_0\sin\vartheta_0$ rather than ϑ_0. Thus, in immersed coatings, angle-of-incidence effects are invariably enhanced. Polarization effects are particularly pronounced but so, too, are the simple wavelength shifts associated with a change in angle of incidence.

Even in coatings that are not immersed, the changes in angle of incidence associated with a highly divergent or convergent beam can cause problems, especially if the component is tilted with respect to the axis. Sometimes the

problems can be eased by deliberately introducing a variation in coating thickness over the surface of the component. This can be particularly effective when a point source is used close to a component, when the small source dimensions ensure that only a small range of angles of incidence correspond to each point on the component surface.

A point to watch concerns polarization effects associated with skew rays. Both *p*- and *s*-polarization performance is calculated with respect to the plane of incidence. A skew ray possesses a plane of incidence that is usually rotated with respect to the principal plane of incidence containing the axial ray of the system. This can cause problems in large aperture polarizers, for example, where, although the s-transmittance for the skew rays can be very low, the corresponding plane of polarization is actually rotated and can lead to an appreciably large leakage of light that is *s*-polarized with reference to the plane of incidence of the axial ray. As a rough example, we can consider a cone of 1° half-angle incident at 45° on a polarizing beam splitter. The plane of incidence of the marginal azimuthal rays will be rotated at an angle of approximately 1°/sin 45°, or 1.4° with respect to the plane of incidence of the axial ray. Let us assume that both axial ray and marginal ray have zero transmittance for *s*-polarized light and unity for *p*-polarized light. Because of the rotation of the plane of incidence the effective transmittance of the marginal ray in the *s*-plane of the axial ray will then be $\sin^2(1.4°)$ or 0.06%.

A very useful account of problems associated with the integration of thin-film coatings into optical systems has been written by Matteucci and Baumeister [1].

15.1 Potential Energy Grasp of Interference Filters

It is worthwhile considering why interference filters are used in preference to other types of wavelength selecting devices such as prism and grating monochromators. Of course the size and mechanical stability of the thin-film filter are in themselves powerful arguments in favor of its use, and, especially in cases where space and weight are at a premium, in satellite-borne instruments, for example, they are probably sufficient. However, there is an even more compelling reason for adopting thin-film filters, and this is the greatly increased potential grasp of energy over dispersive systems.

Compared with a grating monochromator, for instance, the thin-film filter with the same bandwidth is capable, provided the rest of the system be correctly designed round it, of collecting several hundred, and in some cases thousand, times the amount of energy collected by the monochromator. This section, therefore, is devoted to a comparison of the interference filter with the diffraction grating, particularly from the point of view of the potential total energy grasp.

To compare the energy-gathering properties of various components, we have to assume that each is used in an ideal system designed to make maximum use of its energy-gathering powers, that the bandwidths of the various systems are equal, and that any dispersive components are used well within their limiting resolutions so that their response functions are not complicated by large diffraction effects. We shall also assume that the source of illumination is of equal radiance in all cases and that the collecting condensing optics are such that the entrance apertures of all systems are completely filled. The energy grasp under these conditions is then computed in each case as a function of the appropriate area of the component, and the comparison made based on these figures.

In fact, this analysis has been carried out by Jacquinot [2] for a diffraction grating, a prism, and a Fabry–Perot interferometer. He has shown first that there is always a clear advantage in using a diffraction grating rather than a prism, the advantage varying from around 3 to perhaps 100 with the dispersion of the prism materials. Because of this, the comparison that primarily concerns us is between the interference filter and the diffraction grating. Jacquinot has also compared the Fabry–Perot interferometer with an air cavity, with the diffraction grating, and showed that there is a clear gain of 3–400 times in the energy grasp of an interferometer over a grating of the same area. The case of an interference filter is similar but the cavity layer has an index appreciably greater than unity, especially in the infrared, which increases its grasp still further. In the analysis that follows, we shall follow the main lines of Jacquinot's argument, but shall extend the analysis to include a cavity of index other than unity.

Jacquinot considers a spectrometer consisting of an input slit, a collector and collimator of some description, a dispersive element that here is a grating, and an output element imaging the entrance slit on the exit slit, the final element in the system. It is assumed that the resolution is limited by the width of the slits and that the grating is capable of higher resolution if required. This means that we can define the resolution purely in terms of slit width and dispersion. In this condition, the maximum luminosity for a given resolution will be achieved with equal entrance and exit slit widths, expressed in terms of spectral interval, when a triangular response function will be obtained from the instrument. It is assumed that the source that is an extended one, is monochromatic and of uniform radiance (formerly known as brightness).

There will be an imaging system to produce an image of the source on the entrance slit. The radiance of the source image will be equal to that of the actual source, except for the transmission of the imaging system, which we can take to be unity without affecting the final result, since all systems to be compared will have a similar arrangement before the entrance aperture. Given that the radiance of the image is identical to that of the source, it only remains for the aperture of the imaging system to be made large enough for the aperture of the collector and collimator before the grating

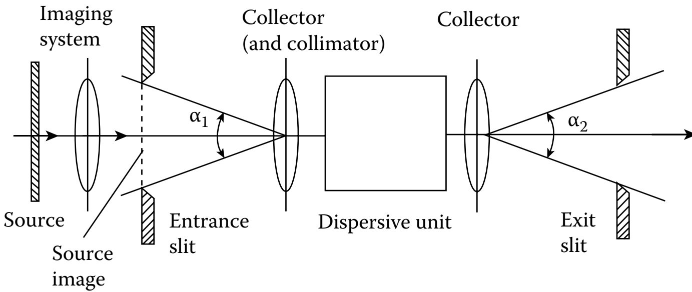

FIGURE 15.2
An idealized dispersive monochromator. (After Jacquinot, P., *Journal of the Optical Society of America*, 44, 761–765, 1954.)

to be completely filled. Again, we can assume that this has been carried out in all arrangements without any loss in generality. The situation is sketched in Figure 15.2. The notation used here is similar to that used by Jacquinot in his original paper to make the comparison easier, except that we will use L for radiance. Let the monochromator be adjusted so that the image of the entrance slit falls directly on the exit slit and let both slits have the same width and length. This corresponds to the apex of the triangle. The energy transmitted by the system will be given by

$$E = LS\omega T$$

where ω is the solid angle subtended by either slit at the appropriate collector element and S the area of the beam at the collector. $S\omega$ will be the same for both the entrance and the exit slit since we have arranged for the image of one to coincide with the other. T is the transmittance of the monochromator. If the width of the exit slit is α_2 and the length β_2, then the expression becomes

$$E = LST\,\beta_2\alpha_2$$

If we denote the resolving power of the system by R, then we have that $\alpha 2 = \lambda D_2/R$ where D_2 is the angular dispersion of the system referred to the output slit, i.e.,

$$E = LST\,\beta_2(\lambda D_2/R)$$

For the grating monochromator the angular dispersion is derived from the equation

$$\sigma(\sin i_1 + \sin i_2) = m\lambda$$

where σ is the grating constant, i.e., the interval between grooves, m is the order number, and i_1 and i_2 are the angles of incidence and diffraction, respectively, at the grating.

$$D_2 = \frac{di_2}{d\lambda} = \frac{m}{\sigma \cos i_2} = \frac{\sin i_1 + \sin i_2}{\lambda \cos i_2}$$

i.e.,

$$\lambda D_2 = \frac{\sin i_1 + \sin i_2}{\cos i_2}$$

Now

$$S = A \cos\ i_2$$

where A is the area of the grating and we assume that it is completely illuminated and that no light is lost, so that

$$S\lambda D_2 = A(\sin i_1 + \sin i_2)$$

Jacquinot shows that $S\lambda D_2$ is a maximum for the Littrow mounting (where i_1 and i_2 are as nearly equal as possible) used on the blaze angle that we denote by φ. For that mounting,

$$S\lambda D_2 = 2A \sin\varphi$$

and

$$E = \left(LT\beta_2/R\right)2A\sin\varphi$$

φ we can take as 30°, say, when $\sin\varphi = ½$ and

$$E = LT\beta_2\, A/R$$

We shall now consider the interference filter and compare it with the diffraction grating. The case considered by Jacquinot is that of the conventional Fabry–Perot interferometer made up of a pair of plates in an etalon with a cavity of unity refractive index. Here we are more concerned with the interference filter where the cavity layer has an index greater than unity. As in Chapter 8, we introduce the concept of an effective index of refraction that governs the angular behavior of the filter. We shall use a similar analysis to that of Jacquinot, but recast it in the form of the results of Chapter 8.

Jacquinot suggests that the filters be used with an acceptance angle such as to make the effective bandwidth of the filter √2× the value at normal incidence. Equation 8.41 gives

$$W_\Theta^2 = W_0^2 + \left(\Delta\nu'\right)^2$$

where W_0 and W_Θ are the half-widths corresponding to collimated light at normal incidence and to a cone of semiangle Θ. If Θ is measured in air, then

$$\Delta\nu' = \nu_0\Theta^2/2n^{*2}$$

For $W_\Theta = \sqrt{2} \times W_0$, we must have $W_0 = \Delta\nu'$, i.e.,

$$W_0 = \nu_0\Theta^2/2n^{*2}$$

and, from Equation 8.42,

$$\hat{T}_\Theta = (W_0/\Delta\nu')\arctan(\Delta\nu'/W_0) = \arctan(1) = \pi/4 = 0.78 \qquad (15.1)$$

where $\hat{T}_\Theta$ is the effective peak transmittance of the filter for a cone of incident light of semiangle Θ referred to the incident medium, which we are assuming is air.

If R_0 is the resolving power for perfectly collimated light at normal incidence and R_Θ that for a cone of semiangle Θ, then

$$R_0 = \nu_0/W_0$$

and since $\Delta\nu'$ is small compared with ν_0

$$R_\Theta = \nu_0/W_\Theta = R_0/\sqrt{2}$$

But $W_0 = \Delta\nu'$ so that

$$R_0 = \nu_0/\Delta\nu' = 2n^{*2}/\Theta^2$$

and so

$$\Theta^2 = \sqrt{2}n^{*2}/R_\Theta \qquad (15.2)$$

If L is again the radiance of the source and A is that area of the filter that is fully illuminated, then the energy collected will be

$$E = LAT\left(\pi/4\right)\omega \qquad (15.3)$$

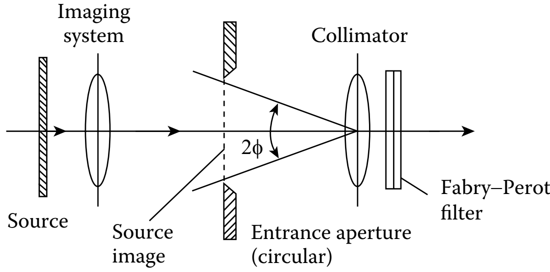

FIGURE 15.3
An arrangement of a monochromator using an interference filter.

where ω is the solid angle subtended by the aperture and T is the normal incidence transmittance. The factor $(\pi/4)$ is included from Expression 15.1. From Figure 15.3

$$\omega = 2\pi(1-\cos\Theta) \approx \pi\Theta^2 \tag{15.4}$$

Then, from Equations 15.2 through 15.4,

$$E = LAT\frac{\pi^2}{2}\frac{n^{*2}}{\sqrt{2}R_{\Theta}}$$

This is similar to the form given by Jacquinot except for the factor n^{*2} that is missing in his expression.

We are now in a position to compare efficiencies. The relative energy grasp of the two systems is

$$\frac{E_{\text{filter}}}{E_{\text{grating}}} = \frac{LAT(\pi^2/2)n^{*2}\ /(R\sqrt{2})}{LT\beta_2 A/R} \tag{15.5}$$

We can assume for this comparison that the resolution and areas and transmittances of the two systems are equal (that is, transmittance at normal incidence in collimated light for the interference filter). Equation 15.5 then simplifies to

$$\frac{E_{\text{filter}}}{E_{\text{grating}}} = \frac{\pi}{2\sqrt{2}}\cdot\frac{n^{*2}}{\beta_2} = 3.4\frac{n^{*2}}{\beta}$$

Jacquinot estimates the usual value of β to be 0.01 radian. With extreme care in design, values of 0.1 have been achieved, although this probably represents the limit. For an n^* of unity, then, the value of the energy ratio varies between 34 and 340.

However, n^* in the visible region is usually in excess of 1.5, which alters the range to 76–760. For the infrared the advantage of the filter is even greater, for n^* is usually of the order of 3.0, so that the range becomes 306–3060, a massive advantage. This means that we can happily make the interference filter much smaller than the grating and still have a very significant increase in energy grasp over it.

This analysis dealt with the single Fabry–Perot type of filter. The advantage with the DHW type of filter is slightly greater still, since the effective transmittance in a cone of illumination is higher than that of Fabry–Perot.

15.2 Narrowband Filters in Astronomy

This section was written for the first edition of the book, published in 1969. There have been considerable advances since then in detection methods, but the calculations and discussion in this section are still valid and they illustrate how filters are integrated into an interesting system of measurement. We therefore leave it unchanged.

The problem of detecting faint astronomical objects is rendered even more difficult than it would otherwise be by the light of the night sky. This light consists mainly of starlight scattered by dust both in the atmosphere and in interstellar space (including light from our own Sun) together with emission from the upper atmosphere and may be considered to be mainly of a continuous spectral nature although there are a number of emission lines as well. The sky light causes an overall fogging of the photographic plates, which are the most common detectors used in this work (although in recent years increasing use has been made of image tubes). Maximum contrast between the photographic image of a star or other object and the sky background is obtained when the sky fog is just apparent on the plate. The exposure time is chosen to give just this amount of fogging. The efficiency of the photographic detector falls off rapidly on either side of this optimum. The limit of detection of a faint object will be reached when the image is just discernible against the background.

The way in which the limit of detection varies with the parameters of the system has been studied particularly by Baum [3]. A simplified account of the analysis is given by Bowen [4] and it is this latter form that we follow here. The notation used by Bowen, which we also use here, differs slightly from that used by Baum.

The signal received from the object will consist of discrete photons arriving at a constant mean rate but randomly spaced. Provided the mean rate is sufficiently small (satisfied for the signals we are considering) we can consider the photons as forming a Poisson distribution (the distribution that deals with sequences of events where the probability of an occurrence in any

particular time interval is vanishingly small, but where the total observing time is sufficiently long to ensure a finite number of events). For the Poisson distribution, the standard deviation of successive measures of the number of photons N arriving in a certain constant time is simply $\sqrt{N}$.

Let D be the telescope aperture diameter, f the focal length of the telescope, t the observation time, β the diameter of the image of the object, n the number of photons from the object received per unit area of telescope aperture per second, s the number of background photons received per unit area of telescope aperture per unit solid angle of sky per second, p the limit of linear resolution of the emulsion, q the quantum efficiency of the entire system, which includes the photographic emulsion and the transmission of the optical system, and m the number of photons recorded per unit area of photographic plate that will produce the correct level of background fog.

In his paper, Bowen defines the faintness of a star or object as $1/n$. We shall now examine the way in which the limiting detectable faintness varies with the parameters of the system. The fractional error in a measurement is denoted by B and is defined as the standard deviation associated with the measurement divided by the measurement itself. Thus in a measurement of a number of photons N, the fractional error would be $B = (\sqrt{N})/N = 1/\sqrt{N}$.

The number of photons recorded from the object and from an equal area of sky in time t is given by

$$D^2ntq + \beta^2 sD^2tq$$

where we are omitting factors of $\pi/4$. The standard deviation in successive measurements will be

$$\left(D^2ntq + \beta^2 sD^2tq\right)^{1/2}$$

and the fractional error in the measurement will be

$$\begin{aligned}\beta &= \frac{(D^2ntq + \beta^2 sD^2tq)^{1/2}}{D^2ntq}\\ &= \frac{(n + \beta^2 s)^{1/2}}{Dnt^{1/2}q^{1/2}}\end{aligned}$$

For very faint objects, $n << \beta^2$ so that

$$B = \frac{\beta s^{1/2}}{Dnt^{1/2}q^{1/2}} \tag{15.6}$$

and the limiting faintness is given by

$$\left(\frac{1}{n}\right)_1 = \frac{B_1 D t^{1/2} q^{1/2}}{\beta s^{1/2}}, \tag{15.7}$$

where B_1 is the highest possible value of B where the object is still just detectable. Bowen suggests that B_1 should be 0.2. This formula applies as it stands to photoelectric detectors and shows how the faintness that can be detected increases with increasing aperture. For the photographic detector, however, the position is not quite the same. Here the time of exposure t must be chosen to give the correct background fog. The efficiency of the plate drops so quickly if the density of the background is incorrect that any other exposure time is of very much less value. This correct exposure time t_0 is given by

$$D^2 t_0 sq = mf^2$$

i.e.,

$$t_0 = \frac{mf^2}{D^2 sq}$$

and, substituting in Equation 15.7,

$$\left(\frac{1}{n}\right)_1 = \frac{B_1 D q^{1/2}}{\beta s^{1/2}} \sqrt{\left(\frac{mf^2}{D^2 sq}\right)} = \frac{B_1 m^{1/2} f}{\beta s} \tag{15.8}$$

In the equation we are assuming that β is larger than the resolution limit of the plate. If this is not the case, where f is small for example, then β must be replaced by p/f, giving

$$\left(\frac{1}{n}\right)_1 = \frac{B_1 m^{1/2} f^2}{ps} \tag{15.9}$$

These results, obtained by Bowen, are not what we might have expected, because they seem to show that the all-important parameter for photographic detection of faint objects is the focal length of the telescope and not the aperture. The longer the focal length, the greater is the faintness that may be observed, regardless of the diameter of the aperture of the system. So far, however, we have neglected to notice that observation time is limited to one night. Increasing the focal length without a corresponding increase in aperture, increases the necessary exposure time, which varies as the square of the focal length. Let t_m be the longest allowable exposure time. Then, for any given system, the largest value of focal length f_m will be given by

$$f_m^2 = \frac{t_m D^2 sq}{m}, \text{ i.e., } f_m = \frac{t_m^{1/2} D s^{1/2} q^{1/2}}{m} \tag{15.10}$$

which, when substituted in Equations 15.8 and 15.9, gives for f large or β large,

$$\left(\frac{1}{n}\right)_1 = \frac{B_1 t_m^{1/2} D q^{1/2}}{\beta s^{1/2}} \tag{15.11}$$

and for f small and β small

$$\left(\frac{1}{n}\right)_1 = \frac{B_1 m^{1/2} t_m D^2 sq}{psm} = \frac{B t_m D^2 q}{pm^{1/2}} \tag{15.12}$$

These expressions* show that, indeed as might be expected, there is a gain in going to larger telescopes.

Given the maximum possible value of D and f, how can the situation be improved by the use of filters? If there is a difference in spectral distribution of the radiation from the object and the sky background, then it is possible that a filter inserted in the system might modify the ratio of photons received from the object to those received from the sky. If this process results in a reduction in n by a factor x to xn, and a reduction in s to ys, then the ratio n/s becomes xn/ys, and if x/y is sufficiently large, then a positive gain in faintness may result. Substituting these values in the expression for the case where the resolution of the emulsion is not the limiting factor, Equation 15.11 becomes

$$\left(\frac{1}{n}\right)_1 = \frac{x B_1 t_m^{1/2} D q^{1/2}}{y^{1/2} \beta s^{1/2}}$$

and, assuming we adjust the focal length of the system as before to give the longest exposure time t_m, then the result† is obtained that a gain in $1/n$ is achievable provided that $x > \sqrt{y}$.

For the case where the emulsion resolution is a limiting factor, Expression 15.12 for $1/n$ shows that there is no possibility of altering the situation by filtering. The filtering will work only when the object is extended, or when the focal length of the telescope is large enough, or when the grain of the plates is fine enough, to ensure that the plate resolution is not a limiting factor.

The great bulk of the sky light is scattered light that has a more or less continuous spectrum. Only the emission from the upper atmosphere has a component consisting of discrete lines. Since, for a gain due to filtering,

* Reciprocity failure, which effectively means that q is reduced slightly as t is increased, has been neglected in this derivation.

† This, at first sight, odd result follows from the assumption made early in the derivation that the object is faint so that $n \ll \beta^2 s$.

it is not sufficient to ensure that $x > y$ but that $x > \sqrt{y}$, in cases where n has a continuous spectral distribution and there is no great difference between the distributions of n and s, there is probably very little to be gained by filtering. In fact, slight enhancement of the ratio of detected photons accompanied by a drop in transmittance could lead to a loss in performance rather than a gain. However, there are classes of objects characterized by line spectra, and in these cases it is possible by using filters centered on the lines to retain n only slightly reduced but to have s greatly reduced. Such a class of objects is the hydrogen emission nebulae. It is now known that hydrogen is one of the elements of interstellar gas, probably the most abundant. Where hydrogen clouds are near bright stars, the atomic hydrogen is ionized by the x-ray and extreme ultraviolet radiation from the stars, and, when the electrons and protons recombine, the characteristic hydrogen spectra are produced. The principal line emitted in the wavelength range detectable at the surface of the Earth is the first line of the Balmer series, $H\alpha$ at 656.3 nm, which, although not always the brightest line, is the one where contrast can be greatly improved.

The use of an interference filter centered on 656.3 nm greatly increases the contrast between the nebulae and the night sky, and gives a large increase in the faintness of nebulae that can be detected.

Equation 15.10 shows that when the interference filter is installed the focal ratio of the telescope must be adjusted to give the correct level of background fog.

$$\frac{f}{D} = \frac{t_m^{1/2}}{m}(ys)^{1/2}q^{1/2}$$

Generally, with typical interference filters, the focal ratio should be near unity. Such a focal ratio incident directly on a narrowband interference filter would have a disastrous effect on both the bandwidth and peak transmittance. However, the optical arrangement of the big telescopes permits an alternative arrangement. The primary mirror of a large telescope usually produces a pencil of focal ratio around *f*/5. As we have seen in Chapter 8, a narrowband filter for the visible region with a bandwidth of around 1% of peak wavelength will accept such a pencil quite satisfactorily and it is usual to insert the interference filter at or very near the prime focus. Beyond the prime focus a camera is installed, which reduces the focal ratio of the system to the desired value. The arrangement is shown in Figure 15.4a. With this layout the variation with field angle of the pass band of the filter (due to angle of incidence variation) is kept very small. If necessary, it could be eliminated altogether by use of an extra lens, as in Figure 15.4b.

In Figure 15.4, the filter acts as a field stop and may limit the field of view of the instrument. Filters up to 6 in in diameter have been constructed, although 4 in is probably a more usual figure. Filters with a diameter of 2 in are readily available.

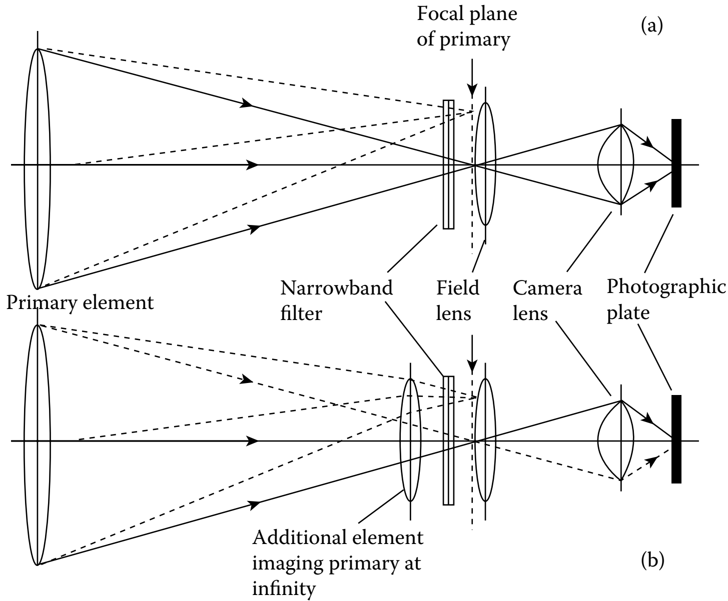

FIGURE 15.4
A narrowband filter in an astronomical telescope. The primary is shown here as a lens, but in the big telescopes would usually be a mirror. The field lens in (a) images the primary aperture on the aperture of the camera lens. If necessary, an additional element can be added as in (b) to alter the inclination or the off-axis pencils so that the effective peak wavelength of the filter is constant over the entire field.

Some particularly fine examples of photographs taken with relatively broad combinations of colored-glass filters and ones with interference filters of very much narrower bandwidths are given by Courtes [5]. Ring was the first successfully to use all-dielectric filters for this purpose, pioneering the development of these filters in the United Kingdom, and a paper by him [6] includes several photographs. A paper by Meaburn [7], who took the excellent photographs in Figure 15.5, illustrates extremely well the type of problem solved by interference filters and is well worth reading. Since this section appeared in the first edition, a particularly useful book by Meaburn [8] has been published and should be consulted for further information.

15.3 Atmospheric Temperature Sounding

In the middle 1960s, work began on a series of radiometers to be flown in satellites with the aim of measuring the distribution of temperature in the upper atmosphere. This program was extremely successful. The first of these

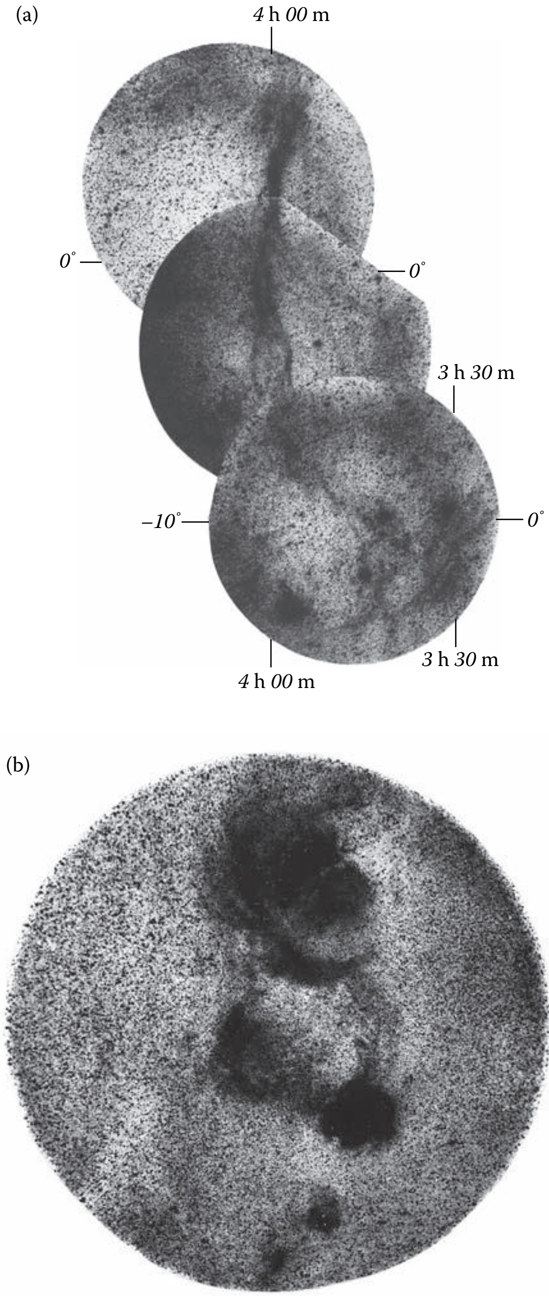

Figure 15.5
(a) Nebulosities in the Cetus arc. $H\alpha$ (656.3 nm) photographs of 1 h exposure taken on a 6-in *f*/1 Schmidt camera through a 4-nm bandwidth filter. (After Meaburn [7].) (b) Nebulosities in the galactic anti-center. Photograph taken through a 4-nm bandwidth filter centered on $H\alpha$ with a 6-in aperture Schmidt camera. The exposure was 1.75 h. (Courtesy of Dr. J. Meaburn.)

radiometers was designed by a joint team from the University of Oxford and the University of Reading in the United Kingdom, the team at Reading moving to Heriot-Watt University at a late stage of the project. The radiometer was flown in the Nimbus IV spacecraft. The radiometer was known as the *selective chopper radiometer* (SCR) because of the basic principles of its design and it made extensive use of filters. It made measurements with a height resolution of 10 km of the temperature of that part of the atmosphere of height between 15 and 50 km, that is, the troposphere and part of the stratosphere. The basic method used in the SCR and in other subsequent radiometers for temperature sounding is the detection and measurement of the radiation from atmospheric carbon dioxide.

Some ideas of the temperature structure of the atmosphere had already been formed, typical temperatures being of the order of 200K at a height of 10 km rising to 240–280K at heights of around 50 km. The peak of the black-body curve for a temperature of 200K, lies at a wavelength of 15 µm, while that for 280K is at 11 µm. The most favorable wavelength region for the measurement of the temperature of the atmosphere by detection of emitted radiation is therefore the band 11–15 µm. Of course the atmosphere will emit radiation only in the regions where it absorbs (the equivalence of absorptance and emittance is a basic physical principle) and this, coupled with the fact that the radiation emitted from a given level must traverse the remainder of the atmosphere above that level to reach the detector in the spacecraft, allows an ingenious method to be used for the deduction of the temperature structure that was first suggested by Kaplan [9].

Carbon dioxide is evenly distributed in the atmosphere and has extensive absorption bands around 15 µm so that it can be used as an indicator of the temperature of the atmosphere as a whole. Fortunately, over most of the important region, carbon dioxide is the only constituent of the atmosphere showing absorption (water vapor would interfere but is important only near the ground, and O_3 at 14 µm in the 25–40 km region can be avoided) simplifying considerably the calculations. The absorption spectrum of CO_2 consists, at very low pressures, of a number of discrete lines that become gradually broader with increasing pressure. The detector in the spacecraft is arranged so that it responds to only a very narrow band of wavelengths in the CO_2 spectrum. If a waveband is chosen within which the absorption is high, then the radiation emitted at the bottom of the atmosphere will not reach space because the transmission of the atmosphere above it is low. At greater heights, a much greater proportion of the energy emitted will reach the detector.

However, also at greater heights, the energy emitted by the atmosphere will fall, because of decreasing density and pressure of CO_2, and, at a height that will depend on the absorption within the particular waveband chosen, the second process will overtake the first with the result that a major portion of the energy received by the detector will emanate from a narrow range of depths in the atmosphere. The mean depth can be changed by varying

the center wavelength of the band that is being detected, and so altering the variation of absorption with height. The experiment and apparatus are described elsewhere [10–14].

The following account is a much simplified version that follows directly work by Sir John Houghton. First, we find the emittance of any layer by calculating the absorptance that is equivalent to the emittance. Consider a layer of the atmosphere situated at a depth z below the spacecraft. Let the transmittance of the atmosphere, at frequency ν, above this layer be T_z. In passing through a layer of thickness dz of the atmosphere the fractional loss in irradiance will be the absorptance of the layer. Next, consider radiation of initial irradiance I at frequency ν at depth z. The fraction of this appearing at the level of the detector in the spacecraft will be either IT_z, or $(I - dI)T_{(z-dz)}$ and as these quantities will be equal we can write

$$(I - dI)T_{(z-dz)} = IT_z$$

With some adjustment we find

$$A_{dz} = \frac{dI}{I} = \frac{T_z - T_{(z-dz)}}{T_{(z-dz)}} = \frac{-(dT_z/dz)dz}{T_{(z-dz)}}$$

where A_{dz} is the absorptance and hence emittance of the layer. If $\mathcal{T}$ is the mean temperature of the layer, then the black-body emission per unit frequency interval associated with it will be given by $B(\mathcal{T})$ at frequency ν. The irradiance actually emanating from the layer will be given by this expression multiplied by the emittance, i.e.,

$$dI_z = KT_{(z-dz)}A_{dz}B_\nu(\mathcal{T})$$

where dI_z is the irradiance per unit frequency interval reaching the radiometer, which emanates from a layer of thickness dz at depth z and K is a constant.

Then

$$dI_z = -K\frac{dT_z}{dz}B_\nu(\mathcal{T})dz$$

If the detector in the spacecraft has a bandwidth of $\Delta\nu$, then the expression for the power over this band becomes

$$\int_{\Delta\nu} dI_z d\nu = \int_{\Delta\nu} -K\frac{dT_z}{dz}B_\nu(\mathcal{T})dz\, d\nu$$

and if R_v/K is the response of the radiometer at frequency v, then the output of the instrument will be given by

$$D_z/dz = \int_{\Delta v} -R_v \frac{dT_z}{dz} B_v(T) dz\, dv$$

We can choose the frequency interval Δv small enough for $B_v(T)$ to be a constant over the interval. $B_v(T)dz$ can then be moved outside the integral sign. What is left is the function

$$W_z = \int_{\Delta v} -R_v \frac{dT_z}{dz} dv$$

which is known as the weighting function, and represents the response of the system to radiation from depth z. We shall now look a little closer at the form of the weighting function, assuming that a single isolated absorption line is involved.

The absorption coefficient k_v for radiation of frequency v is defined by the relationship

$$dI_v = -k_z I_z du$$

where dI_v is the change in irradiance I_v after traversing path length du of the absorbing gas. u is measured in terms of the quantity of gas traversed rather than physical distance and has such units as g cm^{-2} or atmo-cm (the equivalent path length in the gas at normal atmospheric pressure and temperature). The strength of the line S is defined as the absorption coefficient integrated over the whole width of the line.

For radiation of wave number v near the center of a single gaseous absorption line, k_v is given by the Lorentz formula for pressure broadening*:

$$k_v = \frac{S}{\pi} \cdot \frac{\gamma}{(v - v_0)^2 + \gamma^2}$$

γ is the half-width of the line, which is proportional to pressure and can be written $\gamma = \gamma_0(p/p_0)$. (γ is also inversely proportional to the square root of the absolute temperature, but, as this exhibits much less variation than pressure through the part of the atmosphere that we are considering, we can omit temperature from the calculation.)

* See for example p. 47 of Houghton J and Smith S D 1966 Infra-Red Physics (Oxford: Oxford University Press).

If the frequency ν is such that $\gamma^2 \ll (\nu - \nu_0)^2$, then we can write

$$k_v = \frac{S}{\pi} \cdot \frac{\gamma_0 p}{p_0(\nu - \nu_0)^2} = \beta p$$

Now CO_2 is uniformly mixed through the atmosphere so that the mass of CO_2 per unit area between the top of the atmosphere and depth z will be proportional to the atmospheric pressure at that depth, i.e.,

$$u = cp$$

where c is a constant. The transmittance of the atmosphere above depth z, at which the pressure is p, will therefore be

$$\begin{aligned} T_z &= \exp\left(-\int_{p=0}^{p} k_v du\right) \\ &= \exp\left(-\int_{p=0}^{p} ck_v dp\right) \\ &= \exp\left(-\frac{1}{2} c\beta p^2\right) \end{aligned}$$

To simplify the analysis, we can assume that p varies linearly with z, i.e.,

$$p = fz$$

(Alternatively, we could use p as the measure of the depth z since it is a single-valued function of z that increases continuously with z.) The weighting function for a single monochromatic line of frequency ν, assuming that $R = 1$, is then

$$W_z = -\frac{dT_z}{dz} = \beta c f^2 z \exp\left(-\frac{1}{2} \beta f^2 c z^2\right)$$

The form of this function is shown in Figure 15.6. For the purposes of drawing this, a new variable $y = (\frac{1}{2}\beta c f^2)^{\frac{1}{2}} z$ has been introduced so that

$$-\frac{dT}{dz} = (2\beta c f^2)^{\frac{1}{2}} y e^{-y^2}$$

and the function, which is actually plotted in Figure 15.6, is ye^{-y^2}

By choosing the appropriate wavelength, the form of the variation of the absorption coefficient can, to some extent, be controlled and the position of the maximum in terms of the height, or rather depth, varied. The absorption spectrum of CO_2 at 15 µm consists of a large number of separated lines. The teams at Oxford and Reading have made a special study of these, tabulating the positions and strengths, and have been able to choose a series

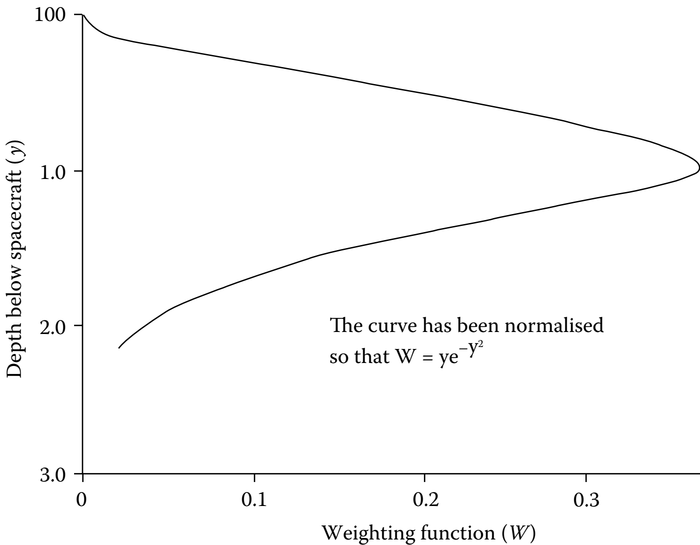

FIGURE 15.6
The form of the radiometer weighting function.

of wavelengths to permit examination of the temperature structure of the atmosphere between 15 and 50 km with a resolution of 10 km.

One of the difficulties that exist is the finite bandwidth of the radiometer. The bandwidths of practical filters cannot be made arbitrarily small and, because the CO_2 absorption coefficient varies with wavelength, the bandwidth of the radiometer will cause a reduction in the height resolution. For the channels designed to look deep into the atmosphere, the bandwidth does not affect the result too much and can be 10 cm^{-1}—well within the capabilities of an interference filter. The channels designed to look at the top of the atmosphere, however, must be positioned on the centers of the most intense lines, the Q-branch at 667 cm^{-1}, and the bandwidth must not effectively be greater than 1 cm^{-1}. This is beyond the current state of the art at 15 μm. The ingenious solution that has been adopted and gives the radiometer its name is the use of a chopper filled with CO_2.

To explain the action of this selective chopper, we shall first consider the operation of the simpler channels with the acceptable filters. In these channels, partly to ensure that the noise in the electronics is sufficiently low and partly to ensure that the radiometer registers radiation from the atmosphere only, and not from the components of the radiometer itself, which will all be emitting at 15 μm, a chopper is placed in the entrance aperture. Radiation emanating from the atmosphere will be chopped, while radiation from the radiometer itself will not, and will escape detection. Of course, the chopper will also radiate and so the usual method of alternately inserting and removing a blanking shutter in front of the radiometer entrance aperture would be quite useless, because the radiation from the shutter would also

be chopped and detected along with the signal. The method that is used is extremely neat. The entrance aperture of each channel is divided into two equal parts so that one half of the aperture views, reflected in a fixed mirror, deep space, which can be assumed to be at a temperature of absolute zero and to represent a reference of zero radiation provided the reflectance of the mirror is sufficiently high, while the other half views the Earth's atmosphere reflected in a second mirror, which can be varied in position for calibration purposes. A chopper consisting of a vibrating black blade is arranged so that it obscures the fixed and variable mirrors alternately and, therefore, effectively chops the incoming signal. The radiation from the chopper blade is not detected because the blade remains within the aperture of the system all the time.

The selective chopper channel of the radiometer is similar to these other channels. However, a narrower filter is used, having a bandwidth of 3.2 cm^{-1} at 667 cm^{-1}, the narrowest achievable at the time at this frequency. In addition, a cell containing CO_2 is included in front of each section of the entrance aperture and the black blade of the chopper is exchanged for a mirror that looks at deep space. If the chopper mirror were completely removed, both parts of the entrance aperture would look at the atmosphere, reflected in a mirror, which again can be varied in position. With the chopper mirror in position and vibrating, one section of the aperture will look at deep space while the other section will look at the atmosphere through the appropriate CO_2 cell, and vice versa. The effect is just as if the input radiation were being chopped by alternate cells of CO_2. The simplest arrangement is to have one cell empty and one filled with CO_2, when, provided the CO_2 is at the correct pressure, the chopping will be effective only over the line centers. This, together with the narrowband filter, gives an effective bandwidth of around 1 cm^{-1}. Since the cells of CO_2 are within the aperture of the system all the time, the radiation from them will not be chopped and will not be detected. The radiation detected in this way originates from the very top of the atmosphere. The addition of a little CO_2 to the empty cell absorbs out the narrow line centers, leaving an extremely narrow width on either side of center and giving a still sharper weighting function that allows regions just below the top of the atmosphere to be examined. Various combinations of filter and chopper have been proposed and a set of weighting functions is shown in Figure 15.7. Each satellite installation consists of six separate channels.

To maintain the accuracy of the instrument in flight, it is possible to recalibrate it. The principal components in the calibration system are the variable mirrors that are placed in front of each channel and normally reflect radiation from the atmosphere into the apertures. These mirrors are driven by small stepping motors and can be tilted to view the atmosphere, deep space, or a calibration black body giving a reference for both gain and zero in each channel. The proposed calibration sequence, which will repeat itself indefinitely in flight, is atmospheric radiation for 20 minutes, space for 2 minutes and

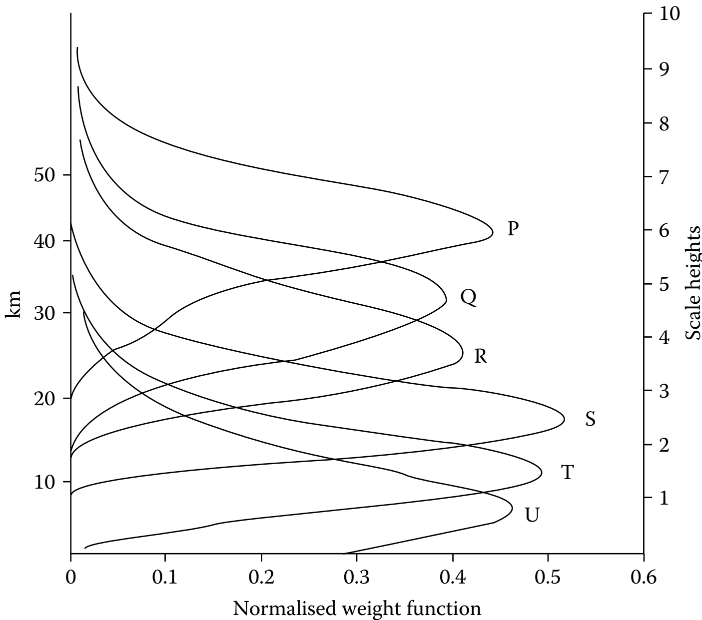

FIGURE 15.7
Proposed weighting functions for a satellite radiometer. The letters P, Q, R, S, T, and U refer to different channels. (Courtesy of Dr. S. D. Smith.)

calibration black body for 2 minutes. The channels having the extra CO_2 cells also have a balance calibration to ensure that the only difference between each half of the aperture is due to the CO_2 in the chopper cells. The narrowband filter that is used in the channel is replaced by a broadband filter at a wavelength outside the CO_2 absorption region, which views the Earth's surface. Any signal detected under these circumstances is due to a difference in sensitivity between the two halves of the channel and can be corrected if necessary.

Curves showing the measured transmittance of two of the basic filter elements are reproduced in Figure 15.8. The sidebands are suppressed in the instrument by filters of the type shown in Figure 7.22. The interference section of the blocking filter is deposited on one of the germanium lenses and an indium antimonide filter is fitted to the end of the light pipe over the detector. In addition, since it was found that the suppression in the wings of the Fabry–Perot filter was not quite high enough, a filter centered on the same wavelength but of the type

$$L \mid Ge \mid L\ HLHHLH\ L\ HLHHLH \mid Air,$$

which is a rather broader two-cavity type of around 20 cm^{-1} half-width, rather broader than that of Figure 15.8b, is placed in series with each Fabry–Perot. The composite filter possesses the narrow half-width of the Fabry–Perot together with the high sideband rejection typical of the two-cavity filter.

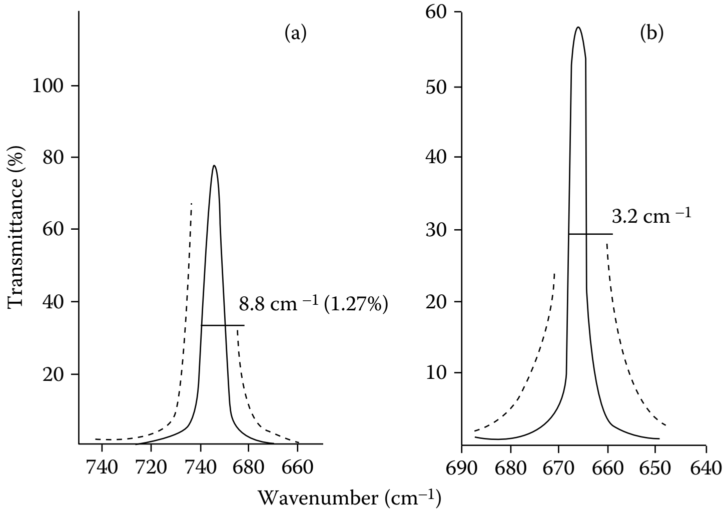

FIGURE 15.8
Measured transmittance of filters manufactured for the radiometer. 1 broken curves are merely the full line curves × 10.

(a) Air | *HLHHLH L HLHLHHLHL* | Ge substrate | *L* | Air

Peak transmittance 78% at 694.4 cm^{-1}.

(b) Air | *HLHLHHLHLH L* | Ge substrate | *L* | Air

Peak transmittance 58% at 666.4 cm^{-1}.
L = ZnS; *H* = PbTe. (Courtesy of Dr. S. D. Smith and Sir Howard Grubb, Parsons & Co. Ltd.)

The construction of the radiometer is shown in Figure 15.9. The optical system has been designed to use the full area of the narrowband filters together with the maximum range of angles that can be accommodated without destroying the spectral profile. It was this that prompted the work of Pidgeon and Smith on the angular dependence of filter characteristics discussed in Chapter 8.

The radiometer was successfully launched in April 1970 and made exceptionally useful temperature surveys of the upper atmosphere revealing much that was novel and unexpected. An early account of the instrument will be found in references [15–17].

15.4 Order Sorting Filters for Grating Spectrometers

There is a considerable advantage in using a diffraction grating rather than a prism for the selection of wavelengths in a monochromator or spectrometer, because the luminosity is so very much greater for the same resolution. A problem exists, however, with the diffraction grating, which does not

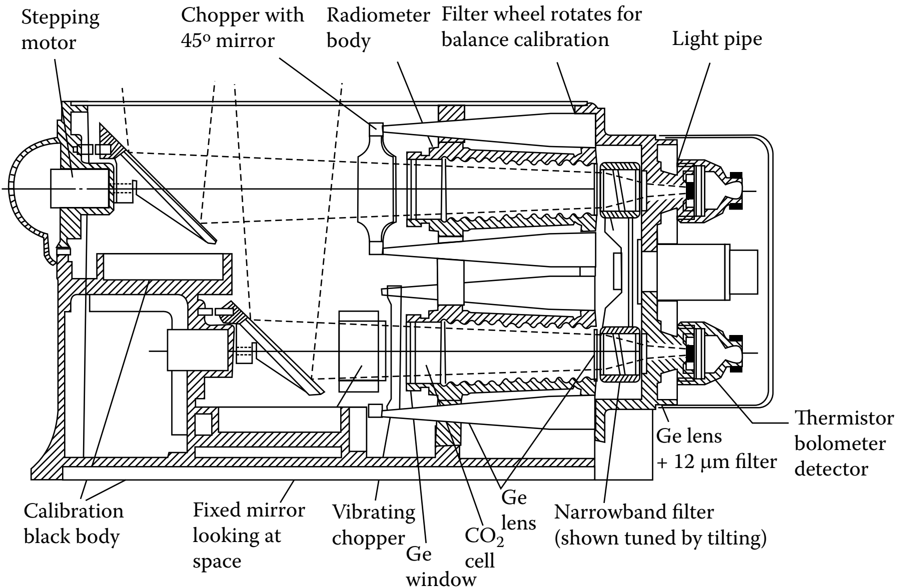

FIGURE 15.9
Schematic diagram of the selective chopper radiometer. (Courtesy of Dr. S. D. Smith.)

exist with the prism. This is the appearance of other orders in the spectrum, which must be eliminated. The problem is particularly severe in the infrared, and the solution usually adopted has been the use of a low-resolution prism monochromator in series with the higher-resolution grating monochromator. The lower resolution of the prism section, which is all that is necessary since order sorting is its sole function, means that the luminosity can be made as high as the grating section and the advantage associated with the grating thereby retained. The grating and prism must be driven so that their respective wavelengths remain in step, a difficulty being that their angular dispersions vary in quite different ways. A simpler and attractive alternative is a longwave-pass thin-film filter. Recently several instruments have appeared on the market that use this system rather than the prism.

A paper by Alpert [18] gives an account of the various factors involved in the specification of such filters for infrared instruments. The most important feature is the rejection required in the stop regions. Before we can make an estimate of this rejection, we must first consider the way in which the energy varies in the various grating orders. Included in the assessment must be the characteristics of both the source and the detector.

A simple theory of the diffraction grating is considered in most textbooks on optics. For our present purpose it is sufficient to note two points. The first is that the angles of incidence and diffraction for any particular wavelength are given by the grating equation

$$\sin\vartheta + \sin\varphi = \pm m\lambda/\sigma \qquad (15.13)$$

where ϑ and φ are the angles of incidence and diffraction, respectively, the sign convention being as shown in Figure 15.10a. σ is the grating constant, that is the spacing of the grooves, and m is the order number. From Equation 15.13, we can see immediately the source of our present problem, that the angles corresponding to any wavelength, λ, in the first order also exactly correspond to $\lambda/2$ in the second order, $\lambda/3$ in the third order, and so on. A second point is that the energy distribution in the various diffracted orders of any wavelength will be given by the pattern of lines in Expression 15.13 modulated by the single-slit diffraction pattern of any one of the grooves at the appropriate wavelength. Modern diffraction gratings are invariably of the reflection type with the grooves "blazed" or tilted, so that the single-slit diffraction pattern has its maximum at a particular wavelength in the first order, known as the blaze wavelength, rather than in the zero order, which increases considerably the efficiency of the grating over a range of wavelengths. To estimate the shape of the energy distribution, we can assume the form of the grooves to be as in Figure 15.10b, although in practice the form may vary from that shown. α and β are the angles of incidence and diffraction referred to the normal to the groove, instead of the grating normal, but with the same sign convention applying. The power in the diffracted beam is given by an expression of the form

$$I = I_0 \frac{\sin^2[\pi \nu \sigma \cos \psi (\sin \alpha + \sin \beta)]}{[\pi \nu \sigma \cos \psi (\sin \alpha + \sin \beta)]^2} \tag{15.14}$$

where it is assumed that the grating will be sufficiently large to intercept the entire incident beam regardless of the angle of incidence. This expression is

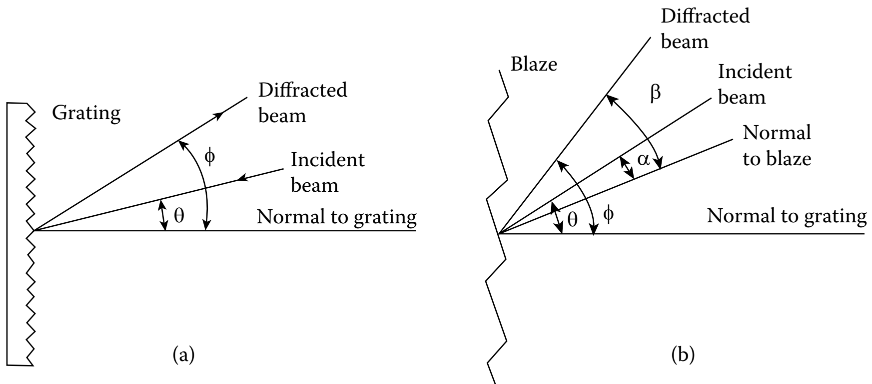

FIGURE 15.10
(a) Sign convention for ϑ and φ. They have the same sign if they are on the same side of the grating normal. One side is chosen arbitrarily as positive. (b) Sign convention for α and β. They have the same sign if they are on the same side of the blaze normal. They are chosen positive when they have the same sense as the positive direction of ϑ and φ.

not strictly accurate over the entire range because at some angles the steps at the ends of the grooves may interfere slightly with the process, but it is good enough for our purpose. ψ is the angle between the grating and the blaze normal.

Most monochromators are of a type where the entrance and exit slits are fixed in position and the grating is rotated to scan the spectrum and where the angle of incidence is almost equal to the angle of diffraction. Little is lost by assuming that they are equal. With this assumption the curves shown in Figure 15.11 have been derived for a typical grating and show the power distributions in the various orders. An important point is that, for the groove arrangement shown in Figure 15.10b, the dispersion, which is inversely proportional to the groove spacing, balances the alteration in the width of the diffraction pattern as the groove width varies, with the result that the variation of power with wavelength in any order depends solely on the blaze wavelength. A good rule of thumb is that the useful range of a grating blazed for a wavelength of λ_0 in the first order is from $2\lambda_0/3$ to $2\lambda_0$ in the first order, from $2\lambda_0/5$ to $2\lambda_0/3$ in the second order, and from $2\lambda_0/(2n + 1)$ to $2\lambda_0/(2n - 1)$ in the nth order. This is rather simpler in terms of wave number, the range being given by $\nu_0 \pm \frac{1}{2}\nu_0$ in the first order and $n\nu_0 \pm \frac{1}{2}\nu_0$ in the nth order. The bandwidth is more or less constant in terms of wave number. Measurements that have been made on gratings confirm the shape of the curves in Figure 15.11. Some such measurements are reproduced by Alpert.

Now let us make the assumption that the diffraction grating is to be used in the first order and that the filter problem is the elimination of the second and higher orders. As far as the filter is concerned, the parameter that matters is the ratio of the detector signal in the first order to that in any of the other higher orders. The factors involved are, first of all, the variation of sensitivity of the detector; second, the variation in efficiency of the grating, already dealt with above; third, the dispersion of the grating in the various orders so that the energy in any order transmitted by the slits in the monochromator

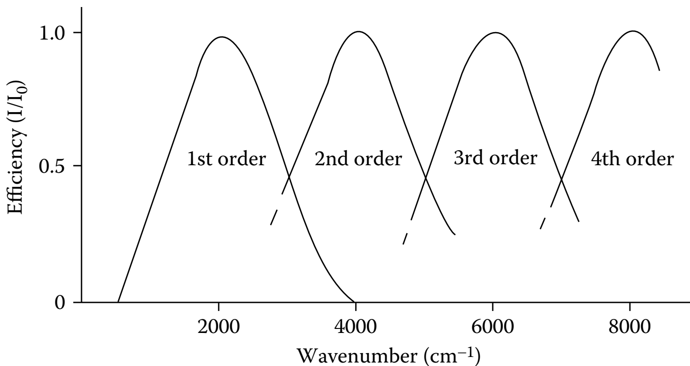

FIGURE 15.11
Intensity distribution in the various orders or a typical diffraction grating (theoretical) blazed for 2000 cm^{-1} (5 µm) in the first order.

can be calculated; and last, the variation of output of the source. Of course, in some applications there may well be other operating factors, such as the transmittance of some optical components, or the variation of reflectance of mirrors.

The detectors commonly used in this part of the infrared are thermal detectors that have reasonably flat response curves. In what follows, we assume that they are perfectly flat. Any variation can be readily included in the analysis if required.

At any wavelength, the slits will pass a small band of wavelengths. If we assume that the slits are narrow enough so that energy variations over the range of wavelengths passed by the slit are negligible, then the energy transmitted in any order will be inversely proportional to the bandwidth of the slits in that order. From Equation 15.13, the bandwidth is inversely proportional to the order number, which does help to reduce the requirements for filter performance.

In this part of the infrared, the sources generally used are either Nernst filaments or globars. For our present purpose we can assume, without too much error, that the source will be a black body probably peaking at around 2 μm, although this particular wavelength does not matter very much. The variation of energy with wavelength for a black-body source is given by Planck's equation:

$$E_\lambda = \frac{c_1}{\lambda^5[\exp(c_2/\lambda T) - 1]} \tag{15.15}$$

where E_λ is the spectral emissive power, and c_1 and c_2 are the first and second radiation constants with values 3.74×10^{-16} Wm^2 and 1.4388×10^{-2} mK, respectively.

For any wavelength λ, let the efficiency of the grating be denoted by ε_λ, and the transmittance of the order sorting filter by T_λ. Then the stray light due to the *m*th order, expressed as a fraction of the energy in the first order, will be given by

$$r_m = \frac{\varepsilon_{\lambda/m} E_{\lambda/m} T_{\lambda/m}}{m\varepsilon_\lambda E_\lambda T_\lambda} = \frac{\varepsilon_{\lambda/m}(\lambda/m) E_{\lambda/m} T_{\lambda/m}}{\varepsilon_\lambda \lambda E_\lambda T_\lambda}$$

where we have multiplied the numerator and denominator by λ. The permissible magnitude of r_m depends on the number of orders that are involved in producing significant leakage. Let this number be N and let the total amount of permissible stray light be given by S, which is expressed as a fraction of the total first-order energy. Then we can require that

$$r_m = S/N$$

and the maximum transmittance permitted at wavelength λ/m is given by

$$T_{\lambda/m} = T_\lambda \frac{S}{N} \cdot \frac{\lambda E_\lambda}{(\lambda/m)E_{\lambda/m}} \cdot \frac{\varepsilon_\lambda}{\varepsilon_{\lambda/m}} \tag{15.16}$$

Now $\varepsilon_\lambda/\varepsilon_{\lambda/m}$ will be greater than unity except on the blaze wavelength. Without affecting the accuracy too greatly, we can make the assumption that each order m is effective only over the range $2\lambda_0/(2m + 1)$ to $2\lambda_0/(2m - 1)$ and that $\varepsilon_\lambda/\varepsilon_{\lambda/m}$ is unity over this range. Elsewhere we can assume that the mth order does not produce leakage and omit it.

To complete the calculation, we need the value of $\lambda E_\lambda/(\lambda/m)E_{\lambda/m}$. The function λE_λ is plotted in Figure 15.12. To make it possible to apply this figure generally, the variables have been normalized in the manner shown and the scales are logarithmic so that any particular set of conditions can be reproduced simply by sliding the scales along the axes.

The first step in drawing up the specification for a practical set of filters will be to decide on the required number of filters. Even one single diffraction grating has a useful wavelength range of 3:1, which is greater than the range that can be covered by just one filter.

Let the limits of the wavelength region over which the grating or set of gratings are to be used be λ_F and λ_S, where $\lambda_F > \lambda_S$. If we start with the longest wavelength, then the final filter in the series must block wavelengths $\lambda_F/2$ and shorter. An ideal longwave-pass filter would have a rectangular edge shape and it would be possible to use it over the whole of the range $\lambda_F/2$ to λ_F.

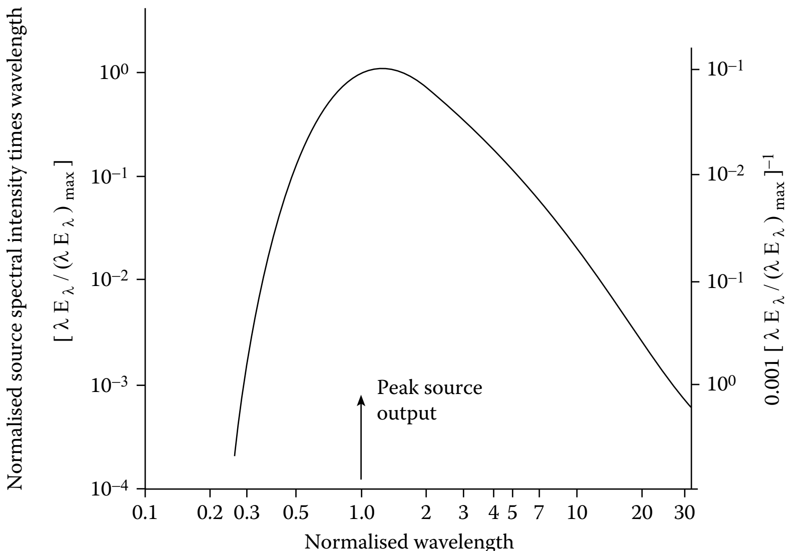

FIGURE 15.12
Curve showing the variation of λE_λ with wavelength for a black-body source.

Real filters have sloping edges and must be allowed some tolerance in edge position otherwise manufacture becomes impossible. This means that the specification must show the start of the transmission region of the final filter as $(1 + \gamma)\lambda_F/2$. Assuming that all the filters in the set are of more or less similar construction, then the same expression will also apply to the next filter in the set, which will have a transmission region specified to start at a wavelength given by $[(1 + \gamma)^2/2^2]\lambda_F$ and to finish at $[(1 + \gamma)/2]\lambda_F$. The regions for the other filters are found in exactly the same way. If there are n filters in the set, then the first filter must have the specified start wavelength at $[(1 + \gamma)^n/2^n]\lambda_F$. We can equate this start wavelength to λ_S and solve for γ:

$$\gamma = 2(\lambda_S/\lambda_F)^{1/n} - 1$$

This expression can be evaluated in a practical case for several possible values of n and the set of filters giving the optimum arrangement of filters and the best degree of tightness of tolerance selected.

The advantage of using this type of specification is that any particular filter from any set of filters made to the specification is interchangeable with the corresponding filter in any other set. If this interchangeability is not required, it is possible to slacken the tolerances slightly, but this makes the problem of making up each individual set rather more of a puzzle.

To illustrate the method, let us consider the specification for a set of filters for use with a pair of gratings for the region 3–30 μm. The first grating can be the one already considered with blaze at 5 μm, while the second will be a similar one with blaze at 15 μm. The region 3–3.3 μm will not be covered with quite as great efficiency as the rest of the region, but the source will be rather more efficient here, and that should counterbalance the fall off in grating efficiency to some extent.

First, we decide on the number of filters. By inspection we arrive at the conclusion that the minimum number of filters is four, but that this number leads to a rather tight specification, and it is better to use five filters. If we assume that the tolerances should be shared equally amongst them, then the limits of the pass regions and the edges of the rejection zones are as shown in Table 15.1.

We then decide on the acceptable level of leakage light in this case as, say, 1% of the true first-order signal. We must also decide on the acceptable minimum transmittance of the filters in the pass region, say 50%. In practice, the level will almost certainly be rather greater than this, but the use of a low figure in setting up the specification gives a pessimistic figure for the specified levels in the rejection region.

Next we compute the regions over which the various orders are effective in producing leakage, or stray, light. The results are shown in Table 15.2. Both the actual wavelength of the leakage and the corresponding wavelengths in the first order with which it interferes are given. We can choose to use germanium as substrate material for the filters and therefore safely neglect all

TABLE 15.1

Preliminary Filter Specifications

Filter Number	Pass Region (μm)	Longwave Edge of Rejection Zone (μm)
5	19–30	15
4	12–19	9.5
3	7.6–12	6
2	4.8–7.6	3.8
1	3–4.8	2.4

TABLE 15.2

Effective Ranges of the Grating Orders

Order	Range (μm)	Corresponding Range in the First Order (μm)
15 μm Grating		
1st	30–10	30–10
2nd	10–6	20–12
3rd	6–4.29	18–12.85
4th	4.29–3.33	17.15–13.33
5th	3.33–2.72	16.70–13.65
6th	2.72–2.31	16.35–13.85
7th	2.31–2.00	16.15–14.00
8th	2.00–1.76	16.00–14.10
9th	1.76–1.58	15.90–14.20
10th	10th and higher order beyond germanium edge	
5 μm Grating		
1st	10–3.33	10–3.33
2nd	3.33–2.00	6.67–4.00
3rd	2.00–1.43	6.00–4.28
4th	4th and higher orders beyond germanium edge	

wavelengths shorter than 1.6 μm, because they will be effectively suppressed by the intrinsic absorption of the germanium.

The first filter we consider is filter number 4, which includes the blaze wavelength of the longer-wave grating in its transmission region. At the blaze wavelength, the highest significant order is the ninth and N therefore is 8, i.e.,

$$T_{\lambda_0} S/N = 0.5 \times 0.01/8 = 0.000625$$

We therefore set the scale on the right-hand side of Figure 15.12 to correspond to 0.000625 at 15 μm and read off the allowable transmissions at the higher-order wavelengths from the curve. This is shown in Figure 15.13.

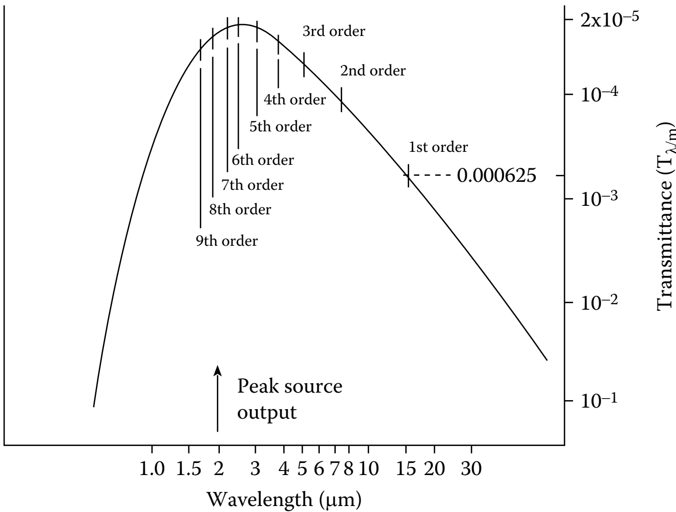

FIGURE 15.13
How the maximum transmittance levels are established for filter number 4.

To simplify the task of setting up the specification, we assume that the transmission levels thus established apply to the complete range for each appropriate order, i.e., for the *m*th order, the transmittance found in this way applies to the range $2\lambda_0/(2m + 1)$ to $2\lambda_0/(2m - 1)$, a slightly pessimistic result. The only exception we make to this is that portion of the rejection zone immediately beside the edge of the transmission zone. Here it is important that the specification should not be tighter than is strictly necessary. The end of the transmission region is 19 μm. From the range of the higher order interference we see that only one order, the second, is effective at that wavelength. $T_\lambda S/N$ is therefore $0.5 \times 0.01/1.0 = 0.005$. Setting this value on the right scale of Figure 15.13 against the point on the curve corresponding to 19 μm, we read off 0.0009 against 9.5 μm, which is therefore the maximum allowable transmittance at that wavelength. At 18 μm, the second and third orders are involved and the value of $T_\lambda S/N$ becomes 0.0025. Setting this against the point on the curve corresponding to 18 μm, we read off 0.0004 against 9 μm, which is the maximum allowable transmittance at that point. At 17.15 μm, there are three orders involved so that the transmittance at 8.6 μm should be not greater than 0.0003. This procedure is repeated at each wavelength where a further order becomes significant until the full number of orders is reached. Points corresponding to these are plotted on a diagram and a horizontal line through each is linked with a vertical line through the adjacent point on the shortwave side. The specification for the filter is then completed by adding a minimum transmittance level of 0.50 from 12 to 19 μm. Figure 15.14 shows the complete arrangement.

Next we consider the longest-wave filter, number 5. Here the conditions are not nearly so severe, because the filter covers a region that does not include

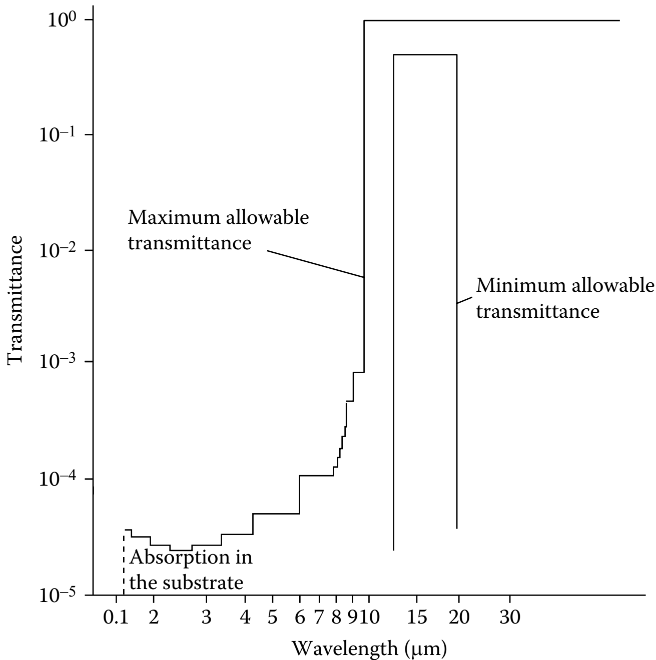

FIGURE 15.14
Specification of filter number 4.

the first-order blaze wavelength and therefore there is only slight higher-order leakage. According to Table 15.2, the second-order leakage is falling off sharply beyond 20 μm and the third order is not effective anywhere within the pass region. The critical region is therefore 9.5–10 μm.

$T_\lambda S/N$ is once again 0.005, and setting this value against the point corresponding to 20 μm in Figure 15.12, we find the permissible transmission in the rejection region at 10 μm as 0.0009. Outside the 9.5–10 μm range, the simple theory that predicts no leakage at all is again not sufficiently accurate. A convenient pessimistic assumption is that the transmittance at the very edge of the rejection zone, i.e., at 15 μm, should be around 0.01 and then a straight line can be drawn from this point to that at 10 μm. On the shortwave side of 9.5 μm, we can retain the transmittance as 0.0009. The resulting transmission specification for the filter is given in Figure 15.15.

Filter number 3 covers the changeover from one grating to the next. Beyond 10 μm, the grating is blazed at 15 μm. The significant range for second-order leakage is 12–20 μm so that, except just at 12 μm, second-order leakage will be low. At 12 μm, $T_\lambda S/N$ is 0.005, and from Figure 15.12 the permissible transmission at 6 μm is just over 0.001. We can specify this level of transmission as far as 5 μm, which corresponds to 10 μm in the first order, the grating changeover wavelength. On the short wavelength side of 10 μm, the 5 μm grating is

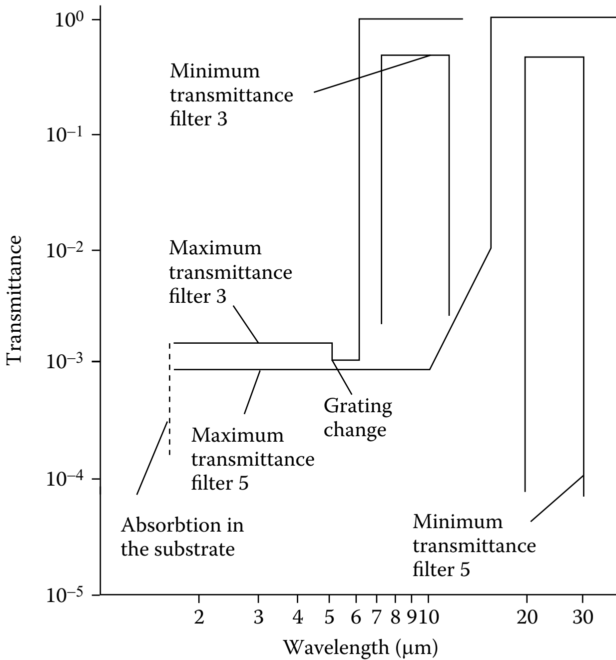

FIGURE 15.15
Specification of filter numbers 3 and 5.

used. Table 15.2 predicts that there will be no interference from the edge of the pass band at 7.6 μm right to 10 μm. However, to be safe, we assume that there will be second-order interference at 7.6 μm, and setting a value of 0.005 against 7.6 μm in Figure 15.12, we establish a value for the transmittance at 3.8 μm, the second-order wavelength. This is shown in Figure 15.15 and we further assume that it applies to the whole region between the germanium edge and 5 μm.

The specification for filter number 2 (Figure 15.16) is set up in exactly the same way as for filter number 4 since it includes the blaze wavelength. However, the requirements are not nearly so severe, because both the peak of the source and the absorption edge of the germanium substrates are much closer to the pass band of the filter.

Filter number 1 is similar to the others (Figure 15.17). The short band from 1.6 to 2 μm, where the simple theory predicts no higher-order leakage (second order missing and third order corresponding to first-order wavelengths beyond 4.8 μm, the edge of the pass band), is filled in by a horizontal line at the same level as the allowable transmittance at 2 μm.

As far as the optical performance of the filters is concerned, there is only one further point to be specified: the bandwidth of the measuring spectrometer used for inspecting the filters. The requirement here is that the bandwidth should be not greater, nor appreciably less that the bandwidth of the

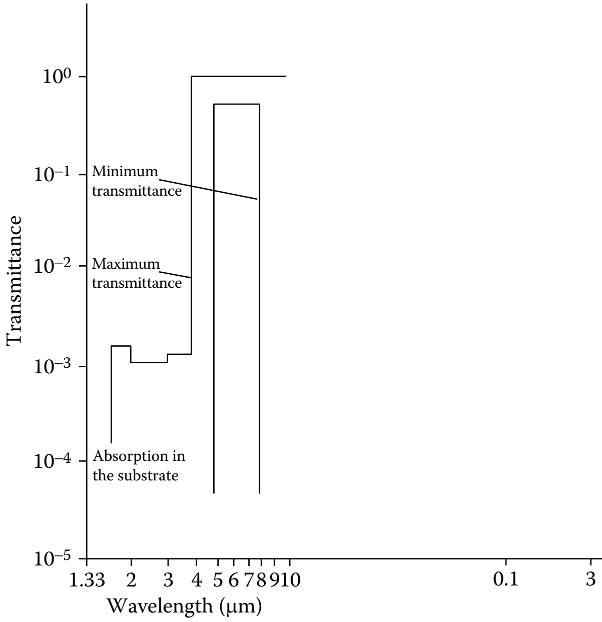

FIGURE 15.16
Specification of filter number 2.

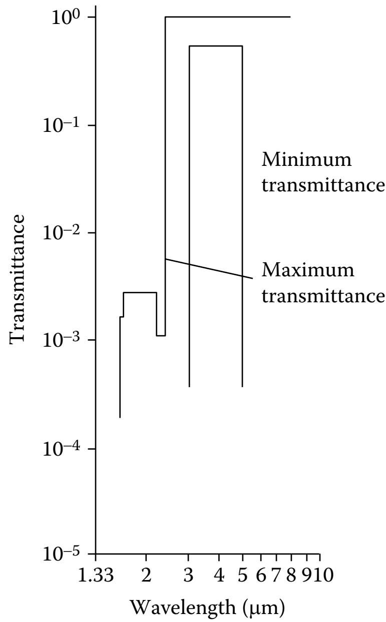

FIGURE 15.17
Specification of filter number 1.

final instrument in which the filters are to be used.* Any spikes of transmittance not resolved by this arrangement will not be resolved by the instrument itself. There is clearly no point in carrying out too strict a test, which would not only be an unnecessary waste of time and expense, but could also lead to a filter's being rejected when in fact it is perfectly satisfactory for the application.

Once the specification has been established, the design of the filters is just a straightforward application of the principles discussed in Chapter 7. A study of the results suggests some general rules. The first is that the filters that include the first-order blaze wavelength in their pass regions are the most critical in their specifications, and to ease, as far as possible, their edge steepness the blaze wavelength should be arranged to be nearer the shortwave limit of the pass region than the longwave limit. The second point is that since those filters that do not include the first-order blaze have very much reduced rejection requirements, it is useful to make sure that the longest-wave filter, that will be the most difficult to fabricate, has a pass region clear of the blaze wavelength even if in some applications it means an extra filter.

15.5 Glare Suppression Filters and Coatings

Glare is a term that is extensive in its coverage. What we mean by the term in this context is specular reflection of illumination from a bright source that enters the eyes and masks a, usually weaker, desired, visual image.

Polarizing sunglasses represent an early example of glare reduction. Sunlight reflected by water or silica sand is a common source of glare. When the sun is at an angle that makes the glare a problem, the reflection is usually in the vertical plane and at or near the Brewster angle so that the reflected light is principally *s*-polarized. A person who is upright will receive this glare light as primarily linearly horizontally polarized, and it can therefore be virtually eliminated by a suitably oriented polarizer.

This solution depends on reflection in the vicinity of the Brewster angle and is not available for the now common glare caused by unsuitable lighting where visual display units are concerned. In this case, the signal light from an emitting phosphor at the rear surface of a glass plate is masked by specularly reflected ambient light from the two surfaces of the plate. The orientation of the plane of incidence can vary enormously and the glare can be reflected at angles that are near normal. A solution that has been much used in electronic instruments consists of a circular polarizer inserted before the display. Specular reflection at near normal incidence reverses the handedness of the

* i.e. the fractional bandwidth of the measuring instrument should be equal to the fractional bandwidth of the final instrument in the transmission region of the particular filter under test.

circularly polarized glare light that has already passed through the polarizer on its inward journey and makes it impossible for it to pass through it again on the outward journey. This works well when the specular reflectance of the outer surface of the polarizer is appreciably less than that of the underlying display. In other cases, the reflectance must be reduced by application of an antireflection coating. Since the circular polarizer protects against glare from its own rear surface, the antireflection coating is required over the front surface only.

Later, it was found that a quite satisfactory reduction in glare could be achieved by replacing the circular polarizer by a simple neutral density filter such as a sheet of absorbing glass or plastic. Specular reflectance from the filter is eliminated by antireflection coatings front and back. Glare light then passes through the filter twice, while signal light passes through only once. This nominally reduces the glare-to-signal ratio by a factor equal to the transmittance of the filter. However, the brightness of the display can be raised to compensate, and so a typical glare reduction is equal to the square of the transmittance. A transmittance of 50%, then, reduces the glare by a factor of 4, a quite acceptable figure.

The glare reduction filter of this type is a separate component that is fitted, at a late stage, as an accessory to the display unit. A recent tendency is to make the glare reduction component an integral part of the display unit. In its simplest form, this is a coating that presents absorption and acts also as an antireflection coating. The simplest way of achieving this is to replace the normal completely transparent high-index materials by high-index absorbing materials. The most common arrangement takes the four-layer high-efficiency antireflection coating and replaces the usual zirconia or titania with indium tin oxide (ITO). A good antireflection coating that is completely transparent reduces the glare by 50%. Normally, it is arranged to have a certain amount of absorption that acts to reduce the glare still further. Figure 15.20 shows a calculated characteristic that uses ITO data from Gibbons et al. [19]. The overall transmittance of the coating is around 90%, and so the glare is further reduced by a factor of 0.8. The glass in the display faceplate is frequently absorbing, too, and this also contributes to a reduction. The ITO in the coating is a conducting material and acts to reduce electromagnetic emission and static electric fields but not low-frequency magnetic fields.

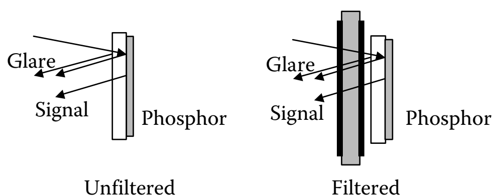

FIGURE 15.18
The principle of an external antiglare filter. Glare light passes through the filter twice while signal light passes through only once.

FIGURE 15.19
Glare reduction filter applied to the face of a display. The high index material is made both absorbing and conducting.

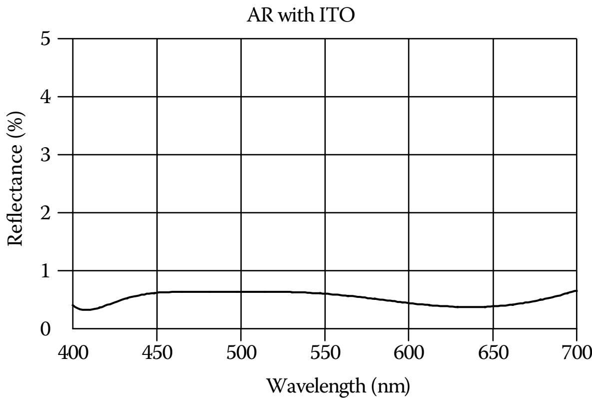

FIGURE 15.20
Response of a four-layer antireflection coating using silica and ITO. The ITO constants are taken from Gibbons et al. [19].

To enhance the absorption still further and improve the glare suppression, materials that are still more absorbing may be used. Transition metal nitrides, such as titanium nitride, are one possibility [20]. Wolfe [21] has used layers of silver and nickel to increase the absorption and at the same time ensure the electrical conductance. Silver was incorporated in the form of a subsystem consisting of around 8 nm of silver surrounded by 1.2 to 2.0 nm of $NiCrN_x$ that was in turn surrounded by some 20 to 30 nm of SiN_x or $SiZrN_x$. An outer layer of SiO_2 then completed the coating. Alternatively, a layer of nickel, perhaps 6 to 9 nm thick surrounded by protecting layers of SiN_x to protect it from oxidation, was found to be satisfactory. Coatings involving these materials could be made to have transmittances in the range of 30%–80%.

An ingenious family of two-layer coatings for glare reduction was recently proposed. Early development was carried out by a group at the Asahi Glass Company Ltd. in Japan [22], who termed the coating *ARAS*. A

further description is given by Ishikawa and Lippey [23]. Absorbing two-layer coatings are also discussed in detail by Zheng and colleagues [24]. At the shortest wavelength, the coating can be considered to consist essentially of a typical V-coat with a thin high-index layer next to the substrate and a rather thicker low-index layer outermost. For simplicity, the substrate in this description is transparent, but this is not a necessary condition. Now let the wavelength move to a longer value. The physical thicknesses of the layers will remain constant, but in the absence of dispersion, both optical thicknesses will become smaller fractions of the wavelength and so the admittance loci will shrink. Now imagine that as the wavelength changes, the reflectance of the coating remains at zero. The outermost low-index layer can be considered to be a normal dielectric material, like silica, and so it will exhibit negligible dispersion. The end point is firmly fixed at unity on the real axis, the admittance of the incident medium, and so, since the locus is shorter, the starting point moves around the existing circle. Similarly, if the index of the high-index inner layer remains constant and the starting point is firmly fixed at the admittance of the substrate on the real axis, the end point will move around the high admittance circle and a gap will open up in the locus so that it is no longer valid. Now let the optical constants of the inner layer, the high-index layer, be completely adjustable. By adjusting both the index of refraction and the extinction coefficient, the end point of the locus can be swept over a quite large area of the admittance diagram. The gap in the admittance locus can be closed so that it becomes valid and the reflectance remains at zero. By arranging for appropriate smooth variations in both n and k, the reflectance can be retained at zero over the entire visible region.

The properties of tungsten-doped titanium nitride are very close to ideal. Measured values extracted from Ishikawa and Lippey (estimating from their graph) are given in Table 15.3. The thicknesses of the tungsten-doped titanium nitride film and the silica film were 10 nm and 80 nm, respectively.

We use a cubic spline interpolation to smooth the constants given in Table 15.3 and then calculate the performance assuming a normal dispersive index for the glass substrate to give Figure 15.21. This is impressive.

The calculated transmittance of the coating is shown in Figure 15.22. It is surprisingly neutral and will contribute to a satisfactory reduction in glare. Although no figures are given the coating also reduces emissions from the display unit.

TABLE 15.3

Optical Constants of Tungsten-Doped Titanium Nitride

Wavelength	Refractive Index	Extinction Coefficient
405.00	2.5	0.7
510.00	1.8	1.3
632.80	1.2	1.7

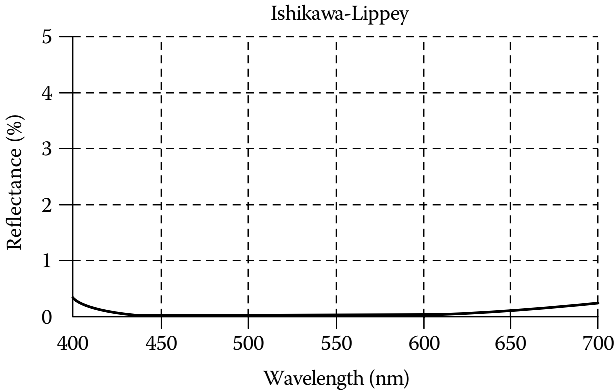

FIGURE 15.21
The performance calculated for design: Air | SiO_2: 80 nm | TiN_xW_y: 10 nm | Glass. (Calculation parameters from Ishikawa, H. and Lippey. B., *Two layer broad band antireflection coating* in *Tenth International Conference on Vacuum Web Coating Fort Lauderdale, Florida*, Bakish Materials Corporation, Englewood, NJ, 1966.)

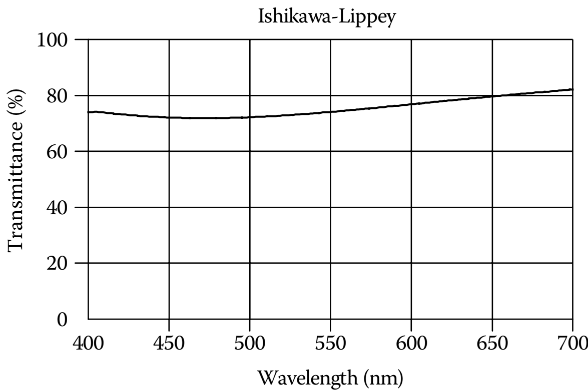

FIGURE 15.22
The calculated transmittance of the coating of Figure 15.21.

The admittance diagram in Figure 15.23 shows clearly the way in which the dispersion of the optical constants of the absorbing layer holds the termination of the locus in the vicinity of the incident medium admittance and keeps the reflectance low.

15.6 Some Coatings Involving Metal Layers

15.6.1 Electrode Films for Schottky-Barrier Photodiodes

A simple diode photodetector consists of a metal layer deposited over a semiconductor forming a Schottky barrier. High quantum efficiency can be

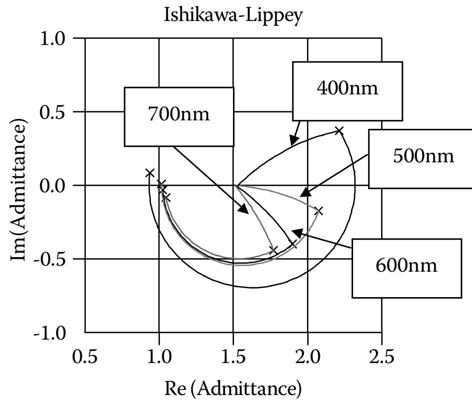

FIGURE 15.23
The admittance locus of the antireflection coating of Figure 15.21 showing how the dispersion of the optical constants of the layer next to the substrate compensates for the shortening of the locus as the wavelength increases.

achieved. The incident light passes through the metal layer into the depletion layer of the diode where it creates electron-hole pairs. The metal contact layer must transmit the incident light and since it has intrinsically high reflectance, it must be coated to reduce its reflection loss. We give here a very simple approach to the design of a combination of electrode and antireflection coating. A number of workers [25–27] have made contributions in this area, with probably the most complete account of an analytical approach being that of Schneider [27].

The substrate for the thin films is the semiconducting part of the diode, and it is fixed in its optical admittance. The metal layer goes directly over the semiconductor (in some arrangements, there is a very thin insulating layer that has negligible optical interference effect), and so the potential transmittance is fixed entirely by the thickness of the metal. All that can be done to maximize actual transmittance is simply to reduce the reflectance to zero.

We take as an example a gold electrode layer deposited on silicon. We assume a wavelength of 700 nm and optical constants of $0.131 - i3.842$ for gold and $3.92 - i0.05$ for silicon [28]. The optical constants of silver and copper are quite similar to those of gold at this wavelength and the results apply almost equally well to these two alternative metals. The admittance locus of a single gold film on silicon is shown in Figure 15.24. An antireflection coating must bridge the gap between the appropriate point on the metal locus to the point (1,0) corresponding to the admittance of air. We can assume that the maximum and minimum values of dielectric layer admittance available for antireflection coating are 2.35 and 1.35, respectively. Using these values, we can add to the admittance diagram two circles that pass through the point (1,0) and correspond to admittance loci of dielectric materials of characteristic admittances 2.35 and 1.35, respectively. These loci define the limits of a region in the complex plane. Provided a metal locus ends within this region,

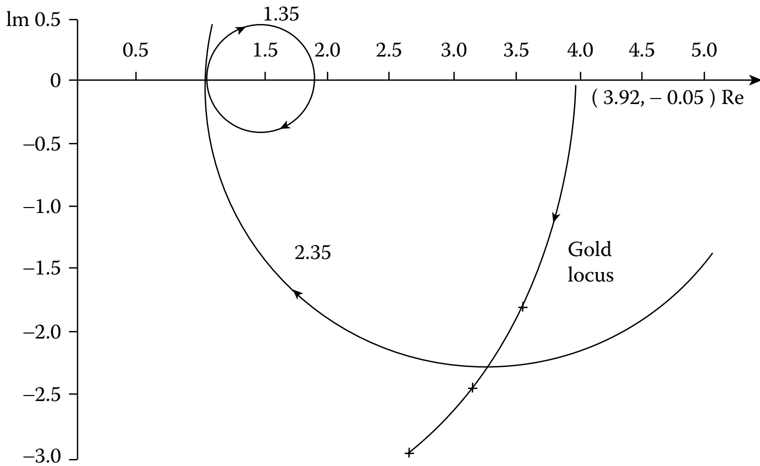

FIGURE 15.24
Admittance diagram showing some of the factors in the antireflection of a metal electrode layer in a photodiode. The optical constants of gold are assumed to be (0.131 – i3.842) at a wavelength λ_0 of 700 nm. The gold is deposited on silicon with optical constants (3.92 – *i*0.05). The crosses on the gold locus mark thickness increments of $0.005\lambda_0$ i.e., 3.5 nm. Also shown are loci corresponding to dielectric layers of indices 1.35 and 2.35 that terminate at the point 1.00.

then it will be possible to find a dielectric overcoat of admittance between 1.35 and 2.35 that, when the thickness is correctly chosen, will reduce the reflectance to zero. It is clear from the diagram that the thicker the metal film, the higher must be the admittance of the antireflection coating. Once the metal locus extends beyond this region, a single dielectric layer can no longer be used and a multilayer coating (or a single absorbing layer, although it would reduce transmittance and so would not be very useful in this particular application) becomes necessary. We have already considered multilayer coatings in the section on induced transmission filters. Here, we limit ourselves to a single layer and take the highest available index of 2.35.

The remaining task in the design is then to find the thicknesses of metal and dielectric corresponding to the trajectories between the substrate and the point of intersection and between the point of intersection and the point (1,0) in Figure 15.24. The points marked along the metal locus correspond to intervals of $0.005\lambda_0$ in geometrical thickness, that is, to thickness intervals of 3.5 nm. Visual estimation suggests a value of $0.013\lambda_0$ for the thickness to the point of intersection. More accurate calculation gives $0.0133\lambda_0$, that is a thickness of 9.3 nm. The dielectric layer has an optical thickness of somewhere between an eighth-wave and a quarter-wave, and accurate calculation yields $0.186\lambda_0$.

The calculated performance of this coating is shown in Figure 15.25. Of course, the thickness of the metal film is rather small and it is unlikely that the values of optical constants measured on thicker films would apply without correction, but the form of the curve and the basic principles of the coating are as discussed here.

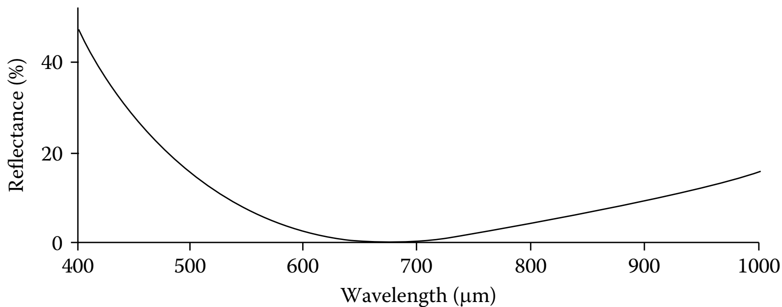

FIGURE 15.25
The calculated transmittance, including dispersion, of the gold electrode film and antireflection coating designed in the text.

15.6.2 Spectrally Selective Coatings for Photothermal Solar Energy Conversion

Coatings for application in the field of solar energy represent a complete subject in their own right. They have been discussed in detail by Hahn and Seraphin [29]. Here we consider simply a limited range of coatings based on antireflection coatings over metal layers that have much in common with the electrode film of the previous section.

Solar absorbers that operate at elevated temperatures can lose heat by radiation unless steps are taken to reduce their emittance in the infrared. Yet to operate efficiently they must have high solar absorptance in the visible and near infrared. Optimum results are obtained from an absorbing coating that exhibits a sharp transition from absorbing to reflecting at a wavelength in the near infrared that varies with the operating temperature of the absorber. One way of constructing such a coating is to start with a thick metal film or a metal substrate and apply an antireflection coating that is efficient over the visible but becomes ineffective in the infrared, so that at longer wavelengths the reflectance is high and the thermal emittance, as a result, is low. Fortunately. we are interested simply in a reduction of reflectance.

Transmittance is unimportant. The energy that is not absorbed in the coating is absorbed in the substrate. Thus, the antireflection coating can include absorbing layers.

A useful approach to the design is the use of a semiconducting layer over a metal. The semiconductor becomes transparent in the infrared beyond the intrinsic edge and so in that region the reflectance of the underlying metal predominates. In the visible and near infrared, the absorption in the semiconductor is sufficient to suppress the metallic reflectance, and to complete the design, it is sufficient to add an antireflection coating to reduce the reflectance of the front face of the semiconductor. Since the metal is to dominate the infrared performance, either the semiconductor layer must be relatively thin in the infrared or the metal must have sufficiently high k/n to be only slightly affected by the high index of the semiconductor in its transparent

region. From the point of view of optical constants, silver is therefore the most favorable metal but it suffers from a lack of stability at elevated temperatures that cause it to agglomerate so that its optical constants are shifted and its reflectance reduced. Seraphin and his colleagues (see [29] for a readily available summary and more detailed references) have developed coatings in which the silver is stabilized by layers of chromium oxide (Cr_2O_3), which act as diffusion inhibitors. The silicon films are produced by chemical vapor deposition in which the silicon-hydrogen bonds in silane gas flowing over the substrate are broken by elevated substrate temperature and, as a result, silicon deposits. Adding oxygen or nitrogen to the gas stream gives an antireflection coating of silicon oxide or nitride that can be graded in composition by continuous variation of gas-stream composition. Such coatings can withstand temperatures in excess of 600 °C without degradation.

The design of such coatings is straightforward. First, the thickness of silicon must be such that the visible absorption is sufficiently high to mask the underlying silver but not so thick that interference effects reduce reflectance and increase emittance in the infrared. In the visible region, the light that enters the silicon layer and is reflected from the silver at the rear surface should be sufficiently attenuated that only a very small proportion ever reemerges. We can assume that the attenuation of this light depends on a law of the form $\exp(-4\pi kd/\lambda)$ and for the entire round trip from front surface to rear of film and back again to the front surface we should have a value roughly in the range 0.01–0.05. Let us choose a design wavelength of 500 nm in the first instance at which silicon in thin-film form has optical constants of $4.3 - i0.74$ [28]. Then for $\exp(-4\pi kd/\lambda)$ to be 0.05, the value of d must be 160 nm. Since this is for the entire round trip, the film thickness should be half this value, or 80 nm. An antireflection coating must then be added to reduce the visible reflectance of the front surface of the silicon layer. Since we have reduced the interference effects to a low level, the front surface will be similar to bulk silicon with optical constants characteristic of the material. Seraphin and his colleagues used a graded-index film of silicon nitride and silicon dioxide, but for simplicity we assume here a homogeneous film of roughly 2.0 admittance and a quarter-wave thick at 500 nm. We can take zirconium dioxide with its characteristic admittance of 2.07 as an example. The performance of the complete coating is shown in Figure 15.26. The extra dip at 600 nm is a result of the thickness of the silicon. The silicon admittance locus spirals around, converging on the optical constants. At 600 nm, the spiral is somewhat shorter but the end point is passing through a region where the zirconium oxide layer can act as a reasonably efficient antireflection coating once again and so the dip appears. The silver begins to assert itself at around 700 nm in this design. We can shift the reflectance trough to a longer wavelength, say 750 nm, by carrying out a completely similar procedure but this time using $4.17 - i0.37$ for the optical constants. Now a double-pass reduction of 0.05 leads to a round-trip thickness of 480 nm, representing a film thickness of 240 nm. The performance is also shown in Figure 15.26.

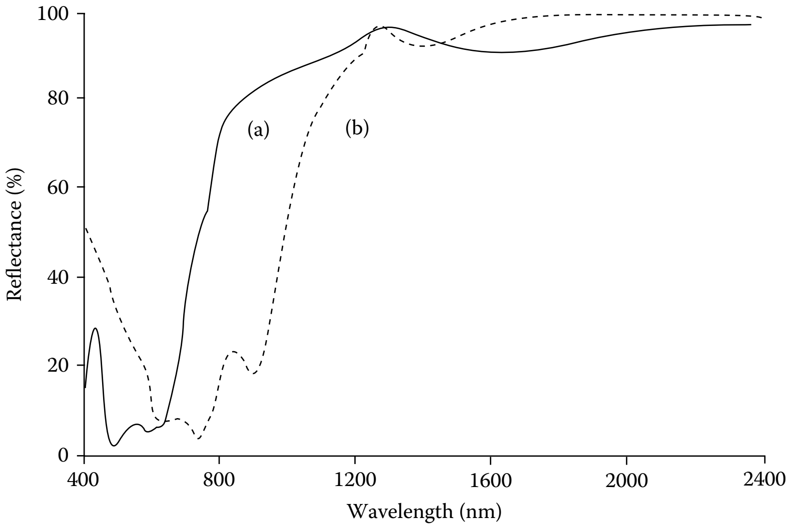

FIGURE 15.26
The calculated performance including dispersion of solar absorber coatings consisting of antireflected silicon over silver. Designs

	ZrO_2	Si	
(a)	$0.25\lambda_0$	80 nm	Ag $\lambda_0 = 500$ nm

	ZrO_2	Si	
(b)	$0.25\lambda_0$	240 nm	Ag $\lambda_0 = 750$ nm

Further details are given in the text.

In both traces, the optical constants of silicon and silver were derived from Hass and Hadley [28].

An alternative arrangement makes use of metal layers as part of an antireflection coating for silver. The great problem in designing an antireflection coating for a high-efficiency metal using entirely dielectric layers is that the admittance where the locus of the first dielectric layer, that is, the layer next to the metal, first cuts the real axis is far from the point (1,0) where we want to terminate the coating, and with each pair of subsequent quarter-waves we can modify that admittance by only $(n_H/n_L)^2$. Many quarter-waves are needed, as we have seen with the induced transmission filters. A metal layer, on the other hand, follows a different trajectory from a dielectric layer, cutting across dielectric loci, and can be used to bridge the gap between the large radius circle of the dielectric next to the metal and a dielectric locus that terminates at (1,0).

The metal locus itself can be arranged to pass through (1,0), but the extra dielectric layer is capable of giving a slightly broader characteristic and also some protection to the metal layer. Silver could be used as the matching

metal but its high k/n ratio leads to rather narrow spike-like characteristics even with the terminating dielectric layer, and a metal with rather greater losses is better. We use chromium here as an illustration with aluminum oxide as dielectric. These materials have figured in published coatings (see Hahn and Seraphin [29] for further details). We choose a wavelength of 500 nm for the design and the optical constants we assume for our materials are silver: 0.05 – i2.87; aluminum oxide: 1.67; and chromium; 2.86 – i4.11. Again the optical constants of the metals were obtained from Hass and Hadley [28] with interpolation if necessary. An admittance diagram of a coating of design:

$$\text{Air}\left|\begin{array}{c}\text{Al}_2\text{O}_3\\ 0.1841\lambda_0\end{array}\right|\begin{array}{c}\text{Cr}\\ 7.5\ \text{nm}\end{array}\left|\begin{array}{c}\text{Al}_2\text{O}_3\\ 0.184\lambda_0\end{array}\right|\text{Ag}\ (\lambda_0 = 500\ \text{nm})$$

is shown in Figure 15.27. The chromium locus bridges the gap between the two dielectric layers. Because of its rather lower k/n ratio than silver, its trajectory is flatter and the entire characteristic less sensitive to wavelength changes. The arrangement helps to keep the final end point of the coating in the vicinity of (1,0) as the loci increase or decrease in length with changing wavelength or g.

No attempt was made to refine this design, although, clearly, because of the wide range of possible thickness combinations that would lead to zero reflectance at the design wavelength, there must be scope for performance improvement by refinement. The characteristic of the coating is shown in Figure 15.28.

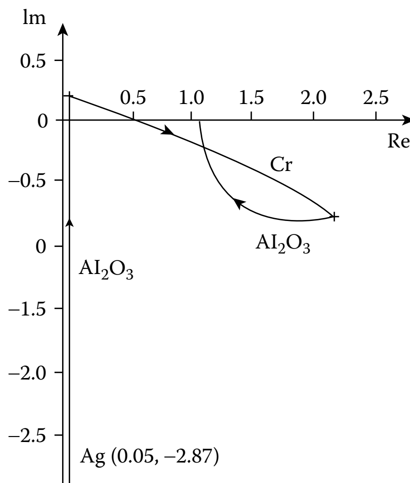

FIGURE 15.27
Admittance diagram at λ_0 of an absorber coating of design:

$$\text{Air}\left|\begin{array}{c}\text{Al}_2\text{O}_3\\ 0.184\lambda_0\end{array}\right|\begin{array}{c}\text{Cr}\\ 7.5\ \text{nm}\end{array}\left|\begin{array}{c}\text{Al}_2\text{O}_3\\ 0.184\lambda_0\end{array}\right|\text{Ag}\ (\lambda_0 = 500\ \text{nm})$$

See the text for an explanation.

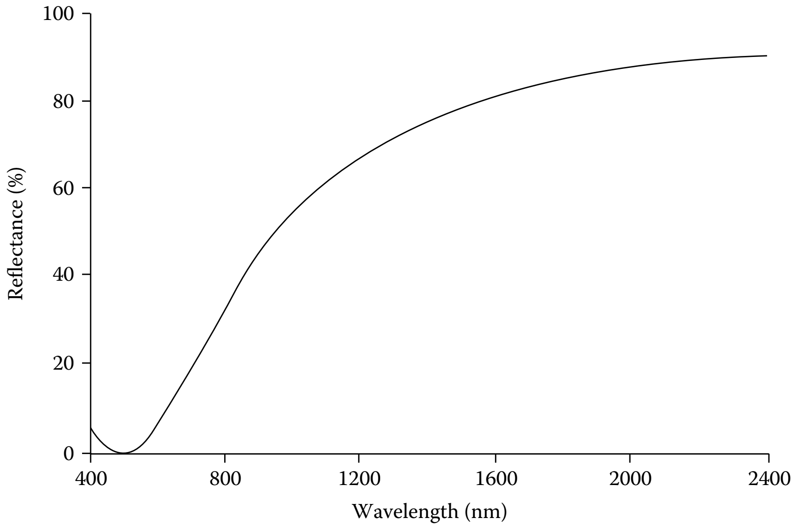

FIGURE 15.28
The calculated performance, including dispersion, of the absorber coating of Figure 15.27.

The reflectance minimum can be shifted to longer wavelengths by repeating the design process with appropriate values of the optical constants.

This gives the desired zero, but then at shorter wavelengths, where the dielectric loci are departing further and further from ideal and the chromium layer is unable to bridge the gap between them, a peak of high reflectance is obtained. At still shorter wavelengths, there is a second-order minimum where the dielectric layers make a complete revolution and are once again in the vicinity of the correct position. For the ideal values we have used in these calculations, the central peak of high reflectance is very high indeed. Practical coatings also show this double minimum (see Hahn and Seraphin [29]), but the central maximum is very much less prominent, the most likely explanation being that the layers in practice have much greater losses than we have assumed. In particular, the thin chromium layers are unlikely to have ideal optical constants. High losses would make the loci spiral in toward the center of the diagram and reduce the wavelength sensitivity.

The major problems associated with such coatings are not their design but the necessary high-temperature stability. Spectrally selective solar absorbers are only economically viable when they are used to produce high temperatures and, indeed, it is only at high temperatures that they offer an advantage over the more conventional spectrally flat black absorbing surfaces that can be produced very much more cheaply. They are used under vacuum to eliminate gas conduction heat losses, and so the major degradation mechanism is diffusion within the coatings. Silver is particularly prone to agglomerate at high temperatures, and much development effort has resulted in the incorporation of thin diffusion barriers such as chromium oxide that inhibit

diffusion and agglomeration of the components without affecting the optical properties. The achievements in terms of lifetime at high temperatures are impressive. Further details will be found in Hahn and Seraphin [29].

15.6.3 Heat Reflecting Metal–Dielectric Coatings

There are several applications where a cheap and simple heat-reflecting filter would be valuable. For example, a normal, spectrally flat solar absorber can be combined with such a filter so that the combination acts as a spectrally selective absorber. It is possible to construct a very simple band-pass filter that has the desired characteristics from a single metal layer surrounded by two dielectric matching layers [30–33]. The filter is similar in some respects to the induced transmission filter, although the maximum potential transmittance that is theoretically possible cannot usually be achieved. One design technique uses the admittance diagram and we can illustrate it with an example in which we consider a glass substrate and an incident medium of air or vacuum. Silver, with optical constants of $0.06 - i3.75$ at 600 nm can serve as metal and we assume a dielectric layer material of index 2.35. Zinc sulfide, which has such an index, has been used in this application, but the most durable and stable coatings are ones incorporating a refractory oxide. Figure 15.29 shows an admittance diagram in which one dielectric locus begins at the substrate and a second terminates at (1,0) corresponding to the incident medium. If the complete coating is to have zero reflectance then the remaining layers must bridge the gap between these two loci. Again, it is easy to see that a metal layer can do this and also that the particular optical constants of the metal are unimportant. They

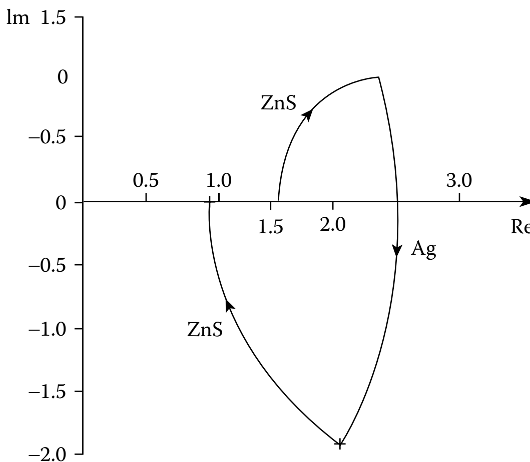

FIGURE 15.29
Admittance diagram of a metal–dielectric heat-reflecting filter. The diagram shows the locus at a wavelength of 600 nm of a ZnS | Ag | ZnS combination deposited on glass.

will simply alter somewhat the points of intersection with the two loci. The loci shown correspond approximately to the thickest silver film that will still give zero reflectance. To increase the silver thickness without sacrificing the zero reflectance requires that the indices of the two dielectric layers be increased. A small increase in thickness of metal without a gross alteration in the design could be achieved by the insertion of a low-index quarter-wave layer next to the substrate to move the starting point of the next high-index dielectric layer, the upper one in the admittance diagram, further along the real axis toward the origin. The new locus would be outside the existing one, demanding a thicker metal matching layer. In the absence of such a low-index layer, the final three-layer design is:

	ZnS	Ag	ZnS	Glass	
Air	2.35	$0.06 - i3.75$	2.35	1.52	$\lambda_0 = 600$ nm
	$0.146\lambda_0$	15 nm	$0.141\lambda_0$		

with performance shown in Figure 15.30. The steep fall toward the infrared is partly due to the drop in efficiency of the matching, but an inspection of the admittance diagram quickly reveals that the reduction in length of each locus accompanying an increase in wavelength should not by itself change the reflectance grossly. Metals, however, show large dispersion, the nature of which is a k that increases in step with λ into the infrared. This keeps the value of $(2\pi kd/\lambda)$ high, and that, together with the increasing k, lengthens the locus through the infrared, inducing a considerable increase in reflectance.

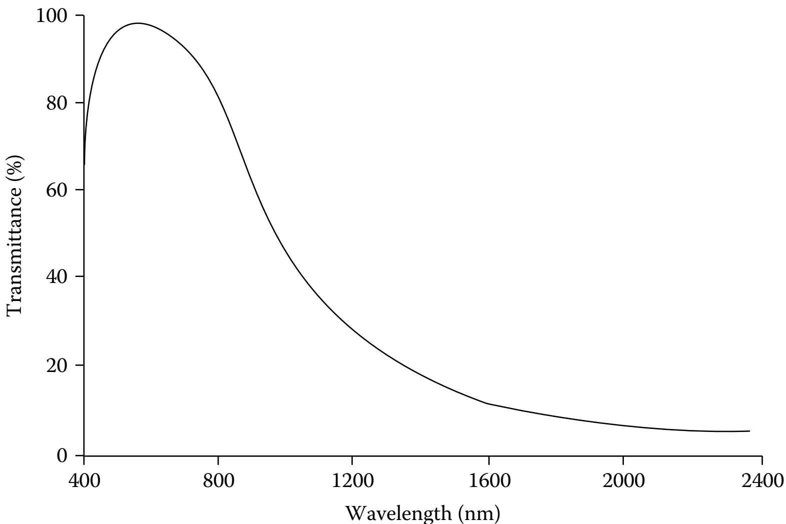

FIGURE 15.30
Transmittance, calculated with dispersion included, of the heat-reflecting coating of Figure 15.29. Details of the design are given in the text.

The coating could be based on virtually any metal with high infrared reflectance and high-index dielectric material. Gold and bismuth oxide have been successfully used [33].

Silver tends to oxidize if the coating is exposed to the air, and it is normal to surround it with thin diffusion barrier layers. These can be nickel, chromium, titanium, and so on, and it is likely that these protecting metals oxidize *in situ* so that they expand and the consequent high packing density makes them an effective barrier. These thin oxide layers have very little optical effect.

References

1. Matteucci J and Baumeister P W 1980 Integration of thin-film coatings into optical systems *Proceedings of the Society of Photo-Optical Instrumentation Engineers* **237** 478–485
2. Jacquinot P 1954 The luminosity of spectrometers with prisms, gratings or Fabry-Perot etalons *Journal of the Optical Society of America* **44** 761–765
3. Baum W A 1962 *Chapter 1: The detection and measurement of faint astronomical sources*, in *Stars and Stelar Systems* Hiltner W A Editor (Chicago: University of Chicago Press)
4. Bowen I S 1964 Telescopes *Astronomical Journal* **69** 816–825
5. Courtes G 1964 Interferometric studies of emission nebulosities *Astronomical Journal* **69** 325–333
6. Ring J 1956 *The Fabry-Perot interferometer in astronomy*, in *Astronomical Optics and Related Subjects* Kopal Z Editor (Amsterdam: North Holland) 381–388
7. Meaburn J 1967 A search for nebulosity in the high galactic latitude radion spurs *Zeitschrift für Astrophysik* **65** 93–104
8. Meaburn J 1976 *The detection and spectrometry of faint light* (Boston: D Reidel Pub Co)
9. Kaplan L D 1959 Inference of atmospheric structure from remote radiation measurements *Journal of the Optical Society of America* **49** 1004–1007
10. Houghton J T 1961 The meteorological significance of remote measurements of infra-red emission from atmospheric carbon dioxide *Quarterly Journal of the Royal Meteorological Society* **87** 102–104
11. Houghton J T 1963/4 Stratospheric temperature measurements from satellites *Journal of the British Interplanetary Society* **19** 381–385
12. Houghton J T and Shaw J H 1965 The deduction of stratospheric temperature from satellite observations of emission by the 15 micron CO_2 band *Memoires de la Société Royale des Sciences de Liège 5ième Serie* **9** 350–356
13. Smith S D 1961 Design of interference filters for the observation of infra-red emission from atmospheric carbon dioxide by an earth satellite *Quarterly Journal of the Royal Metereological Society* **87** 431–434
14. Smith S D and Pidgeon C R 1963 Application of multiple beam interferometric methods to the study of CO2 emission at 15 μm *Memoires de la Société Royale des Sciences de Liège 5th Series* **9** 336–349

15. Ellis P J, Peckham G, Smith S D, Houghton J T, Morgan C G, Rogers C D, and Williamson E J 1970 First results from the Selective Chopper Radiometer on Nimbus 4 *Nature* **228** 139–143
16. Houghton J T and Smith S D 1970 Remote sounding of atmospheric temperature from satellites. I. Introduction *Proceedings of the Royal Society of London, A* **320** 23–33
17. Abel P G, Ellis P J, Houghton J T, Peckham G, Rodgers C D, Smith S D, and Williamson E J 1970 Remote sounding of atmospheric temperature from satellites. II. The selective chopper radiometer for Nimbus D *Proceedings of the Royal Society of London, A* **320** 35–55
18. Alpert N L 1962 Infra-red filter grating spectrophotometers - design and properties *Applied Optics* **1** 437–442
19. Gibbons K P, Carniglia C K, Laird R E, Newcomb R, Wolfe J D, and Westra S W T 1997 *ITO coatings for display applications* in *40th Annual Technical Conference New Orleans* Society of Vacuum Coaters 216–220
20. Bjornard E J Viratec Thin Films 1992 *Electrically-conductive, light attenuating antireflection coating* US Patent 5,091,244
21. Wolfe J 1995 *Anti-static, anti-reflection coatings using various metal layers* in *38th Annual Technical Conference Chicago* Society of Vacuum Coaters 272–275
22. Oyama T and Katayama Y *Light absorptive antireflector* US Patent 5,691,044
23. Ishikawa H and Lippey B 1996 *Two layer broad band antireflection coating* in *Tenth International Conference on Vacuum Web Coating Fort Lauderdale, Florida* Bakish Materials Corporation, POB 148, Englewood, NJ 07631, USA 221–233
24. Zheng Y, Kikuchi K, Yamasaki M, Sonoi K, and Uehara K 1997 Two-layer wideband antireflection coating with an absorbing layer *Applied Optics* **36** 6335–6339
25. Hovel H J 1976 Transparency of thin metal films on semiconductor substrates *Journal of Applied Physics* **47** 4968–4970
26. Yeh Y C M, Ernest F P, and Stirn R J 1976 Practical antireflection coating for metal-semiconductor solar cells *Journal of Applied Physics* **47** 4107–4112
27. Schneider M V 1966 Schottky barrier photodiodes with antireflection coating *Bell System Technical Journal* **45** 1611–1638
28. Hass G and Hadley L 1972 *Optical constants of metals*, in *American Institute of Physics Handbook* Gray D E Editor (New York and London: McGraw Hill Book Company) 6.124–6.156
29. Hahn R E and Seraphin B O 1978 Spectrally selective surfaces for photothermal solar energy conversion *Physics of Thin Films* **10** 1–69
30. Fan J C C and Bachner F J 1976 Transparent heat mirrors for solar energy applications *Applied Optics* **15** 1012–1017
31. Fan J C C, Bachner F J, Foley G H, and Zavracky P M 1974 Transparent heat-mirror films of TiO2/Ag/TiO2 for solar energy collection and radiation insulation *Applied Physics Letters* **25** 693–695
32. Bhargava B, Bhattacharya R, and Shah V V 1977 A broad band (visible) heat reflecting mirror *Thin Solid Films* **40** L9–L11
33. Holland L and Siddall G 1958 Heat-reflecting windows using gold and bismuth oxide films *British Journal of Applied Physics* **9** 359–361

16

Other Topics

16.1 Rugate Filters

The term *rugate* is derived from biology where the meaning is essentially that of corrugated. It was introduced to describe a structure exhibiting a regular cyclic variation of refractive index resembling a sine or cosine wave. Such structures have the property of reflecting a narrow spectral region and transmitting all others. They exhibit properties similar to a quarter-wave stack but without the higher-order reflection bands. Thus, they are notch filters and particularly useful in removing bright spectral lines from weaker continua. Many of their applications involve laser sources, and they are especially relevant in the field of laser protection. This strict original definition of rugate has been relaxed somewhat, so that the term is also sometimes used for any layer system in which there is a deliberate attempt to induce an inhomogeneity whether or not it is of a cyclic kind.

We begin with the strict original meaning of rugate. It can easily be shown that all the beams emerging from the front surface of a multilayer constructed from a series of quarter-wave layers of alternate high and low index are exactly in phase. This leads to high reflectance but is limited in width in terms of wavelength or frequency because the constructive interference condition applies only to the wavelength for which the layers are exact quarter-waves. Outside the zone of high reflectance, it is the transmittance that is high. The quarter-wave stack, therefore, acts as a notch filter. The lower the ratio of the high to low refractive index at the interfaces, the lower will be the amplitude reflection coefficients and the greater the number of beams required to achieve a given reflectance. The rate at which the interference condition decays with change in wavelength determines the width of the high reflectance zone. Smaller index contrast implies more beams, faster decay of the constructive interference, and hence, narrower reflectance zones. A narrow zone of high reflectance in turn implies a large number of layers of low index contrast. All this is considered in greater detail in Chapters 5 and 6.

A limitation of systems made up of discrete dielectric layers is that a change in wavelength does not change the amplitude of the beams, except for slight changes due to dispersion. The same beams with the same amplitudes exist

over a wide spectral region. It is impossible to distinguish between the interference effect between two beams with phase difference φ and two beams of exactly the same amplitude and phase difference $\varphi \pm 2m\pi$ where m is an integer. In the case of the quarterwave stack, the interference condition that exists at wavelength λ_0 also exists at wavelengths $\lambda_0/3$, $\lambda_0/5$, $\lambda_0/7$, and so on, leading to the higher order reflectance zones that limit its usefulness as a notch filter. A typical characteristic curve plotted in terms of g, that is λ_0/λ, is shown in Figure 16.1.

The higher orders may not present any problem in certain applications, and for these the discrete layer design will be quite satisfactory. For those others where the peaks are a problem, we do need to suppress them. They have their origins in the interference between beams reflected at all the interfaces. In other words, their origin is distributed throughout the multilayer. We need, therefore, a distributed solution. We need to retain the beams at the fundamental peak at $g = 1.0$, but we must remove them at all other integral values of g. An antireflection coating that does not affect the performance at $g = 1$, but that operates at values of g greater than unity, is required for each interface. An inhomogeneous layer is such an antireflection coating.

We shall return shortly to the derivation of performance of such systems. For the moment, let us accept the two possible profiles for inhomogeneous layers shown in Figure 16.2. If we assume that the layers have an optical thickness of one-quarter wavelength at $g = 1.0$, then the performances in terms of reflectance against g are those shown in Figure 16.3.

This antireflection coating must now be inserted at each interface in the discrete layer coating. Figure 16.4 shows the resulting profile of optical admittance. The coating now has a sinusoidal variation of index throughout and is known as a rugate structure because of the smooth cyclic variation.

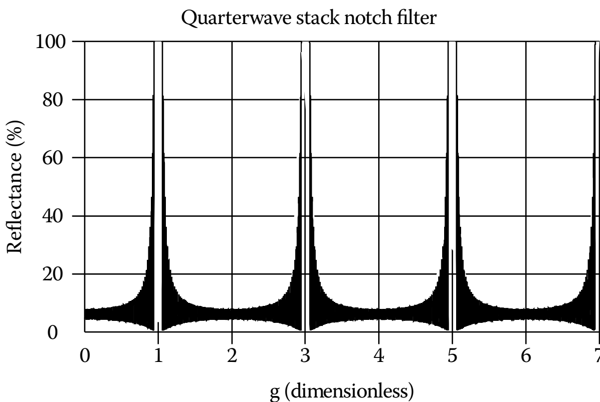

FIGURE 16.1
A typical characteristic of a quarter-wave stack used as a notch filter showing the higher orders at g of 3, 5, and 7. The fringes in the pass regions are so tightly packed they cannot be distinguished.

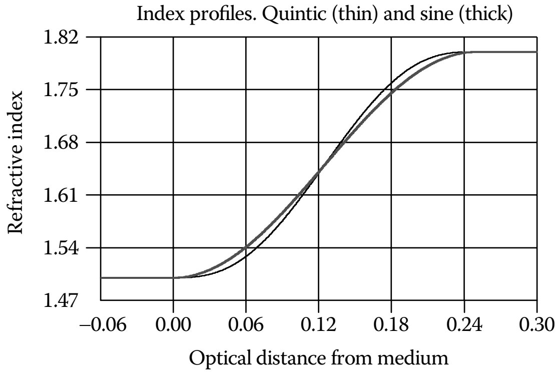

FIGURE 16.2
Inhomogeneous layer profiles rising from 1.50 to 1.80. The layers are one quarter of a wavelength in optical thickness and the profile of refractive index follows a sine law (shallower curve, *thick line*) or a fifth-order polynomial (steeper curve, *thick line*) with zero first and second derivatives with respect to thickness at the end points.

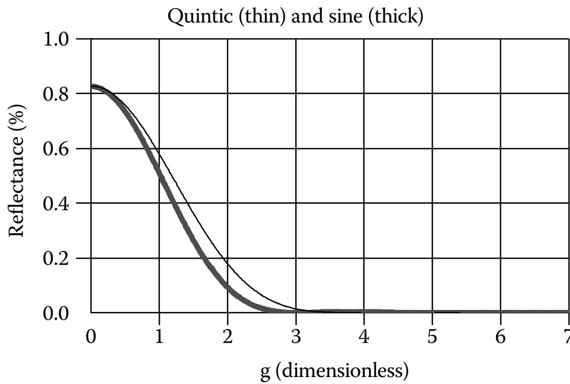

FIGURE 16.3
Reflectance against g for the inhomogeneous layers shown in Figure 16.2. The sine law variation is less steep than the fifth-order polynomial so the curve of reflectance (left curve, *thick line*) drops faster but the fifth-order polynomial (right curve, *thin line*) gives lower reflectance at greater values of g.

The inhomogeneous antireflection coating is a very robust one from the point of view of errors. There is an insensitivity to the actual profile of index. As long as the thickness at a given wavelength is greater than roughly a half-wave, then the reflectance at that wavelength should be very low. Thus, even quite large errors in the profile of a rugate filter are not normally serious unless they are systematic and lead to a change in the pitch of the cycle. Such errors tend to broaden the fundamental peak. Quite severe errors are required before the higher order peaks begin to return. This has useful implications for the manufacturing of such filters.

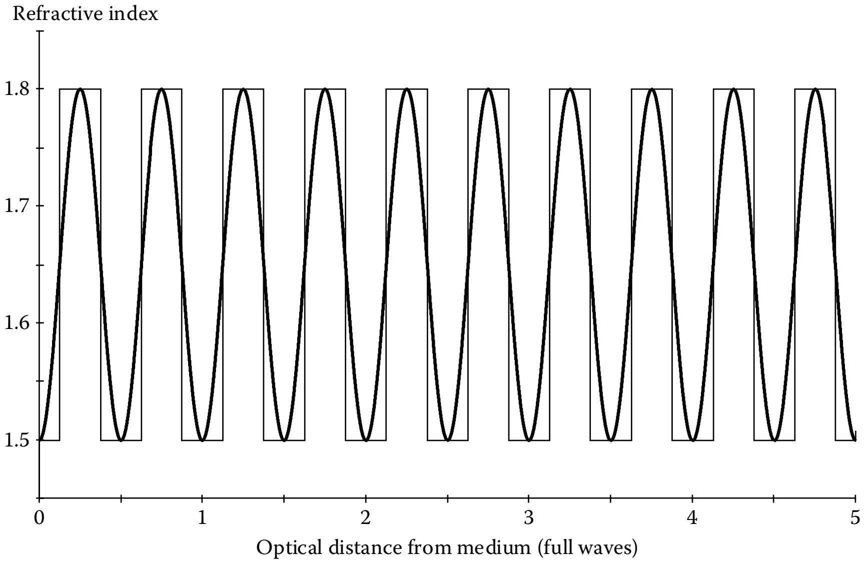

FIGURE 16.4
The result of replacing each discrete interface (square plot, thin line) by one graded to have a sine profile (rounded plot, thick line). This gives the rugate structure. The new variation of reflectance is shown in Figure 16.5. Note the small residual peak at $g = 2.0$. This is due to the failure of the sinusoidal variation of refractive index to act completely like the absentee half-wave layers of the discrete design. The slight residual reflectance change accumulates in a coating with a large number of layers and gives the slight perturbation from the regular fringe pattern that appears elsewhere. Southwell [1] has pointed out that an inhomogeneous layer based on an exponential sine does act as an absentee layer at even values of g even though its profile is almost indistinguishable from that of a sine function.

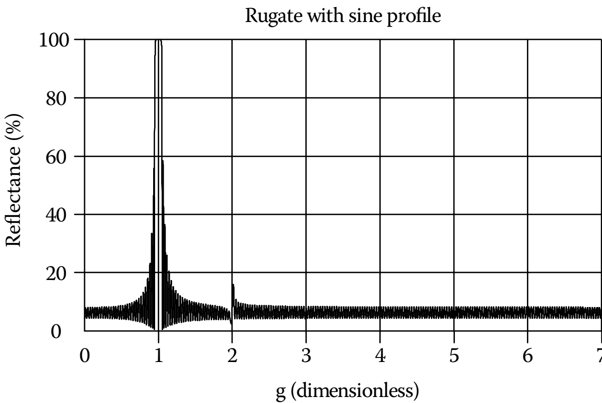

FIGURE 16.5
The reflectance curve of the rugate filter. The variation of index is shown in Figure 16.4 except that the filter actually calculated had the equivalent of 64 discrete layers.

The control of the deposition of rugate filters is a rather more involved task than for a simple discrete layer quarter-wave stack. In discrete layer deposition, it is optical thickness that has always been the object of the closed loop control system. Refractive index has been considered to be characteristic of the particular material being deposited and so the control of that aspect of the layers has been open loop. The deposition methods have concentrated on the control of source temperature, rate of deposition and so on. The rugate filter represents a greater challenge because there is no natural material that yields the desired profile of refractive index. It must be engineered. Compositional changes are necessary and, in the true rugate filter these changes should be smooth. This tends to imply some form of active index control.

The absence of the need for direct index control, however, makes discrete layers very attractive. Although they are not strictly true rugates, nevertheless it is possible to create discrete layer structures that have, up to a point, similar properties. To replace a rugate structure by a discrete layer structure, we can imagine slicing a rugate period into a large number of thin layers of equal optical thickness. Each thin slice has an inhomogeneous index profile, but we can convert it into a homogeneous index that has simply the central value. This gives a staircase profile of index. In fact, and we return to this point later in this section, the calculation of the properties of rugate filters with arbitrary profile is normally carried out in this way with the thicknesses chosen to be so thin that further subdivision makes no changes to the results. Here we use rather thicker slices.

Figure 16.6 shows the profile of a rugate filter that has been converted in this way. The steps are arranged so that in each rugate cycle there are 10 of them. This means that at the reflectance peak where the rugate cycle is one half-wave thick, the individual discrete layers are just one twentieth of a wave thick. As long as the individual layers are thin compared with a quarter-wave, then the discrete version works well. However, as the wavelength reduces, the phase

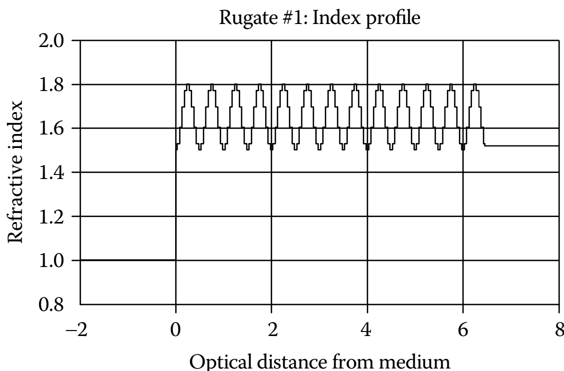

FIGURE 16.6
The profile of a rugate filter with a cycle consisting of ten discrete layers rather than a continuously varying profile.

thickness of the individual layers increases and eventually becomes much thicker compared with a wavelength. However, the behavior of the system does not just simply deteriorate but is quite regular and understandable. At a value of g of zero, the layers are effectively of zero phase thickness and so the reflectance of the system is that of the uncoated substrate. At $g = 1.0$, the rugate cycle is now a half-wave and the reflectance is high. As g increases, the cycle, at first, retains its antireflecting properties and the higher-order peaks are suppressed. Now let us jump to the case where g is large enough for the layers to be of half-wave thickness. Here we have absentee layers and the reflectance is that of the uncoated substrate. At this value of g, we still have exactly the same beams taking part in the interference as at all other values of g. The phase shifts between them, however, are exactly the same as at $g = 0$ except that, in every case, there is an additional path difference of a wavelength, that is 360°, which is indistinguishable from zero. Furthermore, as we now reduce g from this value, we find exactly the same interference pattern as a function of the reduction in g that we find as a function of the increase in g from zero in the normal way. Thus, if we have 10 equal steps or discrete layers making up the rugate cycle with a fundamental peak at $g = 1$, then there will be a similar peak at $g = 9$. A cycle made up of four layers will have a further peak at $g = 3$ and so on. Figure 16.7 illustrates this for the rugate of Figure 16.6. Figure 16.8 shows similar performance for a rugate with a four-layer cycle. In this case the harmonics begin at $g = 3$ and so the sole peak that is eliminated is at $g = 2$. This may not appear to be any different from a two-layer cycle but, in fact, the extra layers help to suppress the half-wave-hole peak that appears at $g = 2$ when the coating based on the two-layer cycle is tilted.

Southwell [1] has indicated that the slight lack of symmetry in the result in Figure 16.7 is a consequence of the use of a set of sublayers of identical

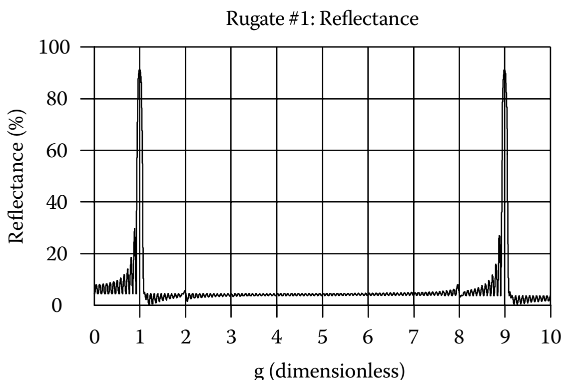

FIGURE 16.7
The performance of the rugate of Figure 16.6 as a function of g showing the harmonic peak at $g = 9.0$. Note the subtle differences in the low reflectance performance from $g = 0$ to $g = 2$ and from $g = 8$ to $g = 10$. This is due [1] to the use in Figure 16.6 of a half-cycle that is the mirror image of the alternate half cycle only if the outer layers are half the thickness of the others.

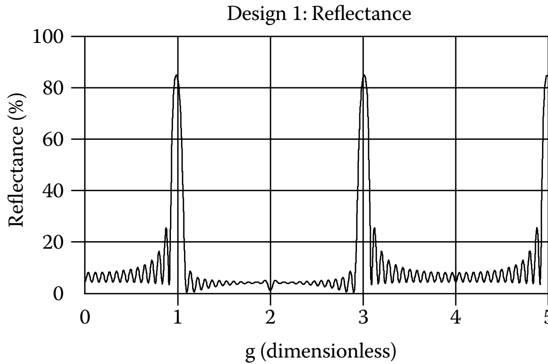

FIGURE 16.8
The performance of a rugate similar to that of Figure 16.6 except that the cycle is made up of four discrete layers of equal thickness. The harmonic peak appears now at $g = 3.0$.

thickness such that there are no two adjacent sublayers with the same index. This effectively makes the rugate period symmetrical only if the two outermost layers are considered to be half the thickness of the others. A rearrangement where the outermost sublayers have the same index and the full sublayer thickness, implying a merging of the innermost layer pair and the ending layer of each cycle with the starting of the next, gives a perfectly symmetrical performance.

An alternative technique for the replacement of the continuous variation with a series of discrete layers uses two materials with fixed indices of refraction. One of the indices must be equal to or less than the lowest in the rugate structure and the other equal to or greater than the highest. The method uses the properties of the characteristic matrices of the films. There are two variants. The first uses the result that the matrix of any symmetrical arrangement of layers, absorbing and inhomogeneous layers included, can be replaced by the characteristic matrix of a single equivalent homogeneous layer [2,3]. This equivalence is dealt with more fully in Chapter 4 and is a purely analytical relationship and certainly not physical, but it is valid wherever the properties involve only the characteristic matrices. This relationship can be reversed, so that the homogeneous film matrix can be replaced by the matrix of a symmetrical combination of layers. Since the eventual result involves identical matrices, properties such as reflectance and transmittance at one particular angle of incidence and wavelength are unchanged when the equivalent sequences are interchanged. One of the most useful aspects of this relationship is the replacement of a layer of intermediate index by a symmetrical combination of layers of given high and low index. At one angle of incidence and one wavelength, this equivalence holds completely for any property that can be calculated using the characteristic matrices. For the equivalence to be retained exactly with changes in wavelength demands a particular dispersion of the indices of the replacement layers. This implies that when real layers are involved

with their natural dispersion the equivalence becomes gradually poorer as the wavelength changes, especially as the wavelength decreases.

The equivalence strictly does not extend to changes in angle of incidence although the deterioration is not usually very rapid. The second variant uses an approximate method based on pairs of layers. When both members of a layer pair are thin compared with a wavelength, then the characteristic matrix of the combination of the two layers is equivalent to that of a single layer of intermediate index [4]. Again, this relationship is not valid for changes in angle of incidence and it becomes poorer as the wavelength decreases. Both variants can take the staircase approximation to the rugate cycle and convert it into an equivalent series of alternate high- and low-index layers of differing thicknesses. We illustrate the method by using the second variant, the two-layer approximation. The product of two thin-film matrices can be considerably simplified if the layers are thin compared with the wavelength. Following Southwell [4], let a layer be dielectric and of physical thickness d, refractive index n, and admittance $y = n$ free space units:

$$\begin{bmatrix} \cos\delta & \dfrac{i\sin\delta}{y} \\ iy\sin\delta & \cos\delta \end{bmatrix} \rightarrow \begin{bmatrix} 1 & i\dfrac{2\pi}{\lambda}d \\ i\dfrac{2\pi}{\lambda}n^2 d & 1 \end{bmatrix} \tag{16.1}$$

Then, the product of two thin film matrices becomes:

$$\begin{bmatrix} \cos\delta_1 & \dfrac{i\sin\delta_1}{y_1} \\ iy_1\sin\delta_1 & \cos\delta_1 \end{bmatrix}\begin{bmatrix} \cos\delta_2 & \dfrac{i\sin\delta_2}{y_2} \\ iy_2\sin\delta_2 & \cos\delta_2 \end{bmatrix} \rightarrow \begin{bmatrix} 1 & i\dfrac{2\pi}{\lambda}d_1 \\ i\dfrac{2\pi}{\lambda}n_1^2 d_1 & 1 \end{bmatrix}$$
$$\begin{bmatrix} 1 & i\dfrac{2\pi}{\lambda}d_2 \\ i\dfrac{2\pi}{\lambda}n_2^2 d_2 & 1 \end{bmatrix} = \begin{bmatrix} 1 & i\dfrac{2\pi}{\lambda}(d_1+d_2) \\ i\dfrac{2\pi}{\lambda}(n_1^2 d_1 + n_2^2 d_2) & 1 \end{bmatrix} \tag{16.2}$$

where we are neglecting terms in $d_1 d_2$. Then, comparing Expression 16.2 with Expression 16.1, we find

$$d = d_1 + d_2$$
$$n^2 = \frac{n_1^2 d_1 + n_2^2 d_2}{d_1 + d_2}$$

Now, knowing n_1 and n_2 and specifying n and d, the equivalent parameters of the two-layer combination we have for d_1 and d_2:

$$d_1 = \left(\frac{n^2 - n_2^2}{n_1^2 - n_2^2} \right) d$$
$$d_2 = d - d_1 \tag{16.3}$$

Note that the total physical thickness remains constant so that the total physical thickness of the rugate to be replaced is preserved. The order, too, of the layers is unimportant. Interchanging the two layers makes no difference to the equivalent parameters of the combination. The important consideration is that n must lie between n_1 and n_2; otherwise negative thicknesses would result.

Figure 16.9 shows a single cycle that has been replaced in this way. (There is an extra layer at the end that is strictly the first layer of a following cycle.) The performance of a rugate filter based on 14 of these cycles in series is shown in Figure 16.10.

The important point about these calculations is that a discrete layer approximation to a rugate filter can give performance that is nevertheless acceptable. The range of transparency of the materials is rarely greater than the clear ranges shown in Figure 16.7 and Figure 16.9. Many of the techniques for coating production lend themselves much better to the construction of discrete layer systems than to the creation of smoothly varying index profiles.

We now turn to the broader meaning of rugate as presenting any continuous variation of index, and consider the theoretical problems in more

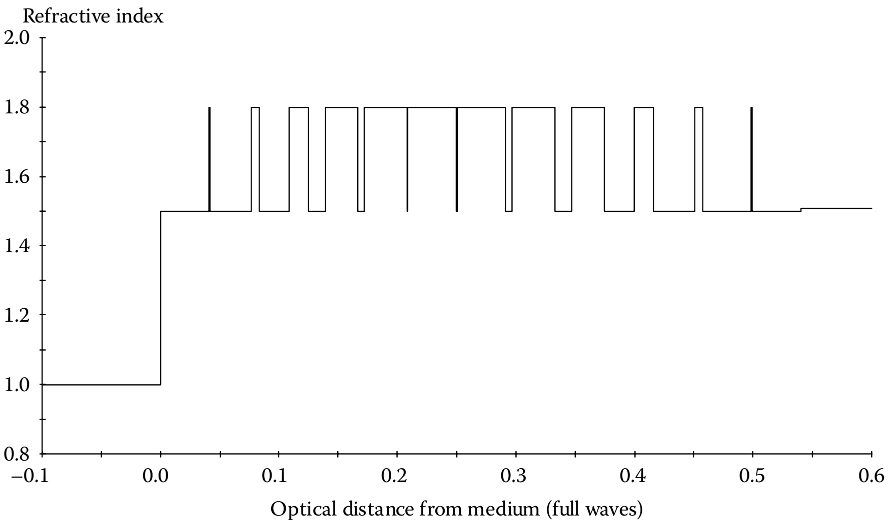

FIGURE 16.9
A 22-layer representation of a single half-wave rugate cycle. The layers are either of high (1.8) index or low (1.5) and their thicknesses are varied so that the overall effect is similar to the smooth variation of the classic rugate.

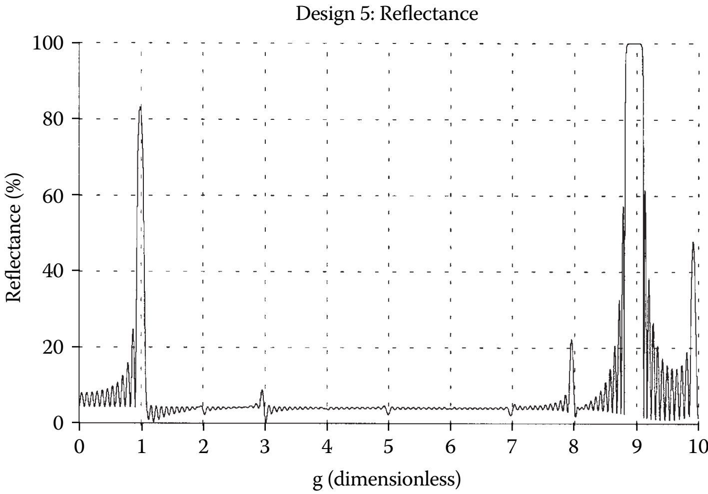

FIGURE 16.10
The performance of the rugate of Figure 16.9. The performance has characteristics similar to those of the stepped version from which it was derived.

detail. Figure 16.11 shows a representation of an inhomogeneous layer that is linking two media. The optical admittance, y, is plotted against the optical thickness, z. Accurate calculation of such layers involves the slicing of them into sufficiently thin homogeneous sublayers and then using the normal calculation techniques. The slices should be rather thinner than a quarter-wave at the shortest wavelength in the calculation. It is rarely necessary to use less than one-tenth of a wave. To test the adequacy of the approximation, the layers can be made still thinner and the calculation repeated. A completely unchanged performance is an indication that the approximation is satisfactory. For the design of such structures, it is usual to use an approximate technique based on what is essentially an application of the vector method. If the performance is to be calculated at the plane

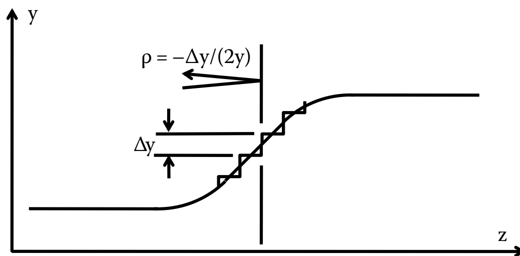

FIGURE 16.11
To derive an expression for the performance of a dielectric inhomogeneous layer, we first divide the layer into a series of separate steps. These steps are chosen close enough so that closer spacing still yields an unchanged result. Each step has an amplitude reflection coefficient of $-\Delta y/(2y)$.

denoted by $z = 0$, then the vector that is derived from the step at the plane z will be given by

$$\rho \exp(-i2\delta) = \frac{\Delta y}{2y} \exp(-i2\kappa z)$$

where κ, the wave number, is given by $2\pi/\lambda$, λ being the free space wavelength. If we represent twice the optical thickness, z, by x, then we can write the sum of all the various vectors as

$$\sum \frac{\Delta y}{2y} \exp(-i\kappa x) \tag{16.4}$$

In the simple vector method, this sum is simply equal to the amplitude reflection coefficient. However, when many such vectors are involved with a quite thick inhomogeneous structure, a correction may be made that represents a better approximation. The conversion of the sum of Expression 16.4 to an integral then yields

$$\int_{-\infty}^{\infty} \frac{dy}{dx} \cdot \frac{1}{2y} \cdot \exp(-i\kappa x) \cdot dx = Q(\kappa) \cdot \exp[i\varphi(\kappa)] \tag{16.5}$$

connecting a function of performance with a function of the distribution of characteristic admittance through a Fourier integral expression. This may be inverted so that the distribution of y may be calculated from the distribution of performance. Q is a function of performance, $\kappa = 2\pi/\lambda$ and x is twice the optical path. $\varphi(\kappa)$ is a phase factor that must be an odd function to ensure that $n(\kappa)$ is real. Although multiple beam effects are neglected, a judicious choice of Q can reduce the errors that arise from this approximation. Note that the Equation 16.5 is frequently written with a positive argument for the exponential. This is simply a consequence of the particular sign convention that is used.

Functions that have been proposed and used for Q include (the first represents the simple amplitude reflection coefficient):

$$\begin{aligned} Q &= \sqrt{R} \\ Q &= \sqrt{\frac{R}{T}} \\ Q &= \sqrt{\frac{1}{2}\left(\frac{1}{T} - T\right)} \\ Q &= \sqrt{\frac{1}{\sqrt{T}} - \sqrt{T}} \end{aligned} \tag{16.6}$$

For a more complete and detailed treatment, see Bovard [5].

The great advantage of this approach is the analytical connection in either direction of a function of design with a function of performance. If we know the performance we can find a design and vice versa. Disadvantages are that the technique is approximate and considerable skill and experience are required in the choice of the appropriate Q function and phase factor φ. Although the resulting design is a continuously varying admittance profile, it can be converted into a discrete-layer design, the thicknesses being chosen thin enough not to affect performance at the shortest wavelength of interest.

16.2 Ultrafast Coatings

Traditionally, coating designers have been able to rely on the steady-state nature of the effects they seek to produce. There are now laser systems, known as ultrafast, capable of generating pulses of light that are short enough for transient response to become significant. A normal high reflector consisting of a quarter-wave stack might be some 25 quarter-waves in thickness. At a wavelength of 1 μm, this implies a trip length for light traveling from the front to the rear of the coating and back again of 12.5 μm or a trip time of around 42 fs. (One femtosecond is 1/1000th picoseconds.) Pulses that are around 50 fs in length are now common and the shortest current pulses are some 5 fs in length. It is clear that transient response of coatings must now be considered important in such applications, but the effects, in fact, can be significant even with pulses some two or three orders of magnitude longer. The idea that coating properties should have an influence on short pulses and that they might be engineered to have prescribed effects is not new. It is, however, only recently that the field has expanded and the technology advanced to the stage where the application is becoming of major importance.

A short pulse can be thought of as an envelope over a carrier. The carrier contains the phase information associated with the pulse and it travels at what is known as the *phase velocity*. The energy is obviously associated with the envelope that travels at what is known as the *group velocity*. In the presence of dispersion, the group velocity and the phase velocity are different, with normal dispersion making the phase velocity greater. Thus, the carrier appears to run through the pulse envelope. A short pulse with Gaussian envelope is shown in Figure 16.12.

The pulse may also be visualized in a different way, as a collection of monochromatic component waves with a continuous distribution of frequencies over a given band. The coherent combination of these monochromatic waves yields the envelope and carrier of the alternative model. Both of the models are entirely equivalent, and if we wish, we can pass from one to the other by way of a Fourier transform.

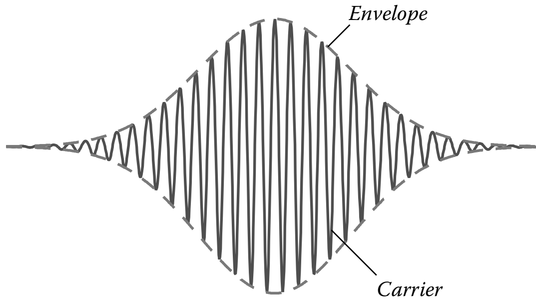

FIGURE 16.12
A short Gaussian-shaped pulse consisting of an envelope over a carrier of constant frequency. The carrier phase may move faster than the pulse when it will appear to run through the envelope as it travels.

Pulse envelopes frequently have a Gaussian shape [6,7]. For simplicity, we can look at the temporal variation at the origin of our coordinates, $z = 0$, and then, if the peak of the pulse corresponds to $t = 0$,

$$F(t) = \mathcal{A}e^{-\frac{t^2}{2\mu^2}} \tag{16.7}$$

where μ has the dimension of time. The Fourier transform gives the frequency distribution and it is also a Gaussian function,

$$G(\omega) = \mathcal{B}e^{-\frac{\mu^2(\omega-\omega_0)^2}{2}} \tag{16.8}$$

If the time between the half-maximum points is τ and the width of the pulse (angular) frequency distribution also at half-maximum is $\Delta\omega$, then

$$\tau \cdot \Delta\omega = 4 \cdot \log_e 2$$

Note that both these quantities are functions of μ. For example,

$$\tau = 2\sqrt{\log_e 2} \cdot \mu$$

The center of the pulse is the point where all of the component waves are exactly of identical phase. If all the component waves travel at the speed of light *in vacuo*, then the phase coincidence will also travel at that speed and the center of the pulse will move with it. Similarly, if all waves slow down equally, then the pulse will slow down to the same extent but will otherwise be unchanged.

The relative phase of the carrier within the pulse is set by the value of phase where all the component waves coincide. If the phase of the waves is zero, then the carrier will have a peak exactly at the peak of the pulse. We can find the position of the pulse peak at any time by a simple procedure.

The pulse can be considered to be made up of monochromatic component waves. As these propagate, the phase relationships between them will change, but if the pulse shape is unaltered as it propagates, then at any particular time there must be a distance along the path where the phase is identical for all the component waves, and this must correspond to the pulse center. We use the normal thin film convention of $(\omega t - \kappa z)$ in the phase factor where $\kappa = 2\pi n/\lambda$ with λ the free space wavelength. We write the component wave phase at distance z and time t as $\varphi = \varphi_0 + \Delta\varphi$. Then for coincidence of all component phases, $\Delta\varphi$ must be zero.

This condition is

$$
\begin{aligned}
(\omega_0 + \Delta\omega)t - (\kappa_0 + \Delta\kappa)z &= \varphi_0 + \Delta\varphi \\
\omega_0 t - \kappa_0 z &= \varphi_0 \\
\Delta\varphi = 0 &= \Delta\omega t - \Delta\kappa z \\
z &= \frac{\Delta\omega}{\Delta\kappa} t = v_g t
\end{aligned}
\tag{16.9}
$$

The quantity $\Delta\omega/\Delta\kappa$ is known as the group velocity, v_g, and clearly it must remain constant if the position z is to be the same for all the component waves and the shape of the pulse unchanged.

An alternative visualization involves a simple diagram. We plot the z-direction horizontally and ω vertically. We sketch the bundle of component waves making up the pulse, as a set of lines through the appropriate values of ω and parallel to the z-axis. We mark contours of constant φ on the lines. Provided there is one contour that runs normally across the lines, so that

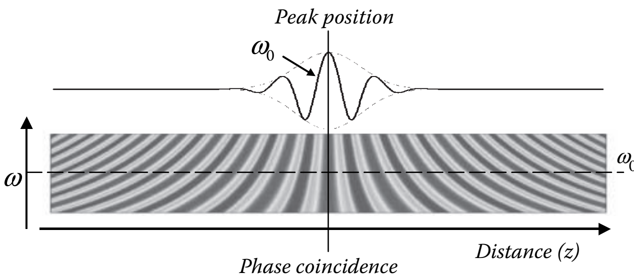

FIGURE 16.13
Sketch showing the component waves of the pulse as a continuous distribution of horizontal lines along the direction of propagation and with their relative phases marked as contours across them. The pulse peak coincides with the position where the phase of all the components is exactly equal.

there is an exact phase coincidence, then the pulse peak will be positioned there and the pulse shape will be unchanged.

In a nondispersive medium, the phase at the peak will be zero because all the component waves will be traveling at an identical velocity even though it may be less than the velocity in free space. In a dispersive medium, the component waves travel at different velocities according to the particular value of refractive index. Provided the variation in velocities still permits a phase coincidence somewhere, then the pulse will appear there and will be unchanged in shape although the phase of the carrier wave will be altered. It is clear from Equation 16.9 that the critical condition is for the group velocity to remain constant across the frequency spectrum of the pulse.

In a dispersive medium, the refractive index changes with frequency. We can calculate the group velocity in terms of this change.

$$\kappa = \frac{2\pi n(\omega)}{\lambda} = \frac{\omega n(\omega)}{c}$$

$$\frac{d\kappa}{d\omega} = \frac{n(\omega)}{c} + \frac{\omega}{c} \cdot \frac{dn(\omega)}{d\omega}$$

$$v_g = \frac{c}{n(\omega) + \omega \cdot \dfrac{dn(\omega)}{d\omega}} \tag{16.10}$$

In a medium with normal dispersion, this is not constant.

There is thus no guarantee that the group velocity should be constant with changing frequency. If the second derivative of κ with respect to ω is nonzero, then there can be no phase coincidence and the pulse will be perturbed. Again, we can consider the operation in two different equivalent ways. If we limit ourselves to the second derivative, then we can write the expression for the phase of an arbitrary component wave as:

$$(\omega_0 + \Delta\omega) \cdot t - \left(\kappa_0 + \Delta\omega \cdot \left.\frac{d\kappa}{d\omega}\right|_0 + \frac{1}{2}(\Delta\omega)^2 \cdot \left.\frac{d^2\kappa}{d\omega^2}\right|_0 \right) \cdot z = \varphi + \Delta\varphi \tag{16.11}$$

and we can immediately identify a problem. The third term in the coefficient of z is even in $\Delta\omega$ and so cannot be compensated by the other terms. We must therefore split the frequency distribution of the pulse into two parts, one with positive $\Delta\omega$ and the other with negative $\Delta\omega$, and look at each separately. In each case, we ensure that the value of $\Delta\varphi$ is zero. This gives two equations instead of the usual one. We keep the value of z the same in each and introduce a different time t representing the interval in time between the pulse centers that correspond to each part of the split distribution. If the spectral width of the split distribution were halved, then each component

pulse would have twice the basic pulse width. As a crude correction for this effect, therefore, we treat the $\Delta\omega$ in the following expressions as the width of the frequency distribution of the basic initial pulse.

$$\Delta\omega \cdot t_1 - \Delta\omega \cdot \left.\frac{d\kappa}{d\omega}\right|_0 \cdot z - \frac{1}{2}(\Delta\omega)^2 \cdot \left.\frac{d^2\kappa}{d\omega^2}\right|_0 \cdot z = 0$$

$$-\Delta\omega \cdot t_2 + \Delta\omega \cdot \left.\frac{d\kappa}{d\omega}\right|_0 \cdot z - \frac{1}{2}(\Delta\omega)^2 \cdot \left.\frac{d^2\kappa}{d\omega^2}\right|_0 \cdot z = 0$$

Then, since

$$\frac{d}{d\omega}\left(\frac{d\kappa}{d\omega}\right) = -\frac{1}{v_g^2} \cdot \frac{d}{d\omega}(v_g)$$

$$\Delta t = (t_1 - t_2) = -\Delta\omega \cdot \frac{d^2\kappa}{d\omega^2} \cdot z = \Delta\omega \cdot \frac{dv_g}{d\omega} \cdot \frac{1}{v_g^2} \cdot z \tag{16.12}$$

and the result, Expression 16.12, actually corresponds to that of a much more strict derivation using Gaussian pulses. For very short pulses that are considerably broadened, then Equation 16.12 gives the width of the broadened pulse. For longer pulses or smaller broadening, it is a little more complicated.

Alternatively, we can use the diagram to see the way in which the phase coincidences are affected by the variation of group velocity. Figure 16.14 shows the modified arrangement of the various component waves and their contours of equal phase. The phase broadening itself causes a widening of the pulses corresponding to each band of frequencies, so there is a still greater broadening as the pulse propagates. The change in the carrier frequency through the width of the resultant pulse is known by the term *chirp*. The pulse is broadened and chirped.

The effect, because it is due to a change in the group velocity across the frequency range of the pulse, is usually known as group velocity dispersion. Similar effects occur in waveguides and optical fibbers. Group velocity dispersion, often abbreviated to GVD, is measured in units of $(\text{time})^2/(\text{unit length})$ and is given by

$$\textit{Group Velocity Dispersion} = \left.\frac{d^2\kappa}{d\omega^2}\right|_0 \tag{16.13}$$

If the original pulse is of Gaussian shape as in Expression 16.7, then if we write:

$$\tau_g^2 = \left.\frac{d^2\kappa}{d\omega^2}\right|_0 \cdot z$$

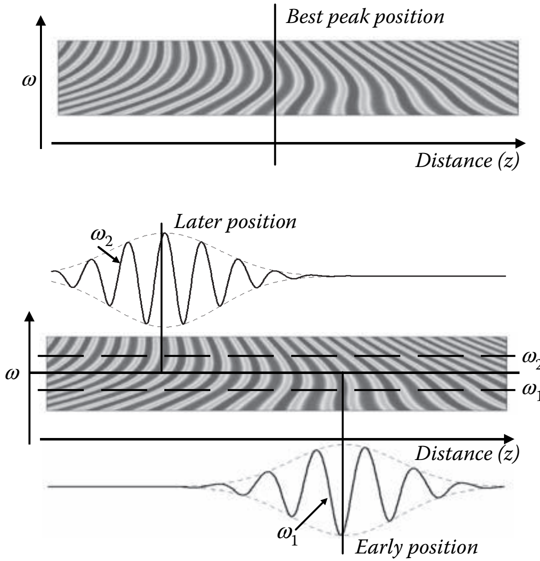

FIGURE 16.14
The pulse frequency distribution in the upper figure is notionally split into two parts in the lower. Each of these parts can be looked on as representing a component pulse with its own center position. Since the group velocity is different for the two component pulses they separate such that one lags behind the other and the combined pulse is broadened. The carrier of the combined pulse shifts from, in this figure, a lower value at the front to a greater value at the rear. This shift in carrier frequency through the pulse is known as a *chirp*. The pulse is said to be broadened and chirped.

it can be shown [6] that the new pulse width is given by

$$\tau_{new} = \tau\left[1+\frac{\tau_g^4}{\mu^4}\right]^{1/2} \tag{16.14}$$

All of these effects are linear and so they can be undone by a similar but opposite effect. Further, the order in which the effects occur is unimportant. A dispersive broadening may be cancelled by an opposite dispersion.

A pulse, consisting of an envelope over a carrier, may be subjected to a modification, by passing through a crystal modulator for example, in which the phase of the carrier is gradually varied throughout the length of the pulse. If this variation is a linear function of time then the effect is just as though the frequency of the carrier had been changed. There is little other effect. However, if the phase is changed as a quadratic function of time, then it is as though the frequency of the carrier were shifted gradually throughout the length of the pulse [7].

$$\cos(\omega t + at^2) = \cos[(\omega + at)t] \tag{16.15}$$

The pulse has frequency ($\omega + at$) and, in other words, is chirped. This chirped pulse appears indistinguishable from a short pulse that has been dispersion broadened, except that the apparent dispersion can be opposite in sign to normal dispersion. The pulse can then be subjected to the action of a dispersive medium where there is significant group velocity dispersion. Provided this dispersion is of the correct magnitude and sense, then it will undo the artificially induced effect in the pulse, leaving it considerably narrowed. Various components have been used for this purpose, but the flexibility of optical coatings makes them particularly attractive in this application [8–11].

Optical coatings affect both the amplitude and the phase of incident light. They can, therefore, in principle make the kinds of adjustments to incident light that we have been considering. They have an advantage over dispersive systems in that the correction is made immediately. We first must consider the nature of the effect that thin film coatings have on the pulse.

Amplitude reduction over part of the range of frequencies leads to pulse broadening because the narrower the frequency spectrum the broader is the pulse. We therefore limit ourselves to consideration of those systems that have flat performance in terms of either transmittance or reflectance and that make adjustments to the phase.

The sign convention is important. We use the normal thin film convention. The coordinate system has its origin at the surface where the reflection is said to be taking place and the phase shift is measured at that surface. The electric field retains its incident positive direction. An incident wave, say, $\mathcal{E}\cos(\omega t - \kappa z + \varphi_{inc})$, say, suffers a phase change φ_{ref} at the surface $z = 0$. The electric field at that surface for the reflected beam therefore becomes $\mathcal{E}\cos(\omega t - \kappa z + \varphi_{inc} + \varphi_{ref})$. This then forms a reflected beam that has expression $\mathcal{E}\cos(\omega t + \kappa z + \varphi_{inc} + \varphi_{ref})$. The returned beam is now propagating along the negative direction of the z-axis. We can avoid the sign change in z if we introduce the idea of the total path traveled by the wave that we denote by x, which always increases as the wave propagates and is along the positive direction of the z-axis before reflection and along the negative direction after reflection. [Note the temptation when using the alternative phase factor convention of ($\kappa z - \omega t$) to reverse the direction of the wave by incorrectly writing ($\kappa z + \omega t$), reversing the direction of time rather than, correctly ($-\kappa z - \omega t$), reversing the propagation direction.]

The expression for the wave now becomes

$$\mathcal{E}\cos(\omega t - \kappa x + \varphi_{inc} + \varphi_{ref}) \tag{16.16}$$

where x is always positive for increasing propagation length.

Now let us examine the effects of the various phase angles on the pulse and its components. We take Equations 16.10 and we rewrite the left-hand side to include a change of phase on reflection. Then

$$\begin{aligned}
&\omega_0 t - \kappa x + \Delta\omega\cdot t - \Delta\omega \left.\frac{d\kappa}{d\omega}\right|_{\omega_0} x - \frac{1}{2}(\Delta\omega)^2 \left.\frac{d^2\kappa}{d\omega^2}\right|_{\omega_0} x + \varphi_0 + \Delta\omega \left.\frac{d\varphi}{d\omega}\right|_{\omega_0} \\
&\quad + \frac{1}{2}(\Delta\omega)^2 \left.\frac{d^2\varphi}{d\omega^2}\right|_{\omega_0} = (\omega_0 t - \kappa L) + \Delta\omega\left\{t - \left(\left.\frac{d\kappa}{d\omega}\right|_{\omega_0} x - \left.\frac{d\varphi}{d\omega}\right|_{\omega_0}\right)\right\} \\
&\quad - \frac{1}{2}(\Delta\omega)^2\left(\left.\frac{d^2\kappa}{d\omega^2}\right|_{\omega_0} x - \left.\frac{d^2\varphi}{d\omega^2}\right|_{\omega_0}\right)
\end{aligned} \tag{16.17}$$

– $(d\varphi/d\omega)$ has units of time and we can identify it as equivalent in its effect to the group delay due to dispersion and it is therefore known as the group delay, sometimes abbreviated to GD. The next term, $-(d^2\varphi/d\omega^2)$, has an effect equivalent to the group velocity dispersion. Since the negative first derivative is known as group delay, this second derivative is known as group delay dispersion, abbreviated to GDD, and has units of (time)^2. Although we have said little about it here, the third derivative is sometimes called the third order dispersion, with units of (time)^3, and abbreviated to TOD. Third order dispersion is usually small but, if it is significant, it can adversely affect the shape of the pulse. The group delay dispersion is particularly important because it can be adjusted in sign and therefore can be used to offset the effects of group velocity dispersion and also to operate on chirped pulses.

For most simple reflectors, φ increases with wavelength. This is the case with the classic quarter-wave stacks. φ increases slowly with λ, the rate of change being a minimum at the central wavelength, and the greater the index contrast in the layers, the slower is the change. An outer low-index layer actually reduces still further the rate of change. The calculated group delay dispersion for a quarter-wave stack is shown in Figure 16.15. The outermost layer in this case is of high refractive index. Although a low-index layer outermost leads to a slight gain, it gives an antinode of electric field at the outer surface and may, therefore, be undesirable. It is obvious that the calculated group delay dispersion for quarter-wave stacks will normally be very small and so it is a particularly safe type of reflector to use with short pulses.

Transparent optical materials with normal dispersion show a refractive index n that reduces as wavelength increases. We can write for κ:

$$\kappa = \frac{2\pi n}{\lambda} = \frac{n\omega}{c}$$

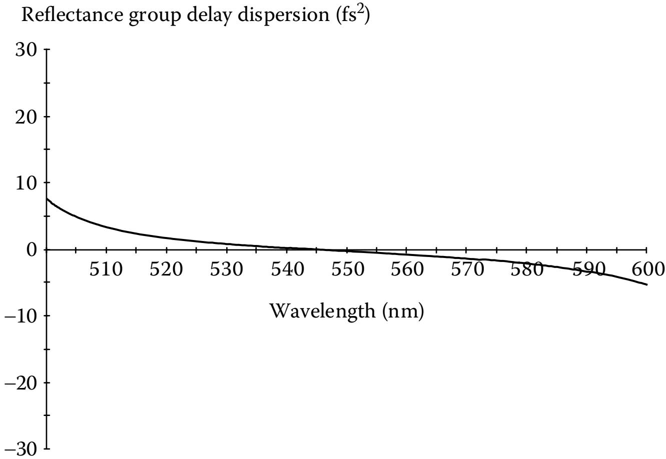

FIGURE 16.15
The calculated group delay dispersion for a 23-layer classic quarter-wave stack of titanium dioxide and silicon dioxide, the titanium dioxide outermost. Reference wavelength is 550 nm. The effect is clearly quite small and this is normal for quarter-wave stacks in general. Variation in the total number of layers makes little difference.

c being, as usual, the velocity of light *in vacuo*. The variation of n in the region of normal dispersion can usually be represented as a Cauchy expression:

$$n = A + \frac{B}{\lambda^2} + \frac{C}{\lambda^4}$$

so that since $\lambda = 2\pi c/\omega$

$$\kappa = \frac{n\omega}{c} = \frac{A\omega}{c} + \frac{B\omega^3}{4\pi^2 c^3} + \frac{C\omega^5}{16\pi^4 c^5}$$

and the group velocity dispersion is given by

$$\begin{aligned}\frac{d^2\kappa}{d\omega^2} &= \frac{6B\omega}{4\pi^2 c^3} + \frac{20C\omega^3}{16\pi^4 c^5} \\ &= \frac{1}{2\pi c^2}\left(\frac{6B}{\lambda} + \frac{20C}{\lambda^3}\right)\end{aligned} \tag{16.18}$$

Typical values for B might be of the order of 10^4 nm^{-2} and for C, 10^9 nm^{-4}. c is approximately 300 nm/fs. Thus, Expression 16.18 becomes of the order of 10^{-4} fs^2 nm^{-1} or 100 fs^2 mm^{-1}.

Figure 16.16 shows the group velocity dispersion calculated from the manufacturer's data for SK7 glass [12]. Clearly, for very short pulses of a few

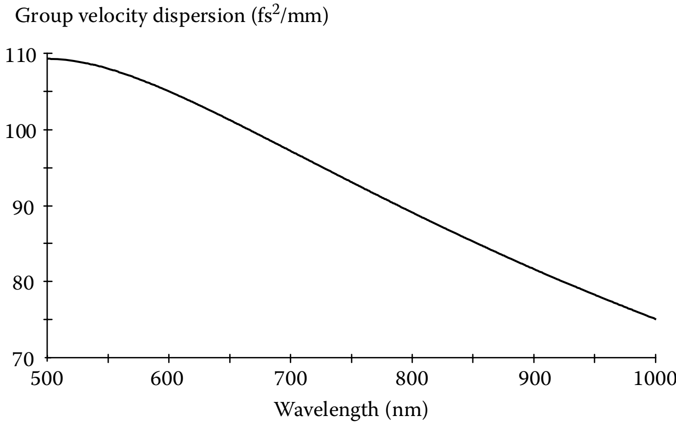

FIGURE 16.16
Group velocity dispersion in $fs^2\ mm^{-1}$ for SK7 glass calculated from the manufacturer's data (Schott, *Schott Optical Glass*, Schott Glass Technologies Inc, Duryea, PA, 1992).

femtosecond length, propagation of even a very few millimeters in a dispersive medium can degrade the pulse.

Rather longer pulses with length measured in picoseconds are used in telecommunications. Here, propagation in media like optical fibers can be over lengths measured in kilometers. Now the effect of group velocity dispersion and third order dispersion can be sufficiently great to affect even these much longer pulses.

TABLE 16.1
Design of Chirped Reflector (Courtesy of Thin Film Center Inc.)

λ_0 700 nm					
Layer	**Material**	**Optical Thickness**	**Layer**	**Material**	**Optical Thickness**
Medium	Air	Massive			
1	TiO_2	0.048	13	TiO_2	0.282
2	SiO_2	0.239	14	SiO_2	0.285
3	TiO_2	0.336	15	TiO_2	0.275
4	SiO_2	0.208	16	SiO_2	0.291
5	TiO_2	0.231	17	TiO_2	0.306
6	SiO_2	0.197	18	SiO_2	0.324
7	TiO_2	0.225	19	TiO_2	0.362
8	SiO_2	0.292	20	SiO_2	0.320
9	TiO_2	0.292	21	TiO_2	0.355
10	SiO_2	0.287	22	SiO_2	0.323
11	TiO_2	0.279	23	TiO_2	0.273
12	SiO_2	0.288	Substrate	Glass	Massive

The net group delay dispersion is given by

$$\left(\frac{d^2\kappa}{d\omega^2}\bigg|_0 L - \frac{d^2\varphi}{d\omega^2}\bigg|_0 \right) \tag{16.19}$$

Straightforward quarter-wave stacks show small group delay dispersion implying that, although useful in reflecting short pulses without distortion, they are not useful as they stand for the correction of the effects of group velocity dispersion. The principle of coatings for the correction of the dispersive effects is that light may penetrate into them to a rapidly varying extent and therefore show rapid phase dispersion, which in turn is translated into the high group delay dispersion that is required. Broad band reflectors with extended zones exhibit this effect and, incidentally, may have a considerable broadening effect when used as simple reflectors. They are, however, useful for operating on chirped pulses [10,11], and because they have often a structure that exhibits a gradual tapering of layer thickness through the structure, they are often known as chirped mirrors. Table 16.1, Figure 16.17, and Figure 16.18 show the details of the design and calculated performance of such a coating with a group delay dispersion of –30° over the region 750 nm to 900 nm. This is an example of a design arrived at purely by synthesis with no starting information other than the materials silica and titania that were to be used. Szipöcs and Köházi-Kis [10,13] give more detailed accounts of a more systematic approach to the design of such chirped mirrors.

The chirped mirror is less useful for compensating for the group velocity dispersion of a longer pulse passing through a considerable thickness of optical material. Here the requirement is a much narrower spectral range but a much higher group delay dispersion. Some way of increasing the magnitude of the negative values of group delay dispersion of an optical coating is required. The addition of a weak cavity to the front of the quarter-wave stack has been

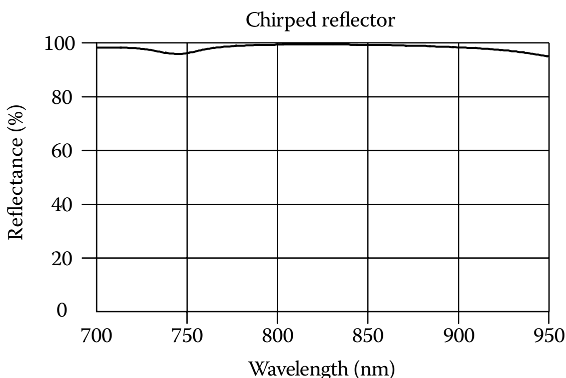

FIGURE 16.17
Calculated reflectance of the coating of Table 16.1.

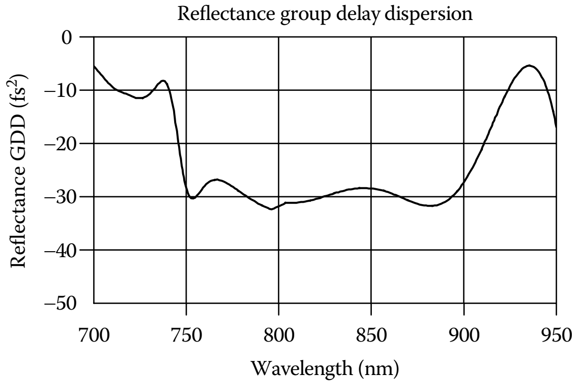

FIGURE 16.18
Calculated group delay dispersion of the coating of Table 16.1.

shown to be one fairly successful way of achieving this result provided the wavelength region is limited—that is, the pulse is reasonably long. The presence of the cavity can be thought of as causing a variable group delay that has a maximum at resonance and falls away on either side. Such an arrangement is usually known as a Gires-Tournois interferometer after the originators [14,15]. The weak cavity does not reduce the reflectance too much, but the result is a very rapid change of phase on reflection that leads to the desired effect.

Figure 16.19 shows the dispersive parameters of a simple Gires-Tournois interferometer of design

$$Air \mid (HL)^6 HH(LH)^6 L(HL)^9 H \mid Glass \qquad (16.20)$$

using tantalum pentoxide and silicon dioxide as materials. This type of interferometer is particularly useful for compensating for third order dispersion in optical fibers [16]. Its characteristic with the large central lobe and much less pronounced secondary lobes makes it particularly suitable for mounting in a cascade of reflecting components, each with slightly shifted resonances so as to broaden the resultant characteristic.

In some versions of the interferometer, the final quarter-wave stack is largely replaced by a silver film. This saves many layers. The same considerations that apply to enhanced metal reflectors to avoid reducing rather than increasing the reflectance apply in this case.

16.3 Automatic Methods

Given a possible solution to a thin film design problem, can we devise an objective method to change the parameters so that it becomes a better design?

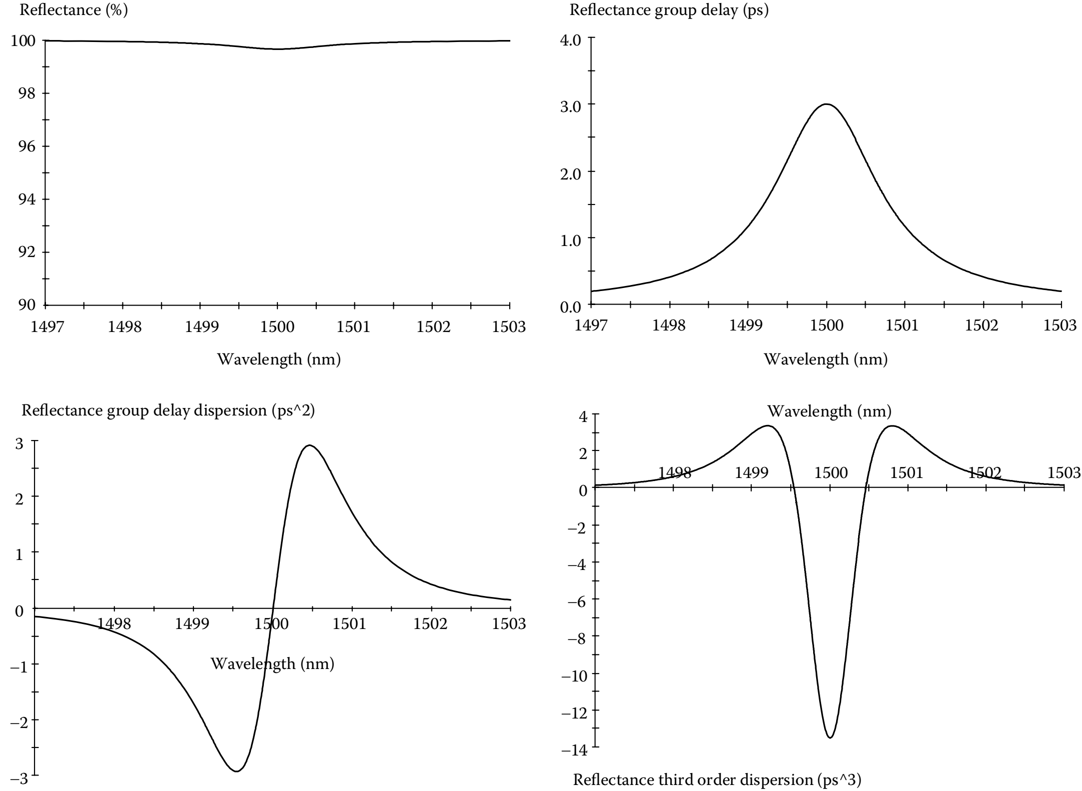

FIGURE 16.19
The various dispersive parameters of the Gires Tournois interferometer of design given in Expression 16.20. These are several orders of magnitude greater than those of the chirped coating but over much narrower spectral regions and are appropriate for telecom pulses rather than ultrafast.

Can we continue the process to make the design as good as possible? And, of course, can we finally devise a way of achieving all this using an automatic computer? The answer to all these questions is a conditional affirmative.

An automatic process that makes adjustments to an already existing design without making major changes is known as *refinement*. An automatic process that involves an element of design construction is usually known as *synthesis*. The term synthesis may denote anything from a mild complication of an almost acceptable design to a process that builds an acceptable design from nothing more than a list of materials and a performance specification. The term *optimization* simply means improving performance and includes both refinement and synthesis. These are not by any means universal definitions and there is no universal agreement on the meanings of the terms.

Before we can make a coating better, we must define what we mean by *better*, and our definition must be one that can be applied to automatic methods. At the current stage of development of the subject, the concept is invariably expressed in terms of changes in a single number, the *figure of merit*. The usual arrangement is for a smaller figure of merit to be better than a larger one and a figure of merit to be zero if the coating has exactly the desired performance. However, automatic processes can work as well with a figure of merit that increases as the merit improves. The figure of merit is derived from a comparison of the actual calculated performance of a design and a specification of a desired performance. The derivation involves the application of a set of rules and it is important that the rules should yield a completely unambiguous figure of merit.

Performance may include any attributes of the coating that can be quantified, but it is frequently taken as the reflectance, or transmittance, or some such normal expression of performance, at specified points over a prescribed wavelength range. Each individual expression of performance is known as a *target*. Usually the form of the rules for calculating the figure of merit will be similar to the following expression.

$$F = \frac{\sum_j [W_j \,|\, T_j - P_j \,|^q]}{\sum_j W_j} \tag{16.21}$$

where F is the figure of merit, T_j is the jth target, P_j is the corresponding calculated value of performance, and W_j is a weight that indicates the relative importance of the particular target, or its tolerance, and which, especially if there are mixed quantities among the targets, will usually include an allowance for the scale of the particular performance attribute represented in the target. It is usual to normalize the expression so that the refinement or synthesis process has always approximately the same working range and this is indicated in Expression 16.5 by dividing by the sum of the weights. The quantity q, the power to which the performance gap is raised, may be completely

free for the user to choose or may, in some procedures, be completely defined. Experience shows that a value of q of 2 works well in many cases. Increasing the value of q makes the process more responsive to larger performance gaps at the expense of smaller.

The figure of merit depends on the particular set of design parameters, and we can consider it as a function of the design parameters as variables. In this case, we call it the *function of merit*. For efficient and reliable optimization, the function of merit should be a continuous, single-valued function of the parameters. Abrupt changes in the function of merit as parameters vary inhibit efficient refinement and should be avoided. Hard constraints on the process can have the same effect as abrupt changes, and so it is often more efficient to soften the constraints by expressing their effect in terms of penalty functions attached to the function of merit rather than rigid boundaries.

If we have the same number of targets in the definition of the merit function as we have parameters in the design, then, in principle, provided the targets are attainable and not mutually exclusive, the problem should be completely soluble, although it may require impossible optical constants or thicknesses. In most cases, however, we will have rather fewer parameters, or those that we have will be incapable of achieving completely the desired performance, and then the objective of the optimization process becomes to make the figure of merit as small as possible. We can visualize the function of merit as represented by a surface in multidimensional space, one dimensions for each adjustable parameter and one for the figure of merit. Making the figure of merit as small as possible, then, is translated into finding a minimum of the merit function, and thence into finding the lowest possible minimum, or, as it is known, the *global minimum*. If there are constraints on the parameters, such as permissible ranges, then the lowest possible minimum within the constraints is known as the *constrained global minimum*. Since there always are constraints (we cannot permit infinite thicknesses, for instance), the minimum that concerns us will be the constrained global minimum. Unfortunately, although it is relatively easy to find a minimum of the merit function, it is not nearly as easy to find, or even to be sure that one has found, the constrained global minimum. Unless the function of merit is analytically friendly, the only way to be absolutely sure is to carry out an exhaustive search of the given parameter region. We can illustrate the problems involved in this, by assuming a 20-layer design with 20 possible values of thickness for each layer, where refractive indices are already prescribed. Assume that one complete figure of merit can be generated in 1 ns. Then an exhaustive search of all possible designs will occupy a time of 20^{20} ns, that is around 2×10^9 years. This problem is considerably constrained, but already it gives some idea of what is involved in an exhaustive search. All optimization techniques, therefore, carry out a more limited procedure that arrives at a local minimum that may be as good a minimum as is economically possible. The adjective *global* is sometimes applied to processes that essentially search in constrained parameter space for more than one merit function

minimum so that they have an improved chance of finding the constrained global minimum.

We may have major gaps in our ideas of a starting design. Perhaps we do not have any idea of the indices for the layers beyond the range of possibilities that are available, or we may not know the number of layers beyond perhaps a prescribed maximum. In that case we have the synthesis problem. If we have a reasonably good design that simply needs minor adjustment, then we have refinement. Synthesis clearly has rather greater dimensions than refinement. To begin, we will concentrate on refinement and assume that we have a starting design of a certain number of layers that the process will alter only in some limited way such as in terms of layer thicknesses or refractive indices or possibly both.

In optical thin film design, we do have many techniques capable of establishing good designs that can be already almost satisfactory. In other words, they are already in the region of an acceptable minimum of the merit function and all that is required is to reach the actual minimum as quickly as possible. This is the objective of many of the optimization techniques that are used in optical coating work. Such is the complicated nature of the function of merit that all do not necessarily find the same minimum from the same starting design. Then there are techniques designed especially so that they do not necessarily choose a neighboring minimum. Instead they range over a region of the parameter space, in a gradually more and more constrained manner. This permits them the opportunity of discovery of any other merit function minimum that might offer improved performance over that nearest to the point of departure.

There are many ways of classifying the various optimization techniques. They can be divided into those that use a single design that is gradually altered in prescribed ways until a minimum is reached, and those that use a family of designs, rejecting members of the family and replacing them by other designs, and reaching the minimum in this way. They may also be classified as those that attempt continuously to move toward a minimum of the merit function and those that may take some time before they finally choose the particular merit function minimum, and, therefore, have greater chance of finding a more satisfactory minimum.

Only an analytical technique can involve continuous alteration of parameters. In computer optimization, the parameters are altered in finite steps that are usually adjusted in size as the process continues. It consists, essentially, of probing the merit function surface. The results of previous probing are used to guide the choice of future ones. The optimization is normally divided into repeated units called iterations. Each iteration will usually involve a single or multiple adjustment of the design or designs according to a set prescription and a reassessment of a new figure of merit. The process is continued until either a satisfactory outcome is attained or fresh iterations are unable to achieve any further improvement. The nature of the adjustment of the design and the way in which it is predicted is what principally distinguishes the various techniques [17].

It is tempting to find the best slope of the merit function as a function of the adjustable design parameters and simply to move down this slope as quickly as possible by changing the design parameters depending on the steepness of the slope. However, it is easy for the technique to become violently unstable with one overcorrection following another if precautions are not taken. The *steepest descent* method picks the maximum slope and follows it but the parameter changes are usually restrained according to the derivative of the slope. If this is high, indicating that the slope appears to be changing rapidly, then the parameter changes are kept small. The steepest slope may not lead directly to the desired minimum. A zigzag path is a frequent feature of the convergence. The method of *damped least squares* is more efficient. Here the path is chosen to minimize a figure of merit based on the squares of the deviation between actual and target performance values. The calculation of the direction requires details of the local merit surface slope. Ideal convergence is achieved if the merit surface has a quadratic form. Stability is assured by restraining the movement by an adjustable damping parameter. Then there are several *univariate search techniques* in which only one parameter is altered at each iteration. The commonest is probably the *golden section* technique. Here a minimum of the merit function is achieved for each parameter in turn. The parameters may be chosen in the order of some prescribed scheme or at random. The search for the minimum in each case involves the process of bracketing, where three values of the parameter are maintained, with the figure of merit of the central one less than either of the two outer values. This means that a minimum exists between the two outer parameters. By always dividing the appropriate region in the ratio of $1:(3 - \sqrt{5})/2$, that is, 1:0.382, the golden section, the most efficient search, can be performed.

Linear search techniques are like the univariate search techniques but they may freely choose the directions along which they search in parameter space. The most effective techniques change the directions from time to time based on previous progress. They are usually called *direction set methods*. The most efficient try to find a set of conjugate directions, that is a set of directions that are decoupled from each other with respect to the minimization process—minimizing along a second direction after a first should not alter the minimum of the first direction. Just one pass through the directions is then sufficient to reach the minimum. This works perfectly for simple quadratic functions. Unfortunately, the thin film functions are very complicated and they have to be searched over quite large regions so they rarely reach the final minimum in just one pass but the search can be made more efficient if a continuous attempt is made to achieve conjugate directions.

Flip-flop optimization [4] is a relatively new term. It is a digital technique, in a sense. A design is set up consisting of a large number of very thin layers of equal geometrical or optical thickness. These thin layers may have either of only two possible indices, or admittances, usually a high value and a low value. A merit function is set up and the figure of merit calculated. Now the layers of the design, from one end to the other, are scanned. At each iteration step, the

figure of merit of the coating is assessed, with the index of the appropriate layer set to both of the permitted values in turn. The better arrangement, in the sense of a lower figure of merit, is chosen, and the index of the layer set to that value. The process then passes to the adjacent layer, and so on. Several complete passes of the design may be employed, and the order in which the layers are examined may be changed. Usually the design stabilizes at a minimum of the merit function after only a few passes. The designs often consist of quite long blocks of one or the other index, corresponding to normal discrete layers, separated by blocks that clearly correspond to discrete layers of intermediate index, and occasionally a structure that represents a thicker inhomogeneous layer is obtained. The process appears very stable. It is relatively easy to take a normal discrete layer design and turn it into a suitable starting design for this process, although it appears to work quite well with all layers initially set to one or the other of the two indices.

A process that does not immediately necessarily choose the minimum toward which it shall move, is *simulated annealing* [17]. This uses a Bolzmann probability distribution:

$$\mathrm{Prob}(E) = \exp(-E/kT). \tag{16.22}$$

where E is replaced by a merit function and kT by an annealing parameter T. Then if the existing figure of merit is $E1$ and a suggested new design has $E2$, the probability that the new design is accepted in place of the old is

$$p = \mathit{probability} = \exp[-(E_2 - E_1)/T] \tag{16.23}$$

except that for $E_2 < E_1$, the probability is unity. The process involves calculating a new figure of merit based on a random choice of parameters within an assigned domain. If the merit function is less than the old, the new design replaces the old. If the merit function is greater than the old, it will be accepted with probability p based on the drawing of a random number. An *annealing schedule* is required that decides on the way in which T is allowed to fall until no further improvement is achieved.

One of the better techniques that uses a family of designs rather than one single one is the *simplex* technique, sometimes called *nonlinear simplex* to distinguish it from a similarly named technique in linear programming. The family of designs is known as the simplex, and numbers one more than the number of design parameters involved. At each iteration, the worst design, that is the design with the greatest figure of merit, is rejected in favor of a new better design. The alternative new designs are generated in three possible ways. First, the worst design is reflected in the center of gravity of the simplex and the figure of merit calculated. If this yields a better design, then a further equal move is made in the same direction and, again, the corresponding figure of merit calculated. The better of these two designs replaces the existing worst design. If the first move fails to yield a better performance,

then the worst design is moved halfway toward the center of gravity, which will then normally be an improvement. In the rare cases where none of the alternatives yields a better design, a completely new simplex is generated by moving all the designs half way toward the existing best design [17].

The *statistical testing* method of Tang and Zheng [18] also involves a family of designs. Like simulated annealing, it does not move immediately down a particular slope but takes rather longer and so has a better chance of finding a more acceptable minimum. A starting region of parameter space is chosen and then this region gradually shrinks around, it is hoped, a good, and perhaps even a global, minimum. Designs are chosen at random within the starting domain until a prescribed number have been found with merit function less than a starting target. The region then shrinks until it contains only those designs and a new target that is now the mean of the merit functions is chosen. The process is repeated until a final minimum is reached.

There is a great deal of debate about which technique is better than another, and it is clear that there are differences in performance for different starting designs and coating types. A few comparative studies have been performed [19,20], but they have not unambiguously identified any technique always superior to all others. The secret of success in refinement is a good starting design that offers scope for improvement. In that context, there is little difference between the various methods.

Synthesis is similar to refinement but involves some construction of the design beyond the adjustment of the existing layers. The number of possible designs is infinite and so the synthesis problem can be solved only by introducing some constraints. Imagine that we have a very efficient refinement technique that is capable of dealing with starting designs that are rather far from ideal. Let us now set up targets and merit function in the normal way. Next we create a starting design that uses a very small number of layers, perhaps only one. We refine this design until it is optimum. Then we add layers according to some prescribed rules. Perhaps the figure of merit will now be rather larger than before, but we refine again and eventually achieve an optimum figure of merit that is lower. Again we add layers according to our prescription and refine as before. We continue this process until we reach a stage where no improvement is taking place and at that stage we accept the best design. This is a viable synthesis technique and represents fairly well the few techniques that are sometimes used in practice. The way in which layers are added is the major difference between them.

Dobrowolski [21] was the major pioneer in this field. He recognized that the addition of one single layer was often ineffective and addition of more layers was indicated. Some spectacular results have been obtained by the *needle variation* method [22]. This searches the design for the best place to add a thin slice of material, initially of zero thickness. The definition of best is a maximum negative derivative of the merit function with respect to the added layer thickness. The addition of this vanishingly thin slice, known as the needle, effectively adds two layers because it cuts the existing layer

in two. Some commercial techniques, not otherwise published, add varying numbers of layers depending on the stage of the synthesis and on the constraints. All depend on a powerful and efficient refinement technique. The statistical refinement techniques tend to be less suitable because already they use considerable computer time, and it is more usual to use either the gradient, damped least squares or linear search techniques in synthesis.

It may sometimes be said in support of a particular technique that it opens up new possibilities in design and arrives at performance levels that cannot be achieved in any other way. However, any design, regardless of how it is achieved, lies in the constrained parameter space. We may think of it as already existing. All that the various techniques can do is to search the constrained parameter space to find a suitable merit function minimum. They cannot find a minimum that does not exist. Although it may seem that synthesis is an ideal technique, the difficulties in finding the constrained global, or even a very good, minimum, which are compounded by the rapid increase in complexity as layers are added, mean that the final design may not be as good as one arrived at by a process of establishing a very good starting design and then carrying out a minimum of refinement [23]. In some techniques, quite thin layers that are difficult to manufacture may form part of the final design, which must then be processed to remove them. The needle method, for example, introduces such thin layers as a necessary part of the process and they may remain at termination. Synthesis is therefore best used when the designer is hard pressed with little idea of how to proceed and it works most effectively when the total number of layers is not large.

Refinement and synthesis work best when the targets call for high transmittance. High reflectance presents certain problems. The performance of an optical coating is essentially a set of interference fringes. Refinement targets should be set so that they are closer together than the fringe spacing; otherwise, the performance between the targets may be seriously in error. The problem is sometimes called *aliasing*. For sine or cosine fringe profiles, avoidance of aliasing implies roughly that if the film is m quarter-waves thick, then the spacing for wavelength target points should be λ/m. We often tend to work in constant increments of wavelength rather than wave number and so the target for a film m quarter-waves thick at λ should have $m + 1$ points to cover the octave λ to 2λ. A film that is 25 wavelengths thick, then should have a target function with 100 wavelength points per octave. This modest requirement is adequate for coatings with low reflectance but, unfortunately, completely inadequate for coatings where reflectance must be high [24]. The reason is that fringe profiles are not always approximately sine or cosine functions. In an antireflection coating, the reflectance is small and multiple beam interference is weak. The fringes are then virtually sinusoidal and so the simple calculation applies. In high reflectance coatings, the fringes are invariably the result of multiple-beam interference and therefore are very narrow. This increases enormously the required number of targets necessary to ensure that a fringe cannot creep in between them.

Additionally, there is a definite tendency for narrow fringes of lower reflectance to appear in coatings where high reflectance is required. We can readily understand the reason. Figure 16.20 shows the reflectance curves of two similar coatings. One is a quarter-wave stack with high reflectance. The other is derived from it by increasing the thickness of one of the central quarter-waves to one half-wave. Although this converts the coating into a single-cavity narrow band filter, the width of the high reflectance zone is considerably increased. The price is a very narrow central fringe. A density curve, Figure 16.21, of the same filter, shows that there is really no fundamental gain but most merit functions are based on reflectance or transmittance and would assign a lower figure of merit to the broader curve. Small changes

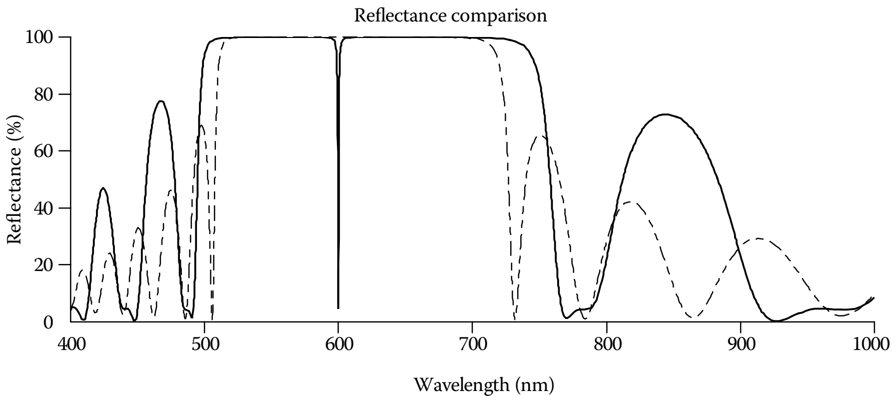

FIGURE 16.20
The insertion of a narrow fringe into the center of a high reflectance coating can actually cause an apparent increase in the width of the high reflectance zone. The basic quarter-wave stack high reflector is the *broken line.*

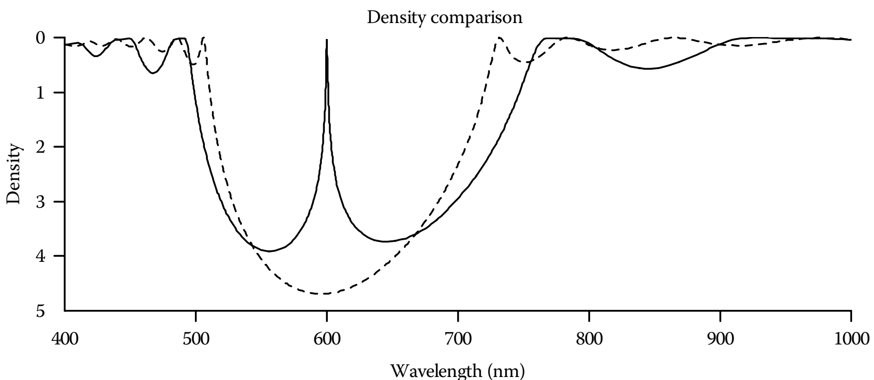

FIGURE 16.21
A look at the density variation shows that the performance is not better, but most merit functions are based on transmittance or reflectance not density and would prefer the broader zone in Figure 16.20.

in the thickness of the nominal half-wave layer can then adjust the lateral position of the fringe with virtually no other changes. Thus, the appearance of such features, sitting between the target points in broadband reflectors, is not surprising. They are persistent and exceedingly difficult to eliminate, particularly by automatic means. Adding extra target points at the fringe is not very successful because a simple adjustment of the cavity layer thickness can move the fringe to where the target points are wider. It is therefore a very simple process for the refinement to alter slightly the thickness of one layer and move the sharp fringe exactly midway between two target points, with resulting substantial decrease of the figure of merit. This is a much easier operation for the process than the removal of a fringe, and sharp deep fringes are, therefore, persistent features that naturally position themselves between the target points, because a small change in the thickness of virtually any layer, but especially the cavity layer, will simply translate the fringe with almost no change in shape.

The fringe peaks are at their narrowest when the coating takes the form of a single cavity in the center of the coating surrounded by maximum reflectors. Let us assume a total thickness for the coating of x full waves and arrange it as a series of quarter-waves of alternate high and low index and with a central half-wave cavity layer. The half-width of such an assembly is given approximately by

$$\frac{\Delta\lambda}{\lambda} = \frac{4y_L^{2x-1}y_{sub}}{\pi y_H^{2x}} \tag{16.24}$$

where we neglect any dispersion of phase shift. The spacing of the wavelength points should be perhaps half this value:

$$\frac{\Delta\lambda}{\lambda} = \frac{2}{\pi}\cdot\frac{y_L^{2x}}{y_H^{2x}} \tag{16.25}$$

where we have assumed the substrate admittance equal to y_L. We can take the wavelength interval as λ to 2λ, say, and the ratio of admittances as $\sqrt{2}$, so that the total number of points in the specification becomes:

$$N = \pi 2^{x-1} \approx 2^x \tag{16.26}$$

Every time another full wave is added the number of points in the specification for the merit function should double.

It can be argued that the calculations are too pessimistic, but it is certainly clear that there is an inexorable increase in computing requirements with coating thickness. The increased burden of calculation becomes rapidly severe, if not impossible. Many of the newer processes are capable of very large numbers of layers and, especially in the case of polymeric films, coatings with thousands of layers are achievable.

Automatic methods have revolutionized the design of coatings. They have not eliminated the older techniques but have rather changed their role. The drudgery of hand calculation has been completely removed. However, as the complexity of optical coatings increases, the completely automatic methods approach a barrier to further progress in the form of suitable measures of merit and further developments in design techniques are required. The advent of the computer has certainly not reduced the need for the skill, experience, and innovation that have characterized the field until now.

16.4 Gain in Optical Coatings

Little seems to have been written on the subject of gain in optical coatings. This may be because the topic is not of any great practical importance at the present time. However, there are some interesting, even fascinating, effects that are connected with gain, so we include some notes on it here. Gain calculations are handled through the extinction coefficient in the same way as absorption, except that the coefficient has opposite sign. This section relies heavily on a paper presented at the 2006 Workshop of European Vacuum Coaters [25].

A particularly useful way of visualizing the difference between a positive and a negative value of k is to plot an admittance locus. A locus with a positive value of k, representing a material with loss, is a gradually collapsing spiral that eventually, if enough material is present, reaches the point $(n - ik)$ (Figure 16.22). The spiral for a layer with negative k, or gain, opens out. If the material is thick enough, the spiral eventually reaches the imaginary axis and will actually pass through it to the other side. At that point it reverses direction and spirals inwards toward the point $-(n - ik)$ (Figure 16.23). The value of k used in Figure 16.23 is intentionally very large to show the spiral clearly. In a real case, the value would be much lower and the spiral much slower.

In any real case, gain is a consequence of a population inversion maintained by some process of pumping and there is a depletion rate that is a function of irradiance. The gain will eventually stabilize at a level where the depletion is just canceled by the pumping. Thus, in any real case, k will be constant only for very low power levels. We will not include such effects in this short discussion. We are effectively assuming that power levels are very low. The effect of the gain is to increase the transmittance and reflectance that now, because of the gain, can exceed unity. Figure 16.24 shows the behavior of both transmittance and reflectance in a system consisting of 4000-nm-thick film with optical constants $(1.5 + i0.1)$ with incident medium of air and emergent of BK 7 glass. The incident medium of air implies a much higher reflection loss than the emergent medium of BK 7 glass. This makes

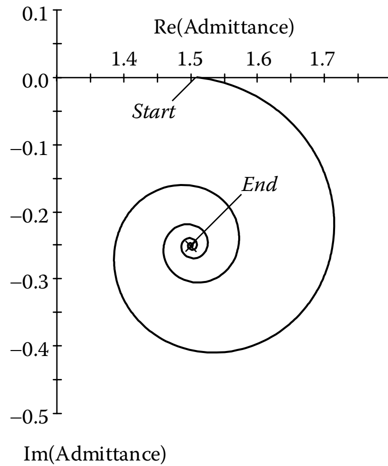

FIGURE 16.22
The locus of a thick absorbing layer deposited over glass. The end point corresponds to $(n - ik)$ that in this figure has a value $(1.5 - i2.5)$.

the transmitted output rather larger than the reflected output. Both are considerably greater than 100%. Again, for simplicity and to show the effects clearly, we are assuming a very large gain.

An adjustment of both gain and wavelength will yield a reflectance of infinity, that is, will result in oscillation of the system. The power output will determine the ultimate level of extinction coefficient. If the reflectance is high enough, that is, the termination point of the locus is close to $-y_0$, then spontaneous emission in the film will be enough to start the oscillation. Note

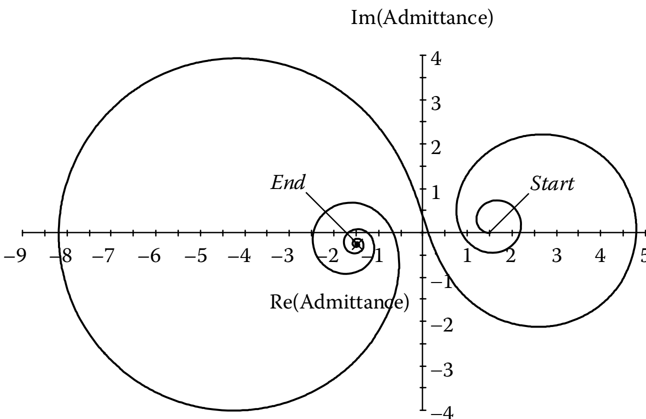

FIGURE 16.23
The locus of a material with negative k, or gain. The spiral reverses direction as it enters the left side of the admittance diagram and gradually collapses toward the point $-(n - ik)$. The reflectance in the left side of the diagram is everywhere greater than 100% and is infinity at the point $-y_0$.

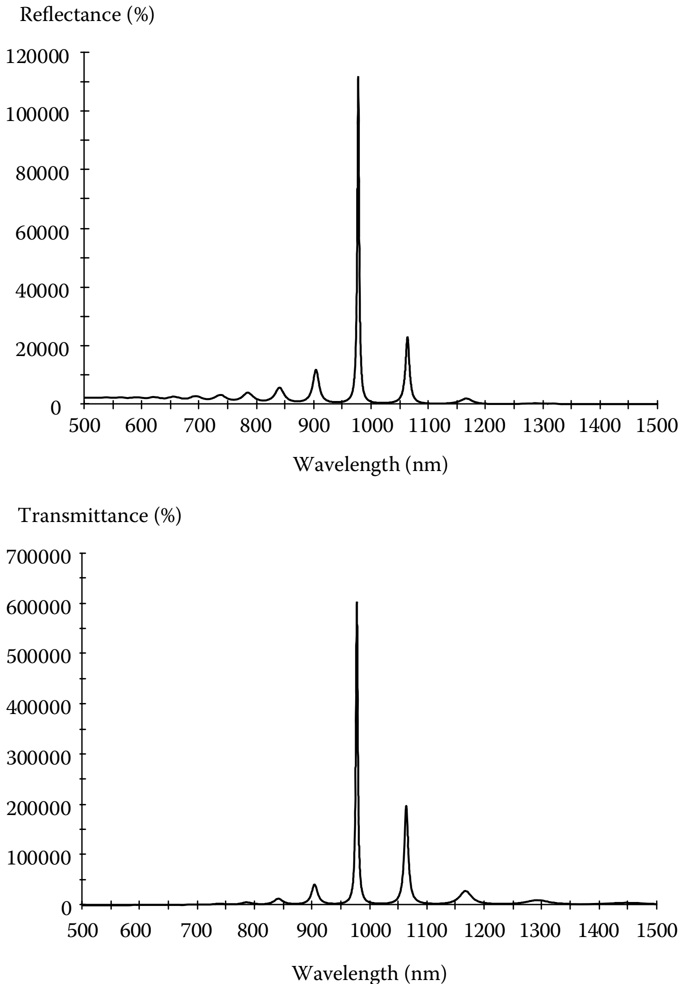

FIGURE 16.24
Reflectance (*upper*) and transmittance (*lower*) of a 4000-nm-thick film with optical constants (1.5 + *i*0.1) with incident medium of air and emergent of BK 7 glass. The unbalanced residual reflectances are responsible for the lack of symmetry in the results.

that the normal thin-film calculations, those that we are using, do always assume an input from the incident medium. As the reflectance rises, so this input becomes smaller and smaller with respect to the output, but the calculations themselves do not take spontaneous emission into account.

If the reflectance at the output side (0.11%—the emergent medium is BK 7) is removed by a perfect antireflection coating, then the reflectance becomes that of the front surface and the device acts as an ideal amplifier (Figure 16.25). Again, the gain is set enormously high so that the effect can be seen clearly. In this case, however, any small irregularity such as a small inhomogeneity,

residual reflectance, or spontaneous emission could affect the stability of the device as evidenced by a sudden expansion of the admittance locus. These need to be taken into account in any real amplifier so that such instability is prevented. An important requirement is that the output reflectance should be sufficiently low.

Added dielectric layers in the left side of the complex plane behave almost in the normal way. The loci of dielectrics are still circular and centered on the real axis, and the quarter-wave rule holds. The difference is that the loci are described counterclockwise instead of clockwise. If the starting point for a dielectric layer is on the left of the imaginary axis, then the entire locus, and that of any following dielectrics, will remain on the left side.

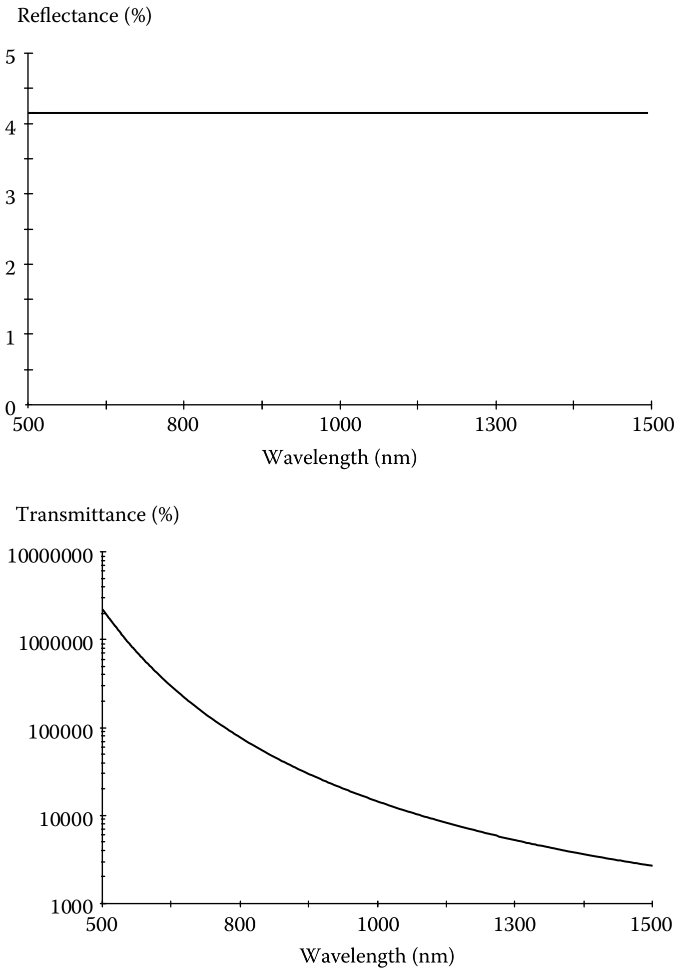

FIGURE 16.25
The reflectance and transmittance of the system of Figure 16.24 with the output side perfectly matched to the substrate.

Matching the rear of the gain layer to the eventual emergent medium presents some interesting aspects. In the case of the rear surface of an absorbing substrate, maximum throughput is the criterion for the optimum matching system. Then a useful definition of transmittance [26] is suggested in Chapter 2 (Equation 2.80):

$$T = \frac{4y_0 y_0^* \,\mathrm{Re}(Y)}{\mathrm{Re}(y_0)[(y_0 + Y)(y_0 + Y)^*]} \tag{16.27}$$

where y_0 is the absorbing incident medium admittance and Y is the admittance of the rear surface. This transmittance is maximized when Y is the complex conjugate of the incident admittance y_0. Provided the matching system is without loss, it can readily be shown that if the direction of the light is reversed, then this coating will be an exact antireflection coating for the absorbing material. The same definition of transmittance could be used for the gain material. Maximum transmittance would be obtained with an exit admittance given by the complex conjugate of the characteristic admittance. In an amplification application, however, this is not a useful definition.

In an amplifier, it is most important to avoid any standing wave in the gain medium or, alternatively, there should be no counterpropagating wave. The existence of such a condition is indicated by an opening admittance spiral. To prevent the spiral from opening, the exit admittance for the gain medium must be equal to the characteristic admittance of the gain medium, not the complex conjugate. If this condition is satisfied, then the locus will be a point and the reflectance of the front surface simply that of the bulk material. An antireflection coating at the front surface will follow the normal rules. Note that the matching applies to the given value of gain only. A gain change will disturb the matching, and the spiral will begin to open.

16.4.1 Oblique Incidence

Modified, tilted admittances were introduced in Chapter 9 where the expressions for absorbing materials were given in Equations 9.10 and 9.11. These are repeated in Equations 16.28 and 16.29.

$$\eta_s = \frac{\sqrt{n^2 - k^2 - n_0^2 \sin^2 \vartheta_0 - 2ink}}{\cos \vartheta_0} \quad \text{(4th quadrant)} \tag{16.28}$$

$$\eta_p = \frac{(n - ik)^2}{\eta_s} \tag{16.29}$$

We recall that the modified admittances are normalized so that the incident medium retains its normal incidence value making the admittance

diagram easier to interpret. These expressions are, of course, valid also for a completely dielectric layer, that is where k is zero when they have a particularly simple form. As long as n is greater than $n_0\sin\vartheta_0$, then η_s is positive real, and so must be η_p. If n is greater than n_0, then η_s rises toward infinity as ϑ_0 tends to 90° and, consequently, η_p falls toward zero. Matters are a little more complicated when n is less than n_0. Then, as the angle of incidence increases, η_s falls toward zero while η_p rises toward infinity. These values are reached at the critical angle when $n_0\sin\vartheta_0$ becomes equal to n. Beyond the critical angle η_s is negative imaginary and slides down the negative limb of the imaginary axis towards negative imaginary infinity as ϑ_0 tends to 90°. At the critical angle, η_p switches to imaginary infinity and moves down the imaginary axis toward zero as ϑ_0 increases. While the admittances are on the real axis, the phase shift on reflection is either zero or 180°. Beyond the critical angle, when the admittances are on the imaginary axis, the reflectance becomes 100%, usually referred to as total internal reflection, and the phase shift for *s*-polarization moves through the first quadrant into the second, while for *p*-polarization, through the third quadrant into the fourth. All this is indicated in Figure 9.8.

An absorbing material changes the results only slightly. The value of η_s moves off the real or imaginary axis into the fourth quadrant of the complex plane and η_p into the first quadrant, Figure 16.26. Total internal reflection is replaced by high reflectance and the phase shift on reflection is slightly modified, Figure 16.27. There is a slight rounding of the corners that occur with the lossless material (thin lines) but otherwise there is virtually no change.

There is, however, a drastic change when gain is involved. Now k in Equation 16.28 is negative and the quantity under the square root sign is in the first or second quadrant. The two possible roots, therefore, must be in the first or third quadrants. Physical conditions, discussed shortly, require that the chosen solution must be the first quadrant one. Figure 16.28 shows the variation of tilted admittance as a function of angle of incidence when the index of the incident medium is greater than that of the emergent medium. Total internal reflection does not quite occur, similar to the case of slightly absorbing emergent media. Comparison with Figure 16.26, however, shows that the admittances have jumped into different quadrants. Figure 16.28 is virtually an inverted Figure 16.26.

A particularly interesting effect [25] concerns the surface plasmon resonance that, in its normal form, is described in Chapter 9. The *p*-polarized metallic admittance locus that would normally lead to a plasmon resonance must start in the fourth quadrant and, clearly, is unable to move to the point corresponding to the incident medium admittance. The lower part of Figure 16.29 shows the resulting locus, which can be compared with that for an absorption-free emergent medium in the upper part of the same diagram. Figure 16.30 compares the performance with and without gain. With gain, the resonance, therefore, disappears completely.

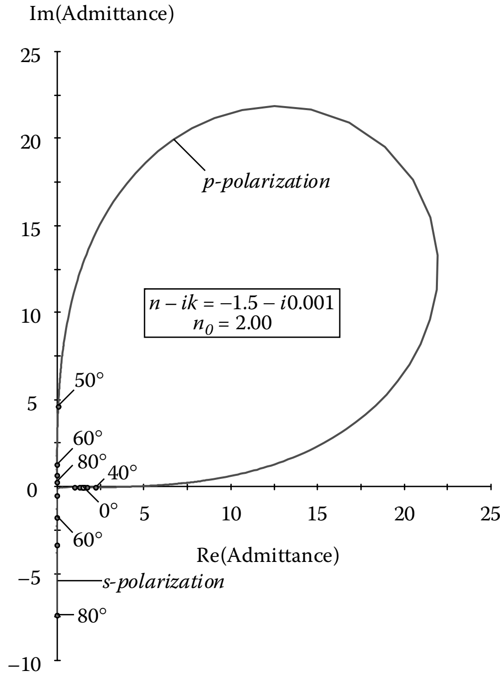

FIGURE 16.26
When the material is slightly absorbing, the tilted admittances move off the axes into the first quadrant for *p*-polarization and fourth quadrant for *s*-polarization. (See color insert following page 398.)

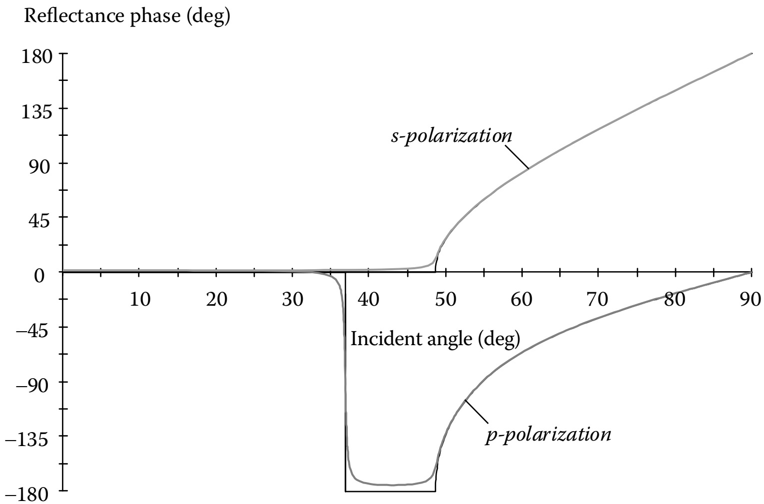

FIGURE 16.27
The form of the phase shift on reflection for a lossless dielectric and for a slightly absorbing material. The thin lines indicate the lossless results.

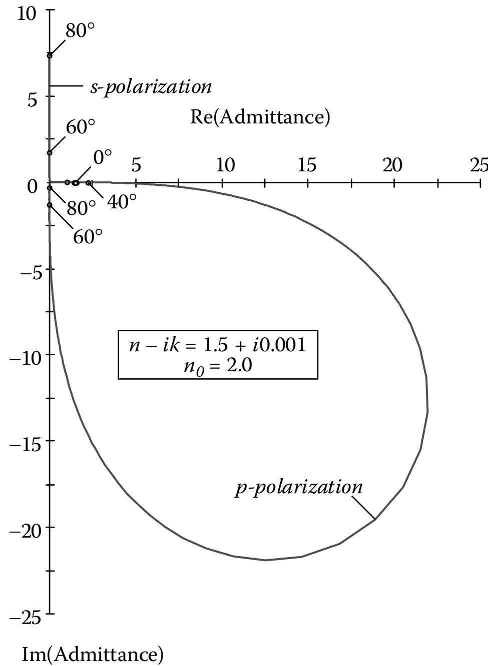

FIGURE 16.28
When the material has slight gain, the tilted admittances move off the real and imaginary axes but, unlike the case of slight absorption, they jump into opposite quadrants. The *s*-admittance is in the first quadrant and the *p*-admittance in the fourth. (See color insert following page 398.)

To understand what is happening, we need to think of the complete expression for the wave, which in a gain medium is given by:

$$E = \mathcal{E}\exp\left[i\left\{\omega t - \frac{2\pi}{\lambda}\left(n_0 \sin\vartheta_0 x + [\xi + i\zeta]z\right)\right\}\right]$$
$$= \mathcal{E}\exp\left(\frac{2\pi\zeta z}{\lambda}\right)\exp\left[i\left\{\omega t - \frac{2\pi}{\lambda}(n_0 \sin\vartheta_0 x + \xi z)\right\}\right] \quad (16.30)$$

Here ξ and ζ are both positive. The direction of propagation of phase of the wave is given by the coefficients $n_0\sin\vartheta_0$ and ξ while the increase in amplitude of the wave is governed by ζ and is purely along the *z*-direction. Such a wave where planes of constant amplitude and constant phase are no longer parallel is known as inhomogeneous. ξ is small beyond critical, and the wave skims close to the interface at an angle of $\arctan[\xi/(n_0\sin\vartheta_0)]$. The angle is smaller with smaller gain. Since it is an infinite plane wave, it can travel enormous distances in the presence of small gain. The propagation angle effect compensates the gain effect, and so we have an increasing exponential into the emergent medium. For zero gain and no absorption, the wave becomes parallel to the interface, but for an absorbing emergent medium, it again is inhomogeneous and inclined to the surface but this time with a

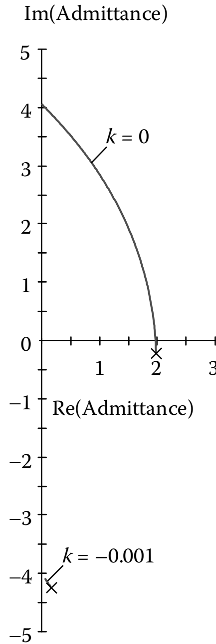

FIGURE 16.29
The *upper part* of the diagram shows the locus of a metal layer (gold in this case) exhibiting a typical surface plasmon resonance. The metal locus starts at the imaginary axis and moves round to the admittance of the incident medium, or close to it. However, when gain is present in the emergent medium, the starting admittance for the metal locus is now in the fourth quadrant (*lower part* of the diagram) and the metal locus simply moves to a termination point that tends to be that of the metal admittance corresponding to high reflectance.

decreasing exponential into the emergent medium. The phase jump and the switch in admittance quadrant can thus be readily understood.

Little seems to have been published on this effect, but the gain-induced phase jump (using a different convention) has been described by A. E. Siegman [27] including a proposed experiment to detect it. Then Brudny [28] helps with a discussion of evanescent tunneling.

There are few phenomena in optics that would exhibit such a major effect in response to such a small stimulus. A gain of 10^{-20} at 1000 nm represents a signal increase of 1 dB in a distance that is roughly 5000 times around the earth. Yet under certain circumstances, this small, virtually immeasurable, effect can produce changes in reflectance of almost 100%.

16.5 Photonic Crystals

Recently, we have started to see the term *photonic crystal* appearing in the optical thin-film literature. The term was first coined by Yablonovitch and

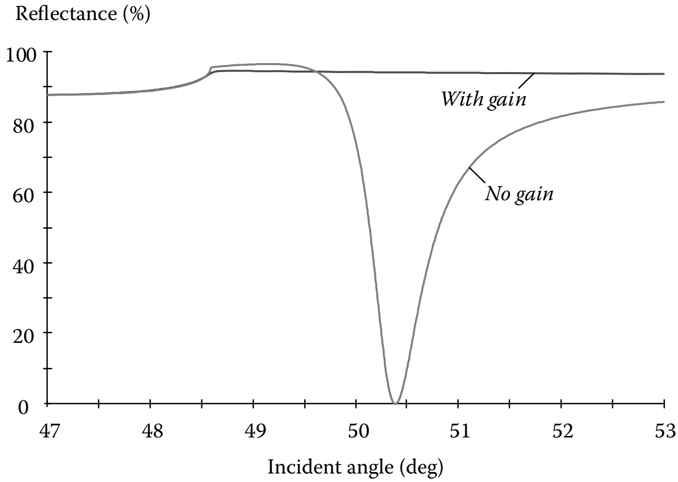

FIGURE 16.30
As soon as gain is introduced into the emergent medium, the surface plasmon resonance collapses and the reflectance rises close to that corresponding to the metal. Below the critical angle, the two curves are virtually indistinguishable. The phase behavior also shows a large jump that accompanies even the slightest gain. Below the critical angle there is virtually no difference between gain, loss, and lossless. The behavior changes abruptly as soon as the critical angle is exceeded.

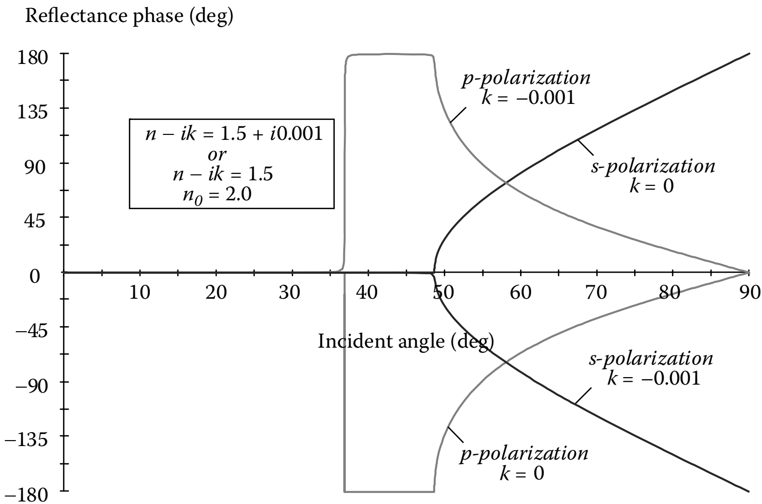

FIGURE 16.31
The phase shift on reflection with and without gain shows the very large jump in phase that occurs beyond the critical angle. (See color insert following page 398.)

more information will be found elsewhere [29,30]. This section attempts to explain, from the point of view of optical coating practitioners, the concept of photonic crystal and its application to optical coatings.

16.5.1 What Is a Photonic Crystal?

The band structure associated with electrons in crystals is a consequence of their wave nature. The electron wavelength is of the same order as the lattice spacing and the consequence is an interference phenomenon that is related to the electron wavelengths and hence their energies. The principal effect is a forbidden energy zone, called the *band gap*, between the energy possessed by bound valence electrons and free electrons, and this gap has enormous influence on the optical properties of the crystal. For example, an interaction between an optical photon and a bound electron is not possible if the electron would acquire energy that would place it in the forbidden zone. In such a case, the photon would simply be transmitted by the crystal. If the photon were to have higher energy, sufficient to shift the electron energy into the allowed band beyond the band gap, the conduction band, then it would be absorbed. This explains the high infrared transmittance and high visible absorptance of the semiconductors. The light, however, has a very large wavelength compared with the lattice spacing and so the lattice has no direct effect. The interaction with the light is indirect. The lattice influences the electrons and the electrons then affect the photons. All of this involves three dimensions, and it is normal to assume that the crystal medium is infinite in extent.

For the lattice directly to affect the photons, its spacing should be comparable with the wavelength of light. Thus, the scale has to be several orders of magnitude greater than that of a crystal. We are led to the idea of a regular three-dimensional assembly of blocks of one refractive index in a matrix of a different one with spacing chosen to induce interference effects in light propagating through it. As we would expect, such an assembly exhibits a pattern of regions where propagation is forbidden and regions where it is permitted. By analogy with normal crystals and their electronic properties, this much larger structure is called a *photonic crystal* and the forbidden propagation regions are *photonic band gaps*.

There are two major problems associated with three-dimensional photonic crystals. The first is the calculation of the properties, and the second, fabrication. Both problems can be eased by reducing the number of dimensions.

16.5.2 Two-Dimensional Photonic Crystals

Two-dimensional photonic crystals can be constructed by the pulling process used for the construction of optical fibers. Here the matrix is the normal dielectric glass material used for the fiber while the scattering features are cylindrical holes running parallel to the axis. This can effectively convert

into a fiber by removing the central hole so that the light propagates along its path and is contained by the reflection from the surrounding photonic crystal structure. Since the process effectively removes an "atom" from the lattice, this absence of the hole is called a *defect* even though it is an intentional feature of the structure. Defect is used in this sense frequently in photonic crystal terminology.

16.5.3 One-Dimensional Photonic Crystals

A reduction in the number of dimensions to one represents a considerable decrease in complexity and allows rapid development of photonic crystal theory. A one-dimensional photonic crystal is a multilayer optical coating under a different name. Unfortunately, this appears to have been not completely understood in the early photonic crystal studies. Also the language, and the approach adopted, owe much to solid-state theory. The problems and their proposed solutions are generally described in this different language. Adding confusion is that many of the quite fundamental results in traditional thin-film theory were developed some time ago. The flood of recent literature is such that older papers are less likely to be recognized. As a result, earlier one-dimensional photonic crystal publications would sometimes repeat results already well known and understood in the field of optical coatings. More recently, the close links between optical coatings and photonic crystals have become recognized. In fact, Yablonovitch, the originator, has recommended reserving the term *photonic crystal* for the two- and three-dimensional structures, which are truly different from optical coatings [30]. Unfortunately, the term is still being used for one-dimensional structures, and an accompanying side effect is that some developments that are of more importance to the thin-film community are nevertheless presented as developments in photonic crystals. This section is an attempt to bridge the gap.

A term that is often used is *photonic band gap*, with the acronym PBG. In one dimension, a photonic band gap is simply a high reflectance zone. We know that any repeated dielectric structure will exhibit a performance in terms of wavelength that will consist of well-defined reflecting regions where the reflectance simply rises steadily as a function of the number of repeats of the structure and regions where the transmittance is high but where there is ripple oscillating between two well-defined envelopes. As the number of repeats increases, the density of the ripple oscillations increases but the ripple continues to follow exactly the same envelopes. The high reflectance regions are the photonic band gaps, and the coating is known as a *photonic band gap structure.*

One of the early assumptions about the one-dimensional photonic crystal was that it would be completely impossible for it to support a forbidden gap over a range of angles from zero to 90° or, in optical coating terms, that the reflectance could remain high from normal incidence to an incidence of 90°.

No good proof of this assumption appears to exist, so it is difficult to be certain of its origin. Photonic crystal theory, by analogy with solid-state crystal theory, tends to treat infinite assemblies. It is natural for a photonic crystal theorist, therefore, to be thinking in terms of propagation within the crystal, whereas the thin-film theorist is well aware of restrictions on the number of layers and of the presence of an incident and emergent medium. If propagation is visualized as within the crystal, then it is clear that propagation laterally would be along the layers and not across them and the resistance to propagation would disappear. Also, it was recognized that there would be a particular propagation direction that would correspond to the Brewster condition between the two materials of the crystal and this would mean a collapse of the band gap, or reflecting zone, for *p*-polarized light. The fact that it is possible, when the incident medium is air and there is sufficient contrast between the high index and low index of the materials, to construct a reflector that, for a limited range of wavelengths, can exhibit high reflectance for both *p*- and *s*-polarizations over all angles of incidence from zero to 90° came, therefore, as a surprise to the photonic crystal community. The effect was called either the *omnidirectional reflector* [31] or, sometimes, the *perfect mirror.*

A quarter-wave stack is the basic dielectric reflector. As the multilayer is tilted to greater angles of incidence, the characteristic moves to a shorter wavelength. But some wavelengths remain within the shifted high-reflectance zone. An omnidirectional mirror is one where there is at least one wavelength that remains within the high reflectance zone right up to grazing incidence. To construct such a reflector, we know that we should do two things. We should make the high-reflectance zone as wide as possible and move as little as possible with changing incidence. To make the zone wide, we choose two materials with very different refractive indices, and to minimize the high-reflectance zone movement, we give one of the materials a maximum refractive index. One other thing that we must do is to use sufficient layers to realize the high reflectance over the whole range.

The limits of the high reflectance zone of a repeated two-layer structure are given by the expression

$$\cos\delta_A \cos\delta_B - \frac{1}{2}\left(\frac{y_B}{y_A} + \frac{y_A}{y_B}\right)\sin\delta_A \sin\delta_B = \pm 1 \tag{16.31}$$

where the quantities have their usual meaning. At normal incidence and for a quarter-wave stack, where $2\delta_A$ and δ_B are equal, the expression is easily inverted to give the high reflectance zone edges and width. At oblique incidence, it is more complicated and not analytically friendly. But it is not difficult to arrange a numerical method on a computer, and once we have the calculation programmed we can readily and almost painlessly calculate any

particular case. Here, we have chosen to use materials of indices 1.45 and 2.5 that are typical of the visible and near infrared regions.

The high-reflectance zone edges could be plotted against ϑ_0, the angle of incidence in the incident medium. But a much more convenient quantity is $n_0\sin\vartheta_0$ because this is the basis for Snell's law and makes the diagram much more general. Also, we can make $n_0\sin\vartheta_0$ negative for p-polarization [31], which has no effect on the results but makes the plots easier to read. Figure 16.32 shows the edges of the high reflectance zone for the first three orders. At normal incidence, the orders at $g = 2.0$ and $g = 4$ are missing because all the layers are absentees. However, as the layers are detuned by tilting, a reflectance zone appears. This is the well-known *half-wave hole* phenomenon that is a major problem in shortwave-pass filters. The Brewster angle between the film materials is to the left where the p-reflectance zone boundaries cross.

The range of $n_0\sin\vartheta_0$ for an incident medium of air runs from zero to unity and so, on the figure, if we include both p- and s-polarizations, it runs from –1.0 to +1.0. It is fairly easy to see that in first order the reflectance will stay within the high reflectance zone for values of g from 1.1012 to 1.1713. This is a wavelength range of 854 to 908 nm for a reference wavelength of 1000 nm. Figure 16.33 shows the performance of a 31-layer structure, Air | $(0.5H\ L\ 0.5H)^{15}$ | Glass, with reference wavelength 1000 nm and calculated for normal incidence (black) and for p-polarization at 85° incidence (red). The reflectance clearly remains high over the 854 nm to 908 nm region. The curves for s-polarization (not shown) are wider. Between 85° and grazing incidence, 90°, the reflectance simply rises everywhere as is normal at grazing incidence.

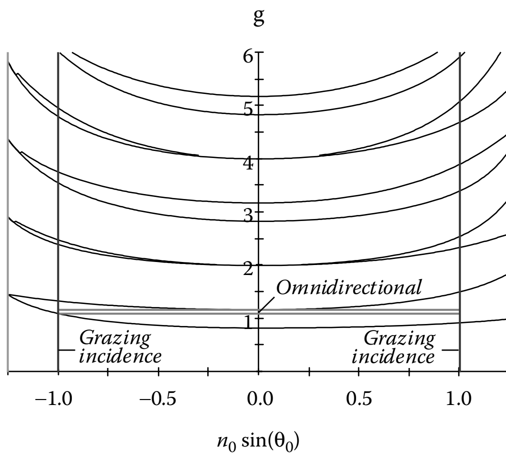

FIGURE 16.32
The limits of the high reflectance regions plotted in terms of g against $n_0 sin\vartheta_0$. The right half of the diagram shows results for s-polarization and the left for p-polarization. The inner vertical lines mark grazing incidence in air. The materials have indices of 1.45 and 2.5. The outer line on the extreme left marks the Brewster angle between the layer materials.

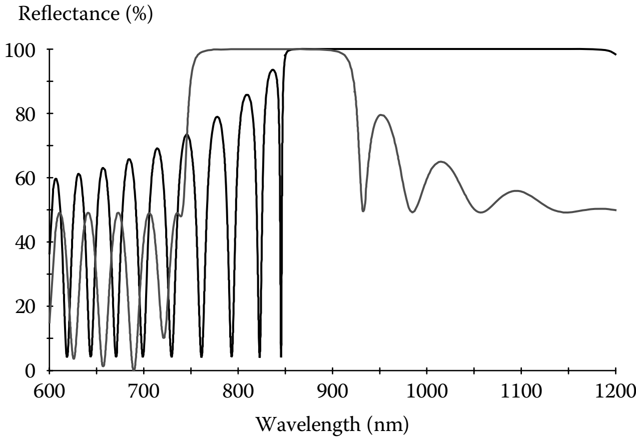

FIGURE 16.33
The reflectance of a 31-layer structure, Air | 0.5*H L* 0.5*H* | Glass with indices *H*: 2.5, *L*: 1.45, and Glass 1.52. *Black curve*, normal incidence, *red*, *p*-polarization at 85°. The reflectance clearly remains high over the region 854 nm to 908 nm.

In the study of electrons in solids, much importance is attached to diagrams of energy against momentum. If the *x*-*z* plane is the plane of incidence with *z* normal and *x* parallel to the surface, then the complete phase factor of a wave propagating obliquely in the plane of incidence is

$$\exp[i\{\omega t-(\kappa_x x+\kappa_z z)\}] \tag{16.32}$$

where ω, the angular frequency, is analogous to energy and κ, the wave number, to momentum. In thin-film optics, it is the *z*-component that interests us and we ignore the *x*-component. Here, however, we choose the *x*-component. κ_x can be written as

$$\kappa_x=\frac{2\pi n_0\sin\vartheta_0}{\lambda}=\frac{2\pi}{\lambda_0}\cdot g\cdot n_0\sin\vartheta_0 \tag{16.33}$$

and ω as

$$\omega=\frac{2\pi c}{\lambda}=\frac{2\pi c}{\lambda_0}\cdot g \tag{16.34}$$

where *c* is the free space velocity of light. We can normalize the expressions by removing the constant factors $2\pi/\lambda_0$ and $2\pi c/\lambda_0$ and this gives us a plot of g against $g\cdot n_0\sin\vartheta_0$, which is the same as the curves of Figure 16.32 but with the horizontal scale multiplied by g. Vertical lines of constant $n_0\sin\vartheta_0$ now become lines emanating from the origin with slope $1/n_0\sin\vartheta_0$, sometimes called *light lines*. If n_0 varies with frequency, that is, if the incident medium

is dispersive, then the lines will become curves. Figure 16.34 shows the new style. Light lines at grazing incidence for air incident medium are shown as two tilted straight lines passing through the origin. A similar plot is given by Fink [31]. Here we have used parameters more familiar to the thin-film community.

The photonic band gap structure can have what is termed a *defect.* The defect consists of extra or missing material. The commonest form of defect is a missing quarter-wave layer in a quarter-wave stack. The result is a half-wave layer surrounded by reflectors, in other words, a single-cavity coating. If the structure around the defect is symmetrical, then the performance of the device exhibits a narrow transmission band, a single-cavity filter. If the structure is not symmetrical, then the result will depend on the degree of asymmetry. In the case where the asymmetry is pronounced, we have a Gire-Tournois interferometer [14]—that is, a device exhibiting reflectance with a resonant group delay. Structures with multiple defects become multiple-cavity filters, or multiple-peak filters, depending on the details of the structure.

Certain other terms associated with electron behavior in crystals are sometimes used to describe optical behavior of thin-film structures. *Bloch waves* is a term used in the band structure of solids. In optics, its meaning is associated with the equivalent properties of the multilayer. In particular, the dispersion relation

$$\cos(K\Lambda) = \cos\left(\frac{\omega n_1 d_1}{c}\right)\cos\left(\frac{\omega n_2 d_2}{c}\right) - \frac{1}{2}\left(\frac{n_2}{n_1} + \frac{n_1}{n_2}\right)\sin\left(\frac{\omega n_1 d_1}{c}\right)\sin\left(\frac{\omega n_2 d_2}{c}\right) \tag{16.35}$$

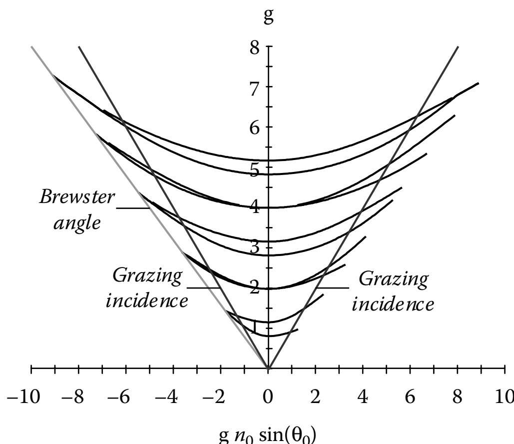

FIGURE 16.34
The band limits plotted in the style of energy against momentum.

where $\Lambda = d_1 + d_2$ can be identified as the expression for the equivalent phase thickness. K is known as the *Bloch wave number*. The forbidden bands or the band gap are those regions where K becomes imaginary.

Quantum tunneling is another term associated with photonic band gap structures. Quantum tunneling is essentially another term for the effects predicted by induced transmission theory.

Although the one-dimensional photonic crystal is, strictly, a multilayer optical coating, nevertheless the expression of its properties from a different point of view can help to bring a greater depth of understanding to the field.

References

1. Southwell W H 1998 *Rugate filter structures* Rockwell Science Center Private Communication
2. Epstein L I 1952 The design of optical filters *Journal of the Optical Society of America* 42 806–810
3. Epstein L I 1955 Improvements in heat reflecting filters *Journal of the Optical Society of America* 45 360–362
4. Southwell W H 1985 Coating design using very thin high- and low-index layers *Applied Optics* 24 457–460
5. Bovard B G 1993 Rugate filter theory: an overview *Applied Optics* 32 5427–5442
6. Saleh B E A and Teich M C 1991 *Fundamentals of Photonics* (New York: John Wiley and Sons Inc)
7. Yariv A and Yeh P 1984 *Optical Waves in Crystals* (New York: John Wiley & Sons)
8. Ferencz K and Szipöcs R 1993 Recent developments of laser optical coatings in Hungary *Optical Engineering* 32 2525–2538
9. Stingl A, Spielmann C, Krausz F, and Szipöcs R 1994 Generation of 11-fs pulses from a Ti:sapphire laser without the use of prisms *Optics Letters* 19 204–206
10. Szipöcs R, Ferencz K, Spielmann C, and Krausz F 1994 Chirped multilayer coatings for broadband dispersion control in femtosecond lasers *Optics Letters* 19 201–203
11. Szipöcs R and Krausz F 1998 *Dispersive dielectric mirror* US Patent 5,734,503
12. Schott 1992 *Schott Optical Glass* (Duryea, PA: Schott Glass Technologies Inc)
13. Szipöcs R and Köházi-Kis A 1997 Theory and design of chirped dielectric laser mirrors *Applied Physics B* 65 115–135
14. Gires F and Tournois P 1964 Interféromètre utilisable pour la compression d'impulsions lumineuses modulées en fréquence *Contes Rendus de l'Academie de Science* 258 6112–6115
15. Kuhl J and Heppner J 1986 Compression of femtosecond optical pulses with dielectric multilayer interferometers *IEEE Transactions on Quantum Electronics* QE-22 182–185
16. Jablonski M, Takushima Y, and Kikuchi K 2001 The realization of all-pass filters for third-order dispersion compensation in ultrafast optical fiber transmission systems *Journal of Lightwave Technology* 19 1194–1205

17. Press W H, Flannery B P, Teukolsky S A, and Vetterling W T 1986 *Numerical recipes. The art of scientific computing* ed 1 (Cambridge/New York: Cambridge University Press)
18. Tang J F and Zheng Q 1982 Automatic design of optical thin-film systems: merit function and numerical optimization method *Journal of the Optical Society of America* 72 1522–1528
19. Aguilera J A, Aguilera J, Baumeister P, Bloom A, Coursen D, Dobrowolski J A, Goldstein F T, Gustafson D E, and Kemp R A 1988 Antireflection coatings for germanium IR optics: a comparison of numerical design methods *Applied Optics* 27 2832–2840
20. Dobrowolski J A and Kemp R A 1990 Refinement of optical multilayer systems with different optimization procedures *Applied Optics* 29 2876–2893
21. Dobrowolski J A 1965 Completely automatic synthesis of optical thin film systems *Applied Optics* 4 937–946
22. Furman S A and Tikhonravov A V 1992 *Basics of Optics of Multilayer Systems* ed First (Gif-sur-Yvette: Editions Frontières)
23. Thelen A 1998 *Computer aided design*, in *Optical Interference Coatings* (Washington, DC: Optical Society of America) 268–270
24. Macleod H A 1996 Recent trends in optical thin films *Review of Laser Engineering* 24 3–10
25. Macleod A and Clark C 2006 *The strange case of the disappearing plasmon resonance* in *7th Symposium of European Vacuum Coaters Anzio, Italy* Romana Film Sottili 1–13
26. Macleod H A 1995 *Antireflection coatings on absorbing substrates* in *38th Annual Technical Conference Chicago* Society of Vacuum Coaters 172–175
27. The effect is described by A E Siegman in a slide show that can be downloaded at www.stanford.edu/~siegman/optics_with_gain.pdf
28. Brudny V L and Mochàn W L 2001 On the apparent superluminality of evanescent waves *Optics Express* 9 561–566
29. Yablonovitch E 1993 Photonic band-gap structures *Journal of the Optical Society of America, B* 10 283–297
30. Yablonovitch E 2007 Photonic crystals: what's in a name? *Optics and Photonics News* (March) 12–13
31. Fink Y, Winn J N, Fan S, Chen C, Michel J, Joannopolous J D, and Thomas E L 1998 A dielectric omnidirectional reflector *Science* 282 1679–1682

17

Characteristics of Thin-Film Dielectric Materials

This list gives some details of the commoner thin-film dielectric materials. It is not a definitive list but is intended to show the wide range of available materials. The metals exhibit enormous dispersion and so an abbreviated table of values is of little use. For extended tables of the optical constants of metals, consult other work [1–4]. Surveys of many thin-film materials are given by Ritter [5,6] and by Palik [2–4]. For a fuller account of the fluorides of the rare earths, consult Lingg [7].

In most cases, the materials in the table can be deposited by many different processes. Where thermal evaporation is possible, it is the main process listed. Many of the materials, with the principal exception of the fluorides, can be sputtered in their dielectric form by either radiofrequency sputtering or neutral ion-beam sputtering. A few materials, the nitrides especially, are not capable of evaporation or reactive evaporation and require an energetic process such as ion-assisted deposition.

The optical properties of thin films are very dependent on deposition conditions and other factors. The values quoted should be interpreted simply as values that were reported at some time and not as necessarily intrinsic and repeatable properties of the materials.

Materials	Deposition technique	Refractive index		Region of transparency	Remarks	References
Aluminium oxide (Al_2O_3)	E-beam	1.62 at 0.6 μm 1.59 at 1.6 μm 1.62 at 0.6 μm 1.59 at 1.6 μm	T_s = 300 °C T_s = 40 °C		Can also be produced by anodic oxidation of Al in ammonium tartrate solution [8]	[9]
Aluminium oxynitride (AlO_xN_y)	E-beam evaporation of Al with nitrogen ion assist and oxygen background	1.71–1.93 at 350 nm 1.65–1.83 at 550 nm		<300 nm–6.5 μm	Index varies continuously as function of composition.	[10,11]
Antimony trioxide (Sb_2O_3)	Molybdenum boat	2.20 at 366 nm 2.04 at 546 nm		300 nm–1 μm	Important to avoid overheating otherwise decomposes	[12]
Antimony sulfide (Sb_2S_3)		3.0 at 589 nm		500 nm–10 μm	Brief note [13] p. 189	[14,15]
Beryllium oxide (BeO)	Tantalum boat. Reactive evaporation of Be metal in activated oxygen.	1.82 at 193 nm 1.72 at 550 nm		190 nm–infrared	Highly toxic	[16]
Bismuth oxide (Bi_2O_3)	E-beam [17]. Also reactive sputtering of bismuth in oxygen [18]	2.7 at 600 nm 2.2 at 9 μm 2.45 at 550 nm	(E-beam) (Sputter)	<550 nm–12 μm	Good infrared material but less abrasion resistant than other oxides [17]	[17,18]
Bismuth trifluoride (BiF_3)	Graphite Knudsen cell	1.74 at 1 μm 1.65 at 10 μm		260 nm–20 μm		[19]
Cadmium sulfide (CdS)	Quartz crucible with spiral filament in contact with charge	2.6 at 600 nm 2.27 at 7 μm		600 nm–7 μm	Avoid overheating. Filament temperature must be 1025 °C	[14,20]
Cadmium telluride (CdTe)	Molybdenum boat	3.05 in near IR				[21] (brief)

Calcium fluoride (CaF_2)	Molybdenum or tantalum boat. E-beam [17]	1.23–1.26 at 546 nm 1.40 at 600 nm 1.32 at 9 µm	(porous) (E-beam)	150 nm–12 µm		[14,17,21,22]
Ceric oxide (CeO_2)	Tungsten boat	2.2 at 550 nm 2.18 at 550 nm. T_s = 50 °C 2.42 at 550 nm. T_s = 350 °C 2.2 in near IR		400 nm–16 µm	Tends to form inhomogeneous layers. Suffers from moisture adsorption.	[23–26]
Cerous fluoride (CeF_3)	Tungsten boat. E-beam [17]	1.63 at 550 nm 1.59 at 2 µm 1.57 at 9 µm (E-beam)		300 nm–12 µm	Hot substrate. Crazes on cold substrate [23]. High tensile stress	[17,21,23,24, 27]
Chiolite ($5NaF \cdot 3AlF_3$)	Howitzer or tantalum boat				Similar to cryolite	[21]
Chromium oxide (Cr_2O_3)	E-beam	2.242 at 700 nm 2.1 at 8 µm		<600 nm–8 µm		[17]
Cryolite (Na_3AlF_6)	Howitzer or tantalum boat	1.35 at 550 nm		<200 nm–14 µm	Slightly hygroscopic. Soft, easily damaged	[14,21–23, 28,29]
Gadolinium fluoride (GdF_3)	E-beam	1.55 at 400 nm		140 nm–>12 µm		[7]
Germanium (Ge)	E-beam or graphite boat	4.25 in IR (usually slightly higher than bulk value)		1.7–100 µm	Absorption band centered at ~25 µm	[21,23]
Hafnium dioxide (HfO_2)	E-beam	2.088 at 350 nm 2.00 at 500 nm 1.88 at 8 µm		220 nm–12 µm		[17,24,30,31]
Hafnium fluoride (HfF_4)	E-beam	1.57 at 600 nm 1.46 at 10 µm		<600 nm–12 µm		[17]

Materials	Deposition technique	Refractive index	Region of transparency	Remarks	References
Lanthanum fluoride (LaF_3)	Tungsten boat. E-beam [17]	1.59 at 550 nm 1.57 at 2 μm 1.52 at 9 μm (E-beam)	200 nm–12 μm	Heated substrate	[17,23,24,27, 32,33]
Lanthanum oxide (La_2O_3)	Tungsten boat	1.95 at 550 nm 1.86 at 2 μm	350 nm–>2 μm	Hot substrate (300 °C)	[23,24,27]
Lead chloride ($PbCl_2$)	Platinum or molybdenum boat	2.3 at 550 nm 2.0 at 10 μm	300 nm–>14 μm		[21,34]
Lead fluoride (PbF_2)	Platinum boat. E-beam [17]	1.75 at 550 nm 1.70 at 1 μm 1.3 at 10 μm (E-beam)	240 nm–>20 μm		[17,21,23,35, 36]
Lead telluride (PbTe)	Tantalum boat	5.5 in IR	3.4 μm–>30 μm	Avoid overheating. Hot substrate (see text)	[37–39]
Lithium fluoride (LiF)	Tantalum boat	1.36 to 1.37 at 546 nm	110 nm–7 μm		[14,40]
Lutetium fluoride (LuF_3)	E-beam	1.51 at 400 nm	140 nm–12 μm		[7]
Magnesium fluoride (MgF_2)	Tantalum boat	1.38 at 550 nm 1.35 at 2 μm	210 nm–10 μm	Films on heated substrates much more rugged. High tensile stress.	[14,21,22,24, 30,41–43]
Magnesium oxide (MgO)	E-beam	1.7 at 550 nm. T_s = 50 °C 1.74 at 550 nm. T_s = 300 °C	210 nm–8 μm		[44]
Neodymium fluoride (NdF_3)	Tungsten boat. E-beam [17]	1.60 at 550 nm 1.58 at 2 μm 1.60 at 9 μm (E-beam)	220 nm–12 μm	Hot substrate 300 °C	[17,23,24,27]
Neodymium oxide (Nd_2O_3)	Tungsten boat	2.0 at 550 nm 1.95 at 2 μm	400 nm–>2 μm	Hot substrate 300 °C. Decomposes at high boat temperature	[23,27]

Praseodymium oxide (Pr_6O_{11})	Tungsten boat	1.92 at 500 nm 1.83 at 2 μm	400 nm–>2 μm	Hot substrate 300 °C	[27]
Samarium fluoride (SmF_3)	E-beam	1.56 at 400 nm	160 nm–>12 μm		[7]
Scandium oxide (Sc_2O_3)	E-beam	1.86 at 550 nm	350 nm–13 μm		[45]
Silicon (Si)	E-beam with water-cooled hearth. Sputtering.	3.5 in IR	1.1–14 μm		[23]
Silicon monoxide (SiO)	Tantalum boat or howitzer	2.0 at 550 nm 1.7 at 6 μm	500 nm–8 μm	Fast evaporation at low pressure	[21] (brief) [9,14,23, 30, 46]
Disilicon trioxide (Si_2O_3)	Tantalum boat or howitzer	1.52–1.55 at 550 nm	300 nm–8 μm		[9, 23, 47–52]
Silicon dioxide (SiO_2)	E-beam. Mixture in tungsten boat.	1.46 at 500 nm 1.445 at 1.6 μm	<200 nm–8 μm (in thin films)		[9,23,53,54]
Silicon nitride (Si_3N_4)	Low-voltage reactive ion plating	2.06 at 500 nm	320 nm–7 μm		[55]
Sodium fluoride (NaF)	Tantalum boat	1.34 in visible	<250 nm–14 μm		[14] (brief)
Strontium fluoride (SrF_2)	E-beam	1.46 at 600 nm 1.3 at 10 μm	<600 nm–>12 μm		[17]
Tantalum pentoxide (Ta_2O_5)	E-beam and sputtering	2.16 at 550 nm 1.95 at 8 μm	300 nm–10 μm		[17,24]

Materials	Deposition technique	Refractive index	Region of transparency	Remarks	References
Tellurium (Te)	Tantalum boat	4.9 at 6 μm	3.4 μm–20 μm		[21,23,56,57]
Titanium dioxide (TiO_2)	Reactive evaporation of TiO, Ti_2O_3 or Ti_3O_5 in O_2. E-beam reactive evaporation.	2.2–2.7 at 550 nm depending on structure	350 nm–12 μm	Can also be produced by subsequent oxidation of Ti film	[14,23,47,52, 53,58–63]
Thallous chloride (TlCl)	Tantalum boat	2.6 at 12 μm	Visible–>20 μm		[21,64]
Thorium oxide (ThO_2)	E-beam	1.8 at 550 nm 1.75 at 2 μm	250 nm–15 μm	Radioactive	[21,23,65–67]
Thorium fluoride (ThF_4)	Tantalum boat	1.52 at 400 nm 1.51 at 750 nm	200 nm–>15 μm	Radioactive. Note: Thorium oxyfluoride ($ThOF_2$) actually forms ThF_4 when evaporated.	[21,23,65–68]
Ytterbium fluoride (YbF_3)	E-beam	1.52 at 600 nm 1.48 at 10 μm	<600 nm–12 μm		[17]
Yttrium oxide (Y_2O_3)	E-beam	1.82 at 550 nm 1.69 at 9 μm	250 nm–12 μm		[17,24,30,69]
Zinc selenide (ZnSe)	Platinum or tantalum boat	2.58 at 633 nm	600 nm–>15 μm		[66]
Zinc sulfide (ZnS)	Tantalum boat or howitzer	2.35 at 550 nm 2.2 at 2.0 μm	380 nm–~25 μm		[14,21,23,26, 29,39,41,67]

Zirconium dioxide (ZrO_2)	E-beam	2.1 at 550 nm 2.05 at 9.0 μm	340 nm–12 μm		[17,24,46]
Substance H1[1*] (zirconia/titania)	Tungsten boat or E-beam	2.1 at 550 nm	360 nm–7 μm	Does not melt completely [70]	[70,71]
Substance H2* (mixed praseodymium and titanium oxides)	E-beam	2.1 at 550 nm	400–7 μm	Some weak absorption bands in visible [70]	[70]
Substance H4* (Lanthanum and titanium oxide)	E-beam with molybdenum liner	2.1 at 500 nm. T_s = 300 °C	360 nm–7 μm		[70]
Substance M1* (mixed praseodymium and aluminium oxides)	E-beam	1.71 at 500 nm. T_s = 300 °C	300 nm–9 μm		[70]

* Substance H1, Substance H2, Substance H4, and Substance M1 are members of the Patinal series of optical coating materials manufactured by E Merck, Darmstadt, Germany.

References

1. Hass G and Hadley L 1972 *Optical constants of metals*, in *American Institute of Physics Handbook* Gray D E Editor (New York/London: McGraw-Hill Book Company) 6.124–6.156
2. Palik E D, ed 1985 *Handbook of Optical Constants of Solids* (New York: Academic Press Inc)
3. Palik E D, ed 1991 *Handbook of Optical Constants of Solids II* (San Diego/London: Academic Press)
4. Palik E D, ed 1998 *Handbook of Optical Constants of Solids III* (San Diego/London: Academic Press)
5. Ritter E 1975 *Dielectric film materials for optical applications*, in *Physics of Thin films* Hass G, Francombe M H, and Hoffman R W Editors (New York/San Fransisco/London: Academic Press) 1–49
6. Ritter E 1976 Optical film materials and their applications *Applied Optics* **15** 2318–2327
7. Lingg L J 1990 *Lanthanide trifluoride thin films: structure, composition and optical properties* PhD Dissertation University of Arizona
8. Hass G 1949 On the preparation of hard oxide films with precisely controlled thickness on evaporated aluminum mirrors *Journal of the Optical Society of America* **39** 532–540
9. Cox J T, Hass G, and Ramsay J B 1964 Improved dielectric films for multilayer coatings and mirror protection *Journal de Physique* **25** 250–254
10. Hwangbo C K, Lingg L J, Lehan J P, Macleod H A, and Suits F 1989 Reactive ion-assisted deposition of aluminum oxynitride thin films *Applied Optics* **28** 2779–2784
11. Targove J D, Lingg L J, Lehan J P, Hwangbo C K, Macleod H A, Leavitt J A, and McIntyre L C, Jr 1987 *Preparation of aluminum nitride and oxynitride thin films by ion-assisted deposition* in *Materials Modification and Growth using Ion Beams Symposium Anaheim, CA, USA* Materials Research Society, Pittsburgh, PA, USA 311–316
12. Jenkins F A 1958 Extension du domaine spectral de pouvoir réflecteur élevé des couches multiples diélectriques *Journal de Physique et le Radium* **19** 301–306
13. Heavens O S, Ring J, and Smith S D 1957 Interference filters for the infra-red *Spectrochimica Acta* **10** 179–194
14. Heavens O S 1960 Optical properties of thin films *Reports on Progress in Physics* **23** 1–65
15. Billings B H and Jr M H 1947 The infra-red refractive index and dispersion of evaporated stibnite thin films *Journal of the Optical Society of America* **37** 119–121
16. Ebert J 1982 Activated reactive evaporation *Proceedings of the Society of Photo-Optical Instrumentation Engineers* **325** 29–38
17. Kruschwitz J D T and Pawlewicz W T 1997 Optical and durability properties of infrared transmitting thin films *Applied Optics* **36** 2157–2159
18. Holland L and Siddall G 1958 Heat-reflecting windows using gold and bismuth oxide films *British Journal of Applied Physics* **9** 359–361
19. Moravec T J, Skogman R A, and Bernal G E 1979 Optical properties of bismuth trifluoride thin films *Applied Optics* **18** 105–110

20. Hall J F and Ferguson W F C 1955 Optical properties of cadmium sulphide and zinc sulphide from 0.6 micron to 14 micron *Journal of the Optical Society of America* **45** 714–718
21. Ennos A E 1966 Stresses developed in optical film coatings *Applied Optics* **5** 51–61
22. Heavens O S and Smith S D 1957 Dielectric thin films *Journal of the Optical Society of America* **47** 469–472
23. Ritter E 1961 Gesichtspunkte bei der Stoffauswahl für dünne Schichten in der Optik *Zeitschrift für Angewandte Mathematische Physik* **12** 275–276
24. Smith D and Baumeister P W 1979 Refractive index of some oxide and fluoride coating materials *Applied Optics* **18** 111–115
25. Hass G, Ramsay J B, and Thun R 1958 Optical properties and structure of cerium dioxide films *Journal of the Optical Society of America* **48** 324–327
26. Cox J T and Hass G 1958 Antireflection coatings for germanium and silicon in the infrared *Journal of the Optical Society of America* **48** 677–680
27. Hass G, Ramsay J B, and Thun R 1959 Optical properties of various evaporated rare earth oxides and fluorides *Journal of the Optical Society of America* **49** 116–120
28. Pelletier E, Roche P, and Vidal B 1976 Détermination automatique des constantes optiques et de l'épaisseur de couches minces: application aux couches diélectriques *Nouvelle Revue d'Optique* **7** 353–362
29. Netterfield R P 1976 Refractive indices of zinc sulphide and cryolite in multilayer stacks *Applied Optics* **15** 1969–1973
30. Borgogno J P, Lazarides B, and Pelletier E 1982 Automatic determination of the optical constants of inhomogeneous thin films *Applied Optics* **21** 4020–4029
31. Baumeister P W and Arnon O 1977 Use of hafnium dioxide in mutilayer dielectric reflectors for the near uv *Applied Optics* **16** 439–444
32. Bourg A, Barbaroux N, and Bourg M 1965 Propriétés optiques et structure de couches minces de fluorure de lanthane *Optica Acta* 151–160
33. Targove J D, Lehan J P, Lingg L J, Macleod H A, Leavitt J A, and McIntyre L C 1987 Ion-assisted deposition of lanthanum fluoride thin films *Applied Optics* **26** 3733–3737
34. Penselin S and Steudel A 1955 Fabry-Perot-Interferometerverspiegelungen aus dielektrischen Vielfachschichten *Zeitschrift für Physik* **142** 21–41
35. Carl-Zeiss-Stiftung 1965 *Interference filters* UK Patent 994,638
36. Lès Z, Lès F, and Gabla L 1963 Semitransarent metallic-dielectric mirrors with low absorption coefficient in the ultra-violet region of the spectrum (3200-2400A) *Acta Physica Polonica* **23** 211–214
37. Smith S D and Seeley J S 1968 *Multilayer filters for the region 0.8 to 100 microns* Final Report on Contract AF61(052)-833 (Air Force Cambridge Research Laboratories)
38. Yen Y-H, Zhu L-X, Zhang W-D, Zhang F-S, and Wang S-Y 1984 Study of PbTe optical coatings *Applied Optics* **23** 3597–3601
39. Ritchie F S 1970 *Multilayer filters for the infrared region 10-100 microns* PhD Thesis University of Reading
40. Schulz L G 1949 The structure and growth of evaporation LiF and NaCl films on amorphous substrates *Journal of Chemical Physics* **17** 1153–1162
41. Hall J F Jr and Ferguson W F C 1955 Dispersion of zinc sulfide and magnesium fluoride films in the visible spectrum *Journal of the Optical Society of America* **45** 74–75

42. Wood O R, II, Craighead H G, Sweeney J E, and Maloney P J 1984 Vacuum ultraviolet loss in magnesium fluoride films *Applied Optics* **23** 3644–3649
43. Hall J F 1957 Optical properties of magnesium fluoride films in the ultraviolet *Journal of the Optical Society of America* **47** 662–665
44. Pulker H K 1979 Characterization of optical thin films *Applied Optics* **18** 1969–1977
45. Arndt D P, Azzam R M A, Bennett J M, Borgogno J P, Carniglia C K, Case W E, Dobrowolski J A, Arndt D P, Gibson U J, Hart T T, et al. 1984 Multiple determination of the optical constants of thin-film coating materials *Applied Optics* **23** 3571–3596
46. Hass G and Salzberg C D 1954 Optical properties of silicon monoxide in the wavelength region from 0.24 to 14.0 microns *Journal of the Optical Society of America* **44** 181–187
47. 1957 *Improvements in or relating to the manufacture of thin light transmitting layers* UK Patent 775,002
48. Ritter E 1962 Zür Kentnis des SiO und Si2O3-Phase in dünnen Schichten *Optica Acta* **9** 197–202
49. Okamoto E and Hishinuma Y 1965 Properties of evaporated thin films of Si2O3 *Trans 3rd Int Vac Congress* **2** 49–56
50. Bradford A P, Hass G, McFarland M, and Ritter E 1965 Effect of ultraviolet irradiation on the optical properties of silicon oxide films *Applied Optics* **4** 971–976
51. Bradford A P and Hass G 1963 Increasing the far-ultra-violet reflectance of silicon oxide protected aluminium mirrors by ultraviolet irradiation *Journal of the Optical Society of America* **53** 1096–1100
52. Auwärter M 1960 *Process for the manufacture of thin films* US Patent 2,920,002
53. Reichelt W 1965 Fortschritte in der Herstellung von Oxydschichten für optische und elektrische Zwecke *Transactions of the Third International Vacuum Congress* **2** 25–29
54. Libbey-Owens-Ford Glass Company 1947 *Method of coating with quartz by thermal evaporation* UK Patent 632,442
55. Bovard B B, Ramm J, Hora R, and Hanselmann F 1989 Silicon nitride thin films by low voltage reactive ion plating: optical properties and composition *Applied Optics* **28** 4436–4441
56. Moss T S 1952 Optical properties of tellurium in the infra-red *Proceedings of the Physical Society* **65** 62–66
57. Greenler R G 1955 Interferometry in the infrared *Journal of the Optical Society of America* **45** 788–791
58. Hass G 1952 Preparation, properties and optical applications of thin films of titanium dioxide *Vacuum* **2** 331–345
59. Brinsmaid D S, Keenan W J, Koch G J, and Parsons W F Eastman Kodak Co 1957 *Method of producing titanium dioxide coatings* US Patent 2,784,115
60. Balzers Patent und Lizenz Anstalt 1962 *Improvements in and relating to the oxidation and/or transparency of thin partly oxidic layers* UK Patent 895,879
61. Pulker H K, Paesold G, and Ritter E 1976 Refractive indices of TiO2 films produced by reactive evaporation of various titanium-oxide phases *Applied Optics* **15** 2986–2991
62. Heitmann W 1971 Reactive evaporation in ionized gases *Applied Optics* **10** 2414–2418

63. Chiao S-C, Bovard B G, and Macleod H A 1998 Repeatability of the composition of titanium oxide films produced by evaporation of Ti2O3 *Applied Optics* **37** 5284–5290
64. Perkin Elmer Corporation 1961 *Infrared filters* UK Patent 970,071
65. Heitmann W and Ritter E 1968 Production and properties of vacuum evaporated films of thorium fluoride *Applied Optics* **7** 307–309
66. Heitmann W 1966 Extrem hochreflektierende dielektrische Spiegelschichten mit Zincselenid *Zeitschrift für Angewandte Physik* **21** 503–508
67. Behrndt K H and Doughty D W 1966 Fabrication of multilayer dielectric films *Journal of Vacuum Science and Technology* **3** 264–272
68. Ledger A M and Bastien R C 1977 *Intrinsic and thermal stress modeling for thin-film multilayers* (The Perkin Elmer Corporation, Norwalk, Connecticut 06856)
69. Lubezky I, Ceren E, and Klein Z 1980 Silver mirrors protected with Yttria for the 0.5 to 14 μm region *Applied Optics* **19** 1895
70. Fritz M, Koenig F, Merck E, and Feiman S 1992 *New materials for production of optical coatings*, in *35th Annual Technical Conference Proceedings* (Albuquerque, New Mexico: Society of Vacuum Coaters) 143–147
71. Stetter F, Esselborn R, Harder N, Friz M, and Tolles P 1976 New materials for optical thin films *Applied Optics* **15** 2315–2317

Bibliography

A complete bibliography of primary references would stretch to an enormous length. This list is, therefore, primarily one of secondary references wherever possible. Primary references are given usually only where secondary references are difficult to obtain or do not exist.

Anders H 1965 *Dünne Schichten für die Optik (English translation: Thin Films in Optics, Focal Press, 1967)* (Stuttgart: Wissenschaftliche Verlagsgesellschaft mbH)

Bach H and Krause D eds 1997 *Thin Films on Glass* (Berlin/Heidelberg: Springer-Verlag)

Baumeister P W 2004 *Optical Coating Technology* (Bellingham, WA: SPIE Press)

Dobrowolski J A 1995 *Optical properties of films and coatings*, in *Handbook of Optics* Bass M, *et al.* Editors (New York: McGraw-Hill, Inc) 42.1–42.130

Flory F R ed 1995 *Thin Films for Optical Systems* (New York: Marcel Dekker Inc)

Frey H and Kienel G eds 1987 *Dünnschicht Technologie* (Düsseldorf: VDI-Verlag GmbH)

Furman S A and Tikhonravov A V 1992 *Basics of Optics of Multilayer Systems* (Gif-sur-Yvette: Editions Frontières)

Hartnagel H L, Dawar A L, Jain A K, and Jagadish C 1995 *Semiconducting Transparent Thin Films* (Bristol/Philadelphia: Institute of Physics Publishing)

Heavens O S 1955 *Optical Properties of Thin Solid Films* (London: Butterworths Scientific Publications)

Hodgkinson I J and Wu Q h 1997 *Birefringent Thin Films and Polarizing Elements* (Singapore: World Scientific Publishing Co Pte Ltd)

Holland L 1956 *Vacuum Deposition of Thin Films* (London: Chapman and Hall)

Hummel R E and Guenther K H eds 1995 *Thin Films for Optical Coatings* Handbook of Optical Properties (Boca Raton, FL: CRC Press)

Jacobson M R ed 1989 *Deposition of optical coatings* SPIE Milestone Series ed Thompson B J MS 6 (Bellingham, WA: SPIE)

Jacobson M R ed 1990 *Design of optical coatings* SPIE Milestone Series ed Thompson B J MS 26 (Bellingham, WA: SPIE)

Jacobson M R ed 1992 *Characterization of optical coatings* SPIE Milestone Series ed Thompson B J MS 63 (Bellingham, WA: SPIE)

Kaiser N and Pulker H K eds 2003 *Optical Interference Coatings* Optical Sciences ed Rhodes W T (Berlin/Heidelberg/New York: Springer-Verlag)

Knittl Z 1976 *Optics of Thin Films* (London: John Wiley and Sons)

Liddell H M 1981 *Computer-aided techniques for the design of multilayer filters* (Bristol: Adam Hilger Ltd)

Lissberger P H 1970 Optical applications of dielectric thin films *Reports of Progress in Physics* **33** 197–268

Perilloux B E 2002 *Thin Film Design: Modulated Thickness and Other Stopband Design Methods* (Bellingham: SPIE Optical Engineering Press)

Pulker H K 1999 *Coatings on Glass* ed 2nd (Amsterdam: Elsevier)

Rancourt J D 1987 *Optical Thin Films: Users' Handbook* (New York: Macmillan Publishing Company)
Thelen A 1988 *Design of Optical Interference Coatings* (New York: McGraw-Hill Book Company)
Vasicek A 1960 *Optics of Thin Films* (Amsterdam: North Holland)
Willey R R 2002 *Practical Design and Production of Optical Thin Films* ed 2nd (New York/Basel: Marcel Dekker Inc)